Advances in Fracture and Damage Mechanics VII

Edited by
H.S. Lee, I.S. Yoon, M.H. Aliabadi

TRANS TECH PUBLICATIONS

Advances in Fracture and Damage Mechanics VII

Advances in Fracture and Damage Mechanics VII

Selected, peer reviewed papers from 7th International Conference on Fracture and Damage Mechanics, FDM 2008, 9-11 September, 2008, Korea

Edited by

H.S. Lee, I.S. Yoon, M.H. Aliabadi

TRANS TECH PUBLICATIONS LTD

Switzerland • UK • USA

Copyright © 2008 Trans Tech Publications Ltd, Switzerland

All rights reserved. No part of the contents of this book may be reproduced or transmitted in any form or by any means without the written permission of the publisher.

Trans Tech Publications Ltd
Laubisrutistr. 24
CH-8712 Stafa-Zurich
Switzerland
http://www.ttp.net

Volumes 385-387 of
Key Engineering Materials
ISSN 1013-9826
Full text available online at *http://www.scientific.net*

Distributed *worldwide by*

Trans Tech Publications Ltd.
Laubisrutistr. 24
CH-8712 Stafa-Zurich
Switzerland

Fax: +41 (44) 922 10 33
e-mail: sales@ttp.net

and in the Americas by

Trans Tech Publications Inc.
PO Box 699, May Street
Enfield, NH 03748
USA

Phone: +1 (603) 632-7377
Fax: +1 (603) 632-5611
e-mail: sales-usa@ttp.net

Steering Committee

M.H. Aliabadi Imperial College, London
B. Abersek University of Maribor, Slovania
J. Alfaiate Instituto Superior Tecnico, Portugal
F.G. Buchholz Univ. Paderborn, Germany
J.K. Kim KAIST, Korea
S-I. Nishida Saga University, Japan
S.W. Shin Hanyang University, Korea
Q. Li Harbin Engineering University, China

Conference Organizing Committee

M. H. Aliabadi, Department of Aeronautics, Imperial College, London, UK
I.S. Yoon, Dept. of Civil Engineering , Induk Institute of Technology, Seoul, Korea
H.S. Lee, School of Architecture & Architectural Engineering, Hanyang University, Ansan, Korea

International Scientific Committee

B. Abersek, University of Maribor, Slovenia
M.M. Abdel Wahab, University of Surrey, UK
J. Alfaiate, Instituto Superior Tecnico, Portugal
R. Al-Khoury, Delft University of Technology, The Netherlands
A. Apicella Alenia, Italy
S. Baragetti, UniversitÃ degli Studi di Bergamo, Italy
Z.P. **Bazant,** Northwestern University, USA
F. Brennan, Cranfield University, UK
M. Boulfiza, Saskatchewan University, Canada
W. Brocks, GKSS Research Centre, Germany
I.Cerny SVUM , Czech Rep
G. Chai,. Sandvik Materials Tech, Sweden
C.S. Lee, University of Seoul, Korea
G. Dhondt, MTU Aero Engines, Germany
M. Doblare, University of Zaragoza, Spain
D.S. Song Sungkyunkwan University, Korea
D.J. Kim, Induk Institute of Technology, Korea
E.K. Kim, Seoul National University of Technology, Korea
P.E.J Flewitt, BNFL Magnox Generation, UK
T. Fujimoto, Kyushu Sangyo University, Japan
M. Guagliano, Politecnico di Milano, Italy
H. Hadavinia, Kingston University, UK
P. Horst, IFL, Braunschweig, Germany
J. Hole, Fraunhofer-Institut fuer Werkstoffmechanik, Germany
J. Hornikova, Brno University of Technology, Czech,Republic
W. Hui, Harbin engineering University, China
A. Ivankovic, University College Dublin, Ireland
J.J. Kim, Hanyang University, Korea

J.K. Kim, KAIST, Korea
J.S. Seol, Hyokwang Construction Co. Ltd, Korea
K.H. Lee, Andong National University, Korea
K.S. Lee, Chunnam National University, Korea
N. Kawagoishi, Kagoshima University, Japan
K.B. Park, Kangwon National University, Korea
M. Kotoul, Brno University of Technology, Czech Republic
E.A.B. Koenders, Delft University of Technology, The Netherlands
A.M. Korsunsky, Oxford University, UK
M.S. **Kumosa,** University of Denver, USA
M. Kuna, Technische UniversitÃ¤t Bergakademie Freiberg, Germany
K.D. Song Hanyang University, Korea
C. Leung, HKUST, Hong Kong
D. Leguillon, CNRS, France
L. Li Harbin Engineering University, China
Q.F. Li, Harbin Engineering University, China
Y. Liu, The University of Western Australia, Australia
K. Nikbin, Imperial College London, UK
L. Nobile, University of Bologna, Italy
T. Nykanen, Lappeenranta University of Technology , Finland
O.S. Lee InHa University, Incheon, Korea
C. Pappalettere, Politecnico di Bari, Italy
C. Park, Kangwon National University, Korea
J. Pastor, ESIGEC, University of Savoie, France
R. Piat, University of Karlsruhe, Germany
A. Saimoto, Nagasaki University, Japan
S.Y. Noh. Hanyang University, Korea
S.W. Jung Korea Institute of Construction Materials (KICM)
G. Savaidis, National Technical University of Athens, Greece
E. Schlangen, Delft University of Technology, The Netherlands
L.**J. Sluys,** Delft University of Technology, The Netherlands
A. Soprano, Second University of Napales, Italy
R. Souchet, Ecole Nationale Superieure de Mecanique et d'Aerotechnique, France
L. Susmel, University of Ferrara, Italy
H. Takuda, Kyoto University, Japan
D. Taylor, Trinity College Dublin, Ireland
V. Tvergaard, DTU, Denmark
H. Theilig, Univ. Appl. Sci. Zittau/Gorliz, Germany
J. Toribio, University of Salamanca, Spain
E. Viola, University of Bologna, Italy
Z.Q. Wang, Harbin Engineering University, China
S.Y. Yan, Harbin Engineering University, China
Y.S. Cho, Hanyang University, Korea
Y.S. Yoon, Korea University
Y. Zheng Harbin Engineering University, China
Ch. Zhang, Univ. Appl. Sci. Zittau, Germany
S.F. **Zhu,** Harbin Engineering University, China

Preface

This volume is a collection of edited papers presented at the 7th International Conference on Fracture and Damage Mechanics (FDM2008), held in COEX Convention Centre, Seoul, Korea, during 9-11 September 2008. Previous meetings were held in London, UK(1999), Milan, Italy (2001), Paderborn, Germany (2003), Mallorca, Spain (2005), Harbin, China (2006) and Madeira, Portugal (2007).

The conference which was attended by researchers from 22 countries served as a forum to promote and exchange latest theoretical, computation and experimental research works on fracture and damage mechanics as well as structural integrity and durability. Two special symposium on *Sustainable Technology of Structures including Architecture and Civil Engineering Fields and Diagnosis, Damage Evaluation, Rehabilitation, Repair, Strengthening, Durability Design technology of Structures* were organised by Prof. Lee, Han Seung.

Keynote lectures were presented by Prof. Sung-Woo, Shin *Director of Sustainable Building Research Center, Professor of Hanyang University and Vice president of Architectural Institute of Korea and* Prof. Erik Schlangen, *Delft University of Technology, The Netherlands.*

The FDM2008 covers a wide range of topics: Fracture Mechanics, Failure analysis, Corrosion, Creep, Non-linear problems, Dynamic Fracture, Residual Stress, Environmental effects, Crack Propagation, Repair Techniques, Composite, Ceramics, Polymers, Metallic and concrete materials, Probabilistic Aspects, Risk Analysis, Damage Tolerance, Fracture Control, Computer Modelling Methods (Finite Elements, Boundary Elements and Meshless), Microstructural and Multiscale Aspects.

The organisers would like to thanks the following institutions:

- Sustainable Building Research Center (SUSB), Hanyang University, Ansan, Korea
- Korea Sustainable Architecture Professional Education Center(SAPEC), Hanyang University, Seoul, Korea
- Harbin Engineering Univeristy, Harbin, China

for sponsoring the conference.

The Editors would like to thanks the members of the Steering Committee and International Scientific Committee for their help and support that were essential to the success of the conference

Editors
Lee, Han Seung, I.S Yoon and Ferri M.H Aliabadi

Table of Contents

Committees

Preface

A Consideration of Cleavage Crack Propagation in Fe_2Si Steel
F. Sorbello, P.E.J. Flewitt, A.G. Crocker and G.E. Smith 1

Fatigue Crack Growth Rate Analysis in a Titanium Alloy
A.M. Korsunsky, D. Dini and M.J. Walsh 5

A Criterion for Crack Kinking Out of an Interface
D. Leguillon and S. Murer 9

Geomatrically Nonlinear Analysis of Cracked Stiffened Curved Panels by DBEM
P.M. Baiz and M.H. Aliabadi 13

A Finite Element Analysis of Scarf Joint for Controlling the Triaxiality Function in Adhesive Bonding
I. Hilmy, M.M. Abdel Wahab, I.A. Ashcroft and A.D. Crocombe 17

A Study of the Dynamic Plane Strain Fracture Toughness of Concrete by SHPB
J. Qu and G.P. Zou 21

About the Effects of Residual Stress States Coming from Manufacturing Processes on the Behaviour of Riveted Joints
F. Caputo, G. Lamanna and A. Soprano 25

Failure Analysis of Diesel Engine Intake Valve
A. Göksenli and B. Eryürek 29

An Analysis of Aging Characteristics of Tilting Train under Accelerated Aging Environment
J.P. Nam, S.H. Yoon, Y.E. Hwang, H. Li and Q.F. Li 33

Analysis for Mechanical Properties of Spiral Accumulating Core Used for Permanent Magnet Motor
N. Noda, B. Zhang, K. Yonemaru, S. Higo and Y. Takamatu 37

Test Analysis for RC Beams Strengthened with Externally Bonded Prestressed CFRP Laminates
S.Q. Cui, J.S. Wang, Z.Z. Pei and Z. Liu 41

Analysis of Critical Damage of Thin Plate Subjected to Contact Explosions
S. Wang, J. Zhang and X.H. Shi 45

Assessment of Extrinsic Crack Tip Shielding in Austenitic Steel near Fatigue Threshold
J. Pokluda, Y. Kondo, K. Slámečka, P. Šandera and J. Horníková 49

Cavity Dynamic Formation and Bifurcation of the Rubber-Like Sphere
G.H. Wu, Y. Wang, L.Q. Tang and Y. Yang 53

Contact Fatigue Behaviour of PVD-Coated Spur Gears
S. Baragetti, A. Terranova and F. Tordini 57

Cement Loop Damage Mechanism in the Process of Repairing Casing
L.Q. Tang, S.Z. Sun, C.C. Wu and X.M. Yu 61

Computational Program for Non-Equilibrium Grain Boundary Segregation Kinetics
J. Wang, Q.F. Li and E.B. Liu 65

Crack Development in Concrete, Part 1: Fracture Experiments and CT-Scan Observations
E. Schlangen 69

Crack Development in Concrete, Part 2: Modelling of Fracture Process
E. Schlangen 73

The Rationale of Adhesive Postinstalled Method to Estimate the Concrete Strength
S.Q. Cui, J.S. Wang, X.W. Kong and H.W. Li 77

Cracking Cohesive Law Thermodynamically Equivalent to a Non-Local Damage Model
F. Cazes, A. Simatos, M. Coret, A. Combescure and A. Gravouil 81

Crushing Behaviour of CFRP Composite Structure
H. Ghasemnejad, H. Hadavinia and E. Lewis 85

Crack Spacing and the Flow Stress in NiTi Thin Films Deposited on Cu Substrate
Y.H. Li, F.L. Meng, C.S. Liu and Y.M. Wang 89

Crack Width of SRC Members Based on Fracture Mechanics
B. Wang, S.S. Zheng, M.Z. Wu, L. Li and L. Zeng 93

Damage Analysis of the SRHSHPC Frame Columns under Low Cyclic Reversed Horizontal Loading
S.S. Zheng, L. Zhang, B. Wang, L. Li and L. Zeng 97

Dynamic Growing Crack Tip Field in Visco-Elastic Compressible Material
Y. Yang, L.Q. Tang, Y. Wang and C. Feng 101

Dynamic Stress Intensity Problem of SH-Wave by Double Linear Cracks near a Circular Hole
H.L. Li, H. Li and Y. Yang 105

Effect of Supporting Conditions on the Fatigue Life of Shaft Based on Product Lifecycle Management
Y.T. Li, P. Ma and M. Song 109

Effects of Microstructure and Humidity on Fatigue Strength of Maraging Steel
M. Miyazono, N. Kawagoishi, Q.Y. Wang, E. Kondo and T. Nagano 113

Effects of Rim and Web Thickness on Gear Tooth Root, Rim and Web Stresses
G. Marunić 117

Electrochemical Behavior of Cu-Bearing CrMo Steel in H_2S Saturated Aqueous Brine Solution
Q.C. Tian, X.M. Dong and Q.A. Zhang 121

Numerical Investigation of Stress Singularities in Cracked Bimaterial Body
L. Náhlík, L. Šestáková and P. Hutař 125

Evaluation of Perforation Resistance of Magnesium Alloy by Hypervelocity Impact
R. Kubota, A. Shimamoto, D. Numata and K. Takayama 129

Fatigue Resistance Assessment of Slurry Coating Steel Substrate Compounds under Cyclic Loading
K.G. Anthymidis, C. David and D.N. Tsipas 133

Excavation Damage in Unsaturated Porous Media
C. Arson and B. Gatmiri 137

Experimental Investigations on the Effects of Thermal Residual Stresses on the Efficiency of Repaired Panels with Glass/Epoxy Composite Patch
H. Hosseini-Toudeshky, M. Shamboli and B. Mohammadi 141

Experimental Study on Seismic Damage Model of the SRHSHPC Composite Frame Columns
S.S. Zheng, L. Zhang, L. Li, B. Wang and M. Xie 145

Experimental Study on the Shear Behaviors of the SRHSHPC Composite Frame Columns
L. Zhang, S.S. Zheng, Q.N. Li, L. Li and B. Wang 149

Numerical Characterization and Validation of Vehicle Collisions
A. Grimaldi, A. Soprano and F. Caputo 153

Far Field Solution of SH-Wave Scattered by a Circular Cavity and a Mode III Crack in Half Space
B.T. Sun, P.L. Yan and Z.L. Yang 157

Fatigue Strength of Maraging Steel at Elevated Temperatures
T. Iwamoto, N. Kawagoishi, N. Yan, E. Kondo and K. Morino 161

Fatigue-Cumulative Damage Model of RC Crane Girders Strengthened with FRP Strips
S.S. Zheng, B. Wang, L. Li, L. Zhang and P.J. Hou 165

FEM Analysis for Sealing Performance of Hydraulic Pressure Brake Hose Caulking Portion
H. Kawahara, S. Yoshimura and N. Noda 169

Fitness-For-Service Assessment of the Pipelines with Localized Geometric Imperfections such as Buckles and Wrinkles
Z.M. Yang, S.B. Kumar and J.P. Tronskar 173

Fracture Behavior and Microstructure of Ti_3AlC_2 Ceramics Prepared by SHS/PHIP Method
Z.Y. Ren, C. Li and Q.F. Li 177

Theoretical Approach to Calculate Surface Chloride Content C_s of Submerged Concrete under Sea Water Laden Environment
I.S. Yoon 181

High Cycle Fatigue Properties and Failure Mode in Ni-Cr-Mo Steel Tempered at Low Temperature
Y. Mochizuki, M. Nakajima and T. Shimizu 185

Inference Engine and Explanation Mechanism in the Expert System of Fracture Mechanics Analysis for Component Design
S.F. Zhu, Q.F. Li and Z.H. Yu 189

Influence of Anisotropic Properties Upon Stress Intensity Factors under Biaxial Stress
A. Shimamoto, H. Ohkawara and J.H. Nam 193

Influence of Grain Size on Notch Sensitivities in Fatigue of Carbon Steel
T. Kanemaru, N. Kawagoishi, E. Kondo, Q.Y. Wang and Y. Ohzono 197

Investigation into Damage of Aluminum Multi-Wall Shield under Hypervelocity Projectiles Impact
G.S. Guan, B.J. Pang, R.Q. Chi and N.G. Cui 201

Failure of Polyurethane Foams under Different Loading Conditions
L. Marsavina, T. Sadowski, D.M. Constantinescu and R. Negru 205

Low-Cycle Fatigue Life Prediction by a New Critical-Plane Method
D. Jin, J.H. Wu and Y. Zhang 209

Mechanical Behaviors of Torsion Actuator of Shape Memory Alloy
B. Zhou, Z.Q. Wang, S.H. Yoon and G.P. Zou 213

A New Method to Calculate Dynamic Stress Intensity Factor for V-Notch in a Bi-Material Plate
Y.T. Li, Z.Y. Rui and C.F. Yan 217

Micromechanics Method to Evaluate Fatigue Life of Ni-Based Superalloys during Morphological Evolution
W.P. Wu, Y.F. Guo and Y.S. Wang 221

Effect of Recessing Length in Adhesive Layer on the Cleavage Joints
M. You, Z. Li, X.L. Zheng and Z.M. Yan 225

Non-Linear Step-by-Step Seismic Response and the Push-Over Analysis Comparison of a Reinforced Concrete of Ductile Frames 15 Level Building
J.A. Avila and E. Martínez 229

Numerical Simulation on Mixed Mode I-II Crack Propagation Process in Concrete
Q. Xu, W. Dong and Z.M. Wu 233

On the Evaluation of the Service Life of Shaft-Bushing Tribosystems at Low Speed
A. Calabrese, P. Morelli, A. Morri, G. Sambogna and F. Tarterini 237

On the Tensile and Compressive Fatigue Behaviour of Notched CFRP Laminates
G. Minak and P. Morelli 241

On the Growth, the Arrest and the Restart of a Crack during a Dynamic Brittle Fracture Experiment
D. Grégoire, H. Maigre and A. Combescure 245

Optimum Dimensions of Thin Walled Tube on the Mechanical Performance of Super Stud Bolt
Y. Xiao, M. Kuhara, N. Noda, K. Saito, M. Nagawa, A. Yumoto and A. Ogasawara 249

Postbuckling Analysis of Laminate with Delamination Based on the Improved Damage Model of 2-D
G. Yang, A.F. Zhang, H.B. Wang and P. Niu 253

Reliability Analysis of Structure System Considering Failure Modes of Strength, Fatigue and Buckling
W.G. An, H. An and Y.Y. Zhang 257

Reliability-Based Structural Optimization of Stochastic Structure Systems Considering Stability
X.C. Yan 261

Research on Performance of Reduced Web Connections in Steel Frame
Y.S. Shao, L. Jin, H.B. Liu and L.L. Xie 265

Risk-Based Research on Failure Mode of High-Arch Concrete Dam
Z.T. Chen 269

Scattering of SH-Waves and Dynamic Stress Intensity Factor by an Interacting Mode III Crack and a Lining Structure in Half Space
Z.L. Yang, M.J. Xu and B.T. Sun 273

Damage Evolution of Laminated Composites Using Continuum Damage Mechanics Incorporate with Interface Element
B. Mohammadi, H. Hosseini-Toudeshky and M.H. Sadr-Lahidjani 277

Simple Approach for Computing Chloride Diffusivity of (Non)Carbonated Concrete
I.S. Yoon 281

Statistical Analysis for Fatigue Life of Concrete
D.F. Zhao, W.W. Kong and X.R. Song 285

Studies on Expansion Properties in Concrete Containing Waste Glass, Silica Fume, Rice Husk Ash and Polypropylene Fibers
A. Sadrmomtazi, O. Alidoust and A.K. Haghi 289

On Fracture Mechanics Testing Technique Based on Compliance of Specimens
L.X. Cai, L. Jin and C. Bao 293

Crack Propagation Behavior of Asphalt Concrete; Part I: A Study into Influence of Different Materials
T. Xie, Z.Z. Jiang, Y.J. Qiu and B. Lan 297

Crack Propagation Behavior of Asphalt Concrete; Part II: A Study into Influence of Loading Rates
Z.Z. Jiang, T. Xie, Y.J. Qiu and B. Lan 301

Study on Restrained Expansive Deformation of Steel Fiber Reinforced Self-Stressing Concrete
H.N. He and C.K. Huang 305

Studying on the Synchronization of a Mechanical Centrifugal Flywheel Governor System
Y.D. Chu, J.G. Zhang, X.F. Li and Y.X. Chang 309

The Directly Damaged Identification Method of Frame Structures Based on Residual Force Vector
W.J. Zou and W.L. Qu 313

The Effect of the Singularity Induced by the Free Surface on Fatigue Crack Growth in Thin Structures
P. Hutař, L. Náhlík and Z. Knésl 317

The Elastic-Viscoplastic Field at the Mixed-Mode Crack-Tip under Compression and Shear
W.Y. Liang, Z.Q. Wang, B. Zhou and H.Q. Lv 321

The Influence of Stiffness Decay on Fatigue Reliability of Truss System
H. An, W.G. An and Y.Y. Zhang 325

The Mesoscopic Investigation on Moduli Prediction in Visco-Elastic Particle Reinforced Composites
X.Z. Ding and L.Q. Tang 329

Application of Mesh Free Method to Evaluation of Woven Fabric Composite Elastic Moduli
P.H. Wen and M.H. Aliabadi 333

Flexural Toughness and Crack Strength of Fiber Reinforced Cementitious Composite
A. Sadrmomtazi, F. Zerafatangiz, O. Alidoust and A.K. Haghi 337

Fatigue Crack Monitoring Using Image Correlation
P. López-Crespo, A. Shterenlikht, E.A. Patterson, J.R. Yates and P.J. Withers 341

Review of Experimental Models for Confirmation of Mathematical Models of Gears
B. Aberšek and J. Flašker 345

Flexural Performance of U-Shaped Precast Concrete Beams with Non-Contact Lapped Splice
S.S. Ha and S.H. Kim 349

Bending and Shear Strength of I-Slab with Polystyrene Forms
S.H. Kim, K.K. Lee, H.S. Lee, K.J. Lee and I.S. Kang 353

The Effect of Mechanical Stress on Barkhausen Noise from Heat-Treated Permalloy Plates
H. Nishihara, K. Kojima, S. Taniguchi, T. Sagae, M. Harada, T. Ogino, S. Matsumoto, H. Maeda, Y. Shindo and N. Ohtsuka 357

Real-Time Measurements on Crack-Tip Deformation Fields of LY12 Samples under Impact Tension
S.Y. Chen, T. Lan, X.M. Chen, W.G. Kong and G.Q. Ni 361

Stress Analysis of Composite Plates with Non-Circular Cutout
J. Rezaeepazhand and M. Jafari 365

Numerical and Experimental Analysis of Crack Closure
P. López-Crespo, D. Camas-Peña, A. González-Herrera, J.R. Yates, E.A. Patterson and J. Zapatero 369

Dynamic Damage Analysis of SRC Frame Structure under Earthquake Action
S.S. Zheng, B. Wang, L. Zhang, L. Li and W. Wang 373

Buckling of Perforated Plates Repaired with Composite Patches
J. Rezaeepazhand and H. Sabori 377

Experimental Study on Compressive Strength of Recycled Aggregate Concrete
W. Wang, H. Ling, X.N. Wang, T. Xia, D.Z. Wang and Y.B. Jiang 381

Corrosion Behavior and Mechanism of a Cu-Ni Alloy in Marine Environment
Q.F. Li, C.H. Li and Y.J. Qiao 385

Dynamic Anti-Plane Behaviors of a Semi-Infinite Piezoelectric Medium with a Circular Cavity and a Crack near the Surface
T.S. Song, D. Li, X.W. Wang and S.L. Dong 389

Blade Failure in Second Stage Turbine
K. Mohammadi and A.K. Haghi 393

Effect of Humidity on Fatigue Strength of Squeeze Cast Al Alloy
Y. Sofuku, N. Kawagoishi, M. Adachi, K. Okutani and Y. Maeda 397

Numerical Simulation and Experimental Investigation of the Failure of a Gas Turbine Compressor Blade
N. Nourbakshnia, S. Ziaei-Rad, A. Kermanpur and H. Sepehri Amin 401

Thermal Fatigue of Thermal Barrier Coatings by Atmospheric Plasma Spraying
H.Y. Qi, H.Q. Ma, X. Li, X.G. Yang and D.Q. Shi 405

A Comparison of Two Direct Methods of Generalized Stress Intensity Factor Calculations of Bi-Material Notches
J. Klusák, T. Profant and M. Kotoul 409

Welding Behavior Analysis of Stiffened Stainless Steel Structure
H. Li and H.L. Ren 413

A Numerical Analysis of Double Notch on Stress Distribution in Single Lap Aluminium Joints
X.L. Zheng, Z. Li, M. You, S. Yu and M.R. Zhao 417

Study on Enhancement of Mechanical Strength by Knotted Shape Memory Alloy Fiber in TiNi Fiber Composites
Y.L. Zhao, J. Li and M. Jin 421

Effect of Nitrogen on Creep Properties of 22Cr-25Ni Austenitic Heat-Resistant Steels
Y.U. Kim, W.S. Jung, Y.H. Chung and S.I. Kwun 425

Comparison of Impact Properties of Sn-9Zn and Sn-3Ag-0.5Cu Lead-Free Solder Ball Joints
I. Shohji, S. Shimoyama, H. Ishikawa and M. Kojima 429

Effect of Thermal Cycle Conditions on Thermal Fatigue Life of Chip Size Package Solder Joint
I. Shohji, T. Tohei, K. Yoshizawa, M. Nishimoto, Y. Ogawa and T. Kawano 433

Approximate Method for Predicting Inelastic Displacement of SDF Systems
M.S. Bae, J.B. Kim and S.W. Han 437

Mechanical Properties of Scandia Stabilised Zirconia with Alumina Addition
W. Araki, H. Norigoe and T. Adachi 441

Wood Fibre Reinforced Cement Matrix: A Micromechanical Based Approach
M.G. Sierra Beltran and E. Schlangen 445

Crack Size Dependency of Shear-Mode Fatigue Crack Threshold in Bearing Steel
S. Muramoto, H. Matsunaga, S. Moriyama and M. Endo 449

A Study of Crack Propagation in BCC Iron by Molecular Dynamics Method
Y. Gao, C. Lu, G. Michal and A.K. Tieu 453

Atomic Simulation of Effect of Stacking Fault and Dislocation on Fracture Behavior in Fe Crystal
C. Lu, Y. Gao, H.T. Zhu and A.K. Tieu 457

Pore Properties of Eco-Material for Erosion Control of Slope and its Fractal Features
J. Wang, Z.L. Hu, J.R. Zhang and M.Z. Zhang 461

Stability Maps of a Cracked Timoshenko Beam Resting on Elastic Soils under Sub-Tangential Forces
E. Viola, A. Marzani and W. Hasan 465

Investigation of Static and Dynamic Response of Graphite and Carbon Fiber Modified Conductive Asphalt-Based Composite
N. Li, S.P. Wu and C.H. Liu 469

Temperature Sensitivity of Asphalt-Aggregate Adhesion via Dynamic Mechanical Analysis
S.P. Wu, Y. Xiao, Q.T. Liu and T.W. Cao 473

Thin Liquid Crystal Film for Corrosion Sensing
F. Kossivas and A. Kyprianou 477

The Effect of Ageing on Rheological Properties and Chemical Conversions of Asphalts
S.P. Wu, L. Pang and G.J. Zhu 481

Contributions in the Study of Hybrid Layered Composites under Static and Variable Loads
N. Constantin, V. Anghel, M. Găvan and Ş. Sorohan 485

Experimental Investigation on Fracture and Tensile Characteristics of Micro-Surfacing Containing Crumb Rubber
Z. Chen, S.P. Wu, T. Zhang and L. Pang 489

Influences of Aging History on Low Temperature Performance of Asphalt Concrete
S.P. Wu, G.J. Zhu, L. Pang and C.H. Liu 493

Preparation of Amido Modified Silicone in Microemulsion
J.S. Liu, S.Q. Huang and S.P. Wu 497

Investigation of Flow Instability in High Temperature Deformation of INCONEL Alloy 783 Using Processing Map Approach
J.T. Yeom, E.J. Jung, J.H. Kim, J.K. Hong, N.K. Park, S.S. Choi and C.S. Lee 501

Effect of Strain-Induced Martensitic Transformation on Coaxing Effect of Austenitic Stainless Steels
J.W. Jung, M. Nakajima, Y. Uematsu, K. Tokaji and M. Akita 505

Characteristics of Deformation-Induced Transformation in Steel 2.25Cr1Mo
Q.F. Li and H.B. Chen 509

Stress Analysis for Shrink Fitting System Used for Ceramics Conveying Rollers
Hendra, M. Tsuyunaru, N. Noda and Y. Takase 513

A Study of Residual Stresses in Al/SiC$_p$ Linear Friction Weldment by Energy-Dispersive Neutron Diffraction
T.S. Jun, F. Rotundo, L. Ceschini and A.M. Korsunsky 517

Mathematical Model for Compressive Stress-Strain Curve of Recycled Aggregate Concrete
W. Wang, L.J. Yang and X.N. Wang 521

Equivalent Stress Intensity Factor of Pre-Northridge Connections
L. Ding, H.B. Liu, Y.S. Shao and C.H. Zhai 525

Fast Analytical Algorithm for Fatigue Crack Life Estimations of Integrally Stiffened Metallic Panels
S.M. Häusler and P. Horst 529

Application of Artificial Neural Network to Forecast the Tensile Fatigue Life of Carbon Material
X.L. Liao, W.F. Xu and Z.Q. Gao 533

Study on the Fatigue Behavior of Carbon/Carbon Composites
X.L. Liao, W.F. Xu and Z.Q. Gao 537

On the Inclined Surface Crack Terminating at the Orthotropic Bimaterial Interface
T. Profant and M. Kotoul 541

Fatigue Behavior of Non-Crimp Fabrics
P. Horst and S. Adden 545

Fatigue Analysis on a Full Scale Fuselage Panel
A. Apicella, E. Armentani and S. Priore 549

Fatigue Properties Improvement of Notched Structural Steel Sheets
N. Hattori, K. Nakayama, M. Zhang and S. Nishida 553

Sensitivity of Fatigue Crack Growth Data to Specimen Geometry
S. Seitl, P. Hutař and Z. Knésl 557

Electro-Mechanical Admittance-Based Damage Detection Using Extreme Value Statistics
C.P. Providakis 561

Evolution of Relevant Parameters on Fretting Fatigue Tests
M. Buciumeanu, A.S. Miranda and F.S. Silva 565

The Thermoelectromechanical *J*-Integral and the Thermal Permeability of Cracks
A. Ricoeur and M. Kuna 569

Stress Singularity of Thermal Stresses in Three-Dimensional Bonded Structures with an Interlayer
H. Koguchi and A. Taniguchi 573

Generalized Quasi-Variational Principles and Application in Nonlinear Non-Conservative Elasto-Dynamics
T. Fan and H.Y. Song 577

Low Cycle Fatigue of Cast Superalloy Inconel 738LC at High Temperature
K. Obrtlík, A. Chlupová, M. Petrenec and J. Polák 581

Stress Fields near Mode II Interface Crack Tip of Two Dissimilar Orthotropic Composite Materials
S.Q. Zhang, H.S. Yao and J.L. Li 585

Damage Evaluation Based on Electrical Resistance Measurement
L.J. Yang, B.X. Sun and Y.M. Guo 589

An Experimental Study on the Fatigue of Structural Steels with Various Welding Details
B.C. Goo 593

Numerical Simulation of Temperature Stress on Asphalt Pavement of Concrete Bridge Deck in Cold Region
H. Wang, S.P. Wu, B. Li and C.H. Liu 597

Investigating Vibration Sources of Faulty Gear Units
A. Belsak and J. Flasker 601

Experimental Study on the Development of New Corrosion Inhibitor Contained a lot of $Ca(No_2)_2$ Using Concrete Structure
B.C. Moon, H.S. Lee and Y.J. Kim 605

Structural Similitude for Buckling of Delaminated Beams
J. Rezaeepazhand 609

Experimental Study on the Adhesion Properties of Zn-Al Metal Spray Method for Steel Structures
J.H. Jin and H.S. Lee 613

The Analytical Trial Function Method (ATFM) for Finite Element Analysis of Plane Crack/Notch Problems
X.R. Fu, S. Cen, Y.Q. Long, X.G. Jiang and J.S. Ju 617

Reliability Assessment of Corrosion Initiation of Harbor Concrete Structure Using FOSM
S.H. Han and W.S. Park 621

A Study on the pH Value Changes of Blended Cement Paste According to the Carbonation
S.H. Lee and H.S. Lee 625

Numerical Simulation of Autogenous Shrinkage in High-Performance Cement Paste Based on a Multi-Component Hydration Model
S.M. Lim, H.S. Lee and X.Y. Wang 629

Prediction of the Carbonation Depth of Concrete with a Mortar Finish
H.S. Lee and X.Y. Wang 633

Mechanical Property of Porous Titanium Produced by Spark Plasma Sintering
Y. Sakamoto, S. Moriyama, M. Endo and Y. Kawakami 637

An Analysis of the Behavior of Small Fatigue Cracks Emanating from Stress Concentrators
S. Ikeda, D. Koyanagi, M. Endo and Y. Sakamoto 641

A Study on the Fatigue Test of Bogie Frame by Stress Measurement
S.C. Yoon, C.S. Jeon, W.K. Kim, J.G. Kim and S.H. Chang 645

Fatigue Life Evaluation of Automotive Engine Mount Insulator
C.S. Woo, W.D. Kim and S. Hur 649

Structural Safety Assessment of Railway Freight Car during Static Loading
J.G. Kim, S.C. Yoon, J.W. Seo and S.T. Kwon 653

An Integrated Approach to Durability Design of Steel Structures Against Atmospheric Corrosion
L. Cascini, R. Landolfo and F. Portioli 657

Analysis of Chloride Diffusion in Cracked Concrete
X.Y. Wang and H.S. Lee 661

An Experimental Study on the Application of Cathodic Protection Method Applying Zn-Al Metal Spray on the RC Structure
M.H. Han and H.S. Lee 665

Thermographic Investigation of Hot Spots in Railway Brake Discs
J.G. Kim, B.C. Goo, S.C. Yoon and S.T. Kwon 669

Experimental Study on the Flexural Fatigue Damage Evolution of Layered Fiber Reinforced Concrete
J. Wang, M.Z. Zhang and X.C. Fan 673

Analytical Study on the Chloride Ion Permeation of Reinforced Concrete Repaired by Finishing Material
S.Y. Yun, S.H. Shin and H.S. Lee 677

Experimental Study on the Water Penetration into Mortar under Water Pressure Condition
J.Y. Yoo, H.S. Lee and Y.J. Kim 681

Crash Tests of Tension Bolts in Light Safety Collision Devices
J.S. Kim, H. Huh, W.M. Choi and T.S. Kwon 685

Analysis of Heat Generation during Fracture in Ceramic Matrix Composites
J.G. Kim 689

Modeling of a Long-Term Creep Curve of Alloy 617 for a High Temperature Gas-Cooled Reactor
W.G. Kim, S.N. Yin, I.H. Jung and Y.W. Kim 693

Mechanical Properties of Ductile Fiber Reinforced Cementitious Composites for Rehabilitation on Concrete Structures
G.S. Ryu, K.T. Koh, S.T. Kang and J.J. Park 697

The Influence of the Amount of Silica Fume on the Mechanical Property of Ultra-High Performance Concrete
J.J. Park, G.S. Ryu, S.T. Kang and S.W. Kim 701

Creep Curve Modeling to Generate the Isochronous Stress-Strain Curve of Type 316LN Stainless Steel
S.N. Yin, W.G. Kim, I.H. Jung, Y.W. Kim and S.J. Kim 705

Fracture Model for PT Flat Plate Connections under Seismic Loading
K.H. Moon, H.B. Jin and S.W. Han 709

Study on Calculation Method of Fracture Parameters of the Tubular Based on 3D VCCT
Q.Y. Wang, Y.J. Liu, X.G. Zeng and H.Y. Chen 713

Study on the Optimum Mixing Condition for Control of Spalling in High Strength Concrete by a Orthogonal Array
M.H. Lee, Y.H. Kim and J.C. Lee 717

Effects of Equal Channel Angular Pressing and Heat Treatment on Low Cycle Fatigue Properties of 6005 Al Alloy
W.H. Kim, H.H. Cho, J.H. Cha, S.I. Kwun and D.H. Shin 721

The Low Cycle Fatigue Behavior of Equal-Channel Angular Pressed Al 5052 Alloy
J.H. Cha, H.H. Cho, W.H. Kim, S.I. Kwun and D.H. Shin 725

Application Technique of PZT Sensors to Detect Structural Damage
Y. Hong, S.H. Hwang, G.P. Wang and D.P. Hong 729

Fracture Analysis of an Oblique Crack Propagation in a Pre-Stressed Glass-Epoxy Composite
E.M. Craciun, A. Carabineanu and N. Peride 733

Computational Fracture Analyses of a Compact Tension Shear (CTS) Specimen with an Inclined Crack Plane
Q.F. Li, G.Y. Qi, S.Y. Yan and F.G. Buchholz 741

Impact Properties of Sn-0.75Cu Lead-Free Solder Ball Joint
I. Shohji, T. Osawa, T. Okashita and H. Watanabe 745

Evaluation of the Failure Elongation of Steel Sheets for an Auto-Body at the Intermediate Strain Rate
S.B. Kim and H. Huh 749

Investigation of Rheological Properties of Asphalt Binders Containing Conductive Fillers
S.P. Wu, B. Li, J.F. Huang and Z.F. Liu 753

Dimple Fracture Simulation under Mixed Mode Loading Condition
M. Kikuchi and S. Sannoumaru 757

Fatigue Crack Growth Simulation by Using S-Version FEM
M. Kikuchi, Y. Wada, Maigefeireti and Y. Li 761

Modeling of Chloride Penetration in Surface Treated Concrete
I.S. Yoon 765

Influence of Cracks on the Durability of RC Structures
L. Nobile 769

Weibull Stress Analysis for an Embedded Crack in Reactor Pressure Vessels under Pressurized Thermal Shock
X.D. Qian and R.H. Dodds Jr. 773

The Enhancement of Corrosion Resistance of Titanium in High Temperature Acidic Solutions by Microarc Oxidation
J.S. Lu and C. Lu 777

The Effect of Volume Fraction of Steel Fiber on the Tensile Softening Behavior in Ultra High Performance Concrete
S.T. Kang, J.J. Park, S.W. Kim and K.N. Hong 781

Reinforcement of Aluminum by TiB Dissolution
P. Agrianidis, K.G. Anthymidis and C. David 785

Fiber Alignment of Steel Fiber Reinforced High Strength Concrete (SFR-HSC) in Flexural Members and its Effect on the Flexural Strength
S.T. Kang, J.J. Park, G.S. Ryu and S.W. Kim 789

An Iterative Algorithm of Hypersingular Integral Equations for Crack Problems
K. Oda and N. Noda 793

Observation of the Behavior of Fatigue Cracks in Friction Stir Welded Aluminum Alloy Joints
K. Katsuki, M. Gutensohn, M. Endo and D. Eifler 797

An Orientation-Dependent Failure Criterion for FCC Crystals
N.N. Huynh, C. Lu, L.Y. Si and K.A. Tieu 801

Influence of Rolling Reduction on Fatigue Behaviour of AA6016/FeP06 Material Compound
A. Lamik, H. Leitner and W. Eichlseder 805

Dynamic Stability of Lateral Vibration of Bottom Hole Assemblies
G.H. Zhao and Z. Liang 809

Shape Optimization of Metal Welded Bellows Seal Based on the Turing Reaction-Diffusion Model Coupled with FEM
M. Gheni and M. Kikuchi 813

Shrinkage Performance and Cracking Resistance Mechanism of Rubberized Lightweight Aggregate Concrete with Polymer
J. Wang, Y. Li and M.Z. Zhang 817

Delamination of Laminates Governed by Free Edge Interlaminar Stresses Using Interface Element
H. Hosseini-Toudeshky, M. Jalalvand and B. Mohammadi 821

On Sensitivity of Thermal Parameters for Concrete Box Girder in the Sunshine
J.Z. Xiao, Z.W. Song and C.Z. Zhang 825

Effects of DLC on Fatigue Properties of Eutectoid Steel
M. Zhang, N. Hattori and S. Nishida 829

Plastic Limit Analysis of an Elbow with Various Wall-Thinning Geometries
S.M. Lee, Y.H. Choi, H.D. Chung, Y.S. Chang and Y.J. Kim 833

Fracture Analysis for Stiffened Aircraft Fuselage Using Substructure Method
J.S. Ju, X.G. Jiang and X.R. Fu 837

Research on the Metal Forming Process of the Muffler Tube Using Finite Element Method
K.T. Han and Y.J. Jin 841

Life Cycle Cost Management Strategy on Corrosion Deterioration and Fatigue Damage of Steel Girder Bridge
M.M.S. Cheung, K.K.L. So and X.Q. Zhang 845

Fatigue Properties of Al-Li Plates Joined by Friction Stir Welding
P. Cavaliere, F.W. Panella and A. Squillace 849

A Viscoplastic Constitutive Model for Single Crystals and its Application in a Numerical Simulation of Creep-Plasticity Behaviors
X.G. Zeng, H.Y. Chen and Z.H. Gao 853

An Experimental Study on Shear Reinforcement Methods of Interior Flat Plate-Column Connections
H.K. Choi, J.S. Kim, E.S. Jin and C.S. Choi 857

A Study on Retrofit Methods of Shear Walls with New Openings
H.K. Choi, J.A. Lee, M.S. Lee, Y.C. Choi and C.S. Choi 861

A Study on Shear Reinforcement of Exterior Joints for Flat Plate
H.K. Choi, S.W. Beck, Y.S. Baik and C.S. Choi 865

Elastic-Plastic Torque Analysis of Notched Cross-Section Bars Using the Finite Difference Method
H.P. Liu, X.R. Fu, S. Cen, X.G. Jiang, J.S. Ju and W.J. Wang 869

Dynamic Tensile Properties of TiCp/Ti Composite
F. Jiang, D. Zhao and J.G. Ning 873

Damage Identification of Mechanical System with Artificial Neural Networks
L.J. Cao, S.J. Li and Z.C. Shangguan 877

Crack Analysis of 3D Functionally Graded Materials by a BEM
J. Wang, X.W. Gao and C.Z. Zhang 881

Finite Element Modelling of Piezoelectric Sensors for Damage Identification in Composite Panels
M.H. Aliabadi, A. Apicella and A. Sanqirgo-Rodriguez 885

Application of Instrumented Indentation Technique to Evaluate Residual Stress and Stress Directionality
M.J. Choi, I.G. Kang, K.H. Kim and D.I. Kwon 889

Nondestructive Estimation of Fracture Toughness Using Instrumented Indentation Technique
K.W. Lee, H.U. Kim, S.W. Park, J.S. Lee, K.H. Kim and D.I. Kwon 893

Key Engineering Materials Vols. 385-387 (2008) pp 1-4
© (2008) Trans Tech Publications, Switzerland
doi:10.4028/www.scientific.net/KEM.385-387.1

A Consideration of Cleavage Crack Propagation in Fe2Si Steel

F Sorbello[1,a] PEJ Flewitt[1,2b] AG Crocker[3,c] and GE Smith[3,d]

[1] Interface Analysis Centre, University of Bristol, Bristol BS2 8BS
[2]Dept. of Physics, HH Wills Laboratory, University of Bristol, Bristol BS8 1TL
[3]Dept. of Physics, University of Surrey, Guildford, Surrey GU2 7XH

[a] fabiosorbello@hotmail.com, [b] peter.flewitt@bristol.ac.uk,
[c] a.crocker@surrey.ac.uk,
[d] gillian.smith@surrey.ac.uk

Keywords: brittle fracture, Fe2Si steel, single crystal, focused ion beam, fractography, twins.

Abstract: It is well established that within the lower-shelf temperature range of Fe2-3Si polycrystalline steels, the brittle fracture occurs predominately by transgranular cleavage, unless subject to embrittling heat-treatments. The cleavage fracture develops on the well established {001} planes of the bcc structure. In this paper we revisit the growth, of these cleavage cracks by considering crack propagation in single crystals of Fe2Si steel. Three point bend specimens manufactured from oriented crystals have been tested by impact loading at a temperature of -196ºC. High spatial resolution focused ion beam imaging combined with ion milling is used to examine in detail the crack propagation path and has provided a new insight into the mechanisms involved. In particular it has been established that within the process zone of the propagating cracks local strain is accommodated by the formation of {112} twins. The results are discussed with respect to the overall crack propagation mechanism.

1. Introduction

In polycrystalline ferritic steels, crack initiation and growth mechanisms change with temperature. This results in the well established variation of Charpy impact energy or fracture toughness with temperature arising from brittle fracture at low temperatures and ductile fracture at high temperatures. [1] Certainly, there have been advances in the ability to model fracture in polycrystalline materials, including 3D models describing brittle fracture at the micro-scale. [1,2] For ferritic steels at lower temperatures, transgranular cleavage on {001} planes predominates. However, for interfaces such as grain boundaries or sub-boundaries (e.g. twins), it has been demonstrated that significant accommodation is required at the interface to compensate for the mismatch between cleavage planes on either side of the interface. [2] It is noteworthy that in bcc polycrystals and single crystals of materials, such as α-iron and Fe2-3wt.%Si steel, the role of twins in the initiation of {001} cleavage cracks has been considered extensively. However, less attention has been given to the contribution of such {112} deformation twins on crack propagation. For example, {112} twins that form as precursors to cleavage crack initiation provide sub-boundaries that have to be overcome during the propagation stage. [3] However, various workers, particularly using atomistic modelling have proposed that deformation twins may form ahead of a growing crack tip. [4,5] In this paper for single crystals of Fe2wt.%Si steel, the role of {112} deformation twins on the propagation of {001} cleavage cracks is considered and discussed with respect to the propagation mechanism.

2. Experimental Procedure

The materials investigated were single crystals of iron-silicon steels with a chemical composition shown in table 1. Single crystal samples were grown at the Academy of Science (Prague, Czech Republic) using the floating zone melting technique under induction heating. The plane normal to

the axis of the extracted single crystal sample was {1-10}. The crystallographic orientation of the selected crystal was verified by using the X-ray Laue back-diffraction method.

The single crystals were cut into matchstick specimens of ~10mm long x 2mm x 2mm, V-notched and impact-fractured at -196ºC using a three-point bend loading jig; the stress was applied along the [44-3] direction. A focused ion beam (FIB) workstation, the FEI FIB201, was used to study the cleavage crack propagation. This system uses a liquid gallium ion source accelerated at 30 keV and has been used for imaging and milling: a low current, 0.001nA, was selected for imaging, whereas the higher current, 11nA, was used for ion milling cross-sections. Fracture facets were identified by topographic contrast, whereas the sub-surface microstructure was imaged by channelling contrast.

Table 1.Elemental composition of the Fe-2wt.% Si crystal

Element	Si	C	P	Fe
wt.%	1.9	0.014	0.009	bal

3. Results and Discussion

A typical fracture surface obtained after testing at -196ºC is shown in Figure 1. Here the cleavage facet has been assigned a specific (001) plane. The cleavage crack has interacted with local features to produce small additional fracture facets, typically ≤ 5μm long. There are two interactions which are the result of cleavage crack propagation across {112} twins that formed prior to crack initiation. [3] Figure 2(a) shows a FIB milled cross section through one of the many smaller diverted cracks which reveals that the path is associated with a thin twin. As a result of the interaction local plastic strain has been promoted to accommodate the mismatch between the twin boundary fracture and the main cleavage crack path to effect final separation. Figure 2(b) shows a diverted crack at X and propagation across a pre-existing {112} twin, at Y. Details of the sub-surface are shown in this FIB milled cross-section which was recorded after tilting the stage at an angle of 45º relative to the [-110] direction. The image contrast shows that at X and Y the twins are ~60nm and ~1.5μm thick respectively. These twins are differently inclined to the (001) cleavage plane. At the twin X, the crack has propagated along one twin boundary and stopped within ~2μm below the original crack surface. By comparison, at twin Y, the crack has propagated on a (001) mirror plane without promoting twin boundary fracture. The broken line superimposed in the cross-section image enhances the topographic variation of the (001) cleavage facet as it crosses the twin. A measure of the inclination of the twin boundaries relative to the (001) cleavage plane allows the identification of the specific twins activated at positions X and Y. [7] Here twin boundaries were inclined at angles of 35.3º and 65.9º to the (001) plane respectively, within a deviation of ~ 1.5º. These twin boundaries were identified as the (-112) and the (-121) planes respectively. Having identified these, all other twins formed in the single crystal were defined.

Experimentally it has been shown, Figures 1 and 2, that {001} cleavage cracks can locally deviate and fracture along a short length of twin boundary. This occurs at small twins (≤100nm thick) which are postulated to form in the process-zone of a propagating crack. A proof of this is given by the twin thickness which proportionally increases with the time elapsed between twin nucleation and stress relief. Since thin twins have only a very brief time to grow, they must nucleate near to the

crack tip. By comparison, the larger twins, such as that shown at position Y in Figure 2 (b) have been demonstrated by the present workers to be associated with load drops in load-displacement curves derived from disc specimens tested at -196ºC. [3] The load drops occur prior to the onset of fracture. Hence, there is evidence that the twins form during the deformation stage which is a pre-cursor to fracture. For a specific (001) cleavage plane the only potentially active thin twins are (112), (-112), (1-12) and (11-2). For example, in the process-zone of a crack propagating, along the

[-1-10] direction of the single crystal, Figure 1, twin boundary fracture occurred mainly on the (112) plane. This correlation is schematically illustrated in Figures 3(a,b,c) which proposes the propagation mechanism of a sharp (001) cleavage crack that spreads in the [-1-10] direction. During fracture, the crack promotes dislocations in the process-zone, Figure 3(a). The dislocations induce stacking faults in the plane of shear resulting in two symmetrical {112} twins, inclined 35.3º to the cleavage plane, Figure 3(b).This description is consistent with the model of twin formation in bcc crystals proposed by Cottrell and Bilby. [8] As the twin grows, the energy required for twinning reduces the crack driving force and makes crack propagation more difficult. Thus, if the stress at the crack tip decreases below a threshold limit, the twin growth eventually arrests. The propagating crack advances and on reaching the twin interface splits as demonstrated in Figures 2(a)(b). While the main crack surrounds the twin by cleavage fracture, a micro-crack propagates along the twin boundary. Since the twin is small, the surrounding cleavage crack forces the micro-crack, which propagated along the twin interface, to rejoin the main fracture path. This process results in a region of high local strain and irrational, possibly ductile fracture. Then, the other small twin disappears and the cleavage crack advances and new dislocations form together with new {112} twins, Figure 3(c).

The twins that form by this mechanism in the process zone will be activated at local points of higher stress concentration that develop along the 3-D crack front. This accounts for the limited size of the twins and the associated fracture facets, Figure 1. Moreover it can be shown that for the density of twin boundary fracture in Figure 1 there will be an associated increase in overall crack propagation energy of about fifty percent compared with simple cleavage based upon a geometrical argument [10]. However, the proportion of twin facets that form on individual {001} cleavage facets in polycrystalline materials will vary according to the orientation of the particular fracture plane relative to the stress axis. This will influence the specific {112} twins that may be formed. In addition Sorbello [9] has observed similar cleavage crack propagation in polycrystalline Fe3Si steel, ά-iron and C-Mn steel.

4. Acknowledgement: The authors are indebted to EPSRC for funding.

5. References

[1] AG Crocker, PEJ Flewitt and GE Smith, Int. Mat. Rev. 50, 99 (2005).
[2] GM Hughes, GE Smith, AG Crocker and PEJ Flewitt, Mat. Sci. Technol., 21, 1268 (2005).
[3] GM Hughes, F Sorbello, GE Smith, PEJ Flewitt and AG Crocker, Fracture of Nano and Engineering Materials and Structures. Proc. 16th European Conf. of Fracture, Ed. Gdoutos (2006).
[4] T Šmida and J Bošanský, Mat. Sci. Eng. A323, 198 (2002).
[5] A Machová and GJ Ackland, Modell. Sim. Mat. Sci. Eng. 6, 521 (1998).
[6] F Guo, H Heinisch and RJ Kuntz, J. Nucl. Mat. 351, 133 (2006).
[7] V Randle and D Dingley, Scripta Metall., 23, 1565 (1989).
[8] AH Cottrell and BA Bilby, Phil. Mag. 42, 573 (1951).
[9] F Sorbello, PhD Thesis, Bristol University (2007).

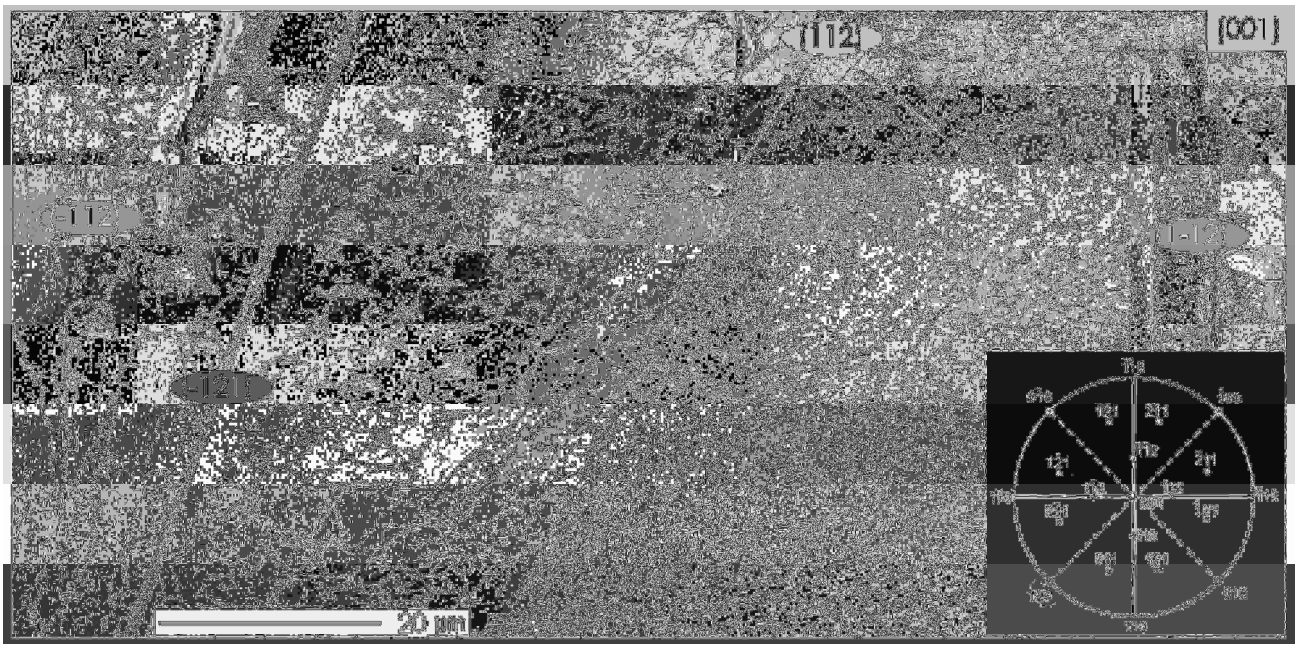

Figure 1. Fractograph showing mutual interaction between (001) cleavage, river patterns and many {112} twins. The crack propagated along the [-1-10] direction on the left hand side and near the [-100] at the centre-right of the image. Inset shows a (001) stereographic projection.

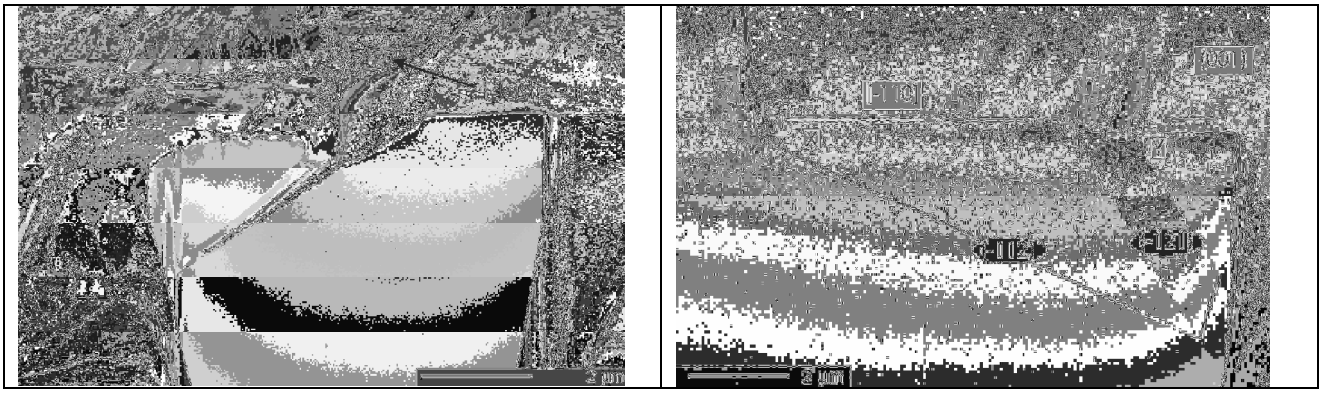

Figure 2. Detail of the main (001) cleavage crack interacting with {112} twins, the ion beam milled cross sections reveal (a) the fracture follows a thin twin boundary and arrests a few micro-metres below the cleavage plane, (b) detail of a locally diverted crack along a twin boundary 'X' and a larger pre-existing (-121) twin 'Y'where the (001) cleavage has propagated across the twin.

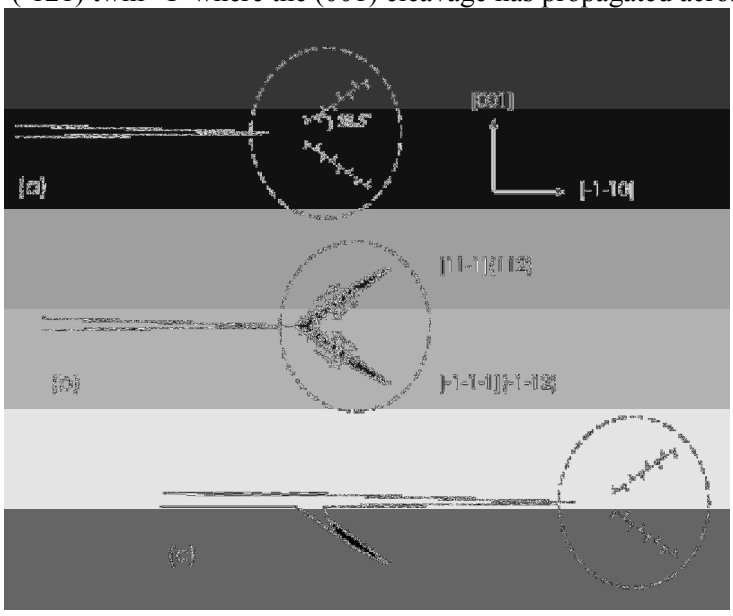

Figure 3. Proposed mechanism of twin formation in the crack process-zone (a) shows dislocations along planes inclined to the (001) cleavage; (b) as the crack propagates the twinning dislocations nucleate thin twins; arrows indicate direction of twinning shear; (c) the crack advances producing local fracture along a boundary of the lower twin and the process repeats ahead to the propagating tip.

Key Engineering Materials Vols. 385-387 (2008) pp 5-8
© (2008) Trans Tech Publications, Switzerland
doi:10.4028/www.scientific.net/KEM.385-387.5

Fatigue crack growth rate analysis in a titanium alloy

Alexander M. Korsunsky[1,a], Daniele Dini[2,b] and Michael J. Walsh[3,c]

[1] Department of Engineering Science, University of Oxford, Parks Rd, Oxford OX1 3PJ, UK

[2] Department of Mechanical Engineering, Imperial College, Exhibition Road, London SW7 2AZ, UK

[3] Combustion Systems Engineering, Rolls-Royce plc, P.O. Box 31, Derby DE24 8BJ, UK

[a]alexander.korsunsky@eng.ox.ac.uk, [b]d.dini@imperial.ac.uk, [c]michael.walsh@rolls-royce.com

Keywords: fatigue, crack growth, elastic-plastic deformation, titanium alloy, aerospace

Abstract. Reliable prediction of fatigue crack growth rates in aerospace materials and components underpins the so-called defect-tolerant approach to lifing. In this methodology the presence or appearance of defects and cracks in components is accepted. However, safe operation is guaranteed by regular inspections and health monitoring, and ensuring (by means of reliable modelling) that no crack may grow far enough to reach the critical size in the interval between inspections. Under such circumstances it is clear that particular attention has to be paid to the development and validation of predictive modelling capabilities for fatigue crack propagation. The situation is complicated by the fact that it is often a challenge to represent correctly the in-service loading experienced by a cracked component. In practice, on top of the major cycles associated with each flight (LCF component), cycles of higher frequency and lower amplitude are also present (HCF component). Sensitivity to dwell at maximum load is also often observed. Furthermore, it is well established that complex load sequences involving overloads and underloads result in fluctuations of fatigue crack growth rates (retardation and acceleration) that must be accounted for in crack growth calculations. In the present study we consider the application of an approach due to Noroozi et al. [1] to the analysis of *R*-ratio effects in Ti-6Al-4V material, on the basis of the experimental crack growth rate data collected under the auspices of AGARD programme [2]. The approach shows promising results, and has the capacity to capture loading sequence effects.

Introduction

Since the beginning of 1970's, damage tolerant design (DTD) has become accepted as a method of fatigue lifing of airframe structures, following the introduction of the military specification MIL-A-83444 in 1971 [3]. This approach offered substantial improvements in safe lives and brought with it significant associated savings in design and operating costs. Subsequently damage tolerant design became the topic of both academic research and industrial development. The Advisory Group for Aerospace Research and Development (AGARD) based in France in 1982 tasked its Structures and Materials Panel with forming sub-committees to address this methodology [4]. Sub-committee SMP/SC.33 formed in 1983 organized a cooperative test programme involving NATO countries with the purposes of (i) promoting familiarity of laboratories with test techniques for DTD of engine disc materials, (ii) standardizing test specimen geometries and test techniques, and (iii) calibrating the results from participating laboratories through a round robin test programme.

For consideration within the test programme, typical engine disc materials were chosen: Ti-6Al-4V, IMI 685 and Ti-17. Realistic engine loading sequences were also identified and selected. The purpose of the extensive multi-laboratory test programme was to generate experimental data that could serve as a basis and reference for the evaluation of different modelling methodologies for the prediction of fatigue crack growth rates (FCGRs) and component lives. The so-called Core Programme used specific test procedures [5] in the round robin study and focused on the Ti-6Al-4V material provided by Rolls-Royce from RB211 fan disc forgings, with the total of 216 tests being carried out by 12 different laboratories. The results confirmed good repeatability of crack growth

data between labs, and it was further confirmed that the potential drop technique provided a highly accurate means of measuring crack sizes. The database FCGR data for Ti-6Al-4V was then used in the Supplemental Programme that focused on life prediction modelling. All predictive models used in this programme used Elber's plasticity-induced crack closure concept [6] and effective stress intensity factor range ΔK_{eff}, with the single exception. The Rolls-Royce approach used the Walker model [7] in the form

$$\frac{da}{dN} = \left(\Delta K (1-R)^m\right)^n \quad , \tag{1}$$

where R denotes the ratio of minimum to maximum stress (or stress intensity factor).

The present paper is devoted to re-analysis of a selection of data from this database using the recently proposed approach due to Noroozi et al. [1].

Experimental

Specimens of Ti-6Al-4V alloy used in the experimental study are shown in Figure 1.

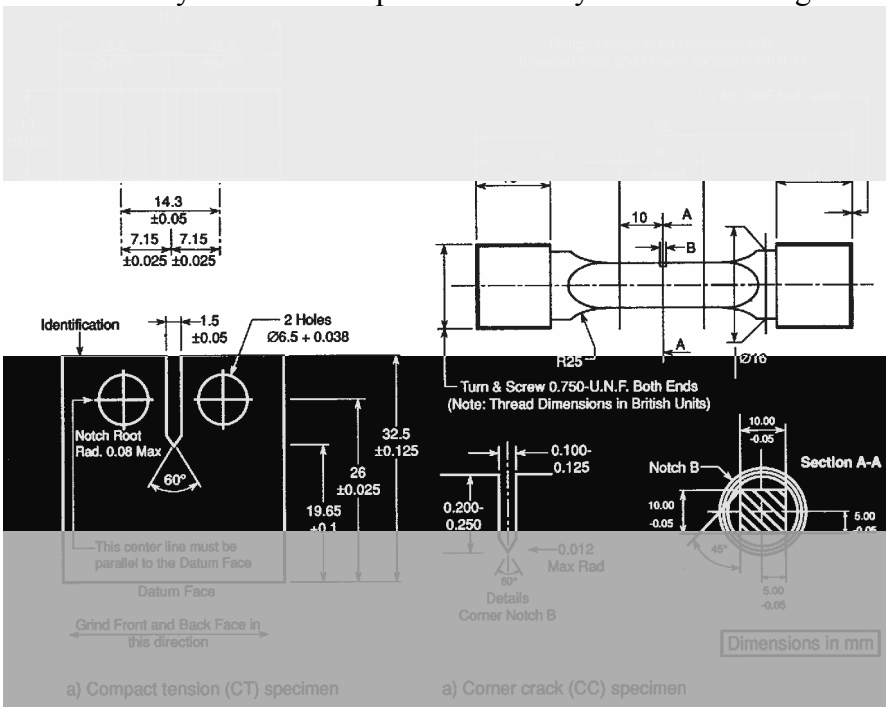

Figure 1. (a) Compact tension (**CT**) and (b) corner crack (**CC**) specimen geometries [2].

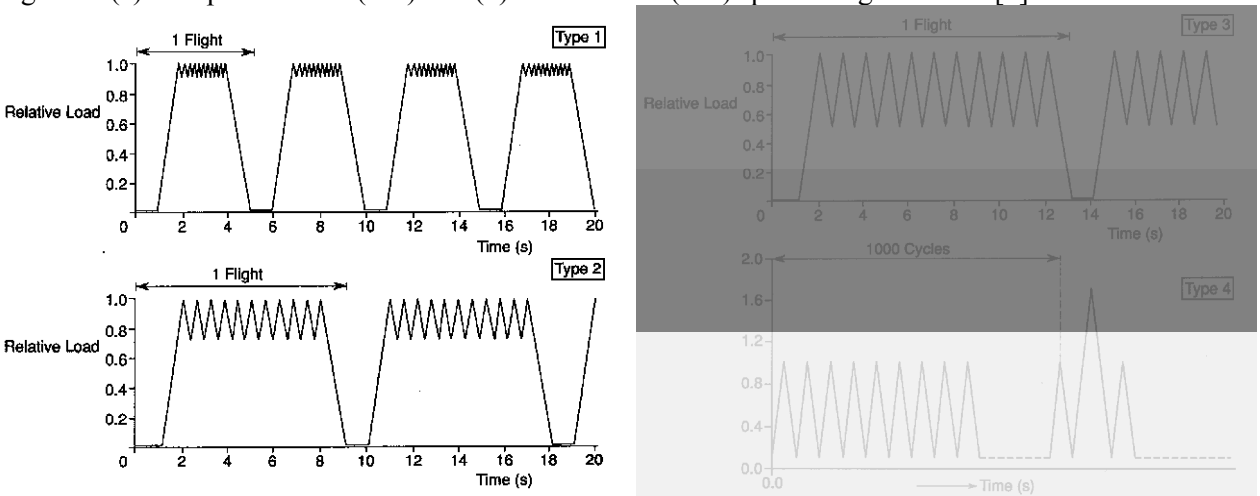

Figure 2. Illustration of 'simple' loading sequences types 1, 2, 3 and 4 (SS1, SS2, SS3 and SS4) [2].

Figure 2 shows the so-called 'simple' loading sequences used for FCGR evaluation. Results sets were denoted using alpha-numeric code referring to laboratory, specimen type and test number. Fatigue crack growth rates obtained from different tests are shown in Figure 3.

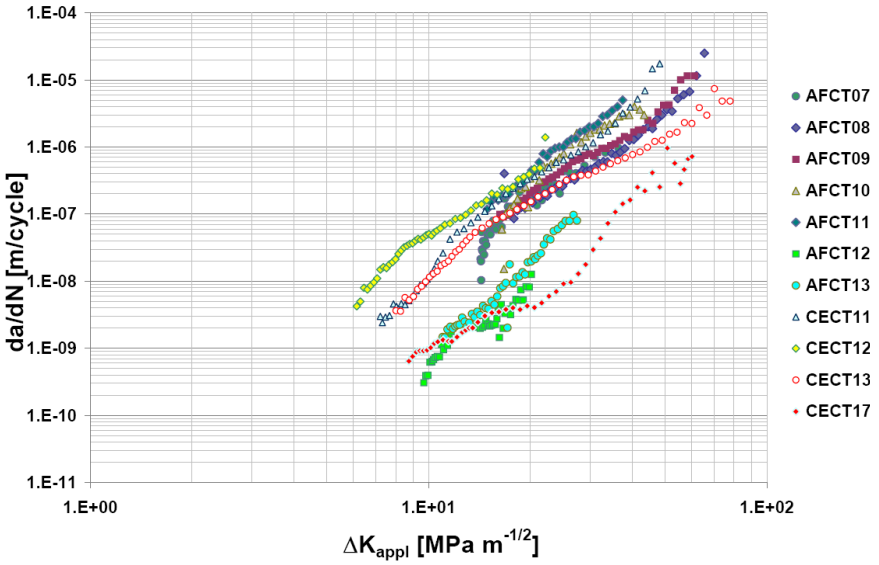

Figure 3. Experimental results for fatigue crack growth rate (FCGR) vs applied stress intensity factor range ('simple' sequences) for compact tension (CT) specimens from AGARD test series [2].

The tests represented in Figure 3 were analysed using the so-called two-parameter driving force approach, with the purpose of 'collapsing' the data into a form of a 'master curve' [8].

Analysis using two-parameter crack driving force

In the approach developed by Glinka and co-workers (e.g. [1]), the driving force for crack propagation is expressed through a combination of the maximum stress intensity factor, $K_{\max}$, and the stress intensity range, ΔK, with both parameters being corrected for the effect of residual stress. Importantly, detailed finite element modelling of the near-tip deformation is not required in this approach. Instead, the crack is assumed to be blunted to a certain material-specific radius, ρ^* (also associated with the elemental material volume). Ramberg-Osgood strain-stress relations are used to describe near crack tip deformation, with the Neuber strain energy rule accounting for reversed inelastic deformation. Crack propagation is thought to occur by sequential failure of elementary material volumes. Failure prediction is based on the Coffin-Manson strain-life curve in combination with the Smith-Watson-Topper parameter:

$$\sigma_{\max}\frac{\Delta\varepsilon}{2}=\frac{(\sigma'_f)^2}{E}(2N)^{2b}+\sigma'_f\,\varepsilon'_f(2N)^{b+c}. \tag{2}$$

Final predictions for fatigue crack growth rate (FCGR) were expressed in the following form:

$$\frac{da}{dN}=C\Delta\kappa^{\gamma}$$
$$\Delta\kappa=K_{\max,tot}^{p}\Delta K_{tot}^{1-p} \tag{3}$$

Furthermore, specific regimes could be considered corresponding to the cases of predominantly elastic behaviour (near the lower fatigue crack growth threshold) and predominantly plastic behaviour (i.e. at higher values of stress intensity factor range). In each of the regimes specific values of parameters p and γ could be identified. However, a difficulty arose in describing the complete range of fatigue response. This is due to the fact that the definition of the combined driving force parameter depends on the value of parameter p, that in turn depends on the regime

considered. In order to overcome this problem it is possible to seek a function that would capture the transition between the two regimes [8]. Figure 4 illustrates fits using a function of the form

$$\frac{da}{dN} = C_{fit}\Delta\kappa^{\gamma_{el}}\left[1+\left(\frac{\Delta\kappa}{\Delta\kappa_0}\right)^{\frac{\gamma_{el}-\gamma_{pl}}{\chi}}\right]^{-\chi} \tag{4}$$

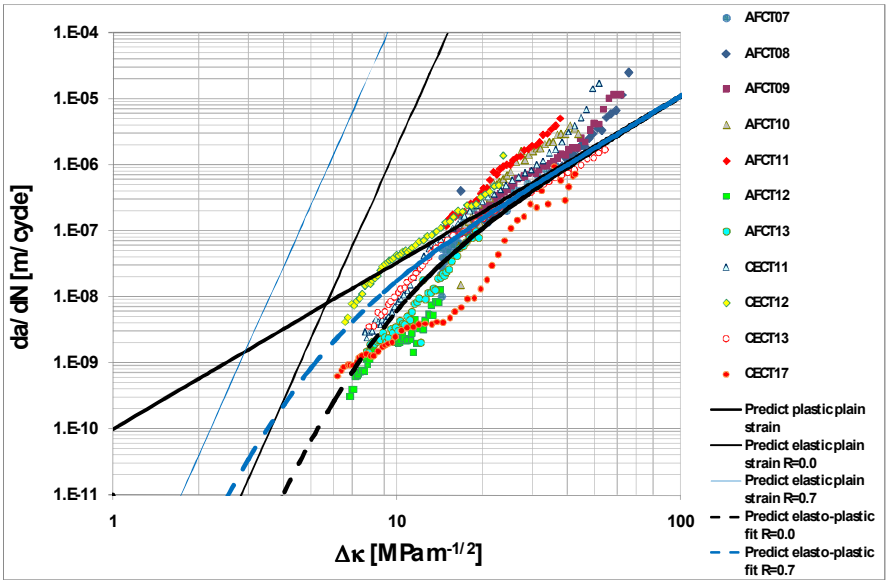

Figure 4. Correlation obtained for FCGR's using two-parameter fatigue crack driving force for simple loading sequences.

Conclusion

The Noroozi et al [1] two-parameter fatigue driving force has been used for the analysis of the data from AGARD addendum report [2]using material properties of alloy Ti-6Al-4V taken from experimental cyclic dogbone sample tests. Encouraging quality of agreement was observed. Improvements in the reliability of prediction of the effects of over/underloads on fatigue crack growth rates can only be achieved if more careful analysis is carried out of the plastic deformation and damage at the crack tip. A merging function was used to describe the transition from elastic to plastic regimes of FCGR, providing a useful tool for developing design correlations.

References

[1] A.H. Noroozi A.H., G. Glinka and S. Lambert: Intl J Fatigue Vol. 27 (2005) p. 1277.
[2] AGARD report R-766 (addendum), AGARD engine disc cooperative test programme, (1993).
[3] Military Specification MIL-A83444, Airplane Damage Tolerance Requirements (U.S.) (1971).
[4] AGARD Conf. proc. 393, Damage tolerance concepts for critical engine components (1985).
[5] A.J.A. Mom, Working document for the AGARD cooperative test programme on titanium alloy engine disc material, NLR TR 84022L (1984).
[6] W. Elber, in: Damage tolerance in aircraft structures, STP 486, ASTM, Philadelphia, PA (1971) p. 230.
[7] E.K. Walker, in: Effect of environment and complex load history on fatigue life, STP 462, ASTM, Philadelphia, PA (1970) p. 1.
[8] A.M. Korsunsky, D. Dini, M.J. Walsh, in: Multiscale Fatigue Crack Initiation and Propagation of Engineering Materials; Structural Integrity and Microstructural Worthiness, edited by G.C. Sih, Springer (2008).

Key Engineering Materials Vols. 385-387 (2008) pp 9-12
© (2008) Trans Tech Publications, Switzerland
doi:10.4028/www.scientific.net/KEM.385-387.9

A criterion for crack kinking out of an interface

Dominique Leguillon[a], Sébastien Murer[b]

[a,b] Institut Jean Le Rond d'Alembert – CNRS UMR7190

Université Pierre et Marie Curie

4 place Jussieu, 75005 PARIS - FRANCE

[a] leguillo@lmm.jussieu.fr , [b] murer@lmm.jussieu.fr

Keywords: Brittle fracture, interfaces, crack kinking, matched asymptotics.

Abstract. Cotterell and Rice theory (1980) on the kinking of a crack submitted to a biaxial loading in a homogeneous material has been recently revisited (Leguillon and Murer 2008). The mixed criterion for fracture which involves both an energetic and a stress condition (Leguillon 2002) allows defining a positive threshold of the *T*-stress below which no branching can occur (Selvarathinam and Goree 1998). This analysis enters within a more general mixed-mode analysis (*I*+*II*+*T*-stress). Despite the complex terms and the oscillations, results extend to interfacial cracks. The assumption of a crack jump as a consequence of the energy balance allows getting rid of the problem brought by the oscillations due to these complex terms. This approach brings a new insight on the prediction of crack kinking out of a bimaterial interface.

Introduction

Within the plane strain elasticity framework, the displacement field in the vicinity of a crack tip at the interface between two homogeneous materials can be described by the so-called Williams' series made of power terms (1). The leading terms involve a complex singularity exponent $\lambda = 1/2 + \mathrm{i}\varepsilon$ associated with a complex mode $\underline{u}$ and the conjugates. The first non singular term called "*T*-stress" corresponds to a tension acting in a direction parallel to the crack. The related power is 1; the associated mode is denoted $\underline{t}$ and T holds for the corresponding intensity factor, i.e. the remote tension

$$\begin{cases} \underline{U}^0(r,\theta) = \underline{R} + K\, r^{1/2+\mathrm{i}\varepsilon}\, \underline{u}(\theta) + \overline{K}\, r^{1/2-\mathrm{i}\varepsilon}\, \overline{\underline{u}}(\theta) + T\, r\, \underline{t}(\theta) + \dots \\ \underline{\underline{\sigma}}^0(r,\theta) = K\, r^{-1/2+\mathrm{i}\varepsilon}\, \underline{\underline{s}}(\theta) + \overline{K}\, r^{-1/2-\mathrm{i}\varepsilon}\, \overline{\underline{\underline{s}}}(\theta) + T\, \underline{\underline{\tau}}(\theta) + \dots \end{cases} \tag{1}$$

where r and θ are the polar coordinates, with the crack tip O chosen as origin. The meaning of index 0 will be explained in the next section. The constant vector $\underline{R}$ is for consistency only. The dots refer to modes with higher order real parts (3/2, 2, 5/2 ...). Oscillations are due to the terms $r^{\pm\mathrm{i}\varepsilon}$ and $(1)_2$ bring into evidence the singular behaviour in the vicinity of the crack tip.

It is worth noting that many authors ([3], [5], [6]) emphasize on the difficulty to extract T from a finite element approximation of (1), even in the real homogeneous case. They propose different procedures leading to quite large inaccuracies. Herein, the path-independent integral H ([4], [9]) is used and proved to be a simple and accurate procedure to determine either the real intensity factor T or the complex one K.

Introducing dimensionless mix mode parameters

$$m(r) = \frac{\overline{K}}{K} r^{-2\mathrm{i}\varepsilon};\ M(r) = \frac{T}{K} r^{1/2-\mathrm{i}\varepsilon} \tag{2}$$

equation (1) can be rewritten as follows

$$\begin{cases} \underline{U}^0(r,\theta) = \underline{R} + K\, r^{1/2+\mathrm{i}\varepsilon}\, (\underline{u}(\theta) + m(r)\, \overline{\underline{u}}(\theta) + M(r)\, \underline{t}(\theta) + \dots) \\ \underline{\underline{\sigma}}^0(r,\theta) = K r^{-1/2+\mathrm{i}\varepsilon} (\underline{\underline{s}}(\theta) + m(r)\, \overline{\underline{\underline{s}}}(\theta) + M(r)\, \underline{\underline{\tau}}(\theta) + \dots) \end{cases} \tag{3}$$

See [2] and [10] for the r dependency of m. The parameter M depends on r as well and is a generalisation of the so-called "stress biaxiality ratio" B used by Leevers and Radon [6].
The aim of this paper is to extend Leguillon's criterion ([7], [12]) in order to include the *T*-stress in the analysis. This criterion is a combination of energy and stress conditions which avoids any arbitrary choice of a critical length and has proved to work well to predict crack initiation at V-notches under symmetric [7] and complex loadings [12] in homogeneous materials. Williams' expansion (1) is used to derive the stress field and a matched asymptotic expansions procedure provides the energy release rate due to the onset of a short crack increment.

Matched asymptotics

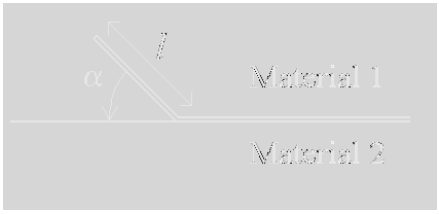

Figure 1. Crack kinking out of an interface.

The main difference with previous works is twofold, a complex singularity holds at the crack tip and the *T*-stress is taken into account in addition to singular modes. The crucial point lies in the comparison between two states: one relies on the initial structure, prior to crack initiation; the other refers to the same structure after onset of a short crack increment (length ℓ) making an angle α with the primary crack (figure 1). The corresponding displacement fields are denoted respectively $\underline{U}^0(r,\theta)$ and $\underline{U}^\ell(r,\theta)$. The asymptotic procedure is carried out with respect to the small crack increment length and matching conditions with (1) lead to

$$\begin{cases} \underline{U}^0(r,\theta) = \underline{U}^0(\rho\ell,\theta) = \underline{R} + K\ell^{1/2+i\varepsilon}\rho^{1/2+i\varepsilon}\underline{u}(\theta) + \overline{K}\ell^{1/2-i\varepsilon}\rho^{1/2-i\varepsilon}\overline{\underline{u}}(\theta) + T\ell\ \rho\underline{t}(\theta) + \dots \\ \underline{U}^\ell(r,\theta) = \underline{U}^\ell(\rho\ell,\theta) = \underline{R} + K\ell^{1/2+i\varepsilon}\ [\rho^{1/2+i\varepsilon}\underline{u}(\theta) + \underline{V}(\rho,\theta)] + \overline{K}\ell^{1/2-i\varepsilon}\ [\rho^{1/2-i\varepsilon}\overline{\underline{u}}(\theta) + \overline{\underline{V}}(\rho,\theta)] \\ \qquad\qquad + T\ell\ [\rho\underline{t}(\theta) + \underline{W}(\rho,\theta)] + \dots \end{cases} \tag{4}$$

where $\rho = r/\ell$ holds for the dimensionless radial coordinate, and where the complex function $\underline{V}$ and the real one $\underline{W}$ are solutions to well-posed problems and vanish at infinity. They depend neither on the global geometry of the structure nor on the loading, and can be computed once and for all as functions of the crack initiation angle α.

The fracture criterion

Using the previously described matched asymptotic analysis (section 2), it has been shown [7] that the initiation of a crack at a V-notch in a homogeneous material can be accurately predicted using two conditions involving both stress and energy. Furthermore, the proposed criterion coincides with Griffith's one for a pure crack. As a consequence of exponents greater than 1/2 in the Williams' expansion in the general case, this initiation process is shown to be unstable; the crack jumps a short length. The presence of the *T*-stress term leads to a similar reasoning which is carried out herein.
Energy condition. The first condition results from an energy balance between two states of the structure prior and after the onset of a short crack increment. It states that the incremental energy release rate $G = -\delta W_p/\delta S$ has to exceed the toughness G_c of the material, δW_p being the elastic potential energy change and δS the newly created crack surface. In plane elasticity, using equations (3) and (4) and asymptotic expansions with respect to the crack increment length ℓ ($\delta S = \ell \times d$, where d holds for the specimen thickness), the energy condition leads to

$$G = K\overline{K}\ X(\alpha, m(\ell), M(\ell)) + \dots \geq G_c \tag{5}$$

where X is a coefficient depending on the crack initiation angle α. It derives directly from the functions $\underline{V}$ and $\underline{W}$ and can be computed using the path-independent integral H ([4], [9]).

Stress condition. The second condition is based on the maximum tension that a material can sustain before failure. It states that fracture can occur only if the opening stress along the expected crack path (defined above by the angle α and the length ℓ) exceeds the material strength σ_c. Due to the oscillations, the forthcoming reasoning can be carried out using only an analogy with the approach used in the real case [8]. The stress condition $\sigma_{\theta\theta} \geq \sigma_c$ leads to the relation

$$K\overline{K}\ Y(m(\ell),M(\ell)) = \ell\ \sigma_c^2 \quad \text{with } Y(m(\ell),M(\ell)) = \left| s_{\theta\theta}(\theta) + m(\ell)\ s_{\theta\theta}(\theta) + M(\ell)\ \tau_{\theta\theta}(\theta) + .. \right|^2 \tag{6}$$

where the index $\theta\theta$ stands for the hoop component of the tensors $\underline{\underline{s}}$ and $\underline{\underline{\tau}}$.

Mix criterion. The compatibility between (5) and (6) gives an equation for the crack initiation length ℓ_c as a function of α

$$\ell_c \frac{X(\alpha, m(\ell_c), M(\ell_c))}{Y(m(\ell_c), M(\ell_c))} = \frac{G_c}{\sigma_c^2} \tag{7}$$

Finally eq. (5) with $\ell = \ell_c$ gives a condition on $|K|$ for crack initiation in the direction α:

$$|K| \geq K_\alpha = \sqrt{\frac{G_c}{X(\alpha, m(\ell_c), M(\ell_c))}}\ , \quad K_f = \min_\alpha K_\alpha \tag{8}$$

The critical value K_α depends on α and the actual kink angle α_f maximizes the denominator, i.e. minimizes K_α giving K_f (i.e. $|K|$ at failure).

Discussion

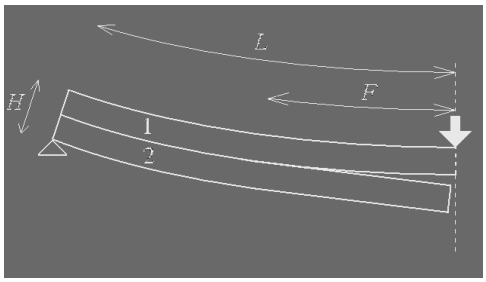

Figure 2. 3-point bending test, $F/L = 0.25$, $H/L = 0.2$ (1/2 specimen).

The kink of a crack in a homogeneous material has been widely studied in the literature, but it is difficult to find experiments to corroborate the predictions for a bimaterial. Many data are involved in the results: the elastic (Young's modulus E and Poisson's ratio ν) and fracture parameters (strength σ_c and toughness G_c) of the two materials. Simulations are carried out on a bimaterial in flexion (figure 2), the stiffer material being alternatively in the upper ($R > 1$) and lower ($R < 1$) position, R is the Young's modulus ratio, $\nu = 0.3$ in both materials. Two cases are analysed: a weak and a strong contrast $E_1 = 300$ GPa, $\sigma_{1c} = 400$ MPa and $G_{1c} = 0.05$ MPa.mm ($K_{Ic} = 4.06$ MPa.m$^{1/2}$), and either $E_2 = 150$ GPa, $\sigma_{1c} = 200$ MPa and $G_{1c} = 0.025$ MPa.mm ($K_{Ic} = 2.03$ MPa.m$^{1/2}$) or $E_2 = 6$ GPa, $\sigma_{1c} = 75$ MPa and $G_{1c} = 0.35$ MPa.mm ($K_{Ic} = 1.52$ MPa.m$^{1/2}$). The stiffer material looks roughly like Alumina while the other looks either like a porous Alumina (weak contrast) or a polymer (strong contrast).

Results are in table 1. The presence of complex terms makes the interpretation quite entangled. A complete sensibility analysis is now in progress for a better understanding of the influence of the various parameters mentioned above. As already observed in the real case [8], K_f defined in (8)

decreases as T increases (not illustrated herein). The particular case $R=1$ (no contrast) is given for comparison taking $K = K_I + \mathrm{i}\, K_{II}$. It is worth noting that the sign of ε is a convention since both + and – occur in eq. (1).

Table 1.

R	ε	$\mathrm{Im}(K)/\mathrm{Re}(K)$	$T/\mathrm{Re}(K)$	α_f (°)	K_f (MPa.m$^{1/2}$)	ℓ_c (μm)
1	0	0.93	1.29	60	2.27	17
2	0.03	1.32	2.79	50	1.39	16
0.5	-0.03	0.89	1.33	60	0.88	18
50	0.09	0.41	1.20	90	0.48	51
0.02	-0.09	1.58	0.38	70	0.81	68

Conclusion

The *T*-stress together with the mix criterion defines an initiation length that allows getting rid of the oscillation terms in the prediction of the critical load and the deflection angle of a crack kinking out of an interface. For a complete analysis the competition between the deflection mechanism and the delamination growth must be analysed. It requires in addition the knowledge of the interface toughness, which determination is difficult, since it depends in particular on the modes mix.

References

[1] Cotterell B and Rice J R (1980) Slightly curved or kinked cracks. Int. J. Fract. 16(2):155–169.
[2] He M Y and Hutchinson J W (1989) Kinking of a crack out of an interface. J. Appl. Mech. 111:270-278.
[3] Kfouri A P (1986) Some evaluations of the elastic T-term using Eshelby's method. Int. J. Fract. 30:301–315.
[4] Labossiere P E W and Dunn M L (1998) Calculation of stress intensities at sharp notches in anisotropic media. Eng. Frac. Mech. 61(5-6):635–654.
[5] Larsson S G and Carlsson A J (1973) Influence of non-singular stress terms and specimen geometry on small-scale yielding at crack tips in elastic-plastic materials. J. Mech. Phys. Solids 21:263–277.
[6] Leevers P S and Radon J C (1982) Inherent stress biaxiality in various fracture specimen geometries. Int. J. Fract. 19:311–325.
[7] Leguillon D (2002) Strength or toughness? A criterion for crack onset at a notch. Eur. J. Mech. A/Solids 21:61–72.
[8] Leguillon D. and Murer S. (2008) Crack deflection in a biaxial stress state, Int. J. Fract. submitted.
[9] Leguillon D and Sanchez-Palencia E (1987) Computation of singular solutions in elliptic problems and elasticity. J. Wiley, New-York Masson, Paris, pp121–128.
[10] Rice J R (1988) Fracture mechanics concepts for interfacial cracks. J. Appl. Mech. 55:98–103.
[11] Selvarathinam A S and Goree J G (1998) *T*-stress based fracture model for cracks in isotropic materials. Eng. Frac. Mech. 60(5-6):543–561.
[12] Yosibash Z, Priel E and Leguillon D (2006) A failure criterion for brittle elastic materials under mixed mode loading. Int. J. Fract. 141(1):289–310.

Key Engineering Materials Vols. 385-387 (2008) pp 13-16
© (2008) Trans Tech Publications, Switzerland
doi:10.4028/www.scientific.net/KEM.385-387.13

Geometrically Nonlinear Analysis of Cracked Stiffened Curved Panels by DBEM

P.M. Baiz and M.H. Aliabadi
Department of Aeronautical Engineering, Imperial College London
South Kensington campus, London SW7 2AZ
p.m.baiz@imperial.ac.uk, m.h.aliabadi@imperial.ac.uk

Keywords: Fracture Mechanics, Shear Deformable, Plate and Shallow Shell Assemblies.

Abstract. This paper presents applications where the DBEM formulations presented by Dirgantara and Aliabadi [3, 4] is combined with the multi region BEM presented recently by Baiz and Aliabadi [2], for the analysis of cracked shear deformable plates and shallow shell assemblies. Stress intensity factors are obtained using the CTOD technique. Several examples are solved to demonstrate the capabilities of the proposed technique. Comparing DBEM with FEM, it was clear that good accuracy and efficiency can be achieved with the present multi region DBEM.

Introduction. Cracks are present in most structural members either as a result of the manufacturing process or due to a localized damage during service life. These cracks may grow by fatigue, corrosion or creep, decreasing the strength and leading to the failure of the structure. The dual boundary element method (DBEM) is based on the use of different equations on each crack surface (displacement and traction integral equations). During the past years, the dual boundary element method has emerged as a robust numerical method for fracture mechanics problems [1]. Applications of the dual boundary element method to fracture mechanics of shear deformable plates have been reported independently by Rashed, Aliabadi and Brebbia [6] and Ahmadi-Brooghani and Wearing [7] while DBEM for shear deformable shallow shells have been derived by Dirgantara and Aliabadi [3].

Multi-region BEM (Plates and Shallow Shells). Lets consider M assembled cylindrical shallow shells or plates joined at J_n. The global coordinate system is given by -x_1-x_2-x_3, and the local coordinate systems for each region by -x_1^m-x_2^m-x_3^m $(m = 1, M)$. The plates or shallows shells have an uniform thickness h, Young's modulus E and Poisson's ratio ν. Generalized displacements and tractions are denoted as, $w_\alpha - p_\alpha$ for rotations of the middle surface, $w_3 - p_3$ for out-of-plane displacement, and $u_\alpha - t_\alpha$ for in-plane displacements. Shallow shells are defined using a curvilinear coordinate system. This means that contrary to flat plates which have a fix normal (local coordinate system) through the whole plate, the local coordinate system of a shallow shell changes with the curvature.

Because two or more angled plates or shallow shells joined together are considered, an approach similar to that proposed in [9] is adopted. To simplify this approach, the local coordinate systems of each region is assumed to be defined such that the x_2^m directions are all aligned with the global direction x_2, following the implementation for plate assemblies presented by Wen *et. al.* [8] or Di Pisa [5]. Based on the above simplification, compatibility equations for each pair of adjacent shallow shells (e.g. $m = 1$ and $m = 2$) could be written as follows:

$$\begin{aligned}
u_1^1(n_{11}^{1c}n_{11}^1 + n_{31}^{1c}n_{13}^1) + w_3^1(n_{13}^{1c}n_{11}^1 + n_{33}^{1c}n_{13}^1) &= u_1^2(n_{11}^{2c}n_{11}^2 + n_{31}^{2c}n_{13}^2) + w_3^2(n_{13}^{2c}n_{11}^2 + n_{33}^{2c}n_{13}^2) \\
u_1^1(n_{11}^{1c}n_{31}^1 + n_{31}^{1c}n_{33}^1) + w_3^1(n_{13}^{1c}n_{31}^1 + n_{33}^{1c}n_{33}^1) &= u_1^2(n_{11}^{2c}n_{31}^2 + n_{31}^{2c}n_{33}^2) + w_3^2(n_{13}^{2c}n_{31}^2 + n_{33}^{2c}n_{33}^2) \\
u_2^1 &= u_2^2 \\
w_1^1 &= w_1^2 \\
w_2^1 &= 0 \\
w_2^2 &= 0
\end{aligned} \tag{1}$$

where n_{ik}^{m} are the components of the rotation matrix of the shallow shell base plane m from local to global coordinates [9], and n_{ik}^{mc} are the components of the rotation matrix from the curvilinear coordinate system to the shallow shell base plane m. The components of n_{ik}^{mc} are given by:

$$\begin{array}{lcllll} n_{11}^{mc} & = & \cos(\alpha_c^m); & n_{12}^{mc}=0; & n_{13}^{mc}=\cos(90+\alpha_c^m) \\ n_{21}^{mc} & = & 0; & n_{22}^{mc}=1; & n_{23}^{mc}=0 \\ n_{31}^{mc} & = & \cos(90-\alpha_c^m); & n_{32}^{mc}=0; & n_{33}^{mc}=\cos(\alpha_c^m) \end{array} \tag{2}$$

where α_c^m is measured with respect to the shallow shell base plane. Equations in (1) result in a system of $5M-4$ compatibility conditions, and have to be supplemented with 4 equilibrium conditions as follows:

$$\begin{aligned} \sum_{m=1}^{M}[t_1^m(n_{11}^{mc}n_{11}^m+n_{31}^{mc}n_{13}^m)+p_3^m(n_{13}^{mc}n_{11}^m+n_{33}^{mc}n_{13}^m)] &= 0 \\ \sum_{m=1}^{M}[t_1^m(n_{11}^{mc}n_{31}^m+n_{31}^{mc}n_{33}^m)+p_3^m(n_{13}^{mc}n_{31}^m+n_{33}^{mc}n_{33}^m)] &= 0 \\ \sum_{m=1}^{M} t_2^m &= 0 \\ \sum_{m=1}^{M} p_1^m &= 0 \end{aligned} \tag{3}$$

to produce the required $5M$ equations. This approach relies on the assumption that the plate or shallow shell flexural rigidity in its own plane is so large that it is possible to ignore its associated deformation, in another words, there is no drilling rotation.

Boundary Integral Formulation. The dual boundary element method is based on the use of two independent equations, the displacement and traction boundary integral equations, at each pair of coincident source points on the surfaces that define a crack. Boundary integral equations for fracture mechanics analysis of shear deformable shells can be found in [3], while boundary integral equations for nonlinear analysis of shear deformable shells can be found in [4]. In order to avoid an ill-conditioned system, the traction integral equations are used for collocations on the other crack surface ($\mathbf{x}^- \in \Gamma^-$):

$$\begin{aligned} &\frac{1}{2}p_\alpha(\mathbf{x}^-)-\frac{1}{2}p_\alpha(\mathbf{x}^+)+n_\beta(\mathbf{x}^-)\neq_\Gamma P^*_{\alpha\beta\gamma}(\mathbf{x}^-,\mathbf{x})w_\gamma(\mathbf{x})d\Gamma(\mathbf{x})+n_\beta(\mathbf{x}^-)\neq_\Gamma P^*_{\alpha\beta3}(\mathbf{x}^-,\mathbf{x})w_3(\mathbf{x})d\Gamma(\mathbf{x}) \\ &\quad = n_\beta(\mathbf{x}^-)\neq_\Gamma W^*_{\alpha\beta\gamma}(\mathbf{x}^-,\mathbf{x})p_\gamma(\mathbf{x})d\Gamma(\mathbf{x})+n_\beta(\mathbf{x}^-)\int_\Gamma W^*_{\alpha\beta3}(\mathbf{x}^-,\mathbf{x})p_3(\mathbf{x})d\Gamma(\mathbf{x}) \\ &\qquad +n_\beta(\mathbf{x}^-)\int_\Omega W^*_{\alpha\beta3}(\mathbf{x}^-,\mathbf{X})q_3^*(\mathbf{X})\,d\Omega(\mathbf{X}) \end{aligned} \tag{4}$$

$$\begin{aligned} &\frac{1}{2}p_3(\mathbf{x}^-)-\frac{1}{2}p_3(\mathbf{x}^+)+n_\beta(\mathbf{x}^-)\neq_\Gamma P^*_{3\beta\gamma}(\mathbf{x}^-,\mathbf{x})w_\gamma(\mathbf{x})d\Gamma(\mathbf{x})+n_\beta(\mathbf{x}^-)\neq_\Gamma P^*_{3\beta3}(\mathbf{x}^-,\mathbf{x})w_3(\mathbf{x})d\Gamma(\mathbf{x}) \\ &\quad = n_\beta(\mathbf{x}^-)\int_\Gamma W^*_{3\beta\gamma}(\mathbf{x}^-,\mathbf{x})p_\gamma(\mathbf{x})d\Gamma(\mathbf{x})+n_\beta(\mathbf{x}^-)\neq_\Gamma W^*_{3\beta3}(\mathbf{x}^-,\mathbf{x})p_3(\mathbf{x})d\Gamma(\mathbf{x}) \\ &\qquad +n_\beta(\mathbf{x}^-)\int_\Omega W^*_{3\beta3}(\mathbf{x}^-,\mathbf{X})q_3^*(\mathbf{X})\,d\Omega(\mathbf{X}) \end{aligned} \tag{5}$$

and

$$\frac{1}{2}t_\alpha(\mathbf{x}^-)-\frac{1}{2}t_\alpha(\mathbf{x}^+)+n_\beta(\mathbf{x}^-)\neq_\Gamma T^*_{\alpha\beta\gamma}(\mathbf{x}^-,\mathbf{x})u_\gamma(\mathbf{x})d\Gamma(\mathbf{x})$$

$$= n_\beta(\mathbf{x}^-) \oint_\Gamma U^*_{\alpha\beta\gamma}(\mathbf{x}^-, \mathbf{x}) t^{(i)}_\gamma(\mathbf{x}) d\Gamma(\mathbf{x}) + n_\beta(\mathbf{x}^-) \int_\Omega U^*_{\alpha\beta\gamma}(\mathbf{x}^-, \mathbf{X}) q^*_\gamma(\mathbf{X})\, d\Omega(\mathbf{X})$$
$$+ \frac{1}{2} n_\beta(\mathbf{x}^-) B \left[(1-\nu) k_{\theta\psi} + \nu \delta_{\theta\psi} k_{\phi\phi}\right] w_3(\mathbf{x}^-) \tag{6}$$

where the body force terms $f(\mathbf{X})$ and membrane tractions $t^{(i)}_\gamma$ are given as,

$$t_\alpha = t^{(i)}_\alpha + t^{(ii)}_\alpha + t^{(n)}_\alpha = N^{(i)}_{\alpha\beta} n_\beta + N^{(ii)}_{\alpha\beta} n_\beta + N^{(n)}_{\alpha\beta} n_\beta \tag{7}$$

$$q^*_3(\mathbf{X}) = q_3 - k_{\gamma\theta} N_{\gamma\theta} + \left[\left(N_{\gamma\theta} w_{3,\theta}\right)_{,\gamma}\right] \tag{8}$$

$$q^*_\gamma(\mathbf{X}) = q_\gamma + N^{(ii)}_{\gamma\theta,\theta} + \left[N^{(n)}_{\gamma\theta,\theta}\right] \tag{9}$$

Due to the limited space in this conference paper, a complete description of the geometrically nonlinear DBEM for shear deformable shallow shells is not presented. The reader is referred for more details of the DBEM for shallow shells to [3] or to [4] for more details on large deflection analysis of shear deformable shallow shells. Equations (4-6) represent traction integral equations and together with the displacement integral equations for collocation on the rest of the boundary Γ^e, form the dual boundary integral formulation in shallow shell problems. It is worth notice that as the source points $\mathbf{x}^+$ and $\mathbf{x}^-$ are coincident, extra free terms appear in equations (4-6) for collocation on both crack surfaces.

The implementation of the dual boundary element formulation requires the discretization of the boundary Γ. Additionally, several uniformly distributed domain points are required for the application of the dual reciprocity method (DRM). In the case of the boundary: continuous, semi discontinuous and discontinuous quadratic isoparametric boundary elements are used to describe the geometry of each region (plate or shallow shell).

Numerical Example. A curved stiffened panel with a centre crack as shown in Fig. 1 is analyzed. The material properties and dimensions are also presented in Fig. 1. The curved panel is simply supported along all the boundary and is subjected to an uniform internal pressure q. In order to validate the DBEM in shallow shell and plate assemblies, results are compared with the FEM. The FEM half model has a total of 5922 elements and 18133 nodes. The DBEM model contains 7 shallow shells and 6 flat plates, with a total of 248 elements and 214 DRM points (14 elements per crack side). Fig. 1 presents the out of plane displacement w_3 contour plot for a central cracked curved stiffened panel.

Conclusion. In this work, applications of the DBEM for the fracture mechanics analysis of geometrically nonlinear shear deformable plate and shallow shell assemblies were presented. A multi-region technique was used to model plate and shallow shell assembled structures subjected to arbitrary loading. Additional equations were obtained by imposing compatibility and equilibrium equations along the interface boundaries. The DBEM shallow shell formulation was developed by coupling boundary element formulations of shear deformable plate bending and two dimensional plane stress elasticity; as a result, domain integrals appear in the formulation and are treated with the Dual Reciprocity Technique. Traction integral equations were applied on one crack surface and the usual displacement integral equations on the other crack surface and non-crack boundaries. Special crack tip elements are used to model accurately the displacement field. Comparing DBEM with FEM models, it was clear that good accuracy and efficiency can be achieved with the present nonlinear multi region DBEM. This simple strategy is very robust, making the DBEM an effective tool for the modeling of general crack problems.

References

[1] Aliabadi, M.H., *The Boundary Element Method, vol II: application to solids and structures*, Chichester, Wiley (2001).

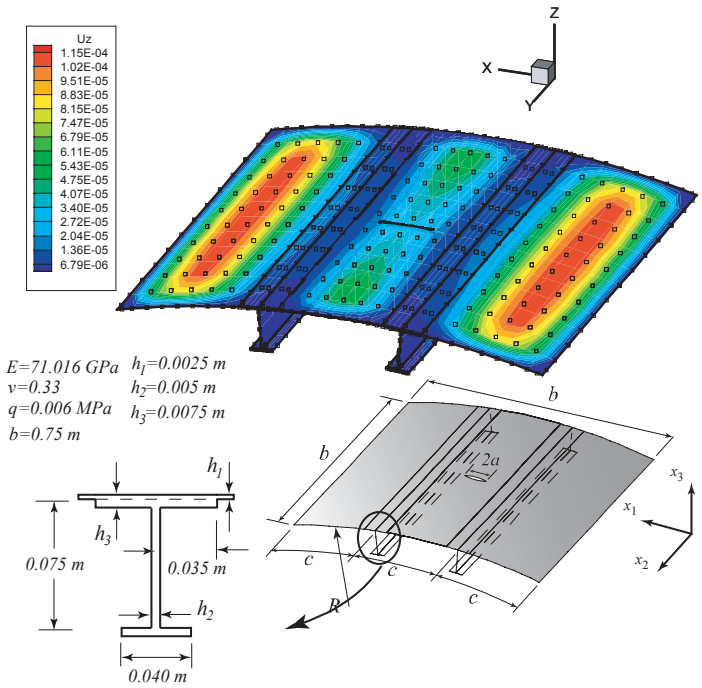

Figure 1: Crack Opening Displacement for Curved Stiffened Panel.

[2] P.M. Baiz, M.H. Aliabadi, Local Buckling of Thin-Walled Structures by the Boundary Element Method. Submitted to *Engineering Analysis with Boundary Elements.*

[3] Dirgantara, T., Aliabadi, M.H., Dual Boundary Element Formulation for Fracture Mechanics Analysis of Shear Deformable Shells, *Internationa Journal of Solids and Structures*, **38**, 7769-7800 (2001).

[4] Dirgantara, T., Aliabadi, M.H., A Boundary Element Formulation for Geometrically Nonlinear Analysis of Shear Deformable Shells, *Computer Methods in Applied Mechanics and Engineering*, **195**, 4635-4654 (2006).

[5] Di Pisa, C., *Boundary Element Analysis of Multi-layered Panels and Structures*, PhD Thesis, Department of Engineering, Queen Mary University of London (2005).

[6] Rashed, Y. F., Aliabadi, M. H. and Brebbia, C. A., Hyper-singular boundary element formulation for Reissner plates, *International Journal of Solids and Structures,* **35**, 2229-2249 (1998).

[7] Wearing, J.L., Ahmadi-Brooghani, S.Y., Fracture analysis of plate bending problems using boundary element method, in *Plate Bending Analysis with Boundary Elements*, *Advanced in Boundary Element Series*, M. H. Aliabadi (Ed.), Computational Mechanics Publications, Southampton (1998).

[8] Wen, P.H., Aliabadi, M.H., Young, A., Crack growth analysis for multi-layered airframe structures by boundary element method, *Engineering Fracture Mechanics*, **71**, 619-631 (2004).

[9] Zienkiewicz, O.C., Taylor, R., *The Finite Element Method, Vol 2: Solid Mechanics*, B-H, Oxford, (2000).

Key Engineering Materials Vols. 385-387 (2008) pp 17-20
© (2008) Trans Tech Publications, Switzerland
doi:10.4028/www.scientific.net/KEM.385-387.17

A Finite Element Analysis of Scarf Joint for controlling the Triaxiality function in Adhesive Bonding.

I. Hilmy[1,a], M.M. Abdel Wahab[1,b], I.A. Ashcroft[2,c] and A.D. Crocombe[1,d]

[1]Faculty of Engineering, University of Surrey, Guildford, Surrey, GU2 5XH,

[2]Department of Mechanical Engineering, Loughborough, Leicestershire, LE11 3TU

[a]i.hilmy@surrey.ac.uk, [b]M.Wahab@surrey.ac.uk, [c]I.A.Ashcroft@lboro.ac.uk[d],
A.Crocombe@surrey.ac.uk

Keywords: Triaxiality Function, Scarf Joint, Low Cycle fatigue Damage, Finite Element Analysis

Abstract:

Triaxiality function (Rv) has been known as one of the important factors that responsible for damage initiation in adhesive bonding. Damage evolution law for low cycle fatigue (LCF) is function of Rv, von Mises equivalent stress (Seqv) and number of cycles (N). From previous research, it was found that the Rv values of two cases: bulk adhesives and single lap joint (SLJ), were close to unity. Those values are uncontrollable. Meanwhile, the damage equation for general solution contains Rv as an independent variable. There is need to choose another joint type that can characterise Rv as an independent variable. This paper presents the choice of scarf joint as specimen that can simulate variation of Rv. Several types of adhesive joints have been modelled and analysed using ANSYS as finite element analysis (FEA) tool. In ANSYS, Rv values were calculated directly from direct output results: von Misses equivalent stress and Hydrostatic stress. From FEA, it was shown that Rv changed as a function of adhesive bondline angle of the scarf joint. The values of Rv are constant along adhesive line except at the free edges. This choice is better than Cleavage joint where the values of Rv are not constant along adhesive line due to the presence of bending moment.

Introduction

Structural engineer in general considers that uniaxial tensile test is suitable to describe the behaviour in structures. But, in multi-axial loading state, this understanding need to be updated. Scaffer et al [1] stated that void nucleation models, void growth models, and void coalescence models depend on triaxiality. If triaxiality value rises, tendency to failure increases. He also states that proper calculation of triaxiality need 3D non-linear analysis. The unique behaviour of triaxiality is that it can be controlled by adjusting the geometry or loading mode. Barsoum [2] has performed research where triaxiality is controlled and is kept constant during a test by maintained the ratio between tension and torsion fixed. Decreasing torsion will also decrease triaxiality and vice versa. Seppala et al [3] explained that void growth occurs because system tries to relax from an applied tension load in order to minimize elastic energy. Material around the void will deform plastically to accommodate void growth. Naturally, plastic deformation emerges because of local shear stress that might occur from applied load or from the stress field around the void, even if it is a hydrostatic stress. Dutta [4] found that the stress state is an important factor in crack initiation and strain failure. The stress state generally can be presented by the stress triaxiality, which has very important role in ductile failure. Higher triaxiality value show how dominate hydrostatic stress in stress field. On the contrary, stress deviatoric component has important role compared to hydrostatic stress at low triaxiality values. Void growth rate related directly to the stress triaxiality value and plastic strain accumulation. Scahfer et al [1] has performed non-linear finite element analysis of a round bar with a notch, which was subjected to a small-scale tension load. They analysed stress levels at failure and

found that failure locations are consistent with locations where the stress triaxiality are higher in all cases considered.

Triaxiality Formula

In the formula to calculate triaxiality function [5], as shown in Eq. 1, there is triaxiality variable T_x, which represent ratio of *Hydrostatic* stress over von-Mises equivalent stress.

$$R_v = \frac{2}{3}(1+\nu)+3(1-2\nu)T_x^2 \tag{1}$$

Hydrostatic stress is a stress that can cause elements to shrink or grow without a change in shape. The hydrostatic stress itself can be extracted from principal stresses values. Since the principal stresses are three stresses from three-dimensional directions, it raises questions on whether to use three-dimensional or two-dimensional analyses to extract the stress values. Is it enough to model the joint as two-dimensional element without sacrificing its accuracy? If triaxiality calculation can be performed in two dimensions, for example by using a plane-stress or plane-strain assumption,the complexity and computing time can be reduced. Triaxiality is like map of the stress state of a structure in this case of an adhesive joint. Triaxiality state in adhesive region is unique belong to particular type of adhesive joint. The main issue presented in this paper is the selection process to choose which joint has good and simple relation between changing load or geometry and triaxiality values. Triaxiality from several types of adhesive joints in three-dimensional models is evaluated and compared. Comparison between three-dimensional and two-dimensional models is also presented.

Finite Element Analysis

Finite element analyses of three adhesive joints model as shown in Fig 1: butt joint based on ASTM STP [6], cleavage joint based on ASTM D 1062 [7] and scarf joint have been performed. For 3D analysis, adhesive joint has been modelled using 20-noded solid element with mid-side nodes while for 2D analysis, adhesive joint has been modelled using 2D plain strain 8-noded solid elements. This is a 2D higher order element. With the presence of nodes in the middle of the element's edges, this element has many advantages: a) more accurate results for mixed (quadrilateral-triangular) automatic meshes and b) irregular shapes can be tolerated without much loss of accuracy. In this model, substrates were made from *Mild Steel* with *Young Modulus* = 210000 N/mm^2, *Poisson's Ratio* = 0.3. Adhesive was made from FM-73™ film-form from Cytec. Material properties of FM-73 are as follow: *Young Modulus* = 1211 N/mm^2, *Poisson's Ratio* = 0.38. The model uses multilinear kinematic hardening material.

Results

Fig. 2 shows how the triaxiality contour an the mid-layer adhesive surface in the butt joint changes when a mixed-load condition is considered. The shape is in-between two extreme loads, pure torsion and pure tension. For pure shear due to torsion, the triaxiality contour remains constant at 0.92, despite spike arises at the centre. For pure tension, except at edge, triaxiality is constant and at its highest value 3.5. Fig. 3 shows the triaxiality contour on the mid-layer adhesive surface in cleavage joint (left) compared with results from a 2D analysis (right). There is a line across the thickness that has zero moment, which is related to the minimum triaxiality value, i.e. 0.92. Also, it can be seen that the range of triaxiality values is between 0.92 and 3.6. This range is still consistent with the result from butt joint. Fig. 4 (left) shows that the triaxiality contour located away from the edges have nearly constant value, i.e. 1.67. The effect of the change of orientation angle is also shown in Fig. 4 (right).

Conclusion

Triaxiality in butt joints can be controlled by adjusting the combination load between tension and torsion. Numerically, triaxiality can be easily controlled, but in practical or laboratory scale, adjusting and maintaining torsion-tension load combination at fixed value, is impossible during fatigue test conditions. Characterization of triaxiality is influenced by loading state and not just the geometry. Changing in the magnitude of loading does not affect triaxiality. This statement is true for case pure tension and pure torsion but not for mixed loading case. This can be explained by the fact that hydrostatic stress always compensates the changing value of von-Mises equivalent stress. The profile of triaxiality in the cleavage joint does not follow simple function shape; beside the shape itself is not consistent if the bondline angle is changed. Triaxiality values in scarf joint along its bondline are constant for all orientations considered except small region at the edges, triaxiality drops due to the effect of singularity. Scarf joint for fatigue test is more feasible to implement in laboratory. Relatively simple joint, easy to manufacture, and the most important advantage is its constant Rv value when fatigue load is applied.

Reference

[1] B. W. Schafer, M. S. Zarghamee: *Triaxiality and Fracture of Steel Moment Connections*, Journal Of Structural Engineering, October 2000 / 1131

[2] I. Barsoum: *Ductile Failure And Rupture Mechanisms in Combined Tension and Shear*, Licentiate Thesis no. 96, 2006, Stockholm, Sweden

[3] E. T. Seppala, J. Belak, R. E. Rudd: *Effect of Stress-Triaxiality on Void Growth In Dynamic Fracture of Metals: a Molecular Dynamics Study*, October 13, 2003

[4] B.K. Dutta, H.S. Kushwaha: *A Modified Damage Potential to Predict Crack Initiation: Theory and Experimental Verification*, Eng. Fracture Mechanics 71 (2004) 263–275

[5] J. Lemaitre, R Desmorat: *Engineering Damage Mechanics*, Springer-Verlag, 2005

[6] E.M. Petrie: *Handbook of Adhesives and Sealants*, McGraw-Hill, 2000

[7] ASTM D 1062-02: *Test Method for Cleavage Strength of Metal-to-Metal Adhesive Bonds*, Vol. 15.06, 2003

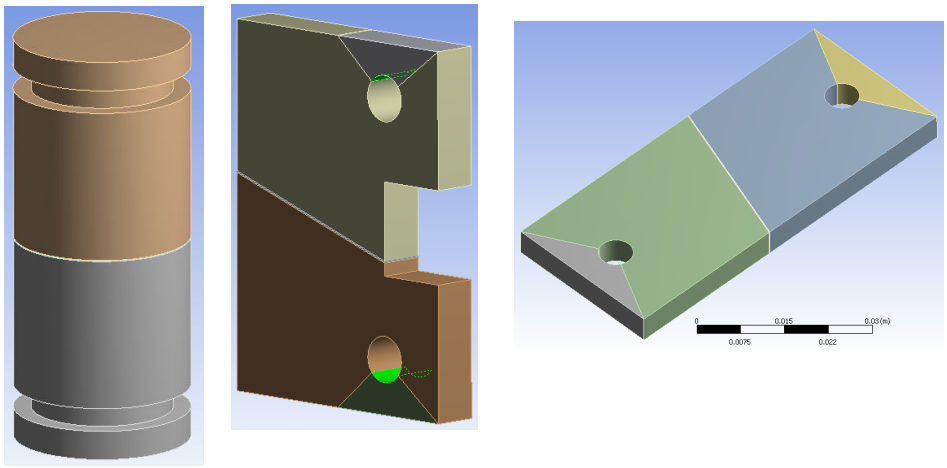

(a) (b) (c)

Figure 1: Adhesive joint solid models: (a) Butt joint, (b) cleavage joint and (c) scarf joint

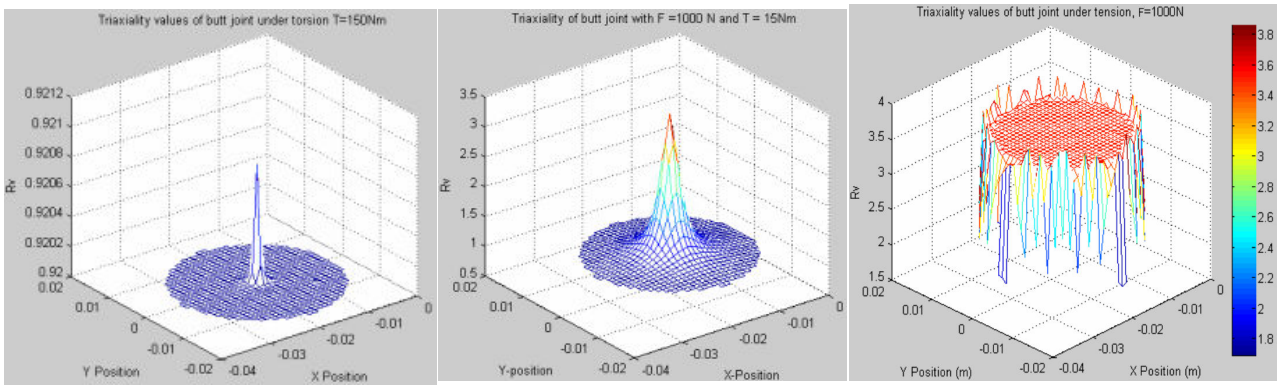

Figure 2: Triaxiality comparison in butt joint: (left) pure torsion, (centre) mixed load, (right) pure tension

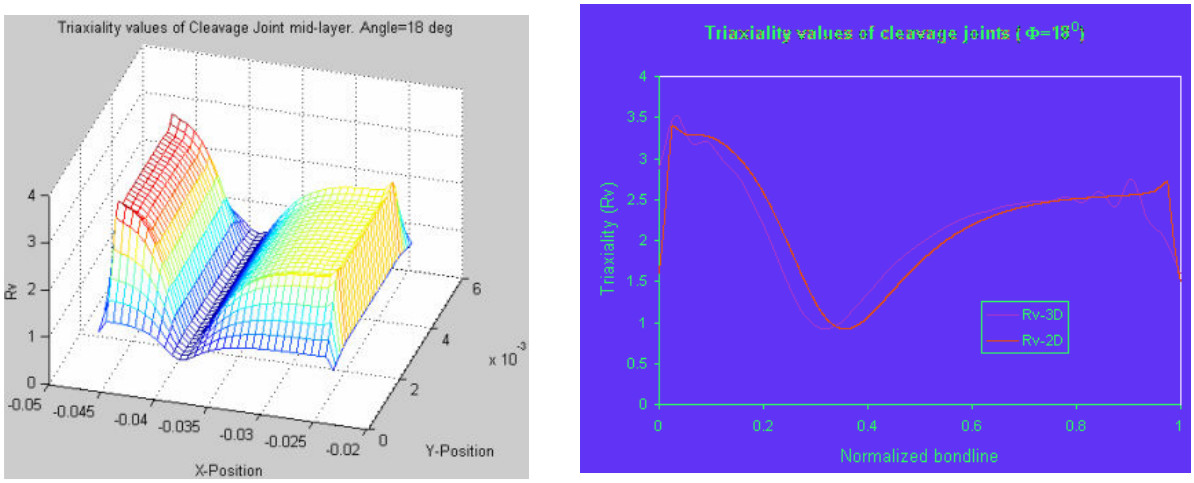

Figure 3: Triaxiality in cleavage joints: (left) 3D result, (right) 3D result in middle line vs plane strain

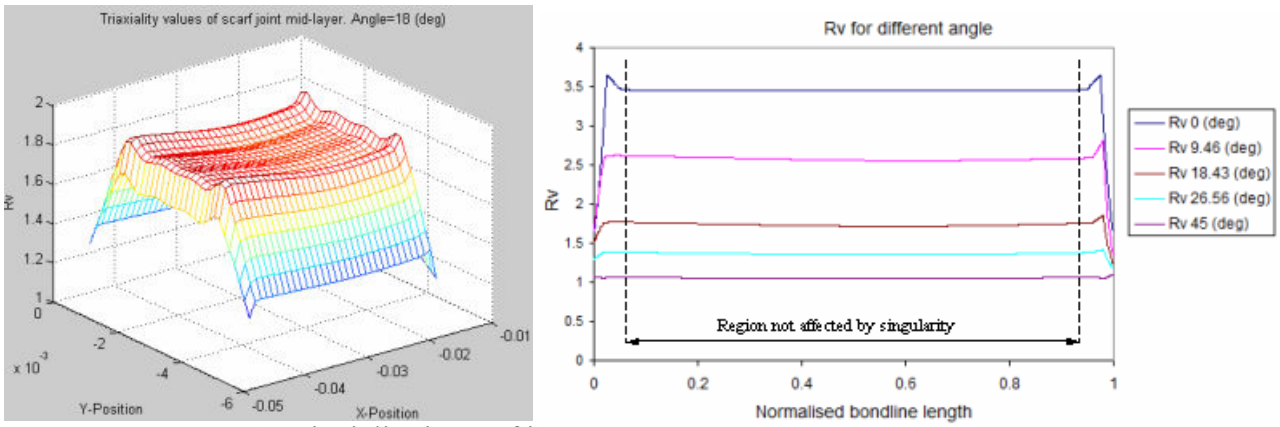

Figure 4: Triaxiality in scarf joints: (left) 3D result, (right) plane strain result for several bondline angles

Key Engineering Materials Vols. 385-387 (2008) pp 21-24
© (2008) Trans Tech Publications, Switzerland
doi:10.4028/www.scientific.net/KEM.385-387.21

A STUDY OF THE DYNAMIC PLANE STRAIN FRACTURE TOUGHNESS Of CONCRETE BY SHPB

Qu Jia[1, a] ,Zou Guang-ping[1, b]

[1]Harbin Engineering University ,Heilongjiang china 150001
[a]qujia@hrbeu.edu.cn, [b]gpzou@163.vip.com.cn

Keywords: concrete; plane strain fracture toughness; strain rate; Hopkinson press bar

Abstract: Concrete is a type of engineering composites which is widely used in military and civil structures. The static performance of concrete can not be used to estimate the variation of concrete under high strain rates under dynamic loads. By introducing the three point bending test under static and dynamic loads, the plane strain fracture toughness K_{IC} and K_{Id} were measured. Using the application of experimental-numerical method a three-dimensional model has been established by FEM software Ansys/LS-DYNA, to carryout transient analysis, and the response curves of stress intensity factor-time through the opening displacement of fracture. Thus, with obtaining the cracking time by the method of strain-gauge, the dynamic plane strain fracture toughness K_{Id} can be determined. By comparing K_{Ic} and K_{Id} we could conclude the result which meant concrete was more liable to crack under dynamic load.

1 Introduction

Concrete is a commonly used engineering composite, which is widely used in military and civil structures such as buildings, defense works and support units of tunnels and underground construction. Similar to other ceramic products, concrete shows the same sensitivity to strain rate under compression, tension and bending, which means that the static performance obtained in the laboratory cannot be applied to predict the change under high strain rate related to dynamic loads. Common static instrument cannot obtain high loading speed. Therefore, a specific instrument is needed. There is still no detection criterion for concrete impact test in our country.

2 Sample Design and Curing

Concrete is the composite with complex ingredients, which is different from metal and polymer with their good homogeneous property. The size of one ingredient, aggregate, is large and different sizes and shapes of defects, such as fracture and gas cavity, are distributed in and around the aggregate. The size of test sample should be large enough to do the test. Because of the limitation of the instrument, the Hopkinson compression bar with the diameter of 37mm is used in the test.

2.1 Material Mixture Ratio

Material	Concrete	Sand	Water
Property	Portland cement 425	Maximum particle diameter 5mm	Main-water
Mass ratio	1	1.65	0.35

To do impact test for concretes, on the one side, aggregate sizes should be reduced properly and on the other side, the diameter of SHPB should be as large as possible. [1] Material mixture ratio is shown in the table for the 37mm-diameter bar used in the test.

2.2 Curing Condition

Based on the common concrete mechanical performance testing method [2], the surface of the test sample under standard curing should be covered after molded in order to prevent water evaporation and should be under stewing for one or two days in 20±5°C. Then, number the sample and remove the mould. Lack of standard curing room, the curing of the test sample is in the stagnant water with PH value under 7 in 20±3°C. The test sample should be taken out immediately after 28 days curing.

2.3 Material Size

Determination of the test sample is commonly by certain geometric and size requirements. Any test sample with K_I calibrated expression and easy to test can be applied to determine K_{IC}. In the present paper, by GB4161-84 national criterion, a three-point bending test sample is applied, where W is 70mm, a is the length of precast fracture with a=W/2=35mm. It has to be mentioned that in the present paper, test samples with the same size is used in the determination of stress intensity factor under static and dynamic loads.

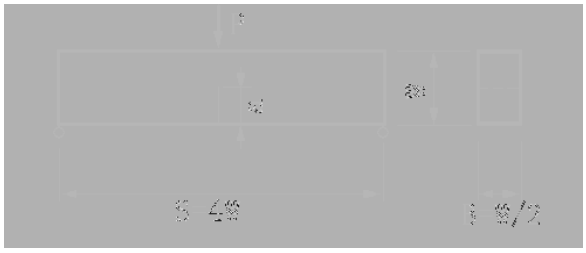

Fig.1 Measurement of pre-crack three-points bending specimen

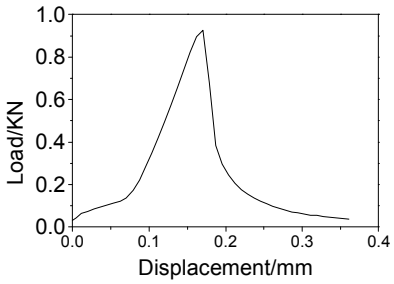

Fig. 2 Load-displacement relationship of three-points bending specimen

3 Test of Static Stress Intensity Factor in Plane Strain Problem

Instron4505 universal test machine is applied to do three-point bending test. The load-displacement curve is shown in Fig.2. From the figure, it can be seen that visible fragile fractural feature appears in concretes.

The moving velocity of INSTRON4505 universal test machine is 0.2mm per minutes constantly. The stress intensity rate obtained from the loading rate is 300 $MPa\sqrt{m}/s$ approximately. Thus, P_C=0.92KN. Substituting P_C into (1), it can be achieved that the static plane strain SIF K_{IC} is 1.06 $MPa\sqrt{m}$ approximately.

$$K_I = \frac{PS}{BW^{3/2}} f\left(\frac{a}{W}\right) \qquad (1)$$

4 Dynamic Fracture Toughness in Plane Strain Problem

4.1 Instruments and Test Principle

The instrument is derived from separated Hopkinson compression bar. The basic principle is that the cylindrical bullet with the length of 1m and the diameter of 37mm is launched by aerodynamic gun and impacts coaxially on incidence bar with the diameter of 2m. When the compression stress impulses transmitted onto the contact surface of incidence bar and the sample, some return to incidence bar and others load on the sample, which exert shock on the sample and make the sample collapse. Load on the sample P(t) is obtained by one-dimensional stress wave theory as

$$P(t) = EA(\varepsilon_i + \varepsilon_r) \qquad (2)$$

where ε_i and ε_r are incidence impulse and reflective impulse recorded by strain gauges on the bar, respectively, E and A are Young's modulus and the cross-sectional area of the compression bar, respectively and c is the velocity of elastic wave.

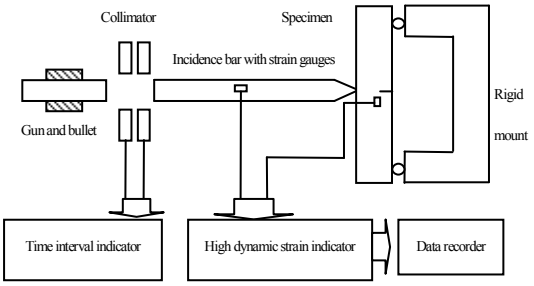

Fig. 3 Device for stress wave loading test

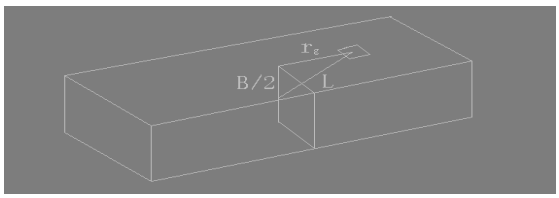

Fig. 4 Pattern for gluing strain-gauge

4.2 The Crack Initiating Time

The crack initiating time is determined by electric resistance strain gauge method. The basic principle is that a strain gauge is bonded near the crack tip and as the sample is under load, the strain is measured by the strain gauge increases with the load. When the crack initiates, unloading wave occurs that makes the strain decrease drastically. Thus, the crack initiating time t_f is the time corresponding to the maximum strain measured minus the time needed for strain wave transmitted from the crack tip to the strain gauge.[3]

4.3 The Loading Function of the Test Sample

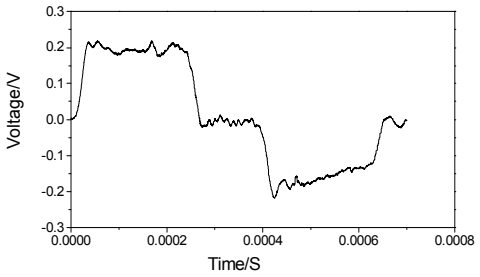

Fig. 5 The original voltage signal from the strain-gauge on the bar

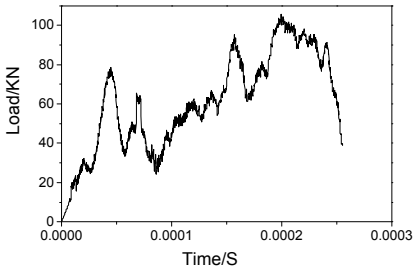

Fig. 6 Load-time curve obtained by the theory of one-dimension stress wave

Under shock loads, typical testing results are shown in Fig.5 and Fig.6. The original voltage signal data obtained by the strain gauge bonded on the incidence bar is illustrated in Fig.5. Fig.6 shows the load-time curve on the test sample obtained by 1-D stress wave theory.

4.4 Analysis by FEM

Due to the symmetry of the sample structure only one half of the sample is discreitsed. With the step size of 2×10^{-6}S, instantaneous FEM analysis proceeds. The total steps is 100 in computation. Similar to static FEM methods [4], polar coordinates is established on the crack tip and by the displacement equation near the Mode I crack tip, we have

$$U_i(r,0) = \frac{K_I}{\mu}\sqrt{\frac{r}{2\pi}} f_i(\theta) \qquad i = x, y \qquad (3)$$

where Ux is COD, Uy is the displacement in the load direction, $\mu$is the shear modulus. The right-handed

coordinates is established with the origin of Cartesian coordinates as the center point of the loading surface and the x direction parallel to the normal direction of the fracture surface, seen in Fig.4.6. In the equation above,

$$fx(\theta)=\frac{1}{4}\left[(2k+1)\sin\frac{\theta}{2}-\sin\frac{3\theta}{2}\right] \quad (4) \qquad fy(\theta)=\frac{1}{4}\left[(2k+1)\cos\frac{\theta}{2}-\cos\frac{3\theta}{2}\right] \quad (5)$$

In the plane strain condition: $k=\frac{3-\upsilon}{1+\upsilon}$, K_I can be obtained when substituting the displacement by FEM into (4). Because the displacement change at crack opening is significant, a relative accurate approximate solution can be achieved. Thus,

$$K_I=\frac{2\mu}{k+1}\sqrt{\frac{2\pi}{r}}Ux(r,\pi) \quad (6)$$

The equation above is accurate near the crack tip r→0. Therefore, displacement can be calculated by different r on the fracture surface. Substituting it into (6), the corresponding K_I can be obtained. $K_I\sim\frac{r}{W}$ curve is an approximate straight line when r is in a very small scale. By epitaxial method, the crossing point of this line and the longitudinal coordinate is the K_I.

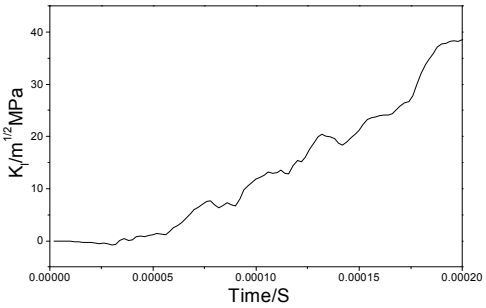

Fig. 7 Stress intensity factor vs. time

By method of extrapolation, the correct SIF-time curve can be obtained. Namely, elongate K_I~r/W line and make it intersect with longitudinal coordinate, the value of the longitudinal coordinate at the cross point is selected as the corresponding K_I, seen in Fig.7. Thus, the SIF rate of shock three-point bending can be derived from the differentiation with time. Then, the plane strain fracture toughness of the given test sample is $K_{Id}=0.88MPa\sqrt{m}$ and the SIF rate is $\dot{K}_{Id}=2\times10^5 MPa\sqrt{m}/s$ approximately.

5 Conclusions

During the testing of concrete three-point bending, fracture toughness is different under dynamic and static loads in contrast test samples. Moreover, the dynamic plane strain fracture toughness is lower than the static value. There are great differences between dynamic and static property. Thus, the influence of dynamic load on the structure should be considered in structural design. The investigation on concrete dynamic fracture toughness has significant importance to military bunkers and directional blasting.

References

[1] Hu Shi-sheng , W ang Dao-rong: Explosion and Shock Waves, 3, Vol22 (2002).
[2] *GB4161-84 Nat. Stan. Exp. Meth. plane strain fracture toughness K_{IC} of metal*(1985).
[3] J.W.Dalley, R.J.Sanford: Experimental Mechanics,Vol6:381-388(1987).
[4] Wang Duo: *Fracture Mechanics*.(Harbin institute of technology press, China 1989).

Key Engineering Materials Vols. 385-387 (2008) pp 25-28
© (2008) Trans Tech Publications, Switzerland
doi:10.4028/www.scientific.net/KEM.385-387.25

About the effects of residual stress states coming from manufacturing processes on the behaviour of riveted joints

F. Caputo[a], G. Lamanna[b], A. Soprano[c]

Dept. of Aerospace and Mechanical Engineering, 2nd Univ. of Naples, Aversa (CE), Italy

[a]francesco.caputo@unina2.it, [b]giuseppe.lamanna@unina2.it, [c]alessandro.soprano@unina2.it

Keywords: riveted joint, residual stress, bearing resistance.

Abstract. A very large number of variables affect the response of bolted or riveted joints typically used in aerospace applications: geometry of the joint, characteristics of the sheets, friction between sheets, geometry of head and kind of fastener, amplitude of clearance before assembly, mounting axial load, pressure effects after manufacture. It must be also recalled that these parameters influence the many failure modes existing for such joints, among which a relevant importance is attributed to bearing.
The present paper deals with the study of the influence of assembly parameters on the joint operational behaviour and in particular with the analysis, performed through numerical simulations, of the influence of the residual stress-strain state coming from the riveting operation on the bearing resistance of an aluminium alloy joint.
This work has been developed within the FP6 research project called MUSCA (Non linear static multiscale analysis of large aero-structures).

Introduction

The load transfer mechanism within as well as among fasteners has been recognized for a long time as one of the main causes which affect both static resistance and fatigue life of joints; unfortunately, such components, which are often considered as very simple, exhibit such a complex behaviour that it is far from being deeply understood and only in recent times the coupling of experimental tests with numerical procedures has let researchers begin to obtain some knowledge about the effects which come from assuming one of the available designs.

A wide spectrum of results and theories about load transfer mechanism in the riveted or bolted joints have appeared since the end of the Second World War, as their use has been increasingly spreading; we have just to observe that they deal, for the largest part, with bolted joints, which require a more limited number of parameters than riveted ones, but in any case in the more recent years also a quite noteworthy series of papers have been published with reference to the case of riveted joints [1, 7].
The requirement of a wide range of different researches dealing with the case of riveted joints is to be found in the large number of variables which can affect the response of such components, among which we can list: geometry of the joint (single or several rows, simple- or double-lap joints, clamping length, fastener geometry), characteristics of the sheets (metallic, non metallic, degree of anisotropy, composition of laminae and stacking order for laminates), friction between sheets, geometry of head and kind of fastener (solid, blind – or cherry – and self- piercing rivets, besides many types now available), amplitude of clearance before assembly, mounting axial load, pressure effects after manufacture.

Besides the aforesaid parameters, it must be recalled that different failure modes exist for such joints: shear, bearing and so on.

From all above it follows that today a great interest is increasingly being devoted to the problem of load transfer in riveted joints, but that no exhaustive analyses have been still carried out insofar: the studies remembered above, in fact, deal with peculiar aspects of such joints, and little efforts

have been directed for example to the connection between riveting operation and response of the joint.

The activity developed within this paper deals with the following aspects:

1. modelling and simulation of the riveting operation, with reference to a solid rivet;
2. development of bearing experimental tests in order to set-up numerical model of each sheet of the riveted joint (especially for what concerns material properties);
3. assessment of a numerical procedure to transfer stress/strain state from the FE explicit analysis of the riveting process to the FE implicit analysis of the joint structural behaviour;
4. investigation of the influence of the riveting process on the bearing resistance of a riveted joint.

For what concerns the modelling and the simulation of the riveting operation, the adopted procedure is illustrated in [8].

Bearing test and FE model set-up

Using an apparatus (Zwick Roell Z010-10kN) which is available at laboratories of the Second University of Naples, a series of bearing experimental tests (ASTM E238-84) have been carried out on a simple aluminium alloy 6xxx T6 holed plate (28.5 x 200 x 3 mm^3, hole diam. 6 mm), equipped with a 6 mm steel pin, obtaining the response curves shown in Fig. 1.

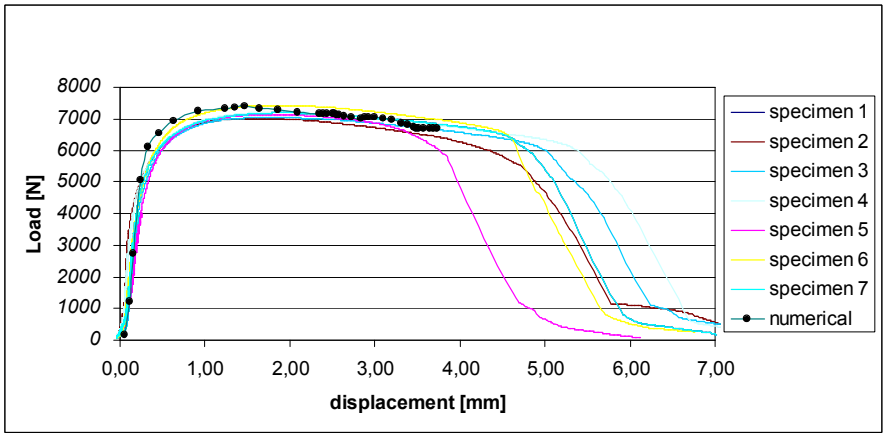

Figure 1: Results from experimental bearing tests

In the same graph numerical results have been illustrated, carried out from non linear static FE simulations developed by using ANSYS ver. 10 code. As it is possible to observe the agreement between numerical and experimental results is very good. This experimental activity allowed to set-up and develop the FE model (Figure 2) of each single sheet of the joint and, in particular, their elastic-plastic material behaviour.

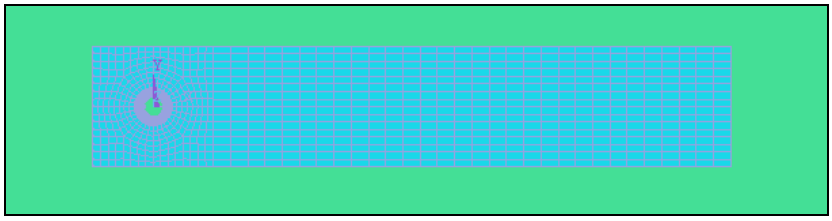

Fig. 2: FE model of single joint sheet.

Effect of riveting process on the joint behaviour

In order to investigate on the influence of the riveting process, it has been necessary at first to transfer the residual stress-strain distribution around the hole coming from the riveting process, which was obtained by means of the FE explicit analysis of the riveting operation illustrated in [8], to the model of the riveted joint (sheets dim. 28.5 x 200 x 1 mm^3, hole diam. 6 mm). The procedure

applied to transfer the residual stress-strain state from riveting operation to the ANSYS FE model, consists in the fitting of the deformed rivet into the undeformed plates (fig. 3a) and in the subsequent recovery of the real interference as the first steps of the implicit FE analysis; some of the results obtained by using this technique are shown in figures 3 and 4 where rivet and sheets results coming from the implicit analysis after interference recovery (fig. 3b and 4a) can be compared with those obtained from explicit analysis [8] after riveting operation (fig. 3c and 4b). As it is possible to observe the results are in a very good agreement from both a qualitatively and a quantitatively point of view.

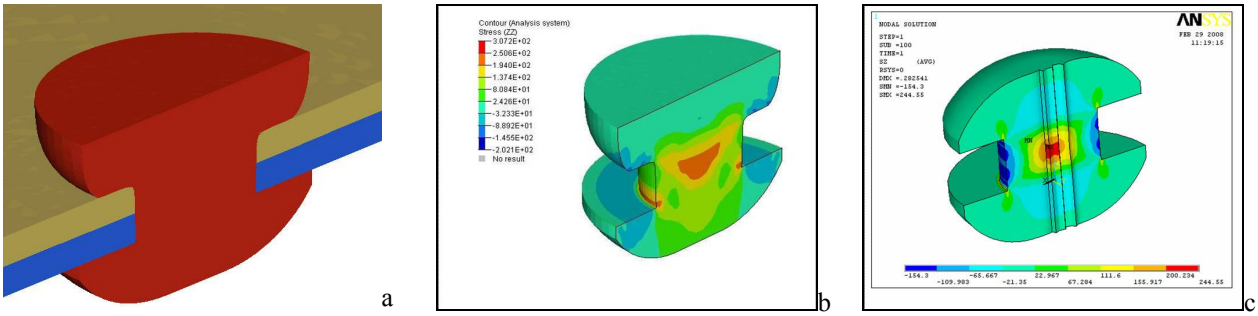

Fig. 3: Axial stress in rivet as coming from explicit and implicit analysis

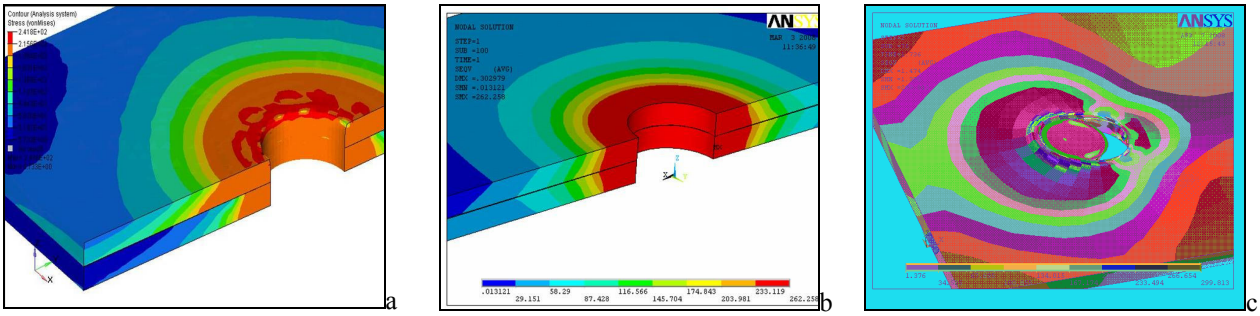

Fig. 4: Von Mises stress in sheets as coming from explicit and implicit analysis

After the riveting effect has been transferred to the joint the sheets have been loaded along the longitudinal direction and results in terms of axial load vs. axial displacement have been compared (fig. 5) with results obtained from the analysis of the same joint without taking into account the riveting effect.

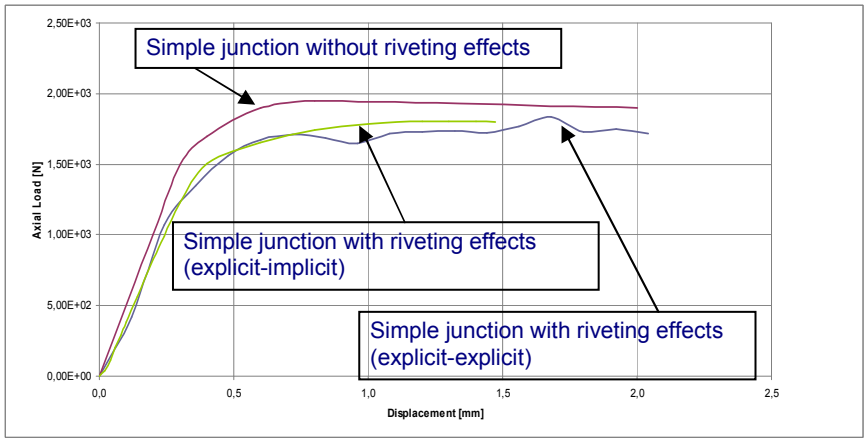

Fig. 5: bearing behaviour of the joint

In figure 4c it is illustrated the distribution of Von Mises stress around the hole of one sheet of the joint corresponding to the maximum load value.

On the same graph, results obtained by analysing both the riveting operation and the axial loading by means of the explicit codes are illustrated too. This procedure is obviously very time consuming compared to the use of an explicit to implicit scheme.

As it is possible to observe from the graph in figure 5, the riveting operation effects cause a reduction of the bearing resistance of the joint of about 10%.

Conclusion

The application of the proposed methodology to the study of the influence of the residual stress-state coming from the riveting operation on the bearing behaviour of a simple joint provided significant results and it can be successfully applied to any type of joint/rivet configuration. The most difficult step in the procedure, once simulated separately the riveting operation of a single rivet, has been to transfer displacement results from explicit analysis to the implicit one, which for high value of initial rivet-hole interference can be time consuming due to the convergence difficulties encountered in recovering the final interference by using implicit FE contact algorithms. Other procedures have been considered, as for examples to analyse by explicit FE solver both the riveting operation and the axial loading of the whole joint, but it revealed to be excessively time expensive.

Anyway, by considering results from the reference case analysed in this work it is possible to conclude that residual stress-strain state from riveting operation can influence sensibly the final bearing resistance of the joint.

References

[1] - T.J. Fitzgerald, J.B. Cohen: Residual Stresses in and around Rivets in Clad Aluminium Alloy Plates, Materials Science & Technology, vol. AI88, pp. 51-58 (1994);

[2] - J. Zhang, J.H. Park, S.N. Atluri: Analytical Fatigue Life Estimation of Full-Scale Fuselage Panel, in: Proc. of FAA-NASA Symposium on the Continute Airworthiness of Aircraft Structures, DOT/FAA/AR-97/2, vol. 1, pp. 51-62 (1997);

[3] - B. Langrand, E. Deletombe, E. Markiewicz, P. Drazétic: Numerical Approach for Assessment of Dynamic Strength for Riveted Joints, Aerospace Science & Technology, vol. 3, pp. 431-446 (1999);

[4] - B. Langrand, E. Deletombe, E. Markiewicz, P. Drazétic: Riveted Joint Modeling for Numerical Analysis of Airframe Crashworthiness, Finite Elements in Analysis and Design, vol. 38, pp. 21-44 (2001);

[5] - B. Langrand, L. Patronelli, E. Deletombe, E. Markiewicz, P. Drazétic: Full Scale Characterisation for Riveted Joint Design, Aerospace Science & Technology, vol. 6, pp. 333-342 (2002);

[6] - B. Langrand, J. Fabis, A. Deudon, J.-M. Mortier: Experimental Characterisaion of Mechanical Behaviour and Failure Criterion of Assemblies under Mixed Mode Loading. Application to Rivets and Spotwelds, Mècanique & Industries, vol. 4, pp. 273-283 (2003);

[7] - L. Ryan, J. Monaghan: Failure Mechanism of Riveted Joint in Fibre Metal Laminates, J. of Materials Processing Technology, vol. 103, pp. 36-43 (2000);

[8] - A. Soprano, F. Caputo, A. Grimaldi: A numerical Investigation about the effects of the riveting operation on the strength of joints, Key Engineering Materials, vols 348-349, pp 265-268, 2007.

Key Engineering Materials Vols. 385-387 (2008) pp 29-32
© (2008) Trans Tech Publications, Switzerland
doi:10.4028/www.scientific.net/KEM.385-387.29

FAILURE ANALYSIS OF DIESEL ENGINE INTAKE VALVE

Ali GÖKSENLİ[1, a] and Barlas ERYÜREK [1,b]

[1] Faculty of Mechanical Engineering, Istanbul Technical University, Taksim, Istanbul, Turkey.

[a] goksenli@itu.edu.tr, [b] eryurekb@itu.edu.tr

Keywords: Valve, Failure analysis, Faulty assembly, Impact ratio

Abstract. In this study failure analysis of a mini van diesel engine intake valve is analyzed in detail. Failure occurred at the groove of the valve. First mechanical and chemical properties of the valve are determined. After visual investigation of the fracture surface it is concluded that fracture occurred due to fatigue. Damaged valve, valve seat, cylinder block and piston surface is investigated and construed. Failure constituted 300 kilometers after the rectification of the engine. Therefore rectification and assembly steps of valve and engine parts are analyzed in detail. Considering assembly, design and working conditions of the engine, stresses occurring at the failure surface are calculated. Endurance limit and fatigue safety factor is determined. Because of high fatigue safety factor, reasons for failure are investigated and effects causing stress increase at groove of the valve are established. These effects are faulty assembly of the valve and valve seat causing a high impact effect. In conclusion effect of impact ratio on stress increase is explained.

Introduction

Intake valve, investigated in this paper, was used in a diesel engine of a minivan. Failure occurred at the groove of the valve (Fig.1). It is reported that fracture constituted 300 kilometers after the rectification of the engine.

Figure 1: Damaged valve

Investigations

Material Identification. As no information with respect to the chemical composition of the valve material was available, the first task in the failure analysis was the material identification. The chemical analysis of the valve was carried out by Atomic Absorption Spectroscopy and is reported in Table 1. Later micro structural analysis was carried out. The hardness of the valve, measured using Rockwell hardness tester, is 54 HRC at the surface and 39 HRC at the center of the valve, which indicates that surface hardening is applied to the valve. Considering chemical, microstructural and hardness values, valve material is estimated as Martensitic Stainless Steel T410 (X15Cr13). T410 has high corrosion resistance even in high temperatures and it is widely used as valve material. According catalogue data [1], its tensile strength is 986 MPa.

Table 1: Chemical composition of the valve

C	0,147	**Ni**	0,38	**P**	0,031	**Si**	0,96
Cr	12,47	**Mn**	0,97	**S**	0,028		

Visual Investigation Of Fracture Surface and Damaged Engine. After macroscopic investigation it is revealed that fracture occurred at the valve groove (Fig. 2). The valve is connected to the valve retainer by the help of locks.

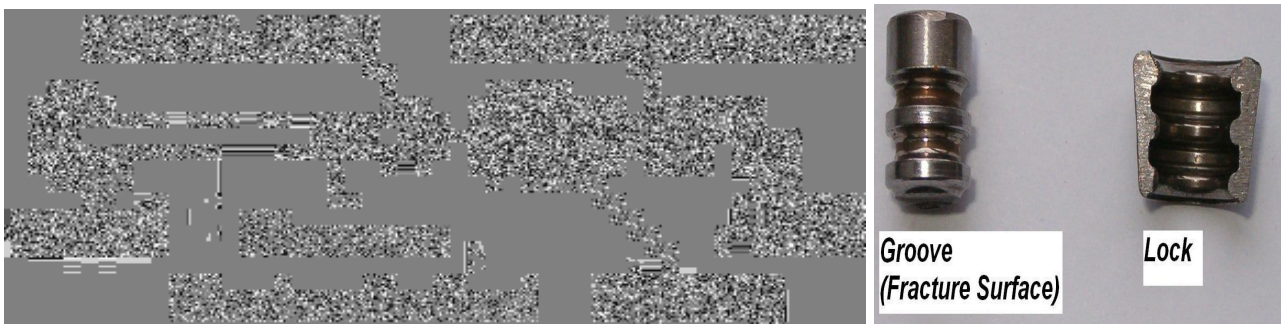

Figure 2: Valve system and fractured valve groove

By surface examination fatigue lines are determined. Figure 3 shows a typical tensile bending fatigue fracture surface. Fatigue cracks initiated circular and moved almost along the whole surface. The small area of brittle fracture surface indicates a low maximum applied stress.

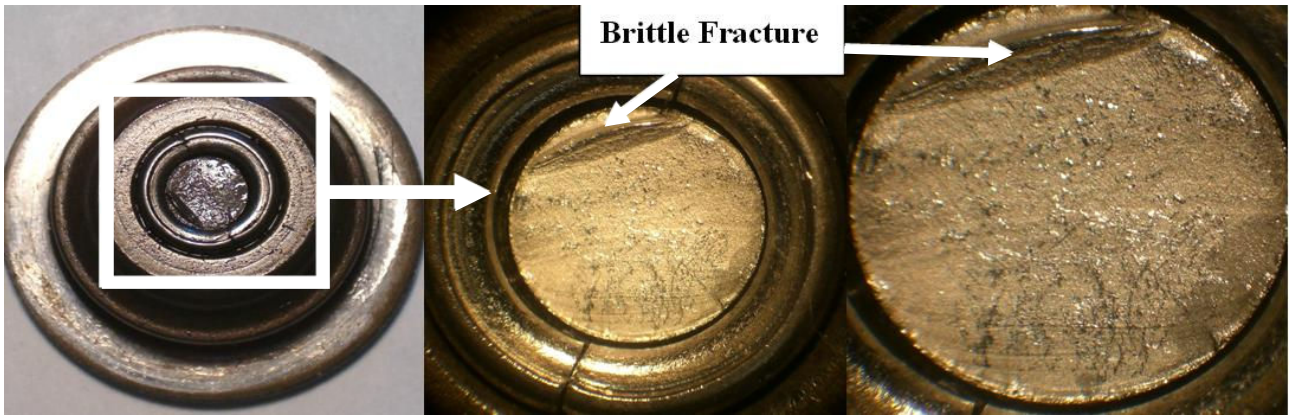

Figure 3: Fracture Surface

After surface investigation of the cylinder block and piston surface, deep split marks are determined (Fig. 4). These marks are formed by the damaged valve seat which was broken, probably at the last cycles of the engine.

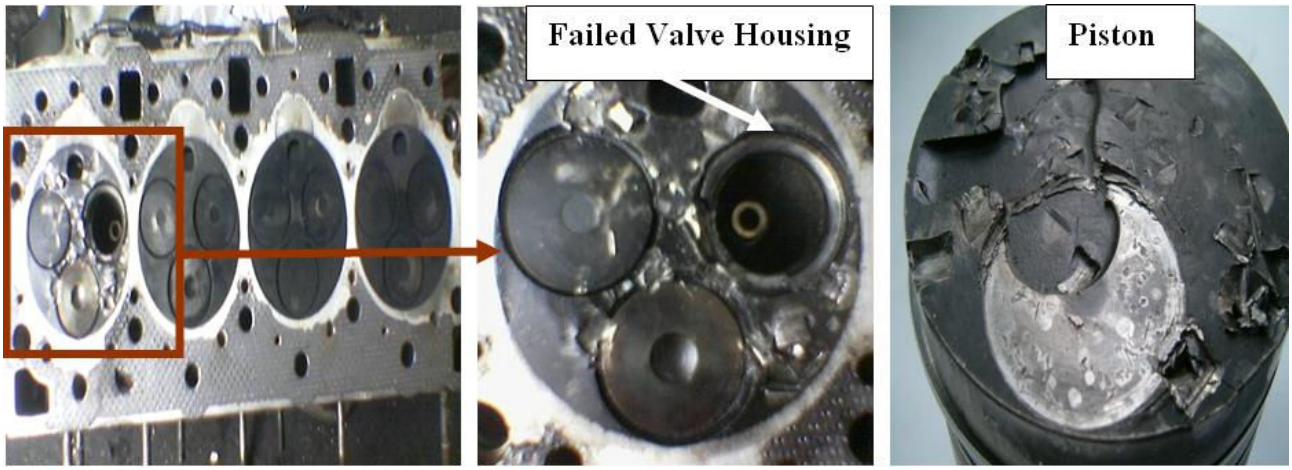

Figure 4: Damaged piston block and piston surface

Stress Calculations. Analytical analysis was performed to determine normal stresses at the groove of the valve where fracture occurred. Using Profile Projector, radius of curvature was measured as

0.75 mm and diameter of the valve as 5 mm. Theoretical notch effect is determined as 1,82 using relevant tables [2]. Fatigue notch effect depending on material and geometry is calculated (using related equation) as 1,38. Impact ratio coefficient is 1,2. To determine stress value at the groove of the valve, forces acting on the valve is investigated. During operation two kind of forces are acting on the valve; spring force (caused by the deformation of the spring) and inertia forces. During assembly of the valve, the free length of the spring is decreased 8,5 mm. During exhaust process, the valve performs a displacement of 3,25 mm. Therefore maximum deformation of the spring is 11,75 mm. Spring stiffness coefficient is 38 N/mm. As a result, acting maximum spring force is 446 N. By maximum engine speed (6300 rot/min), acceleration of the valve is 6,3 mm/sec^2 [3]. The weight of the valve and retainer is 0,269 kg. Inertia force is calculated as 1695 N. Maximum total force acting on the valve, considering spring and inertia forces, is 2141 N. Stress value, originating at the fracture surface (σ_F), using fatigue notch effect and impact ratio coefficient, is σ_F = 179 MPa.

Endurance limit (σ_E) can be calculated as $\sigma = 0{,}5 \cdot 986 = 493 MPa$. Considering size factor (k_D) as (for diameter 5 mm) k_D=0,99 and surface factor (very fine polished) k_S= 0,98 [4], the modified endurance limit (σ^I_E) is $\sigma^I_E = 479 MPa$. In this case, fatigue safety factor (υ) can be calculated as;

$$\upsilon = \frac{\sigma^I_E}{\sigma_F} = \frac{479}{179} = 2{,}68 . \quad (1)$$

Determining Cause of Failure. From equation 1 can be clearly be seen that a high fatigue safety factor is present and stresses occurred at the fracture surface is quite under the endurance limit. Therefore no fatigue fracture ought to be originated. For this reason carefully analysis was carried out to find the reason for failure. Probably cause of stress raise might be; high micro notch effect, increase in valve spring deformation amount or high impact effect. Carefully macroscopic analysis was carried out on lock and valve grooves but no micro cracks are determined causing notch effect and raise in stress value. Later assembly steps are investigated in detail, because failure occurred only 300 km after the rectification of the engine. It is reported that during the rectification, valve, valve guide and valve seat are modified. A new valve seat is placed inside the housing (Fig. 5).

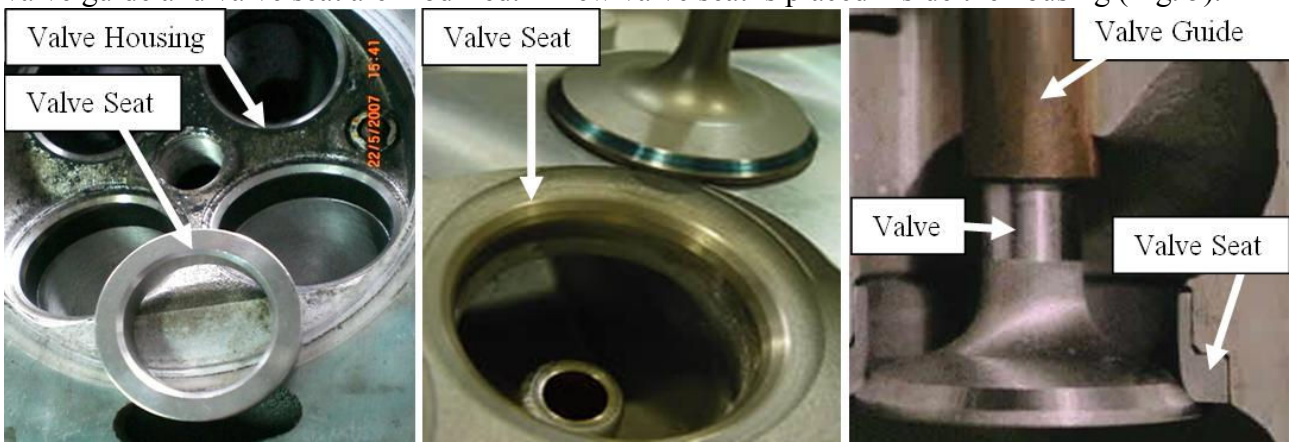

Figure 5: Valve, valve guide and valve seat after assembly

By faulty and incorrect assembly of the valve seat, the seat might not be exactly mounted in its housing and about 2-3 mm thickness of valve seat would be outside of the housing. Because of this the valve would hit the piston surface during engine operation at the top dead center (TDC), because the distance of the piston TDC and valve during operation is 2-2,5 mm [3]. By observation of cylinder surface, a bright circular area can be seen (Fig. 6), which is caused by the contact (impact) of the valve with the piston surface, which also supports our explanation that valve seat is not correctly assembled in its housing and is X mm (Fig. 6) outside of the housing. This contact caused a very high impact effect concluding in enormous raise in stress values.

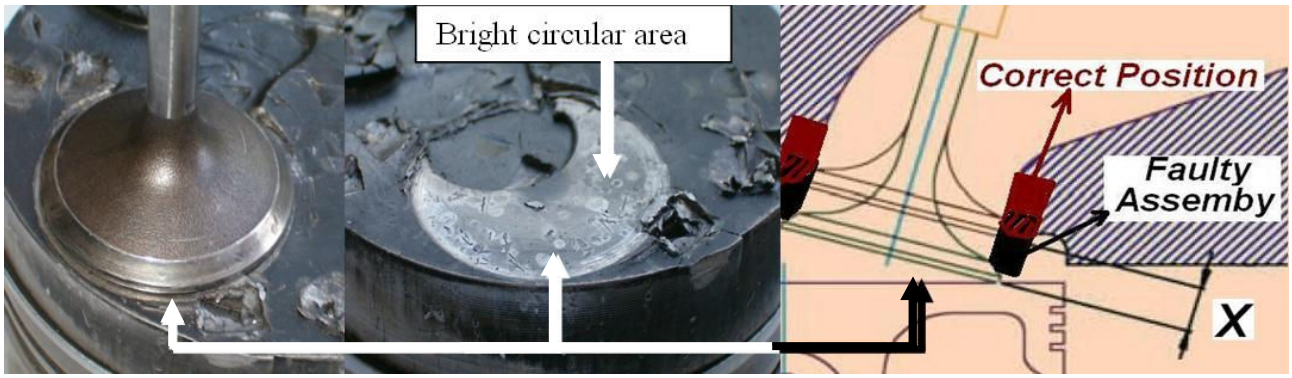

Figure 6: Bright circular area, which is caused by the contact of the valve with the piston surface

Fatigue Calculations. For fatigue analysis, average vehicle velocity is assumed to be 65 km/h and average diesel engine speed as 2400 rot/min. Until failure occurred (300 km), valve is exposed to be in contact with the piston $6{,}6 \cdot 10^5$ times. This contact caused a high impact effect and raise in stress values. To estimate the impact effect, stress-cycle and stress-impact ratio graphics are constituted (Fig.7). In figure 7-a it can be seen that stress value constituted at fracture surface, considering cycle number, $6{,}6 \cdot 10^5$, is 503 MPa. To achieve this stress value, impact ratio must increase from 1,2 (assumed value in calculations considering no contact of the valve with the piston) to 3,38 (Fig. 7-b). In this case fatigue safety factor is decreased to 0,95.

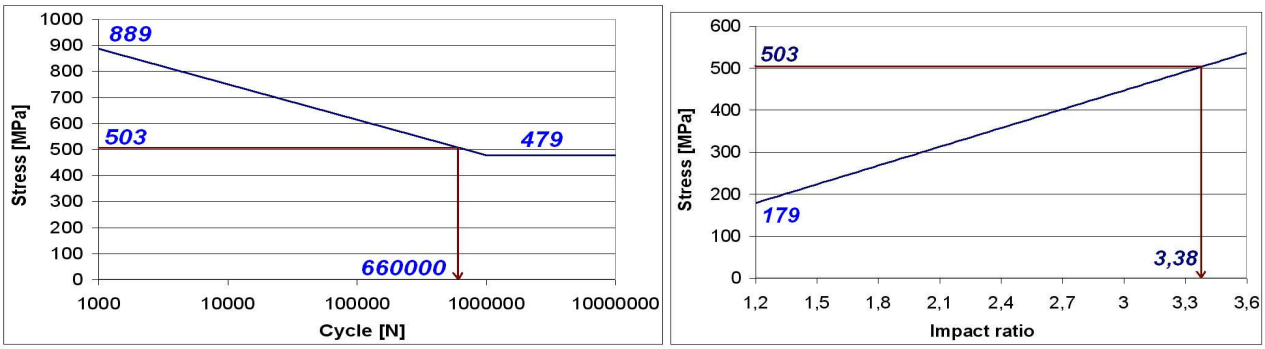

*Figure 7: S*tress-cycle (a) and stress-impact ratio (b) relations

Summary

Failure analysis of a minivan diesel engine intake valve is analyzed. First mechanical and chemical properties of the valve are determined. After visual investigation of the fracture surface it is concluded that fracture occurred due to fatigue. Damaged valve, valve seat, cylinder block and piston surface is investigated and construed. Rectification and assembly steps of valve and engine parts are analyzed in detail. Stresses occurring at the failure surface, endurance limit and fatigue safety factor is calculated. Because of high fatigue safety factor, reasons for failure are investigated and effects causing stress increase at groove of the valve are determined. These effects are faulty assembly of the valve and valve seat causing a high impact effect. In conclusion effect of impact ratio on stress increase is analyzed.

References

[1] A. Buch: Fatigue Data Handbook, (Trans Tech. Publisher, 1998).
[2] B.I.Eryürek: Failure Analysis, (Birsen Pub., Istanbul, 1993).
[3] H. Zhao and N. Ladammatos; Engine Combustion Instrumentation and Diagnostics, (SAE International, 2001).
[4] S. Gülec and A. Aran: Fatigue Strength of Steels and Cast Irons, (TUBITAK Pub., 1983).

Key Engineering Materials Vols. 385-387 (2008) pp 33-36
© (2008) Trans Tech Publications, Switzerland
doi:10.4028/www.scientific.net/KEM.385-387.33

An analysis of aging characteristics of tilting train under accelerated aging environment

Jeong-Pyo Nam[1, a], Sung-Ho Yoon[2, b],Young-En Hwang[2, c], Hong LI[3, d] , Qingfen LI[4, e]

[1]College of Materials Science and Chemical Engineering, Harbin Engineering University, Harbin 150001, China

[2]College of Mechanical Engineering, Kumoh National Institute of Technology, Kumi, Korea

[3] College of Civil Engineering, Harbin Engineering University, Harbin 150001, China

[4]College of Mechanical and Electrical Engineering, Harbin Engineering University, Harbin 150001, China

[a]urin7942@hotmail.com, [b]shyoon@kumoh.ac.kr, [c]hwangye21@hotmail.com
[d]leeh2005@sohu.com, [e]qingfli@yahoo.com.cn

Keywords: Tilting train; Environmental factors; Thermo-mechanical couple; UTM; DMA.

Abstract. In this study, the effect of combined environmental factors such as ultraviolet ray, high temperature and high moisture on mechanical and thermal analysis properties of glass fabric and phenolic composites are evaluated through a 2.5KW accelerated environmental aging tester. The environmental factors such as temperature, moisture and ultraviolet ray applied of specimens. A xenon-arc lamp is utilized for ultraviolet light and exposure time of up to 3000 hours are applied. Several types of specimens - tensile, bending, and shear specimens that are warp direction and fill direction are used to investigate the effects of environmental factors on mechanical properties of the composites. Mechanical degradations for tensile, bending and shear properties are evaluated through a Universal Testing Machine (UTM). Also, storage shear modulus, loss shear modulus and tan δ are measured as a function of exposure time through a Dynamic Mechanical Analyzer (DMA). From the experimental results, changes in material properties of glass fabric and phenolic composites are shown to be slightly degraded due to combined environmental effects.

1. Introduction

High-speed rail is becoming a popular mode of travel in East Asia. Although national governments may be ready for trains speeding along at 300 km/h or more, the regional geography is not. Tracks must often snake through mountainous terrain and other obstacles, which can create problems at high speeds. Tilting trains can keep the speeds up without causing passengers uncomfortable. Polymeric composite materials have high specific properties and specific strength, and superior corrosiveness, so they have been widely used for aerospace, port facilities, and train carbody. Specially glass fabric/phenolic composites are advantageous to manufacture the structural materials which curve shape and heat-resisting property are demanded by properties of fabrics form and phenolic resin. However, they can bring about problems in operating real composites structure. Because mechanical properties, thermal properties, and physical properties are changed by environmental factors on during long time exposure. In this study, the durability by aging of glass fabric/phenolic composites, which can be applied in real train carbody, were tested with using accelerated environmental aging tester. Specimens applied in accelerated aging are separated with Warp direction and Fill direction, those were performed in evaluation of mechanical properties through UTM, evaluation of thermal dynamic properties through DMA.

2. Materials and Methods

Glass fibric/phenolic composites used in this experiment were molded through the autoclave with using prepreg (Glass fabric #650/ AP300, Hankuk Fiber Glass co., LTD) that glass fiber fabrics

(Glass fabric #650) were added in phenolic resins (AP300) for high temperature hardening. Tensile specimens (175mm×25mm×3mm), bending specimens (125mm×25mm×3mm) and shear specimens (76mm×20mm×3mm) were molded with applying the autoclave after to laminate 0.5mm-thickness of glass fiber fabrics prepreg up to 6 layers.

Accelerated aging tester shown in Fig. 1 has heating wire, water spray, and 2.5KW xenon-arc lamp inside so that it can accelerate conditions of temperature, rain and snow, and ultraviolet light by sunlight. Test conditions are suggested by ASTM G155-00a[7] and ATLAS, one of accelerated aging environmental tester manufacturer to do accelerated aging test, water was sprayed for 18 minutes every 2hours when lamp was on, and at this time it considered that 60°C of temperature, 80%RH of humidity. The data, which is collected to identify whether temperature, moisture, and ultraviolet are met to the setting-up condition, is shown in Fig. 2. It indicates that moisture is well-matched to the set-up 80%RH, relative humidity gets higher when to spray water for 18 minutes every 2hours, and internal temperature of chamber is well-matched to the set-up 60°C. it indicates that it is 80°Cin specimens installed on specimen fixed equipment due to ultraviolet light and radiant heat, and where ultraviolet light is uniform according to exposure time.

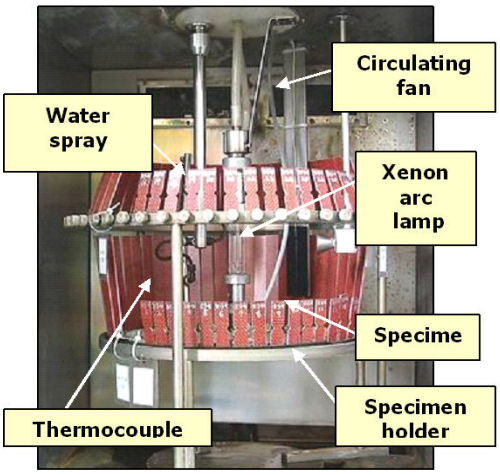

Figure 1 Internal Chamber

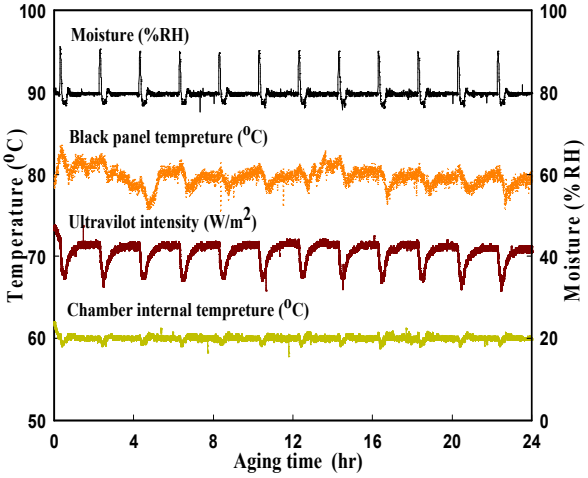

Figure 2 Acquisition data of control parameters

Mechanical property testers, which is consist of load tester, signal amplifier, A/D converter (National Instruments, USA), and data collector, was used to evaluate mechanical properties such as tensile, bending, and shear properties of glass fabric/phenolic composites exposed in environmental for long time. Load tester is Zwick/Z100, and the strain to the load of action was measured with adhesive strain such as strain gage or non-adhesive strain sensor such as LVDT and extensometer. Mechanical properties of composites were evaluated by regulated procedure in ASTM. Each per second to analyze the experimental results are conducted statistical treatment to incline presumed value of average, remove outlier that increases the presumed value of accuracy, and get high reliable result value from the result data. Chauvenet standard[8] was applied to detect outlier, the way that remove vertex points if the probability value including each declination from data average is smaller than 1/2n, and re-decides statistical value from residual data was adapted.

Dynamic Material Analysis (DuPont DMA983) was applied to examine thermal analysis properties, such as storage shear modulus G', loss shear modulus G" and tanδ, which are against Warp direction and Fill direction of Glass fabric/Phenolic composites exposed in environmental factors (Eq.1~Eq.3).

$$G'(\omega) = \frac{\sigma_0}{\varepsilon_0}\cos\ \delta \tag{1}$$

$$G''(\omega) = \frac{\sigma_0}{\varepsilon_0}\sin\ \delta \tag{2}$$

$$\tan \delta = \frac{G''}{G'} \tag{3}$$

Specimen was installed on specimen fixed equipment in chamber charged with nitrogen gas with 32mm of span, and scoped by 0.2mm of amplitude, 1Hz of cycle. At this time, temperature was increased from 30°C to 300°C by 2°C/min of rate of temperature increase.

3. Result of Evaluation of Environmental Aging Properties

Changes of tensile, bending, and shear properties by exposure time are show in Fig. 3. These result are from performing on 6 specimens each, modulus and strength in Warp direction are presented higher than those in Fill direction because of fiber density of specimens length direction. As exposure time is increasing, modulus and strength are decreased little by little as compared to before to be exposed. Specially if specimens in Warp direction are exposed for 1000hours, tensile, bending, and shear modulus are decreased by 10.9%, 6.5%, and 2.2% each before the exposure, and tensile, bending, and shear strength are decreased by 2.5%, 7.0%, and 1.7% each. When it is exposed in environmental factors for 3000hours, bending and shear modulus are increased by 0.5% and 0.1% each more than when it is exposed for 1000hours, as the reason of these phenomenon, firstly it can be caused from post-curing of composites exposed in environmental factors when exposure time is increased, and secondly it is estimated that properties of each specimen are not even as each of specimens are mass produced. When it is exposed in environmental factors for 1000hours, bending properties in Warp direction are seriously decreased than those in Fill direction, because exfoliation on plastic layer occurred on surface of composites has greater properties decrease in Fill direction where relatively more plastics are as one major factor of aging.

Typical storage shear modulus G', loss shear modulus G", tanδ to DMA specimens before to be exposed are shown in Fig. 4. Here storage shear modulus that is glass state at normal temperature has primary flatness area, it is decreased slowly as temperature is higher, and it is rapidly decreased around at glass transition temperature that glass state is changed into rubber state. Loss shear modulus and tanδ diagram before and after transition temperature are caused from interference effect of phenol by effect of bubble by adduct, such as moisture or carbonic acid gas occurred during composites during molding, and wide distribution of molecular weight, it is difficult to read loss shear modulus and tanδ storage shear modulus with being different from storage shear modulus.

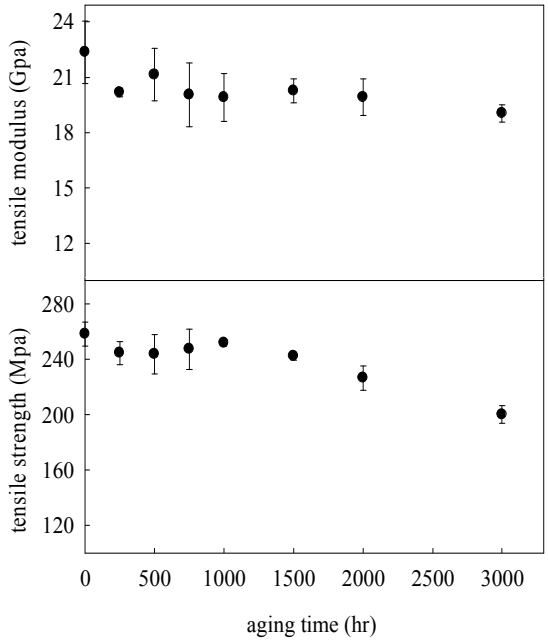

Figure 3 Variation of mechanical properties w.r.t aging time of warp direction acquisition data of control parameters

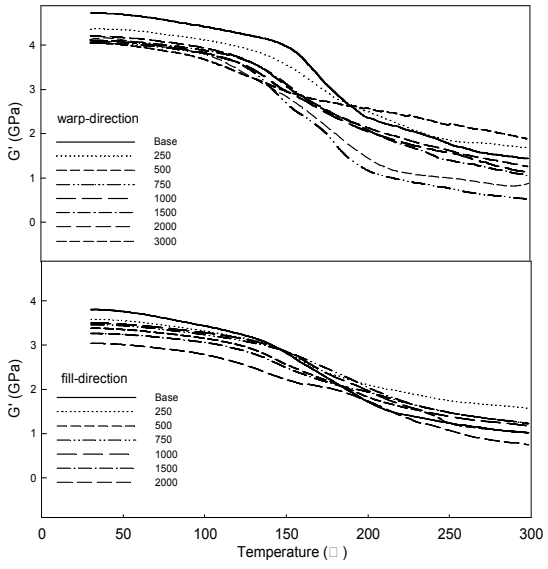

Figure 4 DMA result of glass fabric/phenolic composite

4. Conclusion

We could have following conclusion through the study to assessment of environmental factors by using accelerated aging tester to materials applicable on composites driver-cap of Tiltiing train.

Modulus by Warp direction and Fill direction of glass fabric/phenolic composites exposed in environmental factors is relatively insensible, but strength can be sensitive more than modulus, and these properties tend to be decreased as the exposure time is increased.

Storage shear modulus and glass transition temperature are decreased in both of Warp direction and Fill direction as the exposure time is increased. Glass transition temperature was increased a little in early exposure stage because of post-curing of composites, but if the exposure time is longer, chain cutting of composites occurs dominantly, and then it is gradually decreased.

5. Postscript

This study was progressed as a part of railroad technical development project of Korea Railroad Administration

References

[1] J. R. Reeder, D. H. Allent, and W. L. Bradley, in: *Accelerated Strength Testing of Thermoplastic composites*, NASA Langley Research Center Hampton. (1998)

[2] Thomas S. Gates, and Michael A. Grayson, in: *On The Use of Accelerated Aging Methods for Screening High Temperature Polymeric Composite Materials*, NASA AIAA (1999)., vol. 2, pp.925~935.

[3] Dennis A. Russell, Larry B. Fogdall, and Gail Bohnhoff-Hlavacek, in: *Simulated Space Environmental Testing on Thin Films*, NASA Technical Publication (2000), April 2000-210101.

[4] James R. Reeder, in: *Prediction of Long-Term Strength of Thermoplastic Composites Using Time-Temperature Superposition*, NASA Technical Publication (2002), August 2002-211781.

[5] Tomas S. Gates (2003), in: *On the Use of Accelerated Test Methods for Characterization of Advanced Composite Materials*, NASA Technical Publication, May 2003-212407.

[6] Thomas K. Tsotsis, Scott keller, Kyejune Lee, Jason Bardis, and Jack Bish, in: *Aging of Polymeric Composite Specimens for 5000 Hours at Elevated Pressure and Temperature*, Composite Science and Technology, vol. 61 (2001), pp.75~86.

[7] ASTM G155-00a, Annual Book of ASTM Standards, 14.04, American Society for Testing and Materials. (2001)

[8] J. P. Holman, in: *Experimental Methods for Engineers*, McGraw-Hill. (2001)

[9] S. H. Hong, K. B. Shin, B. Jeong in:*Prediction of Long - Term Performance of a Composite Material Using Accelerated Environmental Test*, Korean Society for Composite Materials Vol.11 (1998), pp.1-13.

[10] S. H. Yoon, S. J. Lee and J. K. Lee, in: *Effects of Combined Environmental Factors on Mechanical and Thermal Analysis Properties of Graphite/Epoxy Composites,* Korean Society of Mechanical Engineering Vol.26, pp.1416-1425. (2002)

Key Engineering Materials Vols. 385-387 (2008) pp 37-40
© (2008) Trans Tech Publications, Switzerland
doi:10.4028/www.scientific.net/KEM.385-387.37

Analysis for Mechanical Properties of Spiral Accumulating Core Used for Permanent Magnet Motor

Nao-Aki NODA[1,a], Biao ZHANG[2,b], Kazuhiko YONEMARU[1,c]

Shota HIGO[1,d] and Yoshihiro TAKAMATU[1,e]

[1] Department of Mechanical Engineering, Kyushu Institute of Technology, 1-1 Sensui-cho, Tobata-ku,Kitakyushu, 804-8550 Japan

[2] Department of Mechanical Engineering, Kyushu Institute of Technology, 1-1 Sensui-cho, Tobata-ku,Kitakyushu, 804-8550 China

[a] noda@mech.kyutech.ac.jp, [b] f344156h@tobata.isc.kyutech.ac.jp

[c] f344156h@tobata.isc.kyutech.ac.jp, [d] f344156h@tobata.isc.kyutech.ac.jp

[e] f344156h@tobata.isc.kyutech.ac.jp

Key words: spiral, accumulating, finite element method, bending, deterioration

Abstract. Recently, permanent magnet motors are widely used in many industrial fields because they are suitable for compact mechanical system. The motor core is usually manufactured from magnetic steel sheet with press machine. However, usually most parts of the plate are scraped, and only small percent of the sheet is used for the core. The spiral accumulating core system is suitable for manufacturing the core more ecologically because in this system more than 50% of the magnet steel sheet can be used. In this study, therefore, the effective Young's modulus of the spiral accumulating core is considered in order to find out a good method to fix the core. In this analysis, the finite element method is applied to 3D models, whose layers and slits are periodically arranged. Stress and thickness distributions are also analyzed in the bending process. When the spiral core is manufactured through spiral accumulating system with plate-bending process, the thickness change should be minimized because that may deteriorate dimensional accuracy of the spiral core. Also residual bending stress is investigated because that may cause an electric loss. The results indicate that plastic zone is limited at localized regions and therefore an electric loss is not very large. The effective Young's modulus of the 3D dimensions model of the real spiral accumulating core is estimated about 127.5 GPa.

Introduction

The PM synchronous motor is a rotating electric machine where the stator is a classic three phase stator like that of an induction motor and the rotor has surface-mounted permanent magnets. Recently, permanent magnet motors are widely used in wide industrial fields because they are suitable for compact mechanical system. The motor core is usually manufactured from magnetic steel sheet with press machine. However, usually most parts of the plate are scalped, and only small percent of the sheet is used for the core. The spiral accumulating core system is suitable for manufacturing the core more ecologically because in this system more than 50% of the magnet steel sheet can be used (see Fig.1).

In this study, therefore, the effective Young's modulus of the spiral accumulating core is

considered in order to find out a good method to fix the core. In this analysis, the finite element method is applied to 3D models, whose layers and slits are periodically arranged. Also stress distributions and thickness changes will be analyzed at the bending process. When the spiral core is manufactured through spiral accumulating system with plate-bending process, the thickness change should be minimized because that may cause deterioration of the dimensional accuracy of the spiral core. Also residual bending stress is investigated because that may cause an electric loss.

Method of analysis

Figure 2 shows (a) Axis and Rotor and (b) Housing and stator after shrink fitting. The compressive stress always acts in the direction of the circumference when the stator is fixed on the outside housing. Since the slit sustains the compressive stress, there is little effect on the Young's modulus. However, when the rotor is fixed on the axis, the tensile stress appears in the circumference direction. Therefore it is necessary to analyze the effective Young's modulus for rotor in order to fix it properly. Figure 3 shows three types of layers. Assume three layers are in the range of $\theta = 0^\circ \sqcup 90^\circ$ (see Fig.3). For example, each layer of core shape in the range of $90^\circ \sqcup 180^\circ$ coincide with that in the range of $0^\circ \sqcup 90^\circ$. The fourth layer is the same as the first layer. In this study, the effective Young's modulus of the spiral accumulating core is evaluated by applying the finite element method to this model.

Figure 4 shows the example of FEM mesh for 3D model. In this study, the linear hexahedron element is used. The total number of elements is 60450, and total number of nodes is 77868. Figure 5 shows the boundary condition of the model. As shown in Fig.5, the displacement in the y direction at $\theta = 0^\circ$ is fixed, and displacement in the x direction at $\theta = 90^\circ$ is fixed, that is, $u_x=u_y=0$ at $\theta=0,90^\circ$. The displacement in the z direction is fixed at the top and bottom surface of the 1st layer and of the 3rd layer, that is $u_z=0$ at the top and bottom surfaces. Then the constant displacement in the r-direction $u_r=\Delta R$ is given at r = R.

The effective Young's modulus of the 3D dimensions model is given by Eqs. (1). In Fig.6, $\sigma_{\theta 1}$, $\sigma_{\theta 2}$, $\sigma_{\theta 3}$ are the average stress of first layer, second layer and third layer of the model respectively, the stress $\sigma_{\theta av}$ is the average stress of three layer accumulating model, and ε_θ is a strain of the

Fig.1 Automatic spiral accumulating

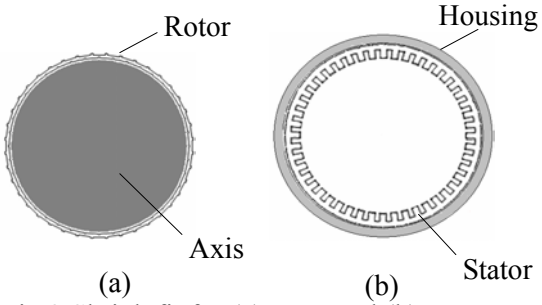

Fig.2 Shrink fit for (a) rotor and (b) stator

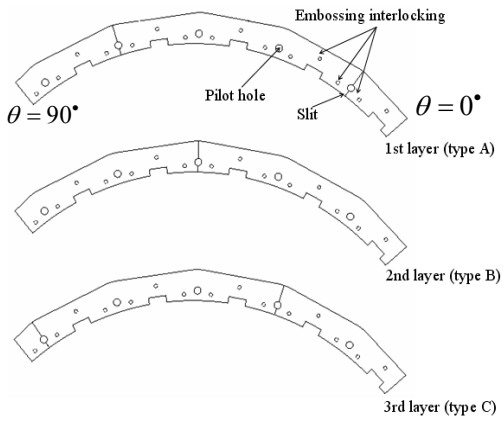

Fig.3 Three types of layers

$$E^* = \frac{\sigma_{\theta av}}{\varepsilon_\theta} = \frac{\sigma_{\theta 1} + \sigma_{\theta 2} + \sigma_{\theta 3}}{3(\Delta R / R)} \quad \ldots (1)$$

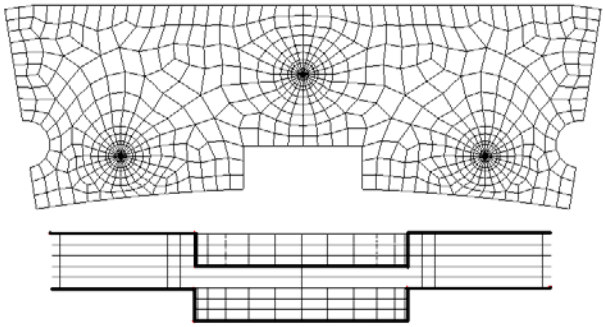

Fig.4 Example of FEM mesh for 3D model

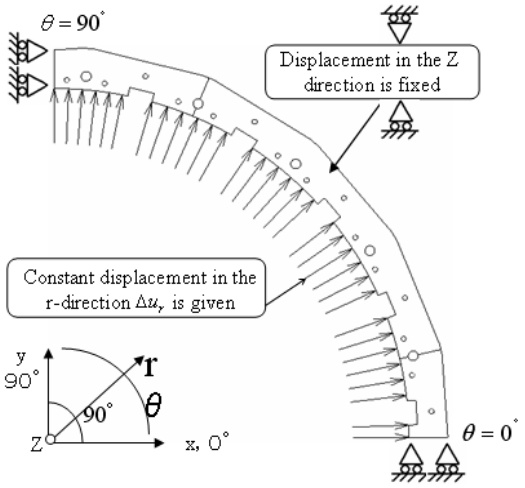

Fig.5 Boundary conditions of the model

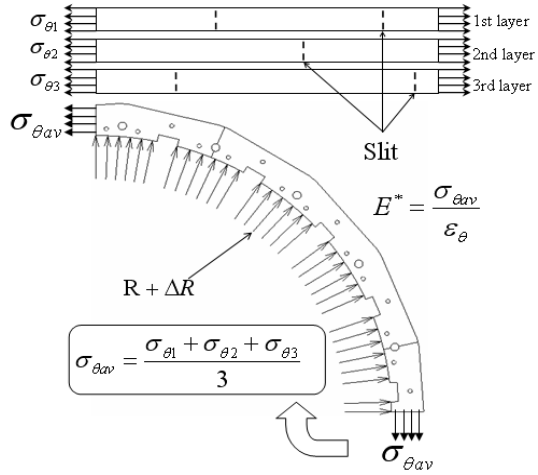

Fig.6 Method of analysis

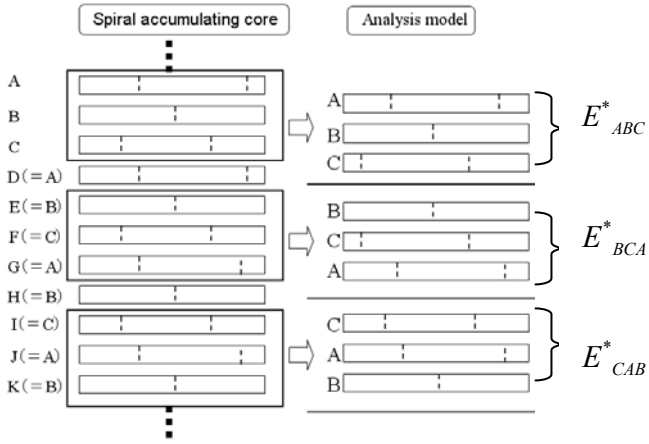

Fig.7 Three kinds of models analyzed

direction of θ, and the value is equal to the strain value of the direction of R. Moreover, R is a radius in the core, and ΔR is constant displacement in the radial direction.

Results and discussion

Three kinds of models are analyzed as shown in Fig.7. The effective Young's modulus of three kinds of model are E^*_{ABC} = 124.5 GPa, E^*_{BCA} = 129.6 GPa, E^*_{CAB} = 128.4 GPa. The average effective Young's modulus is E^*_{av} = 127.5 GPa. Since periodic conditions at the top and bottom surfaces can't be applied, the results are slightly different.

Figures 8 and 9 show the thickness distributions after the spiral accumulating core is bended. When the rotor and stator are subjected to the bending stress, the largest thickness change appears at y=0, and y=0.7 mm. The difference of the thickness between FEM and experiment results is less than 0.02mm. Figures 10 and 11 show the thickness distributions in the section A-A' in Fig.8 and Fig.9. Figure 12 and 13 show the equivalent stress over the yield stress σ_{yield} for stator and rotor at the plasticity zone after bending. The results indicate that plastic zone is limited at the localized region and therefore an electric loss is not very large.

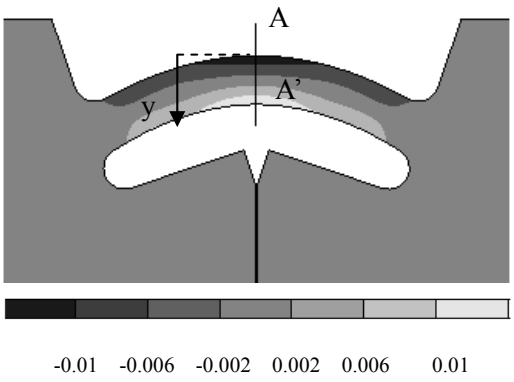

Fig.8 Thickness distribution

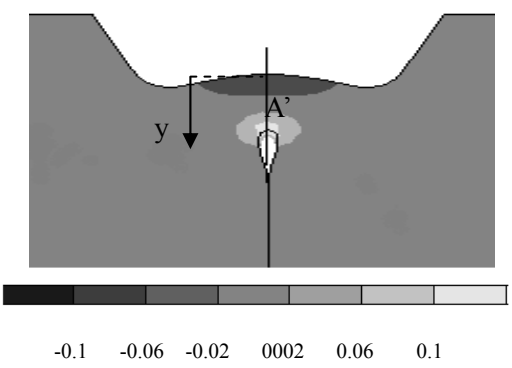

Fig.9 Thickness distribution

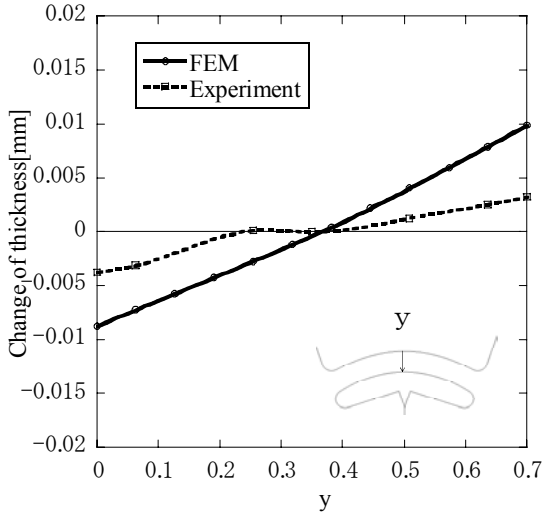

Fig.10 Thickness distribution at A-A'

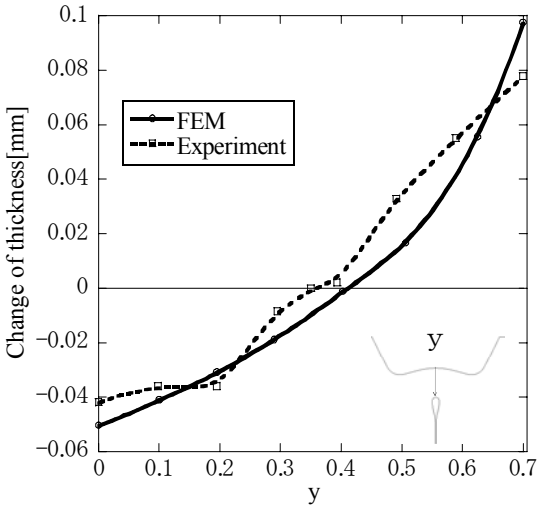

Fig.11 Thickness distribution at A-A'

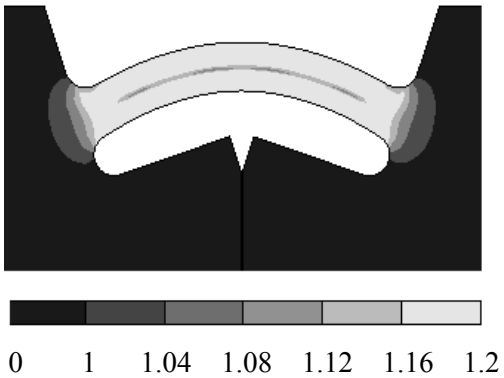

Fig.12 $\sigma_{eq}/\sigma_{yield}$ in stator

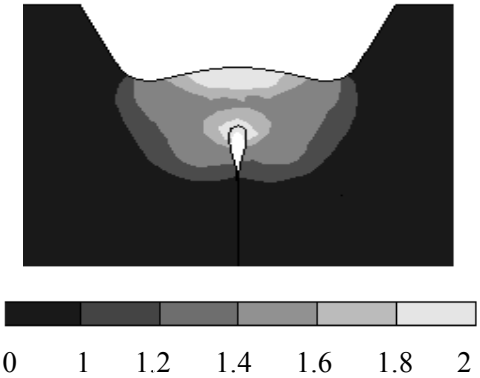

Fig.13 $\sigma_{eq}/\sigma_{yield}$ in rotor

References

[1] Abb research ltd., "Method of forming motor", Japan patent (in Japanese), 2004-505595
[2] Kumai, S., and Yaskawa electric corp., "Winding accumulating core of motor", Japan patent (in Japanese), s51-40506
[3] Kikuchi, Y., Fukuda, Y., Maeyama, K., and Fujitsu general ltd., "Motor", Japan patent, 2005-160170
[4] Sakanishi, S., Asai, T., Koyama, M., and Kuroda precision ind. ltd., Mitsuba electric mfg. co. ltd., "Method and device for manufacturing winding stator core", Japan patent, h2-106151
[5] Mizutani, K., and Toshiba corp., "Manufacture of annular core", Japan patent, h1-264548
[6] Kaido, C., "Spiral Core made of Grain-oriented Electrical Steel Sheet", IEEJ Transactions on Industry Applications, Vol. 116, No. 3 (1996), pp. 265-270

Key Engineering Materials Vols. 385-387 (2008) pp 41-44
© (2008) Trans Tech Publications, Switzerland
doi:10.4028/www.scientific.net/KEM.385-387.41

Test Analysis for RC Beams Strengthened with Externally Bonded Prestressed CFRP Laminates

Shiqi Cui[1, a], Jinshan Wang[1,b], Zhaozhen Pei[1,c] and Zhi Liu[1,d]

[1] Structure Institute of Shandong Province Academy of Buildings, Jinan, Shandong province, China.

[a]cfrp@sina.com, [b]wangjinshan@gmail.com, [c]pzz_616@163.com, [d]liuzhi_cn@eyou.com

Keywords: Prestressed CFRP, Strengthened, RC Beam, Deform

Abstract. Reinforced concrete beams strengthened with externally bonded CFRP sheet and prestressed CFRP are analyzed in this paper. Crack developments and displacements with curvatures for different beams are analyzed. Test results show that prestressed CFRP are able to control the development of macro cracks in concrete and prestressed CFRP is an effective method to improve the toughness of concrete, reduce strengthening cost and meanwhile enhance bearing capacity of concrete beams.

Introduction

The rehabilitation or strengthening of reinforced concrete can increase bearing capacity and lessen the deflection when the bearing capacity and deflection of the concrete beam are insufficient which can be due to any of the following factors including: incorrect selection of materials, errors in design calculations and detailing, poor construction methods and inadequate quality control and supervision, chemical attack, and external physical or mechanical factors. The applications of carbon fiber reinforced plastic (CFRP) laminates as tensile reinforcement have been widely used in repair and upgrading of concrete structures with many advantages: corrosion resistance, high strength-to-weight ratio and high stiffness-to-weight ratio[1], however, the modulus of elasticity of CFRP is almost the same as that of the steel, the CFRP come into its own ultimate strength at the expenses of the axial deflection of the beam. The prestressed CFRP laminates would solve this problem.

Design of test members and test schemes

Four-point bending tests are carried out for rectangular section beams with span l=2400mm, the net span l_0 =2100 mm. Table 1 lists the cross-sectional dimensions and strengthening schemes of the beams. The steel reinforcement ratio of test concrete beam is 0.9%. The beams are subject to static loading mode of two-point load distribution in accordance with the GB 50152-92 *Standard Methods for Testing of Concrete Structures*. The compressive strength of concrete is 32.0MPa. Material properties of CFRP laminates used to strengthen concrete beams are indicated in Table 2.

Table 1. Cross-sectional dimensions and strengthening schemes of the test specimens

Specimen number	Cross-sectional dimensions (mm^2)	CFRP dimensions (mm^2)	Prestress (MPa)
L1	150×250		
L2	150×250	13.32	
L3	150×250	13.32	200

Table 2. Material properties of CFRP laminates

Theoretical thickness (mm)	Elasticity modulus (GPa)	Tensional strength (MPa)
0.111	220	3750

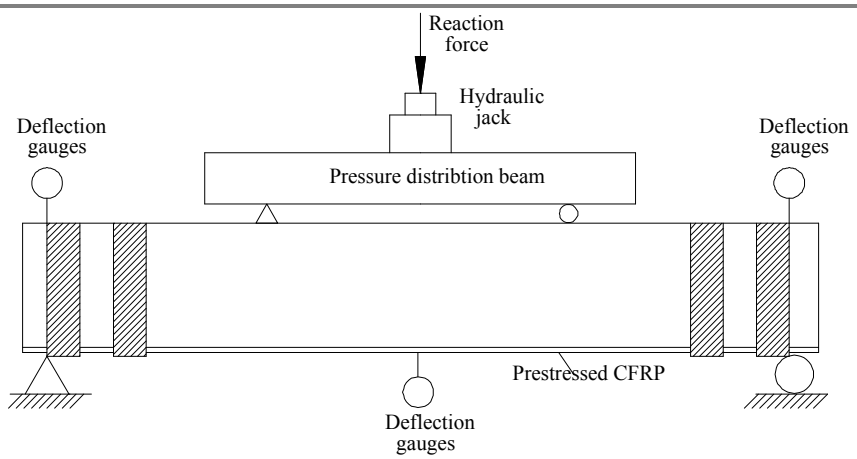

Fig. 1 Measure scheme of test

Figure 2 shows the device used for the application of prestress to the CFRP laminates. The CFRP laminates were initially positioned by adhesive at one end of the beam. After a complete cure of the adhesive, prestress load was applied by a hydraulic jack throw the rolling shaft (Figure 2). The tensile load to be applied to the CFRP laminates was determined by multiplying the nominal prestress percentage by the ultimate load of the plate. The latter was based on the strengths found in the material characterization tests (Table 2).

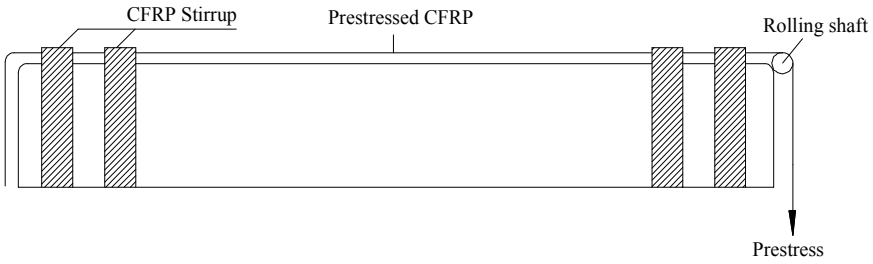

Fig. 2 Device used to apply prestress to CFRP laminates

Analysis of test results

Concrete is a weak material in tension and cracks when subjected to high local tensile stresses. Its low tensile capacity can be attributed to the high stress concentration under load. Flexural cracking in beams is not only unavoidable but is necessary to allow tension reinforcement to play its part. The formation and propagation of cracks depend on the tensile strength of the concrete. When the principal tensile stress in concrete exceeds its tensile strength, cracks form perpendicular to the direction of this stress. Cracking started with vertical flexural cracks in the constant moment region. The crack formation became stabilized once again after a load of 40 kN. Table 2 shows cracking loads of beams where it can be seen that the cracking loads for L2 and L3 beams are approximately 107% and 158% that of the L1 beam, respectively. The spacing of cracks decreased when the CFRP laminates was prestressed (Figure 3 and Table 2). This indicates the significant contribution of the prestressed CFRP laminates to the initial cracking load.

Table 2. Comparison of structure capacity by specimen

Specimen	Initial cracking load (kN)	Failure load (kN)	Spacing of cracks (mm)	Modes of failure
L1	16.5	64.7	135	Steel yielding
L2	17.6	80.1	112	Concrete crushing
L3	26.1	85.6	80	Concrete crushing

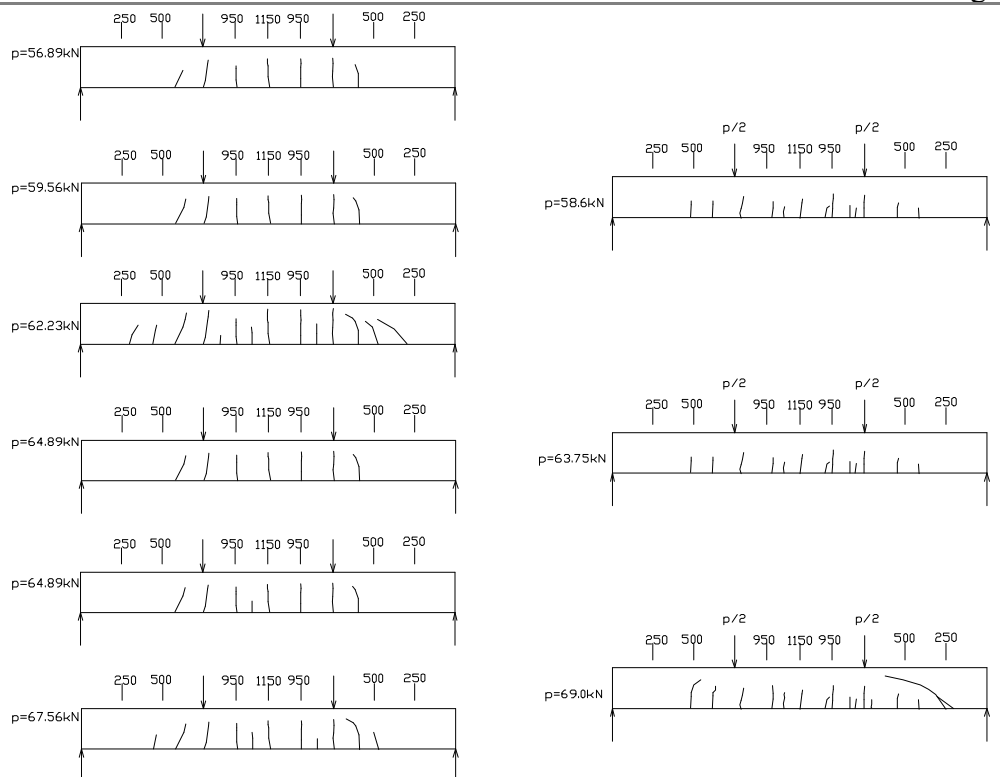

Fig. 3 Comparison of the crack of the L2 and L3 beam (the left is the crack of L2)

One of the important factors that affect the serviceability of a RC flexural member is its deflection. Deflection is function of load, span length, second moment of are and modulus of elasticity of material. The stiffness of member is largely dependant on both the second moment of area and the modulus of elasticity. Fig. 4 shows the experimental load–deflection curves. The initial linear part of the graphs has a very steep slope which corresponds to the uncracked condition of these beams. In this region the deflection is proportional to the applied load and the entire concrete section is considered effective in resisting the loads. The ultimate load of L1 beam was around 19% lower than L2 beam while that of L2 beam was only 6% lower than L3 beam, which indicates that CFRP laminates contribute to enhancement of the bearing capacity remarkably and the prestressed CFRP also enhance the bearing capacity but not remarkably.

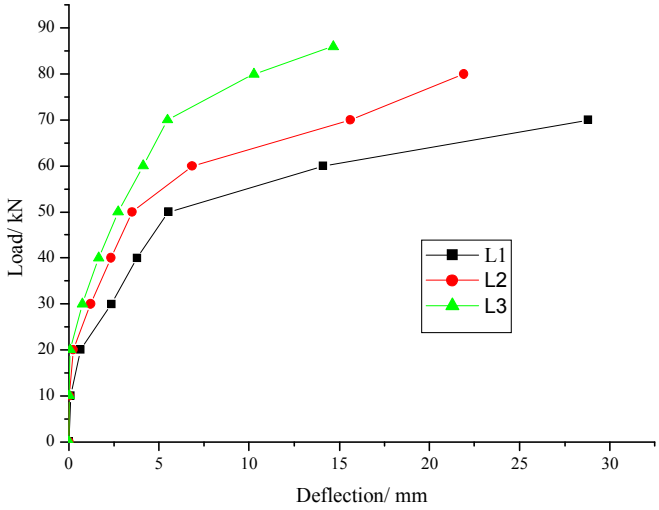

Fig. 4 Load–displacement curves of specimens

Summary

The results of experimental testing on CFRP and prestressed CFRP beams were presented. The important features of the comparison of behaviour between CFRP and prestressed CFRP beams are listed as follows:

1. The prestressed CFRP laminates can enhance the initial cracking load of the beam remarkably compared with that of the non-strengthened beam and the non-prestressed CFRP beam.
2. The prestressed CFRP laminates can lessen the spacing of cracks compared with that of the non-strengthened beam and the non-prestressed CFRP beam.
3. The failure load for CFRP and prestressed CFRP beams was nearly the same and much higher than that of the non-strengthened beam.

References

[1] M.A.Shahawy, T.Beitelman, M.Arockiasamy and R.Sowrirajan: Composites Part B: Engineering, Volume 27, Issues 3-4 (1996), p 217-224

[2] H.N. Garden and L.C. Hollaway: Composites Part B: Engineering, Volume 29, Issue 4 (1998), p 411-424

[3] Frederick Stoll, Joseph E. Saliba and Laura E. Casper: Composite Structures, Volume 49, Issue 2, (2000), p 191-200

[4] Charles W. Dolan and Derek Swanson: Composites Part B: Engineering, Volume 33, Issue 1 (2002), p 1-6

[5] Owen Rosenboom, Tare K. Hassan and Sami Rizkalla: Construction and Building Materials, Volume 21, Issue 4 (2007), p 764-776

[6] Patrick X.W. Zou and Shouping Shang: Construction and Building Materials, Volume 21, Issue 4 (2007), p 777-788

[7] P. Colombi, A. Bassetti and A. Nussbaumer: Theoretical and Applied Fracture Mechanics, Volume 39, Issue 1 (2003), p 61-71

[8] Christoph Czaderski and Masoud Motavalli: Composites Part B: Engineering, Volume 38, Issues 7-8 (2007), p 878-886

Key Engineering Materials Vols. 385-387 (2008) pp 45-48
© (2008) Trans Tech Publications, Switzerland
doi:10.4028/www.scientific.net/KEM.385-387.45

Analysis of Critical Damage of Thin Plate Subjected to Contact Explosions

Shan Wang[1,a], Jing Zhang[1,b], Xinghua Shi[1,c]

[1]School of Civil Engineering, Harbin Engineering University, Harbin 15001, P.R. China.

[a]wangshan@hrbeu.edu.cn, [b]zhangjing8270@163.com, [c]shixinghua9@163.com

Key Words: Contact explosions, Critical damage, Dynamic fracture, Critical blasting charge, Critical deformation

Abstract：The damage of thin steel plate subjected to contact explosions was a very complex nonlinear process. The initial crevasse of plate subjected to contact explosions had influence upon the whole damage process, so the critical damage study was significant on the anti-explosion of ship structure. In virtue of the wave solution of the plate plastic dynamic response and the dynamic fracture theory, the critical blasting charge was derived theoretically when onset of initial circumferential crack namely critical damage happened. And the expression of critical deformation was also obtained. Lastly the results calculated using proposed method was compared with numerical simulation and the experiment in the published literature, which were almost coincided. It could be seen that the present method could perfectly solve the critical damage of thin plate under contact explosions theoretically, and provide references for defensive engineering.

Introduction

The great plastic dynamic response and the local or whole fracture would appear when the structure subjected to explosions. A lot of researches of plastic dynamical response of thin plate subjected to explosions were developed inside and outside. Based on the principle of the energy equilibrium, the expressions were obtained for the final deflections of the shock wave upon the plates subjected to the impulse loading in reference [1]; Failure by petalling occurs when thin plates were struck by cylindro-conical projectiles in reference [2]; the petalling was researched in reference [3] by energy equilibrium. But few people did the research about the critical destroy of plate subjected to contact explosions. In this paper, based on the dynamic fracture theory, the critical blasting charge and critical displacement were derived theoretically when onset of initial circumferential crack namely discing happened in clamped plate subjected to contact explosions.

1 Wave solution of plastic response of the plate

The calculating model was shown in Fig.1, where the circular membrane of a finite radius R_0 was considered initially at rest on a plane and at $t=0^+$ an impulsive transverse load was applied over a central circular zone of radius R_1.

The solution was discontinuity because blasting load was acted local in center of plate. A complete analysis of all possible shock waves, rarefaction waves, and acceleration waves was necessary. Considering the local effect of explosions to plate, $\xi_0 \in \left(0,1/2\sqrt{2}\right)$, so the displacement of arbitrary point in plate was reached as follows in reference [4]

$$W(\xi)=\begin{cases} 2\left(\sqrt{2}-1\right)V\xi_0^2-\dfrac{V}{8\xi_0}\left(3\xi_0^2+\left(\xi-3\xi_0\right)^2\right), \xi\in\left(0,2\xi_0\right) \\ V\xi_0^2\left(2\left(\sqrt{2}-1\right)-\dfrac{1}{\xi}\right), \xi\in\left(2\xi_0,\dfrac{1}{\sqrt{2}}\right) \\ 2V\xi_0^2\left(\xi-1\right), \xi\in\left(\dfrac{1}{\sqrt{2}},1\right) \end{cases} \tag{1}$$

Where $W = w/r$, w was deflection; $\xi = R/R_0$; $\xi_0 = R_1/R_0$; $V = I_0/c_0\rho_0 h$, I_0 was initial unit impulse, ρ_0 was plate density, c_0 was sound velocity in plate, σ_0 was yield intensity of plate.

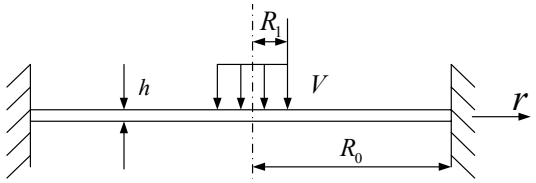

Fig.1 Plate geometry and loading configuration

2 Fracture criterion

The local ductile fracture criterion for uncracked bodies was adopted [5]

$$\int_0^{\bar{\varepsilon}_f} f\left(\frac{\sigma_m}{\bar{\sigma}}, \dot{\bar{\varepsilon}}, T\right) d\bar{\varepsilon} = D_c \tag{2}$$

Where $\bar{\varepsilon}$ was the equivalent plastic strain; $\bar{\varepsilon}_f$ was equivalent fracture strain; $\sigma_m/\bar{\sigma}$ was the ratio of hydrostatic mean stress $\bar{\sigma}_m$ to Von Mises equivalent stress, which defined stress triaxiality; $\dot{\bar{\varepsilon}}$ was the ratio of equivalent strain; f was weighting function depending on the stress triaxiality, strain rate, and temperature; D_c was critical damage value of material.

The effect of strain rate and temperature was much smaller than that of the stress triaxiality [6], so these were not be considered. Feature of fracture envelope was shown in Fig.2. For deformation of clamped thin plate, stress state (σ_1, σ_2) always stayed in the first tension-tension quadrant. The corresponding stress triaxiality remained between $1/3$ (uniaxial tension)and $2/3$ (equi-biaxial tension), Eq.(1) could be further reduced to

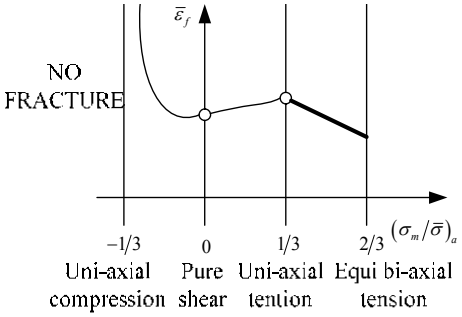

Fig.2 Feature of the fracture envelope

$$\int_0^{\bar{\varepsilon}_f} \frac{\sigma_m}{\bar{\sigma}} d\bar{\varepsilon} = D_c, \quad \left(\frac{\sigma_m}{\bar{\sigma}}\right)_{av} = \frac{1}{\bar{\varepsilon}_f}\int_0^{\bar{\varepsilon}_f} \frac{\sigma_m}{\bar{\sigma}} d\bar{\varepsilon}$$

The fracture criterion could be rewritten as

$$\left(\frac{\sigma_m}{\bar{\sigma}}\right)_{av} \bar{\varepsilon}_f = D_c \tag{3}$$

3 The critical blasting charge and displacement

3.1 The Solution of V

The impulse per unit area I_0 was defined as

$$I_0 = \int_{\frac{l}{D}}^{\infty} p_b(t) dt \tag{4}$$

Where p_b was pressure; l was length of dynamite; D was explosive velocity.

The dynamite contacted to the plate was ignited from $x = 0$, shock wave spread to right at speed of D and it reached the surface of plate at $t = l/D$.

The relation of p_b and c_b was as follows at the arbitrary time

$$\frac{p_b}{p_H} = \left(\frac{c_b}{c_H}\right)^3 = \frac{64}{27}\left(\frac{c_b}{D}\right)^3 \tag{5}$$

The velocity u_b of the production of blasting in the interface was written as

$$c_b = \frac{x}{t} - u_b \tag{6}$$

The u_b and D at the interface could be written

$$\frac{u_b}{D}=\frac{u_{b0}}{D}\left(\frac{l}{Dt}\right)^{\beta} \qquad \left(t\geq\frac{l}{D}\right) \tag{7}$$

Where u_{b0} was initial parameter of shock wave; β was the parameter of dynamite and plate, when the dynamite was TNT and plate was steel, $\beta=2.2488$.

Eq.(6) and the integral in Eq.(7) both sides were taken into Eq.(5)

$$\frac{p_b}{p_H}=\frac{64}{27}\left(\frac{l}{Dt}\right)^3\left\{1+\frac{\beta u_{b0}}{(1-\beta)D}\left(\frac{l}{Dt}\right)^{\beta-1}-\frac{u_{b0}}{(1-\beta)D}\right\}^3 \tag{8}$$

Eq.(8) was taken into Eq.(4), I_0 was written as

$$I_0=\int_{l/D}^{t}p_H\frac{64}{27}\left(\frac{l}{Dt}\right)^3\left\{1+\frac{\beta u_{b0}}{(1-\beta)D}\left(\frac{l}{Dt}\right)^{\beta-1}-\frac{u_{b0}}{(1-\beta)D}\right\}^3,\ p_H=\frac{\rho D^2}{(\gamma+1)g} \tag{9}$$

Where γ was exponent, $\gamma=3$, ρ was dynamite density, g was acceleration of gravity.

$$I_0=\frac{8l\rho D\cdot\lambda}{27g} \tag{10}$$

Where $\lambda=\left[\frac{2(\beta A)^3}{3\beta-1}-6\beta A^2(A-1)+\frac{6\beta A(A-1)^2}{\beta+1}-(A-1)^3\right]$; $A=\frac{u_{b0}}{(1-\beta)D}$

The total impulse was written as

$$I=A_0I_0=\frac{8mD\cdot\lambda}{27g},\quad I_0=\frac{8mD\cdot\lambda}{27gA_0}$$

Where A_0 was the blasting area, m was the blasting charge.

According to Eq.(1), $V=I_0/c_0\rho_0h$.

So the V was written as

$$V=\frac{8mD\cdot\lambda}{27\rho_0gA_0c_0h} \tag{11}$$

3.2 The Solution of The Critical Blasting Charge and Displacement

D_c was the constant to certain material from Eq.(2). But ultimate strain $\bar{\varepsilon}_f$ depended on not only material, but also load style. Fracture strain could be reached from experiment of uniaxial tension, $(\sigma_m/\bar{\sigma})_{av}=1/3$, value of D_c was got from Eq.(3).

When plate fractured, $(\sigma_m/\bar{\sigma})_{av}=0.6$, the dynamic fracture strain was written as $\bar{\varepsilon}_f=D_c/(\sigma_m/\bar{\sigma})_{av}=5D_c/3$. The maximum slope of plate was constant from Eq.(3), $\partial w/\partial r=\partial W/\partial\xi=3V/4$, so $\varepsilon=1/2(\partial w/\partial r)^2=9/32V^2$.

At the point of rupture $\varepsilon=\bar{\varepsilon}_f$

$$V=2.434\sqrt{D_c} \tag{12}$$

Eq.(12) was taken into Eq.(11)

$$m=8.215\frac{\rho_0gA_0c_0h}{D\lambda}\sqrt{D_c} \tag{13}$$

The critical blasting charge were derived theoretically when onset of initial circumferential crack happened in clamped plate subjected to contact explosions. The corresponding critical displacement could be reached by Eq.(3).

4 Example

According to [7], the data were as followed: $h=1.6\text{mm}$, $R_1=12.5\text{mm}$, $R_0=50\text{mm}$, $\rho_0=7840\,\text{kg/m}^3$, $\bar{\varepsilon}_f=0.3$, $\sigma_0=330\text{MPa}$, $\rho=1620\,\text{kg/m}^3$, $D=7000\,\text{m/s}$, $u_{b0}=810\,\text{m/s}$.

From Eq.(3), $D_c=\bar{\varepsilon}_f(\sigma_m/\bar{\sigma})_{av}=0.3\times(1/3)=0.1$

From Eq.(10), $\lambda=0.892$

The above data were taken into Eq.(13), the critical blasting charge $m_{cr} = 5.09\text{g}$.

$V = 2.434\sqrt{D_c} = 0.770$, $\xi_0 = R_1/R_0 = 0.25$, once these were taken into Eq.(1), the critical deformation was obtained as follows

$$W(\xi,\tilde{\tau}) = \begin{cases} -0.0326 - 0.385\times(\xi - 0.75)^2, & \xi \in (0,0.5) \\ 0.048\times\left(0.828 - \dfrac{1}{\xi}\right), & \xi \in \left(0.5, \dfrac{1}{\sqrt{2}}\right) \\ 0.096\times(\xi - 1), & \xi \in \left(\dfrac{1}{\sqrt{2}}, 1\right) \end{cases}$$

Tab.1 The comparison of results

	The experiment result in [7]	Simulation result	Theoretical result
Critical blasting charge	4.75g	4.65g	5.09g

The plate above was simulated by LS-DYNA, results of experiment, simulation and theoretical result in this paper were shown in Tab.1.The error between theoretical result in this paper and experiment was 7.16%, and that with simulation was 9.46%. So the present result, experiment and simulation coincided well.

5 Conclusions

This paper adopted the dynamic fracture rule, the critical blasting charge was derived theoretically when thin plate subjected to explosions. It could be seen:

(1) The method in this paper was simple, and the conception was definite. Furthermore, the theoretical result, experiment and simulation was compared showing good agreement, it was satisfied the requirement of engineering. So this method was reasonable and feasible.

(2) The formula of critical blasting charge considered comprehensively the influence of dynamite and plate, it was important for the designing of defensive structure.

6 Acknowledgment

This paper was supported by the National Natural Science Foundation of China and China Academy of Engineering Physics (Grant No. 10276013).

References

[1] WU Cheng, JIN Yan, LI Huaxin. A study on square plate dynamic response under underwater explosion. Chinese Journal of High Pressure Physics, 2003, vol.17, No.4, pp.275-282

[2] Tomasz Wierzbicki. Petalling of plates under explosive and impact loading. International Journal of Impact Engineering, 1999, vol.22, pp.935-954

[3] ZHANG Zhenhua, ZHU Xi. Petaling of rigid plastic plate under contact explosive loading of cylindrical dynamite. Journal of Ship Mechanics, 2004, vol.8, No.5, pp.113-119

[4] M. Mihailecu-Suliciu, T. Wierzbicki. Wave solution for an impulsively loaded rigid-plastic circular membrane. Arch. Mech, 2002, vol.54, No.5-6, pp.553-575

[5] Young-Woong Lee, Tomasz Wierzbicki. Fracture prediction of thin plates under localized impulsive loading. Part Ⅱ: discing and petalling. International Journal of Impact Engineering, 2005, vol.31, pp.1277-1308

[6] Hopperstad OS, Borvik T, Langseth M etl. On the influence of strain rate on the behavior of a structural steel.Part Ⅱ.Numerical study. Eur J Mech A/Solids, 2001, vol.20, pp.685-712

[7] Nurick GN, Radford AM. Deformation and tearing of clamped circular plates subjected to localized central blast loads. In: Reddy BD (editor) Recent developments in computational and applied mechanics. A volume in honor of John B. Martin, 1997, pp.276-301

Key Engineering Materials Vols. 385-387 (2008) pp 49-52
© (2008) Trans Tech Publications, Switzerland
doi:10.4028/www.scientific.net/KEM.385-387.49

Assessment of Extrinsic Crack Tip Shielding in Austenitic Steel near Fatigue Threshold

Jaroslav Pokluda[1], Yoshiyuki Kondo[2], Karel Slámečka[1], Pavel Šandera[1] and Jana Horníková[1]

[1]Brno University of Technology, Technická 2, 616 69 Brno, Czech Republic

[2]Kyushu University, 744, Moto-oka, Nishi-ku, 819-0395 Fukuoka, Japan

pokluda@fme.vutbr.cz, ykondo@mech.kyushu-u.ac.jp, slamecka@fme.vutbr.cz, sandera@fme.vutbr.cz, hornikova@fme.vutbr.cz

Key words: Fatigue threshold, austenitic steel, extrinsic toughening, unified closure model, effective fatigue threshold

Abstract. Asymmetric arrangements of stored crack-wake dislocations and low values of the size ratio SR, the plastic zone size / the characteristic microstructural distance, were found to be of basic importance for the shear misfit of crack flanks causing the roughness-induced crack closure in case of plain strain conditions. The crack wake dislocations produce also the plasticity induced crack closure as a result of a near-tip mismatch perpendicular to crack flanks. According to a recently published theoretical concept, an estimation of these extrinsic shielding effects in the threshold region of fatigue crack propagation was made for austenitic steel of Japan provenience. Related fatigue experiments were based on a standard load shedding technique associated with monitoring of the crack closure level. The surface roughness was analysed by means of the optical chromatography that enables a 3D reconstruction of fracture morphology. Calculated and measured effective threshold values of about 2.2 MPa.m$^{1/2}$ are practically identical. Total levels of the extrinsic toughening induced by the austenitic microstructure are rather low when compared to those identified in ferritic- and ferritic-austenitic steels.

Theoretical background

The plasticity induced crack closure (PICC) and the roughness induced crack closure (RICC) are known as two important mechanisms for fatigue crack tip shielding and lead to an apparent increase in the resistance to fatigue crack propagation [1]. Although a plenty of studies on these mechanisms have been done hitherto [2, 3], our understanding and a prediction capability remain still rather insufficient. Recently, some new concepts concerning the closure effects were proposed [4, 5]. Asymmetric arrangements of stored crack-wake dislocations and low values of the size ratio S_R (the characteristic microstructural distance divided by the plastic zone size) were found to be of basic importance for the shear misfit of crack flanks causing RICC under plain strain conditions. The crack wake dislocations cause also PICC as a result of a near-tip mismatch perpendicular to crack flanks. According to newly derived formulae including these effects, an estimation of maximum levels of both RICC and PICC can be made for metallic materials in the whole fatigue crack propagation regime.

The crack-wake dislocations on both sides of crack flanks independently contribute to PICC [4]. As a simple model, only two narrow bands of dislocations can be considered here to tilt the volume elements in the crack wake. This transfers the material to the crack tip and results in PICC under plain strain conditions. When the arrangement of crack-wake dislocations is asymmetric, the shear misfit of crack flanks causes a long-range RICC on rough fracture surfaces. An additional short-range contribution to RICC comes from the shear irreversibility ahead the crack tip [5]. The necessary conditions for RICC (the asymmetry and the roughness) are well fulfilled when $S_R \geq 1$, i.e. when the characteristic microstructure distance (the mean grain size or the interparticle spacing) is comparable or higher than the plastic zone size [5, 6]. On the other hand, when the plastic zone em-

braces, at least, several grains or particles, i.e. $S_R << 1$, the RICC can be neglected. However, the size ratio does not have any significant considerable effect on the PICC ratio.

The aim of this paper is to apply the unified model [7] to investigation of the extrinsic fracture toughness component and the effective fatigue-threshold value of the austenitic steel made in Japan.

Considering the local stress intensity factors (SIFs) K_{I} and K_{II} and associated displacements produced by the totally asymmetric dislocation band near the crack tip, one can derive the following expression for the maximum long-range (LR) closure ratio:

$$\left(\frac{\delta_{cl}}{\delta_{\max}}\right)_{LR} = C\sqrt{S_R\left(R_S^2 - 1\right)}, \tag{1}$$

where C is a dimensionless constant ($C = 0.125$ is usually employed), nearly independent on the material and R_S is the surface (area) roughness of the fracture surface [8]. The maximal short-range (SR) component (a totally irreversible slip) can be written as

$$\left(\frac{\delta_{cl}}{\delta_{\max}}\right)_{SR} = \frac{3\left(R_S - 1\right)}{\sqrt{6} + 3\left(R_S - 1\right)}. \tag{2}$$

Due to an enormous variability in the characteristic microstructure distance in engineering materials and for the sake of simplicity, one can divide the grains (or interparticle spacings) into two categories; to those of $S_R \geq S_{Rc}$ (maximal level of RICC, $S_R \geq 1$) and those of $S_R < S_{Rc}$ (no RICC, $S_R \to 0$), where $S_{Rc} = d_c / r_p$ is a critical boundary value of about 0.5 ($S_{Rc} \in \langle 0.2,\ 1\rangle$ [8]). Then, the parameter

$$\eta = \int_{S_{Rc}}^{\infty} p\left(S_R\right) \mathrm{d}S_R \approx \exp\left[-\left(\frac{0.886\, S_{Rc}}{S_{Rm}}\right)^{2.2}\right], \tag{3}$$

where $p(S_R)$ is the Weibull probability density and S_{Rm} is the mean value of the size ratio, expresses a statistically averaged weight of S_R in the phenomenon of RICC.

On the contrary to RICC, dislocation arrays on both sides of crack flanks contribute to PICC. This effect remains practically unaffected by the size ratio and can be simply assessed [7] as

$$\left(\frac{\delta_{cl}}{\delta_{\max}}\right)_{PICC} = 2C. \tag{4}$$

Assuming Eqs. (1) and (2) multiplied by the probability parameter (3), and Eq. (4), the total level of the closure ratio reads

$$\left(\frac{\delta_{cl}}{\delta_{\max}}\right)_{tot} = \frac{K_{cl}}{K_{\max}} = C\eta\sqrt{R_S^2 - 1} + \frac{3\eta\left(R_S - 1\right)}{\sqrt{6} + 3\left(R_S - 1\right)} + 2C. \tag{5}$$

Because $\Delta K_{eff} = K_{\max} - K_{cl}$, and according to Eq. (5), the effective value of the SIF range can be expressed as

$$\Delta K_{eff} = \left(1 - C\eta\sqrt{R_S^2 - 1} - \frac{3\eta\left(R_S - 1\right)}{\sqrt{6} + 3\left(R_S - 1\right)} - 2C\right)\frac{\Delta K}{1 - R}, \tag{6}$$

where ΔK is the applied SIF range and R is the cyclic ratio. Values of ΔK_{eff} can be identified experimentally by measuring the crack closure. The effective threshold value ΔK_{eff} represents a pure material resistance against the crack propagation and should be nearly independent on the cyclic ratio and microstructure parameters of a particular material.

Experimental methods and results

Fatigue crack growth (FCG) rate tests were carried out using 18 mm thick compact C(T) specimens made of austenitic steel SUS316L (the chemical composition in Table 1) in a MTS servo-hydraulic machine. The first two tests were performed at room temperature using the cyclic ratios $R = 0.1$ and $R = 0.3$ for steadily decreasing ΔK. In the third test the value $K_{\max} = 15.5$ MPa.m$^{1/2}$ was kept constant. The threshold values ΔK_{th} and $\Delta K_{eff,th}^{\exp}$ in all tests correspond to the crack growth rate $\mathrm{d}a/\mathrm{d}N = 10^{-11}$ m/cycle. Crack closure was evaluated by analyzing the load versus crack opening displacement (COD) curves.

Table 1 Chemical composition

Material	C	Ni	Cr	Mo	Si	Mn	P	S
SUS316L	0.019	12.30	17.32	2.87	0.49	0.83	0.028	0.001

The mean grain size of the steel was of 28 μm. Values of the area roughness R_S were measured by means of the profilometer MicroProf FRT (based on the chromatic aberration method) for z-axis measurement, equipped by the FRT Mark III software for 3D surface reconstructions. All the experimental data are summarised in Table 2.

Table 2 Experimental data

Test No	$R_p0.2$ [MPa]	R_S	R	ΔK_{th} [MPa.m$^{1/2}$]	$\Delta K_{eff,th}^{\exp}$ [MPa.m$^{1/2}$]
1	217	1.37	0.1	3.54	2.19
2	217	1.40	0.3	2.93	2.20
3	217	1.42	0.8	2.65	2.65

Estimation of Extrinsic Components and Effective Thresholds

The computed values of the statistical factor η and the effective SIF range $\Delta K_{eff,th}^{cal}$ are displayed in Table 3. The values C = 0.125 and $S_{Rc} = 0.5$ were used in agreement with above mentioned presumptions. The calculated and the measured effective threshold values are practically identical (about 2.2 MPa.m$^{1/2}$) – compare Tables 2 and 3. Note that, in ferritic steels, this value is of 2.75 MPa.m$^{1/2}$ [6, 9]. As expected, no closure was identified in the threshold region of the test No. 3 because of very high value $R = 0.8$ reached at $\mathrm{d}a/\mathrm{d}N = 10^{-11}$ m/cycle. In this case, obviously, the identity $\Delta K_{eff,th}^{\mathrm{cal}} = \Delta K_{th}$ can be applied.

Table 3 Computed values

Test No	η	$\Delta K_{eff,th}^{cal}$ [MPa.m$^{1/2}$]	Extrinsic component [%]
1	0.76	2.13	39
2	0.70	2.30	22
3	–	(2.65)	0

The last column in Table 3 shows a percentage contribution of the total extrinsic component $\Delta K_{eff,th}^{cal}$ (corresponding to the crack closure) to the measured values ΔK_{th}, expressed as $\left(\Delta K_{th} - \Delta K_{eff,th}^{cal}\right).100 / \Delta K_{th}\,[\%]$. The values reveal a rather low participation of the extrinsic toughening induced by the austenitic microstructure when compared to 53% in the ferritic steel [5] and 75% in the ferritic-austenitic duplex steel [10].

Conclusions

The fatigue threshold behaviour of the austenitic steel at room temperature has been investigated by means of experimental and theoretical approaches. The main results can be summarised as follows:

(i) The calculated values of effective fatigue thresholds (closure corrected) are in very good agreement with experimental data.

(ii) Total levels of the extrinsic toughening induced by the austenitic microstructure are rather low when compared to those identified in ferritic- and ferritic-austenitic steels.

Acknowledgment

This work was supported by the Ministry of Education, Youth and Sports of the Czech Republic in the frame of the project MSM 0021630518.

References

[1] Ritchie, R. O. (1988). Mater. Sci. Eng. 103, 15.

[2] Suresh, S. (1998). Fatigue of materials. Cambridge (MA): Cambridge University Press.

[3] McClung, R. C. and Newman J. C. (1999). Advances in fatigue crack closure measurement and analysis. ASTM STP 1343, West Conshohocken, PA.

[4] Pippan, R., Strobl, G., Kreuzer H. and Motz C. (2004). Acta Mater. 52, 4493.

[5] Pokluda, J., Šandera, P. and Horníková, J. (2004). Fat. Fract. Engng. Mater. Struct. 27, 141.

[6] Pokluda J., Šandera P. and Horníková J. (2005). J. ASTM Int. 2, JAI11997.

[7] Pokluda J., Šandera P. and Pippan J. (2006). In: "Fatigue 06", Ed. W. S. Johnson, Elsevier, Atlanta, Georgia, USA, p. 0107A_03.

[8] Pokluda J. and Pippan R. (2007). Mater. Sci. Eng. A 462, 355.

[9] Pippan R. (1991). Mater. Sci. Eng. A 138, 1.

[10] Pokluda J., Podrábský T., Slámečka K., Pospíšilová S. and Chai G. C. (2008). Mater. Sci. Forum 567-568, 101.

Key Engineering Materials Vols. 385-387 (2008) pp 53-56
© (2008) Trans Tech Publications, Switzerland
doi:10.4028/www.scientific.net/KEM.385-387.53

Cavity Dynamic Formation and Bifurcation of the Rubber-like Sphere

Guohui Wu[1,a], Yong Wang[1,b], Liqiang Tang[1],Yong Yang[1]

[1]College of Civil Engineering, Harbin Engineering University, Harbin 150001,China

[a]wuguohui@hrbeu.edu.cn,[b]wangyong3502@163.com

Keywords: incompressibility; sphere; bifurcation; dynamic formation; cavity

Abstract. Based on the strain energy function proposed by GAO Y C and the theory of finite deformation dynamics, the question about the cavity dynamic formation and bifurcation of the incompressible homogeneous solid sphere under a suddenly applied uniform tensile dead-load was studied. The condition under which a dynamic bifurcated solution exists was examined. The relationship between the dead-load and the cavity radius, the critical load, the stress distributions after the cavity formation, the vibration phase diagram of the cavity radius and the approximate vibration period were also determined.

Introduction

In recent years, void nucleation and growth in rubber-like material have become a hot topic because this phenomena can help people realize the damage and failure mechanical mechanism of the rubber-like material. In 1958, the phenomena of sudden void formation was observed experimentally in vulcanized rubber by Gent and Lindley[1]. But until in 1982, Ball[2] successfully used the nonlinear bifurcation theory to explain this phenomena. After then further investigations of such bifurcation problems have also been made in [3-6]. For the static case, the sphere consisting of the incompressible homogeneous isotropic rubber was studied by L. Q. Tang[3]. While X. C. Shang[4] considered the compressible case. For the dynamic case, the large amplitude vibrations of hollow incompressible elastic cylinder was firstly considered by Knowles[5]. Then an incompressible elastic solid sphere composed of neo-Hookean material under a suddenly applied uniform radial tensile dead-load was considered by Chou-Wang[6]. In this paper, the problem on the cavity dynamic formation and bifurcation of the incompressible homogeneous solid sphere under a suddenly applied uniform tensile dead-load was considered. In order to own the obvious physical meaning, the question was discussed in the material coordinates.

The mathematical model of the problem

We consider a finite deformation dynamic model of an incompressible hyperelastic solid sphere which is set into motion at time $t=0$ by a suddenly applied uniform radial dead-load p_0. The spherical coordinates are adopted and the material and spatial coordinates are respectively denoted by (R,Θ,Φ), (r,θ,ϕ). So the undeformed configuration (initial configuration) can be described by $C_0=\{(R,\Theta,\Phi)/0\le R\le A,0\le\Theta\le\pi,0\le\Phi\le 2\pi\}$.

Let a point (R,Θ,Φ) in the undeformed sphere move to (r,θ,ϕ) at time t, so the motion can be described by

$$r=r(R,t)>0,\theta=\Theta,\phi=\Phi, \tag{1}$$

where $r(R,t)$ is to be determined and $r(0^+,t)\ge 0$.

Define the principal stretches

$$\lambda_r = \partial r(R,t)/\partial R; \lambda_\theta = \lambda_\phi = r(R,t)/R. \quad (2)$$

Then through the equation (1), the deformation gradient and the left Cauchy-Green deformation tensors can be given by $\boldsymbol{F} = \mathrm{diag}(\lambda_r, \lambda_\theta, \lambda_\theta)$, $\boldsymbol{B}=\boldsymbol{F}\cdot\boldsymbol{F}^T = \mathrm{diag}(\lambda_r^2, \lambda_\theta^2, \lambda_\theta^2)$. So the first invariant is $I_1 = \lambda_r^2 + 2\lambda_\theta^2$. Through the incompressible condition $\det \boldsymbol{F} = 1$, we have $\lambda_r = \lambda_\theta^{-2}$. Then with the help of equation (2), a differential equation is obtained. Solving it, we can gain

$$r = (R^3 + K^3(t))^{\frac{1}{3}}. \quad (3)$$

It is obviously found that if $K(t) = 0$ for $t \geq 0$, the above equation indicates that the sphere remains solid in the current configuration which corresponds to the trivial solutions. While if $K(t) > 0$, a cavity will occur in the sphere, and its radius is $K(t)$ which corresponds to the singular solutions. It is worth noting that in the dynamic case the cavity radius makes nonlinear vibration with the time.

Combining the equation (2) and (3), we can gain

$$\lambda_r = [1 + (\frac{K(t)}{R})^3]^{-2/3}, \lambda_\theta = [1 + (\frac{K(t)}{R})^3]^{1/3}. \quad (4)$$

The strain energy function proposed by Y.C.Gao is given by

$$W = a(I_1^n - 3^n), \quad (5)$$

where $a > 0, n > 0$ .When $a = \mu/2$, $n = 1$, the above equation can degenerate into the famous Neo-Hooken material. So the document [6] can be viewed as the special case of this paper.

Cauchy stress tensor are given by

$$\boldsymbol{\sigma} = -p\boldsymbol{I} + 2\partial W/\partial I_1 \boldsymbol{B} - 2\partial W/\partial I_2 \boldsymbol{B}^{-1}, \quad (6)$$

where p is the hydrostatic pressure and $\boldsymbol{I}$ is the unit tensor.

Substituting the equation (5) into (6), we can gain

$$\sigma_{rr} = -p(R,t) + 2an(\lambda_\theta^{-4} + 2\lambda_\theta^2)^{n-1}\lambda_\theta^{-4}, \sigma_{\theta\theta} = \sigma_{\phi\phi} = -p(R,t) + 2an(\lambda_\theta^{-4} + 2\lambda_\theta^2)^{n-1}\lambda_\theta^2; \quad t \geq 0, \quad (7)$$

where λ_θ is given by the equation (4) and $p(R,t)$ represents the arbitrary hydrostatic pressure.

If the body force is not considered, the equation of motion in the initial configuration can be described by

$$\frac{\partial \sigma_{rr}}{\partial R} = \lambda_r \rho \frac{\mathrm{d}^2 r}{\mathrm{d}t^2} - \frac{2(\sigma_{rr} - \sigma_{\theta\theta})}{R}\frac{\lambda_r}{\lambda_\theta} \quad t \geq 0, \quad (8)$$

where ρ is the material density.

The boundary conditions are

$$\sigma_{rr}(A,t) = p_0 A^2 / r^2(A), \quad \sigma_{rr}(0,t) = 0, \quad t \geq 0, \quad (9)$$

where the second equation denotes that if the cavity forms, its surface is free.

Assume that the sphere is in the undeformed state and at rest at time $t = 0$. So the conditions $r(R,0) = R, \dot{r}(R,0) = 0$ can be obtained. Then from the equation (3), the initial conditions can be given by

$$K(0) = 0, \dot{K}(0) = 0. \quad (10)$$

At present the problem to be solved is the following: for a prescribed value of the tensile dead-load $p_0 > 0$, we seek the hydrostatic $p(R,t)$ and a time dependent function $K(t) \geq 0$ under the boundary conditions (9) and the initial conditions (10) from solving the equation (8). In this paper, the singular solutions of $K(t) > 0, t \geq 0$ is only considered.

Solutions

Substituting the equations (3) and (7) into the equation (8), then integrating with respect to R from $0 \to R$ and using the boundary condition（9-2）, we can gain

$$\sigma_{rr}(R,t) = \int_0^R \rho[1 + (\frac{K(t)}{R})^3]^{-\frac{2}{3}}\{\{\frac{2K(t)}{[R^3 + K^3(t)]^{\frac{2}{3}}} - \frac{2K^4(t)}{[R^3 + K^3(t)]^{\frac{5}{3}}}\}[\frac{\mathrm{d}K(t)}{\mathrm{d}t}]^2 + \frac{K^2(t)}{[R^3 + K^3(t)]^{\frac{2}{3}}}\frac{\mathrm{d}^2 K(t)}{\mathrm{d}t^2}\}\mathrm{d}R$$

$$-\int_0^R \frac{2}{R}\lambda_\theta^{-3}2an(\lambda_\theta^{-4}+2\lambda_\theta^{2})^{n-1}(\lambda_\theta^{-4}-\lambda_\theta^{2})\mathrm{d}R. \tag{11}$$

With the help of the equations (3) and (4), we can respectively make the replacement of integral variable for the first and the second integral in the equation (11) and gain

$$\begin{aligned}\sigma_{rr}(R,t)=\rho[\frac{\mathrm{d}K(t)}{\mathrm{d}t}]^2\left\{\frac{3}{2}-\frac{2K(t)}{[R^3+K^3(t)]^{1/3}}+\frac{K^4(t)}{2[R^3+K^3(t)]^{4/3}}\right\}\\ +\rho\frac{\mathrm{d}^2K(t)}{\mathrm{d}t^2}\left\{K(t)-\frac{K^2(t)}{[R^3+K^3(t)]^{1/3}}\right\}-\int_{[1+(\frac{K(t)}{R})^3]^{1/3}}^{\infty}\frac{4an(\lambda_\theta^{-4}+2\lambda_\theta^{2})^{n-1}(\lambda_\theta^{-5}-\lambda_\theta)}{\lambda_\theta^{3}-1}\mathrm{d}\lambda_\theta\end{aligned}. \tag{12}$$

Using the equation (7), we can also obtain

$$\sigma_{\theta\theta}(R,t)=2an(\lambda_\theta^{-4}+2\lambda_\theta^{2})^{n-1}(\lambda_\theta^{2}-\lambda_\theta^{-4})+\sigma_{rr}(R,t). \tag{13}$$

The equations (12) and (13) are the stress analytical solutions to this question.

With the equations（9-1）and（12）, we gain

$$\begin{aligned}p_0[1+(\frac{K(t)}{A})^3]^{-2/3}=\rho[\frac{\mathrm{d}K(t)}{\mathrm{d}t}]^2\times\left\{\frac{3}{2}-\frac{2K(t)}{[A^3+K^3(t)]^{1/3}}+\frac{K^4(t)}{2[A^3+K^3(t)]^{4/3}}\right\}\\ +\rho\frac{\mathrm{d}^2K(t)}{\mathrm{d}t^2}\left\{K(t)-\frac{K^2(t)}{[A^3+K^3(t)]^{1/3}}\right\}-\int_{[1+(\frac{K(t)}{A})^3]^{1/3}}^{\infty}\frac{4an(\lambda_\theta^{-4}+2\lambda_\theta^{2})^{n-1}(\lambda_\theta^{-5}-\lambda_\theta)}{\lambda_\theta^{3}-1}\mathrm{d}\lambda_\theta\end{aligned}. \tag{14}$$

This second-order nonlinear differential equation provides a relationship between the tensile dead-load p_0 and cavity radius $K(t)$. Replacing $K(t)$ in equations (12)-(14) by the constant K, we can conveniently gain the stress distributions and the relationship between the tensile dead-load and cavity radius in the static case, which are the same as the conclusions in document [3]. So it is founded that the dynamic case can degenerate into the static case conveniently.

Let $x(t)=K(t)/A$, $v=\frac{\mathrm{d}x}{\mathrm{d}t}$ in the equation (14) , then integrate with respect to x from $0\to x$, we obtain

$$2p_0[(1+x^3)^{1/3}-1]=\rho A^2x^4v^2[\frac{1}{x}-\frac{1}{(1+x^3)^{1/3}}]+8an\int_0^x y^2\int_{[1+y^3]^{1/3}}^{\infty}\frac{(\lambda_\theta^{-4}+2\lambda_\theta^{2})^{n-1}(\lambda_\theta-\lambda_\theta^{-5})}{\lambda_\theta^{3}-1}\mathrm{d}\lambda_\theta\mathrm{d}y. \tag{15}$$

From the theory of vibrations, we know that the motion $x(t)$ is periodic if and only if the phase diagram is the closed curve in the $x\sim v$ plane with a finite period.

Assuming $v=0$ in the equation (15), we can gain

$$2p_0[(1+x^3)^{1/3}-1]=8an\int_0^x y^2\int_{[1+y^3]^{1/3}}^{\infty}\frac{(\lambda_\theta^{-4}+2\lambda_\theta^{2})^{n-1}(\lambda_\theta-\lambda_\theta^{-5})}{\lambda_\theta^{3}-1}\mathrm{d}\lambda_\theta\mathrm{d}y. \tag{16}$$

For a given p_0, if there is a root and the root is $x>0$ in the equation (16), the root denoted by x_m corresponds to the maximum of the cavity radius in the process of the vibration.

When $x\to 0^+$, by the equation (16) the critical load is obtained by

$$p_{cr}=4an\int_1^{\infty}\frac{(\lambda_\theta^{-4}+2\lambda_\theta^{2})^{n-1}(\lambda_\theta-\lambda_\theta^{-5})}{\lambda_\theta^{3}-1}\mathrm{d}\lambda_\theta. \tag{17}$$

If the critical load p_{cr} is a finite value, the constitutive parameter n must be demanded that $n<1.5$ which is same as the static case. The above equation provides the condition under which a dynamic bifurcated solution exists. When $a=\mu/2, n=1$, that is to say, the material is the famous Neo-Hooken material, we can gain $p_{cr}=2.5\mu$ from the above equation which is the same as the conclusion in the document [6]. So the model built in the document [6] can be seen as a special case of this paper.

Discussions

From the equation (16), we can give the fig.1 where $p_0^{\#}=p_0/a$. It is seen that the maximum of the cavity radius increases with the increment of the constitutive parameters a,n from fig. 1.

Through the equation (15), we can gain the relationship between v and x, which provides the phase diagram fig.2 if $n=1.2$ and $p_0=11.05a$. In this condition the load $p_0=11.05a$ is larger than the critical load $p_{cr}/a=10.85$, so the cavitation phenomena occurs. Then by the periodic formula $T=\oint\frac{1}{v}dx$, we can obtain the approximate vibration period of the cavity radius $T=3.09A\sqrt{\rho/a}$.

From the fig.2, it is found that the curve of $x\sim v$ is a closed curve and is a symmetric about the x-axias. It starts at the initial point $x=0,v=0$ at time $t=0$. Then the velocity v firstly increases quickly and secondly decreases as the cavity radius x increases from zero. When the x reaches the maximum x_m, v decreases to zero. Later x decreases, while v firstly increases, secondly decreases rapidly. When x reaches zero, the velocity v also decreases to zero. So the curve is closed. The fact that the curve is approximately parallel to the v axis near the zero point indicates that the cavity occurs suddenly and increases rapidly.

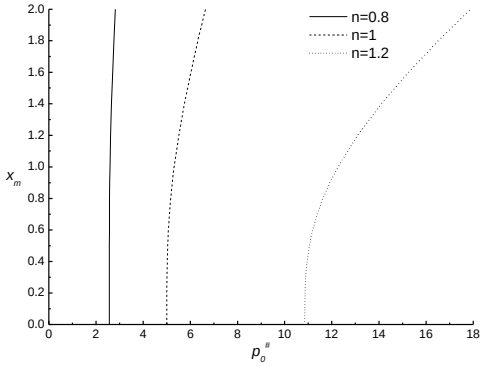

Fig. 1 the relationship plot between x_m and p_0

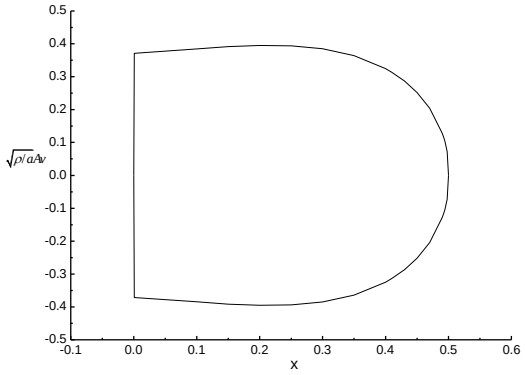

Fig.2 the phase diagram when $n=1.2, p_0=11.05a$

Conclusions

Through the full paper, we can gain the following conclusions: 1）the dynamic case built here may degenerate into the static case conveniently; 2）only if the constitutive parameter n meets $0<n<1.5$, the rubber solid sphere exists dynamic bifurcated solution. The critical load which is only relative to the material constitutive parameters reflects the material's intrinsic property and increases with the increment of the constitutive parameters; 3）when the tensile dead-load is larger than the critical load, a cavity suddenly appears in the centers of the sphere and can grow quickly. The cavity displayed a periodic nonlinear vibration; 4）the constitutive parameter n has the important influences on the critical load and the relationship between the load and the maximum amplitude.

Acknowledgements

This research was supported by the Nature Foundation of Heilongjiang Province in China under Grant No.A2004-08 and by the Foundation of Harbin Engineering University under Grant No. HEUF04005.

References

[1] A. N. Gent, P. B. Lindley: Proc. R. Soc. Lond. Vol. A249 (1958), p. 195
[2] J. M. Ball: Phil. Trans. Roy. Lond. Vol.306 (1982), p. 557
[3] L. Q. Tang, Z. Q. Fan and Y. Yang: J. of Harbin Engineering University Vol. 26 (2005), p. 624
[4] X. C. Shang, C. J. Cheng: Int. J. Eng. Sci. Vol. 39 (2001), p. 1101
[5] J. K. Knowles: J. Appl. Mech. Vol. 29 (1962), p. 283
[6] M. S. Chou-wang, C. O. Horgan: Int. J. of Engng, Sci, Vol. 27 (1989), p.967

Key Engineering Materials Vols. 385-387 (2008) pp 57-60
© (2008) Trans Tech Publications, Switzerland
doi:10.4028/www.scientific.net/KEM.385-387.57

Contact Fatigue Behaviour of PVD-coated Spur Gears

Sergio Baragetti[1,a], Angelo Terranova[2,b] and Federico Tordini[1,c]

[1]Dipartimento di Progettazione e Tecnologie, Università degli Studi di Bergamo, Viale Marconi 5, 24044, Dalmine (BG), Italy

[2]Dipartimento di Meccanica, Politecnico di Milano, Via La Masa 34, 20156, Milano, Italy

[a]sergio.baragetti@unibg.it, [b]angelo.terranova@polimi.it, [c]federico.tordini@unibg.it

Keywords: PVD coatings, Residual stresses, Contact fatigue, Spur gears, Numerical models

Abstract. In this paper the contact fatigue behaviour of gears coated with PVD (Physical Vapor Deposition) thin hard film was studied. Contact fatigue tests (R = 0) were carried out on both coated and uncoated automotive transmission spur gears. The bulk material and the coating analysed throughout the tests were, respectively, case hardened 18NiCrMo5 and CrN. The influence of the coating was both experimentally and numerically evaluated. Several FEM models were developed to assess the stress and strain distributions from tooth flank surface to in-depth layers. The influence of the surface treatments on the bulk material was taken into account with the models and the Coffin-Manson equation was used to predict the number of load cycles necessary for initial fatigue damage to occur. All the tested tooth flanks were observed using optical microscope and SEM.

Introduction

The need to lower fuel consumption with more power available is becoming a fundamental issue for several mechanical applications, especially in the automotive and aerospace fields. From this point of view, lightening structural components using suitable light alloys would prove to be effective. Thin hard coatings may improve surface hardness, wear and corrosion resistance of mechanical components [1] and so even the fatigue and contact fatigue behaviour, as demonstrated in recent research studies [2-5]. PVD-coated light alloys with similar or better performances than steels would be highly beneficial to a lot of structural applications. As far as the authors know, no significant theoretical-numerical studies on both the contact fatigue behaviour of PVD-coated gears and the effect of the surface residual stresses induced with deposition and case hardening processes are available. In this work the contact fatigue in both PVD-coated and uncoated case hardened spur gears was investigated by means of numerical models and the Coffin-Manson relationship between deformation amplitude and number of cycles required for fatigue damage initiation [6]. Furthermore, suitable experimental tests were performed to check and set up the numerical analyses. The models enabled to assess the number of cycles necessary to promote the initial fatigue crack formation at the contact area [6, 7].

Material and methods

Standard automotive transmission spur gears made of 18NiCrMo5 steel alloy were tested under contact fatigue (R = 0) on a computer-controlled universal testing machine (BRT VT250) at room temperature and at a frequency of 20 Hz. The case hardening depth was in the interval 0.5-0.6 mm, and the surface hardness 560 HV. The material yield strength was 690 MPa, while the ultimate tensile strength 828 MPa [8]. Some of the gears were coated with a PVD arc-deposited CrN film: the average film thickness was 10.0 μm and the surface hardness after deposition 700 HV. The module of the gears was 2.95 mm, the number of teeth 24, the pitch diameter 70.80 mm and the tooth width 13.34 mm. The tests were carried out by introducing a cylindrical roller having a diameter of 8 mm between each couple of adjacent teeth. The contact between cylindrical roller and tooth flanks was very close to the outer point of single teeth pair engagement (Fig. 1), which is the most critical contact loading area during gear meshing. A suitable device made it possible to keep the gear fixed while the pulsating load was being applied to the roller along the vertical direction.

Six load levels ranging from 0.625 to 15 kN were used. Table 1 gives the resultant normal force on each tooth flank at each load level and the corresponding maximum contact Hertzian pressure in the case of steel-on-steel contact without friction. The experiments were performed without lubrication. The material of the cylindrical roller was hardened 100Cr6, which has higher strength - *i.e.* yield equal to 1650 MPa and ultimate to 1900 MPa - and hardness - namely 848 HV - than the gear material. After the tests, the tooth flanks were investigated with optical microscope (Leica MZ75) and SEM (ZEISS EVO 40) to assess and quantify the contact fatigue damage.

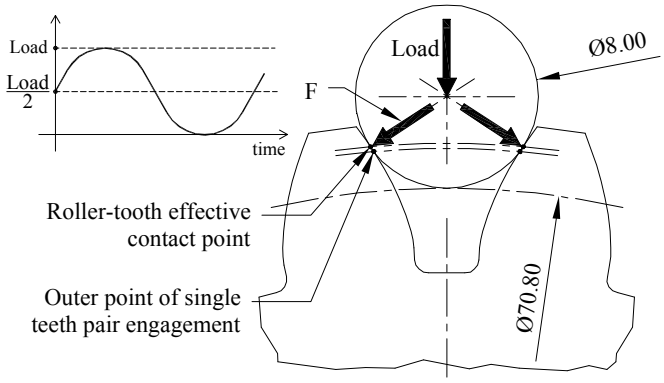

Figure 1 – Load application scheme.

Load [kN]	F [kN]	p_{Hertz} [MPa]
0.625	0.56	671
1.25	1.13	949
2.5	2.26	1343
5	4.51	1899
10	9.03	2685
15	13.54	3289

Table 1 – Test loads on tooth flanks.

Results and discussion

Experimental tests. Fig. 2 and 3 summarize the main results from experimental tests. Fig. 2 shows the extension of the damaged areas on the tooth flanks with respect to load cycle number at a load of 1.25 kN for both coated and uncoated gear. Fig. 3 shows the areas at constant load cycle number with the applied load varying in the afore reported range. Both the diagrams indicate that coated gear has a worse behaviour with respect to uncoated one and that the correlation between areas and both number of cycles and load levels is nearly linear. Nevertheless, in the presence of the coating a remarkable increase (Fig. 3) in fatigue damage between 5 and 10 kN at both 10000 and 50000 load cycles took place. Large coating detachments were observed on the tooth flanks tested at 10 and 15 kN. Furthermore, even at low loads and number of load cycles the coating showed damage or delamination - as SEM analyses evidenced, confirming that lower thicknesses - *i.e.* not higher than 1 μm - or other coatings [2] could prove more effective under contact or rolling contact fatigue. As far as uncoated gear is concerned, no surface damage was detected after 10000 cycles only at the lowest applied load - *i.e.* 0.625 kN.

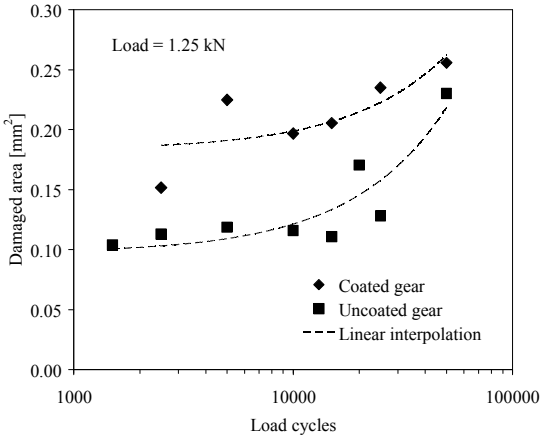

Figure 2 – Damaged area vs. Load cycles diagram.

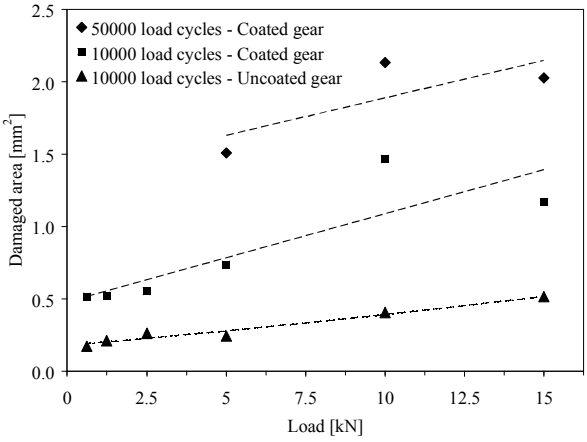

Figure 3 – Damaged area vs. Load diagram.

Fig. 4 shows the damaged area of a coated tooth flank tested under one of the most severe test conditions - namely at 10 kN and 50000 load cycles. It is quite clear that coating delamination occurred and wide pieces of coating were detached from the substrate. Fig. 5 depicts spall formation

in coated gear. The inclination of the crack suggests that the presence of the coating does not influence the typical pitting or spalling mechanism which takes place under rolling contact fatigue for uncoated components [6-9].

Numerical models. The stress distribution on and below the contact surface for both coated and uncoated gears was numerically determined by means of the FE code ABAQUS 6.6-1. Several 2D models were developed and the submodeling technique was also used to refine the calculations at the contact area. CPE4 4-node bilinear plane strain elements were used for the bulk material, while CPE3 3-node linear plane strain ones for the coating. Models and submodels with more than 40000 dof were solved at each test load level.

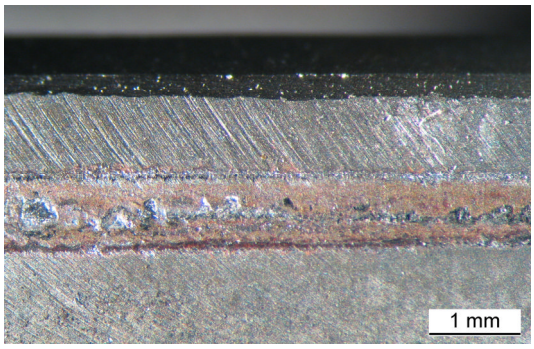

Figure 4 – Magnification (2x) of a coated tooth flank tested at 10 kN and 50000 load cycles.

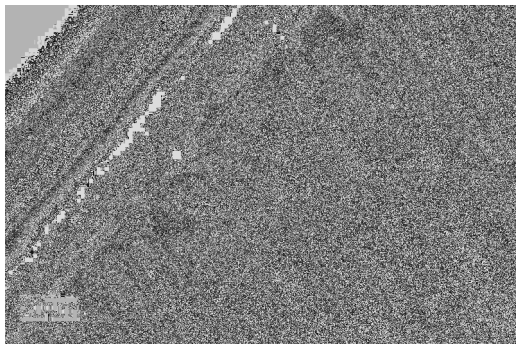

Figure 5 – SEM micrograph of incipient spall formation in a coated tooth flank tested at 1.25 kN and 50000 load cycles.

In order to use the models to predict the number of loading cycles necessary for fatigue damage initiation, a suitable cyclic softening behaviour of gear base material was introduced [8, 10] and the Coffin-Manson law [6] was applied:

$$\frac{\Delta\varepsilon}{2} = \frac{\sigma'_f}{E}\left(2N_f\right)^b + \varepsilon'_f\left(2N_f\right)^c \qquad (1)$$

where $\Delta\varepsilon$ is the cyclic deformation amplitude, N_f the number of loading cycles to initial damage, σ'_f the fatigue strength coefficient, ε'_f the fatigue ductility coefficient, b and c, respectively, the strength and the fatigue ductility exponent. For 18NiCrMo5 the following values were used: σ'_f = 1890 MPa, ε'_f = 0.848, b = -0.115 and c = -0.734 [8, 10].

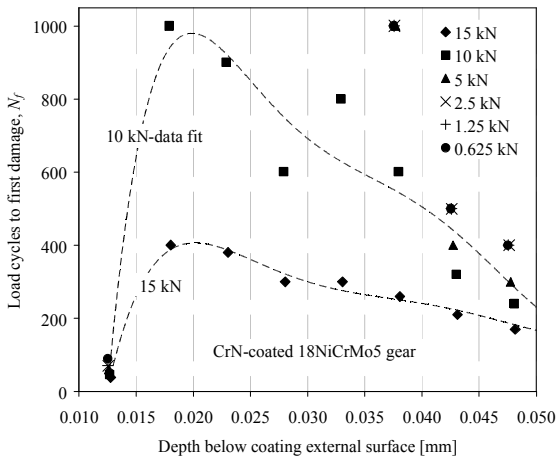

Figure 6 – Damaged area vs. Load cycles diagram.

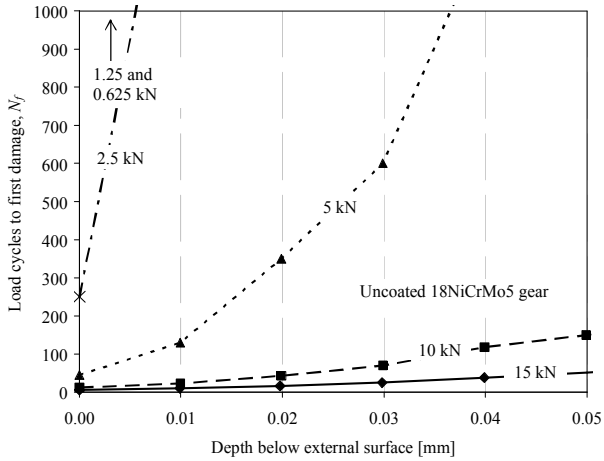

Figure 7 – Damaged area vs. Load diagram.

A bilinear elastic-perfectly plastic behaviour was adopted for cylindrical roller material and a perfectly elastic one for the coating. Suitable surface residual stress fields were applied to take into account the PVD deposition [4] and the case hardening [11] treatments. The maximum compression stresses were set at surface and were -2400 MPa for coated gear and -150 MPa for uncoated one. The tangential contact behaviour was considered by introducing a friction factor of 0.5 to reproduce

the unlubricated condition. The models enabled to calculate the maximum cyclic deformations and to assess their position over the contact area. The main results are summarized in Fig. 6 and 7, which show the numbers of cycles to first damage from the surface to the core of the tooth for each applied load. The minimum N_f was at bulk material external surface for both the coated and the uncoated gear, showing good agreement with SEM observations. Furthermore, the number of cycles to initial damage in uncoated gear calculated with the load of 0.625 kN was higher than 10000, while at higher loads N_f was very low - *i.e.* lower than 300 - for both coated and uncoated gear (Fig. 6 and 7). This confirmed the experimental evidence.

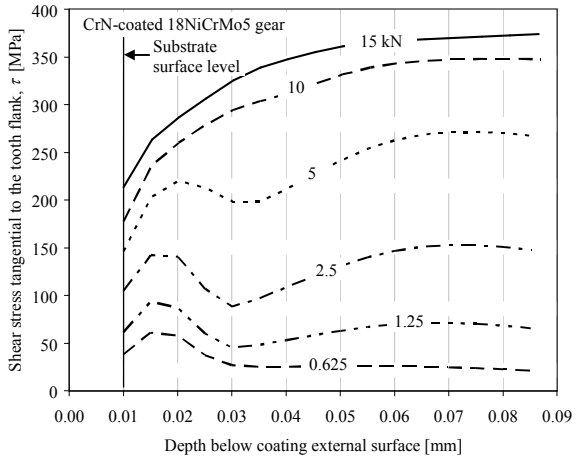

Figure 8 – Coated gear: Shear stress vs. Depth bel. surf.

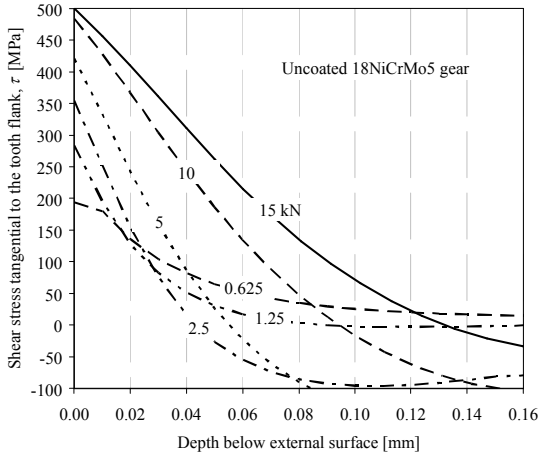

Figure 9 – Uncoated gear: Shear stress vs. Depth bel. surf.

Summary

A suitable theoretical-numerical model able to foresee the number of cycles to initial contact fatigue damage in coated and uncoated gears was developed. The contact fatigue experimental tests showed that the 10 μm-thick CrN coating is unsuitable in the presence of contact fatigue. The damaged areas in coated gear were wider than in uncoated one, even if it is possible to address them to extra quotes from coating failure. FEM analyses showed that maximum deformation amplitudes promoting initial damage occurred at external surface for uncoated gear and at coating-bulk material interface for coated one. This should have been due to the high friction from unlubricated condition and the residual stress fields from surface treatments and it was in good agreement with the experimental evidence. The shear stresses at coating-substrate interface (Fig. 8) and the peak values approached at uncoated external surface (Fig. 9) fit well the actual initial damage positions. The experimental damage-load graph for uncoated gear was quite more uniform than for coated one (Fig. 3). This suggests that the high residual stresses induced by PVD deposition may play a detrimental role under contact fatigue, even if it is important to underline that, as far as the higher test loads are concerned - *i.e.* 10 and 15 kN, the coating could be led to fracture statically (Table 1).

Acknowledgements

The Authors wish to thank BRT (Casei Gerola, Italy) for the experimental tests, eng. Stefano Cavalleri for his help in FEM analyses and tests and LAFER (Piacenza, Italy) for the execution of the coatings.

References

[1] A.M. Merlo: Surf Coat Technol Vol. 174-(175) (2003), pp. 21-26.
[2] S. Stewart, R. Ahmed: Wear Vol. 235 (2002), pp. 1132-1144.
[3] K.R. Kim, C.M. Suh, R.I. Murakami, C.W. Chung: Surf Coat Tech. **171** (2003), pp. 15-23.
[4] S. Baragetti, G.M. La Vecchia, A. Terranova: Int J Fat Vol. 27(10-12) (2005), pp. 1541-1550.
[5] S. Baragetti: Int J Fat Vol. 29 (2007), pp. 1893-1903.
[6] M. Šraml, J. Flašker: Int J Adv Manuf Technol Vol. 31 (2007), pp. 1066-1075.
[7] S. Glodež, B. Aberšek, J. Flašker, Z. Ren: Engng Fract Mech Vol. 71 (2004), pp. 429-438.
[8] *ASM Metals Handbook*, edited by ASM International, 10th edition, Materials Park, OH (1993).
[9] S. Suresh: *Fatigue of Materials*, edited by Cambr Univ Press, 2nd edition, Cambridge (2004).
[10] Y. Higashida, J.D. Burk, F.V. Lawrence Jr.: Weld Res Suppl Vol. 5083 (1978), pp. 334s-344s.
[11] M. MackAldener, M. Olsson: Int J Fat Vol. 23 (2001), pp. 329-340.

Key Engineering Materials Vols. 385-387 (2008) pp 61-64
© (2008) Trans Tech Publications, Switzerland
doi:10.4028/www.scientific.net/KEM.385-387.61

Cement loop damage mechanism in the process of repairing casing

Liqiang Tang[1,a], Shuzhang Sun[1], Congcong Wu[1],Xuemei Yu[1]

[1]College of Civil Engineering, Harbin Engineering University, Harbin 150001, China

[a]ccheu@163.com

Keywords: cement loop damage; fibrous composite model; the distribution of stress and displacement field; debonded length

Abstract: Based on the theories of fracture mechanics and composite materials mechanics, fibrous composite model that interacted on stratum, cement loop and casing was firstly established. Boundary conditions that the repaired force acted in fibrous composite model were also given. The influences of interface damage evolution and fracture process of fiber and matrix on the cement loop mechanical properties were studied as well. Meanwhile the distributions of stress and displacement fields were obtained. Finally, the debonded length and variation of the optimum repaired force were also determined, which can restrict the cement damage length to the lowest scale. The results given here can provide a reliable design references for improving the technology of repairing casing damage well.

Introduction

In traditional casing design, simple stimulation test was mainly used to study and analyse casing strength under the conditions of bearing nonhomogenous external applied load, homogenous external applied load and diametrical concentrated load[1]. There are few studies on the interactions between the formation, cement loop and casing. Based on the theories of fracture mechanics and composite materials mechanics, fibrous composite model that interacted on stratum, cement loop and casing was firstly established. Boundary conditions that the repaired force acted in fibrous composite model were also given. The influences of interface damage evolution and fracture process of fiber and matrix on the cement loop mechanical properties were studied as well. Meanwhile the distributions of stress and displacement fields were obtained. Finally, the debonded length and variation of the optimum repaired force were also determined, which can restrict the cement damage length to the lowest scale. The results given here can provide a reliable design references for improving the technology of repairing casing damage well.

Mechanical model of composite materials in the process of rolling-plastic

In the process of repairing casing damaged wells, it would cause stress redistribution of the casing-cement loop-formation system, and result in the cement loop damage. If we look stratum layer and cement loop cementation surface as matrix (using subscript m as physical quantity in the matrix), casing as fiber(using subscript f as physical quantity in the matrix), then the casing-cement loop-formation system can be abstracted as fiber composite materials, and the process of cement loop damage can be simulated as fiber-matrix debonding problem of fiber composite materials in the interface. [2]

Interface damage mechanic model of cement loop in the process of rolling plastic is showed as figure 1. Casing deformation take place at the H from the ground, and earth stress is σ_{H}. $0 \le z \le l$ is debonding area, $l \le z \le s$ is bonding area. In order to facilitate the calculation, following assumptions are made:

(1)P is tensile load applied on the casing, that is :.

$$P = \sigma_{zf}\pi(b^2 - a^2) \qquad z = 0 \quad . \tag{1}$$

where σ_{zf} is fiber stress in the z direction.

(2)Ignore initial stress of casing in the process of repairing well and influence of well liquid. Assume fiber and matrix as linear elastic material, and ignore influence of volume force.

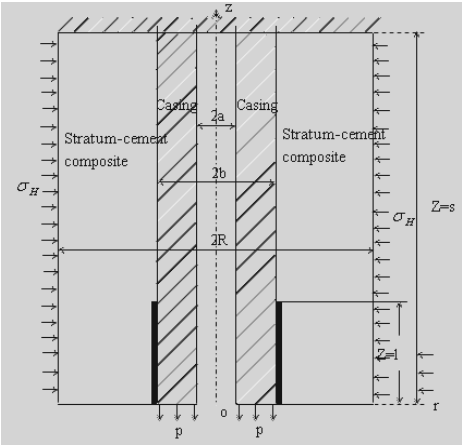

Fig1. Mechanical model of bonding area destroyed between casing and cement loop

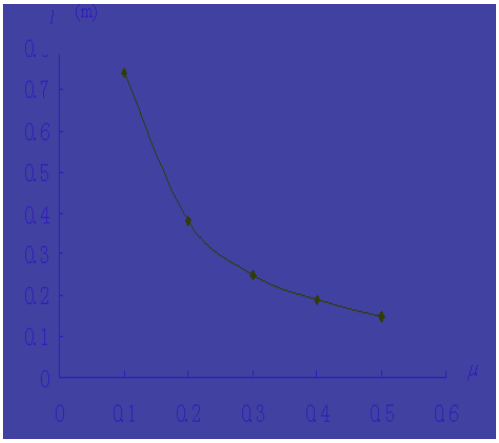

Fig2. Curve of friction coefficient and cement loop damage length

1. The bonding area

Stress and displacement meet continuous conditions, that is :

$$[\sigma_{ij} n_j]_\Gamma = 0 \quad , \quad [u_i]_\Gamma = 0 \quad , \tag{2}$$

where $[\phi_n]_\Gamma$ is gap quantity of physical quantity ϕ in the interface Γ , $[\phi_n]_\Gamma = \phi_{n+} - \phi_{n-}$.

When $z = s$, displacement equation is :

$$u_f(z) = u_m(z) = 0 \quad . \tag{3}$$

2. The debonding area ($0 \le z \le l$)

Assume tensile load applied on casing in the z direction is T_f , $T_f = \sigma_{zf}\pi(b^2 - a^2)$. Under the action of T_f , casing will contract in the lateral and matrix will has expand, so additional stress q^* would be generated in the interface. Assume $q_f^* = (\sigma_{rf} + \sigma_{\theta f})$ is additional stress that generated by casing, $q_m^* = (\sigma_{rm} + \sigma_{\theta m})$ is additional stress that generated by matrix, so stress-strain relationships of casing and matrix in the z direction can be expressed:

$$\varepsilon_{zf} = \frac{\mathrm{d}u_f}{\mathrm{d}z} = \frac{1}{E_f}\left[\sigma_f - \gamma_f(\sigma_{rf} + \sigma_{\theta f})\right] = \frac{1}{E_f}\left(\frac{T_f}{\pi(b^2 - a^2)} - \gamma_f q_f^*\right)$$
$$\varepsilon_{zm} = \frac{\mathrm{d}u_m}{\mathrm{d}z} = \frac{1}{E_m}\left(\frac{T_m}{\pi(R^2 - b^2)} - \gamma_m q_m^*\right) \tag{4}$$

where $E_f, E_m, \gamma_f, \gamma_m$ are Young's modulus and Poisson's ratio of casing (fiber) and matrix respectively. T_m is the tensile load in the matrix , and $T_m = \sigma_{zm}\pi(R^2 - b^2)$. There is a shear stress acting on the debonded zone due to the interface pressure, which meets Coulomb friction law. That is:

$$\tau_s = -\mu\sigma_n = -\mu\sigma_{rf} - \mu\sigma_{rm} \quad . \tag{5}$$

3.The whole area. ($0 \le z \le s$) ,we have

$$\sigma_{rm} = -\sigma_H \qquad r = R, \qquad \sigma_{rf} = 0 \qquad r = a \quad , \qquad T_f + T_m = P \quad . \tag{6}$$

The equilibrium equation in the z direction：

$$\frac{\mathrm{d}T_m}{\mathrm{d}z} = -\frac{\mathrm{d}T_f}{\mathrm{d}z} = 2\pi b\tau_s \quad , \quad T_f = P \quad , \quad T_m = 0 \tag{7}$$

Stress-displacement field of casing-cement loop in the process of rolling-plastic

Stress and displacement distribution in casing can be obtained, that is:

$$\sigma_{rf} = \frac{B_1}{r^2} + c_1, \quad \sigma_{\theta f} = -\frac{B_1}{r^2} + c_1, u_{rf} = -\frac{1+\gamma_f}{E_f}\cdot\frac{B_1}{r} + (\frac{1-\gamma_f}{E_f}c_1 - \frac{\gamma_f}{E_f}\sigma_{zf})r, \tag{8}$$

Ihe matrix, the distributions of stress and displacement are:

$$\sigma_{rm} = \frac{B_2}{r^2} + c_2, \sigma_{\theta m} = -\frac{B_2}{r^2} + c_2, \quad u_{rm} = -\frac{1+\gamma_m}{E_m}\cdot\frac{B_2}{r} + (\frac{1-\gamma_m}{E_m}c_2 - \frac{\gamma_m}{E_m}\sigma_{zm})r \quad , \tag{9}$$

where B_1 , B_2 , c_1 , c_2 are undetermined constants, which are determined by boundary conditions and interfacial continuous conditions.

When stress is applied, the displacements of casing u_f and matrix u_m can be determined by elastic constitutive equation, boundary conditions and continuous displacement conditions.

1. Interface bonding area ($l < z < s$)

$$u_f = u_m = (z-s)\frac{1}{E_f}\left[P^* + \sigma_H^*\right], \tag{10}$$

where P^* and σ_H^* represent the contributions of applied force and earth stress to the displacements of casing and matrix, and

$$P^* = \frac{c_f\tilde{P}}{c_m KA}(A - 2(\alpha\gamma_f^2 + \gamma_m^2 c_f / c_m)), \sigma_H^* = \frac{2\tilde{\sigma}_H}{KA}(\gamma_m A + 2\left[(\gamma_f - \gamma_m)c_f / c_m - \gamma_m\gamma_f c\right]),$$
$$K = \alpha + c_f / c_m - 2c^2 / A. \tag{11}$$

where $A = \alpha\left(a^2/b^2+1\right) + \gamma_f(a^2/b^2-1) + c_f/c_m\left[\left(R^2/b^2+1\right) + \gamma_m(R^2/b^2-1)\right], \alpha = E_m/E_f$

$\tilde{P} = P/(\pi b^2 - \pi a^2), c_f = (b^2-a^2)/(R^2-a^2), c_m = (R^2-b^2)/(R^2-a^2), c_f + c_m = 1.$

2. Interface debonding area ($0 < z < l$)

From constitutive equations, displacements of debonded zone can be given.

Displacement intermittent quantity that generated in debonded zone is given by:

$$\upsilon(z) = \left|u_f(z) - u_m(z)\right|. \tag{12}$$

The discussions on calculations and the results :

1.For given casing inner diameter, external diameter and material constants $E_f, E_m, \gamma_f, \gamma_m$, displacement difference could be determined by equation (12). When the stress in the z direction is determined, the stress and displacement fields could be given by equation (8) and (9).

2.With the increasing of friction coefficient, interfacial shear stress and the length of the rupture surface will increase. The largest shear will appears where l is the largest. The maximum of displacement difference occur in the end, and increases with the friction coefficient increasing.

Determining failure length of cement loop

For fiber composite materials debonded problems, Shan [3] proposed the concept of debonding parameter ξ , that is:

$$\zeta = \frac{1}{2}\frac{\partial}{\partial S}\left[\int_{S_T}\vec{T}\cdot\delta\vec{u}ds - \frac{1}{2}\int_{S_F}\tau_s\delta v ds\right] \quad . \tag{13}$$

From analysis and calculations in section 2 , we obtain:

$$\frac{4bA\alpha B^*}{b^2-a^2}\zeta=\left[\alpha\left(A-2c\gamma_f\right)\widetilde{P}-\left(2c-\gamma_m A\right)\widetilde{\sigma}_H-\frac{B^*}{c}\left(\alpha\gamma_f\widetilde{P}-2\widetilde{\sigma}_H\right)\left(e^{\lambda l}-1\right)\right]^2, \tag{14}$$

$$B^*=A\left(\left(\alpha+c_f/c_m\right)A-2c^2\right),$$

where equation (14) is debonding critical formula.

The damage length of cement loop can be obtained from equation (14). Basic parameters are: $2a=124.3\text{mm}, 2b=139.7\text{mm}, R=700\text{mm}, E_f=2.06\times10^{11}\text{Pa}, E_m=9\times10^9\text{Pa}, \gamma_f=0.26, \gamma_m=0.35$.

1. (assume $\sigma_H=20\text{MPa}$, $\tilde{P}=2.4\text{MP}a$). The relationship between cement loop damage length l and friction coefficient μ (friction coefficient of cement loop and casing) is given by figure 2.

It can be seen: with the increasement of the friction coefficient, the damage length of cement loop gradually become smaller, and damage length is inversely proportional to the friction coefficient.

2. Calculation results about damage length of cement loop l and earth stress σ_H is given by table1(assume μ =0.3, bit stress $\tilde{P}=2.4\text{MP}a$).

Table1: Calculation result about cement loop damage length and earth stress

earth stress (MPa)	10	15	20	25	30
cement loop damage (m)	0.70	0.48	0.37	0.30	0.20

With increasing of earth stress, the damage length of cement loop will decrease, the reason can be explained that the increasement of earth stress resulting in the increasing the friction of cement and casing. It must be stated that the influence of earth stress on the casing deformation is not took into account. In fact, when the earth stress increases to a certain degree, the casing deformation will lead to cement fracture.

3. The relationship between cement loop debonding work ζ and bit stress $\widetilde{P}$ is given by the table 2 (assume $l=0.2\text{m}, \sigma_H=15\text{MP}a$)

Table2. Calculation result about cement loop debonding toughness and bit stress

debonding work(J/m^2)	20	60	100	140	180	220	260	300
bit stress (MPa)	51.3	93.5	122.6	146.2	166.6	184.8	201.5	216.9

When damage length of cement loop is determined, larger the debonding work is, the larger bit stress $\widetilde{P}$ leading to the damage of cement loop. The cement debonding work is determined by its own physical and chemical properties. This shows that from another view the cement loop properties have great influence on damage. Therefore, in order to enhance the quality of repaired well, people should not only focus on improving technology, but also improve the properties of cement loop.

The true situation indicated that the casing damage tend to take place in the deep stratum. That is to say, when earth stress is very large, cement loop damage in the process of repairing is unobvious. Therefore, when earth stress is small, this model is suitable. [4]

Acknowledgements

This research was supported by the Nature Foundation of Heilongjiang Province in China under Grant No.A2004-08 and by the Foundation of Harbin Engineering University under Grant No. HEUF04005.

References

[1] J.H. Nester: Drilling Prod. Practice (1987), p.314

[2] Y.C. Gao,Y.M.Mai and B.Cotterell: J.Appl. Math. Phy. Vol. 39(1988), p.550

[3] H. Stang, S.P. Shan: Mater. Sci. Vol. 21(1986), p.953

[4] M.Z. Jiang: Dis.for the Degree of Doctor. Harbin Engineering University (2003)

Key Engineering Materials Vols. 385-387 (2008) pp 65-68
© (2008) Trans Tech Publications, Switzerland
doi:10.4028/www.scientific.net/KEM.385-387.65

Computational Program for Non-equilibrium Grain Boundary Segregation Kinetics

Wang Jun[1,a], Li Qing-fen[1,2,b], Liu Er-bao[2]

[1]College of Mechanical and Electrical Engineering, Harbin Engineering University,

[2] College of Material Science and Chemical Engineering, Harbin Engineering University,

Harbin 150001, China

[a] wangjun@hrbeu.edu.cn, [b]qingfli@yahoo.com.cn

Keywords: Fracture failures; non-equilibrium grain-boundary segregation (NGS) kinetics; simulation

Abstract. The solute segregation to grain boundaries may be classified into equilibrium and non-equilibrium segregation. The models and kinetics calculation equations were proved in previous work. However, the computational task for grain-boundary segregation kinetics process is complex and cumbersome as it can involve a vast amount of numerical data. It is therefore necessary to develop an easily usable computational program which can provide the researchers with a powerful tool in grain-boundary segregation kinetics process analysis in addition to having a sound theory. A computational program of non-equilibrium grain-boundary segregation (NGS) kinetics of solute is therefore developed in this paper. It includes programs for critical time calculation, effective time calculation and diffusion coefficients calculation, the program of Auger Electron Spectroscopy test data disposal, the program of curve fitting and the program of NGS kinetics simulation. A simulation example by using the computation program of NGS kinetic equations is in good accordance with the experimental observation of phosphorus in steel 12Cr1MoV. The computational program of NGS is therefore proved to be appropriate and helpful.

Introduction

Material grain boundaries comprise of narrow zones of weakness. When failure occurs in material, it often occurs catastrophically by fracture along grain boundaries and often by the micro-segregation of embrittling impurity to these grain-boundaries. Therefore, for a long time, the study of grain boundary micro-segregation has been one of the most attractive fields in material science and engineering [1].

The segregation of solute atoms in grain boundaries is classified into equilibrium and non-equilibrium segregation. McLean [2] first proposed models for the thermodynamics and isothermal kinetics of equilibrium segregation. Seah and Hondros [3] and Guttmann [4] furthered the theories of equilibrium segregation and made them more perfect. Ogura [5] developed McLean's work to enable the calculation of the equilibrium segregation level during cooling. In the late 1960s, a NGS theory with respect to the solute atoms was proposed by Aust et al. [6] and Anthony [7]. A NGS kinetic model was derived by Xu [8-11]. The models and kinetics calculation equations are proved in the above work.

The analysis and computational task for the grain-boundary segregation kinetics process is complex and cumbersome as it can involve a vast amount of numerical data. It is therefore necessary to develop an easily usable computation program which can provide the researchers with a powerful tool in NGS kinetics process analysis. In the present work, a set of computation programs of NGS kinetics of solute is developed.

Kinetic equations

The fact that a critical time exists is the most characteristic aspect of non-equilibrium segregation [1]. A formula for the critical time was worked out in references [8]:

$$t_c(T) = d^2 \ln(D_c/D_i)/[4\delta(D_c - D_i)] \quad (1)$$

Where d is the average grain size, δ is the critical time constant, D_c is the coefficient of complex diffusion and D_i is the coefficient of impurity diffusion in the matrix.

An isothermal kinetic model of NGS both for segregation processes and desegregation processes was developed in references [8 - 11].

In the segregation processes, the isothermal kinetic relationship for non-equilibrium segregation is given in Eq. 2 as

$$[C_b(t) - C_b^m(T_i)]/[C_b^m(T_{i+1}) - C_b^m(T_i)] = 1 - \exp\left(4Dt/\alpha_{i+1}^2 d^2\right)\ erfc[2(Dt)^{1/2}/\alpha_{i+1}d] \quad (2)$$

Where

$$erfc\left[2(Dt)^{1/2}/\alpha_{i+1}\,d\right] = 1 - erf\left[2(Dt)^{1/2}/\alpha_{i+1}d\right] = 1 - \left(2/\sqrt{\pi}\right) \times \int_0^{2(Dt)^{1/2}/\alpha_{i+1}d} \exp\left(-y^2\right)dy$$

In which $C_b(t)$ is the concentration of the solute atoms at the grain boundary, $C_b^m(T)$ is the maximum concentration (supposing that the sample is cooled quickly from temperature T_i down to T_{i+1}), $D = D_c$ is the diffusion coefficient of complexes, t is the isothermal holding time at the constant temperature .

Eq. 2 describes the non-equilibrium segregation concentration, $C_b(t)$, of the solute atoms at the grain boundary as a function of the isothermal holding time t at the constant temperature when t is shorter than the critical time t_c ($t < t_c$), i.e. the segregation process of the complexes to the grain boundaries from the center is dominant.

In the de-segregation processes, the equation is given as:

$$C_b(t - t_c) = C_g + \frac{1}{2}(C_b(t_c) - C_g)\{erf[(x + d/2)/[4D_i(t - t_c)]^{1/2}] - erf[(x - d/2)/[4D_i(t - t_c)]^{1/2}\} \quad (3)$$

Where D_i is the diffusion coefficient of solute, C_g is the concentration of solute atoms within the grain.

Eq. 3 describes the non-equilibrium segregation concentration, $C_b(t)$, of the solute atoms at grain boundary as a function of the holding time t at constant temperature when $t > t_c$, i.e. the diffusion process of solute atoms from grain boundaries to center is dominant.

Computation program

A set of computation programs of NGS kinetics is developed. It includes: the critical time calculation program, the effective time calculation program, the diffusion coefficients calculation program, the Auger Electron Spectroscopy (AES) test data disposal program, the least square fitting curve program and the NGS kinetics simulation program.

A simulation example by using the computation program of NGS kinetic equations is given. The flowchart of AES test data disposal is shown in Fig.1 and the running result of the program is given in Fig.2. Fig. 3 gives the flowchart of the least square fitting curve and the running result is given in Fig.4 .

Experimental result, i.e. the variation of segregation level of phosphorus for 12Cr1MoV steel at the isothermal holding temperature of 540ºC is shown in Fig.5 (C_p-curve)[12].

The critical time $t_c(T)$ was calculated for specimens solution heated at 1050°C according to the equation (1). The isothermal holding temperature is 540°C, i.e. 813K. The calculated value of $t_c(T)$ for steel 12Cr1MoV is 516h, which is in good agreement with the experimental result which is about 500h [12] (see Fig. 5).

The C_b-curve in Fig. 5 is the simulation of the experimental data with equations (2) and (3).

For the segregation process, the diffusion coefficient of complexes, D_c, can be calculated according to the Eq. 2. The relation of D_c vs holding time t is as follow:

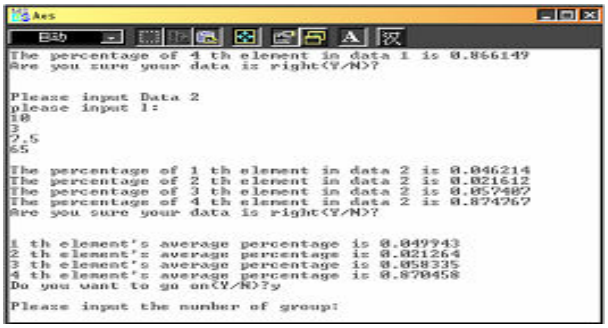

Fig.2 Running result of AES test data disposal

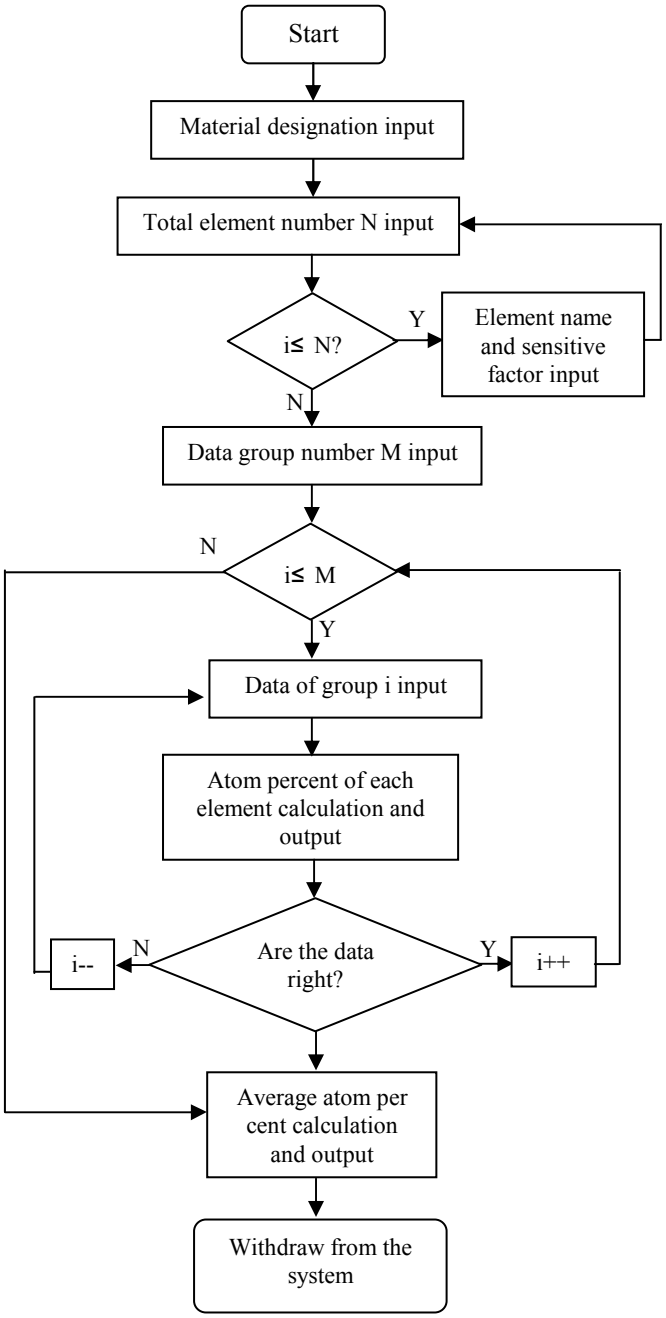

Fig.1 Flowchart of AES test data disposal

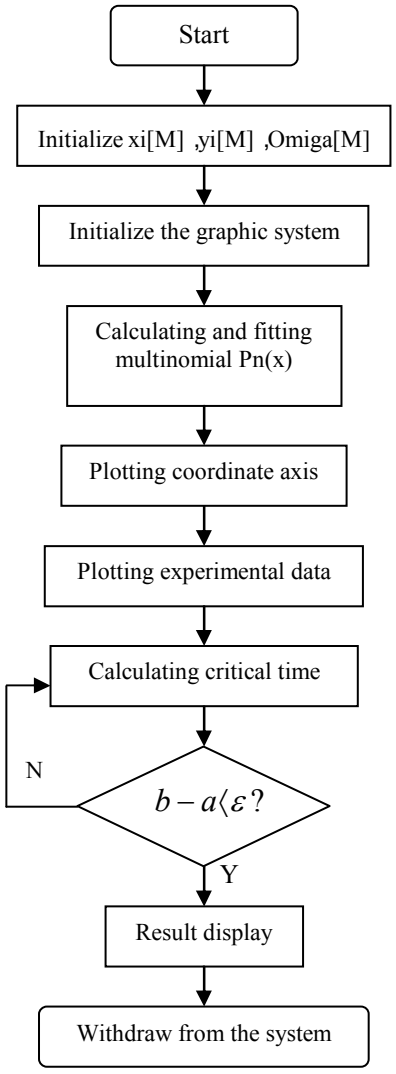

Fig.3 Flowchart of least square fitting curve

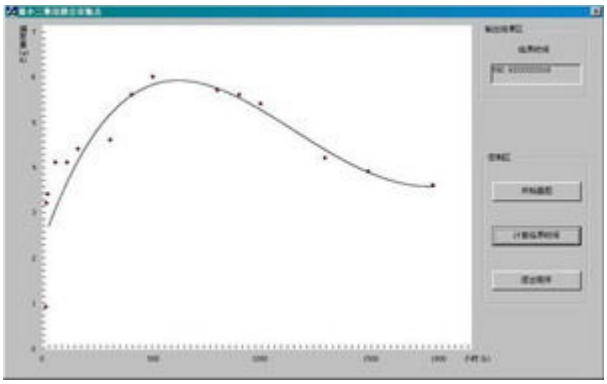

Fig.4 Running result of least square fitting curve

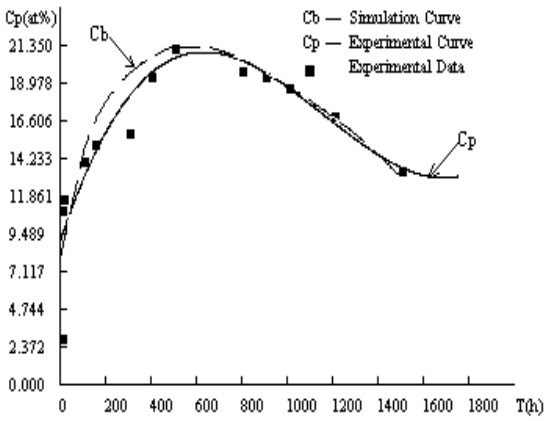

Fig. 5 Experimental and simulation results

D_c=5.6226e-16exp(-2.7030e-5t)+5.2156e-17. (4)

For the de-segregation process, the diffusion coefficient of solute, D_i, can be calculated according to the Eq. 3. The relation of D_i vs holding time t is as follow:

D_i=1.8900e-27exp(1.2900e-6t)+2.5972e-24. (5)

Results (see Fig. 5) show that the simulation result by using the computation program of NGS kinetic equations perfectly fits with the experimental observations for phosphorus in steel 12Cr1MoV. The computation program of NGS is therefore proved to be proper and helpful.

Summary

A set of computation program of NGS kinetics is developed in this paper. A simulation example by using the computation program is in good accordance with the experimental observation of phosphorus in steel 12Cr1MoV. The computation program of NGS is therefore proved to be proper and helpful.

References

[1] T.D. Xu, B.Y. Cheng *Prog. Mater. Sci.*, **49**, 109-208 (2004).

[2] D. McLean, *Grain-Boundaries in Metals*, Oxford University Press, UK (1957).

[3] M.P. Seah and E.D. Hondros *Int. Metals Rev*, 222-262 (1977).

[4] M. Guttmann *Metal. Sci.*, **10**, 337-341 (1976).

[5] T. Ogura, *Trans. Japan Inst. Metals*, **22**, 109 (1981).

[6] K.T. Aust., S.J. Armijo. and E.F. Koch *et al. Trans. Am. Soc. Metals.*, **60**, 360 (1976).

[7] T.R. Anthony *Acta Metall.*, **17**, 603-611 (1969).

[8] T.D. Xu *J.Mater. Sci.*, **22**, 337-345 (1987).

[9] T.D. Xu: Scrippta Materialia, 37, 1643-1650 (1997).

[10] T.D. Xu: Mater.Sci. Technol., 1999; 15: 659.

[11] T. D. Xu, S. Song, Acta Metall. 1989; 37: 2499.

[12] Q. F. Li, S. L. Yang, L. Li, L. Zheng and T. D. Xu, Scripta Materialia, 2002; 47: 389.

Key Engineering Materials Vols. 385-387 (2008) pp 69-72
© (2008) Trans Tech Publications, Switzerland
doi:10.4028/www.scientific.net/KEM.385-387.69

Crack Development in Concrete, Part 1: Fracture Experiments and CT-scan Observations

E. Schlangen

Microlab, M & E, Faculty of Civil Engineering and Geosciences, Delft University of Technology, P.O. Box 5048, 2600 GA Delft, The Netherlands

h.e.j.g.schlangen@tudelft.nl

Keywords: Concrete, Fracture, CT-Scan, Tension, Softening.

Abstract

This paper describes a method to measure the 3D-microstructure of a material which can be used to perform fracture simulations. A model concrete is made and the 3D structure is obtained with a CT-scanner. Uni-axial tensile tests are performed on cylindrical specimens of the model concrete a regular concrete and of a mortar. The model concrete shows more micro-cracking, a more tortuous crack path, a lower tensile load and a less brittle behaviour compared to the mortar and the regular concrete. Furthermore it is found that the opening of the crack is more uniform when the material is more heterogeneous, which results in a more stable fracture.

Introduction

Fracture properties of materials are closely related to the microstructure of the material. In a material like mortar or concrete the microstructure is well defined, at least on the meso-scale of the material, where aggregate particles (mm-scale) are embedded in a cement matrix. Concrete is, however, heterogeneous on various scales, ranging from nano (nano-meters) to macro (metres) scale. On the lower scales (nano and micro) the microstructure is constantly changing, especially in the early stage during hydration when the cement matrix is formed. Experimental studies have shown that if we zoom in on the material, we can explain why we have a softening behaviour. A zone of micro-cracks is formed and crack bridging, branching and friction effects all have a contribution to the toughness of concrete. The micro-structure of the material has a large influence on the crack patterns in concrete. Cracks follow the weakest link in the material which is often the interfacial transition zone (ITZ). Transport of gases, moisture and ions takes place through the pore structure and cracks in the concrete. Durability of concrete structures is very closely related to these transport properties. Understanding the fracture mechanisms and how this is related to the microstructure is therefore of utmost importance. In this paper a method is described to measure fracture properties and determine the particle arrangements inside the material. This information is then used to model the behaviour of the material as described in [1].

Materials and Experiments

In the experimental program in this research uni-axial tensile tests are performed on cylindrical specimens. The specimens are glued between non-rotating steel platen. The boundary conditions strongly influence the results that are obtained in the tests, i.e. both the maximum load as well as the post-peak behaviour [2,3,4]. In this paper the influence of the material structure on the non-uniform opening is studied. For this purpose mortar specimens are produced, consisting of sand particles with a maximum aggregate size of 2 mm. An Ordinary Portland Cement is used with a water to cement ratio of 0.5. Next to this mortar, a concrete with large aggregates of size 8-16 mm and model concrete specimens are produced with special spherical aggregates with a very low bond with the cement paste. The aggregates are plastic spheres with a diameter of 12 mm and a density around 1050 kg/m3. The model concrete and the 8-16 mm concrete are also made with the same mortar in which 25 % of the mortar volume is replaced by the aggregates.

The specimens are cast in cylindrical plastic cups with a diameter of 55 mm and a height of 80 mm. The cups are closed with a lid and stored at 20oC for 14 days after which the specimens are taken out of the cup and sawn to a height of 70 mm which is needed in the test (top and bottom part are removed). At half height a notch is made with a depth of 4 mm. After that the specimens are stored until the age of testing (28 days) at 40% RH and 20oC.
In order to determine the exact distribution of the spherical particles in the mortar, the specimens are put in a CT-scanner (nanotom of Phoenix x-ray Systems). For this case the lowest possible resolution of the machine is used, which is sufficient for this purpose, i.e. a voxel-size of 122 micrometer. The exact location of particles is needed for the 3D-simulations of the fracture process [1]. Using CT-scan images for relating the microstructure to fracture behaviour and other properties of materials is a technique which is becoming popular [5].
At 28 days the specimens are glued in a uni-axial tensile testing machine and tested in deformation control, using the average of 4 LVDT's with a measuring length of 30 mm as feed back signal.

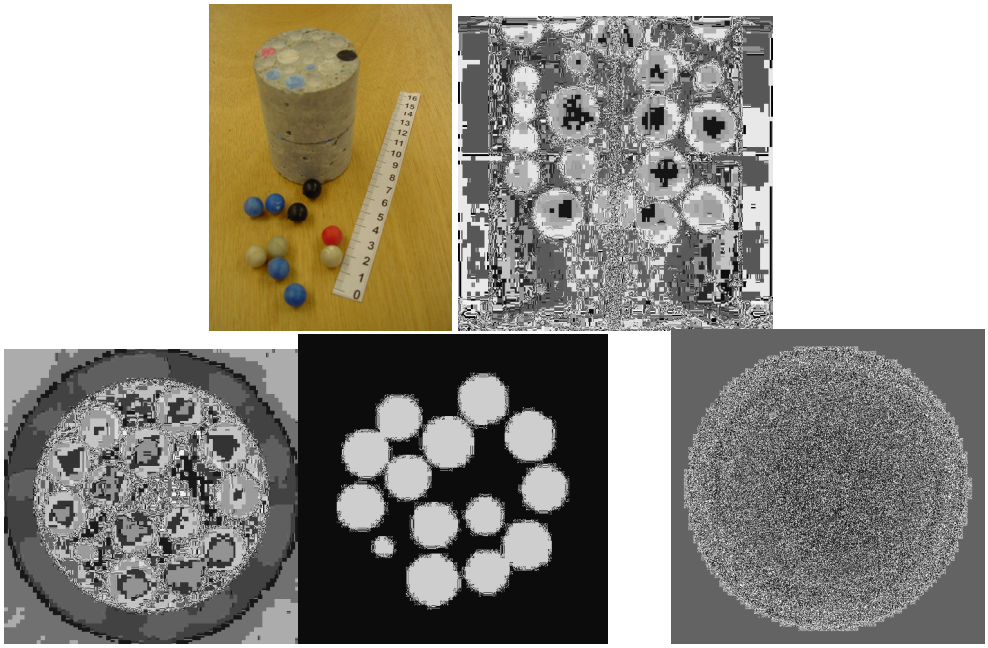

Fig. 1. Cylindrical specimen, vertical cross section from CT-Scan, horizontal cross section, particle arrangements after image processing and CT-scan of a 8-16 mm concrete specimen.

Results of Experiments

In figure 1 a cylindrical specimen is shown that is used in the test. Also a vertical and a horizontal cross section taken from the 3D image that is obtained with the CT-scanner, as well as the particle configuration obtained from this image after image-processing. Due to the low density of the plastic particles some segregation is observed. However, this is not influencing the fracture behaviour a lot, since enough particles are present in the region of the notch. The CT-scan on the 8-16 mm concrete did not show enough detail. From the obtained cross section the aggregates in the specimen can be seen by the naked eye. However image processing tools, even after using different filter techniques, are not able to distinguish between aggregates and matrix. The reason for this is the fact that the densities of aggregates and cement matrix are very close.
Figure 2 shows the set-up that is used for the tensile tests and also a model concrete specimen after the test. It can be clearly seen that all the spherical particles debond from the mortar, which indicates that this is the weakest link in the material. In the case of the 8-16 mm concrete it was also observed that some of the large aggregates were cracked after the test and that aggregates were also covered with some cement matrix in the final crack.
The load-deformation curves for a mortar, a model-concrete (BB) and an 8-16 mm concrete test are given in figure 3. The mortar specimens have a strength which is about three times higher then the model-concrete specimens. With the image processing software used on the CT-scan image it was

found that in the model concrete specimens, the area of the mortar part is also about 33% of the total area of the cross section of the specimen in the notch area. The 8-16 mm concrete specimen has almost the same maximum load as the mortar specimen. This indicates that the bond between the aggregates and the concrete is rather good and is close to the strength of the mortar. From figure 3 it can also be observed that the mortar specimens are more brittle. Some of the tests on mortar showed a snap-back behaviour and it was not even possible to determine the full softening curve for these tests.

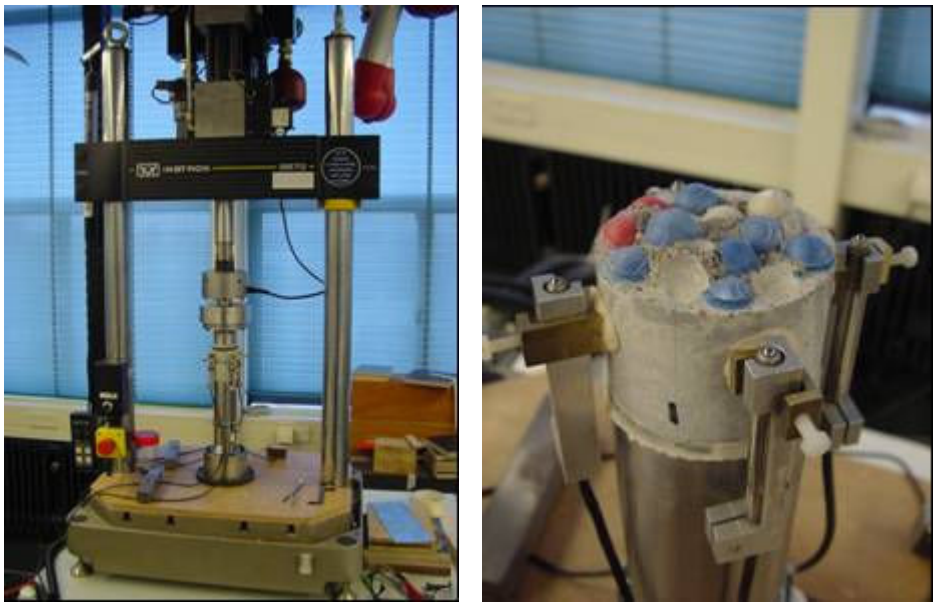

Figure 2. Set-up for deformation controlled uni-axial tensile test and fractured specimen.

The reason for this snap-back is the non-uniform opening of the specimen. Although it is loaded between non-rotating end-platen, the heterogeneity of the material itself creates this non-uniformity, see also [2,3]. This can be clearly seen in figure 4, where the load-deformation curves for the individual LVDT's are plotted for tests on the three materials. A little disorder in the material as present in the mortar is enough to first open the specimen at one side and close it at the opposite side. If the deformation is increased the crack jumps to the other side and a snap back is observed in the load-deformation curve. If the disorder is larger, as is the case in the model-concrete, the opening of the total crack becomes more uniform again and no snap-back is observed. The 8-16 mm concrete has some more heterogeneity than the mortar, but less than the model concrete. It shows non-linear opening, but no snap-back behaviour is obtained.

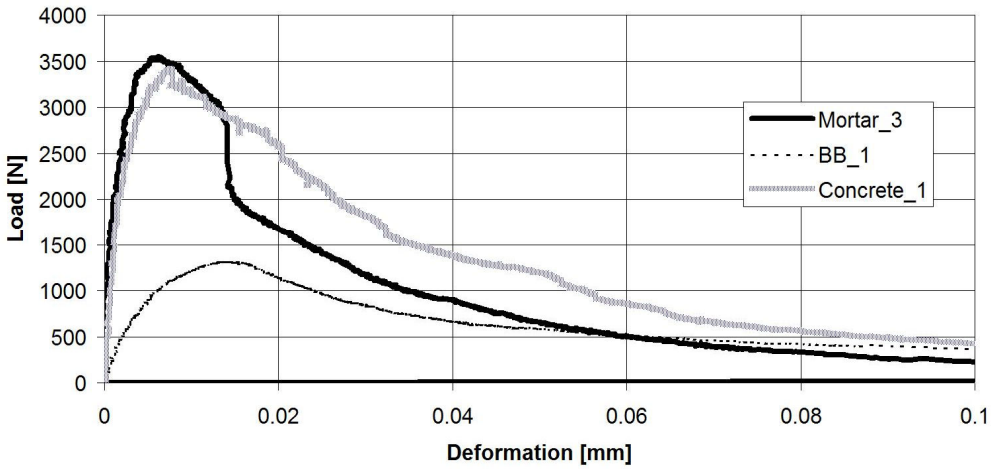

Figure 3. Load deformation curves for a mortar (Mortar_3), a model concrete (BB_1) and a 8-16 mm concrete (Concrete_1) specimens tested in tension.

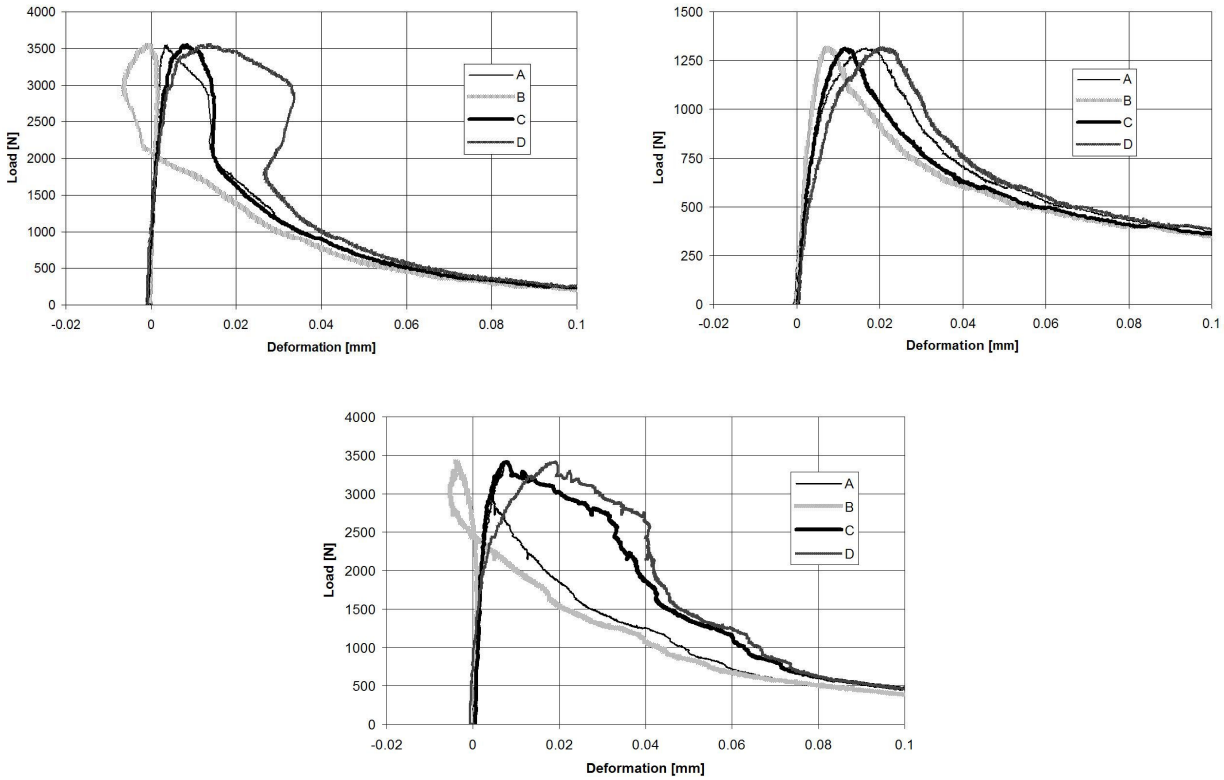

Figure 4. Load deformation curves for individual LVDT's in a mortar (top-left), a model concrete (top-right) and an 8-16 mm concrete (bottom) specimen tested in tension.

Conclusions

A procedure is presented to produce specimens, measure fracture properties and obtain 3D images of the particle structure in heterogeneous materials as concrete. With this procedure a set of data is obtained that can be used to model the 3D behaviour of mortar and concrete in a more precise way. This is needed to able to predict (micro-) crack distributions in concrete, which is required to perform durability and life time prediction analyses for concrete structures. Furthermore it is found that the opening of the crack is more uniform when the material is more heterogeneous, which results in a more stable fracture.

References

[1] Schlangen, E. 2008. "Crack Development in Concrete, Part 2: Modelling of Fracture Process." In Fracture and Damage Mechanics (FDM08), Seoul, Korea, 9-11 September.

[2] Van Mier, J.G.M. and Schlangen, E. 1989. "On the Stability of Softening Systems", In Fracture of Concrete and Rock – Recent Developments (eds. S.P. Shah, S.E. Swartz & B. Barr), Elsevier, London/New York, pp.387-396.

[3] Hordijk, D.A. 1991, Local approach to fatigue of concrete, PhD thesis, Delft University of Technology, The Netherlands, pp. 210.

[4] Carpinteri, A. and F. Maradei, F. 1995. "Three-jack solution to obtain a truly stable and symmetric tensile concrete test", Experimental Mechanics, Vol. 35, 19-23.

[5] Landis, E.N. and Nagy, E.N. 2000. "Three-dimensional work of fracture for mortar in compression" Engineering Fracture Mechanics, Vol. 65 No. 2-3, 223-234.

Key Engineering Materials Vols. 385-387 (2008) pp 73-76
© (2008) Trans Tech Publications, Switzerland
doi:10.4028/www.scientific.net/KEM.385-387.73

Crack Development in Concrete, Part 2: Modelling of Fracture Process.

E. Schlangen

Microlab, M & E, Faculty of Civil Engineering and Geosciences, Delft University of Technology, P.O. Box 5048, 2600 GA Delft, The Netherlands

h.e.j.g.schlangen@tudelft.nl

Keywords: Concrete, Tensile test, Lattice model, Fracture, Softening.

Abstract

In a companion paper in this conference [1] an experimental study is presented that deals with measuring fracture properties and obtaining 3D images of the particle structure in heterogeneous materials as mortars and concrete. The fracture mechanisms observed in the tests are modelled with a 3D lattice model. The heterogeneity of the model is directly implemented from the 3D images obtained in a CT-scanner. With this method realistic crack patterns can be obtained.

Introduction

Fracture of disordered materials can be simulated very well with network or lattice models [2]. In these models the material is represented by a network of small springs or beams. All the single elements have a linear elastic behaviour. Heterogeneity is implemented in the network by variation of properties. After loading the network a crack is formed by just removing an element of which a limit (strength or strain) is exceeded. With this method realistic crack patterns can be obtained. Furthermore a ductile global behaviour of the material is found while the local behaviour is brittle. The method of simulating fracture with a lattice model is applied for concrete a lot in the last decade in 2D [3] but also in 3D [4]. Heterogeneity of the material can be implemented in different ways, using distributions of strengths and stiffness, random orientation of elements or a generated or digital image of microstructures of the material [5]. The best and most realistic results are obtained when the implemented heterogeneity is as close as possible to the real microstructure of the material. In this paper a method is proposed to use 3D images of the material obtained with CT-scanning as input for the fracture simulations. 3D-crack patterns and crack widths can be accurately predicted in this way, which is of importance for transport simulations which make predictions of durability and service life of concrete structures possible.

Description of simulations

In [1] the procedure is described how to produce cylindrical specimens with plastic spherical particles. These cylinders are put in a CT-scanner to obtain the exact location of particles inside the specimen. The public domain image processing software package ImageJ is used to separate and locate the particles. The obtained binary image with particles is used to implement disorder in the mesh for the fracture simulations. In the lattice simulations a 3D regular square lattice of beam elements is used. All the beams have the same length and cross section. However, the stiffness and strength of the elements are different. For this the binary image of particles is used. In figure 1 the 3D mesh is given of the model concrete with the spheres. Also a mesh for a homogeneous material is shown in which all the properties are equal to mortar materials. The third mesh in the figure is for a material with random distributed material properties. In this case the same amount of particle, ITZ, and Mortar beam elements are used but now randomly distributed in the zone of the sample where the particles are located. The values in table 1 are used as input. For the background of the equations that have to be solved for performing the fracture simulations the reader is referred to [5].

The 3D cylinder is modelled with 35232 elements and 12379 nodes, with 12 degrees of freedom in each node.

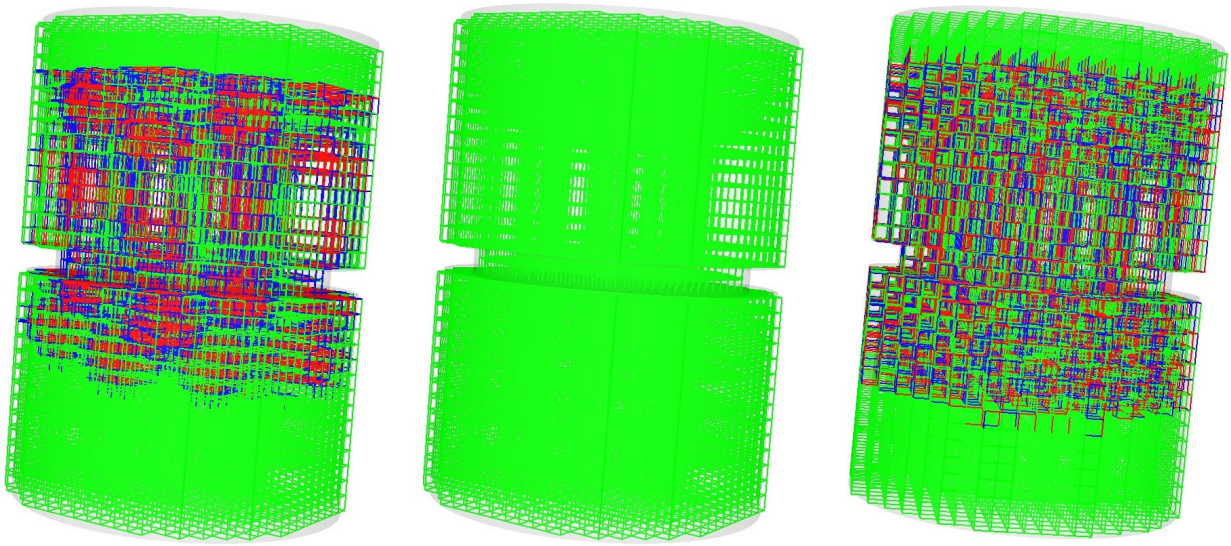

Fig. 1. 3D lattice mesh: model concrete, homogeneous material (mortar) and random material.

Location	Stiffness [GPa]	Strength [MPa]
Particle	10.0	6.25
Mortar	30.0	5.0
ITZ	5.0	0.625

Table. 1. Input values for 3D fracture simulations

Results and comparison with experiments

In the experiments [1], the cylinders are tested in uni-axial tension. The boundary conditions at top and bottom are such that no rotation is allowed. Similar to the experiments a case with homogeneous properties (resembling the mortar specimens) and a case with embedded spherical particles (resembling the model concrete) are modelled. For comparison also a random material is simulated with properties as discussed above. The resulting crack patterns (projection of all the cracks) are given in figure 2.

In the case of the homogeneous material a single plane of cracks is obtained. In the case of the material with embedded spheres first micro-cracks at the boundary between particles and mortar (ITZ) develop, which later are connected with cracked mortar-elements to form a localized crack which separates the specimen in two parts. In case of a random material first micro-crack develop distributed through the complete section of the material with random properties. After that a localized crack between the notches is found. In case of the model concrete the micro-cracks are localised more around the spheres and stay in a certain band around the main crack.

In figure 3 the load-deformation curves for the three simulations are given. It can be seen that homogeneous material has a much more brittle outcome and a higher maximum load. The maximum loads compare very well to the experimental findings. However, the overall response is a bit too brittle in both cases. Omitting too much details of the microstructure in the simulations is the main reason for this [5]. A possible solution is implementing local softening behaviour in the elements as for instance used in [6]. The random material has a higher maximum load compared to the model concrete. Reason for this is that if the weak zones are grouped together in the ITZ, the micro-cracks grow together to some localised bigger cracks. This reduces the strength of the material.

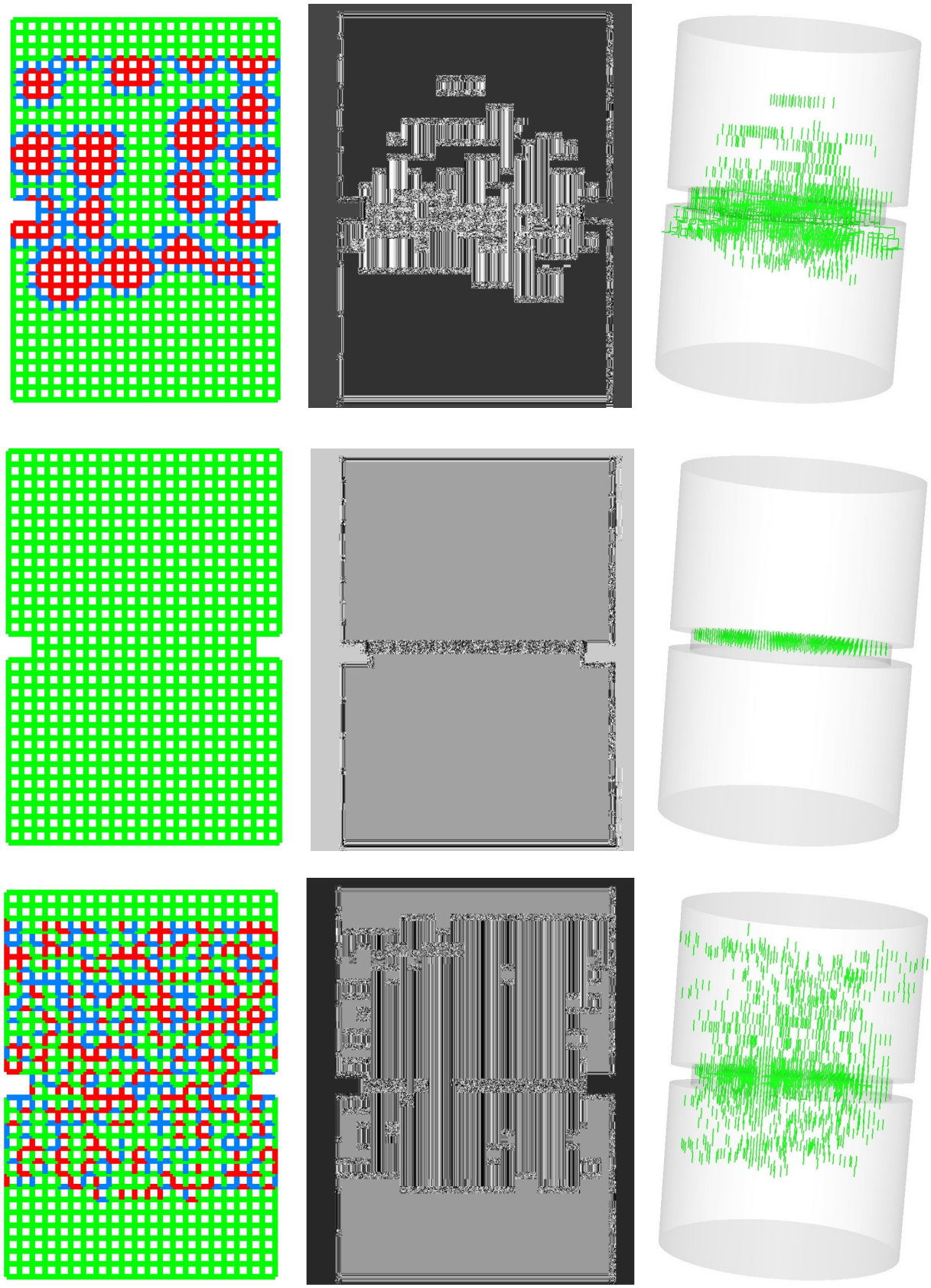

Figure 2. Projected cracks in 3D simulations: model concrete, homogeneous material (mortar) and random material.

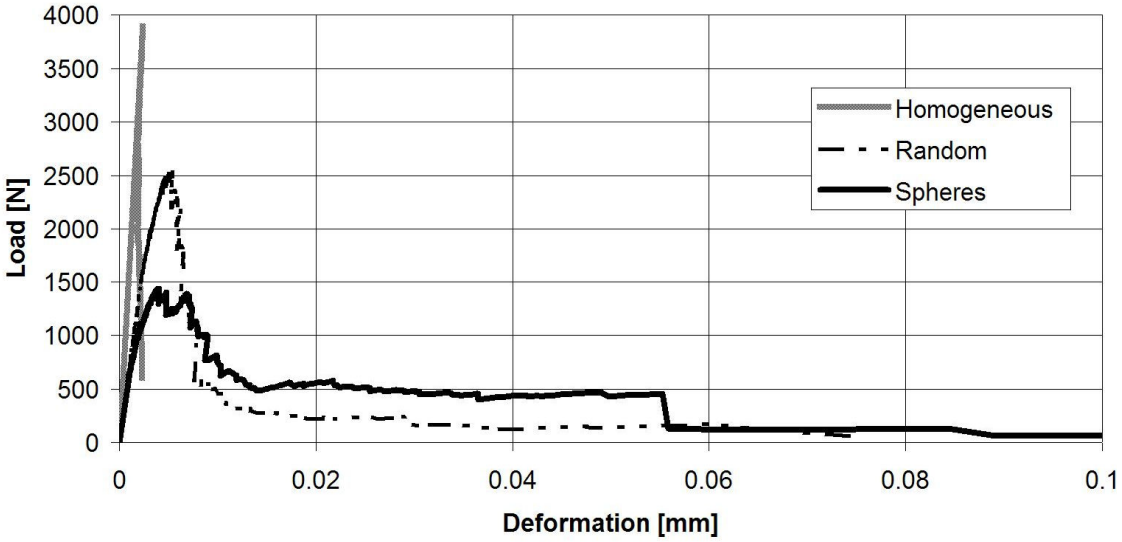

Figure 3. Load-deformation curves for simulations on model concrete, homogeneous material (mortar) and random material.

Conclusions

In this paper and the companion paper [1] a procedure is presented to produce specimens, measure fracture properties and obtain 3D images of the particle structure in heterogeneous materials as concrete, which are then implemented in a 3D lattice model for fracture simulations. Realistic modelling of 3D fracture is now possible. The determination of the local material properties can be added to this procedure by using a combination of micro-structural observation with microscopy and nano-indentation measurements as described in [7]. In [1] it was observed that in the uni-axial tensile experiments non-uniform opening occurs which is more pronounced if the material is less heterogeneous. The same was found in the simulations.

References

[1] Schlangen, E. 2008. "Crack Development in Concrete, Part 1: Fracture Experiments and CT-scan Observations." In Fracture and Damage Mechanics (FDM08), Seoul, Korea, 9-11 September.

[2] Herrmann, H.J. and Roux, S. eds, 1990. Statistical models for the fracture of disordered media, Elsevier/ North Holland, Amsterdam.

[3] Schlangen, E. and van Mier, J.G.M. 1992, Experimental and numerical analysis of micromechanisms of fracture of cement-based composites, Cem. Conc. Composites, 14: 105-118.

[4] Schlangen, E. and van Mier, J.G.M. 1994, Fracture simulations in concrete and rock using a random lattice. In Siriwardane, H.J. and Zaman, M.M. (eds.), Computer Methods and Advances in Geomechanics, Balkema, Rotterdam, pp. 1641-1646.

[5] Schlangen, E. and Garboczi, E.J. 1997, Fracture simulations of concrete using lattice models: computational aspects, Engineering Fracture Mechanics, 57(2/3): 319-332.

[6] Ince, R., Arslan, A. and Karihaloo, B.L. 2003. Lattice modelling of size effect in concrete strength, Engineering Fracture Mechechanics, 70, 2307–2320.

[7] Copuroglu, O. and Schlangen, E. 2007. Modeling of frost salt scaling. Cement & Concrete Research, 38, pp. 27-39.

Key Engineering Materials Vols. 385-387 (2008) pp 77-80
© (2008) Trans Tech Publications, Switzerland
doi:10.4028/www.scientific.net/KEM.385-387.77

The Rationale of Adhesive Postinstalled Method to Estimate the Concrete Strength

Shiqi Cui[1, a], Jinshan Wang [1,b], Xuwen, Kong[1,c], Hiwen, Li[1,d]

[1] Structure Institute of Shandong Provincial Academy of Building Research, Jinan, China.

[a]cfrp@sina.com, [b]wangjinshan@gmail.com, [c]kongxuwen@sina.com, [d]lhworg@sina.com

Keywords: Rationale, adhesive postinstalled method, concrete strength.

Abstract. In the adhesive postinstalled method, headed anchor is anchored into concrete by means of a high strength epoxy resin adhesive. To measure the concrete compressive strength, the metal anchor is "pulled" from the concrete. There occur four types of failure when the metal anchor is pulled out. This paper introduces the rationale of the adhesive postinstalled method to estimate the in-place concrete strength. The embedment depth and the diameter of the reaction ring are specified by experimental phenomenon and theoretical analysis.

Introduction

The pullout test is used during construction to estimate the in-place strength of concrete to help decide whether critical activities such as form removal, application of post-tensioning, or termination of cold weather protection can proceed. Because the compressive strength is usually required to evaluate structural safety, the ultimate pullout load measured during the in-place test is converted to an equivalent compressive strength by means of a previously established relationship. Unlike some other tests used to estimate the in-place strength of concrete, the pullout test subjects the concrete to a slowly applied load and measures an actual strength property of the concrete. The concrete is subjected, however, to a complex three-dimensional state of stress, and the pullout strength is not likely to be related simply to uniaxial strength properties. Nevertheless, by use of a previously established correlation, the pullout test can be used to make reliable estimates of in-place strength [1, 2] .

Structure Institute of Shandong Province Academy of Buildings tried an innovative adhesive postinstalled method to estimate concrete strength in 2006. The adhesive postinstalled method measures the ultimate load required to pull an adhesive-bonded metal insert from a concrete specimen or structure. The pulling load is applied by a tension jack, which reacts against the concrete surface through a reaction ring concentric with the insert. As the insert is pulled out, a roughly cone-shaped fragment of the concrete is also extracted. Bonded anchors transfer load differently than do headed cast-in-place or post-insert anchors. Headed anchors and post-insert anchors transfer load through bearing of the anchor head on the concrete. Bonded anchors transfer load by adhesion to the concrete along the entire embedded portion of the anchor.

Failure Modes of Adhesive-bonded Anchors

Figure 1 presents four typical failure modes observed for adhesive anchors installed in hardened concrete. For a very small embedment depth of an adhesive anchor, a concrete cone is usually pulled out as shown in Figure 1a. When the embedment of the anchors increased, a bond failure below a shallow concrete cone is observed (Figure 1b). If the embedment is very deep, the bond is so strong that the steel failure occurs in the anchor (Figure 1c). In some installations, bond failure without a concrete cone, as shown in Figure 1d, may occur if the bonded surface lacks adequate strength due to the adhesive itself, improper curing, or inadequate hole preparation.

Failure Pullout Force of Adhesive Anchors

For postinstalled anchors with combined cone and bond failure, the pullout force can be seen as the combination of the cone and bond (Figure 2) :

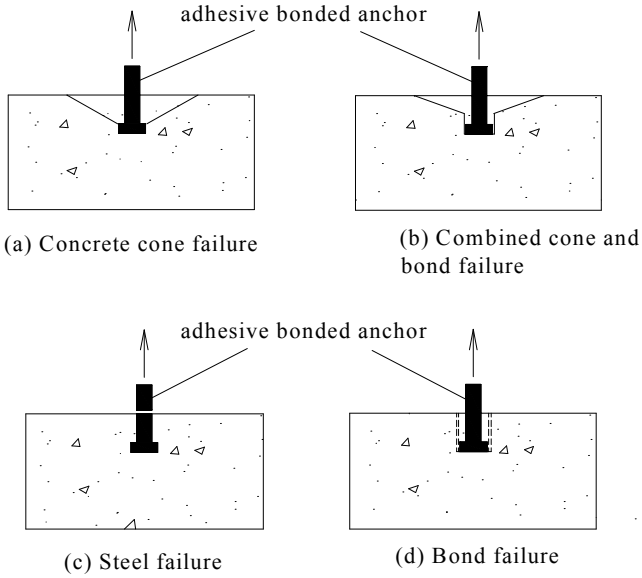

Fig.1 Failure modes for adhesive anchors.

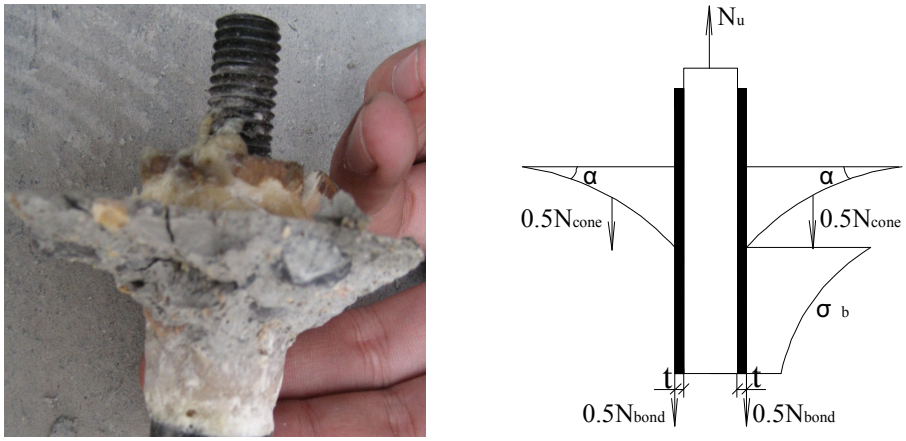

Fig. 2 Failure specimen and scheme of the pullout force

$$N_u = N_{cone} + N_{bond} \tag{1}$$

Based on a database of chemically bonded-threaded rod anchors, Eligehausen et al. (1984) [3] suggested the following equation for pullout capacity of concrete cone failure:

$$N_{cone} = 0.92 h_{ef}^2 \sqrt{f_c} \tag{2}$$

The uniform bond-stress model is commonly used in design and is easy to apply. It predicts the capacity of the anchor as a function of the uniform failure stress. This model does not account for compatibility between the concrete, bonding agent, and threaded rod. The following equation is used to predict the strength for a uniform bond-stress distribution [4~7] :

$$N_{bond} = \tau_0 \pi d_0 (h_{ef} - h_{cone}) \tag{3}$$

Combining the concrete cone model of (2) with the uniform bond-stress model of (3) gives the following:

$$N_u = 0.92 h_{ef}^2 \sqrt{f_c} + \tau_0 \pi d_0 (h_{ef} - h_{cone}) \quad (4)$$

By minimizing this combined cone-bond capacity equation with respect to cone depth hcone the depth of the concrete cone at the minimum failure load can be determined:

$$\frac{dN_u}{dh_{cone}} = 0 \quad (5)$$

which yields the following equation for cone depth in mm:

$$h_{cone} = \frac{\tau_0 \pi d_0}{1.84\sqrt{f_c}} \quad (6)$$

Where N_u=failure pullout force; h_{ef}=the embedded depth of the anchor; τ_0=the shear strength of the adhesive and f_c=compressive strength of the surrounding concrete at the time of testing.
Equation (6) indicates that cone depth hcone is found to be the function of the adhesive mechanical properties and the compressive strength of the surrounding concrete at the time of testing . When the embedded depth of the anchor is less than the cone depth hcone, the concrete cone failure would occur and equation (4) indicates that the failure pullout force is the unique function of compressive strength of the surrounding concrete at the time of testing. Only under this circumstances, the compressive strength could be estimated by the pullout force accurately in theory.

Failure Mechanism

The pullout test subjects the concrete to static load. Therefore, it should be possible to calculate the internal stresses in the concrete and to predict the onset of cracking and the ultimate pullout load. This is desirable so that the ultimate pullout load could be related to the uniaxial strength properties of concrete.

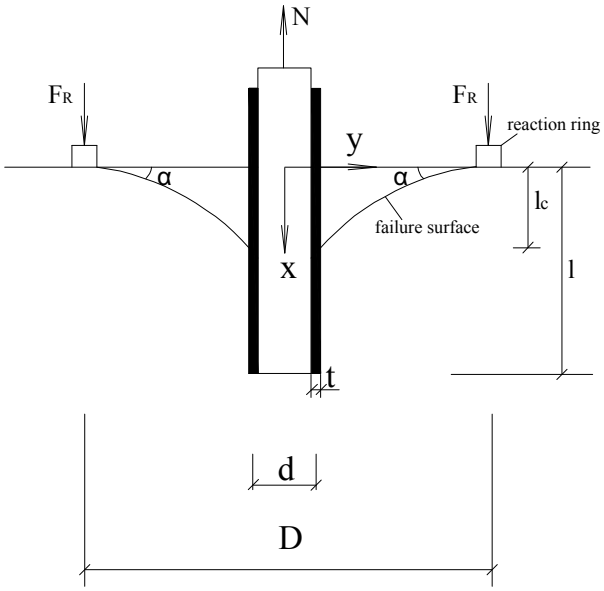

Fig. 3 Scheme of analysis of the stress on the failure surface

Stresses on Failure Surface

Figure 3 illustrates the forces acting on the anchor system. Based on the macromechanics, the pullout force N equals the algebraic sum of the F_R for the equation of equilibrium for forces in the y direction:

$$N = \pi D F_R \quad (7)$$

By symmetry, it is assumed that all cross sections are in the same condition, the components of the stress induced by the F_R and N are expressed as following equations (8) and (9), respectively.

$$\sigma_x^{F_R} = -\frac{2F_R}{\pi}\frac{x^3}{\left[x^2+\left(\frac{D-d}{2}\right)^2\right]^2};\quad \sigma_y^{F_R} = -\frac{2F_R}{\pi}\frac{x\left(\frac{D-d}{2}\right)^2}{\left[x^2+\left(\frac{D-d}{2}\right)^2\right]^2};\quad \tau_{xy}^{F_R} = -\frac{2F_R}{\pi}\frac{x^2\left(\frac{D-d}{2}\right)}{\left[x^2+\left(\frac{D-d}{2}\right)^2\right]^2} \quad (8)$$

$$\sigma_x^{N} = \frac{2N}{\pi}\frac{x^3}{\left[x^2+\left(\frac{d}{2}\right)^2\right]^2};\quad \sigma_y^{N} = \frac{2N}{\pi}\frac{x\left(\frac{d}{2}\right)^2}{\left[x^2+\left(\frac{d}{2}\right)^2\right]^2};\quad \tau_{xy}^{N} = \frac{2N}{\pi}\frac{x^2\left(\frac{d}{2}\right)}{\left[x^2+\left(\frac{d}{2}\right)^2\right]^2} \quad (9)$$

The principal stress of the combination of F_R and N is expressed as follows:

$$\sigma_1 = \frac{1}{2}(\sigma_x^{N+F_R} + \sigma_Y^{N+F_R}) + \sqrt{\left(\frac{\sigma_x^{N+F_R} - \sigma_y^{N+F_R}}{2}\right)^2 + \left(\tau_{xy}^{N+F_R}\right)^2} \quad (10)$$

In which x= embedment depth of the anchor; y= the semidiameter of the reaction ring;σ_x =normal stress on plane perpendicular to the x axis; σ_y =normal stress on plane perpendicular to the y axis; τ_{xy} =shear stress on plane perpendicular to the x, y axes andσ_1 =principal stress.

Equations (8)-(10) show that the ultimate pullout load increased gradually as the diameter decreased from 140 mm to about 85 mm. As the diameter was reduced further, the ultimate pullout load increased rapidly. Ultimate pullout load increased gradually as the embedment depth increased from 10 mm to 50 mm. As the embedment depth increases, the depth of the concrete cone failure surface decreases. To ensure the occurrence of the concrete cone failure type, experiments show the embedment depth of the anchor for the compressive strength to be estimated is chosen to be 30mm and the diameter of the reaction ring is chosen 120mm.

Summary

The theoretical analysis on the rationale of the adhesive postinstalled method to estimate the concrete strength was introduced from the points of the macromechanics and micromechanics, and the results of experimental give the specific dimensions of the experimental apparatus.

References

[1] V.Mohan Malhotra and Nicholas J. Carino, in: Handbook on Nondestructive Testing of Co ncrete, chapter, 3, CRC Press LLC (2004).
[2] J.H.Bungey and S.G.Millard, in Testing of Concrete in Structures, chapter, 4, Chapman & Hall (1996).
[3] Eligehausen, R., Mallbe, R., and Rehm, G. Betonwerk+ Fertigteil-Technik, 10, 686-692, 1984.
[4] Cook, R. A., Fagundo, F. E., Biller, M. H., and Richardson, D. E. Structures and materials res. rep. no.91-3, Univ. of Florida, Gainesville, Fla, (1991).
[5] Ronald A. Cook, Journal of Structural Engineering. Vol. 9(119), p. 2744-2762 (1993).
[6] R.A.Cook, G.T.Doerr, and R.E., Klingner, ACI Structural Journal. Vol. 5(90), p. 514-524 (1993).
Ronald A .Cook, Gacob Kunz, Werner Fuchs, and Robert C. Konz, ACI Structural Journal. Vol. 1(95), p. 9-26 (1995).

Key Engineering Materials Vols. 385-387 (2008) pp 81-84
© (2008) Trans Tech Publications, Switzerland
doi:10.4028/www.scientific.net/KEM.385-387.81

Cracking cohesive law thermodynamically equivalent to a non-local damage model

Fabien Cazes[1,a], Anita Simatos[1,b], Michel Coret[1,c], Alain Combescure[1,d] and Anthony Gravouil[1,e]

[1]LaMCoS, INSA-Lyon, CNRS UMR 5259

18-20 rue des sciences F69621 Villeurbanne France

[a]fabien.cazes@insa-lyon.fr, [b]anita.simatos@insa-lyon.fr, [c]michel.coret@insa-lyon.fr, [d]alain.combescure@insa-lyon.fr, [e]anthony.gravouil@insa-lyon.fr

Keywords: Cohesive crack, damage, non-local models, energetic balance

Abstract. This paper deals with the transition from a localized damage state to crack formation. Several attempts have already been made in this field. Our approach is in the continuity of studies where thermodynamic considerations lead to the definition of an equivalent crack concept. The main idea consists in replacing a damaged localized zone by a crack in order to recover the same amount of dissipated energy. On the one hand, a nonlocal model is used to modelize accurately localized damage. On the other hand, an elastic model which authorizes the formation of a crack described by a cohesive zone model is used. This cohesive zone model is defined thermodynamically in order to be in concordance with the damage model. The method allows obtaining the cohesive zone model traction curve from the knowledge of the nonlocal damage model solution. The numerical implementation is done using a Lagrangian multiplier that ensures the energetic equivalence between both models.

Introduction

Localized damage and fracture mechanics are two ways of modelling the same phenomena. Both methods introduce a characteristic length in the behaviour and can be considered as localization limiters. Our study aims at bridging those two theories in a well defined thermodynamic framework. In this view, we use the equivalent crack concept defined by Mazars [1] where energy dissipation is the value which has to be preserved in order to bridge models. This concept was used by Mazars and Pijaudier-Cabot in [2] with a non-local damage model. Another important ingredient of the method is the thermodynamical definition of the cohesive zone model, within the framework defined by Gurtin [3]. It is assumed that unload occurs linearly, as for a damage model. After presenting in detail the method, we will show an application with the Mazars non–local damage model where the corresponding cohesive zone model is incrementally constructed. We will then discuss the validity of the method. Finally we will present our current work which deals with the generalization of the method when plastic strains are taken into account.

The bridging method.

Energetic criterion for bridging models. We assume isothermal processes. The energetic criterion concerns the energy dissipation of the structure noted Φ. If we note $\breve{\Phi}$ the non-local damage model dissipated energy and $\hat{\Phi}$ the cohesive zone model dissipated energy, the criterion writes:

$$\hat{\Phi} = \breve{\Phi} .$$

For the non-local damage model, $\breve{\Phi}$ is calculated with the formula:

$$d\breve{\Phi} = \int_{\Omega} -Y\, dD\, dV ,$$

with D the scalar damage variable, and Y its conjugate variable.

Additional constraints on the cohesive zone model. In addition to the energetic criterion, we impose that the cohesive model unloads in the same way as a damage model, which means that we observe no energy dissipation and a linear behaviour. In order to take into account these assumptions for the cohesive zone model, we use the thermodynamic framework defined by Gurtin in [3] for interfaces. With this construction of the cohesive zone model, it can be shown that the expression of the dissipated energy increment writes:

$$d\hat{\Phi} = \frac{1}{2}\int_{\Gamma} (\sigma d\delta - \delta d\sigma),$$

with σ the stress and δ the displacement jump across the cohesive crack.

Application to the incremental construction of a cohesive law.

For this study, we assume that the nonlocal damage model is given, whereas the cohesive law is unknown and has to be determined. The dissipated energy is calculated from the nonlocal damage model and then used with the energetic criterion to construct incrementally the cohesive law of the equivalent crack. For the cohesive zone model, we assume that there is only one crack and that it appears in the middle of the beam.

The nonlocal model. We here present the results obtained with a nonlocal damage model. The evolution law chosen for damage follows Mazar's model. For this model, damage is linked to an equivalent strain ε_{eq} which writes for a one-dimensional problem:

$$\varepsilon_{eq} = |\varepsilon| .$$

The maximum of ε_{eq} during time is noted κ. Damage is then computed with the formula:

$$D = 1 - \frac{\varepsilon_0(1-A_t)}{\kappa} - \frac{A_t}{\exp(B_t(\kappa-\varepsilon_0))} \qquad \text{if } \kappa > \varepsilon_0,$$

where ε_0, A_t and B_t are material constants. The nonlocal features of the model are obtained by using a smoothed strain, calculated with the help of a Gaussian function. An analytical solution of the nonlocal problem serves of reference for the calculation of the cohesive law. The analytical solution is obtained with the use of the nonlocal smoothening function on a discontinuous strain field. This method was introduced in [4] and can be considered in itself as a way of bridging the gap between nonlocal models and fracture mechanics. The calculation of the nonlocal strain field is schematized bellow:

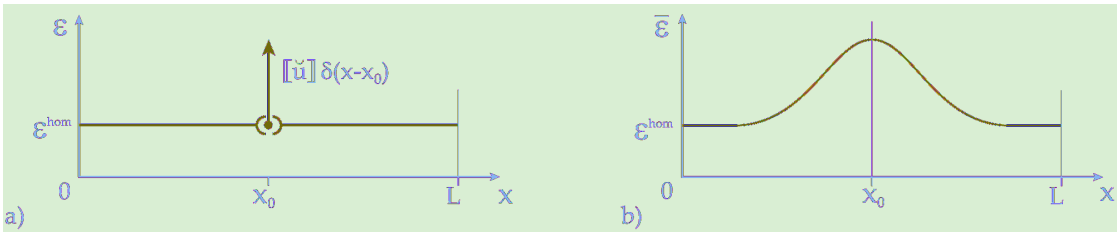

Fig 1

The cohesive zone model. The knowledge of the solution of the nonlocal problem allows us to calculate dissipated energy increments that will be transferred in the cohesive zone model. This information is sufficient to compute incrementally the solution of the problem with a cohesive crack. This calculation requires a special numerical implementation that will be presented now.

Numerical calculation of the cohesive law. The resolution of the problem with a cohesive crack is treated by isolating the elastic part of the structure. This means that cohesive stresses are considered as external loads. We choose to consider the lips of the crack as a prescribed-displacement zone. A Lagrangian multiplier imposes the wanted dissipated energy increment on the crack between two time steps. The incremental-calculation process of the cohesive law and the obtained cohesive law are represented on the following graph:

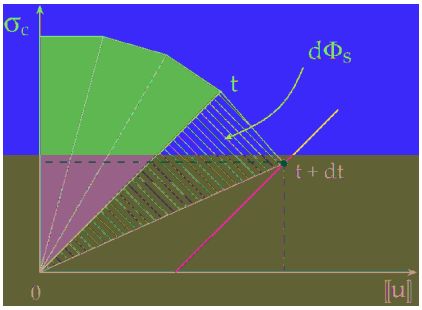

Fig. 2

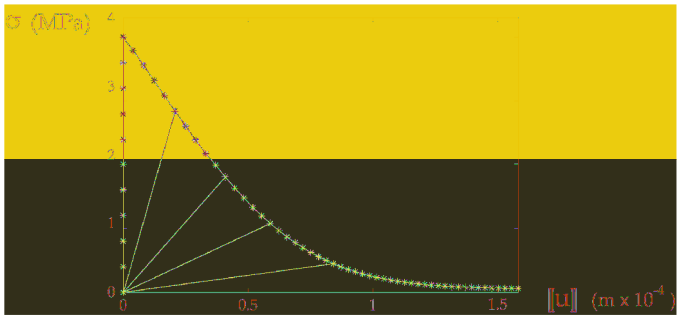

Fig. 3

Validity of the method.

We define the total energy E as the energetic quantity that remains stable during time. If we neglect kinetic energy and temperature variations, the First and Second Principles of thermodynamics give the following expression of E:

$$E = \Psi - W_{ext} + \Phi ,$$

where Φ, W_{ext} and Ψ are respectively the dissipated energy, the external-loads work and the free energy of the whole structure. The proposed energetic criterion imposes that dissipated energy is the same for both models. An interesting property of the method proposed is that Ψ and W_{ext} are also kept identical for both models. The key feature that allows concluding on this is the fact that both models unload in a linear manner, which allows us to write:

$$d\Psi = \int_{\Gamma} \underline{F}\,\underline{u}\, dS ,$$

with $\underline{F}$ and $\underline{u}$ the external loads and displacements applied to the structure. This property is obviously true for the damage model and was also preserved for the cohesive zone model during its thermodynamic construction.

Generalization to plasticity.

Our current work deals with the generalization of the method to more sophisticated models. We will next present our first results in the use of the method when plastic strains are taken into account.

Difficulties arisen by the presence of plastic strains. Plastic strains complicate the study of the energetic behaviour of the structure because, even if the unloading is done inside the elastic domain, the free energy of the unloaded state isn't equal to zero. There are two reasons for this: the first one is the fact there is some free energy stored in the microstructure of the material and the other one is the presence of residual stresses in the unloaded state. The first problem can be tackled by building a fictitious free energy potential from the knowledge of the mechanical behaviour of the material. This potential is defined so that dissipated energy is not directly linked to heat production, but merely to unrecoverable energy.

New bridging criterion. The cohesive model is defined in the same way as for damage, with the only difference that we now allow the presence of a plastic displacement jump across the cohesive zone. This new parameter in the cohesive zone requires refining the energetic criterion, which now writes:

$$d\hat{\Phi}^p = d\breve{\Phi}^p ,$$
$$d\hat{\Phi}^e = d\breve{\Phi}^e ,$$

with $d\Phi^p$ the dissipated energy increment associated with the variation of the plastic internal variables and $d\Phi^e$ the increment of dissipated energy associated with the damage variation.

Conclusion

The method proposed here allows building incrementally a cohesive zone model from the knowledge of the solution of a nonlocal damage problem. This method is generalized so that it can be used with plastic-damageable models. Further work has to be done for the three dimensional generalization of the method.

References

[1] J. Mazars: Application de la mécanique de l'endommagement au comportement non-linéaire et à la rupture du béton de structure, PhD thesis, ENSET (1984).

[2] J. Mazars and G. Pijaudier-Cabot: International Journal of Solids and Structures, Vol. 33, Num. 20-22 (1996), p. 3327-3342.

[3] Gurtin, M.: Zeitschrift für Angewandte Mathematik und Physik (ZAMP), Vol. 30, Num. 6 (1979), p. 991-1003.

[4] Planas, J., Elices, M., Guinea, G.: International Journal of Fracture, Vol. 63, Num. 2 (1993), p. 173-187.

[5] A. Hillerborg, M. Modéer and PE. Petersson: Cement and Concrete Research, Vol. 6 (1976), p. 773-782.

Key Engineering Materials Vols. 385-387 (2008) pp 85-88
© (2008) Trans Tech Publications, Switzerland
doi:10.4028/www.scientific.net/KEM.385-387.85

Crushing behaviour of CFRP composite structure

H. Ghasemnejad [1, a], H. Hadavinia [1, b] and E. Lewis [1, c]

[1] Faculty of Engineering, Kingston University, SW15 3DW, UK

[a] h.ghasemnejad@kingston.ac.uk, [b] h.hadavinia@kingston.ac.uk, [c] e.lewis@kingston.ac.uk

Keywords: Specific sustained crushing stress; Composite; Stiffened box

Abstract. The present paper investigates specific sustained crushing stress (SSCS) of various composite laminate designs and stiffened boxes under axial crushing test. In this regard, an optimum composite crash box design is sought by studying the effect of laminate design and stiffeners on SSCS. Crash boxes were fabricated from carbon/epoxy twill-weave fabrics of $[0]_4$, $[45]_4$ and $[0,45]_2$. The progressive failure with three distinct crushing modes of transverse shearing, lamina bending and brittle fracture was observed for three laminate designs. Two new assembled composite boxes were made from channels and V-shape stiffener and tested in quasi-static condition. Adhesive bonding was used in joining the channelled and stiffened boxes. Measured amount of SSCS for all models were compared to find an optimum crash box. It was found SSCS increases with increasing proportion of 0° plies in the laminate.

Introduction

The fibre reinforced polymer (FRP) composite materials are known as excellent energy absorbers due to their high strength-to-weight and stiffness-to-weight ratios. For crashworthiness design, FRP composite structural elements such as box are able to collapse in progressive controlled manner. The highest energy absorption occurs in two progressive crushing mechanisms which are brittle fracture and lamina bending [1-2]. These two crushing mechanisms absorb the energy due to interlaminar, intralaminar crack growth and fracturing of lamina bundles. Jacobe *et al.* [3] have extensively reviewed previous works related to the effect of fibre type, matrix type, fibre architecture, specimen geometry, process conditions, fibre volume fraction and testing speed on energy absorbing capabilities of crash elements. Bolukbasi *et al.* [4] studied the energy absorption in composite stiffeners to conduct expensive and time- consuming design support tests at the element and sub-assembly level prior to fabrication of the fuselage structure in aircraft. The present work studies the specific sustained crushing stress (SSCS) of composite boxes which are laminated from carbon/epoxy twill-weave fabrics of $[0]_4$, $[45]_4$ and $[0,45]_2$. The most effective laminate design was chosen in laminating channels and V-shape stiffener. Adhesive bonding was used in making

channelled and stiffened boxes. The specific sustained crushing stress (SSCS) of stiffened composite boxes was compared to SSCS of the best laminate design of simple composite box.

Experimental studies

The crush box specimens were made of carbon/epoxy twill-weave fabrics by hand lay-up with three fibre orientations with respect to weft direction. The dimensions of all boxes were the same and chosen regarding the previous reported works which have shown progressive failure [5]. The side of each box was 80 mm with thickness around 3 mm and the total length was 100 mm. One end of specimens was bevelled to make a trigger for progressive crushing with an angle of 60°. Each specimen was crushed between two parallel plates for 50 mm stroke using Universal Testing Machine with 500 kN load cell. The crush speed was set at 2 mm/min. Composite boxes with laminate design of $[0]_4$ crushed in lamina bending failure mode. Brittle fracture and transverse shearing crushing modes were observed for other two laminate designs of $[0,45]_2$ and $[45]_4$ (see Figure 1).

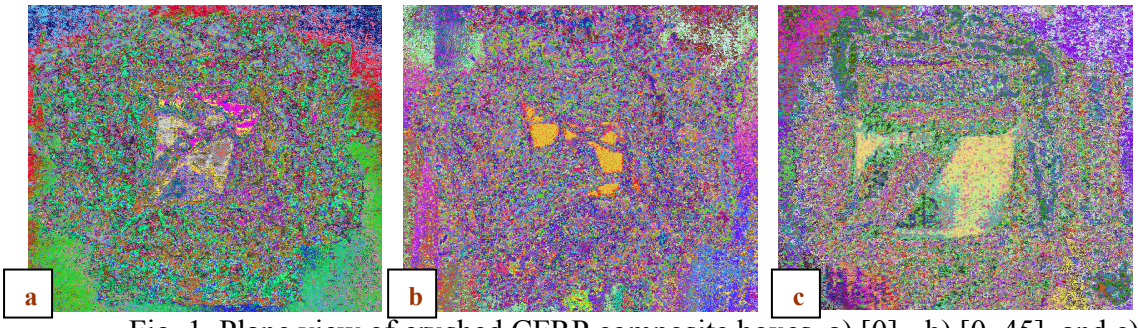

Fig. 1. Plane view of crushed CFRP composite boxes. a) $[0]_4$, b) $[0, 45]_2$ and c) $[45]_4$.

The force-crush distance diagrams were recorded automatically and the results are compared in Figure 2. The specific sustained crushing stress (SSCS) is a measure of the energy absorption capability of the material which is defined by,

$$SSCS = \frac{\sigma_{sc}}{\rho} \tag{1}$$

where, σ_{sc} is sustained crushing stress which is defined as the ratio of mean force to cross-sectional area, and ρ is material density. From experimental results, it was found that the SSCS increases with increasing the proportion of 0° plies in the laminate. $[0]_4$ laminate has the highest mean force and consequently the highest SSCS with respect to other laminates made from the same materials and the same cross-sectional area.

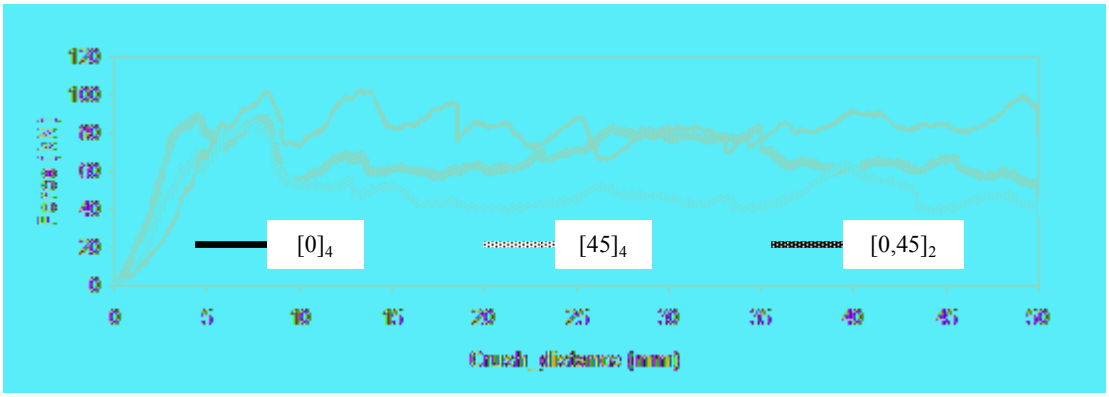

Fig. 2. The comparison of force-crush distance of CFRP composite boxes.

Two types of boxes were made from assembling channels and V-shape stiffener using the $[0]_4$ laminate which showed the highest SSCS in simple box tests. The thickness of channels was the same as simple composite box but the V-shape stiffener thickness was 2.25 mm. The type I specimens consisted of two bonded channels and the type II specimens were made from bonding two channels and one V-shape stiffener (Figure 3). The channels and the stiffener were bonded together using Betamate 1493 epoxy adhesive which is cured for 30 min at 180°C. All boxes were tested at the same conditions as in the simple box tests.

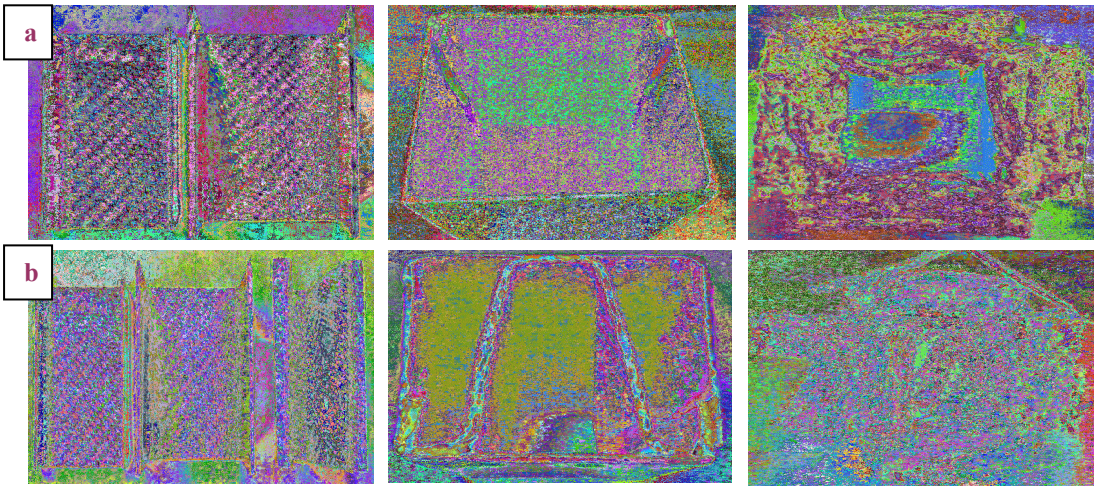

Fig. 3. Assembled crash boxes made from bonding (a) Two channels and b) Two channels stiffened with V-shape stiffener before and after crushing.

In Figure 4 the force-crush distance diagrams of assembled specimens are compared to the crushing response of simple box with $[0]_4$ laminate.

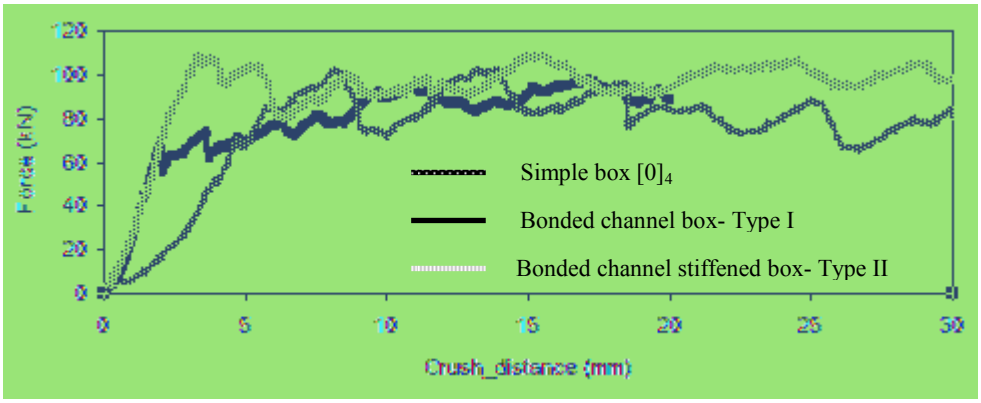

Fig. 4. Comparison of force-crush distance of CFRP assembled and simple boxes (All made from $[0]_4$ lay-up).

Conclusions

In this paper, the specific sustained crushing stress (SSCS) of simple and stiffened CFRP composite boxes which were laminated from carbon/epoxy twill-weave fabrics was studied experimentally. It was found that the highest specific sustained crushing stress (SSCS) was achieved for simple composite box with the fibre orientation of $[0]_4$. The assembled boxes from two channels with the $[0]_4$ lay up bonded by epoxy adhesive showed roughly the same SSCS as the simple box. The assembled box stiffened with a V-shape stiffener has 4% higher SSCS relative to its higher mean force in comparison with simple box.

References

[1] A.G. Mamalis, D.E. Manolakos, G.A. Demosthenous and M.B. Ioannidis. *The static and dynamic collapse of fibreglass composite automotive frame rails*. Composite Structures, 34(1996), p.77-90.

[2] H. Ghasemnejad, B.R.K Blackman, H. Hadavinia and B. Sudall. *Experimental studies on fracture characterisation and crashworthiness of GFRP composite box.* To be published.

[3] G.C. Jacob, J.F. Fellers, S. Simunovic and M. Starbuck. *Energy absorption in polymer composites for automotive crashworthiness.* Journal of Composite Materials 36(2002), p.813-850.

[4] A.O. Bolukbasi and D.H. Laananen. *Energy absorption in composite stiffeners*. Composites 26(1995), p. 291-301.

[5] G.L. Farley and R.M. Jones. *Energy absorption capability of composite tubes and beams*. NASA TM-101634, AVSCOM TR-89-B-003, 1989.

Key Engineering Materials Vols. 385-387 (2008) pp 89-92
© (2008) Trans Tech Publications, Switzerland
doi:10.4028/www.scientific.net/KEM.385-387.89

Crack spacing and the flow stress in NiTi thin films deposited on Cu substrate

Y. H. Li[1,a*], F. L. Meng[2,3,b*], C. S. Liu[3,c], Y. M. Wang[2,d]

[1] School of Sciences, Harbin Engineering University, Harbin 150001, China

[2] Department of Materials Science, Key Laboratory of Automobile Materials of MOE, Jilin University, Changchun 130012, China

[3] School of Materials and Metallurgy, Northeastem University, Shenyang 110004, China

[a] yonghuali@hrbeu.edu.cn, [b] mfl@jlu.edu.cn, [c] csliu@mail.neu.edu.cn, [d] **wangym32@yahoo.com**

Keyword: NiTi thin film; The flow stress; Fracture toughness; Cracks propagation;

Abstract: Ti-51.45at.%Ni thin films were deposited onto copper substrates by magnetron sputtering. The copper substrates were pre-punched into dog-bone specimens with 4.5mm×30mm(gauge portion) ×35μm(thickness). The substrate temperature was about 673K. The thin films were about 20μm thick. The as-deposited films were first solution treated at 1073K for 1h, and then aged at 773K for 30min. The grain size was estimated to be 1.5μm from scanning electron microscopy micrographs. Tensile tests were carried out on CSS-44100 electron universal test-machine. The strain rate was 1.1×10^{-4} s^{-1}. The stress-strain curves of the free-standing film were obtained from the experimental stress-strain curves of copper substrate together with the thin film adherent to the substrate compared with the curves of copper substrate without film. The Hall-Patch coefficient was calculated, k=205Mpa.$\mu m^{1/2}$. It seems that the Hall-Patch coefficient decreases with increasing film thickness. The experimental results showed that a series of parallel cracks grew in a concerted fashion across the thin film and the cracks were equally spaced. The cracks were more closely spaced if the film stress was increased. The fracture toughness of the film was estimated, K_{1c}=0.96MPa·$m^{1/2}$. Therefore, the minimum crack spacing is predicted by the film stress given.

1. Introduction

Among several types of functional materials proposed for fabricating microactuators, TiNi shape memory alloys have great recovering force after deformation [1,2]. The environment temperature, the crystallographic texture, the grain size and the thickness of film should affect the flow stress development [3]. However, in order to achieve the effective development and a comprehensive understanding of shape memory thin films, the studying of mechanical properties of sputter-deposited thin films is necessary. In the present article, we investigated the stress-induced crack propagation, and predict the flow stress of thin film before its fracture. In this work the Hall-Patch coefficient and the fracture toughness of the film were obtained.

2. Experimental

The Ni-rich NiTi thin films were deposited onto Cu substrates by magnetron sputtering in an argon atmosphere using a sputtering target of an equiatomic NiTi alloy. The copper substrates were pre-punched into dog-bone specimens with 4.5mm×30mm(gauge portion) ×35μm(thickness). The sputtering conditions were as follows: argon pressure, 4×10^{-2} Pa; sputtering power, 640 W; deposition rate, 95 nm/min; substrate-to-target distance, 65 mm. The substrate temperature was about 673K. The

NiTi films thickness was about 20μm. The films composition determined by energy dispersive X-ray spectroscopy was about Ti-51.45at.%Ni. To produce the crystallization of NiTi, in a vacuum furnace the as-deposited films were first solution treated at 1073K for 1h, and then aged at 773K for 30min. Tensile tests were carried out at ambient temperature. Tensile tests were carried out on CSS-44100 electron universal testing machine. The strain rate was 1.1×10^{-4} s^{-1}. The stress-strain curve of the free-standing film was obtained from the experimental curve of copper substrate together with the thin film adherent to the substrate compared with the curve of copper substrate without film. The micrographs of the NiTi thin film were obtained using scanning electron microscopy (SEM).

3. Results and Discussion

Griffin [4] and Bravman [5] recently showed that the strength of polycrystalline thin films depends on both their grain sizes and their thicknesses. The total flow stress is simply determined by the sum of two mechanisms [6]:

$$\sigma_{flow,total} = \sigma_{flow} + kd^{-1/2} \tag{1}$$

where d is median grain size and k is the Hall-Petch coefficient. For bcc structures, Chen [7] showed that real slip plane only occurred on the {110} plane. For a {110} oriented film, the slip direction is <111>.

$$\sigma_{flow} = 2.121\times\frac{b\mu_f}{4\pi(1-\upsilon)}\ln(\frac{d}{b})(\frac{2}{0.866d}+\frac{1}{h}) \tag{2}$$

$$\sigma_{flow,total} = 2.121\times\frac{b\mu_f}{4\pi(1-\upsilon)}\ln(\frac{d}{b})(\frac{2}{0.866d}+\frac{1}{h}) + kd^{-1/2} \tag{3}$$

A film that is attached to a substrate and subjected to a tensile stress may fail in a number of ways. If the stress in the film is uniaxial or if the fracture properties of the film are sufficiently anisotropic, a series of cracks will grow parallel to one another [8,9]. The minimum spacing can exist between a series of parallel cracks propagating in a thin film [10].

$$\sigma_{cr} \geq 0.7K_{Ic}/\sqrt{t} \tag{4}$$

Where t is the thickness of the film, K_{Ic} is the fracture toughness of the film. σ_{cr}, is the critical stress. A number of cracks may propagate when the stress reaches this critical value. If the film stress exceeds σ_{cr}, the maximum possible crack density is increased, and the minimum crack spacing is given by

$$\lambda/t \approx 8(1-\sqrt{1-0.5(\sigma\sqrt{t}/K_{Ic})^{-2}}) \tag{5}$$

The stress-strain curves of the free-standing NiTi thin film is shown in Fig. 1.

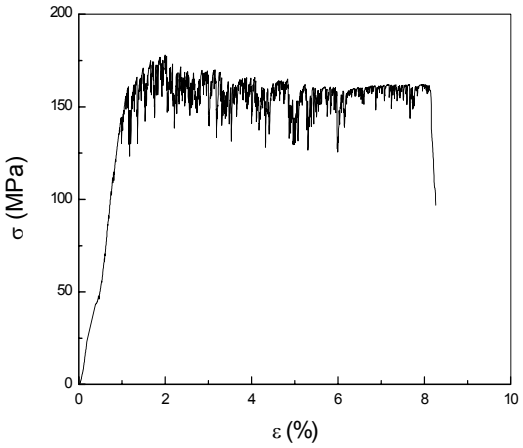

Fig.1 stress-strain curve of free-standing NiTi thin film

Fig. 2 shows the microstructures of the thin film after heat treatment. The Fig. 3 shows the SEM micrograph of NiTi thin film fractured.

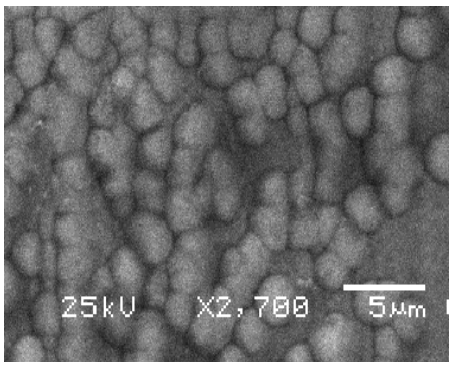

Fig. 2 SEM micrographs of NiTi thin film.

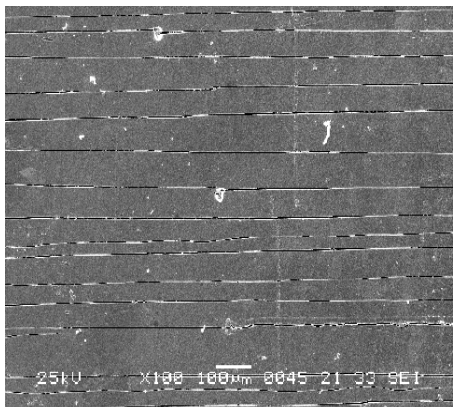

Fig. 3. SEM micrograph of NiTi thin film fractured.

From Fig. 2 the grain size of the film is estimated to be 1.5μm. For NiTi alloy[11], $\mu_f = 27 \times 10^3 Mpa$, $b = 0.2596nm$, $\upsilon = 0.28$. From Eq. 3, the Hall-Patch coefficient is calculated, k=205Mpa.μm$^{1/2}$. Ishida [12] showed that the total flow stress of Ti-51.5at%Ni thin film was about

600Mpa at 317K, h=8μm, d=0.5μm. The Hall-Patch coefficient was calculated to be 383Mpa.μm$^{1/2}$ from Eq. 3. It seems that the Hall-Patch coefficient decreases with increasing film thickness which agrees with Venkatraman's work [5]. In Fig. 3, a series of cracks grow parallel to one another, and the direction of crack extension is perpendicular to the one of tension. The fracture toughness of the film, K_{Ic}, can be determined from Eq. 4, K_{Ic}=0.96MPa·m$^{1/2}$. The minimum crack spacing is about $\lambda = 87\mu m$ according to Eq. 5.

4. Conclusions

The mechanical properties of sputtering-deposited Ti-51.45at.% Ni thin film are investigated. The experimental results show that a series of parallel cracks grew in a concerted fashion across the thin film and the cracks are about equally spaced. The cracks are more closely spaced if the film stress is increased. The fracture toughness of the film is estimated, K_{Ic}=0.96MPa·m$^{1/2}$. Therefore, the minimum crack spacing is predicted by the film stress given, $\lambda = 87\mu m$. The Hall-Patch coefficient is calculated, k=205Mpa.μm$^{1/2}$. It seems that the Hall-Patch coefficient decreases with increasing film thickness.

Acknowledgments

Projects supported by the National Science Foundation for Post-doctoral Scientists of China (Grant No. 20060390969 and 20060390432).

References

[1] S. Miyazaki, Y. Ohmi, K. Otsuka: J. Phys. (France) Vol. 43 (1982), p. C4-255.
[2] S. Miyazaki, K. Otsuka: ISIJ Int. Vol. 29 (1989), p. 353.
[3] J. E. Sanchez and E. Arzt: Scripta Metall. Mater. Vol. 27 (1992), p. 285.
[4] A.J. Griffin, F.R. Brotzen and C. Dunn: Scripta Metall, Vol. 20(9) (1986), p. 1271.
[5] R. Venkatraman, and J. C. Bravman: J. Mater. Res., Vol. 7 (1992), p. 2040.
[6] P. Richard and J. J. Vlassak: Annu. Res. Mater. Sci., Vol. 26 (1996), p. 431.
[7] R. Maddin and N. K. Chen: Progr. Met. Phys., Vol. 5 (1954), p. 53.
[8] M. S. Hu and A. G. Evans: Acta Metall. Vol. 37 (1989), p. 917.
[9] D. C. Agrawal and R. Raj: Acta Metall. Vol. 37 (1989), p. 1265.
[10] M. D. Thouless: J. Am. Ceram. Soc., Vol. 72 (1990), p. 2144.
[11] F. Shan, Y. Huo, F. Teng and Y. Wang: Rare Metal Materials And Engineering (Chinese), Vol. 27 (1998), p. 199.
[12] A. Ishida, M. Sato, T. Kimura and S. Miyazaki: Philosophical Magazine A, Vol. 80 (2000), p. 967.

Key Engineering Materials Vols. 385-387 (2008) pp 93-96
© (2008) Trans Tech Publications, Switzerland
doi:10.4028/www.scientific.net/KEM.385-387.93

Crack Width of SRC Members Based on Fracture Mechanics

Bin WANG[a], Shansuo ZHENG[b], Minzhe Wu[c], Lei LI[d], and Lei ZENG[e]

School of Civil Engineering, Xi'an University of Architecture and Technology, Xi'an 710055, China

[a]wangbin1853@sohu.com, [b]zhengshansuo@263.net, [c]minzhewu@sohu.com,
[c]lilei1004@163.com, [c]zenglei28@126.com

Key words: Steel reinforced concrete; Fracture energy; Tension stiffening; Crack width

Abstract. Steel reinforced concrete (SRC) structure is a kind of building structure with excellent mechanical performance, but the theory of crack width is not very clear. In recent years, the fracture energy is more and more applied to research concrete materials, which has opened up a new field for concrete materials modeling. In this paper, crack width model for SRC structure based on fracture energy concept is put forward. A uniaxial tension model is employed in the analysis for simplification. On the ground of the stress equilibrium as well as the relation among relative slip, steel strain and concrete strain, the basic equations are derived. By introducing the interfacial nonlinear bond stress versus slip constitutive relation between embedded steel and concrete, the analytical solution for distribution of slip along the interface is obtained. And based on this result, the influence of the interfacial bond-slip on tension stiffening of the steel is considered. The displacements of steel and concrete at the crack face under different load levels are computed and analyzed respectively. Finally according to the principle of work and power as well as the fracture energy concept of plain concrete, expression for fracture energy of SRC structures is obtained, and the relation of crack width and concrete fracture energy is established. The comparison shows that the fracture energy based on the model agrees with the test results well.

Introduction

Steel reinforced concrete (SRC) structure is used in high-rise and super high-rise buildings extensively because of its excellent seismic performance, rigidity and fire resistance. The present computing methods about crack width of SRC members are different, the bond slip effect between steel and surrounding concrete is neglected. Several research results [3] have shown bond slip exists in SRC structure and obviously affects the mechanical property of members. Based on fracture mechanics a new method is proposed for the computation of crack width of SRC members considering bond slip between steel and concrete. Fracture mechanics supplies a new means for computing crack width. Fracture energy is a very important parameter in fracture mechanics, which studies on crack expansion mechanics under load in the view of energy and tensile softening of concrete is considered. Based on a uniaxial tension crack width test and fracture energy theory, considering bond slip and the tension stiffening effect the maximum crack width calculation method of SRC members is studied in this paper.

Relationship of Crack Width and Fracture Energy for Plain Concrete

The relationship between the material properties of concrete and the maximum crack width is linear (Morcos 1991), in a more general form, which can be expressed as

$$w_0 = C\frac{G_f}{f_t} \tag{1}$$

where, G_f is fracture energy; f_t is tensile strength of concrete; C is a constant that depends on the mathematical model used to describe the descending branch of tensile strain-softening curve. w_0 can

be determined from Eq. (1) for any concrete mixture ratio as long as tensile strength and fracture energy are known.

Distribution of bond slip

Bond slip value $s(x)$ is equal to the strain difference between steel and surrounding concrete in crack surface, which is expressed as

$$\frac{ds}{dx} = \varepsilon_s(x) - \varepsilon_c(x) = \frac{\sigma_s(x)}{E_s} - \frac{\sigma_c(x)}{E_c} \tag{2}$$

where, σ_c and σ_s are stresses of surrounding concrete and steel, respectively; E_c and E_s are Young's moduli of concrete and steel, respectively.

A uniaxial tension model is adopted, as shown in Fig.1. The load P is carried by steel and surrounding concrete together. The concrete stress can be expressed as

$$\sigma_c = \frac{P}{A_c} - \frac{\sigma_s A_s}{A_c} \tag{3}$$

Inserting Eq. (3) in Eq. (2) and differentiating with respect to x yields

$$\frac{d^2 s}{dx^2} = \frac{d\sigma_s}{dx}\left(\frac{1+n\rho}{E_s}\right) \tag{4}$$

where, $n = E_s/E_c$; $\rho = A_s/A_c$; A_s and A_c are cross-section areas of steel and concrete, respectively.

The distribution of the bond stress at the interface between surrounding concrete and steel is different. In order to simplify calculation the average bond stress $\bar{\tau}$ is introduced, and it is assumed that the relationship of bond stress and slip is linear, $\bar{\tau}[s(x)] = E_b \cdot s(x)$, E_b is the slip modulus and is assumed to be 1.826×104MN/m^3.

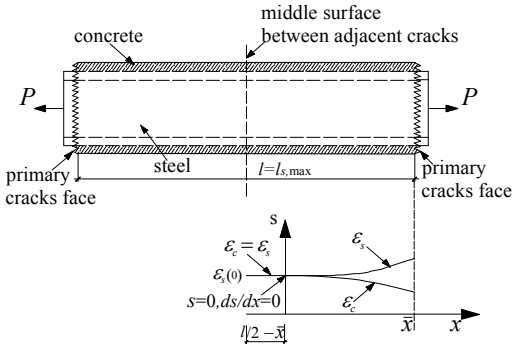

Fig.1. Distribution of bond slip and strain in shaped steel and concrete

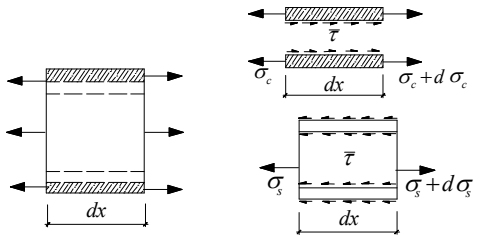

Fig.2. Free body for SRC member

Consider a segment dx of a SRC member, as shown in Fig.2. The equilibrium equations of steel can be expressed as

$$\frac{d\sigma_s}{dx} = \frac{\bar{\tau}[s(x)] \cdot L}{A_s} \tag{5}$$

where, L is the perimeter of steel. Substituting Eq.(5) into Eq.(4) yields

$$\frac{d^2 s}{dx^2} - \frac{\bar{\tau}\left[s(x)\right] L}{A_s} \cdot \frac{1+n\rho}{E_s} = \frac{d^2 s}{dx^2} - k^2 \bar{\tau}\left[s(x)\right] = 0 \tag{6}$$

where, $k^2 = \frac{L}{A_s} \cdot \frac{1+n\rho}{E_s}$ is a constant. In order to avoid numerical problems arising from spatial discretization at this model, the general solution of Eq.(6) can be derived by analytical solution.

Determination of maximum crack spacing

The maximum crack spacing is computed in an iterative manner. The starting point is the known force in the concrete at the middle surface between the two adjacent cracks, i.e., at $x = 0$. The load, which carried by the concrete, is given by

$$P_c(0) = \sigma_c A_c = f_t A_c \tag{7}$$

Then, at $x = l/2$, $P_c(l/2)$ is obtained from the average bond stress $\bar{\tau}\left[s(x)\right]$ between steel and surrounding concrete, shown as

$$P_c(l/2) = P_c(0) - L\int_0^{l/2} \bar{\tau}\left[s(x)\right] dx \tag{8}$$

During the iteration, the length of the composite model l is continuously increased until $P_c(l/2)$ close to zero, the iteration is over. In this paper, l represents the maximum crack spacing, giving $l_{s,\max} = l$. Finally, the average crack spacing can be estimated as $l_s = (2/3) l_{s,\max}$ according to CEB-FIP (1990).

Tension stiffening

In order to consider tension stiffening effect in the context of fracture energy concept, the length of the model l is equal to the average crack spacing l_s. The respective displacement measured at the crack face is divided in the following three stages (see in Fig.1):

The first stage: $\varepsilon_c = \varepsilon_s$, $l/2 - \bar{x} \le x \le 0$

$$u(0) = u(l/2) = \varepsilon_c \frac{l}{2} = \frac{f_t}{E_c} \frac{l}{2} \tag{9}$$

The second stage: $\varepsilon_c < \varepsilon_s$, $0 \le x < \bar{x}$

$$u(\bar{x}) = \varepsilon_s(0)\left(\frac{l}{2} - \bar{x}\right) + \int_0^{\bar{x}} \left(\varepsilon_s(0) + \frac{P_{bs}(x)}{A_s E_s}\right) dx \tag{10}$$

The third stage: $\varepsilon_c < \varepsilon_s$, $\bar{x} = l/2$

$$u = \int_0^{l/2} \left(\frac{P_s(0) + P_{bs}(x)}{A_s E_s}\right) dx \tag{11}$$

where, at $x = \bar{x}$, $P_{bs}(x)$ is a load which is transferred from steel to concrete by the average bond stress. When $0 \le x < \bar{x}$, $P_{bs} = L\int_0^{\bar{x}} \bar{\tau}\left[s(x)\right] dx$, when $\bar{x} = l/2$, $P_{bs} = L\int_0^{l/2} \bar{\tau}\left[s(x)\right] dx$; $P_s(0) = \rho_s n P_c(0)$.

Crack width of SRC members

The fracture energy is introduced to simulate the cracking process of concrete and assumed to be a constant material property. Energy release in consequence of both cracking of concrete and bond slip, which are looked as a parameter. Based on load–displacement response of composite material, the energy released can be expressed as

$$W = W_{sc} - W_s = \int_0^{\infty} \frac{P_{sc} - P_s}{A_c} du \tag{12}$$

Consequently, according to the fracture energy concept, $W = G_f$, Eq. (1) can be rewritten as

$$w_0 = C\frac{W}{f_t} \tag{13}$$

where, P_{sc} and P_s are computed on the basis of a composite model of length l_s.

Comparison with the test results

The comparison of test results and calculation values is supplied by Ref. [5] and in this paper (see table 1), which shows that the method supplied in this paper agrees with the test results well.

Table 1 crack width Comparison of calculation and test

Specimen No.	concrete strength grade	specification of steel	types of steel	w_{test}	w_c	$w_{c[5]}$	$\frac{w_c}{w_{test}}$	$\frac{w_{c[5]}}{w_{test}}$	Specimen section
SRCⅠ a		H140×110×4.5×6.0	Q235	0.102	0.106	0.118	1.039	1.157	
SRCⅠ b	C60	H140×80×4.5×6.0	Q235	0.134	0.139	0.154	1.037	1.149	
SRCⅠ c		H140×50×4.5×6.0	Q235	0.169	0.180	0.200	1.065	1.183	
SRCⅡ a		H140×110×4.5×6.0	Q235	0.096	0.103	0.106	1.072	1.103	
SRCⅡ b	C80	H140×80×4.5×6.0	Q235	0.124	0.132	0.112	1.065	0.903	
SRCⅡ c		H140×50×4.5×6.0	Q235	0.154	0.155	0.160	1.006	1.039	

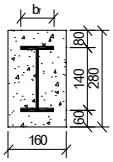

Conclusion

In this paper, based on a number of uniaxial tension test, the calculation method of SRC members crack width is obtained considering bond-slip behavior and tension stiffening of material. The results shows that the calculated crack width agrees with test well. This project is sponsored by National Natural Science Foundation of China (Grant No. 50378080) and the Educational Office of Shaan'xi Province in China (Grant No. 06JK263).

References

[1] Morcos, S. *Fracture in Continuous Composite Beams*. PhD dissertation, Unversity of Pittsburgh, Pa

[2] *Comite´Euro-International du Be´ton-Fe´de´ration International de la Pre´-contrainte* (*CEB-FIP*). (1990). Model code 1990, bulletind'information. CEB, Lausanne, Switzerland

[3] S. S. Zheng, G. Z Deng. *Experimental study on bond-slip performance between steel shape and concrete in SRC structures*. Engineering Mechanics, Vol. 20, No. 5 (2003), p.63-69

[4] Bai Guoliang, Jiang Weishan, ect.. *Calculation crack width on SRC beam*. J. Xi'an Univ. Of Arch. & Tech.. Vol. 27(1995), No. 3, p. 320-328

Key Engineering Materials Vols. 385-387 (2008) pp 97-100
© (2008) Trans Tech Publications, Switzerland
doi:10.4028/www.scientific.net/KEM.385-387.97

Damage Analysis of the SRHSHPC Frame Columns under Low Cyclic Reversed Horizontal Loading

Shansuo ZHENG[a], Liang ZHANG [b], Bin WANG[c],Lei LI[d], Lei ZENG[e]

School of Civil Engineering, Xi'an University of Architecture and Technology, Xi'an 710055, China

[a]zhengshansuo@263.net, [b]gztrzl@126.com, [c]wangbin1853@sohu.com, [d]lilei1004@163.com, [e]zenglei28@126.com

Keywords: Steel Reinforced High Strength and High Performance Concrete (SRHSHPC), Frame Column, Low Cyclic Reversed Loading Test, Damage Analysis, Accumulative Damage Model.

Abstract. Based on tests under low cyclic reversed horizontal loading, damage behaviors of steel reinforced high strength and high performance concrete (SRHSHPC) frame columns are analyzed. The strength attenuation that considered as damage variable is figured out, and the influence of axial compression ratio, shear span ratio, stirrup ratio and concrete strength on the strength attenuation is discussed. The accumulative damage model, which can reveal the effect of cyclic loading and maximum deformation, is established for the SRHSHPC frame columns. The different phases of damage growth and their features for the SRHSHPC frame columns are analyzed, and the relation of damage and displacement is ascertained. Furthermore, the influence of axial compression ratio, shear span ratio, stirrup ratio and concrete strength on the damage development is also discussed. The results show that the damage model could give a rational description for damaging process of the SRHSHPC frame columns.

Introduction

The earthquake-resistance behaviors of structure depend on its energy absorption capability and elastic-plasticity deformation capacity strongly, but the damage of structure is price for realizing these capacities. In general, if the energy absorption capacity and elastic-plastic deformation ability is better, the seismic behaviors of structure are more excellent whose seismic damage is less. In the paper, the hysteretic performance as well as the failure mechanism of the columns is analyzed based on experimental results. Besides, the damage cumulative process is studied.

Damage Model

Because the resistance of structures is different, there are different damage phases in the whole low cyclic reversed horizontal loading process. The damage variable D is applied to describe different damage phases. And it has the following characteristics: (1) the dimension of damage variable D is [0, 1]. If the $D = 0$, it is indicated that there is no damage in which the structure is relative safe. If the $D = 1$, it is indicated that the damage reaches limit phase in which the structure is failure. If the value of D is between 0 and 1, it is indicated that the structure is in a particular damage state; (2) the damage of structure is irreversible. Besides, the damage variable D is monotone increasing function.

The damage value of the SRHSHPC structure is multivariate function. The effect factors include maximum deformation, cycle cumulative effect, original damage, shrinkage, creep and so on. The damage stages of the SRHSHPC structure under low cyclic load can be described by a function of the parameters $x_i (i = 1, 2, \cdots, n)$. Namely, the change of these parameters reflects the variation of damage. The parameters $(x_1, x_2, \cdots, x_n)$ are corresponding to the damage components $d_j (j = 1, 2, \cdots, n)$. Thus, the damage value D can be considered as the mapping function of $d_j (j = 1, 2, \cdots, n)$. Besides, it should satisfy the following conditions:

1: When $d_j(j=1,2,\cdots,n)=0$, $D=f(d_1, d_2, \cdots, d_j)=0$;

2: D is monotone increasing function of $d_j(j=1,2,\cdots,n)$.

Supposing $f_j=f(0, \cdots, d_j, \cdots, 0)=d_j$ $(j=1, 2, 3,\cdots,n)$, Then $D\geq \max d_j(j=1,...,n)$, namely $D=\max d_j+\alpha$.

Usually, the earthquake failure of frame columns can be attributed to cumulative damage generated by great deformation and cycle loading effect. Therefore, the cumulative damage phase of the SRHSHPC columns can be expressed by maximum deformation damage component D_d and cycle damage component D_c. The parameter α reflects the maximum deformation and cycle damage effect influencing the damage of components, whose value is influenced by some factors, such as character of component, character of earthquake motion and so on. For the sake of reflecting main influencing factors and calculating conveniently, the simplification formula is adopted as: $D=D_d+D_c$, where D_d is expressed as maximum deformation damage, namely $D_d=\Delta/\Delta_u$; Δ is maximum action deformation; Δ_u is limit deformation under monotone loading. A great deal of experiment certificate that, under low cyclic reversed horizontal loading, the damage accumulation of structural members is mainly expressed as the accumulation of damage produced in every time circle.

For example, before the limit phase, the bearing capacity of component decreases following times of circulation loading till convergence in specified displacement cycle. It is named as strength attenuation following with damage value of low cyclic reversed loading increasing. Therefore, strength attenuation can be applied to express damage component under cycle load. The strength attenuation (shown in Fig.1) produced in one time cycle loading is expressed by the strength corresponding to the ending time of cycle in certain displacement P_i and cycle initial strength P_{0i}. For the first deformation cycle of loading process, P_0 is in the monotone loading line. Supposing there are K cycles, the deformation value corresponding to each cycle is $\Delta_1,\Delta_2,\cdots,\Delta_k$ respectively, and initial strength of each cycle is P_{01}, P_{02}, $\cdots$, P_{0K} respectively; the strength corresponding to the ending time of each cycle is P_1, P_2, $\cdots$, P_K respectively. The $D_{ci,0}$ and $D_{i,0}$ is applied to express initial cumulative cycle damage and total damage value in the i $(1\leq i\leq K)$ cycle respectively. The $D_{ci,0}$ and $D_{i,0}$ is employed to express cumulative cycle damage and total damage value corresponding to ending time of the i cycle respectively. Because the damage process is irreversible, so there is:

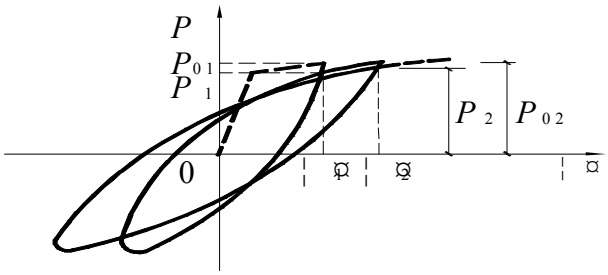

Fig.1 Strength attenuation

$$\begin{cases} D_{c1,0}=0, D_{d1}=\Delta_1/\Delta_u, D_{1,0}=\Delta_1/\Delta_u \\ D_{di}=\begin{cases} D_{ci,0}=0, & D_{i,0}=D_{ci,0}+D_{di} \\ D_{di\text{-}1,} & \Delta_i<\Delta_{i\text{-}1} \\ \Delta_i/\Delta_u & \Delta_i\geq\Delta_{i\text{-}1} \end{cases} \end{cases} \tag{1}$$

Generally, the failure process of component under cycle loading includes concrete cracking, crack expanding, yielding till failure. In the beginning of cycle, the load which reaches appointed displacement keeps reducing, and crack expanding. The damage of component becomes worse. But after some of cycles, the hysteretic curve astringes, the strength no longer reduces, and the damage no

longer develops. Therefore, it is considered that change rate of damage is direct ratio with rate of strength attenuation, namely $\mathrm{d}D_{ci,e} = \lambda \mathrm{d}P_i$. It must satisfy following conditions: (1) if $P_i = P_{0i}$, $D_{ci,e} = D_{ci,0}$. (2) If $P_i \to P_{fi}$, $D_{ci,e} = 1 - D_{di}$, where P_{fi} is residual strength of low cyclic endurance failure in the i cycle.

According to the upper formula, the final result can be obtained as following:

$$D_{ci,e} = D_{ci,0} + (1 - D_{ci,0} - D_{di})(1 - P_i / P_{0i}) / (1 - P_{fi} / P_{0i}) \tag{2}$$

Finally, the total damage value can be attained as following:

$$D_{i,e} = D_{\mathrm{d}i} + D_{\mathrm{c}i,e} = D_{\mathrm{d}i} + D_{\mathrm{c}i,0} + (1 - D_{ci,0} - D_{di})(P_{0i} - P_i) / (P_{0i} - P_{fi}) \tag{3}$$

where P_{fi} can be taken as $P_{fi} = P_u \Delta_i / \Delta_u$ referring to the reinforced concrete members; P_u is the strength of component which corresponds to limit deformation Δ_u under monotone loading.

Damage Evolution of the SRHSHPC Frame Columns

From beginning loading to final failure, the damage evolution of the SRHSHPC frame columns under low cyclic reversed horizontal loading includes approximately three stages: no damage stage before cracking; damage increasing stably stage following plastic deformation and cycle times increasing; damage increasing sharp after reaching limit load. These three stages also indicate that the damage of the SRHSHPC frame columns is a process evolving and accumulating gradually. The test parameters, for example, axial compression ratio, concrete strength, shear span ratio, stirrup ratio and loading system influence the evolution of damage obviously.

Fig.2 is the relation curves of displacement and corresponding damage value of the SRHSHPC test specimens in the some deformation stages. Because of steel skeleton function, the limit bearing capacity increases obviously. Before reaching the limit bearing capacity, damage caused by the cyclic effect grows stably, till astringing after 2~3 circulations. After reaching the bearing capacity which corresponds to monotone load-on, cycle damage increases quickly, whose value can not be neglected in total damage value. When cycle times are more, the cycle damage finally becomes the main reason to cause the component failure. According to damage variation curves by calculating the frame column SRC-5 and SRC-9 respectively, it is indicated that if the axial compression ratio is more, the damage value is greater. If the axial compression ratio is more, the growth rate of $\Delta - D_c$ curves and $\Delta - D$ curves after yielding is also bigger. If the concrete strength is more, the damage value is greater evolving quickly. But, if the shear span ratio is more, the damage value is less, and evolves relatively slowly.

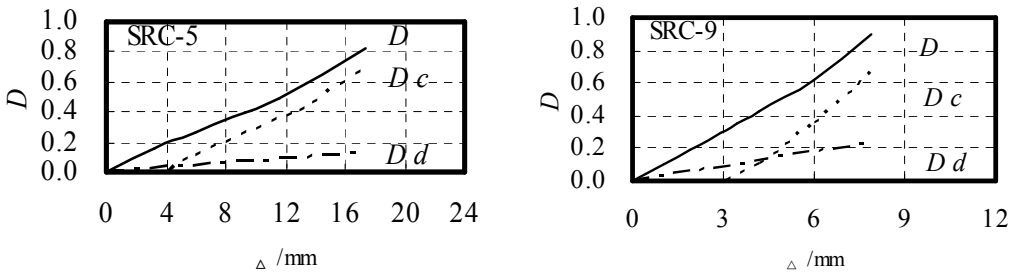

Fig. 2 $\Delta - D$ curves of specimens

Damage Value of the SRHSHPC Frame Columns Corresponding Failure

Experimental results indicate that, if the shear span ratio of specimen is more ($\lambda > 2$), its failure type is usual flexure failure whose failure is same to reinforced concrete column. The failure zone is usual

end of column. The increase of damage value is indicated as crack occurring and expanding, steel yielding, and plastic strain increasing. The macroscopic view phenomena are displacement of column top increasing and the bearing capacity decreasing. However, if the shear span ratio of specimen is less ($\lambda \leq 2$), the failure mode is different obviously. Firstly, some diagonal crack appears at the column root. The diagonal crack grows continually along with the load increasing and cycling, which causes the damage increasing. When the shear span ratio is quite smaller, the shear compression zone of column is divided into some small inclined columns, and the specimens start to yield. With the cycle displacement increasing, the small inclined columns are compressed to failure and the load decreases sharply. The damage process is very quickly with bad ductility.

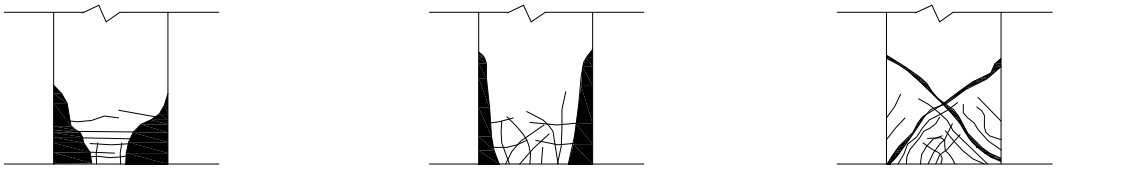

D=1.02 Flexure failure | *D*=1.06 Shear splitting failure | *D*=1.09 Shear compression failure

Fig. 3 Damage values and failure models of the SRHSHPC frame columns

When the shear span ratio of samples is moderate ($1.5 < \lambda < 2.5$), the failure model will be shear splitting failure. With increasing of load, the lengthwise bond cracks appear suddenly to the flange girth outside of compression shape steel .it extends very quickly. Finally, the protective layer of the SRHSHPC columns outside the flange girth of shape steel begins to desquamating badly, and the horizontal load decreasing sharply till the samples is broken. The damage process of the SRHSHPC columns is slower than reinforced concrete columns. The damage value also increases more slowly. This is mainly because of the final function of shaped steel. Because the failure of small shear span ratio column is usually caused by concrete being crushed or reaching shear compression limit strength, so the damage value increases sharply comparing with flexure failure. In the total damage, proportion of final damage value is more. In general, when the cycle times are less, deformation damage occupies an important position in total damage. But, cyclic damage can not be neglected. With the cycle increasing, especially near failure stage, the proportion of cyclic damage increases outstandingly, even becomes main factor which causes component failure.

Conclusion

In the paper, the damage model which is applicable to the SRHSHPC column is attained, by which the damage process of the SRHSHPC column under low cyclic reversed horizontal loading was analyzed. The analytical results have good agreements with the test results. This project is sponsored by National Natural Science Foundation of China (Grant No. 50378080) and the Educational Office of Shaan'xi Province in China.

Reference

[1] Saatcioglu. M., Ozcebe. G.: *Response of reinforced columns to simulated seismic loading*. ACI structural Journal, Vol. 86, 1985, p.3-12

[2] Lemaitre J.: *A continuous damage mechanics model for ductile fracture.* ASME, Journal of Engineering Materials and Technology, Vol. 107, 1985, p.83-89

[3] Park. Y. J., Ang. A. H.S: *Mechanistic seismic damage model for reinforced concrete*. Journal of Structural Engineering, ASCE, Vol. 111, No.4 (1985), p.740-756

[4] Bai Guoliang, Qin Fuhua: *Principle and design of composite structures of steel and concrete*. Science and Technology Press, Shanghai, China (2000)

Key Engineering Materials Vols. 385-387 (2008) pp 101-104
© (2008) Trans Tech Publications, Switzerland
doi:10.4028/www.scientific.net/KEM.385-387.101

Dynamic Growing Crack Tip Field in Visco-Elastic Compressible Material

Yong Yang[1,a], Liqiang Tang[1,b], Yong Wang[1,c], Chen Feng[1,d]

[1]College of Civil Engineering, Harbin Engineering University, Harbin 150001, China

[a]yangharbin@163.com, [b]tlq8854@126.com, [c]wangyong3502@tom.com, [d]beier5217@163.com

Keywords: visco-elastic compressible material, crack tip, dynamic growing

Abstact. A mechanical model of the visco-elastic compressible material is established in order to investigate the viscous effect in dynamic growing crack-tip field. The constitutive equations on the visco-elastic compressible material are deducted. Through asymptotic analysis, it is shown that in the stable creep growing stage, the elastic-deformation and the visco-deformation are equally dominant in the near-tip field, as $r^{-1/(n-1)}$. The asymptotic solutions of separative variable in the crack-tip field are aslo obtained. According to numerical calculation, the curves of stress, stain and displacement are given. The results indicate that the near-tip fields are mainly governed by the creep exponent n and Mach number M; the stress fields of mode I and mode II is slightly affected by the elastic compressible deformation; the strain and displacement fields of mode I are deeply affected by the elastic compressible deformation. However, the strain and displacement fields of mode II are less affected by the elastic compressible deformation. The asymptotic solutions of dynamic growing crack-tip field gained here can conveniently degenerate the incompressible case, when the Poisson ratio $\nu \to 0.5$, named as HR field. The conclusions can provide the references for further studying the dynamic growing crack-tip field in compressible material.

Introduction

Under high temperature, many metals show viscoelastic properties, which are closely related to environmental factors and strain rate. Engineering practice also shows that time-dependent deformation of materials have great effects on the structural strength, rigidity and life duration. So visco-elasticity has drawn much attention in the mechanical and engineering fields.

In 1968, Hutchinson[1], Rice and Rosengren[2] studied the asymptotic crack tip field for plane strain stationary crack independently. When elastic deformation is neglected, the so-called HRR field is obtained for power law hardening materials. Hui and Riedel[3] addressed the quasi-static mode III and mode I crack problem where elastic-power-creeping constitutive equations are introduced to model the rate-dependent materials. HR field was obtained, where stress and strain possess the same singularity, as $r^{-1/(n-1)}$, with n, the power law exponent. HR field is self-government which means that crack tip stress and strain fields are not dependent on the applied load, and no geometrical parameters related to the crack are included. Once the crack propagation velocity $\dot{a}$ is given, crack tip fields can be fully determined. Gao[4,5] gave a simplified elasto-visco-plastic model in which it was assumed that during the elastic deformation stage, viscous effects can be ignored. When plastic deformation occurs, viscous effects are taken into account. For mode I crack, solutions with logarithm singularity and power singularity were given separately. Tang[6] investigated the mode I crack tip field for incompressible elasto-viscous materials.

At present, more studies on the crack tip focus on the incompressible material. However,

incompressibility is an ideal assumptation. In most cases, considering the material compressibility is more reasonable. Crack tip fields on mode I and mode II dynamic growing crack in compressible visco-elastic material are given in present paper where the distribution law of the stress fields and the strain fields are discussed.

1. Basic Equations

Fig. 1 shows a mechanical model of a planar crack steadily propagating along the positive direction of X, in which the common origin is at the crack tip of planar crack , XOY is the fixed coordinate system, xoy is the moving coordinate system, and the moving rectangular and polar coordinate system denoted respectively by (x,y) and (r,θ). Supposing that the crack grows at the steady velocity V, the material derivative of any physical quantity $\boldsymbol{\Phi}$ in steady field can be expressed as

$$D = V\left[\frac{\sin\theta}{r}\frac{\partial}{\partial\theta} - \cos\theta\frac{\partial}{\partial r}\right]. \tag{1}$$

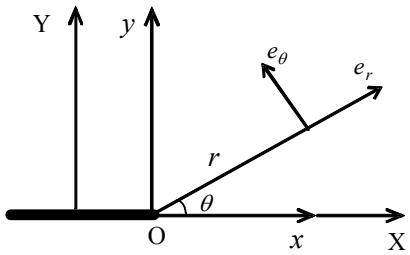

Fig.1 Coordinate with crack

The strain rate of the visco-elastic material is composed of elastic and viscous strain rate, named as

$$\dot{\varepsilon}_{ij} = \dot{\varepsilon}^e_{ij} + \dot{\varepsilon}^c_{ij}. \tag{2}$$

where, $\dot{\varepsilon}^e_{kk}$ and $\dot{\varepsilon}^c_{kk}$ is respectively expressed as elastic volume strain ratio and viscous volume strain ratio. The case where elastic deformation is compressible and viscous deformation is incompressible is studied in this paper, as $\dot{\varepsilon}^e_{kk} \neq 0, \dot{\varepsilon}^c_{kk} = 0$. The constitutive equations are given by

$$\dot{\varepsilon}_{ij} = \frac{1+\nu}{E}\dot{s}_{ij} + \frac{1-2\nu}{3E}\dot{\sigma}_{kk}\delta_{ij} + \frac{3}{2}B\sigma_e^{n-1}s_{ij}, \tag{3}$$

Where, the modulus of elasticity E, the exponent of creep strain n, the material parameters of power-law creep material B, and the equivalent stress is $\sigma_e = \left[(3/4)\left(\sigma_r - \sigma_\theta\right)^2 + 3\sigma_{r\theta}^2\right]^{1/2}$. The case that elastic deformation is compressible is considered, so the Poisson's ratio $\nu < 0.5$. The equations of motion and geometry are

$$\nabla\cdot\boldsymbol{\sigma} + \mathbf{F} = \rho\,\ddot{\boldsymbol{u}},\ \ \boldsymbol{\varepsilon} = \frac{1}{2}\left(\boldsymbol{u}\nabla + \nabla\boldsymbol{u}\right),\ \ \nabla\times\dot{\boldsymbol{\varepsilon}}\times\nabla = 0. \tag{4}$$

2. Governing Equations

When $r \to 0$,supposed that the form of separate variable of potential function of displacement and separate variable of potential function of stress are

$$u_r = r^{s_1-1}f_1(\theta,n)\quad, u_\theta = r^{s_1-1}f_2(\theta,n)\ , \tag{5}$$

$$\sigma_r = r^{s-2}\left[P(\theta)+F(\theta)\right], \sigma_\theta = r^{s-2}\left[P(\theta)-F(\theta)\right], \sigma_{r\theta} = r^{s-2}T(\theta). \tag{6}$$

In stable creep growing stage, elastic-deformation and visco-deformation are equally dominant in the near-tip field, as a result, the stress and the strain have the same singularity, as $s = s_1 = s_2 = (2n-3)/(n-1)$.

Introducing the relevant quantities to equations of motion and constitutive equations, by noticing that the derivation laws (1) of material derivative and by dimensionless arrangement, as:

$$(s-2)P(\theta) + sF(\theta) + T'(\theta) = M^2\left\{\sin^2\theta\tilde{f}_1'' + (2-s)\sin(2\theta)\tilde{f}_1' + (s-2)\left[\sin^2\theta + (s-1)\cos^2\theta\right]\tilde{f}_1 - 2\sin^2\theta\tilde{f}_2' + (s-2)\sin(2\theta)\tilde{f}_2\right\};$$

$$P'(\theta) - F'(\theta) + sT(\theta) = M^2\left\{\sin^2\theta\tilde{f}_2'' + 2\sin^2\theta\tilde{f}_1' + (s-2)\left[\sin^2\theta + (s-1)\cos^2\theta\right]\tilde{f}_2 - (s-2)\sin(2\theta)\tilde{f}_1 + (2-s)\sin(2\theta)\tilde{f}_2'\right\};$$

$$\sin\theta(s-2)(\tilde{f}_1'-\tilde{f}_2)-\cos\theta(s-1)(s-2)\tilde{f}_1=\sin\theta(1-2\nu)P'(\theta)+\sin\theta(1+\nu)F'(\theta)-2\sin\theta(1+\nu)T(\theta)+(2\nu-1)\cos\theta(s-2)P(\theta)$$
$$-(1+\nu)\cos\theta(s-2)F(\theta)+\frac{3}{2}A\cdot 3^{\frac{(n-1)}{2}}\left[F^2(\theta)+T^2(\theta)\right]^{\frac{(n-1)}{2}}F(\theta)\ ;$$
$$\sin\theta\left[2\tilde{f}_1'+\tilde{f}_2''+(s-2)\tilde{f}_2\right]-\cos\theta(s-2)(\tilde{f}_1+\tilde{f}_2')=\sin\theta\left\{\left[(1-2\nu)P'(\theta)-(1+\nu)\left[F'(\theta)-2T\right]\right\}+\cos\theta(s-2)\left[(2\nu-1)P(\theta)\right.\right.$$
$$\left.+(1+\nu)F(\theta)\right]-\frac{3}{2}A\cdot 3^{\frac{(n-1)}{2}}\left[F^2+T^2\right]^{\frac{(n-1)}{2}}F(\theta)\ ;$$
$$\sin\theta\left[\tilde{f}_1''+2(s-2)\tilde{f}_1+(s-4)\tilde{f}_2'\right]-\cos\theta(s-2)\left[\tilde{f}_1'+(s-2)\tilde{f}_2\right]=(1+\nu)\left[2\sin\theta T'(\theta)+4\sin\theta F(\theta)-2\cos\theta(s-2)T(\theta)\right]$$
$$+A\cdot 3^{\frac{(n-1)}{2}}\left[F^2(\theta)+T^2(\theta)\right]^{\frac{(n-1)}{2}}T(\theta)\ . \qquad (7)$$

3. Numerical calculation and Discussions

For mode I crack, the conditions to determine the solution are given as follows:

$$\tilde{f}_2(0)=0\,,T(0)=0\,,P(\pi)-F(\pi)=0\ \ ,T(\pi)=0\,,(2-s)\tilde{f}_1'(0)=0\,,$$
$$-(1-s)(2-s)\tilde{f}_1(0)=(2\nu-1)(s-2)P(0)-(1+\nu)(s-2)F(0)+(3/2)\,A\cdot 3^{(n-1)/2}F^n(0)$$
$$(2-s)\left[\tilde{f}_1(0)+\tilde{f}_2'(0)\right]=(2\nu-1)(s-2)P(0)+(1+\nu)(s-2)F(0)-(3/2)\,A\cdot 3^{(n-1)/2}F^n(0) \qquad (8)$$

For mode II crack, the conditions to determine the solution are given as follows:

$$P(0)=0\,,F(0)=0\,,P(\pi)-F(\pi)=0\,,T(\pi)=0\,,$$
$$(s-1)(2-s)\tilde{f}_1(0)=0\,,(2-s)\left[\tilde{f}_1(0)+\tilde{f}_2'(0)\right]=0\,,$$
$$(2-s)\left[\tilde{f}_1'(0)+(s-2)\tilde{f}_2(0)\right]=2(1+\nu)(2-s)T(0)+A\cdot 3^{(n+1)/2}T^n(0) \qquad (9)$$

In view of Eqs. (8) and (9), there are not enough conditions to solve the governing differential equations. To solve the problem with two-parameter shooting method, the boundary value problem should be transformed into initial value problem. The angular distribution curves of the stress and the strain on the crack tip are separately given by Fig. 2-13, in which the stresses and the strains are normalized separately with requirement of $\max\tilde{\sigma}_e(\theta)=1$, $\max\tilde{\varepsilon}_e(\theta)=1$, $\max(\tilde{u}_i)=1$, $0\le\theta\le\pi$.

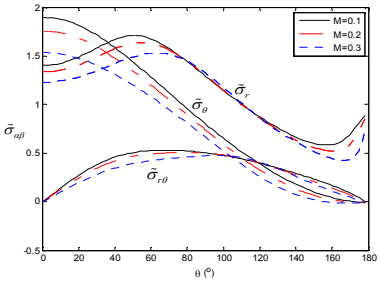

Fig.2 curves of stresses with M (Mode I)

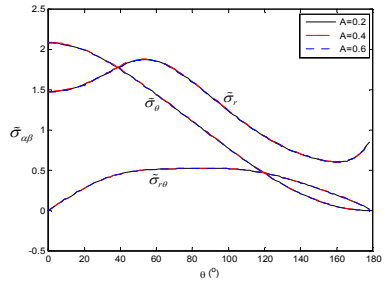

Fig.3 curves of stresses with A (Mode I)

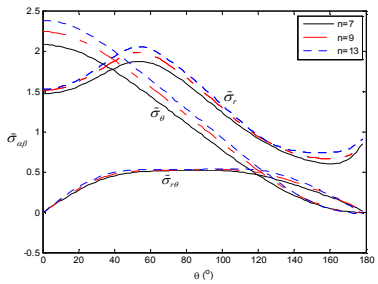

Fig.4 curves of stresses with n (Mode I)

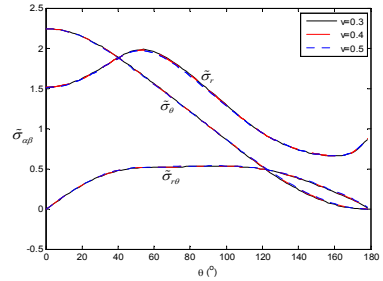

Fig.5 curves of stresses with ν (Mode I)

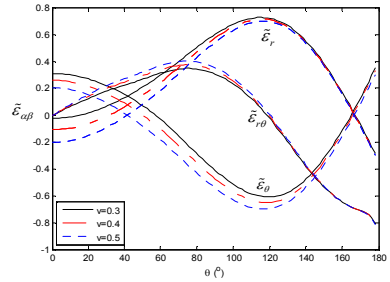

Fig.6 curves of strains with ν (Mode I)

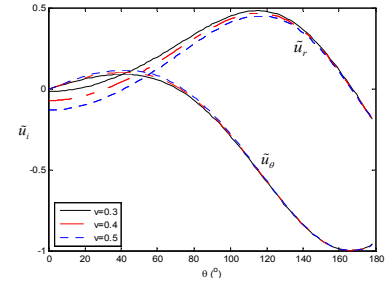

Fig.7 curves of displacement with ν (Mode I)

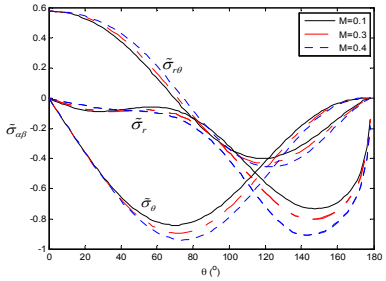

Fig.8 curves of stresses with M(Mode II)

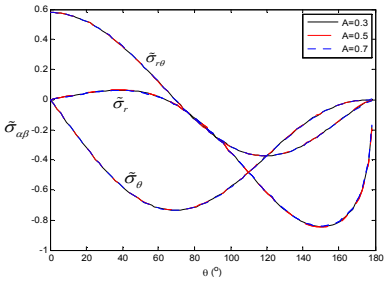

Fig.9 curves of stresses with A(Mode II)

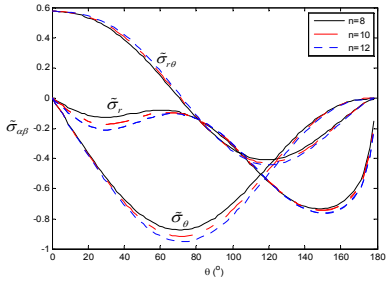

Fig.10 curves of stresses with n(Mode II)

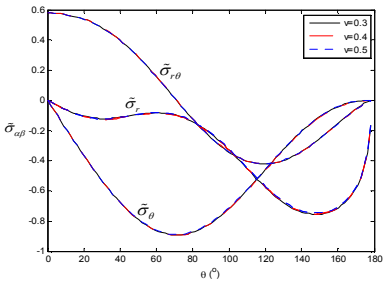

Fig.11 curves of stresses with ν (Mode II)

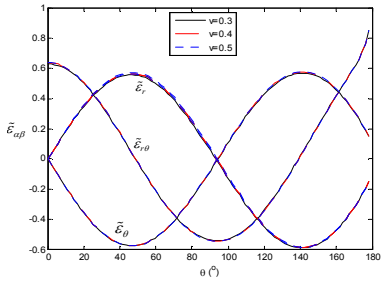

Fig.12 curves of strains with ν (Mode II)

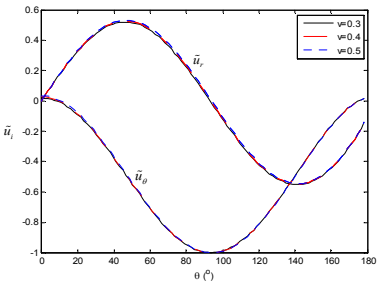

Fig.13 curves of displacement with ν (Mode II)

4.Conclusions

(1) Crack tip fields on mode I and mode II dynamic growing crack in visco-elastic material, where the elastic deformation is compressible and the viscous deformation is incompressible, are studied in this paper. By analysis, it shows that elastic deformation and viscous deformation are equally dominant in the near-tip, and the stresses, strains have the same singularity, namely, $(\boldsymbol{\sigma},\ \boldsymbol{\varepsilon}) \propto r^{-1/(n-1)}$.

(2) The stress fields obviously change with March number M, and the stress components decrease when March number M increases; the stress fields change slightly when the parameter A changes. However, the stress components increase with the increasing creep exponent n. The variation of the stress field caused by n is opposite to M. The trend of the stress fields in Fig.5-7 and Fig.8-10 is consistent with Ref. [3].

(3) Through Fig.5-7 and Fig.8-10, the Poisson's ratio has less influence upon the stress fields on the crack tip, it has great effect upon the strain fields and the displacement fields on mode I. When the Poisson's ratio $\nu = 0.5$, the March number $M = 0$ the tip field tends towards HR field [6]. So the compressibility of material has more influenced on the tip field. And the field approaches to the reality when compressibility of materials is considered.

References

[1] Hutchinson J.W.: Journal of Mechanics and Physics of Solids, Vol. 16(1968): p13.

[2] Rice J.R., Rosengren G.F.: Journal of Mechanics and Physics of Solids, Vol. 16(1968): p1.

[3] C.Y.Hui, H.Riedel. International Journal of Fracture, Vol.17(1981): p409.

[4] Gao Y.C.: Mechanics Research Communcations. Vol. 15, (1988):p307.

[5] Gao Y.C.: Theo. Appl. Frac. Mech., Vol. 14(1990): p233.

[6] Tang L. Q. and Can yanhong: Acta. Mater, Vol.37 (2005), p573 (in Chinese).

Key Engineering Materials Vols. 385-387 (2008) pp 105-108
© (2008) Trans Tech Publications, Switzerland
doi:10.4028/www.scientific.net/KEM.385-387.105

Dynamic Stress Intensity Problem of SH-Wave by Double Linear Cracks near A Circular Hole

HongLiang Li [1, a],Hong Li [1,b],Yong Yang[1,c]

[1] School of Civil Engineering, Harbin Engineering University, Harbin, 150001,China

[a]leehl@sina.com, [b]lihong@hrbeu.edu.cn, [c]yangyong@hrbeu.edu.cn

Keywords: composite crack; circular hole; Green's Function; SH-wave scattering; dynamic stress intensity factor(DSIF)

Abstract. In mechanical engineering, circular hole is used widely in structure design. When the structure is overloaded or the load is changed regularly, cracks emerge and spread. Based on the former study of dynamic stress concentration problem of SH wave by a crack originating at a circular hole edge, in this paper, the method of Green's function is used to investigate the problem of dynamic stress intensity problem of double linear cracks near a circular hole impacted by incident SH-wave. The train of thought for this problem is that: Firstly, a Green's function is constructed for the problem, which is a fundamental solution of displacement field for an elastic space possessing a circular hole and a linear crack while bearing out-of-plane harmonic line source force at any point; Secondly, in terms of the solution of SH-wave's scattering by an elastic space with a circular hole and a linear crack, anti-plane stresses which are the same in quantity but opposite in direction to those mentioned before, are loaded at the region where the second crack is in existent actually, we called this process "crack-division"; Finally, the expressions of the dynamic stress intensity factor(DSIF) of the cracks are given when the circular hole and double linear crack exist at the same time. Then, by using the expressions, an example was provided to show the effect of circular hole and cracks on the dynamic stress intensity factor of the cracks.

Introduction

In mechanical engineering, circular hole is used widely in structure design. When the structure is overloaded or the load is changed regularly, cracks emerge and spread. The problem of scattering of SH wave by a circular hole and linear cracks around the hole is one of the important and interesting questions in mechanical engineering for the latest decades. There are lots of materials obtained by theoretical research and earthquake damage investigation. These problems are complicated, because there are many factors influenced. Researchers solved these problems by analysis and numerical methods[1-3]. It is hard to obtain analytic solutions except for several simple conditions.

In this paper, the method of Green's function is used to investigate the problem of dynamic stress concentration of the circular hole and double linear cracks around the hole for incident SH wave. The train of thoughts for this problem is that: Firstly, a Green's function is constructed for the problem, which is a fundamental solution of displacement field for an elastic space possessing a circular hole and a linear crack around the hole while bearing out-of-plane harmonic line source force at any point; Secondly, in terms of the solution of SH-wave's scattering by an elastic space with a circular hole and a linear crack, anti-plane stresses which are the same in quantity but opposite in direction to those mentioned before, are loaded at the region where the second crack is in existent actually, we called this process "crack-division"; Finally, the expressions of the displacement and stresses are given when the circular hole and double linear crack exist at the same time. Then, by using the expressions, an example was provided to show the effect of circular hole and cracks on the dynamic stress intensity factor of the cracks.

Model and Solution of assistant problem

The model is shown as Fig.1, an elastic space containing a circular hole and double linear cracks around the hole. In this paper, the anti-plane shear wave model is studied. The displacement is expressed as $W(x, y, t)$.

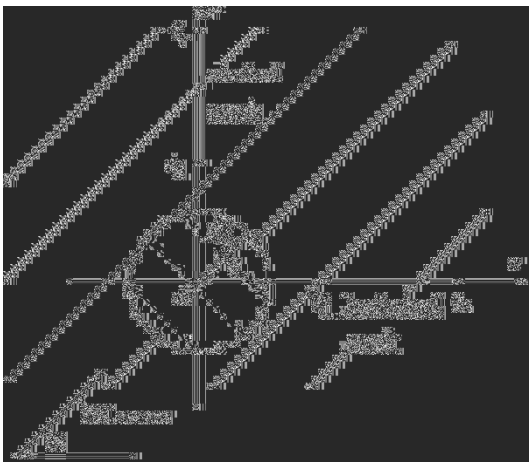

Fig.1 Model of the problem

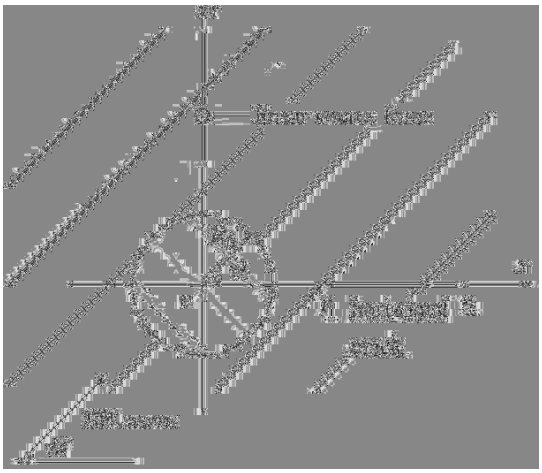

Fig.2 Model of Green's Function

The problem of scattering of SH waves by a circular hole and a linear crack around the hole has been solved by me. The displacement field W of the problem can be given as follows[4,5]:

$$W = W^{(t)} - \int_{\vec{r}_1}^{\vec{r}_2} \tau_{\theta z}^{(t)} |_{\vec{r}=\vec{r}_0} \times G(r, r_0, \theta, \theta_0) d\vec{r}_0 \tag{1}$$

And it is named as the solution of assistant problem.

Green's function

The Green's function used in this paper is regarded as the displacement response to the elastic space containing a circular hole and a linear crack around the hole impacted by anti-plane harmonic linear source force at any point. The dependence of the displacement function $G^{(t)}$ on time t is $e^{-i\omega t}$. The model is shown as Fig.2.

In the polar coordinate system, the governing equation of $G^{(t)}$ can be written as:

$$\frac{\partial^2 G^{(t)}}{\partial r^2} + \frac{1}{r}\frac{\partial G^{(t)}}{\partial r} + \frac{1}{r^2}\frac{\partial^2 G^{(t)}}{\partial \theta^2} + k^2 G^{(t)} = \delta(\vec{r} - \vec{r_0}) \tag{2}$$

The displacement in the elastic space is expressed as $G^{(t)}(r, \theta, t)$, $\vec{r}_0$ stands for the position of the linear source force in polar coordinates. The boundary conditions can be expressed as below:

$$\tau_{rz}|_{r=R} = 0, \tau_{\theta z} = 0 (where \quad crack \quad is \quad \text{in existent}) \tag{3}$$

The basic solution which satisfies the control equation (2) and the boundary conditions (3) should include two parts of motion: the disturbance of anti-plane linear source force and the scattering wave incited by the circular hole and a linear crack around the hole.

the wave field $G^{(t)}$ can be written as:

$$G^{(t)} = G^{(i)} + G^{(is)} \tag{4}$$

where $G^{(i)}$ is the wave displacement of the complete elastic space due to the line source load $\delta(\vec{r} - \vec{r}_0)$ on the arbitrary position, $G^{(is)}$ is the scattering wave incited by the circular hole.

According to the solution of assistant problem, $G^{(t)}$ can be obtained, and it is the Green's function that should be used in this paper.

Expression of displacement and stress for the model

The stress on the second crack produced by incident SH-wave and the scattering wave incited by the circular hole and a linear crack can be obtained. A pair of opposite forces is applied to the crack; therefore the resultant force on the crack is zero, which can be thought as crack. The above constructing process is called crack-division technique which can be used to obtain the expression of displacement and stress for the model. The detail can be discussed as follows.

Firstly, we consider the incidence of SH-wave on the infinite linear-elastic space containing a circular hole and a linear crack around the hole.

According to solution of assistant problem, The displacement and stress produced by the hole and a linear crack's scattering can be obtained,

$$W^{(s)} = W^{(t)} - \int_{\vec{r}_1}^{\vec{r}_2} \tau_{\theta z}^{(t)} |_{\vec{r}=\vec{r}_0} \times G(r, r_0, \theta, \theta_0) d\vec{r}_0 \ , \tau_{\theta z}^{(s)}\Big|_{\vec{r}=\vec{r}_d} = \tau_{\theta z}^{(t)}\Big|_{\vec{r}=\vec{r}_d} - \int_{\vec{r}_1}^{\vec{r}_2} \tau_{\theta z}^{(t)} |_{\vec{r}=\vec{r}_0} \times \frac{\mu}{r} \frac{\partial G}{\partial \theta}\Big|_{\vec{r}=\vec{r}_d} d\vec{r}_0 \tag{5}$$

where $\vec{r}_d$ represent any point in the second crack.

According to incident field and scattering field in the elastic space containing a hole and only a linear crack, the crack-division technique is used to construct the model of SH-wave scattering by an elastic space containing a circular hole and double linear cracks.

The constructing process is that: the space is separated along the second crack and a pair of anti-plane opposite forces with the multitude $-\tau_{\theta z}^{(s)}$ are applied to up and down section of the region where the second crack will appear, therefore the resultant force on up (or down) section of the region is zero, which can be thought as crack. The above constructed Green's function indicates that the basic displacement solution can be obtained wherever the anti-plane linear source force's position it is. Consequently, we can obtain the total displacement field and stress field under the interaction of the circular hole and the cracks for incident SH-wave.

The force $-\tau_{\theta z}^{(s)} |_{\vec{r}=\vec{r}_d}$ is applied on the crack and the tectonic additional displacement field can be obtained:

$$-\tau_{\theta z}^{(s)} |_{\vec{r}=\vec{r}_d} \times G^{(t)}(r, r_d, \theta, \theta_d) \tag{6}$$

Hence, the total displacement field can be written as follows:

$$W^{(d)} = W^{(s)} - \int_{\vec{r}_3}^{\vec{r}_4} \tau_{\theta z}^{(s)} |_{\vec{r}=\vec{r}_d} \times G^{(t)}(r, r_d, \theta, \theta_d) d\vec{r}_d \tag{7}$$

And the total stress field at the horizontal crack's inner tip is that:

$$\tau_{rz}^{(d)}\Big|_{\vec{r}=\vec{r}_{1-0}} = \tau_{rz}^{(s)}\Big|_{\vec{r}=\vec{r}_{1-0}} - \int_{\vec{r}_3}^{\vec{r}_4} \tau_{\theta z}^{(s)} |_{\vec{r}=\vec{r}_d} \times \mu \frac{\partial G^{(t)}}{\partial r}\Big|_{\vec{r}=\vec{r}_{1-0}} d\vec{r}_d \tag{8}$$

So the dynamic stress intensity factor (DSIF) at the horizontal crack's inner tip is given by

$$k_3 = \frac{\tau_{rz}^{(d)}\Big|_{\vec{r}=\vec{r}_{1-0}}}{\tau_0 Q} \tag{9}$$

where $\tau_0 = \left|\tau_{rz}^{(i)}\right| = \mu W_0 k$, Q is characteristic length of the crack.

Example

In this paper, we pay attention to a representative kind of models, which is shown as Fig.1. The radius of the hole is 1. The angle of incident wave is 45°. Fig.3 show that compared with the condition there is only a horizontal crack in elastic space, DSIF at the inner tip of the horizontal crack is changed a lot if there is another crack or a hole. The influence is more obvious at medium frequencies than at high frequencies. Fig.4 shows that the influence of second crack is bigger when the distance between two cracks is short than that is long. Fig.5 shows that if the distance between the horizontal crack and the hole with the vertical crack is long enough, the influence of the hole and the vertical crack could be neglected.

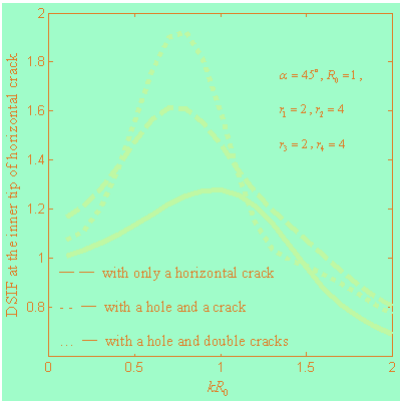

Fig.3 Variation of DSIF vs. kR_0

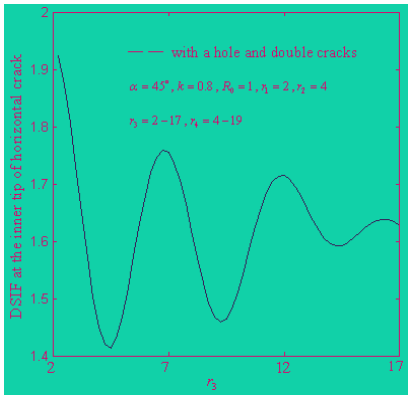

Fig. 4 Variation of DSIF vs. r_3

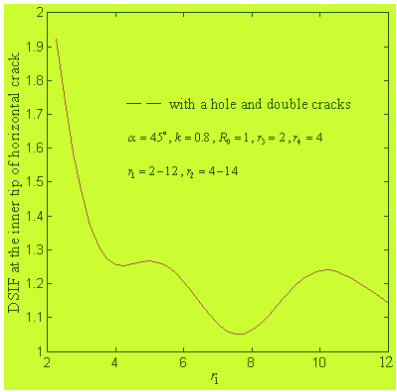

Fig. 4 Variation of DSIF vs. r_1

Summary

In this paper, by using the technique of crack-division, a new method is given to solve the interaction problem of Circular hole and double Linear Cracks by incident SH-wave. By using the method an example is solved, and some new conclusion is given. The method in the paper could be used to study some other correlative problem.

Acknowledgments

Thanks for the support by the Natural Science Foundation of Heilongjiang Province(A2004-07) and the Basis Research Foundation of Harbin Engineering University(HEUFP05007).

References

[1] Y. Yang and A. Norris: Shear Wave Scattering from a Debonded Fiber. Mech. Phys.Solids, Vol.39(1991),p.273-280

[2] Wang Yuesheng, Wang Duo: Dynamic Stress Intensity Factors of Circular Arc-shaped Interface Cracks Subjected to Shear Wave. Acta Mechanica Solida Sinica, Vol.14(1993),No.4,p.362-367

[3] Karim M.R., Awal M.A., Kundu T.: Elastic Wave Scattering by Cracks and Inclusions in Plates: In-Plane Case. International Journal of Solids and Structures,Vol.29(1992),No.19,p.2355-2367

[4] Li HongLiang, Liu DianKui: Interaction of SH-Waves by Cracks with Circular Inclusion(in Chinese).Journal of Harbin Engineering University, Vol.25(2004),No.5,p.618-622

[5] Li HongLiang: The Interaction of Circular Cavity, Inclusion with Beeline Cracks by SH-wave [D] (in Chinese). Harbin Engineering University, 2004

Key Engineering Materials Vols. 385-387 (2008) pp 109-112
© (2008) Trans Tech Publications, Switzerland
doi:10.4028/www.scientific.net/KEM.385-387.109

Effect of supporting conditions on the fatigue life of shaft based on product lifecycle management

Youtang Li [a], Ping Ma [b] and Ming Song [c]

Key Laboratory of Digital Manufacturing Technology and Application, Ministry of Education, Lanzhou University of Technology, Lanzhou 730050, China

[a]liyt@lut.cn, [b]gddx@lut.cn, [c]songming2004@163.com

Keywords: Anti-fatigue design, Fatigue life, Supporting condition, Assessment method, Product lifecycle management

Abstract. An anti-fatigued criterion of annularly breached shaft on mechanical design has been put forward, and the main factors that affect fatigue life of shaft are discussed. The interrelation of the main factors and the framework is founded. A new assessment method to fatigue life of shaft has been put forward according to Corten-Dolan's theory modified Miner's rule. The effect of supporting conditions to fatigue life of shaft is discussed and the influencing parameters are obtained. The results show that the fatigue life of broad support in two sides is longer than that of narrow support in two sides. The results will establish the base of anti-fatigue design of shaft.

Introduction

The Product lifecycle management (PLM) concept holds the promise of seamlessly integrating all the information produced throughout all phases of a product's life cycle to everyone in an organization at every managerial and technical level, along with key suppliers and customers [1]. A lifecycle assessment (LCA) gives a general overview of resource consumption and environmental stress in the entire lifecycle of the product [2].

Anti-fatigue design is a key content in product lifecycle management. The shaft is used in engineering widely, such as machine tool, automobile, steamship and so on. There are many factors that affect the fatigue life of component. Therefore, it is very difficult to determine a design criterion exactly. An anti-fatigued criterion of annularly breached spindle on mechanical design [3] and a uniform model and fracture criteria of annularly breached bars under bending [4] have been put forward, respectively. The cumulative damnification is the effective method in limited lifecycle design, and Miner's rule, modified Miner's rule, relative Miner's rule, Manson's bilinear theory and Corten-Dolan's theory are applied in actual design at present and the precisions of lifecycle estimate are between 1/3 and 3 [5]. These methods are suitable for the strength assessment and life estimation of finite life under variable amplitude loading. An assessment rule of fatigue life of shaft based Corten-Dolan's theory and modified Miner's rule has been put forward [6], but the influencing factors that considered in the rule is not roundly. For designing the fatigue life of shaft exactly and putting forward an effective assessment method, the influencing factors must be analyzed completely. In the present work, the mechanics model for assessing the fatigue life of shaft is set up, the main factors that affect the fatigue life of shaft are summarized, the assessment method of fatigue life for shaft is put forward according to the traditional fatigue life estimation and the effective factor, and the effect of supporting conditions to fatigue life of shaft is discussed and the influencing parameters are obtained.

Factors Affecting the Fatigue Life and Mechanical Model

Influencing Factors of Fatigue Life of Shaft. There are many factors such as materials properties, geometrical factors, notched factors, boundary conditions, environmental conditions and loading conditions that affect the fatigue life of shaft. The main factors can be classified as shown in Fig.1. These factors are affected each other in the machine lifetime.

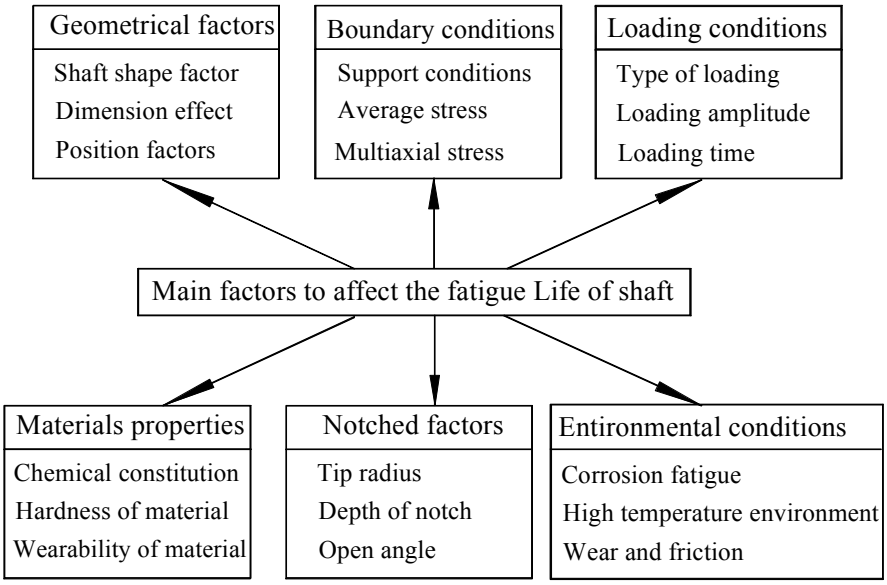

Fig.1 Factors that affect the fatigue life of shaft

Mechanical Model of Shaft for Life Estimation. The annular notch is the main factor to affect the fatigue life of shaft in engineering practice. The annular notches such as tool back groove and installation groove are existed usually in shaft and the stress concentration is existed at the tip field of notch. On the other hand, the crack may be existed in the shaft and the singularity at the tip of crack should be expressed by stress intensity factor. If we regard tip radius, depth and field angle of notch or crack as descriptive parameter, the crack and notch can be served as breach uniformly. The mechanical model of shaft for life estimation can be shown as Fig.2.

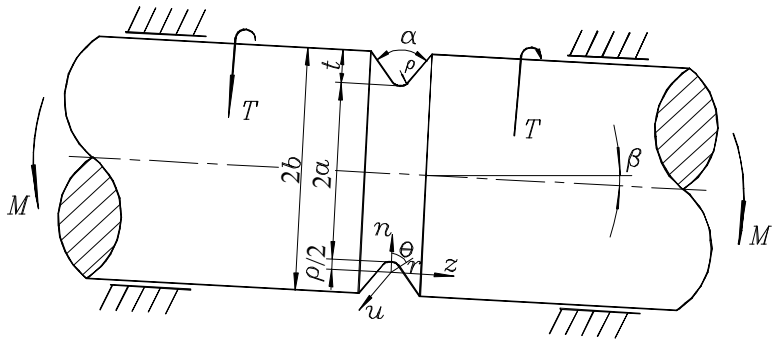

Fig.2 Mechanical model of shaft for life estimation

Fatigue Strength and Fatigue Life Estimation

Fatigue Strength. The strength criterions of modified miner's rule and the Corten-Dolan's theory can be written as following, respectively

$$n = \frac{\sigma_{-1D}}{\left(\sum_{i=1}^{l} n_i \sigma_i^m / aN_0\right)^{1/m}} \geq [n] \tag{1}$$

$$n = \frac{\sigma_1}{\sigma_q} = \frac{\sigma_1}{\left(\sum_{i=1}^{l} n_i \sigma_i^d\right)^{1/d}} \geq [n] \tag{2}$$

where a is calibrated to the test value of cumulative damage in loading chart, and σ_1 is the maximal stress (MPa), N_1 fatigue life in maximal stress(c), d the exponential of Dortem-Dolan express, m the exponential of S-N curve.

Traditional Fatigue Life Estimation. For every circular loading, the damage can be calculated according to the loading chart method and the fatigue life can be estimated according to certain cumulative damage theory. For modified miner's rule and Corten-Dolan's theory, the fatigue life of shaft can be written as followings [6].

$$N = a\sum_{i=1}^{l} n_{0i} \Big/ \sum_{i=1}^{l} \frac{n_{0i}}{N_i} \tag{3}$$

$$N = N_1 \Big/ \sum_{i=1}^{l} \alpha_i \left(\frac{\sigma_i}{\sigma_1}\right) \frac{n_{0i}}{N_i} \tag{4}$$

Modified Fatigue Life Estimation. The precisions of fatigue life estimation of traditional fatigue life estimation are between 1/3 and 3. The source of errors are due to the complicated conditions, such as materials capability, geometrical factors, notched parameters, boundary conditions, environmental conditions and loading conditions. The equation of fatigue life estimation for modified miner's rule and Corten-Dolan's theory can be modified as following, respectively.

$$N = K_1 K_2 K_3 K_4 K_5 K_6 a\sum_{i=1}^{l} n_{0i} \Big/ \sum_{i=1}^{l} \frac{n_{0i}}{N_i} \tag{5}$$

$$N = K_1 K_2 K_3 K_4 K_5 K_6 \, N_1 \Big/ \sum_{i=1}^{l} \alpha_i \left(\frac{\sigma_i}{\sigma_1}\right) \frac{n_{0i}}{N_i} \tag{6}$$

where K_1, K_2, K_3, K_4, K_5 and K_6 are the influencing coefficients for materials capability, geometrical factors, notched parameters, boundary conditions and environmental conditions and loading conditions, respectively. The influencing coefficient of notched parameters, K_3, can be estimated by the chart of tip radius, depth and open angle of notch to stress concentration factor [7].

Effect of Supporting Conditions on the Fatigue Life of Shaft

The fatigue life of shaft is affected by average stress and multi-axial stress, which can be described by influencing coefficient, K_4. The effect of supporting conditions to fatigue life of shaft means that the deflection, β, will be changed, and the average and multi-axial stress will be changed also.

Deflection for Different Supporting Condition. There are three kinds of supporting conditions for two supported shaft, i.e. a) narrow supports in two sides, b) narrow support in one side and broad support in other side, c) wide supports in two sides. The deflections conditions of three supporting in a shaft in lathe are shown in Table 1.

Table 1. The deflections in three supporting for a shaft

loads	200N	400N	600N	800N	1000N	1200N	1400N	1600N
Support a)	0.012	0.025	0.037	0.049	0.062	0.074	0.086	0.098
Support b)	0.008	0.015	0.023	0.029	0.037	0.045	0.052	0.059
Support c)	0.006	0.012	0.018	0.024	0.030	0.036	0.042	0.048

Effect of Supporting Conditions to Fatigue Life of Shaft. The combined bending and torsional ~~composite~~ loading will be applied to the shaft when the deflection, β, is existed. The influencing coefficient, K_4, in I-III mode can be written as following

$$K_4 = f_{3,\alpha} / \sqrt{(f_{1,\alpha}^2 + f_{3,\alpha}^2)(1-\nu^2)} \tag{7}$$

where $f_{1,\alpha}$ and $f_{3,\alpha}$ are the dimensionless factor near the tip of notch of bending stress, σ_1, and torsional stress, σ_3. The $f_{1,\alpha}$ and $f_{3,\alpha}$ can be calculated with finite element method and the results in different deflection, β, when ρ/b=0.2, a/b=0.85 and α=60^0, are shown in Fig.3. We can know from Fig.3 that dimensionless factor, $f_{1,\alpha}$, increase with the increase of deflection, β, and $f_{3,\alpha}$ are not changed nearly. The results of influencing coefficient, K_4, with different deflection, β, are shown in Table 2.

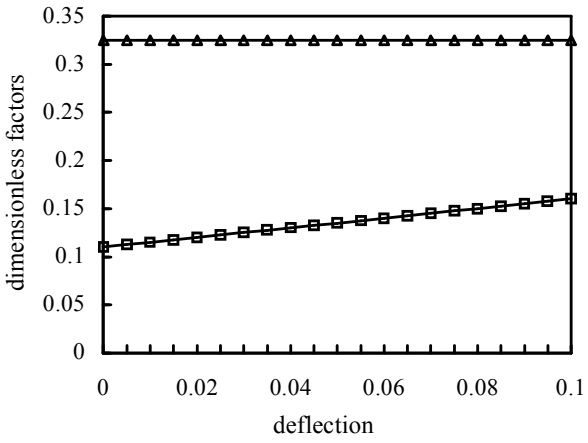

Fig.3 Dimensionless factor vs deflection, β

We can know from Table 2 that the influencing coefficient, K_4, will decrease gradually with the increase of deflection, β, i.e. the fatigue life will decrease gradually with the increase of deflection. Therefore, the fatigue life of broad supports in two sides is longer than that of narrow supports in two sides. The kind of support of shaft may affect the wear, installation and other condition. The environmental conditions, K_5, and other influencing coefficient may be affected by the support, they can be determined by experiment or other method.

Table 2. The influencing coefficient, K_4, vs deflection

Deflection	0.01	0.02	0.03	0.04	0.05	0.06	0.07	0.08
$f_{1,\alpha}$	0.166	0121	0.126	0.132	0.137	0.142	0.148	0.153
$f_{3,\alpha}$	0.325	0.326	0.327	0.328	0.329	0.330	0.330	0.331
K_4	0.981	0.977	0.972	0.966	0.962	0.957	0.951	0.945

Conclusions

(1) The fatigue life of shaft is affected by many factors, such as materials capability, geometrical factors, notched parameters, boundary conditions, environmental conditions and loading conditions.

(2) The fatigue life can be estimated by modified rule, in which the effect of materials capability, geometrical factors, notched parameters, boundary, environmental conditions and loading conditions have been considered.

(3) The support conditions affect the fatigue life of shaft. The fatigue life of broad support in two sides is longer than that of narrow support in two sides. The broad support should be selected in the design of machine.

References

[1] R.Sudarsan, S.J.Fenves, R.D.Sriram. *Computer-Aided Design,* Vol.37 (2005), p.1399

[2] J. Glahn, K. Heydenreich. *Corporate Environmental Strategy.* Vol.8 (2001), p.186

[3] Y.T.Li, P.Ma, C. F. Yan. *Key Engineering Materials.* Vol.321-323 (2006), p.755

[4] Y.T.Li, Z.Y.Rui, C.F.Yan. *Key Engineering Materials.* Vol.321-323 (2006), p.751

[5] S. B. Zhao. *J. of machine design.* Vol.17, No.6 (2000), p.5

[6] Y.T.Li, P.Ma, J.T.Zhao. *Materials Science Forum* 561-565, 2253 (2007)

[7] Y.T.Li, Z.Y.Rui, C.F.Yan. *Key Engineering Materials.* Vol.274-276 (2004), p.211

[8] Y.T.Li and C.F.Yan: Key Engineering Materials. Vols.306-308 (2006), p.7

[9] S.Lahiri, B.V.Sankar & P.A.Mataga: Eng. Fract. Mech. Vol.53 (1996), p.289

Key Engineering Materials Vols. 385-387 (2008) pp 113-116
© (2008) Trans Tech Publications, Switzerland
doi:10.4028/www.scientific.net/KEM.385-387.113

Effects of Microstructure and Humidity on Fatigue Strength of Maraging Steel

M. Miyazono[1,a], N. Kawagoishi[1,b], Q.Y. Wang[2,c],
E. Kondo[1,d] and T. Nagano[3,e]

[1] Kagoshima University, 1-21-40 Korimoto, Kagoshima 890-0065, Japan
[2] Sichuan University, Chengdu 610065, China
[3]Miyakonojo National College of Technology, 473-1 Miyakonojo 885-8567, Japan
[a] m0781043@mech.kagoshima-u.ac.jp, [b] hiro@mech.kagoshima-u.ac.jp,
[c] wanggy@scu.edu.cn, [d] kondo@mech.kagoshima-u.ac.jp,
[e] takanori@cc.miyakonojo-nct.ac.jp

Keywords: Fatigue, Maraging Steel, Humidity, Grain Size, Reversion Austenite, Crack Initiation, Crack Propagation

Abstract. Rotating bending fatigue tests were carried out for maraging steels with different grain size in moist air in order to investigate the effects of humidity, grain size and reversion austenite on fatigue strength of the steel. Fatigue strength was decreased by humidity, and the decrease in fatigue strength was large in larger grain sized steel. Both of the initiation and propagation of a crack were promoted by humidity. Many cracks initiated at the specimen surface and intergranular cracks were observed at specimen surface and on fracture surface when humidity was high. The decrease in fatigue strength by humidity was suppressed by formation of reversion austenite.

Introduction

Recently, high strength steels have been widely used as materials for machines and structures, because service conditions have become sever and sever and requirements for light weight and safety increase. In general, endurance ratios of high strength steels are fairly low in comparison with the ones in low and medium strength steels [1]. This is mainly caused by their high sensitivity for notch [2].

Maraging steel [3] is an ultra-high strength steel which is hardened by the precipitation of intermetallic compounds such as Ni_3Ti, FeMo or Ni_3Mo in martensitic structure. The maraging steel has both high tensile strength and high ductility. Although many studies on fatigue strength of maraging steel have been carried out, studies on the behavior of a crack initiation and propagation are very limited.

In the present study, the effects of humidity, grain size and reversion austenite on the initiation and propagation behavior of a fatigue crack were investigated for a maraging steel under rotating bending.

Material and experimental procedures

Material used was a 300 grade maraing steel whose chemical composition in mass percent was 0.005C, 0.03Si, 0.04Mn, 0.002S, 18.69Ni, 4.89Mo, 8.92Co, 0.10Al, 0.91Ti and remainder Fe. In order to change the grain size, the material was solution treated for 3.6ks at three different temperatures of 1093K, 1273K and 1463K.

Fig. 1 shows their microstructures. The mean grain sizes were about 21μm, 40μm and 105μm. In the following, these materials will be denoted by symbols of S, M and L, respectively. After solution treatment, the materials were aged at 753K for 48ks, which was under-aged condition without reversion austenite (γ=0%). Moreover, parts of steel L were aged at 783K for 48ks, which was over-aged condition formed reversion austenite of 2 vol. % (γ=2%) and had the same hardness but different microstructure. The steels of L without and with reversion austenite are divided to symbols L_1 and L_2, respectively. Table 1 summarizes their mechanical properties.

Fig. 2 shows shape and dimensions of specimen. Prior to fatigue testing, all of the specimens were electro-polished about 25μm from the surface layer to remove the work affected layer and make the surface observation easier.

Observation and measurement of the change in specimen surface and a crack due to stress repetitions were carried out by plastic replication technique. Fatigue tests were carried out using the Ono type rotating bending fatigue testing machine with capacity of 15 Nm operating at 50 Hz. The humidity was controlled by setting the machine in a cabin maintained constant relative humidity of 25% and 85%.

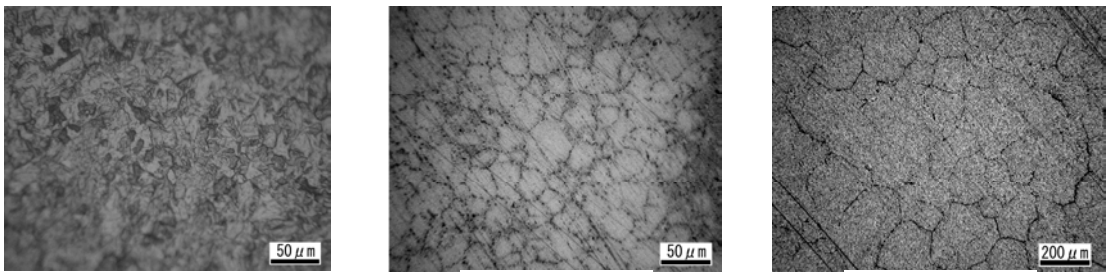

(a) S (b) M (c) L_1

Fig.1 Microstructures

Table 1 Mechanical properties

Material	$\sigma_{0.2}$(MPa)	σ_B(MPa)	δ (%)	HV
S	2073	2156	8.5	667
M	2064	2153	7.7	640
L_1	2069	2158	7.0	655
L_2	2159	2144	7.2	680

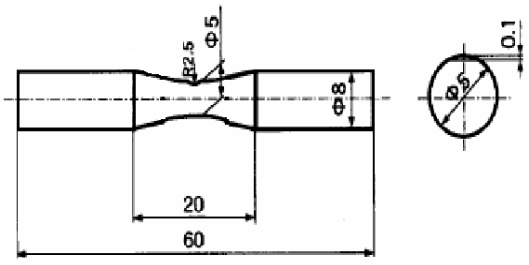

Fig.2 Shape and dimensions of specimen

Results and discussion

Fig. 3 shows *S*-N_f curves for the steels of S, M and L_1 whose have no reversion austenite tested in relative humidity of 25% or 85%. Endurance ratios, σ_{w0}/σ_B (σ_{w0}: fatigue limit, σ_B: tensile strength), of materials S, M and L_1 are very low of 0.29,0.23 and 0.21 even in low humidity of 25%, where fatigue limits were defined by the fatigue strength at 10^7. Fatigue strength is decreased by high humidity. The decrease in fatigue strength is large with increase in grain size. In general, the endurance ratios of high strength steels are very low in comparison with the ones of low or medium strength steels. This is mainly caused by their high notch sensitivity. However, Fig. 3 means that the influence of humidity on the fatigue strength must be also considered in high strength steel, especially in large grain sized steel.

Fig. 4 is crack growth curves of steel L_1 showing the effect of humidity on the crack initiation and propagation. As seen from the figure, both of initiation and propagation of a crack are

accelerated by humidity and the influence of humidity is marked in crack initiation process.

By successive observation on specimen surface during fatigue test, it was observed that a crack initiated as a transgranular crack in low humidity, while at grain boundary of prior austenite in high humidity, consequently crack propagated in zigzag manner. Moreover, when humidity was high, many cracks initiated from grain boundary not at any corrosion pits, though cracks initiated from corrosion pits in many high strength steels [4].

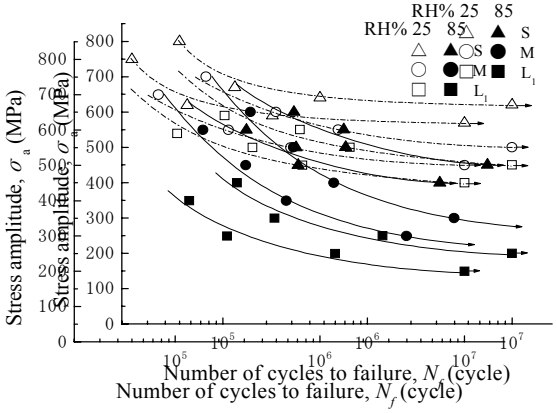

Fig.3 *S*-N_f curves

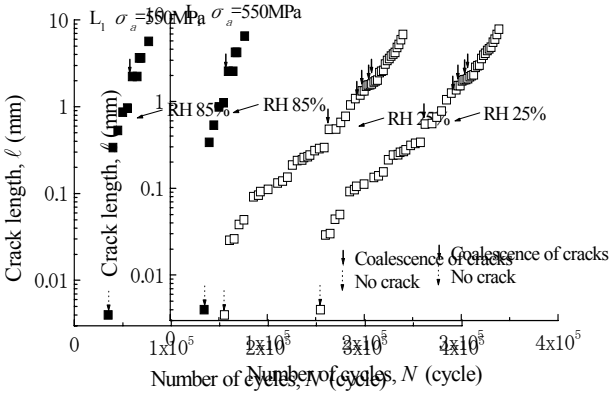

Fig.4 Crack growth curves

Fig. 5 shows fracture surfaces of specimens of steel L_1. Many intergranular cracks through prior austenite grain boundaries are observed when humidity is high, though most of fracture surface is covered with cracking of martensite rath in low humidity environment.

From the results mentioned above, one of the reasons for low endurance ratio of a maraing steel is large influence of humidity causing accelerations of both of initiation and propagation of a crack in addition to high notch sensitivity. As the factors of the accelerations in both processes of initiation and propagation of a crack, lowering of surface energy due to water absorption and hydrogen embrittlement are considered.

In the following, the influence of reversion austenite on the sensitivity of fatigue strength for humidity is investigated, because it has been reported that austenite structure becomes one of trap sites of hydrogen and has high resistance to stress corrosion cracking [4]

Fig. 6 is *S*-N_f curves of steels L_1 and L_2 showing the effect of reversion austenite on the fatigue strength and Fig.7 shows fracture surface of steel L_2, respectively. By formation of reversion austenite, fatigue strength is increased and also the influence of humidity on the fatigue strength is decreased. Moreover, there are no or little intergranular cracking on the fracture surface. These results suggest that reversion austenite distributed at boundaries of rath, packet and block of martensite and prior austenite suppresses the acceleration of crack propagation due to hydrogen embrittlement.

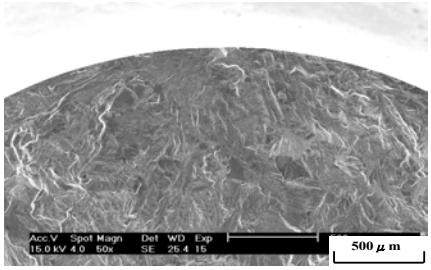

(a) RH25%, N_f=3.4×10^{5}cycles

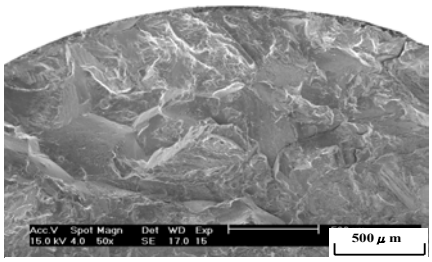

(b) RH85%, N_f=1.3×10^{5}cycles

Fig.5 Fracture surfaces of steel L_1 (σ_a=550MPa)

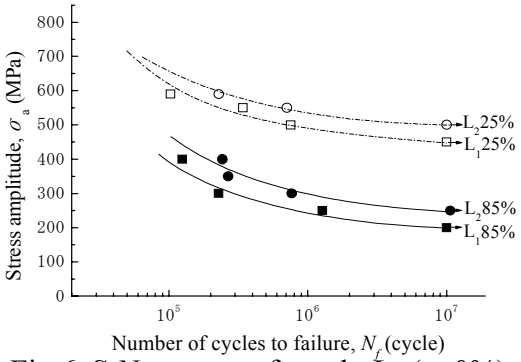

Fig.6 *S*-N_f curves of steels L_1 (γ=0%) and L_2(γ=2%)

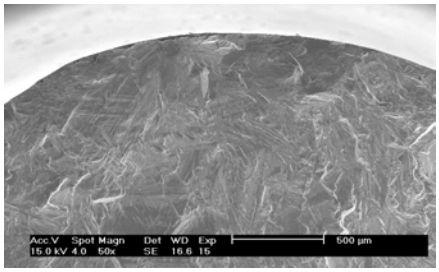

Fig.7 Fracture surface of steel L_2 (RH85%, σ_a=550MPa, N_f=3.4×10^5 cycles)

Conclusions

The effects of humidity, grain size and reversion austenite on the initiation and propagation behavior of a fatigue crack were investigated for a maraging steel under rotating bending. Fatigue strength was decreased by humidity. The decrease was marked in larger grain size and caused by the acceleration of crack initiation and its propagation. Intergranular cracks were observed on fracture surface in high humidity. On the other hand, the decrease in fatigue strength due to high humidity was suppressed by formation of reversion austenite.

References

[1] M.F. Garwood, H.H. Zurburg and M.A. Erickson, Interpretation of Test and Correlation with Service, ASM, (1951), p.1

[2] Y. Murakami, M. Shimizu, Trans. Jpn. Soc. Mech. Eng., A, Vol.54, (1983), p.413

[3]Y. Kawabe, Bull. of Jpn. Institute of Metals, Vol. 14, (1974), p.767

[4] N. Kawagoishi, T. Nagano, M. Moriyama, Y. Ohzono and T. Ura, Trans. Jpn. Soc. Mech. Eng., A, Vol.71, (2005), p.600

Key Engineering Materials Vols. 385-387 (2008) pp 117-120
© (2008) Trans Tech Publications, Switzerland
doi:10.4028/www.scientific.net/KEM.385-387.117

Effects of Rim and Web Thickness on Gear Tooth Root, Rim and Web Stresses

Gordana Marunić

University of Rijeka Faculty of Engineering, Vukovarska 58, 51000 Rijeka, Croatia
gmarunic@riteh.hr

Keywords: Spur Gear, Tooth Root Stress, Rim Stress, Web Stress, Rim Thickness, Web Thickness, FEM

Abstract. The paper presents a study on the tooth root, rim and web stresses of thin-rimmed spur gear structure with symmetrical web, based upon 3D FEM calculations. In order to identify some gear design directions, the effects of rim and web thickness on gear stress behaviour are investigated, and maximum stresses resulting from actual rim and web contribution are compared.

Introduction

Through the numerous investigations dealing with the assessment of rim thickness effects on external spur gear stresses, the web contribution to the stress behaviour, and consequently the simultaneous effect of rim and web on a gear structure stresses, have been not considered very often.

The research into the rim thickness influence on tooth root stress has developed gradually, starting from 2D approach to the stress calculation of thin-rimmed gears without web [1,2]. However, the results of further investigations based upon 3D approach [3,4] have pointed to the appearance of complex stress field in a spur tooth root area, including non-uniform stress distribution along a spur tooth face width.

As regards analytical methods for the assessment of tooth bending strength i.e. the teeth load capacity, the standard ISO [5] introduced the rim thickness factor for the calculation of nominal tooth root stress, but the parameters related to the web effects are not taken into account.

The development of 3D numerical models of thin-rimmed webbed gears, that are possible to simulate the load distribution along the tooth face width, has enabled the insight into and the examination of gear structure stresses [6, 7, 8, 9, 10]. These investigations have been in the main directed to the tooth root, rim and web stresses by taking into account the variation of only one related parameter i.e. the rim or web thickness. The accomplished deeper insight into has undoubtedly met the requirements related to actual demands for smaller design weight.

In this paper the attention is devoted to stress behaviour of gear structure with thin-rimmed body connected to the hub by symmetric web. Maximum stress that appears at tooth root, rim and web surface is determined through 3D FEM calculations, considering simultaneous contribution of rim and web thickness to actual gear deformation and the emergence of these stresses. The stress comparison is based on maximum equivalent von Mises stress that brings into prominence a spur gear 3D state of stress.

Basic Considerations of 3D FEM Calculation

The basis for 3D FEM stress calculation is the developed pinion-wheel model that simulates the transmitted load distribution along the tooth face width, resulting from actual gear pair structure.
The pinion and wheel are taken of equal teeth geometrical parameters (number of teeth $z_1=z_2=20$; module $m=10$ mm; pressure angle $\alpha_n=20°$; profile shift coefficient $x_1= x_2=0$; face width $b=100$ mm; contact ratio $\varepsilon_\alpha=1,56$).

In order to reduce computational effort, two different pinion-wheel models are established at the outer point of single pair tooth contact, in relation to the calculation of toot root stress and on the other hand, the rim and web stresses. For tooth root calculation, a solid pinion and thin-rimmed wheel with middle web are always gear segments corresponding to four teeth. This model choice is made after the analysis of tooth root stress in relation to the influence of embraced model portion. In the case of rim and web stresses calculation, thin-rimmed wheel with middle web position is performed as full gear structure. The calculation of rim and web stresses doesn't allow model simplification as previously mentioned for tooth root stress calculation, and the deformation of wheel as a whole is considered. Furthermore, one half of pinion-wheel face width is modelled, another one being taken into account by proper boundary conditions. The developed FEM numerical pinion-wheel models are described in [11].

The rim thickness s_R is varied in the range with slightly overcome upper and lower limits included in the standard ISO (s_R/h_t =0,5….1,2), and expressed by the backup ratio s_R/h_t (h_t - tooth height, mm), is taken : s_R/h_t =0,44; 0,64; 0,92; 1,34.

The adopted web thickness b_S covers the range of interest, and expressed by the tooth face width b, is: b_S/b=0,1; 0,2; 0,3; 0,4.

There are separated at the wheel surface for the analysis and comparison, following equivalent stresses: -maximum stress at tensile side of the loaded tooth root, regardless of its position along the fillet and the face width, -maximum stress at internal rim surface at the rim and web joint, regardless of its position in angular direction related to the loaded tooth centre line, and - maximum web stress regardless of its position in angular and radial direction, but away from stress concentration regions.

Maximum Tooth Root Stress

The results of 3D FEM calculation show that maximum equivalent tooth root stress at tensile side of the loaded tooth always appears in the middle of the tooth face width. The position at the tooth fillet varies as the gear geometrical parameters under consideration change, but it is not the subject of this paper.

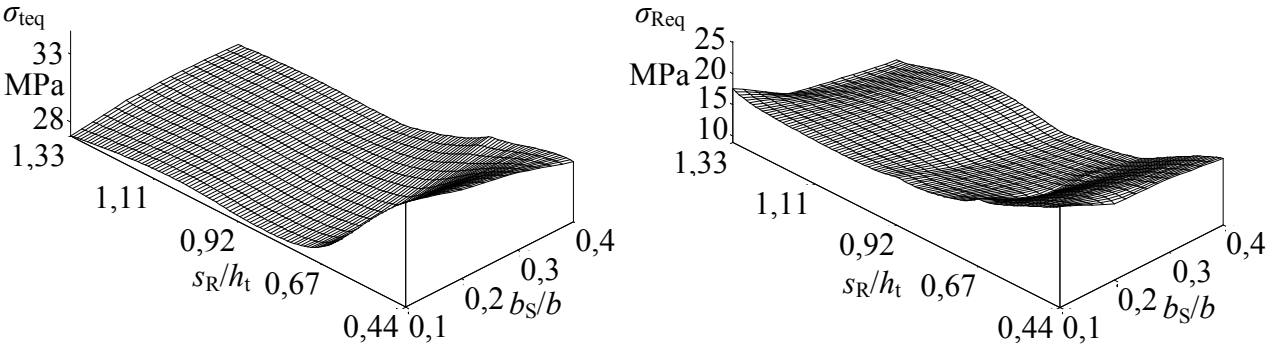

a) b)

Figure 1. Variation of maximum equivalent toot root stress (a) and rim stress (b) as rim and web thickness varies

On Fig. 1a the variation of maximum tooth root stress σ_{teqmax} is presented for the adopted ranges of rim and web thickness. In the case of the thinnest rim, the thicker web noticeably contributes to the load distribution and to the deformation of tooth and its foundation. Therefore, the effect of web thickness increment on maximum tooth root stress is mostly expressed for the thinnest rim under consideration (s_R/h_t =0,44), when tooth root stress decreases for about 10% when the thickest web of b_S/b=0,4 is reached.

The influence of rim thickness upon maximum tooth root stress is more expressed in relation to

the previously mentioned contribution of web thickness. Maximum stress sharply increases going towards the thinnest rim and web. The effect of greater gear blank rigidity introduced by the web, upon the tooth root stress is obvious as the stress increment diminishes when the web gets thicker.

In the case of the thinnest web of b_S/b=0,1, maximum tooth root stress value rises about 29% going from the thickest rim, but the rise is about 15% for the web thickness of b_S/b=0,4.

Maximum Rim Stress

Maximum equivalent stress σ_{Reqmax} at internal rim surface, always occurs at the rim and web joint. In relation to the position in angular direction going from the loaded tooth centre line, maximum stress appears under the compressive side of the loaded tooth within the area affected by gear geometrical parameters under consideration.

σ_{Reqmax} is presented in Fig. 1b related to the rim and web thickness. The obtained stress results point to obviously predominant influence of rim thickness upon maximum rim stress variation, in comparison with the influence of web thickness, especially for thicker webs. For the thickest web (b_S/b=0,4), rim stress increases more than two times when the thinnest rim (s_R/h_t =0,44) is reached.

In the case of the thickest rim (s_R/h_t =1,34) and going towards the thinnest web, maximum rim stress considerably increases, about 97%, but the web influence diminishes and for the thinnest rim (s_R/h_t =0,44) this stress increment is lower, about 28%.

Maximum Web Stress

In the positions determined in angular direction from the centre line of the loaded tooth towards compressive side, as well as in radial direction, maximum equivalent web stress σ_{Weqmax} appearance is strongly influenced by the web and rim thickness. As shown in Fig. 2 both, the rim and web thickness, contribute to the variation of maximum stresses. As the rim becomes thinner, the web thickness effect diminishes; the web stress is larger going from the thickest to thinnest web from more than two times (s_R/h_t =1,34), to about 34% (s_R/h_t =0,44), respectively.

The influence of rim thickness is mostly expressed in the case of the thickest web (b_S/b=0,4), where actual gear structure rigidity supported by thick web, causes the increment of web stress for about two times going from the upper (s_R/h_t =1,34) to lower (s_R/h_t =0,44) limit of the adopted rim thickness range.

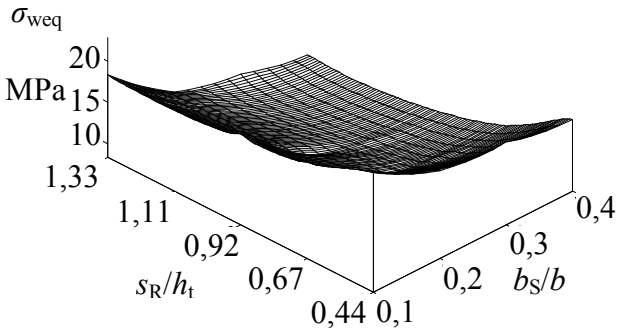

Figure 2. Relation between maximum web stress and rim and web thickness

Comparison of Maximum Stresses

Maximum principal tooth root stress at tensile side of the loaded tooth is the basis for rating the bending strength of gear teeth [5]. Unlike the proposals of ISO standard, maximum equivalent stress resulting from FEM calculations at critical tooth section, is compared with maximum equivalent rim stress, in order to examine another possible critical area located at the gear body with middle web

position.

Generally, for the chosen gear structure and the adopted ranges of two varied geometrical parameters, maximum equivalent rim stress doesn´t overcome the corresponding tooth root stress. Maximum rim stress approaches to tooth root stress in the case of the thinnest rim and web, mostly, when the deviation of rim stress from tooth root one is about 38%. The thicker are the web and rim, maximum rim stress deviates more from the tooth root stress.

The tooth root stress is effected by the web thickness only for the thinnest rims, and the rim thickness decrease causes uniform stress increment regardless of web thickness.

Maximum equivalent web stress is always lower than the corresponding rim one, and reaches peak value for the thinnest rim and web, when is about 10% lower.

Conclusions

The analysis and comparison of maximum equivalent stresses that occur in thin-rimmed spur gear with middle web position indicate that both, maximum rim and web stresses are smaller than maximum tooth root stress. With the decrease of rim and web thickness, maximum rim stress increases and takes 72% of tooth root stress. Maximum web stress is smaller than tooth root and rim stress, but shows the same tendency of considerable increment as the rim and web thickness decreases.

The tooth root stress is influenced by the deformation of rim part and web contributes to this deformation. Therefore, the effect of web thickness on tooth root stress is neglectable for larger rim thickness, but this effect becomes more obvious as the rim and web are thinner.

Based upon the accomplished insight into maximum equivalent stresses that appear at the tooth root, rim and web, it can be recommended maximum rim stress evaluation, additional to tooth root one, for extreme values of rim and web thickness. This evaluation has to take into account actual gear structure by the model that is able to properly simulate the load distribution along the tooth face width, and the resulting deformation of teeth and gear body as a whole.

References

[1] H. Eiff, K. Hirschman, and G. Lechner : Trans. ASME: J. Mech., Transmiss. And Autom. Des., (1990), p. 575

[2] C. Baret, et al.,in:*Proceedings of InternationalPowerTransmissions and Gearing Conference,* ASME, Chicago (1989).

[3] G. Curti, F. A. Raffa, D. Garavelli and C. Baret, in : *Proceedings of JSME International Conference on Motion and Powertransmissions,* JSME, Hiroshima (1991).

[4] ISO 6336-3, (2006)

[5] H. C. Kim et al., in: *Proceedings of International Congress-Gear Transmissions 96,* edited by K. Arnaudov, TUME-Bulgaria, Sofia (1996).

[6] H. Linke, W. Mitschke, and M. Senf: Maschinenbautechnik, Vol. 32 (1983), p. 450

[7] H. C. Kim, J. P. de Vaujany, M. Guingand and D. Play: Journal of Mechanical Design, Vol.120 (1998), p. 349

[8] S. Li,: Journal of Mechanical Design, Vol. 202 (2002), p. 511

[9] C. A. Blazakis and D. R. Houser, in: *Proceedings of the International Gearing Conference*, edited by J. N. Fawcett, UK National Gear Metrology, Univ. of Newcastle Upon Tyne, British Gear Assn., Newcastle Upon Tyne (1994).

[10] G. Marunić, in: *Proceedings of 5th International Scientific Conference RIM 2005*, edited by I. Karabegović, M. Jurković and V. Doleček, Univeresity of Bihać, Bihać (2005).

Key Engineering Materials Vols. 385-387 (2008) pp 121-124
© (2008) Trans Tech Publications, Switzerland
doi:10.4028/www.scientific.net/KEM.385-387.121

Electrochemical behavior of Cu-bearing CrMo steel in H_2S saturated aqueous brine solution

Qingchao TIAN[1,a], Xiaoming DONG[1,b] and QingAn. Zhang [2,c]
[1] Baosteel Research Institute, Baoshan Iron and Steel Co., Ltd., Shanghai 201900, China
2 Anhui University of Technology, Maanshan, Anhui 243002, China
[a]tctian@163.com , [b]dongxiaoming@baosteel.com, [c] qazhang@ahut.edu.cn

Keywords: Electrochemical testing, sulfide stress corrosion cracking, phase characterization.

Abstract. Electrochemical measurement techniques were applied to investigate the polarization and hydrogen permeation behavior of Cu-bearing CrMo steel in a H_2S saturated aqueous brine solution. The observation on microstructure and precipitate phases of the steel was conducted by transmission electron microscopy (TEM), and the corrosion product was investigated by using X-ray diffractometer (XRD), X-ray photoelectron spectroscopy (XPS), and scanning electron microscopy (SEM). It is disclosed that copper addition could effectively influence the electrochemical behavior of the investigated steel, and the dissolution behavior of iron matrix and carbide precipitates in the H_2S solution acts as a key role for the steel resistance to hydrogen sulfide corrosion.

Introduction

In order to improve the resistance of steel to H_2S damage, it is important to understand the corrosion behavior in H_2S environments. H_2S corrosion of low-alloy steels have been linked with anodic dissolution [1], and the corrosion film produced on the steel surface influences the behavior of H_2S damage. It has been disclosed that the corrosion of carbon steel in aqueous chloride solutions containing H_2S involves a two-stage mechanism, i.e., a charge transfer process that occurs at the interface between the iron sulfide corrosion product and the metal and a transport process through the sulfide film [2-3], and the failure behaviors are highly dependent on chemical composition, microstructure, density and type of traps, etc. It is accepted that CrMo steel with tempered martensite has good resistance to sulfide stress corrosion cracking (SSC) [4], thus it is important to optimizing the alloy composition design to improve the corrosion films for enhancing the corrosion resistance properties. However, few reports concerning the corrosion mechanism of low alloy steel have been found. Therefore, it is necessary to further investigate the effects of alloying elements on the corrosion mechanism for CrMo steels in H_2S environments.

Experimental

The Cr-Mo steels used were prepared with a composition in weight percent of 0.27 C, 0.5 Cr, 0.5 Mo, 0.30 Si, 0.45 Mn, 0.005 P, 0.001 S and Fe balanced, without (noted as AH1) and with (noted as AH2) addition of 0.2Cu for a comparison, respectively. After rolling, the steel plate was heated to austenitize followed by quenching and tempering at temperature higher than 650^{o}C. Polarization behavior was measured at room temperature (RT) using a conventional three-electrode cell. A saturated calomel electrode and a platinum plate were used as the reference electrode and counter electrode, respectively. The NACE solution (5 wt% NaCl + 0.5 wt% CH_3COOH) was injected into the electrolytic cell to immerse electrodes. After deoxygenation by bubbling nitrogen, H_2S was charged to saturate the NACE solution. A scan rate of 0.5 mV/s was used for the measurement. Hydrogen permeation experiment was carried out using an electrochemical method developed by Devanathan and Stachurski [5]. The cubic samples were immersed in the H_2S-saturated NACE solution at RT for 50 hours, and then dried carefully for X-ray photoelectron spectroscopy (XPS) and scanning electron microscopy (SEM). The morphologies of the corrosion products on the sample surfaces were examined using a XL30 scanning electron microscope. The X-ray photoelectron spectra were obtained using a PHI-550 spectrometer with an Al Kα

non-monochromatic source. XRD measurements were performed to analysis the phase constitution using 'D/max IIIA' automatic diffractometer, and a H-800 transmission electron microscopy (TEM) was used to observe the precipitates distribution of the steel matrix. TEM specimens were first mechanically polished, then prepared by a twin-jet electro-polishing apparatus in an electrolytic solution with an approximate composition in volume per cent of $CH_3COOH:HClO_4$ =92.5:7.5.

Results

Electrochemical Behavior

The two steels show similar electrochemical behavior. Fig. 1 represents the polarization curve of freshly polished steel in the H_2S-saturated NACE solution at RT. It can be seen that the anodic curve does not exhibit a stage of passivation but an active dissolution property. The corrosion currents for AH1 and AH2 were determined to be 76 and 45 μA / cm^2, respectively. Apparently, Cu addition in CrMo steel can effectively increase the corrosion resistance.

Fig. 2 shows the hydrogen permeation curves of investigated steels, obviously indicating a three-stage corrosion process. It can be seen that the hydrogen permeation flux increases significantly at the initial stage of immersion, and the maximum hydrogen permeation flux appears when the immersion time is up to 1 hour (stage I). This indicates that the fresh surface of steel is sensitive to H_2S and hydrogen atoms can easily enter the steel matrix. Further increasing the immersion time leads to the decrease of hydrogen permeation flux (stage II), which gradually reaches a steady value after the immersion time is about 15 hours (stage III). During the whole process, the hydrogen permeation flux for AH1 is about 2 μA / cm^2 higher than that for AH2, and a fluctuation is observed at stage III, as indicated by the arrow in Fig. 2.

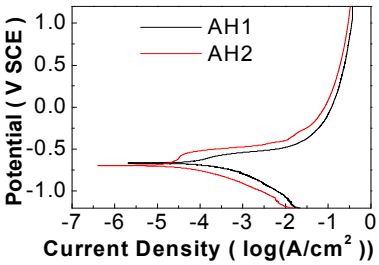

Fig.1 Polarization curves.

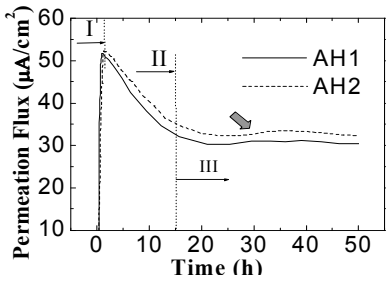

Fig. 2 Permeation curves

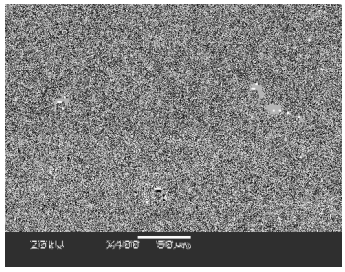

Fig. 3 SEM image

Characterization of Corrosion Product

Fig. 3 shows a SEM image of the corrosion scale on the surface of steel AH1 after 50 hours of immersion in the H_2S-saturated NACE solution. It is found that there are a lot of cracks in the corrosion scale. This implies that the corrosion film is not compact in solution. Observation of the cross-section of the corrosion scale discloses that the thickness for AH1 and AH2 was about 8 and 6μm, respectively.

For understanding the structure of corrosion scale, XPS is used to survey the chemical state of element species, and only iron, molybdenum and sulfur are identified on the outer surface of the scale. Fig. 4a represents the narrow scan of Fe2p spectrum of corrosion scale. It can be seen that the Fe2p3/2 at about 710.9 eV corresponds well to Fe in Fe_3O_4. During the experiment, the H_2S-saturated NACE solution was deoxygenated by bubbling nitrogen. However, the oxygenation probably occurred when the corrosion product was exposed in the air. Fig. 4b shows the Mo3d XPS spectrum. The Mo3d5/2 binding energy for MoS_2 occurs at 228.8 eV, but at the present experiment, Mo3d5/2 peak is found to be at 231.7eV, near the typical binding energy of Mo(VI) (232eV). Fig. 4c presents the narrow scan of S2p spectrum of this sample, which also shows two peaks at 161.7 and 166.7 eV. The peak occurring at 161.7 eV matches the binding energy of FeS. The peak with a higher binding energy of 166.7 eV is attributed to sulfate or sulfite species, which might be caused by oxidation of sulfide.

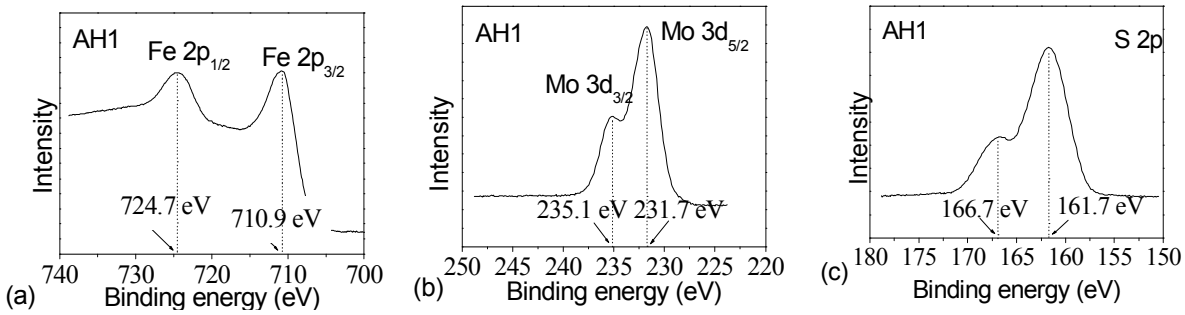

Fig. 4 Narrow scans of Fe2p (a), Mo 3d(b), and S2p (c) spectrum of the surface corrosion scale

The phase constitution of the corrosion product on the steel surface was determined by XRD analysis, and the results show that the matrix phase is α-Fe, and two other main phases are two kinds of iron sulfide, i.e., pyrrhotite ($Fe_{1-x}S$) and mackinawite($Fe_{1+x}S$). The rest including Cu_2S, MoS_2, Cr_2O_3 and Fe_3O_4 can also be discriminated. However, except Fe_3O_4, these phases have not been identified by XPS. Owing to the higher depth resolution of XRD than that of XPS, it can be safely deduced that these phases located at the inner layer of the corrosion scale.

TEM Observation

After quenching and tempering, the microstructure of the investigated steel exhibits a mixture of ferrite and carbides. Fig.6 shows the precipitates distribution of steel carbides. Selected zone diffraction discloses that cementite, molybdenum carbide and chromium carbide homogeneously scatters over the iron matrix, and the sizes of all these carbides are smaller than 200nm in diameter. The Cu-rich phase has not been found in the experiment.

Discussions

The electrochemical behavior should correspond to the formation of corrosion product. It has been reported that iron sulfide particles initially form on the fresh surface and then grow into multiple-layer films [1]. Considering the result of a first increase of permeation flux to maximum then a decrease to a relatively steady level, as indicated in Fig. 2, the corrosion mechanism for CrMo steels is deduced as shown in Fig. 7, different from the two-stage mechanism.

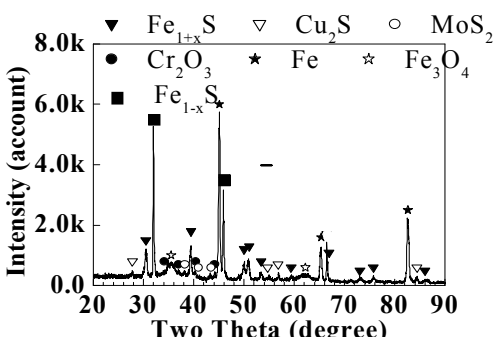

Fig. 5 XRD pattern of corrosion scales

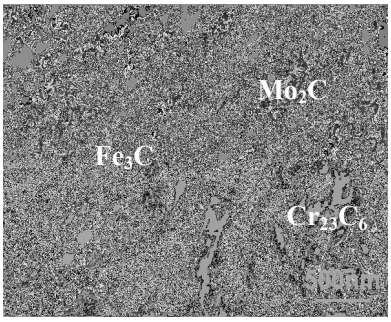

Fig.6 TEM observation of AH2

It is generally believed that tetragonal mackinawite exists below 100 °C and transforms into the hexagonal pyrrhotite above 138 °C [6]. In this study, both mackinawite and pyrrhotite exist during the corrosion process. It is proposed that the reaction of ferrite and cementite with H_2S might be responsible for their formation, respectively. However, further investigation is needed for better understanding. Irrespective the difference in the two kinds of non-stoichoimetric iron sulfides (pyrrhotite and mackinawite), based on the results above, it is believed that the stoichoimetric FeS particles and hydrogen atoms form on the fresh steel surface during stage I (Fig. 7a). The initial electrochemical reactions of steel matrix in solution can be described as Reaction (R.) I:

R. I: $Fe + H_2S \rightarrow FeS + 2H + 28.80$ KJ/mol

$2H \rightarrow H_2$ - 97.16 KJ/mol

The product FeS might either adhere to the steel surface or dissolve into the solution, while the produced H atom might either form H_2 bubbling up or diffuse into the steel matrix directly. The hydrogen permeation flux increases as this main reaction intensifies. It is understandable that soon after a layer of thin iron sulfide film covers the fresh steel surface, hydrogen permeation flux arrives at the maximum, indicating the start of stage II (Fig.7b). However, the formed film acts as a barrier to the transportation of both H_2S from the solution / film interface to the film / steel interface and H_2 the other way around. As a result the hydrogen permeation flux decreases until the ion transportation process reaches equilibrium (stage III). Thus during stage II, the film thickness may increase steadily, and the formation of a certain thickness of iron sulfide film is responsible for the relative stability of hydrogen permeation flux (stage III, Fig.7c). XPS and XRD results disclose the different constituent phases between the outer and the inner sides of the corrosion scale, and this is considered to answer for the fluctuation exhibiting in stage III, and then the possible electrochemical reaction can be written as:

R.II: $Mo_2C + 4H_2S \rightarrow 2MoS_2 + CH_4 + 2H_2$ -396.32 KJ/mol

R.III: $Cu + H_2S \rightarrow Cu_2S + H_2$ -52.58KJ/mol

R.IV: $Cr_{23}C_6 + 23H_2S \rightarrow 23CrS + 6CH_4 + 11H_2$ -2829.76 KJ/mol

The Gibbs free energies in R.I-IV are calculated according to [7]. When the corrosion product is exposed in the air, Fe_3O_4, Cr_2O_3, molybdate, sulfate or sulfite might form, as indicated in Fig.7d.

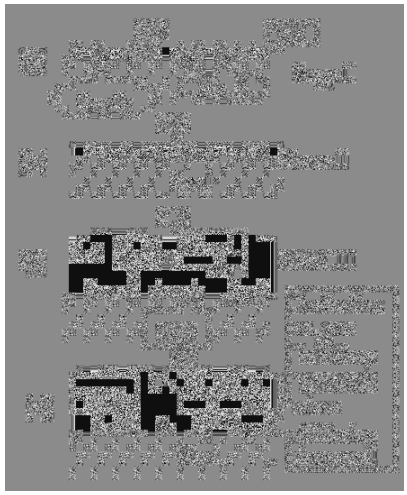

Fig. 7 Schematic of solution mechanism of CrMo steel

The decrease in permeation rate in steel has been explained in terms of metal carbides acting as obstacles to ion transport [3]. In the present case, Cu addition alters the anodic dissolution rate, and effectively increases the corrosion resistance of CrMo steel. As a result, the corrosion scale of AH1 is a little thicker than that of AH2. Therefore, it is considered that on the one hand, the reaction of Fe with H_2S might be retarded more effectively for AH1 than for AH2, and then the hydrogen permeation flux for AH2 is a little higher than that for AH1. On the other hand, it is well known that Cu addition leads to the precipitation of Cu-rich phase at RT and thus cause a rise of vacancy concentration, which may be helpful to accelerate the hydrogen permeation rate.

Summary

A three-stage corrosion process of CrMo steels with and without Cu addition has been deduced according to the electrochemical behavior and the corrosion product in H_2S saturated aqueous brine solution. It is found that the steel matrix, besides Fe_3C, also contains Mo_2C and $Cr_{23}C_6$ carbides, and the corrosion scale is made up of FeS, MoS_2, Cu_2S and Cr_2O_3, among them, Cu_2S, MoS_2 and Cr_2O_3 phases lie near the inner side of corrosion scale, while molybdate near the outside of scale. The electrochemical behavior corresponds to the formation of corrosion product, and the dissolution behavior of iron matrix and carbide precipitates in the H_2S solution acts as a key role for the steel resistance to the hydrogen sulfide corrosion.

References

[1] S.Y. Tsai, H.C. Shih, J. Electrochem. Soc. 145 (1998), p. 1968-76.
[2] H. Vedage, T.A. Ramanarayanan, J.D. Mumford and S.N. Smith, Corrosion 49 (1993), p. 114-121
[3] W.C. Luu, J.K.Wu, Corrosion Science 38(1996), p. 239–45.
[4] B.D. Craig, G. Krauss. Metallurgical Transactions A 11(1980), p. 1799–808.
[5] M.A.V. Devanathan, Z. Stachurski, Proc. Roy. Soc. A 270 (1962), p. 90-102.
[6] M. Ueda, Corros. Engin. 44 (1995) 159-74.
[7] J.A. Dean, *Lange's Handbook of Chemistry* (McGraw-Hill Book Company, Switzerland,1985)

Key Engineering Materials Vols. 385-387 (2008) pp 125-128
© (2008) Trans Tech Publications, Switzerland
doi:10.4028/www.scientific.net/KEM.385-387.125

Numerical Investigation of Stress Singularities in Cracked Bimaterial Body

L. Náhlík[1,2,a], L. Šestáková[1,2,b] and P. Hutař[1,c]

[1]Institute of Physics of Materials, Academy of Sciences of the Czech Republic, Žižkova 22, 616 62 Brno, Czech Republic

[2]Institute of Solid Mechanics, Mechatronics and Biomechanics, Brno University of Technology, Technická 2, 616 69 Brno, Czech Republic

[a] nahlik@ipm.cz , [b] sestakova@ipm.cz, [c] hutar@ipm.cz

Keywords: bimaterial interface, stress singularity exponent, corner singularity, vertex singularity, general singular stress concentrator.

Abstract. Composite materials or generally materials with interfaces are nowadays used in many varied engineering applications. In comparison with classical engineering materials the existence of material interface causes locally different stress distribution, which can strongly influence behaviour of whole structure and can have an important influence on failure mechanisms of such materials. The paper presented is devoted to the investigation of stress singularity exponents of a crack growing in a bimaterial body perpendicularly to the interface and touching the material interface. Discrepancies between value of stress singularity exponent in the centre of bimaterial body and on the free surface were found. The assumptions of linear elastic fracture mechanics (LEFM) and small scale yielding (SSY) are considered. For numerical calculations finite element analysis was used. Results obtained can contribute to a better understanding of failure of materials with interfaces.

Introduction

The perpendicular crack touching the interface between two dissimilar elastic materials represents kind of general singular stress concentrator. The stress respectively displacement distribution (perfect adhesion between materials is assumed) around the tip of such concentrator can be expressed in general form as follows (e.g. [1-3]):

$$\sigma_{ij} = \frac{H_I}{\sqrt{2\pi}\ r^p}\ f_{ij}(p,\alpha,\beta)\ ,\ u_i = \frac{H_I}{\sqrt{2\pi}} r^{1-p} g_i(p,\alpha,\beta), \tag{1}$$

where $f_{ij}(p,\alpha,\beta)$ and $g_i(p,\alpha,\beta)$ are known functions of bimaterial parameters α and β [1] and $0 < p = p(\alpha,\beta) < 1$ is the stress singularity exponent. Parameters α and β express elastic mismatch and can be understood as elastic constants of bimaterials. For plane strain conditions are given as:

$$\alpha = \frac{\frac{E_1}{E_2}\cdot\frac{1+\nu_1}{1+\nu_2} - 1}{4(1-\nu_1)}, \qquad \beta = \frac{E_1}{E_2}\cdot\frac{1-\nu_2^2}{1-\nu_1^2},$$

where E_1, E_2 are Young moduli and ν_1, ν_2 Poissons ratios of material 1 or 2 respectively, see Figs 1 or 2.

For given materials and loading conditions, the stress distribution around the crack tip is determined by the value of the generalised stress intensity factor H_I. The value of H_I is proportional to the applied load and has to be estimated numerically. For homogeneous materials, where p = ½, H_I corresponds to the stress intensity factor K_I.

The stress singularity exponent p = 1 - λ, where eigenvalue λ can be determined from characteristic equation [1]:

$$\lambda^2\left(-4\alpha^2+4\alpha\beta\right)+2\alpha^2-2\alpha\beta+2\alpha-\beta+1+\left(-2\alpha^2+2\alpha\beta-2\alpha+2\beta\right)\cos\left(\lambda\pi\right)=0\,. \qquad (2)$$

The stress singularity exponent p can be so determined from the asymptotic stress and displacement fields near the crack tip, e.g. [4,5]. Figs 1(a) and (b) show asymptotic solution of the crack opening stress ahead of crack tip and displacements perpendicular to the crack faces calculated by finite element method. On the base of knowledge of numerical asymptotic solution near the crack tip of a crack touching the interface, the stress singularity exponent p can be easily determined from log-log plots. Described procedure was used in next numerical calculations.

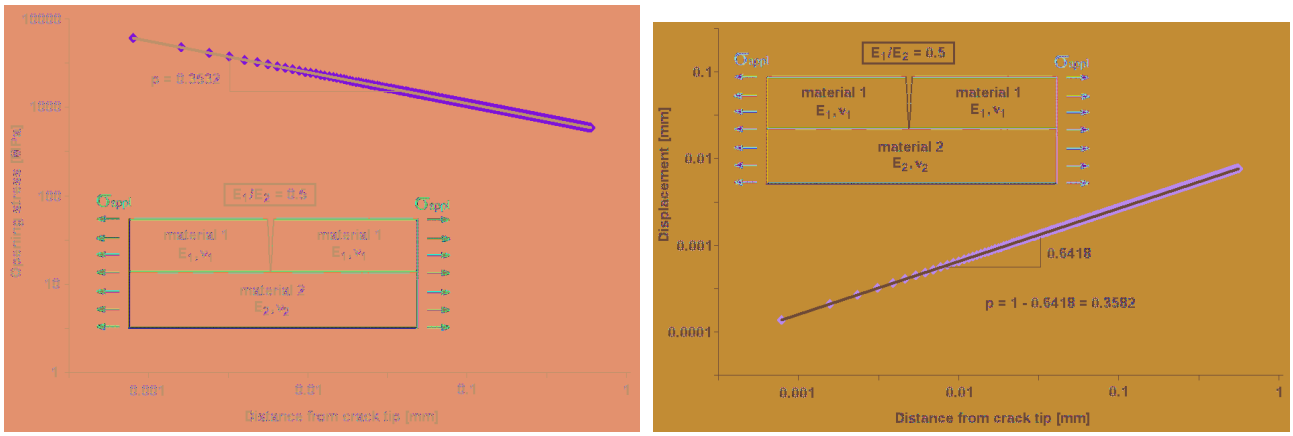

(a) **(b)**

Fig. 1. Opening stresses (a) and displacements (b) versus distance from the crack tip along $\theta = 0$ in log-log plots for ratio of Young moduli $E_1/E_2 = 0.5$

Numerical calculations

A bimaterial body shown in Fig. 2 subjected to the remote tensile load $\sigma_{appl} = 100$ MPa was used for numerical calculations of stress singularities. The dimensions of the bimaterial body were chosen as 100 x 20 x 30mm (length x width x thickness), see Fig. 2. The considered thickness of both materials (1 and 2) was the same, i.e. t = 15 mm. The elastic properties of the bimaterial were: Poissons ratio $\nu_1 = \nu_2 = 0.3$ and ratios of Young moduli of materials 0.5, 0.67, 1, 1.5 and 2.

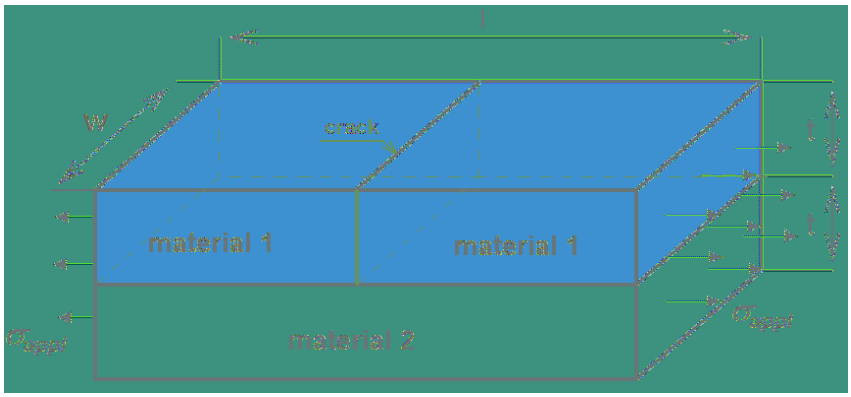

Fig. 2. Tensile bimaterial specimen considered for numerical calculations

The calculations were performed for different numerical models: for an appropriate 2D body under plane strain conditions and for a 3D body. Singularities around the crack tip were determined for mutual comparison from opening stresses and displacements perpendicular to the crack faces. The procedures showed in Figs 1(a) and (b) were used. In the case of 3D bimaterial cracked body both mentioned procedures were used and stress singularities determined in the centre of the body and in place of so-called vertex point, i.e. in the intersection between crack front and free surface. The crack front was touching the interface along all its length.

For finite element analysis FE system ANSYS was used and numerical calculations were performed in mathematical software Matlab. Results obtained were compared with analytical solution given by Eq. 2. All calculated results are summarized in Table 1.

Table 1. Stress singularity exponents obtained from analytical solution, numerical 2D and 3D solutions for the centre of specimen and surface of bimaterial specimen for different ratio E_1/E_2

E_1/E_2	Analytical sol.	Numerical solution				
		2D model	3D model			
			centre		surface	
			open. stress	displacement	open. stress	displacement
0.50	0.43389	0.4292	0.4277	0.4284	0.3532	0.3582
0.67	0.46053	0.4588	0.4599	0.4535	0.3941	0.3927
1.00	0.50000	0.5000	0.5026	0.4898	0.4548	0.4445
1.50	0.54279	0.5422	0.5441	0.5276	0.5180	0.4985
2.00	0.57451	0.5723	0.5723	0.5543	0.5617	0.5358

Table 2. Deviations between exact analytical solution and numerical 3D solution obtained from asymptotic stresses and displacements in the centre of specimen and differences in stress singularities between centre and surface of bimaterial specimen in dependence on E_1/E_2 ratio

E_1/E_2	Deviation – singularity from stresses [%]	Deviation – singularity from displacements [%]	Difference between centre – surface [%]
0.50	1.4	1.3	17.4
0.67	0.1	1.5	14.7
1.00	0.5	2.0	11.1
1.50	0.2	2.8	8.2
2.00	0.4	3.5	6.7

Discussion and summary

The stress singularity exponents of a crack touching the interface between two dissimilar elastic materials were determined by exact 2D analytical and purely numerical solutions and mutually compared. In next the numerical solution were used for determination of stress singularities in 3D cracked bimaterial body. Stress singularities were computed from asymptotic crack opening stresses as well as from displacements perpendicular to the crack faces. The accuracy of stress singularities evaluated from stress component and displacements is comparable, see Table 2.

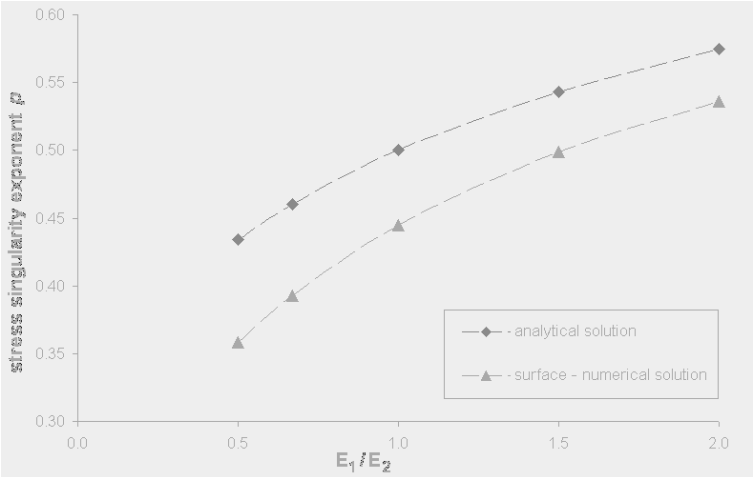

Fig. 3. Shift of stress singularities between centre and surface of specimen for different E_1/E_2 ratio

Discrepancies between value of stress singularity in the centre of specimen and on the free surface were found. The systematic fall of singularities on the free surface and in the centre of a bimaterial body can be explained by existence of so-called corner (vertex) singularity. This phenomenon was during the last 20 years described for cracks in homogeneous bodies in detail, e.g. [6-8]. Values of stress singularities in the centre of the body very well correspond to values obtained from analytical or numerical 2D solution respectively.

The values of stress singularity on the surface are systematically lower than in the centre and depend on Poissons ratio of both material components, see e.g. [6-8] for details. This fall can lead to the different behaviour of shallow cracks in composite materials or cracks in thin bodies in comparison to thicker ones. The decrease of stress singularity causes decrease of a fatigue crack propagation rate in comparison to thicker specimens, which are not, due to their sufficient thickness, so strongly influenced by the existence of corner singularity.

Procedure for evaluation of the fatigue crack propagation rate can be found for similar kind of general singular stress concentrator e.g. in [9]. The change of the stress singularity leads to different crack behaviour of a crack growing (propagating) through the interface between two dissimilar materials. In mentioned cases the decrease of stress singularity influences threshold values (or critical values in case of brittle fracture) and direction of further crack propagation after its pass through the material interface. This effect can influence time to failure of structures made from materials with interfaces (e.g. composite materials). For reliable estimation of behaviour of thin structures made from such materials or behaviour of shallow cracks, the change of stress singularity should be considered.

Acknowledgements

This research was supported through the grant No. 106/08/1409 and No. 106/06/P239 of the Czech Science Foundation and grant No. GAAV KJB200410803 of the Grant Agency of the Academy of Sciences of the Czech Republic.

References

[1] K.Y. Lin and J.W. Mar: Int. Journal of Fracture, 12 (1976), p. 52.

[2] S.A. Meguid, M. Tan and Z.H. Zhu: Int. Journal of Fracture 73 (1995), p. 1-23

[3] D.N. Fenner: International Journal of Fracture 12 (1976), p. 705-721

[4] C-S. Huang and P. Labossiere, in: Proceedings of Fatigue and Damage Mechanics 2003, p.35.

[5] P. Labossiere, M. Dunn and S. Cunningham: Journal of the Mechanics and Physics of Solids 50 (2002), p. 405.

[6] Z.P. Bažant, L.F. Estenssoro : Int. J. Solids Structures Vol. 15 (1979), p. 405-426

[7] J.P. Benthem : Int. J. Solids Structures Vol. 13 (1977), p. 479-492

[8] C.R. Pictu, V. Gupta : J. Mech. Phys. Solids Vol. 45 (1997), p. 1495-1520

[9] P. Hutař, L. Náhlík and Z. Knésl: Key Engng. Mater., Vols. 348-349 (2007), p. 377.

Key Engineering Materials Vols. 385-387 (2008) pp 129-132
© (2008) Trans Tech Publications, Switzerland
doi:10.4028/www.scientific.net/KEM.385-387.129

Evaluation of Perforation Resistance of Magnesium Alloy by Hypervelocity Impact

Ryo KUBOTA[1, a], Akira SHIMAMOTO[2,b], Daiju NUMATA[3,c] and Kazuyoshi TAKAYAMA[4,d]

[1]Graduate School of Eng., Saitama Institute of Technology, 1690, Fusaiji, Fukaya, Saitama, 369-0293, Japan

[2]Advanced Science Laboratory, Saitama Institute of Technology, 1690, Fusaiji, Fukaya, Saitama, 369-0923, Japan

[3]Graduate School of Eng., Tohoku University, Katahira 2-1-1, Aoba, Sendai, Miyagi, 980-8577, Japan

[4]Biomedical Engineering Research Organization, Tohoku University, Katahira 2-1-1, Aoba, Sendai, Miyagi, 980-8577, Japan

[a]q7002upo@sit.ac.jp, [b]shimamot@sit.ac.jp, [c]numata@rainbow.ifs.tohoku.ac.jp, [d]takayama@rainbow.ifs.tohoku.ac.jp

Keywords: Hypervelocity impact, Ballistic range, Magnesium alloy,

Abstract. Magnesium alloy is the lightest metal that is used as a structural material. It has a higher specific tensile strength and specific stiffness than Iron and Aluminum alloy, and the dent is not caused easily from Iron and Aluminum alloy at the impact. Therefore, Magnesium alloy is widely used in many areas, especially as an external shell of a mobile device and automotive parts which replaces iron and plastic, etc., and its demand is expected to grow in the future. In this paper we studied the hypervelocity impact with a ballistic range to clarify the characteristic of Magnesium alloys which had such a characteristic. The effect of impact velocity, temperature and the size of perforation hole were investigated experimentally. The perforation resistance of Magnesium alloys and their impact behavior were characterized.

Introduction

Recently, the weight reduction and recycling more than the past are requested as for structural material, because of environmental preservation and energy conservation points of view. Therefore, Magnesium alloy with the smallest specific gravity in a practical metal, the exquisite specific tensile strength and specific stiffness, and abundant resources is paid to attention. Magnesium alloy has the attractive characteristics such as machinability, dent resistance and dimensional stability etc., however, it has the problem in the application because it has low corrosion resistance, poor plastic formability and it is active metal. As a result, majority of Magnesium were used for non-structural material of the addition element etc. However, application of Magnesium alloy as the light weight and high strength material which takes the place of Aluminum alloy and Plastic has expanded to structural material such as aerospace structural member and vehicle components etc. by the advancement of molding method and coating technology [1].

It is important to clarify fracture behavior by the external force from the antiplane when Magnesium alloy is used for a structural material of space structure. In the severest one of such an impact phenomenon, space debris impact to space structure and bird strike to airplane, etc. exist. In such cases, the impactor has a very large relative velocity though small mass. Consequently, the damage of structure grows because the impactor has an enormous kinetic energy, and this phenomenon is very dangerous. Moreover, environmental temperature should be different from normal temperature, and environment in high- and low-temperature region be considered. Authors had clarified fracture behavior at hypervelocity impact of CFRP before [2]. Then, we did hypervelocity impact experiment which used Ballistic range to clarify impact characteristic of Magnesium alloy of cryogenic temperature from normal temperature in range, and examined fracture behavior in this research.

Specimen and Experimental device

Specimen. Table1 shows mechanical properties of Magnesium alloy ZK60A-T5 used for this research. Table2 shows details of specimen, structural wall and projectile.

Table 1 Mechanical Properties of ZK60A-T5

Tensile Strength (MPa)	275.5
Yield Strength (MPa)	150.1
elongation (%)	15.0

Table 2 Detail of Mocked parts

Item (Mocked parts)	Material	Shape	Size
Specimen (Bumper shield)	Zk60A-T5	Plate	110×110×2.3 (mm)
Structural wall (Space structure)	Al 2024-T3	Plate	200×200×5.0 (mm)
Projectile (Space debris)	Al 2017-T4	Sphere	7.938 (mm) dia., 0.74 (g) mass

Experimental Device. Experimental device used in this research is Ballistic range (Institute of Fluid Science, Tohoku University) shown in Fig.1. It uses the single-stage gun or the two-stage light gas gun by velocity which is necessary. In this experiment, the single-stage gun was used. The projectile is built in the sabot of division into four as shown in Fig.2, and projectile and sabot are launched together. The sabot is stopped before cryogenic chamber reaches by stopper, and only projectile goes into cryogenic chamber. The cryogenic chamber was double tank constitution, and specimen and structural wall were set up in the inside tank as shown in Fig.3 (there distance are 104mm), and it was set up in Ballistic range. Impact phenomenon was made visible by the shadow graph method, and it took a picture with the ultra high-speed camera (DRS Hadland Co. Ltd.,. Imacon200).

Experimental Condition. Experimental conditions were assumed to be each three conditions of impact velocity, 0.5, 1.0 and 1.7 km/s and temperature were 25 ºC: Normal temperature, -50 ºC: Low temperature and -120 ºC: Cryogenic temperature.

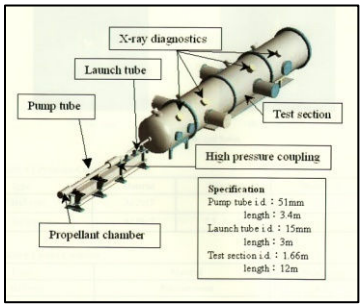

Fig.1 Schematic drawing of Ballistic range

Fig.2 Projectile built into Sabot

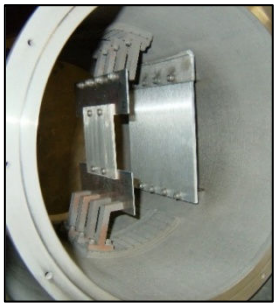

Fig.3 Specimen and Structural wall set up in Cryogenic chamber

Experimental result and discussion

In this research, space debris impact to space structure was mocked, projectile (space debris) was made to impact with specimen (bumper shield) and structural wall (space structure), and it examined it. As a result, it was confirmed that projectile perforated specimen in all experimental conditions. Fig.4 shows the relation between area of perforation hole and impact velocity. Area of perforation hole increased in proportion to impact velocity as Fig.4 showed, and the effect by temperature was not admitted so much. Then, Figs.5-7 shows one example of perforation hole of each velocity in -50 ºC and Fig.8 shows cross section of perforation hole. For impact velocity 0.5 km/s, perforation hole was extended from the front toward the rear of specimen, and it deformed like the petal in the rear and crack occurred was admitted. And, it was confirmed that deformation of specimen increased slightly decreasing in temperature. However, it has been understood that fracture surface of perforation hole is almost straight though the deformation is admitted. As a result, it is thought that neither spurt of debris to the front nor form of debris cloud to the rear it happened. For impact velocity 1.0 km/s,

partial projection was caused on perforation hole edge and it was confirmed to the front that crack which enclosed perforation hole occurred (Refer to Fig.6). The fracture surface confirmed the composition of the taper which narrows toward from the front to inside of perforation hole and the taper which broadens toward from inside of perforation hole to the rear. In addition, it was confirmed that fracture surface on the rear side was partially straight. Projection and taper in the front are formed with spurt of specimen which became debris by the deformation of specimen and rarefaction wave and taper in the rear is formed with becoming of projectile and specimen the debris cloud because of the multiple spall phenomenon by interaction of deformation of specimen, shock waves and rarefaction waves [3]. As a result, fracture surface of perforation hole has a lot of ruggedness. In this, it is cause that Magnesium alloy is hexagonal close packed structure with few slip systems, and slip plane exists in parallel for plate face in the wrought products [4, 5]. As a result, it is thought that it is a part of specimen couldn't become debris because crack caused by hypervelocity impact propagated complexly, and it remained without spurting. For impact velocity 1.7 km/s, the generation of deformation and crack is not admitted in perforation hole and it's neighborhood. In addition, ruggedness and crack in fracture surface for impact velocity 1.7 km/s are large or increase compared with that of impact velocity 1.0k m/s. Therefore, it was confirmed to have received the effect by an increase in impact velocity.

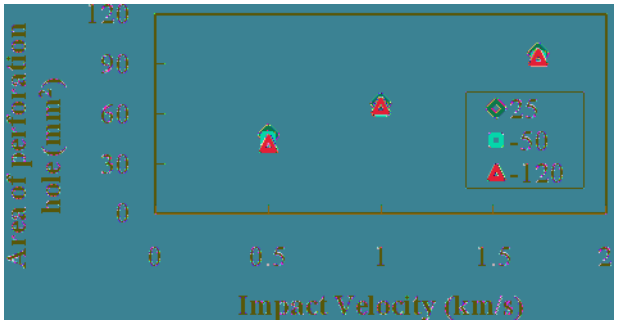

Fig.4 Relation between Area of Perforation hole and Impact Velocity

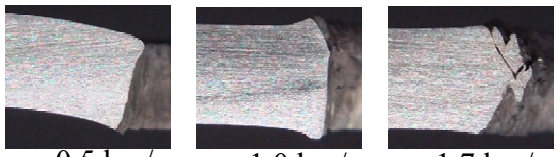

v = 0.5 km/s ***v*** = 1.0 km/s ***v*** = 1.7 km/s

(a) Experimental Temperature 25 ºC

v = 0.5 km/s ***v*** = 1.0 km/s ***v*** = 1.7 km/s

(b) Experimental Temperature -50 ºC

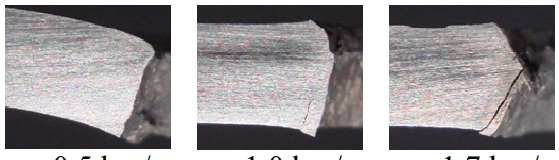

v = 0.5 km/s ***v*** = 1.0 km/s ***v*** = 1.7 km/s

(c) Experimental Temperature -120 ºC

Fig.8 Cross section of perforation hole edge

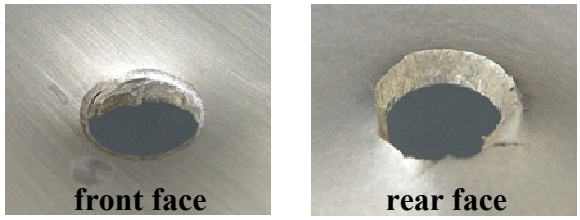

Fig.5 Macro Photography of Perforation hole (***v*** = 0.5 km/s, ***t*** = -50 ºC)

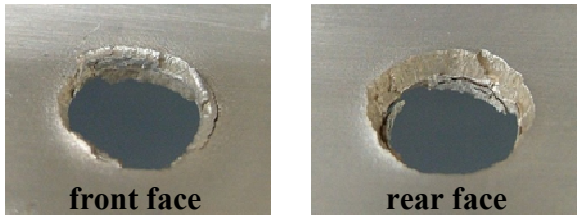

Fig.6 Macro Photography of Perforation hole (***v*** = 1.0 km/s, ***t*** = -50 ºC)

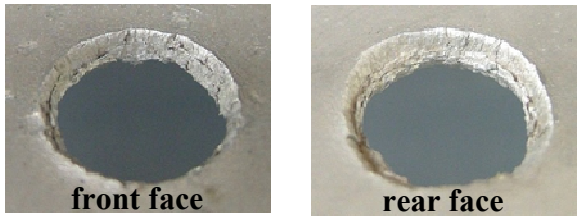

Fig.7 Macro Photography of Perforation hole (***v*** = 1.7 km/s, ***t*** = -50 ºC)

Fig.9 shows one example of debris cloud at 25 ºC temperature. For impact velocity 0.5 km/s, debris cloud was not formed, and spurt of debris was not admitted in the front of specimen as Fig.9 showed. It differed for impact velocity 0.5 km/s, and for impact velocity 1.0 and 1.7 km/s, debris cloud was

formed, and spurt of debris was confirmed to the front. A. Francesconi et. al [6] are clarifying the effect by temperature on geometry of debris cloud in hypervelocity impact examination at cryogenic temperature of Aluminum alloy. Then, we compared and examined geometry of debris cloud by difference of temperature in impact velocity 1.7 km/s (Refer to Fig.10). Debris cloud was formed to symmetry for incidence axis of projectile as shown in Fig.10, and the effect for it's form by temperature was not admitted.

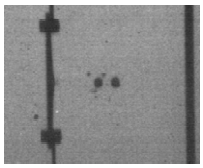
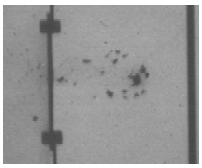
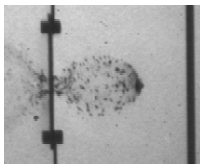

v = 0.5 km/s ***v*** = 1.0 km/s ***v*** = 1.7 km/s

Fig.9 Photographs of debris cloud (***t*** = 25 ºC)

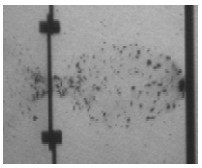
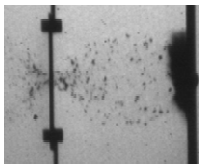
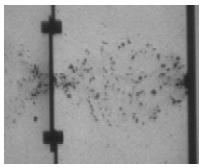

t = 25 ºC ***t*** = -50 ºC ***t*** = -120 ºC

Fig. 10 Photographs of debris cloud (***v*** = 1.7 km/s)

Conclusions

In this research, we did the experiment which mocked space debris impact phenomenon to clarify impact characteristic of Magnesium alloy. The experiment made spherical Aluminum alloy impact with Magnesium alloy specimen by using Ballistic range under the conditions whose impact velocity and experimental temperature were 0.5, 1.0 and 1.7 km/s, and 25, -50 and -120 ºC respectively. We examined the fracture behavior of Magnesium alloy and obtained the following findings based on examination result.

1. The form of debris cloud was not admitted for impact velocity 0.5 km/s. The effect at temperature on it was not admitted though it was confirmed for impact velocity 1.0 and 1.7 km/s.
2. Area of perforation hole increased in proportion to impact velocity, and difference of fracture style was confirmed from geometry of perforation hole in difference of impact velocity.

In impact velocity 0.5 km/s, it was confirmed to deform perforation hole like the petal in the rear.

In impact velocity 1.0 km/s, it was confirmed that causing projection on edge of perforation hole in the front occurred as crack's enclosing perforation hole.

In impact velocity 1.7 km/s, neither deformation of specimen nor occurrence of crack were admitted in perforation hole neighborhood.

3. A lot of ruggedness were confirmed for impact velocity 1.0 and 1.7 km/s in fracture surface.

References

[1] Yo Kojima and Tadao Ito: Technologies & Applications of Magnesium Alloys, CMC Publishing Co.,Ltd, (2006), p.219-226

[2] Ryo Kubota, Akira SHIMAMOT, Daiju NUMATA, Masayuki ANYOUJI, Kazuki TAKAYAMA, Evaluation of penetration resistance by highpervelocity impact of CFRP composite, Proceedings of 39th Symposium on Stress-strain Mesurement and Strength Evaluation, (2008), p.23-28

[3] CHARLES E. ANDERSON, JR., TIMOTHY G. TRUCANO, SCOTT A. MULLINT: DEBRIS CLOUD DYNAMICS, Int. J Impact Eng., 9, 1, (1990), p.89-113

[4] JMA, in: Handbook of Advanced Magnesium Technology, KALLOA PUBLISHING CO., LTD., (2000), p.114

[5] Nobuhiro KOGA, Kazunari HATO and Ratchanee PISARN: Journal of Japan Institute of Light Metals, 51, 9, (2001), p. 452-456

[6] A. Francesconi, D. Pavarin, C. Giacomuzzo, F. Angrilli: Impact experiments on low-temperature bumpers, Int. J Impact Eng, 33, (2006), p. 264-272

Key Engineering Materials Vols. 385-387 (2008) pp 133-136
© (2008) Trans Tech Publications, Switzerland
doi:10.4028/www.scientific.net/KEM.385-387.133

Fatigue resistance assessment of slurry coating steel substrate compounds under cyclic loading

K.G. Anthymidis[1, a], C. David[2,b] and D.N. Tsipas[1,c]

[1]Laboratory of Physical Metallurgy, Mechanical Engineering Department,

Aristotle University of Thessaloniki, 54006 – Thessaloniki, Greece

[2]Technical University of Serres, Mechanical Engineering Department,

Magnesias Campus, 62124 – Serres, Greece

[a]kanth@teiser.gr, [b]david@teiser.gr, [c]tsipas@eng.auth.gr

Keywords: slurry coatings, impact testing, fatigue resistance.

Abstract. Slurry coatings have been used for the protection of gas turbine materials in power plants during the last years. These coatings can be applied by spaying, brushing or dipping. The main constituent elements are silicon, chromium, potassium, borium, carbon and zirconium. They are characterized by high hardness and very good resistance against corrosion, erosion, abrasive and adhesive wear. To guarantee the reliability of coated steam turbines components used in power plants, the lifetime assessment of the coatings and their failure prediction become very important. Microhardness, scratch, adhesion and pin-on-disk sliding tests are commonly used for rapid evaluation of the mechanical properties of these coatings [F. Loeffler: Thin Solid Films, Vol. 339 (1999), p. 181]. However, the above testing methods do not model the dynamic cyclic fatigue. In this paper we evaluate the fatigue resistance of slurry coatings working under cyclic loading conditions by the impact testing method. The coating failure mode and its extent were assessed by SEM observations and EDX analysis. From the experimental results it was concluded that the Si,Cr,O,B,C coatings deposited on P91 steel substrate showed an improved fatigue strength compared to that of Si,Cr,O deposited on the same substrate.

Introduction

Modern power generation steam turbines are being designed to have higher efficiencies and to meet the stringent environmental regulations, ensuring plant reliability, availability and maintainability, - without increased cost. High efficiencies can be achieved at higher temperatures. Therefore the operating temperature is expected to rise from 550˚C to 650˚C. At these service conditions, turbine components have to be protected using spallation and oxidation resistant coatings, such as Si,Cr,O,B,C and Si,Cr,O slurry coatings. The fatigue failure resistance of these slurry coatings working under cyclic load conditions were assessed by means of the impact testing method.

The working principle of impact testing is described in great detail elsewhere [1,2]. Briefly, during the impact testing a coated specimen is cyclically loaded by a cemented carbide ball that repetitively impacts on the specimen surface. The superficially developed Hertzian pressure induces a complex stress field within the coating, as well as, in the interfacial zone between the coating and the substrate. Both these stress states are responsible for distinct failure modes, such as a cohesive or adhesive one. The subjection of the layered compounds to impulsive stresses creates real conditions for the appearance of coating fatigue phenomena - based upon structural transformation, crack generation and crack growth - which are responsible for the gradual micro-chipping and the degradation of the coating. Consequently the appearance of the substrate due to gradual coating degradation or abrupt coating release from the substrate indicates the coating failure.

Experimental procedure

The examined slurry coatings were characterized regarding their fatigue resistance using the impact testing method illustrated in figure 1.

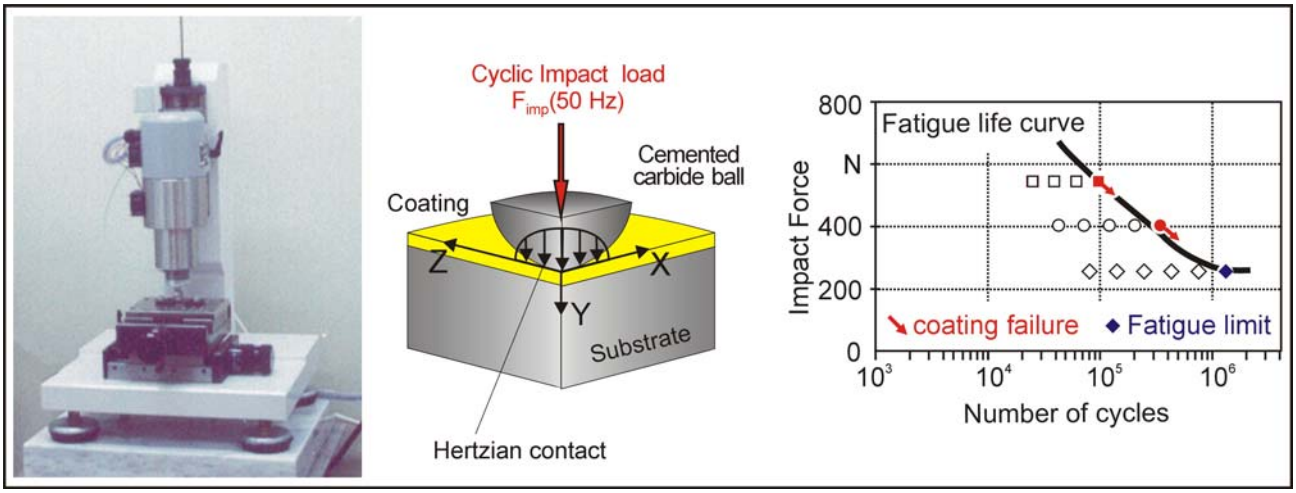

Figure 1: Impact testing method

The test bench where the experiments were carried out is simple and user friendly and allows the determination of the fatigue behavior of a wide range of single and multielement coatings. The working principle of the impact test is based on the alternate Laplace magnetic forces produced by the electromagnetic field, which is induced within the mechanical unit depicted in figure 1. A cemented carbide ball of 5 mm diameter impacts the coated specimen at 50 Hz, so that the coating substrate compound is stressed cyclically. The stress strain problem related to the impact test is the Herzian contact, which develops between the spherical indentor and the examined layered space. The superficially developed Hertzian pressure induces a complex stress field within the coating, as well as in the interfacial zone between the layer and the substrate. Both these stress states are responsible for distinct failure modes such as cohesive or adhesive one. Gradual intrinsic coherence release and coating microchipping (degradation) is assigned as coating cohesive damage. On the other hand the abrupt coating adhesive fracture and consequent exposure of the substrate material designate the coating failure. So depending on the stress state and the microstructural properties of the coating as well as on the adhesion in the interfacial zone two distinct coating failure modes can be identified, either a cohesive or an adhesive one. In all craters resulted from the experiments three different zones were identified. A central zone in the mid of the impact cavity, where the coating is strained with compressive stresses and a gradual cohesive degradation usually takes place. The indermediate zone inside the piled up rim formed around the impact cavity, where tensile and shear stresses are building up and both cohesive and adhesive coating fracture arises. Finally, the peripheral zone outside the impact cavity, where macrocracks might propagate depending on the coating brittleness and adhesive coating failure occurs. The coating failure mode and its extent in all conducted experiments were assessed by means of SEM observations and EDX analysis. The impact load leading to coating fatigue failure was recorded in fatigue diagrams (*Wöhler curve*) versus the number of impacts applied. The impact load for which the coating after 10^6 impacts does not fail designates its fatigue limit.

Results and discussion

In Figure 2 the high cycle fatigue diagram of the Si,Cr,O slurry coating deposited on P91 steel substrate is shown. This coating had an average thickness of 50 μm and Vickers microhardness values of 550-600Hv. From the conducted impact tests it was concluded that the fatigue limit of the current coating amounts approximately 100 N. The coating failure of the examined coating-substrate compound in all experiments applied at various loads occurred in the central zone of the impact crater in terms of gradual coating degradation, namely the coating underlies in cohesive failure mode (Fig.3).

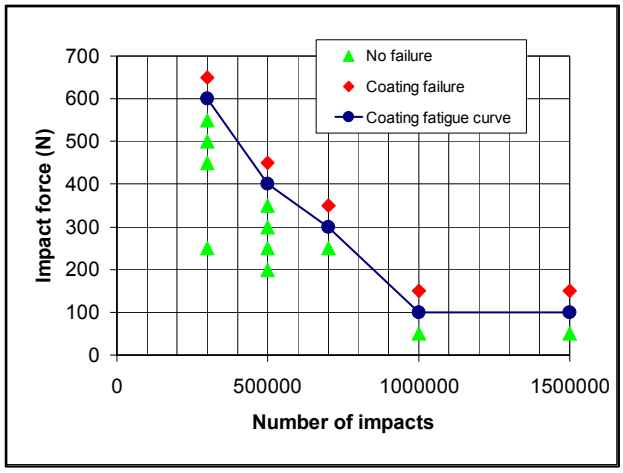

Figure 2: Fatigue curve of the Si,Cr,O slurry coating deposited on P91 steel substrate.

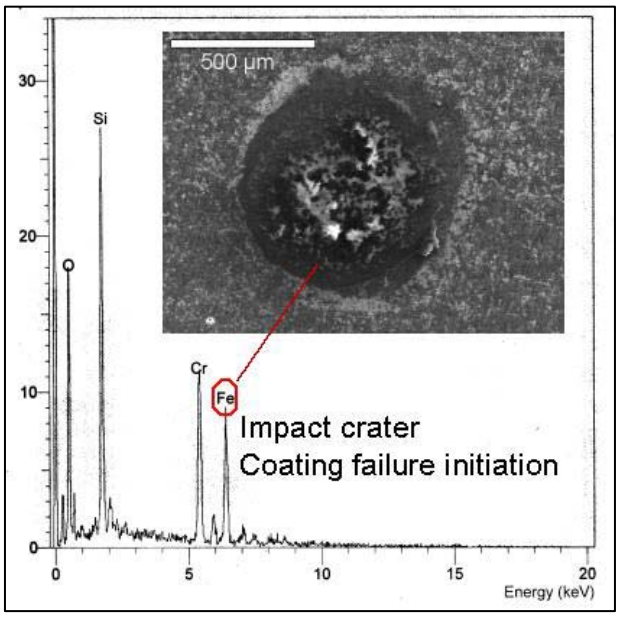

Figure 3: Impact crater SEM and EDX analysis of the Si,Cr,O slurry coating deposited on P91 steel substrate after 10^6 impacts by an impact load of 100 N.

In Figure 4 the high cycle fatigue diagram of the other Si,Cr,O,B,C slurry coating deposited on P91 steel substrate is shown. This coating was produced as the previous one with the difference that the constituent element Silica has been partial substituted with BC. The coating appears an average thickness of 50 μm and increased Vickers microhardness values of 1100-1200Hv. In this case where the coating microstructure is tougher with higher wear resistance at the same time, the coating layer sustains the cyclic impacts without any sign of degradation failure at impact loads similar to the previous one. Indeed this coating demonstrates an improved fatigue resistance with a fatigue limit approximately 150 N (Fig.5).

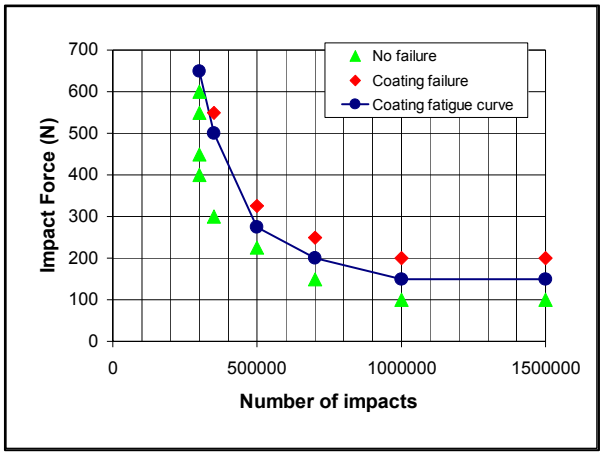

Figure 4: Fatigue curve of the Si,Cr,O,B,C slurry coating deposited on P91 steel substrate.

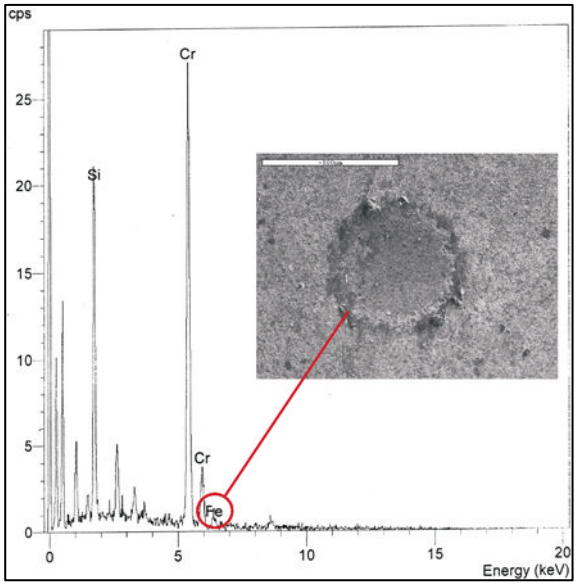

Figure 5: SEM and EDX analysis of the Si,Cr,O,B,C slurry coating deposited on P91 steel substrate after 10^6 impacts with an impact force of 150 N. Failure initiation around the rim of impact crater.

Conclusions

The work presented here outlines the failure mechanisms and gives an assessment of the fatigue strength against cyclic loading of slurry coatings. In this sense provides a feedback approach for optimizing the design of surface engineering components. More specifically the paper reports the results of an experimental approach capable to investigate the endurance performance of coating systems with refer to their mechanical properties and to deliver a semi-empirical design approach. Current impact testing investigations revealed the good fatigue strength of slurry coatings reinforced with BC in order to have high toughness.

Acknowledgment

We express our gratitude to the E.U. for financing this work through the projects SUPERCOAT and Interreg IIIA and to Technical University of Serres, Greece for partial funding provided.

References

[1] A.A. Voevodin, R. Bantle and A. Matthews: Wear Vol. 185 (1995), p. 151
[2] R. Bantle and A. Matthews: Surface and Coatings Technology Vol. 74-75 (1995), p. 857

Key Engineering Materials Vols. 385-387 (2008) pp 137-140
© (2008) Trans Tech Publications, Switzerland
doi:10.4028/www.scientific.net/KEM.385-387.137

Excavation damage in unsaturated porous media

Arson C.[1, a], Gatmiri B.[2, 1, b]

[1] Univ. Paris-Est, U.R. NAVIER (CERMES), Ecole Nationale des Ponts-et-Chaussées, 6-8 av. Blaise Pascal, Cité Descartes, Champs-sur-Marne, 77455 Marne-la-Vallée cedex 2, France

Tel: 00 33 1 64 15 35 24, Fax: 00 33 1 64 15 35 62

[2] University of Tehran, Department of Civil Engineering, IRAN

[a] arson@cermes.enpc.fr, [b] gatmiri@cermes.enpc.fr

Keywords: mixed damage model, unsaturated porous medium, hydro-mechanical and damage couplings, micro-mechanics, phenomenological approach, fracture flow

Abstract. This paper presents a damage model dedicated to unsaturated brittle rocks. It mixes phenomenological and micro-mechanical concepts, and is formulated based on the use of independent state variables (net stress and suction). The expression of the liquid permeability is modified in order to represent the influence of fracturing on interstitial fluid flows.

Introduction

The purpose of this study is to describe the Excavation Damaged Zone (EDZ) surrounding deep galleries dig in unsaturated brittle clay-host rock. Up to now, damage models dedicated to the representation of fracturing in continuous unsaturated porous media have mainly been designed by means of a Biot's stress concept. Alternatively, the present model involves independent state variables (net stress and suction), in order to emphasize the role of suction rigidity. The strain tensor is split in accordance with the choice of separated, independent stress state variables (part 1). The behaviour laws are derived from a postulated expression of the free energy (part 2). Combining micro-mechanical and phenomenological modelling approaches makes it possible to determine the reversible and irreversible components of the damaged strain tensor (part 3). Fracturing induces huge flow perturbations, through permeability changes. Consequently, the diffusive model of Gatmiri [1,2] has been transformed (part 4).

1. Strain splitting

The internal damage variable is a tensor, $\underline{\underline{\Omega}}$, defined in its principal base, following the principle of spectral decomposition:

$$\underline{\underline{\Omega}}(t) = \sum_{i=1}^{3} d_i(t)\ \underline{n_i}(t) \otimes \underline{n_i}(t) \qquad (1)$$

The meso-crack densities and directions d_i and $\underline{n_i}$ require the definition of a Representative Volume Element (RVE). Denoting the total stress tensor, the liquid pore pressure and the gas pore pressure by $\underline{\underline{\sigma}}$, p_w and p_g respectively, the stress state variables chosen to formulate the model are net stress $\underline{\underline{\sigma''}} = \underline{\underline{\sigma}} - p_g \underline{\underline{Id}}$ and suction $s = p_g - p_w$. In compliance with the former works of Gatmiri [1,2], it is assumed that the reversible strain tensor can be split into two components, each of which being thermodynamically-associated to a stress state variable, and being dependent on the damage variable $\underline{\underline{\Omega}}$:

$$\begin{cases} d\underline{\underline{\varepsilon}}_M^{rev}(\underline{\underline{\Omega}}) = \underline{\underline{\underline{\underline{D}}}}_e^{-1}(\underline{\underline{\Omega}}) : d\underline{\underline{\sigma}}'' \\ d\underline{\underline{\varepsilon}}_S^{rev}(\underline{\underline{\Omega}}) = \underline{\underline{D}}_s^{-1}(\underline{\underline{\Omega}})\ ds \end{cases} \quad (2)$$

Moreover, irreversible cracking is described by additional, irreversible components of deformations:

$$d\underline{\underline{\varepsilon}} = d\underline{\underline{\varepsilon}}_M^{rev}(\underline{\underline{\Omega}}) + d\underline{\underline{\varepsilon}}_S^{rev}(\underline{\underline{\Omega}}) + d\underline{\underline{\varepsilon}}_M^{irr} + d\underline{\underline{\varepsilon}}_S^{irr} \quad (3)$$

Suction effects are assumed to be isotropic:

$$d\underline{\underline{\varepsilon}}_S^{rev} = \frac{d\varepsilon_{S_v}^{rev}}{3}\underline{\underline{Id}}, \qquad d\underline{\underline{\varepsilon}}_S^{irr} = \frac{d\varepsilon_{S_v}^{irr}}{3}\underline{\underline{Id}}, \qquad \underline{\underline{D}}_s(\underline{\underline{\Omega}}) = \beta_s(\underline{\underline{\Omega}})\ \underline{\underline{Id}} \quad (4)$$

2. Behaviour laws (phenomenological approach)

For an unsaturated porous medium, the Inequality of Clausius-Duhem (ICD) writes [3]:

$$\underline{\underline{\sigma}}'' : d\underline{\underline{\varepsilon}} - sd(nS_w) - d\psi_s(\underline{\underline{\varepsilon}}, nS_w) \geq 0, \quad (5)$$

in which $\psi_s(\underline{\underline{\varepsilon}}, nS_w)$ is Helmholtz free energy. The thermodynamic conjugations corresponding to the assumed split of deformations (Eq. 3) and to the definition of net-stress- and suction-related rigidities (Eq. 2) lead to a new form of the ICD:

$$\underline{\underline{\sigma}}'' : d\underline{\underline{\varepsilon}}_M + sd\varepsilon_{S_v} - d\psi_s(\underline{\underline{\varepsilon}}_M, \varepsilon_{S_v}, \underline{\underline{\Omega}}) \geq 0 \quad (6)$$

The expression of the free energy is postulated as follows:

$$\psi_s(\underline{\underline{\varepsilon}}_M, \varepsilon_{S_v}, \underline{\underline{\Omega}}) = \frac{1}{2}\underline{\underline{\varepsilon}}_M : \underline{\underline{\underline{\underline{D}}}}_e(\underline{\underline{\Omega}}) : \underline{\underline{\varepsilon}}_M + \frac{1}{2}\varepsilon_{S_v}\beta_s(\underline{\underline{\Omega}})\varepsilon_{S_v} - g_M\underline{\underline{\Omega}} : \underline{\underline{\varepsilon}}_M - \frac{g_S}{3}\varepsilon_{S_v}Tr(\underline{\underline{\Omega}}) \quad (7)$$

$\frac{1}{2}\underline{\underline{\varepsilon}}_M : \underline{\underline{\underline{\underline{D}}}}_e(\underline{\underline{\Omega}}) : \underline{\underline{\varepsilon}}_M$ and $\frac{1}{2}\varepsilon_{S_v}\beta_s(\underline{\underline{\Omega}})\varepsilon_{S_v}$ are damaged elastic deformation energies. $-g_M\underline{\underline{\Omega}} : \underline{\underline{\varepsilon}}_M$ and $-\frac{g_S}{3}\varepsilon_{S_v}Tr(\underline{\underline{\Omega}})$ are potentials attesting the presence of residual deformations after unloading, g_M and g_S being material parameters [4].The definition of the free energy (Eq. 7) provides the damage-related behaviour laws of the stress state-variables:

$$\begin{cases} \underline{\underline{\sigma}}'' = \dfrac{\partial\psi_s(\underline{\underline{\varepsilon}}_M, \varepsilon_{S_v}, \underline{\underline{\Omega}})}{\partial\underline{\underline{\varepsilon}}_M} = \underline{\underline{\underline{\underline{D}}}}_e(\underline{\underline{\Omega}}) : \underline{\underline{\varepsilon}}_M - g_M\underline{\underline{\Omega}} \\ s = \dfrac{\partial\psi_s(\underline{\underline{\varepsilon}}_M, \varepsilon_{S_v}, \underline{\underline{\Omega}})}{\partial\varepsilon_{S_v}} = \beta_s(\underline{\underline{\Omega}})\ \varepsilon_{S_v} - \dfrac{g_S}{3}Tr(\underline{\underline{\Omega}}) \end{cases} \quad (8)$$

3. Computation of the reversible and irreversible components of the strain tensor (micro-mechanical approach)

Reversible strains. A damaged stress tensor is defined, using the operator of Cordebois and Sidoroff [5]:

$$\underline{\underline{\hat{\sigma}}}'' = \underline{\underline{\underline{\underline{M}}}}(\underline{\underline{\Omega}}) : \underline{\underline{\sigma}}'' = \left(\underline{\underline{Id}} - \underline{\underline{\Omega}}\right)^{-1/2} \cdot \underline{\underline{\sigma}}'' \cdot \left(\underline{\underline{Id}} - \underline{\underline{\Omega}}\right)^{-1/2} \tag{9}$$

Applying the Principle of Equivalent Elastic Energy ($\delta W_e\left(\underline{\underline{\hat{\sigma}}}'', \underline{\underline{\Omega}} = 0\right) = \delta W_e\left(\underline{\underline{\sigma}}'', \underline{\underline{\Omega}}\right)$), leads to:

$$\underline{\underline{\underline{\underline{D_e}}}}(\underline{\underline{\Omega}}) = \underline{\underline{\underline{\underline{M}}}}^{-1}(\underline{\underline{\Omega}}) : \underline{\underline{\underline{\underline{D_e^0}}}} : \underline{\underline{\underline{\underline{M}}}}^{-T}(\underline{\underline{\Omega}}), \qquad \underline{\underline{\underline{\underline{M}}}}^{-1}(\underline{\underline{\Omega}}) = \underline{\underline{\sigma}}'' \otimes \left[\left(\underline{\underline{Id}} - \underline{\underline{\Omega}}\right)^{-1/2} \cdot \underline{\underline{\sigma}}'' \cdot \left(\underline{\underline{Id}} - \underline{\underline{\Omega}}\right)^{-1/2}\right]^{-T} \tag{10}$$

Recalling that suction effects are assumed to be isotropic, a damaged suction is similarly defined:

$$\mathrm{Tr}\left(\hat{s}\ \underline{\underline{Id}}\right) = \mathrm{Tr}\left(\underline{\underline{\underline{\underline{M}}}}(\underline{\underline{\Omega}}) : \underline{\underline{Id}}\ \ s\right) = s\ \ \mathrm{Tr}\left(\left(\underline{\underline{Id}} - \underline{\underline{\Omega}}\right)^{-1/2} \cdot \underline{\underline{Id}} \cdot \left(\underline{\underline{Id}} - \underline{\underline{\Omega}}\right)^{-1/2}\right) \tag{11}$$

and the same reasoning provides the expression of the damaged suction rigidity:

$$\beta_s(\underline{\underline{\Omega}}) = \frac{9\beta_s^0}{\left(Tr\left[\left(\underline{\underline{Id}} - \underline{\underline{\Omega}}\right)^{-1}\right]\right)^2}. \tag{12}$$

Irreversible strains. Now that the degraded rigidities are known (Eqs. 10,12), incremental reversible deformations are perfectly determined, and may be combined with the behaviour laws (Eq. 8) to obtain the incremental irreversible strains:

$$\begin{cases} \mathrm{d}\underline{\underline{\varepsilon}}_M^{irr} = -\underline{\underline{\underline{\underline{D_e}}}}^{-1}(\underline{\underline{\Omega}}) : \left(\dfrac{\partial \underline{\underline{\underline{\underline{D_e}}}}(\underline{\underline{\Omega}})}{\partial \underline{\underline{\Omega}}} : \underline{\underline{\varepsilon}}_M\right) : \mathrm{d}\underline{\underline{\Omega}} + g_M \underline{\underline{\underline{\underline{D_e}}}}^{-1}(\underline{\underline{\Omega}}) : \mathrm{d}\underline{\underline{\Omega}} \\ \mathrm{d}\varepsilon_{S_v}^{irr} = -\beta_s^{-1}(\underline{\underline{\Omega}}) \left(\dfrac{\partial \beta_s(\underline{\underline{\Omega}})}{\partial \underline{\underline{\Omega}}} \varepsilon_{S_v}\right) : \mathrm{d}\underline{\underline{\Omega}} + \dfrac{g_S}{3} \beta_s^{-1}(\underline{\underline{\Omega}})\ \underline{\underline{Id}} : \mathrm{d}\underline{\underline{\Omega}} \end{cases} \tag{13}$$

The increment of damage $\mathrm{d}\underline{\underline{\Omega}}$ may be computed by means of an associated flow rule.

4. Flow modelling in fractured unsaturated porous media

In the present model, the effect of damage on fluid flows will be impacted on the permeability of the liquid phase only. As in the works of Gatmiri [1,2], transfers are assumed to be diffusive. A specific cracking-related component $\underline{\underline{\underline{\underline{k_{int}^2}}}}\left(n^{frac}, \underline{\underline{\Omega}}\right)$ is added to the intrinsic permeability of the intact material $\underline{\underline{\underline{\underline{k_{int}^1}}}}\left(n^{rev}, \underline{\underline{\Omega}}\right)$:

$$\underline{\underline{v_w}} = -\underline{\underline{\underline{\underline{K_w}}}} \cdot \underline{\nabla}\left(\frac{p_w}{\gamma_w} + z\right), \qquad \underline{\underline{\underline{\underline{K_w}}}} = k_r(S_w)\ \left(\underline{\underline{\underline{\underline{k_{int}^1}}}}\left(n^{rev}, \underline{\underline{\Omega}}\right) + \underline{\underline{\underline{\underline{k_{int}^2}}}}\left(n^{frac}, \underline{\underline{\Omega}}\right)\right) \tag{14}$$

$k_r(S_w)$ is the relative permeability, depending on the saturation degree. n^{rev} and n^{frac} are reversible and fracturing porosities. The flow inside each micro-crack damaging the RVE is assumed to follow the cubic law [6]:

$$\underline{v_w}^{i}(\underline{n_i}) = -\frac{1}{12\mu_w}(e_i)^2\left(\underline{\underline{Id}} - \underline{n_i}\otimes\underline{n_i}\right)\cdot\underline{\nabla}(p_w + \gamma_w z), \qquad i = 1...N \tag{15}$$

in which it is supposed that the RVE is damaged by N penny-shaped micro-cracks characterized by a radius r_i and an opening e_i. Due to the homogenized definition of damage (Eq. 1), the flow in a meso-crack may be quantified by:

$$\underline{v_w}^{frac} = -\underline{\underline{k_2}}(n^{frac}, \underline{\underline{\Omega}})\cdot\underline{\nabla}\left(\frac{p_w}{\gamma_w} + z\right) = \frac{1}{V_{REV}}\sum_{i=1}^{3}\left(\underline{v_w}^{i}(\underline{n_i})\ V_i\right),\ V_{REV} = b^3,\ V_i = e_i\pi(r_i)^2 \tag{16}$$

which results in:

$$\underline{\underline{k_2}}(n^{frac}, \underline{\underline{\Omega}}) = \frac{\gamma_w}{12\mu_w}\frac{\pi}{b^3}\sum_{i=1}^{3}(e_i)^3(r_i)^2\left(\underline{\underline{Id}} - \underline{n_i}\otimes\underline{n_i}\right) \tag{17}$$

Conclusion

This paper presents a mixed damage model based on the use of independent state variables (net stress and suction), combining phenomenological and micro-mechanical concepts. Supposing that all the hydro-mechanical parameters characterizing the intact porous material are known, few additional data are required to represent damage: one characteristic dimension of the RVE (b), one dilatancy parameter relating crack openings (e_i) to crack radii (r_i), two energetic coefficients (g_M and g_S), eventual damage load function parameters, and the initial damage tensor $\underline{\underline{\Omega^0}}$ (12 scalar parameters, falling to 7 scalars in axisymmetric configurations, and to 5 coefficients if the initial damaged state is assumed to be isotropic).

Acknowledgements

This research is supported by the European project TIMODAZ ("Thermal Impact on the Damaged Zone Around a Radioactive Waste Disposal in Clay Host Rocks"), launched by EURATOM.

References

[1] B. Gatmiri, Non Linear Behaviour Of A Multiphase Engineering Barrier In Nuclear Waste Disposal" 16th ICSMGE, OSAKA (2005), pp. 2261-2264.

[2] B. Gatmiri, M. Seyedi, P. Delage, J.-J. Fry, A new suction-based mathematical model for thermo-hydro-mechanical behavior of unsaturated porous media, NUMOG VI, Quebec, CANADA (1997), pp. 291-296.

[3] O. Coussy, P. Dangla P., *Approche énergétique du comportement des sols non saturés*, in: O. Coussy, J.M. Fleureau (Ed), Mécanique des sols non saturés, Hermes, pp. 137-174 (2002)

[4] A. Dragon, D. Halm, Modélisation de l'endommagement par méso-fissuration : comportement unilatéral et anisotropie induite, C.R. Acad. Sci. Paris, T. 322, Série IIb, 275-282 (1996).

[5] J.P. Cordebois, F. Sidoroff, Endommagement anisotrope en élasticité et plasticité, Journal de Mécanique théorique et appliquée spec. Issue, 45-60 (1982).

[6] J.F. Shao, H. Zhou, K.T. Chau, Coupling between anisotropic damage and permeability variation in brittle rocks, Int. J. Num. An. Meth. Geomech., 29, 1231-1247 (2005).

Key Engineering Materials Vols. 385-387 (2008) pp 141-144
© (2008) Trans Tech Publications, Switzerland
doi:10.4028/www.scientific.net/KEM.385-387.141

Experimental Investigations on the Effects of Thermal Residual Stresses on the Efficiency of Repaired Panels with Glass/Epoxy Composite patch

H. Hosseini-Toudeshky[1,a], M. Shamboli[1,b] , B. Mohammadi[1,c]
[1]Aerospace Engineering Department & Centre of Excellence in Computational Aerospace Engineering
Amirkabir University of Technology, 424 Hafez Ave, Tehran, Iran
Fax: +98-21 6695 9020, Tel: +98-21 6454 3224
[a]Hosseini@aut.ac.ir, [b]mshambooli@gmail.com, [c]Bijan_Moh@aut.ac.ir

Keywords: Repair, Single-side, Composite, Aluminium Panels, Curing Temperature

Abstract. The aim of this experimental investigation is to study the effect of various curing temperatures on crack-front shape and crack growth life of centrally cracked aluminium panels in mode-I condition with single-side glass/epoxy composite patches. The aluminium panels are made of Al 2024-T3 with the thicknesses of 2.29 mm. Unidirectional four layers lay-up perpendicular to the initial crack length were used for the patches of all specimens and the adhesive was Araldite LY564. The cyclic remote stress of 118 MPa with the R-ratio of 0.05 was applied for all models. The experiments were performed for different curing temperatures of room temperature, 50°C, 80°C, 100°C and 120°C. It is shown that the fatigue crack growth life of the repaired panels with curing temperatures of 100°C and 120°C is considerably smaller than those obtained for specimens cured at room temperature and 50°C.

Introduction

Thermal residual stresses in the aluminium repaired panels using boron/epoxy and graphite/epoxy patches has been recognized as a disadvantage of repair technology using composite patches. This is due to the relatively low coefficient of thermal expansion of composites compared to the parent material which results in the residual tensile stresses of the repaired components [1]. During the heat-up phase, both materials are allowed to expand or contract almost freely because the adhesive has not yet cured and locked in its structure. When the adhesive is sufficiently cured, the three-dimensional molecular cross-linked structure limits its ability to viscoelstically respond to stress. When the repair has been cooled to the ambient temperature, the thermal expansion coefficient mismatch becomes clearly visible.

Numerical studies have been carried out by Chow and Atluri [2] to examine the effect of the thermal cycling on the fatigue response of the aluminum panels repaired with the boron/epoxy patch. They found that, the fatigue life of the specimens, which undergoes cycles of high stress at low-temperature and low stress at high-temperature is dramatically reduced. Crooker [3] investigated the thermal residual strain occurred in the 7075-T6 aluminum panel with double-side repairs of 15-ply graphite/epoxy patches. He concluded that reducing the curing cycle temperature could decrease thermal residual strains by 26.5% between the patch and the aluminum panels when FM73 adhesive is used to bond them together, and 7.4% when EA 9696 is used.

Theoretical analyses to compute the stress intensity factor after repair had been conducted for both mechanical and thermal loadings by Rose, [4] and Wang et al., [5]. Sabelkin et al., [6] performed investigations to characterize the fatigue crack growth of repaired stiffened aluminum panels with boron/epoxy composite using both experiments and analyses. They performed three-dimensional finite element analysis using the three layers technique that included the thermal residual stresses developed during the composite patch bonding. They showed that the temperature range affects stress intensity factor ranges almost in a similar manner in both un-stiffened and stiffened panels. They didn't simulate the real crack-front shape in single-side repaired panels which is a curved shape during the crack propagation period.

A single-side repair usually produces out-of-plane bending, which occurs due to the shift in the neutral axis of the panel under tension loading. This causes stress variations over the thickness of the cracked panel and therefore produces non-uniform crack propagation along the panel's thickness

leading to a curved crack-front shape. The crack-front shape also affects the magnitude of stress intensity factors along the crack-front and therefore affecting the crack growth rate. In the real application the curvature of the crack-front shape is affected by the out-of-plane bending due to the asymmetric (single-side) repair configuration and distribution of thermal residual stresses along the panel thickness. Therefore it is worth to investigate the effect of curing temperatures on the crack-front shape of the repaired panels. Effect of thermal residual stresses due to various curing temperatures on the fatigue life of repaired panels with composite patches has not been reported in the literatures yet.

In this study experimental fatigue crack growth life and crack-front shape of centrally cracked aluminium panels in mode-I condition with single-side repairs of glass/epoxy patches are curried out. The experimental results obtained from various curing temperatures of 50^{o}C, 80^{o}C, 100^{o}C and 120^{o}C are compared with those obtained at room curing temperature.

Experiments

Typical geometry and loading of the aluminium panels, adhesive layer and composite patch and also a typical experimental specimen are shown in Figure 1. The specimens were made of 2024-T3 aluminium alloy with the thickness of 2.29 mm containing a central sharp flaw of 0.2 mm wide followed by the production of fatigue crack to reach the crack size of 2a = 10.0 mm. Specimens' dimensions followed the ASTM E-647 standard. The surface of each specimen was prepared with a P2 etching process [7]. After that the specimens are bonded with 4 layers unidirectional UND Composite Interglass 92145/LY564 (glass/epoxy). Two specimens of each repaired panel with the same panel and patch configuration were prepared to repeat the tests. The patches were made using the hand lay-up technique. Each specimen remained in the room temperature for two hours to pass the gel time without any pressure. Then they were kept under the pressure for 18 hours in the room temperature. Then the specimens cured under specific curing temperatures and cycles.

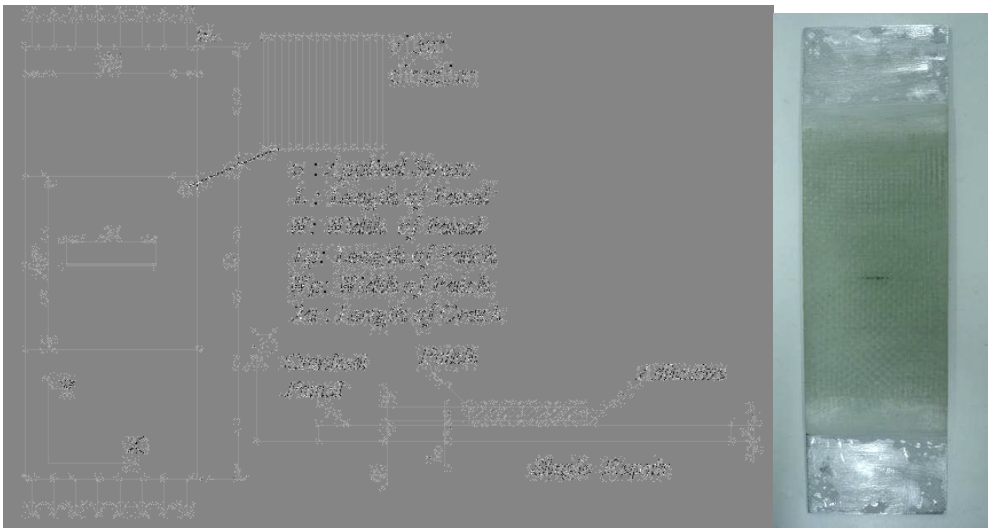

(a) (b)

Figure 1. Typical geometry, loading (a) and experimental specimen (b) of repaired panels

Finally, cyclic loads were applied to both repaired and un-repaired specimens with the frequency of 5 Hz, load ratio of R=0.05 and the maximum applied remote stress of 116 MPa at ambient temperature using a servo-hydraulic DARTEC 9600 machine. The initial crack size was a=5.0 mm. When the crack length at the un-patched surface of the panel reaches to the value of 10.25 mm, tests stopped and a static tensile load applied to each specimen until failure occurs. Therefore, the crack-front shape due to the fatigue crack growth can be detected on the broken surface of the repaired panels.

Results and Discussions

Figure 2 shows the comparison of crack-front shapes obtained at a certain crack growth length for repaired panels with glass/epoxy patches under various curing temperatures. The results obtained for the curing temperature of 120°C are not presented to prevent crowding. This figure shows that there are only small differences between the obtained crack-front shapes under various curing temperatures between room and 120°C temperatures. It also shows that when the curing temperature is increased the crack-front curvature radius becomes larger and closer to a perpendicular crack-front shape. The more perpendicular crack-fronts can produce higher stress intensity factors leading to the faster crack extension or smaller fatigue crack growth life of the repaired panels.

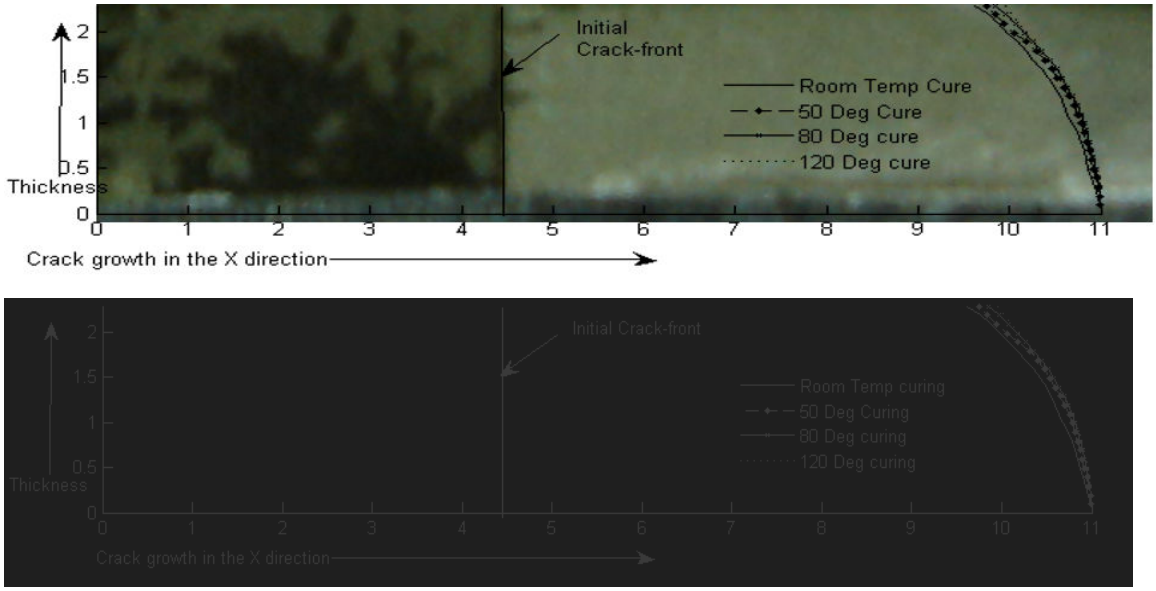

Figure 2. Comparison of crack-front shapes for repaired panels with glass/epoxy patch under various curing temperatures

Figure 3 shows the crack growth behaviour of repaired panels under various curing temperatures based on the recorded crack extensions at un-patched surfaces. This figure shows that there is almost a similar overall behaviour of the crack growth for repaired panels under various curing temperatures. There are significant differences between the crack growth lives obtained at room and 50 °C curing temperatures during the crack extension. There are not significant differences between the crack growth behaviour and lives obtained for curing temperatures of 100°C and 120°C. The fatigue life differences under various curing temperatures occurred at small crack growths are considerably smaller than those obtained at large crack extensions.

Fatigue crack growth lives of the repaired panels with various curing temperatures for a small initial growth of 0.5 mm and a certain growth of 5.25 mm (X_{ctip}=10.25 mm) at un-patched surface are listed in Table 1. It shows that the fatigue life of the repaired panels for both a small crack growth of 0.5 mm (indication of almost restarting the crack growth) and certain growth of 5.25 mm are decreased by increasing the curing temperature. This table shows that the obtained lives for a very small crack growth at various curing temperatures of between 50°C and 120°C may decreased by 29% to 53% when compared with the life obtained for room temperature curing cycle. The results also show that the obtained life for the certain crack growth of 5.25 mm at 50°C curing temperature is decreased by 13.9% when compared with the life obtained at room temperature curing cycle, however, the life obtained at 120°C is decreased by 37.2%.

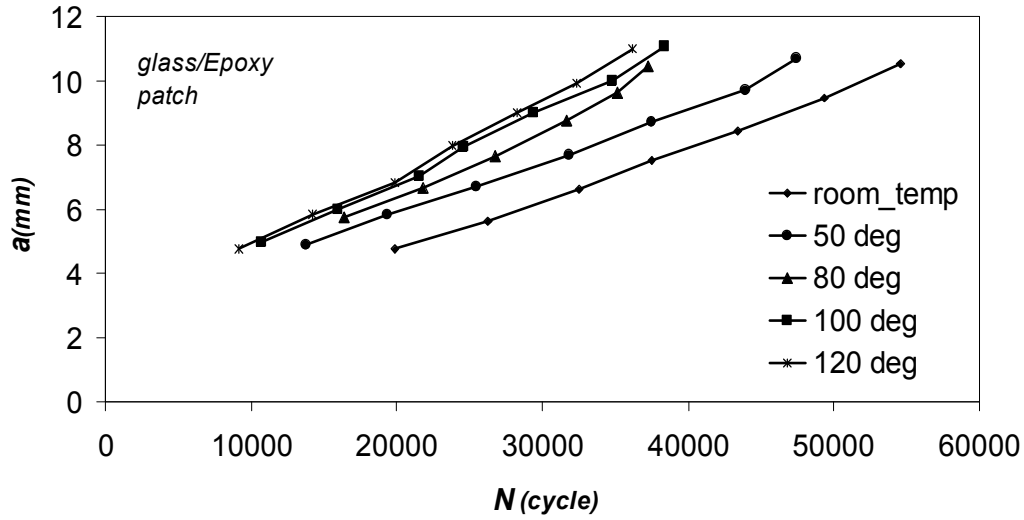

Figure 3. Crack growth behaviour of repaired panels under various curing temperatures

Table 1. Crack growth life of repaired panels with various curing temperatures

Curing Temperatures	Small initial crack growth (×1000) Cycle	Certain crack growth of 5.25 mm (×1000) Cycle
Room Temperature	19.8	53.3
50 °C	14.0	45.9
80 °C	-	36.8
100 °C	10.0	35.2
120 °C	9.2	33.48
Un-repaired	11.17	

Conclusion

It was shown that there are small differences between the obtained crack-front shapes under various curing temperatures. The fatigue life differences under various curing temperatures occurred at small crack growths are considerably smaller than those obtained at large crack extensions. The fatigue crack growth lives of repaired panels for small and large crack extensions were considerably decreased with increasing the curing temperatures. The effect of thermal residual stresses on the crack growth life reduction at the curing temperatures of 50°C and 120°C were 13.9% and 37.2% respectively when compared with the life obtained at room curing temperature.

References

[1] AA. Baker, R. Jones, (1988), Bonded Repair of Aircraft Structure, Dordrecht: Martinus Nijhoff, Netherlands.
[2] W.T. Chow, S.N. Atluri, (1997), AIAA Journal, Vol. 35(9), pp. 1528-1535.
[3] H.R. Crooks, (2003), MSc Thesis, USAF, Air Force Institute of Technology.
[4] L.R.F. Rose, (1998), Bonded Repair of Aircraft Structures, Kluwer Academic Publisher 1988.
[5] C.H. Wang et al., (2000), Int. J. of Sol. and Struc., Vol. 37, pp. 4577–4599.
[6] V. Sabelkin, S. Mall, J.B. Avram, (2006), Eng. Frac. Mech., Vol. 73, pp. 1553–1567.
[7] H.M. Clearfield, D.K. McNamara, and G.D. Davis, (1990), Engineered Materials Handbook, Vol. 3 Adhesives and Sealants, Brinson, H.F., ASM International, p. 260.

Key Engineering Materials Vols. 385-387 (2008) pp 145-148
© (2008) Trans Tech Publications, Switzerland
doi:10.4028/www.scientific.net/KEM.385-387.145

Experimental Study on Seismic Damage Model of the SRHSHPC Composite Frame Columns

Shansuo ZHENG[a], Liang ZHANG [b], Lei LI[c], Bin WANG[d], Ming XIE[e]

School of Civil Engineering, Xi'an University of Architecture and Technology, Xi'an 710055, China

[a]zhengshansuo@263.net, [b]gztrzl@126.com, [c] lilei1004@163.com, [d] wangbin1853@sohu.com, [e]kpxtx@163.com

Keywords: Steel Reinforced High Strength and High Performance Concrete (SRHSHPC), Composite Frame Column, Seismic Damage Model, Cumulative Dissipated Hysteretic Energy, Damage Index.

Abstract. Based on experimental investigation under low cyclic reversed loading, the seismic behaviors and seismic damage model for steel reinforced high strength and high performance concrete (SRHSHPC) composite frame columns are studied. Several existing seismic damage models are firstly presented and their characteristics are comparatively analyzed. From the test results of low cyclic reversed loading, the variation history of cumulative dissipated hysteretic energy of the SRHSHPC composite frame columns under different loading cycle levels is figured out, and the influence of axial compression ratio, shear span ratio, stirrup ratio and concrete strength on the cumulative dissipated hysteretic energy is also discussed. The damage index of the SRHSHPC composite frame columns is compared according to the existing seismic damage models, and the seismic damage model adapted for the SRHSHPC composite frame columns is established. According to the variation history of the damage index under different loading cycle levels, the rule of damage development for the SRHSHPC composite frame columns is proposed. The influence of axial compression ratio, shear span ratio, stirrup ratio and concrete strength on the damage development is also discussed. The results indicate that the seismic behaviors of the SRHSHPC composite frame column are outstanding, and the seismic damage model could give a quantitative description for damaging process of the samples, which is reference for establishing more rational damage criteria for the SRHSHPC earthquake-resistant composite structure.

Introduction

The steel reinforced high strength and high performance concrete (SRHSHPC) structure is a kind of new composite structure that applies high strength and high performance concrete (HSHPC) to the steel reinforced concrete (SRC) structure. This type of structure system can make full use of the excellent mechanical behaviors and high durability of the HSHPC. Therefore, its application in the structure engineering becomes more and more widespread. The earquake-resistance behaviors of structure depend on its energy absorption capability and elastic-plasticity deformation capacity strongly, but the damage of structure have great influence on these capacities. Namely, the original energy absorption capability and elastic-plasticity deformation capacity of structure will be inevitably decreased once the damage arises in structure. For the sake of researching the whole response process and failure mechanism of the SRHSHPC structure the earthquake, and evaluating seismic behaviors and establishing seismic failure criterion reasonably, the seismic damage model need to be studied. In this paper, experiment on the SRHSHPC frame columns under low cyclic reversed loading is completed, and the hysteretic performance as well as the failure mechanism of the column is investigated. Besides, some main parameters that have great influence on seismic behaviors and damage evolvement of the SRHSHPC frame columns, such as shear span ratio, axial compression ratio, stirrup ratio and concrete strength are analyzed.

Analysis of the Experimental Results

There are four main factors influencing seismic behaviors of the SRHSHPC frame columns. They are shear span ratio, axial compression ratio, stirrup ratio and concrete strength. All these factors are taken into consideration in experiment. Fig.1 is the typical load-displacement hysteresis curve of specimens in this experiment. From the experimental $P-\Delta$ hysteresis curves, following characteristics can be found: (1) With the increase of shear span ratio, the hysteresis curve is more sufficiency, which indicates the good ductility of the column. (2) The stirrup ratio has the same effect on hysteresis curves as that of shear span ratio. The capacity of energy dissipative and the ductility performance of the column will be improved as the increase of stirrup ratio. (3) With the growth of concrete strength, the hysteresis curves become thin, and the area of curve enclosing reduces, so the capacity of ultimate deformation and stability decreases obviously. (4) The hysteresis curves of the SRHSHPC columns can astringe to those of pure steel columns basically. Because of the core steel, the ductility performance of the SRHSHPC columns is much better than RC column. It has superior ability for resisting the secondary earthquake.

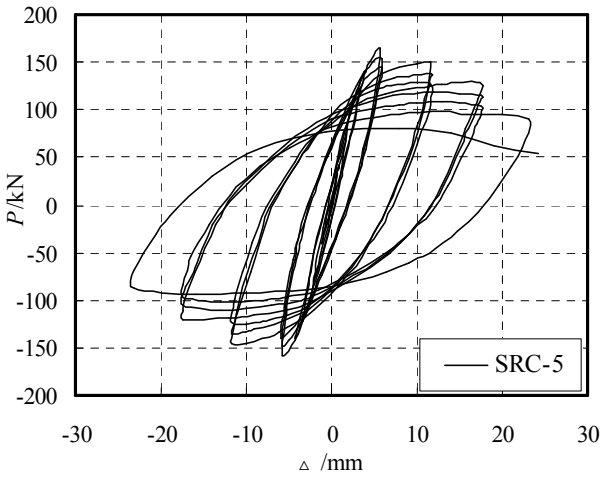

Fig.1 $P-\Delta$ hysteresis curve of specimen

Earthquake Damage Model

The damage is one of the most intuitionistic behaviors when structure is subjected to the earthquake load. According to the historical earthquake data, seismic design intensity and structure importance, the seismic damage performance-based design was proposed in the premise of allowing earthquake damage. However, according to the earthquake disaster experience and research results in the last several decades, it is indicated that earthquake is reciprocating motion of ground, and the duration of earthquake is shorter, so seismic damage of structure is not only related to maximum deformation, but also related to accumulation damage which is induced by low-cycle fatigue. Therefore, the inelastic performance should be described by the parameters which can reflect the deformation and accumulation damage effect. Generally, the damage of structure is described by damage parameters which reflect different failure mechanism based on deformation and energy or both of the comprehensive aspect.

Although domestic and international scholars have put forward a lot of two-parameter earthquake damage models, the Park damage model is still more mature, and it is applied extensively. For the sake of considering cumulative hysteretic energy dissipation based on deformation analysis, the Park Y. J., Ang A. H. S. and Wen Y. K.(1985, American) put forward the seismic damage model firstly which is linear combination maximum deformation and cumulative hysteretic energy dissipation . The damage index D is defined as $D=\left(\delta_m/\delta_u\right)+\alpha\left(E_h/F_y\delta_u\right)$, where δ_u is the limit deformation by monotone loading; F_y is the yield shear force; δ_m and E_h are the actual maximum elastoplasticity deformation and cumulative hysteretic energy dissipation of component in the earthquake respectively; α is the energy dissipation factor. Shear type structure is calculated by this formula: $\alpha = (0.073\lambda + 0.24n + 0.314\rho_s - 0.447) \times 0.7^{100\rho_\omega}$, where λ is the shear span ratio; ρ_s is the longitudinal reinforcement rate; ρ_ω is volume stirrup ratio. For flexure type structure, α can

be calculated by the formula: $\alpha = \left[0.37n + 0.36\left(k_\rho - 0.2\right)^2\right] \times 0.9^{100\rho_\omega}$, where k_ρ is normalization stirrup ratio, $k_\rho = \rho_s f_y / 0.85 f_c^{'}$. f_y and $f_c^{'}$ are strength design value of reinforcing bar and axis compression strength design value of concrete respectively.

Because the boundary condition of Park-Ang model is not religious enough, Kunnath put forward the correction Park-Ang model, namely $D = \left[\left(\delta_m - \delta_y\right) / \left(\delta_u - \delta_y\right)\right] + \alpha\left(E_h / F_y \delta_u\right)$. The correction Park-Ang model defines the earthquake damage by two-parameter deformation exceeding yielding point and hysteretic energy dissipation, which is more rationality.

In 1987, according to the assumption that speed of accumulative damage is proportional to existed damage value, Wang and Shah put forward the earthquake damage model basing on the accumulative damage, namely Wang Model: $D = \left(e^{k\beta} - 1\right) / \left(e^k - 1\right)$, where k is a experimental constant; β is cyclic loading parameters, $\beta = c\sum_{i=1}^{n}\left(\delta_{m,i} / \delta_u\right)$, where c is a experimental constant; δ_u is limit deformation by monotonic loading test; $\delta_{m,i}$ is the maximum displacement in i cycle.

Cumulative Hysteretic Energy Dissipation

The cumulative hysteretic energy dissipation of specimen E is defined as the area of hystereis curve, $E = F\int dx$.

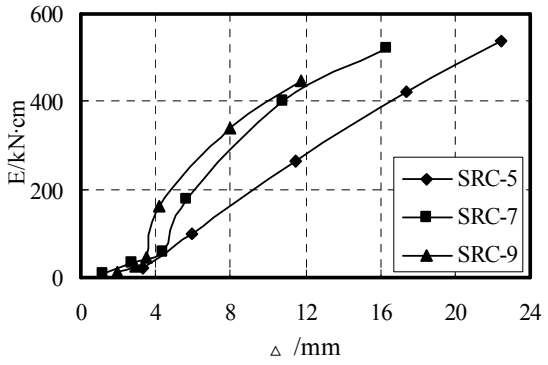

Fig.2 Influence of shear span ratio on E

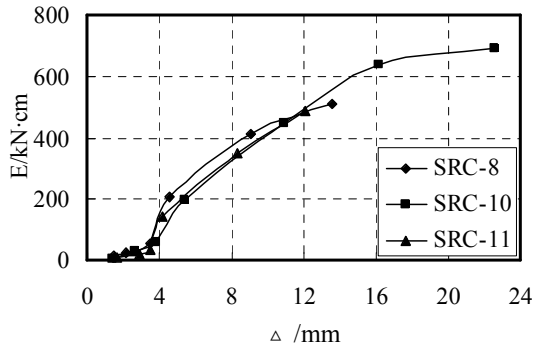

Fig.3 Influence of axial compression ratio on E

Fig.2 and Fig.3 show that the changing of cumulative hysteretic energy dissipation with cycle loading. The abscissa in figure is cycle loading level. Before yielding it corresponds to the single cycle loading. After yielding it corresponds to the second or third cycle in a certain displacement similarly. It is indicated that, when the axial compression ratio increases, cumulative hysteretic energy dissipation becomes less and less. The cumulative hysteretic energy dissipation of the SRHSHPC columns is more than ordinary reinforced concrete column's, which indicates that the SRHSHPC columns have excellent seismic behaviors. In the premise of same axial compression ratio, the cumulative hysteretic energy dissipation has tightly relationship with shear span ratio, stirrup ratio and concrete strength. With shear-span ratio rising, the cumulative hysteretic energy dissipation increases correspondingly. With stirrup ratio rising, the cumulative hysteretic energy dissipation also increases correspondingly. When concrete strength of specimens rises, the cumulative hysteretic energy dissipation decreases correspondingly, so seismic behaviors of the SRHSHPC column debase.

Damage Index

According to contrast analysis to different type of seismic damage models, the seismic damage model basing on linear combination of maximum deformation and cumulative hysteretic energy dissipation

is recommended for analyzing damage performance of the SRHSHPC columns. According to regression analysis to test results, The energy dissipation factor of the SRHSHPC columns is calculated by following formula: $\alpha = 0.792\rho_\omega \times (0.072\lambda + 0.56n + 0.133\rho_s - 0.224)$, where ρ_ω is transverse stirrup ratio; ρ_s is steel ratio; λ is shear-span ratio, $n = N/(f_c A_c + f_s A_s)$ is axial compression ratio.

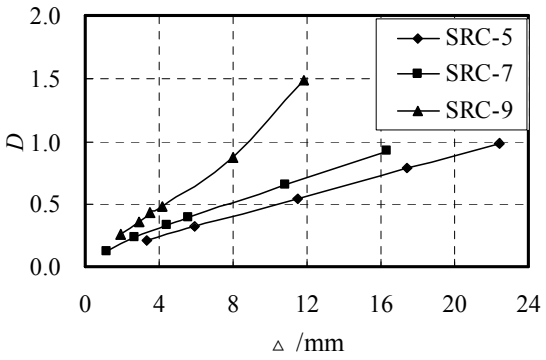

Fig.4 Influence of shear span ratio on damage

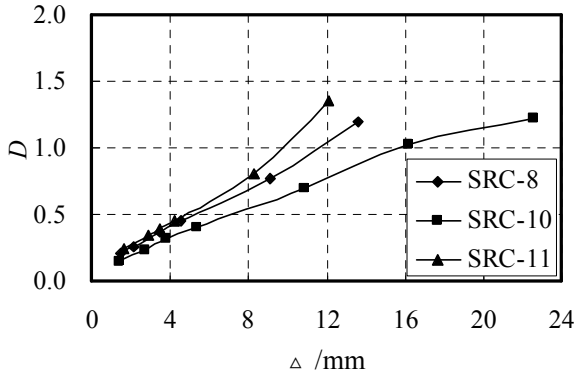

Fig.5 Influence of axial compression ratio on damage

According to the calculation results, it is indicated that with shear-span ratio rising, energy dissipation factor increases correspondingly; with axial compression ratio enhancing, damage factor also increases correspondingly; with stirrup ratio rising, energy dissipation factor increases correspondingly. However energy dissipation factor almost has no relationship with concrete strength. Therefore, the major factors affecting damage of the SRHSHPC columns are shear-span ratio, axial compression ratio, stirrup ratio, and steel ratio.

Summary

Based on experimental investigation under low cyclic reversed load, seismic performance and seismic damage model for the SRHSHPC composite frame columns are studied. It is indicated that the SRHSHPC columns has excellent seismic behaviors. When the axial compression ratio decreases, stirrup ratio and steel ratio increases, the cumulative hysteretic energy dissipation of the SRHSHPC composite column increases correspondingly. The major factors affecting damage of the SRHSHPC columns are shear-span ratio, axial compression ratio, stirrup ratio, and steel ratio. According to the test results and contrast analysis to different type of seismic damage models, the damage model of the SRHSHPC columns is attained, and the seismic damage model could give a quantitative description for damaging process of the samples, which is reference for establishing more rational damage criteria for the SRHSHPC earthquake-resistant composite structure. This project is sponsored by National Natural Science Foundation of China (Grant No. 50378080) and the Educational Office of Shaan'xi Province in China.

Reference

[1] Park. Y. J., Ang. A. H.S: *Mechanistic seismic damage model for reinforced concrete*. Journal of Structural Engineering, ASCE, Vol. 111, No.4 (1985), p.740-756

[2] Ou Jinping, He Zheng: *Seismic damage performance based design of reinforced concrete structures*. Earthquake Engineering and Engineering Vibration, China, Vol. 19, No.1 (1999), p.21-30

[3] Bai Guoliang, Qin Fuhua: *Principle and design of composite structures of steel and concrete*. Science and Technology Press, Shanghai, China (2000)

[4] Saatcioglu. M., Ozcebe. G.: *Response of reinforced columns to simulated seismic loading*. ACI structural Journal, Vol. 86, 1985, p.3-12

Key Engineering Materials Vols. 385-387 (2008) pp 149-152
© (2008) Trans Tech Publications, Switzerland
doi:10.4028/www.scientific.net/KEM.385-387.149

Experimental Study on the Shear Behaviors of the SRHSHPC Composite Frame Columns

Liang ZHANG[a], Shansuo ZHENG[b], Qingniing LI[c], Lei LI[d], Bin WANG[e]

School of Civil Engineering, Xi'an University of Architecture and Technology, Xi'an 710055, China

[a]gztrzl@126.com, [b]zhengshansuo@263.net, [c]lilei1004@163.com, [d]qingningli@126.com, [e]wangbin1853@sohu.com,

Keywords: Steel Reinforced High Strength and High Performance Concrete (SRHSHPC), Composite Frame Column, Failure Pattern, Shear Mechanism, Truss model of concrete, Shear strength.

Abstract. The shear behaviors of steel reinforced high strength and high performance concrete (SRHSHPC) composite frame columns are studied through the test on a number of SRHSHPC specimens with grade of concrete strength varied from C80 to C120 subjected to constant axial compression and cyclically varying horizontal load. Four influencing factors, namely, shear span ratio, axial compression ratio, stirrup ratio and concrete strength, are taken into consideration in the test, and strain gauges are respectively placed on steel web, stirrups as well as reinforcement bars to study the shear mechanism of SRHSHPC composite columns. According to test results, the shear failure patterns and shear mechanism of the specimens are discussed. By analyzing the contribution of the steel web, concrete, stirrups and reinforcement bars to the shear capacity, the shear mechanism of the SRHSHPC composite columns is figured out. Therefore, the influence of shear span ratio, axial compression ratio, stirrup ratios and concrete strength on shear behaviors of the SRHSHPC frame columns is clear. Finally, concrete truss model and principle of accumulation are applied to discuss the shear capacity and a calculation model for shear strength of the SRHSHPC composite columns is established. It is indicated that the shear behaviors of the SRHSHPC frame composite columns are excellent, and the calculated results of shear strength have good conformity with test results.

Introduction

When the structure is subjected to earthquake loading, the columns with high axial compression ratio and small shear span ratio in the structure will be destructed suddenly if the shear capacity is not sufficient. It is demonstrated for several times by the earthquakes in the world. Therefore, the understanding of the shear behaviors and enhancing the bearing capacity of diagonal section are crucial to ensure seismic safety of the structure. Taking some main factors into consideration, the concern of this paper is the experimental study about shear behaviors of the SRHSHPC composite columns with the concrete strength from C60 to C120. The shear failure mechanism of the SRHSHPC columns subjected to constant axial compression and cyclically varying horizontal load are studied. Four influencing factors, namely, shear span ratio, axial compression ratio, stirrup ratio and concrete strength, are taken into consideration in the test. The concrete truss model and principle of accumulation are applied to discuss the shear capacity and a calculation model for shear capacity of the SRHSHPC composite columns is established.

Analyses of the Main Factors for Shear Capacity

Shear Span Ratio. The shear span ratio is the most important factor which affects the shear capacity of SRHSHPC composite columns. From Fig.1, the conclusion can be got easily that with the increase of the shear span ratio, the resistance of the specimen decreases accordingly. At the meantime, when the shear span ratio is small, the curve between shear span ratio and shear capacity is sharp. The curve becomes more and more even as the shear span ratio increases. This shows that when the shear span

ratio is small, it can affect the shear capacity of the SRHSHPC composite columns obviously. The impact of the shear span ratio on the shear capacity of the SRHSHPC composite columns is mainly decided by the impact on the failure modes. Generally speaking, if the shear span ratio of the specimens $\lambda \geq 2.5$, the failure mode of the specimens tends to be flexure failure. When the shear span ratio of the specimens is moderate ($\lambda \approx 2.0$), the failure model tends to be shear splitting failure. The shear capacity of this failure model is determined by the bond strength between the steel and concrete and the tensile strength of concrete, so the capacity is low. The shearing compression failure model mainly occurs on the specimens of smaller shear span ratio ($\lambda \leq 1.5$). The shear capacity is determined by the concrete strength of the columns. So the bearing capacity of this kind of failure is perfect.

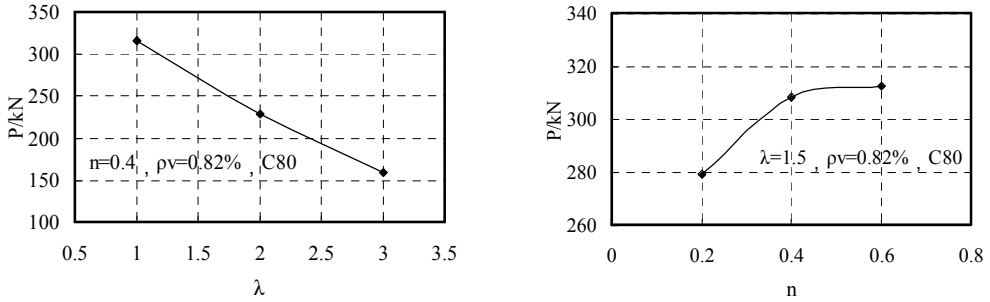

Fig. 1 Influence of shear span ratio and axial compression ratio on shear capacity

Axial Compression Ratio. The axial compression ratio (Shown in Fig.1) is the important factor that affects the shear bearing capacity of the SRHSHPC columns. The shear capacity of the SRHSHPC columns increases with the axial compression ratio. When the axial compression ratio is small (n<0.40), the shear capacity increases rapidly accordingly with the growth of axial compression ratio. After the axial compression ratio increases to certain degree (n≥0.40), the change rate of shear capacity decreases gradually and the curve becomes more and more smooth. The effect of axial compression ratio on samples is within a certain domain.

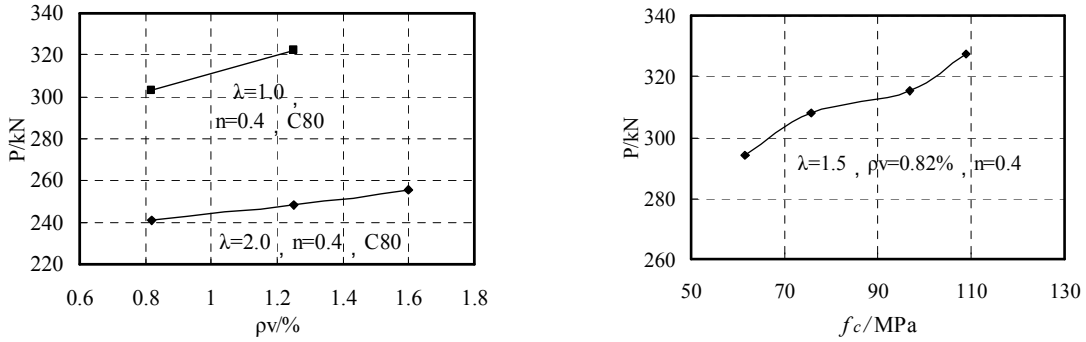

Fig. 2 Influence of stirrup ratio and concrete strength on shear capacity

Stirrup Ratio. The stirrup ratio (Shown in Fig.2) is one of the other important factors that influence the shear capacity of the specimen. The curve of the shear capacity versus stirrup ratio shows that the shear capacity of the SRHSHPC column growth with the stirrup ratio. But its affect is different to specimens with the different shear span ratio. When the shear span ratio is small, the rate of slope is large and the increasing speed of shear capacity is sharp. The effects of the stirrup ratio on shear capacity are obvious. With the increase of the shear span ratio, the curve becomes more and more even and the increasing speed of the shear capacity decrease with the stirrup ratio increasing. When the shear span ratio $\lambda \geq 2.5$, the curve is parallel to the X-axis nearly and the increase of the hoop reinforcement ratio almost has no effect to the shear capacity of the component.

Concrete Strength. The shearing failure of the SRHSHPC columns occurs because of the stress in concrete reaching the ultimate strength. So the concrete strength will have a significant influence on

the shear capacity of samples (Shown in Fig.2). It is indicated easily that if the other conditions are similitude, shear capacity of the component will be greater when the concrete strength increases. But the increase of bearing capacity would be different when the shear span ratio is different. When the shear span ratio is small, the shear capacity will increase sharply with raising of concrete strength.

Analysis of the Shear Capacity

Shear Capacity of Steel V_y^s. When the samples reach the ultimate strength phase, the web in tension side becomes yielding, but the web in compression side does not yield completely. So it is assumed that average shearing stress equals to αf_{ys} ($\tau = \alpha f_{ys}$), in which α should be less than 1.0 and f_{ys} refers to the yield strength value of steel. According to Misess yield theory, the formula $f_{ys} = \sigma^2 + 3\tau^2$ can be get. If the normal stress need not be taken into consideration and the web of the steel is pure shear yielding, there is $\tau = f_{ys}/\sqrt{3}$, or $\alpha = 1/\sqrt{3} = 0.58$. In fact, there is normal stress besides the shear stress, and the distribution of shear stress is not uniform, so α will be slightly less than 0.58. According to the test results, the average value of the α is equal to 0.40. The calculation procedure for shear capacity of steel under the reciprocating loading can be simplified by referring to the standards. According to the regression analysis of the test data, the formula is suggested as follows: $V_y^s = \dfrac{1.48}{\lambda + 1.5} f_{sy} t_w h_w$. f_{sy} refers to the yield strength of steel, h_w and t_w are the height and width of steel web respectively. If $\lambda < 1.0$, then $\lambda = 1.0$. If $\lambda > 2.5$, then $\lambda = 2.5$.

Shear Capacity of Hoop Reinforcement V_{sv}. The stress of the hoop reinforcements becomes larger quickly after the shear crack appearing even yielding. The hoop reinforcements not only bear the shear load, but also restraints the expansion of the concrete. The shear capacity of the hoop reinforcement can be taken as tension web member in the truss mode [1]. The calculation formula could be gotten as $V_{sv} = \dfrac{\lambda + 3}{2(\lambda + 1)} f_{yv} \dfrac{A_{sv}}{S} h_0$. h_0 is effective depth of the cross-section which is taken as the projected length of crack for the safety. f_{yv} is the yield strength of the hoop reinforcements, and A_{sv} refers to the sum of the section area of the hoop reinforcement which is in the same cross-section. S is the stirrup space length.

Shear Capacity of Concrete V_c. The experimental results show that, when the displacement angle is less than $1/200$ and the width of crack is not large, the concrete can support 50 percent of the total shear approximately. With the increasing of displacement angle and the increasing of repeated loading, concrete is separated into many small rhombuses by cross-cracks. That makes the compression and shear strength decrease. The final failure of the SRHSHPC columns is that the part of shear-compression area is crushed. However the concrete still has certain shear capacity because the hoop reinforcements and steel have restraint to concrete. The shear-compression pole model is used for calculating the bearing capacity of concrete (Shown in Fig.3). If the quantity λ is large and the quantity θ is small, the shear capacity of

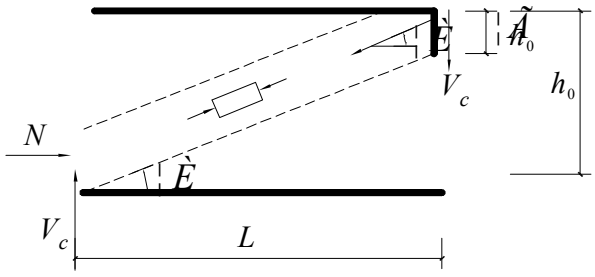

Fig. 3 Shear-compression pole model

concrete is also small. According to the experimental results, the formula can be used as follows: $V_c = \gamma h_0 b h_c \sin\theta = \frac{0.23}{2\lambda+1}\alpha_c b h_0 f_c$. γ refers to the height coefficient of shear-compression area. α_c is the reduction coefficient of the high strength and high performance concrete ($\alpha_c = \sqrt{23.5/f_c}$).

Calculation of Shear Capacity

According to the analysis mentioned above, it is indicated that the main factors affecting the shear capacity of the SRHSHPC columns are shear span ratio, axial compression ratio, stirrup ratio, steel ratio and concrete strength. Based on the experimental results and principle of accumulation, the shear capacity of the SRHSHPC composite columns is established as:

$$V = \frac{0.23}{2\lambda+1}\alpha_c b h_0 f_c + \frac{\lambda+3}{2(\lambda+1)} f_{yv}\frac{A_{sv}}{S}h_0 + \frac{1.48}{\lambda+1.5} f_{sy} t_w h_w + 0.07N \quad (1)$$

where, N refers to the design value of axis compression load. If $N \geq 0.3(f_c A_c + f_s A_s)$, then $N = 0.3(f_c A_c + f_s A_s)$. And $A_c = A - A_s$. A is sectional area of sample. A_s refers to sectional area of steel.

Tab.1 Comparison of calculation and test results

Item	SRC-5	SRC-7	SRC-9	SRC-13	SRC-14	SRC-18
Test value V_s/kN	159.12	228.25	316.12	315.45	327.27	248.25
Calculating value V_c/kN	172.21	239.76	250.69	266.65	245.33	263.56
V_s/V_c	0.924	0.952	1.261	1.183	1.334	0.942

According to the Comparison of calculation and test results (Shown in Tab.1), average value of V_s/V_c is equal to 1.0993, and mean square deviation is equal to 0.1819. It is indicated that the calculated results of shear capacity have a good conformity with test results.

Conclusion

According to the test results and analysis, it is indicated that, there are three failure types for the SRHSHPC composite columns under the combined action of axial compression and horizontal loads. The main factors affecting the shear strength of the SRHSHPC columns are shear span ratio, axial compression ratio, stirrup ratio, and concrete strength. The contributions of those factors which affect the shear capacity of samples are non-linearity. The shear behaviors of the SRHSHPC frame composite columns are excellent, and the calculated results of shear capacity have a good conformity with test results. This project is sponsored by National Natural Science Foundation of China (Grant No. 50378080) and the Educational Office of Shaan'xi Province in China.

Reference

[1] Koichi Minami: *Rational analysis of shear in reinforced concrete columns*. IABSE Colloquium, 1981

[2] Tang Jiuru, Pang Tonghe: *Test and analysis of shear capacity of SRC short-column*. Journal of Southeast University, China, Vol. 21, No.4 (1991), p.74-81

Key Engineering Materials Vols. 385-387 (2008) pp 153-156
© (2008) Trans Tech Publications, Switzerland
doi:10.4028/www.scientific.net/KEM.385-387.153

Numerical Characterization and Validation of vehicle collisions

A. Grimaldi[1, a], A. Soprano[2,b], F. Caputo[2,c]

[1]Accident Investigation, Elasis S.C.p.A, Pomigliano D'Arco (NA), Italy

[2]Dept. of Aerospace and Mechanical Engineering, Second University of Naples, Aversa (CE), Italy

[a]alfonso.grimaldi@elasis.it, [b]alessandro.soprano@unina2.it, [c]francesco.caputo@unina2.it

Keywords: road accident, collision analysis.

Abstract. In the recent years the road accident analysis has been one of the main fields of research for automotive engineering, because of the heavy costs which Europe has to sustain each year in terms of injuries, fatalities and related costs. In this paper, starting from an impulsive model available in literature, a numerical characterization of vehicle collisions and deformation process is proposed and validated, identifying the main parameters which describe the vehicle impact behaviour. The study, conducted by using both empirical and numerical data (simulated trough Ls-Dyna), analyses the impact process by considering several situations, with different severity and geometry of impact; furthermore, with reference to the main parameters which describe the vehicle behaviour in the impact, the authors present a wide analysis, classified according to the severity of impact and to the different parts of the vehicle structure which absorb the impact energy.

Introduction

In the European Union alone 2.000.000 road accidents with physical injuries and 50.000 fatalities occur every year: furthermore, the costs directly related to those accidents were estimated in 162 billions Euros for 1997 alone by the European Transport Safety Council (ETSC), which explain why the present target in Europe is to reduce by 50% the number of accident from 2000 to 2010. Because of the many and complex features, the study of road accidents has to be dealt by means of an integrated approach, studying the aspects and the relations of its main components: vehicle, driver and environment. For those reasons, road safety can be defined as a real challenge for Governments, vehicle industry, insurance companies, customer organizations and so on. Regarding the vehicle industry, today the safety rating is one of most important distinctive features when buying a new car. In this context, all the design activities finalized to the analysis and improvement of the vehicle performance during an impact event are integrated.

With reference to accident reconstruction, it must be pointed out that a reliable evaluation of the crush process, which starts at the moment of the first contact between the vehicle and the opponent (obstacle or other vehicle) and lasts till separation, is one of the main aspects to be analyzed, as deceleration is highest during this phase, increasing up to 20/30g. It is usual today to qualify crush by means of the energy absorbed by the structure of the vehicle, in turn conventionally evaluated through the EES (Equivalent Energy Speed), which represents the velocity required in an impact against a rigid and fixed barrier to obtain the same crush level of the real accident. EES assessment is usually carried out by comparison with specific crash test results, analysing the similarity of the residual crush.

The authors investigated the behaviour of an impacting vehicle, aiming to numerically characterize its performance and the consequent deformations; in particular, taking into account the available accident investigation methodologies, they tried to validate the force and energy analysis methods, together with the most important parameters, considering the vehicle residual crush. The study was carried out by means of a numerical characterization of the vehicle behaviour and it was meant to give a contribution to both road accident analysis and reconstruction methodologies, in

order to be useful during the design activities, helping to improve the energy absorbing structures and the safety systems.

Macmillan's model

As a first step, a preliminary study has been carried out with about the mathematical and physical models, which give an estimation for collision forces and energy distribution through a detailed measure of the residual crush, also taking into account the test crash results and the mechanical properties of the involved structures.

Following that procedure, the authors analyzed Campbell's model [1, 2], which is adopted in Crash 3 code (NHTSA) [3], with a specific attention to the energy evaluation methodology [6], to the vehicle impact characteristic parameters [7, 8] and obviously to the subsequent validation analysis [9].

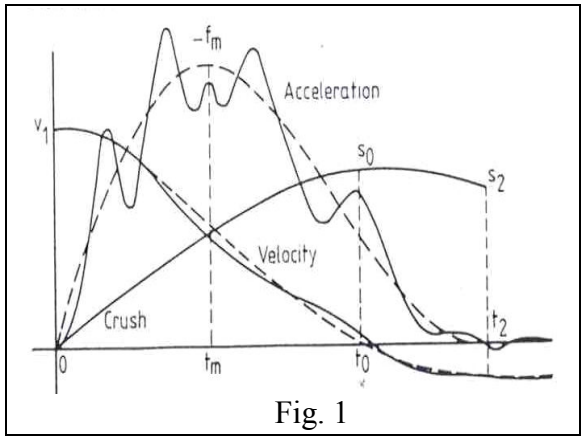

Fig. 1

Moreover, a further study was performed with regard to another physical model, conceived by R.H. Macmillan [10], which, even if somehow analogous to Campbell's model – as it defines, for example, some coefficients to represent the vehicle – is based on different/alternative hypotheses.

Macmillan's model was introduced to analyse the impact dynamics as a contribution to the design of vehicle and restraint systems as well as to accident analyses, in order to define the conditions existing before the impact (i.e. speeds, positions, ecc) on the basis of the position and the state of vehicle and its occupants after the accident. The model, which deals with the case of a centered impact, analyses the "typical" curves of acceleration, velocity and displacement recorded in barrier impact test.

The main objective of the Macmillan model is to obtain an analytical representation for the smoothed curves such as to follow with a sufficient approximation the behaviour of the vehicle, as it is shown in Fig.1. That analytical formulation, through the definition of reference parameters, allows to numerically characterize an impact and to foresee the behaviour of vehicles with different crush characteristics.

All that characterization is based on three parameters, besides the energy restitution coefficient, which are known as the *structural index* β_0, the *crush modulus* C_m and the *impact resistance factor* K_r, on whose basis calibration of the experimental curves can be obtained and through which it is possible to built some useful adimensional groups, among which is the *impact number*, which let us to evaluate the vehicle behaviour in impacts which occur in different conditions, giving a very valuable generalization of the analysis.

Test case application

The peculiarities of MacMillan model were tested with specific reference cases, carrying out a correlation procedure between experimental and numerical data. Therefore, the main target of this phase was to evaluate the model capability to represent numerically and with a good approximation the behaviour of a real vehicle during a crash.

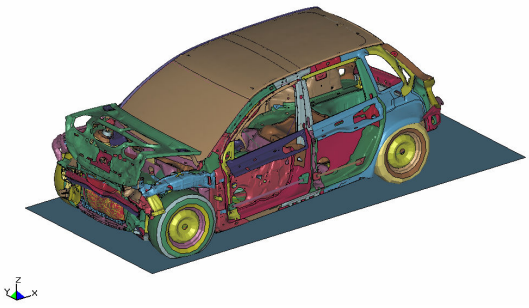
Fig. 3 – Full central impact

To determine the range for the characteristic parameters, The investigation examined several crash tests performed with different impact velocities or with different

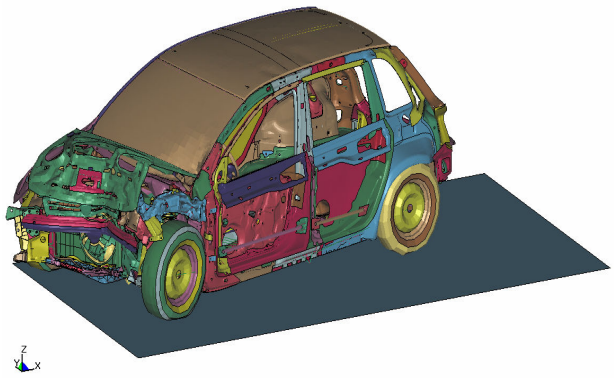

Fig. 4 – Frontal impact with 40% overlap

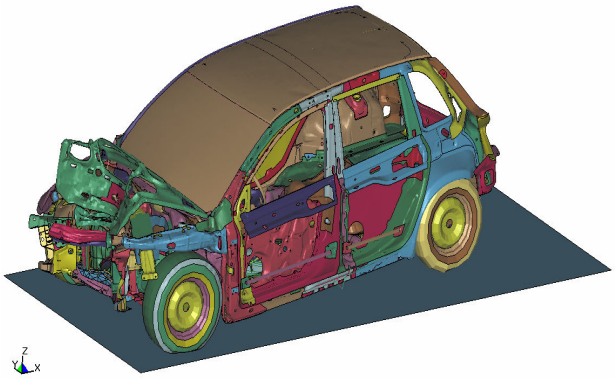

Fig. 5 – Pole centered impact

impact configurations, as it is shown in Fig. 3-5, in order to define the ranges for the experimental parameters.

For each test it was first controlled if the characteristic parameters, which had been evaluated at a given speed following the model procedure, were able to represent the vehicle behaviour also for different impact speeds. In a second phase we examined the variation of the characteristic parameters as a function of impact configuration.

According to the correlation procedure, (in Fig. 6 we show broken line curves to represent the results according to MacMillan model and continuous line curve to represent experimental results for one test) it has been found that the model is able to reproduce, with a fair accuracy, all the reference cases (both experimental and numerical) only if the characteristic parameters are considered as functions of the impact velocity and configuration, as their values largely depend on the residual deformation and on the particular parts of the structure which is involved in the crash.

The said dependence is obviously stressed if values obtained at low speed are used to evaluate or correlate the vehicle behaviour at higher velocities and vice versa.

This can be explained observing the different crashworthy structure involved in the crash according to different speed and to different impact configuration and, moreover, taking account of the effects of deformation speed on several mechanical properties of material of the crashworthy structures.

This said dependence, however, is not to be strictly assumed, as in some cases, even if light differences of the values for most interesting parameters were present, the correlation could be accepted according to the desired approximation.

This circumstance has assessed that, also if an impact number is available, in order to guarantee a complete and correct vehicle characterization several experimental/numerical reference tests have to be available, carried out at different velocities and with different impact configurations; only in this case it is possible to compute the correlation and to define the characteristic parameters as a function of the relevant variables.

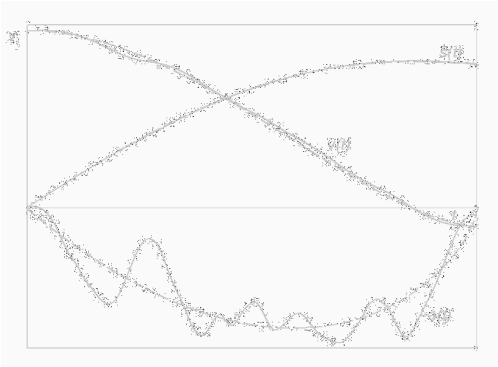

Fig. 6 – Correlation of results

Conclusive consideration

The present analysis, aiming to evaluate the capability of Macmillan model to obtain the main characteristic parameters from the collision test of a real vehicle, brought us to investigate the dependence and variability of the said vehicle parameters as a function of the velocity and the structure directly involved in the impact.

In fact, we found that, with regard to vehicle characterization, it is possible to evaluate the three parameters for a given velocity and impact typology,

which, following the above mentioned correlation, show a sufficiently good approximation also for other impact velocities, if the impact configuration is the same.

In terms of suitability of this methodology, a reliable numerical characterization of the vehicle during an impact can be obtained through the typical testing activity usually performed during the vehicle design and improvement; besides, the numerical test and design tools, for example FEM, allow to extend the investigation range, as it is the case of the present study.

Taking into account the above mentioned variability, the numerical impact characterization, abreast of the prefixed objective, allow to evaluate numerically, with a sufficiently good approximation, all the main entities of interest, for instance the maximum acceleration, the maximum force, the absorbed energy and so on.

Such a condition gives an useful advantage in term of the severity evaluation and of road accident reconstruction. In fact, starting from the residual deformations suffered in the accident and taking into account the configuration of an impact, it is possible to identify, from the vehicle characterization reached as exposed in this activity, the three characteristics parameters which reliably represent the behaviour of the vehicle and consequently, following the formulation proposed in the model, to evaluate numerically all the main values of interest for the impact.

References

[1] K.L Campbell, *Energy Basis for collision severity,* Enviromental activities staff, General Motor Corporation; SAE paper 740565.
[2] Brian G.McHenry, *The algorithms of CRASH*, Southeast Coast Collision Conference, Aug 2001.
[3] *Crash3 User's Guide and technical Manual*, Department of transportation, National Highway Traffic Safety Administration, Washinghton, 1986.
[4] Raymond R. McHenry and Brian G.McHenry, *A revised Damage Analysis Procedure for CRASH Computer Program*, SAE paper 861894.
[5] Aloke Kumar Prasad, *Crash3 Damage Algorithm Reformulation for Front and Rear collision*, TRC of Ohio, SAE paper 900098.
[6] Aloke Kumar Prasad, *Energy absorbed by vehicle structures in side-impacts*, TRC of Ohio, SAE paper 910599.
[7] James A. Neptune, *A method for determining Accident specific Crush Stiffness Coefficients*, Neptune Engineering and J_2 Engineering; SAE paper 940913.
[8] James A. Neptune, *A method for determining Crush Stiffness Coefficients from Offset Frontal and Side Crash Tests*, Neptune Engineering and J_2 Engineering, SAE paper 980024.
[9] Timothy J. Long, *A validation study for the balance Method in determination of stiffness coefficients*, Collision Research and Analysis, SAE paper 1999-01-0079.
[10] R.H Macmillan, *Dynamics of vehicle Collisions*, Interscience enterprise Ltd., 1983.

Key Engineering Materials Vols. 385-387 (2008) pp 157-160
© (2008) Trans Tech Publications, Switzerland
doi:10.4028/www.scientific.net/KEM.385-387.157

Far Field Solution of SH-wave Scattered by a Circular Cavity and a mode III Crack in Half Space

Baitao Sun [1, 2, a], Peilei Yan [1, b], Zailin Yang [1, c]

[1]School of Civil Engineering, Harbin Engineering University, Harbin 150001, China

[2]Institute of Engineering Mechanics, China Earthquake Administration , Harbin 150080, China

[a]sunbt@iem.net.cn, [b]yanpeilei325@sohu.com, [c]yangzailin00@163.com

Key words: Scattering of SH-waves; Green's function; Interaction of circular cavity and crack; Displacement mode of scattering wave for far field

Abstract: Based on Green's function, complex function and multi-polar coordinate system, the far field solution of SH wave scattered by an elastic half space with a circular cavity and a crack at an arbitrary position and orientation is investigated. First, a suitable Green's function is constructed, which is the fundamental solution of the displacement field for a half space with a circular cavity subjected to an out-plane time-harmonic line force at an arbitrary position in half space. Second, by means of crack-division technique, a crack with any location and orientation can be constructed in the region of the half space. The displacement field and stress field are established in the situation of coexistence of circular cavity and crack. At last expressions of far field, such as displacement mode of scattering wave are deduced. Some examples and numerical results are illustrated. The influences of the combination of different media parameters on solutions of far field are discussed.

I Introduction

When a composite material with interface defects is impacted by the dynamic load, the scattering field produced by the interface defects presents many characteristic parameters of the defects such as the defect composition, location and shape, so the research on the scattering far field is important to the geological prospects, seismological investigation, non-destruction evaluation and the other fields. In the ocean acoustics, the scattering far field of the acoustic wave is also used in the under-water survey, object distinguishing and so on. In theory, the scattering solution of elastic waves is one of the basic topics of reverse problems on elastic wave. On the basis of literature [1-4], the paper concentrates on the scattering far field solution of SH-wave by a circular cavity interface inclusion. A new model and a new method are presented in order to investigate deeply on this kind of complex interface.

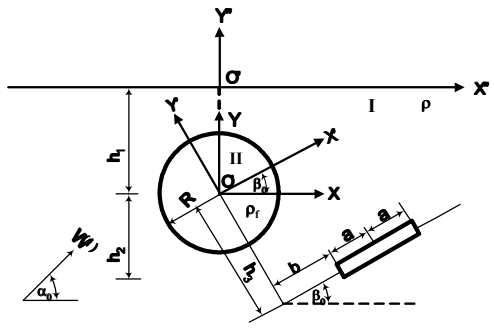

Fig. 1 The half space model with a circular cavity and a crack impacted by SH wave

II Green's Function

The model of half space is shown in Fig.1. It contains a circular cavity and a crack in any position. ρ and c_s are the mass density and the shear wave velocity of the media respectively.

Governing Equation and Boundary Condition. The Green's function in this paper is the fundamental solution

of displacement field for an elastic half space containing a circular cavity impacted by a time harmonic out-plane line source loading at an arbitrary point in half space. The dependence of the displacement function G on time is $e^{-i\omega t}$, and G satisfies the following governing equation

$$\frac{\partial^2 G}{\partial z \partial \bar{z}} + \frac{1}{4}k^2 G = 0 \tag{1}$$

The corresponding stresses are given by

$$\tau_{rz} = \mu\left(\frac{\partial G}{\partial z}e^{i\theta} + \frac{\partial G}{\partial \bar{z}}e^{-i\theta}\right) \qquad \tau_{\theta z} = i\mu\left(\frac{\partial G}{\partial z}e^{i\theta} - \frac{\partial G}{\partial \bar{z}}e^{-i\theta}\right) \tag{2}$$

Boundary conditions

$$\tau_{\theta^* z^*} = 0 \quad \theta^* = 0, \pi \qquad \tau_{rz} = 0 \quad |z| = R \tag{3}$$

Derivation of Green's Function. According to the boundary conditions mentioned above, the fundamental solution satisfying governing equation (1) can be decomposed into two parts, one is the disturbance impacted by out-plane line source loading and the other is the scattered wave excited by the circular cavity.

In a full elastic space, the wave field excited by the out-plane line source loading $\delta(\vec{r} - \vec{r}_0)$ is $G^{(i)}$, which can be described as a known incident wave, it takes the form

$$G^{(i)} = \frac{i}{4\mu} H_0^{(1)}\left(k\left|z'' - z_0''\right|\right) \tag{4}$$

The reflection wave from half-space surface can be expressed as

$$G^{(r)} = \frac{i}{4\mu} H_0^{(1)}\left(k\left|z'' - \bar{z}_0''\right|\right) \tag{5}$$

The scattered wave excited by the circular cavity and satisfying the stress free condition on the horizontal interface automatically can be considered as follows[5-6]

$$G^{(s)} = \sum_{n=-\infty}^{\infty} A_n\left[H_n^{(1)}\left(k|z|\right)\left(z/|z|\right)^n + H_n^{(1)}\left(k\left|z - 2ih_1\right|\right)\left(z - 2ih_1/\left|z - 2ih_1\right|\right)^{-n}\right] \tag{6}$$

in which A_n are unknown coefficients to be determined from the zero-stress condition on the edge of circular cavity. The total wave field is

$$G^{(t)} = G^{(i)} + G^{(r)} + G^{(s)} \tag{7}$$

Substitution of Eqs. (4)、(5) and (6) into Eq.(2), the stresses from incident wave $G^{(i)}$、reflected wave $G^{(r)}$ and scattered wave $G^{(s)}$ can be obtained, and then substituting the expression of stresses in boundary conditions (3), we have

$$\sum_{-\infty}^{\infty} A_n \varsigma_n = \varsigma \tag{8}$$

Multiplying both sides of Eq. (8) by $e^{-im\theta}$ and integrating over the interval $(-\pi, \pi)$, a set of infinite algebraic equations to determine the coefficients A_n can be obtained.

III Scattering of SH-waves by the Circular Cavity and the Crack near the Interface

As shown in fig.1, the steady-state SH-wave $W^{(i)}$ incident on an elastic half space will cause the reflected wave $W^{(r)}$ from the half space surface. In the complex plane, $W^{(i)}$ and $W^{(r)}$ can be given by

$$W^{(i)} = W_0 \exp\{\frac{ik}{2}[(z - ih_1)e^{-i\alpha_0} + (\overline{z} + ih_1)e^{i\alpha_0}]\} \tag{9}$$

$$W^{(r)} = W_0 \exp\{\frac{ik}{2}[(z - ih_1)e^{i\alpha_0} + (\overline{z} + ih_1)e^{-i\alpha_0}]\} \tag{10}$$

Where α_0 is incident angle.

The scattered wave $W^{(s)}$ excited by the circular cavity in the half space can be described by expression (6), in which A_n are unknown coefficients. And the process of solving A_n is the same as that of the Green's function discussed in this paper. The displacement field of the elastic half space with a circular cavity can be written as

$$W = W^{(i)} + W^{(r)} + W^{(s)} \tag{11}$$

For an arbitrary point in the elastic half space, the total stresses from the incident wave $W^{(i)}$, the reflected wave $W^{(r)}$ and the scattered wave $W^{(s)}$ can be solved. If the additional stresses with the same magnitude and opposite direction to the total stresses are applied on the same point, the ultimate stresses of this point are zero. Therefore, when a pair of forces with the same magnitude and opposite direction is loaded along the region where the crack wants to be set, the resultant forces on the region are zero, which can be thought as a crack.

Ⅳ Displacement Mode of Scattering Wave for Far Field

The total scattering wave field includes the scattering wave caused by circular cavity and the scattering wave fields produced by the additional interface force. The total scattering displacement in half space is:

$$W^{(ts)} = W^{(s)} - \int_{(b,-h_3)}^{(2a+b,-h_3)} \tau_{\theta z} G dz' \tag{12}$$

in which G is the expression of Green's function (7).

The scattering wave can be expressed as a series of Hankel function, and their common item $H_n^{(1)}(Kr)$ can be abstracted. Make use of the asymptotic expression of Hankel function as the independent variable is large enough:

$$H_n^{(1)}(z) = (-i)^n \sqrt{2/\pi z} \cdot e^{i(z-\pi/4)} \tag{13}$$

The scattering far-field displacement can be expressed as:

$$W^{(zs)}(r,\theta)=\sqrt{8\pi/kr}\cdot e^{i(kr-\frac{\pi}{4})}F(\theta) \tag{14}$$

Where: $z=r(\cos\theta+i\sin\theta)$, $F(\theta)$ is displacement mode of scattering wave for far field.

V Summary

According to the above theoretical derivation, the numerical examples are investigated and the computational results are provided.

Fig.2. show displacement mode of scattering wave for far field when $kr=0.1,0.5,1.0,2.0$ respectively. When $kr=0.1$ quasi-static , displacement mode of scattering wave for far field is standard semicircle and it show that displacement of each point is the same. As shown in fig.a, crack is just below the circular cavity center, $\alpha=90^0$, displacement mode of scattering wave for far field is symmetrical distribution; b, show the results when crack is declining, $\alpha=90^0$; c, show the results when crack is declining, $\alpha=45^0$.These examples show that, displacement mode of scattering wave for far field tends to be complex with the increase of the wave number.

Fig.3. show the results when $h_2=1.1,3.0,5.0$ respectively. In low frequency, displacement mode of scattering wave for far field tends to be enhancive with the increase of h_2; in high frequency, even $\alpha=90^0$ or $\alpha=30^0$, displacement mode of scattering wave for far field tends to be complex, and the value of the displacement changes greatly.

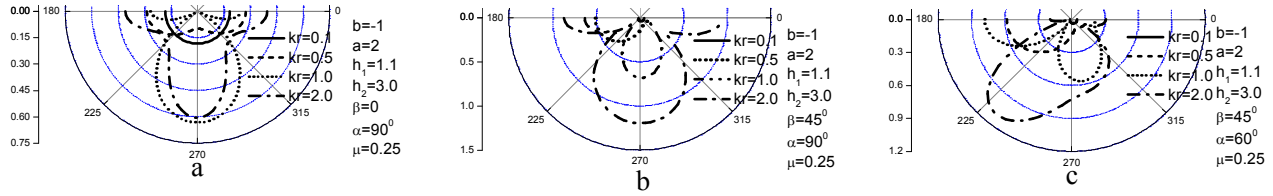

Fig. 2 Far Field Solution of SH-wave Scattered by a Circular Cavity and a mode III Crack

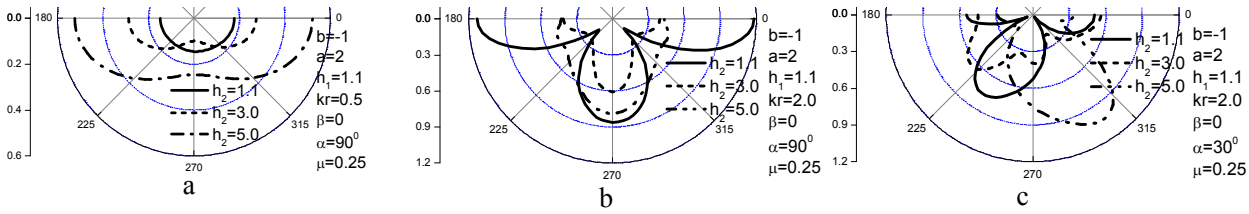

Fig. 3 Far Field Solution of SH-wave Scattered by a Circular Cavity and a mode III Crack

References

[1] Pao Y. H. Elastic Waves in Solids [J]. ASME Journal of Applied Mechanics, 1983,50(4): 1152-1164.

[2] Zheng Zhemin, Zhou Heng, Zhang Hanxin. Trends of Development in Mechanics in the Early 21st Century [J]. Advances in Mechanics. 1995, 25(4): 433-449

[3] Wang Duo, Wang Yuesheng. Recent Progress in Dynamics of Interface [J](in Chinese). Shanghai Journal of Mechanics. 1993,.14(4): 1-15

[4] Wang Ren, Huang Kezhi, Yang Wei, Zheng Quanshui, He Yousheng. An Introduction to the 19th ICTAM [J]. Mechanics and Practice. 1997, 19(1): 57-64

[5] Liu Diankui, Liu Hongwei. Scattering of SH-wave by Cracks Originating at A Circular Hole Edge and Dynamic Stress Intensity Factor [J]. Acta Mechanica Sinica. 1999, 31(3): 292-299

[6] Yang Zailin, Liu Diankui, Shi Wenpu. Scattering far field solution of SH-wave by movable rigid cylindrical interface [J]. Acta Mechanica Solida Sinica. 2002,15(3): 214-220

Key Engineering Materials Vols. 385-387 (2008) pp 161-164
© (2008) Trans Tech Publications, Switzerland
doi:10.4028/www.scientific.net/KEM.385-387.161

Fatigue Strength of Maraging Steel at Elevated Temperatures

T. Iwamoto[1,a], N. Kawagoishi[1,b], N. Yan[2,c],
E. Kondo[1,d] and K. Morino[3,e]

[1] Kagoshima University, 1-21-40 Korimoto, Kagoshima 890-0065, Japan
[2] Sichuan University, Chengdu 610065, China
[3]Tokuyama College of Technology, 3538 Gakuenndai, Shunan 745-3538, Japan
[a] m0781004@mech.kagoshima-u.ac.jp, [b] hiro@mech.kagoshima-u.ac.jp,
[c] yannu@me.tokushima-u.ac.jp, [d] kondo@mech.kagoshima-u.ac.jp,
[e] morino@tokuyama.ac.jp,

Keywords: Fatigue, Maraging Steel, Elevated Temperature, Crack Initiation, Crack Propagation

Abstract. Rotating bending fatigue tests were carried out to investigate the effects of temperature on the fatigue strength and the fracture mechanism of an 18 % Ni maraging steel at room and elevated temperatures of 473K and 673K. Fatigue strength was higher at elevated temperatures than at room temperature, though static strength was decreased by softening at elevated temperature. There was no effect of temperature on crack morphology and fracture mechanism. On the other hand, during fatigue process at elevated temperature, the specimen was age-hardened and the specimen surface was oxide. That is, the increase in fatigue strength at elevated temperature was mainly caused by the increase in hardness due to age-hardening and suppression of a crack initiation due to surface oxidation.

Introduction

Maraging steel is hardened by the precipitation of intermetallic compounds in martensitic structure. The steel has the highest tensile strength and high ductility among steels [1],[2]. Therefore, this steel has been applied to materials for parts and components of machines used under sever service conditions, e.g. die steel, major parts of engine for aircraft, etc. It is significant to clarify the fatigue properties at elevated temperature, because the microstructure of the age-hardened steel may be affected by the thermal exposure in fatigue process [3]. However studies on fatigue properties at elevated temperature were very limited.

In the present study, rotating bending fatigue tests were carried out at elevated temperatures to investigate the effects of temperature on the fatigue strength and the fracture mechanism of an 18 % Ni maraging steel.

Material and experimental procedures

Material used was a 300 grade maraing steel whose chemical composition in mass percent was 0.005C, 0.03Si, 0.04Mn, 0.002S, 18.69Ni, 4.89Mo, 8.92Co, 0.10Al 0.91Ti and remainder Fe. The material was solution treated at 1123K for 5.4ks, then aged at 753K for 48ks. The mean grain size was about 21μm. Table 1 shows the mechanical properties at room and elevated temperatures.

Fig. 1 shows shape and dimensions of specimen. Specimens have a blunt and narrow notch to localize the crack initiation site. Prior to fatigue testing, all of the specimens were electro-polished about 20μm from the surface layer to remove the work affected layer and make the surface observation easier.

Observation and measurement of the change in specimen surface and crack length due to stress repetitions were carried out by plastic replication technique. Fatigue tests were carried out using the Ono type rotating bending fatigue testing machine with electric furnace (capacity: 100 Nm, frequency: 50 Hz). The fatigue tests were carried out at room temperature, 473K and 673K. The temperature was automatically controlled within the deviation of ±5K.

Table 1 Mechanical properties

Temperature	$\sigma_{0.2}$(MPa)	σ_B(MPa)	ψ(%)	δ(%)
R.T.	2073	2156	47	8.5
473K	1775	2025	53	4.2
673K	1641	1837	54	4.3

$\sigma_{0.2}$: 0.2% proof stress σ_B : Tensile strength

ψ: Reduction of area δ : Elongation

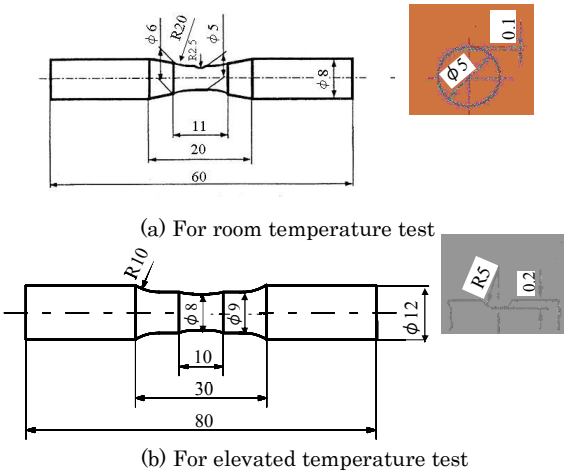

Fig.1 Shape and dimensions of specimen

Results and discussion

Figs. 2 and 3 show S-N_f curves and σ_a/σ_B-N_f curves at room temperature, 473K and 673K, where σ_B is the tensile strength at each temperature. Fatigue strength was higher at elevated temperatures than at room temperature except for the short life region in spite of decrease in static strength due to softening at elevated temperature. Endurance ratios, σ_{w0}/σ_B, were 0.28, 0.37 and 0.41 at room temperature, 473K and 673K, respectively, where fatigue limits, σ_{w0}, was defined by the fatigue strength at 10^7. Moreover there was no or little difference between fatigue strengths at 473K and at 673K. That is, the change in static strength due to elevated temperature was not reflected to the change in fatigue strength.

Figs.4 and 5 show examples of crack morphology and fracture surface at room temperature and 673K. There is no difference in the feature of crack morphology and fracture mechanism. Therefore, it is difficult to explain the temperature dependence on the fatigue strength from these results. On the other hand, surface oxidation and change in aged condition may be yielded in addition to softening at elevated temperature.

Actually, the specimen surface was heat tinted and hardened after fatigue test at elevated temperature.

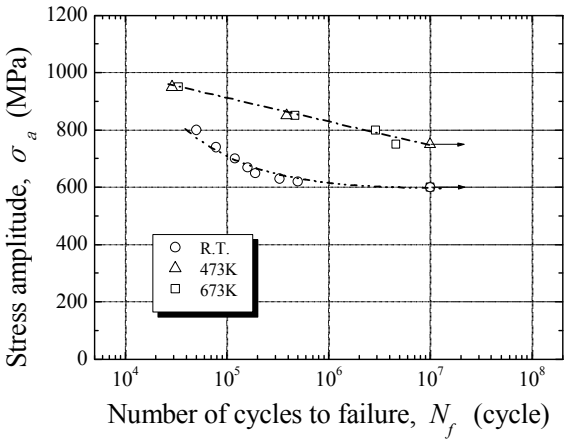

Fig. 2 S - N_f **curves**

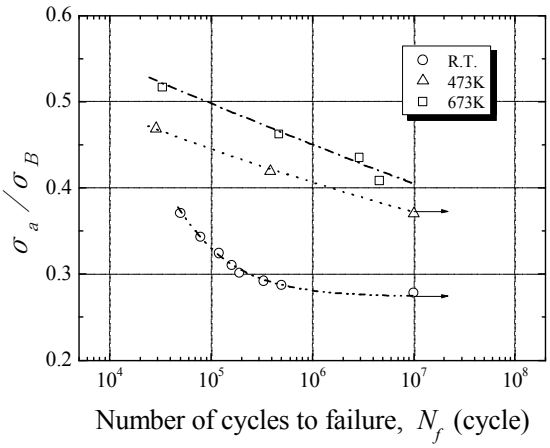

Fig. 3 σ_a / σ_B - N_f **curves**

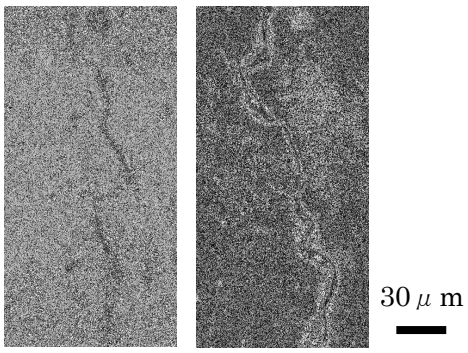

(b) R.T. σ_a**=950MPa** N_f**=8.59×10^4**

(a) 673K σ_a**=950MPa** N_f**=3.33×10^4**

Fig.4 Crack morphology

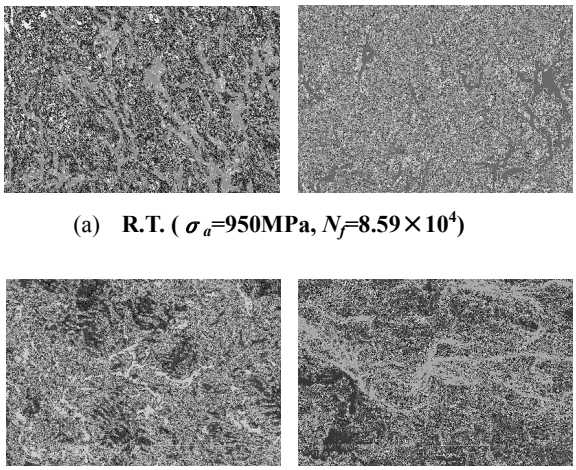

(a) **R.T. (** σ_a**=950MPa,** N_f**=8.59×10^4)**

(b) 673K (σ_a**=950MPa,** N_f**=3.33×10^4)**

Fig.5 Fracture surfaces

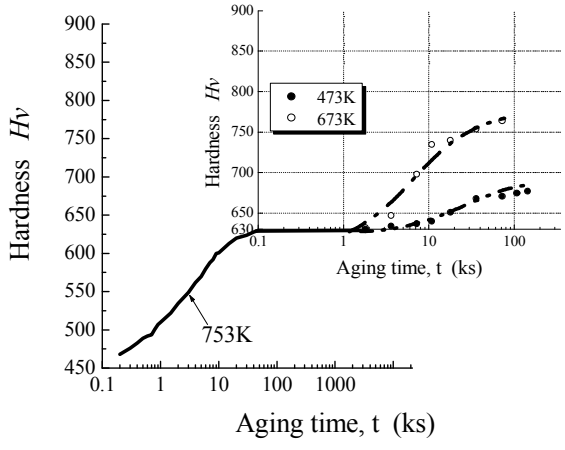

Fig.6 Aging curves

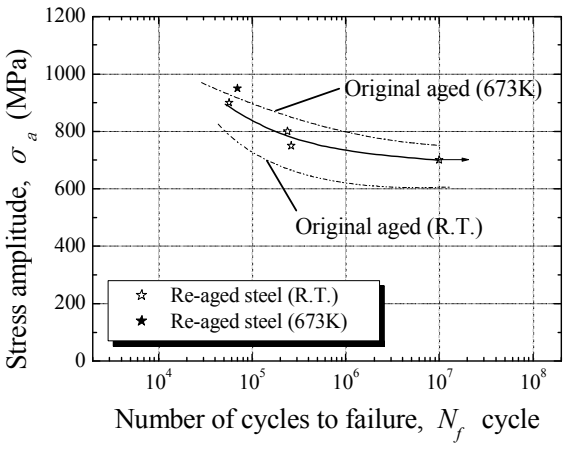

Fig.7 S - N_f **curves of re-aged steel**

Fig. 6 shows aging curves which measured at room temperature after heating to original aged steel at 473K and 673K for appropriate time. At both temperatures, steels were hardened.

These results indicate that the steel was hardened by aging and the specimen surface was oxide at elevated temperature, suggesting that the increase in fatigue strength at elevated temperature may be caused by the increase in hardness due to age-hardening in addition to suppression of crack initiation by surface oxidation. In order to confirm the above stated consideration, fatigue tests were carried out using specimens re-aged at 673K for 180ks, corresponding time to 10^7 stress repetitions, to the original aged specimens. The hardness of re-aged specimen was about HV760 before fatigue test.

Fig. 7 is results showing the effect of age-hardening during fatigue process at elevated temperature on fatigue strength. In the figure, open and solid symbols mean the results of re-aged specimens tested at room temperature and at 673K, respectively. And the results of original aged specimens were also shown by lines only. Fatigue strength was increased by re-aging not only at room temperature but also at 673K even in short life region. From these results, the main reason for the increase in fatigue strength at elevated temperature is age-hardening during fatigue process at elevated temperature. Therefore, it can be explained from the insufficient age-hardening due to short aging time that there was small difference in fatigue strength between room and elevated temperatures in short life region. Moreover, no or little difference in fatigue strength between 473K and 673K can also explained from that there were two opposite effects of softening and age-hardening on the strength of material at elevated temperature.

Conclusions

In order to investigate the fatigue properties of maraging steel at elevated temperature, rotating bending fatigue tests were carried out at room and elevated temperatures of 473K and 673K. Main results were concluded as follows;

1. Fatigue strength was higher at elevated temperatures than at room temperature despite of decrease in static strength due to softening.
2. There was no difference in fracture mechanism at all of the temperatures tested.
3. Material was hardened by aging during fatigue process at elevated temperature. This is a main reason for the increase in fatigue strength at elevated temperature.

References

[1] J.M. Marder and A.R. Marder, Trans of Metals, Vol. 62 (1969), p.1

[2] Y. Kawabe, Bull. of Japan Institute of Metals, Vol. 14 (1974), p.767

[3] D. Zheng and H. Ghonem, Metall. Trans. A, Vol.23A (1992), p.3169

Key Engineering Materials Vols. 385-387 (2008) pp 165-168
© (2008) Trans Tech Publications, Switzerland
doi:10.4028/www.scientific.net/KEM.385-387.165

Fatigue-Cumulative Damage Model of RC Crane Girders Strengthened with FRP Strips

Shansuo ZHENG[a], Bin WANG[b], Lei LI[c], Liang ZHANG[d], and Piji HOU[e]

School of Civil Engineering, Xi'an University of Architecture and Technology, Xi'an 710055, China

[a]zhengshansuo@263.net, [b]wangbin1853@sohu.com, [c]lilei1004@163.com, [d]gztrzl@126.com, [e]pijihou@163.com

Key words: Cumulative damage model; CFRP strip; Flexural rigidity; RC crane girder

Abstract. The cumulative damage of the reinforced concrete (RC) crane girders occurred by overload, fatigue and other reasons in service may deteriorate the safety of RC crane girders seriously, so it is necessary to analyze the damage mechanism and rationally reinforce them in good time. In this paper, RC crane girder strengthened with CFRP strips is taken as a target, and the mechanical performance degradation under fatigue load is studied. According to the basic theory of continuum damage mechanics, a damage variable is defined by flexural rigidity, and fatigue- cumulative damage model, which describes the process of damage and fracture, is established. The variation law of cumulative damage of RC crane girders strengthened with FRP strips under crane load is discussed, and the failure patterns such as concrete cracking, debonding between CFRP strips and concrete, yield of steel bars etc., are studied. The criterion which can be used to estimate the cumulative damage degree of strengthened RC crane girders is proposed. Finally, the evolution of the fatigue damage in the RC crane girders strengthened with CFRP strips is numerically simulated, and the results show that the proposed model can correctly describe the damage and failure process of strengthened RC crane girders. The research will provide a reference for the damage analysis and reinforcement of RC crane girders strengthened with CFRP strips.

Introduction

RC crane girder is one of the important structural members in industrial factory building. The working condition of crane may affect the production efficient of the factory. RC crane girder exits serious fatigue damage phenomenon under heavy loading, which is discovered in the relevant researches [1, 4]. Under the repeated loading, crane girder may be subjected to fatigue failure, which is a process of fatigue cumulative damage essentially. Therefore, the proper reinforcement approaches are very important to increase the fatigue life. Owing to high rigidity, strength, good fatigue-resistance performance, etc., CFRP strips as an advance reinforcement material is studied and used extensively in RC members. Under the repeated loading, the original flaw of RC crane girder may develop into macro-crack with damage increase and rigidity degradation gradually [2, 3]. If the cumulative damage value reaches a critical value, RC crane girder or the whole structure may be failed. In this paper, the degree of the rigidity degradation is employed to describe the fatigue damage of RC crane girder based on damage mechanics. The fatigue damage is regarded as a random process according to Miner's cumulative damage. Based on the cumulative damage model, the evaluation model for fatigue life of RC crane girder strengthened with CFRP strips is proposed.

Fatigue Cumulative Damage Model

In residual rigidity model, the stress redistribution can be reasonably considered and three stages of structural members (damage nucleation, damage stable and unstable expansion) can be easily represented. Moreover, the rigidity can be measured through deflection, frequency, etc.. Therefore, the fatigue life of RC members can be precisely predicted by residual rigidity. Therefore, the damage state of RC crane girder strengthened with CFRP strips can be described through the flexural rigidity

of the strengthened crane girder. As Lemaitre's classical damage equation, the damage variable can be expressed as

$$D = 1 - \frac{B_N}{B_0} \tag{1}$$

where, D is the value of the cumulative damage; B_0 is the original flexural rigidity when the member has no damage; B_N is the residual flexural rigidity after the N times of load cycle. The cumulative damage variable D aims at every circle obviously, the variable range is from 0 to 1: $D = 0$ corresponds to the no damage state of members, and $D = 1$ corresponds to the fatigue failure state.

The mid-span deflection of the strengthened RC crane girder is given by [3]

$$f = \alpha \frac{M}{B_N} l_0^2 \tag{2}$$

After the N times of the load cycle the residual flexural rigidity B_N can be obtained

$$B_N = \alpha \frac{M}{f_N} l_0^2 \tag{3}$$

where, l_0 is the span of the RC crane girder; M is the value of the moment at pure bending part for RC crane girder strengthened with CFRP strips; α is the deflection factor related to load mode and supporting condition, In this paper, $\alpha = 23/216$.

The fatigue damage variation curve of the strengthened girder should be satisfied with three-stage variation law in the whole loading circle. The cut-off points should be fixed at the 10% and 90% of the life curve [4]. So the fatigue damage evolution process of strengthened crane girder can be divided into three phases which are damage nucleation, damage stable and unstable expansion. Different test results indicate that three phase law described by residual rigidity is more reasonable. On the basis of the above discussion, the three phase linearity cumulative damage model can be established as follow

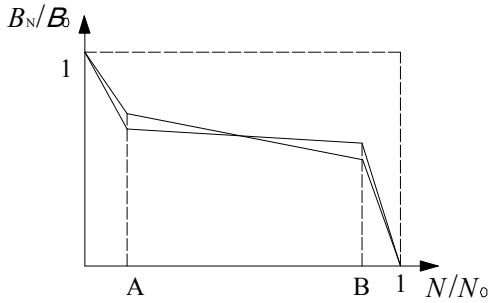

Fig.1 Ideal three-stage curve

$$B_N/B_0 = \begin{cases} k_1 x & (0 \le x \le 0.1) \\ B_{A,N}/B_0 - k_2(x - 0.1) & (0.1 < x \le 0.9) \\ B_{B,N}/B_0 - k_3(x - 0.9) & (0.9 < x \le 1.0) \end{cases} \tag{4}$$

where , k_1, k_2, k_3 are damage increment rates of the first, second and third deformation stage, respectively; according to the test results of literature [3], the value of 1.187, 0.203, 0.096 is used in this paper, B_N/B_0, $B_{A,N}/B_0$, $B_{B,N}/B_0$ are the value of the standardized residual rigidity under any cyclic loading, the end of the first and second phase, respectively; $B_{A,N}$, $B_{B,N}$ are the residual rigidity corresponding to the point A and B in the Fig.1, respectively; All these can be obtained by Eq. (3). $x(=N/N_0)$ is the ratio of the loading cycle times to fatigue life.

Fatigue Life Analysis Based on Cumulative Damage Model

At present, there are many methods about the evaluation of residual fatigue life for structure members. All these methods can be summarized into two means as follows: the first one is based on the $S-N$ curve and the principle of cumulative damage; the other one is based on fracture mechanics. The $S-N$ curve is extensively used in practice engineering, because of the advantages of direct-viewing, use- convenience. This method, usually obtained through constant amplitude circle load test for structure or material, is the most fundamental approach to describe the fatigue durability of structure or material. It reflects the relationship between the constant-amplitude stress range and the stress circle times, and it can be expressed as

$$N_i S_i^m = A \tag{5a}$$

The log-log form of the above equation is

$$\log N_i = \log A - m \log S_i \tag{5b}$$

where, N_i is the invalidation circle times under the circle of constant-amplitude stress range S_i; m is the fatigue strength index; A is the performance parameter of material.

The repeated loading that acts on crane girder is usually irregular. This means the load form can not be regard as constant-amplitude circle load. Under the crane cycle loading, the Miner linearity cumulative damage theory can be described as following

$$D = \sum_i \Delta D_i = \sum_i \frac{n_i}{N_i} \tag{6}$$

where, D is the value of cumulative damage; N_i is the fatigue life of strengthened girder under constant-amplitude stress range S_i; n_i is practical circle times corresponding to constant-amplitude stress range S_i, $N = \sum_i n_i$.

Substituting Eq. (5a) into Eq. (6) yields

$$D = \sum_i \frac{n_i S_i^m}{A} = \frac{N S_e^m}{A} \tag{7}$$

$$S_e^m = \sum_i n_i S_i^m \Big/ N \tag{8}$$

where, S_e is the value of equivalent constant-amplitude stress range.

Based on the cumulative damage model, substituting Eq. (7) into Eq. (1) yields the expression of $B_N/B_0 - N$ curve

$$N S_e^m = A\left(1 - \frac{B_N}{B_0}\right) \tag{9a}$$

The log-log form can be expressed as

$$\log N = \log A + \log\left(1 - B_N/B_0\right) - m \log S_e \tag{9b}$$

where, A, m are obtained by test or the specification, the value of equivalent constant-amplitude stress range S_e is obtained statistically based on the stress time-history or load history curve.

Result Analysis of Fatigue Life

The flexural rigidity of RC crane girder strengthened with CFRP strips takes on obviously the three-stage development law in fatigue cumulative damage: damage nucleation of structure and members, damage stable and unstable expansion, respectively. In the first stage, the advantage of CFRP strips doesn't be made full use of. Therefore, the concrete initial crack develops continuously and the mid-span deflection of crane girder increases rapidly. In the second stage, the strain of the CFRP strips increases rapidly and CFRP is subjected to great tension. Hereby, the crack develops stably, the deflection of crane girder increases relatively steady and the flexural rigidity of strengthened crane girder decrease slowly. In the third stage, after debonding between CFRP strips and concrete, the deflection of the mid-span increases rapidly and then steel bars yield, eventually, the strengthened RC crane girder is destroyed.

In the course of calculation, the standardized residual rigidity and fatigue damage of RC crane girder strengthened with CFRP strips keep to linearly varying law in the I, II, III stage, respectively. Based on fatigue cumulative damage model supplied in this paper and used the test data [3], the value of $S_e = 120$, 150, 180 (MPa) are used in this paper. Finally, the value of the standardized residual for the strengthened RC crane girder in each phase is obtained through Eq. (3), Eq. (4), Eq. (9) (see Fig. 2). In different damage stages, the standardized residual rigidity is linear relationship with load cycle times. Hence, the residual fatigue life can be predicted easily through comparing the load cycle times of the strengthened RC crane girder with B_N/B_0 , $B_{A,N}/B_0$, $B_{B,N}/B_0$.

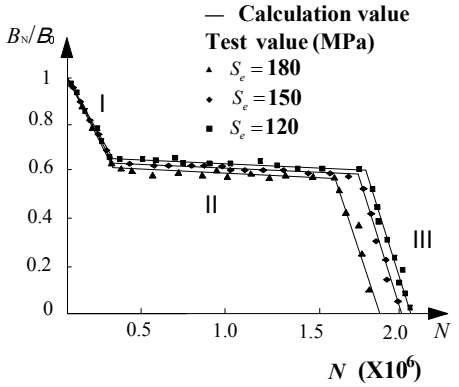

Fig.2 Comparison of test resluts and calculation resluts

Conclusion

In this paper, the three-stage cumulative fatigue damage model for RC crane girder strengthened with CFRP strips is established. Based on the Miner linearity cumulative damage theory, the $B_N/B_0 - N$ curve is obtained through the three-stage cumulative fatigue damage model. Comparing the model with test data, the calculation model proposed in this paper can well describe the evolution of the fatigue cumulative damage for RC crane girder strengthened with CFRP strips. This project is sponsored by National Natural Science Foundation of China (Grant No. 50378080) and the Educational Office of Shaan'xi Province in China (Grant No. 06JK263).

References

[1] Yao Guowen, Huang Peiyan: *A Study on the faatigue behavior of RC beams strengthened with fiber laminates*. Joural of China Civil Engineering, China, Vol. 39, No. 4(2006), p.35-38

[2] Xing Kuntao, TongXiaoli: *Fatigue reliable life assement of steel cran structures under crane loading*. Chinese Journal of Computational Mechanics, China, Vol. 21, No.5 (2004), p.636-640

[3] TANG Hong-we, LI Shi-bin: *A Fatigue Cumulative Damage Model of RC Beam Based on Stiffness Degradation*. Journal of China Railway Socity, China, Vol. 29, No.3 (2007), p.84-88

[4] Zhang Qingzhong: *The fatigue behaviors of crane RC beams strengthen by CFRP*. Civil Eng. Thesis, Jiang Su University, China (2007)

Key Engineering Materials Vols. 385-387 (2008) pp 169-172
© (2008) Trans Tech Publications, Switzerland
doi:10.4028/www.scientific.net/KEM.385-387.169

FEM Analysis for Sealing Performance of hydraulic pressure Brake Hose Caulking Portion

Hirofumi KAWAHARA[1.a], Shinpei YOSHIMURA[1.b], Nao-Aki NODA[1.c]
[1] Department of Mechanical Engineering, Kyushu Institute of Technology,
1-1 Sensui-cho, Tobata-ku,Kitakyushu-si, 804-8550 Japan
[a]g344121h@tobata.isc.kyutech.ac.jp, [b]d104136s@tobata.isc.kyutech.ac.jp
[c]noda@mech.kyutech.ac.jp

Keywords: Stress analysis, Finite element method, Sealing performance, Brake hose, Hose life.

Abstract. Usually, development of automobile brake hose and power steering hose has been realized through evaluating several actual prototype hoses experimentally. Recently, high durability and high development effect for brake hose has been required because periodic exchange for the brake hose has not been requested any more. In this study, therefore, stress analysis by FEM is performed to the crimped portion of hydraulic pressure brake hose in order to promote the development of the automobile hoses more efficiently. It is found that large normal stresses σ_r in the radial direction appear at the crimped portion between the nipple and inner rubber. The results suggest that several grooves on the nipple surface may be useful because they cause large σ_r, which may improve the sealing performance. The effect of permanent deformation of the rubber on the sealing performance is discussed by assuming initial deformation of the rubber at the crimped portion.

1. Introduction

Hydraulic brake hoses have been used in automobiles to conduct the oil pressure generated by the master cylinder to the brake as shown in Fig. 1. Rubber material has high flexibility with no volume change, which is called incompressibility. Because of this property, at the caulking portion in Fig. 2(a), high compressible stresses appear between the nipple and inner rubber, which causes high sealing performance. Previously brake hoses in automobiles have been changed in a few years. However, a new regulation enacted in 1995 has not asked this regular renewing anymore.[1] Therefore high durability of brake hose is necessary for recent automobile. Brake hose at the crimped portion consists of nipple, sockets, inner rubber, reinforced layer, and outer rubber, as show Fig. 2. The nipple in Fig. 2(a) usually has grooves, which may improve sealing performance. Usually, development of automobile brake hose has been realized by evaluating a lot of materials and shapes of nipple and crimping socket experimentally.[2]

In this study, therefore, stress analysis by FEM will be performed for the crimped portion of hydraulic pressure brake hose in order to promote the development of the automobile hoses more efficiently.

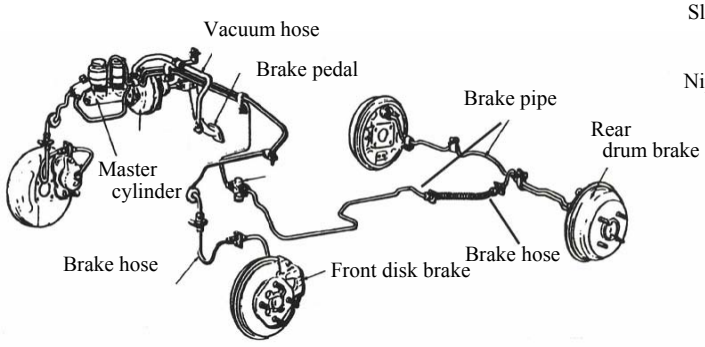

Fig. 1 Brake hose in automobiles

(a) Sockets consisting of nipple and sleeve

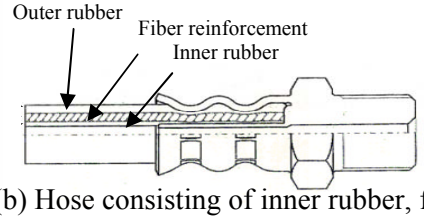

(b) Hose consisting of inner rubber, fiber reinforcement and outer rubber

Fig. 2 Hydraulic brake hose

2. Method of Analysis

As shown in Fig. 2(b), the brake hose consists of three layers, that is, the inner rubber, reinforced layer, and the outer rubber. Usually the stress-strain relation of rubber is expressed by using Mooney-Rivlin material model, Ogden material model, or Arruda-Boyce material model. In this study, Arruda-Boyce material model is applied. Figure 3 shows the stress-strain relations for inner and outer rubbers. It is seen that the experimental and analytical results for inner rubber and outer rubber are in good agreement. The reinforced layer is composed of a complicated net structure of Polyvinyl Alcohol (PVA) material.(see Fig. 4 and Fig. 5) In this study, therefore, the reinforced layer is modeled as an anisotropic elastic material whose elastic constants are E_r, $E_\theta=E_z$, $\nu_{r\theta}$, $\nu_{\theta z}$, ν_{zr}. Most suitable elastic consultants will be found from the displacement at the caulking portion assuming that these three layers are bonded completely. The coefficients of friction are assuming to be 0.3 between outer rubber and sleeve, and between inner rubber and nipple. Table 1 shows materials and elastic constants of each layer. The sleeve material is S10C (JIS) whose Young's modulus is 207[GPa] and the Poisson ratio is 0.29. Nipple can be assumed as a rigid body because elastic deformation is found to be small. Here, four nodes axi-symmetric elements and applied as shown in Fig. 5. Sealing as performance of brake hose may be evaluated by normal stress appearing between nipple surface and the inner rubber. Three types of nipples with brake hoses are considered, that is, no groove, four grooves, and eight grooves. (see Fig. 6)

3. Results and Discussion

Table 2 shows thicknesses of three layers with varying material constants of reinforced layers. The error is indicated in the parenthesis. When $E_r=40$[MPa], $E_z=E_\theta=100$[MPa], $\nu_{r\theta}=\nu_{zr}=\nu_{\theta z}=0.2$, the thicknesses coincide with the experimental results within 10%.

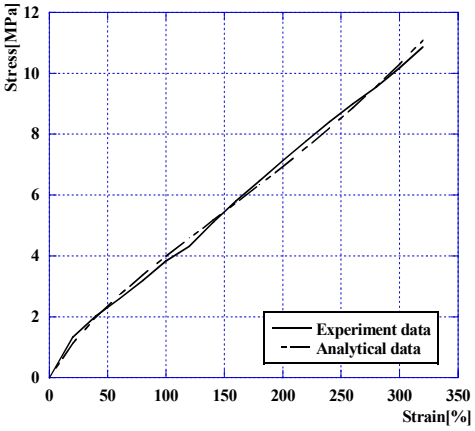

(a) Inner rubber

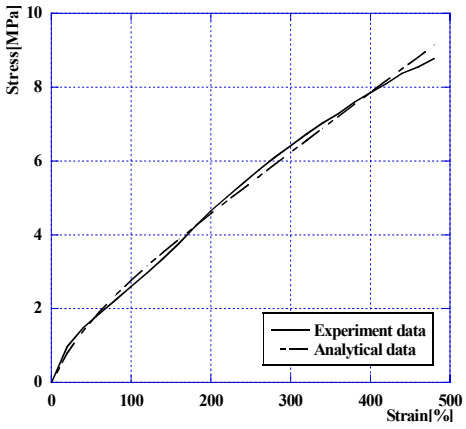

(b) Outer rubber

Fig. 3 Stress strain relation of the rubber

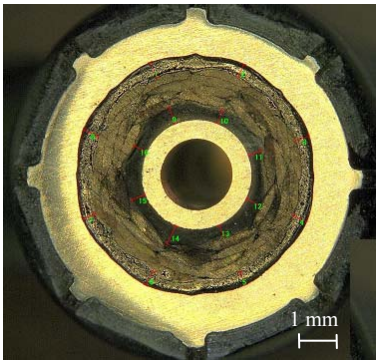

(a) Picture of first crimped portion A-A' in Fig .5

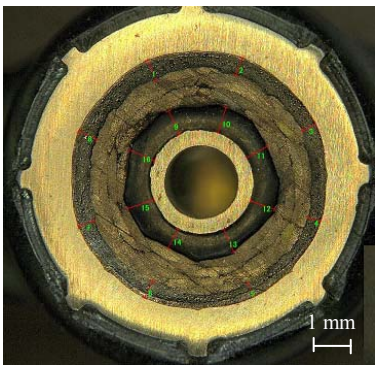

(b) Picture of second crimped portion B-B' in Fig .6

Fig. 4 Cross section at crimped portions

Table 1 Material data used in EFM analysis

	Material	Young's modulus (GPa)	Poisson's ratio
Outer rubber	EPDM	Use of experimental data	Use of experimental data
Inner rubber	EPDM	Use of experimental data	Use of experimental data
Sleeve	S10C	207	0.29
Nipple and Caulking tool	Rigid body		

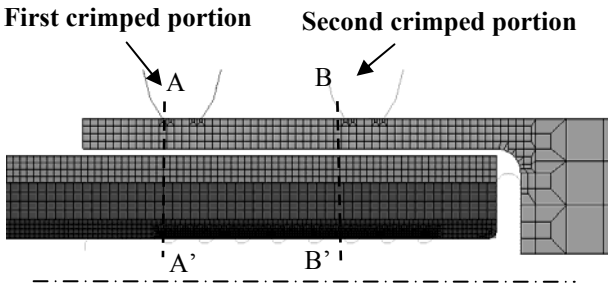

Fig. 5 FEM mesh model

Figure 6 indicates the principal strains for three models, that is, no groove, four groove, and eight grooves models. The maximum strain is about 60% for both no groove, and four groove models. For eight groove model the maximum strain 100% appears at No.8 grooves because the first caulking portion is just above the No.8 grooves. Figure 7 shows the normal stress σ_n appearing between inner rubber and nipple. The broken line shows the results of no groove, the dashed-dotted line shows the results of four grooves, and the solid line shows the results of eight grooves. From Fig. 8 it is found that values of the normal stress σ_n is not changed at the same position of the different models. The maximum the normal stress σ_n for eight groove models is larger than the maximum σ_n for four groove models. The largest the normal stress σ_n at the No.8 groove may be useful for prevent oil leakage.

Table 2 Thickness of three layers

(a) First crimped portion

E_r [MPa]	E_θ=E_z [MPa]		Inner rubber	Reinforcement	Outer rubber
40	100	Thickness [mm]	0.436	1.044	0.461
		Error [%]	(4.803)	(3.956)	(-6.713)
40	80	Thickness [mm]	0.43	1.03	0.483
		Error [%]	(6.113)	(5.244)	(-11.806)
60	100	Thickness [mm]	0.404	1.103	0.437
		Error [%]	(11.790)	-1.471941122	-1.15740741
40	120	Thickness [mm]	0.444	1.055	0.445
		Error [%]	(3.057)	(2.944)	(-3.009)
60	120	Thickness [mm]	0.415	1.11	0.421
		Error [%]	(9.389)	(-2.116)	(2.546)
Experiment		Thickness [mm]	0.458	1.087	0.432

(b) Second crimped portion

E_r [MPa]	E_θ=E_z [MPa]		Inner rubber	Reinforcement	Outer rubber
40	100	Thickness [mm]	0.657	1.147	0.506
		Error [%]	(10.123)	(-9.866)	(0.197)
40	80	Thickness [mm]	0.66	1.133	0.531
		Error [%]	(9.713)	(-8.525)	(-4.734)
60	100	Thickness [mm]	0.635	1.201	0.483
		Error [%]	(13.133)	(-15.038)	(4.734)
40	120	Thickness [mm]	0.66	1.16	0.487
		Error [%]	(3.057)	(2.9439)	(-3.009)
60	120	Thickness [mm]	0.646	1.207	0.468
		Error [%]	(11.628)	(-15.613)	(7.692)
Experiment		Thickness [mm]	0.731	1.044	0.507

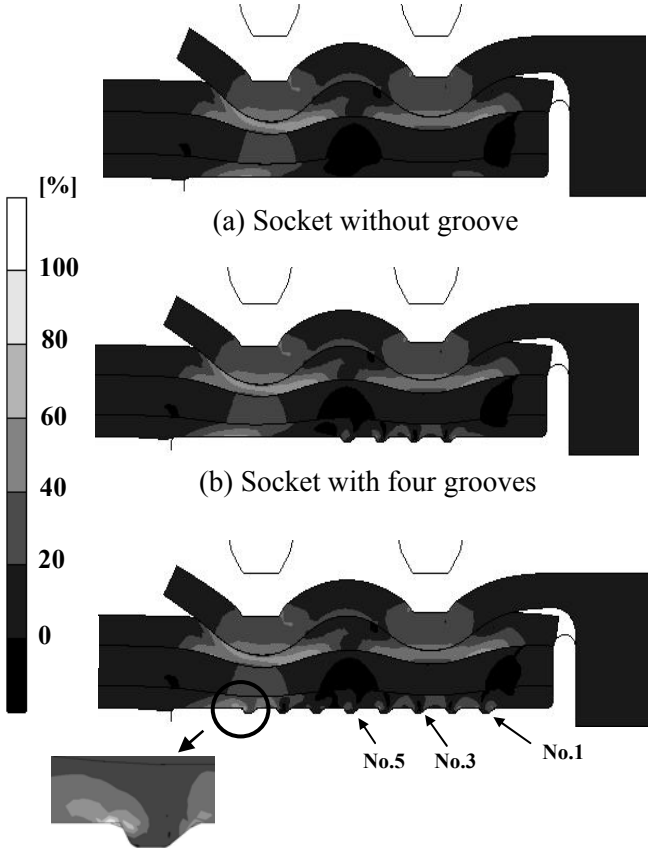

(a) Socket without groove

(b) Socket with four grooves

(c) Socket with eight grooves

Fig. 6 Principal strain distributions

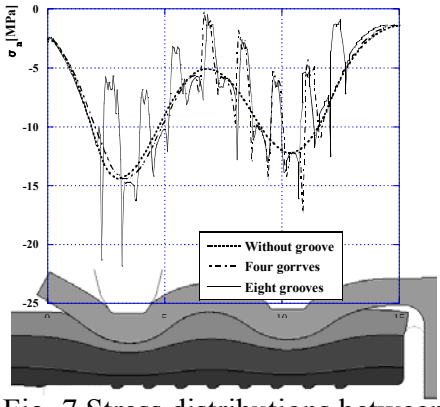

Fig. 7 Stress distributions between inner rubber and nipple

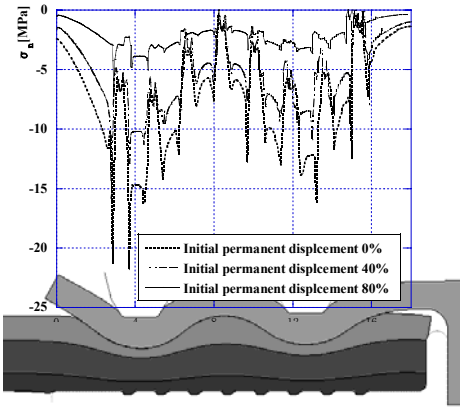

Fig. 9 Analysis result of re-crimped model

(a) Brake hose used many years

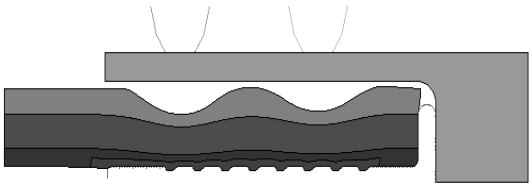

(b) Shape of re-crimped model (compression set rate 80%)

Fig. 8 (a) Real shape of the brake hose used many years and (b) re-crimped model

Figure 8(a) shows an example of permanent deformation after using many years. In this study, the effect of this permanent deformation on the sealing performance is investigated. Here, we assume initial deformation as show in Fig. 8(b). Then, the FEM analysis is performance by applying the displacement at the crimped portions. In this analysis, we assume the inner rubber, reinforcing layer, and the outer rubber have the same elastic properties of new materials.

Figure 9 shows the normal stress σ_n between nipple and inner rubber after re-crimped. The broken line shows the results of no permanent deformation, the dashed-dotted line shows the results of 40% permanent deformation, and the solid line shows the results of 80% permanent deformation. When the permanent deformation is 80%, the normal stress is only about 20% of the value of no permanent deformation, and therefore may deteriorate sealing performance seriously.

4. Conclusions

(1) The reinforcement layer was assumed as an anisotropic elastic material with varying the elastic constants. Then, the thickness at the crimped portions coincides with the experiment with 10%. The FEM results are found to simulate real brake hose accurately.

(2) The maximum the normal stress σ_n for eight groove models is larger than the maximum σ_n for four groove models. The largest the normal stress σ_n at the No.8 groove may be effective for preventing oil leakage.

(3) The effect of this permanent deformation on the sealing performance was investigated. When the permanent deformation is 80%, the normal stress is only about 20% of the value of no permanent deformation, and therefore may deteriorate the sealing performance seriously.

References

[1] Ishikawa, T., Hagiwara, H., Uno, A., Brake Hose with High Durability and Low-cost, Hitachi Cable, No.20 (2001) , pp.137-142

[2] Ishii, K., FEM Analysis for Crimp of Hydraulic Brake Hose, Technical Report of Meiji Rubber & Chemical, Vol.44 (2003) , pp.3-6.

Key Engineering Materials Vols. 385-387 (2008) pp 173-176
© (2008) Trans Tech Publications, Switzerland
doi:10.4028/www.scientific.net/KEM.385-387.173

Fitness-For-Service Assessment of the Pipelines with Localized Geometric Imperfections such as Buckles and Wrinkles

Yang Zhengmao[a], Kumar Shashi Bhushan[b] and Tronskar Jens P.[c]

Materials Technology and Structural Integrity Testing Laboratories, Det Norske Veritas,

DNV Technology Centre, Singapore 118224

[a]Zhengmao.Yang@dnv.com, [b]Shashi.Bhushan.Kumar@dnv.com, [c]Jens.P.Tronskar@dnv.com

Keywords: Pipeline; Fitness for Service; Buckles; Wrinkles;

Abstract. In this paper, FFS assessment procedure for the buckle damaged pipeline with cracks in the girth welds is presented. For FFS assessment the tensile and J R-curve data from a pre-strained pipeline material, API 5L X65 were obtained in the laboratory to study the influences of the large plastic strain on the material properties and the fracture resistance of the pipeline girth welds. Tensile and single edge notch bend specimens in as-received, 10% pre-strained and 20% pre-strained conditions were tested. The test results show significant increase in yield and tensile strength in the pre-strained specimens. Generally, the elongation and fracture resistance decreased after pre-straining. In FFS material specific failure assessment diagrams (FADs) generated based on the stress-strain curves obtained from testing were used. The critical flaw sizes of the pipeline girth welds were calculated, and the influence of the large plastic strain on the FFS results was discussed.

Introduction

A major threat to the integrity of subsea pipelines is mechanical damage, caused by excessive movement of lay barge during pipeline laying or third party tools such anchor chain drop etc. A survey has revealed that 39% of offshore pipeline and 37.7% onshore pipeline failures were caused by outside force damage.

During the installation of offshore pipelines with thinner wall thickness the pipe wall at the 6 o'clock position see large compressive strain and local buckling may occur. This kind of imperfection changes the local geometry of the pipe, and therefore, a stress concentration and local bending stress will be induced. On the other hand, because of large local deformation the pipeline has undergone large local plastic strains i.e. 10-20% plastic strains, the material properties of the pipe with large plastic strain will be drastically changed, and therefore the fracture resistance of the pipe is expected to be decreased, especially when the damage is located at the seam or girth welds. To assess the criticality of such damage, Fitness-For-Service (FFS) required. At present there are no definitive assessment guidelines that consider these aspects.

In this paper, material tests of the buckled pipeline was performed to study the influence of the large plastic bending strain on the material properties, and nonlinear finite element (FEM) analysis was performed to study the local stress distribution around the buckles or wrinkles. Based on these results, FFS assessment for the buckled pipeline with cracks in the girth welds is presented. The critical flaw sizes of the pipeline girth welds were calculated, and the influence of the large plastic strain on the FFS results was discussed.

Local Buckling and Wrinkle Bends

Local buckling and wrinkle bends are associated with the bending of pipe that results in creating local indentations that may be regularly or irregularly spaced, along the length of the affected area. During the installation of offshore pipeline, the shape of the pipe takes in the overbend is controlled by the stinger geometry as shown in Fig. 1. If the stinger curvature did not match the suspended-

span curvature, then excessive bending will occur at the end of stinger, the pipe wall at the 6 o'clock position will be subjected to large compressive strain, and therefore local buckling or wrinkle bends may occur in this area as shown in Fig. 2, especially for the pipeline with small wall thickness to pipeline diameter ratio.

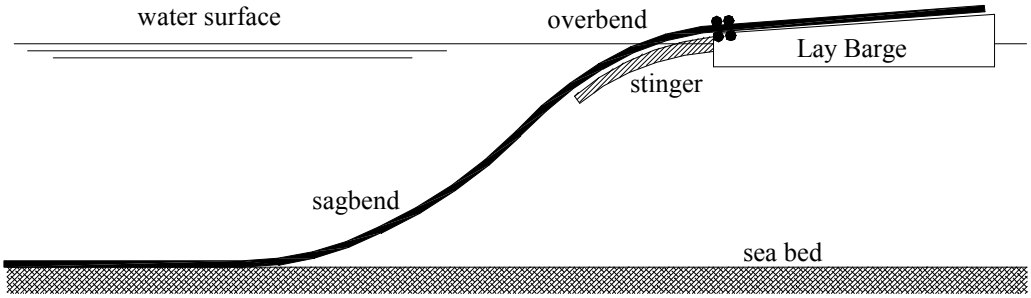

Fig. 1. S-Lay scheme

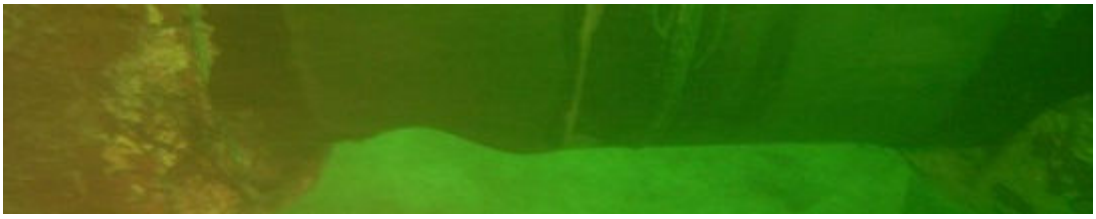

Fig. 2. Wrinkle bends in 6 o'clock of a pipeline

Because of the large local deformation, the materials in the buckled pipe region have undergone large local plastic strains. Based on the experimental efforts by American Petroleum Institute [1], it was found that although depth of the wrinkle is important, the more important factor is the profile shape of the damage, the change in radius of curvature along the length of the line is directly related to bending strain. This plastic strain may be estimated using the formula proposed in ASME B31.8 Appendix R for the strain estimating in dents. Based on the in-situ measurement of the deformation contour, the profile of the wrinkle can be obtained as shown in Fig. 3, and the plastic strain was estimated and tabulated in Table 1.

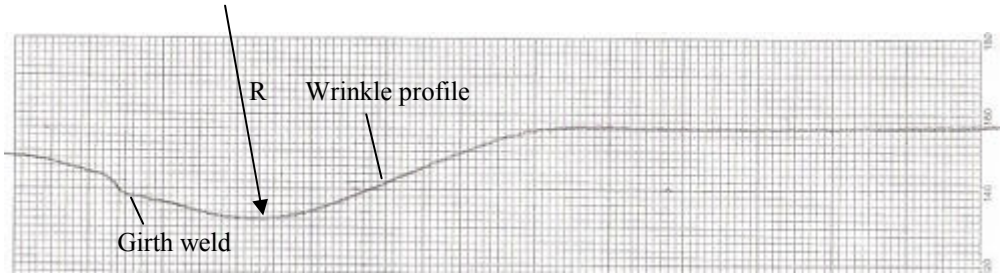

Fig. 3. The wrinkle profile along the longitudinal direction

Table 1 The estimated maximum longitudinal bending strains

Buckle No.	***d*/OD**	**R (mm)**	**Plastic strain (ASME)**
B-1	5.2%	28.8	22.0%
B-2	3.4%	58.3	10.9%
B-3	3.1%	59.9	10.6%
B-4	4.5%	60.5	10.5%

From Table 1, the plastic bending strain can be up to 20%. The material properties of the pipe with such a large plastic strain will be drastically changed, and therefore the fracture resistance capacity of the pipe is expected to be decreased, especially when the damage is located at the seam or girth welds as shown in Fig. 3.

Material Tests of the Buckled Pipe

In order to understand the influence of the local buckling or wrinkle bends on the material properties, the tensile and J-R curve tests were performed in the material technology laboratory of DNV Singapore. Three sets of specimens were tested, say as received, pre-strained 10% and pre-strained 20%. All of these specimens were cut from the same pipe that the winkle bends were detected in the inspection. As received specimens were extracted from the original pipe, pre-strained 10% and 20% specimens were extracted from the pipe walls which were pre-strained by bending up to the maximum strain of 10% and 20% in the pipe outer surface. The stress strain curves of the specimens were plotted in Fig. 4.

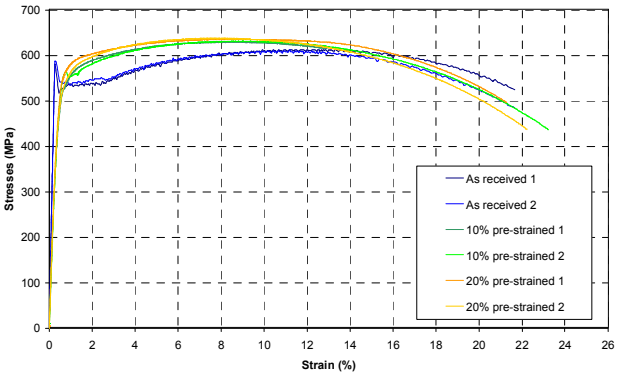

Fig. 4. Engineering Stress strain curves

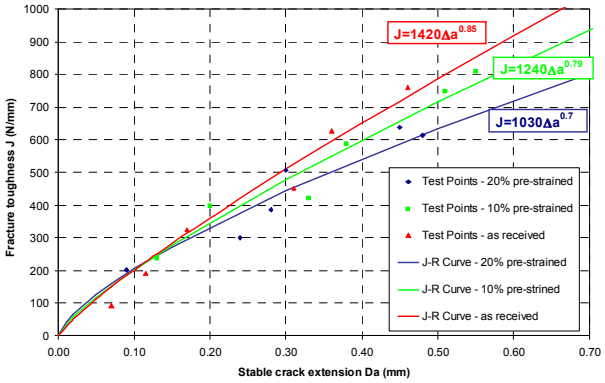

Fig. 5. J-R curve of the materials

It can be seen that the yield strength of the material is increased with the pre-strain level, but the strain corresponding to the ultimate tensile strength is decreased with the increasing of the pre-strain level, and the yield plateau which can be found in the stress strain curve of as received specimens disappears in the pre-strained specimens.

The J-R curves of the specimens were plotted in Fig. 5. As predicted previously, the specimens with higher pre-strain level obtain lower fracture toughness. As Δa equal to 0.4 mm, the J values are 542 N/mm, 601.2 N/mm and 651.7 N/mm for as received, 10% pre-strained and 20% pre-strained specimens respectively. The fracture toughness of J value was decreased 8.4% and 20.2% for the 10% pre-strained and 20% pre-strained specimens respectively.

Assessment of the Buckled Pipeline

Local changes in wall shape, such as dents, local buckling or wrinkle bends, concentrate stress [2]. In the assessment of the buckled pipeline, the local bending stress induced by the changes of wall shape should be considered; the stress distribution in the buckled region can be obtained by finite element analysis. The local deformation of the pipe wall has been measured from the in-situ inspection as shown in Fig. 3, and the deformed pipe was modeled in ABAQUS as shown in Fig. 6.

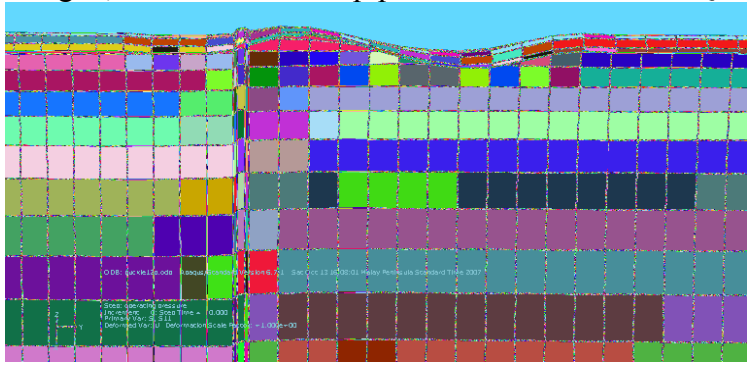

Fig. 6. Numerical model of buckled pipe

Based on this numerical model, longitudinal axial stress cross the wall thickness can be calculated as shown in Fig. 7. According to this stress condition and the material properties of the 20% pre-strained specimens obtained from the tests, the buckled pipeline was assessed as per BS7910: 2005 [3], the critical flaw sizes were plotted in Fig. 8. It can be seen that one of the defects detected in the in-situ inspection is unacceptable. Therefore, the operation pressure has to be dropped down to 800 psig before the buckled pipeline was repaired.

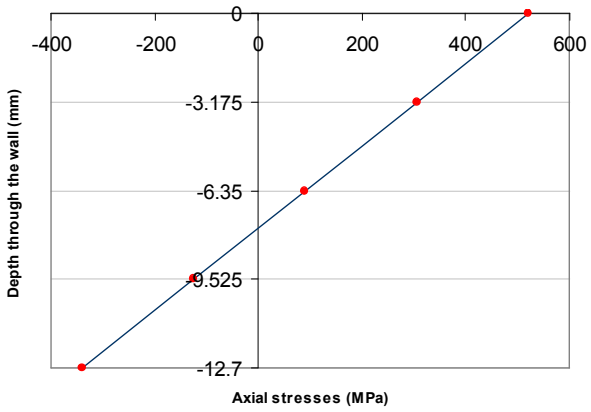

Fig. 7. Longitudinal axial stress of buckle B-1 under the operation pressure (1650 psig)

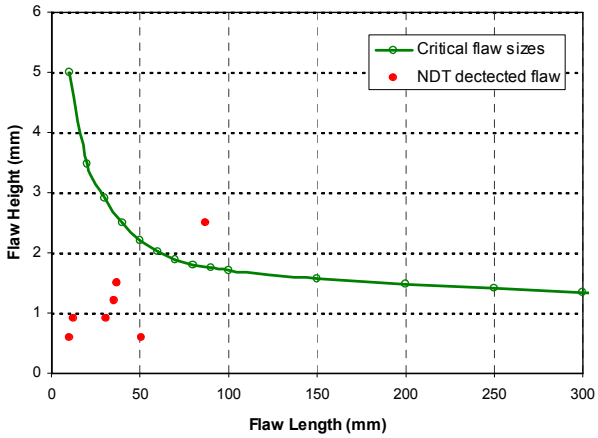

Fig. 8. Critical flaw size of buckle B-1 under operation pressure (1650 psig)

Conclusion

Due to local deformation in the buckled region, large plastic strain was accumulated and lower fracture toughness of the material was obtained from the material tests. Because of the shape changes of the pipe wall, stress concentrates in the buckled area. Based on the stress condition obtained from finite element analysis and the material properties from the material tests, critical flaw size of the buckled pipeline was obtained and it was found that the operation pressure of the pipeline has to be dropped down to half of the design operation pressure before this imperfection was repaired.

References

[1] C.R. Alexander and J.F. Kiefner: *Effects of Smooth and Rock Dents on Liquid Petroleum Pipelines*. API Publication 1156 (First Edition), American Petroleum Institute, Washington, D.C. (1992).

[2] A.J. Rinehart and P.B. Keating: *Stress Concentration Solution for a 2D Dent in an Internally Pressurized Cylinder.* Journal of Engineering Mechanics, Vol. 133, pp. 792-800, (2007).

[3] BS7910: *Guide on Methods for Assessing the Acceptability of Flaws in Fusion Welded Structures*. British Standards Institution, London, UK. (2005).

Key Engineering Materials Vols. 385-387 (2008) pp 177-180
© (2008) Trans Tech Publications, Switzerland
doi:10.4028/www.scientific.net/KEM.385-387.177

Fracture Behavior and Microstructure of Ti_3AlC_2 Ceramics Prepared by SHS/PHIP Method

Ren Zheng-yi[1,a], Li Chong[1,b], Li Qing-fen[2,3,c]

[1]Engineering Education Center, Harbin Engineering University,

[2]College of Material Science and Chemical Engineering, Harbin Engineering University,

[3]College of Mechanical and Electrical Engineering, Harbin Engineering University,

Harbin 150001, China,

[a] zyren8005@vip.sina.com, [b]lichong@hrbeu.cn, [c] qingfli@yahoo.com.cn,

Keywords: Fracture behavior; Ti_3AlC_2 Ceramics; SHS/PHIP method; compressive deformation

Abstract. Fracture behavior and the microstructure of Ti_3AlC_2 ceramics prepared by SHS/PHIP method were studied. Stress-strain curves at different temperature with a strain rate of 1×10^{-3} s^{-1} were obtained. Fracture toughness, flexural strength, crack propagation behavior and compressive deformation of specimens were investigated. Results show that the microstructure of the large size Ti_3AlC_2 ceramics prepared by SHS/PHIP method has typical layered feature of ternary carbide compound. The bridge-link phenomena induced by the flaky grains occurred in three-point bending test. It restrained the crack propagation and improved the fracture toughness of the material. Cylindrical specimens under axial compression usually smashed into chips for most of the ceramics materials, however, for the Ti_3AlC_2 ceramics prepared by SHS/PHIP, shear fracture along 45º incline of the specimen occurred at room temperature, and bulging deformation without any crack exhibited when temperature was high. It is concluded that the Ti_3AlC_2 ceramics prepared by SHS/PHIP has better fracture-resistance properties.

Introduction

It is well known that ceramics materials have many excellent mechanical properties, such as high strength, high hardness, high melting point, and high stability, etc. However, ceramics also has the vital weakness that is high brittleness, because ionic bond and covalent bond are the mainly bond type in ceramics. It is necessary to induce weak bond type, such as metal bond into crystal of the ceramics so that the brittleness may be improved [1].

Ti_3AlC_2 ceramics is a novel structural and functional material which combines the merits of both metals and ceramics. The unique advantages make it a promising material that will be widely used in many industrial fields. However, Ti_3AlC_2 block material prepared by different methods has different properties [2-4].

It is the first time, a Φ150mm Ti_3AlC_2 ceramics block material prepared by SHS/PHIP (Self-propagating High-temperature Synthesis / Pseudo Hot Isostatic Pressing) method was obtained by our research group[5]. In this paper, the fracture behavior and microstructure of the Ti_3AlC_2 ceramics block material was studied. Fracture toughness, flexural strength, crack propagation behavior and compressive deformation of specimens were investigated.

Experimental

Fracture toughness, flexural strength and compressive properties of Ti_3AlC_2 tests were carried out on Instron-1186 testing machine and Gleeble-1500 hot-simulation machine respectively. Specimens were made by the Ti_3AlC_2 ceramics block. The composition is given in table 1. Three-point bend specimens were used for the testing of fracture toughness K_{1c} and flexural strength σ_b, according to the Chinese Test Standard GB/T6569-2006 and GB/T14389-14390-93, respectively. Specimen size is Φ 8mm×12mm for compressive test. The strain rate is $0.1s^{-1}$, $0.01s^{-1}$, $10^{-3}s^{-1}$, and $10^{-4}s^{-1}$ respectively. Tests were carried out at different temperature. The microstructure of Ti_3AlC_2 ceramics was studied with scanning electron microscopy (SEM).

Table 1 Composition of the test material Ti_3AlC_2

Materials	Grain size (μm)	chemical composition (wt%)				
Ti-powder	≤45	Ti	Fe	Si	C	Cl^-
		≥99.2	≤0.03	≤0.01	≤0.035	≤0.04
Al-powder	≤45	Active Al	Fe	Si	Cu	N
		≥99	≤0.6	≤0.3	≤0.05	≤0.01
C-powder	1	C	water	ash	volatile	S
		≥96	≤1.0	≤0.3	≤2.0	≤0.4

Specimen is 3 × 4 × 36mm^3 for bending test and the σ_b is calculated according to equation (1):

$$\sigma_b = \frac{3P_f L}{2h^2 w}. \tag{1}$$

Where P_f is the load at fracture, L is the span, h and w are the height and width of specimen respectively.

For fracture toughness test, specimen with a prefabricated crack is 2 × 4 × 22mm^3 and the crack depth is 2mm. K_{1c} is calculated according to the equation (2):

$$K_{IC} = Y \cdot \frac{3PL}{2wh^2}\sqrt{a}\ . \tag{2}$$

Where Y is the calibration factor and α is the crack depth.

Results and discussion

Compressive stress-strain curves at different temperature with a strain rate of $1\times10^{-3}/s$ were showed in Fig.1. The load-displacement curve for fracture toughness K_{1c} test is given in Fig. 2. The variation of flexural strength with temperature is given in Fig.3. Experimental results show that the test material exhibited brittle fracture with very little plastic deformation from room temperature to 800°C. Obvious plastic deformation occurred when temperature was higher than 800°C, and the higher the temperature, the higher the plastic deformation was. The flexural strength at room temperature was 330.8MPa, and decreased with increasing temperature. The fracture toughness K_{1c} at room temperature was 5.7MPa·$m^{1/2}$, which is much higher than other ceramics, such as SiC and Al_2O_3.

Microstructure of Ti_3AlC_2 is shown in Fig.4. The SEM fractographs of the compressive samples fractured at room temperature and 1100°C are given in Fig. 5 and 6 respectively. Fig.7 shows the unit cell of Ti_3AlC_2. Fig.8 gives the photos of compressive samples distorted at room temperature and 1300°C respectively. The bridge-link phenomena induced by the flaky grains are shown in Fig.9.

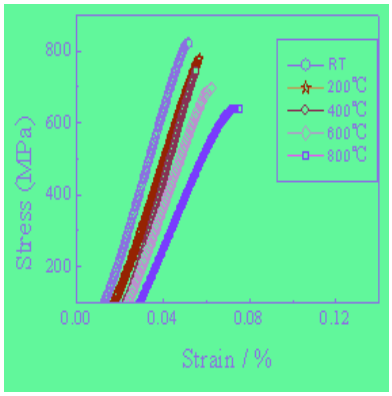

(a) Lower temperature

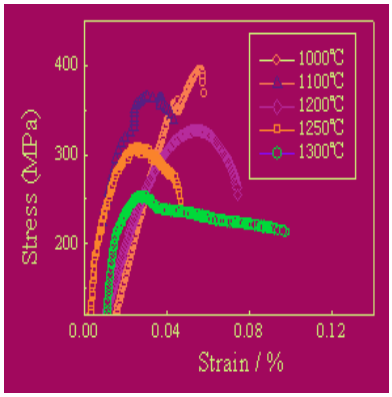

(b) Higher temperature

Fig.1 Stress-strain curves at different temperature

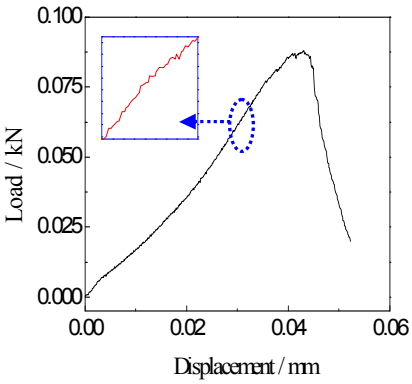

Fig 2 Load-displacement curve for K_{1c} test

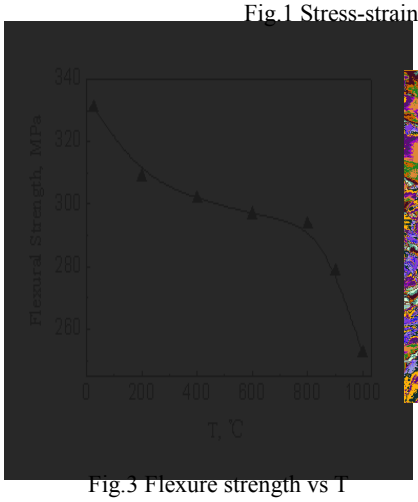

Fig.3 Flexure strength vs T

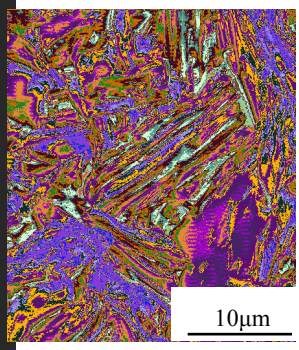

Fig 4 Microstructure of Ti_3AlC_2

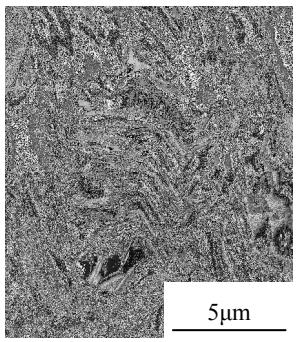

Fig 5 Fractured at room temperature

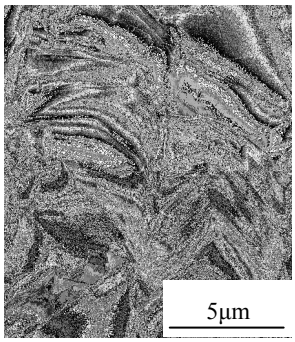

Fig 6 Fractured at 1100°C

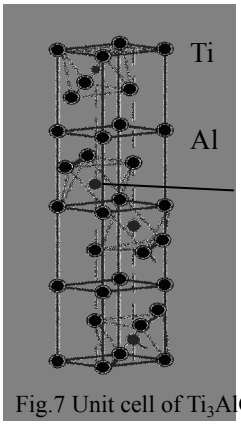

Fig.7 Unit cell of Ti_3AlC_2

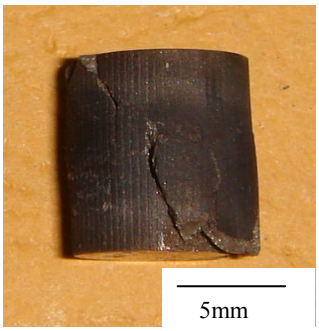

(a) Distorted at room temperature

(b) Distorted at 1300°C

Fig 8 Compressive sample

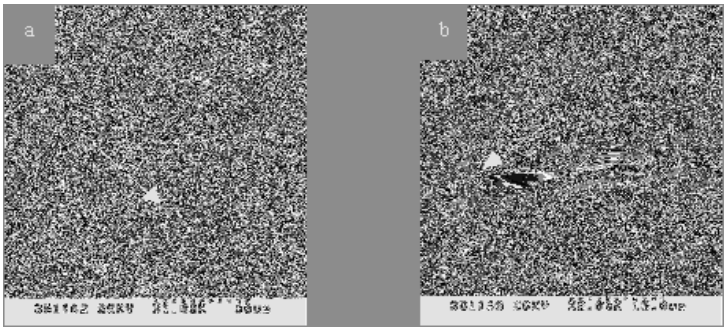

(a) Grain bridging (b) Grain pull-out

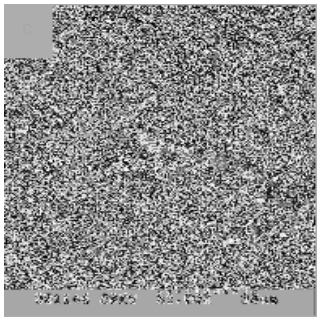

(c) Final crack

Fig.9 Bridge-link fracture phenomena

From Fig.4, we may see that there are a number of plate-like Ti_3AlC_2 grains which consisted of many thin slices distributed in the sample. It indicated that the microstructure of Ti_3AlC_2 ceramics prepared by SHS/PHIP has the typical layered feature of ternary carbide compound.

Fig.5 shows that the thin slices were distorted and delaminated in the compressive sample fractured at room temperature. The distortion behavior of Ti_3AlC_2 ceramic is similar with that of hexagonal crystal structure metal. Transgranular crack and grain torsion may be observed in the compressive sample fractured at 1100°C (Fig.6), and obvious plastic deformation occurred at 1100°C. They both show that the plasticity of the test ceramics is higher than most of the other ceramics.

The crystal structure of carbide ternary compound Ti_3AlC_2 is hexagonal (see Fig.7), and has the space group $P6_3/mmc$. Where, the Ti_6C octahedrons are linked together through Al atoms and formed the layered structure of Ti_3AlC_2 ceramic [6]. The layered structure revealed that Ti_3AlC_2 ceramic has a unique combination of merits of both metals and ceramics.

Cylindrical specimens under axial compression usually smashed into chips for most of the ceramics materials, however, for the Ti_3AlC_2 ceramics prepared by SHS/PHIP, shear fracture along 45º incline of the sample occurred at room temperature, and branching and deflection of the main crack can be seen in Fig.8 (a). From Fig.8 (b), we see that bulging deformation without any crack occurred when temperature was high. It is obvious that the Ti_3AlC_2 ceramics prepared by SHS/PHIP has much better plastic behavior.

The bridge-link phenomena induced by the flaky grains occurred in three-point bending test (Fig.9). It restrained the crack propagation and improved the fracture toughness of the material.

It is concluded that the Ti_3AlC_2 ceramics prepared by SHS/PHIP has better fracture-resistance properties.

Summary

Fracture behavior and the microstructure of Ti_3AlC_2 ceramics prepared by SHS/PHIP method were investigated. Results show that the microstructure of the testing material has the typical layered feature of ternary carbide compound. The testing Ti_3AlC_2 ceramics has much better plastic behavior and fracture-resistance properties than most of the other ceramics materials.

References

[1] M. W. Barsoum: Progress Solid State Chemistry, Vol. 28 (2000), p.201

[2] N. V. Tzenov, M. W. Barsoum: J. Am. Ceram. Soc., Vol. 83 (2000), P.825

[3] X. H. Wang, Y .C. Zhou: Acta Materialia, Vol. 50 (2000), P.3141

[4] X. H. Wang, Y .C. Zhou: Journal of Materials Chemistry, Vol. 12 (2002), P. 455

[5] C. Li, X. D. He, Q. F. Li: Tool Technique, Vol. 41 (2006) , p.30

[6] H. X. Zhai, Z. Y. Huang, M. X. Ai, et al: Journal of the American Ceramic Soc, Vol. 88 (2005), p.270

Key Engineering Materials Vols. 385-387 (2008) pp 181-184
© (2008) Trans Tech Publications, Switzerland
doi:10.4028/www.scientific.net/KEM.385-387.181

Theoretical Approach to Calculate Surface Chloride Content C_s of Submerged Concrete under Sea Water Laden Environment

In-Seok Yoon[1,a]

[1] Dept. of Civil Eng., Induk Institute of Technology, Seoul, Korea

[a] isyoon@induk.ac.kr

Keywords: surface chloride content, service life design, seawater, salt ingredient

Abstract. The ingress of chloride ions plays a crucial role for service life design of reinforced concrete structures. In view of durability design of concrete structures under marine environment, one of the most essential parameters is the surface chloride content of concrete. With the social and technical backgrounds, the research approach of this study starts with the calculation of the amount of chloride ingredients in normal sea water. The capillary pore structure is modeled by numerical simulation model HYMOSTRUC and it is assumed to be completely saturated by the salt ingredients of seawater. In order to validate this approach, the total chloride content of the mortar and concrete slim disc specimen was measured after the immersion into the artificial sea water solution. Additionally, the theoretical, the experimental and in-situ investigation results of other researchers are compiled and analyzed. Based on this approach, it will follow to calculate the maximum surface chloride content of concrete in the tidal zone, where the environment can be considered as subjected to dry-wetting cycles.

Introduction

The literatures have been flooded with methodological approaches to carry out the durability design of concrete, since 1980s. In the process of durability design, the surface chloride content, C_s, has been regarded as one of the crucial parameters. At the same time, the surface chloride content is considered as a standard parameter to define environmental degree of chloride laden concrete. However, many researchers and engineers have determined this value empirically. It is not easy to define this value because of its variation with elapsed time, environmental condition and, especially microclimatic condition at the concrete surface. In this study, a rational and practical way is suggested for the calculation of the maximum C_s in the submerged portion.

Significance and Approach to Calculate C_s

Effect of environmental condition. The concrete sections exposed to marine environment are mainly divided into three parts: atmospheric zone, tidal zone, submerged zone. The origin chloride sources of concrete are air borne chloride carried from sea for atmospheric zone, brackish water or sea water for tidal zone, and sea water for submerged zone, respectively. For this reason, equivalent chloride concentration, C_{env} can be expressed as maximum equivalent surface chloride content (C_{sea}) which is described by Eq. (1).

$$C_{env} = C_{sea}\, f(h) \tag{1}$$

in which, C_{sea}: concentration of chlorides in the seawater, C_{env}: maximum equivalent chloride concentration, f(h) : function of height above tidal zone.

In the tidal zone where intermittent drying-wetting cycles occur, chloride ingredients can be accumulated at the surface of concrete if sea water is dried out. The evaporation can increase C_s of concrete in the tidal zone to a higher value than the chloride content of sea water. In the submerged zone, C_s does not increase infinitely because the value is governed by the degree of saturation. That is, the C_s initially will fluctuate about a steadily rising level and then increase with elapsed time slowly

and continuously. Finally, this value will stagnate if it equals the concentration of sea water approximately. Maximum C_s can be regarded as an imperative parameter to predict a service life of concrete for long term and a constant value after a certain short period has elapsed. Thus, in order to characterize the chloride build-up, the rational expression can be depicted by [1]:

$$C_s(t) = C_{max}(1 - e^{-at}) \tag{2}$$

in which, C_{max}: maximum surface chloride content = f(C_{sea}) , t: elapsed time, a: a constant for rate of chloride accumulation.

Calculation of amount of composite salts in sea water. C_{max} depends on the amount of chlorides (C_{sea}) in sea water. Symbol e and c mean chemical element and composite salts in sea water, respectively. The amount (C_c) of composite salt can be calculated as:

$$C_c = Q_e W_e \tag{3}$$

in which, Q_e: quantity of chemical element e,(see Table 1), W_e : atomic weight of chemical element e. (Na : 22.990, Cl : 35.453, Mg : 24.305)

Table 1 Chemical element of sea water [2]

Chemical Element (e)	Cl	Na	Mg	SO_4	K	Ca	HCO_3
Volume (m mol/ l)	548	470	54	28	10	10	2

Now, we can calculate an amount of composite salt c. Because they are the major composite salts of sea water, composite salts are confined as NaCl, $MgCl_2$ in this study. The mass fraction (Ω_c) of composite salts can be obtained if total salt ingredients are assumed to be 35 g/l[2].

Calculation of mass quantity of composite salts in unit volume. The mass quantity of composite salt (Q_c) per unit volume of sea water is calculated as a given equation below:

$$Q_c = \Omega_c \cdot \rho_c \tag{4}$$

in which, Ω_c : mass fraction of composite salt c of seawater, ρ_c: density of the composite salt c.(NaCl: 2.160 kg/dm^3, $MgCl_2$: 2.310 kg/dm^3).

Calculation of mass of Cl^- in composite salts. The quantity of composite salts should be translated into a quantity of only the quantity of Cl^- to consider an atomic weight of ingredients of salt as:

$$Q_c^{Cl} = Q_c \frac{W_{Cl}}{(W_c + W_{Cl})} \tag{5}$$

in which, Q_c^{Cl}: quantity of Cl- in competitive salts c, W_{Cl}: atomic weight of Cl^- ions.

Calculation of total Cl^- mass. Total quantity of Cl^- composite salts (Q_{Total}^{Cl}) can be calculated as a given equation:

$$Q_{Total}^{Cl} = Q_{NaCl}^{Cl} + Q_{MgCl_2}^{Cl} \tag{6}$$

in which, Q_{NaCl}^{Cl}: quantity of Cl^- in NaCl, $Q_{MgCl_2}^{Cl}$: quantity of Cl^- in $MgCl_2$.

Calculation of quantity of Maximum surface chloride content, C_{max}. If the capillary pore of cementious materials is fully filled with sea water, the maximum amount of chloride content in concrete can be calculated, as given in Eq. (7). This value can be used as a maximum surface chloride content for submerged concrete under seawater laden marine environment.

$$C_{\max} = Q_{Total}^{Cl} \cdot \phi_{cap} \tag{7}$$

in which, C_{max}: maximum surface chloride content, ϕ_{cap} : capillary porosity of cementious materials (see Fig. 3). Now, we can calculate the maximum chloride content according to the unit weight of concrete ($W_{con'c}$) can be expressed as:

$$C_{\max} = \frac{1.371 \cdot \phi_{cap}}{W_{con'c}} \ [g_{Cl}/g_{conc}] \tag{8}$$

Experimental Program

Effect of environmental condition. C_s depends on many parameters such as the ingredient of sea water, the geographical location, and the exposure condition with water level. Many researchers have confirmed this value, based on the result of in-situ investigation of old concrete structure.

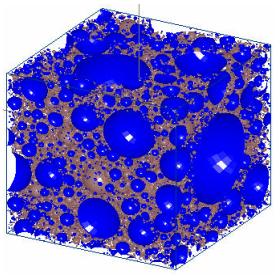

Fig. 1 Microstructure modeling

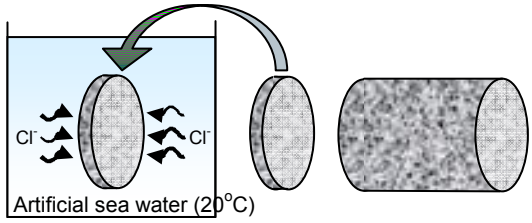

Fig. 2 Chloride immersion testing

Table 2 Mix Proportion of concrete: ( ) is not contained in mortar

Type \ Item	*W/C* (%)	Unit weight (kg/m^3)			
		Water	Cement	Sand	Gravel
OPC-45	45	185	411	735	(1248)
OPC-50	50	185	370	742	(1207)
OPC-55	55	185	336	746	(1072)

Results and Discussions

The C_s of the mortar disk and concrete disk is calculated and presented in Table 2. At the end of the 20°C water curing period, the top 2 mm of the specimens was sawn and then immersed in artificial sea water with same composition as given in Table 1. Total chloride ion content in the specimens was measured in accordance with the technique described in ASTM C1152-97 and expressed as a weight ratio of chloride to concrete (g_{Cl}/ g_{conc}) for mortar and concrete specimens.

Fig. 4 and Fig. 5 present comparisons of measured C_s and calculated C_s in mortar and concrete, respectively. For concrete, accurate relationship between experiment and calculation is not formulated because of skin effect and sporadic existence of coarse aggregates. However, it should be noticed that predicted values of C_s are approximately in reasonable agreement with the measured values in case of mortar. More than anything else, the maximum C_s theoretically depends on *w/c* ratio because dense concretes have finer pore structures and should absorb less chloride in view of build-up rate of chloride, according to this result.

Fig. 6 depicts the result of comparison of this result and other studies[3]~[6]. As shown in this figure, C_s depends on *w/c* ratio, but is mostly in the range of 5.5 to 7 × 10^{-3} g_{Cl}/g_{conc}, which coincides with the result of in-situ investigation of Takeda and calculated result of Bazant approximately.

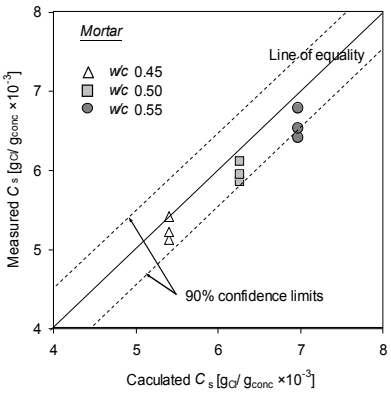

Fig. 4 Comparison of calculated and measured C_s (in mortar)

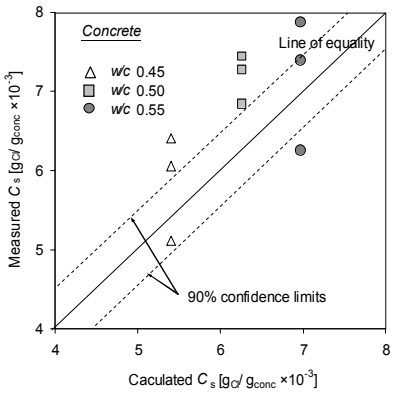

Fig. 5 Comparison of calculated and measured C_s (in concrete)

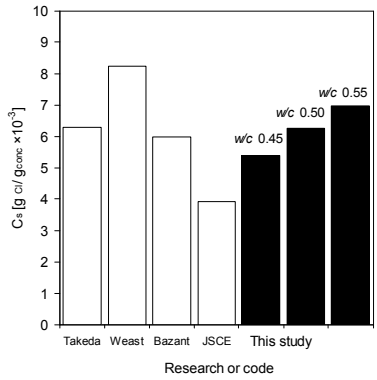

Fig. 6 Comparison of this result and other studies

Summary

The accuracy of this approach is dependent on pore structural properties of concrete and the microclimatic condition at near surface concrete. C_s is mainly an environmental parameter, however, that is also a little governed by material properties of concrete such as *w/c* ratio, cement content, and the type of cement. For these reasons, it is not easy to define this value of C_s in concrete deterministically. This approach is theoretically based on the ingredient and amount of seawater, and microstructural characteristics of cementious materials. This result can be used for reasonable durability design of concrete structures. On the basis of the approach suggested, the calculation of C_s in tidal concrete can be performed.

References

[1] P. Arora, B.N. Popov, B. Haran, M. Ramasubramanian, S. Popova, and R.E. White, "Corrosion Initiation Time of Steel Reinforcement in a Chloride Environment – A One Dimensional Solution, " *Corrosion Science*, Vol.39, No.4, pp.739-759, 1997.

[2] E.H. Lieb, A. Gianguzza, S. Sammartano, E. Pelizzetti, Chemistry of Marine Water and Sediments, Springer, 2002.

[3] N. Takeda, S. Sogo, S. Sakoda, and T. Idemitu, "An Experimental Study on Penetration of Chloride Ions into Concrete and Corrosion of Reinforcing Bars in Various Marine Environment," (in Japanese language) *Journal of JSCE*, No.599, No.40, 1998.8.

[4] "CRC Handbook of Chemistry and Physics," R.C. Weast and M.J. Astle (Eds.), 63rd, pp.299, CRC Press, Boca Raton, FL, F-154, 1982.

[5] Z.P. Bazant, "Physical Model for Steel Corrosion in Concrete Sea Structure – Application," *Journal of Structure, Div., ASCE*, No.105, Vol.6, pp.1137-1153, 1979.

[6] JSCE, Concrete Standard Specification, Part of Durability (in Japanese language), 1999.

Key Engineering Materials Vols. 385-387 (2008) pp 185-188
© (2008) Trans Tech Publications, Switzerland
doi:10.4028/www.scientific.net/KEM.385-387.185

High Cycle Fatigue Properties and Failure Mode in Ni-Cr-Mo steel Tempered at Low Temperature

Yu Mochizuki[1], Masaki Nakajima[2,a] and Toshihiro Shimizu[2]

[1] Advanced Course Student, Toyota National College of Technology, JAPAN

[2] Toyota National College of Technology, 2-1 Eisei-cho, Toyota 471-8525, JAPAN

[a] nakajima@toyota-ct.ac.jp

Keywords: High cycle fatigue, Rotating bending, Axial loading, Fish-eye, Ni-Cr-Mo steel.

Abstract. High cycle fatigue properties and failure mode in high strength steel tempered at low temperature were studied. The material used was Ni-Cr-Mo steel, JIS SNCM439, which was tempered at 453 K. After heat treatment, round bar specimens with hourglass shape were machined. Fatigue tests were performed using two kinds of specimens with two surface conditions, *i.e.*, as-ground specimen and buff-finished specimen. Tests were conducted under rotating bending and axial loading. Under rotating bending, in as-ground specimens, fatigue failure took place in high cycle region above 10^7 cycles and failure mode was surface-related. On the other hand, buff-finished specimens exhibited the step-wise *S-N* curve, *i.e.*, the subsurface fracture with a fish-eye was observed. However, under axial loading, even in buff-finished specimens the subsurface fracture didn't occur due to small nonmetallic inclusions. Based on the results, the fatigue limit was estimated by the statistics of extremes. The prediction gave the conservative values.

Introduction

In a step-wise *S-N* curve observed in high strength steels, different fracture mechanisms operate at short life region and long life region more than 10^7 cycles, *i.e.*, surface-related crack initiation in the former and fish-eye fracture in the latter [1]. There are many factors that influence the transition from surface-related fracture to subsurface fracture. Of those factors, it seems that surface finishing condition should play an important role [2, 3], because high strength steels are generally very sensitive to surface defects. In addition, the existence of stress gradient exerts an influence on subsurface fracture [4], because of the size of critical volume including the nonmetallic inclusion.

In the present study, fatigue tests under rotating bending and axial loading were performed using specimens with different surface finishing conditions, *i.e.*, as-ground specimen and buff-finished specimen. The effects of surface finishing condition of specimens and loading condition on step-wise *S-N* characteristics, particularly on high cycle properties and failure mode, were studied.

Experiments

Material. The material used in this study is Ni-Cr-Mo steel, JIS SNCM439 (equivalent to AISI 4340), whose chemical compositions are given in Table 1. The materials were oil-quenched at 1123 K and then tempered at 453 K. The mechanical properties after heat treatment are listed in Table 2. After heat treatment, two kinds of round bar specimens for rotating bending and axial loading were machined to the configurations illustrated in Fig. 1 (a) and (b), respectively. Two kinds of specimens with different surface conditions were prepared, *i.e.*, as-ground specimen and buff finished specimen. The stress concentration factors, K_t, of the specimens are given in Fig. 1.

Procedures. Fatigue tests were performed at a stress ratio, *R*, of -1 using cantilever-type rotating bending fatigue testing machine and multi-type axial loading fatigue testing machine with a cyclic frequency of 53 Hz and 80 Hz, respectively. After experiments, fracture surfaces of all the specimens were examined in detail using scanning electron microscope (SEM). A particular attention was paid to the failure mode in long life region.

Experimental results

***S-N* characteristics.** The *S-N* curves obtained under rotating bending and axial loading are shown in Fig. 2, where fatigue lives are plotted against the maximum stress, σ_{max}. Under rotating bending, in as-ground specimens fatigue failure took place in high cycle region above 10^7 cycles and failure mode was surface-related, except for the one example of subsurface fracture at 900 MPa. It seems that the fatigue limit of as-ground specimen is about 850 MPa, because of run-out specimen can be found at 850 MPa for 10^9 cycles. On the other hand, in buff-finished specimens, fatigue lives were longer than those of as-ground specimens and failure mode above 10^7 cycles was subsurface fracture with a fish-eye, resulting in the step-wise *S-N* curve. Under axial loading, even in buff-finished specimens, subsurface fracture was not observed in high cycle region. The fatigue limits of as-ground specimens and buff-finished specimens are 850 MPa each.

SEM observations. Although it was expected that subsurface fracture would be seen in as-ground specimens under both loading conditions, subsurface fracture was not observed, except for one case. Fig. 3 shows the fracture surfaces in as-ground specimens. Nonmetallic inclusion which caused the subsurface fracture is shown in Fig. 3 (a), whose size is 21.47 μm and is exceptionally large. Surface defects as shown in Fig. 3 (b) were observed in as-ground specimen and caused the surface-related fracture in high cycle region above 10^7 cycles. On the other hand, in buff-finished specimens, subsurface fracture was seen in high cycle region under rotating bending. However, under axial loading, subsurface fracture was not found.

Table 1 Chemical composition (wt. %).

SNCM439	C	Si	Mn	P	S	Ni	Cr	Mo	Cu
Rotating bending	0.41	0.24	0.66	0.018	0.016	1.71	0.75	0.21	0.13
Axial loading	0.39	0.24	0.65	0.019	0.018	1.7	0.76	0.21	0.14

Table 2 Mechanical properties.

0.2% proof stress $\sigma_{0.2}$ (MPa)	Tensile strength σ_B (MPa)	Elongation δ (%)	Reduction of area (%)	Vickers hardness *HV*
1491	1960	15	40	557

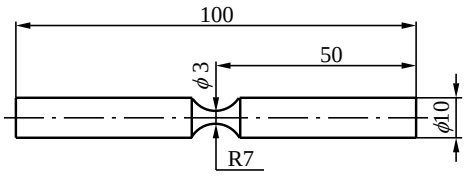

(a) Rotating bending (K_t=1.06)

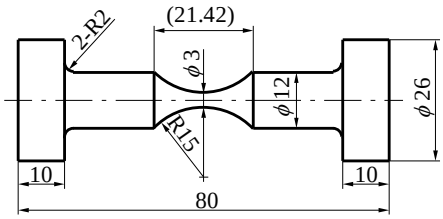

(b) Axial loading (K_t=1.04)

Fig. 1 Specimen configurations (unit : mm).

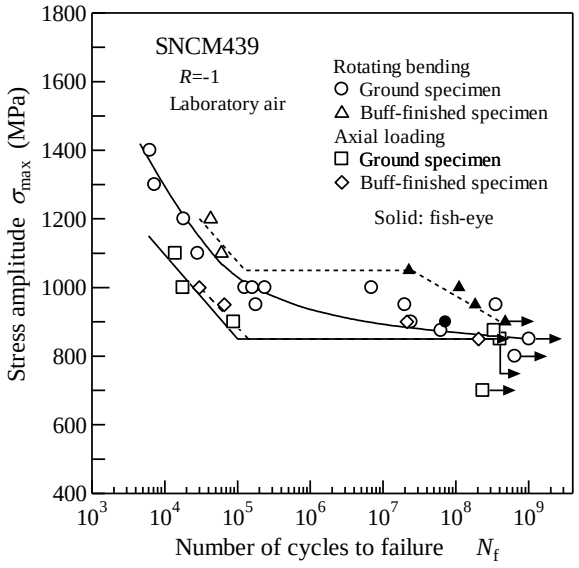

Fig. 2 *S-N* curves.

Discussions

Extreme value distributions of nonmetallic inclusion. The sizes of maximum nonmetallic inclusion in a standard area, S_0=0.0031 mm^2, were measured using SEM. The results obtained are shown in Fig. 4. As can be seen in the figure, the sizes of non-metallic inclusion in SNCM439 used for rotating bending are statistically larger than those in SNCM439 for axial loading. This is the reason of surface-related fracture in buff-finished specimens under axial loading. It seems that the difference between both SNCM439s is due to cleanliness of alloy elements [5].

The estimation of fatigue limit was conducted using the extreme value distribution of inclusion shown in Fig. 4. According to the previous study using the same material [6], the inclusions that acted as fracture origin were located within 0.2 mm from the specimen surface. This is because of the presence of stress gradient under rotating bending. Thus, the critical area, S, under rotating bending is obtained to be 1.76 mm^2. Using this value, the return period, T, is obtained from the equation, $T=S/S_0$. The inclusion size for the return period of T=569 is 10.96 μm, as seen in Fig.4. Based on this value, fatigue limit, σ_w, was calculated by the following Eq. 1 [7].

$$\sigma_w = 1.56(HV+120)/\left(\sqrt{area}\right)^{1/6} \quad (1)$$

Where $\sqrt{area}$ is the estimated inclusion size and Vickers hardness HV is 557. The estimated fatigue limit is 730 MPa for rotating bending. The similar calculation was also performed for axial loading. The critical area, S, and the return period, T, obtained were 7.07 mm^2 and 2280, respectively. The inclusion size for the return period of T=2280 was 5.37 μm. Using this value, fatigue limit under axial loading was calculated by Eq. 1 and predicted to be 800 MPa. Since the experimental run-out stresses are 850 MPa each under both loading conditions, the predicted values give the conservative estimation.

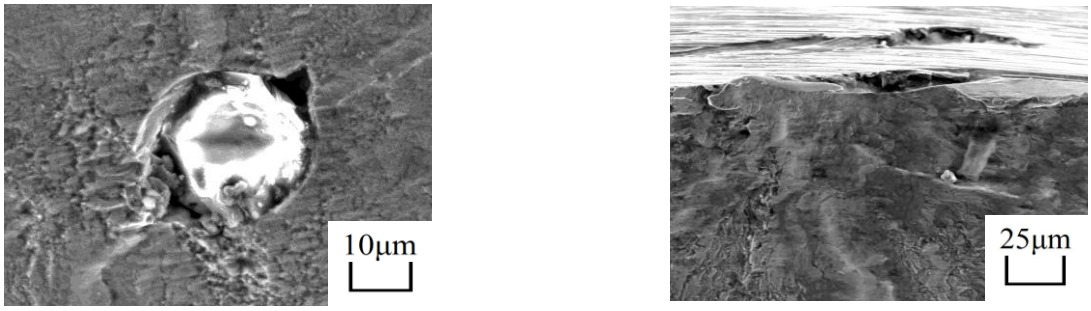

(a) Inclusion in fish-eye (σ_a=900MPa, N_f=7.16×10^7)

(b) Defect on surface (σ_a=875MPa, N_f=6.19×10^7)

Fig. 3 SEM micrographs showing fracture surface of as-ground specimen.

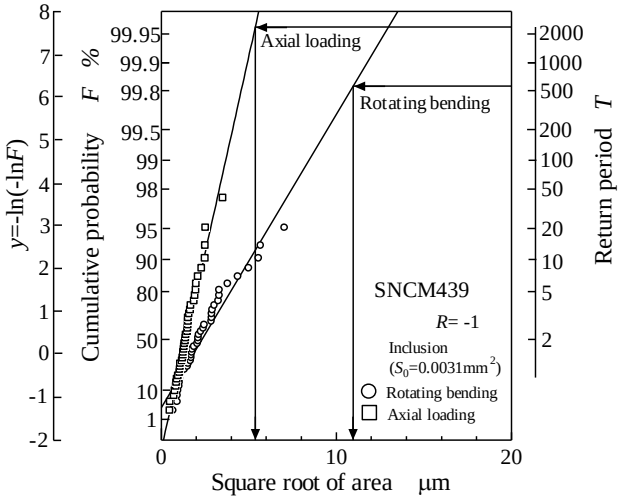

Fig. 4 Extreme distributions of inclusion.

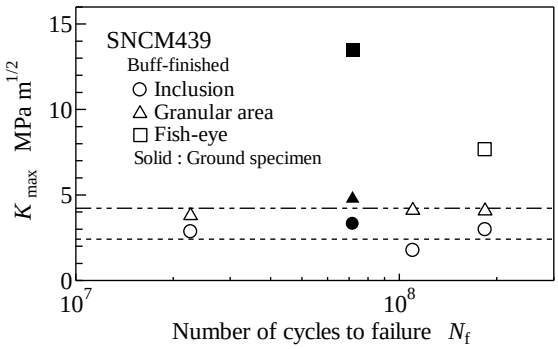

Fig. 5 K_{max} for inclusion, granular area and fish-eye as a function of fatigue life, N_f.

Quantitative analysis of nonmetallic inclusion and granular area. Subsurface fracture was seen for buff-finished specimen under rotating bending. Nonmetallic inclusions and granular areas observed in fish-eyes were analyzed quantitatively using the $\sqrt{area}$ parameter model [8]. After the tests, the sizes of nonmetallic inclusions and granular areas were measured, and the maximum stress intensity factor, K_{max}, was calculated by the following Eq. 2 [8],

$$K_{\max} = 0.5\sigma_{inc}\sqrt{\pi\sqrt{area}} \tag{2}$$

where σ_{inc} is the stress level at the location of inclusion and $\sqrt{area}$ is the inclusion size obtained from experiment. Figure 5 shows the K_{max} values for nonmetallic inclusion and the granular area as a function of the number of cycles to failure, N_f. The K_{max} values for nonmetallic inclusion and the granular area indicate the condition of subsurface crack initiation and the transition condition from the granular area to flat and featureless area in fish-eye, respectively. As can be seen in the figure, the K_{max} values for inclusion are nearly the same regardless of N_f, *i.e.*, K_{max} =1.77~3.32 MPa $m^{1/2}$. K_{max} values for the granular area are also similar irrespective of N_f, *i.e.*, K_{max} =3.79~4.78 MPa $m^{1/2}$. On the other hand, K_{max} values for fish-eye were scattered, depending on the location of nonmetallic inclusion with maximum size.

Conclusions

High cycle fatigue properties and failure mode in Ni-Cr-Mo steel tempered at low temperature were studied under rotating bending and axial loading. The conclusions obtained are as follows.

(1) Under rotating bending, failure mode of as-ground specimen failed in high cycle region above 10^7 cycles was surface-related fracture caused by grinding defects. On the other hand, in buff finished specimen, fatigue lives were longer than those of as-ground specimens and failure mode above 10^7 cycles was subsurface fracture, resulting in the step-wise *S-N* curve.

(2) Under axial loading, even in buff-finished specimens, subsurface fracture was not seen in high cycle region.

(3) The sizes of nonmetallic inclusion in SNCM439 used for rotating bending were larger than those in SNCM439 for axial loading. This is the reason of surface-related fracture in buff-finished specimens under axial loading.

References

[1] H. Emura and K. Asami: Transactions of the JSME, A55-509 (1989), p. 45

[2] M. Goto, T.Yamamoto, H. Nisitani, T. Sakai, and N. Kawagoishi: J. Soc. Mater. Sci., Japan, 49-7 (2000), p. 786

[3] H. Itoga, K. Tokaji, M. Nakajima, H-N. Ko: Int. J. Fatigue, 25 (2003), p. 379

[4] Y. Murakami: Proc. of Int. Conf. on Fatigue in the Very High Cycle Regime, Vienna, (2001), p. 11

[5] H. Itoga, H-N.Ko, K. Tokaji and M. Nakajima: Transactions of the JSME, A69-686 (2003), p. 1450

[6] M. Nakajima, K.Tokaji, T. Shimizu, H, Itoga and H-N. Ko: J. Soc. Mater. Sci., Japan, 50-9 (2001), p. 954

[7] Y. Murakami and M. Endo: Int. J. Fatigue, 16 (1994), p.163

[8] Y. Murakami, S, Kodama and S. Konuma: Transactions of the JSME, A54-500 (1998), p. 688

Key Engineering Materials Vols. 385-387 (2008) pp 189-192
© (2008) Trans Tech Publications, Switzerland
doi:10.4028/www.scientific.net/KEM.385-387.189

Inference Engine and Explanation Mechanism in the Expert System of Fracture Mechanics Analysis for Component Design

Zhu Shi-fan [1,a], Li Qing-fen[1,b], Yu Zhi-hong[2,c]

[1] College of Mechanical and Electrical Engineering, Harbin Engineering University, Harbin 150001, China

[2] China Warship Research and Design Centre, 268 Zhiyang Road, Wuhan, 430064, China

[a]zhushifan@hrbeu.edu.cn, [b]qingfli@yahoo.com.cn, [c]yzhzsl@163.com

Keywords: Inference engine; explanation mechanism; expert system; fracture mechanics

Abstract. An expert system (ES) prototype in structural component design based on fracture mechanics analysis was developed recently. The system consists of several main functional parts. Among them, the inference engine is the control structure of ES which allows the expert to use searching strategies to test different hypotheses and arrive at ES conclusions. A general inference engine which can perform different inference by loading up different knowledge bases and a set of track explanation mechanism which ensure the inference process visible and reliable were established and discussed in this paper.

Introduction

Engineering failures may occur in some well-designed component and structures, and the cause has very often been a pre-existing crack or other defect. Fracture mechanics is a method which aids in predicting the remaining service life of a component that contains a defect such as a crack. It is a tool which relates the size of a defect to the likelihood of its causing fracture in a given material under a given stress regime. Stress intensity factor (K_1), crack opening displacement (COD), J-integral, FATT, etc, having been adopted for many industrial applications. The design engineers can greatly improve the reliability and serviceability of a structure using fracture mechanics.

AI and system technology are the major factor in the knowledge age. For determining the fracture characteristic of materials and structures, knowledge-based system could be very useful [1]. Several expert systems related to fracture mechanics were developed, where the usefulness of an AI approach to some deterministic problems were discussed and some ES approaches to fracture mechanics problems were devised [2-4].

An expert system prototype in structural component design based on fracture mechanics analysis was developed recently [5]. The system was a useful tool to assist a non-expert (with basic mechanics knowledge) make a quick access in mechanical component design and analysis. In this paper, the inference engine and explanation mechanism in the expert system is discussed.

Main Functional Components

An ES has at least three major components: “dialog structure”, “inference engine” and “knowledge base” [4]. Our system is composed of several functional components: a general inference engine, a set of knowledge bases and data bases, an explanation model, a bases administration system, an engineering calculation model, an on-line help service and the interface. The framework of the system is shown in Fig.1.

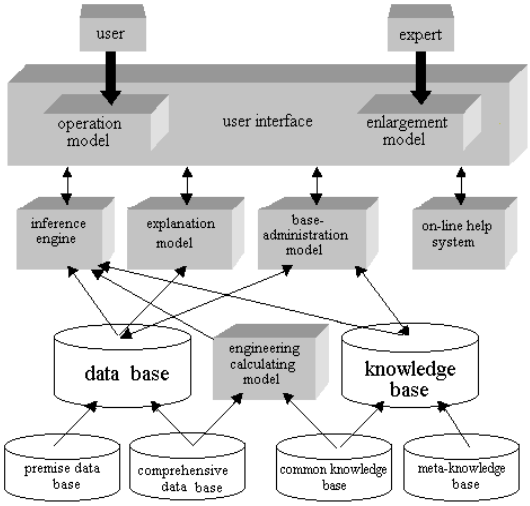

Fig.1 Framework of the ES

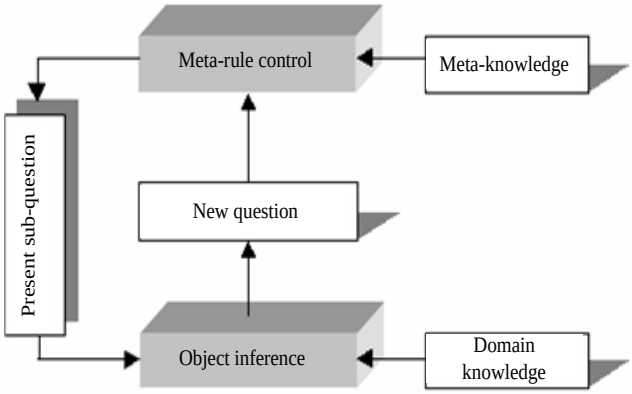

Fig.2 Two-level control inference structure

Inference Engine

The inference engine is the problem processing part of the expert system. It is the control structure of the system which allows the expert to use search strategies to test different hypotheses and arrive at expert system conclusions. The inference engine is related to the structure of knowledge databases and the expression form of knowledge.

There are three inference engines in the ES. The first one is the object inference engine which may accomplish the index and arrange the tasks, and it also has the function of controlling and coordinating the other inference engines. The second is the rule-sets inference engine which may implement the inference operation of rule-sets by using forward chaining strategy. The third is the method inference engine which finally explains the conclusions.

Production rules and an approximate inference model of the logical deduction models are used in the ES. A meta-rule control which may avoid the blindness in searching and a data-driving control strategy are used in this system. They give friendly human computer interface and aid the user in searching. The two-level control inference structure of the ES is shown in Fig. 2.

A complete matching of rule-matching method is adopted in the inference engine. In order to eliminate the conflicts of inferences, the following strategies are used:

(1) Context confine: each type of engineering component has its own knowledge bases;

(2) Rules arrangement is in confidence level order;

(3) For the rules which have the same confidence level, the first rule has the first priority to be chosen for inference.

The inference engine can perform different inference by loading up different knowledge bases in the system. The flow chart of the inference is shown in Fig.3.

Explanation Model

Explanation model allows the users to question and challenge the results from the expert system as well as to understand how the results are achieved. The structure of the explanation model is shown in Fig. 4.

There are two parts in our explanation model. One is “prepared test”, also called “canned explanation”, which is used for answering the questions of users and explaining the initial inference data. Another part is for explaining the reasoning of the expert system where both “canned

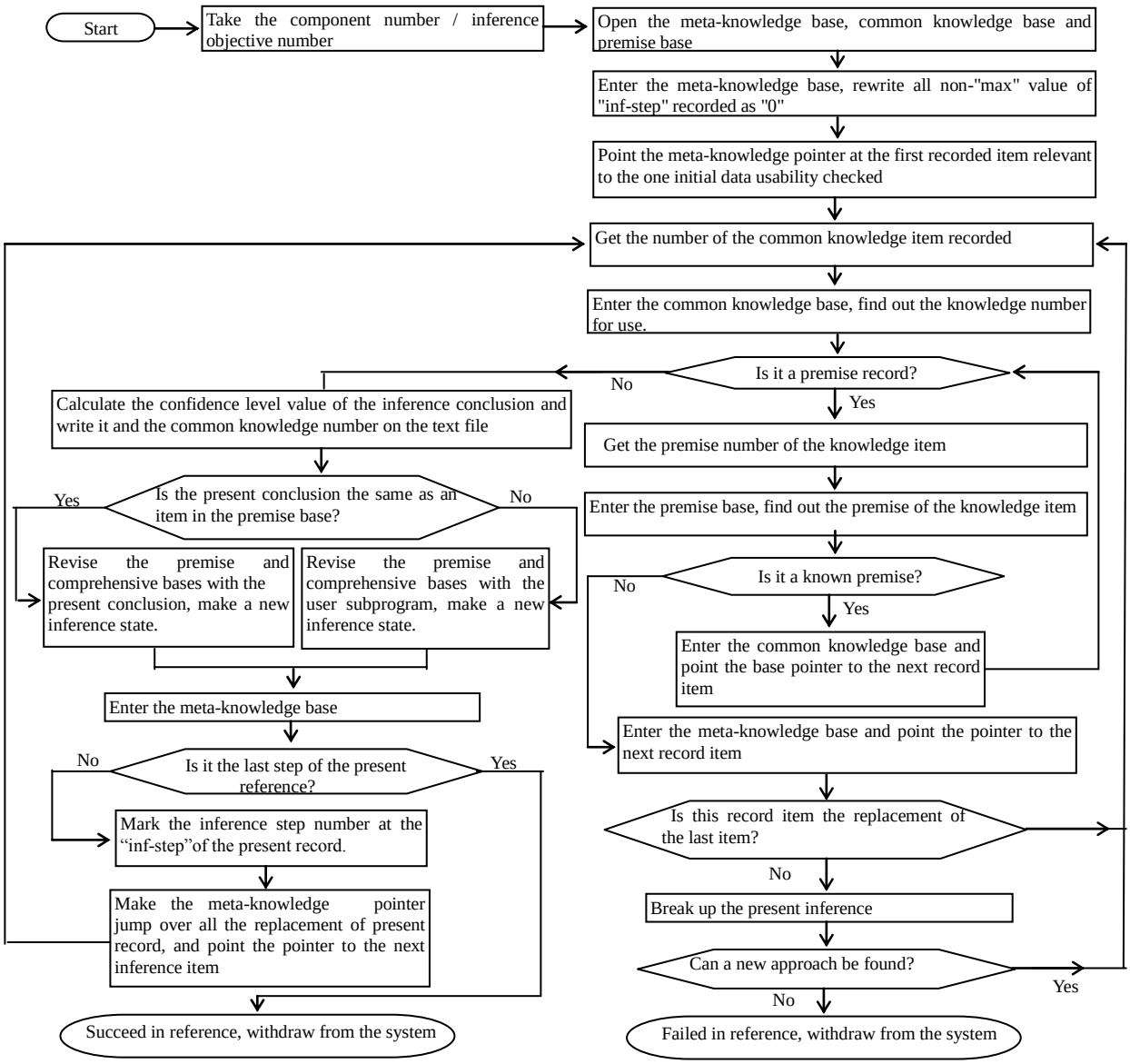

Fig. 3 Flowchart of the inference

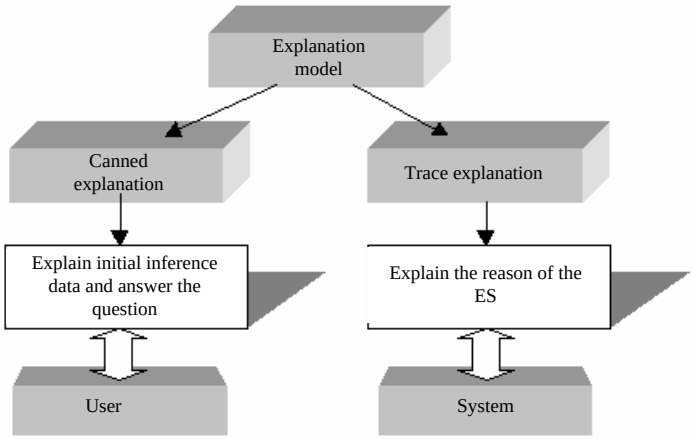

Fig.4 Structure of the explanation model

explanation" and "trace explanation" were used. When users want to know the inference process or the explaining, they may push the "track" or "explain" button and look through them. It may ensure the inference process visible and reliable.

An Analysis Example

In the ES, the most important types of defects are simplified for fracture analysis. Stress, strain, and crack-size analysis can be carried out for different component. By specifying the nature of loading, material type, component geometry and size, the critical crack size at which rapid fracture occurs can be automatically determined from the system. This includes the time history of crack growth such that a non-destructive inspection procedure can be established. It will also indicate whether the structure has or has not failed. One way of determining the structural integrity is to compare the calculated fracture toughness to the fracture toughness of the material or to some other fracture parameters. If the crack length and then the resulting fracture toughness determined by the ES are lower than the fracture toughness of the material, then the structure is judged to be safe. One can also use the threshold values determined experimentally, for fatigue life of material / component as the fracture criteria.

We take the analysis of the crack tip opening displacement (COD), δ , in the pressure vessel as an example. The stress of pressure vessel is defined as follow:

$$\sigma = PD/2t \,. \tag{1}$$

Where, *P* is the inner pressure of vessel, *t* is the thickness of vessel wall, *D* is the inner diameter of vessel.

The crack tip opening displacement δ is calculated according to the D-B model equation:

$$\delta = \frac{8\sigma_s \bar{a}}{E\pi} \ln Sec\left[\frac{\pi(M\sigma)}{2\sigma_s}\right]. \tag{2}$$

Where, $\bar{a} = \alpha_1^2 a$, and $M = (1+\alpha\frac{\bar{a}^2}{R_t})^{1/2}$, in which, σ_s is the yield strength of the vessel material, *a* is the half crack length, *R* is the inner radius of the vessel, α and α_1 are the correction factors, and *E* is the elasticity modulus.

When the loading, the material type, the component geometry and size are determined, δ is then determined based on equations above. The ES system may compare δ calculated with the material parameter δ_c, if $\delta < \delta_c$, the structure is judged to be safe, whereas, if $\delta \geqq \delta_c$, the structure is judged to be failed.

Summary

The inference engine and explanation mechanism of the expert system prototype in structural component design based on fracture mechanics analysis, were established and discussed in this paper. An analysis of the COD in the pressure vessel, as an example, was also discussed.

References

[1] H. Liebowitz: Engineering Fracture Mechanics, Vol.50 (1995), p. 601

[2] K.Y. Lee, H.Liebowitz: Engng Fracture Mech., Vol. 50 (1995), p. 609

[3] H. Liebowitz, J. S. Sandhu, J.D lee: Engineering Fracture Mechanics, Vol.50 (1995), p. 653

[4] Q. F. Li, H. F. Liu, J.T Zhang : Material & Design, Vol.18 (1997), p. 1

[5] Z.Y. Ren, Q. F. Li: Key Engineering Materials, Vols. 297-300(2005), p. 2681

Key Engineering Materials Vols. 385-387 (2008) pp 193-196
© (2008) Trans Tech Publications, Switzerland
doi:10.4028/www.scientific.net/KEM.385-387.193

Influence of Anisotropic Properties upon Stress Intensity Factors under Biaxial Stress

Akira Shimamoto[1, a], Hiroshi Ohkawara[1, a]
and Jeonghwan Nam[2, b]

[1]Saitama Institute of Technology, 1690, Fusaiji, Fukaya, Saitama 369-0293, Japan

[2]Hi-tech Mechanical Design Research Center, Yeungnam University, Kyoungbuk, Korea

[a]shimamot@sit.ac.jp, [b]nam@jj.ac.kr

Keywords: Anisotropy, Stress Intensity Factor, Experimental Stress Analysis, Fracture Mechanics, Biaxiality Ratios

Abstract. In this study, stress intensity factors were investigated and determined by photoelastic and caustics methods to clarify the mechanical behavior of crack tips under various biaxiality ratios. Polycarbonate (PC) plates with isotropic and anisotropic properties were used as specimens. The results confirmed that regardless of biaxiality ratio or the material's property only 'K_I' was generated in cases of a crack angle $\theta = 0^o$. It was also confirmed that only K_I was generated in the isotropic PC plate with crack angle $\theta = 45^o$ under a biaxial load (1:1). When the biaxiality ratio is more than 1:1 with a crack angle $\theta = 45^o$, both K_I and K_{II} are simultaneously generated in the isotropic specimen. Furthermore, K_I, and K_{II} values are influenced most by the extrusion direction in the anisotropic specimens as the biaxiality load ratios increase.

Introduction

To maintain low weights for upsizing machines and structures, polymeric materials that have high strength and elastic moduli are employed as structural materials in aircraft, ships and automobiles. Due to increasing machine performance, materials today face more complicated fracture phenomena. Instead of one-dimensional stress, these fracture phenomena usually create biaxial or multi-axial stress conditions; therefore, it has become increasingly important to understand basic deformation behaviors and characteristics of the fracture processes of polymeric materials under multi-axial stress conditions. Understanding this will ensure reliability for such structures and reduce the probability of accidents.

This study aims to analyze the effect of anisotropy upon deformation behavior near the tip of a crack under biaxial stress conditions. Polycarbonate materials were used as specimens since they are widely used as industrial materials and have both isotropic and anisotropic properties. Careful observation of the stress intensity factors using photoelastic and caustics methods were carried out on specimens at various bi- axial loading ratios. Data from the two methods were then analyzed and the effect of anisotropy clarified.

Specimens and experimental methods

Specimens. Two types of specimens, polycarbonate (PC) band plates having an isotropic property (casting: PS1S) and ones having an anisotropic property (extrusion: LEXAN 9030) were used in this experiment. Figure 1 shows the shapes and dimensions of the specimens. The thicknesses of the isotropic and anisotropic specimens were 6 mm and 3 mm, respectively. Specimens were machined with an end mill with a vertical machining center. A crack was created in each specimen with a long end mill of diameter 0.8 mm until it reached a length of 28 mm. Then, the edge of a razor with a thickness of 0.08 mm was pushed into both crack tips to add 1 mm to the crack length. This made the crack more like a natural one. The extrusion direction of the PC band plate with anisotropic

properties was defined as the Y-axis and the cracks were made at notch angles (θ) of 0 and 45 degrees from the Y-axis in both the isotropic and anisotropic specimens.

Experimental methods. A hydraulic high-speed biaxial material testing device [1], vertical with four actuators that face one another at right angles, developed by the authors was used for this study. The actuators are independent in each direction and the load ratio can be varied. In the experiments, the loading velocity was fixed at 0.1 mm/s, and the load for the X-axis was fixed at 980 N and the load for the Y-axis increased in four steps from 980 N to 3920 N (1:1 to 1:4). We defined β as the biaxial load ratio, P_y / P_x. Stress intensity factors were then analyzed by photoelastic and caustics methods. The photoelastic fringe patterns and the caustics patterns near the crack tips were continuously observed under each load ratio and pictures taken in sequence. To measure the dimensions of the caustics patterns, reference lines were inserted at 10 mm intervals on the screen.

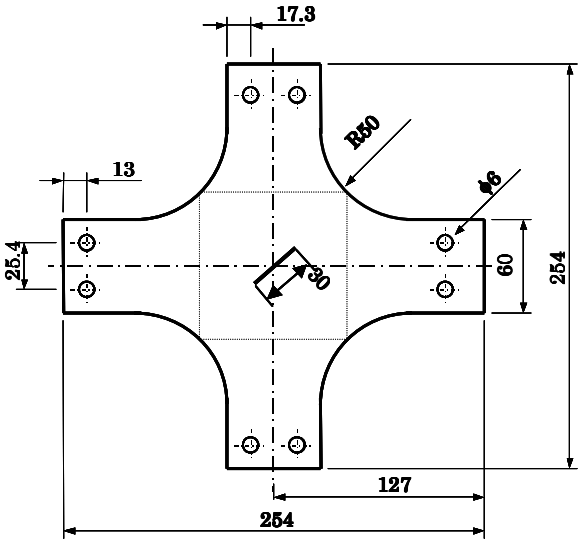

(Unit: mm)

Fig. 1 Dimensions of cruciform specimen

Caluculation of stress intensity factors

Photoelasticity. For calculation of the stress intensity factors, K_I and K_{II}, pictures of the isochromatic fringe patterns under each load were captured into a personal computer, and the necessary values measured. The factors were then calculated for Mode I using the Irwin's method [2], and by Equations for the mixed mode using the Smith's method [3].

Caustics method. A He-Ne laser (LHG-3223: TOSHIBA) was used as the light source. The parallel incident light produced by the collimator (Auto Collimator: Nikon) passed through the specimen under a biaxial tensile load. Caustics pattern images were captured from the rear of the screen. It is known that when only K_I exists, the pattern is an almost perfect circle, while the pattern loses its circular shape and becomes a more spiral caustics curve [4-6] when both K_I and K_{II} exist. For the mixed mode, K_I and K_{II} were calculated using individual equations [7, 8].

Results and discussion

The relationship between stress intensity factor K_I and the load ratio under biaxial stress. The influence of the difference between the isotropic and anisotropic properties of the PC materials upon the area near the crack tip was examined under biaxial stress conditions using photoelasticity and caustics methods. Especially, we were interested in the behavioral differences between isotropic and anisotropic PC materials. Figures 2(a) to (d) show some of the isochromatic fringe patterns (left side) and the caustics images (right side) under each load ratio for isotropic material with 0º notch angle. As shown in Figure 2, the isochromatic fringe patterns of both the isotropic and the anisotropic PC band plates were generated symmetrically and almost perpendicular to the direction of the crack under biaxial stress conditions with load ratios from 1:1 to 1:4. Their caustics images were almost perfect circles. This shows that only K_I acted no matter what the load ratio or the material's property was when notch angle (θ) is 0º. Further, the stress intensity factor K_I in Mode I was determined using the above noted equations corresponding to the photoelastic and caustics methods. Figure 3 shows the relationship between load ratios and the normalized stress intensity factors K_I / K_0 ($K_0 = \sigma_0(\pi a)^{1/2}$, $\sigma_0 = P_y / (w \cdot t)$) when notch angle ($\theta$) is 0º for isotropic and anisotropic materials, respectively. The values of K_I / K_0 determined by photoelasticity agree well with those by the caustics method; with there being no influence from isotropic or anisotropic properties.

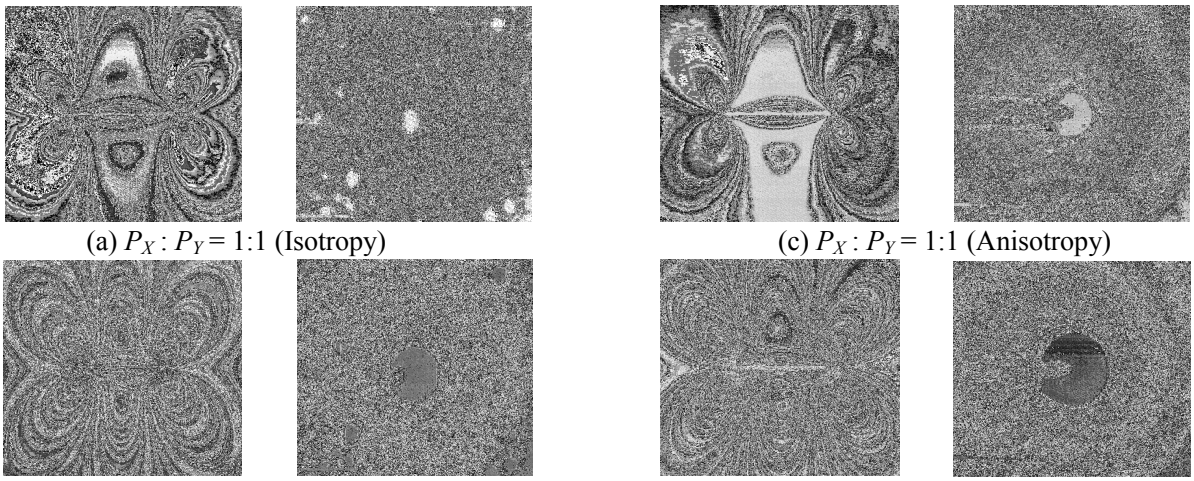

(a) $P_X : P_Y = 1:1$ (Isotropy) (c) $P_X : P_Y = 1:1$ (Anisotropy)

(b) $P_X : P_Y = 1:4$ (Isotropy) (d) $P_X : P_Y = 1:4$ (Anisotropy)

Fig. 2 Isochromatic fringe patterns and caustics images near crack tip under biaxial stress conditions ($\theta = 0^o$)

The relationship between the stress intensity factors, K_I and K_{II}, and the load ratio under biaxial stress conditions. The photoelastic fringe patterns and the caustics images of the PC material with isotropic properties under equal biaxial load conditions (load ratio, 1:1) in Figures 4(a) to (d) show that only K_I acted when the notch angle (θ) is 45º, generally the same as when θ is 0º. As the load ratio became more than 1:1, the isochromatic fringe loop became asymmetrical and oblique. The caustics image lost its circular shape, and became a spiral, as shown in Figures 4(a) and (b). This shows that not only the opening stress intensity factor, K_I, but also the in-plane shearing stress intensity factor, K_{II}, was brought into play. For the material with anisotropic properties, as shown in Figure 4(c) and (d), the caustics image lost a little of its perfectly-circular shape to become a spiral (mixed-mode), and the isochromatic fringe pattern was also ansymmetrical to the crack (mixed-mode) under equal biaxial stress conditions (1:1). This was due to the extrusion direction, that is, the anisotropic properties. It is also shown that as the load ratio increased the photoelastic fringe loop became asymmetrical and oblique. The caustics image became a spiral, as with the material with isotropic properties.

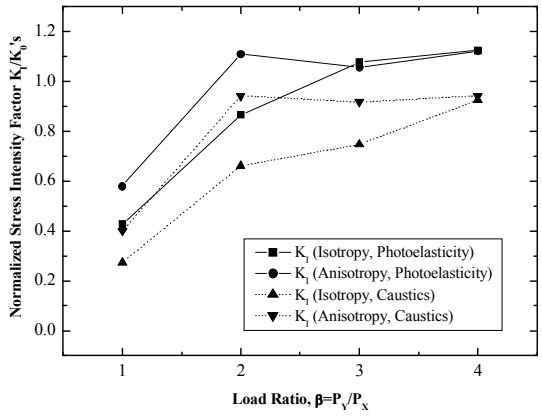

Fig. 3 Relationships between biaxial load ratio and stress intensity factor ($\theta = 0^o$)

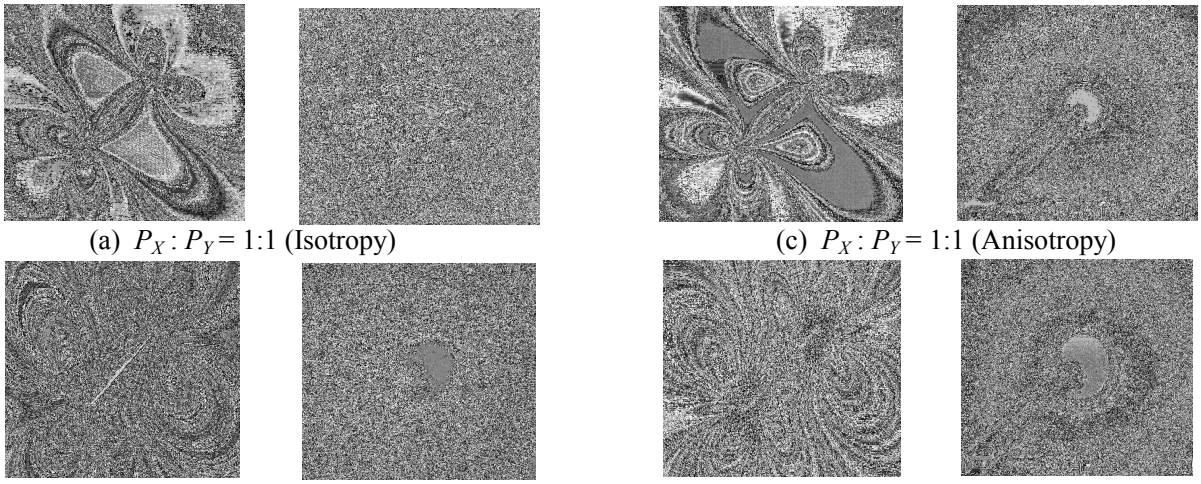

(a) $P_X : P_Y = 1:1$ (Isotropy) (c) $P_X : P_Y = 1:1$ (Anisotropy)

(d) $P_X : P_Y = 1:4$ (Isotropy) (d) $P_X : P_Y = 1:4$ (Anisotropy)

Fig. 4 Isochromatic fringe patterns and caustics images near crack tip under biaxial stress conditions ($\theta = 45^o$)

Figure 5 shows the relationship between the load ratios and the values of the normalized stress intensity factors, K_I / K_0 and K_{II} / K_0, found using photoelastic and caustics methods. In Figure 5, the solid lines show the relationships obtained from photoelastic method and the dot lines show the ones obtained from caustic method. As shown in Figure, the normalized stress intensity factor K_I / K_0's are increase and almost constant, but K_{II} / K_0 are increase as increasing load biaxiality ratio. As shown in Figure 5, in the case of materials with anisotropic properties, the relationships between the extrusion direction, the load ratios and the stress intensity factors, K_I and K_{II}, are influenced most by the extrusion direction, that is, the anisotropic property as the biaxial load ratioβ increases. Consequently, when materials with anisotropic properties are used in machines or structural members, it is important to consider the extrusion direction of the material and the load ratios incorporated in their design.

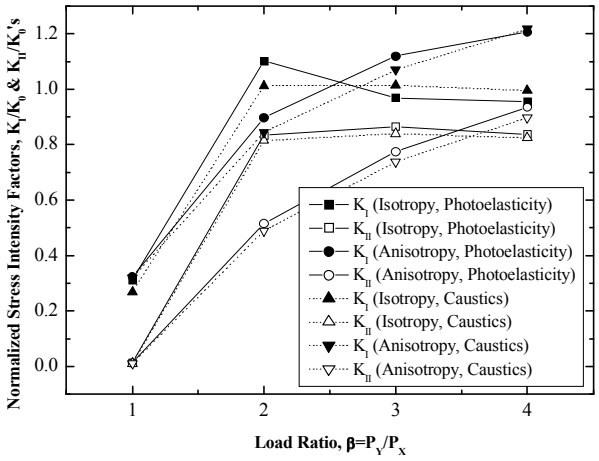

Fig. 5 Relationships between biaxial load ratio and stress intensity factor (θ = 45º)

Conclusions

The stress intensity factors K_I, K_{II}, of PC band plates with isotropic and anisotropic properties were determined by photoelastic and caustics methods under biaxial stress conditions. The following conclusions can be drawn from the results:

1. When the notch angle θ is 0˚ under biaxial load conditions, there is no influence from either isotropic or anisotropic properties, only K_I is affected.
2. For PC band plates with isotropic properties, only K_I is generated under equal biaxial load, and both K_I and K_{II} are generated under unequal biaxial load when the notch angle θ is 45˚.
3. K_I, and K_{II} values are influenced greatly by anisotropic properties as the load ratio β increases.

Acknowledgement

This work was supported by the High-Tech Research Center in Saitama Institute of Technology.

References

[1] J. Nam, A. Shimamoto, T. Shimomura and S. Tsukagoshi: ATEM'99, Proceeding Vol. 1 (1999), pp.350-355.

[2] G.R. Irwin: Proc. of SESA, Vol. 16-1(1958), pp.93-96.

[3] D. Smith and C.W Smith: Eng. Frac. Mech., Vol. 4 (1972), pp.357-366.

[4] J.M. Etherridge and J.W. Dally: Experimental Mechanics, Vol. 17 (1977), pp.248-254.

[5] K. Shimizu, H. Shimada and T. Sasaki: Transaction JSME, Seriase. A, Vol. 46-411 (1980), pp.1196-1202.

[6] P. S. Theocaris and E. Gdoutos: Trans. ASME, Ser. E, Vol. 39-1 (1972), p.75.

[7] S. Takahashi and K. Shimizu: Science of Machine, Vol. 37-5 (1985), pp.621-626.

[8] A. Shimamoto and S. Takahashi: Bulletin of JSME, Vol. 27-229 (1984), pp.1346-1352.

Key Engineering Materials Vols. 385-387 (2008) pp 197-200
© (2008) Trans Tech Publications, Switzerland
doi:10.4028/www.scientific.net/KEM.385-387.197

Influence of Grain Size on Notch Sensitivities in Fatigue of Carbon Steel

T. Kanemaru[1,a], N. Kawagoishi[1,b], E. Kondo[1,c],
Q.Y. Wang[2,d] and Y. Ohzono[1,e]

[1] Kagoshima University, 1-21-40 Korimoto, Kagoshima 890-0065, Japan
[2] Sichuan University, Chengdu 610065, China
[a] m0781016@mech.kagoshima-u.ac.jp, [b] hiro@mech.kagoshima-u.ac.jp,
[c] kondo@mech.kagoshima-u.ac.jp, [d] wanggy@scu.edu.cn,
[e] xpsohzno@jm.kuas.kagoshima-u.ac.jp

Keywords: Fatigue, Carbon Steel, Notch Sensitivity, Grain Size, Crack Initiation, Crack Propagation

Abstract. In order to investigate the influence of grain size on notch sensitivities in fatigue of a fine-grained carbon steel, rotating bending fatigue tests were carried out using specimens with a V-grooved circumferential notch of commercial fine-grained carbon steel with grain size of 6.5μm. The results were compared with those of a larger grain sized carbon steel (grain size: 20 μm) and the notch sensitivities were evaluated based on Linear notch mechanics proposed by Nisitani. Notch sensitivities for both of fatigue limits for a crack initiation and its propagation of the fine grained steel were high. The results were discussed from the view points of the size of area related to crack initiation and the crack growth resistance.

Introduction

In general, although the fatigue limit of a smooth specimen in carbon steel is increased similar to static strength by refining the grain size, the one for crack propagation in a sharply notched specimen is hardly influenced [1]. This is related to the phenomenon that there is no or little influence of grain size on the crack growth rate [2]. These results were obtained by steels with conventional grain size larger than about 10μm. Recently, ultra-fine-grained steels with grain size smaller than a few μm have been developed and the mechanical properties were investigated. It was reported that the steels have not only a higher fatigue strength but also an excellent crack growth resistance [3]. These results suggest that fatigue properties of notched member with a fine grain are different from the ones in conventional grain sized steel.

In this study, in order to investigate the notch sensitivities in fatigue for commercial fine-grained carbon steel, rotating bending fatigue tests were carried out using specimens with a V-grooved circumferential notch and smooth specimens. The results were evaluated based on Linear notch mechanics [4] and discussed through the observation of surface fatigue damage due to stress repetitions.

Material and experimental procedures

Material used was a commercial rolled carbon steel with a mean grain size of 6.5μm. The chemical composition is shown in Table 1. The material was annealed at 950˚C for 2h in order to get a different grain size of 20μm.

Fig. 1 shows microstructures of the as received and the annealed materials. In the following, these materials were called as a fine-grained steel and a coarse-grained steel, respectively.

Table 2 shows their mechanical properties.

Table.1 Chemical composition (wt.%)

C	Si	Mn	P	S	Cu	Ni
0.16	0.35	1.4	0.014	0.002	0.02	0.01
Cr	Sn	T.Al	B	Nb	V	Mo
0.02	0.001	0.018	1.00E-04	0.001	0.055	0.002

Table.2 Mechanical properties

	σ_y (MPa)	σ_B (MPa)	ψ (%)
6.5 μ m	451	603	69.2
20 μ m	321	515	65.1

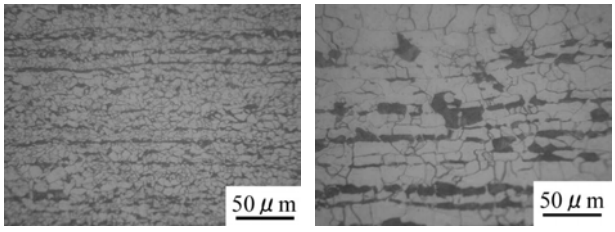

(a) Fine-grained steel (b)Coarse-grained steel

Fig.1 Microstructures

Fig. 2 shows shape and dimensions of specimens. Fatigue tests were carried out using specimens

with a V-grooved circumferential notch and smooth specimens for evaluation of notch sensitivity. Moreover specimens with a partial notch of 0.1mm in depth and 2.5mm in notch radius as shown in Fig.2 (c) at the center part of smooth specimen to localize the crack initiation site were also used for the successive observation of surface damage. The fatigue strength reduction factor in a partially notched specimen was smaller than 1.1. Therefore this specimen can be regarded as a smooth specimen. After machining, all of the specimens were annealed at 600˚C for 1h in N_2 gas to release the residual stress and then electro-polished about 10-20μm from the surface layer. Crack initiation and propagation behavior was measured by using plastic replication method. The crack length ℓ was defined as the length of the circumferential direction along the specimen surface. Testing machine used was a rotating bending machine operated at 50 Hz in ambient air.

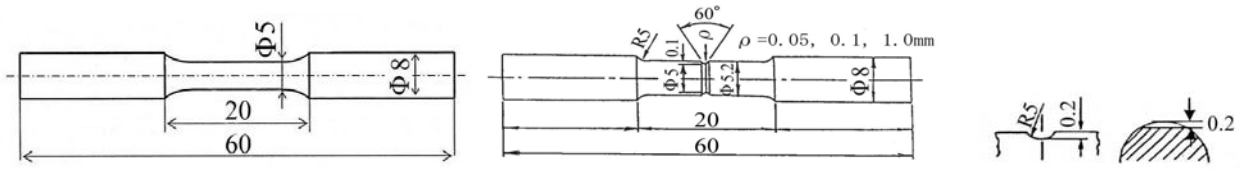

(a) Smooth specimen (b) Notched specimen (c) Detail of partial notch

Fig.2 Shape and dimensions of specimens

Results and discussion

Figs. 3 and 4 show *S-N*$_f$ curves and *S-(N*$_f$*-N*$_{0.05}$*)* curves for partially notched specimens, respectively. In the figure, $N_{0.05}$ means 0.05mm crack initiation life in the partially notched specimen. By refining grain size, not only the resistance to crack initiation but also the resistance to crack propagation are increased.

Fig. 5 shows examples of non-propagating cracks in sharply notched specimen with notch radius of ρ=0.05mm. Morphology of a crack is more zigzag in the coarse-grained steel than in the fine one, corresponding to their grain sizes.

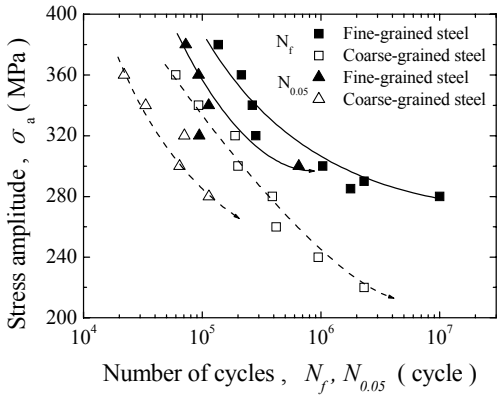

Fig.3 *S-N*$_f$ curves

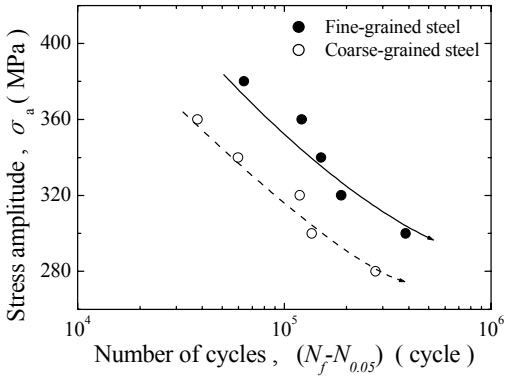

Fig.4 *S*-(*N*$_f$*-N*$_{0.05}$) curves

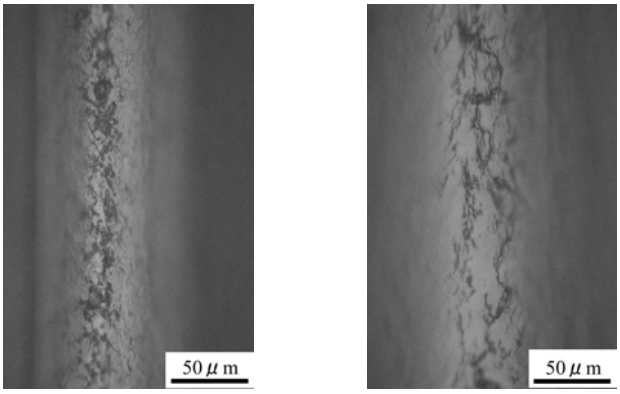

(a)Fine-grained steel (b)Coarse-grained steel

Fig.5 Non-propagating cracks in sharply notched specimen (ρ=0.05mm)

Fig. 6 shows fatigue limits for crack initiation and propagation σ_{w1} and σ_{w2} against for stress concentration factor K_t. Both of fatigue limits σ_{w1} and σ_{w2} are increased by refining grain size, though

the increase is small in σ_{w2}. The increase in σ_{w1} is caused by the constraint of a grain boundary [5]. However, many studies showed that there is no or little influence of grain size on σ_{w2} as mentioned before [1]. In the following, crack growth resistances in both steels will be compared by evaluating the growth rate of a small crack using partially notched specimens.

Fig. 7 shows relation between crack growth rate and the term $(\sigma_a/\sigma_B)^n\ell$ which is effective parameter evaluating the growth rate of a small crack [6]. In both steels, crack growth rate can be expressed by a relation, $d\ell/dN=C(\sigma_a/\sigma_B)^n\ell$ (C, n: constants, n≃7 is fine-grained steel,n≃9.5 is coarse one). In the relation, a reciprocal of C means crack growth resistance. The resistance of the fine-grained steel is larger than the one of the coarse one, corresponding to the difference in σ_{w2}.

Fig. 8 shows fatigue damage around a crack tip in both steels, under the same mechanical severity $(\sigma_a/\sigma_B)^n\ell$ at the crack tip. Slipped zone corresponding to the grain size at the crack tip is observed in both steels, meaning that the slipped zone is affected by grain boundary. This may be main reason for the high resistance to a crack growth in the fine-grained steel.

Fig. 9 shows the notch sensitivity based on Linear notch mechanics proposed by Nisitani [4]. It is sensitive in both of limits for a crack initiation and its propagation in fine-grained steel.

Fig. 10 is an example showing the change in surface state of a partially notched specimen due to stress repetitions in fine-grained steel. Similar to the results reported before [2], a crack initiated after whole of a grain was covered with slip bands. That is, the area related to a crack initiation is one grain size. From this result and the fact that fatigue limit of notched specimen is determined by the maximum stress and stress gradient at notch root [4], the influence of the maximum stress on fatigue limit for crack initiation is larger in a fine-grained steel than in a coarse one. That is, the sensitivity for crack initiation is high in a fine-grained steel. On the other hand, the higher notch sensitivity for crack propagation in a fine-grained steel can be explained from that the influence of grain size is larger in σ_{w0} than in σ_{w2}.

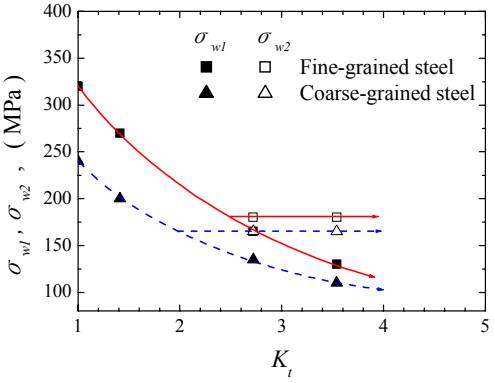

Fig.6 Relation between σ_{w1}, σ_{w2} and K_t

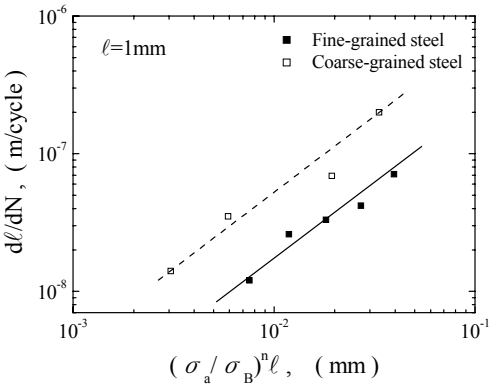

Fig.7 Relation between crack growth rate and $(\sigma_a/\sigma_B)^n\ell$

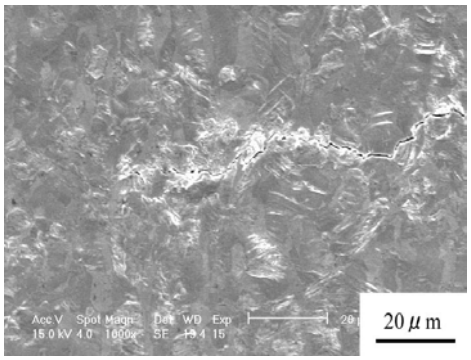

(a) Fine-grained steel

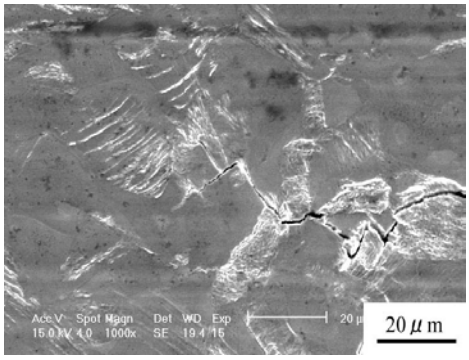

(b) Coarse-grained steel

Fig.8 Fatigue damage around a crack tip ($(\sigma_a/\sigma_B)^n\ell$≃$9.7\times10^{-3}$mm)

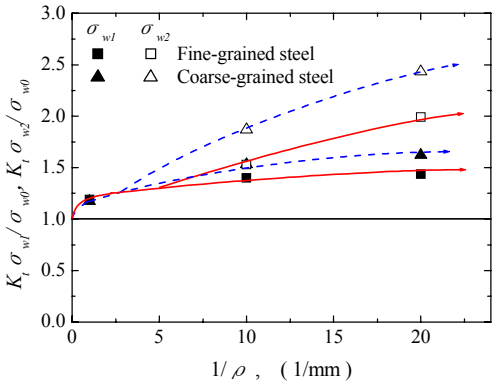

Fig.9 Relation between $K_t\sigma_{w1}/\sigma_{w0}$, $K_t\sigma_{w2}/\sigma_{w0}$ and $1/\rho$

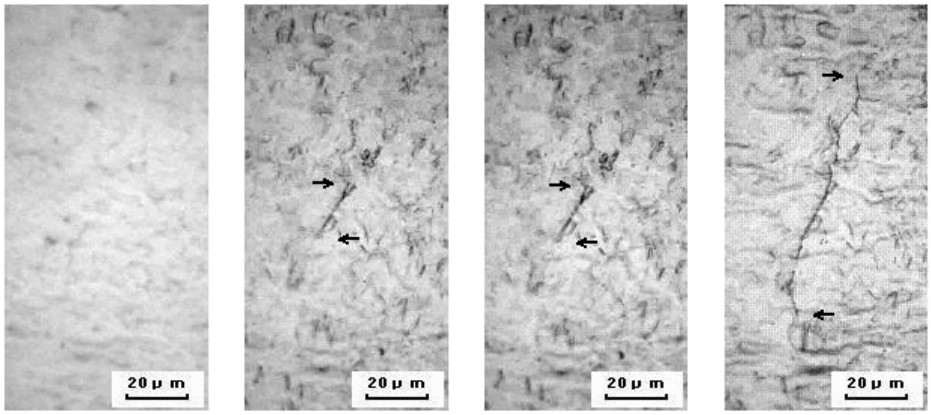

N=0 N=4×10^4 N=5×10^5 N=7.5×10^5

Fig. 10 Change in surface state of a partially notched specimen due to stress repetitions (Fine-grained steel ⇔ axial direction) (σ_a=360MPa)

Conclusions

In order to investigate the notch sensitivities in fatigue for a commercial fine-grained carbon steel with grain size of 6.5μm, rotating bending fatigue tests were carried out using specimens with a V-grooved circumferential notch and smooth specimens. The results were evaluated based on Linear notch mechanics through the surface fatigue damage due to stress repetitions. The steel has higher fatigue limits and notch sensitivities for a crack initiation and its propagation than larger grain sized steel.

Acknowledgement

The authors express their sincere thanks to Nakayama Steel Works, Ltd. for supplying the material, and to Mr. M. Yamakita for his effort to the experiment.

References

1. H. Nakazawa, H. Kobayashi, A. Morita, S. Iikura, K. Miyauchi and Y. Ishii, Trans. of the J. Soc. of Mech. Eng., Japan, 40-329 (1974), pp. 9-22 (in Japanese).
2. M. Kage and H. Nisitani, Trans. of the J. Soc. of Mech. Eng., Japan, 51-461 (1985), pp. 3-9 (in Japanese).
3. H. Kimura, Y. Akiniwa, K. Tanaka, J. Kondo and T. Ishikawa, J. Soc. Mater. Sci., Japan, 51-7 (2002), pp. 795-800 (in Japanese).
4. H. Nisitani, Trans. of the J. Soc. of Mech. Eng., Japan, 49-447 (1983), pp. 1353-1359 (in Japanese).
5. T. Yokobori, Kikai no Kenkyu, 12-12(1960), pp.1623-1628 (in Japanese).
6. H. Nisitani, Mechanics of Fatigue, ASME AMD (edited by T. Mura), 47(1981), pp.151-166.

Key Engineering Materials Vols. 385-387 (2008) pp 201-204
© (2008) Trans Tech Publications, Switzerland
doi:10.4028/www.scientific.net/KEM.385-387.201

Investigation into Damage of Aluminum Multi-Wall Shield under Hypervelocity Projectiles Impact

Gongshun Guan[1,a], Baojun Pang[1, a], Runqiang Chi[1, a] and Naigang Cui[1, a]

[1]P. O. Box 3020, Science Park, Harbin Institute of Technology, Harbin, 150080, P. R. China

[a]ggsh@hit.edu.cn

Keywords: Hypervelocity impact; Multi-wall; Damage; Crack; Experiment

Abstract. In order to study the hypervelocity impact of space debris on spacecraft through hypervelocity impact on aluminum alloy multi-wall structure, a two-stage light gas gun was used to launch 2017-T4 aluminum alloy sphere projectiles. The projectile diameters ranged from 2.74mm to 6.35mm and impact velocities ranged from 1.91km/s to 5.58km/s. Firstly, the advanced method of multi-wall shield resisting hypervelocity impacts from space debris was investigated, and the effect of amount and thickness of wall on shield performance was discussed. Finally, by regression analyzing of experiment data, the experience equations for forecasting the diameter of the penetration hole on the first wall and the diameter of the damaged area on the second wall of aluminum multi-wall shield under hypervelocity normal impact of Al-spheres were obtained. The results indicated that the performance of multi-wall shield with more amount of wall is excellent when area density is constant. At the same time, intensity of the first wall and protecting space play the important roles.

Introduction

Hypervelocity impacts on spacecrafts in low earth orbit by meteoroids and space debris posed a threat to space missions [1,2]. Therefore, the design of spacecraft for an earth–orbiting mission must take into account the possibility of such impacts and their effects on the spacecraft structure. The dual-wall structure is the conventional shield type used to protect space structures by hypervelocity meteoroids and orbital debris impacts [3,4]. Comparing dual-wall shield, multi-wall shield is better resistance shielding systems [5]. The hole size on the first wall, the damaged area on the second wall and the crack length on the third wall can be used to evaluate the protection ability of multi-wall shield. The main factors affecting the damage mode and resist character of multi-wall shield from hypervelocity impact are impact velocity of projectile, diameter of projectile, thickness of bumper, amount of wall and protection spacing.

In this study, dual-wall structure, three-wall structure and four-wall structure were investigated experimentally in a systematic manner to generate a large database of impact results and enable a better understanding of the processes that occur upon impact of hypervelocity particles on multi-wall shield. Results showed that the performance of multi-wall shield with more amount of wall is excellent when area density is constant. At the same time, intensity of the first wall and protecting space play the important roles.

Hypervelocity impact test

Test facility. The tests were performed with a gas driver two-stage light gas gun at Harbin Institute of Technology, which is capable of accelerating projectiles up to 0.7g at a maximum velocity of 7km/s. The pump tube caliber is 57mm, and the launch tube calibers are 7.6mm and 10mm respectively. In a typical shot operation, high-pressure nitrogen gas is stored in the first stage of the gun, until it is discharged on the back of the piston through the opening of a custom fast valve. The driver gas coming from the first stage pushes the piston along the pump tube, thus compressing the hydrogen gas in the second stage up to very high pressure and temperature. The projectile velocities were measured by magnetic induction. The uncertainty in these measurements is approximately ± 2%. Test samples were fixed in the vacuum target chamber, which simulates space environments. The pressure in test chamber was approximately 200Pa. The projectile was contained in a cylindrical plastic sabot

consisting of two pieces. The sabot was separated from the projectile by the gas dynamic drag force in flight and as such was deflected from the path of the projectile, i.e. the ballistic line.

Testing. The impact tests have been performed onto multi-wall shield, each of them consisting of 2A12 aluminum alloy bumpers and 5A06 aluminum alloy rear wall. The total thickness of bumpers is 2mm. The space between the first wall and the rear wall was 100mm. Table 1 shows the test condition of aluminum alloy multi-wall structure. d_p, V_p, t_1, S_1,, t_2, S_2, t_3, S_3 and t_w are projectile diameter, impact velocity, the first wall thickness, space between the first wall and the second wall, the second wall thickness, space between the second wall and the third wall, the third wall thickness, space between the third wall and the rear wall, rear wall thickness respectively. For this study, 2017-T4 aluminum alloy spheres were launched, with the protection of sabots, at velocities between 1.91km/s and 5.58km/s. The diameter of projectiles ranged from 2.74mm to 6.35mm. The impact angle was 0°for all the tests. The pressure of nitrogen gas in the first stage reservoir ranged from 3MPa to 20MPa. The pressure of hydrogen gas in pump tube ranged from 0.1MPa to 0.15MPa.The impact event was recorded by two flash x-ray stations. The first x-ray station viewed the projectile about 2cm prior to impact the bumper. This allowed the condition of the projectile to be viewed to insure it was still intact after the launch and sabot stripping. The second x-ray station was positioned to capture the debris-cloud formation.

After each test, a digital microscope was used to measure the perforation diameter on the first wall and the diameter of the damaged areas on the second wall of aluminum multi-wall shield.

Test results. After Al-sphere projectile penetrated through the first wall, debris clouds comprising particles of projectile and bumper was brought behind the first wall. Particles size and material state in debris clouds depends on projectile impact velocity and material characteristics of projectile and the first wall. Accordingly, debris clouds impact can generate craters, spallations and perforation on the second wall.

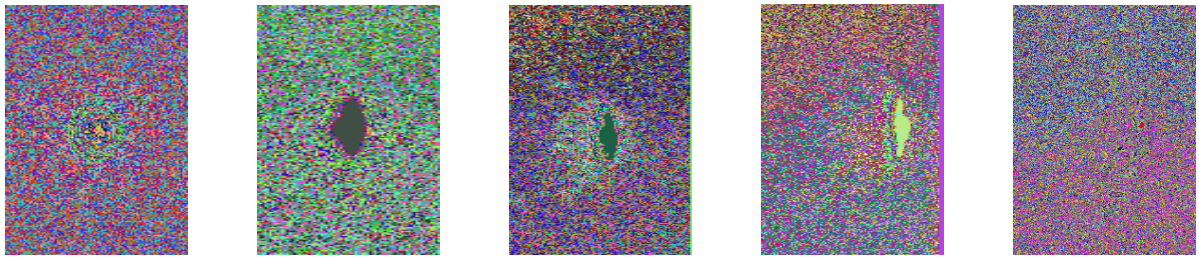

(a) velocity 1.91km/s (b) velocity 3.21km/s (c) velocity 3.55km/s (d) velocity 3.96km/s (e) velocity 4.31km/s

Fig. 1 radiographs of debris cloud in test

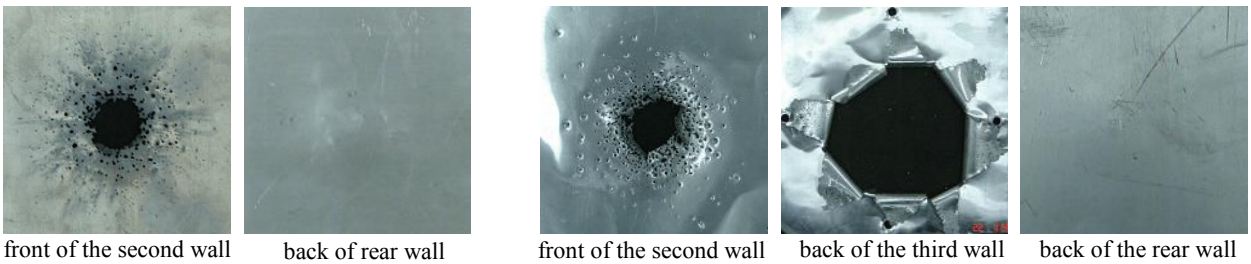

front of the second wall back of rear wall front of the second wall back of the third wall back of the rear wall

(a) three-wall shield, velocity 4.24km/s, diameter 5.00mm (b) four-wall shield, velocity 4.31km/s, diameter 5.00mm

Fig.2 Damages of multi-wall shield under hypervelocity impacts

When projectile impact velocity is less than the impact velocity of projectile fragmentation, the projectile will impact on the second wall with integrated body (see Fig. 1a), and bring a large hole or crater on the second wall, damage mostly come from projectile. For example, at 1.91km/s the projectile partially fragmented. When impact velocity is larger than the impact velocity of projectile fragmentation, projectile will break up, and forming debris cloud behind the first wall (see Fig. 1e). Debris clouds impacted on the second wall, forming damaged dense zones [6]. The second wall damage is characterized by a ring of holes surrounding the impact center and a large splash of finely

fragmented and liquid material (see Fig. 2). For aluminum projectiles, the impact velocity of projectile fragmentation is about 3km/s. In addition to a hole, the third wall of a multi-wall structure impacted by high velocity debris clouds can also experience cracking and petaling (see Fig. 2b). The damaged areas on the second wall can be described by diameter of central damaged area D_{cc} and diameter of ring damaged area D_{rc}. Crack length on the third wall is simply the largest distance between two crack tips in the star-shaped petal pattern.

From table 1, it can be found that amount of bumpers is an important factor effecting on the damage modes of the rear wall of the multi-wall shield. When keeping the total thickness of bumper t_b and protection spacing S constant, as the amount of bumpers increased, the damage on the rear wall mitigated.

Table 1 Test condition and damage on the rear wall of aluminum alloy multi-wall structure

No.	d_p [mm]	V_p [km/s]	t_1 [mm]	S_1 [mm]	t_2 [mm]	S_2 [mm]	t_3 [mm]	S_3 [mm]	t_w [mm]	Damage of rear wall
MW075	2.74	3.96	2.00	100	--	--	--	--	3	no bulge
MW070	3.18	4.05	2.00	100	--	--	--	--	3	tiny bulges
MW071	3.97	4.10	2.00	100	--	--	--	--	3	tiny bulges
MW072	4.76	4.07	2.00	100	--	--	--	--	3	tiny spallations, tiny bulges
MW073	5.00	1.91	2.00	100	--	--	--	--	3	central hole
MW075	5.00	4.08	2.00	100	--	--	--	--	3	tiny spallations, tiny bulges
MW074	5.00	5.58	2.00	100	--	--	--	--	3	tiny bulges
MW083	6.35	4.01	2.00	100	--	--	--	--	3	central hole, small bulges
MW084	2.74	3.55	1.50	50	0.50	50	--	--	3	no bulge
MW085	3.18	4.06	1.50	50	0.50	50	--	--	3	no bulge
MW086	3.97	4.10	1.00	50	1.00	50	--	--	3	small bulges
MW087	4.76	3.96	1.75	50	0.25	50	--	--	3	large central bulge, bulge height 2.18mm
MW088	4.76	5.37	1.50	50	0.50	50	--	--	3	small bulges
MW076	5.00	4.17	0.50	50	1.50	50	--	--	3	large central bulge, bulge height 3.54mm
MW077	5.00	4.24	1.50	50	0.50	50	--	--	3	large central bulge, bulge height 1.02mm
MW078	5.00	4.31	1.00	50	1.00	50	--	--	3	large central bulge, bulge height 1.68mm
MW079	5.00	4.55	1.75	50	0.25	50	--	--	3	large central bulge, bulge height 1.61mm
MW089	6.35	4.31	1.00	33.3	0.50	33.3	0.50	33.3	3	small central bulge
MW069	2.74	4.10	1.00	33.3	0.50	33.3	0.50	33.3	3	no bulge
MW091	3.18	4.08	1.50	33.3	0.25	33.3	0.25	33.3	3	no bulge
MW092	3.97	4.11	1.50	33.3	0.25	33.3	0.25	33.3	3	no bulge
MW093	4.76	4.13	1.00	33.3	0.50	33.3	0.50	33.3	3	no bulge
MW081	5.00	3.21	1.50	33.3	0.25	33.3	0.25	33.3	3	tiny bulges
MW082	5.00	4.31	1.50	33.3	0.25	33.3	0.25	33.3	3	no bulge

Damage analysis.

A correlation from regression analysis was developed to relate the hole size on the first wall D_h, and damage zones on the second wall D_{cc}, D_{rc}, with other relevant test parameters, such as the projectile diameter d_p, projectile impact velocity V , the first wall thickness t_b, the protection spacing S and the velocity of sound in aluminum c. As a first step, the all test data were used to find out a correlation in the form $(D_h\text{-}d_p)/d_p=f(V/c,\ t_b/d_p)$, $D_{cc}/S=f_{cc}\ (V/c,\ t_b/S,\ d_p/t_b)$, and $D_{rc}/S=f_{rc}\ (V/c,\ t_b/S,\ d_p/t_b)$, These equations were obtained using a multiple regression tool. The equations were given as follows:

$$\frac{D_h - d_p}{S} = 2.18\left(\frac{V}{c}\right)^{1.11}\left(\frac{t_b}{d_p}\right)^{0.69} \tag{1}$$

$$\frac{D_{cc}}{S} = 2.928\left(\frac{V}{c}\right)^{1.399}\left(\frac{t_b}{S}\right)^{0.531}\left(\frac{d_p}{t_b}\right)^{0.251} \tag{2}$$

$$\frac{D_{rc}}{S} = 2.883\left(\frac{V}{c}\right)^{0.691}\left(\frac{t_b}{S}\right)^{0.427}\left(\frac{d_p}{t_b}\right)^{0.317} \tag{3}$$

Then, using these equations, the relationship between test parameters and diameter of the damage zones on the second wall are shown in Fig. 3 and Fig. 4.

Fig. 3 shows the relationship between the diameters of the damaged zones on the second wall D_{cc},

D_{rc} and the projectile diameter d_p. When keeping impact velocity V, thickness of bumper t_b and protection spacing S constant, as the projectile diameter increased, the diameter of the damaged area on the second wall increased. Therefore, projectile diameter is a dominant factor with respect to damage on the second wall.

Fig. 4 shows the relationship between the diameters of the damaged zones on the second wall D_{cc}, D_{rc} and impact velocity V. When keeping projectile diameter d_p, thickness of bumper t_b and protection spacing S constant, as the impact velocity increased, the diameter of the damaged area on the second wall increased. Therefore, impact velocity is another dominant factor with respect to damage on the second wall.

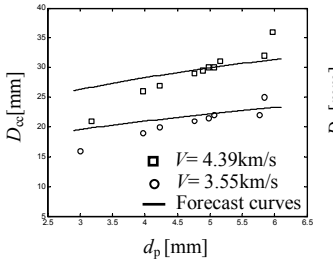

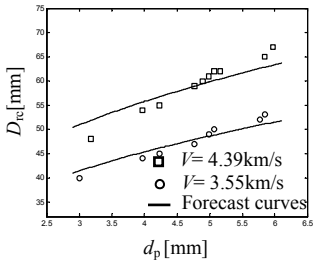

Fig.3 Relationship between the damaged zones on the second wall and d_p

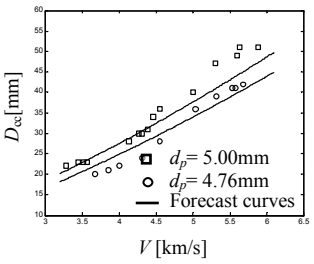

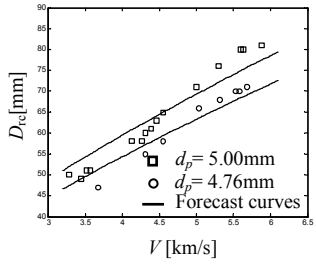

Fig.4 Relationship between the damaged zones on the second wall and V

Summary

This paper discussed the results obtained from all impact tests performed by launching aluminum spheres onto aluminum multi-wall shield configuration. This was done to search for resist capability about aluminum multi-wall structure under hypervelocity impact. In this study, the advanced method of multi-wall shield resisting hypervelocity impacts from space debris was investigated, and the effect of amount and thickness of wall on shield performance was discussed. By regression analyzing of experiment data, the experience equations for forecasting the diameter of the penetration hole on the first wall and the diameter of the damaged area on the second wall of aluminum multi-wall shield under hypervelocity normal impact of Al-spheres were obtained. The results indicated that the performance of multi-wall shield with more amount of wall is excellent when area density is constant. At the same time, intensity of the first wall and protecting space play the important roles.

References

[1] P. P. Bernhard, E. L. Christiansen and J. Hyde: Int J Impact Eng. Vol. 17 (1995), p. 57

[2] M. Lambert: Adv. Space Res. Vol. 19(1997), p. 369

[3] P. W. Schonberg and E. J. Williamsen: Int J Impact Eng. Vol. 20 (1997), p. 711

[4] E. L. Christiansen and J. H. Kerr: Int J Impact Eng. Vol. 26 (2001), p. 93

[5] E. A. Tayla, P. J. Glanville and R. A. Clegg: Int J Impact Eng. Vol. 29 (2003), p. 691

[6] M. Lambert, F. Schafer and T. Geyer: Int J Impact Eng. Vol. 26 (2001), p. 369

Key Engineering Materials Vols. 385-387 (2008) pp 205-208
© (2008) Trans Tech Publications, Switzerland
doi:10.4028/www.scientific.net/KEM.385-387.205

Failure of polyurethane foams under different loading conditions

Liviu Marsavina[1,2 a], Tomasz Sadowski[2,b], Dan M. Constantinescu[3,c], Radu Negru[1,d]

[1] University Politehnica of Timisoara, Department of Strength of Materials, ROMANIA

[2] Lublin University of Tehnology, Faculty of Civil and Sanitary Engineering, POLAND

[3] University Politehnica of Bucharest, Department of Strength of Materials, ROMANIA

[a]msvina@mec.upt.ro, [b]t.sadowski@pollub.pl, [c]dancon1@form.resist.pub.ro, [d]radun@mec.upt.ro

Keywords: polyurethane foam, impregnation, tensile test, three point bend test, compression test.

Abstract. Polyurethane foam materials are widely used as cores in sandwich composites, for packing and cushioning. This paper presents the experimental results obtained for the mechanical properties of polyurethane foams in different loading conditions and the influence of impregnation on the mechanical properties. A 200 kg/m^3 density polyurethane foam was tested in tension, compression and three point bending. The experimental results show that the impregnation layer has no effect on the strength of the foam, but has considerable influence on the tensile and flexure modulus.

Introduction

Polyurethane foam materials are widely used as cores in sandwich composites, for packing and cushioning. They are made of interconnected networks of solid struts and cell walls incorporating voids with entrapped gas. The main characteristics of foams are light weight, high porosity, high crushability, and good energy absorption capacity, [1].

Many efforts were made in recent years to characterize the behavior of different types of foams in different loading conditions. Viana and Carlsson [2] tested commercial foams in uniaxial tension and investigated the fracture behaviour. Tu et al. [3] presented the plastic deformations of rigid polyurethane foam under static compressive loading and proposed a theoretical approach to describe the deformation localisation. The non-linear behaviour of PVC foam was investigated by Berthelot and Lolive [4] and they showed results for compressive, tensile and shear tests. Lin [5] emphasized the variation of the mechanical properties of plastic foams with the internal structure and with the loading conditions (strain rate and temperature). The effect of the density and filler size was also investigated by Saint-Michel et al. [6,7]. Ramsteiner et al. [8] analyzed the parameters influencing the mechanical properties of foam. The following parameters were identified and studied: the structure of the foam, the matrix material of the foam, the density of the foam, cell orientation and testing temperature. The size effect on stress–strain relation of neat polyurethane foam was investigated by Chiang and Ding [9] using the multi-scale speckle method. Their important conclusion was that at the macro-scale the foam material may be treated as a homogeneous and isotropic material, but deformation pattern becomes progressively heterogeneous when the length scale is reduced. The effect of impregnation on mechanical properties of foams is pointed out by Apostol et al. [10] but is less studied comparing with effect of density, strain rate or temperature.

For the characterization of the mechanical behaviour of polyurethane foams tensile, compression and three point bending tests were considered. A 200 kg/m^3 density foam was used in the experimental program. The foam was impregnated with polyester and epoxy resins and a study of the effect of impregnation on the mechanical properties was studied.

Mechanical testing of PU foam

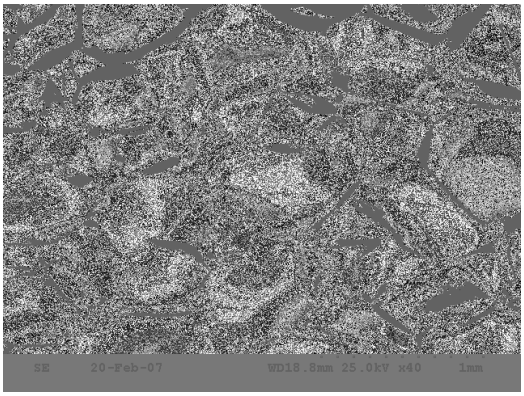

Fig. 1 The microstructure of PU foam

The investigated foam is a 200 kg/m^3 closed cell polyurethane (PU) rigid foam. The foam was manufactured and supplied in form of flat panels with 12 mm thickness. The microscopic structure of the foam is presented in Fig. 1 and the characteristic dimensions are cell – wall size 200 – 500 μm and wall thickness 3 – 4 μm. The foam faces were impregnated with epoxy (layer of 170 μm) and polyester (layer of 100 μm) resin in order to increase durability of the foam used for lightweight boats.

All tests were done at room temperature.

Tensile tests. The tensile properties of the foam were determined from plate specimens. In order to prevent failure of the specimen in the gripping region a transition to a reduced cross-section of dimensions 12 x 6 mm was performed. The length of the reduced cross section was 50 mm. An MTS extensometer with 25 mm length gage was used to measure displacement. A MTS static and dynamic testing machine type 858 Table Top System was used for tensile tests with a speed of 1 mm/min. Fig. 2 presents typical load – displacement curves for un-impregnated and impregnated specimens. It can be observed that the impregnation influence the load – displacement response, by increasing the stiffness of the specimen.

Three point bend tests (TPB). The MTS static and dynamic testing machine type 858 Table Top System was used for bending tests, using 2.5 kN load cell range. Three point bend specimens un-impregnated and impregnated with epoxy and polyester resin (12 x 12 x 135 mm) were adopted, and a span of 90 mm was used for the test (span/depth ratio 7.5:1). During tests the specimens were stiff enough and crushing is not taking place. The absence of crushing is highlighted by the brittle fracture of specimens, without plastic deformations. Fig. 3 presents comparatively the load – displacement curves for three point bend tests for un-impregnated and impregnated specimens. For the three point bend test the impregnation has important effect on the stiffness of the foam and no effect on flexural strength. For some impregnated specimens damage occurs, a drop of load corresponding with cracking of the impregnation layer, continued by an increase in load.

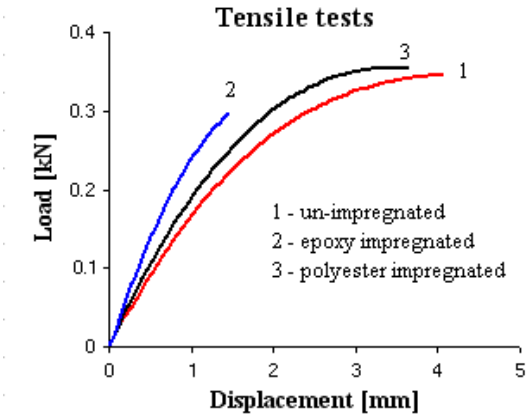

Fig. 2 Load–displacement curves for tensile tests

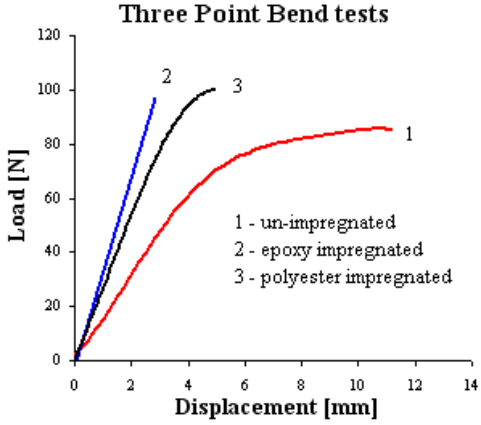

Fig. 3 Load–displacement curves for TPB tests

Compression tests. The tests were carried out using a Zwick universal testing machine with a 2.5 kN load cell. Cubic specimens with 12 mm length were used for compression test. The load – displacement data were recorded and post processed in order to obtain stress – strain curve. The

influence of the loading direction: in plane (1-2) and out of plane (3), Fig. 3.a and of the loading rate, Fig. 3.b.

The engineering stress – engineering strain curve highlights the nonlinear behaviour of the polyurethane foams in compression, Fig. 3. The following parts could be identified: an initial linear elastic response leading to yield, a small drop in stress after yield, a post-yield plateau and a final sharp rise in compressive stress, corresponding to foam densification.

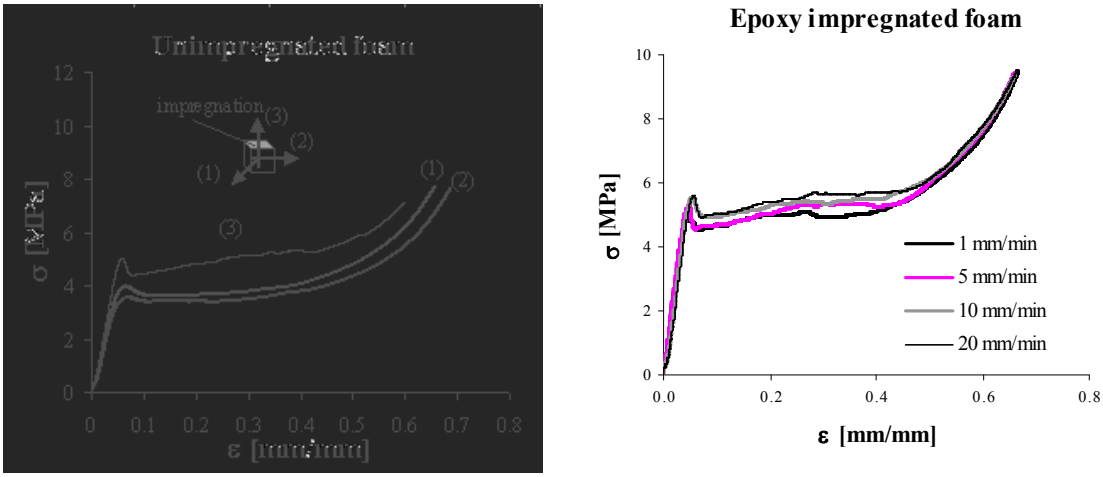

a. effect of loading direction b. effect of loading rate

Fig. 4 Engineering stress – engineering strain curves from compression tests

It can be observed in Fig. 4.a the anisotropic behaviour of foam. Different behaviour was obtained mainly when the load was applied on direction (3), for which there is no stress plateau. On the other hand Fig. 4.b shows the influence of the strain rate. The compression yield stress and the stress plateau slightly increases with 10%, respectively 7.8% for testes at 20 mm/min, comparing with 1 mm/min.

Conclusions

The static mechanical properties of the polyurethane foam were determined by three different tests. The effect of impregnation with two different resins was investigated. The results for strength and modulus of the three tests are presented in Fig. 5 comparatively for un-impregnated and impregnated foams.

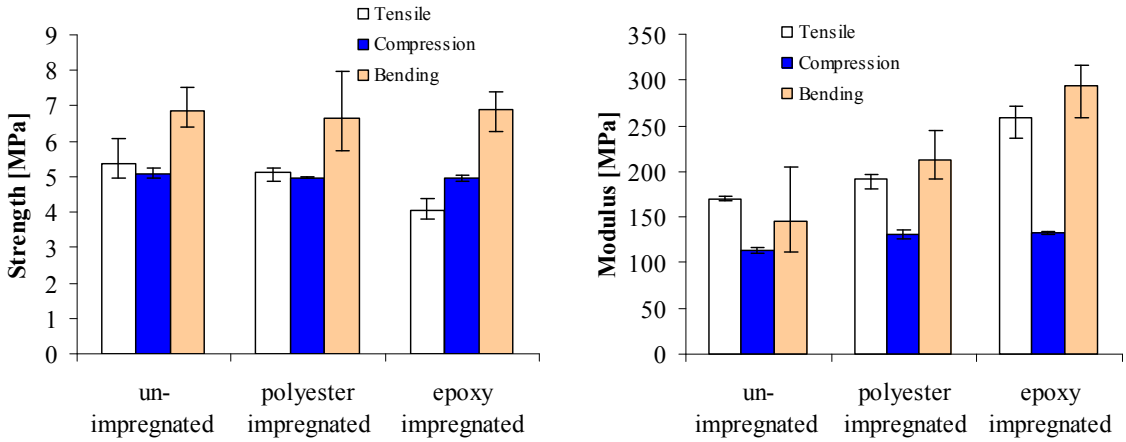

a. strength of foam b. modulus of foam

Fig. 5 Comparison of the mechanical properties of foam

The highest values for the strength of the foam were obtained in three point bend tests around 6.8 MPa. Values for tensile and compression strength are close: for tension between 4 MPa for epoxy impregnated to 5.4 MPa for un-impregnated foam and approx. 5 MPa for compression. It can be

observed in Fig. 5 that the impregnation has no effect on flexural and compression strengths (Fig. 5.a). A slight decrease of tensile strength was observed with the impregnation. On the other hand the impregnation has an important effect on the foam stiffness. The flexural modulus is 146 MPa for un-impregnated foam, 211.8 MPa for polyester impregnated foam and 294.5 MPa for epoxy impregnated foam (double than for un-impregnated foam), Fig. 5.b. An increase of the tensile modulus was observed too, but only with 13 % for polyester impregnation (thickness of layer 100 μm) and with 53% for epoxy impregnated foam (thickness of layer 170 μm). The impregnation has no effect on the compressive modulus. The values for the compression modulus are smaller than the tensile, respectively the flexure modulus.

The anisotropy of the foam was examined by compression tests using cubic specimens with the load oriented in-plane (1), (2) and out of plane (3). An increase of the mechanical properties of the foam was observed with increasing the strain rate.

Acknowledgments

The research was supported by the Marie Curie Transfer of Knowledge project MTKD-CT-2004-014058 and by Research for Excellence Grant 202/2006 awarded by the Romanian National Authority for Scientific Research.

References

[1] L.J. Gibson, M.F. Ashby: *Cellular Solids. Structure and properties* (Cambridge University Press, Cambridge, 1997).

[2] G. M. Viana, L.A. Carlsson: Mechanical Properties and Fracture Characterization of Cross-Linked PVC Foams, Journal of Sandwich Structures and Materials, 4 (2002), p. 99 – 113.

[3] Z. H. Tu, V. P. M. Shim, C.T. Lim: Plastic deformations modes in rigid polyurethane foam under static loading, International Journal of Solids and Structures, 38 (2001), p. 9267 – 9279.

[4] J.-M. Berthelot, E. Lolive: Non-linear Behaviour of Foam Cores and Sandwich Materials, Part 1: Materials and Modelling, Journal of Sandwich Structures and Materials, 4 (2002), p. 219 – 247.

[5] H.-R. Lin: The structure and property relationships of commercial foamed plastics, Polymer Testing, 16 (1997), p. 429 – 443.

[6] F. Saint-Michel, L. Chazeau, J.-Y. Cavaille, E. Chabert: Mechanical properties of high density polyurethane foams: I. Effect of the density, Composites Science and Technology, 66 (2006), p. 2700–2708.

[7] F. Saint-Michel, L. Chazeau, J.-Y. Cavaille: Mechanical properties of high density polyurethane foams: II. Effect of the filler size, Composites Science and Technology, 66 (2006), p. 2709–2718.

[8] F. Ramsteiner, N. Fell, S. Forster: Testing the deformation behaviour of polymer foams, Polymer Testing, 20 (2001), p. 661 – 670.

[9] F.-P. Chiang, Y. Ding: Size effect on stress–strain relation of neat polyurethane foam, Composites: Part B, 39 (2008), p. 42–49.

[10] D. Apostol, M. Miron, D. M. Constantinescu, Experimental evaluation of the mechanical properties of foams used in sandwich composites, 24th Danubia - Adria Symposiom, Sibiu, (2007), p. 35-36.

Key Engineering Materials Vols. 385-387 (2008) pp 209-212
© (2008) Trans Tech Publications, Switzerland
doi:10.4028/www.scientific.net/KEM.385-387.209

Low-cycle Fatigue Life Prediction by a New Critical-plane Method

Dan Jin[1,a], Jianhua Wu[1,b], Yang Zhang[1,c]

[1]School of Mechanical Engineering, Shenyang Institute of Chemical Technology, Shenyang, 110142, P.R.China

[a]jindan76@163.com, [b]zhangcm2004@126.com , [c]yz_1983@hotmail.com

Keywords: linear damage rule; irregular loading; multiaxial fatigue; rainflow cycle counting; critical plane.

Abstract: A series of low-cycle fatigue experiments of axial-torsional loading of variable amplitudes were performed on the tubular specimens of 304 stainless steel. Two models of multiaxial low-cycle fatigue life, KBM and FS method, are evaluated based on the fatigue life data of 304 stainless steel. Rainflow cycle counting and the Liner Damage Rule are used to calculate fatigue damage. It was shown that the part prediction results are nonconservative for the two models. The life prediction is done again based on the weight function critical plane method for the two models. The prediction results are better by using the weight function critical plane method than the previous results for KBM model. But the prediction results are improved little for FS model in spite of the weight function critical plane method being used.

Introduction

Engineering components are often subjected to complex multiaxial loading in which not only the principal axes rotate but also the applied loading is of variable amplitude. There have been many earlier researches under constant amplitudes, out-of-phase tension-torsion loading and some other simple non-proportional loading condition. Smith, Watson and Topper[1] proposed the SWT model for the material showing tensile failure. The maximum normal strain plane was considered as the critical plane in the model. Wang and Brown[2] applied the Kandil-Brown-Miller[3] (KBM) model to variable amplitude tension-torsion loading with the maximum shear strain range plane as the critical plane. Fatemi and Socie[4] (FS) proposed a fatigue model for shear fracture materials. The maximum shear strain plane was considered as the critical plane and the normal stress on the plane was used to replace the normal strain in the KBM model. Rainflow counting algorithms were developed for uniaxial fatigue and they were later modified to use with multiaxial fatigue[5,6]. Though many damage models have been developed, unfortunately, none of them enjoys universal acceptance. Linear damage rule is still dominantly used in design, in spite of its major shortcomings[7]. It is a common practice that a life computation procedure employs rainflow cycle counting on an appropriate strain/stress history on the critical plane and a linear damage rule (LDR).

The critical plane-based life analysis can follow one of several different approaches. Findley et al[8] initially defined the critical plane as the plane subjected to the largest cycle of shear strain. Socie[9] proposed that the maximum shear or normal strain plane as the critical plane depending on the material, loading mode, and strain amplitude. The controversy with the critical plane is that while the observed crack initiation plane is the critical plane, shear or normal, the maximum value of the fatigue parameter employed for life calculation is achieved on a different plane[10].

In this paper, KBM and FS fatigue parameters are employed for correlating fatigue data under random multiaxial loading. A life computation procedure is employed in which rainflow cycle

counting on a maximum shear strain plane for the parameter and the LDR are used to calculate the damage. The life prediction is done again by using the weight function critical plane method. The consequences will be examined.

Experimental procedure

The material used in this investigation is type 304 stainless steel. The fatigue data have been previously reported. The details of strain history in one loading block and the experimental results are given in the previous works[10].

Multiaxial fatigue models

The multiaxial fatigue models employed in this paper are given as follows:

1. The KBM model [3]

$$\frac{\Delta\gamma}{2}+s\varepsilon_n^*=[1+\upsilon+(1-\upsilon)s]\frac{\sigma_f^{'}-\sigma_0}{E}(2N_f)^b+(1.5+0.5s)\varepsilon_f^{'}(2N_f)^c \qquad (2)$$

where s is the material constant and it can be determined by uniaxial and torsional tests. For type 304 stainless steel used for evaluation in this study, $s=1.2$.

2. The FS model [4]

$$\frac{\Delta\gamma_{\max}}{2}(1+k\frac{\sigma_n^{\max}}{\sigma_y})=\frac{\tau_f^{'}}{G}(2N_f)^{b_0}+\gamma_f^{'}(2N_f)^{c_0} \qquad (3)$$

where k is a material constant determined from uniaxial and torsional tests in a similar manner as s for KBM, and k=0.85 for the current material.

In the two equations, $\tau_f^{'}$, $\gamma_f^{'}$, b_0 and c_0 are fatigue properties in Coffin-Manson equations and $\tau_f'=831, b_0=-0.1003, \gamma_f'=0.1402$, $c_0=-0.339$. G is the shear modulus, σ_n^0 is the mean normal stress, ε_n^* is the normal strain excursion, σ_y is the yield stress of material.

Results and discussions

Two fatigue models previously defined (KBM, and FS) are used in conjunction with rainflow cycle counting on a suitable critical plane for each model and LDR for damage computation. The stress and strain are calculated for planes with angle $0^\circ\le\theta\le180^\circ$ from the axis of the specimen with an increment of 1°. The critical plane is the maximum shear strain plane for the KBM and FS models.

The prediction results of two models are shown in Fig.1 and Fig.2. The solid lines in these figures represent perfect correlation and the dotted lines are for the factor-2 band. It can be seen that the KBM model gives non-conservative predictions for partial TnA and AV specimens. The life predictions for FS model are better than the previous models. The normal stress is used instead of normal strain in this model, and the effect of additional hardening under irregular loading path is treated better.

The states of stress and strain under fatigue loading are generally time-varying, and they may be complex multiaxial states. A plane may experience maximum damage at some time points, but

another plane may sustain greater overall damage, though diffused over time. Chen et al proposed a weight function critical plane approach[11].A new critical plane is defined by applying a weight function on the instantaneous critical plane. The fatigue life prediction is done by the rainflow cycle counting and the liner damage rule for the KBM and FS model considering the new critical plane. The prediction results are shown in Fig.3 and Fig.4.

The difference between the maximum shear strain plane and the weight function-based critical plane depends on the loading path. The difference may be large for some loading paths but others may show no difference. It can be seen that for the AV and TV loading paths, the weight function changes much with time but the maximum shear strain plane remains unchanged. So it is no effect for that paths, whether considering the weight function, or not. It may be said that the weight function method is unnecessary for proportional loading paths. But for some multiaixal paths, TB, R, TnA and so on, the variation is fairly large. So it is necessary to consider the weight function for these loading paths. From the result comparing, it can be seen that the weight function critical plane method influenced the KBM model more than that of FS model.

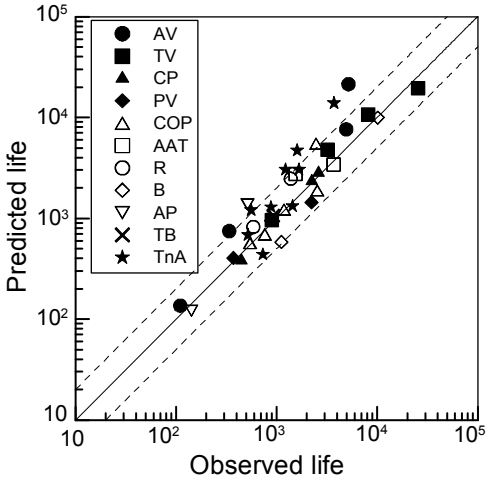

Fig.1 Fatigue life predictions of KBM model

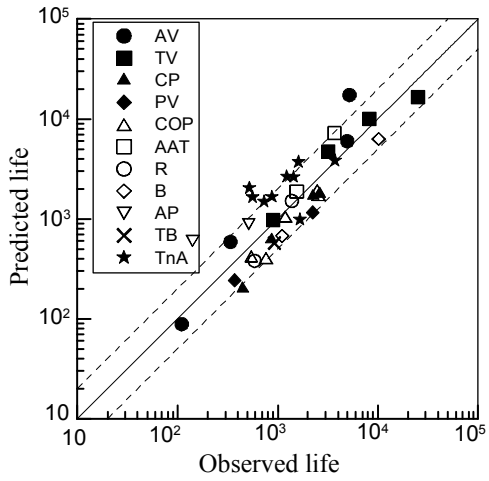

Fig.2 Fatigue life predictions of FS model

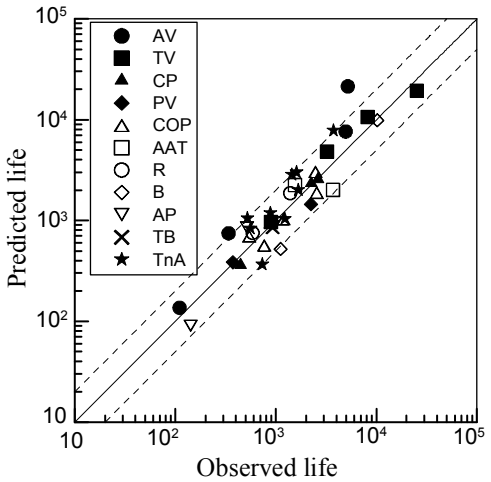

Fig.3 Fatigue life predictions of KBM considering weight function

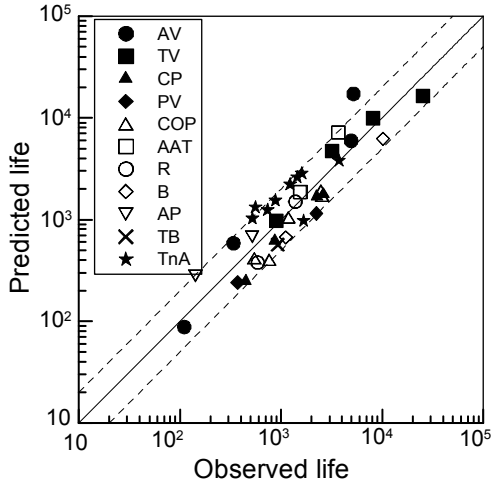

Fig.4 Fatigue life predictions of FS considering weight function

Conclusions:

Two damage models are employed for correlating low cycle fatigue data under irregular loading, i.e. KBM and FS. A life computation procedure is employed in which rainflow counting on an appropriate plane for each model and LDR are used to calculate the damage. The prediction results

show that the KBM model gives non-conservative predictions for partial TnA and AV specimens. The life predictions for FS model are better than the previous models. The weight function-critical plane method was tried with the KBM and FS model. It improved the results based on the maximum shear strain planes for the same parameter, especially for KBM model and the results were acceptable.

Acknowledgements

The authors gratefully acknowledge financial support for this work from National Natural Science Foundation of China and the Teaching and Liaoning Province Education Office (2005324). The authors are also thankful for the partial financial support provided from the Brain Korea 21 Program at Pohang University of Science and Technology.

References

[1] K.N. Smith, Watson P. and T.H. Topper, A stress-strain function for the fatigue of metals, Journal of Materials 1970, 5(4): 767

[2] C.H. Wang and M.W. Brown, A path-independent parameter for fatigue under proportional and non-proportional loading. Fatigue Fract. Engng. Mater. Struct., 1993, 16: 1285

[3] F.A. Kandil, M.W. Brown and K.J. Miller, Biaxial low-cycle fatigue fracture of 316 stainless steel at elevated temperature, Book 280, The Metal Society, London, 1982, 203

[4] A.Fatemi and D.F. Socie, A critical plane approach to multiaxial fatigue damage including out-of-plane loading. Fatigue Fract. Engng. Mater. Struct, 1988, 14: 149

[5] R.J. Anthes, Modified rainflow counting keeping the load Sequence. Int. J. Fatigue, 1997, 19: 529

[6] T.E. Langlais, J.H. Vogel and T.R. Chase, Multiaxial cycle counting for critical plane methods. Int. J. Fatigue, 2003, 25: 641

[7] A. Fatemi and L. Yang, Cumulative fatigue damage and life prediction theories: a survey of the state of the art for homogeneous materials. Int. J. Fatigue, 1998, 20: 9

[8] W.N. Findley, J.J. Coleman and B.C Handley., Theory for combined bending and torsion fatigue with data for 4340 steel. In: International conference on fatigue of metals, New York, 1956. The Institution of Mechanical Engineers: 1956, 150

[9] D.F. Socie, Multiaxial fatigue damage models. Transactions ASME, J. Engng. Mat. Tech., 1987, 109: 293

[10] K.S. Kim, B.L. Lee and J.C. Park, Biaxial fatigue of stainless steel 304 under irregular loading. fatigue and fracture mechanics: ASTM STP 1389, Halford G.R. and Gallagher, Eds., American Society for Testing and Materials, West Conshohocken, PA 2000, 31: 79

[11] X. Chen, D. Jin and K.S. Kim, A weight function-critical plane approach for low-cycle fatigue under variable amplitude multiaxial loading. Fatigue Fract. Engng. Mater. Struct., 2006, 29: 331

Key Engineering Materials Vols. 385-387 (2008) pp 213-216
© (2008) Trans Tech Publications, Switzerland
doi:10.4028/www.scientific.net/KEM.385-387.213

Mechanical Behaviors of Torsion Actuator of Shape Memory Alloy

Bo Zhou[1,a], Zhen-Qing Wang[1,a], Sung-Ho Yoon[2,b] and Guang-Ping Zou[1,a]

[1]College of Civil Engineering, Harbin Engineering University, Harbin, 150001, P. R. China

[2]School of Mechanical Engineering, Kumoh National Institute of Technology, Gumi, 730-701, Korea

[a]zhoubo@hrbeu.edu.cn, [b]shyoon@kumoh.ac.kr

Keywords: Mechanical model; Torsion actuator; Shape memory alloy

Abstract. A shape memory alloy (SMA) torsion actuator is designed by using SMA wires and a thin-walled tube. A mechanical model, which predicts the thermo-mechanical behaviors of the SMA torsion actuator, is developed based on the knowledge of solid mechanics and constitutive relation of SMA. The relationship of the torsion-angle and temperature of the SMA torsion actuator is numerically described by using the mechanical model coupled with Tanaka's, Liang's and Zhou's phase transformation models of SMA respectively. Results show the mechanical model well predict the thermo-mechanical behaviors of the SMA torsion actuator.

1. Introduction

Shape memory alloy (SMA) is a smart material with special mechanical properties associated with super elasticity and shape memory effect. Compared with the other smart materials, such as piezoelectricity and magnetostriction materials, SMA can produce larger recovery strain or stress. This makes it become current excellent candidates for the designs of various actuators and sensors. Self-adaptive wings can improve the aerodynamic performance of airplanes significantly. There are actuators assembled by smart materials and ordinary structural materials in adaptive wings. SMA torsion actuator is one of the key approaches to realize adaptive wings in the airplanes [1-3].

2. Phase transformation model of SMA

Reasonable and simple phase transformation models play an important role in the practical applications of SMA. Tanaka [4] developed an exponential-type model based the nucleation kinetics differential equation for metal materials. Liang and Rogers [5] suggested a cosine-type model according to experimental results. Brinson [6] suggested another cosine-type model which is able to describe the phase transformation from twinned martensite to detwinned martensite. Zhou and Yoon [7] developed a triangle-type model based on the differential relation between the martensite volume fraction and free energy during the phase transformation of SMA. Compared with the models of Tanaka's, Liang's and Brinson's, it formulated on the phase transformation peak temperature as well as the phase transformation starting and finishing temperatures. Its equivalent expressions can be expressed as

$$\xi = \xi_0 \begin{cases} \dfrac{a_1}{a_1+a_2}\cos\left(\dfrac{T-A_s^\sigma}{a_1}\right)+\dfrac{a_2}{a_1+a_2} & (A_p^\sigma > T > A_s^\sigma) \\ -\dfrac{a_2}{a_1+a_2}\sin\left(\dfrac{T-A_p^\sigma}{a_2}\right)+\dfrac{a_2}{a_1+a_2} & (A_f^\sigma > T > A_p^\sigma) \end{cases} \quad (M \to A) \tag{1a}$$

and

$$\xi = \xi_0 + (1-\xi_0)\begin{cases} -\dfrac{m_1}{m_1+m_2}\cos\left(\dfrac{T-M_s^\sigma}{m_1}\right)+\dfrac{m_1}{m_1+m_2} & (M_p^\sigma < T < M_s^\sigma) \\ \dfrac{m_2}{m_1+m_2}\sin\left(\dfrac{T-M_p^\sigma}{m_2}\right)+\dfrac{m_1}{m_1+m_2} & (M_f^\sigma < T < M_p^\sigma) \end{cases} \quad (A \to M) \tag{1b}$$

where

$$m_1 = \frac{2(M_{po} - M_{so})}{\pi},\quad m_2 = \frac{2(M_{fo} - M_{po})}{\pi},\quad a_1 = \frac{2(A_{po} - A_{so})}{\pi},\quad a_2 = \frac{2(A_{fo} - A_{po})}{\pi}$$

$$M_s^\sigma = \frac{\sigma}{C_M} + M_{so},\quad M_p^\sigma = \frac{\sigma}{C_M} + M_{po},\quad M_f^\sigma = \frac{\sigma}{C_M} + M_{fo}$$

$$A_s^\sigma = \frac{\sigma}{C_A} + A_{so},\quad A_p^\sigma = \frac{\sigma}{C_A} + A_{po},\quad A_f^\sigma = \frac{\sigma}{C_A} + A_{fo}$$

The notations M→A and A→M indicate the phase transformations from martensite to austenite and from austenite to martensite respectively. A_{so}, A_{po} and A_{fo} are phase transformation starting, peak and finishing temperatures from martensite to austenite in the free-stress state respectively. M_{so}, M_{po} and M_{fo} are phase transformation starting, peak and finishing temperatures from austenite to martensite in the free-stress state respectively. C_M and C_A are material constants describing the relations between the phase transformation critical temperature and stress from austenite to martensite and from martensite to austenite respectively. ξ_0 is the initial value of martensite volume fraction.

3. Mechanical model of SMA torsion actuator

In this study, the SMA torsion actuator consists of SMA wires and a thin-walled tube, shown in Figure 1. The pre-elongated SMA wires are twisted and plastered around the surface of the thin-walled tube with an angle, $\boldsymbol{\alpha}$, referenced to the center axis, $\boldsymbol{X}$, of the tube, called as twist-angle. The length, external diameter and wall thickness of the tube are expressed by $\boldsymbol{L}$, $\boldsymbol{D}$, and $\boldsymbol{t}$ respectively. The length and number of SMA wires in the actuator are expressed by $\boldsymbol{l}$ and $\boldsymbol{N}$ respectively. Only one SMA wire is plot in Figure 1, which makes it clear to illustrate the structure of SMA torsion actuator. The length $\boldsymbol{l}$ of SMA wires, the tube length $\boldsymbol{L}$ and the twist-angle $\boldsymbol{\alpha}$ should be related by

$$l = \frac{L}{\cos\alpha} \tag{2}$$

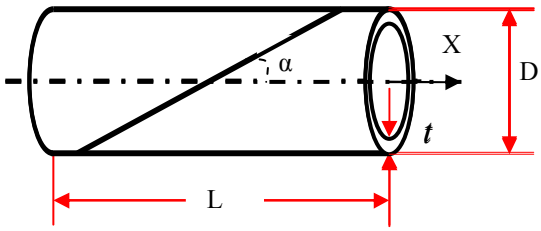

Fig. 1 Structural diagram of SMA torsion actuator

The number of SMA wires, $\boldsymbol{N}$, diameter of SMA wires, $\boldsymbol{d}$, and the external diameter of thin-walled tube, $\boldsymbol{D}$, should satisfy the inequality

$$N \le \frac{\pi D}{d}\cos\alpha \tag{3}$$

For SMA in one-dimension state, the relationship of stress, $\boldsymbol{\sigma}$, strain, $\boldsymbol{\varepsilon}$, martensite volume fraction, $\boldsymbol{\xi}$, and temperature, $\boldsymbol{T}$, reads as

$$\varepsilon_0 - \varepsilon = \frac{\sigma_0 - \sigma}{E_s} + \varepsilon_L(\xi_0 - \xi) + \frac{\Theta_s}{E_s}(T - T_0) \tag{4}$$

where $\boldsymbol{E}_s$, and $\boldsymbol{\Theta}_s$ are elastic modulus and thermo-expansion modulus of SMA respectively. $\boldsymbol{\varepsilon}_L$ is a material constant of SMA, called as maximal residual strain, which can be determined through tensile test. $\boldsymbol{\sigma}_o$, $\boldsymbol{\varepsilon}_o$, $\boldsymbol{\xi}_o$ and $\boldsymbol{T}_o$ are the initial values of $\boldsymbol{\sigma}$, $\boldsymbol{\varepsilon}$, $\boldsymbol{\xi}$ and $\boldsymbol{T}$ respectively.

The increments of length in SMA wire and thin-walled tube are expressed by $\Delta\boldsymbol{l}$ and $\Delta\boldsymbol{L}$ respectively. The geometrical continuity condition of the torsion actuator requires

$$\Delta l\cos\alpha = \Delta L \tag{5}$$

The static equilibrium condition along the axis X (shown in Fig. 1) leads to

$$N\frac{\pi}{4}d^2\sigma\cos\alpha-\pi Dt\sigma_t=0 \tag{6}$$

and the moment equilibrium condition around the axis X (shown in Fig. 1) leads to

$$\pi Dt\tau_t\frac{D}{2}-N\frac{\pi d^2}{4}\sigma\frac{D}{2}\sin\alpha=0 \tag{7}$$

In Equation (6) and (7), $\boldsymbol{\sigma}_t$ and $\boldsymbol{\tau}_t$ are the normal and shear stresses in the cross-section of thin-walled tube.

Based on the geometrical and equilibrium conditions, Equations (5), (6) and (7), the driven-stress and torsion-angle equations of SMA torsion actuator are expressed as

$$\sigma=\beta[\sigma_0+E_s\varepsilon_L(\xi_0-\xi)+\Theta_s(T-T_0)] \tag{8}$$

and

$$\phi=\frac{2L\alpha_s\beta}{DG_t}[\sigma_0+E_s\varepsilon_L(\xi_0-\xi)+\Theta_s(T-T_0)] \tag{9}$$

respectively. In Equations (8) and (9),

$$\beta=\frac{E_t}{E\alpha_c+E_t},\quad \alpha_c=\frac{Nd^2\cos\alpha}{4Dt},\quad \alpha_s=\frac{Nd^2\sin\alpha}{4Dt},$$

$\boldsymbol{E}_t$ and $\boldsymbol{G}_t$ is the elastic and shear modulus of the thin-walled tube.

4. Numerical examples

The thermo-mechanical behaviors of SMA torsion actuator are simulated by using the driven-stress and torsion-angle equations coupled with Tanaka's, Liang's and Zhou's SMA phase transformation models of SMA respectively. During the numerical calculations, the material constants and geometrical dimensions are listed in Table 1.

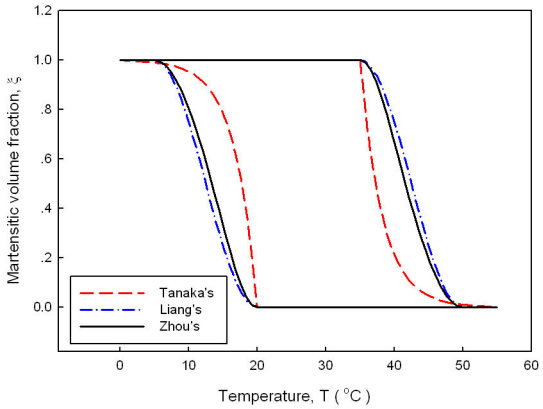

Fig.2 Martensite volume fraction- Temperature curves with different phase transformation models

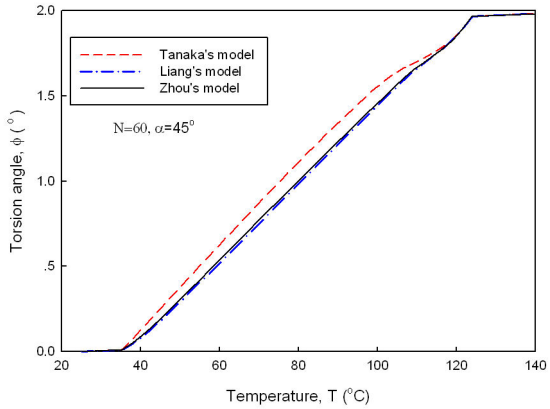

Fig.3 Torsion angle-Temperature curves with different phase transformation models

Figure 2 shows the martensite volume fraction-temperature curves of SMA in free-stress state described by Tanaka's, Liang's, and Zhou's SMA phase transformation models respectively. It can be well known that the curve shape described by Tanaka's phase transformation model is prominently different from that described by Liang's or Zhou's phase transformation model. While the difference of the curve shapes predicted by Liang's and Zhou's phase transformation models is not evident. This is because that Tanaka's model is formulated with an exponent-type function, however both of Liang's and Zhou's models are formulated with triangle-type functions. It is easy to numerically demonstrate the phase transformation behaviors of SMA described by Liang's and

Zhou's are same if the values of phase transformation peak temperature equal the average values of phase transformation starting and finishing temperatures, so Liang's phase transformation model can be considered as a special case of Zhou's phase transformation model with the conditions of $\boldsymbol{A}_{po}=0.5(\boldsymbol{A}_{so}+\boldsymbol{A}_{fo})$ and $\boldsymbol{M}_{po}=0.5(\boldsymbol{M}_{so}+\boldsymbol{M}_{fo})$.

Table 1 Material constants and geometric dimensions

Material constants and geometric dimensions of SMA wires					
M_{fo}	M_{po}	M_{so}	A_{so}	A_{po}	A_{fo}
5 °C	15 °C	20 °C	35 °C	40 °C	50 °C
E	Θ	ε_L	C_M	C_A	d
40 Gpa	0.55Mpa/°C	0.07	5 Mpa/°C	14 Mpa/°C	0.5 mm
Material constants and geometric dimensions of thin-walled tube					
E_t	G_t	D	t	L	
120 Gpa	40 Gpa	20 mm	0.5 mm	50 mm	

Figure 3 shows the relationship curves of the torsion-angle and temperature in the SMA torsion actuator predicted by the torsion-angle equation coupled with Tanaka's, Liang's, and Zhou's phase transformation models of SM respectively. During the numerical calculations the initial values of martensite volume fraction, ξ_0, temperature, T_0 are 0.6 and 25°C respectively. The twist-angle and number of SMA wires are 45 degree C and 60 respectively. Results reveals that the relationship of the torsion angle and temperature associated with Tanaka's phase transformation model is distinctly different from that associated Liang's or Zhou's phase transformation model. While both relationships associated with Liang's and Zhou's phase transformation models are similar. This is also due to that Tanaka's model is formulated with an exponent-type function while both of Liang's and Zhou's models are formulated with triangle-type functions, as above mentioned in the explanation for Figure 2.

5. Conclusions

SMA wires and a thin-walled metal tube are used to design the SMA torsion actuator. The driven-stress and torsion-angle equations of the SMA torsion actuator are developed respectively. The relationship of the torsion-angle of the SMA torsion actuator and temperature is numerically simulated by the torsion-angle equation coupled with Tanaka's, Liang's and Zhou's SMA phase transformation models respectively. Results show that both driven-stress and torsion-angle equations can describe the thermo-mechanical behaviors of the SMA torsion actuator effectively.

References

[1] F. M. Davidson and C. Liang: Proc. of the Conf. on Smart Structures and Materials, SPIE, Vol.2717(1996), p.672
[2] A. P. Jardine, B. C. Jonathan and J. Flanagan: Proc. of the conf. on Industrial and Commercial Applications of Smart Structures Technologies, SPIE, Vol.3674(1999), p260
[3] A. C. Keefe and G. P. Carman: Proc. of the Conf. on Smart Structures and Materials, SPIE, Vol.3675(1999), p.295
[4] K. Tanaka: Res. Mechanica, Vol.18(1986), p251
[5] C. Liang and C. A. Rogers: Journal of Intelligent Systems and Structures, Vol.1(1990), p207
[6] L. C. Brinson: Journal of Intelligent Material Systems and Structures, Vol.4(1993), p.229
[7] B. Zhou and S. H. Yoon: Smart Materials and Structures, Vol.15 (2006), p.1967

Key Engineering Materials Vols. 385-387 (2008) pp 217-220
© (2008) Trans Tech Publications, Switzerland
doi:10.4028/www.scientific.net/KEM.385-387.217

A New Method to calculate dynamic stress intensity factor for V-notch in a bi-material plate

Youtang Li [a], Zhiyuan Rui [b] and Changfeng Yan [c]

Key Laboratory of Digital Manufacturing Technology and Application, Ministry of Education, Lanzhou University of Technology, Lanzhou 730050, China

[a]liyt@lut.cn, [b]ruizy@lut.cn, [c]changf_yan@163.com

Keywords: Bi-material; V-notch; Eigen-equation; Dynamic stress intensity factor; Finite element method

Abstract. The stress singularity eigen-equation for V-notch in a bi-material plate is obtained. A new definition of dynamic stress intensity factor of a crack perpendicular to bi-material interface is put forward, and then is extended to any V-notch in bi-material plate. A formula of stress extrapolation method to calculate dynamic stress intensity factors of V-notch in bi-material plate is obtained. As an example, the three points bending sample with two materials is investigated.

Introduction

People always use crack or notch to achieve the fracture process of solid material in thousands years history of human being. The new surface forming method of solid materials is an important part in advanced manufacturing. A new surface forming method of solid material using crack and its propagation has been put forward and this new method was named crack technique [1]. In the applying research of crack theory, how to make crack quickly is a key problem that meets demand of high efficient production in engineering. Using artificial crack that formed with bi-material may be a feasible way to achieve efficient production.

The problem of a crack perpendicular to and terminating at bi-material interface has been the fully researched theoretically, but the research was restricted only in semi-infinite crack in infinite bi-material medium [2-3]. The crack or notch formed by bi-materials are the main point of fracture theory and the research of matrix crack that can be used in active fracture have made great progress [4-6].The stresses in bonded materials with a crack perpendicular to the interface were studied by Cook T.S. [7], and the stress intensity factor of the perpendicular interface crack of bi-material was defined by Seweryn A [8].

A method to calculate the stress intensity factor for V-notch in bi-material plate has been proposed [9]. The stress intensity factor of bi-material crack was redefined and a new definition of stress intensity factor for perpendicular interfacial V-notch of bi-material was put forwarded in the method. A generalized expression for calculating K_I of V-notch of perpendicular bi-material was obtained by means of stress extrapolation method. The method is extended to dynamic problem in this paper. As an example, the three points bending sample with two materials was calculated.

Stress Singularity Eigen-Equation of Bi-Material V-Notch

The perpendicular interfacial V-notch of bi-material is shown in Fig.1. Two plates with elastic module E_1 and E_2, and Poisson's ratio μ_1 and μ_2 are perfectly joined along their common interface. In material 1 there is a notch perpendicular to the interface, the notch tip is exactly at the interface of the two plates and the opening angle is 2α. The Ariy's stress function, $\Phi(r,\theta)$, which satisfies the bi-harmonic equation, can be chosen as following.

$$\Phi(r,\theta) = r^{\lambda+1}F(\theta) \tag{1}$$

$$F(\theta) = a\sin(\lambda+1)\theta + b\cos(\lambda+1)\theta + c\sin(\lambda-1)\theta + d\cos(\lambda-1)\theta \tag{2}$$

In polar coordinates system, the stresses σ_r, σ_θ, $\tau_{r\theta}$ can be expressed as following.

$$\sigma_r = \frac{1}{r^2}\frac{\partial^2\Phi}{\partial\theta^2} + \frac{1}{r}\frac{\partial\Phi}{\partial r} = r^{\lambda-1}[F''(\theta) + (\lambda+1)F(\theta)] \quad (3)$$

$$\sigma_\theta = \frac{\partial^2\Phi}{\partial\theta^2} = r^{\lambda-1}[\lambda(\lambda+1)F(\theta)] \quad (4)$$

$$\tau_{r\theta} = -\frac{1}{r}\frac{\partial^2\Phi}{\partial r\partial\theta} + \frac{1}{r^2}\frac{\partial\Phi}{\partial\theta} = -\lambda r^{\lambda-1}F'(\theta) \quad (5)$$

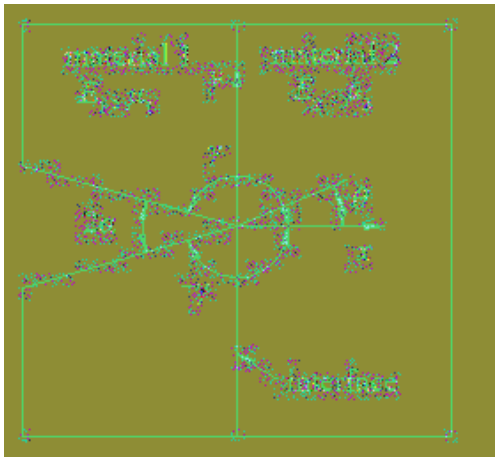

Fig.1 V-notch model of bi-material

The material 1 and 2 should have the same stress function given by eq.(1) and different coefficients *a*, *b*, *c*, *d*. In order to assure the continuity of displacement along the interface, the eigen-values, λ_1 and λ_2 of material 1 and material 2 must be equal in order to assure continuity of displacement along the interface. The stress function in material 1 and 2 can be written as follows

$$\Phi_1(r,\theta) = r^{\lambda+1}\left[a_1\sin(\lambda+1)\theta + b_1\cos(\lambda+1)\theta + c_1\sin(\lambda-1)\theta + d_1\cos(\lambda-1)\theta\right] \quad (6)$$

$$\Phi_2(r,\theta) = r^{\lambda+1}\left[b_2\cos(\lambda+1)\theta + d_2\cos(\lambda-1)\theta\right] \quad (7)$$

Because the boundary of the V-notch should be free and the stress and displacement in the interface should be continuous. Taking into consideration of the generic condition ($\pi/2<\gamma<\pi$), a series of equations for a_1, b_1, c_1, d_1, b_2, and d_2 can be obtained. In order to make the homogeneous equation have a solution for the unknown a_1, b_1, c_1, d_1, b_2, and d_2, the determinant of the coefficients of the unknowns should be zero. The eigen-equation for λ can be obtained as follows

$$\begin{aligned}&\left[1 - \beta + 2\alpha(1 + \alpha - \alpha\lambda^2 + \beta(\lambda^2-1))\right]\sin\pi\lambda + \alpha(\beta-\alpha)\lambda^2\sin(\pi\lambda - 2\gamma) - (\alpha + \alpha^2 - \alpha\beta)\\ &\sin\left[2\lambda(\pi-\gamma)\right] + \lambda\sin2\gamma - (1+\alpha)(\alpha-\beta)\sin2\lambda\gamma + (\alpha\beta\lambda^2 - \alpha^2\lambda^2)\sin(\pi\lambda + 2\gamma) = 0\end{aligned} \quad (8)$$

where

$$\alpha = \frac{\mu_1/\mu_2 - 1}{1 + k_1} \qquad \beta = \frac{\mu_1}{\mu_2}\frac{1+k_2}{1+k_1} \qquad k_{1,2} = \begin{cases}(3-\mu_{1,2})/(1+\mu_{1,2}) & \text{for plane stress}\\ 3 - 4\mu_{1,2} & \text{for plane strain}\end{cases} \quad (9)$$

If the linear symmetrical crack would be considered alone, $\gamma = \pi$ should be substituted into eq.(9), so that the following equation could be obtained.

$$\sin\lambda\pi\left[\lambda^2(-4\alpha^2 + 4\alpha\beta) + 2\alpha^2 - 2\alpha\beta + 2\alpha - \beta + 1 - (2\alpha^2 - 2\alpha\beta + 2\alpha - 2\beta)\cos\lambda\pi\right] = 0 \quad (10)$$

λ=0 and λ=1 are the solutions of above equation, if λ=0, all the stress should be zero, and if λ=1, all the stress should be constant. Besides λ=0 and λ=1, the other solutions (for $0<\lambda<1$) can be obtained as follows

$$\lambda^2(-4\alpha^2 + 4\alpha\beta) + 2\alpha^2 - 2\alpha\beta + 2\alpha - \beta + 1 - (2\alpha^2 - 2\alpha\beta + 2\alpha - 2\beta)\cos\lambda\pi = 0 \quad (11)$$

The eigen-solution, λ, should be 1/2 only when $0<\lambda<1$, showing the singularity ($1/\sqrt{r}$) of stress near the tip of crack. Thus it can be seen that the stress singularity near the tip of V-notch of bi-material is dependent on the exponent, λ, and it depends not only on the parameter of material, but also on the opening angle of V-notch. The eq. (8) is the stress singularity eigen-equation for V-notch with bi-material, and it can be regarded as the generalization of Zak's eigen-equation of perpendicular interface crack of bi-material and Williams's eigen-equation of V-notch.

A New Numerical Method to Calculation of Stress Intensity Factor

For the perpendicular interface crack of bi-material, the stress intensity factor can be defined as

$$K_{ij}(t) = \lim_{r\to 0}\sqrt{2\pi}r^{1-\lambda}\sigma_{ij}(r,\theta) \tag{12}$$

where the parameter, λ, expressing the singularity of stress and it can be solved with eq.(10). According to the definition of stress intensity factor of V-notch [8], the stress intensity factor of perpendicular V-notch of bi-material can be written as follows

$$K_{\mathrm{I}}(t) = \lim_{r\to 0}(2\pi r)^{1-\lambda}\sigma_{\theta}(r,0) \tag{13}$$

where λ can be obtained from eq.(8), and it depends not only on the two materials for V-notch of bi-material but also on the opening angle of V-notch. For perpendicular V-notch of bi-material, the stress intensity factor, $K_{\square}$, can also be expressed in the form of eq.(13) and it can be regarded as the universal definition of stress intensity factor for crack, V-notch, perpendicular interface crack with bi-material and perpendicular V-notch with bi-material. The stress intensity factor is calculated by using the results of stress $\sigma_{\theta}(r, 0)$ extrapolated along the direction of notch. The stress near the tip of crack orientation perpendicular to the crack can be expressed as following

$$\sigma_{\theta}(r,0) = \frac{K_{\mathrm{I}}(t)}{(2\pi r)^{1-\lambda}}(1+cr) \tag{14}$$

where $K_{\square}$(t) and c are unknown. The stresses at the points r_1 and r_2 from V-notch tip on the prolongation of V-notch can be obtained as follows

$$\sigma_{\theta}(r_1,0) = \frac{K_{\mathrm{I}}(t)}{(2\pi r_1)^{1-\lambda}}(1+cr_1) \qquad \sigma_{\theta}(r_2,0) = \frac{K_{\mathrm{I}}(t)}{(2\pi r_2)^{1-\lambda}}(1+cr_2) \tag{15}$$

The stress intensity factor for mode I problem in bi-material system can be calculated as follows

$$K_{\mathrm{I}}(t) = \frac{(2\pi r_1 r_2)^{1-\lambda}[\sigma_{\theta}(r_1,0)r_2^{\lambda} - \sigma_{\theta}(r_2,0)r_1^{\lambda}]}{r_2 - r_1} \tag{16}$$

When λ=1/2, the above equation can be simplified for the case of single material as follows

$$K_{\mathrm{I}}(t) = \frac{\sqrt{2\pi r_1 r_2}\left(\sigma_{\theta}(r_1,0)\sqrt{r_2} - \sigma_{\theta}(r_2,0)\sqrt{r_1}\right)}{r_2 - r_1} \tag{17}$$

Numerical Examples

Three points bending specimen. The specimen and its dimension are shown in Fig. 2. The impact loading can be written as following

$$F(t) = tF_{\max}/t_f \qquad (t \le t_f)$$
$$F(t) = 0 \qquad (t > t_f) \tag{18}$$

where t_f is the time of $F(t)$ to maximum. The material 1 is medium carbon steel and material 2 alloy steel (20CrMnTi), they are linearly elastic with the shear modulus E_1=210GPa, E_2=205.67GPa, Poisson's ratio $\mu_1 = 0.27$, $\mu_2 = 0.28$ and density are 7.85g/cm^3. The normalized dynamic stress intensity factor is defined as

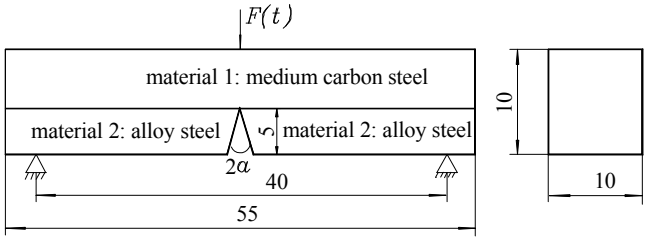

Fig. 2 Specimen and its dimension

$$K_{DI}(t) = K_{\mathrm{I}}(t)/\sigma_0(t)\sqrt{\pi a} \tag{19}$$

The results of normalized dynamic stress intensity factor $K_{DI}(t)$ for t_f equal to 90*us*, 135*us* and 180*us* are shown in Fig. 3.

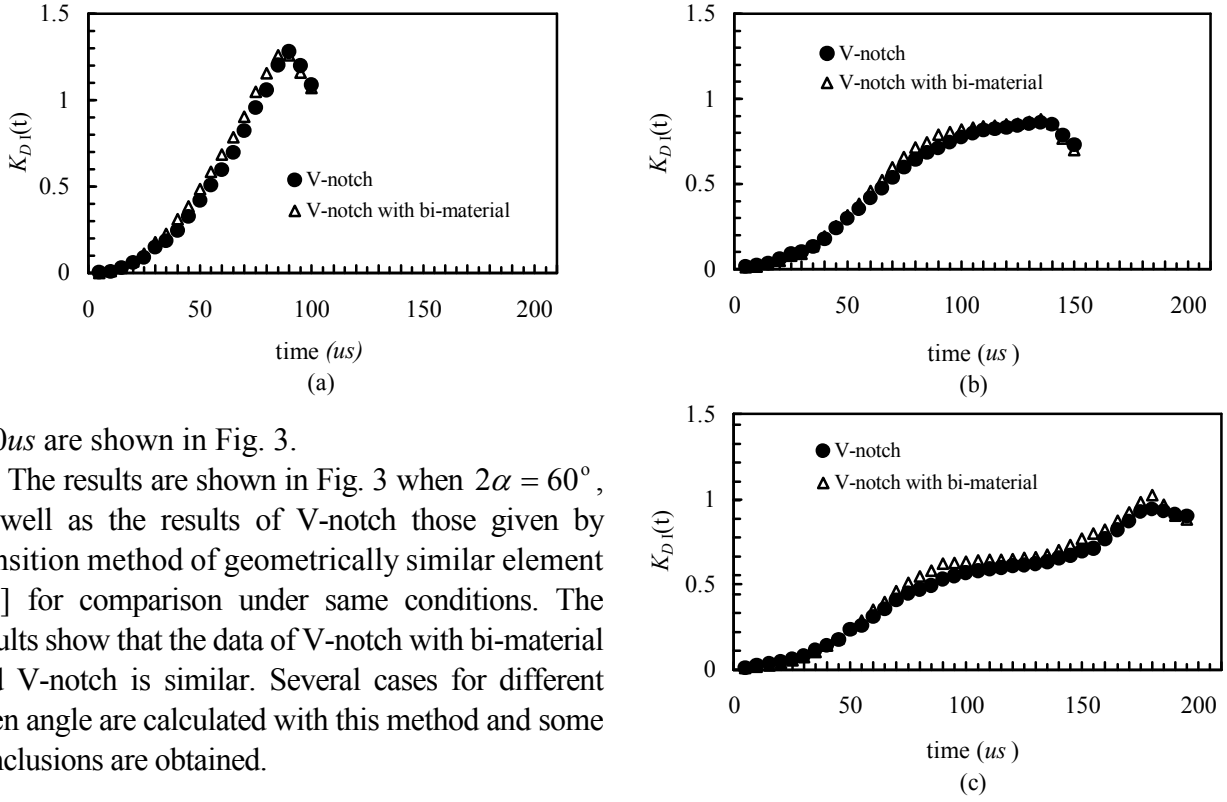

Fig.3 Results of dynamic stress intensity factor (a) 90us (b) 135us (c) 180us

The results are shown in Fig. 3 when $2\alpha = 60^{\circ}$, as well as the results of V-notch those given by transition method of geometrically similar element [11] for comparison under same conditions. The results show that the data of V-notch with bi-material and V-notch is similar. Several cases for different open angle are calculated with this method and some conclusions are obtained.

Conclusions

1) The stress intensity factor $K_I(t)$ decreases with the opening angle of notch, and it increases with the ratio of Poisson's ratio, μ_1/μ_2. The change is very small when $2\alpha \leq 30°$, showing that the effect of opening angle of notch on the singularity of stress near the notch tip is not obvious.

2) In the calculation of stress intensity factor of V-notch with bi-material, the singularity of stress depends on the exponent, λ-1, and λ is related not only to the property of the two materials but also to the opening angle of V-notch. Therefore, it is complicated to model the singularity of stress at the V-notch tip of with the singularity element and displacement method as well, which would additionally concern the expression displacement field near the V-notch tip. It is not difficult to calculate the stress intensity factor with the stress method of common element presented.

References

[1] Zhao B J, Lang F Y, Wei Q T. Engng Fract Mech 1988; 31: 923-929
[2] Riemelmoser FO, Pippan R. Int J Fracture 2000; 103: 397-418
[3] Zak AR and Williams ML. J Appl Mech, 1963; 30: 142.
[4] Li Y T, Yan C F and Huang H. Materials Science Forum Vols.437-438 (2003) p.309
[5] Li Y T, Ma P and Yan C F. Key Engineering Materials Vols.324-325 (2006) p. 503
[6] Li Y T and Yan C F. Key Engineering Materials Vols.306-308 (2006) p. 7
[7] Cook T S and Erdogan F. Int J Engin Science, 1972, 10: 677-697.
[8] Seweryn A. Int. J. Solids and Structures, 2002, 39: 4787-4804
[9] Carpinteri A, Paggi M, Pugno N. Int J Solids and Structures. 2006; 43: 627-641
[10] Li Y T and Song M. 8th int. conf. on fundamentals of fracture, 2008, Hong Kong , China
[11] Li Y T, Yan C F and Kang Y P. Key Engineering Materials Vols.306-308 (2006) p. 61

Key Engineering Materials Vols. 385-387 (2008) pp 221-224
© (2008) Trans Tech Publications, Switzerland
doi:10.4028/www.scientific.net/KEM.385-387.221

Micromechanics method to evaluate fatigue life of Ni-based superalloys during morphological evolution

Wen-Ping Wu[a], Ya-Fang Guo[b], Yue-Sheng Wang[c]

Institute of Engineering Mechanics, Beijing Jiaotong University, Beijing, 100044, P.R. China
[a]06115206@bjtu.edu.cn, [b]yfguo@bjtu.edu.cn, [c]yswang@bjtu.edu.cn

Keywords: Ni-based superalloys, fatigue life, micromechanics, morphological evolution.

Abstract. A quantitative life prediction method has been proposed to evaluate fatigue life during morphological evolution of precipitates in Ni-based superalloys. The method is essentially based on Eshelby's equivalent inclusion theory and Mori-Tanaka's mean field method. The shape stability and life prediction are discussed when the external stress and matrix plastic strain are applied. The calculated results show that the fatigue life is closely related with microstructures evolution of precipitates. The magnitude and sign of the external stress and matrix plastic strain have an important effect on fatigue life of Ni-based superalloys during the morphological evolution of precipitates.

Introduction

Ni-based superalloys have been inevitable materials for the blades and vane applications in gas turbines, because of their excellent reliability and mechanical properties. Generally, the superalloys have naturally developed composite microstructures consisting of γ matrix and γ' precipitates. The morphological evolution of precipitates is generally associated with the creep resistance [1-3]. Several theoretical methods have been proposed to simulate the equilibrium microstructure morphologies of precipitates and explain rafting mechanism [3-5], while less attention has been focused on the effects on the high temperature fatigue properties during morphological evolution of precipitates. In this paper we introduce a reasonable and simplified micromechanics model based on Eshelby's inclusion theory and Mori-Tanaka's mean field method. The life prediction is discussed by taking account of both microscope failure mechanism and role of microstructure. A particular attention is paid to the evolution of the microstructure in relation with the fatigue life of the material. The results of these calculations are used to evaluate the fatigue life of Ni-based superalloys during the morphological evolution of precipitates.

Model of analysis

The microstructure of Ni-based superalloy is modeled by a composite material system in which the γ' precipitates distribute uniformly in the γ matrix. The material properties of the matrix and precipitates used for calculations are [2]: Young's modulus C^m=85GPa, C^p=100GPa, Poisson's ratio $\nu^m = \nu^p = 0.3$, the volume fraction $V_f^m = 0.36$, $V_f^p = 0.64$, and the misfit strain δ=-0.15%. In this work, δ_{ij} is assumed to have isotropic components,

$$\delta_{11} = \delta_{22} = \delta_{33}, \text{ and the other } \delta_{ij} = 0 \qquad (1)$$

Fig.1a and b show the microstructure of Ni-superalloys and a three-dimensional simplified model for precipitates. The simplified ellipsoidal model can denote various shapes of the precipitates by a shape factor α. The shape factor α is defined as $\alpha = a_1 / a_2$ or $\alpha = a_1 / a_3$ with $a_2 = a_3$.

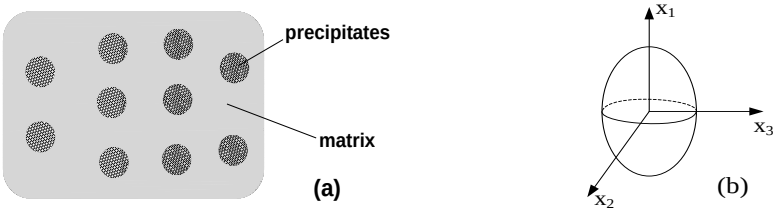

Fig.1. (a) Model of Ni-based superalloys microstructure containing ellipsoidal precipitates. (b) Schematic diagram of an ellipsoidal precipitates in an infinite matrix, the semi-axes a_1, a_2 and a_3 are coincident with x_1, x_2 and x_3 directions respectively.

Morphological evolution

As a morphological evolution resulting from the external load [3], the matrix plastic strain [5] is well known. Here, suppose a material system undergoes a plastic deformation under an external load. One of the simplest states is that only the matrix undergoes a plastic strain ε_p along the loading axis direction under a uniaxial load. According to Eshelby's inclusion theory and mean field method [6, 7], the stress in the precipitates associated with a matrix plastic deformation is given by

$$\begin{aligned}\sigma_{ij}(\delta,p) &= C^p_{ijkl}\{S_{klmn}\varepsilon^*_{mn}(\delta,p)V^p_f - S_{klmn}I\varepsilon^*_{mn}(\delta,p) + \delta\varepsilon^*_{kl}(\delta,p)\} - \delta\sigma_{ij}(\delta,p)\\ &= C^m_{ijkl}\{S_{klmn}\varepsilon^*_{mn}(\delta,p)V^p_f - S_{klmn}I\varepsilon^*_{mn}(\delta,p) + \delta\varepsilon^*_{kl}(\delta,p)\} - \delta\sigma_{ij}(\delta,p)\end{aligned} \tag{2}$$

where S_{klmn} is the Eshelby's tensor depending on the geometrical shape of the ellipsoidal precipitates [7], $\varepsilon^*_{11} = \delta - \varepsilon_p, \varepsilon^*_{22} = \delta + \varepsilon_p/2, \varepsilon^*_{33} = \delta + \varepsilon_p/2$, and the other $\varepsilon^*_{ij} = 0$.
Consider the material system in which a remote external load is applied; the stress state in the precipitates is written as

$$\begin{aligned}\sigma_{ij}(\delta,p,inh) &= C^p_{ijkl}\{\varepsilon^0_{kl} + S_{klmn}\cdot\varepsilon^{**}_{mn}(\delta,p,inh) - V^p_f(S_{klmn}-I)\varepsilon^{**}_{mn}(\delta,p,inh) - \varepsilon^*_{kl}(\delta,p)\}\\ &= C^m_{ijkl}\{\varepsilon^0_{kl} + S_{klmn}\cdot\varepsilon^{**}_{mn}(\delta,p,inh) - V^p_f(S_{klmn}-I)\varepsilon^{**}_{mn}(\delta,p,inh) - \varepsilon^{**}_{kl}(\delta,p,inh)\}\end{aligned} \tag{3}$$

The total energy of the material system can be expressed as

$$E_{el} = E_0 + E_{(inh)}(\delta,p,inh) + E(\delta,p) + E_{(int)}\sigma(\delta,p), \tag{4}$$

with

$$E_{(inh)}(\delta,p,inh) = -\frac{1}{2}\sigma^0_{ij}\cdot\varepsilon^{**}_{ij}(\delta,p,inh)\cdot V^p_f; \qquad E(\delta,p) = -\frac{1}{2}\sigma_{ij}(\delta,p)\cdot\varepsilon^*_{ij}(\delta,p)\cdot V^p_f$$

$$E_{(int)}(\sigma,\delta,p) = -\frac{1}{2}\sigma^0_{ij}\cdot\varepsilon^{**}_{ij}(\delta,p)\cdot V^p_f \tag{5}$$

By solving equations (2) and (3), the total energy is evaluated for the material system which undergoes a plastic deformation under an external load. Naturally, the microstructure morphologies having the lowest energy are obtained if the contribution of the interfacial energy is ignored.

Table 1 shows the total energy with five representative microstructures of precipitates which undergo a plastic strain under an external stress along the x_1 direction. As seen in Table 1, when the external tensile stress is applied, the total energy becomes larger as the matrix plastic strain and external stress increases. The limiting case of $\alpha \to 0$ for the disc shape has the lowest energy. Therefore, the disc-shaped particles are energetically favored for a negative misfit alloy when the material undergoes a plastic deformation under a tensile stress. When the compressive stress is applied and the matrix plastic strain is smaller, the needle-shaped particles have the lowest energy. However, if the matrix plastic strain exceeds a certain value, the spherical particles will yield the smallest total energy as shown in Table 1. This result indicates that the magnitude of the matrix

plastic strain plays an important role in the morphological evolution of the precipitates.

Table 1. Total energy associated with the plastic strain under an external stress along the x_1 direction.

Microstructure morphologies		$\alpha \to 0$	$\alpha = 0.5$	$\alpha = 1$	$\alpha = 1.5$	$\alpha \to \infty$
The total energy associated with the plastic strain under an external load (MJ/m^3)						
Tensile	$\sigma_{11} = 200MPa$ $\varepsilon_p = 0.002$	0.692 (lowest)	0.744	0.775	0.795	0.853
	$\sigma_{11} = 100MPa$ $\varepsilon_p = 0.002$	0.277 (lowest)	0.323	0.352	0.369	0.422
	$\sigma_{11} = 200MPa$ $\varepsilon_p = 0.005$	1.175 (lowest)	1.248	1.337	1.399	1.611
Compressive	$\sigma_{11} = -200MPa$ $\varepsilon_p = -0.002$	0.478	0.403	0.383	0.376	0.370 (lowest)
	$\sigma_{11} = -100MPa$ $\varepsilon_p = -0.002$	0.245	0.174	0.156	0.149	0.142 (lowest)
	$\sigma_{11} = -200MPa$ $\varepsilon_p = -0.005$	1.187	0.972	0.945 (lowest)	0.947	1.013

Life estimation

In order to investigate the effect of the microstructure evolution on fatigue failure, it is necessary to express "fatigue damage" by an appropriate parameter. Since damage is irreversible process, it should be represented by a plastic work density, W_p, which can reasonably denote energy dissipation process. Here, W_p is defined by

$$W_p = \int \sigma_{ij} \cdot d\varepsilon_{p,ij} \tag{6}$$

where $d\varepsilon_{p,ij}$ is a plastic strain increment.

According to the Manson–Coffin's law [8], the following linear equation is assumed to combine the fatigue life:

for the γ matrix $$W_p^0 \cdot N_f^0 = C(\gamma) \tag{7-1}$$

and for the γ' precipitates $$W_p \cdot N_f = C(\gamma') \tag{7-2}$$

where N_f^0 and N_f are the fatigue life of the γ matrix and γ' precipitates; $C(\gamma)$ and $C(\gamma')$ are the material constants, respectively. The fatigue life of the composite material system is supposed to be governed by a shorter value of either N_f or N_f^0. Thus we can qualitatively discuss the effect of microstructure changes on the fatigue life by comparing the values of W_p or W_p^0, even without knowing the actual values of $C(\gamma)$ and $C(\gamma')$.

Fig. 2a, b, c and d show summary of the calculated values of $1/W_p$, a parameter corresponding to the fatigue life. This figure can be directly compared with Table 1. It is found by the comparison that fatigue life is closely related with the shape stability of precipitates during morphological evolution. The more stable the shape is during morphological evolution of precipitates, the longer fatigue life of Ni-based alloys is. Moreover, the magnitude and sign of the external stress and matrix plastic strain strongly influence the fatigue life. The smaller external stress and matrix plastic strain

have a longer fatigue life. Therefore, the fatigue life changes with the change of the external stress and matrix plastic strain.

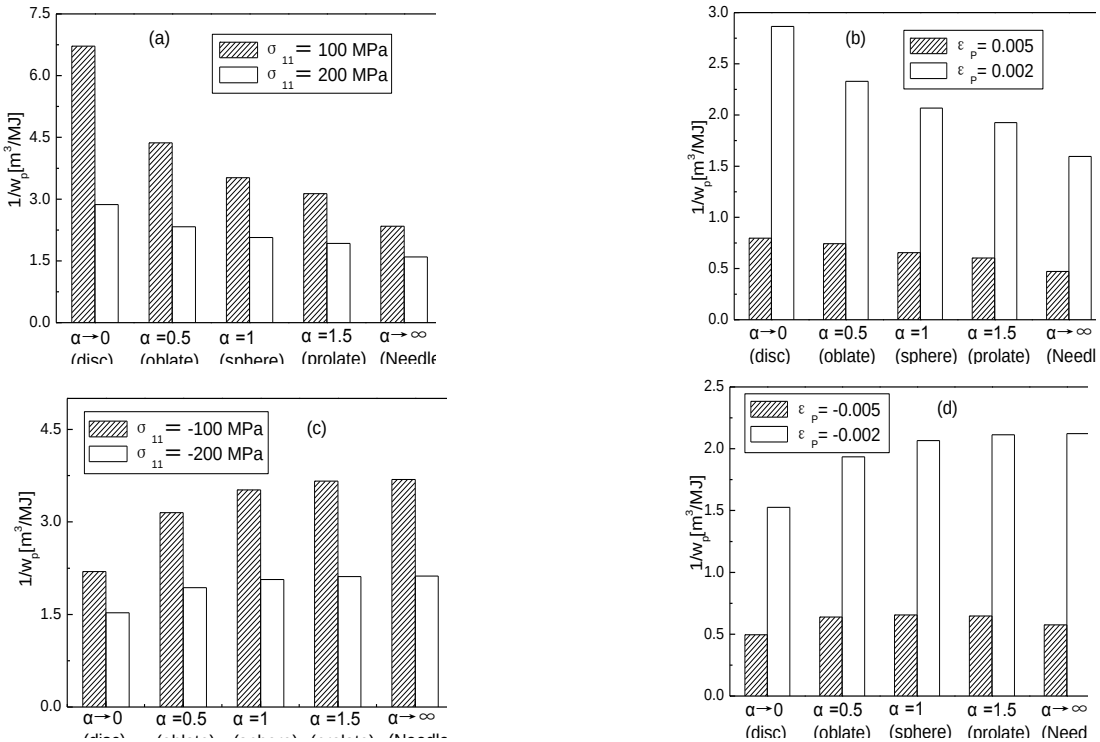

Fig.2. Predicted fatigue life of various microstructures of precipitates. (a) different tensile stresses; (b) different positive plastic strains; (c) different compressive stresses; (d) different negative plastic strains

Summary

A simplified micromechanics model has been proposed to evaluate the fatigue life of Ni-based superalloys during morphological evolution of precipitates. Life estimation was discussed by taking account of microscope failure mechanism and the effect of microstructure. The calculated results show that the fatigue life is closely related with the microstructures evolution of precipitates. The magnitude and sign of the external stresses and matrix plastic strain play an important role on the fatigue life of Ni-based superalloys during the morphological evolution of precipitates.

Acknowledgements

The research was supported by Chinese Nature Science Foundation (Grant No. 10672016 and No.10572019) and Beijing Jiaotong University Science Foundation (No. 2005SM0035).

References

[1] T. M. Pollock, A. S. Argon: Acta Metall. Mater. Vol. 42 (1994), p.1859
[2] M.Sakaguchi and M. Okazaki: Int. J. Fatigue. Vol.29 (2007), p.1959
[3] A. Pineau: Acta Metall. Vol.24 (1976), p.559
[4] R. Mueller and D. Gross: Comp. Mater. Sci. Vol.11 (1998), p.35
[5] N. Ratel, G. Bruno, P. Bastie, T. Mori : Acta Mater. Vol. 54 (2006), p. 5087
[6] T. Mori, K.Tanaka : Acta Metall. Vol. 21(1973), p.571
[7] T. Mura, in: Micromechanics of Defects in Solids, Martinus Nijhoff Publishers (1987).
[8] D.E. Martin : Trans. Am. Soc.Mech.Eng, J.Basic.Eng. Vol.83(1961), p.565

Key Engineering Materials Vols. 385-387 (2008) pp 225-228
© (2008) Trans Tech Publications, Switzerland
doi:10.4028/www.scientific.net/KEM.385-387.225

Effect of Recessing Length in Adhesive Layer on the Cleavage Joints

Min You [a], Zhi Li, Xiaoling Zheng [b] and Zhanmou Yan

College of Mechanical and Material Engineering, China Three Gorges University
Yichang 443002, China

[a] youmin@ctgu.edu.cn, [b] zhengxiaoling@ctgu.edu.cn

Key words: epoxy; steel; stress distribution; recessing; cleavage

Abstract: The elastic finite element analysis (FEA) and the experimental method of testing the cleavage strength of the joint were used to investigate the effect of the recessing as well as its length on the stress distribution in both the mid-bondline and the adherend near the interface along the bondline of adhesively bonded steel cleavage joint. The results from the FEA simulation showed that the peak values of the stresses distributed in the mid-bondline were nearly the same when the length of the arranged recessing was not greater than 10 mm except that the shear stress *Sxy* was increased a little when the length of the recessing was increased. For the normal stress *Sy* near the interface of the joint with a 16 mm length recessing, the peak stress in the adherend is about 49% higher than the one in the adhesive at the left edge of the joint. And it is supported with the results from the experiments that the ultimate load of the steel-to-steel cleavage joint decreased a little when the gap length was less than 10 mm.

Introduction

In recent years, more attention is paid to study the load-carrying capacity of the adhesively bonded joints with recessing or gap in it. In general, some researchers was interesting in this issue to take them as defects such as de-bonding, gap, crack etc. (Olia and Rossetos [1], Lang and Mallick [2], de Moura et al. [3]). But in authors' opinion it may be named intermittent bonding and taken as one of the new bonding technologies. The authors analyzed the effect of off-center recessing on the strength of adhesively bonded single-lap joint [4] and the the effect of the recessing in adhesively bonded double lap joints [5]. However, it is necessary to study the effect of the recessing on the other types of joints such as cleavage joint [6-7]. The aim of this paper is to investigate the influence of it on the stress and strength of adhesively bonded cleavage joint.

Experimental conditions and FEA model

The cleavage joint is shown in Fig. 1(a). Its width was 25mm. The adherends were made from AIS 1045 structural steel and bonded with an epoxy adhesive (layer thickness 0.2 mm) and their properties are given in Table 1. The model was built using ANSYS software as shown in Fig. 1(b) and the detail mesh in Fig 1(c). The element PLANE183 was used for both adherend and the adhesive. The load applied was 3.75 kN. All the stresses were from the mid-bondline (y = 0.1 mm) or the adherend near the interface (y = 0.25 mm). The adherends were first polished using emery paper, then degreased with acetone and dried. Finally they were bonded with the adhesive. A special technology had been developed to prepare the joints with desired recessing length (L = 5mm to 16mm). After the specimen being cured in the oven for 2 h at 50°C, then placed them in room temperature (about 20°C) for 24h. The cleavage strength tests were performed at a crosshead speed of 5 mm/min.

TABLE 1 Materials property

Materials	Elastic modulus (MPa)	Poisson's Ratio
Steel 1045	209,000	0.27
Epoxy adhesive	3000	0.42

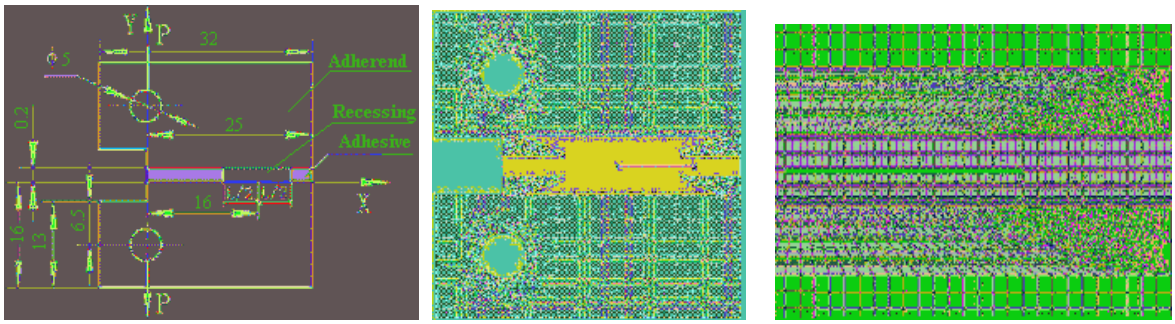

(a) (b) (c)

Fig. 1 (a) Dimension of the specimen, (b) finite element model, (c) detail mesh

Results and discussion

The effects of the recessing length on the stress distribution in the joint are given in Fig.2 and Fig.3. Where there was no adhesive, there was no any stress component at all in the mid-bondline. All the peak values and the stresses distribution in the mid-bondline and the adherend near the interface are nearly the same while the recessing length was not great than 10 mm. For example, the peak value of the normal stress Sy at the point x = 0.5 mm in the mid-bondline are all about 26 MPa (i.e. 26.80 MPa for the normal joint L =0 mm, 26.82 MPa for L =5 mm or 26.96 MPa for L =10 mm recessing) but increased to 42.95 MPa at the same point when L = 16 mm. In Fig. 3b, the same tendency can be seen (the peak value of Sy at the left point in the adherend near the interface maintained about 38 MPa when L ≤10 mm or reached to 64 MPa when L =16 mm). From Fig.2 and Fig.3 one can imagine that the load-carrying capacity of the cleavage joint may be almost not affected by a recessing arranged in the adhesive when its length is not great than 10 mm.

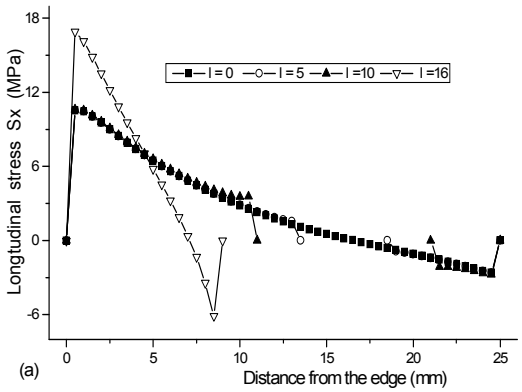

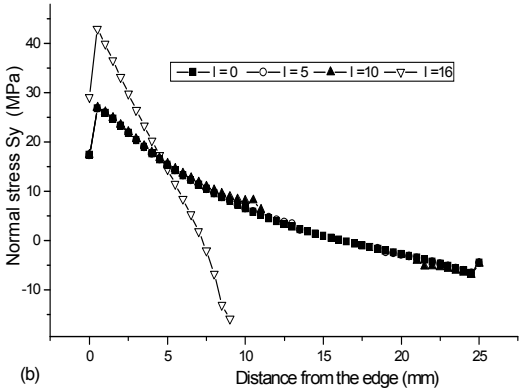

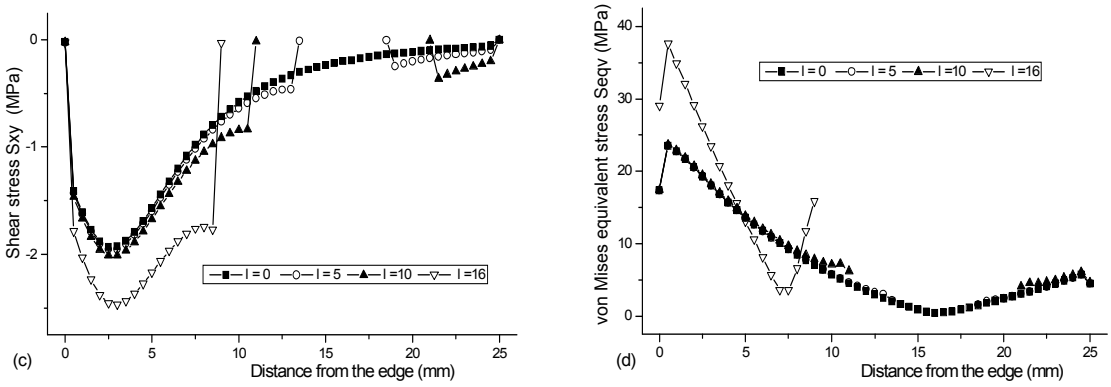

Fig. 2 Recessing length L vs. the stress distribution in the mid-bondline of the joint: (a) longitudinal stress Sx, (b) peel stress Sy, (c) the shear stress Sxy and (d) von Mises equivalent stress Seqv.

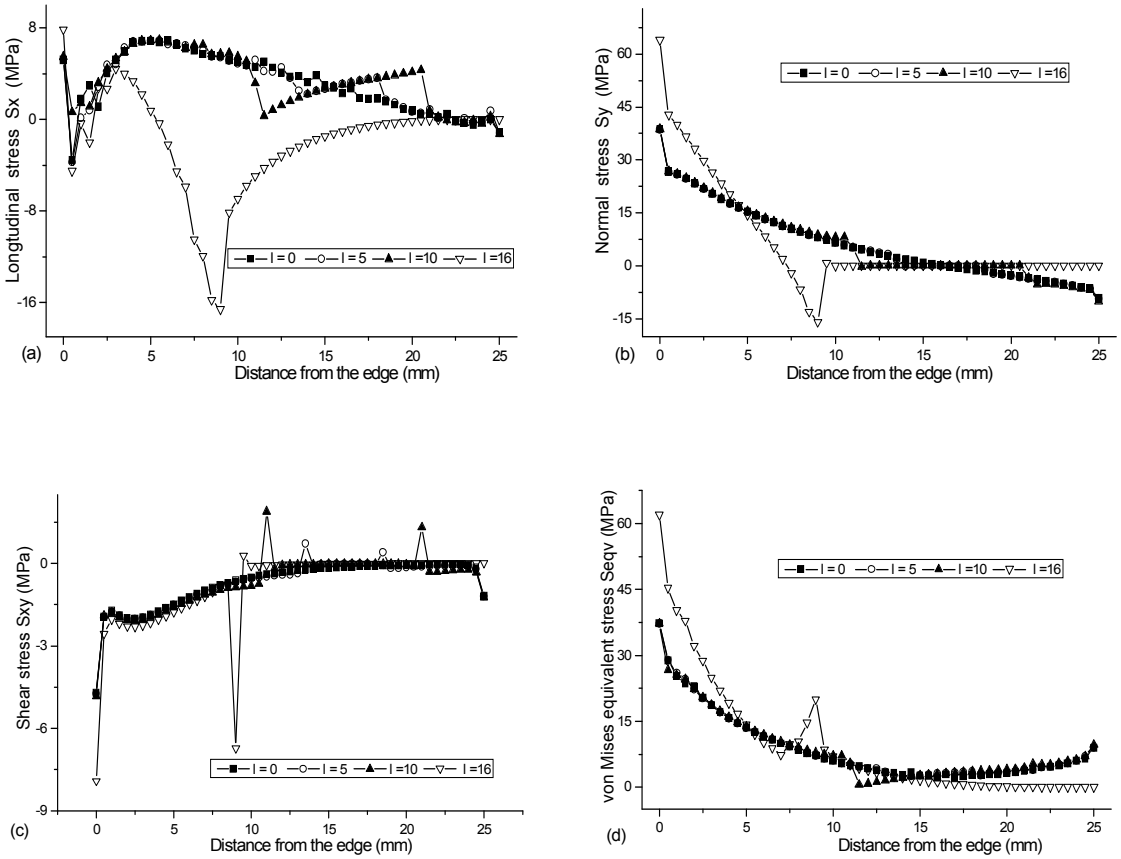

Fig. 3 Recessing length L vs. the stress distribution in the adherend near the interface of the joint: (a) longitudinal stress Sx, (b) peel stress Sy, (c) shear stress Sxy and (d) von Mises equivalent stress Seqv.

The effect of the recessing length on the failure load of the adhesively bonded lap joints made of aluminium adherends and an epoxy adhesive are shown in Fig.4 where the symbol "▼" presents the highest failure load and the symbol "▲" presents the lowest one in same group (included at least 4 specimens). From Fig. 4 it can be seen the failure load of the joint was decreased a little as the length of the recessing was increased to 10 mm and then decreased rapidly when the length reached 16 mm. The average failure loads of the joints were 4.59 kN (L =0), 4.27 kN (L =5 mm, about 6.97% lower than the normal joint), 4.16 kN (L =10 mm, about 9.37% lower) and 1.62 kN (L =16 mm, about 64.71% lower) respectively but the derivation of the test results was higher when L = 5

mm or 10 mm. It is obviously that the shorter recessing in the adhesive is not important to the ultimate load of the joint and they are in compliance with the ones obtained from the finite element simulation.

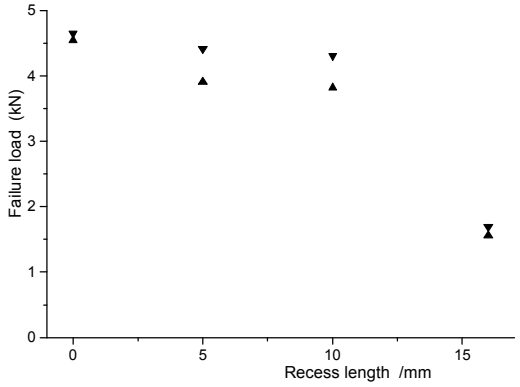

Fig. 4. Recessing length L vs. the failure load

Summary

Under the condition of this work, results obtained from the FEA simulation showed that the peak values of the stresses distributed in the mid-bondline were nearly the same when the length of the arranged recessing was not greater than 10 mm except that the shear stress *Sxy* was increased a little when the length of the recessing was increased. The failure load of the joint was decreased a little as the length of the recessing was increased to 10 mm and then decreased rapidly when the length reached 16 mm. The derivation of the test results was higher when the recessing length was equal to 5 mm and 10 mm. The results from the experimental were in compliance with the ones obtained from the finite element simulation.

Acknowledgements

The authors would like to acknowledge the financial supported by the Major Research Programs of Science and Technology of Hubei Provincial Department of Education (2003Z001), China.

References

[1] M. Olia, J. N. Rossetos. *Int J of Solids and Structures*, 1996, 33(18): 2681–2693.

[2] T. P. Lang, P. K. Mallick. *Int J Adhes Adhes*, 1999, 19: 257-271.

[3] M. F. S. F. de Moura, R. Daniaud, A. G. Magalhaes. *Int J Adhes Adhes,* 2006, 26: 464-473.

[4] X.L. Zheng, M You, Y Zheng, et al. *Proc. of 7th Int. Conf. on Structural Adhesives in Engineering*, IOM Communications Ltd. London, 2004: 171-174

[5] M. You, Z. M. Yan, X. L. Zheng, et al. *Int J Adhes Adhes*, 2007, 27: 696-702

[6] X.L. Zheng, M.S. Zhang, M. You, et al. *Key Engineering Materials,* 2007, Vols. 348-349: 949-952

[7] F.R. Kong, M. You, X. L. Zheng, et al. *Int J Adhes Adhes* 2007, 27: 298-305

[8] F.R. Kong, M. You, X. L. Zheng. *J of Adhesion*. 2008, 84(2):105-124

Key Engineering Materials Vols. 385-387 (2008) pp 229-232
© (2008) Trans Tech Publications, Switzerland
doi:10.4028/www.scientific.net/KEM.385-387.229

Non-linear step-by-step seismic response and the Push-over analysis comparison of a reinforced concrete of ductile frames 15 level building

Jorge A. Avila[1,a] and Eduardo Martinez[1]

[1] Institute of Engineering, National University of Mexico (UNAM)

Ciudad Universitaria, Coyoacan 04510, Mexico, D.F.

[a] javr@pumas.iingen.unam.mx

Abstract. Based on a ductile frames 15 level building, a non-linear analysis with increased monotonically lateral loads (Push-Over) was made in order to determine its collapse and its principal responses were compared against the elastic and inelastic time-history seismic responses determined with the SCT-EW-85 record. The seismic-resistance design and faced to gravitational loads was made according to the Complementary Technical Norms of Concrete Structures Design (NTC-Concrete) and the NTC-Seismic of the Mexico City Code (RDF-04), satisfying the limit service states (relative lateral displacement between story height maximum relations, story drifts ≤ 0.012) and failure (seismic behavior factor, Q= 3). The compressible (soft) seismic zone IIIb and the office use type (group B) were considered. The non-linear responses were determined with nominal and over-resistance effects. The comparison were made with base shear force–roof lateral displacement relations, global distribution of plastic hinges, failure mechanics tendency, lateral displacements and story drift and its distribution along the height of the building, local and global ductility demands, etc. For the non-linear static analysis with increased monotonically lateral loads, it was important to select the type of lateral forces distribution.

Introduction

The design criteria in Mexico City are ruled by the Mexico City Construction Code, used since 2004 (RDF-04) [1], and its Complementary Technical Norms (NTC). In this work the elastic and inelastic behavior (time-history and static with lateral loads monotonically increased Push-Over procedure) of a reinforced concrete 15 level building, with office use (group B) and located in Mexico City's III_b compressible seismic zone, are compared. The spectral modal dynamic analysis was used for the design, checking that, in the service condition, the maximum relations of the relative horizontal displacement between story height (drifts) did not exceed the permissible limit of γ_p = 0.012 (design condition in which the non-structural elements are not linked to the main structure), and also that the failure limit state (resistances) were accomplished, assuming that the elastic seismic forces were reduced by the seismic behavior factor, Q=3; the designs satisfy the special requirements of ductile frames, in addition to those general requirements, as the NTC-Seismic [2] and NTC-Concrete [3] specify when Q = 3 or 4 is used. When the designs were known, inelastic step-by-step dynamic analysis were performed with the SCT accelerogram, EW component, recorded during the September 19th of 1985 earthquake in Mexico City. For the Push-over analysis, different options for the seismic forces were checked: a) according to the spectral modal dynamic analysis results; b) according to the accepted static method in the NTC-Seismic, RDF-04; c) according to the results of the initial elastic stage of the step-by-step dynamic analysis; and, d) according to the most intense stage in the inelastic range of the time-history dynamic analysis, without and with over-resistance effects. During the performance of the Push-over analysis, and without the necessity of achieving the failure mechanism, the instant in which the supposed maximum local ductility values could be reached (30 for beams and/or 20 for columns) was monitored.

Structure description

Its foundation is made of a two level rigid box with a parking basement, foundation beams grid, and under the foundation slab, a group of point piles. The plant is rectangular with three 6 meters bays

in Y direction (short direction), and five 9 meters bays in X direction (longitudinal) (see Fig. 1). The story height is 3.5 meters, from the roof level to the first level; the ground level story height is 4.5 meters (PB-N1), and 3.5 meters for the basement story height (PB-basement).

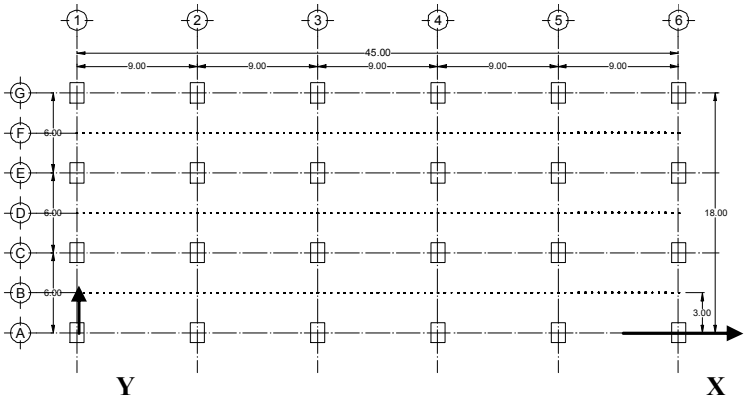

Fig. 1 Type-plant [meters]

Elastic responses

Vibration periods. Table 1 presents the periods for the first three modes vibration for the directions: X (long), Y (short) and torsion of the 15 levels building, according to the NTC-Seismic criteria. For both directions the fundamental periods of vibration result very alike.

Ratios of relative lateral displacement between the story height. Fig. 2 shows the maximum story distortion of the 15 levels building, with the earthquake acting in both directions X and Y, respectively; they are compared against the of 0.012.

Table 1. Vibration periods [seconds]

Direction	Period, T_i (s)		
	Mode 1	Mode 2	Mode 3
X	1.527 (57.73)	0.505 (7.76)	0.289 (2.97)
Y	1.551 (56.51)	0.502 (9.26)	0.276 (3.42)
θ	1.300 (55.49)	0.428 (8.40)	0.240 (3.27)

( ) Effective modal mass, %

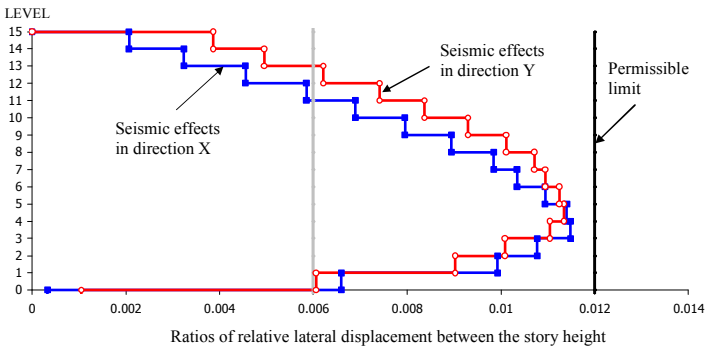

Fig. 2 Ratios of relative lateral displacement between the story height, spectral modal dynamic analysis

Inelastic responses

The time-history inelastic responses were calculated for the structural 2 (transversal direction) and C (longitudinal direction) axes; in this paper are shown the C axe responses. The step-by-step inelastic dynamic responses are determined with the SCT-EW record. Each axis was calibrated with the mass and stiffness dynamic properties that were representative for each direction of the structure. The fundamental periods of vibration of both directions are separated of the critical zone of the SCT-EW-85 record elastic spectra (see Fig. 3), and it is to be expected that in at the beginning of the seismic forces action, the effects will be minor and with less damages. Despite the direction analyzed it is a building in which the corresponding elastic and inelastic spectral ordinates (global ductility of 3) of the design and response spectra are similar.

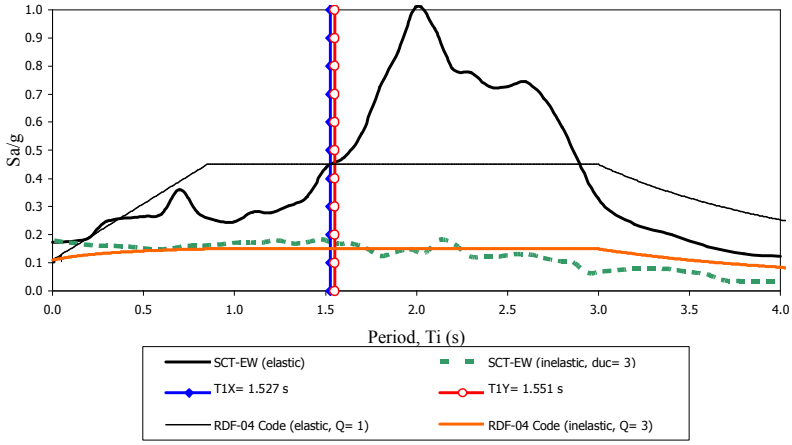

Fig. 3 Location of the fundamental periods of vibration of the 15 level building, seismic zone III_b, design spectra RDF-04 and response spectra SCT-EW (ξ= 5%)

Ratios of Base Shear Force-Roof Lateral Displacement. When the inelastic dynamic comparisons are done, it is observed a behavior in the non-linear range, with higher hysteretic area with nominal resistances; the help that over-resistances offer makes the response to tend to be elastic (see Figs. 5 and 6).

Plastic Hinges Global Distribution and Local Ductility Demands. The plastic hinges get diminished in number and plastic rotation amplitude when we take notice of the possible over-resistance sources. When we compare the maximum local ductility demands developed in the beams and columns of C axe, without and with over-resistance effects (see Fig. 4), it is corroborated that in both directions we have a similar inelastic behavior.

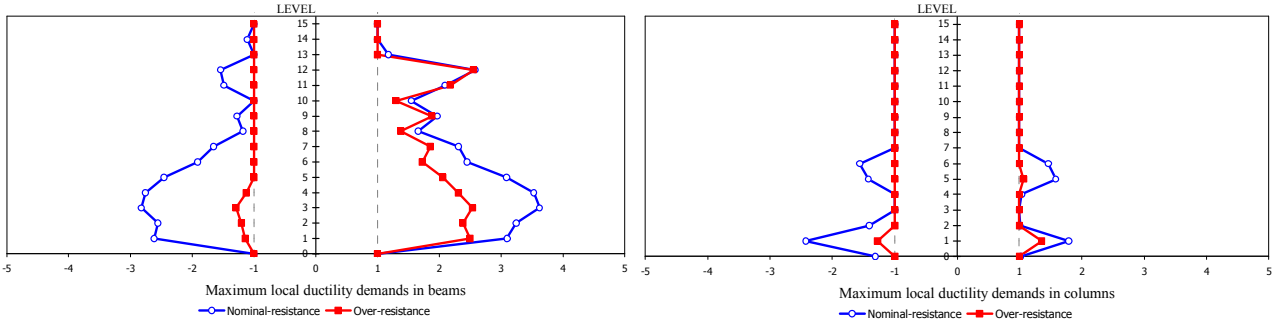

Fig. 4 Beam and columns ductility maximum demands of C axe, time-history analysis (without and with over-resistance effects)

After checking the form of each forces distribution Fi and comparing versus the step-by-step analysis results, only the case a) results are showed with the Push-over procedure. In C axe the local ductility maximum limit, established for the columns of PB-N1 story, predominated; the beams developed, practically in a generalized way in all the levels, local ductility under 20, inferior to the assumed permissible limit. In general, the results are congruent with the observed behavior in the responses of the inelastic analysis in time-history, versus the SCT-EW record effects. Figs. 5 and 6 show the comparisons of the hysteretic step-by-step inelastic analysis curves, in function of the ratios of base shear force–roof lateral displacement, versus to those determined in the Push-over analysis. The failure mechanism was never reached, because the established yield maximum limit dominated in beams or columns. It is to be noticed in these graphics that certainly there is a correspondence between resistance and lateral stiffness (equivalent slope) available determined with

both type of non-linear analysis (step-by-step and static Push-over type) and that, in the other hand, with the time-history analysis, it is not possible to determine the real deformation capacity of each structure before the collapse mechanism is formed, limited in this work if the local ductility maximum demands showed in beams and columns, over the acceptable values in a practical design point of view.

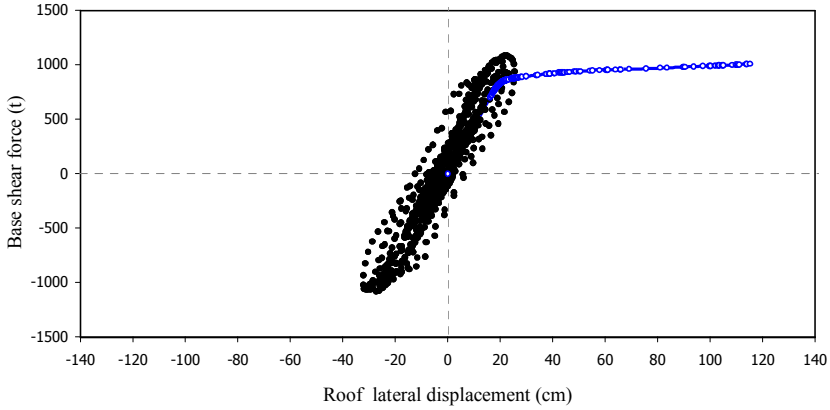

Fig. 5 Comparisons of the step-by-step inelastic analysis curves, in function of the ratios of base shear force–roof lateral displacement, versus to those determined in the Push-over analysis (nominal resistance effects)

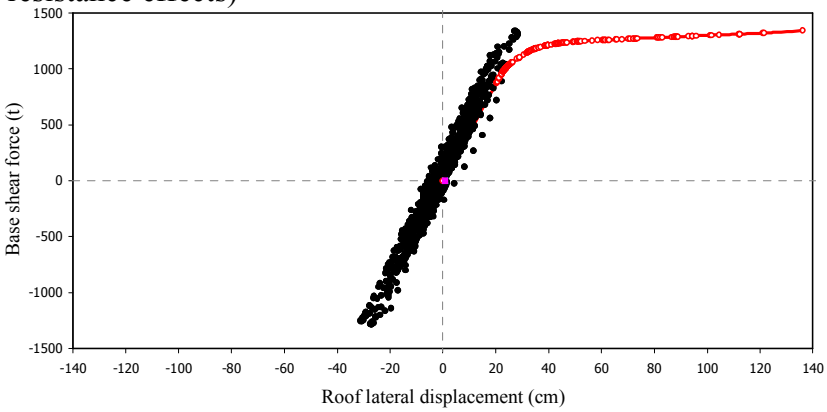

Fig. 6 Comparisons of the step-by-step inelastic analysis curves, in function of the ratios of base shear force–roof lateral displacement, versus to those determined in the Push-over analysis (over-resistance effects)

Conclusions

The structure presents inelastic behavior, mainly in the beam ends; the general tendency of the failure mechanism of both directions accomplish with the philosophy of "strong column–weak beam", as it is recommended in the modern Codes. With the step-by-step dynamic analysis we are able to estimate in a better way the structural behavior closest to reality in case of a severe earthquake. With the Push-over analysis the failure mechanism was never reached, because the established maximum limit of yield dominated in beams or columns. The effects of the possible over-resistance sources that structures have, not included in a conventional design, give us an additional security margin in the response of the structures in front of intense solicitations, allowing us to estimate in a better way the seismic-resistant behavior of the structures.

References

[1] Mexico City Construction Code, 2004 (RDF-04).

[2] Complementary Technical Norms (NTC), NTC-Seismic, RDF-04.

[3] Complementary Technical Norms (NTC), NTC-Concrete, RDF-04.

Key Engineering Materials Vols. 385-387 (2008) pp 233-236
© (2008) Trans Tech Publications, Switzerland
doi:10.4028/www.scientific.net/KEM.385-387.233

Numerical simulation on mixed mode I-II crack propagation process in concrete

Qing Xu[1,a] , Wei Dong [2,b] , Zhimin Wu [2,c]

[1]School of Civil and Hydraulic Engineering, Dalian University of Technology
[2,3]State Key Laboratory of Coastal and Offshore Engineering, Dalian University of Technology, Dalian 116024, P.R. China
[a]xuqing@dl.cn, [b]dlutdw@yahoo.com.cn, [c]zhiminwu2002@yahoo.com.cn

Keywords: concrete; mixed modeI-II fracture; crack propagation criterion; numerical simulation

Abstract: A crack propagation criteria is proposed for mixed mode I-II fracture in concrete based on the initial cracking K_I-K_{II} curve obtained from experiment. Once the difference between the stress intensity factor at the crack tip caused by the external load and the one caused by the cohesive force attains the above K_I-K_{II} curve, the crack begins to propagate. Based on this criteria, the finite element method was used to simulate the mixed mode I-II crack initiation, stable propagation and unstable failure in concrete. For the four-point shear concrete specimens, the crack propagation trajectory and *P-CMSD* (Crack Mouth Sliding Displacement) curve were obtained. Upon the comparison with the experimental results, the calculated results show good agreement. It is concluded that, if the elastic modulus E, the uniaxial tensile strength f_t and the initial cracking K_I-K_{II} curve of concrete are measured from experiment, the complete process of mixed mode I-II crack propagation can be simulated using the proposed criterion.

Introduction

The finite element method was applied successfully to simulate the propagation of mixed mode I-II cracks in concrete in recent years. Crack initiation and propagation in concrete can be modeled in two different ways: (i) smeared crack model [1] or (ii) discrete crack model [2]. The softening behavior described by an appropriate stress-strain relation is characterized by reducing the material stiffness in smeared model or described by a relation between stress and relative displacement along the localized surfaces of discontinuity in discrete crack model. For the two approaches, it is fundamental to choose an accurate criterion to estimate crack initiation and predict crack direction in numerical analysis. Maximum principal stress criterion and maximum circumferential stress criterion are frequently adopted because they are easy to implement [3-6].

It has been approved that the crack propagates when the load gets its maximum. Therefore, in this paper, a crack propagation criterion is proposed for mixed mode I-II fracture in concrete based on the initial cracking K_I-K_{II} curve obtained from experiment according to the initial load. Based on the criteria, the finite element method is used to simulate the mixed mode I-II crack initiation, stable propagation and unstable failure in concrete. Upon the comparison with the experimental results, the calculated ones show good agreement.

Evaluation of crack propagation criterion

An experiment of four-point shear notched beams of concrete was carried out to determine the initial cracking state according to sudden decrease of the strain gauges' values. Then the initial cracking load P_{ini} can be given. Besides, the quarter point singular element approach was used to

calculate the stress intensity factors $K_{\mathrm{I}}^{\mathrm{ini}}$ and $K_{\mathrm{II}}^{\mathrm{ini}}$ corresponding to P_{ini} in the present study. Moreover, different combinations of $K_{\mathrm{I}}^{\mathrm{ini}}$ and $K_{\mathrm{II}}^{\mathrm{ini}}$ were obtained according to different positions of pre-cracks. Correspondingly, the mixed mode I-II initial cracking criterion for concrete can be obtained using the fitting curves of track formed by the different combinations of $K_{\mathrm{I}}^{\mathrm{ini}}$ and $K_{\mathrm{II}}^{\mathrm{ini}}$ [7]. In this paper, for the specimen of Series 600 (long×wide×high=2500×600×200mm, a_0 =120mm, f_{cu}=42.9Mpa), the fitting curve through different combinations of $K_{\mathrm{I}}^{\mathrm{ini}}$ and $K_{\mathrm{II}}^{\mathrm{ini}}$ is shown in Fig. 1

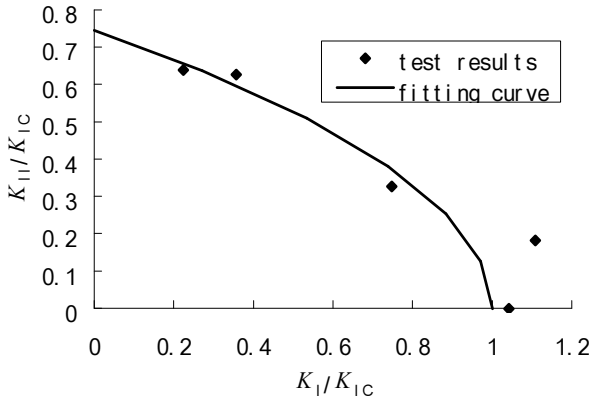

Fig.1 The fitted curve for Series 600 specimen

Then the I-II mixed mode initial cracking criterion equation is given by Eq. (1) based on the fitted curve.

$$K_{\mathrm{II}}^2 + 0.508K_{\mathrm{I}}K_{\mathrm{Ic}} - 0.508K_{\mathrm{Ic}}^2 = 0 \tag{1}$$

A superposition approach for calculating the stress intensity factor at the crack tip in a four-point shear notched beam caused by the external load P and the cohesive force on the fictitious crack zone can be determined using the following simple relationship:

$$K_{\mathrm{I,II}} = K_{\mathrm{I,II}}^{\mathrm{P}} - K_{\mathrm{I,II}}^{\sigma} \tag{2}$$

Where $K_{\mathrm{I,II}}^{\mathrm{P}}$ is the stress intensity factor caused by the external load P, $K_{\mathrm{I,II}}^{\sigma}$ is the stress intensity factor caused by the cohesive stress σ_{w}.

During the crack propagation, each step of the crack length increase was regarded as a whole fracture process, i.e. fracture may be divided into two steps: the crack initiation and the crack stable propagation in each crack extended step. Therefore, it is assumed that the difference between $K_{\mathrm{I,II}}^{\mathrm{P}}$ and $K_{\mathrm{I,II}}^{\sigma}$ satisfies the equation of the above K_{I}-K_{II} curve, the crack begins to propagate.

$K_{\mathrm{I,II}}^{\mathrm{P}}$ and $K_{\mathrm{I,II}}^{\sigma}$ are directly calculated by the quarter point singular element approach in virtue of the external load P and the cohesive stress σ_{w}, respectively. The expression [8] of σ_{w} is given in Eq. (3).

$$\frac{\sigma_{\mathrm{w}}}{f_{\mathrm{t}}} = \left\{1+\left(c_1\frac{w}{w_0}\right)^3\right\}\exp\left(-c_2\frac{w}{w_0}\right) - \frac{w}{w_0}(1+c_1^3)\exp(-c_2)\text{, for } w\in[0,w_0] \tag{3}$$

Where c_1 and c_2 are the material constants, f_{t} is the uniaxial tensile strength of concrete, w_0 is the maximum crack opening width when the stress becomes zero. With the experimental values of these parameters, $c_1 = 3$, $c_2 = 7$ and w_0 =160 μm are adopted in the present calculation.

$K_{\mathrm{I,II}}^{\mathrm{ini}}$ is determined by the initial load P_{ini} and the initial crack length a_0. At the beginning of crack propagation, $K_{\mathrm{I,II}}^{\mathrm{ini}}$ represents ability of the body to resist an external load. Therefore, $K_{\mathrm{I,II}}^{\mathrm{ini}}$ can be treated as the appearance of crack propagation during the whole fracture process. In this paper, $K_{\mathrm{I,II}}^{\mathrm{ini}}$ is utilized as a criterion of crack propagation. According to Eq. (2), $K_{\mathrm{I,II}}^{\mathrm{ini}}$ can be presented by $K_{\mathrm{I,II}}^{\mathrm{P}}$ minus $K_{\mathrm{I,II}}^{\sigma}$. Once the following relation is satisfied, the crack will begin to propagate.

(1) $K_{\mathrm{I,II}}^{\mathrm{P}} - K_{\mathrm{I,II}}^{\sigma} < K_{\mathrm{I,II}}^{\mathrm{ini}}$, the crack can't extend

(2) $K_{\mathrm{I,II}}^{\mathrm{P}} - K_{\mathrm{I,II}}^{\sigma} = K_{\mathrm{I,II}}^{\mathrm{ini}}$, the crack is in the critical state

(3) $K_{\mathrm{I,II}}^{\mathrm{P}} - K_{\mathrm{I,II}}^{\sigma} > K_{\mathrm{I,II}}^{\mathrm{ini}}$, the crack will extend

The iteration process for crack growth in numerical simulation and results

In order to simulate the crack propagation, the proposed crack propagation criterion is used. Fig.2 displays the variety of cohesive force during crack propagation.

The iteration process can be described by the following,

1. Increase the load from zero by a pre-assumed amount ΔP and calculate the stress intensity factor at the initial crack tip until $K_{\mathrm{I,II}}^{\mathrm{P}} - K_{\mathrm{I,II}}^{\sigma} = K_{\mathrm{I,II}}^{\mathrm{ini}}$ is satisfied. The initial load P_{ini} is given, namely load (1) = P_{ini}.
2. Delete all nodes and elements. Increase the crack length by a specified amount Δa and rebuilt the model.
3. Increase the load from the value of load (1) and calculate w, use Eq. (3) to calculate $\sigma(x)$, without moving the fictitious crack tip, until the $K_{\mathrm{I,II}}^{\mathrm{P}} - K_{\mathrm{I,II}}^{\sigma} > K_{\mathrm{I,II}}^{\mathrm{ini}}$ is satisfied. Then, load (2) can be obtained.
4. Repeat steps 2-3 for the next crack propagation. When the result of $K_{\mathrm{I,II}}$ caused by load (i-1) minus $K_{\mathrm{I,II}}^{\sigma}$ caused by cohesive forces exceed the initial fracture criterion $K_{\mathrm{I,II}}^{\mathrm{ini}}$ in the step of i, the $K_{\mathrm{I,II}}^{\mathrm{P}} - K_{\mathrm{I,II}}^{\sigma} > K_{\mathrm{I,II}}^{\mathrm{ini}}$ can be satisfied only by decreasing the applied load (i-1). Therefore, the maximum load $P_{\max}$ is obtained, $P_{\max}$=load (i-1).
5. Repeat step 2 for the next crack propagation. Decrease the load by a pre-assumed amount ΔP and calculate the stress intensity factor at the initial crack tip until $K_{\mathrm{I,II}}^{\mathrm{P}} - K_{\mathrm{I,II}}^{\sigma} > K_{\mathrm{I,II}}^{\mathrm{ini}}$ is satisfied.
6. The program will terminate when the crack approaches the boundary of beam or the load becomes negative.

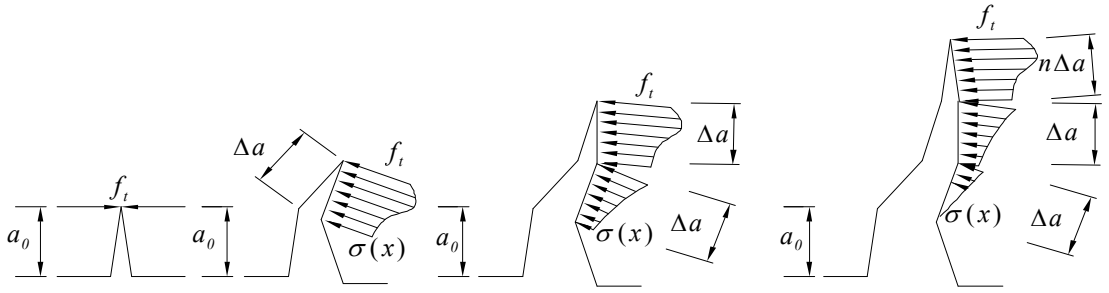

(a) Initial step (b) The first step (c) The second step (d) After n steps

Figure.2 The variety of cohesive force during the crack propagation

Calculated results

The different crack propagation states of specimen L604-2 are shown in Fig.3. Fig.4 shows the comparisons between crack trajectories and *P-CMSD* (crack mouth sliding displacement) curves using numerical simulation and experimental approach for specimen L604-2. The numerical results show good agreement with experimental ones. It should be noted that the descending part of *P-CMSD* curve is not acquired in the test. Therefore, the comparison is only for the ascending part of the curve.

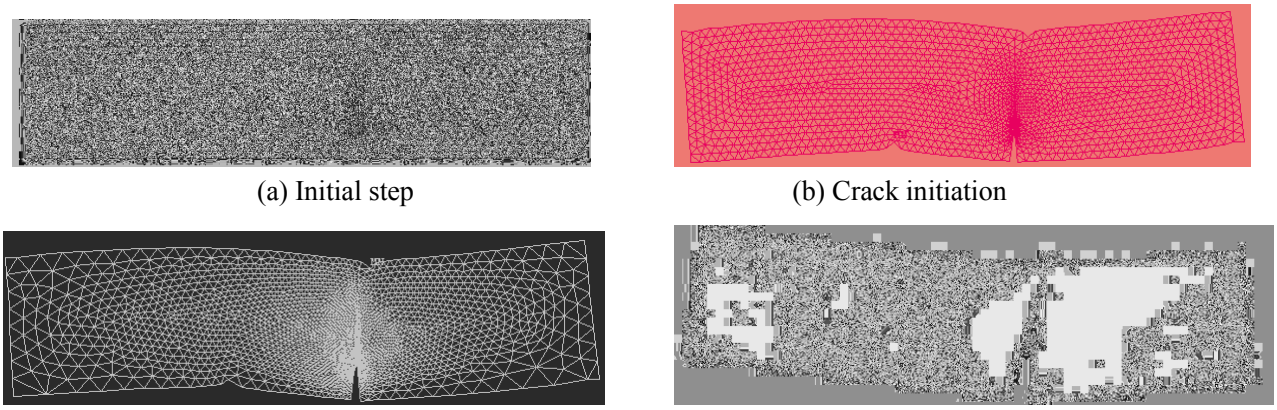

(a) Initial step (b) Crack initiation

(c) Unstable propagation (d) The extend length is 450mm (failed)

Figure.3 The crack propagation of L604-2(long×wide×high=2500×200×600mm, a_0 =120mm, f_{cu}=42.9Mpa)

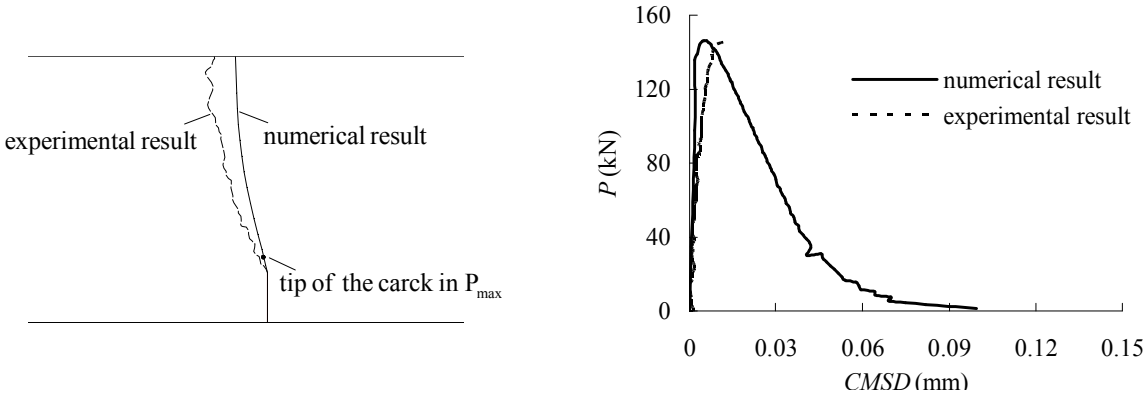

L604-2 (long×wide×high=2500×200×600mm, a_0 =120mm, f_{cu}=42.9Mpa)

Figure.4 Comparisons of crack trajectory and *P-CMSD* curves between simulation and experiment

Conclusions

A crack propagation criterion is proposed. If the uniaxial tensile strength, the elastic modulus, Poisson's ratio and the initial fracture equation of concrete are obtained, the whole process of mixed mode I-II fracture propagation can be simulated by using this criterion and by using the proposed method. Upon the comparison with the experimental results, the calculated ones show good agreement for the crack trajectory and *P-CMSD* curve. Therefore, the proposed method in this paper is feasible.

References

[1]Rashid Y R. Nucl. Engng. Des, Vol.7, No.4(1968), p.334-344.

[2]Ngo D, Scordelis A. J. ACI, Vol.64, No.3(1967), p.152-163.

[3]Alfaiate,J., Wells,G.N, Sluys,L.J. Engng. Fract. Mech. Vol.69 (2002), p.661-686.

[4]Zihai Shi. J. Struc. Engng. Vol.130, No.11(2004), p.1738-1747.

[5]Schröder,J., Löblein,J. Comput. Mech. Vol.36, No.2 (2005), p.139-157.

[6]Bouchard,P.O. Bay,F. Comput. Methods. Appl. Mech. Engng. Vol.192, p.3887-3907.

[7]Zhimin Wu, Wei Dong: Key. Engng. Mat. Vol.348-349(2007), p.961-964.

[8] Reinhardt H W, Cornelissen H A W:J. Struc. Engng. Vol.112, No.11(1986),p.2462-2477.

Key Engineering Materials Vols. 385-387 (2008) pp 237-240
© (2008) Trans Tech Publications, Switzerland
doi:10.4028/www.scientific.net/KEM.385-387.237

On the Evaluation of the Service Life of Shaft-Bushing Tribosystems at low speed

Alessandra Calabrese[1,a], Piero Morelli[2,b], Alessandro Morri[3,c], Giuliano Sambogna[3,d] Fabrizio Tarterini[3,e]

[1]S.I.BO. s.r.l. Società Italiana Boccole - v. G. Puccini 10, 40012 Calderara di Reno (BO) Italy

[2]DIEM Department of Mechanical Engineering - v.le Risorgimento 2, 40136 Bologna Italy

[3]SMETEC Institute of Metallurgy - v. S. Donato 15, 40127 Bologna Italy

[a]alessandra@sibo.eu, [b]piero.morelli@unibo.it, [c]alessandro.morri4@unibo.it, [d]samb@bomet.fci.unibo.it, [e]fabrizio.tarterini@unibo.it

Keywords: Tribology, Wear of Materials, Service Life, Bushing Bearings.

Abstract. This work presents the results of a set of endurance tests performed on steel to steel shaft/bushing tribosystems, without re-lubrication after start-up. The experimental procedure was designed in order to provide simulation for the operative conditions of earthmoving machinery. For this purpose, a new testing machine was specifically manufactured so as to accommodate shaft/bushing assemblies up to a nominal coupling diameter of 90 mm, with a maximum radial load capability of 300 kN.
The machine was operated in alternating rotation, with a span angle of 180 degrees, at an angular speed of 10 rpm. The effects of contact pressure intensity were investigated, as well as the effects of grease lubrication type and of the geometry of grease breeding grooves that were located on the bushings inner surface. The tribology behaviour of the tested assemblies was quantified by means of the transmitted torque, grease temperature at the surface of contact and the metallographic analysis of wear out surfaces.

Introduction

A theoretical study on the bushings wear out was elaborated by Teplyi [1], for the case of thin walled components, while Lyubin [2] proposed a numerical implementation of the "non-wearing-shaft / wearing-bush" model. Some experimental investigations were performed by Campbell et al. [3], concerning the bushings life and maintenance on mining machines.
In this paper, the problem of bushings wear out, lubrication and endurance has been adressed, reproducing the specific experimental conditions of earthmoving machines applications.

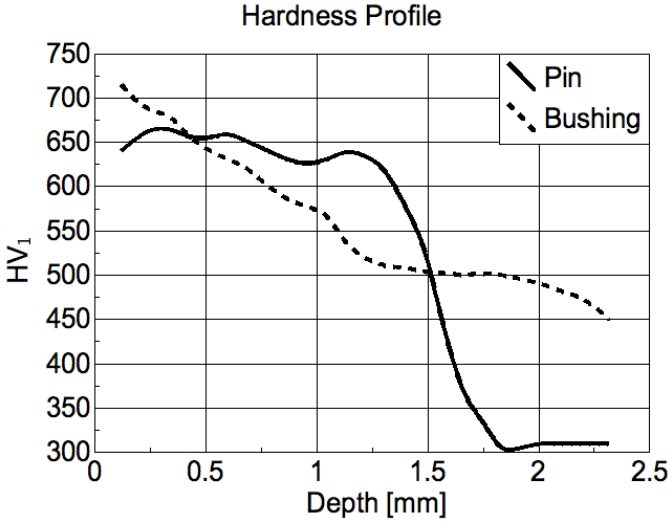

Fig. 1 - In depth hardness of the contact surfaces.

Materials and Methods

Bushings and Pins. The studied bushings were hollow cylindrical shaped, with an inner diameter of 60 mm, an outer diameter of 75 mm and an axial length of 60 mm. The bushings were made in 20MnV6 (Table 1), carburized, oil quenched and then tempered at low temperature. The carburized depth range was between 0.8 and 1 mm (Fig. 1).

	C	Mn	Si	P	S	Cr	Ni	Mo	Pb	Sn	Al	Ti	V	Nb	Co
39NiCrMoS3	0.395	0.67	0.22	0.009	0.023	0.74	0.75	0.15	0.001	0.22	0.032	0.003	0.002	0.003	0.012
20MnV6	0.18	1.55	0.36	0.016	0.027		0.003				0.027	0.002	0.13		

Table 1 - Steel chemical compositions, in weight %.

The pins used for tribological tests were produced with 39NiCrMoS3 (Table 1), induction heated, oil quenched and then tempered at low temperature, with a resulting hardened depth of about 1.5 mm (Fig. 1). After the heat treatment, both the internal and external surfaces of the bushings were characterized by a fine martensite structure, which was not so clearly resolvable in the optical microscope, and retained austenite, as shown in Fig. 2.

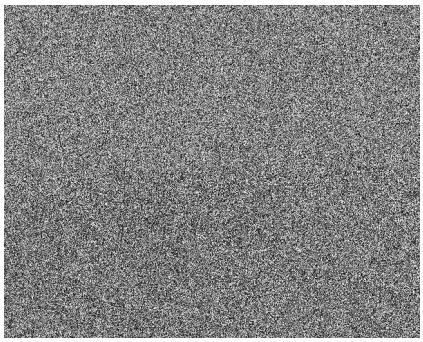

Fig. 2 - Bushings microstructure.

Lubrication. Grease lubrication was provided once for all before starting the endurance tests, which were carried out at room temperature. Two kinds of grease lubrication have been taken into consideration:

- 609360 AGIP Rocol Sapphire 2 bearing grease, with Lithium ions, identified in this work as "grease A"
- 608060 AGIP Rocol Sapphire hi pressure 2, with molybdenum disulfide, which has been called "grease B".

Since bushings were provided with a radial hole, manufactured in order to optimize the lubricant filling procedure, it was possible to insert a thermocouple so to measure the temperature of the grease in direct contact with the friction surface between the bushings and the pins.

Experimental setup. Endurance tests were performed on the test bench of Fig. 3. The pin bushing assemblies were placed between two lateral supports and subjected to the radial load applied by a mechanical device by means of elastic energy accumulation. Usable load was up to 300 kN. An electric gear motor was controlled by a National Instruments system, which was programmed to drive the pin in alternating sinusoidal rotation at the frequency of 10 cycles per minutes. The maximum nominal torque deliverable by the gear reducer was 2 kNm. These loading conditions were meant to simulate the constraints of earthmoving machinery, where bushings are typically employed with high contact pressures at low speeds.

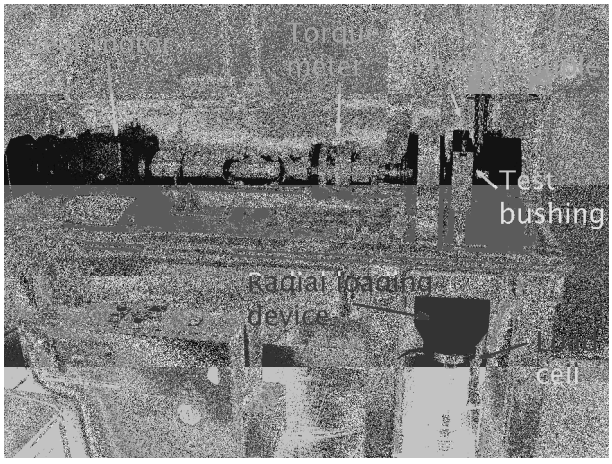

Fig. 3 - Bushing test bench.

The testing machine was instrumented with a torque meter, a thermocouple and a load cell, in order to provide the real time measurements of the torque absorbed by the friction between pin and bushing, the grease temperature and the applied radial load. Endurance testing was protracted until severe wear out or seizure of the fitting occurred.

Results and Discussion

Endurance diagrams. A set of preliminary life tests was performed in order to study the effects of the lubricating grooves geometry. Grooves are obtained by machining the inner surface of the bushings, in order to create channels like webs at the surface of contact, that once filled with grease, are able to release lubrication during the service life. The wider is the extension in length and width of the grooves, the higher is the lubricating efficiency, but the lower is the specific load carrying ca-

pacity of the bushings. The results of preliminary tests allowed to identify the best compromise between smooth and full grooved surfaces.
The experimentation was then addressed to investigate the effects of the intensity of the contact pressure and the type of lubricating grease. Load ratings were assessed by the so called "admissible pressure p_{adm}", defined as the ratio between the radial load and the projected area of the contact surface into a plane containing the bushing axis:

$$p_{adm} = \frac{F}{\varphi \cdot L}, \tag{1}$$

where F is the radial load, φ is the bushing inside diameter and L is the bushing length. Two levels of p_{adm} were chosen, namely 23 MPa and 27 MPa, in order to simulate standard and severe loading conditions. The characteristic endurance behaviours that were observed are shown in the diagrams of Fig. 4 to Fig. 7.

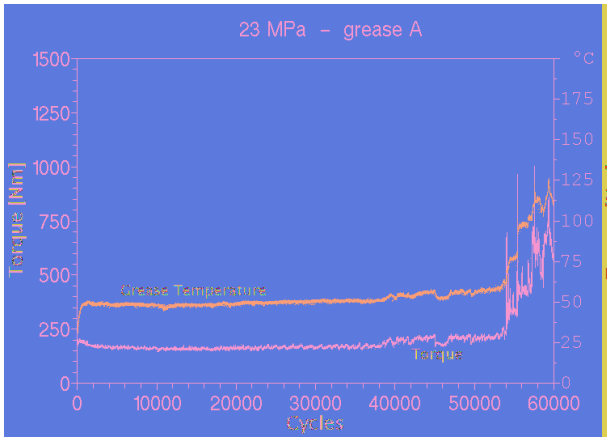

Fig. 4 - Std. load and std. grease.

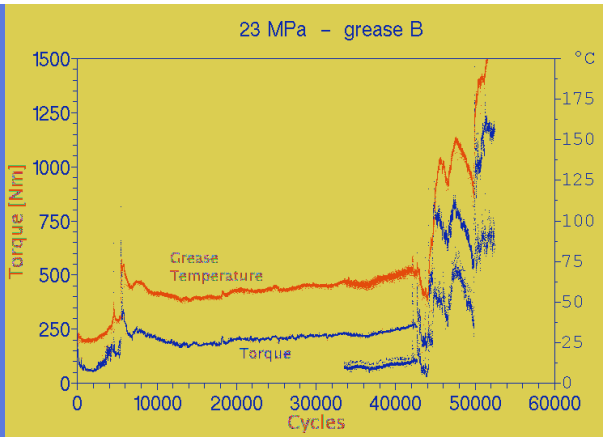

Fig. 5 - Std. load and quality grease.

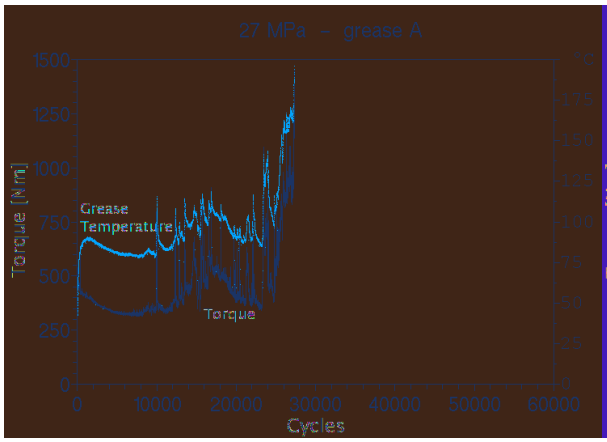

Fig. 6 - Severe load and std. grease.

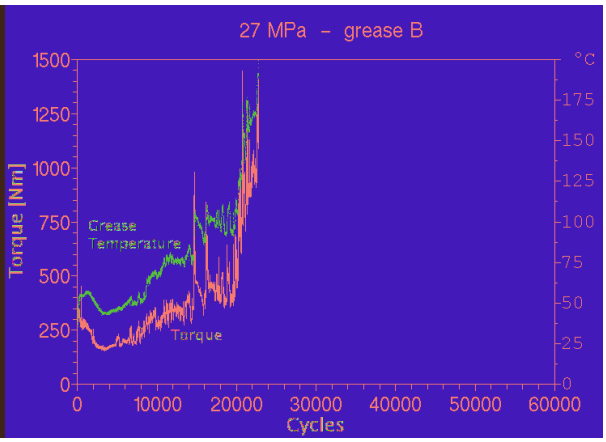

Fig. 7 - Severe load and quality grease.

Break-in was outlined by an initial torque reduction, which was faster for the case of high quality lubrication. Adhesive wear out took place, producing a progressive damage that caused both the torque and grease temperature to gradually increase. Abrasive wear out or major damage were proven by the irregularities and sudden rises shown on the diagrams. In Fig. 5, the dual torque measurement related to the back and forth alternating rotation was probably caused by severe abrasion before complete seizure.
Surface wearing. A SEM analysis of the contact surfaces was performed at different phases of the bushings life. In Fig. 8 is shown the surface state of a new bushing, as machined, which exhibits the typical roughness and straight signs caused by grinding. After break-in, the surface shown in Fig. 9 appears more smooth, but reveals the first markings of micro damage, which occurred during the

useful life due to adhesion wear. Extensive plastic deformation and abrasion grooves are shown in Fig. 10 for the case of a complete bushing seizure. No evidence of oxidative wear was observed.

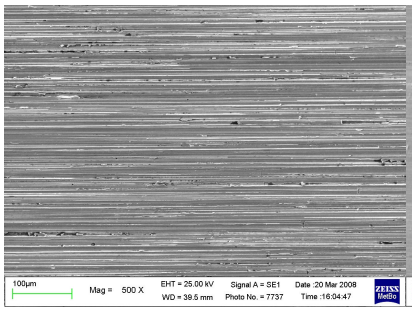

Fig. 8 - Grinding grooves, as machined.

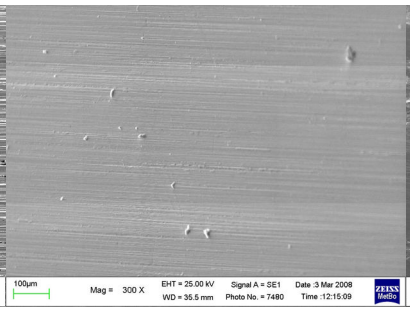

Fig. 9 - Adhesion wear, useful life.

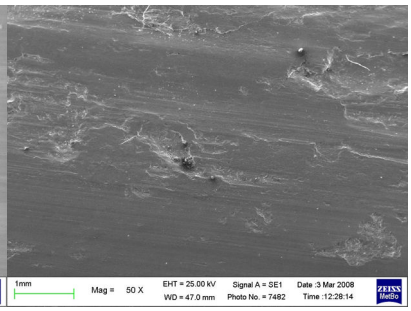

Fig. 10 - Abrasion wear and seizure.

Conclusions

By the analysis of the endurance diagrams and wearing of the contact surfaces, it is possible to draw the following conclusions about the bushings service life in case of slow rotational speeds and lack of maintenance for re-lubrication:

I. The lubrication grooves geometry has proven to be a key parameter for the enhancement of the bushings life.
II. Severe loading conditions can reduce the bushings endurance to half the average life achievable for the case of standard loading conditions.
III. High performance grease lubrication decreases significantly the contact friction, thus reducing the energy required for actuation and the mechanical load of the actuator devices. However, this kind of lubrication is subject to a faster deterioration, if compared to the more economic one; this is the reason why the measured bushing lives were shorter. A proactive re-lubrication maintenance plan should be considered in case of the adoption of high quality greases.

Acknowledgments

The authors express their gratefulness to S.I.BO. s.r.l. “Società Italiana Boccole”, for founding and taking part to this research and for manufacturing the tested materials and the prototype of the experimental testing machine.

References

[1] M.I. Teplyi: *Determination of contact parameters and wear on cylindrical sliding bearings*. Soviet journal of Friction and Wear. Vol. 8 n. 5 (1987), p.99-105

[2] O.H. Lyubin: *Evaluation of the service life of shaft-bush-type tribosystems.* Materials Science. Vol. 41 n. 6 (2005), p.755-763

[3] J. Campbell, N.N. Gray, T. Wiley, E.B. Shields: *Wear testing of bushings during the cyclic process.* ASME Pressure Vessels and Piping Conference 2005, p.239-242

Key Engineering Materials Vols. 385-387 (2008) pp 241-244
© (2008) Trans Tech Publications, Switzerland
doi:10.4028/www.scientific.net/KEM.385-387.241

On the Tensile and Compressive Fatigue Behaviour of Notched CFRP laminates

Giangiacomo Minak[1,a], Piero Morelli[1,b]

[1]DIEM - Department of Mechanical Engineering - v.le Risorgimento 2 - 40136 Bologna, Italy

[a]giangiacomo.minak@unibo.it, [b]piero.morelli@unibo.it

Keywords: CFRP, fatigue, notch effect, Maximum Likelihood Estimation.

Abstract. This paper describes the experimental results of a set of fatigue tests performed on T300 carbon fiber / epoxy resin laminates cured in autoclave.
The effects of anisotropy in laminates lay up have been investigated, as well as the influence of circular hole notches, for both the case of tensile and compressive loading conditions.
Due to the high slenderness of specimens, that have the ASTM D3039 standard suggested geometry, a special gripping device has been designed in order to avoid the axial buckling.
Fatigue failure probability of the material has been assessed by means of Maximum Likelihood Estimates (MLE) of the experimental data, as a function of the lay-up and load conditions.
Eventually, the micrographic analysis of fractured surfaces outlined the combined effects of both the geometry and notches towards the damage behaviour of this kind of material.

Materials and Methods

Laminates lay-up and specimens geometries. The studied laminates were multi-layer composite materials made by Hexcel epoxy matrix prepegs reinforced by T300 unidirectional carbon fibers. The fiber volume ratio was 60%.
Unidirectional $[0]_6$ and quasi-isotropic $[0/+45/-45/90]_s$ lay-ups have been considered. Un-notched specimens were manufactured to comply with the ASTM D3039 standard [1] and their measures were 250 mm in length and 25 mm in width.
Wider laminates (width=40 mm) were machined accordingly to ASTM D5766 [2], in order to produce hole notches with diameters of 2 and 8 mm.
Experimental devices. Quasi-static and fatigue tests have been performed using an Instron 8032 servo-hydraulic machine, equipped with a FastTrack 8800 digital console.
For the case of tensile loading, specimens were latched onto a couple of standard planar grips, while for compressive fatigue loading, the anti-buckling device of Fig. 1 was specifically designed. Specimens were mounted inside a rigid structure, that was meant to prevent lateral deflections.

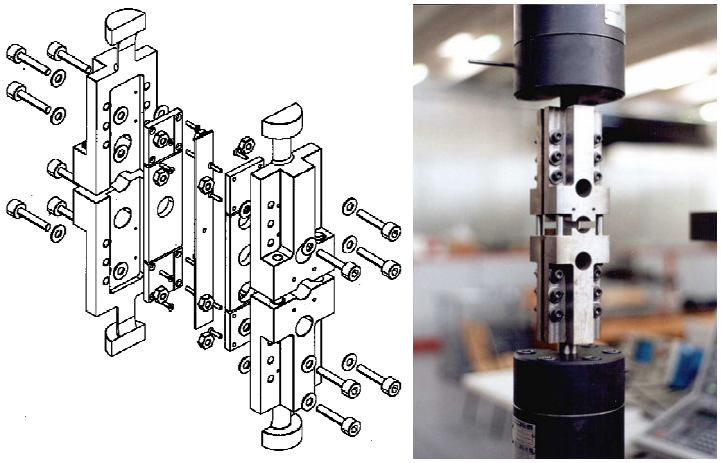

Fig.1 - anti-buckling device

Axial friction was reduced by the interposition of teflon layers and misalignments were measured by 4 connecting pins instrumented with strain gauges.
Statistical data analysis. The fatigue failure probability of specimens was modeled as a function of the applied stress (normalized with respect to the ultimate tensile strength) and the resulting life, on the basis of the two following hypotheses:
a) fatigue life, as the number of cycles N, is a Weibull distributed stochastic variable, whose failure probability density function is:

$$f(N,\alpha,\beta)=\frac{\beta}{\alpha}\left(\frac{N}{\alpha}\right)^{\beta-1}e^{-\left(\frac{N}{\alpha}\right)^{\beta}}, \quad (1)$$

where α is the characteristic life and β the shape parameter of the distribution;
b) the characteristic life α is in power relation [3] with the intensity of the stress σ :

$$\alpha=\gamma_1(\sigma)^{\gamma_2}. \quad (2)$$

Under these assumptions, the failure probability distribution expressed in Eq. 1 is a function of the applied stress, the fatigue life and three unknown parameters of the model:

$$f=f(N,\sigma;\beta,\gamma_1,\gamma_2). \quad (3)$$

The values of the parameters β, γ_1 and γ_2 can be determined by a MLE performed on the experimental data. In the logarithmic form, the likelihood function L is as follows:

$$L(\beta,\gamma_1,\gamma_2)=\sum_{i=1}^{k}L_i+\sum_{j=1}^{h}L_j, \quad (4)$$

where L_i is the i^{th} log-likelihood contribution of the k data set of failed specimens:

$$L_i(\beta,\gamma_1,\gamma_2)=\ln\left[f(N_i,\sigma_i;\beta,\gamma_1,\gamma_2)\right], \quad (5)$$

and L_j is the j^{th} log-likelihood contribution of the h censored data set of run out specimens:

$$L_j(\beta,\gamma_1,\gamma_2)=\ln\left[1-\int_0^{N_j}f(t,\sigma_j;\beta,\gamma_1,\gamma_2)dt\right]. \quad (6)$$

The optimum values of the parameters (β, γ_1, γ_2), that allow the model to provide the best interpolation of the experimental measures, are found by maximizing the log-likelihood function.

Results and Discussion

Ultimate Tensile Strength. The ultimate loads measured during quasi-static testing were divided by the neat cross sections of the specimens, in order to calculate the nominal values of the ultimate tensile stresses. The results are shown in Table 1.

Lay-up	$[0]_6$	$[0/+45/-45/90]_s$	$[0/+45/-45/90]_s$	$[0/+45/-45/90]_s$
notch	un-notched	un-notched	Φ 2 mm hole	Φ 8 mm hole
specimen width	25 mm	25 mm	40 mm	40 mm
σ_{UTS} [MPa]	1705 ± 786	546 ± 35	629 ± 45	517 ± 22

Table 1 - ultimate tensile strength of the material

Unidirectional laminates are characterized by a high spread of the tensile strength values, while the quasi-isotropic lay-up outlines a remarkable notch sensitivity and a dependency on the specimen width. In this regard, a remarkable delamination was observed at the free edges. The absolute delaminated area extension was independent of the specimen width. For this reason, the fraction of delaminated material over the nominal area was higher in the case of narrower specimens. This could explain the higher strength measured for the case of wider laminates.

Fatigue life. Fatigue testing has been performed investigating the effects of pulsating and alternating load conditions. Pulsating fatigue was applied in tensile stress only, with a load cycle shape factor $R=\sigma_{min}/\sigma_{max}$ equal to 0.1. The experimental results are plotted in the Wöhler diagrams of Fig. 2 to

Fig. 5, using circular markers. The stress amplitudes have been normalized with respect to the mean values of the ultimate tensile strength σ_{UTS} of Table 1.
Alternating fatigue was applied in both tensile and compressive stress, with a symmetric load cycle (shape factor R equal to -1). The corresponding experimental points are drawn using triangular markers. For each data set, black filled markers have been used for the case of failed specimens, while empty markers have been employed for run out specimens.

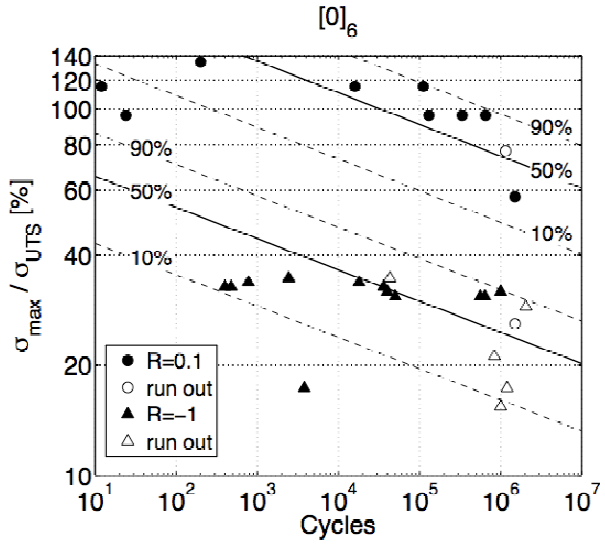

Fig. 2 - unidirectional specimen fatigue behaviour

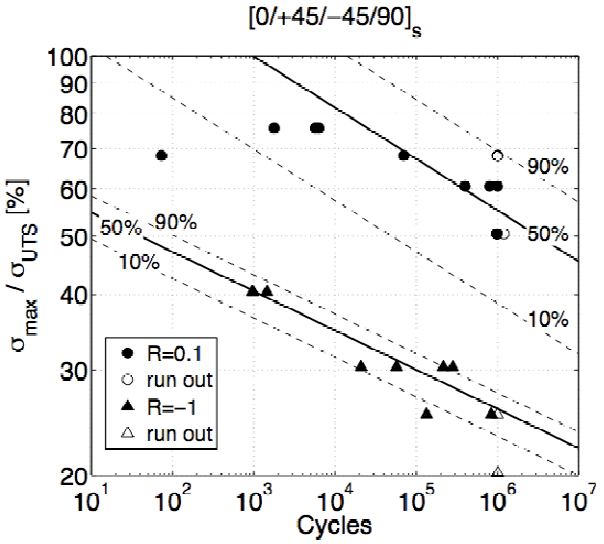

Fig. 3 - quasi-isotropic specimen fatigue behaviour

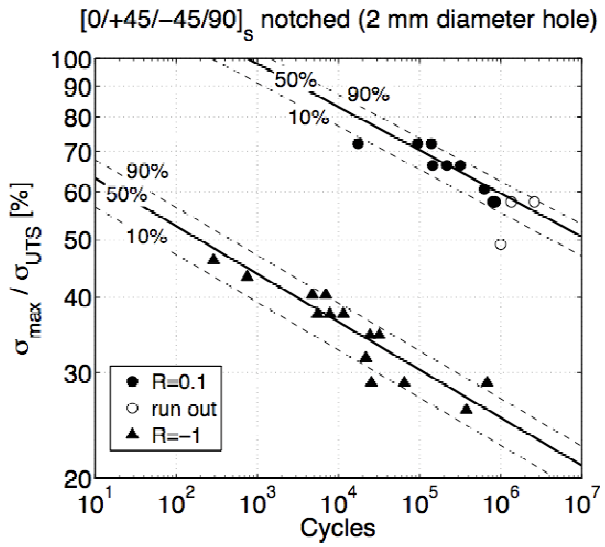

Fig. 4 - quasi-isotropic, light notched specimen fatigue behaviour

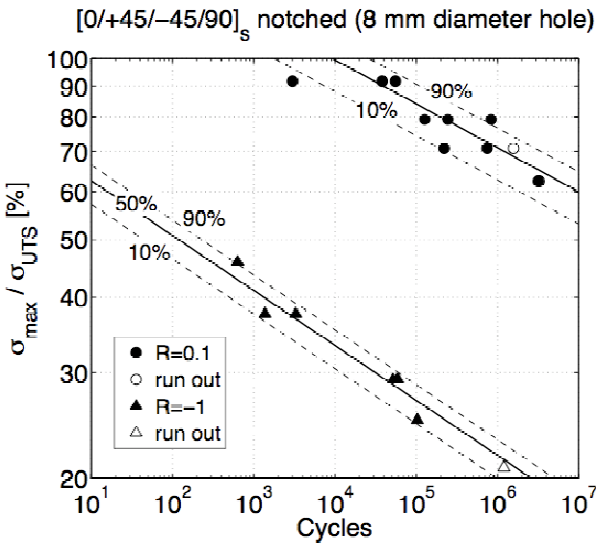

Fig. 5 - quasi-isotropic, heavy notched specimen fatigue behaviour

Fatigue curves were drawn accordingly to the Weibull MLE of the experimental data, once chosen the desired value for the failure probability of the material. In the charts presented above, three iso-failure probability levels, namely 10%, 50% and 90%, have been taken into consideration.
Fracture mechanics. Unidirectional laminate failures were fiber dominated and characterized by a high dispersion of the experimental data, by a good residual strength for run out specimens and by instantaneous fractures of the material with high energy releases. Elevated values of the fatigue endurance have been recorded even though the applied stress intensities were greater than the medium quasi-static tensile strength. This behaviour could be a consequence of the partial matrix failures that take place during the very first stage of fatigue testing, which increase the degree of freedom of fibers and allow the local redistribution of the applied load with an overall strength increase.

Compressive fatigue loadings, on the contrary, were characterized by the domination of matrix failure mechanisms and by a considerably reduced fatigue life.
Quasi-isotropic laminates showed the rapid delamination of the 90° central plies and the subsequently damage of 45° layers, which acted as a stress concentration source and propagated fracture towards the 0° sheets at the specimen surface.
Notch effect was not so clearly recognizable during fatigue testing in tensile conditions, while more remarkable effects came up with compressive loads for heavy notched specimens. Local delaminations at the inner edges of the holes were observed, and could be held responsible for micro localized buckling phenomena which have an influence on damage acceleration [4].

Conclusions

By the analysis of the fatigue diagrams and damage mechanics of the studied laminates, it is possible to draw the following conclusions about the fracture behaviour of the material:

I. The effects of the specimen geometry on damage mechanisms, such as delamination, can not be neglected for both the case of quasi-static and fatigue loading. Wider specimens have proven a higher strength.
II. During quasi-static testing, the quasi-isotropic laminates have shown a higher sensitivity towards stress concentration, as opposed to the unidirectional laminates, which were relatively unaffected by the presence of notches.
III. Notch effect is significantly reduced in fatigue loading.
IV. Compressive loads lead to a considerably reduction on fatigue life. This can be ascribed to matrix failure at the micro scale, which causes a local increase of fiber slenderness and micro-buckling damage.

References

[1] ASTM D3039-00: *Standard test method for tensile properties of polymer matrix composite materials*.

[2] ASTM D5766-95: *Standard test method for open hole tensile strength of polymer matrix composite materials*.

[3] L. Goglio, M. Rossetto: *Comparison of fatigue data using the maximum likelihood method.* Eng. Frac. Mech. Vol. 71 (2004), p.725-736

[4] H.M.S. Belmonte, S.L. Ogin, P.A. Smith: *A physically-based model for the notched strength of woven quasi-isotropic CFRP laminates.* Comp. Part A. Vol. 35 (2004), p.763-778

Key Engineering Materials Vols. 385-387 (2008) pp 245-248
© (2008) Trans Tech Publications, Switzerland
doi:10.4028/www.scientific.net/KEM.385-387.245

On the growth, the arrest and the restart of a crack during a dynamic brittle fracture experiment

David Grégoire[a], Hubert Maigre[b] and Alain Combescure[c]

Mechanics Laboratory Contacts and Structures,
LaMCoS, INSA-LYON, CNRS UMR5259,
20 Avenue Albert Einstein,
F69621 Villeurbanne Cedex, France.

[[a]david.gregoire, [b]hubert.maigre, [c]alain.combescure]@insa-lyon.fr

Keywords: Dynamic brittle fracture, Mixed-mode loading, Crack arrest and restart, X-FEM, Experiments, Kolsky Bars (SHPB), PMMA, crack localization.

Abstract. Our purpose is to propose a methodology for assessing dynamic crack propagation laws under mixed-mode loading. Dynamic brittle fracture experiments are performed on polymethylmethacrylate (PMMA) in which mode combination changes and crack arrest phases occur. Then, these experiments are numerically reproduced by using the eXtended Finite Element Method (X-FEM) in order to validate the algorithms and the criteria assumed.

Introduction

The risks due to crack propagation under dynamic loading are still difficult to estimate. Unlike quasi-static cases, where the loading and crack position can be easily established, in dynamic impact cases, loading conditions, propagation parameter variations and exact crack positions are difficult to control. The determination of relevant constitutive crack propagation laws from dynamic crack propagation experiments is thus a challenging operation. Consequently, the first step for assessing dynamic crack propagation laws is the development of numerical simulation tools. Some numerical tools are now able to represent dynamic crack growth but these numerical results have to be compared with experimental results to ensure that the numerical laws introduced are physically consistent.

In a previous work [1], crack tip position histories have been determined by standard optical tools. The test rig was a split Hopkinson pressure bar (SHPB) and the specimen geometry was chosen in order to provide direct conversion between impacting compressive waves and tensile waves in the vicinity of a machined notch. Since the material used (PMMA) was transparent, the crack tip position history was obtained by using standard optical tools (four cameras providing one picture per camera) and by carrying out the same tests, repetitively and reproducibly. Three different phases were observed: two propagation phases were separated by a crack arrest phase. Using an eXtended Finite Element Method (X-FEM), numerical simulations were performed and both the crack path and the crack position histories fitted the experimental results.

This kind of comparison allowed the validation of a dynamic crack growth criterion but only in a unique case of loading. The previous process leads to a large experiments number for obtaining different crack tip position histories corresponding to different loading rate and the loading rate influence on the transient propagation phases as arrest and restart cannot be represented accurately if several experiments are needed to obtain a crack tip position history.

Therefore the experimental setup has been improved by replacing the cameras with a Zimmer extensometer. It leads to a very accurate crack tip localization and provides the whole propagating crack tip position history for each test performed as shown in [2] in pure mode 1 conditions with several consecutive crack arrest phases.

This paper focuses on the use of the same experimental setup in order to study the influence of the loading rate on the transient propagation phases as arrest and restart in mixed-mode conditions.

Experimental setup

The test rip is a split Hopkinson Pressure Bar (SHPB or Kolsky bars) test developed by Kolsky [3] and primarily used for the measurement of a material dynamic behavior. The test specimen is made of polymethylmethacrylate (PMMA), a transparent brittle material. The bars are chosen made of nylon, a quite similar material, in order to guarantee both a good wave transmission on their interfaces with the specimen and an elastic strain gage response. Details on the experimental setup are presented in [1] and [2].
There is no standard for dynamic impact fracture tests. Therefore a simple, but distinctive, geometry designed is chosen to obtain transient propagation phases as crack arrest and restart. A rectangular specimen with a circular hole is used to provide both the direct wave conversion from compressive waves into tensile waves and the crack arrest zone. A radial initial notch is machined at the border of the hole in order to initiate the crack in mixed-mode conditions as shown Fig. 1.

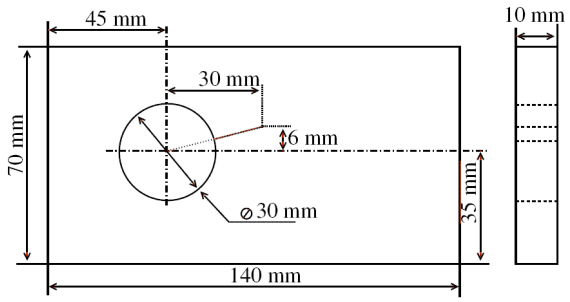

Fig 1. *Specimen geometry.*

The use of SHPB is attractive because it provides both an accurate measurement of the applied loading and the global response of the test specimen during the transient experiment. Wave dispersion and geometry effects are taken into account in the shifting of the mechanical data to the specimen-bar interfaces as in [4].
The experimental test rig includes the striker bar, the input bar, the output bar and the specimen between the bars; 2 strain gages connected to their amplifiers; 2 optical displacement sensors Zimmer 115 and Zimmer 116 with different measuring ranges (see Table 1).

Zimmer	115	116
Measurement range [mm]	100	20
Working distance [mm]	1154	41.1
Measurement width [mm]	5	1
Resolution [mm]	0.01	0.002
Uncertainty [mm]	±0.2	±0.04
Maximum tracking velocity [m/s]	8350	1670

Table 1. *Characteristics of the optical displacement sensors.*

Since the signal delivered by the extensometer takes into account the specimen solid body displacement in addition to the crack tip displacement, a correction is processed in order to obtain the real crack growth. Four different tests are performed at different impact velocities. The experimental conditions are described in Table 2 and the crack tip positions histories for each Zimmer extensometers in Fig. 2.

Experiment	Test 1	Test 2	Test 3	Test 4
Striker velocity [m/s]	8.35	10.3	11.2	12.6

Table 2. *Experimental conditions.*

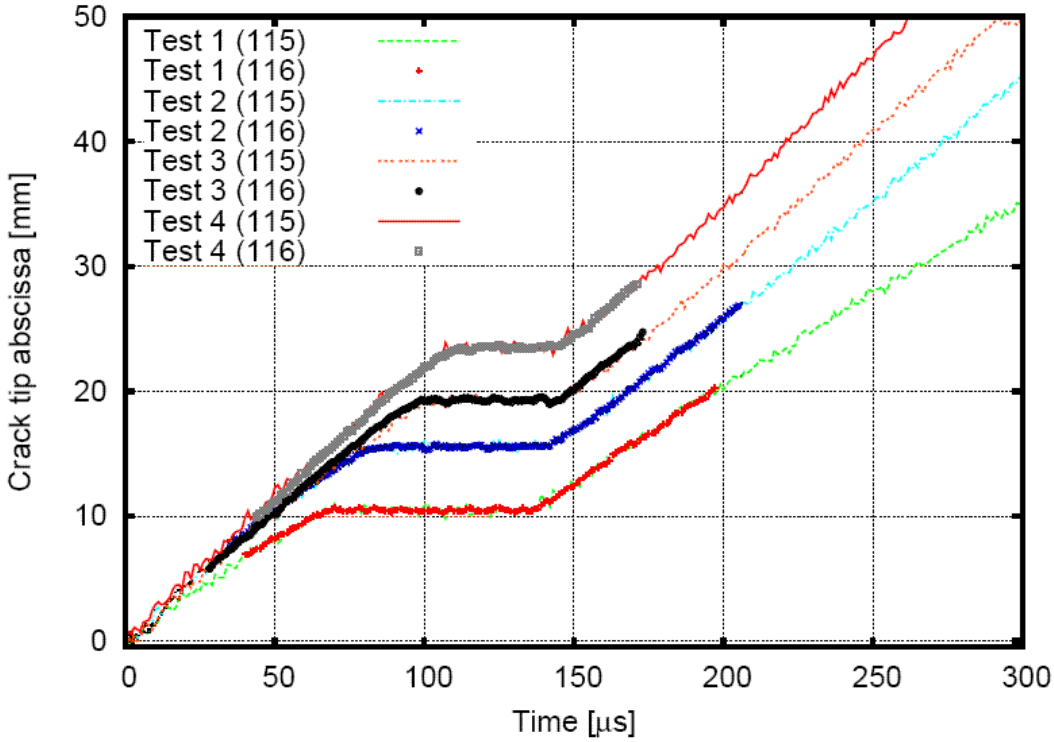

Fig 2. *Experimental crack tip position histories for the four tests (Zimmer 115 and Zimmer 116).*

Fig. 2 reveals that this method based on optical displacement sensor measurement provides an accurate crack tip localization. For each test, the signals delivered by each extensometer agree and the highly transient propagation phases such as arrest and restart are easily distinguishable. Thus, the influence of the loading rate on the crack arrest and restart phases can be noticed. The lower is the striker velocity, the lower is the horizontal crack tip velocity, the earlier occurs the crack arrest phase and the longer lasts the crack arrest phase.

Numerical comparison

The eXtended Finite Element Method is chosen for the simulation because the cracks are not described explicitly by the mesh. It allows the mixed-mode dynamic propagation laws validation because the crack path is considered *a priori* unknown. This method consists inusing an enrichment to the classical finite element approximation in order to capture the discontinuity and the singularity of the strain fiels at the crack tip. It was first developed for quasi-static analysis in [5] and then used for dynamic crack propagation in [1] in the light of [6].

The numerical simulation are carried out using the input velocity collected from the experiments as a boundary condition at the input bar interface and an impedance condition is used to model the contact between the output bar and the specimen.

Even if the PMMA is known to be viscoelastic, a linear elastic behavior is assumed with a dynamic elastic modulus fitted with the velocity of the elastic waves measured during the experiment.

An example of comparison between experimental and numerical results is presented in Fig. 3 in order to show how this numerical tool can be used to validate crack propagation laws. The dynamic crack propagation laws assumed are quite simple, chosen according to the global macroscopic concept of stress intensity factors [7] extended to elastodynamics within the framework of [8,9]. The fracture phenomenon is assumed to be governed by the intensity of the hoop stress near the crack tip as in [10] and a dynamic crack growth criterion is chosen to take the crack growth process into account as in [11] (the formulation can be found in [1]).

On the Fig. 3, a good matching of the numerical and experimental results is obtained but the criteria have to be involved in order to well-represent the loading rate dependencies noticed in Fig. 2.

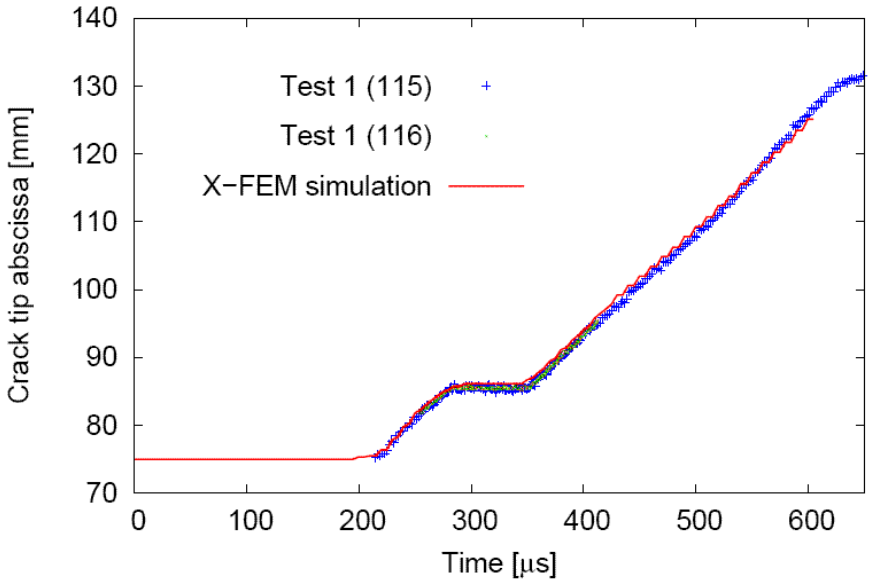

Fig 3. *Comparison of crack tip position histories for the test 1.*

Conclusion

This work shows that a good combination of well-controlled experiments and refined X-FEM simulations enables one to explain the history of brittle dynamic crack propagation and arrest using simple ingredients. The new experimental setup presented allows the assessment and the validation of new dynamic crack growth criteria by studying the highly transient propagation phases such as crack growth, crack arrest and crack restart.

References

[1] D. Grégoire, H. Maigre, J. Réthoré, A. Combescure: Int. J. Solids Struct., 44, 6517-6534, 2007.

[2] D. Grégoire, H. Maigre, F. Morestin : Eur. J. Comput. Mech., accepted, 2008.

[3] H. Kolsky: P. Phys. Soc., B62, 676-700, 1949.

[4] H. Zhao, G. Gary: J. Mech. Phys. Solids, 43(8), 1335-1348, 1995.

[5] N. Moës, J. Dolbow, T. Belytschko: Int. J. Numer. Meth. Eng., 46, 131-150, 1999.

[6] J. Réthoré, A. Gravouil, A. Combescure: Int. J. Numer. Meth. Eng., 63, 631-659, 2005.

[7] G. Irwin: J. Appl. Mech., 24(3), 361-364.

[8] H. D. Bui: Mécanique de la rupture fragile, Masson, Paris, 1978.

[9] L. B. Freund: Dynamic Fracture Mechanics, Cambridge University Press, Cambridge, 1990.

[10] H. Maigre, D. Rittel: Int. J. Solids Struct., 30(23), 3233-3244, 1993.

[11] M. Kanninen, C. H. Popelar: Advanced Fracture Mechanics, Oxford University Press, 1985.

Key Engineering Materials Vols. 385-387 (2008) pp 249-252
© (2008) Trans Tech Publications, Switzerland
doi:10.4028/www.scientific.net/KEM.385-387.249

Optimum Dimensions of Thin Walled Tube on the Mechanical Performance of Super Stud Bolt

Yang Xiao*, Masahiro Kuhara*,Nao-Aki Noda*,
Kinjiro Saito**, Masato Nagawa***,
Atsushi Yumoto****,Ayako Ogasawara****

*Department of Mechanical Engineering, Kyushu Institute of Technology,
1-1 Sensui-cho, Tobata-ku, Kitakyushui, Fukuoka, 804-8550 Japan
**Nittetsu Yawata Engineering Co., Ltd.,
2-2 Tobihata-cho, Tobata-ku, Kitakyushui, Fukuoka, 804-0001 Japan
***Daiki Kogyo Co., Ltd.
11-16 Hama-cho, moji-ku, Kitakyushui, Fukuoka, 801-0856 Japan
****Nittetsu Plant Designing Co., Ltd.,
46-59 Oazanakahara, Tobata-ku, Kitakyushui, Fukuoka, 804-0002 Japan

young@student.dlut.edu.cn, f344116m@tobata.isc.kyutech.ac.jp, noda@mech.kyutech.ac.jp,
A-Yumoto@npdx.co.jp, A-Ogasawara@npdx.co.jp

Keywords: Plastic working, Machine element, Press working, Anti-loosening, Thin walled tube, Prevailing torque

Abstract. The bolts and nuts are widely used in various fields as important joining elements with long history. However, loosening induced by the vibration and external loads is still a big problem. And the loosening sometimes causes very serious accident without notice. This paper deals with a special stud bolt named “Super Stud Bolt (SSB)” which can prevent loosening effectively. There is a thin walled tube between the upper and lower threads, which can be deformed along the axial direction so that the phase difference is produced and SSB is developed. This phase difference induces the contrary force on the surfaces of the upper and lower threads, which brings out the anti-loosening performance. In this study, the processing and fastening-loosening courses are simulated with the finite element method. And the anti-loosening performance is analyzed and realized. In addition, the anti-loosening performances under various phase differences are compared and finally best dimensions for SSB are examined.

Introduction

Threaded connections play a critical role in engineering with long history. Because of their relatively low cost and easy disassembly for maintenance, they are widely used for mechanical products and structures in modern times. However, self-loosening, which is one of the most frequent failure modes for threaded connections, brings out the failure of engineering products and several serious accidents. Therefore, in recent years much attention has been paid to the research on the anti-loosening. Many experiments have been performed in order to find out the reasons and the influence factors of self-loosening. Moreover, Finite Element Method (FEM) is widely used on these types of research (1, 2) with the recent development of the computer. Based on these, all kinds of anti-loosening nuts are invented[3-4]. And some stud bolts are also produced for anti-loosening, for example, shaft end plates (wire type) and bent plates shown in Fig. 1. However, these kinds of anti-loosening bolt can not be used repeatly, dismentling is difficulty and component is complex.

In order to make up these fault, the super stud bolt is developed as shown in Fig. 2 (a). This kind bolt can prevent loosening easily. In this anti-loosening mechanism, the thin walled tube between the upper threads and the lower threads plays an important role as shown in Fig.2 (b). The thin walled tube can be deformed along the axis, and the phase difference of lower and upper threads is designed in the course of processing. Accordingly, the deformation must be produced in order that

the threads meet each other in the course of fastening. Then, the thread contact force shown in Fig. 2 (b) comes out due to this deformation. This force is called the griping force, by which the prevailing torque is produced, so that the self-loosening can be prevented. This is the working principle of the Super Stud Bold (SSB).

Since the thin walled tube is the heart of anti-loosening mechanism, the best original dimensions will be discussed in this study. Moreover, in this paper the M16 SSB is taken as a sample, and the capability of the anti-loosening will be investigated using FEM. Both courses of processing and fastening will be simulated, and the relation between axial force and displacement will be researched. Incording to the results, the best original dimensions will be decided.

Analysis model and method

Analysis model. In Fig.3 (a), the SLN is simplified into an axi-symmetric model to be studied. Here the bottom is fixed, while the forced displacement z (mm) is placed on the top of the model by the rigid body. In this study, the thin walled tube is mainly researched with the finite element method as shown in Fig.3 (b).

The material of the SSB is SC435 (JIS), whose stress-strain relation in Fig.4 is used in the elastic-plastic finite element analysis of the thin walled tube. Here, Young's modulus is 210GPa, Poison's ratio is 0.3, and the yielding stress is 800MPa.

Analysis model. With the axi-symmetric FE model, both courses of processing and fastening-loosening of SSB are simulated. The processing course is shown in Fig. 5, and the course of fastening-loosening is shown in Fig.6. In the Fig. 5 (a), the length L of thin walled tube is produced on the top of normal bolt by machining. At this time, the phase difference of lower and upper threads is 0. As shown in Fig. 5 (b), the thin walled tube is pressed by (p-α) mm. Here, α (mm) is the nominal phase difference of lower and upper threads, which is smaller than the pitch of nut (p=2mm). When the press is removed, spring back happens as shown in Fig. 5 (c). Here, L_1=L-(p-α) and L_2=L-(p-α)+b, so that the real phase difference of lower and upper threads α_2=α+b=p-(L-L_2) appears. Figure 6 (d) is the same as Fig. 5 (c), and Fig. 6 (e) shows the phase difference of lower and upper threads becomes 0 because the threads of the bolt and nut can meet each other while the nut is fastened. In Fig. 6 (f), spring back b′ happens after loosening. In order to simulate both courses which include large plastic strains, elastic-plastic large deformation theory will be applied in this analysis.

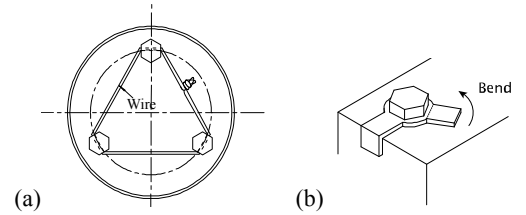

Fig.1 Anti-Loosening stud bolts previously proposed

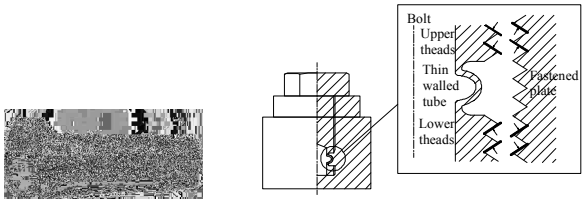

(a) Photo (b) Anti-loosening theory

Fig.2 Super stud bolt recently proposed

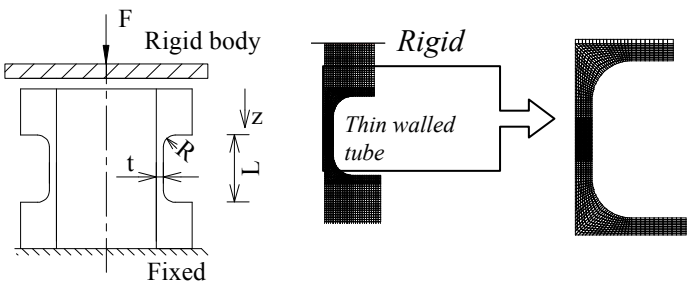

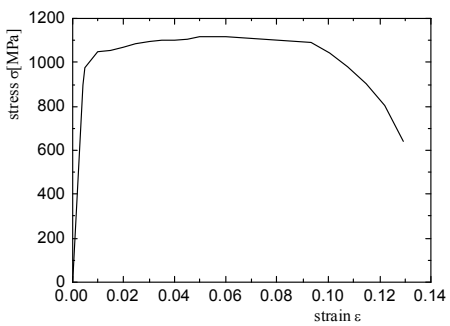

Fig.3 (a) Analysis model (b) Finite element model (c) Detail of thin walled tube Fig.4 Relation between stress and strain for SCM435

Analysis results

The anti-loosening capability A standard model M16 bolt is employed, and the dimension of the thin walled tube is shown in Fig.3(a), here, L=5.8mm, R=1mm and t=0.6mm.

In order to design the phase difference of lower and upper threads (α=0.1mm), the relation between the axial force and the displacement is shown in Fig.7. The course of processing is indicated as the line (a) → (b) →(c); then, the final displacement 1.84mm provides the real phase difference of lower and upper threads 0.16mm. The line from (d) to (e) shows the course of fastening, and the line from (e) to (f) shows the course of loosening. In those loading and unloading courses, the plastic deformation occurs and the permanent deformation 1.94-1.84=0.1mm has been added. Then, only small phase difference of lower and upper threads (2.00-1.94=0.06mm) remains. However, in consecutive fastening-loosening courses, the relation between the axial force and the displacement moves to the line from (f) to (e). Because the deformation in this course is totally elastic, plastic deformation does not occur and the phase difference of lower and upper threads 0.06mm will not be changed anymore. Moreover, the axial force 14.51kN is also unchanging, and therefore, the prevailing torque is the same in the consecutive fastening-loosening courses.

From Fig. 7, it can be shown when the threads meet each other (Fig. 7(e)), the axial force is 14.51kN. Accordingly, the prevailing torque may be evaluated as Ts=20.64 N·m by Eq.(1)[5].

$$T = \frac{d_2}{2} F \tan \rho' + \frac{d_2}{2} F \tan \beta + \frac{d_w}{2} \mu_w F \qquad (1)$$

Where F is axial force,
d is the radius of screw, and approximately
$d_2 = 0.92\, d$, $d_w = 1.3\, d_2$,
ρ' is friction angle between the threads, here $\tan(\rho') = 0.15$
β is lead angle of threads, 2.4796 (deg)
μ_w is average friction factor on the interface between the head of bolt and the clamp.

Influence of the dimension of the thin walled tube on the anti-loosening capability The thin walled tube is the heart of SSB because the dimension has large influence on the anti-loosening capability, stress distribution and spring factor. In this study, the inference of the dimensions *R, L, t* in Fig. 3 will be investigated, and best dimensions will be examined.

(a) Influence of curvature radius *R* In order to improve stress distribution at both ends of thin walled tube, the effect of curvature radius R in Fig. 3(a) is studied. As shown in Fig. 3(a), L and t are fixed as L=6.0mm, t=0.65mm, and R is changed. When R is 0.0, 0.5, 1.0, the stress distributions of the thin walled tube in Fig. 5 (b) are shown in Fig.9 (a), (b), (c), respectively.

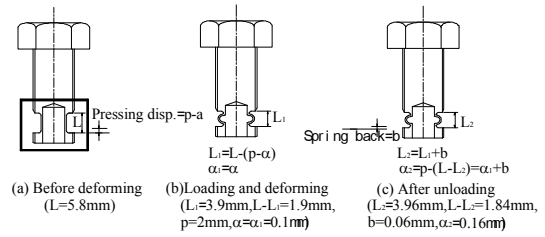

Fig.5 Dimension change in the course of processing
[( ): Values in Fig. 7]

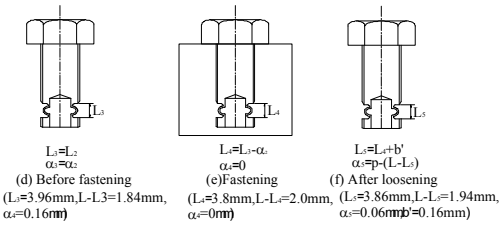

Fig.6 Dimension change in the course of fastening
[( ): Values in Fig. 7]

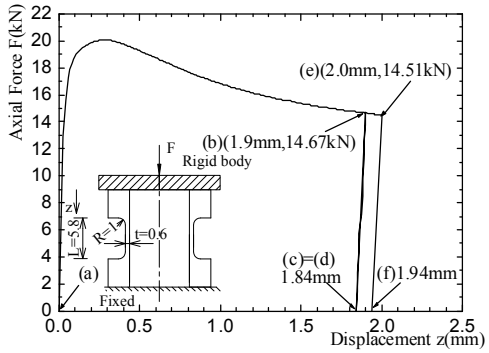

(a) → (c) Processing
(d) → (e) Fastening
(e) → (f) Loosening
(f) → (e) Fastening from second time
(e) → (f) Loosening from second time

Fig.8 Relation between axial force and displacement (L=5.8mm,R=1mm,t=0.6mm)

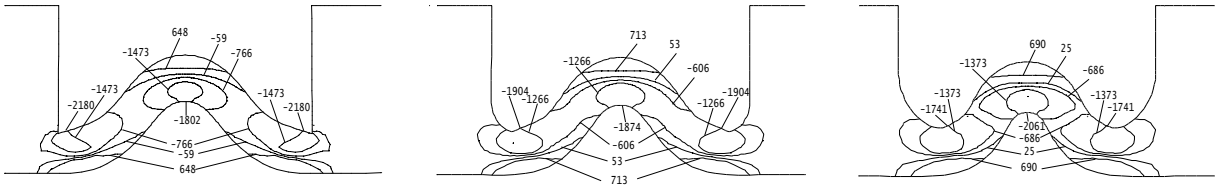

(a) R=0mm (b)R=0.5mm (c) R=1.0mm

Fig.9 Stress distribution σ_z (MPa) for different curvature R (L=5.8mm, t=0.6mm, α_1=0.1mm)

Table.1 Effect of initial length of thin tube L
(L-L_1=1.9mm in Fig.5, R=1.0mm, t=0.6mm in Fig.3(a))

Length of thin walled tube L (mm)	Spring factor k ($\times 10^8$N/m)	Spring back (Elastic deformation) b(mm)	Prevailing torque Ts(N-m)
4.8	4.36	0.04	25.08
5	3.88	0.04	23.86
5.8	2.63	0.06	20.64
6	2.42	0.06	19.83
6.8	1.89	0.07	17.73

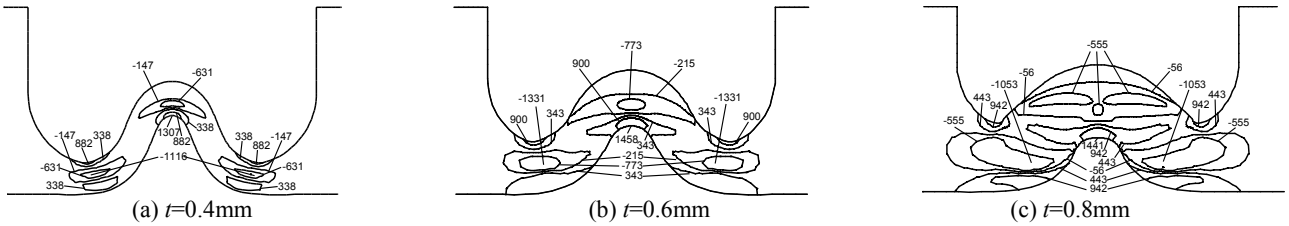

(a) t=0.4mm (b) t=0.6mm (c) t=0.8mm

Fig.10 Distribution of σ_z(MPa) (R=1.0mm, L=5.8mm)

From Fig.9, while R is smaller, the stress concentration is more serious at both ends of the thin walled tube. Conversely, while R is larger, at the center of the thin walled tube the stress become larger. The stress distribution is the most desirable in Fig. 9 (b) while R is 0.5mm.

(b) Influence of Length of Thin Walled Tube *L* To investigate the effect of length L, dimensions R and t are fixed as R=0.5mm, t=0.65mm, and L is changed (see Fig. 3(a)). When L is 5.0, 6.0, 8.0, the results are shown in Table 1.

From Table 1, while L is longer, the spring factor becomes smaller, and spring back b in Fig. 5 becomes larger. Here, spring back b may be regarded as an amount of elastic deformation. It should be noted that this elastic deformation is much smaller than the phase difference of lower and upper threads (0.1~0.15mm). In other words, large plastic deformation always exists in the course of first fastening-loosening whenever L is 5, 6 or 8mm. It can be seen that the prevailing torque becomes smaller while L is longer in Table 1. That is to say, the anti-loosening capability becomes lower as L is longer. In addition, the cost of processing is higher when L becomes longer. According to the above, the length of thin walled tube should be designed as short as possible if the thin walled tube can be deformed as shown in Fig. 3(a). It may be concluded that L=5mm is the best.

(c) Influence of Thickness of Thin Walled Tube *t* In order to improve both processing and fastening courses, the influence of the thickness of the thin walled tube t is studied. While the L and R are fixed, thickness t is changed as 0.4, 0.6, and 0.8mm. The stress distributions σ_z are indicated in Fig. 10 (a), (b) and (c).From Fig.10, it is seen that the stress distribution becomes complicated with increasing the thickness t. The stress distribution of t=0.4mm is desirable, and therefore, it may be concluded that the best thickness t is 0.4mm.

References

[1] Izumi, S., Yokoyama, T., Iwasaki, A., Sakai, S., Three-dimensional finite element analysis of tightening and loosening mechanism of threaded fastener, Engineering Failure Analysis 12(2005), pp.604-615.

[2] Pai, N.G., Hess, D.P., Three-dimensional finite element analysis of thread fastener loosening due to dynamic shear load, Eng. Failure Anal. Vol. 9, (2002), pp.383-402.

[3] Daiki Kogyo KK., 2004, Super Slit Nut, Japan Patent (in Japanese) 2004-218674.

[4] Hard Lock Kogyo KK., 2002, hard lock nut, Japan Patent (in Japanese) 2002-195236.

[5] Kaneta, M., Yamamoto, U., Foundational Mechanical Design Engineering, Rikogakusha, (2003), pp.58-59, (in Japanese)

Key Engineering Materials Vols. 385-387 (2008) pp 253-256
© (2008) Trans Tech Publications, Switzerland
doi:10.4028/www.scientific.net/KEM.385-387.253

Postbuckling analysis of laminate with delamination based on the improved damage model of 2-D

Yang Gang[a], Zhang Aifeng[b], Wang Haibin[c], Niu Peng[d]

Dalian Maritime University, Dalian, China

[a]yanggang@newmail.dlmu.edu.cn, [b]hr98@21cn.com, [c]haibin_81@yahoo.com.cn, [d]np777@mail2.lut.cn

Key words: Delamination, modeling, postbuckling, finite element analysis, energy release rate, laminate theory.

Abstract. The paper presents the compatibility relation of displacement, strain energy expression, and the formulations of Finite Element Method in the transitional region for the improved damage model of 2-D delamination[1]. The postbuckling behaviors of composite laminated plate with a circular delamination are analyzed. Results show that the model mainly improves computational results of energy release rates in the delamination front. The model should only be used in a narrow region near the crack-tip and the normal Mindlin model in other regions. It leads to little increase in the amount of computation, but significant improvement in the results.

Introduction

The post-buckling and delamination of laminated composite plates/shells are an area of active research in the mechanics of composite materials. The structural failure of laminated plates/shells is often related to their post-buckling behavior. Particularly because that the laminated composites can easily fall apart from each other, the composites will further buckle and the delamination will further propagate with the effect of planar loads in between, which will cause the laminated structure lose its strength and rigid promptly, and therefore lose its carrying capacity for external loads. Therefore, delamination has become the main hazard of composite materials. In recent years, the research on the mechanisms of post-buckling and delamination, the interaction between the two, and the behavior of delamination growth has gained attention[2]. But because of the complexity, many problems remain to be solved.

The modeling of delamination has always remained the focus in the studies of delamination, as the assumptions adopted will directly affect the application of the analytical results based on it. In the past, the Mindlin model was usually adopted for the study of delamination, but quasi-three-dimensional analyses show that this assumption is rather unrealistic[3], with overly strong constraint on the deformation near the crack tip. Based on an improved damage model[1], the present paper details the condition for displacement transformation in the transient region $\Omega_{0'}$, the formulae derives the finite element matrix for laminated plates, taking into account the shear effect. Analyses were carried out on the post-buckling behavior of plate with circular delamination, showing some interesting results. In particular, it has been proven that the modified damage model has significant influence on the strain field, displacement field and the energy release rate in the delamination front.

Basic equations in the transient region

The transformation of displacement in the transient region $\Omega_{0'}$. In the delamination front region $\Omega_{0'}$, the normal $S^{(1)}S^{(2)}$ is a straight line before deformation. When buckling occurs, the normal $S^{(1)}S^{(2)}$ will become a broken line $S^{(1)}A^{(1)}A^{*}A^{(0)}A^{(2)}S^{(2)}$, as shown in Fig. 1.

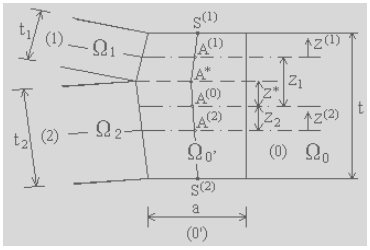

Fig. 1 The delamination front region of the improved damage model

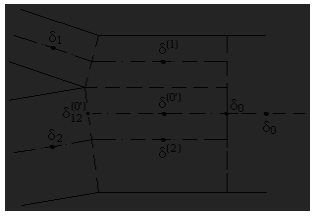

Fig. 2 the displacement fields of delamination front region

Let $\delta^{(0)}, \delta^{(1)}$ and $\delta^{(2)}$ represent the vectors at $A^{(0)}, A^{(1)}, A^{(2)}$ respectively.

$$\begin{aligned} \delta^{(0)} &= \left[u^{(0)}, v^{(0)}, w, w_{,x}\ w_{,y}, \gamma_{xz}^{(1)}, \gamma_{yz}^{(1)}, \gamma_{xz}^{(2)}, \gamma_{yz}^{(2)}\right]^T \\ \delta^{(i)} &= \left[u^{(i)}, v^{(i)}, w, w_{,x}\ w_{,y}, \gamma_{xz}^{(i)}, \gamma_{yz}^{(i)}\right]^T \quad i = 1,2 \end{aligned} \tag{1}$$

Considering the compatibility conditions of displacement at A^*, we obtain the following relation defines their transformation

$$\delta^{(i)} = R_{i0}\,\delta^{(0)} \tag{2}$$

where

$$R_{i0} = \begin{bmatrix} 1 & 0 & 0 & T_1 & 0 & T_2 & 0 & T_3 & 0 \\ 0 & 1 & 0 & 0 & T_1 & 0 & T_2 & 0 & T_3 \\ 0 & 0 & 1 & 0 & 0 & 0 & 0 & 0 & 0 \\ 0 & 0 & 0 & 1 & 0 & 0 & 0 & 0 & 0 \\ 0 & 0 & 0 & 0 & 1 & 0 & 0 & 0 & 0 \\ 0 & 0 & 0 & 0 & 0 & 2-i & 0 & i-1 & 0 \\ 0 & 0 & 0 & 0 & 0 & 0 & 2-i & 0 & i-1 \end{bmatrix} \tag{3}$$

$T_1 = \frac{1}{2}(-1)^i (t - t_i)$, $T_2 = (2-i)\frac{t_1}{2}$, $T_3 = \frac{1}{2}(-1)^{(i-1)}\left[t - (3-i)t_i\right]$. t, t_1 and t_2 are the thickness of the plate (0), (1) and (2), respectively.

The strain energy in the transient region $\Omega_{0'}$. The strain energy in the plate $0'$ may be expressed as

$$U = U^{(1)} + U^{(2)} + U^s \tag{4}$$

in which $U^{(1)}$ and $U^{(2)}$ are, respectively, the tensile and bending strain energy in the region (1) and (2).

$$U^{(i)} = \frac{1}{2}\int_A (N^{\alpha\beta(i)}\varepsilon_{\alpha\beta}^{(i)} + M^{\alpha\beta(i)}\kappa_{\alpha\beta}^{(i)})dA \quad i = 1,2 \tag{5}$$

Clearly, the tensile and bending strain energy, as well as the relevant finite element stiffness matrices in the region $\Omega_{0'}$ may be calculated in a similar fashion as that in the regions Ω_1 and Ω_2. However, the shear strain energy U^s and the corresponding stiffness matrix must be computed over the whole thickness of the plate. In other words, except for the transverse shear, the other aspects may be treated by dividing $\Omega_{0'}$ into two Mindlin plate (1) and (2), and the relationship between them are given by Equation. (2).

The finite element formulation for the improved damage model. The delaminated plate may be divided into four regions $\Omega_1, \Omega_2, \Omega_0$ and $\Omega_{0'}$, as shown in Fig. 1. The degrees of freedom at each

node on the elements in Ω_1, Ω_2 and Ω_0 are seven. $\Omega_{0'}$ is the non-delaminated region in adjacent to the delamination front, and is divided into two layers $\Omega^{(1)}$ and $\Omega^{(2)}$, corresponding to the extended regions of Ω_1 and Ω_2 in $\Omega_{0'}$, respectively. $\Omega^{(1)}$ and $\Omega^{(2)}$ may be discretized to compute all the stiffness matrices other than the shear stiffness matrix $\mathbf{K}^h$, which must be calculated over the total thickness of the plate in region $\Omega_{0'}$.

At the boundary between the two regions, the following transformation equations exist for the displacement fields, as shown in Fig. 2,

$$\begin{aligned}
&\delta^{(i)} = R_{i0}\,\delta^{(0')} \quad \text{between } \Omega^{(i)} \text{ and } \Omega_{0'} \\
&\delta_i = T_{i0'}\delta_{12}^{0'} \quad \text{between } \Omega_i \text{ and } \Omega_{0'} \text{ and } i = 1,2 \\
&\delta^{(0')} = T_{0'}\delta_{12}^{0'} \quad \text{between } \Omega_{0'} \text{ and } \Omega_i \\
&\delta^{(0')} = T_{0'0}\delta_0 \quad \text{between } \Omega_{0'} \text{ and } \Omega_0
\end{aligned} \tag{6}$$

where

$$\begin{aligned}
&\delta_i^T = \left[u_i, v_i, w_i, w_{,xi}, w_{,yi}, \gamma_{xzi}, \gamma_{yzi}\right] \quad i = 0,1,2 \\
&\delta^{(i)T} = \left[u^{(i)}, v^{(i)}, w^{(i)}, w_{,x}^{(i)}, w_{,y}^{(i)}, \gamma_{xz}^{(i)}, \gamma_{yz}^{(i)}\right] \quad i = 1,2 \\
&\delta^{(0')T} = \left[u^{(0)}, v^{(0)}, w^{(0)}, w_{,x}^{(0)}, w_{,y}^{(0)}, \gamma_{xz}^{(1)}, \gamma_{yz}^{(1)}, \gamma_{xz}^{(2)}, \gamma_{yz}^{(2)}\right] \\
&\delta_{12}^{(0')T} = \left[u^{(0)}, v^{(0)}, w^{(0)}, w_{,x}^{(0)}, w_{,y}^{(0)}, \gamma_{xz}^{(1)}, \gamma_{yz}^{(1)}, \gamma_{xz}^{(2)}, \gamma_{yz}^{(2)}, \gamma_{xz1}, \gamma_{yz1}, \gamma_{xz2}, \gamma_{yz2}\right]
\end{aligned} \tag{7}$$

$$T_{i0'} = \begin{bmatrix}
1 & 0 & 0 & T_1 & 0 & T_2 & 0 & T_3 & 0 & 0 & 0 & 0 & 0 \\
0 & 1 & 0 & 0 & T_1 & 0 & T_2 & 0 & T_3 & 0 & 0 & 0 & 0 \\
0 & 0 & 1 & 0 & 0 & 0 & 0 & 0 & 0 & 0 & 0 & 0 & 0 \\
0 & 0 & 0 & 1 & 0 & i-2 & 0 & 1-i & 0 & 2-i & 0 & i-1 & 0 \\
0 & 0 & 0 & 0 & 1 & 0 & i-2 & 0 & 1-i & 0 & 2-i & 0 & i-1 \\
0 & 0 & 0 & 0 & 0 & 0 & 0 & 0 & 0 & 2-i & 0 & i-1 & 0 \\
0 & 0 & 0 & 0 & 0 & 0 & 0 & 0 & 0 & 0 & 2-i & 0 & i-1
\end{bmatrix} \tag{8a}$$

$$T_{0'} = \begin{bmatrix} [I] & [0] \\ (9\times 9) & (9\times 4) \end{bmatrix}, \quad T_{0'0} = \begin{bmatrix}
[I]_{7\times 7} & & & & & & \\
0 & 0 & 0 & 0 & 0 & 1 & 0 \\
0 & 0 & 0 & 0 & 0 & 0 & 1
\end{bmatrix} \tag{8b}$$

and I is the unit matrix.

These transformations and the displacement transformation can both be applied to the element matrices.

The shear stiffness matrix $\mathbf{K}^h$. The shear strain energy of an element may be written in the following format,

$$U^s = \frac{1}{2}\sum_A \{\gamma\}^T [\mathbf{H}]\{\gamma\} dA = \frac{1}{2}\{\mathbf{q}^s\}^T [\mathbf{K}^h]\{\mathbf{q}^s\} \tag{9}$$

where

$$\mathbf{K}^h = \int_A \mathbf{L}^T \mathbf{H} \mathbf{L} dA \tag{10}$$

with $\mathbf{H}$ denoting the shear stiffness matrix[1], $\mathbf{L}$ is the shape function[4], and A the area of the element.

Numerical results and discussion

Square laminate subjected to uniaxial compression with circular delamination. The applied load is $p = 1KN/mm$, and the dimension of the specimen is 100×100 mm. The whole plate consists of eight layers $(0°/90°/0°/90°)_s$. The thickness of the plate 8×0.5mm, with all boundaries are clamped. The delamination is located between the first and the second sublaminates with a diameter of $a = 15mm$. The material is graphite/epoxy, with Young's modulus and Poisson's ratios as follows, $E_1 = 134GPa$, $E_2 = 10.2GPa$, $\gamma_{12} = 0.3$, $G_{12} = G_{13} = 5.52GPa$, G_{23}= 3.43 GPa.

Figs. 3 and 4 plot the load-deflection curve $p - w$ and the energy release rate curve $G - s$. Here, we take layers 1 to 4 as the transition region in the modified damage model, as shown in Fig. 5, and four groups of curves (13-1, 13-2, 13-3, 13-4) are obtained from the analysis.

It can be seen that the modified model has little effect on the load-deflection results, but its influence on the energy release rate at the boundary of delamination, which is the Main parameter governing the propagation of delamination, is significant. Since the model relaxes the stiffness at the boundary of delamination, reduction of the energy release rate is expected. The negative value in the figure was mainly caused by neglecting the contact problem at the boundary of delamination.

It can be seen from the four groups of curves shown in Figs. 3 and 4 that if the transient region takes one layer, the solution is close to that of three-plate model[5], and if it takes 2 to 4 layers, there is very little difference between the solutions and they are very close to the result of ANSYS(3D). Therefore, two layers of elements (approximately 2-3 times thickness of plate) would be sufficient for the transient region to obtain a reasonable solution.

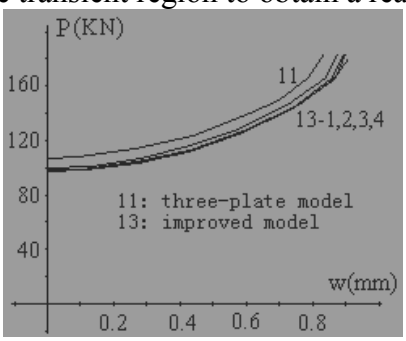

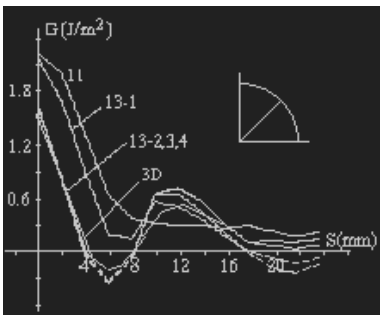

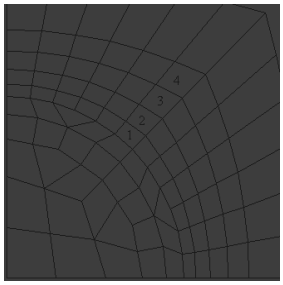

Fig. 3 load to center deflection *Fig. 4 energy release rate along delamination edge* *Fig. 5 mesh of transition region*

Summary

The improved 2D delaminated damage model gives a more realistic representation of the displacement field near the crack-tip. Numerical results show that the model mainly improves computational results of energy release rates over the normal Mindlin model. The modified model should only be used in a narrow region near the crack-tip and the normal Mindlin model should be used in other regions. This leads to little increase in the amount of computation, but significant improvement in the results.

References

[1] Yang Gang, Zhang Aifeng, Hu Weiping, Huang Baozong: Key Engineering Materials Vol. 324 (2006), p. 439
[2] Hwang, Shun-Fa, Huang, Shu-Mei: Composite Structures Vol. 68 (2005), p. 157
[3] Wang xinhong: North-east university Master' paper (1998)
[4] Huang B Z, Shenoy V B, Atlury S N: Comput. Mech. Vol. 13 (1994), p. 295
[5] B. Cochelin, M. Potier-Ferry: Computer Methods in Applied Mechanics and Engineering Vol. 89 (1991), p. 361

Key Engineering Materials Vols. 385-387 (2008) pp 257-260
© (2008) Trans Tech Publications, Switzerland
doi:10.4028/www.scientific.net/KEM.385-387.257

Reliability Analysis of Structure System Considering Failure Modes of Strength, Fatigue and Buckling

An Wei-guang[1,a],An Hai[2,a], Zhang Yong-yi[3,a]

[1,2,3]School of civil engineering, Harbin Engineering University, Harbin 150001,china

[a]anweiguang@hrbeu.edu.cn

Keywords: buckling failure, residual resistance, section modulus, the reliability calculating of system overall instability

Abstract. There could be multi-failure modes in the course of working of the structure system including slender bar members. For example, strength failure, fatigue failure and buckling failure, especially sudden buckling failure would bring large disaster to structure. In this paper, according to Fatigue and Damage Mechanics theory, safe margin expression of the different failure mode of structure (static strength, fatigue and buckling) is given firstly, then by analyzing different failure mode of structural element under static and fatigue loads, and failure mode of the calculating element is confirmed by comparing the failure probability value of different failure mode. In the course of searching for significant failure paths, not only is failure mode that stiffness matrix of structure is zero considered, but also buckling failure mode of compressed residual structure is considered too, so that failure analysis is more reasonable. In the end, the reliability calculating method of the structural system is given, and the validity of the method proposed in this paper is explained combining an example.

Introduction

For structures bearing static loads and fatigue loads simultaneously, especially compressed structures including slender bar members, there could be multi-failure modes in the course of working, for example, static strength failure, fatigue failure and buckling failure and so on. It is very dangerous for structure system because of suddenness of buckling failure, the impact of structural element buckling and structural integrity buckling on structure failure should be considered fully. So, multi-failure modes including static strength failure, fatigue failure and buckling failure should be considered simultaneously in structural reliability analysis according with actual engineering design.

Safe margins of static strength failure, fatigue failure and buckling failure of structural system

Safe margins of static strength failure. For the structure bearing static loads and fatigue loads simultaneously, static strength reliability is analyzed by adopting the method of time-dependent reliability due to structural resistance decreasing. Safe margins of static strength failure [1] can be expressed as follows

$$\overline{Z} = R_r - S_G - S_Q \tag{1}$$

Where, R_r denotes the structural resistance, S_G denotes effect of static loads, S_Q denotes effect of fatigue loads.

Safe margins of fatigue failure. According to the method of fatigue reliability, safe margins of fatigue failure can be expressed [2] as follows

$$\tilde{\mathbf{Z}} = (\mathbf{\Omega}_a^{-1} - \mathbf{\Omega}_b \cdot \mathbf{\Omega}_a^{-1} - \mathbf{\Omega}_c)\mathbf{T} - \mathbf{T_d} \tag{2}$$

Where, $\mathbf{\Omega_a}$, $\mathbf{\Omega_b}$ and $\mathbf{\Omega}_c$ denotes the matrix of stress parameter, $\tilde{\mathbf{Z}} = [\tilde{Z}_1, \tilde{Z}_{2/1}, \tilde{Z}_{3/1,2}, \cdots, \tilde{Z}_{n/1,2,\cdots,(n-1)}]^T$,

$\mathbf{T}=[T_1,T_2,\cdots,T_n]^T$, $\mathbf{T}_d=[0,0,\cdots,T_{\mathrm{D}}]^T$, T_{D} denotes the design life of structural system, $\tilde{Z}_{i/1,2,\cdots,(i-1)}$ is the safe margin of the i th failure element when the former $(i-1)$ th element has failed, $T_i(i=1,2,\cdots,n)$ denotes the fatigue life of the i th failed element when the others isn't failed.

Safe margins of buckling failure. Safe margin $\overline{\overline{Z}}$ of buckling failure of structural element can usually be expressed as follows

$$\overline{\overline{Z}}_i=\frac{C\pi^2EI_i}{l_i^2}-P_i \tag{3}$$

where C is coefficient corresponding supporting condition, E, I_i and l_i denotes elastic modulus, moment of inertia and the length of element respectively, P_i denotes compressed load effect of element.

Safe margin $\overline{\overline{Z}}_s$ of buckling failure of trusses structural system is expressed as follows

$$\overline{\overline{Z}}_s=P_{cr}-P \tag{4}$$

where, P_{cr} denotes critical load of truss structural buckling, P denotes external loads acting on truss structural system.

Reliability analysis of structural system considering buckling failure under static loads and fatigue loads

The expression of safe margin of structural element failure probability and analysis of its failure mode. Every compressed structural element may occur static failure, fatigue failure or buckling failure, their safe margin is $\overline{Z}_i,\tilde{Z}_i$ and $\overline{\overline{Z}}_i$ respectively, corresponding reliability index is $\overline{\beta}_i,\tilde{\beta}_i$ and $\overline{\overline{\beta}}$,failure probability of their series can be expressed as follows

$$P_i=P\left(\overline{Z}_i\le 0\cup\tilde{Z}_i\le 0\cup\overline{\overline{Z}}_i\le 0\right)=P\left(Z_i\le 0\right) \tag{5}$$

where Z_i is equivalent safe margin, can be solved by Reference [3].

The method of searching failure modes in this paper is as follows:

- Firstly, solving failure probability P_i and β_i of Eq.(5);
- Secondly, comparing with the value of β_i of each element of structure, and finding the element of minimum of β_i as first failed element;
- Thirdly, analyzing final failure mode of i th element: if $\overline{\beta}_i$ of the element is minimal, the element is regarded as static failure; if $\tilde{\beta}_i$ of the element is minimal, the element is regarded as fatigue failure; if $\overline{\overline{\beta}}$ of the element is minimal, the element is regarded as buckling failure.

Accumulative damage time calculation of different failure modes of elements. Failure life of every element is needed to solve in the course of structural fatigue failure, so that accumulative damage of fatigue loads to other elements can be calculated during this course.

If the element is fatigue failure, fatigue life of i th element [2] in the structure can be expressed as follows

$$T_i=\frac{\Delta A_i}{B^m\Omega_i} \tag{6}$$

where Δ denotes accumulative damage degree, B denotes uncertain behavior of the calculating model, Ω_i denotes stress parameter of i th element, A_i and m denotes material constant.
if the element is static failure. Its equivalent life[4] is as follows

$$\overline{T}_i = \left[1 - \left(\frac{S_{G_i} + S_{Q_i}}{R_{r_i}}\right)^{\frac{r}{r+\alpha+1}}\right] \frac{A_i}{B^m \Omega_i} \tag{7}$$

where S_G denotes static load, S_Q denotes fatigue load, R_r denotes resistance, r and α denote material parameter.
If the element is buckling failure, its equivalent life[4] is as follows

$$\overline{\overline{T}}_i = \left[1 - \left(\frac{P_i l_i^2}{\pi^2 E}\right)^{\frac{r}{r+\alpha+1}}\right] \frac{A_i}{{B_D}^m {B_{Ii}}^m \Omega_i} \tag{8}$$

In summary, as soon as failure life of the element static failure, fatigue failure and buckling failure is solved, accumulative damage times of the element failure to the next element can be analyzed and calculated truly.
Failure course analysis of structural system and the necessity of considering buckling failure of residual structure. Failure of one or several elements may not lead to failure of structural system for hyper-static structure, but the structural system may turn into new residual structure. Buckling failure probability of the compressed residual structure(high slenderness ratio) may be increased due to fatigue damage and elastic modulus decay of elements. For example, there is $n+1$ elements in a certain failure path, that is, residual structure is static after the n th element failing. Here, structural integrity buckling should be analyzed, and this failure event connecting in parallel with former failure events of n elements makes up of the structural integrity failure path, failure probability of this buckling failure paths can be expressed as follows

$$P_{f_q} = P(Z_1 \le 0 \bigcap \cdots \bigcap Z_n \le 0 \bigcap \overline{\overline{Z}}_s \le 0) \tag{9}$$

where, $\overline{\overline{Z}}_s$ denotes safe margin of residual structure buckling.
If not considering integrity buckling of residual structure, failure probability of the failure path which be made up of $n+1$ elements as stiffness matrix of structure system $|K| = 0$ can be expressed as follows

$$P_{f_j} = P(Z_1 \le 0 \bigcap \cdots \bigcap Z_n \le 0 \bigcap Z_{n+1} \le 0) \tag{10}$$

where, Z_{n+1} denotes equivalent safe margin of the element of max failure probability in residual structure.
It is shown from analysis of failure course that failure probability of Eq.(9) may be more bigger than that of Eq.(10).So, it is necessary for residual structural system to consider integrity buckling failure due to factors of fatigue damage and elastic modulus decay of structural elements etc.
Reliability analysis of structural system. Following above analysis method of structure failure course, the significant failure paths can be searched by adopting Branch-and-Bound Method [3], then correlation coefficient of every significant failure modes need to be educed [3],finally, failure probability of structural system can be solved by using the PNET Method[3].

Numerical example

Consider the plane truss structure shown in Figure1. Parameter data of structure refers to Reference

[4]. The design life is $T_D = 15$ years.

Result: Significant failure paths and reliability index of structural system are shown in table 1.

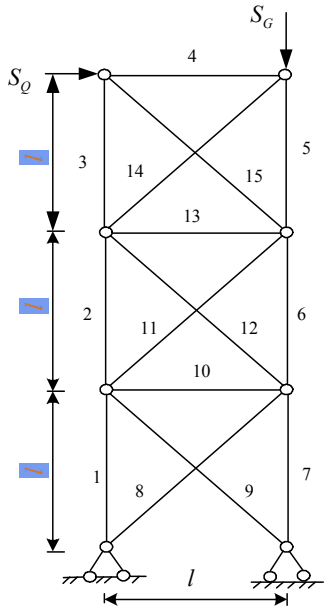

Fig.1 the plane truss structure

Tab.1 Significant failure paths and reliability index of structural system

Number of failure modes	Failure paths	Reliability index of failure modes β_i
1	$\bar{7}-\tilde{1}$	3.685
2	$\bar{7}-\tilde{12}-$ *system buckling*	3.843
3	$\bar{6}-\bar{7}-\tilde{2}$	3.972
4	$\bar{6}-\tilde{10}-\tilde{2}$	4.007
5	$\bar{7}-\bar{3}-$ *system buckling*	4.298
6	$\bar{6}-\tilde{3}-\tilde{2}$	4.733
7	$\bar{7}-\bar{3}-\tilde{16}$	5.017
8	$\bar{6}-\tilde{3}-\tilde{7}-\bar{\bar{2}}$	5.273
Reliability index of system considering residual structural integrity buckling		3.557
Reliability index of system not considering residual structural integrity buckling		3.625

Note: Superscript - , ~ and = denotes static strength failure, fatigue failure and buckling failure respectively

Summary

As can be seen from example: 1) Reliability index (4.298) of the fifth failure mode which considers buckling failure of structural system is smaller than reliability index (5.107) of the seventh failure mode which only considers structure turning to mechanism ($|K^i| = 0$) instead of considering buckling failure, it is shown that the fifth failure mode is more dangerous than the seventh failure mode. So, it is important to consider structure buckling failure; 2) reliability index (3.557) of considering residual structural integrity buckling is smaller than reliability index (3.625) of not considering residual structural integrity buckling, this is shown that reliability demands of structural system may not be satisfied if effect of residual structural integrity buckling is neglect.

In another word, only by considering synthetically static strength failure, fatigue failure and buckling failure of structural system, the results calculated can be reliable and in accordance with actual engineering design.

References

[1] An Wei-guang,Zhao Wei-tao,An Hai. Reliability analysis of stochastic structural system considering static strength, stiffness and fatigue. Science in China , 2007, 37(4):516-526 P

[2] Hu Yu-ren,Chen Bo-zhen. Reliability analysis of ship and ocean engineering structure. Beijing:Demotic Traffic Press(1996)

[3] An Wei-guang,Cai Yin-lin,Chen Wei-dong. Reliability analysis and optimum design for stochastic structure systems. Harbin: Harbin Engineering University Press(2005)

[4] Gu Yong-wei,An Wei-guang,An Hai. Structural Reliability Analysis under Static Load and Fatigue Load. ACTA ARMAMENTARII,2007,28(12):1473-1477 P

Key Engineering Materials Vols. 385-387 (2008) pp 261-264
© (2008) Trans Tech Publications, Switzerland
doi:10.4028/www.scientific.net/KEM.385-387.261

Reliability-based Structural Optimization of Stochastic Structure Systems Considering Stability

Xinchi Yan

College of Civil Engineering, Jiangnan University, Wuxi 214122, China

skywalkeryan@yahoo.com.cn

Key words: Failure mode; stochastic structure system; stability; reliability-based structural optimization; optimum vector method

Abstract: The problem of failure mode analysis of stochastic structural systems, dealing with the design variables expression, reliability-based structural optimization and improved stability of girders, have been studied in this paper. Considering the material intensity, girder section area, panel thickness and loads as stochastic variables, a mathematical model of optimization is constructed. In the iterative procedure, the optimum vector method was adopted to optimize the object and the gradient step; and the optimum vector step have been used alternatively, and these can speed up the iterative procedure. The calculation of a numerical example shows this method is exact and free from the selection of optimum start point, further more the convergence is stable and fast.

Introduction

Stochastic structural systems have many indeterminate mechanics factors; this makes failure mode analysis very difficult. Taking into account the indeterminate factors will make the Reliability-Based Structural Optimization design (RBSO) a more logical design method [1,2]. Further more, it is important for most structures like spatial girder-panel system to have enough stability [3]. In this paper special focus is placed on the stability analysis and the methodology of reliability-based structural optimization of stochastic structural system.

Mathematic Model of Optimization

The mathematic model of this RBSO issue is:

$$\begin{cases} \min W(A) = \sum_{b=1}^{B} C_b A_b \\ s.b.\ g(A) = \beta_s^a - \beta_s(A) \le 0 \\ A^L \le A \le A^U \end{cases} \quad (1)$$

where $\boldsymbol{A}$ is design variable, is section area of the component; β_s is structural system reliability index; β_s^a is admit system reliability index; C_b is the mass of b element's unit section.

Optimum vector method is also called grads edge method, be different from conventional arithmetic, optimum vector method in this paper used alternatively the gradient step and the optimum vector step[4], its searching direction is shown in Fig. 1.

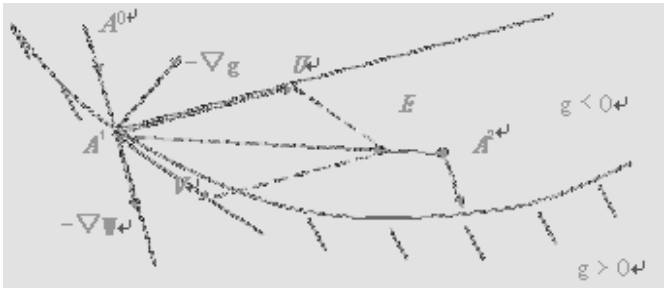

Fig. 1 Direction of optimum vector

Design Variables Focus on Keeping Enough Stability

From Fig. 2, the areas of ventral panel and face panel are regarded as design variables, designated by A_{H_w} and A_{B_f}, respectively. It is clear that $A_{H_W} = H_w t_w$, $A_{B_f} = B_f t_f$.

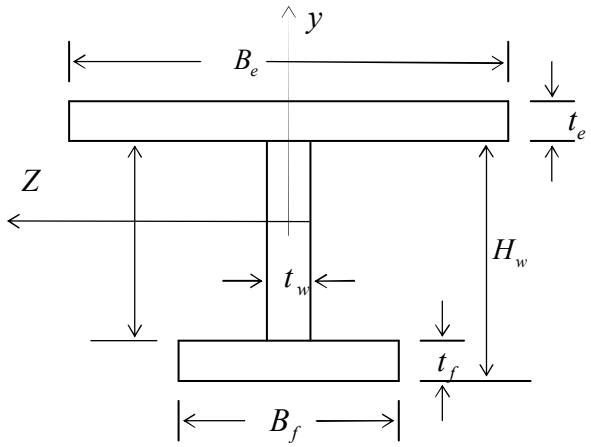

Fig.2 Sketch map of beam section

In order to ensure the panels have enough local stability, height and breadth of ventral panel H_w and t_w are always calculate as follows:

$$\frac{H_w}{t_w} < 1.6\sqrt{\frac{E}{\sigma_s}} \tag{2}$$

So there is

$$t_w > 0.625\sqrt{\frac{\sigma_s}{E}} H_w = 0.0286 H_w \tag{3}$$

thickness and breadth of face panel t_f and B_f should follow $\frac{B_f}{t_f} \le 0.6\sqrt{\frac{E}{\sigma_s}}$, so there is

$$t_f > 1.667\sqrt{\frac{E}{\sigma_s}} B_f = 0.0763 B_f \tag{4}$$

In this way design variables can be given by

$$\left.\begin{aligned} A_{H_w} &= H_w t_w = H_w t_w(H_w)\cdot H_w = 0.0286 H_w{}^2 \\ A_{B_f} &= B_f t_f = B_f t_f(B_f) B_f = 0.0763 B_f{}^2 \end{aligned}\right\} \tag{5}$$

Numerical Examples

Warship cabin between 165th and 200th ribs is shown in Fig. 3. There are 64 kinds of girder, and take optimum design. Before Optimization, system reliability index β_s = 3.1564, and girder system weight is 38405 kg[4 , 5].

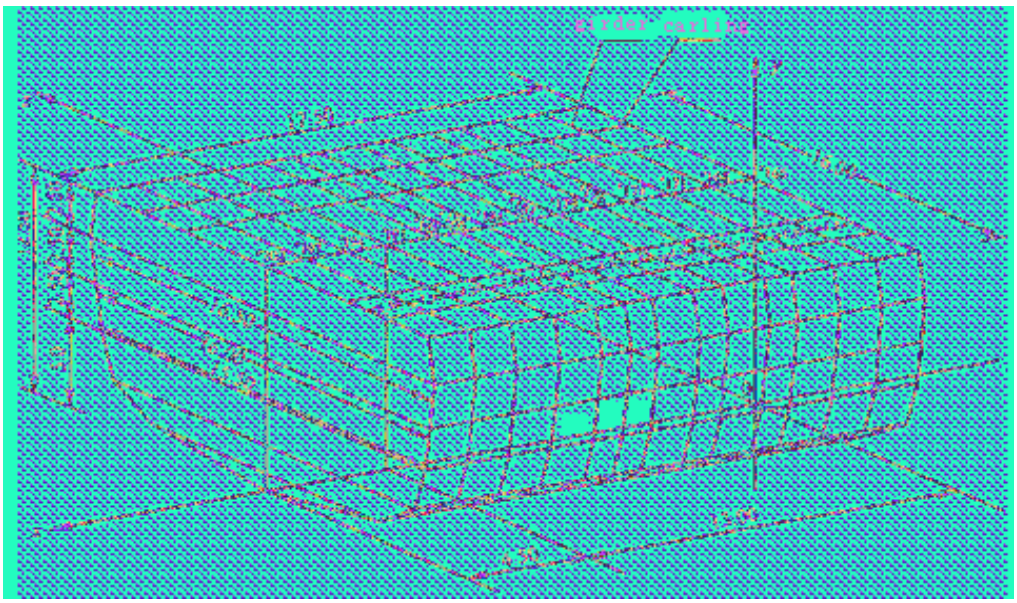

Fig. 3 Spatial girder-panel structural system of ship cabin

The object function is

$$W = W_0 + \sum_{b=1}^{B} A_b C_b = W_0 + \sum_{b=1}^{B} (A_{H_{W_b}} + A_{B_{f_b}}) C_b \tag{6}$$

where W_0 is mass of cincture panel, design variables $A_{H_{wb}}$ is area of b beam element's ventral panel, and $A_{B_{fb}}$ is area of b beam element's face panel. From equation 5, ventral panel height H_{w_b} and face panel breadth B_f can be calculated.

The optimization constraint is $\begin{cases} \beta_s \geq \beta_s{}^a = 3.685 \text{ [6]} \\ 0 < A_{H_{wb}} < 0.0286 m^2 \\ 0 < A_{B_{fb}} < 0.0763 m^2 \end{cases}$. Optimum course is shown in Table 1.

TABLE 1 Optimum course of beams

Iterative time	1	2	3	4	5	6	7	8
β_s	3.703	3.711	3.712	3.697	3.691	3.687	3.686	3.685
W (kg)	38831	35144	33825	33779	33759	33745	33745	33744

Summary

Focus on ensure components having enough stability, the optimum design variables were established, and base on reliability, optimum design methodology for structural systems with multi-random factors is shown in this paper. Optimum vector method was adopted to make convergence quickly and stable. After optimization design, girder system's weight reduce 9.2%, and the searching start point was chosen in unviable area, but it doesn't affect the convergence, The calculation result shows this method is logical , stable and free from the selection of searching start point.

References

[1] Wang Guang-yuan. On the development of uncertain structural mechanics. Advances In Mechanics (2002), 32(2): 205-211

[2] Cheng Geng-dong; Xu Lin. Sequential Approximate Programming Approach to Reliability Based Structural Optimization. Chinese Journal of Computational Mechianics (2006), 23(6): 641-646

[3] Hu Yu-ren, Chen Bo-zhen, Sun Jiu-long. Equation for Predicting Tripping Stress of Stiffeners in Stiffened Panel. Journal of Shanghai Jiaotong University (2002), 36(1): 95-98

[4] Yan Xin-chi, Hua Yuan. Failure Analysis of the Stochastic Structural System. Key Engineering Materials (2006), Vols. 324-325: 223-226

[5] Yan Xin-chi, An Wei-guang, Chen Wei-dong. Reliability analysis for large ship structure[J]. Journal of Harbin Engineering University (2004), 25(2):147-150

[6] Yan Xin-chi. *Genetic Algorithm and SFEM-based for reliability-Based Optimization of Random structural System*. Dissertation for the Degree of Harbin Engineering University, 2005

Key Engineering Materials Vols. 385-387 (2008) pp 265-268
© (2008) Trans Tech Publications, Switzerland
doi:10.4028/www.scientific.net/KEM.385-387.265

Research on Performance of Reduced Web Connections in Steel Frame

Shao Yongsong[1,2,a], Jin Lu[1,b], Liu Hongbo[1,3,c], Xie Lili[1,2,d]

[1]School of Civil Engineering, Harbin Institute of Technology, Harbin 150090, China

[2]Institute of Engineering Mechanics, China Earthquake Administration, Harbin 150080, China

[3]College of Civil Engineering and Architecture, Heilongjiang University, Harbin 150080, China

[a]shaoyongsong@hit.edu.cn, [b]duobeibei@163.com, [c]interdage@163.com, [d]llxie@public.hr.hl.cn

Keywords: steel frame connection; reduced web connection; web opening; failure mechanism; finite element analysis

Abstract: Following the Northridge earthquake, widespread damages in connections have been discovered. Then the research on behavior of new beam-column connections has been being a hot spot in recent several years. Non-linear analysis of reduced web connections with circular and rectangular openings in concentrated loading was carried out with finite element method. The parameters were conducted to study the effect of opening ratio, opening style and opening position on bearing capacity. Results show that bearing capacity of reduced web connection reduces with the increase of opening ratio. The opening ratio of reduced web connection takes little effect on bearing capacity when opening ratio is less than 50%. The bearing capacity of reduced web connection with circular opening is larger than rectangular opening if the opening area is equal.

Introduction

In high-rise steel frame, connection is the key part which insures the structure safety, and it takes an important effect on the performance of the whole structure system. Following the Northridge earthquake in 1994, brittle fractures have been discovered in connections of steel constructions widely[1]. Henceforth, the performance of new type connections including reinforced and reduced connection is becoming a hot research point in domestic and international engineering field[2,3].
Reduced web connection has advantages of lightening weight, and it's easy to laying equipment pipelines through the openings and perfects the space. It will be result in lowering project cost and increasing economic benefit directly. The objective focuses on the performance of connection with reduced beam web in steel frame. Non-linear analysis was carried out on reduced web connections under concentrated static loading with finite element method.

Finite element model

The models are built up using shell 181 element in ANSYS computer program to simulate the performance of connections with opening. Constitutive relationship of steel is bilinear strengthen elastic-plastic model, and yield strength is 235N/mm^2(Fig.1). The Young's Modulus and Poisson's ratio are 2.06e5N/mm^2 and 0.3, respectively. The beam-column connection is considered as hinge joint. A concentrated static loading is applied at end of beam in the vertical direction. During the process of building up the models of reduced web connection, material nonlinear and geometrical

nonlinear are taken into account. Fig.2 shows geometric model and loading style of connection. The finite element model and parameters of specimens are shown in Fig.3 and Table1, respectively.

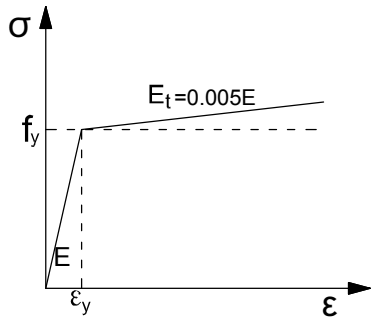

Fig.1 Constitutive relationship

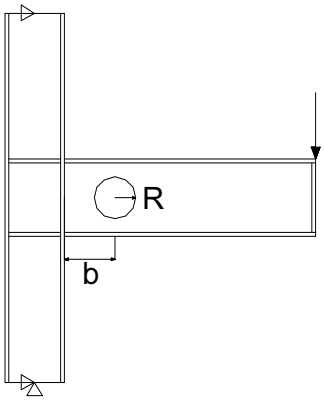

Fig.2 Geometric model

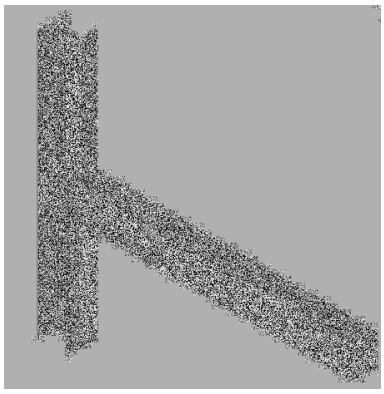

Fig.3 Finite element model

Table 1. Specimen dimensions and parameters of connections

Member	Sectional dimension $h\times b_f\times t_w\times t_f$ [mm]	Area A [cm^2]	Moment of inertia I_x [cm^4]	Gyration radius i_x [cm]	Modulus of section W_x [cm^3]
Beam	440×300×11×18	102.4	59161	24.1	2689
Column	400×400×10×20	120.0	68573	23.9	3429

Opening dimension must assure enough bearing capacity of connection. To reduced web connection with circular opening, main parameters are the distance b from the centre of circular opening to external edge of column flange and radius R of circular opening. The distance from opening edge to column flange is (b-R). Considering the dimension of end plate and welding opening, the relationship of these parameters are b=(0.4~2)b_f, R=(0.1~0.45)h, (b-R)>100mm, where b_f and h are beam flange width and beam height respectively. To rectangular opening, main parameters are the distance b from rectangular opening centre to column flange edge, opening height d (d=2R) and opening length c. The range of these parameters are b=(0.4~2)b_f, h=(0.2~0.9)h, (b-c/2)>100mm.

Reduced web connection with circular opening

In the case of reduced web connection with circular opening, load-deformation curves in different opening ratios are shown from Fig.4 to Fig.6. b means different distance of opening center, where b=0 to un-reduced connection especially.

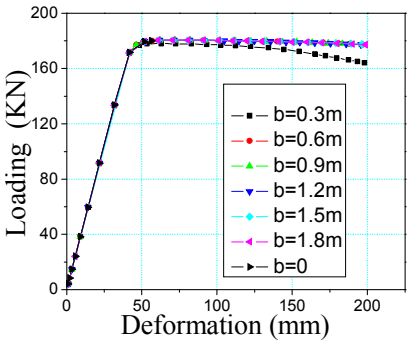

Fig.4 Opening ratio ρ=30%

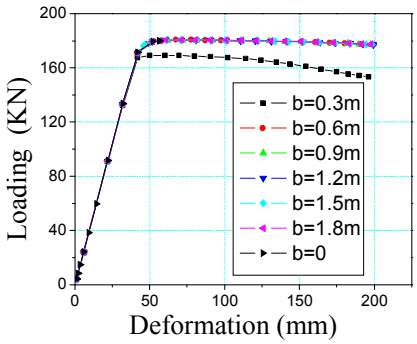

Fig.5 Opening ratio ρ=50%

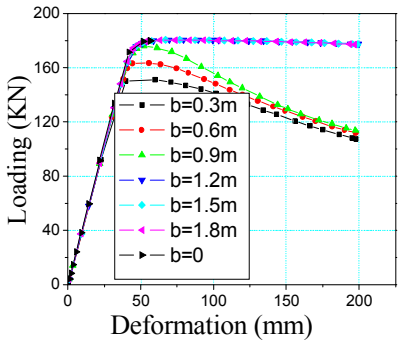

Fig.6 Opening ratio ρ=70%

It could be seen that with the increase of reduced beam web opening ratio, the connection ductility almost doesn't decrease, but ultimate bearing capacity decreases gradually. For different opening ratios, the effect on the connections with opening is becoming more and more smaller with the increase of distance b. When opening edge is closer to column flange (b=0.3m), load-deformation

curve is lower than which of un-reduced connection, but other curves almost coincide with un-reduced connection curve. In the case of opening ratio ρ=70%, bearing capacity decreases a lot, but as opening center is far away from column flange, the influence due to opening is becoming lower so as to be neglected.

Reduced web connection with rectangular opening

Load-deformation diagrams of reduced web connections with rectangular openings in different opening ratios are shown from Fig.7 to Fig.9, where a is length-width ratio of rectangular opening. It could be seen that the basic influence of opening ratio and opening position on bearing capacity is similar to circular opening. In the case of opening ratio ρ=70%, bearing capacity decreases down to 50% of un-reduced connection. Moreover, though opening center is far away from column flange, bearing capacity of opening doesn't increased distinctly. Rectangular opening has large negative effect on connection when a=2. Fig.10 to Fig.12 are in the case of reduced web connection with length-width ratio of rectangular opening a=1. Compared with circular opening and rectangular opening with a=2, negative effect on the connection of square opening is between them.

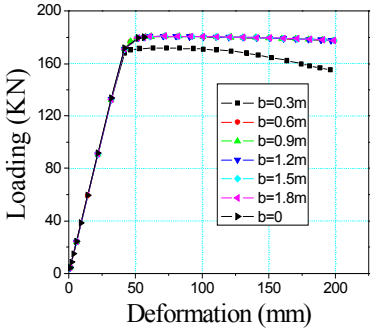

Fig.7 ρ=30% (a=2)

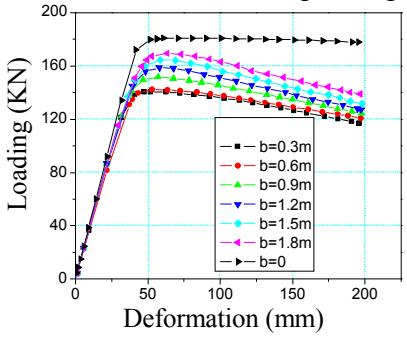

Fig.8 ρ=50% (a=2)

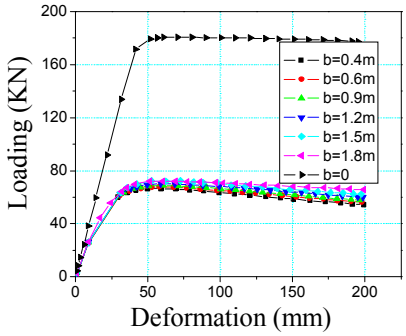

Fig.9 ρ=70% (a=2)

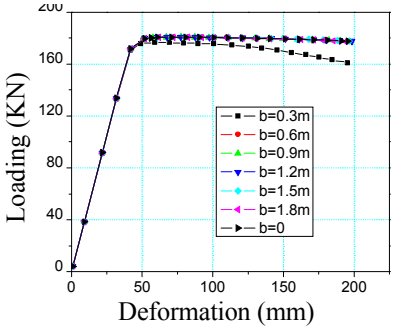

Fig.10 ρ=30% (a=1)

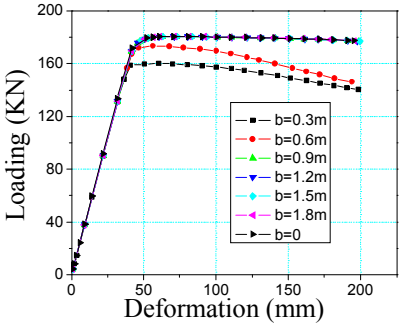

Fig.11 ρ=50% (a=1)

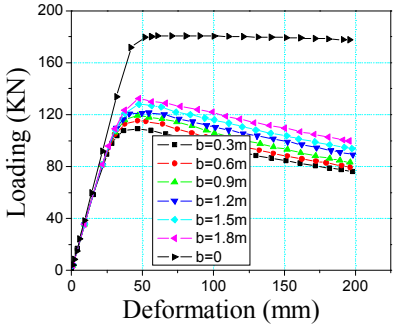

Fig.12 ρ=70% (a=1)

Comparison of circular and rectangular openings

From the above analysis, reduced beam web with rectangular opening has a greater effect on the connection than circular opening. Bearing capacities of different web openings and different opening positions are shown in Fig.13, where c is circular opening and r means rectangular opening. In the same opening ratio, rectangular web opening(r=2) has a greater effect on the connection compared with circular web opening. To lower opening ratio, the effect of opening to bearing capacity of connection decreases. The effect of circular web opening on bearing capacity of connection is still very little even in opening ratio ρ=70%, and bearing capacity is 152.44kN when b=0.3m, which only decreases by 13.31% compared with which of un-reduced connection. In comparison, bearing capacity has a greater decrease in the case of rectangular web opening, especially in larger opening

ratio. When ρ=70% and r=2, the lowest bearing capacity of connection is only 37.99% of un-reduced connection.

As shown in Fig.14, the farther distance from opening to column flange, the lower effect of connection, which can also be gained from the above analysis. If distance from opening center to column flange b=0.3m uniformly, with the increase of opening ratio, bearing capacity of connection decreases whether rectangular or circular web opening. While in the same opening ratio, curve of rectangular web opening is lower than circular opening. So the conclusion could be gained that in application circular web opening is better than rectangular web opening.

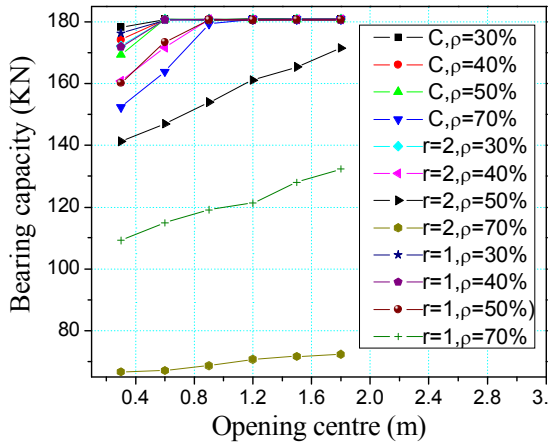

Fig.13 Bearing capacity comparison of different web openings

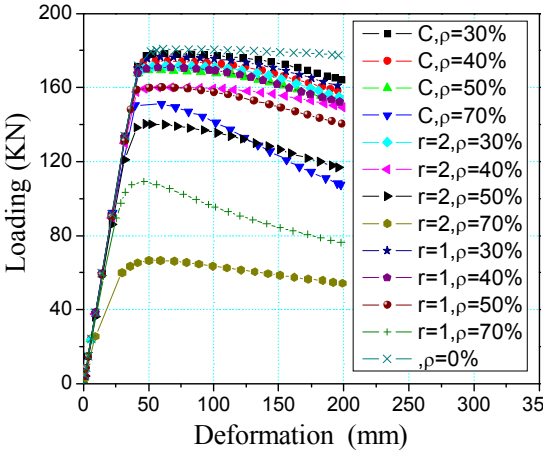

Fig.14 Load-deformation curves of different openings and opening ratios

Summary

In conclusion, bearing capacity of reduced web connections reduces with the increase of opening ratio whether circular opening or rectangular opening. The opening ratio of reduced web connection takes little effect on bearing capacity if opening ratio is less than 50%. Otherwise, reduced beam web with rectangular opening has a greater effect on the connection compared with circular opening if the opening ratio is equal. It is expected that there will be more extensive application of reduced web connections with circular and rectangular openings.

Acknowledges

The work presented in this paper is supported by National Natural Science Foundation of China (50538050) and Foundation of Heilongjiang Educational Committee (11521210).

References

[1] K.F.Chung, T.C.H.Liu: Journal of Constructual Steel Research. Vol. 9(2003), p.1159

[2] V.T.Lian, N.E.Shanmugan: Thin-walled Structures. Vol.41 (2003), p.245

[3] N.E.Shanmugan, V.T.Lian and V.Thevendran: Thin-walled Structures. Vol.40 (2002), p.443

Key Engineering Materials Vols. 385-387 (2008) pp 269-272
© (2008) Trans Tech Publications, Switzerland
doi:10.4028/www.scientific.net/KEM.385-387.269

Risk-based Research on Failure Mode of High-arch Concrete Dam

Zaitie Chen [1,2,a]

[1]Civil Engineering College, Hohai University, Nanjing 210098, China;

[2] Shazhou Institute of Technology, Zhangjiagang 215600, China

[a]Email:chenzaitie@yahoo.com.cn

Keywords: high-arch dams, risk analysis, failure modes, state functions

Abstract: Risk analysis can overcome the weakness of conventional safety evaluation of high-arch dams where the random nature of the load and resistance effect are ignored and the failure mode and failure disaster loss are not taken into account. On the basis of statistical analysis of the data of the failure arch dams and faulty and perilous arch dams in the world, it is deduced that the failure of high arch dam is mainly caused by super elevation floods, highly intense earthquakes, mountain landslides, abnormal temperature variation, explosion load, etc. Five major failure modes for high arch dams are suggested, namely dam abutment rock instability, fundamental plane instability, entire entity instability, excess cracking and extreme dam overflow. Based on the study of the failure mechanism of the major failure modes, a state function is established to calculate the failure probability of the major failure modes. An approach is developed to obtain the statistical quantity and the regularities of distribution of the load and resistance random variables.

1 Introduction

Healthy, harmonious, sustainable economic and social developments of China urgently need the solution to fossil energy shortage and environmental pollution. Hydroelectric power, at present, is the sole source of reproducible clean energy that can be exploited commercially on a large scale. China is abundant in hydropower resources, the possible quantity of technical development of which is ranked first in the world[1]. The exploitation of hydroelectric power cannot do without dams & reservoirs and thus a number of 300-m-level (world top level) major dams, 60% of which are arch dam type, are under construction or planned to be constructed in China[2]. In view of the height and the reservoir capacity of these high-arch dams, when there has an accident, there would be great economic and social losses as well as human casualties. The conventional safety evaluation which is based on stress safety coefficient, overload or strength reserve safety degree ignores the random nature of the load and resistance, takes the failure mode and the consequence of the accidental calamity into no consideration and takes not through risk analysis and evaluation. Although quite a few experts have obtained quite a few achievements in studying the failure modes and risk analysis of earth-rock dams and gravity dams, however, as the earth-rock dam and gravity dam are of simple structure, the failure mechanism conforms to the strength theory and the failure modes are few and relatively independent, the risk evaluation is relatively easy to conduct. High-arch dams are of complex high-order statically indeterminate structure, failure mechanism is complex and interdependent failure modes without explicit formula in terms of state function;

Sponsored by Natural Science Foundation Of China (50539030, 50779009), National Basic Research Program of China (973 Program)(2007CB14104)

moreover, as the high arch dam construction is of a short history and there have been few instances of failure dams and perilous dams, the research and analytical data are deficient and the rare achievements of the research on high arch dam failure mode based on risk analysis are found.

2 The causes of the failure of high arch dams and the recognition of the major failure modes

Researches show that the causes of high arch dam failure, A, mainly involves such natural factors as flood, earthquake, close-range mountain slope-slide, upstream dam failure, aging of dam body and construction joint materials, abnormal temperature variation, as well as some human factors such as war and terrorist attack[3]. In the case of common dam overflow, the high arch dam will not lose its function of water-keeping and no severe loss will be caused; however, the extreme overflow of Italian Vajont Arch Dam led to the death of over 2000 people as well as disastrous economic loss. The dam abutment rock instability, B, the excess cracking, C, the entire entity instability of arch dam and dam foundation, D, the extreme dam overflow, E, and the instability of the dam body along the fundamental plane F are generally the five major failure modes of high arch dams and every two of these major failure modes are not completely independent but correlative to a definite degree. In actual calculation, the dam abutment rock instability, the entire entity instability and the instability of the dam body along the fundamental plane are considered partly correlative and the correlativity must be taken into account, while the remaining major failure modes are of low correlativity and thus can be deemed as relatively independent. Generally, the failure probability, $P(A)$, of high arch dam can be expressed as

$$P(A) = P(B \cup C \cup D \cup E \cup F) = P(C) + P(E) + P(B \cup D \cup F) \tag{1}$$

In view of the fact that the probability of the simultaneous occurrence of the three major failure modes, i.e. the dam abutment rock instability, the entire entity instability and the instability of the dam body along the fundamental plane, is relatively rare, in the actual calculation the formula (1) can be changed into

$$P(A) = P(B) + P(C) + P(D) + P(E) + P(F) - P(BD) - P(BF) - P(DF) \tag{2}$$

Although the correlativity among the dam abutment rock instability, the entire entity instability and the instability of the dam body along the fundamental plane cannot be neglected, they are not highly correlative, so the value range of the correlation coefficient, ρ, is recommended to be $[0.3, 0.5]$ and the specific value is to be discussed and determined by experts, and the upper and lower limits of the intersecting probability between corresponding major failure modes should be determined by means of "dual mode" narrow boundary formula. For example, the formula for calculating the upper and lower limits of the intersecting probability, $P(BD)$, between the dam abutment rock instability and the entire entity instability is

$$\max\left(\Phi(-\beta_B)\Phi\left(-\frac{\beta_D - \rho\beta_B}{\sqrt{1-\rho^2}}\right), \Phi(-\beta_D)\Phi\left(-\frac{\beta_B - \rho\beta_D}{\sqrt{1-\rho^2}}\right)\right) \le P(BD) \tag{3}$$

$$P(BD) \le \Phi(-\beta_B)\Phi\left(-\frac{\beta_D - \rho\beta_B}{\sqrt{1-\rho^2}}\right) + \Phi(-\beta_D)\Phi\left(-\frac{\beta_B - \rho\beta_D}{\sqrt{1-\rho^2}}\right) \tag{4}$$

As far as high arch dams as a dam type is concerned, there are five major failure modes namely the dam abutment rock instability, the excess cracking, the entire entity instability, the extreme dam overflow and the instability of the dam body along the fundamental plane. These major failure modes for high arch dams in general are not necessarily the major failure modes for a specific high arch dam; to determine the major failure modes for a specific high arch dam, it is necessary to work out the risk rate and risk value of the dam in accordance with its shape, dimension, load & resistance features, the geological structure at the dam site as well as the

economic and social status of the region, especially the downstream region of the dam and then to exclude the failure modes with the risk rate and risk value being one or more Magnitude Order(s) smaller from the five major failure modes of high arch dams, and the remaining failure mode/modes is/are the major failure mode(s) for the specific dame.

3 Approach to account for random nature of high arch dam load and resistance effective variables

To calculate the failure probability of the major failure modes of high-arch dams, it is necessary to obtain the observation data of the effective random variables of the load & resistance and thus to get the statistic and regularities of distribution. Among the resistance effective random variables, the mean, variation and distribution regularities of the tensile strength, the compressive strength, the shear strength and the rigidity of the dam body materials can be obtained by means of static and hypothesis test on the measured data by the Quality Inspection Authorities and, if necessary, reference can be made to the strength-stress curve of dam concrete material indicating the aging with time; while the mean, variation and distribution regularities of the strength and rigidity indexes of the dam foundation and dam abutment rock can be obtained by means of static and hypothesis test directly on the data from geologic exploration.

In terms of the load data of high arch dam, the mean, variation and approximate distribution regularities of the flood elevation, the inflow velocity, the earthquake acceleration and the temperature variation can be obtained generally by means of statistic analysis of historical data; while the load-effect random variables are generally all kinds of stress and deformation. As high arch dams are of high-order redundancy complex structure and there exists no analytic relationship between load and load-effect random variables, there is no way to obtain the mean, variation and distribution regularities of the load-effect random variables from the mean, variation and distribution regularities of the load through theoretical analysis and only the following indirect method can be used: first, to establish the finite element numerical calculation model; then, based on the mean, to obtain variation and distribution regularities of the load parameter, to generate a series of random arrays of the load random variables by means of computer simulation; to input the random arrays as respective loads to obtain the value of the required load-effect random variables (stress, deformation, etc.) and repeat the input to get a series of values; to make statistic analysis and carry hypothesis test on these series values as the observation data of load-effect random variables and finally obtain the mean, variation and distribution regularities.

4 State function of the major failure modes of high arch dams

The state function of high arch concrete dam extreme overflow is

$$g(x) = H_{\mathrm{d}} + \Delta H - H \tag{5}$$

where, H_{d} is the dam height; ΔH is the threshold value of the upstream water level higher than the dam top in the case of extreme overflow; H is the upstream water elevation. The state function of dam abutment rock instability is

$$g(x) = \sum_{i=1}^{n} (\sigma_i f_i + c_i) A_i \cos\alpha_i - \sum_{i=1}^{n} A_i \tau_i \cos\beta_i \tag{6}$$

where, n is the number of the joints that the sliding face passes; A_i is the area of the i th joint; f_i and c_i are the frictional coefficient and cohesion coefficient of the i th joint; α_i is the included angle between the tangent line of the i th joint face and the sliding direction; β_i is the included angle between the shear stress of the i th joint face and the sliding direction; σ_i and τ_i are the normal stress and shear stress of the i th joint. The state function of the excess cracking is

$$g(x) = K_{IC} - K_I \tag{7}$$

where, K_I is the stress intensity factor and K_{IC} is the fracture toughness of the material.

There is also no explicit formula for the state function of the instability of the dam's body along the fundamental plane; it is only possible to obtain the safety degree, k_1, of the instability of the dam body along the fundamental plane by means of finite element numerical analog computation and obtain the inexplicit state function as follows

$$g(x) = k_1 - 1 \tag{8}$$

Entire entity's instability refers to the downstream slipping instability of the high arch dam together with the dam foundation along the weak structural face of the bedrock (such as the faults, the embedded stratum, etc.). Generally there is no explicit formula for the state function and it is necessary to obtain the entire entity safety degree, k_1, by means of finite element numerical analog computation and obtain the inexplicit state function as follows

$$g(x) = k_2 - 1 \tag{9}$$

5 Risk evaluation indexes and criteria for high arch dams

In general, risk rate (i.e. failure probability) and economic loss risk value (i.e. the arithmetic product of the risk rate and calamity economic loss) are used as the major indexes for evaluate the risk. In view of the fact that the accident (or failure) of high arch dam will cause not only economic loss but also heavy human casualties, and that increasing importance is attached to the life value of human beings, which the practice of equalizing human life to money is receiving increased moral censures and that there is a great difference between different countries and regions in equating life loss to economic loss, it is, therefore, suggested that the failure risk of high arch dam should be evaluated by means of the three indexes, namely risk rate, P, economic loss risk value, R_L, and life loss risk value, R_N. Only when the three risk indexes of a high arch dam are no greater than the tolerable risk rate $[P]$, the tolerable economic loss risk value $[R_L]$ and the tolerable life loss risk value $[R_N]$, can the risk of the dam be acceptable[4].

6 Conclusion

High-arch concrete dams are of high-order statically indeterminate structure and complex failure mechanism. Apart from adverse geological and environmental conditions, high arch dams are usually located in the area with frequent occurrences of intense earthquakes and the load & resistance effect is of randomness and uncertainty. Besides, risk evaluation involves such disciplines and research fields as mathematics, mechanics, dam structural engineering, calamity evaluation, risk analysis, etc. As a result, the research on high-arch dam failure risk is still at its early stage and, together with the studies of the relationship between hydrological and geological conditions before and after the construction of high-arch dams, the failure mechanism of high arch dams, the method of evaluating dam failure indirect loss, the risk management of high-arch dam operation, the risk control of planned high-arch dam, etc., requires joint exploration in depth by experts and scholars in various fields.

References

[1] Ren Qingwen. Development of theory and methods on high dam structural analysis[A] In: New Developments in Dam Engineering, edited by W. Martin Publications/A.A.Balkema Publishers, The Netherlands (2004),in press

[2] The statistical data of large dams in China on http//.www.icold-cigb.org.cn

[3] Chen Zaitie,Ren Qingwen Research on high arch dam failure probability based on failure mode[J].Key Engineering Materials, , Vol.348-349, 601-604,(2007).

[4] Chen Zaitie,Ren Qingwen.Research on standard of acceptable risk for high arch dam in developing countries[J]. Key Engineering Materials , Vol.348-349,597-600,(2007).

Key Engineering Materials Vols. 385-387 (2008) pp 273-276
© (2008) Trans Tech Publications, Switzerland
doi:10.4028/www.scientific.net/KEM.385-387.273

Scattering of SH-waves and Dynamic Stress Intensity Factor by an Interacting Mode III Crack and a Lining Structure in Half Space

Zailin Yang [1,3,a], Meijuan Xu[2,b], Baitao Sun [3,c]

[1, 2]School of Civil Engineering, Harbin Engineering University, Harbin 150001, China

[3]Institute of Engineering Mechanics, China Earthquake Administration, Harbin 150080, China

[a] yangzailin00@163.com, [b]meijuan242@163.com, [c]sunbt@iem.net.cn

Key words: Scattering of SH wave; Crack, DSIF; Green's function; Lining structure

Abstract. Scattering of SH wave by an elastic half space with a lining structure and a crack in any position and direction is studied with Green's function, complex function and multi-polar coordinate method. First, a suitable Green's function is constructed, which is a fundamental solution to the displacement field for the elastic space possessing circular lining structure while bearing out-of-plane harmonic line source load at arbitrary point. Then a crack in any position and direction is constructed by means of crack-division in half space. Finally the displacement field and stress field are established in the case of coexistence of circular lining structure and crack, and the expression of dynamic stress intensity factor (DSIF) at the tip of crack is given. According to numerical examples, the influences of different parameters on DSIF are discussed.

1. Introduction

The model of lining structure is common in many projects and has practical value and significance. The scattering of SH-wave, which is caused by half-space circular lining structure, had been studied[1]. In this paper, we study the interaction of inclusion and crack impacted by SH-wave. At present, most studies concerning scattering of SH-wave by the inclusion and crack focus on the radial crack, which originates from the boundary of inclusion and along the radius. In fact, when the forces are applied to the composite materials containing inclusions, the cracks are often found in the vicinity of the inclusions[2-3]. The purpose of this paper is to study scattering of SH wave by an interacting mode III crack with any position and a circular lining structure in half space, which can supply some beneficial references to the strength designing and non-destructive inspection of composite materials.

2. Green's Function

The model of the shallow-embedded circular lining structure is given according to Fig.1. ρ_{I} and C_{I}, ρ_{II} and C_{II} are the mass density and the wave velocity of the medium and the inclusion respectively.

Governing Equation and Boundary Condition. In the anisotropic medium, the easiest scattering problem for the elastic wave is the scattering of SH-wave. The displacement $G(x,y,t)$ impacted by the incident wave is vertical to the *xy* plane, it is irrespective with the *z* axis. $G(x,y,t)$ should satisfy:

$$\frac{\partial^2 G}{\partial z \partial \bar{z}} + \frac{1}{4}k^2 G = 0 \tag{1}$$

The corresponding stresses are given by

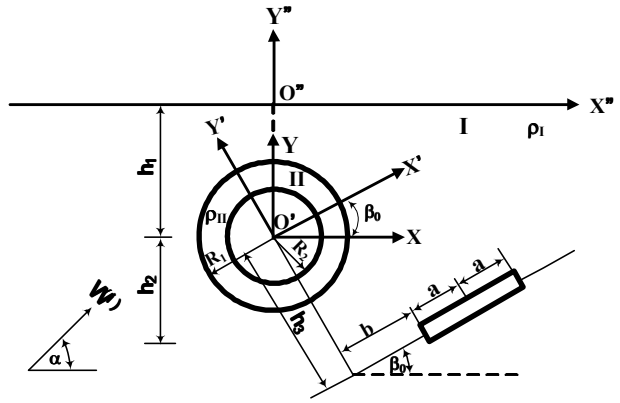

Fig.1 The infinite half space model with a circular lining structure and a crack impacted by SH wave

$$\tau_{rz} = \mu(\frac{\partial G}{\partial z}e^{i\theta} + \frac{\partial G}{\partial \bar{z}}e^{-i\theta})$$

$$\tau_{\theta z} = i\mu(\frac{\partial G}{\partial z}e^{i\theta} - \frac{\partial G}{\partial \bar{z}}e^{-i\theta}) \quad (2)$$

In the complex plane $(z,\bar{z})$, the boundary condition can be expressed as:

$$\begin{cases} G^{(i)} + G_{\mathrm{I}}^{(s)} + G^{(r)} = G_{r_1\Pi}^{(s)} + G_{r_2\Pi}^{(s)}, \ r = R_1 \\ \tau_{rz}^{(i)} + \tau_{rz}^{(r)} + \tau_{rz,\mathrm{I}}^{(s)} = \tau_{rz,r_1\mathrm{II}}^{(s)} + \tau_{rz,r_2\mathrm{II}}^{(s)}, r = R_1 \\ \tau_{rz,r_1\mathrm{II}}^{(s)} + \tau_{rz,r_2\mathrm{II}}^{(s)} = 0, r = R_2 \end{cases} \quad (3)$$

The Scattering Wave around the Circular Lining Structure. Now, using the symmetry of the scattering wave and multi-polar coordinates, the scattering wave in the medium $G_{\mathrm{I}}^{(s)}$ around the circular lining structure can be districted, which should satisfy the equation (1) and the radiation condition beside the stress free condition on the horizontal interface.

In the complex plane $(z,\bar{z})$, $G_{\mathrm{I}}^{(s)}$ can be expressed as:

$$G_{\mathrm{I}}^{(s)} = \sum_{n=-\infty}^{\infty} A_n \left\{ H_n^{(1)}\left(k_1|z|\right)\left[\frac{z}{|z|}\right]^n + H_n^{(1)}\left(k_1|z-2h_1 i|\right)\left[\frac{z-2h_1 i}{|z-2h_1 i|}\right]^{-n} \right\} \quad (4)$$

In which, A_n are unknown coefficients, which are determined by the boundary condition of the circular lining structure.

In the complex plane $(z,\bar{z})$, the scattering wave around the inside and outside of circular lining structure can be expressed as:

$$G_{r_1\Pi}^{(s)} = \sum_{n=-\infty}^{\infty} B_n \left\{ H_n^{(2)}(k_2|z|)\left(\frac{z}{|z|}\right)^n \right\} \qquad G_{r_2\Pi}^{(s)} = \sum_{n=-\infty}^{\infty} C_n \left\{ H_n^{(1)}(k_2|z|)\left(\frac{z}{|z|}\right)^n \right\} \quad (5)$$

Derivation of Green's Function. In a full elastic space, the wave field excitated by the out-plane line source loading $\delta(\vec{r}-\vec{r}_0)$ is $G^{(i)}$, which can be described as a known incident wave, it takes the form

$$G^{(i)} = \frac{i}{4\mu_1} H_0^{(1)}\left(k_1|z''-z_0''|\right) \quad (6)$$

The reflection wave from half-space surface can be expressed as

$$G^{(r)} = \frac{i}{4\mu_1} H_0^{(1)}\left(k_1|z''-\bar{z}_0''|\right) \quad (7)$$

The total wave field is

$$G^{(t)} = G^{(i)} + G^{(r)} + G^{(s)} \quad (8)$$

Substitution of Eqs.(4),(5),(6) and (7) into Eq.(2), the stresses from incident wave $G^{(i)}$, reflected wave $G^{(r)}$ and scattered wave $G^{(s)}$ can be obtained, and then substituting the expression of stresses

into boundary conditions (3), multiplying both sides by $e^{-im\theta}$ and integrating over the interval $(-\pi,\pi)$, a set of infinite algebraic equations to determine the coefficients A_n, B_n, C_n can be obtained.

3. Scattering of SH-waves by the Circular Lining Structure and the Crack near the Interface

As shown in Fig.1, the steady-state SH-wave $W^{(i)}$ incident on an elastic half space will cause the reflected wave $W^{(r)}$ from the half space surface. In the complex plane, $W^{(i)}$ and $W^{(r)}$ can be given by

$$W^{(i)} = W_0 \exp\{\frac{ik_1}{2}[(z-ih_1)e^{-i\alpha} + (\overline{z}+ih_1)e^{i\alpha}]\} \tag{9}$$

$$W^{(r)} = W_0 \exp\{\frac{ik_1}{2}[(z-ih_1)e^{i\alpha} + (\overline{z}+ih_1)e^{-i\alpha}]\} \tag{10}$$

Where α is incident angle.

The scattered wave $W^{(s)}$ excited by the circular lining structure in the half space can be described by expression (4), in which A_n are unknown coefficients. And the process of solving A_n is the same as that of the Green's function discussed in this paper. The displacement field of the elastic half space with a circular lining structure can be written as

$$W = W^{(i)} + W^{(r)} + W^{(s)} \tag{11}$$

For an arbitrary point in the elastic half space, the total stresses from the incident wave $W^{(i)}$, the reflected wave $W^{(r)}$ and the scattered wave $W^{(s)}$ can be solved. If the additional stresses with the same magnitude and opposite direction to the total stresses are applied on the same point, the ultimate stresses of this point are zero. Therefore, when a pair of forces with the same magnitude and opposite direction is loaded along the region where the crack wants to be set, the resultant forces on the region are zero, which can be thought as a crack.

Then the total wave field in domain I is

$$W^{(t)} = W^{(i)} + W^{(r)} + W^{(s)} - \int_{(b,-h_3)}^{(2a+b,-h_3)} \tau_{\theta z} G^{(t)} dz' \tag{12}$$

in which $G^{(t)}$ is the expression of Green's function (8).

4. Dynamic Stress Intensity Factor (DSIF)

The analyses illustrates that in local area near the crack tip, using the stress of a certain point which has minute distance to the crack tip as the nominal stress of crack tip field, the dynamic stress intensity factor according with the practical situation would be obtained[4]:

$$k_3 = \tau_{rz}\big|_{\vec{r}=\vec{r}_1} \Big/ \tau_0 Q \quad , \quad \tau_0 = \left|\tau_{rz}^{(i)}\right| = \mu_1 k_1 W_0 \tag{13}$$

Where $\tau_{rz}\big|_{\vec{r}=\vec{r}_1}$ stands for the nominal stress in the vicinity of crack tip; Q is the characteristic size and has the square root dimension of length.

5.0 Summary

According to the above theoretical derivation, numerical examples are provided to show the effects of various parameters on the DSIF. Here we give two kinds of dimensionless parameters for comparison: $\mu_1/\mu_2 = 2.9$, $k_2/k_1 = 1.5$, concrete lining structure in granite; $\mu_1/\mu_2 = 0.31$, $k_2/k_1 = 0.7$, steel lining structure in granite.

Figures 2~4 give the graphical results of DSIF. In Fig.2,a, the peak value of DSIF is gained when $k_1 a = 4.3$; but in b, the value of DSIF decreases acutely after $k_1 a = 1.5$, and it tends to be stable. As shown in Fig.3, the value of DSIF decreases with the increasing of the value of h_1, and it tends to be stable but with periodical undulation. In Fig.4, it can be seen that DSIF reduces periodically with the increasing of h_2, from the comparison of a and b, we can find that the endurance of DSIF is similar.

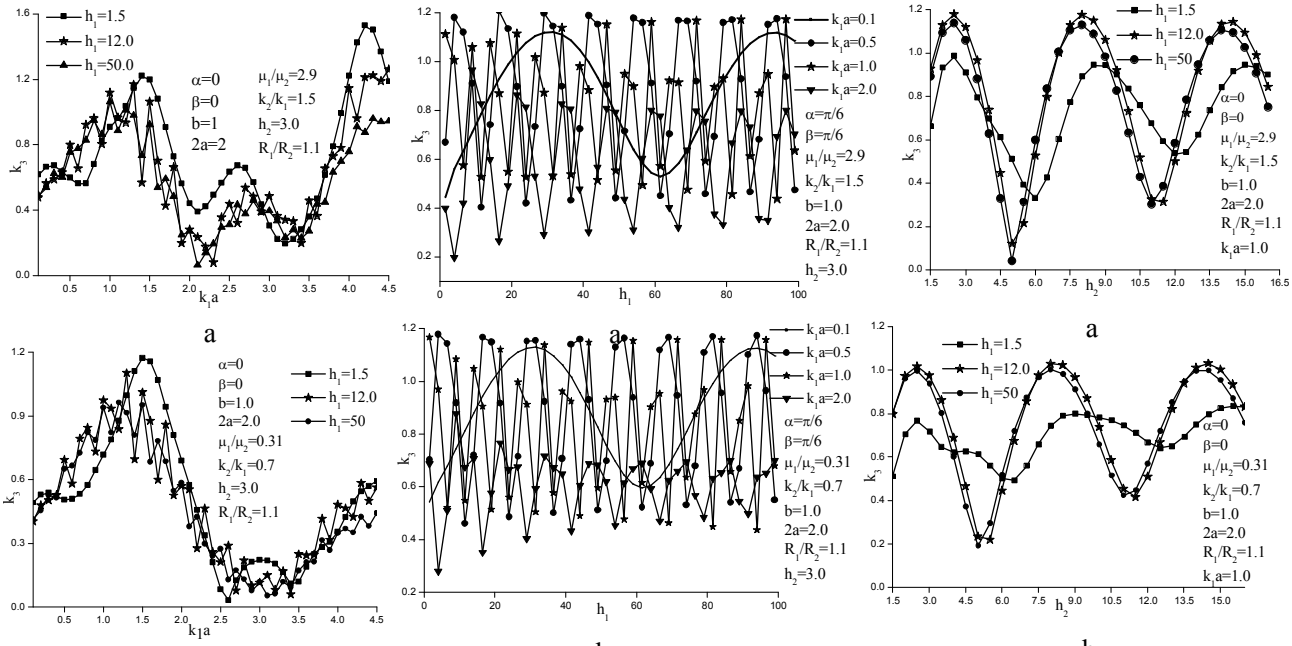

Fig.2 Fig.3 Fig.4

6.0 Reference

[1]. Qi Hui, Wang Yan, Liu Diankui. Dynamic analysis of shallow- embedded lining structure by incident SH-wave [J]. Earthquake engineering and engineering vibration. 2003,23(3):41-46.

[2]. Li Hongliang, Liu Diankui. Interaction of SH-wave by cracks with a circular inclusion. Journal of Harbin Engineering University.2004,25(5):618-622.

[3]. Liu Diankui, Lin Hong. Scattering of SH-waves by an Interface Linear Crack and a Circular Cavity near Bimaterial Interface. ACTA Mechanica Sinica. 2004,20(3):317-326.

[4]. Zailin Yang, Diankui Liu, Xiaotang Lv. Dynamics of a mode III crack impacted by elastic wave in half space with a removable rigid cylindrical inclusion [J]. 5th International Conference on Fracture and Damage Mechanics 2006, p679-682.

Key Engineering Materials Vols. 385-387 (2008) pp 277-280
© (2008) Trans Tech Publications, Switzerland
doi:10.4028/www.scientific.net/KEM.385-387.277

Damage Evolution of Laminated Composites using Continuum Damage Mechanics Incorporate with Interface Element

B. Mohammadi[1,a], H. Hosseini-Toudeshky[1,b], M. H. Sadr-Lahidjani[1,c]
[1]Aerospace Engineering Department & Centre of Excellence in Computational Aerospace Engineering
Amirkabir University of Technology, 424 Hafez Ave, Tehran, Iran
Fax: +98-21 6695 9020, Tel: +98-21 6454 3224
[a]Bijan_Moh@aut.ac.ir, [b]Hosseini@aut.ac.ir, [c]Sadr@aut.ac.ir,

Keywords: Layer-wise – Interface Element – Continuum Damage Mechanics – FEM

Abstract

In this paper, 3D continuum damage mechanics (CDM) incorporated with layer-wise theory and interface element is employed to investigate the progressive damage inside and between the laminate's layers under quasi-static axial loading. For this purpose, a finite element program is developed. To simulate the delamination, a quadratic interface element is used which is compatible with the 8-node numerical layers of layer-wise theory. Matrix cracking and delamination initiation and propagation of $[30_2/-30_2]$s angle-ply laminate are investigated and the obtained results are compared with the available experimental evidence.

Introduction

Today, the knowledge of the behaviour of fibrous composite laminates as far as damage evolution and the construction of reliable tools of analysis and prediction are necessary in order to optimize the use of such laminates. Initial damage such as matrix cracking can appear and begin to accumulate at stress levels much lower than the ultimate strength of the laminate. Delamination may form at the intersection of an existing matrix crack and an adjacent ply. The tendency for the delamination to propagate to significant length depends upon the laminate configuration. Small delaminations may appear in an angled ply group at the free edge of the laminate. The extent of delamination is initially bounded by an adjacent matrix crack and the laminate edge. Propagation of the delamination typically leads to immediate laminate failure. [1]

CDM has been widely used in the modeling of the progression of distributed microscopic damage in composite laminates. Interface elements have also been used to predict both initiation and propagation of delaminations. Implementing of an interface element with layer-wise discretization in CDM is a new approach in damage analyses of laminates which is presented in this paper. Using CDM, distributed microscopic damage, and matrix cracking can be quantified by employing of a damage tensor field that describes the orientation and density of microcracks inside the layers. In addition, the interface layer with de-cohesive constitutive law is used to predict the delamination progress in the laminates. For this purpose, a finite element program was developed using an eight-node 2D layered element including full layer-wise plate theory with interface element assumptions to perform 3D damage analyses. Matrix cracking, delamination initiation and propagation of an angle-ply laminate are predicted and compared with the available experimental evidence.

CDM in Composite Laminate

In the CDM, damage variables can be presented through the internal state variables of thermodynamics for irreversible processes in order to describe the effects of damage and its microscopic growth on the macro-mechanical properties of the materials. The damage tensor that is capable of accurately describing damage mechanisms such as fiber breakage, fiber/matrix debonding, and matrix cracks is a symmetric 2^{nd} order tensor φ whose principal directions are assumed to coincide with the principal material directions. The i^{th} eigenvalue, φ_i, represents the effective fractional reduction in load carrying area on planes that are perpendicular to the i^{th} principal material direction as shown typically in Figure 1.

To define Stress transformation in a general state of deformation and damage, the effective stress tensor is related to the Cauchy stress tensor by the following linear transformation:

$$\bar{\boldsymbol{\sigma}} = \mathbf{M}(\boldsymbol{\varphi}) : \boldsymbol{\sigma} \tag{1}$$

where $\mathbf{M}$ is a fourth-order linear transformation operator called the damage effect tensor. In the framework of irreversible thermodynamics, it is possible to decouple the Helmholtz free energy, ψ, into a potential function for each corresponding internal-state variable. Therefore, an analytical expression for the thermodynamic potential can be given as sum of two terms, the strain energy, $E(\boldsymbol{\varepsilon}^e, \boldsymbol{\varphi})$, and dissipation energy, $\prod^d(\kappa)$, as follows:

$$\rho\psi = E(\boldsymbol{\varepsilon}^e, \boldsymbol{\varphi}) + \prod^d(\kappa) \tag{2}$$

where κ is overall accumulated scalar damage parameter. The state laws can be written from the thermodynamic potential equation in the following form:

$$\boldsymbol{\sigma} = \rho\frac{\partial\psi}{\partial\boldsymbol{\varepsilon}^e}; \quad \mathbf{Y} = -\frac{\partial\psi}{\partial\boldsymbol{\varphi}}; \quad K = -\frac{\partial\psi}{\partial\kappa} \tag{3}$$

where $\boldsymbol{\sigma}$, $\mathbf{Y}$, and K are stress tensor, damage conjugate force tensor, and isotropic hardening/softening conjugate relation, respectively. Using these equations, damage potential and damage evolutions can be defined. Analogous to plasticity, it is postulated that damaging state can be distinguished from non-damaging state on a local basis by a damage surface of:

$$Q = q(\mathbf{Y}, \kappa) = \sqrt{\mathbf{Y} : \mathbf{J} : \mathbf{Y}} - \sqrt{|\mathbf{H} : \mathbf{Y}|} - (K(\kappa) - K_0) \tag{4}$$

where $K(\kappa)$ is damage hardening/softening rule, and K_0 is the initial damage threshold at which damage begins to occur. The Y_i are eigenvalues of damage conjugate force tensor defied in Eq. (3) The $\mathbf{J}$ and $\mathbf{H}$ tensors are determined by available data on a single composite lamina, and K_0 is the initial damage threshold. Q<0 indicates a non-damaging state, Q=0 indicates a damage inducing state, and Q>0 is understood to be inadmissible. Non-associative damage can be used here to derive the evolution equations for the constitutive model which the damage potential, G, is not equal to the damage criterion, Q.

$$G = g(\mathbf{Y}, \kappa) = \sqrt{\mathbf{Y}.\mathbf{J}.\mathbf{Y}} - (K(\kappa) - K_0) \tag{5}$$

In addition, Damage evolution equations are obtained from dissipation potential function defined by the thermodynamic forces. Using the theory of functions of several variables, damage Lagrange multiplier, $\dot{\lambda}^d$ is utilized to determine the evolution equations for the damage tensor, and the corresponding hardening state variables, as follows:

$$\dot{\boldsymbol{\varepsilon}}^{id} = +\frac{\partial G}{\partial\boldsymbol{\sigma}}\dot{\lambda}^d; \quad \dot{\boldsymbol{\varphi}} = -\frac{\partial G}{\partial\mathbf{Y}}\dot{\lambda}^d; \quad \dot{\kappa} = -\frac{\partial G}{\partial K}\dot{\lambda}^d; \tag{6}$$

The implicit backward Euler technique is also used to develop an efficient and more accurate algorithm for stress integration and returning on the damage surface.

Interface in Layer-wise plate theory

In the layer-wise plate theory, it is assumed that the displacements, material properties and element geometry can be approximated by a sum of conveniently separable interpolation functions which each individual 3-D interpolation function can be written as the product of a 2-D and 1-D interpolation functions [3]. The transverse strains are assumed as a piecewise continuous distribution through the laminated thickness. The displacement filed is expressed in the form of:

$$u(x,y,z) = \sum_{m=1}^{n} U^m(x,y)\boldsymbol{\phi}^m(z); \quad v(x,y,z) = \sum_{m=1}^{n} V^m(x,y)\boldsymbol{\phi}^m(z); \quad w(x,y,z) = \sum_{m=1}^{n} W^m(x,y)\boldsymbol{\phi}^m(z) \tag{7}$$

where (u, v, w) are the displacement components, and U^m, V^m, and W^m are unknown displacement variables of each numerical layer, and $\boldsymbol{\phi}^m$ are the global interpolation functions for the discretization of the displacements through the thickness. A typical laminates with interface layers in layer-wise discretization is shown in Figure 2. The interface element is implemented as a very thin numerical layer which behaves different from typical numerical layers. As far as the interface elements contains the out-of-plane stresses only, the in-plane stresses and strains are excluded from the strain energy term in the stiffness matrix calculation of the interface layers.

The constitutive law of interface layers must be formulated using a differential equation in which the response of the structure can be calculated for each load increment. Eq. (8) describes the variation of interlaminar stress components with respect to nonlinear state variables.

$$\boldsymbol{\sigma} = \mathbf{C}\left(\boldsymbol{\varphi}^{\mathrm{Int}}\right)\boldsymbol{\varepsilon} \quad ; \; d\boldsymbol{\sigma} = \mathbf{C}\left(\boldsymbol{\varphi}^{\mathrm{Int}}\right)d\boldsymbol{\varepsilon} + \boldsymbol{\varepsilon}\frac{\partial \mathbf{C}\left(\boldsymbol{\varphi}^{\mathrm{Int}}\right)}{\partial \boldsymbol{\varphi}^{\mathrm{Int}}} d\boldsymbol{\varphi}^{\mathrm{Int}} . \tag{8}$$

where $\boldsymbol{\sigma}$, $\mathbf{C}(\boldsymbol{\varphi})$, $\boldsymbol{\varphi}^{\mathrm{Int}}$, and $\boldsymbol{\varepsilon}$ are stress, interface penalty stiffness matrix in damage state, damage tensor, and strain tensor of interface layer, respectively. For an intact interface, delamination initiates when the interlaminar stresses or a combination of them reach a limit. For an existing delamination, a fracture mechanics approach has proved successful in dealing with its propagation. Treating delamination as a damage process in the context of continuum damage mechanics involves two aspects, the initiation and the growth of the damage. Some justifications of the existence of such a surface in stress space can be found in literature. Combination of the two concepts can be used to present a model for establishing damage evolution law in the interface layer [4]. Then, the damage surface in the σ and $\mathbf{G}$ space is constructed as follows:

$$g(\sigma, G) = \left(\frac{\langle \sigma_{33} \rangle}{\sigma_{33c}}\right)^2 + \left(\frac{\sigma_{23}}{\sigma_{23c}}\right)^2 + \left(\frac{\sigma_{13}}{\sigma_{13c}}\right)^2 - \left[1 - \left(\frac{G_I}{G_{IC}}\right)^2 + \left(\frac{G_{II}}{G_{IIC}}\right)^2 + \left(\frac{G_{III}}{G_{IIIC}}\right)^2\right] = 0 \tag{9}$$

where σ_{ij} are stress components of interface layer, and $\mathbf{G_i}$ (i=I, II, III) are energy release rate components, and the subscript *c* denotes the critical value. Also, $\langle \sigma_{33} \rangle$ means that this term is omitted for compression stress. Evolution of interface damage tensor and corresponding stress relaxation are governed by the normality and flow rules, and consistency condition which are not explained here due to the pages limitation.

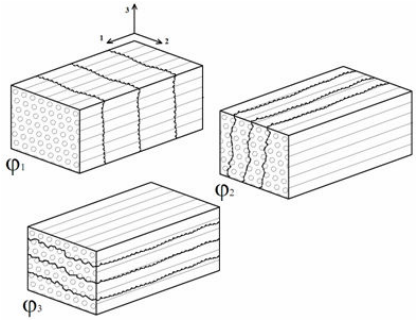

Figure 1. Typical damage eigenvalues of φ1, φ2 and φ3 in the lamina level

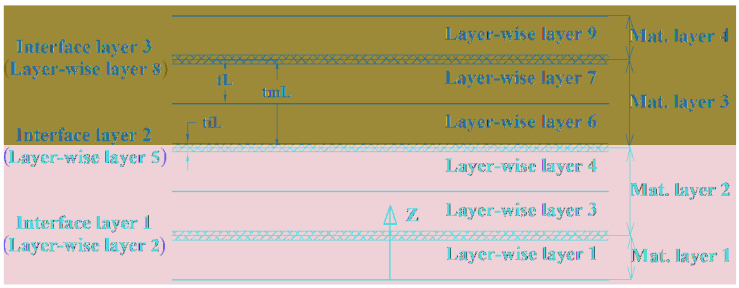

Figure 2. Typical laminate with interface elements

Finite element Analysis

In the incremental form, the weak form of the equilibrium equation with the elastic-damaged material stiffness matrix is used. In the integration scheme, for each integration point in an inelastic state, the implicit backward Euler elastic predictor-inelastic corrector algorithm is used to compute the stresses at numerical or interface layers. The governing equation can be linearized consistently and solved within an incremental iterative Newton-Raphson solution procedure. All stresses and strains quantities are calculated and monitored at each Gaussian integration point and therefore the damage occurrence can be determined at such points. Then, the nodal forces are produced by the stress field that satisfies the elasto-damage conditions. Then the stress and strain terms are adjusted until satisfaction of the inelastic criterion.

The developed finite element program was used to perform the matrix cracking, delamination initiation and propagation of $[30_2/\text{-}30_2]$s graphite/epoxy laminate. The length and width of the lamiante are L=152.4 *mm* and W=44.45 *mm* respectively. Elastic constants for the un-damaged T300/5208 graphite-epoxy are, E_{11}=137.11GPa; $E_{22}=E_{33}$=9.58GPa; $\nu12=\nu13=\nu23$=0.28; and $G_{12}=G_{13}=G_{23}$=4.48GPa with the ply thickness of 0.127 *mm*. Strength and critical energy release rate values of the interface layer are σ_{23c}=35MPa, σ_{13c}=70MPa, σ_{33c}=59MPa, $G_{II}=G_{III}$=0.3 N/mm, and G_I=0.275 N/mm. The diametric material damage tensors, **J** and **H**, can be calculated for a single lamina using Barbero [2] approach as follows: J_{11}=0.15573202e-14; J_{22}=0.50661122e-13;

J_{33}=0.16762622e-13, H_{11}=0.15785511e-6; H_{22}=-0.45710155e-7; H_{33}=-0.30425396e-7. The Hardening constants, $c_1^d = -0.2, \text{and } c_2^d = 9.0e5$ and damage threshold, K_0=0.23, can be determined using the standard in-plane shear test results of single lamina. Due to the symmetric condition of the lay-ups, half of the laminates in the thickness direction was modeled. To predict the high stress gradient near the free edges, very fine meshes are used in these areas. Six uniform elements along the x-direction, 18 non-uniformly distributed elements in the y-direction and 10 numerical layer discretizations through the thickness are used.

Results and Discussions

Figure 3 shows that considering the damage condition in the analysis induce significant non-linear behavior on the average axial stress versus applied axial strain. The non-linear behavior and the stiffness reduction in the results are mainly due to the propagation of matrix cracking. During the solution procedure, it has been observed that matrix cracking and edge shearing delaminations are increased. In a certain load increment, the global behaviour of the laminate becomes unstable due to the complete damage of the interface layer in most of the elements. Therefore, the solution of the problem diverges indicating the unstable delamination propagation. The failure load calculated from the present study is larger than that obtained from the experiments. It can be due to the existence of errors in the used material data and simulation. In the present study, 10 numerical layer discretizations were considered to reduce the CPU time. It can be increased to improve the results. Figure 4 shows the variations of various stiffness degradations along the thickness of the laminate near the free edge at almost the failure load. It shows that the stiffness reductions are not very large except for G_{13} at the interface layer which tend to zero and indicating the complete damage of the interface or shear delamination. The stiffness reduction of E_{22} along the laminate thickness is larger than the others showing the matrix crack propagations.

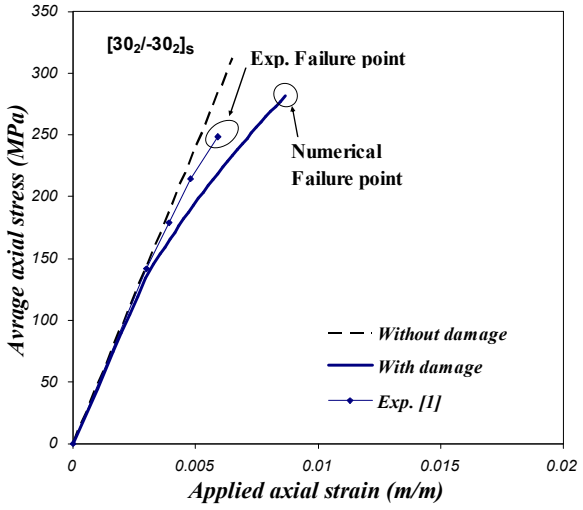

Figure 3. Comparison of numerical and experimental laminate responses

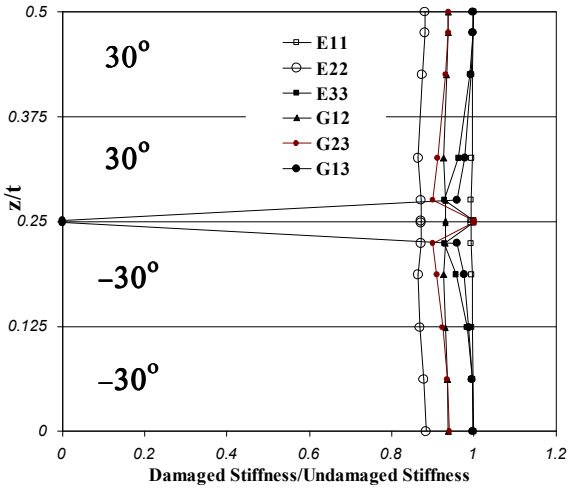

Figure 4. Through the thickness Stiffness degradations near the laminate free edge

Conclusion

In this paper, a new approach of implementing an interface element with layer-wise discretization in continuum damage mechanics was employed for damage analyses of laminates. For this purpose, a finite element program was developed to perform 3D damage analyses. It was shown that using this new approach, matrix cracking, edge delamination, laminate's response and final failure load of the laminates can be predicted.

References

[1] Herakovich C.T. (1998), Mechanics of Fibrous Composites., John Wiley, New York.
[2] Barbero E, Lonetti P. (2002), *J. Composite Mater*, Vol. 36(8), pp. 941-962.
[3] Reddy J. N., (1987), *Commun Appl Numer Methods*, Vol. 3, pp. 173-180.
[4] Zou Z., Reid S.R., Li S.,(2003), *J. of the Mechcs and Physics of Solids*, Vol. 51, pp. 333-356.

Key Engineering Materials Vols. 385-387 (2008) pp 281-284
© (2008) Trans Tech Publications, Switzerland
doi:10.4028/www.scientific.net/KEM.385-387.281

Simple Approach for Computing Chloride Diffusivity of (Non)Carbonated Concrete

In-Seok Yoon[1,a]

[1] Dept. of Civil Eng., Induk Institute of Technology, Seoul, Korea

[a] isyoon@induk.ac.kr

Keywords: Service Life, Chloride Diffusivity, Carbonation, Porosity, Tortuosity

Abstract. The purpose of this study is to establish a simple approach to compute the chloride diffusivity of (non)carbonated concrete. The chloride diffusivity of concrete should is defined, based on engineering and scientific knowledge of cement and concrete materials. In this paper, parameters affecting the chloride diffusivity, such as the diffusivity in pore solution, tortuosity, micro-structural properties of hardened cement paste, volumetric portion of aggregate, are taken into consideration in the calculation of the chloride diffusivity of noncarbonated concrete. For carbonated concrete, reduced porosity due to carbonation is calculated and used for calculating the chloride diffusivity. The results are compared with experimental data and previous research works.

Introduction

Chloride diffusivity is considered as the most crucial parameter for the determination of the service life of concrete and its magnitude have been regarded as an arbitrary constant or determined from regression analysis obtained from experimental results for short-term. A lot of models for the chloride diffusivity of concrete have been developed with various approaches: from empirical solution based on the experimental results to comprehensive multi-scale model with high resolution digital analysis. One of the practical and realistic solutions is to express as a simple formulation with multi-factors regarded as an individual influencing effect. However, the effects of the influencing factors on the chloride diffusivity of concrete were ambiguous in previous studies.[1] Furthermore, the majority of these researches didn't deal with this issue in combination with carbonation of concrete, although carbonation affects the chloride diffusivity of concrete significantly. In this paper a simple model depicting the time evolution of the chloride diffusivity of (non)carbonated concrete is presented.

Material Modeling of Chloride Diffusivity

Chloride diffusivity. One of the practical and reasonable ways to compute the chloride diffusivity of concrete is to consider multi-factors function. However, the solution didn't clearly depict the effect of some important factors such as the temperature and its effect on the viscosity. These have been only depicted using the temperature equation of *Arrhenius* type in most of all researches. This study suggests a new analytical approach with a multi-factor function as illustrated in Fig. 1. A function of multi-factors might be a function of chloride diffusivity in bulk fluid, $F(D_o(S,T)$, a function of pore structural properties, $F(St_{micro})$, a function of tortuosity, $F(\tau_T^2)$, a function of hindrance effect, $F(H)$. In what follows a description of these factors is given.

$$D_{Cl(cp)} = F(D_o(S,T)) \cdot F(St_{micro}) \cdot F(\tau_T^2) \cdot F(H) \quad (1)$$

For saturated concrete, the flow media of chloride ions can be the bulk pore water as the ions can flow through water-filled pores. In this respect, ion diffusivity in bulk fluid can be estimated as Wilke et al[2]:

$$D_o = \frac{1.173 \times 10^{-16} \cdot AF\sqrt{\phi \cdot M}}{\eta \cdot V_m^{0.6}} \tag{2}$$

in which, D_o : ion diffusivity in liquid (m^2/s), T : temperature (K), AF : association factor for the solvent (= 2.26 for water), M : molecular weight of the solvent(= 18.1 g/mol for water), η : viscosity of the solvent (Pa.s), V_m : molar volume of the solute at its boiling point (m^3/K mol).

Microstructural Properties of cementious material. Porosity and pore size distribution function is necessary to consider the effect of micro-structural properties of cementitious materials on chloride diffusion. Maekawa et al.[3] suggested porosity distribution function as;

$$dV_p = Br \exp(-Br)\, d \ln r \tag{3}$$

in which, V_p : fractional pore volume of the distribution up to pore radius r, B: sole porosity distribution parameter, which is a peak point of porosity distribution of the cement paste on a logarithmic scale. Eq.(3) can be rewritten as Eq. (4). If the total porosity ϕ is known, sole porosity distribution parameter B can be calculated from Eq. (5). The total porosity ϕ can be calculated by HYMOSTRUC[4].

$$\phi = B\int_0^\infty \exp(x) \cdot \exp\{-B \cdot \exp(x)\}\, dx \tag{4}$$

Tortuosity. It is quite difficult to define the tortuosity as a specific value. Fig. 1 (a) displays the possible morphology of idealized cement core and Fig. 1 (b) represents cement core existed in one cell, as a formation of two-dimensional particle. In principal, the morphology of cement core is similar to the shape of circle, however, the shape is transformed into a rectangular type in order to simplify the fluid flow, as shown in Fig. 1 (c).[5] The area of the rectangle (A_{sq}) should be equal to that of a circle (A_{cir}) because porosities (b) and (c) should also be equal.

Since the shape of real cement core is similar to circle, a shape function considers differences between rectangle and circle should be introduced. That is, the amount of porosity should be same in (b) and (c) of Fig. 4. Since fluid should flow along the geometric figure of cement core, the ratio of geometric figure of rectangle to that of circle should be considered as a shape function. Considering the shape function, averaged tortuosity can be thus defined as;

$$\tau_T = \sqrt{\pi}\,\frac{\sqrt{1-\phi}\sqrt{\left(\frac{1}{\sqrt{1-\phi}-1}\right)^2 + \frac{1}{4}} + \frac{1}{2}\sqrt{1-\phi} + 1}{4} \tag{5}$$

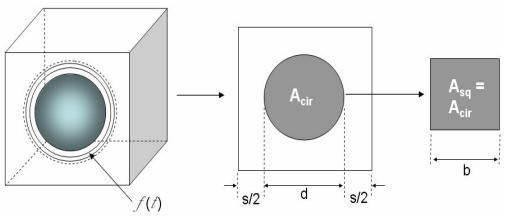

(a) (b) (c)

Fig. 1 Morphology of idealized cement core and transformation of circle shape into rectangle

Effect of hindered diffusion. The forth term of Eq. (1), (d) $F(H)$, means hindrance effect due to narrow pore diameter. As the molecular diameter of the solute approaches the diameter of the pore, the diffusive transport of the solute through the solvent is hindered by the presence of the pore and the pore wall. The function of the hindered diffusion can be expressed as Eq. (16). Two correction factors, $f'(\varphi)$ and $f''(\varphi)$, are theoretically bounded by 0 and 1. Furthermore, both correction factors are function of the reduced pore diameter φ (d_s / d_{pore}). d_s means solute molecular diameter ($\approx$4Å for chloride ions) and d_{pore} means diameter of pore. The first correlation factor, partition coefficient, is based on simple geometrical arguments, as described in Eq. (18). For the

second correlation factor, Renkin equation, which is reasonable for $0 \le \varphi \le 0.6$, is used in Eq. (19).[6] These expressions for the hindrance effects would be useful to depict delayed diffusion rate which is occurred in consequence of narrow pore diameter and collision of chloride ion molecules with each others.

$$F(H) = f'(\varphi) f''(\varphi) \tag{6}$$

$$f'(\varphi) = \frac{\pi(d_{pore} - (t_d + d_s))^2}{\pi(d_{pore} - t_d)^2} = (1-\varphi)^2 \tag{7}$$

$$f''(\varphi) = 1 - 2.104\varphi + 2.09\varphi^3 - 0.95\varphi^5 \tag{8}$$

Effect of aggregate. An interactive behavior in compliance with the presence of aggregates should be taken into accounted in the calculation of composite diffusivity. In this study, EMT (effective medium theory) is used to convert the diffusivity of cement paste into that of concrete.[7] EMT has been developed for the estimation of the overall conductivity of a multiphase material originally, however, this can be applied to variety of situations in disordered or random networks. Based on the EMT model, the effective diffusivity can be expressed as:

$$F(C_{comp}) = \left(\frac{D_2}{k}\right)\left(\frac{1}{1+V(1-k)/k}\right)\left(\delta + \sqrt{\delta^2 + \frac{1}{2}k\varsigma}\right) \tag{9}$$

in which, D_1, D_2: the diffusivities in the two distinct components in the system, V_1, V_2 : the volume fractions of the different components in the multiphase material and may be replaced by $1 - V$ and V, respectively ($V_1 = 1 - V$, $V_2 = V$), C_1, C_2 : the concentrations of the species in the different regions, $k = C_1 / C_2$, a measure of the distribution of the diffusing species between the components in the composite material. When k is equal to 1, a uniform distribution of the diffusion species exists in the material, $\varsigma = D_1 / D_2$, $\delta = (3V - 1 + k\varsigma(2-3V))/4$. The chloride diffusivity of aggregate is assumed to be 1×10^{-12} cm^2/s.

Decreased porosity of concrete. Carbonation of concrete leads to a change of porosity and this can have significant impact on chloride diffusivity. Papadakis [8] had suggested the development of major constituents of cement paste in order to estimate the performance of concrete versus time. Carbonation usually proceeds in the volume of concrete in the form of a front, separating a completely carbonated region from the rest, in which carbonation has not started yet. In this latter region, the value of decreased porosity due to carbonation ($\Delta\phi_c$) is zero, whereas in the former, $\Delta\phi_c$ is approximately equal to

$$\Delta\phi_c = [\mathrm{Ca(OH)_2}]\ \Delta\overline{V}_{CH} + [\mathrm{CSH}]\ \Delta\overline{V}_{CSH} \tag{10}$$

in which, the concentrations of $Ca(OH)_2$ and C-S-H mean those at the completion of hydration and $\Delta\overline{V}_{CH}$ and $\Delta\overline{V}_{CSH}$ equal 3.85×10^{-6} m^3/mol, 15.39×10^{-6} m^3/mol, respectively.

Results and Discussions

Fig. 2 shows the result of calculation of the chloride diffusivity of concrete. The chloride diffusivity decreases significantly after 28 days. The trend shows a noticeable decrease since then, however, this

continues slightly. Fig. 3 provides the comparison of chloride diffusivity of this analytical formulation and experimental data of Van Dalen [9]. The analytical formulation as proposed in this paper shows good agreement with experimental data approximately. In this figure, it is clear that the densification of the microstructure of concrete due to ongoing hydration of cement should lead to a significant reduction of the chloride diffusivity of concrete. Fig. 4 shows the ratio of diffusivity of carbonated concrete to that of noncarbonated concrete. It is clear that carbonation can influence on diffusivity of concrete greatly.

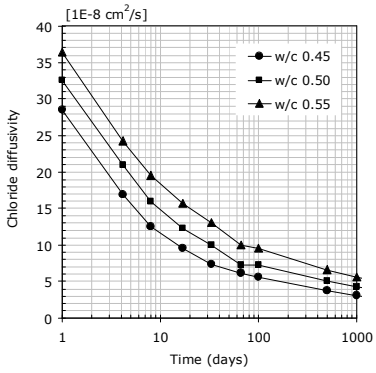

Fig. 2 Chloride diffusion coefficient of concrete

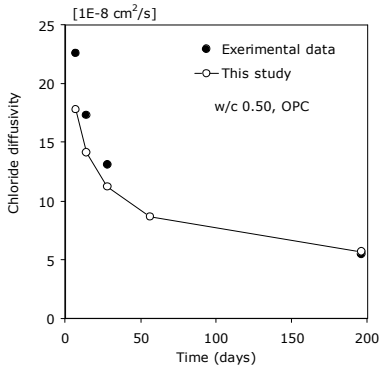

Fig. 3 Comparison of calculated and measured D (in concrete)

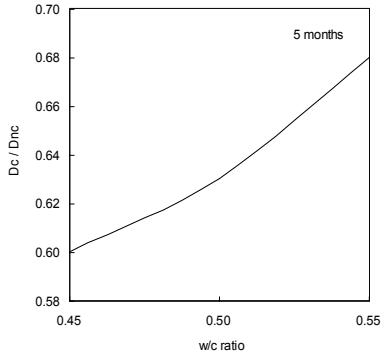

Fig. 4 D_c / D_{nc} with w/c ratio

Summary

The chloride diffusivity is of particular important material parameter for calculating the service life of marine concrete. A comprehensive approach for formulation with the multi-factor function is constructed, considering many affecting factors. The proposed formulation is simple, yet realistic which can be used for reasonable durability design of concrete structures.

References

[1] Saetta, A. V., Scotta, R.V. and Vitaliani, R. V., "Analysis of Chloride Diffusion into Partially Saturated Concrete," *ACI Materials Journal*, **90**(5), 441-451, 1993.

[2] Wilke, C. R. and Chang, P., "Correlation of Diffusion Coefficient in Dilute Solutions," *Journal of American Institute of Chemical Engineering*, 1, 1995.

[3] Maekawa, K. Chaube, R., and Kishi, T., "Modeling of Concrete Performance: Hydration, Microstructure Formation and Mass Transport," E & FN Spon, 1999.

[4] Breugel, K. Van, Simulation of Hydration and Formation of Structures in Hardening Cement-Based Materials, Ph.D Thesis, Delft University of Technology, The Netherlands, 1991.

[5] Yu, B. O. and Li, J. H. (2004), "A Geometry Model for Tortuosity of Flow Path in Porous Media," Chin. Phys. Lett., Chinese Physical Society, **21**(8), pp.1569-1571, 2004.

[6] Welty, J. R., Wicks, C. E., Wilson, R. E. and Rorrer, G., "Fundamentals of Momentum, Heat, and Mass Transfer," 4th Edition, John Wiley & Sons, 2001.

[7] Davis, H. T., "The Effective Medium Theory of Diffusion in Composite Media," *Journal of American Ceramic Society*, **60**, pp.499-501, 1997.

[8] Papadakis, V. G., Vayenas, C. G. and Fardis, M. N., "Physical and Chemical Characteristics Affecting the Durability of Concrete," *ACI Materials Journal*, **88**(2), pp.186-196, 1991.

[9] Dalen, S. H. Van, *Onderzoek naar de RCM methode* (in Dutch), MSc-Thesis, Delft University of Technology, The Netherlands, 2005.

Key Engineering Materials Vols. 385-387 (2008) pp 285-288
© (2008) Trans Tech Publications, Switzerland
doi:10.4028/www.scientific.net/KEM.385-387.285

Statistical Analysis for Fatigue Life of Concrete

Dongfu Zhao [1, a], Weiwei Kong [1, b], Xiaoruan Song[2]

[1]Department.of Civil Engineering, Beijing Institute of Civil Engineering and Architecture, Beijing 100044,China; [2]State Key Laboratory of Coastal Engineering, Dalian University of Technology, Dalian 116024, China zhaodongfu@bucea.edu.cn, kongweiwei2008@sina.com

Key words: fatigue life, statistical test, fuzzy optimization, variance analysis, sample size

Abstract. Statistical analysis is presented for 108 groups of fatigue test data of concrete, including tests of abnormal value, variance and distribution-fitted with fuzzy optimization; analysis of variance, sample size and error. It is chiefly concluded that effect of stress level of repeated loading on the fatigue life of concrete is much more significant than that of stress rate and relative stress amplitude, and effect of stress rate and relative stress amplitude are of the same significance; Relationship of sample size, relative error and significant level is also presented; fatigue life of concrete is more fitted for lognormal distribution than Weibull distribution. Suggestion for relevant code, standard and regulation are presented.

Introduction

Concrete is compound material, the fatigue test data are very discrete, as well as the fatigue life, so statistical method is usually employed to conduct analytical study. But the present statistical survey is basically based on test data from one or two laboratories , synthesis statistical analysis about massive test data has not been conducted. In this paper, 108 groups of fatigue life test data[1-11] of concrete are selected for synthesis statistical analysis. Firstly, statistical tests are conducted including test of the abnormal value, the variance and the distribution fitting, the optimum distribution law of fatigue life of concrete is ascertained. Secondly, variance analysis is presented to ascertain the influence significance degree to fatigue life caused by stress level S, stress rate R and relative stress amplitude $\Delta S'$. Finally, the error and sample size analysis are conducted, error level, sample size and significance level relations of test data are analyzed.

Statistical test of fatigue life of concrete

Tests of abnormal value

Grubbs method[12] is employed to examine one by one of each group of test data: for the figure $x_1, x_2, ..., x_n$, which fit normal distribution $N(\mu, \sigma^2)$, take $G = |x_d - \overline{x}_n| / S_n$ as the statistical variable to be tested. 108 groups of test data[1-11] above mentioned are selected for abnormal value test, take significance level $\alpha = 0.05$, four abnormal values are found, their $G \succ G_{\alpha,n}$. They are abandoned in the following statistical analysis.

Variance test

Bartlett test method[13] is used for variance test of the 108 groups of test data, their stress level S=0.95, 0.9, 0.85, 0.8, 0.75, 0.7, 0.65, 0.6. Take α=0.01, three groups of data are found remarkable different from others, their test results are $B = 35.678 \succ \chi^2 = 30.578$; $B = 64.226 \succ \chi^2 = 37.566$;

The project is financed by Ph.D fund of BUCEA

$B = 25.312 \succ \chi^2 = 18.475$. They are eliminated, so the following analysis is conducted for the residual 105 groups of test data.

Fuzzy optimization for distribution fit

For fatigue life of concrete, lognormal distribution and Weibull distribution are generally proposed to fit test data. The two distributions are compared by fuzzy optimization[14], parts of results for different stress levels are summarized in table 1, where z_1 is the membership degree to optimum of lognormal distribution, and z_2 is that of Weibull distribution. All results indicated that lognormal distribution is more flexible to fit test data.

Table 1 Distribution-fitted with optimization result

literature [3]						literature [7]						literature [9]					
S=0.90		S=0.80		S=0.70		S=0.85		S=0.75		S=0.65		S=0.85		S=0.75		S=0.675	
z_1	z_2	z_1	z_2	z_1	z_2	z_1	z_2	z_1	z_2	z_1	z_2	z_1	z_2	z_1	z_2	z_1	z_2
0.6	0.4	0.6	0.4	0.5	0.5	0.43	0.57	0.77	0.23	0.69	0.31	0.5	0.5	0.67	0.33	0.33	0.67

Variance analysis

The main purpose of variance analysis[15] in this paper is to judge the factorial effect, namely judging the influence and influence degree of different stress level S, stress rate R, relative stress amplitude $\Delta S'$ and so on factors to fatigue life of concrete. Firstly, consider the influence of stress level and stress rate, take test data in literature [1] as an example, take S=0.95, 0.75 , R=0, 0.2, 0.4. Its variance analysis process and result are summarized in Table 2. And for test data in literature [3], take R=0, 0.2, S=0.9, 0.7, the variance analysis process and result are summarized in Table 3.

Table 2 Variance analysis of test data from literature [1]

Variance origin	square sum	freedom degree	equal square	F value	$F_{a,0.05}$
stress level	12.80	1	12.80	45.71	4.28
stress rate	1.10	2	0.55	1.96	3.42
model error	0.55	2	0.28	0.97	3.47
repeat error	6.00	21	0.29	___	___
residual error	6.54	23	0.28	___	___
sum	20.45	26	___	___	___

Table 3 Variance analysis of test data from literature [3]

Variance origin	square sum	freedom degree	equal square	F value	$F_{a,0.05}$
stress level	63.98	1	63.98	533.17	4.24
stress rate	2.56	1	2.56	21.33	3.24
model error	0.28	1	0.28	2.55	4.26
repeat error	2.61	24	0.11	___	___
residual error	2.88	25	0.12	___	___
sum	69.43	27	___	___	___

Secondly, the influence of stress level S and relative stress amplitude $\Delta S'$ to fatigue life is compared. Analysis results indicated that influence of S and $\Delta S'$ to fatigue life is both remarkable,

but the influence of S is more remarkable that of $\Delta S'$.

Therefore, the influence of stress level S to fatigue life of concrete is the most remarkable. The influence of stress rate R and relative stress amplitude $\Delta S'$ takes second place, R and $\Delta S'$ have almost the same influence degree. Present code[16] in china only considers influence of S and R for fatigue problem of concrete, influence of $\Delta S'$ is ignored, which needs further study.

Sample size and error analysis

Concrete is compound material, its strength is very dispersed, which causes the variability of its fatigue life to be bigger, this is the primary reason for which fatigue life more disperses. So, to determine such dispersed strength and the fatigue life of concrete, massive experiments are needed. But as a result of the condition limitation, it is impossible to perform so many experiments. This requests determining reasonably the least test sample under the corresponding condition. According to statistics principle [14], $n = \delta t_{n-1,1-\alpha/2} / e$, where $e = \left(\overline{x} - \mu\right) / \overline{x}$ is the relative error, $\delta = s / \overline{x}$ is the coefficient of variation.

105 groups of test data are analyzed. The results are summarized in table 4.

Table 4 Relative error for corresponding coefficient of variation, sample size

sample size n	coefficient of variation δ	$t_{0.05,n-1}$	relative error e
3	0.008~0.529	4.303	0.019~1.314
4	0.027~0.325	3.182	0.044~0.517
5	0.016~0.344	2.776	0.020~0.427
6	0.091~0.313	2.571	0.096~0.328
7	0.092~0.328	2.447	0.085~0.303
9	0.055~0.303	2.306	0.043~0.233
10	0.035~0.279	2.262	0.025~0.199

The results demonstrated, when sample size $n \geq 5$, relative error $e \leq 50\%$; when $n \geq 7$, $e \leq 30\%$; when $n \geq 10$, $e \leq 20\%$.

Conclusions

In this paper, through statistical analysis for massive fatigue test data of concrete under uniaxial constant-amplitude fatigue load, the following conclusions are conducted:

1. In the 108 groups of fatigue test data, 4 abnormal values are found. Therefore, in fatigue experiments of concrete, the abnormal value test for each group of test data is necessary, and the abnormal value should be eliminated.

2. In the 108 groups of test data, 3 groups of test data have the significance difference in variance test, accounts for 2.8%. Therefore, variance test should be conducted for test data under similar experiment condition.

3. By the fuzzy optimization, lognormal distribution is more flexible than Weibull distribution to describe the fatigue life distribution rule of concrete.

4. The variance analysis result indicated that, the influence of stress level S to fatigue life of concrete is the most remarkable. The influence of stress rate R and relative stress amplitude $\Delta S'$ takes second place, R and $\Delta S'$ have almost the same influence degree.

5. Error and the sample size analysis result indicated that, When the sample size $n \geq 5$, relative error $e \leq 50\%$; when $n \geq 7$, $e \leq 30\%$; when $n \geq 10$, $e \leq 20\%$. In fatigue experiment of concrete, such problem should be taken into account.

References

[1] VAN LEEUWEN IR.J. Miner's rule with respect to plain concrete [J]. Heron, 1979, 24(1): pp12-25

[2] CORNELISSEN H.A.W. Fatigue failure of concrete in tension [J]. Heron, 1984, 29(4): pp59-64

[3] ZHANG B, PHILLIPS D.V. Sustained loading effect on the fatigue life of plain concrete [J]. Magazine of Concrete Research, 1998,50(3): pp263-278

[4] TEPFERS R, HEDBERG B, SZCZEKOCKI G. Absorption of energy in fatigue of plain concrete [J]. Materials of Construction, 1997,17(1): pp59-64

[5] TAN TENG HOOI. Effects of passive confinement on fatigue properties of concrete [J]. Magazine of Concrete Research, 2000,52(1): pp7-15

[6] SHI X.P, FWA T.F, TAN S.A. Flexural fatigue strength of plain concrete [J]. ACI Materials Journal, 1993,90(5): pp435-440

[7] BYUNG HWAN OH. Fatigue life distribution of concrete for various stress levels [J]. ACI Materials Journal, 1991,88(2): pp122-128

[8] KRZYSZTOF DYDUCH. Experimental investigation of the fatigue strength of plain concrete under high compressive loading [J]. Materials and Structures, 1994, 24: pp505-509

[9] Li Yongqiang, Che Huimin. Bending fatigue performance study of concrete under constant-amplitude redundant stress [J]. Railroad journal, 1999, 21 (2): P26-30

[10] MITSURU SAITO, SATORU IMAI. Directensile fatigue of concrete by the use of friction grips [J]. ACI Journal, 1983, 80(5):pp431-438

[11] Ou Jinping, Lin Yanqing. Experiment study of fatigue damage intensity and rigidity attenuation of concrete [J]. Harbin Construction College Xuebao, 1998, 31 (4): P1-8

[12] Wu Chuanyi. Statistics discover of the abnormal data [J]. Mathematical statistic and management, 1984, 2: pp20-24

[13] Deng Bo. Statistics processing method of test data [M]. Beijing: Tsinghua University Press, 1994.

[14] Chen Shouyu. The engineering fuzzy set theory [M]. Beijing: Defense Industry Press, 1998.

[15] Xiang Kefeng, Wu Qiguang. Experiment design and data analysis [M]. Shanghai: Shanghai Science and Technology Press, 1989

Key Engineering Materials Vols. 385-387 (2008) pp 289-292
© (2008) Trans Tech Publications, Switzerland
doi:10.4028/www.scientific.net/KEM.385-387.289

Studies on expansion properties in concrete containing waste glass, silica fume, rice husk ash and polypropylene fibers

A. Sadrmomtazi[1,a], O. Alidoust[2,b], A. K. Haghi[3,c]

[1] University of Guilan, Civil Engineering Department, Rasht, Iran

[2] University of Guilan, Civil Engineering Department, Rasht, Iran

[3] University of Guilan, Textile Chemistry Engineering Department, Rasht, Iran

[a]sadrmomtazi@yahoo.com, [b]Alidoust@yahoo.com, [c]Haghi@Guilan.ac.ir

Keywords: Waste glass, pozzolanic behavior, particle size effect, Expansion, Fiber reinforcement

Abstract. The amount of waste glass sent to landfill has increased over recent years due to an ever growing use of glass products. Landfilling can cause major environmental problems because the glass is not biodegradable material. However, waste glass can be used as fine aggregate, coarse aggregate and powder form in concrete. The fine and coarse aggregate can cause alkali-silica reaction (ASR) in concrete, but the powder form can suppress their ASR tendency and acts as a pozzolanic material. This paper studies the expansion properties in concrete containing waste glass, silica fume, rice husk ash and polypropylene fibers in detail.

Introduction

Studies have been done on the possibility of reusing waste glasses as asphalt additive or road filler [1,2]. Waste glasses were used as aggregates for concrete [3–5]. However, the applications were limited due to the damaging expansion in the concrete caused by alkali–silica reaction (ASR) between high-alkali pore water in cement paste and reactive silica in the waste glasses. The chemical reaction between the alkali in Portland cement and the silica in aggregates forms silica gel that not only causes cracks upon expansion, but also weakens the concrete and shortens its life [6]. Recently, studies have been carried out to suppress the ASR expansion in concrete and find methods to recycle waste glasses [7,8]. Polypropylene fibers, produced by the fibrillation of polypropylene films, have been used in Portland cement concrete since the late 1960s [9]. Polypropylene and other synthetic fibers are added to concrete as secondary reinforcement to control plastic shrinkage [10]. The effect of polypropylene fibers on the properties of hardened concrete varies depending on the type, length, and volume fraction of fiber, the mixture design, and the nature of the concrete materials used. It also revealed the expansion and strength characteristics of concrete due to ASR by mixing reinforcing polypropylene fibers [11]. In this research project, some mixtures were prepared by composite cement was made by replacement of %10 of weight of cement by pozzolans and different volume fracture of PP fiber in the matrix for studying the effects of this materials to control the amount of expansion due to alkali-silica reaction.

Material specifications

Clean flat glass was used in this study. The chemical composition of the glass and other materials was analyzed using an X-ray microprobe analyzer and listed in Table 1 together with that of silica fume and rice husk ash for comparison.

Table 1: Chemical composition of glass, silica fume and rice husk ash (by weight percent)

Materials	Sio_2	Al_2O_3	Fe_2O_3	CaO	MgO	Na_2O	K_2O	CL	SO_3	$L.O.I$
Glass	72.50	1.06	0.36	8.00	4.18	13.1	0.26	0.05	0.18	-
Silica fume	91.1	1.55	2.00	2.24	0.60	-	-	-	0.45	2.10
Rice husk ash	92.15	0.41	0.21	0.41	0.45	0.08	2.31	-	-	-

To study the particle size effect, two different ground glasses were used:

- Type I: ground glass having particles passing a #80 sieve (180µm);
- Type II: ground glass having particles passing a #200 sieve (75µm).

The particle size distribution for two types of ground glass, silica fume, rice husk ash and ordinary Portland cement were analyzed by laser particle size set and have shown in Fig 1. The particle shapes of all materials were also analyzed using scanning electronic microscope (Fig. 2).

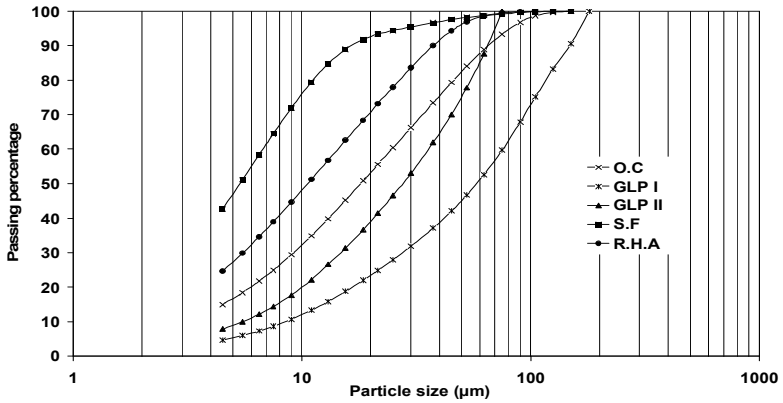

Fig.1: Laser Particle size distribution of ground waste glass type I, type II, silica fume, rice husk ash and ordinary Portland cement

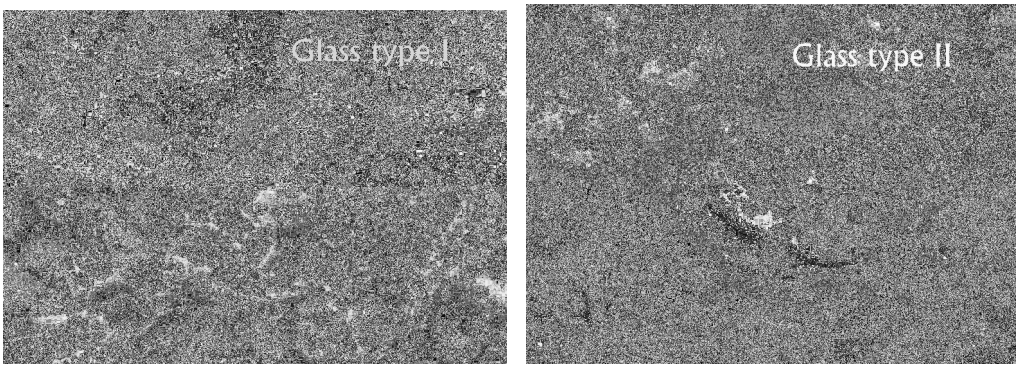

Fig. 2: Particle size and shape of ground waste glass type I, type II

Results and discussion

Analysis of the expansion characteristics of concrete containing waste glass, silica fume and rice husk ash. The expansion–time history curve made by the measurements complying with ASTM C1260 in terms of the additives like silica fume, rice husk ash and tow kind of ground waste glass whit different particle size which replaced by 10% of cement Portland weight are shown in figure 1.

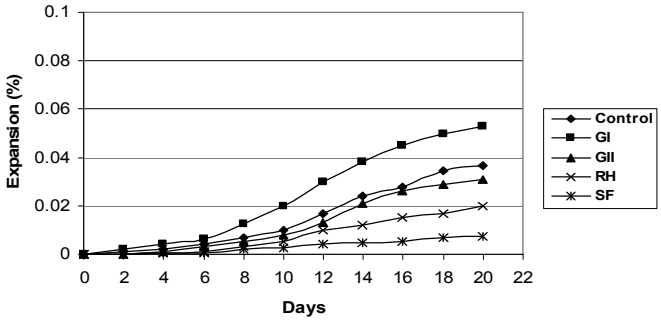

Fig. 3, Expansion time history for concrete bars

According to figure 1 specimens containing ground waste glass type I showed higher expansion rates than the other specimens specially the controls ones. The most important reasons for increase in expansion of samples containing glass type I is because of coarse particle size. In this way the alkali content cement and pore water has grater opportunity to react with silica content in aggregate specially particles if glass type I.

By replacing the cement Portland with ground glass type II the expansion rate of the specimens decrease around 15%. According to last researches materials with pozzolanic characteristics can suppress the alkali-silica reaction (ASR) and decrease the expansion respectively. According to ASTM C618 glass type II has the pozzolanic behavior due to its fine particle size.

By using of rice husk ash in matrix of concrete the amount of expansion decline about 50% of controls. It shows that rice husk ash has more pozzolanic properties the glass type II.

Also application of silica fume instead of 10% Portland cement weight has the most effective impact on expansion of specimens.

Results of mixes incorporating SF showed significantly lower expansion levels at all ages. Specimen incorporating SF expanded 70% less than Control at the end of test.

ASR characteristics of concrete containing reinforcing fiber. Fig 4 display the expansion time history curve for concrete bars having different contents of PP fiber (0.1–1 Vol %), respectively, combine with each type of composite cement. Results show that the ASR expansion decreases with an increase in the contents of PP fibers.

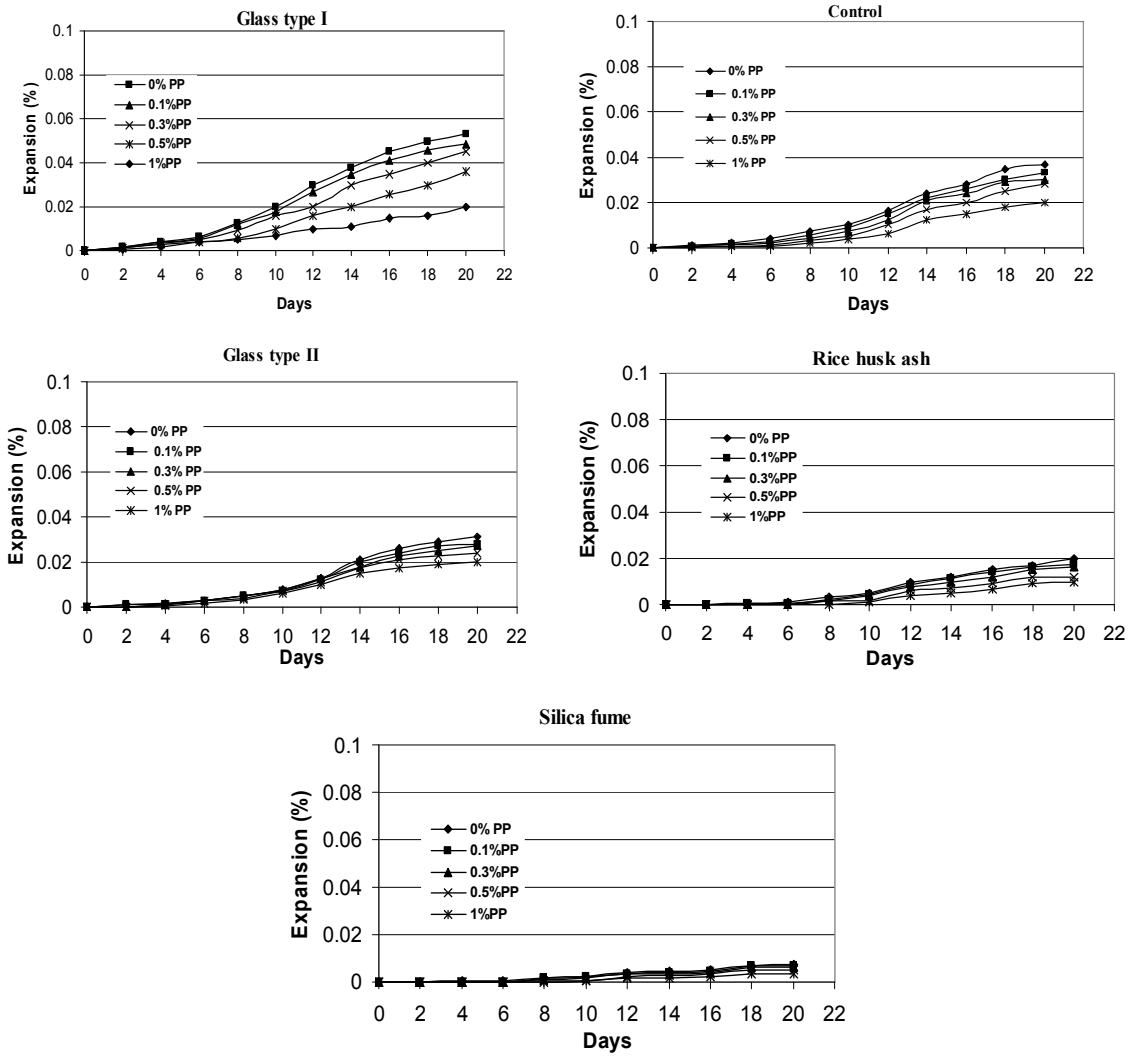

Fig. 4, Expansion time history curves for concrete bars containing different amount of PP fibers

Conclusion

This study intended to find effective ways to reutilize the hard to recycle waste glasses as concrete aggregate. Analysis of the problematic ASR expansion of concrete containing recycled waste glasses, silica fume and rice husk ash and reinforcing fiber gave the following results:

(1) Results show that the expansion rate by ASR in accordance with ASTM C 1260 showed an increasing tendency in specimens containing waste ground glass type I due to its coarse particle size rather than the others.
(2) Utilization of high reactive pozzolans like silica fume and rice husk ash have a great impacts on reduction of ASR expansion.
(3) According to results it is obtained that waste ground glass type II shows pozzolanic behavior like silica fume and rice husk ash, subsequently causes the decline in ASR expansion due to its fine particle size according to ASTM C618.
(4) With the content of waste glass type I and that of PP fiber 0.1-0.3 Vol %, the expansion rate of the specimens decreased by about 15-20%. By increasing amount of fiber to 0.5-1 Vol % , the expansion declined around 50-70%.
(5) In general application of fiber in the matrix is a suitable way to suppress the ASR expansion.
(6) It seems that the composition of high reactive pozzolans and PP fiber is the best way to decrease the harmful effects of ASR expansion.

References

[1] J. Refined, Development of non-traditional glass markets, Resour. Recycl. (1991) 18– 21.

[2] J. Uchiyama, Long-term utilization of the glass reasphalt pavement, Pavement (1998) 3– 89.

[3] C.D. Johnson, Waste glass as coarse aggregate for concrete, J. Test. Eval. 2 (5) (1974) 344–350.

[4] O. Masaki, Study on the hydration hardening character of glass powder and basic physical properties of waste glass as a construction material, Asahi Ceramic Foundation Annual Research Report,(1995).

[5] S.B. Park, Development of Recycling and Treatment Technologies for Construction Wastes, Ministry of Construction and Transportation, Seoul, (2000).

[6] R.N. Swamy, The Alkali– Silica Reaction in Concrete, Van Nostrand Reinhold, New York, (1992).

[7] S. Naohiro, The strength characteristics of mortar containing glass powder, The 49th Cement Technology Symposium. JCA, Tokyo, (1995) 114–119.

[8] I. Kyoichi, K. Atobumi, Effects of glass powder on compressive strength of cement mortar, College of Engineering, Kantou Gakuin University, Study Report 40 (1) (1996) 13–17.

[9] Bentur A, Mindess S. Fiber reinforced cementitious on durability of concrete. Barking: Elsevier, (1990).

[10] Balaguru PN, Shah SP. Fiber reinforced cement composites. New York: McGraw-Hill, Inc, (1992):367p.

[11] S.B. Park, Development of Energy Conserving High Performance Fiber Reinforced Concrete and Instruction for Design and Construction for the Reinforced Concrete, Ministry of Construction and Transportation, Seoul, (1998).

Key Engineering Materials Vols. 385-387 (2008) pp 293-296
© (2008) Trans Tech Publications, Switzerland
doi:10.4028/www.scientific.net/KEM.385-387.293

On Fracture Mechanics Testing Technique Based on Compliance of Specimens

CAI Lixun[1, a], JIN Lei[1,b] and BAO Chen[1,c]

[1] Department of applied mechanics and engineering, southwest jiaotong university, Chengdu, China, 610031

[a]lix_cai@263.net, [b]goodcat2004@163.comt, [c] bchxx@163.com

Keywords: Compliance; fracture toughness; crack growth rate; COD; testing technique; CAMT

Abstract. Based on compliance testing of a straight-notch compact tensile (SN-CT) or a single edge bending (SEB) specimen, this paper present a formula with increment form to calculate plastic part of J-integral, two formulas for a SN-CT specimen and a SEB specimen to transform crack mouth opening displacement (CMOD) v_0 to the crack opening displacement (COD) q along load line, and simplified formulas to estimate crack length a and effective young's modulus E. Furthermore, the relation between v and q of the SN-CT specimens of 45 steel and SEB specimens of 30Cr steel were investigated. The results show that the formulas to describe the relation between the ratio v/q and the dimensionless crack length a/w of the specimens accord with the testing results better.

Introduction

With the development of computer aided material testing (CAMT) in recent ten years, compliance testing of fracture mechanics become a very important technology recommended by fracture testing standards[1,2,3,4] . However, there still exist some aspects for this kind of CAMT technique need to be improved. A J-integral increment formula to display real-time results of J-resistance curve in fracture toughness testing and two transform formulas to calculate load line displacement q from measure result of CMOD v for a SN-CT specimen and SEB specimens were presented. In addition, a simplified formula to calculate Young's modulus E based on compliance C of a CT specimen was recommended. Finally, the transform formulas from v to q for SN-CT and SEB specimens were checked by testing.

Increment formula of J-integral

It needs to display the real-time data of J-resistance curve under multi-step unloading for a single specimen method. According to national standard GB2038-91[1] and America standard ASTM E813-89[2], the plastic part of J-integral recommended by J.R.Rice is expressed as follow

$$J_{\mathrm{p}} = \frac{\eta U_{\mathrm{p}}}{B_N b} \tag{1}$$

where the plastic work U_{p} is the area surrounded by P~q curve and the unloading line from load P, η is equal to $2+0.522b/w$ for CT specimens and to 2 for SEB specimens, B_{N} means the net thickness of a specimen, and $b=w-a$, w and a stand for width and crack length of the specimen, respectively.

Figure 1 gives P~q curve of a single specimen in testing under loading and unloading according to the test standards. In figure 1, beeline $P_{\mathrm{i}}B$ is extended from unloading line at load P_{i}, and then the area $AP_{\mathrm{i}}BA$ or U_{Pi} is plastic power at load P_{i}. From equation 1, $U_{\mathrm{pi}}=J_{\mathrm{pi}}B_{\mathrm{N}}b_{\mathrm{i}}/\eta_{\mathrm{i}}$ at P_{i} and $U_{\mathrm{pi-1}}=J_{\mathrm{p(i-1)}}B_{\mathrm{N}}b_{\mathrm{i-1}}/\eta_{\mathrm{i-1}}$ at $P_{\mathrm{i-1}}$. So, the increment of plastic power U_{P} can be expressed as

$$\Delta U_{pi} = U_{pi} - U_{p(i-1)} = J_{pi} B_N b_i / \eta_i - J_{p(i-1)} B_N b_{i-1} / \eta_{i-1} \quad (2)$$

From figure 1, the plastic work U_{Pi} at load P_i is equal to U_i-$P_i(C_iP_i)/2$, and then the plastic work increment ΔU_{Pi} under loading from load P_{i-1} to load P_i can be expressed as ΔU_i-$[P_i(C_iP_i)/2$-$P_{i-1}(C_{i-1}P_{i-1})/2]$ where the total work increment ΔU_i(=U_i-U_{i-1}) is near to $\Delta q_i(P_i+P_{i-1})/2$. So, the plastic work increment ΔU_{Pi} (=U_{Pi}-$U_{P(i-1)}$) has the expression as follow

$$\Delta U_{pi} = \Delta q_i \frac{P_i + P_{i-1}}{2} - \left[\frac{1}{2} C_i P_i^2 - \frac{1}{2} C_{i-1} P_{i-1}^2 \right] \quad (3)$$

From Equ.1~3, increment formula of J-integral is obtained as

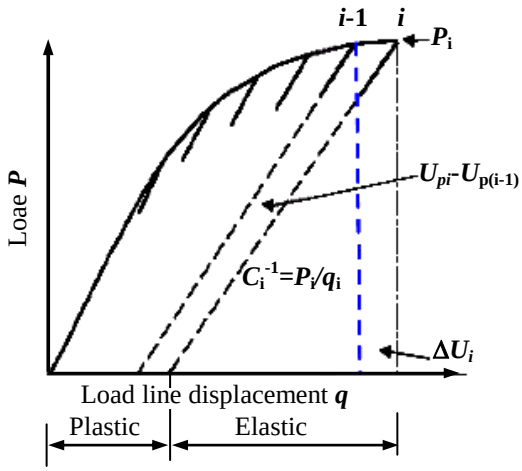

Figure 1 Schematic diagram how to determine plastic power increment of J-integral

$$\left.\begin{aligned} J_{pi} &= \frac{\eta_i}{B_N b_i} \Delta U_{pi} + \frac{\eta_i}{\eta_{i-1}} \frac{b_{i-1}}{b_i} J_{pi-1} \\ \eta_i &= \begin{cases} 2 + 0.522 \dfrac{b_i}{w} & \text{for CT specimens} \\ 2 & \text{for SEB specimens} \end{cases} \\ \Delta U_{pi} &= \Delta V_{LLi} \frac{P_i + P_{i-1}}{2} - \left[\frac{1}{2} C_i P_i^2 - \frac{1}{2} C_{i-1} P_{i-1}^2 \right] \end{aligned}\right\} \quad (4)$$

Formula to describe the relation between *a*/*w* and *q*

According to GB2038-91, GB6398-2000 and ASTM E813-89, dimensionless crack length *a*/*w* has following expression

$$\left.\begin{aligned} \frac{a}{w} &= c_0 + c_1 U_x + c_2 U_x^2 + c_3 U_x^3 + c_4 U_x^4 + c_5 U_x^5 \\ U_x &= \begin{cases} \left[(BEC)^{\frac{1}{2}} + 1 \right]^{-1} \quad (0.2 \le \dfrac{a}{w} \le 0.975) & \text{for CT specimens} \\ \left[\left(BEC_v \dfrac{4w}{S} \right)^{\frac{1}{2}} + 1 \right]^{-1} & \text{for SEB specimens} \end{cases} \end{aligned}\right\} \quad (5)$$

where compliance C=C_q= q/P or C=C_v=v_0/P, q is COD along load line of a CT or SEB specimen and v_0 is CMOD at mouth of the specimen, E is Young's modulus, and S means the span of a SEB specimen. The coefficients c_0~c_5 are given in Table 1.

Table 1 The coefficients in Eq.5

Specimen type	COD		c_0	c_1	c_2	c_3	c_4	c_5
CT	v_0	GB	1.0010	-4.6695	18.460	-236.82	1214.9	-2143.6
		ASTM	1.0000	-4.5000	13.157	-172.55	879.94	-1514.7
	q		1.0002	-4.0632	11.242	-106.04	464.33	-650.67
SEB	v_0		0.99975	-3.9504	2.9821	-3.2141	51.516	-113.03

From ISO 12135:2002(E) [4], compliance C of a SEB specimen is given by

$$\left.\begin{aligned} C_v &= \frac{v_0}{P} = \frac{S(1-\nu^2)}{EB_e w} g_3(\frac{a}{w}) \\ C_q &= \frac{q}{P} = \frac{(1-\nu^2)}{EB_e}(\frac{S}{w-a})^2 g_5(\frac{a}{w}) \\ B_e &= B - \frac{(B-B_N)^2}{B} \end{aligned}\right\} \tag{6}$$

in which, ν is Poisson ratio of materials, function g_3 and g_5 are given in reference [4].

In testing of fracture toughness by standard GB2038-91and ASTM E813-89, the CMOD v_0 of a straight-notch CT specimen or a SEB specimen is allowed to determine J-integral. However, the plastic work U_p of J_p can not straightly obtained from P-v_0 curve of the specimen, and it needs to transform the CMOD v_0 to COD q. Unfortunately, the transform method is not given in the standards. Therefore, according to Eqs.(5~7) and Tab.1, a relation between v_0/q and a/w is specially presented by

$$\left.\begin{aligned} v_0/q &= \alpha \cdot f(\frac{a}{w}) \\ f(a/w) &= \sum_{i=0}^{5} d_i \cdot (\frac{a}{w})^i \\ \alpha &= \begin{cases} 1 & \text{for CT specimens} \\ 6\dfrac{a}{S}(1-\dfrac{a}{w})^2 & \text{for SEB specimens} \end{cases} \end{aligned}\right\} \tag{7}$$

where the coefficient d_0~d_5 are given in table 2.

Table 2 The coefficient d_0~d_5 in Eq.7

Specimen type	d_0	d_1	d_2	d_3	d_4	d_5
CT	3.8260	-15.259	43.200	-64.976	49.003	-14.551
SEB	-85.884	853.66	-3325.2	6490.2	-6329.3	2497.8

The indirect-computational results according to Eq.(5,6) and results obtained straightly by Eq.7 are given in Fig.2 and Fig.3, and the relative error between them are also illustrated in the figures.

The results show that the maximum error of Eq.7 for a CT specimen does not exceed 0.3% when $a/w \in (0.25,0.8)$, and the maximum error of Eq.7 for a SEB specimen does not exceed 0.4% when $a/w \in (0.4,0.75)$. Therefore, equation 8 has high transform accuracy. For effect of large deformation of the specimens, the q given by Eq.7 should be further modified according to methods recommended by standard GB2038 or ISO12135.

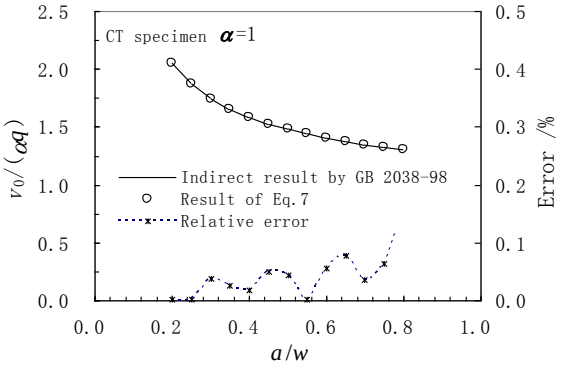

Figure 2 $v_0/(\alpha q)$~a/w curve and the error for a CT specimen

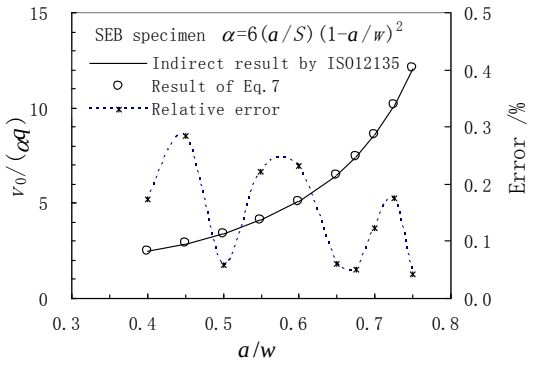

Figure 3 $v_0/(\alpha q)$~a/w curve and the error for a SEB specimen

A simplified formula to determine *a*/*w* or *E* by compliance *C*

It was noticed that for one relation of a CT specimen between *a*/*w* and C_v , Tab.1 and Eq.5 from national standard GB6398-2000 and America standard ASTM E813-89 give two different formulas. This situation reminded us to check them. Figure 4 gives $a/w \sim U_x$ curves from the two formulas and the error of them to predict *a*/*w*. It shows the results are closed each other and relative error of their dimensionless crack length does not exceed 0.1%, and it is accidental that the relation between *a*/*w* and U_x meets linear law. Further, an interest fact was found that there exists a simple linear relation between dimensionless ligament *b* /*w* of CT specimens like follow

$$b/w = 4.187U_x = 4.187/[(B \cdot E \cdot C_v)^{\frac{1}{2}} + 1] \qquad a/w \in (0.25, 0.975) \text{ for CT specimens} \qquad (8)$$

where it has only one coefficient, 4.187. Figure 4 indicates its error relatively to the result from ASTM formula (Eq.5), and it shows that the maximum error does not exceed 0.8% as $a/w \in (0.25,0.975)$ and 0.3% as $a/w \in (0.5,0.975)$.

From Eq.8, Young's modulus can be simply expressed as

$$E = \frac{1}{BC_v}\left(\frac{3.187 + a/w}{1 - a/w}\right)^2 \qquad (9)$$

Eqs.(8,9) are very brief and convenient to use.

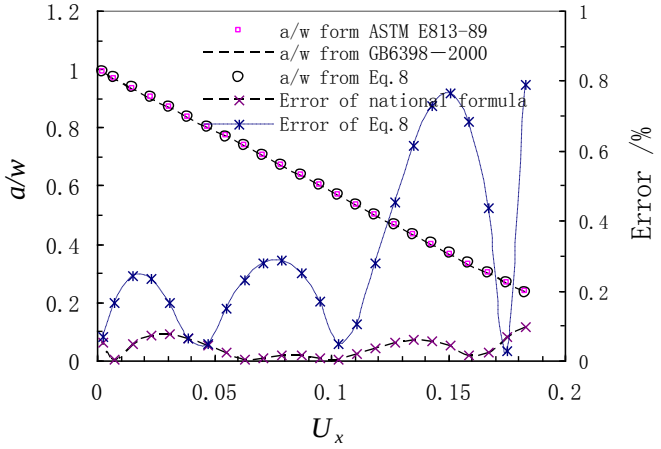

Figure 4 $a/w \sim U_x$ curves for CT and the errors

Discussion and conclusions

To check Eq.7, loadings for five CT specimens of 45 steel with crack length from 25mm to 36mm and with the design in Fig.1 and six SEB specimens of 30Cr with crack length from 20mm to 28mm and with the dimension 160:40:20 of *S*:*W*:*B* were carried out by MTS 809 machine. Two MTS COD gauges, MTS632.03F-20 with 5mm gauge length and MTS632.03c.21 with 12.5mm gauge length, were used for the loadings on the CT specimens. In loading, the COD gauges didn't stop work until they got to their limit 4mm. The experimental results of v_0/q all are closed the predicting results by Eq.7 and the maximum relative error between them does not exceed 4%.

As a conclusion, the increment formula of J-integral given in Eq.4, the transform formulas given in Eq.7 and the simplified formulas given in Eq.(8,9) are very useful in CAMT and all are recommended to used in fracture mechanics tests.

References

[1] GB2038-91: Standard test method for J_{IC}, a measure of ductile fracture toughness. Chinese standard bureau. (1991)
[2] ASTM E813-89:Standard of test method for $J_{IC,}$ a measure of fracture toughness, America Society of Testing and Materials.(1989)
[3] ASTM E399-90:Standard of test method for plain strain fracture toughness of metallic materials, America Society of Testing and Materials.(1990)
[4] ISO 12135-2002(E):International standard of unified method of test for the determination of quasistatic fracture toughness, International Organization for Standardization.(2002)

Key Engineering Materials Vols. 385-387 (2008) pp 297-300
© (2008) Trans Tech Publications, Switzerland
doi:10.4028/www.scientific.net/KEM.385-387.297

Crack Propagation Behavior of Asphalt Concrete

Part I: A Study into Influence of Different Materials

Tao XIE[1,a], Zezhong JIANG[2,b], Yanjun QIU[2,c] and LAN Bo[3,d]

[1]College of Civil and Architecture Engineering, Guizhou University, Guiyang 550003, China

[2]College of Civil Engineering, Southwest Jiaotong University, Chengdu 610031, China

[3]Department of Transportation of Sichuan Province, Chengdu 610041, China

[a]xie_tao96@163.com,[b]qmrjzz@yahoo.com.cn, [c]publicqiu@163.com, [d]sclb2008@163.com

Keywords: asphalt concrete, crack propagation behavior, CT, material

Abstract: The fracture resistance of asphalt materials significantly influences the service life of asphalt pavements and consequently affects the maintenance and rehabilitation costs of the pavement network. Therefore, there is significant interest in understanding the mechanism of fracture in asphalt pavements and in developing analysis tools that would lead to the selection of asphalt materials with increased fracture resistance. Study of cracking behavior of asphalt mixtures should be conducted in a micro-scale level to have a real simulation of crack propagation. Using SIEMENS SOMATOM plus X-ray CT (computerized tomography) and multi-functional testing rig, a dynamic observation of cracking propagation of hot mix asphalt was conducted in this research. Failure process under compressive pressure was recorded using CT images and CT numbers. The direct responses in density change of Marshall Samples under a CT-compressive process are change of CT numbers. Cracking propagation in the samples can be clearly observed and failure mode and stress-strain behavior can then be simulated. The tests reported provide important theoretical fundamentals to study the cracking behavior and failure mechanism of asphalt mixtures.

Introduction

A great effort has been devoted to the development of an accurate and reliable strength criterion for composites. The failure process in a composite is extremely complex and it would be very difficult to analytically describe each successive failure stage in detail[1]. The analysis of composite material failure has traditionally followed two investigative paths: macro-mechanics and micro-mechanics. The macro-mechanics approach is to determine the effects of the constituent materials by the overall material parameters like tensile strength and shear strength. The micro-mechanics approach is to consider the interactive and individual behavior of the composite constituent materials such as the fiber and epoxy resin properties. Therefore, there is significant interest in understanding the mechanism of fracture in asphalt pavements and in developing analysis tools that would lead to the selection of asphalt materials with increased fracture resistance. An experimental method that allows observation of crack initiation and propagation is of great interest to help researchers understand the fracture mechanisms of asphalt mixtures, develop more general and reliable constitutive models, and nominate the influential factors in the process of fracture [2].

This paper reports a research effort of dynamic observation of the micro-fracture process of asphalt mixture under compressed condition using CT method. The CT numbers, CT images and

the other data were analyzed for surveying the influence of different materials on crack propagation behavior of asphalt concrete under compressed condition.

Description of experiment

The specially developed uniaxial loading equipment specially for CT studies on asphalt concrete, measuring Φ240mm×1000mm in sizes, having a 142mm inner diameter of axial compression cylinder that creates a maximum axial compression of 400kN and a confining pressure of 20 *MPa* . By using this testing equipment, one can conduct CT tests of continuous loading failure and unloading damage with this equipment man can make real-time CT on a designated cross section of a specimen in the meantime when he conducts macro tests of complete failure process so as to study the deformation failure situation of the specimen.

The CT unit for our tests is X-ray spiral CT unit of plus type of SIEMENS SOMATOM, having spatial resolutions of 0.35mm×0.35mm (being able to distinguish a minimum volume of 0.12mm^{3}with a layer thickness of 1 *mm* and a density contrast resolution of 0.3%(3HU) [3]. The specially designed loading system is the necessary accessory for the CT machine at the State Key Laboratory of Frozen Soil Engineering of China.

Fig.1 SIEMENS SOMATOM PLUS X-ray CT

Fig.2 loading equipment system

Marshall samples of AC20 (with average density 2.41g/cm^3), SMA16 (with average density 2.30g/cm^3), ATB25(with average density 2.39g/cm^3) were used under uniaxial compressive stress state in normal temperature testing environment. Stress and strain behavior was observed during the compressive failure process of the asphalt mixtures. The indexes of specimens are accorded with the *Specifications for design of highway asphalt pavement* [4]. The CT test was carried out in the State Key Laboratory of Frozen Soil Engineering from Aug.24 to Sept.10, 2006.The asphalt concrete samples were used to study the crack propagation law under uniaxial compression with CT real-in time scanning test. For each sample there were three cross sections from top to bottom for scanning. The rate of strain was 0.2mm/min as a quasi-static loading test.

Analysis of the test results

Tab.1 is the scan test conditions of the samples. The each section of AC20 was scanned in 6 times, and each section of SMA16 and ATB25 was scanned in 5 times. The thickness of each section is 5mm.The internal distance is 8 mm between two sections. The corresponding stress states of 5 or 6 times scanning test are given in Tab.2. The test results of each scan section of AC20, SMA16 and ATB25 are also shown in the Tab.2 [5]. In the Tab.2, ME is the CT value of each section. In order to comparative analysis, there has a unified process for the stress state of each sample, i.e. each stress value is divided by the respective peak strength value of sample. The CT images of the 2nd scan sections are partly given in this paper because of limit of the paper length (Fig.3).

Table 1 Scan test conditions

Voltage/ kV	Current/ mA	Time/ s	Label	Thickness/mm	Amplifying factor	Interval/mm
120	165	2	OM	5	5.0	8

Table 2 Scan test results of 2nd scan sections under different loading rates

Scan order	AC20-1			SMA16			ATB25		
	σ/σ_c	ε / %	ME	σ/σ_c	ε / %	ME	σ/σ_c	ε / %	ME
1	0	0	1994.1	0	0	1903.4	0	0	1966.7
2	0.04	0.63	1997.4	0.21	0.94	1897.1	0.12	0.79	1964.7
3	0.52	2.54	1989.3	0.81	2.52	1883.1	0.92	2.38	1948.9
4	0.93	3.49	1944.7	1.00	4.72	1829.2	1.00	3.49	1897.9
5	1.00	5.56	1876.0	0.81	9.13	1709.0	0.61	9.37	1657.8
6	0.82	9.52	1711.6	-	-	-	-	-	-

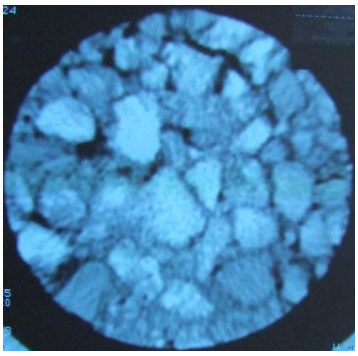

(a) $\sigma/\sigma_c = 1.0$ of AC20-1

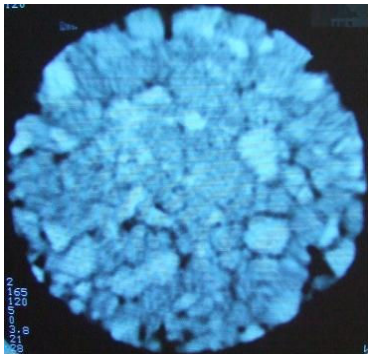

(b) $\sigma/\sigma_c = 1.0$ of SMA16

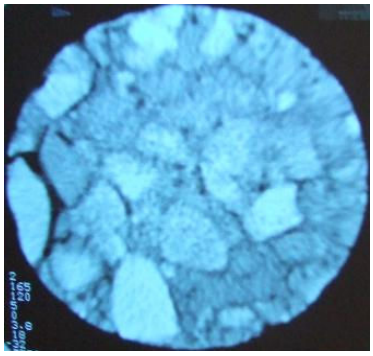

(c) $\sigma/\sigma_c = 1.0$ of ATB25

Fig.3 CT images of 2nd scan section

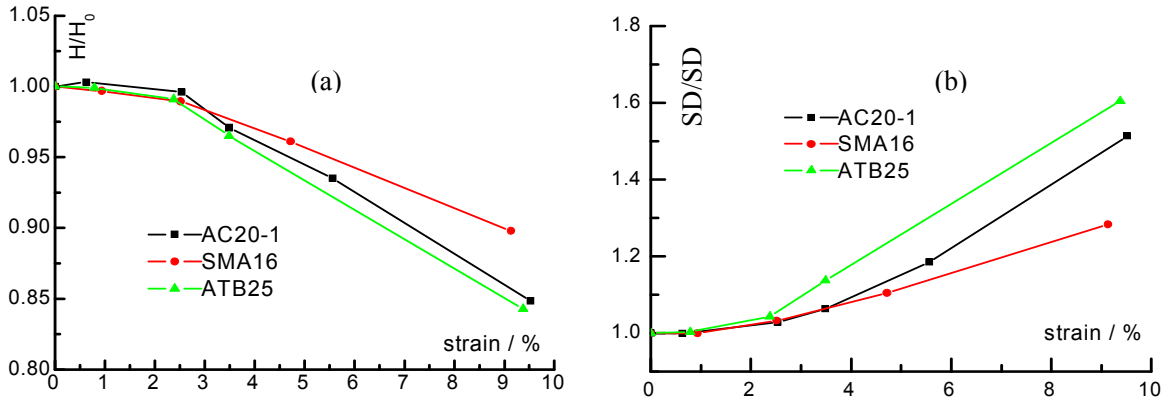

Fig.4 The influence of different materials on CT number and the variance of CT value

In the Fig.4 (b), the SD is the variance of the CT value of each section and SD_0 is the variance of the CT value of initial scan cross section.

In the Tab.2, σ_c is the respective peak strength value of the samples. In order to visual comparative analysis of the influence of loading rate on CT number, Fig.4 is worked out. There also

has a unified process for the CT numbers of each time scan of each sample, i.e. each CT number value and the variance of the CT value of each section. are divided by the respective initial CT number value of sample and the variance of the CT value.

It is obtained from Tab.2, in the stage of the value of ε from 0 to about 0.7%, only the CT value of AC20-1 all three scan sections are rose. In fact, the micro-cracks began to be closed. However, the CT number increases to a small extent, for instance, the CT number of the AC20-1 increases only by 3.3. The CT value of 1st scan sections of ATB25 had increased a few and there were not increase in 2nd and 3rd scan sections. But the CT value of SMA16 all three scan sections is a few decreases. At the same time, the Fig.4 (a) has shown that the change degree of CT number of SMA16 is biggest under the minim value of strain condition and at the beginning of compression.

When ε came to about 2.5%, the CT value began to descend, and it can be seen from Tab.2 and CT images that the microcracks began to lengthen, bifurcate and there are a lot s of microcracks began to grow. The testing result has shown that in continuous loading process, the crack formed in the previous stage will continuously develop with the increment of stress and become longer and wider. On the other hand, the CT value of 3rd scan sections of AC20-1 had increased a few and there were a few of microcracks growth. It shows that there are different damage phenomena in the different sections of the same sample compressed by the same loading.

When ε rose beyond about 3.5%, in this stage, the CT value of each section began to obviously decrease, the microcracks of 1st scan section continue lengthen the microcracks of 2nd scan section began to bifurcate, lengthen and nearly penetrate, many microcracks of the 3rd scan section began to bifurcate. This stage is the failure omen stage, and it was the stage of the fastest speed of microcracks evolution. At the same time, It can be seen from the Fig.4(a) that the CT number of ATB25 is more quickly decrease than that of AC20-1 and SMA16. Because of the values of c and φ of SMA16 are larger than that of AC20-1 and ATB25, the capacity of the cracking resistance is higher, so the change of CT number of SMA16 is smaller. This fact is showed in Fig.4(b) that the curve of the variance of CT value is more comparatively smooth.

Conclusions

The initial test result s illustrate that the different materials has a noticeable influence on crack propagation behavior of asphalt concrete. At the beginning of compression, the CT change value of SMA16 is a few decreases and there is no CT value increased stage. At the stage of damage stable development, the microcracks growth is quicker and the CT value decrease of ATB25 is faster than those of SMA16. The Crack Propagation Behavior is influenced by the materials of it's.

Acknowledgements

This paper is supported by the Guizhou Province's Outstanding Young Science & Technology Talents Project (Z073239).

References

[1] C.H.Kim and H-Y.Yeh, Engng Fracture Mech. 47,569-582,1994

[2] M. M. J. Jacobs. Crack Growth in Asphaltic Mixes. Ph.D. Dissertation, Faculty of Civil Engineering, Delft University of Technology, Delft, 1995

[3] Yang Gengshe, Zhang Changqing. Rock masses damage and identification. Xi'an: Shanxi Science and Technology Press, 1998, 79-90. (in Chinese)

[4] The Professional Standard of China.Specification for Design of Highway Asphalt Pavement(JTJ 014-97). Beijing: China Communications Press,1997.(in Chinese)

[5] Tao XIE. Study on crack propagation behavior of asphalt mixtures based on CT rael-time observation. Ph.D. Dissertation, School of Civil Engineering, Southwest Jiaotong University, Chengdu, 2006

Key Engineering Materials Vols. 385-387 (2008) pp 301-304
© (2008) Trans Tech Publications, Switzerland
doi:10.4028/www.scientific.net/KEM.385-387.301

Crack Propagation Behavior of Asphalt Concrete

Part II: A study into Influence of Loading Rates

Zezhong JIANG[1,a], Tao XIE[2, b] , Yanjun QIU[1,c] and LAN Bo[3,d]

[1]College of Civil Engineering, Southwest Jiaotong University, Chengdu 610031, China

[2]College of Civil and Architecture Engineering, Guizhou University, Guiyang 550022, China

[3]Department of Transportation of Sichuan Province, Chengdu 610041, China

[a]qmrjzz@yahoo.com.cn, [b]xie_tao96@163.com,

[c]publicqiu@163.com, [d]sclb2008@163.com

Keywords: asphalt concrete, crack propagation behavior, CT, loading rate

Abstract: Cracking has long been accepted as a major mode of premature failure in flexible pavements. Expected life of pavements, pavement condition and maintenance cost are directly related to pavement cracking. It is crucial to have a sufficient understanding of cracking mechanism in order to produce a sound and safe material and structural design of asphalt pavements. Simulation, surveying, observation, and measurement of cracking in pavement structures have been reported in literature in last three decades. However, cracking process in asphalt mixtures in a three dimensional scale is still a great challenge to road engineers. Using SIEMENS SOMATOM plus X-ray CT (computerized tomography) and multi-functional testing rig, a dynamic observation of cracking propagation of hot mix asphalt was conducted in this research. Marshall samples of AC20 were used under uniaxial compressive stress state. Stress and strain behavior was observed during the compressive failure process of asphalt mixtures. Cracking propagation in the samples can be clearly observed and failure mode and stress-strain behavior can then be simulated. Research results show that loading rate is a critical factor influencing cracking velocity and cracking density.

Introduction

Asphalt concrete is the most commonly used material in pavement construction today because of its favorable properties such as elasticity, stability, durability, and water resistance. Asphalt mixtures are used as surface or base layers in a pavement structure to distribute and transfer stresses caused by loading and to protect the underlying unbound layers from the effects of water. In order to adequately perform both of these functions over the pavement design service life, the mixture must also withstand the effects of air and water, resist permanent deformation, and resist cracking caused by loading and environment. Despite asphalt concrete is widely used on pavement, the fundamental mechanism of fatigue fracture and permanent deformation, still awaits discovery and a general predictive theory remains to be developed [1].

Little cracks on a highway or airport runway can mean the start of something big. To the monitoring public or the airline pilot, how that crack develops may be a mystery. Early detection, however, is essential to avoid expensive repairs later. This paper focuses on a research effort of the influence of loading rate on crack propagation behavior of asphalt concrete under compressed condition by using CT method.

Description of experiment

The specially developed uniaxial loading equipment specially for CT studies on asphalt concrete, measuring Φ240mm×1000mm in sizes, having a 142mm inner diameter of axial compression cylinder that creates a maximum axial compression of 400kN and a confining pressure of 20 MPa . By using this testing equipment, one can conduct CT tests of continuous loading failure and unloading damage with this equipment man can make real-time CT on a designated cross section of a specimen in the meantime when he conducts macro tests of complete failure process so as to study the deformation failure situation of the specimen. The CT unit for our tests is X-ray spiral CT unit of plus type of SIEMENS SOMATOM, having spatial resolutions of 0.35mm×0.35mm (being able to distinguish a minimum volume of 0.12mm^{3}with a layer thickness of 1 mm and a density contrast resolution of 0.3%(3HU) [2]. The specially designed loading system is the necessary accessory for the CT machine at the State Key Laboratory of Frozen Soil Engineering of China.

Marshall samples of AC20 (with average density 2.41g/cm^3) were used under uniaxial compressive stress state in normal temperature environment. Stress and strain behavior was observed during the compressive failure process of asphalt mixtures. The indexes of specimens are accorded with the *Specifications for design of highway asphalt pavement* [3]. The CT test was carried out in the State Key Laboratory of Frozen Soil Engineering from Aug.24 to Sept.10, 2006.The samples were used to study the crack propagation law under uniaxial compression with CT real-in time scanning test .For AC20-1 there were three cross sections from top to bottom.

In this test, it adopts three kinds of loading rate. The loading rate of AC20-1 is 0.2mm/min; the loading rate of AC20-2 is 0.4mm/min; and AC20-3 is 0.1 mm/min.

Analysis of the test results

Table 1 is the scan test conditions of the samples. The AC20 samples had three cross-sections from the up to down for scanning and each section was scanned in 6 times, then 18 images were obtained. The thickness of each section is 5mm.The internal distance is 8 mm between two sections. The corresponding stress states of 6 or 8 times scanning test are given in Tab.2. The test result s of each scan section of AC20-1 is also shown in the Tab.2 [4]. Limiting to research money, the AC20-2 and AC20-3 only have 2nd scan section test. At the same time, because of the loading rate of AC20-3 is the slowest, it has 8 times scanning test. In the Tab.2, ME is the CT value of each section. In order to comparative analysis, there has a unified process for the stress state of each sample, i.e. each stress value is divided by the respective peak strength value of sample. The CT images of the 2nd scan sections are partly given in this paper because of limit of the paper length (Fig.1 and Fig.2).

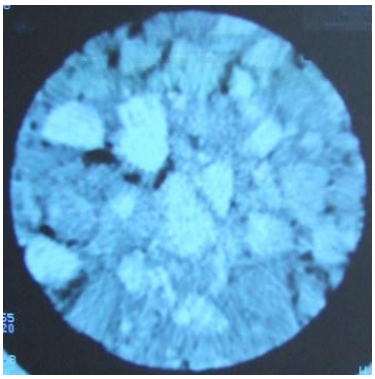

(a) $\sigma/\sigma_c = 0$ of AC20-1

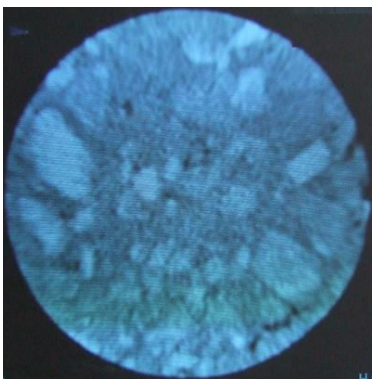

(b) $\sigma/\sigma_c = 0$ of AC20-2

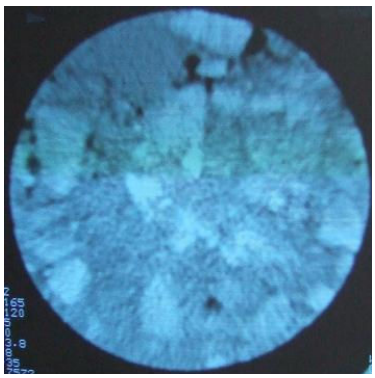

(c) $\sigma/\sigma_c = 0$ of AC20-3

Fig.1 CT images of 2nd scan section

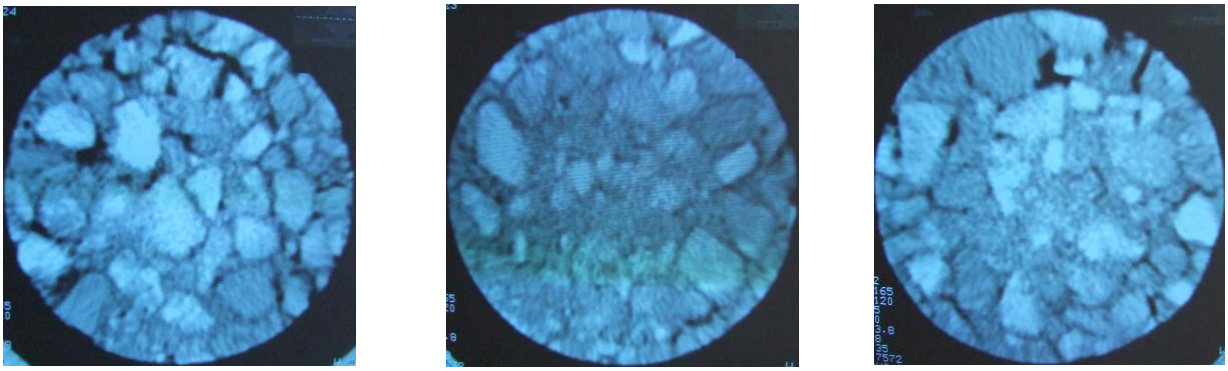

(a) $\sigma/\sigma_c = 1.0$ of AC20-1 (b) $\sigma/\sigma_c = 1.0$ of AC20-2 (c) $\sigma/\sigma_c = 1.0$ of AC20-3

Fig.2 CT images of 2nd scan section

Table 1 Scan test conditions

Voltage/ kV	Current/ mA	Time/ s	Label	Thickness/mm	Amplifying factor	Interval/mm
120	165	2	OM	5	5.0	8

Table 2 Scan test results of 2nd scan sections under different loading rates

Scan order	AC20-1			AC20-2			AC20-3		
	σ/σ_c	ε / %	ME	σ/σ_c	ε / %	ME	σ/σ_c	ε / %	ME
1	0	0	2004.0	0	0	2028.0	0	0	2078.5
2	0.04	0.63	2010.0	0.16	0.61	2034.6	0.06	0.79	2080.8
3	0.52	2.54	1995.9	0.80	2.38	2018.6	0.58	2.38	2074.2
4	0.93	3.49	1945.1	1.00	3.97	1973.5	0.85	3.49	2010.7
5	1.00	5.56	1874.1	0.95	5.08	1943.9	0.97	4.28	1985.0
6	0.82	9.52	1700.2	0.70	9.21	1792.2	1.00	4.75	1957.7
7	-	-	-	-	-	-	0.89	6.50	1881.8
8	-	-	-	-	-	-	0.65	9.51	1729.4

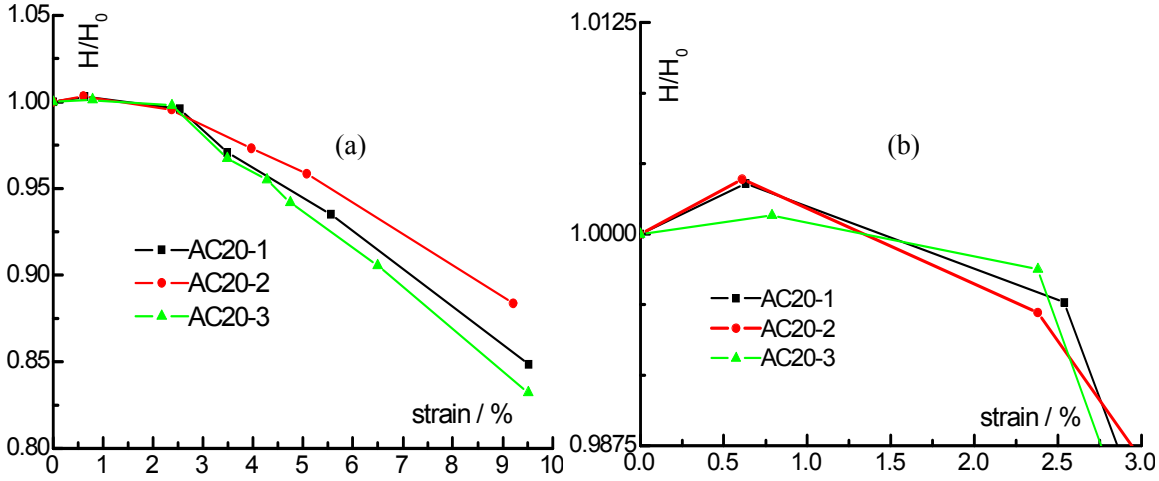

Fig.3 The influence of loading rate on CT number

In the Table 2, σ_c is the respective peak strength value of sample. In order to visual comparative analysis of the influence of loading rate on CT number, Fig.3 is worked out. There also has a unified process for the CT numbers of each time scan of each sample, i.e. each CT number value is divided by the respective initial CT number value of sample. The Fig.3(b) is the

amplification part of Fig.3(a) from $\varepsilon = 0$ to $\varepsilon = 3\%$. It is obtained from Table 2, in the stage of the value of ε from 0 to about 0.7%, all the CT value of three scan sections are rose. In fact, the micro-cracks began to be closed. It can be seen from the Table 2 that the CT number of all layers of the specimen increases. However, the CT number increases to a small extent, for instance, the CT number of the AC20-1 increases only by 6.0, AC20-3 changes a little in amount, having an increment of only 2.3. At the same time, the Fig.3(b) has shown that the change degree of CT number of AC20-2 is biggest under the minim value of strain condition and at the beginning of compression. When ε came to about 2.5%, the CT value began to descend, and it can be seen from Tab.2 and CT images that the microcracks began to lengthen, bifurcate and there are a lot s of microcracks began to grow. The testing result has shown that in continuous loading process, the crack formed in the previous stage will continuously develop with the increment of stress and become longer and wider. On the other hand, the CT value of 3rd scan sections of AC20-1 had increased a few and there were a few of microcracks growth. It shows that there are different damage phenomena in the different sections of the same sample compressed by the same loading. At the same time, It can be seen from the Fig.3(b) that after the initial holes was compressed to be closed, the CT number of AC20-2 is more quickly decrease than that of AC20-1 and AC20-3. It shows the fact that the initial damage is sensitive to the loading rate at the stage of microcracks growth. When ε rose beyond about 3.0%, in this stage, the CT value of each section began to obviously decrease, the microcracks of 1st scan section continue lengthen the microcracks of 2nd scan section began to bifurcate, lengthen and nearly penetrate, many microcracks of the 3rd scan section began to bifurcate. This stage is the failure omen stage, and it was the stage of the fastest speed of microcracks evolution. At the same time, It can be seen from the Fig.3(a) that the CT number of AC20-3 is more quickly decrease than that of AC20-1 and AC20-2. It shows the fact that at the stage of damage stable development, the loading rate is slower, the microcracks growth is quicker and the CT value decrease is faster.

Conclusions

The initial test result s illustrate that the loading rate has a noticeable influence on crack propagation behavior of asphalt concrete. At the beginning of compression, the CT change value is bigger as the loading rate is quicker. At the stage of damage stable development, the microcracks growth is quicker and the CT value decrease is faster as the loading rate is slower. Loading rate is a critical factor influencing cracking velocity and cracking density.

Acknowledgements

This paper is supported by the Guizhou Province's Outstanding Young Science & Technology Talents Project (Z073239).

References

[1] M. M. J. Jacobs. Crack Growth in Asphaltic Mixes. Ph.D. Dissertation, Faculty of Civil Engineering, Delft University of Technology, Delft, 1995

[2] Yang Gengshe, Zhang Changqing. Rock masses damage and identification. Xi'an: Shanxi Science and Technology Press, 1998, 79-90. (in Chinese)

[3] The Professional Standard of China.Specification for Design of Highway Asphalt Pavement(JTJ 014-97). Beijing: China Communications Press,1997.(in Chinese)

[4] Tao XIE. Study on crack propagation behavior of asphalt mixtures based on CT rael-time observation. Ph.D. Dissertation, School of Civil Engineering, Southwest Jiaotong University, Chengdu, 2006

[5] R L Krans. Semi-circular Bending Test: a Practical Crack Growth Test Using Asphalt Concrete Cores Reflective Cracking in Pavements. Journal of Engineering Mechanics, 1996, 116(4):123-132

Key Engineering Materials Vols. 385-387 (2008) pp 305-308
© (2008) Trans Tech Publications, Switzerland
doi:10.4028/www.scientific.net/KEM.385-387.305

Study on restrained expansive deformation of steel fiber reinforced self-stressing concrete

He Huanan[1,a] Huang Chengkui[2,b]

[1]State Key Laboratory Of Coastal and Offshore Engineering, Dalian University of Technology, Dalian, China, 116024

[2]State Key Laboratory Of Coastal and Offshore Engineering, Dalian University of Technology, Dalian, China, 116024

[a]hehuanandl@163.com, [b]huangck@dlut.edu.cn

Keywords: self-stress, steel fiber, expansive deformation, expansion

Abstract. A new sort of high performance concrete is introduced which combines most advantages of prestressed concrete and steel fiber concrete, named steel fiber reinforced self-stressing concrete(SFFRSSC for short). Self-stressing concrete is actually a kind of expansive concrete which self-stresses, namely pre-compressive stresses, are induced by dint of some restrictions generally provided by steel bars to concrete expansion after hydration of expansive cement. As a result of chemical reaction, concrete archived prestresses by itself different from mechanical prestressed concrete, so called self-stressing concrete. By distributing short-cut steel fibers into self-stressing concrete at random, prestresses(self-stress) are created in concrete under combined restriction of steel bars and steel fibers. Thank to the pre-stresses tensile strength of concrete are significantly increased as well as cracking strength. In addition, expansive deformation of SFFRSSC can compensate the shrinkage of concrete to decrease shrinkage crack, and the steel fibers play an important role in post-crack behavior. On the other hand, self-stressing concrete can avoid the troubles of construction compared with conventional mechanical prestressed concrete. For purpose of understanding the properties of SFFRSSC, in this paper some researches were carried out to investigate the special expansive behaviors of restrained expansive deformation with restriction of steel bar as well as steel fiber. The test results indicated that steel bar and steel fiber both provide effective restrict to self-stressing concrete as result of forming prestresses in concrete.

1. Introduction

As we know, concrete has an inherent weakness in resisting tension and crack, this drawback is undesirable. Steel fiber reinforced concrete and prestressed concrete are recognized as two effective approaches to enhance tensile strength of concrete or crack resistance. Nowadays steel fiber concrete has been extensively used in many countries. It is generally believed that randomly distributed fibers in concrete can increase tensile strength, and that the post-crack behavior can be improved involving the decreasing of crack width and increasing of toughness of concrete. Prestressed concrete is widely employed in buildings, bridges, and other structures for some significant contributions to the construction industry such as high cracking resistance performance. In this paper a new type of prestressed concrete named self-stressing concrete is introduced, which the prestresses in concrete are created by chemical reaction itself rather than conventional mechanical action, therefore it is also called chemical prestressed concrete or self-stressing concrete. Actually self-stressing concrete is kind of expansive concrete with high expansive energy, by restrictions of steel bar to expansion the pre-compressive stresses (up to about 7 MP_a) are induced

to concrete, and meanwhile the expansion could compensate shrinkage deformation. In china self-stressing concrete is mostly used to manufacture water pipes in order to increase cracking strength in the past decades.

By distributing steel fibers into self-stressing concrete to form steel fiber reinforced self-stressing concrete, SFRSSC for short, the first-crack strength and ultimate tensile strength are remarkably improved with the combined restriction of steel fibers and steel bars. Furthermore, SFRSSC can also improve ductility, fatigue strength, impermeability and impacting strength of concrete. As a result, the durability will be higher than that of ordinary concrete. In addition, the inclusion of steel fibers can help solve some practical problems of self-stressing concrete, such as low objective self-stress level, the aberrant crack deformation, the long-term self-stress loss and others. The obvious advantages of SFRSSC extend applied fields of self-stressing concrete as well as that of steel fiber reinforced concrete. It is very important to understand the nature of this new type of building material in order to provide a rational accordance for design and construction.

This paper is to investigate expansive deformation of self-stressing concrete under the restrain of steel fibers

2. Expansive deformation

It is well known that free expansion for concrete is not expected, but when the expansion is restrained, pre-compressive stresses (self-stresses) come into being in concrete, which is good for members in tension. Therefore, the restrained expansion is a precondition for self-stressing concrete to create self-stress as well as a foundation to calculate self-stress values which indirectly deduced from the expansive deformation. For an example shown in Figure 1, since the expansion of the self-stressing concrete prism can elongate the steel bar in longitudinal axis, according to the equilibrium of endogenous force in a cross-section, the induced self-stress σ_z in concrete is,

$$A_c\sigma_z = A_s E_s (l_0 - l)/l \tag{1}$$

$$\sigma_z = \rho_s E_s \varepsilon_s \tag{2}$$

Where, A_c= cross-sectional area of self-stressing concrete; A_s= cross-sectional area of steel bar; E_s= elastic modulus of steel bar; l= original length of steel bar, namely original length of a specimen; l_0=elongated length of steel bar, namely length of a specimen after expansion ρ_s= reinforcing ratio; ε_s=tensile strain of steel bar, equal to $(l_0 - l)/l$, namely ratio of the restrained expansive deformation of the self-stressing concrete.

Above two expressions illuminate that ε_s is a key point to study SFRSSC. Accordingly some tests were carried out to investigate the relationships between the restrained expansion and restriction ratio.

One-dimensional restrained expansive deformations of steel fiber reinforced self-stressing concrete were measured from 1 day to 28 days. Two main factors influencing self-stress level were considered, namely reinforcing steel

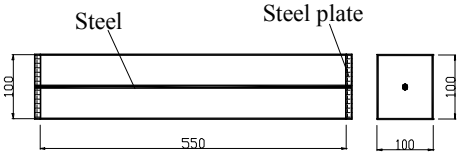

Fig.1 sizes of prism

bar ratio ρ_s and steel fiber volume fraction ρ_f. 4 reinforcing steel bar ratios were 0, 0.78%, 1.36% and 2.87% respectively, reinforcing ratio varied by placing a various diameter steel bar in concrete. 3 steel fiber volume fractions were 0, 1% and 2% respectively.

2.1 Test materials

Matrix materials were composed of sulfoaluminate expansive cement, lime rock coarse aggregate with size of 5~20mm and medium sand. Aspect ratio of steel fibers l/d was 50. All specimens were cast with the same mix proportion, water/cement is 0.38, cement, sand and gravel were 600 kg/m^3,588kg/m^3 and 882kg/m^3. specimens were cured in water after demolding at a constant temperature of 20^{0}C.

2.2 Specimens sizes and measurements

Test specimens are 100mm×100mm×550mm prisms with a single steel bar embedded along longitudinal axial each side anchored by a thick steel plate. Figure 1 shows the specimen's details.

5 strain gauges were attached along the steel bar to record tensile strains, the average of 5 data of the stain gauges present restrained expansive ratio of self-stressing concrete, also expressed as ε_s. 24 hours after casting, the specimens were removed from the molds and cured.

2.3 Relation between restrained expansion ratio ε_s and reinforcing ratio of steel bar ρ_s for self-stressing concrete

The expansive deformations of specimens restrained by steel bar, have a tight relationship with the reinforcing ratio. The more the restraint is, the less the expansive deformation is. But when the reinforcing ratio got higher than a certain one, the restrained expansion no more decreased significantly, and trend towards be gentle, as shown in figure 2. Figure 2 also illustrated that steel bar individual or combination of steel bar and steel fibers can restrain the expansive deformation of self-stressing concrete, but it can be found that steel bar's restraint plays an important role for expansion of self-stressing concrete, and dominates the development of expansion. Hence, for self-stressing concrete reinforced with steel bar, whether reinforced with steel fibers or not, the relationship between restrained expansive ratio ε_s and reinforcing ratio ρ_s adopted a uniform expression, shown as following:

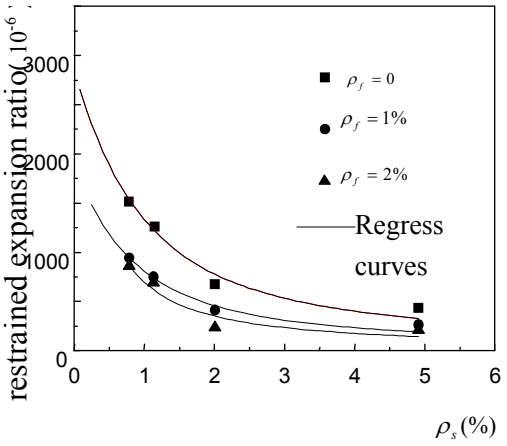

Fig.2 Curves of restrained expansion ratio ε_s *vs* reinforcing ratio ρ_s in different steel fiber volume ρ_f

$$\varepsilon_s = a(1-e^{-x/b})/x, \qquad x>0 \tag{3}$$

where, x= numerator of reinforcing ratio's percent; a,b are regression coefficients of this test respectively. Table1 gives the regression coefficients of a,b in various steel fiber content.

Regression curves of restrained expansion ratio *vs* reinforcing ratio in different steel fiber volume are plotted in figure 2.

Table 1 Regression coefficients of test results

ρ_f / %	0	1	2
$a \times 10^{-6}$	1630	931	702
b	0.56	0.49	0.22

3. Conclusion

According to the test results, an expression of steel reinforcing ration ρ_s and restrained expansive deformation was proposed, and according it the self-stress could be calculated. This simply expression shows a good physical meanings, namely when exceeding a certain ρ_s, the expansive deformation nearly has no development, which indicated the expansive energy is exhausted.

Reference:

[1] Tian Wenling, Li Shichun and Huang Chengkui: Experimental study on mechanical characteristics of steel fiber reinforced expansive concrete, Journal of Building Materials, 2000.9

[2] He Huanan; Huang Chengkui: Research on cracking-resistant capacity of steel-lined steel fiber reinforced self-stressing concrete penstock, Journal of Dalian University of Technology, Vol.46,No.2,2006,p257-261.

[3] He Huannan, Huang Chengkui: Expansive Characteristics and Self-stress Value of Self-stressing Concrete Reinforced with Steel Bar and Steel Fiber, Journal of Building Materials, Vol.7,No.2,2004, p156-160.

[4] Dai Jianguo, Huang Chengkui: Research on the basic mechanical properties of steel fiber reinforced self-stressing concrete, Journal of Building Materials, 2001.1

[5] He Huanan, Huang Chengkui: Calculation of Tensile Strength of Self-stressing Concrete Reinforced with Steel Bar and Fiber, Journal of Building Materials, Vol.5,No.1,2003, p32-36.

Key Engineering Materials Vols. 385-387 (2008) pp 309-312
© (2008) Trans Tech Publications, Switzerland
doi:10.4028/www.scientific.net/KEM.385-387.309

Studying On the Synchronization of a Mechanical Centrifugal Flywheel Governor System

Yandong Chu[a], Jiangang Zhang[b*], Xianfeng Li[c] and Yingxiang Chang[d]

School of mathematics and physics, Lanzhou Jiaotong University, Lanzhou, 730070, China

[a]cyd@mail.lzjtu.cn, [b]zhangjg7715776@126.com, [c]lixf1979@126.com,[d]changyx@mail.lzjtu.cn

Keywords: flywheel governor, Poincaré map, Hopf bifurcation, chaos synchronization,

Abstract: In this paper, the dynamical behaviors of the centrifugal flywheel governor with external disturbance are discussed, and the system exhibits exceedingly complicated dynamic behaviors. The influence of system parameter on the chaotic system is discussed through Lyapunov-exponents spectrum and global bifurcation diagram, which accurately portray the partial dynamic behavior of the system. It is chaotic with proper system parameter, and we utilize Poincaré sections to study the Hopf bifurcation and chaos forming of the centrifugal flywheel governor system. Then, we utilize coupled-feedback control and adaptive control to realize the chaotic synchronization and obtain the conditions of chaos synchronization. Finally, we carry on the theory proof using the Lyapunov stability theory to the obtained conditions, the theoretical proof and number simulation shows the effectiveness of these methods.

Introduction

Chaos is a very interesting nonlinear phenomenon. Since the discovery of chaos synchronization by Pecora and Carroll in 1990[1], and they realize in laboratory, there have been tremendous interests in studying the synchronization of various chaotic systems. Furthermore, chaos synchronization has many potential applications in laser physics, chemical reactor, secure communication and so on [2–4]. In the past 20 years, many techniques for chaos control and synchronization have been developed, such as feedback method, adaptive technique, time delay feedback approach, and back-stepping method [5-6], but many synchronization methods were proposed for low dimension discrete system and autonomous system. At the present, the research on chaos synchronization of non-autonomous system was still not mature, and it has been an important direction of chaos synchronization [7].The chaos synchronization realization on non-autonomous system is quite difficult, because the non-autonomous system includes the force drive, time-dependent non-linear rigidity or damping. In this paper, the adaptive control method is proposed to realize the chaos synchronization, and numerical simulations confirm the validity and feasibility of the proposed methods.

Main equations

The centrifugal flywheel governor system with external disturbance is shown in Fig.1. The motor drives the flywheel to rotate with angular velocity ω. The flywheel is joined with axis through the gear case. The axis rotates with angular velocity $n\omega$. Rod 1 and rod 2 of the length l are joined with a hinge at the end of rod 3, and there is a braced ball of mass m at the end of the rod 1 and rod 2. A linear spring of stiffness k covers on the axis and its one end is against to the end plane of the sleeve. The vapor's flux Q can be adjusted by the mechanical centrifugal flywheel governor,

which makes the flywheel rotates at a certain rotational angular velocity ω_0. When $\Delta\omega = \omega - \omega_0 \neq 0$, the rods will move up and down.

Some basic assumptions for the system are

(1) neglecting the mass of the rods and the spring;

(2) viscous damping in rod bearing of the fly-ball is presented by damping constant *c*.

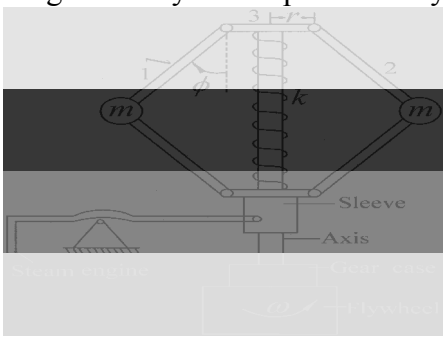

Fig.1 Physical model of the mechanical centrifugal flywheel governor with external disturbance

With the notation used in Fig.1, we can obtain the Lagrangian

$$T = 2\times\{\frac{1}{2}m[(r+l\sin\phi)^2(n\omega)^2 + l^2\dot{\phi}^2]\} = m(n\omega)^2(r+l\sin\phi)^2 + ml^2\dot{\phi}^2 \tag{1}$$

where l, m, r and ϕ represent the length of the rod, the mass of fly-ball, the distance between the rotational axis and the suspension joint, and the angle between the rotational axis and the rod. Then using Lagrange equation of motion for the governor can be derived as follows

$$2ml^2\ddot{\phi} - 2ml^2n^2\omega^2\sin\phi\cos\phi + 4kl^2\times(1-\cos\phi)\sin\phi + 2mgl\sin\phi = -c\dot{\phi} \tag{2}$$

where *c* is the damping coefficient.

For the rotational machine the net torque is the difference between the torque P_1 produced by the engine and the load torque P, which is available for angular acceleration. Applying Newton's Second law, we have

$$I\frac{\mathrm{d}\omega}{\mathrm{d}t} = P_1 - P \tag{3}$$

where I is the moment of inertia of the machine. For a given angular velocity ω, we assume that P_1 substituted for $\overline{P}_1$. As the angle ϕ varies, the position of control valve which admits the fuel is also varied. Thus, we have

$$P_1 = \overline{P}_1 + \alpha(\cos\phi - \cos\phi_0) \tag{4}$$

where ϕ_0 and α represent the angle corresponding to ω_0 and the proportionally constant. Substituting Eq. (4) into Eq. (3), it becomes

$$I\dot{\omega} = \alpha\cos\phi - F \tag{5}$$

where $F = (P + \alpha\cos\phi_0) - \overline{P}_1$, and F is an equivalent torque of the load Eq.(10) is the second differential equation of motion for the system. Eqs. (2) and (5) can be written in three-dimensional non-dimensional form

$$\dot{\phi} = \varphi, \qquad \dot{\varphi} = d\omega^2\cos\phi + (e + p\omega^2)\sin\phi\cos\phi - \sin\phi - b\varphi, \qquad \dot{\omega} = q\cos\phi - F \tag{6}$$

where $q = \frac{\gamma}{J\Omega_n}$, $F = \frac{\beta}{J\Omega_n}$, $d = \frac{n^2mr}{2kl+mg}$, $e = \frac{2kl}{2kl+mg}$, $p = \frac{n^2ml}{2kl+mg}$, $b = \frac{c}{2ml^2\Omega_n}$, $\Omega_n = \sqrt{\frac{2kl+mg}{ml}}$, and the dot presented the derivative with respect to t, φ is $\mathrm{d}\phi/\mathrm{d}t$. Hence, the dynamics of the system of rotational machine with fly-ball governor is described by a three-dimensional autonomous system.

The load torque is assumed to be constant for the system in the Eq. (5). Another condition can be considered. The load torque is now not constant but is represented by a constant term and a harmonic $F + a\sin\omega t$, where F, a, ω are constants. Let $\phi = x$, $\dot{\phi} = y$, $\omega = z$, Eq. (5) can be written in three-dimensional non-autonomous form

$$\dot{x} = y, \quad \dot{y} = dz^2\cos x + \frac{1}{2}(e + pz^2)\sin 2x - \sin x - by, \qquad \dot{z} = q\cos x - F - a\sin\omega t, \tag{7}$$

Bifurcation and routes to chaotic motion

In order to detect periodic motion and chaotic motion, a bifurcation diagram can be constructed, which is proceeded by using numerical integration of Eq. (7). To integrate this nonlinear system, we use the fourth-order Runge-Kutta algorithm. The time step is always $\Delta t = 0.01$, and the integration time is always greater than $t = 10{,}000$. The mechanical centrifugal flywheel governor with $d = 0.08$, $e = 0.5$, $p = 0.01$, $F = 1.942$, $a = 0.4$, $b = 0.4$ and $\omega = 1.0$, have been chosen for analyses, one can find that the Hopf bifurcation occurs in the bifurcation diagram, as shown in Fig.2(a). This phenomenon can be characterized by the Lyapunov exponents (see Fig.2(b)), which coincides well with the bifurcation diagram.

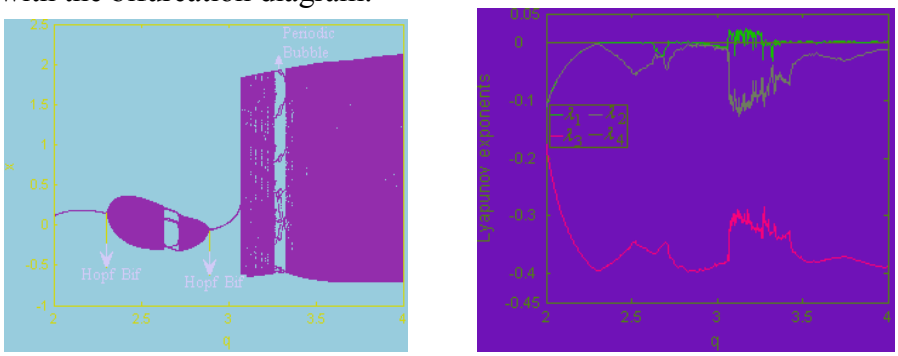

Fig.2 Global bifurcation diagram and the spectrum of Lyapunov exponents of the system

Chaos synchronization

Consider two non-autonomous identical systems

$$\dot{x} = Ax + f(x,t) + g(t) \tag{8}$$

and

$$\dot{y} = Ay + f(y,t) + g(t) + u(x,y) \tag{9}$$

where $x, y \in R^n$ are state vectors, Ax and Ay are the linear parts of system (8) and (9), $f(x,t) \in R^{n\times 1}$ and $f(y,t) \in R^{n\times 1}$ are the nonlinear parts of system (8) and (9), which are differentiable function, $g(t) \in R^{n\times l}$ is exciting force, the system (8) is the drive system, and the system (9) is the response system, $u(x,y)$ is the control input.

In order to achieve synchronization of (8) with (9), we add the coupled feedback control function $u(x,y) = (u_1(t), u_2(t), \cdots, u_n(t))^T = K(x-y)$ to system (9), where $K \in R^{n\times n}$ is a constant diagonal matrix, referred to as the feedback gain matrix or coupling matrix. Then the response system becomes

$$\dot{y} = Ay + f(y,t) + g(t) + K(x-y) \tag{10}$$

Subtracting Eq. (8) from Eq. (10), we obtain the dynamical error system

$$\dot{e} = Ae + (f(y,t) - f(x,t)) - Ke = (A-K)e + (f(y,t) - f(x,t)) \tag{11}$$

where $e = y - x = (e_1, e_2, \cdots, e_n)^T$ is the error state vector. Our goal is to design a suitable constant coupling matrix K such that $\lim_{t\to+\infty} \|e\| = 0$, where $\|\|$ denotes the Euclidean norm.

Theorem1. If $f(y,t) - f(x,t) = F(x,y,t)(y-x)$, $\|F(X,Y,t)\| \le M < \infty$ and choose proper coupling matrix K, the two chaotic systems (8) and (10) can be synchronized.

According to the form of (8), we choose system (7) as the drive system and it becomes

$$\dot{x}_1 = x_2, \quad \dot{x}_2 = dx_3^{\,2}\cos x_1 + \frac{1}{2}(e + px_3^{\,2})\sin 2x_1 - \sin x_1 - bx_2, \quad \dot{x}_3 = q\cos x_1 - F - a\sin \omega t, \tag{12}$$

Where $x = (x_1, x_2, x_3)^T$, $A = \begin{bmatrix} 0 & 1 & 0 \\ 0 & -b & 0 \\ 0 & 0 & 0 \end{bmatrix}$, $g(t) = (0,0,-F - a\sin \varpi t)^T$ and

$$f(x,t)=\begin{bmatrix} 0 \\ dx_3^{\,2}\cos x_1+\frac{1}{2}(e+px_3^{\,2})\sin 2x_1-\sin x_1 \\ q\cos x_1 \end{bmatrix}.$$

We assume that the drive system (12) with three state variables drives the following response system having identical equations denoted above.

$$\dot{y}_1=y_2+k_1(x_1-y_1),\qquad \dot{y}_2=dy_3^{\,2}\cos y_1+\frac{1}{2}(e+py_3^{\,2})\sin 2y_1-\sin y_1-by_2+k_2(x_2-y_2)$$
$$\dot{y}_3=q\cos y_1-F-a\sin\varpi t+k_3(x_3-y_3) \tag{13}$$

where $y=(y_1,y_2,y_3)^T$, $f(y,t)=\begin{bmatrix} 0 \\ dy_3^{\,2}\cos y_1+\frac{1}{2}(e+py_3^{\,2})\sin 2y_1-\sin y_1 \\ q\cos y_1 \end{bmatrix}$.

Consider the systems given in (12) and (13). The system parameters of two systems in simulation are $d=0.08$, $e=0.5$, $p=0.01$, $F=1.942$, $a=0.4$, $b=0.4$, $\varpi=1.0$ and $q=2.5$ so that the two systems exhibit the chaotic behavior. The chaotic attractor is shown in Figs.5. The initial values of the drive system and response system are taken as $x|_{t=0}=(0.2,0.1,0.1)$ and $y|_{t=0}=(-1.1,0.6,1.1)$ respectively. Thus, the initial errors are $e|_{t=0}=(-1.3,0.5,1.0)$. The simulation results are illustrated in Figs.3 (a), Fig.3 (b) shows the simulation results after adding the controller when $t=20$ .As we expect, one can observe that response system starts to trace drive system quickly.

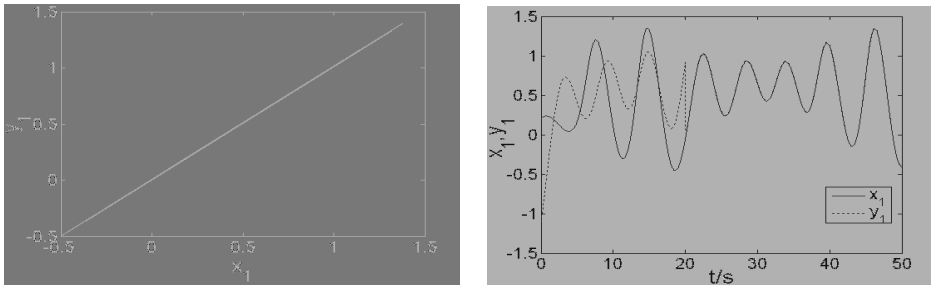

Fig.3 Phase portraits, errors and similarity of unidirectional coupled systems with $k\sin(y-y_1)$, $k=0.66$

Summary

In this letter, we present further numerical results concerning the mechanical centrifugal flywheel governor system. Its chaotic features are fully exposed by all the bifurcation diagrams and Lyapunov exponents. This paper demonstrates chaos synchronization between two identical chaotic centrifugal flywheel governor system systems by using coupling feedback control. The sufficient conditions for achieving chaos synchronization are derived by using Lyapunov stability theory. Numerical simulations are performed to verify the effectiveness of the proposed synchronization techniques.

References

[1] Pecora LM,Carroll TL: Phys Rev Lett Vol.64 (1990), p.821
[2] Terry JR, Thornburg KS: Phys Rev E Vol.359 (1999), p.4036
[3] Yang, T, Chua, LO: Int. J.Bifurcation and Chaos Vol.7 (1997), p.645
[4] Yang, T, Chua, LO: Int. J.Bifurcation and Chaos Vol.8 (1998), p.1657
[5] Tao Chao-hai,Lu Jun-an,Lü Jin-hu: Acta Physica Sinica Vol.51 (2002), p.1497
[6] Z.M. Ge, J.K. Lee: Applied Mathematics and Computation Vol.163 (2005), p.667
[7] Z.M. Ge, J.K. Lee: Journal of Sound and Vibration Vol.282 (2005), p.635

Key Engineering Materials Vols. 385-387 (2008) pp 313-316
© (2008) Trans Tech Publications, Switzerland
doi:10.4028/www.scientific.net/KEM.385-387.313

A Direct Damaged Identification Method of Frame Structures Based on Residual Force Vector

ZOU Wan-jie[1,2,a], QU Wei-lian[1,b]

[1] School of Civil Engineering and Architecture, Wuhan University of Technology, Wuhan, 430070, China.

[2]Department of Civil Engineering, Guangxi University of Technology, Liuzhou, 545006, China.

[a]zouwanjie@tom.com, [b]quwl1946@sina.com

Keywords: damage identification; residual force vector method; stiffness connectivity vector; frame structures

Abstract: By using the intrinsic character of the frame structures, a new direct damage identification method of the frame structures based on residual force vector is presented. The stiffness connectivity matrix is obtained by sensitivity analysis. The stiffness matrix perturbation of the damaged structure can be expanded by the stiffness connectivity matrix, then substituting it into residual force vector equation, the new residual force vector equation expressed by the stiffness connectivity matrix is obtained. This equation can be solved directly, so the stiffness perturbation of layers is got, by it, the damaged locations and the extents of the frame structures are identified. At last, a numerical example of a seven-layer frame structure is given, the identification result shows that, only with the first-order mode of the damaged structure, the damage can be identified accurately. Even in considering of some degreed noise of the mode parameters, the structure damage can be identified well, demonstrating the effectiveness of presented method.

Introduction

The structures damage identification base on the dynamic test data is a subject that has received much attention in recent years, and the model updated is one of the main structures identification methods. These methods mainly include residual force vector method, minimum norm updated method, minimum rank updated method and sensitivity analysis method[1], etc. Residual force vector method was presented by Zimmerman and Kaout[2] at first, and named subspace rotation algorithm at that time, Kahl and Sirkis[3] improved this method and applied it on the beam structures damage identification, they identified the damage locations successfully. This method combined with other method was also used in the damage identification of the concrete frame structures successfully [4]. In general, all these methods base on the residual force vector mentioned above can only identify the damage locations, or the extents of damage in qualitatively, if the identification of damage extents is need, others method such as the sensitivity analysis or GA are needed, and by this process, the additional error is inevitably, it brings the unfavorable influence to the identification results. Doebling[5] extended the minimum rank updated method combined with the residual force vector, used the elements stiffness parameters directly in the minimum rank updated to identify the damage of structures, the damage locations and extents of a eight-bay truss of NASA were identified successfully, and came to the conclusion that the minimum rank updated method was better than the minimum norm updated method. In this paper, the idea of minimum rank updated use the element's stiffness parameters directly is inherited, with the using of character of the shear-type frame structures; a new damage identification method of frame structure base on residual force vector method is presented.

1 The basal theory of residual force vector method

The motion equation of the shear-type frame structure is:

$$[M]\{\ddot{x}\}+[K]\{x\}=\{F\} \tag{1}$$

It's corresponding characteristic equation is:

$$([K]-\lambda_j[M])\{\phi_j\}=\{0\} \tag{2}$$

where [K] and [M] are the global stiffness matrix and the global mass matrix of correct model separately, λ_j and $\{\phi_j\}$ are the jth order eigenvalue and the jth order eigenvector.

To the damaged structure, suppose:

$$[K_d]=[K_u]-[\Delta K]\ ,\ [M_d]=[M_u]-[\Delta M] \tag{3}$$

where $[K_u]$,[Mu] and $[K_d]$,$[M_d]$ are the global stiffness matrix and the global mass matrix of nominal and damaged structure separately, [ΔK] and [ΔM] are the structural stiffness and mass matrix perturbations separately.

To the damaged structure

$$([K_d]-\lambda_{dj}[M_d])\{\phi_{dj}\}=\{0\} \tag{4}$$

where λ_{dj} and $\{\phi_{dj}\}$ are the *j*th order eigenvalue and eigenvector after damage. Substituting the Eq.(3) into Eq.(4) and rearranging to get

$$([K_u]-\lambda_{dj}[M_u])\{\phi_{dj}\}=([\Delta K]-\lambda_{dj}[\Delta M])\{\phi_{dj}\} \tag{5}$$

Since the left-hand side of Eq. (5) is known, the residual force vector $\{R_j\}$ can be defined for each measured mode as

$$\{R_j\}=([K_u]-\lambda_{dj}[M_u])\{\phi_{dj}\} \tag{6}$$

The Eq.(5) can be expressed as

$$([\Delta K]-\lambda_{dj}[\Delta M])\{\phi_{dj}\}=\{R_j\} \tag{7}$$

Eq.(7) is named the residual force vector equation of damaged structure. In general, structure damage mainly begot in the reducing of stiffness, and mass has no perturbation, [ΔM]=0, so the Eq.(7) can be simplified to

$$[\Delta K]\{\phi_{dj}\}=\{R_j\} \tag{8}$$

2 Damaged identification of frame structures

2.1 The expansion of the global stiffness matrix [K] and the stiffness matrix perturbation [ΔK] of damaged structure by using the stiffness connectivity matrix[5]

For a n-layer frame structure, the global stiffness matrix of nominal structure [K] and the structural stiffness matrix perturbation after damage [ΔK] can be expanded as follows

$$[K]=[A][P][A]^T \tag{9}$$

$$[\Delta K]=[A][\Delta P][A]^T \tag{10}$$

A n-layer frame structure can be simplified to a n degree of freedoms system, where [P] and [ΔP] are the diagonal matrices of layer-level stiffness parameters and it's perturbations as follows

$$[P]=diag(k_1,\cdots,k_n)\ ,\ [\Delta P]=diag(\Delta k_1,\cdots,\Delta k_n)$$

where k_i and Δk_i are the *i*th layer's stiffness and it's perturbation after damage. [A] is called the stiffness connectivity matrix, and $[A]=[\{a_1\}\ \{a_2\}\ \cdots\ \{a_n\}]$, where $\{a_i\}$ is the stiffness connectivity vector of the *i*th layer's stiffness k_i, [A] relates to the form of the structures and has no change before and after structures damage.

The calculation of [A]. When the Eq.(10) is expanded, it's element is

$$\Delta K_{ij} = [A_{i1}A_{j1} \quad A_{i2}A_{j2} \quad \cdots \quad A_{in}A_{jn}][\Delta k_1 \quad \Delta k_2 \quad \cdots \quad \Delta k_n]^T \tag{11}$$

Meanwhile, ΔK_{ij} can be derived from the first-order sensitivity analysis of the stiffness matrix

$$\Delta K_{ij} = \frac{\partial K_{ij}}{\partial k_\beta}(\Delta k_\beta) \quad (i, j, \beta = 1, \cdots, n) \tag{12}$$

Colligating Eq.(11) and Eq.(12) to get

$$A_{i\beta}A_{j\beta} = \frac{\partial K_{ij}}{\partial k_\beta} \quad (i, j, \beta = 1, \cdots, n) \tag{13}$$

All of the A_{ij} can be got by solving Eq.(13), so the matrix [A] is got.

2.2 The calculation of the layers' damage stiffness parameters

Eq.(10) can be expanded to

$$[\Delta K] = [A][\Delta P][A]^T = \Delta k_1\{a_1\}\{a_1\}^T + \cdots + \Delta k_n\{a_n\}\{a_n\}^T = \sum_{i=1}^{n} \Delta k_i\{a_i\}\{a_i\}^T \tag{14}$$

Substituting Eq.(14) into Eq.(8) to get

$$\sum_{i=1}^{n} \Delta k_i\{a_i\}\{a_i\}^T\{\phi_{dj}\} = R_j \tag{15}$$

Suppose

$$\Delta k_i\{a_i\}^T\{\phi_{dj}\} = \gamma_i \tag{16}$$

Then Eq.(15) can be expressed as

$$\sum_{i=1}^{n} \gamma_i\{a_i\} = R_j \tag{17}$$

Eq.(17) can be expressed as the matrix form

$$[A]\{\gamma\} = R_j \tag{18}$$

where [A] is a full rank square matrix, so the Eq.(18) can be solved directly, and the γ_i are got, then substituting it into Eq.(16), and solving it, the Δk_i ($i = 1, \cdots, n$) can be got, consequently, the damage locations and extents of frame structure are determined at the same time.

3 Numerical example

A seven-layer shear-type frame structure shown in Fig.1, it's parameters are $m_i = 6\times10^5 kg$, $k_i = 4\times10^8 N/m$, ($i = 1 \sim 7$). Which mass matrix is a diagonal matrix, and stiffness matrix is a three diagonal matrix. Now consider the stiffness of the 1th,4th,5th,6th layers are damaged, stiffness reduce 20% and 10% separately, or k1,k4 reduce to $3.2\times10^8 N/m$ and k5,k6 reduce to $3.6\times10^8 N/m$ separately, use the method presented in this paper to identify it's damage.

Computing all of the A_{ij} from Eq.(13), the stiffness connectivity matrix [A] is got

$$[A] = \begin{bmatrix} 1 & 1 & 0 & 0 & 0 & 0 & 0 \\ 0 & -1 & 1 & 0 & 0 & 0 & 0 \\ 0 & 0 & -1 & 1 & 0 & 0 & 0 \\ 0 & 0 & 0 & -1 & 1 & 0 & 0 \\ 0 & 0 & 0 & 0 & -1 & 1 & 0 \\ 0 & 0 & 0 & 0 & 0 & -1 & 1 \\ 0 & 0 & 0 & 0 & 0 & 0 & -1 \end{bmatrix}$$

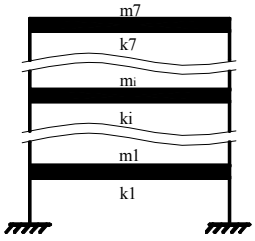

Fig.1 Frame structure

(1) Result of damage identification in no test noise

Assume that only the first mode of the damaged structure is measured, so that λ_{d1} and $\{\phi_{d1}\}$ are known.(In the numerical example, it can be computed from the damaged stiffness matrix.)

$\lambda_{d1}=0.2606\times10^{2}$ rad2/s2, $\{\phi_{d1}\}=10^{-3}\times[0.1555\quad 0.2738\quad 0.3814\quad 0.4973\quad 0.5787\quad 0.6350\quad 0.6608]^{T}$

The residual force vector computed by the first-order mode parameters is

$$\{R_1\}=10^{4}\times[1.2439\quad 0\quad -0.9270\quad 0.6014\quad 0.1005\quad 0.2251\quad 0]^{T}\ \text{N}$$

Then $\{\gamma\}$ can be computed by substituting [A] and $\{R_1\}$ into Eq.(18) to get

$$\{\gamma\}=10^{4}\times[1.2439\quad 0\quad 0\quad -0.9270\quad -0.3256\quad -0.2251\quad 0]^{T}$$

Then, Δk_i is computed by substituting γ_i, $\{\phi_{d1}\}$ and $\{a_i\}$ of [A] into Eq.(16) to get

$$\{\Delta k\}=10^{7}\times[8\quad 0\quad 0\quad 8\quad 4\quad 4\quad 0]^{T}\ \text{N/m}$$

So the layers' stiffness perturbations are got: $\Delta k_1=8\times10^{7}$ N/m, $\Delta k_4=8\times10^{7}$ N/m, $\Delta k_5=4\times10^{7}$ N/m , $\Delta k_6=4\times10^{7}$ N/m, and others $\Delta k_i\,(i=2,3,7,8)$ are zeros. The calculation result accord to the assumption entirely, the damage occurs at the 1th,4th,5th,6th layers, and the stiffness of the 1st,4th layers' reduce 20%, and 5th,6th layers' reduce 10% are confirmed.

(2) Result of damage identification in 5% test noise in mode shapes.

In order to study the influence of the test noise, the level of 5% test noise is added to the first-order mode shapes. Repeat the solution process of (1), the identification result are got

$$\{\Delta k\}=10^{7}\times[7.7524\quad -0.0391\quad 0.08511\quad 8.2862\quad 3.8924\quad 4.1805\quad 0.1105]^{T}$$

The relative errors of Δk_1, Δk_4, Δk_5, Δk_6 are 3.10%, 3.58%, 2.69%, 4.50% separately.

4 Conclusion

Based on the works of Doebling and others, a new method for damage identification of the frame structures using the residual force vector was presented in this paper. By using the character of the shear-type frame structures and the layers' level stiffness parameters constraining the connectivity of the global stiffness matrix, the method is able to identify the locations and the extents of the multiple-layer damage case by only one step calculation. In the numerical example, the influence to the identification result of test noise was discussed too, in the level of 5% test noise of the first-order mode shapes, the maximum error is only 4.50%, and the average error is 3.47%, the identification effect is well. Furthermore, in this method, only the first-order mode parameters of the damaged structures are need, that is to say that the measuring precision of the mode can be ensured. The identification result indicates that the method may be useful for the onsite engineering.

References

[1] S. W. Doebling, C. R. Farrar, M. B. Prime: A summary review of vibration-based damage identification methods.The Shock and Vibration Digest, Vol.30(1998), p. 91-105

[2] D. C. Zimmerman, M. Kaouk: Structural damage detection in beam structures using a subspace rotation algorithm. AIAA Journal, Vol.32(1992), p. 2341-2350

[3] K. Kahl, J. S. Sirkis: Damage detection in beam structures using subspace rotation algorithm with strain data. AIAA Journal, Vol.34(1996), p. 2609-2614

[4] Zhou xianyan, Shen pushing, Cheng xiangyun. Damage Assessment of Reinforce Concretes Structures by Vibration Parameter Identification Technique. China Civil Engineering Journal, Vol.31(1998), p.39-45 (in Chinese)

[5] S. W. Doebling. Minimum- rank optimal update of elemental stiffness parameters for structural damage identification . AIAA Journal, Vol.34(1996), p.2615-2621

Key Engineering Materials Vols. 385-387 (2008) pp 317-320
© (2008) Trans Tech Publications, Switzerland
doi:10.4028/www.scientific.net/KEM.385-387.317

The effect of the singularity induced by the free surface on fatigue crack growth in thin structures

Pavel Hutař[1, a], Luboš Náhlík [1,b] and Zdeněk Knésl[1,c]

[1]Institute of Physics of Materials, Academy of Sciences of the Czech Republic

Zizkova 22, 616 62 Brno, Czech Republic

[a]hutar@ipm.cz, [b]nahlik@ipm.cz, [c]knesl@ipm.cz

Keywords: Fatigue crack, vertex singularity, thin structures.

Abstract. In many industrial applications is necessary to predict fatigue lifetime of thin structures, where the stress field near the crack front have a real three-dimensional nature. Due to the existence of vertex singularity in the point where the crack front touching free surface, crack propagation in 3D structures cannot be reduced to a series of plane strain or plane stress problems along the crack front edge. The paper describes the influence of vertex singularity on the distribution of the stresses around the crack front for three-dimensional body. The distribution of the stress singularity through the thickness of the specimen gives us indication of the crack behavior in thin structures. The estimation of the thickness of the specimen where the change of singularity plays an important role on fatigue crack growth rate (in dependence on Poisson's ratio) is carried out. The results contribute to a better understanding of the crack behavior in thin structures, and can help to more reliable estimates of their residual fatigue life.

Introduction

Crack propagation in thin sheets is undoubtedly influenced by the surface termination of the crack front edge, where the planar elastic solution for crack tip singularity is not applicable and the singular stress field is of three dimensional nature. Due to existence of vertex singularity in the point where crack front intersects free surface, singular stress distribution is changed and can influence fatigue crack behaviour. The three-dimensional singular stress field near the point where the crack front intersecting the free surface was investigated by Bažant and Estenssoro [1] and Benthem [2]. They found that the singularity exponent induced by the free surface differs from 0.5 and dependents on Poisson's ratio. Although, numerous papers are focused last 20 years on this problem [3,4,5,6], solution is usually made for semi-infinite space and can be used only for relatively thick structures.

The paper is focused on the influence of vertex singularity on the distribution of the stresses around the crack front for thin-walled three-dimensional structure. Numerically obtained distribution of the stress singularity through the thickness of the specimen gives us indication of the crack behavior in thin structures.

Numerical model

A middle tension specimen was used as a model of the simple 3D configuration with a straight crack, see Fig.1. Uniform tensile stress was applied and so only loading mode I was considered. Exploiting the symmetry in the specimen geometry and loading, only one-eighth of the MT specimen was modeled by the finite-element method.

Because the power of the singularity close to the free surface is weaker than 0.5 (corresponding to crack in two-dimensional case), the validity of the classical fracture parameters (stress intensity factor K or energy release rate G) are violated. Therefore, we assume stress distribution around the crack tip in each single layer perpendicular to crack front in general form:

$$\sigma_{ij} = \frac{H_I}{r^p} \cdot f_{ij}(p,\theta), \tag{1}$$

where H_I is a generalized stress intensity factor, p is stress singularity exponent and r,θ are cylindrical coordinates. Based on this assumption, singularity exponents along the crack front using log-log regression analysis were estimated [7]. Because this methodology is based on direct interpolation of stress or displacement, it is necessary to make a sufficiently fine mesh around the crack front.

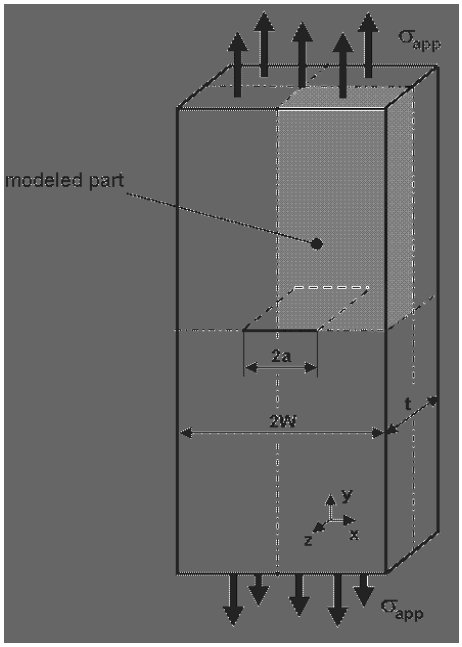

Fig.1 Model used for finite element computations

Discussion of numerical results

Change of the singularity exponent along the crack front for different specimen thickness is presented in Fig.2. In this case Poisson's ratio is ν= 0.5. The results of calculations for thick specimens (10, 20 mm) correspond to previous numerical results obtained in [7] and show that the thickness of the surface region influenced by the vertex singularity does not depend on the specimen thickness but depends on Poisson's ratio ν only. The singularity exponent is close to 0.5 in the middle of the specimen and in the point where the crack front intersects the free surface the stress singularity exponents correspond to Bažant [1] and Benthem [2]. These conclusions are valid only for specimen with thickness greater than boundary regions influenced by vertex singularity, where vertex singularities are not mutually influenced. When the vertex singularities are mutually influenced, distribution of the singular stress field along the crack front is significantly changed and assumption of the semi-infinite space used for semi-analytical estimation of the vertex singularity is not valid. The stress singularity exponent in the middle of the specimen continuously decreases and vertex singularity in the intersection between crack front and free surface increases (specimens with t=1, 2mm). Finally, for the really thin structures singular stress field have the same manner through the thickness of the specimen and stress singularity exponent is roughly constant in the relation with thickness. In the case of Poisson's ratio ν= 0.5 the singularity exponent for thin structures (thinner than 1 mm) is equal to 0.465. To find relation between fatigue crack propagation rate in usual planar problem with stress singularity ½ and the singular stress field with different singularity a concept based on generalized stress intensity factor described in [7] can be used. Generally, decrease of the stress singularity exponent for the same nominal loading leads to decrease of the fatigue crack growth rates.

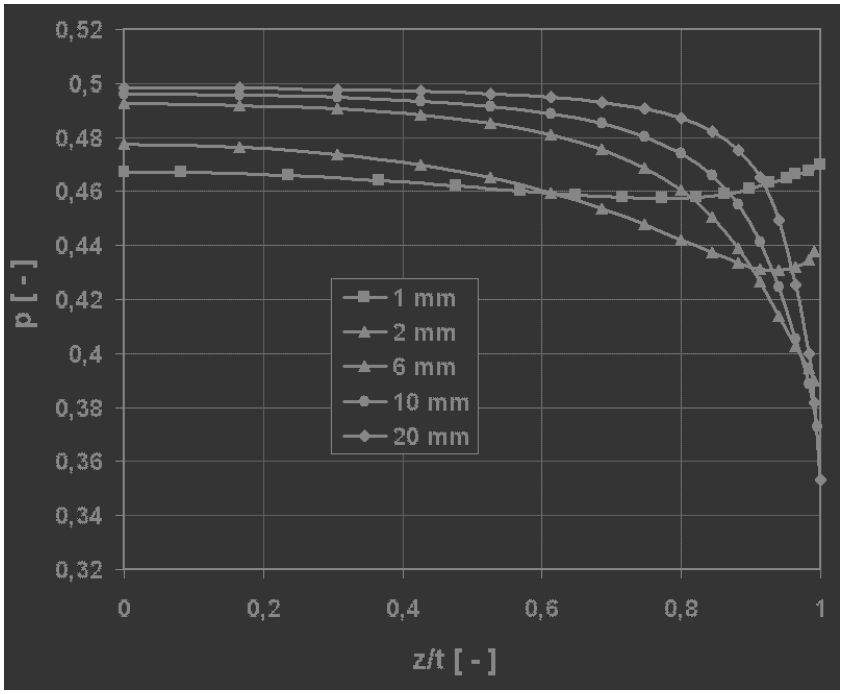

Fig.2. Change of the stress singularity exponent along crack front for specimens with various thickness (1,2,6,10,20 mm) for Poisson's ratio ν= 0.5

Detailed study of the change of vertex singularity exponent with respect to the thickness of the specimen for different Poisson's ratio is well documented in Fig.3. The vertex singularity corresponds to semi-analytical estimation of Bažant and Benthem [1,2] only for thick specimens t = 10, 20 mm. For thin specimens vertex singularity increases. Therefore, difference between stress singularity in the middle of the specimen (Fig.4.) and in the vertex point for the thin-walled structures decreases with decrease of the thickness. Finally, if the structure is thin enough, stress singularity is roughly constant along crack front, smaller than ½, and depends on the Poisson's ratio of the material.

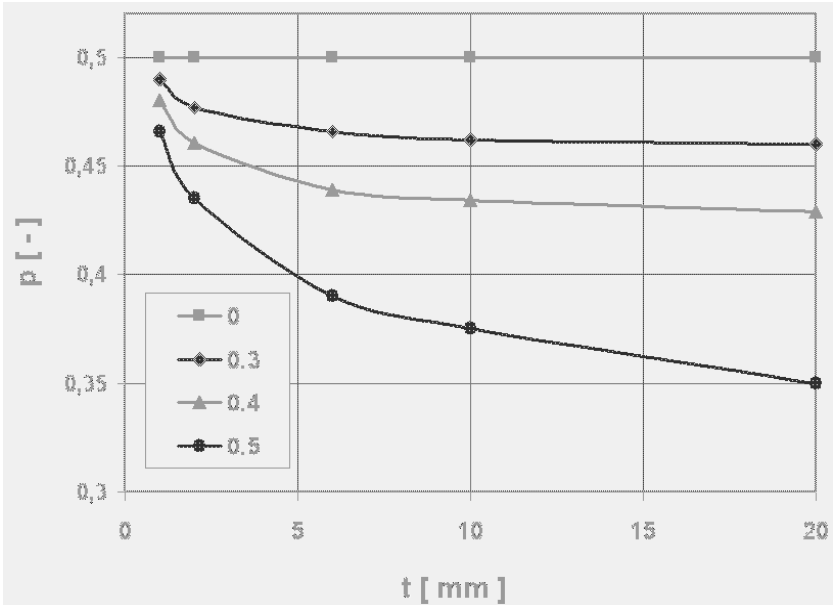

Fig.3. Change of the stress singularity exponent on the free surface for different Poisson's ratios as a function of specimen thickness

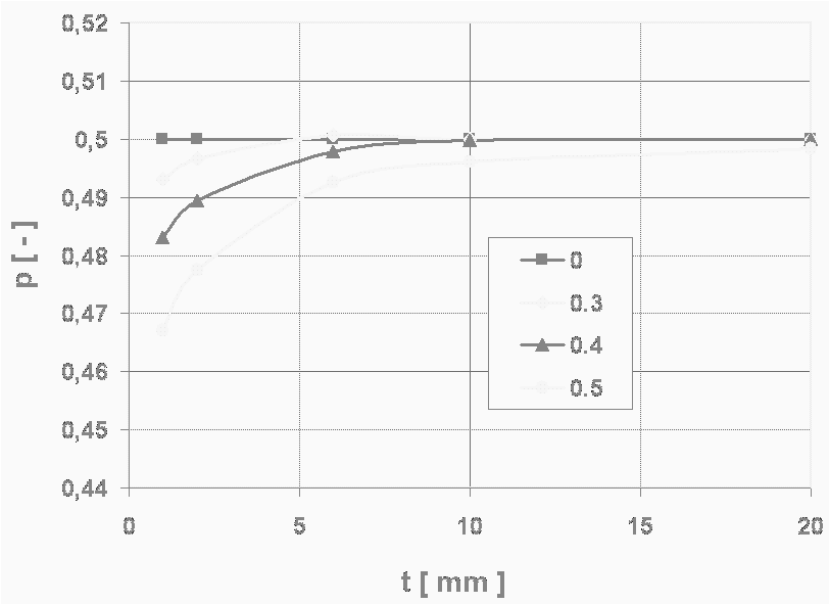

Fig.4. Change of the stress singularity exponent in the middle of the specimen for different Poisson's ratios as a function of specimen thickness

Summary

The influence of the stress singularity induced by the free surface on the behavior of a middle tension specimen is investigated in this paper. Attention is mainly focused on the change of the stress singularity exponent along the crack front of a thin-walled three-dimensional specimen. Displacements and stress obtained by finite element analysis were used to estimate the power of the singularity using a log-log regression analysis. It was found, that vertex singularity corresponds to semi-analytical estimation only for thick specimens. With decrease of the structure thickness vertex singularity increases. For really thin structures ($t < 1$ mm) singular stress field around crack tip have the same manner through the thickness of the specimen and stress singularity exponent is roughly constant in the relation with thickness (e.g. in the case of Poisson's ratio $\nu = 0.5$ the singularity exponent is equal to 0.465). Decrease of the stress singularity exponent for the same nominal loading leads generally to decrease of the fatigue crack growth rates.

Acknowledgments

This investigation was supported by grants nos. 106/06/P239 and 101/08/1623 of the Czech Science Foundation.

References

[1] Z.P. Bažant, L.F. Estenssoro : Int. J. Solids Structures Vol. 15 (1979), p. 405-426

[2] J.P. Benthem : Int. J. Solids Structures Vol. 13 (1977), p. 479-492

[3] M. Heyder, G. Kuhn : International Journal of Fatigue Vol. 28 (2006), p. 627-634

[4] C.R. Pictu, V. Gupta : J. Mech. Phys. Solids Vol. 45 (1997), p. 1495-1520

[5] L.P. Pook : Engineering Fracture Mechanics Vol. 48 (1994), p. 367-378

[6] K.N. Shivakumar, I.S Raju : International Journal of Fracture Vol. 45 (1990), p. 159-178

[7] Hutař, P., Náhlík, L., Knésl, Z.: Key Engineering Materials, Vols. 348-349 (2007), p. 377-380

Key Engineering Materials Vols. 385-387 (2008) pp 321-324
© (2008) Trans Tech Publications, Switzerland
doi:10.4028/www.scientific.net/KEM.385-387.321

The Elastic-viscoplastic Field at the Mixed-mode Crack-Tip under Compression and Shear

Liang Wenyan[1, a], Wang Zhenqing[1, b] , Zhou Bo[1, c] ,Lv Hongqing[1, d]

[1]School of Civil Engineering, Harbin Engineering University, Harbin 150001, China
[a]liangwenyan@hrbeu.edu.cn, [b]wangzhenqing@hrbeu.edu.cn, [c]qingziworld@hotmail.com, [d]balili333@yahoo.com

Keywords: mixed-mode crack-tip under compression and shear; quasi-static propagating; viscosity effect ; elastic-viscoplastic materials

Abstract: Under the assumption that the viscosity coefficient is in inverse proportion to the power law of the equivalent plastic strain rate. The friction touch effect between viscosity and crack-tip surfaces is considered, the asymptotic solution is established for elastic-viscoplastic field at the mixed-mode quasi static crack-tip under compression and shear. The numerical solution at crack-tip without stress and stain gap is obtained. The variation of numerical solution is discussed for the mixed-mode under compression and shear according to each parameter. Through numerical results and analysis for the mixed-mode crack-tip field under compressing and shear, it is whole plastic without elastic unloaded section, viscosity effect is an important factor when propagating crack-tip field.

Introduction

Large amount of nonreversible deformation energy will be created because of higher strain rate in the process of crack propagating, and part of deformation energy release out with hot form that leads temperature power-up at the crack-tip and then material has the viscidity characteristic. As a result, the research about the effect between material viscidity character and material fracture character has been paid more and more attention.

Matching condition of elasticity, plasticity and viscidity is discussed for mode III crack in reference [1], and the change law of numerical value solution for mode I crack and model crack with every parameter is discussed in reference [2,3]. However, all of above researches were based on crack face opening and no friction touch, namely the friction effect between crack faces is ignored[4]. Though this assumption has resolved classical I and II crack problem, but it does not accord with actual project condition that the crack propagates under mixed force effect. The project reality requires that the Mechanics worker must give corresponding rationale to explain and to resolve the parameters' changing conditions of crack-tip filed under mixed force.

1 Basic equations

Mechanical model of mixed-mode crack-tip under compression and shear is shown in Fig.1. Let $X_\alpha(\alpha=1,2)$ be fixed plane coordinate system. Consider a semi-infinitive crack propagating along X_1 with constant velocity V in infinitive solid. X_2 is vertical to the crack plane. Then, following coordinate systems $o-xy$ and $o-r\theta$ are established with crack-tip being initial point, as is shown in Fig.2. For steady propagation, the material derivative of any physical quantity $\boldsymbol{\Omega}$ in crack-tip field is equation (1).

$$\dot{\boldsymbol{\Omega}}=\frac{d\boldsymbol{\Omega}}{dt}=-V\frac{\partial\boldsymbol{\Omega}}{\partial x}=V\left(\frac{\sin\theta}{r}\frac{\partial}{\partial\theta}-\cos\theta\frac{\partial}{\partial r}\right)\boldsymbol{\Omega} \tag{1}$$

Project supported by a grant from the Ph.D. Programs Foundation of Ministry of Education of China (No.20060217010) and Fundamental Research Foundation of Harbin Engineering University (No.HEUFT07005)

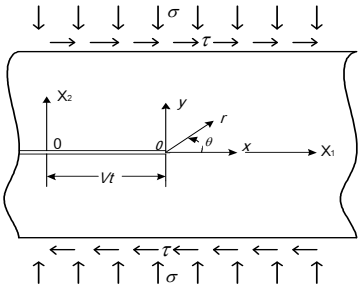

Fig.1 Mechanical model of mixed-mode crack-tip under compression and shear

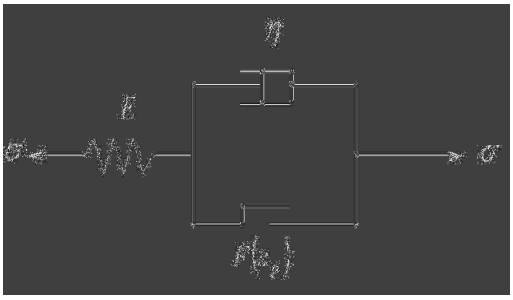

Fig.2 Elastic-viscoplastic constitutive model

Because the viscosity at crack-tip is related to strain rate, assume that viscosity coefficient η is as follows

$$\eta = C\left(\dot{\bar{\varepsilon}}_p\right)^{-\beta} \qquad (0<\beta<1) \tag{2}$$

where C is a non-negative constant. Elastic-viscoplastic constitutive model is given in Fig.2. The three-dimensional elastic visco-plastic constitutive equation[5] is

$$\dot{\varepsilon}_{ij} = \frac{1+\nu}{E}\dot{\sigma}_{ij} - \frac{\nu}{E}\dot{\sigma}_{kk}\delta_{ij} + \frac{3S_{ij}}{2\bar{\sigma}}\left(\frac{2}{3C}\right)^{\frac{1}{1-\beta}} H\left[\bar{\sigma}-\sqrt{3}K\right]\left[\bar{\sigma}-\sqrt{3}K\right]^{\frac{1}{1-\beta}} \tag{3}$$

where Heaviside step function is

$$H\left[\bar{\sigma}-\sqrt{3}K\right] = \begin{cases} 1 & \bar{\sigma}-\sqrt{3}K>0 \\ 0 & \bar{\sigma}-\sqrt{3}K\le 0 \end{cases} \tag{4}$$

Assume that stress has the power singularity as follows

$$\sigma_{ij} \sim r^{-\delta} \qquad (0<\delta<1/2) \tag{5}$$

Further, assume that viscose stress and plastic stress have the same magnitude at crack-tip and the elastic strain and plastic strain also have the same magnitude. By magnitude coordination, we get

$$\delta = \frac{1}{\beta} - 1 \tag{6}$$

From $0<\delta<1/2$, we could only consider the case of $2/3<\beta<1$.

2 Asymptotic equations at the mixed-mode crack-tip under compression and shear

Under incompressible situation, by introducing displacement potential function U, By magnitude matching, assume that the displacement potential function is

$$U = r^{2-\delta} g(\theta) \tag{7}$$

The displacement components are

$$u_r = -\frac{\partial U}{r\partial\theta} = -r^{2-\delta} g(\theta) \ , \ u_\theta = \frac{\partial U}{\partial r} = (2-\delta) r^{1-\delta} g(\theta) \tag{8}$$

The stress tensor σ_{ij} at the crack tip has singularity, namely $r^{-\delta}$,so the stress tensor can be expressed as

$$\sigma_r = r^{-\delta}\left[P(\theta)+S(\theta)\right] \quad \sigma_\theta = r^{-\delta}\left[P(\theta)-S(\theta)\right] \quad \sigma_{r\theta} = r^{-\delta}T(\theta) \tag{9}$$

Where $P(\theta)$, $S(\theta)$ and $T(\theta)$ are the angle functions on the at the crack tip.

Introduce the following dimensionless quantities

$$\tilde{T}=\frac{T}{\mu},\ \ \tilde{S}=\frac{S}{\mu},\ \ \tilde{P}=\frac{P}{\mu},\ \ \tilde{\Sigma}=\frac{\Sigma}{\mu},\ \ \ \ f=\frac{K}{\mu} \tag{10}$$

Introducing the relevant quantities to equations of motion and constitutive equations, the governing equations can be obtained as:

$$\tilde{S}'=\frac{2\delta h'}{\sin\theta}-\frac{2D^{*}\tilde{S}}{\tilde{\Sigma}\sin\theta}\left(\tilde{\Sigma}-\sqrt{3}f\right)^{\frac{1}{1-\beta}}-\delta\tilde{S}\cot\theta+2\tilde{T} \tag{11}$$

$$\tilde{P}'=\frac{2\delta h'}{\sin\theta}-\frac{2D^{*}\tilde{S}}{\tilde{\Sigma}\sin\theta}\left(\tilde{\Sigma}-\sqrt{3}f\right)^{\frac{1}{1-\beta}}-\delta\tilde{S}\cot\theta+\delta\tilde{T} \tag{12}$$

$$\tilde{T}'=\delta\left(\tilde{P}+\tilde{S}\right)-2\tilde{S} \tag{13}$$

$$h''=-\left(1-\delta^{2}\right)h-\delta\tilde{T}\cos\theta-\frac{2D^{*}\tilde{T}}{\tilde{\Sigma}}\left(\tilde{\Sigma}-\sqrt{3}f\right)^{\frac{1}{1-\beta}}-\delta\left(\tilde{P}+\tilde{S}\right)\sin\theta \tag{14}$$

3 Characterization parameters and boundary conditions on mixed-mode crack

3.1 Characterization parameters

The load mixed parameter M_P by Shih[5] is introduced in this paper, for expressing the stress state. According Eq. (9) and Eq. (15), the expression of M_P is

$$M_P=\frac{2}{\pi}arctg\left(\lim_{r\to 0}\left|\frac{\sigma_\theta(r,\theta=0)}{\sigma_{r\theta}(r,\theta=0)}\right|\right) \tag{15}$$

$$M_P=\frac{2}{\pi}arctg\left(\left|\frac{P(0)-F(0)}{T(0)}\right|\right) \tag{16}$$

When $M_P=1$, the crack tip is under tension (compression), belong to the mode I crack. When $M_P=0$, the crack tip is under shear, belong to the mode II crack. And when $0<M_P<1$, the crack tip is under tension (compression) and shear at the same time, belong to the mixed mode crack. Meanwhile, the crack will be close under the compression stress, and the closed crack surfaces will produce the friction shearing slipping along the crack surface.

3.2 Boundary conditions

The boundary conditions for the mixed mode crack comprise the junction conditions at the crack frontage ($\theta=0$) and the friction touch conditions of the crack surfaces.

(1) the junction conditions at the crack frontage ($\theta=0$)

$$g'(\pm 0)=0, g(\pm 0)=0, \tilde{P}(\pm 0)+\tilde{S}(\pm 0)=0, \tilde{P}(\pm 0)-\tilde{S}(\pm 0)<0, \tilde{T}(\pm 0)>0 \tag{17}$$

(2) the friction touch conditions of the crack surfaces

Assumed that the friction of the crack surfaces accords with the Coulomb Friction Law, so the friction touch conditions of the crack surfaces

$$\tilde{P}(\pm\pi)-\tilde{S}(\pm\pi)\le 0, \tilde{T}(\pm\pi)=-\mu[\tilde{P}(\pm\pi)-\tilde{S}(\pm\pi)], g(\pm\pi)=0 \tag{18}$$

4 numerical calculation and results analyse

Four will be defined to meet the junction conditions and the friction touch conditions: the

viscosity effect of the material D^*, the exponent β, the friction coefficient μ and the load mixed parameter M_P. The solution of the governing equations is belong to both ends boundary problem. As the conditions of defining the solutions is insufficient, $h'(0)$ and $T(0)$ are regarded as adjustable parameters, then the boundary problem can be transformed to the initial value problem by the two-parameters shooting method. In this paper, when $M_P = 0.84$ and $M_P = 0.34$, the crack separately approaches to the mode I and the mode II. By the variation of each parameter, the corresponding variation of stress field, strain field and displacement field on the elastic-viscoplastic mixed-mode quasi static crack is given as Fig. 3~4.

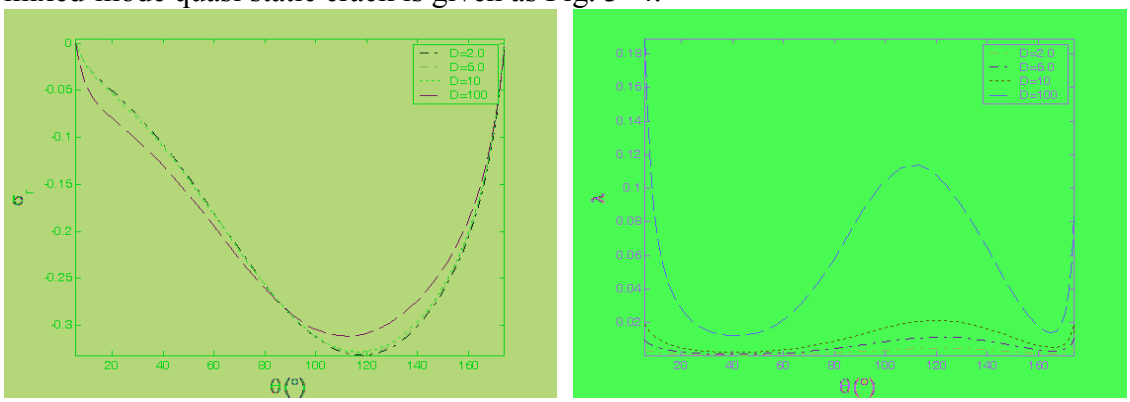

Fig. 3 Angular variations of stress components and plastic flow factor according to different D^* $(\beta = 0.8, Mp = 0.84, \mu = 0.2)$

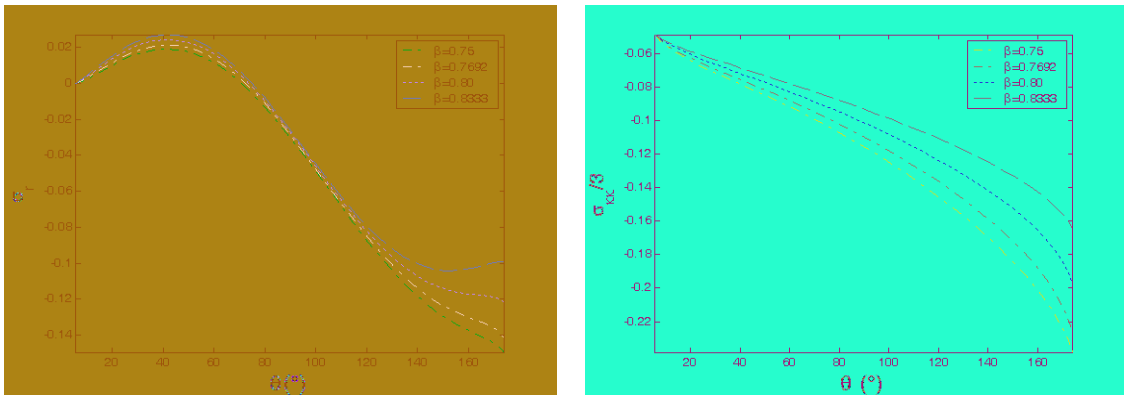

Fig. 4 Angular variations of stress components and hydro-static stresses according to different β $\left(D^* = 10, Mp = 0.34, \mu = 0.2\right)$

5 conclusions

(1) no matter how the parameters change, the numerical results are met the the junction conditions at the crack frontage and the friction touch conditions of the crack surfaces.

(2)as the viscosity effect at the crack tip is considered, the numerical solutions are entirely continuous, and there is no plastic shock wave, which makes clear that the viscosity effect is an important factor in studying the propagating crack tip.

(3) the viscosity coefficient is in inverse proportion to the power law of the equivalent plastic strain rate, and is the function of the angle, where homogeneity of the material is not losed and comforms to the property of the material.

References

[1] Wang Z Q: Acta mechanica sinica Vol. 25(1993),p.159(in Chinese)
[2] Jia B, Wang Z Q and Li Y D: J. Appl. Mech Vol. 20(2003),p.64(in Chinese)
[3] Li Yongdong, Jia Bin : Acta Mechanica Sinica Vol. 37(2005),p.280(in Chinese)
[4]Liang W Y, Wang Z Q: Chinese J. of Theo. and App. Mech Vol. 38(2006),p.618(in Chinese)
[5] Shih C F, in: American Society for Testing and Materials(1974)

Key Engineering Materials Vols. 385-387 (2008) pp 325-328
© (2008) Trans Tech Publications, Switzerland
doi:10.4028/www.scientific.net/KEM.385-387.325

The Influence of Stiffness Decay on Fatigue Reliability of Truss System

An Hai[1,a], An Wei-guang[1,a],Zhang Yong-yi[1,a]

[1]School of civil engineering, Harbin Engineering University, Harbin 150001,china

[a]anweiguang@hrbeu.edu.cn

Keywords: fatigue loads, stiffness reliability index, elastic modulus decrease, residual strength, Stochastic Finite Element Method

Abstract. Physical properties of element are very complex under fatigue loads.The structural system consisted of elements is not a simple topological structure,which the change of its physical properties is more complex.In order to analyze quantitatively the structural stiffness reliability of different design life,it is important to establish the accurate formula of physical properties decrease. In this paper, the formula of elements' elastic modulus decrease is deduced by using damage mechanics theory combining with the model of residual strength of element. Moreover, stiffness reliability index of controlling node of truss system is solved by applying the Stochastic Finite Element Method in different service life.

Introduction

It is widely existent for stiffness decrease of structure to bring many accidents to mechanic industry,aviation industry and ship industry and so on.Now,many fatigue reliability theories of structure seldom research the influence of elastic modulus decrease on structural stiffness.In actual,structural modulus has decreaseed after its damage,in many cases,its stiffness can't satisfy reliability demands although its strength can satisfy.So,it is important to analyze fatigue reliability of structure under its stiffness decrease.

Residual strength after element damage

The formula of strength after element damage. It is known from damage mechanics theory,the surface energy is provided by strain energy stored near its two fracture side when the element fractures.The formula of strength after element damage[1] is

$$\sigma_d = \sqrt{\frac{\gamma \overline{E}}{b}} \tag{1}$$

Where, γ is surface energy density. $\overline{E}$ is elastic modulus of damage element. b is space between crystal lattice.

Strain equivalent assumption. It can be obtained from strain equivalent assumption as follows

$$\varepsilon = \frac{\overline{\sigma}}{E} = \frac{\sigma}{\overline{E}} = \frac{\sigma}{E(1-\omega)} \tag{2}$$

Where, ε is linear elastic strain, E is elastic modulus of no damage element, $\overline{E}$ is elastic modulus of damage element, σ is actual stress, $\overline{\sigma}$ is effective strain, ω is damage factor,and it can be expressed as follows

$$\omega = \frac{A - \overline{A}}{A} \tag{3}$$

Where, A is cross-section area of no damage element, $\overline{A}$ is effective cross-section area of damage element.

Applying eq.(2) and eq.(3),it can be solved as follows

$$\overline{A} = \overline{E}\frac{A}{E} \tag{4}$$

The formula of residual strength under static strength decrease. At present,some scholars have made researches on residual strength under static strength decrease.For metal material, strength decreases slowly at the beginning,and decreases rapidly when repetition-rate n/N is close to 1, further,the structure is destroyed. The model of residual strength proposed by Schaff[2] is adopted in this paper, residual strength σ_d can be expressed as follws

$$\sigma_d = \sigma(n) = \sigma(0) - [\sigma(0) - \frac{F_{fi}}{A(n)}](\frac{n}{N})^c \tag{5}$$

Where, $\sigma(0)$ is static strength of element, F_{fi} is internal force of element under fatigue loads, $A(n)$ is effective cross-section area of element passing n times cycle, c is exponent, n, N is cycle times and fatigue life of element under fatigue loads respectively.
Substituting eq.(1) and eq.(4) into eq.(5),the formula of elastic modulus decreasing of damage element can be obtained as follows

$$\overline{E} = \frac{b}{\gamma}\left\{\sigma(0) - \left[\sigma(0) - \frac{F_{fi}E}{\overline{E}A}\right]\left(\frac{n}{N}\right)^c\right\}^2 \tag{6}$$

By Taylor expansion to eq.(6) and choosing its linear part,the mean value of elastic modulus $\overline{E}$ can be expressed as follows

$$\mu_{\overline{E}} = \frac{b}{\gamma}\left[\mu_{\sigma(0)} - \left(\mu_{\sigma(0)} - \frac{\mu_{F_{fi}}\mu_E}{\mu_{\overline{E}}\mu_A}\right)\left(\frac{n}{N}\right)^c\right]^2 \tag{7}$$

According to eq.(5) and eq.(6), it can be obtained as follows

$$\frac{\partial\overline{E}}{\partial(\sigma(0))} = \frac{2\sigma(n)\frac{b}{\gamma}\left[1-\left(\frac{n}{N}\right)^c\right]}{1+2\sigma(n)\frac{b}{\gamma}\left(\frac{n}{N}\right)^c\frac{F_{fi}E}{A\overline{E}^2}} \tag{8}$$

$$\frac{\partial\overline{E}}{\partial F_{fi}} = 2\sigma(n)\frac{b}{\gamma}\cdot\frac{E}{A\overline{E}}\left(\frac{n}{N}\right)^c \tag{9}$$

So ,the deviation of elastic modulus $\overline{E}$ can be expressed as follows

$$D(\overline{E}) = \left(\frac{\partial\overline{E}}{\partial\sigma(0)}\Big|_\mu\right)^2 D(\sigma(0)) + \left(\frac{\partial\overline{E}}{\partial F_{fi}}\Big|_\mu\right)^2 D(F_{fi}) \tag{10}$$

Where,from eq.(7) to eq.(10), $\mu_{(\bullet)}$ denotes mean and $D(\bullet)$ denotes deviation, $\frac{\partial\overline{E}}{\partial\sigma(0)}\Big|_\mu$, $\frac{\partial\overline{E}}{\partial F_{fi}}\Big|_\mu$ is the mean value of random variables $E, \overline{E}, A, F_{fi}, \sigma(n)$ respectively, $\mu_{\sigma(n)} = \mu_{\sigma(0)} - \left(\mu_{\sigma(0)} - \mu_{S_P}\right)\left(\frac{n}{N}\right)^c$.

So,stochastic characters of elastic modulus $\overline{E}$ can be analyzed by eq.(7) and eq.(10).

Stiffness reliability analysis of truss system with bar elements considering elastic modulus decrease

Numerical characters of node displacements of truss system with bar elements under elastic modulus decrease. To assume that there are same elastic modulus and cross-section area in truss system. The safe margin of stiffness failure mode of node displacements of truss system with bar elements is as follows

$$M_i = \delta^a - \delta_i \tag{11}$$

Where, δ_i is node displacements of truss system, i is node number, δ^a is the allowable value of δ_i. According to Finite Element theory,stiffness matrix of truss system with bar elements after elastic modulus decrease is as follows

$$\left[\overline{K}\right]^e = \begin{bmatrix} \dfrac{\overline{E}\overline{A}}{l} & -\dfrac{\overline{E}\overline{A}}{l} \\ -\dfrac{\overline{E}\overline{A}}{l} & \dfrac{\overline{E}\overline{A}}{l} \end{bmatrix} \tag{12}$$

Applying eq.(4),the part of eq.(12) matrix $\dfrac{\overline{E}\overline{A}}{l}$ can be expressed as follows

$$\frac{\overline{E}\overline{A}}{l} = \overline{E}^2 \frac{A}{lE} \tag{13}$$

According to Finit Element Control Equations, array matrix of damage elements nodes' displacements $\left[\overline{\delta}\right]$ can be expressed as follows

$$\left[\overline{\delta}\right] = \left[\overline{K_{\mathrm{Q}}}\right]^{-1}\left[P\right] \tag{14}$$

Where, $\left[\overline{K_{\mathrm{Q}}}\right]$ is the total stiffness matrix of damage truss system, $\left[P\right]$ is array matrix of loads.

It is known from eq.(13) and eq.(14) that $\overline{\delta}_{\mathrm{i}}$ can be expressed as the function of random variables $E,\overline{E},A,P$.

Applying the Stochastic Finite Element Method[3], by Taylor expansion to eq.(14) and choosing its linear part,the mean value and the deviation of $\left[\overline{\delta}\right]$ can be expressed as follows

$$\mu_{\left[\overline{\delta}\right]} = \mu_{\left[\overline{K_{\mathrm{Q}}}\right]^{-1}}\mu_{[P]} \tag{15}$$

$$\begin{aligned} D\left(\left[\overline{\delta}\right]\right) = &\left(\frac{\partial\left[\overline{\delta}\right]}{\partial\overline{E}}\Big|_{\mu_X}\right)^2 D\left(\overline{E}\right) + \left(\frac{\partial\left[\overline{\delta}\right]}{\partial E}\Big|_{\mu_X}\right)^2 D\left(E\right) + \\ &2\left(\frac{\partial\left[\overline{\delta}\right]}{\partial\overline{E}}\cdot\frac{\partial\left[\overline{\delta}\right]}{\partial E}\right)\Big|_{\mu_X} Cov\left(\overline{E},E\right) + \left(\frac{\partial\left[\overline{\delta}\right]}{\partial A}\Big|_{\mu_X}\right)^2 D\left(A\right) + \left(\frac{\partial\left[\overline{\delta}\right]}{\partial p}\Big|_{\mu_X}\right)^2 D\left(P\right) \end{aligned} \tag{16}$$

Where, $\boldsymbol{X}=(E,\overline{E},A,P)$, $\big|_{\mu_X}$ is mean value of random variable in $\boldsymbol{X}$.

So, the mean value and the deviation of $\overline{\delta_i}$ can be given from that of $\left[\overline{\delta}\right]$,and stiffness reliability index of nodes' displacement can be solved by applying eq.(11).

Numerical example. Truss system with 10 bars is shown in Fig.1,to assum that fatigue ife of elements subject to logarithmic normal distribution and have the same mean-value $S-N$ curve, equal amplitude fatigue load $P=14KN$,the static strength mean $\mu_{R(0)}=373.6MPa$, $c=4.092$, variance coefficient $\nu_{R(0)}=0.05$, $\frac{\gamma}{b}=2\ MPa$, cross-section area of element (1),(2),(3),(6),(7),(10) is $\mu_A=2cm^2$, cross- section area of element (4),(5),(8),(9) is $\mu_A=3cm^2$, variance coefficient $\nu_A=0.01$, $\delta^a=0.8cm$. To evaluate stiffness reliability of truss system in different service life(β is not smaller than 3).

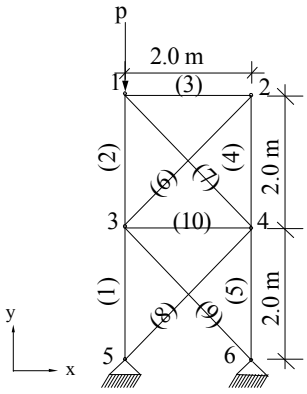

Fig1. Truss system

According to Finit Element calculating,the displacement of node 1 is maximal,so to select node 1 as controlling node.Thus, applying the method of this paper,stiffness reliability of truss system in different life can be evaluated by calculating reliability index β of controlling node 1. Displacement and reliability index β of controlling node 1 is shown in Table 1.

Tab.1 displacement and reliability of controlling node 1

Cycle times in different life	Displacements of node 1(cm)		Reliability index of maximal displacement β
	x	y	
0	-0.392	-0.353	10.41
1.3×10^7	-0.416	-0.375	8.33
2×10^7	-0.518	-0.467	3.53
2.5×10^7	-0.722	-0.651	0.37

As can be seen from the example,along with cycle times of fatigue loads to structure increasing,stiffness reliability index of controlling node begin to decrease slowly,and it will decrease rapidly when the life of element approaches to end.

Summary

The method proposed in this paper considers simultaneously elastic modulus decrease and cross-section area of element to the effect of stiffness reliability of structure, and deduces correlative decreasing formula by using damage mechanics theory combining with the model of residual strength.It is a new attempt for stiffness reliability analysis of system in different service life.

References

[1] Dai Jing-jun ,Zhang Zhao-guo. Research About Fracture Stress of Damaged Material. Journal of Shandong Agricultural University, 2004 , 35 (1) : 102-104P

[2] Schaff J R,Dacidson B D.Life prediction methodology for composite structures.Part I-Ccnstant amplitude and two-stress level fatigue.Journal of Composite Materials, 1997,31(2):128-157P

[3] An Wei-guang,Cai Yin-lin,Chen Wei-dong.Reliability analysis and optimum design for stochastic structure systems.Harbin:Harbin Engineering University Press(2005)

Key Engineering Materials Vols. 385-387 (2008) pp 329-332
© (2008) Trans Tech Publications, Switzerland
doi:10.4028/www.scientific.net/KEM.385-387.329

The Mesoscopic Investigation on Moduli Prediction in Visco-Elastic Particle Reinforced Composites

Xuezhong Ding[1,a], Liqiang Tang[1,b]

[1]College of Civil Engineering, Harbin Engineering University, Harbin 150001, China

[a]dingxz@163.com, [b]tlq8854@126.com

Keywords: Glass/ED6 composites, moduli prediction, visco-elastic model, Eshelby equivalent inclusion theory

Abstract. The visco-elastic mechanism of particles reinforced composites has been investigated through revised Eshelby equivalent inclusion theory. A visco-elastic model is applied. Furthermore, by introducing Heaviside step function and Laplace transform, the creep constitutional equation related to strain rate effect is achieved. Finally, by equivalent inclusion theory, introducing secant modulus, the material moduli with time and volume fraction concerning Glass/ED6 particles reinforced materials have been given. The results show that the visco-elastic property of composite material is mainly determined by the visco-elastic behavior of the matrix, which meet experiment results well. It can be concluded from the results that there exits close relationship between the inclusion shape, volume fraction and loading path.

Introduction

For most metallic composite materials, when entering viscous and plastic phase, the Young's modulus can no longer retain constant. Visco-plastic problem in with the four parameter fluid model, which Maxwell model concatenates Voigt Model, has been studied by Jun Liang and Shanyi Du. In the present work, researches based on a new visco-elastic model, which is more close to the practical material, have been investigated[1,2,3,4].

Fundamental Equations

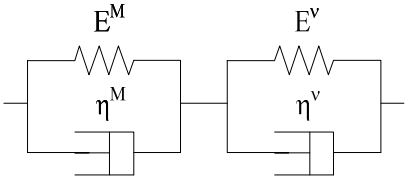

Fig. 1 Four Parameter Visco-Elastic Solid Model

The Laplace transform can transfer partial differential equations with time element and coordinate conversion into ordinary differential equations, which is widely used in elastic visco-plastic mechanics. The Laplace transform is

$$F(s)=\int_0^\infty f(t)e^{-st}dt\,. \tag{1}$$

Based on the principle of correspondence and by Laplace transform, the visco-elastic differential constitutive equation in this model can be transformed into

$$\sigma + \frac{\eta_1 + \eta_2}{E_1 + E_2}\dot{\sigma} = \frac{E_1 E_2}{E_1 + E_2}\varepsilon + \frac{E_1\eta_2 + E_2\eta_1}{E_1 + E_2}\dot{\varepsilon} + \frac{\eta_1\eta_2}{E_1 + E_2}\ddot{\varepsilon} \tag{2}$$

With creep test, $\sigma = \sigma_0 H(t)$, and by inverse Laplace transform, let $\tau_1 = (q_1 + q_2)/q_0$, there is

$$\varepsilon = \sigma_0 \exp(-\frac{t}{\tau_1})(\frac{p_1}{q_1 + q_2} - \frac{1}{q_0}) + \frac{\sigma_0}{q_0} \tag{3}$$

, where

$$p_1 = \frac{\eta_1 + \eta_2}{E_1 + E_2}, q_0 = \frac{E_1 E_2}{E_1 + E_2}, \quad q_1 = \frac{E_1\eta_2 + E_2\eta_1}{E_1 + E_2} \text{ and } q_2 = \frac{\eta_1\eta_2}{E_1 + E_2} \tag{4}$$

Effective Modulus Prediction

Assume that the distant field homogeneous stress acts on the boundary of composites. Then, the mean stress in matrix is

$$\sigma^M = \sigma^A + \tilde{\sigma} = L^M(\varepsilon^A + \tilde{\varepsilon}) \tag{5}$$

, where L^M is Young's Modulus in matrix, $\tilde{\varepsilon}$ is the perturbation strain caused by the interaction of spherical inclusions.

Similarly, the mean stress in spherical inclusions is

$$\sigma^F = \sigma^A + \tilde{\sigma} + \sigma' = L^F(\varepsilon^A + \tilde{\varepsilon} + \varepsilon') = L^M(\varepsilon^A + \tilde{\varepsilon} + \varepsilon' - \varepsilon^*) \tag{6}$$

, where ε^* is the equivalent eigenstrain of spherical inclusions.

By Eshelby equivalent inclusion theory [4], there is

$$\varepsilon' = S\varepsilon^* \tag{7}$$

, where S, which is related to matrix elasticity and the shape of inclusions, is the tetradic Eshelby tensor. From (5), (6), (7), there is

$$\sigma' = L^M(S - I)\varepsilon^* \tag{8}$$

In Eshelby's theory, the volumetric mean stress in composites is equal to the distant field homogeneous stress, namely,

$$\sigma^A = (1 - f)\sigma^M + f\sigma^F \tag{9}$$

, where f is the volume fraction of reinforcement. From (6), (7) and (8), we have

$$\tilde{\sigma} = -f\sigma', \tilde{\varepsilon} = -f(S - I)\varepsilon^* \tag{10}$$

Then, it can be obtained as

$$\varepsilon^* = A\varepsilon^A \tag{11}$$

where $A = \{L^M + (L^F - L^M)[fI + (1 - f)S]\}^{-1}(L^M - L^F)$.

Homogeneous tension stress σ_{11}^{A} acting on x, which is along the fiber and by Hook's law, Young's modulus is

$$\frac{E_{11}}{E_0}=\frac{\varepsilon_{11}^{A}}{\varepsilon_{11}^{A}+f\varepsilon_{11}^{*}}=\frac{1}{1+f(a_1-2\gamma_0 a_2)} \tag{12}$$

Pure shear stress σ_{12}^{A} acting on the plane perpendicular to x and by Hook's law, the shear modulus is

$$\frac{\mu_{12}}{\mu_0}=\frac{\varepsilon_{12}^{A}}{\varepsilon_{12}^{A}+f\varepsilon_{12}^{*}}=\frac{1}{1+fa_3} \tag{13}$$

Homogeneous tension stress acting on x and by Hook's law, Poisson's ratio is

$$\gamma_{12}=-\frac{\varepsilon_{22}^{A}+f\varepsilon_{22}^{*}}{\varepsilon_{11}^{A}+f\varepsilon_{11}^{*}}=\frac{\gamma_0-f[a_2-\gamma_0(a_1+a_2)]}{1+f(a_1-2\gamma_0 a_2)} \tag{14}$$

By Laplace transform, there is

$$\frac{E^{LT}}{E_M^{LT}}=\frac{1}{1+f(a_1^{LT}-2\gamma_0^{LT}a_2^{LT})},\quad \frac{\mu^{LT}}{\mu_M^{LT}}=\frac{1}{1+fa_3^{LT}},$$

$$\gamma^{LT}=\frac{\gamma_M^{LT}-f[a_2^{LT}-\gamma_M^{LT}(a_1^{LT}+a_2^{LT})]}{1+f(a_1^{LT}-2\gamma_M^{LT}a_2^{LT})} \tag{15}$$

a_1, a_2 and a_3 are parameters determined by Eshelby tensor, Lamè coefficients and volume fraction.

Suppose that the granular reinforcements and visco-elastic matrix are isotropic, then, the Young's modulus can be expressed as

$$E_M^{LT}=\frac{q_0+q_1 s+q_2 s^2}{p_1 s}=\frac{E_0^M E_0^{\upsilon}+(E_0^M\eta_0^{\nu}+E_0^{\upsilon}\eta_0^M)s+\eta_0^M\eta_0^{\nu}s^2}{(\eta_0^M+\eta_0^{\nu})s} \tag{16}$$

Based on the correspondence principle, visco-elastic property corresponds with elastic property in Laplace transform. Thus, the visco-elasticity can be obtained from mesomechanical elastic methods.

Results

The mechanical property of Glass/ED6 composite can be seen from the following figures.

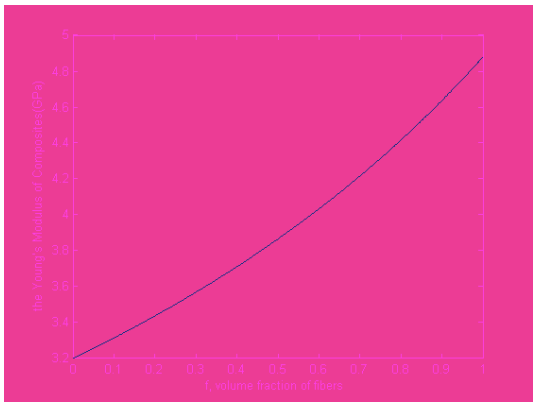

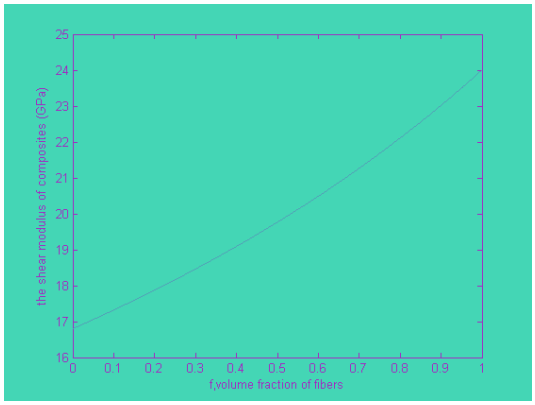

Fig.2 Variation of the Young's modulus with f Fig.3 Variation of the shear modulus with f

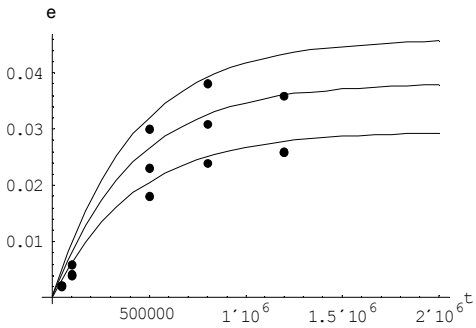

Fig.4 Comparison between Experiment and Theoretical Creep Curves

It can be seen that the Young's modulus and shear modulus of the composites increases in direct proportion with volume fraction of fibers. From the figure we can find that in the initial stage, the composite exhibits instantaneous elasticity, which is in good agreement with the experimental results. Then, instable creep stage occurs and finally, it reaches the stable creep stage, which fits the experimental data well.

Conclusions

The visco-elastic performance of particle reinforced composites is mainly determined by the visco-elasticity of matrix, which is closely related to the inclusion shape and volume fraction. This work will provide theoretical basis to the practical engineering applications such as material design and performance prediction of composites.

References

[1] Findley W N, Lai J S, Onaran K. Creep and relaxation of nonlinear viscoelastic materials. North-Holland, New York, 1976

[2] Christensen R M. Theory of viscoelasticity: An Introduction, 2nd edn [M]. New York, Academic Press, 1982

[3] Li J, Weng G J. Effective creep behavior and complex moduli of fiber and ribbon-reinforced plastics in compression [J]. Polymer Mech, 1983,6:718-722

[4] Yang Liu, Jun L, Mesoscopic Prediction on Dynamic Visco-Elastic Performance of Particular Reinforced Composites, Key Engineering Materials, vol.334-335, 2007

[5] Mura T. Micromechanics of Defects in Solids [M]. Netherlands, Martinus Nijhoff, 1987.

Key Engineering Materials Vols. 385-387 (2008) pp 333-336
© (2008) Trans Tech Publications, Switzerland
doi:10.4028/www.scientific.net/KEM.385-387.333

Application of Mesh Free Method to Evaluation of Woven Fabric Composite Elastic Moduli

P.H. Wen[1,a] and M.H. Aliabadi[2,b]

[1] School of Engineering and Material Sciences, Queen Mary, University of London, UK

[2]Department of Aeronautics, Imperial College, London, UK

[a]p.h.wen@qmul.ac.uk, [b]m.h.aliabadi@imperial.ac.uk

Keywords: Mesh free method, woven fabric composites, elastic moduli.

Abstract. A computational method for the micro-mechanical material model of woven fabric composite material was developed in this paper based on a repeated unit cell approach and two smooth fibre modes were presented. The stiffness matrix was evaluated with a domain integral by the use of radial basis function interpolations without element mesh. The applications of mesh free method to evaluate woven fabric composite elastic moduli have been presented and good accuracy has been achieved compared with the results by other approaches.

Introduction

Composite laminate is extensively utilized in modern shell structures. In different industries, fabric composites are now used to fabricate components, in certain cases, it may even be used for critical parts. Industrial piping has also been made of composite materials in many applications. A variety of pressure vessels are also fabricated from composites. Earlies models for the analysis of woven fabric composites were included in the work by Ishikawa et al [1-2]. The finite element analysis and approximated analytical analysis were carried out by Chung and Tamma [3] and Tanov and Tabiei [4]. Meshless approximations have received much interest since Nayroles *et al* [5] proposed the diffuse element method. Later, Belyschko *et al* [6] proposed element-free Galerkin method and reproducing kernel particle methods, respectively. Recently, Atluri and his colleagues presented a family of Meshless methods based on the Local weak Petrov-Galerkin formulation (MLPGs) for arbitrary partial differential equations [7] with Moving Least Square (MLS) approximation. In this paper, an improved mesh free method is presented with radial basis functions (RBF) interpolation. For the woven fabric composites, it becomes more difficult to utilise FEM since the directions of fibres are variation in the volume cell. However, the mesh free approaches for the problems of micro-mechanical models can be used for the composite material, particularly for the functional elastic moduli in the computational volume cell. In this paper, the accuracy of mesh free method is demonstrated compared with results by FEM and analytical solutions.

The volume cell models

A mosaic model of the woven composite's Representative Volume Cell (RVC) is used for deriving the micromechanical relations used for homogenization as described in [4]. The micromechanical model is the four-cell model described. The micromechanical model is based on the method of cells, which consists in dividing the RVC in different blocks or cells, each of which can be further divided into sub-cells. Assuming that the fibre yarns in both direction (the fill and warp) have the same structure and properties, that part of the woven RVC can be constructed using four-cell model. Therefore, only a quarter of the composite's RVE needs to be considered to derive the homogenized stiffness properties of the whole woven composite's RVC. The homogenized stiffness properties of the woven composite's RVC are then used to predict the stress-strain behaviour of the plain-woven composite at the lamina level.

Two 3D woven fabric composite unit cells were constructed to determine its elastic properties as shown in Figure 1. In this case, the fibres in yarn volume are unidirectional and smooth distributed

along the fill/warp directions. We assume that the variation of bottom fibre in the fill direction on section $y = 0$ is

$$z_1(x) = z_0 - \frac{H}{4} + \frac{H}{4}\cos\frac{\pi x}{2} \tag{2}$$

where z_0 denotes the location of a fibre at $x = y = 0$. For the bottom fibre, $z_0 = H/2$ and the fibre location in the xoz becomes

$$z_1(x) = \frac{H}{4}(1 + \cos\frac{\pi x}{2}) \tag{3}$$

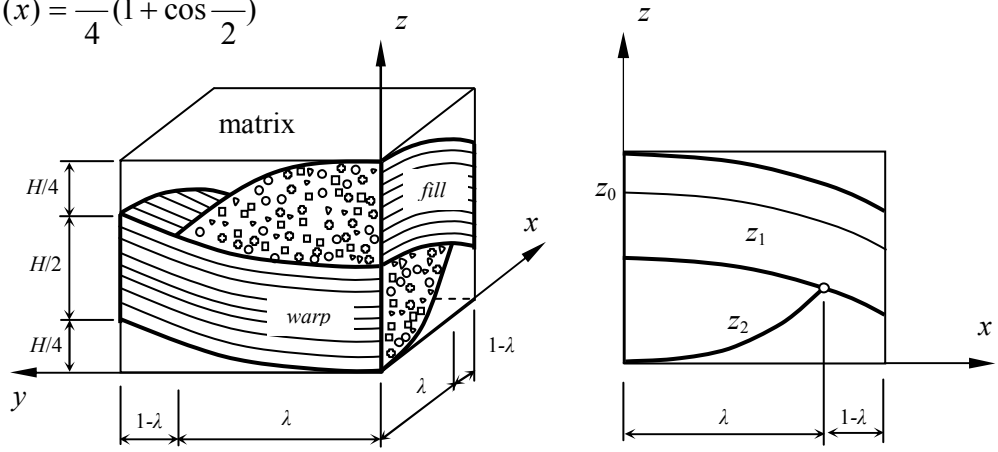

Figure 1. RVC with smooth fibres and geometry of yarn volume for model I.

- Smooth fiber model I.

The geometry of smooth fibre model I is illustrated in Figure 1. Suppose the configuration for the yarn volume in the warp direction to be

$$z_2(x) = \alpha x^2 \tag{4}$$

The coefficient α is determined by considering the location of joint for fibres of fill and warp

$$\alpha = \frac{H}{4\lambda^2}(1 + \cos\frac{\pi\lambda}{2}) \tag{5}$$

where λ denotes the coordinate of joint shown in Figure 1. Considering the portion of fabric yarn volume in the RVC, we have following integral

$$V_y = 2\int_0^{\lambda}\left[\frac{H}{4}(1 + \cos\frac{\pi x}{2}) - \alpha x^2\right]dx \tag{6}$$

Then we have following equation to evaluate the location of joint

$$4\lambda = 6V_y + 3(\lambda - \frac{\pi}{2}\sin\frac{\pi\lambda}{2}) - \lambda(1 - \cos\frac{\pi\lambda}{2}) \tag{7}$$

The root of λ can be easily determined by the alterative method.

- Smooth fibre model II.

The geometry of smooth fibre model II is illustrated in Figure 2. The configuration for yarn volume in the warp direction is assumed to be a half of elliptic and defined as

$$z_2(x) = \frac{H}{4}(1 \pm \sqrt{1 - \frac{x^2}{\lambda^2}}) \tag{8}$$

where λ is the principle axis of elliptic which can be determined by the portion of yarn volume as

$$\lambda = \frac{4V_y}{\pi} \tag{9}$$

Model II is more suitable for a small portion of yarn volume composites. For instance, if the yarn volume portion $V_y = 0.5385$, then $\lambda = 0.8162$ and 0.6856 for the smooth fibre model I and model

II respectively. The yarn volume surfaces for these two smooth fibre modes are illustrated in Figure 3 when y=0 exactly.

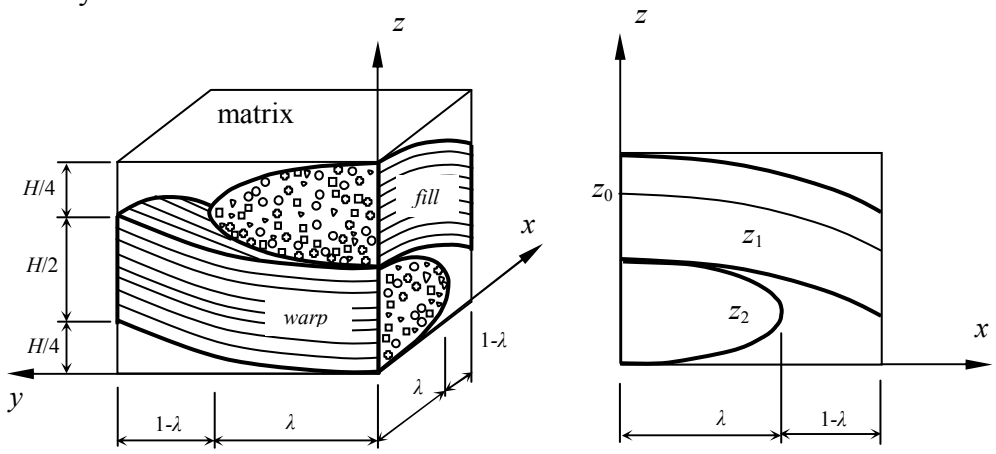

Figure 2. RVC with smooth fibres and geometry of yarn volume for model II.

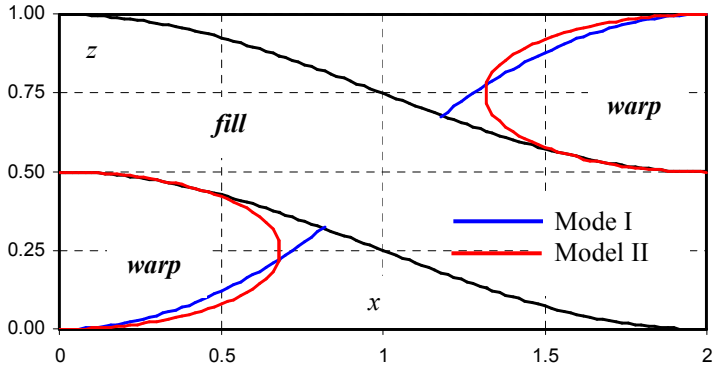

Figure 3. The surfaces of yarn volume for different smooth fibre modes when the yarn volume fraction $V_y = 0.5385$.

The mesh free method

Consider a domain Ω surrounded by a boundary Γ and a sub-domain Ω', which is the neighbourhood of a point $\boldsymbol{\eta}$ $(=\{x, y, z\})$ and is considered as the domain of definition of the RBF approximation for the trail function at $\boldsymbol{\eta}$ and also called as support domain to an arbitrary point $\boldsymbol{\eta}$. To interpolate the distribution of function u in the sub-domain Ω' over a number of randomly distributed nodes $\boldsymbol{\xi}$ $[=\{\xi_1, \xi_2, ..., \xi_n\}, \xi_i = (x_i, y_i, z_i)$, i=1,2,,…,n], the approximation of function u at the point $\boldsymbol{\eta}$ can be expressed by

$$u(\boldsymbol{\eta}) = \sum_{k=1}^{n} R_k(\boldsymbol{\eta}, \boldsymbol{\xi}) a_k + \sum_{j=1}^{t} P_j(\boldsymbol{\eta}) b_j = \mathbf{R}(\boldsymbol{\eta}, \boldsymbol{\xi})\mathbf{a} + \mathbf{P}(\boldsymbol{\eta})\mathbf{b} \tag{10}$$

where $\mathbf{R}(\boldsymbol{\eta}, \boldsymbol{\xi}) = \{R_1(\boldsymbol{\eta}, \boldsymbol{\xi}), R_2(\boldsymbol{\eta}, \boldsymbol{\xi}), ..., R_n(\boldsymbol{\eta}, \boldsymbol{\xi})\}$ is the set of radial basis functions centered around the point $\boldsymbol{\eta}$, $\{a_k\}_{k=1}^{n}$ are the unknown coefficients to be determined. The radial basis function is selected multi-quadrics as

$$R_k(\boldsymbol{\eta}, \boldsymbol{\xi}) = \sqrt{c^2 + \alpha_1 (x - x_k)^2 + \alpha_2 (y - y_k)^2 + \alpha_3 (z - z_k)^2} \tag{11}$$

where c is a free parameter (is chosen to unit in this paper) and α_i are scale factors. In order to guarantee unique solution of the interpolation problem, a polynomial term is added along with the constraints $\sum_{j=1}^{t} P_k(\boldsymbol{\xi}_j) a_j = 0, 1 \le k \le t$. Solving these equations in Eq.(10) gives

$$\mathbf{b} = \left(\mathbf{P}^T\mathbf{R}_0^{-1}\mathbf{P}\right)^{-1}\mathbf{P}^T\mathbf{R}_0^{-1}\mathbf{u}, \qquad \mathbf{a} = \mathbf{R}_0^{-1}\left[\mathbf{I} - \mathbf{P}\left(\mathbf{P}^T\mathbf{R}_0^{-1}\mathbf{P}\right)^{-1}\mathbf{P}^T\mathbf{R}_0^{-1}\right]\mathbf{u} \tag{12}$$

where **I** denotes the diagonal unit matrix. Substituting the coefficients **a** and **b** from Eq.(12) into Eq.(10), we can obtain the approximation of the field function in terms of the nodal values

$$u(\boldsymbol{\eta}) = \sum_{k=1}^{n} \phi_k(\boldsymbol{\eta}, \boldsymbol{\xi}) u(\boldsymbol{\xi}_k). \tag{13}$$

Results and discussion

Consider the second Glass/epoxy woven composite discussed by Marrey and Sankar [19] by the FEM with properties for the yarn $E_{\mathrm{L}} = 58.61\,\mathrm{GPa}$, $E_{\mathrm{T}} = 14.49\,\mathrm{GPa}$, $G_{\mathrm{LT}} = 5.38$, $\nu_{\mathrm{LT}} = 0.25$ and $\nu_{\mathrm{TT}} = 0.247$; the isotropic matrix is of Epoxy with $E = 3.45\,\mathrm{GPa}$, $\nu = 0.37$. The yarn volume fraction $V_y = 0.26$ and the average undulation angle $\theta = 4.2^0$. The thickness of RVC is H=0.2174. As seen from Table 1, all values have good agreement with other approaches.

Table 1. RVC properties by different approaches

Approach	E_x (GPa)	E_y (GPa)	G_{xz}, G_{yz} (GPa)	G_{xy} (GPa)	ν_{xy}	ν_{yz}
Ref [8]	11.81	6.14	1.84	2.15	0.408	0.181
Four-cell model [4]	11.86	6.21	1.70	2.33	0.404	0.166
Single-cell model [4]	11.93	5.67	1.59	2.31	0.436	0.159
Four-cell model	12.01	6.00	1.831	1.75	0.407	0.173
Smooth fibre model I	12.81	5.80	1.625	1.94	0.438	0.149
Smooth fibre model II	11.08	5.49	1.624	1.83	0.438	0.166

Summary

The distribution of the fibres in the RVC can be arbitrary in each numerical model and the prediction of micromechanical properties can be obtained easily by the proposed mesh free method. Compared with the results by FEM and approximated analytical solutions, the accuracy of this paper is very satisfied.

References

[1] T. Ishikawa, Antisymmetric elastic properties of composite plates of satin weave cloth, Fibre Sci. Technol. 15 (1981), 127-145.
[2] T. Ishikawa, T.W. Chou, One-dimensional micromechanical analysis of woven fabric composites, AIAA, J. 21 (12) (1983), 1714-1721.
[3] P.W. Chung, K.K. Tamma, Woven fabric composites – developments in engineering bounds, homogenization and application, Int. J. Numer. Meth. Engng 45 (1999), 1757-1790.
[4] R. Tanov, A. Tabiei, Computationally efficient micromechanical models for woven fabric composite elastic moduli, J. App. Mech. 68 (2001), 553-560.
[5] B. Nayroles, G. Touzot & P. Villon, Generalizing the finite element method: diffuse approximation and diffuse elements, Computational Mechanics 10 (1992), 307-318.
[6] T. Belytschko, Y.Y. Lu & L. Gu, Element-free Galerkin method, Int. J. Numerical Methods in Engineering 37 (1994), 229-256.
[7] S.N. Atluri, The Meshless Method (MLPG) for Domain and BIE Discretizations, Forsyth, GA, USA, Tech Science Press (2004).
[8] R.V. Marrey, B.V. Sankar, A micromechanical model for textile composite plate, J. Compos. Mater. 31 (12) (1977), 1187-1213.

Key Engineering Materials Vols. 385-387 (2008) pp 337-340
© (2008) Trans Tech Publications, Switzerland
doi:10.4028/www.scientific.net/KEM.385-387.337

Flexural toughness and crack strength of fiber reinforced cementitious composite

A. Sadrmomtazi[1,a],F.Zerafatangiz[2,b], O. Alidoust[3,c], A. K. Haghi[4,d]

[1] University of Guilan, Civil Engineering Department, Rasht, Iran

[2] University of Guilan, Mechanical Engineering Department, Rasht, Iran

[3] University of Guilan, Civil Engineering Department, Rasht, Iran

[4] University of Guilan, Textile Chemistry Engineering Department, Rasht, Iran

[a]Sadrmomtazi@yahoo.com, [b]F.z.angiz@guilan.ac.ir [c]Alidoust@yahoo.com, [d]Haghi@Guilan.ac.ir

Keywords: Flexural Strength, Crack Propagation, Fiber Reinforced Composite, Cement Mortar.

Abstract. The main objective of this study is to evaluate the flexural toughness and crack strength of a cement-based composite under the effect of using recycled polypropylene (PP) fiber and recycled glass. This research study proves the feasibility of the use of glass as aggregates replacement and PP fibers for composite reinforcement..

Introduction

Waste carpet fibers have been used in cement-based composites concrete since the late 1960s [1-3]. Natural and other synthetic fibers are added to cement as secondary reinforcement to control plastic shrinkage [4]. The performances of ordinary Portland cement using recycled glass, Silica fume, Rice Husk and fibers as a fraction of aggregates used in a cement-based composite were investigated. [5].The effect of polypropylene fibers on the properties of cement-based composites varies depending on the type, length, and volume fraction of fiber, the mixture design, and the nature of materials used.

Experiments

In the cementitious composite**,** two different ground glasses were used, namely type I: ground glass having particles passing a #80 sieve (180μm) and type II: ground glass having particles passing a #200 sieve (75μm). Silica fume(SF) and rice husk ash (RH) are added to the cementitious composite.

Results and discussion

The effect of fiber volume fraction, and the age of the mortar matrix on the flexural strength are represented in Figure 1.

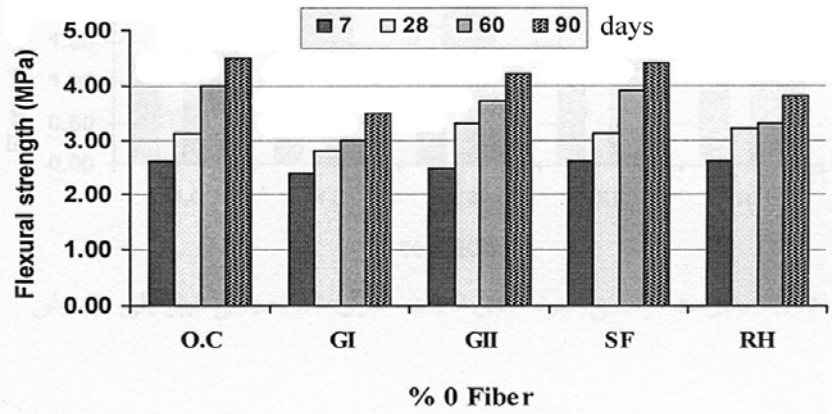

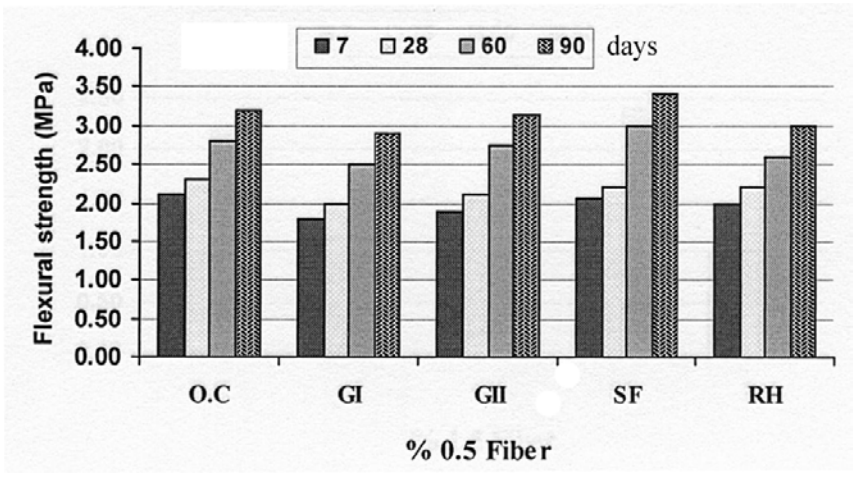

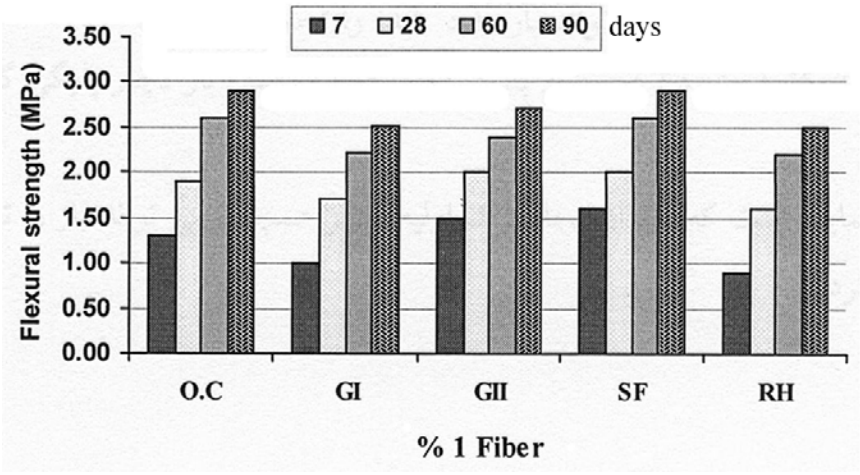

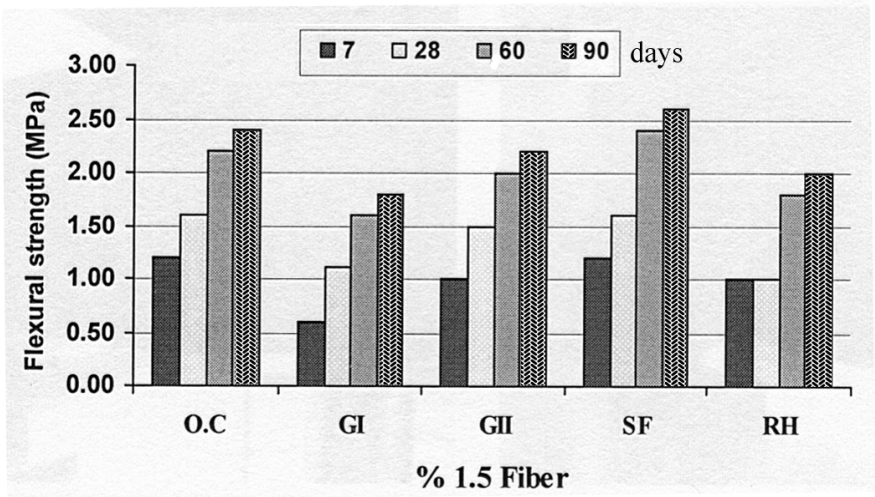

Fig. 1, Flexural strength of mortars in different ages

The $50 \times 50 \times 200 mm$ beam was tasted in three-point (i.e., center-point) bending with the span of 180 mm. The test configuration is shown in Figure 2. The test was controlled automatically by

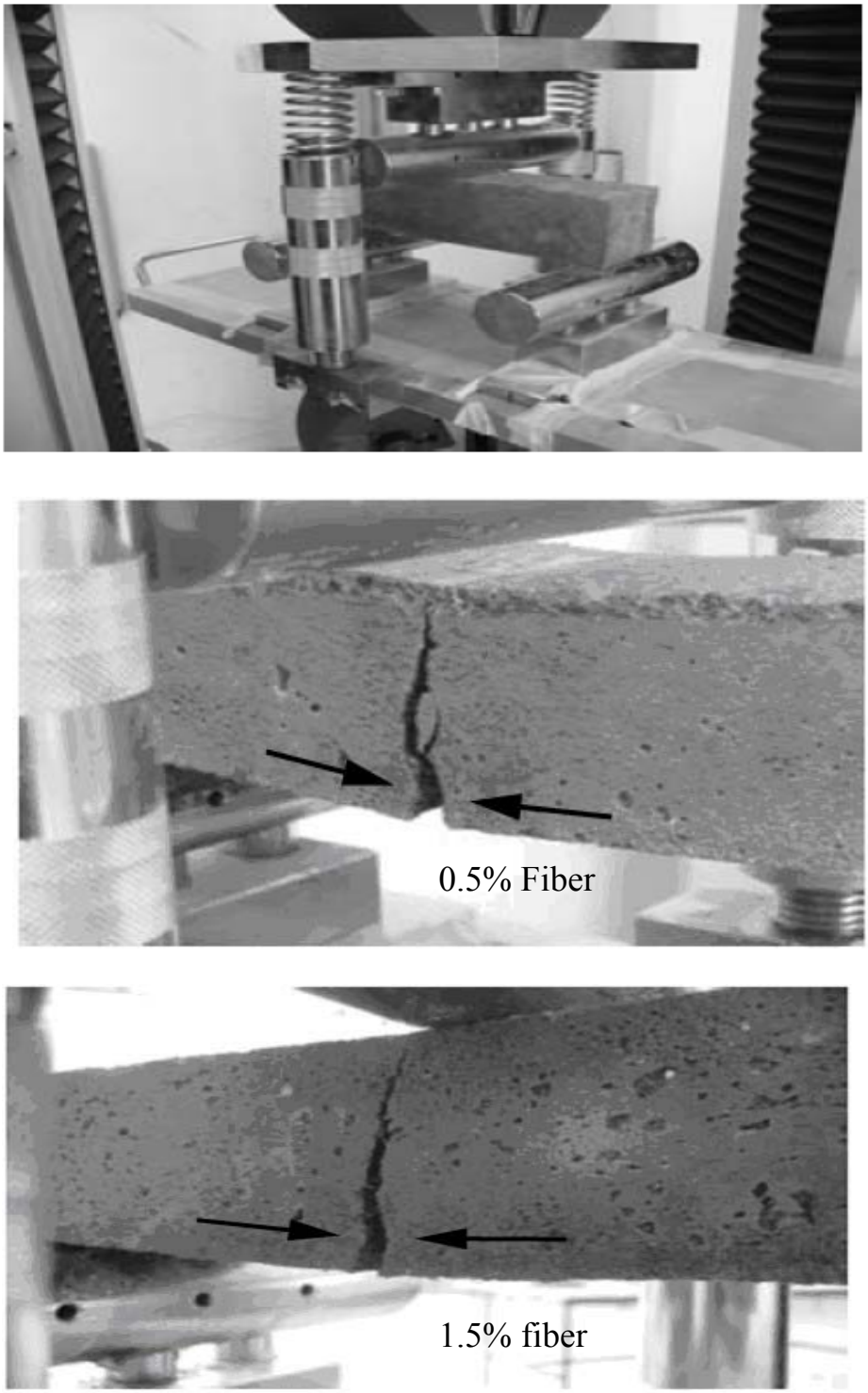

Fig. 2, Cracking of flexural specimens and bridging effect of fiber on cracks

computer with a constant cross head movement of 1 mm/min. Results show, by increasing the amount of fiber in matrix of specimens, the flexural strength tends to decrease.

According to above results, the highest flexural strength was observed in 10%SF and 10%GΠ, which is due to pozzolanic activity mentioned before. the flexural strength of specimens contained 0.5% PP fiber doesn't show considerable increment. Nevertheless, in mixes contained 1% and 1.5% PP fibers, represent a relative increment in flexural strength. It is also observed that the lowest

strength is related to GI in all mixes due to coarse particle size and low pozzolanic behavior. According to Figure 2 it can be observed that after crack initiation, fibers can still carry load and absorb the energy.

Figure 3 represents typical load-deflection responses of plain matrix and mixtures contained 0.5%, 1%, and 1.5% fibers. For plain mortars, the behavior was in a brittle manner. When the strain energy was high enough to cause the crack to self-propagate, fracture occurred almost while the peak load was reached (this is due to the tremendous amount of energy being released). According to Figure 3, the fiber bridging effect helped to control the rate of energy release significantly. Thus, fibers still can carry load even after the peak. With the effect of fibers bridging across the crack surface, fibers were able to maintain the load carrying ability even after the mortar had been cracked. Our laboratory results indicate that, by increasing the amount of fiber in matrix flexural toughness rise up.

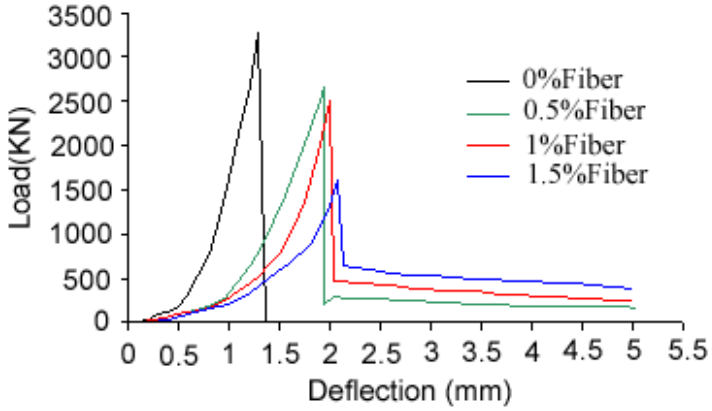

Fig. 3, Load-Deflection Response of plain and polypropylene fiber reinforced mortar

Conclusion

Increasing the fibers in matrix causes low compressive strength, but it increases the flexural toughness substantially. In fact the ability for absorbing the energy rises up. However, mixture of cement based composite with GII and SF containing different percentage of fibers shown close properties to target specimens. Results show the great possibility of usage of ground glass and silica fume in mortars as a replacement in cement.

References

[1] A. Bentur, S. Mindess, Fiber reinforced Cementitious on Durability of Concrete Barking: Elsevier, (1990).

[2] PN. Balaguru, SP. Shah , Fiber Reinforced Cement Composites. New York: McGraw-Hill, Inc, p.367, (1992).

[3] K. Duckett, "Olefin Fiber" and "Nylon Fibers", Project: Textile Science 526 - Nonwovens Science and Technology II, (http://trcs.he.utk.edu/textile/nonwovens/), (Fall 1999).

[4] W.D. Callister, Material Science and Engineering-An Introduction, 4th ed., John Wiley & Sons, New York, (1997).

[5] A.K.Haghi, A.Sadrmomtazi,O.Alidoust,Admixture of Waste Fibers In The Concrete of Tomorrow, Sixth International Conference on Composite Science and Technology , Durban, South Africa, 22-24 January 2007,.

Key Engineering Materials Vols. 385-387 (2008) pp 341-344
© (2008) Trans Tech Publications, Switzerland
doi:10.4028/www.scientific.net/KEM.385-387.341

Fatigue crack monitoring using image correlation

P. Lopez-Crespo[1, a], A. Shterenlikht[2,b], E. A. Patterson[3,c], J. R. Yates[1,d] and P. J. Withers[4,e]

[1]Mechanical Engineering Department, University of Sheffield, Mappin Street, Sheffield S1 3JD, UK

[2]Mechanical Engineering Department, Bristol University, University Walk, Bristol BS8 1TR, UK

[3]Department of Mechanical Engineering Department, Michigan State University, 2555 Engineering Building, East Lansing, MI 48824-1226, USA

[4]Materials Science Centre, Manchester University, Grosvenor Street, Manchester M1 7HS, UK

[a]p.lopezcrespo@sheffield.ac.uk, [b]mexas@bristol.ac.uk,[c]eann@egr.msu.edu, [d]j.yates@sheffield.ac.uk, [e]philip.withers@manchester.ac.uk

Keywords: structural health monitoring, stress intensity factor, image correlation, plastic zone's corrections

Abstract. A novel methodology based on a combination of experimental and analytical methods is used for monitoring the stress intensity factor in fatigue cracks subjected to constant amplitude loads. Full-field displacement information is fitted, following a multi-point over-deterministic approach, to an analytical model. This is developed from Muskhelishvili's complex formulation. The methodology allowed accurate monitoring of the stress intensity factor during three fatigue cycles when small-scale yielding conditions were achieved. Moreover for larger loads where important plastic deformation occurs around the crack tip, Dugdale's correction accounted for the differences between theoretical and calculated stress intensity factors. Accordingly the tool provides an indirect approach for measuring crack tip plasticity. Due to the fact that image correlation is relatively simple to use and is a non-contacting technique, the approach pioneered in this work seems ideal for monitoring fatigue cracks in industrial applications.

Introduction

A variety of parameters are available for characterizing defects or cracks. Amongst them the stress intensity factor (SIF) is probably the most widely used in engineering components prone to linear elastic fracture behaviour. It is employed to assess stable and progressive fatigue crack growth under applied loads. Nevertheless its evaluation often requires detailed finite element analysis which can not be easily achieved for the monitoring the structural integrity of real engineering components.

This work presents a novel methodology for monitoring mixed-mode SIFs from experimental measurements made with image correlation. The approach is based on a procedure previously developed for photo-elasticity [1] and thermo-elastic stress analysis [2]. However the use of image correlation as the experimental technique instead of the aforementioned techniques represents an important step forward: on the one hand no plastic model of birefringent material or bonding of a coating is required, as in the case of photo-elasticity; on the other hand there is no need to apply a cyclic load, as in the case of thermo-elastic stress analysis [3].

Image correlation technique provides maps of displacements of a surface undergoing deformation. It is based on the fact that if the image brightness is approximately constant, surface features will retain similar appearances under small translations and deformations. These features can be then tracked by means of a 2D correlation function to perform pattern matching as a function of the displacement. The displacement is calculated from the location of the maximum value of the correlation function [4].

The aim of the current contribution is to present a new methodology for monitoring experimentally the SIF in real fatigue cracks.

Methodology

The approach for inferring the SIF is based on the multi-point over-deterministic method [5]. It combines an elastic analytical model describing the crack tip field with experimental measures of the displacement field performed by image correlation. The analytical model is based on Muskhelishvili's analytical formulation [6] which proved to generate good results in the case of photo-elastic [7] and thermo-elastic data [2]. In the present case, in order to apply the methodology to image correlation data, the analytical descriptor was developed in terms of displacements. The model employs complex functions incorporating Fourier series. The complex SIF is written as:

$$K_I - iK_{II} = 2\sqrt{\frac{\pi}{a}}\sum_{k=-3}^{3} kb_k \tag{1}$$

where K_I and K_{II} are the opening and shear components respectively of the SIF, a is the crack length and b_k are Fourier coefficients which are determined by fitting the analytical model to the experimental data.

Experimental method

A wedge opening loaded specimen [8] was employed. This was machined in 2024 aluminium alloy. The specimen was fatigue pre-cracked under ΔK_I of approximately 10 MPa√m and load ratio of 0.1 until the crack length was approximately 23 mm.

The features needed for having the random pattern required by image correlation to work were introduced by polishing the surface. This was done with a 120 grade grit paper. The surface was imaged by a 1600 × 1200 pixel CCD with 14 bit dynamic range. The camera was fitted with a 55 mm Canon macro lens and this was located at approximately 200 mm from the surface. In addition the surface was illuminated by a 100 W lamp.

Two different cyclic loads were applied to the sample while images of the crack tip region were recorded. About 21 images were captured throughout each loading cycle, and a full-field map of displacements was obtained for each of these images. These resembled qualitatively to those shown in Fig. 1.

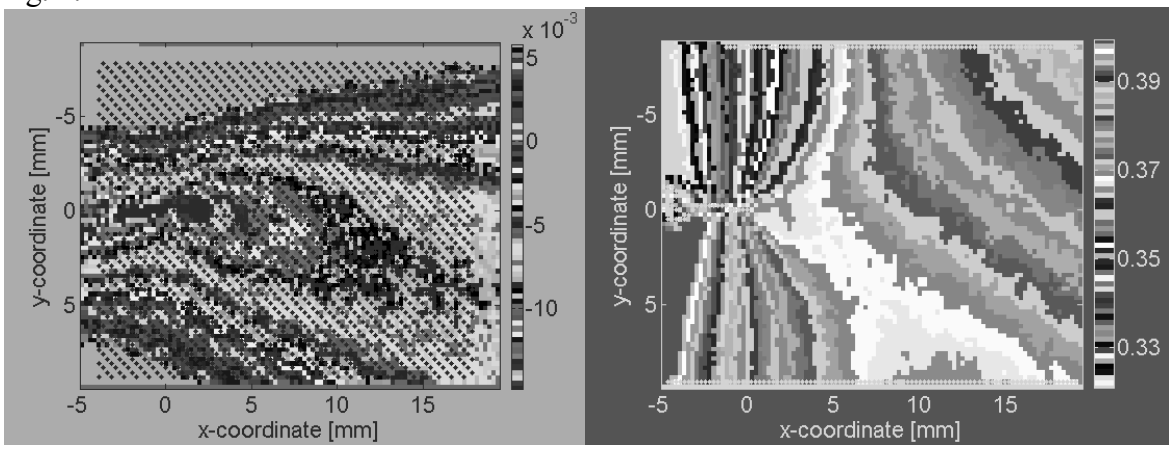

Fig. 1: (a) Horizontal displacement field measured with image correlation showing an array of collected points employed for evaluating the SIF. (b) Vertical displacement field showing the fatigue crack detected with an edge finding routine.

The experimental information required for evaluating the SIFs was collected from the area surrounding the crack tip. U-shaped arrays like the one shown in Fig. 1.a were employed to sample the experimental data. Since the displacement data are representative of the actual displacement field surrounding the crack tip, the SIFs inferred by the technique are *effective* values, and incorporate the influences of crack closure and plasticity.

The origin of coordinates employed for the analytical model was positioned at the tip of the crack. This was found by means of a Sobel edge-finding routine [9] applied to the displacement fields. The vertical displacement field was utilized for this purpose, for having a better signal to noise ratio than the horizontal displacement. An example of the edge detected in this way is shown in Fig. 1.b.

Results and discussion

The results of determining the SIF through two sets of cyclic loads are shown in Figs. 2 and 3. Both mode I and II components of the SIF were estimated. Very good agreement is observed between theoretical and experimental results in the case of the first load (Fig. 2). As regards the second loading case, the experimental results are generally greater than nominal values. This effect is particularly accentuated at the peak of the cycles. At these levels the load approaches the fracture toughness of the material and generates considerable crack tip plasticity.

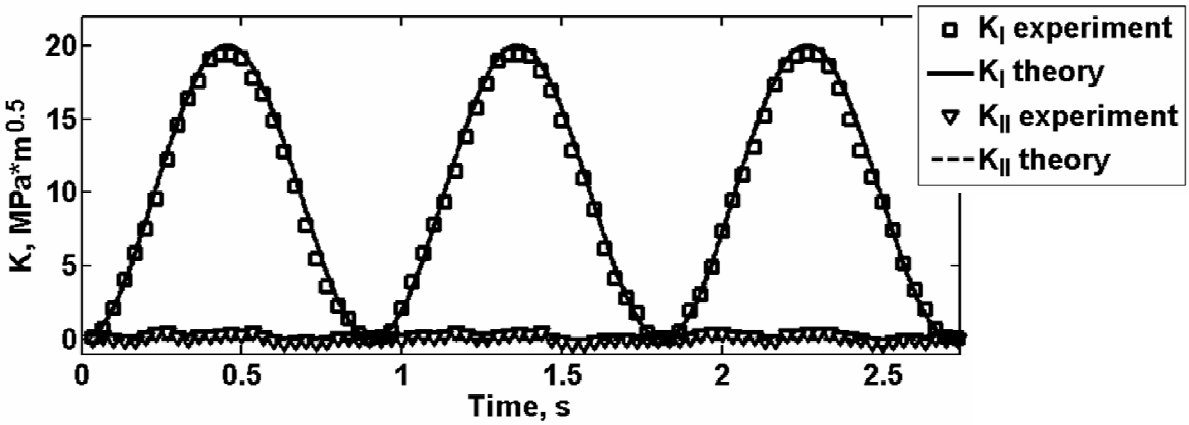

Fig. 2: Inferred and nominal applied K_I and K_{II} monitored during 3 loading cycles in wedge opening loaded specimen.

Unlike the case of stress data, any plastic deformation occurring around the crack tip affects the whole displacement field. As a consequence, the theoretical SIF can be modified to account for the plasticity developed around the crack tip. This is done by increasing, fictitiously, the crack length to $a + 2r_y$, with $2r_y$ being the size of the plastic zone calculated according to Dugdale model [10]. The corrected SIF accounting for the size of the plastic zone, $K_{I\,cor}$, will then be:

$$K_{I\,cor} = K_{I\,the}\sqrt{1+\frac{2r_y}{a}} \tag{2}$$

where $K_{I\,the}$ is the theoretical value calculated according to [8]. The corrected SIF is also plotted in Fig. 3. Good correlation is observed between the experimental values and the theoretical values including the effect of the plastic size. Accordingly the methodology is sensitive to crack tip plasticity, and the experimental SIF measured is an enhanced factor, where part of it is due to the elastic component of the crack tip displacement and another part is due to plasticity.

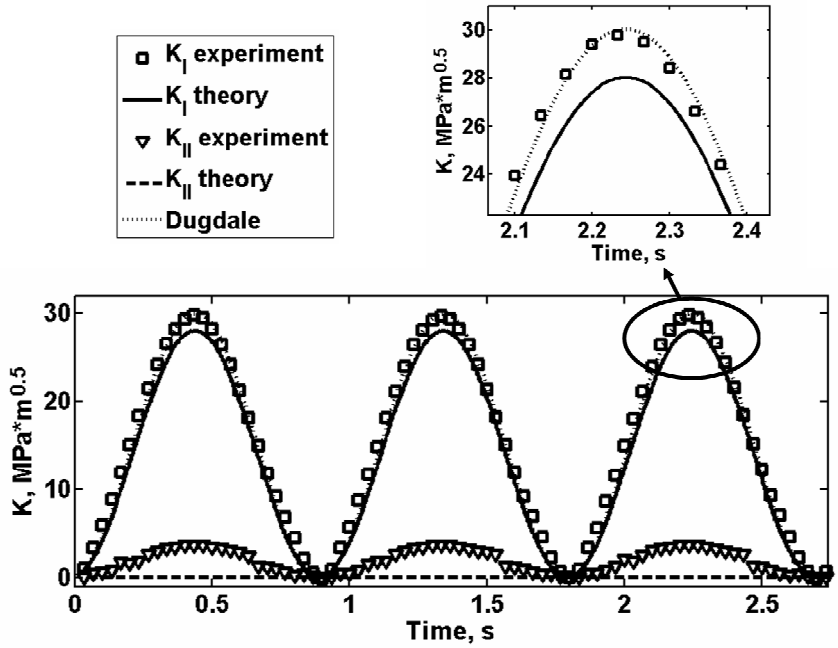

Fig. 3: Inferred and nominal applied K_I and K_{II} monitored during 3 loading cycles in wedge opening loaded. Theoretical K_I corrected by taking into account plasticity around the tip, using Dugdale's approach [10], is also plotted.

Conclusion

The methodology herein described allows monitoring of the *effective* SIF in cracked specimens. Under small-scale yielding conditions, the technique provides accurate estimation of the SIF while fatigue load is applied. If crack tip plasticity is increased further, the experimental value measured contains also information about the plasticity. Therefore the approach seems to measure the true SIF under elastic-plastic conditions.

References

[1] M.N. James, M.N. Pacey, L.-W. Wei and E.A. Patterson: Eng. Fract. Mech. v.70 (2003), p.2473

[2] F.A. Díaz, E.A. Patterson, R.A. Tomlinson and J.R. Yates: Fat. Fract. Eng. Mater. Struc. v.27 (2004), p.571.

[3] E.A. Patterson and E.J. Olden: Fat. Fract. Eng. Mater. Struc. v.27 (2004), p.623.

[4] M.A. Sutton, S.R. McNeill, J.D. Helm and Y.J. Chao, in: *Photomechanics, Topics in Applied Physics*, edited by P.K. Rastogi (2000).

[5] R.J. Sanford and J.W. Dally: Eng. Fract. Mech. v.11 (1979), p.621.

[6] N.I. Muskhelishvili: *Some basic problems of the mathematical theory of elasticity* (Noordhoff Ltd, Netherlands 1953)

[7] A.D. Nurse and E.A. Patterson: Fat. Fract. Eng. Mater. Struc. v.16 (1993), p.1339

[8] Y. Murakami ed.: *Stress Intensity Factors Handbook* (Pergamon Press, Oxford 1987)

[9] M. Sonka, V. Hlavac and R. Boyle: *Image Processing, Analysis and Machine Visio* (Chapman and Hall International 1993)

[10] S. Suresh: *Fatigue of Materials* (Cambridge University Press, Cambridge 2004)

Key Engineering Materials Vols. 385-387 (2008) pp 345-348
© (2008) Trans Tech Publications, Switzerland
doi:10.4028/www.scientific.net/KEM.385-387.345

Review of experimental models for confirmation of mathematical models of gears

B. Aberšek and J. Flašker

University of Maribor, Faculty of Natural Sciences and Mathematics, 2000 Maribor, Slovenia

University of Maribor, Faculty of Mechanical Engineering, 2000 Maribor, SLOVENIA

boris.abersek@uni-mb.si, joze.flasker@uni-mb.si

Keywords: Gears, mathematical models, experiemnt, numerical analyses

Abstract. In order to calculate the service life as precisely and reliably as possible we need good mathematical models for describing loading, geometry, properties of materials and fracture mechanics parameters. It can be established whether a mathematical model is precise and reliable only by comparison of results of the method such as analytical methods in case of simple problems and experiment when real complex structure are deal with. Since gears and gearing belong to the second group, by correctly selected and developed test pieces and carefully planned experiments we obtained results with which we confirmed and justified the mathematical model for calculating mentioned parameters. To this end we will show in this paper series of experimental methods and test pieces used on the gears.

Intriduction

For confirm mathematical models we developed different non-standard test pieces and on this pieces we used combination of mixed experimental methods. The aim of these combinations was to obtain as complete information about the individual influences as possible and to determine the interaction between magnitudes. In this way we confirmed different mathematical/numerical models as a whole and also determined some physical interpretations in models. With this we were able to ensure that our model is not purely a mathematical model but they have also physical meanings.

Experimental determination of crack growth ratio

Since gears and gearings belong to the real complex structures by correctly selected and developed test pieces and carefully planned experiments we obtained results with which we confirmed and justified the use of the mathematical models [1, 2, 5] for calculating the tooth stress intensity factor Z as well as the service life of gears.

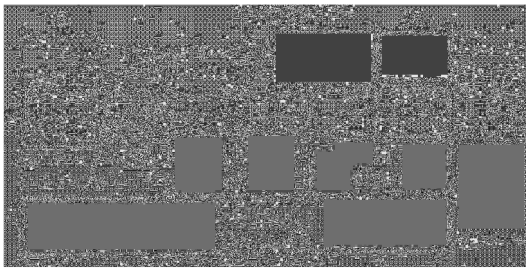

Figure 1: Standard (ASTM-E606) test piece

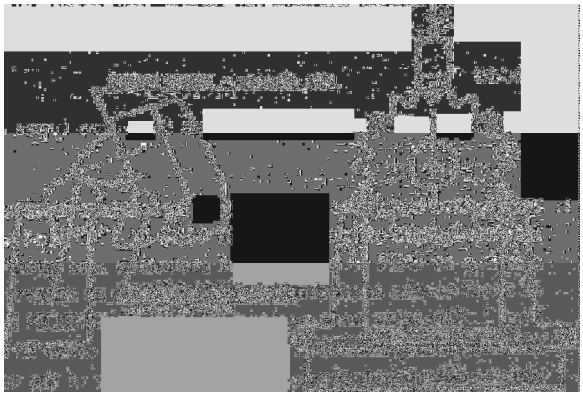

Figure 2: Gear test piece

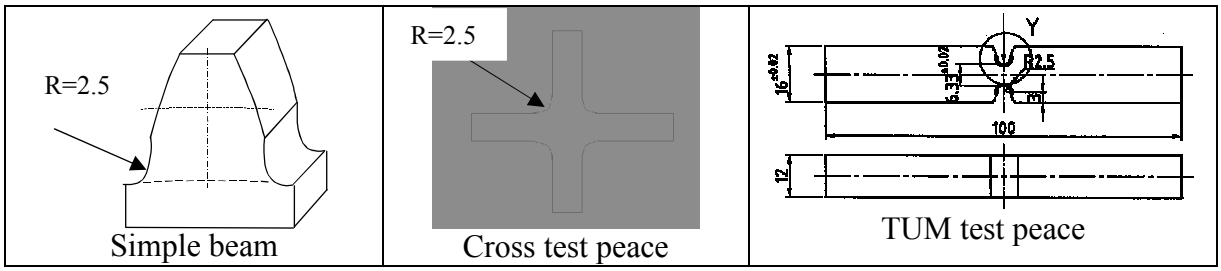

Figure 3: Non-standard gear test peace

Test pieces. We used in our laboratory two types of test pieces:

- Standard test piece for determination of fracture mechanics parameters of material AISI 4130 or 42CrMo4 according to DIN in the area of initiation and growth of short cracks according to ASTM-E606 as shown in Figure 1.
- Non-standard test pieces for determination of parameters of gears. These types of test pieces were gear test pieces developed during previous researches [2, 4]. The arrangement of the individual measuring instruments and test peace is shown in Figure 2.

Different laboratories use different test peaces. Some of them are shown in Figure 3.

Measuring method used.

As we wanted to observe particularly initiation and propagation of short cracks and to determine the conditions occurring in this case [2, 4] (stresses, strains, moment of beginning of fracture etc.), we used mixed experimental methods: photoelastic method, method of measuring of stress/strain by means of strain gauges, replica technique for determination of prevailing initials and measuring of microcracks by means of crack gauges. The aim of these combinations was to obtain as complete information about the individual influences as possible and to determine the interaction between these magnitudes. Individual methods are briefly described below.

Replica on cylindrical test piece. During the tensile test of cylindrical test piece the observed test area had a cross section of 4x10 mm. The replica method was used for determining the length: of short cracks with the replication interval of $2x10^3$ cycles in case of very short cracks because we were particularly interested in this area, while for greater lengths the interval was increased to $2x10^4$ cycles. The tests were stopped when the tensile loading was maximal so that the cracks remained open during replication of the surface area.

The test with surface area replication was affected with examination of loading of stress levels 892 N/mm^2 and 696 N/mm^2, which corresponded to a service life of 22.385 and 80.150 cycles. We performed a few test for each loading ratio, which facilitated studying of a great number of cracks. The triangular form of the pulse at 50 Hz frequency was used.

The replicas obtained at various stages of test were examined on an optical microscope Leitz with 150x to 250x magnification. In this way we determined and/or selected the cracks important for further observation. The length of crack was then measured on the basis of which we calculated the crack growth ratio *da/dN*. For each experimental value *da/dN* obtained from analysis of replicas we calculated the relevant value ΔK. By means of the least square method from equation:

$$\frac{da}{dN} = z_1(\Delta K)^{z_2} \tag{1}$$

for each pair of data thus obtain with the some stress level we determined the corresponding value of coefficient of the material for short cracks:

$$z_1 = 120{,}571742 \quad \text{and} \quad z_2 = 3{,}069$$

The value of the tooth stress intensity factor K is related to propagation of the plastic zone, deformation and orientation of grain in case of short cracks and stress intensity factors in case of long cracks. When we want to approximate the tooth stress intensity factor for general use for crack initiation, propagation of micro and macro crack, the stress intensity factor for gear tooth becomes a more complex form [2, 5]:

$$K = \left(0.2\,\sigma + e^2\right) \ln\sqrt{\pi\, a} \left| \frac{\sigma\, Y(a/S)\, \sqrt{\pi\, a}\, \left(\sigma\, Y(a/S)\right)\sqrt{\pi\, a} - K_{th}\,)}{K_{th}} \right| \tag{2}$$

where the shape factor [4] is:

$$Y(a/S) = \left(\cos\,\varphi - \frac{c}{L}\, \sin\varphi \right) Y_m(a/S) - \frac{S}{6L}\, \sin\varphi\, Y_t(a/S) \tag{3}$$

where $Y_m(a/S)$ is the bending part and $Y_t(a/S)$ is the known shape factor for the compact tension specimen. (4)

Replicas on gears. By the replica method we followed up the propagation of short fatigue cracks in the observed direction, i.e., along the tooth width. The test was performed so that the loadings, i.e., F_{max} = 50 kN, F_{min} = 5 kN and the ration $\Delta F = F_{min}/F_{max}$ = 0,1 was checked. The test was performed at the frequency 50 Hz. Replicas were made in intervals $3x10^3$ during the first three measurements, then the step was increased to $6x10^3$ cycles. After $210x10^3$ the test was stopped and final impressions were made. All impressions were made in critical cross section at the point of maximum tensile stress. In the end we made ground section from the test piece on which we observed the process of occurrence of cracks and their size.

Measurements with crack gauges. For measuring the crack lengths greater than approximately 0,2 mm we used crack gauges made by Measurement Group Vishay Type TK-09-CPB02-005. The measuring gauges were glued to gear test pieces at approx. 0,11 - 0,2 mm from the edge as shown in Figure 2. By means of the gauge and x-y plotter we recorded the crack growth from the initial value to the size of 2,6 mm in ten steps. By means of these measurements we obtained the *a-N* curve. On the basis of this diagram and measurements of short crack lengths we made the diagram *da/dN - a* and diagram *da/dN - ΔK*.

Static measurements. We loaded and relieved the gear test piece with fixed strain gauges from 0-114 kN and measured deformations in the critical cross section of the gear tooth. On the basis of deformations we calculated the stress and residual stress, i.e., plastification in the tooth root. The results are average value of deformations along the entire width of the strain gauge. These data were used for evaluation of results of numerical analyses.

Measurements and fatigue. During the next step we started the fatigue test on the gear test piece at the room temperature and at 50 Hz frequency with the following loading: maximum force F_{max} = 50,1 - 50,2 kN, distance between supports L=294 mm and ratio $R = F_{max}/F_{min}$ = 0,1. During fatigue we measured by means of strain gauges the change of strain as function of number of cycles in the area of micro cracks. The basic aim of the measurements was to obtain a correlation between the micro crack length and stresses and/or how to conclude from the stress what happen in the material, when the crack occurs.

The number of cycle's waried from 0 to 280.000 where the test was stopped. We found out that by such method of measurements of the stress/strain, thought the smallest strain gauge was selected, it

was possible only to evaluate the local stress conditions since the influence of average values in the strain gauge is too great so that it is not possible to get precise insight into local micro conditions.

Since by the measuring method with strain gauges we did not achieve desired results, we tried to measure stresses also by the photo elastic method. We glued photo elastic sheet to both teeth in contact. The data on this lining are: deformation optical constant F = 4,10x10^{-6} m/rad, module of elasticity E=2900 MPa, Poisson's number n=0,36 and thickness of lining h=2 mm.

Because of the possibility of examination and because of comparison of different methods the following measuring components were glued in addition to the photo elastic plastic sheet on the gear test piece front side:

- one strain gauge on the tooth flank in the critical cross section,
- another strain gauge on the rear side in the critical cross section.

During the test micro cracks occurred in the interior of the gear, which was detected by the replica method as well as by the subsequent fractographic. Because of these micro cracks changes occurred in the field of isochromates.

Numerical verification

In order to verify correctness of functioning of the presented model, we have compared the experimental results (FEA) with numerical results [3,4].

Our secondary goal was to tray to find optimal test peace. Because experiment is complicated and expensive we made comparison between different non-standard test piece - beam test peace which is most simplified model, cross test peace and bend test peace with notch in form of tooth according to Figure 3 only with FEA. Results are partly shown in [2].

Conclusion

By experimental researches we can come to the following conclusions:

1. From fractography we can establish that the crack length-number of cycle's ratio is not a continuous smooth.
2. The manner of crack propagation is the form I - combined with form II am III [2, 4]. Therefore stress intensity factor K_I, K_{II}, K_{III} are not appropriate for describing the crack growth because the connections between ΔK and da/dN are no more monotonous function. Therefore, for calculations we have developed the gear stress intensity factor K which takes into account not only the stress of homogeneous material in critical cross section but also the stress concentration due to defects occurring there.

The tests performed also show that the photo elastic method and replica method are suitable for determining the crack initiation since it detects precisely enough the changes in the stress/strain field. It also enables us to find out and follow up the plastic zones. We can simplify some non-standard experiment but we must be extremely carefully with interpretation of the results.

References

[1] D. Taylor and J. F. Knott: *Fatigue crack propagation behaviour of short crack; the effect of microstructure*, Fatigue Engn. Mater. Struct. 4, 147 - 155, (1981)

[2] B. Aberšek, and J. Flašker: *How gears break,* Wit Press, Southampton, Boston (2004)

[3] M.F. Kanninen: *Advanced Fracture Mechanics*, Oxford Press, New York (1985)

[4] B. Aberšek, J. Flašker and S. Glodež: *Review of mathematical and experimental models for determination of service life of gears*. Eng. fract. mech.. vol. 71, iss. 4/6, 439-453, (2004).

[5] B. Aberšek and J. Flašker: *Numerical methods for evaluation of service life of gear*, International Journal for Numerical Methods in Engineering, Vol. 38, 2531-2545, (1995).

Key Engineering Materials Vols. 385-387 (2008) pp 349-352
© (2008) Trans Tech Publications, Switzerland
doi:10.4028/www.scientific.net/KEM.385-387.349

Flexural Performance of U-Shaped Precast Concrete Beams with Non-contact Lapped Splice

Sang-Su Ha [1,a], Seung-Hun Kim [2,b]

[1]Schoolof Architecture, Hankyong National University, Ansung, Gyeonggi-do, 456-749, Korea

[2]Dept. of Architectural Engineering, Hanbat National University, Daejeon, 305-719, Korea

[a]drhaha@naver.com , [b]kimsh@hanbat.ac.kr

Keywords: Precast Concrete, Non-contact, Lapped Splice, Crack

Abstract. In this study, new moment-resisting precast concrete beam-column joint is proposed for moderate seismic regions. The new joint includes the connection reinforcing bars, penetrated the joint and lap-spliced with the bottom bars of precast U-beam. To evaluate the performance for non-contact lapped splice, experimental and analytical work were conducted, for major variables of the length of lap and the diameter of connection reinforcing bars(D19, D22, and D25). Results of experimental and analytical works show that these variables have much influence on flexural strength and ductility, and deformation of lapped joint. Using nonlinear finite element method, analytic research was performed for investigating crack and fracture patterns, load-deflection curve, comparison of internal force, evaluation of ductility, stains of reinforcement bar.

Study background and objective

Precast concrete (PC) provides the advantage of high quality control, construction efficiency and savings in time and cost. However, it was true that PC systems had drawbacks in the relevant to connectivity between elements. Therefore, the use of precast concrete structural systems had been limited primarily to non-seismic areas. To promote the use of precast concrete in moderate and high seismic areas, adequate connection methods between precast members need to be developed and they must have enough strength and ductility.

New moment-resisting precast concrete beam-column joint was proposed for moderate seismic regions[1]. It has the connection reinforcing bars, penetrated the joint and lap-spliced with the bottom bars of U-shaped precast beam, as shown in Fig. 1.

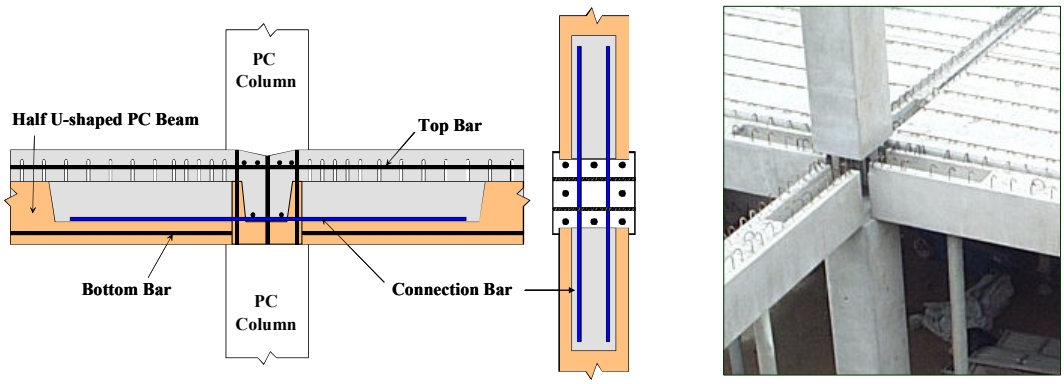

Fig. 1 New moment-resisting precast concrete beam-column joint

In this joint, welding or mechanical splices are not used to lap splice longitudinal bottom reinforcements of the beam to the reinforcements extending from the column. The inner region of the U-shaped PC beam with the connection bars will be grouted to form a monolithic connection.

The load is transferred in the spliced reinforcements by non-contact lap splicing. The aim of the

present research program was to evaluate the flexural performance for non-contact lapped splice between the bottom bars of PC beam and the bottom bars of topping concrete. The present research program consisted of experimental and analytical works.

Experimental and Analytical Program

Specimens. An experimental and analytical program was carried out to investigate the effect of the length of lap and the types of connection reinforcing bars (D19, D22). Six beam specimens of full scale were tested. Table 1 summarizes the specimens. Fig. 2 shows the cross-sections of specimens and shapes. For FEM analysis, Total-RC, nonlinear FEM program for RC structures, was used. The FEM mesh of specimens consists of two-dimensional element as shown as Fig. 3. The clear span of specimen was 5000 mm and the original cross-section was 300 mm in width (B) and 400 mm in depth (D). The distance between lapped bars (t_p) is 10 mm. L_d is the lap length calculated by ACI design code[2].

Table 1 List of specimens

Specimen	Bottom bars	Lap length(mm)	t_p(mm)
B1-1	3-D19	590 (1.0 L_d)	10
B1-3	3-D19	470 (0.8 L_d)	10
B1-4	3-D19	710 (1.2 L_d)	10
B1-5	3-D19	820 (1.4 L_d)	10
B1-6	2-D25	980 (1.0 L_d)	10
B1-7	2-D22	850 (1.0 L_d)	10

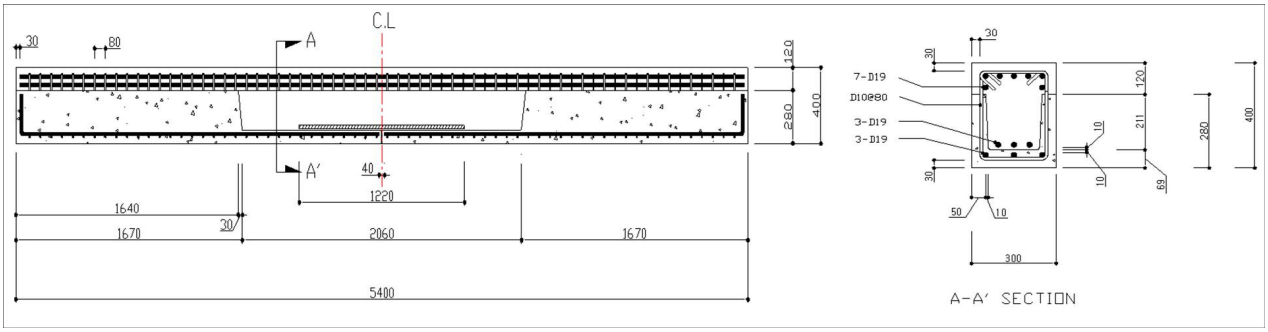

Fig. 2 Details and configuration of B1-1 specimen

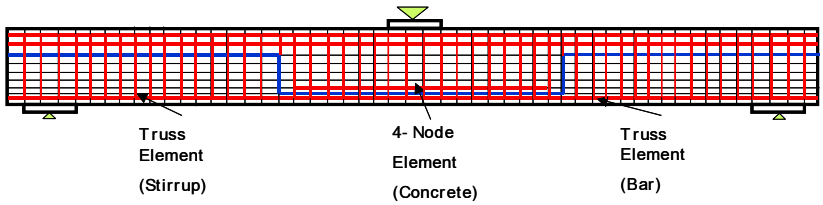

Fig. 3 FEM mesh

Material models. The compressive strengths of PC and RC were 26.5 MPa and 25.2 MPa, respectively. All the reinforcements steel used in the specimens conformed to KS SD40. Mechanical properties of the reinforcing bars are listed in Table 2. As shown as Fig. 4, material and bond models were used for FEM analysis[3]. After cracking, concrete is still able to carry the tensile stresses normal to the cracked plane partially, because of the concrete adhesion to the reinforced bars and the aggregate interlocking. To evaluate this tension stiffening behavior and recombination of crack, the concrete stress strain relationship on the cracked plane is assumed as Fig. 4(c).

Test methods. Concentrated load was applied to the center of specimen by actuator and specimen was controlled by values of LVDT, which was located on the center of specimen.

Table 2 Mechanical properties of reinforcing bars

Type of reinforcing bars	Yield strength(MPa)	Yield strain	Tensile strength (MPa)	Elastic modulus (MPa)	Extensibility (%)
D10	502.1	0.003	734.5	166.7	15.9
D13	535.6	0.0031	747.1	168.7	17.0
D19	525.1	0.0026	760.1	202.0	14.8
D22	508.0	0.0026	756.5	195.2	18.7
D25	514.9	0.0025	791.1	205.9	19.4

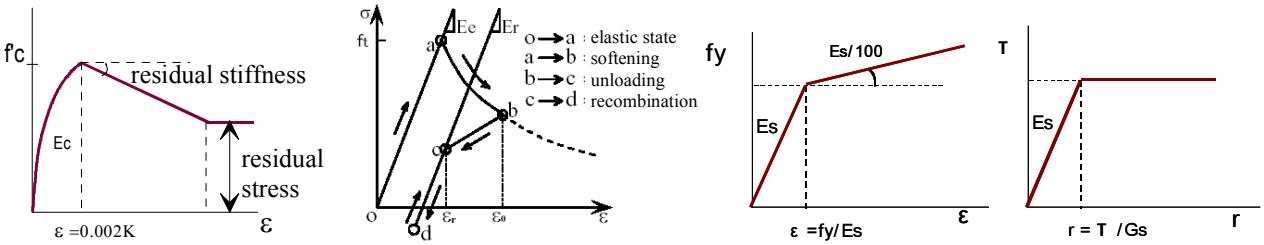

(a) concrete in compression (b) concrete in tension (c) reinforcements (d) bond

Fig. 4 Material models

Test and Analysis Results

Failure patterns. Fig. 5 shows the failure patterns of B1-1 and B1-5 specimen by test and FEM analysis results. In B1-1 and B1-3 specimens, V-shaped cracks occurred by bond failure. The others showed flexural failure as shown as Fig. 5(b).

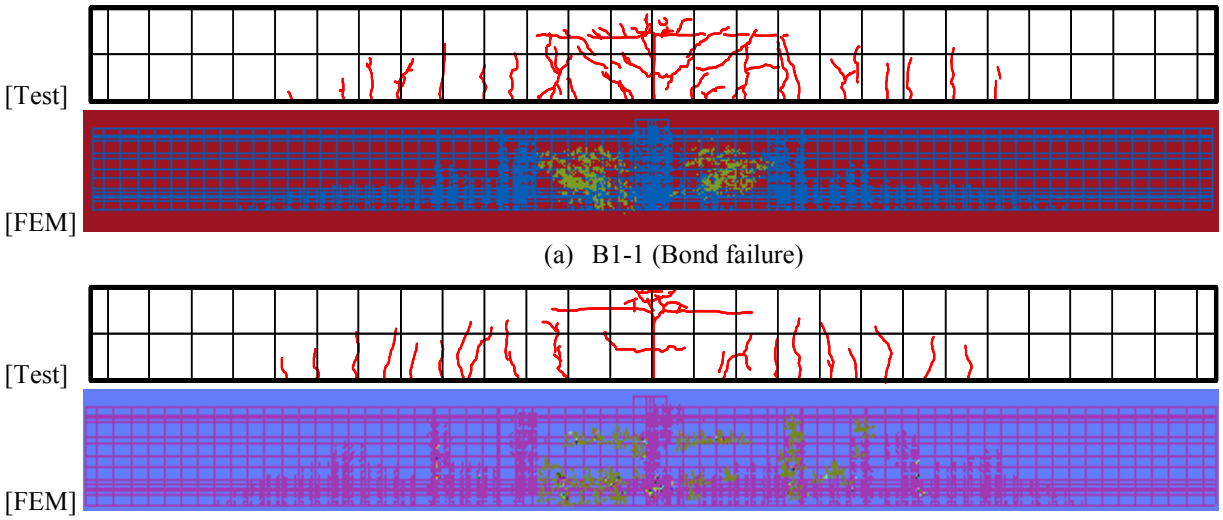

(a) B1-1 (Bond failure)

(b) B1-5 (Flexural failure)

Fig. 5 Failure patterns

Load-displacement response. Fig. 6 shows the load-deflection curves at the center span for all specimens comparing the experimental results with analytical results. For B1-1 and B1-3 specimens, the strengths were reduced after 50 mm in deflection by bond failure of reinforcement bars. For specimens occurred by bond failure, analytical results agree well with experimental results.

Strengths. Table 3 shows the cracking strength (P_{cr}), the yield strength (P_y), and the maximum strength (P_{max}) of all specimens by test and FEM analysis. P_n is the nominal strengths calculated by KCI and ACI design code [4], [2]. In the comparison of maximum strengths by test and nominal strengths, $P_{max\text{-}TEST}/P_n$ measured 0.74~1.23. It showed that B1-1 (1.0 L_d) and B1-3 (0.8 L_d) specimens had an insufficient performance on non-contact lapped splice between the bottom bars of PC beam and the bottom bars of topping concrete. Therefore, for safety design, it is desirable for D19 using as connection bars that Ψ_s (the factor used to modify development length based on reinforcement size) is

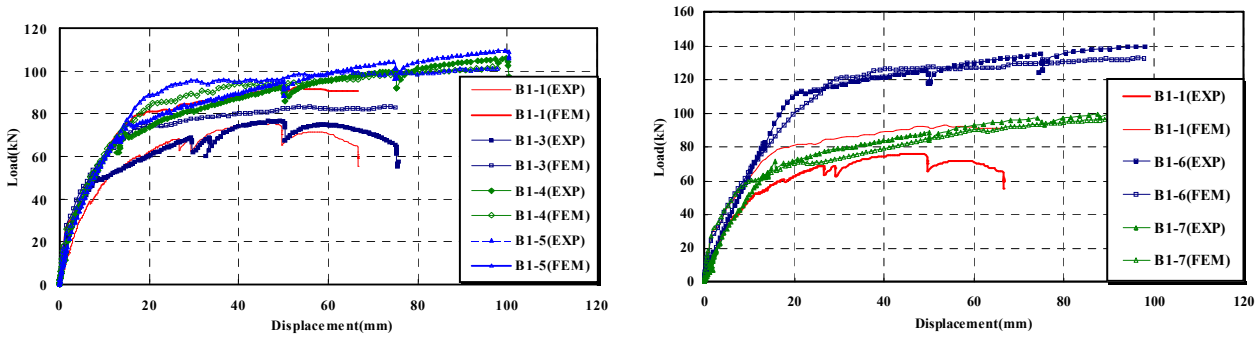

Fig. 6 Load-displacement response

Table 3 Strengths by test and FEM analysis

Specimen	$P_{cr\text{-}TEST}$ (kN)	$P_{cr\text{-}FEM}$ (kN)	$P_{y\text{-}TEST}$ (kN)	$P_{y\text{-}FEM}$ (kN)	$P_{max\text{-}TEST}$ (kN)	$P_{max\text{-}FEM}$ (kN)	P_n (kN)	$P_{max\text{-}TEST}$ / $P_{max\text{-}FEM}$	$P_{max\text{-}TEST}$ / P_n
B1-1	18.4	23.0	59.1	78.98	75.4	92.55	100.8	0.81	0.74
B1-3	18.4	22.4	56.3	66.96	76.6	83.28	101.2	0.91	0.75
B1-4	19.1	25.7	74.6	81.31	106.0	101.84	101.2	1.04	1.05
B1-5	19.4	24.6	73.0	89.98	109.7	105.21	100.1	1.04	1.09
B1-6	17.2	23.6	111.9	103.51	139.2	132.22	112.7	1.05	1.23
B1-7	22.7	26.8	66.8	64.21	101.6	97.44	87.7	1.04	1.15

taken as 1.0. In the comparison of maximum strengths by test and FEM analysis, $P_{max\text{-}TEST}/P_{max\text{-}FEM}$ for specimens with flexural failure measured 1.04~1.05. It showed that FEM analysis results agree well with experimental results. For B1-1 and B1-3 specimens with bond failure, $P_{max\text{-}TEST}/P_{max\text{-}FEM}$ measured 0.81~0.91. It showed that it needs to consider the de-bonding effect between PC and the connection bars with diameter less than D19.

Conclusions

The experimental and analytical works were conducted to evaluate the flexural performance for non-contact lapped splice between the bottom bars of PC beam and the bottom bars of topping concrete. The conclusions obtained in this study can be summarized as follows;

1) For specimens using D19 connection bars with lap length (1.0 L_d) by the previous design code, V-shaped cracks occurred by bond failure. 2) For safety design, it is desirable for D19 using as connection bars that the factor used to modify development length based on reinforcement size is taken as 1.0. 3) For specimens with flexural failure, the maximum strength of FEM analysis agree well with test's. 4) It needs to consider the de-bonding effect between PC and the connection bars with diameter less than D19.

Acknowledgement This work was supported by the Korea Research Foundation Grant funded by the Korean Government (KRF-2005-050-D00017).

References

[1] S. H. Kim, G. C. Ryu, S. S. Ha, J. H. Moon, and L. H. Lee : An Experimental Study of the Structural Behavior on the Precast Concrete, Journal of Architectural Institute of KOREA, Vol. 22, No. 7 (2006)

[2] ACI Committee 318 : Building Code Requirements for Structural Concrete (ACI 318-05) and Commentary (ACI 318R-05) (2005)

[3] Total Information service LTD : Total-LCC Ver. 1.0 User's Manual (2004)

[4] Korea Concrete Institute : Concrete Structure Design Code (2003)

Key Engineering Materials Vols. 385-387 (2008) pp 353-356
© (2008) Trans Tech Publications, Switzerland
doi:10.4028/www.scientific.net/KEM.385-387.353

Bending and Shear Strength of I-Slab with Polystyrene Forms

S. H. Kim[1,a], K. K. Lee[2,b], H. S. Lee[3,c], K. J. Lee[2,b], I. S. Kang[3,d]

[1]Architectural Engineering, Hanbat National University, Daejeon, 305-719, Korea

[2]Samsung Heavy Industries Co., LTD., Seoul, 135-080, Korea

[3] School of Architecture & Architectural Engineering, Hanyang University, Ansan, 425-791, Korea

[a]kimsh@hanbat.ac.kr, [b]kangkun.Lee@samsung.com,

[c]ercleehs@hanyang.ac.kr, [d]ins5kang@hanyang.ac.kr,

Keywords: Precast Concrete, Polystyrene, Failure, Crack

Abstract. Where the self weight of the overall slab needs to be considered, the quantity of in-situ concrete required can be reduced by the introduction of polystyrene void forms supplied and fixed to the precast panel during manufacture. In this study, new I-slab system with polystyrene form and precast concrete deck is proposed to reduce the construction period and the self weight of the slab. This paper presents experimental works on the bending and shear of the I-slabs. Five specimens were tested. The main parameters of experiments were the hole diameter of polystyrene form and the thickness of slab. Structural performance of I-slab was evaluated on the basis of failure mode, load-displacement curve, and ultimate strengths. Based on the test results, the critical punching shear sections were changed as test variables, so the punching shear strengths were very different. Test results indicated that the developed I-slab were very effective to increase the strength because of self weight reduction.

Study background and objective

Concrete deck construction using the precast concrete (PC) wide slab is divided into two separate operations. In the first, PC forms reinforced with lightweight steel trusses and the required bottom steel, accurately positioned in the concrete, are prefabricated off-site. In the second operation, these elements, used as forms, are combined with the balance of the reinforcing steel and the upper, poured-in-place layer of the slab on the structure. The wide slabs replace conventional formwork and become an integral part of the finished deck.[1]

Where the self weight of the overall slab needs to be considered, the quantity of in-situ concrete required can be reduced by the introduction of polystyrene void forms supplied and fixed to the precast panel during manufacture. The void formers developed at America and Europe are normally rectangular form and are fixed between the lattice girders. In this study, I-slab system with new polystyrene form and precast concrete deck is proposed to reduce the construction period and the self weight of the slab, as shown in Fig. 1. New polystyrene form is 400 mm long and 400 mm wide with 200 mm diameter hole, as shown in Fig. 2. The depth of polystyrene form is changed by slab thickness.

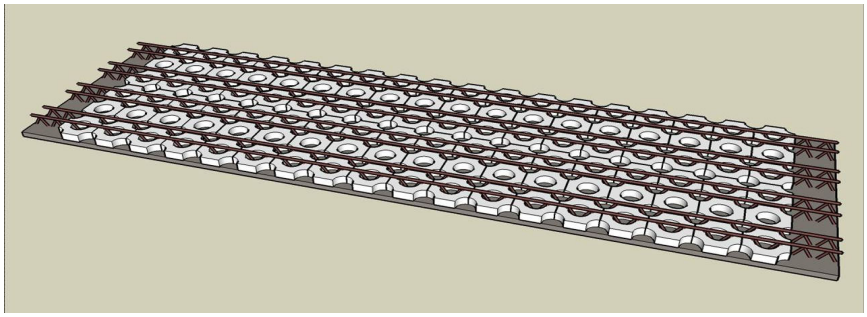

Fig. 1 I-slab system

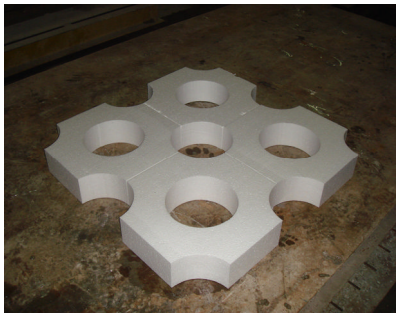

Fig. 2 New polystyrene form

The aim of the present research was to evaluate the bending and shear strength of the I-slabs throughout experimental works. The main parameters of experiments were the hole diameter of polystyrene form and the thickness of slab. Structural performance of I-slab was evaluated on the basis of failure mode, the load-displacement curve, and the ultimate strengths.

Experimental Program

Specimens. An experimental program was carried out to investigate the effect of the hole diameter of polystyrene form (160 mm, 200 mm) and the thickness of slab (210 mm, 310 mm). It consists of two types of test. One is the bending test (S1 series). The clear span of specimen was 5000 mm for slab thickness, t_s = 210 mm and 6000 mm for t_s = 310 mm. The other is the shear test (IS Series). The length of specimen was 2000 mm. Details and configuration of IS specimen are similar to S1 specimen except the span. Total six specimens of full scale were tested. Table 1 summarizes the specimens. Fig. 3 shows the details and configuration of S1-2 and IS-6 specimen.

Table 1 List of specimens

Specimen	Length*width (mm*mm)	Slab thickness, t_s (mm)	Bottom bars	Hole Diameter of polystyrene form (mm)	Volume ratio of polystyrene form
S1-2	1200*5200	210	4-D13+2-D10	200	0.260
S1-6	1200*6400	310	5-D13	200	0.372
S1-7	1200*6400	310	5-D13	160	0.459
IS-2	1200*2000	210	4-D13+2-D10	200	0.260
IS-6	1200*2000	310	5-D13	200	0.372
IS-7	1200*2000	310	5-D13	160	0.459

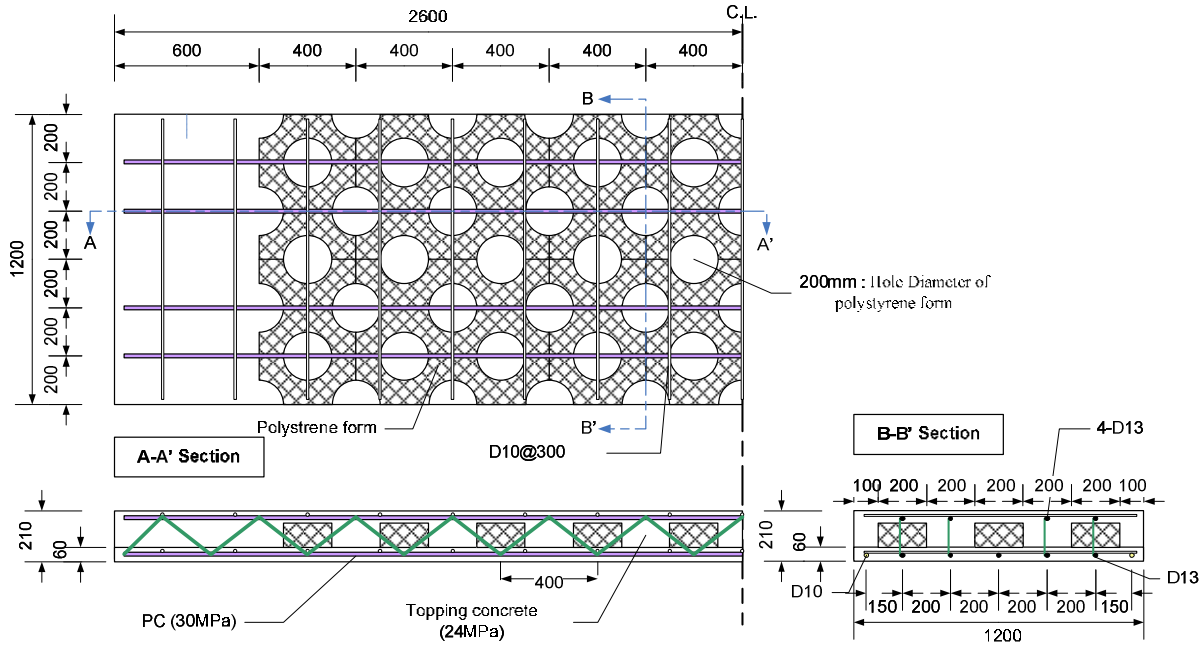

Fig. 2 Details and configuration of S1-2 specimen

Materials. The design strengths of PC and RC were 30 MPa and 24 MPa, respectively. The compressive strengths of PC and RC were 26.5 MPa and 25.2 MPa, respectively. All the reinforcements steel used in the specimens conformed to KS SD40. Mechanical properties of the reinforcing bars are listed in Table 2.

Test methods. For bending test, the two concentrated load was applied to 50mm from the center of specimen by actuator as shown as Fig. 3(a). Specimen was controlled by values of LVDT, which was

Table 2 Mechanical properties of reinforcing bars

Type of reinforcing bars	Yield strength(MPa)	Yield strain ($\times 10^{-6}$)	Tensile strength (MPa)	Elastic modulus (MPa)	Specimen
φ9	339.57	1800	446.05	190.87	S1-2, IS-2
	352.10	3075	527.64	172.54	S1-6, S1-7, IS-6, IS-7
D10	415.62	2200	609.04	247.42	S1-2, IS-2
	461.64	2901	580.46	152.73	S1-6, S1-7, IS-6, IS-7
D13	575.73	4900	673.38	127.81	S1-2, IS-2
	456.48	2911	545.35	167.02	S1-6, S1-7, IS-6, IS-7

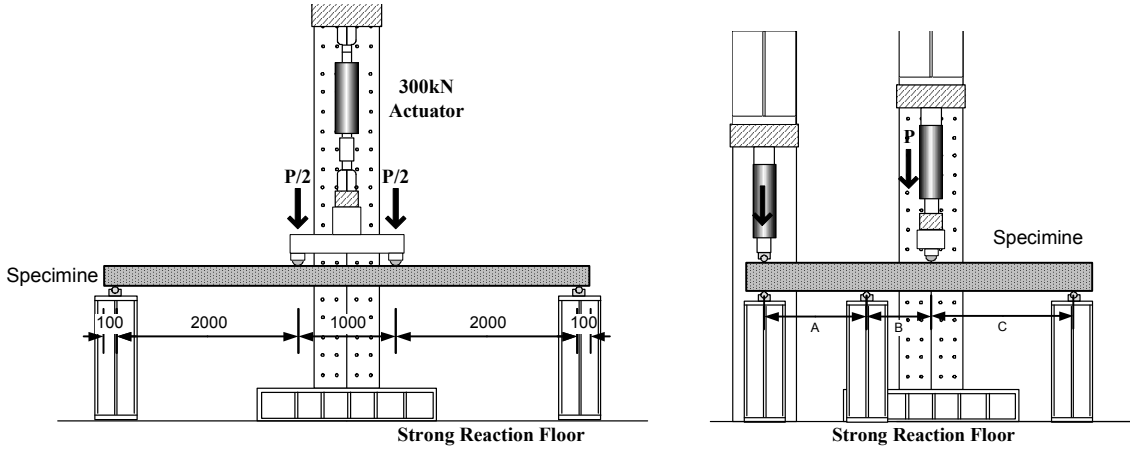

(a) Bending test (b) Shear test

Fig. 3 Test setup

located on the center of specimen. For shear test, maximum shear force and little bending moment act on the center of zone B in Fig. 3(b) as using three supports and two actuators.

Test Results

Failure patterns. Fig. 4 shows the failure patterns of S1-5 and IS-5 specimen by test results. In S1 specimens, flexural failure occurred as shown as Fig. 4(a). In IS specimens, shear failure occurred as shown as Fig. 4(b).

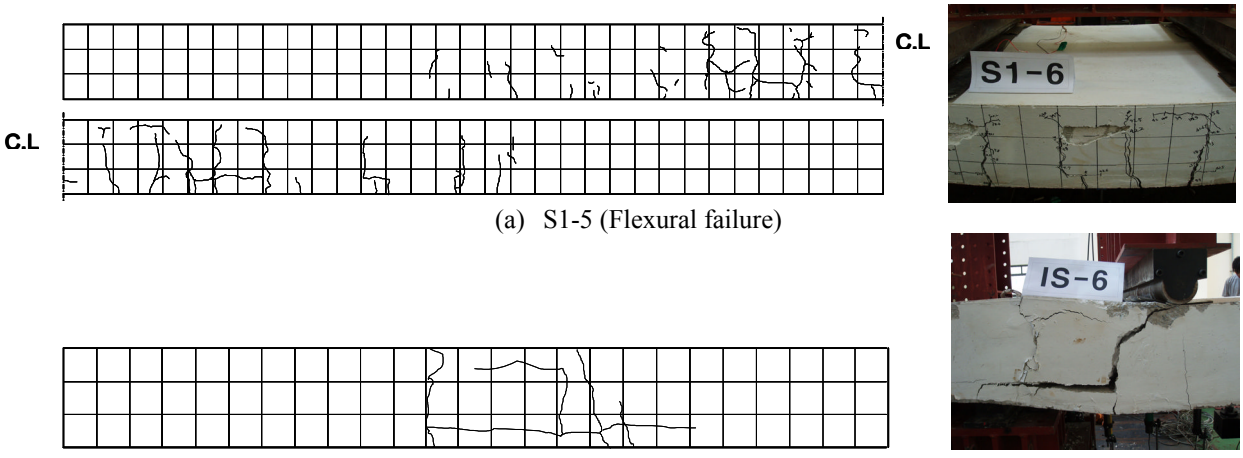

(a) S1-5 (Flexural failure)

(b) IS-5 (Shear failure)

Fig. 4 Failure patterns

Section force-deformation response. Fig. 5 shows the bending moment-rotation curves at the center span for S1 specimens. For S1-6 and S1-7 specimens, the hole size of polystyrene form had no influence on the initial stiffness, ultimate strengths, and deformation. Fig. 6 shows the shear force-displacement curves at the loading point for IS specimens.

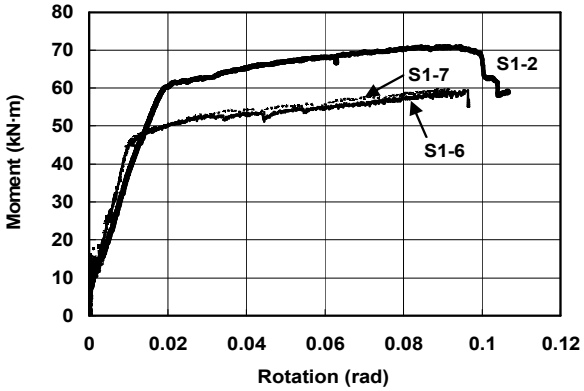

Fig. 5 Bending moment-rotation curves

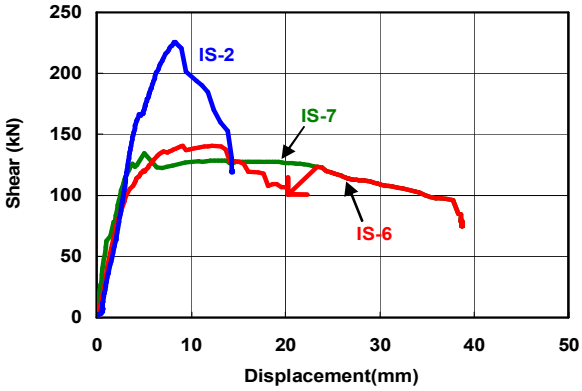

Fig. 6 Shear force-displacement curves

All IS specimens had the ultimate shear strengths before 10 mm in deflection. IS-2 specimen had the greatest ultimate strength, but showed very brittle failure than IS-6 and IS-7 specimens.

Strengths. Table 3 shows the comparison of nominal flexural strength and test flexural strength for S1 specimens. M_n and V_n is calculated by ACI design code [2]. In the comparison of maximum strengths by test and nominal strengths, M_u/M_n measured 0.98~1.04. It showed that nominal strengths by ACI code agreed well with experimental results. Table 4 shows the comparison of nominal shear strength and test shear strength for IS specimens. V_u/V_n measured 1.52~2.18. It showed that I-slab had more shear capacity. It was caused by the effect of lattice girders.

Table 3 Comparison of nominal flexural strength and test flexural strength

Specimen	Nominal flexural strength, M_n (kN·m)	Bending moment by self-weight, M_{u1} (kN·m)	Bending moment by loading, M_{u2}(kN·m)	Test flexural strength, $M_u=M_{u1}+M_{u2}$ (kN·m)	M_u/M_n
S1-2	81.40	13.91	71.11	85.02	1.04
S1-6	83.26	25.00	59.45	84.45	1.01
S1-7	83.26	21.65	60.14	81.78	0.98

Table 4 Comparison of nominal shear strength and test shear strength

Specimen	Nominal shear strength, V_n (kN)	Shear strength by self-weight, V_{u1} (kN)	Shear strength by loading, V_{u2}(kN)	Test shear strength, $V_u=V_{u1}+V_{u2}$ (kN)	V_u/V_n
IS-2	104.61	2.20	225.46	227.66	2.18
IS-6	91.10	3.61	134.53	138.14	1.52
IS-7	91.10	3.17	140.46	143.63	1.58

Conclusions

The experimental works were conducted to evaluate the bending and shear strength of the I-slabs throughout experimental works. The conclusions obtained in this study can be summarized as follows; 1) I-slab with new polystyrene form had a sufficient flexural and shear capacity. 2) The hole size of polystyrene form had no influence on the initial stiffness, ultimate strengths, and deformation. 3) For the accurate calculation of shear strength, it needs to consider the effect of lattice girders.

References

[1] Mid-state Filigree Systems, Inc.: The Filigree Wideslab Method of Concrete Deck Construction (2006)

[2] ACI Committee 318 : Building Code Requirements for Structural Concrete (ACI 318-05) and Commentary (ACI 318R-05) (2005)

Key Engineering Materials Vols. 385-387 (2008) pp 357-360
© (2008) Trans Tech Publications, Switzerland
doi:10.4028/www.scientific.net/KEM.385-387.357

The Effect of Mechanical Stress on Barkhausen Noise from Heat-treated Permalloy Plates

H. Nishihara[a], K. Kojima[b], S. Taniguchi, T. Sagae[c], M. Harada, T. Ogino, S. Matsumoto[d], H. Maeda[e], Y. Shindo[f] and N. Ohtsuka[g]

Faculty of Science and Technology, Ryukoku University, Seta-oecho 1, Otsu 520-2194, Japan

[a]nishihara@rins.ryukoku.ac.jp, [b]kunihiro_kojima_1983116@yahoo.co.jp, [c]sagae@cac-net.ne.jp, [d]QWK02573@nifty.com, [e]hidefumi@rins.ryukoku.ac.jp, [f]shindo@rins.ryukoku.ac.jp, [g]ohtsuka@rins.ryukoku.ac.jp

Keywords: Barkhausen noise; Permalloy; Mechanical stress; Heat treatment

Abstract. The effect of mechanical stress on Barkhausen noise from 45-permalloy plate is reported for as-rolled plate and plates which are annealed at various temperatures up to 1000 K. The data are compared with data of magnetic permeability, coercive force and Vickers hardness. The Barkhausen noise energy detected has been found to increase linearly with nominal stress. The larger the annealing temperature, the less the rate of increase was observed. On the other hand, the magnetic permeability has been found to decrease linearly with nominal stress in a small stress region. Overall features are explained qualitatively by a model in which tensile stress makes the number of effective pinning sites which have appropriate activation energies for discontinuous motion of domain wall more, while annealing process makes just the number of pinning sites such as defects and grain boundaries less.

Introduction

When varying magnetic field is applied to a ferromagnetic material, the magnetization shows discontinuous change due to discontinuous domain wall motion which induces magnetic Barkhausen noise in a pickup coil. The magnetic Barkhausen noise measurements have been reported and discussed in relation to heat treatment, grain size, strain, and hardness [1,2]. However, still a mechanism of the generation of the Barkhausen noise has not been well understood and the measurements are not established as a popular method for non-destructive test (NDT). It has been known that mechanical stress applied to a ferromagnetic material has an effect on the Barkhausen noise from the material [3]. It was found that the Barkhausen noise amplitude in XC10 French steel increases with increasing tensile stress [3]. On the other hand, the stress response of rms value of Barkhausen noise for steel concrete reinforcement cables was found that the rms value steadily decrease as a function of tensile stress up to a level of 1000 MPa [4]. Also the Barkhausen noise energy detected in pure nickel plate has been found generally to decrease with nominal stress [5]. In view of these somewhat conflicting results, it was decided to do experimental study on permalloy specimen which is one of the magnetically softest ferromagnetic materials. The effect of mechanical stress on Barkhausen noises from rolled thin plates of 45-permalloy is reported. The effect has also examined for the plates which are annealed at various temperatures up to 1000 K.

Experimental Results and Discussion

45-permalloy plates which were prepared by rolling with a thickness of 0.20 mm supplied by the Nilaco Corporation with chemical compositions of Ni of 45 %, Fe(+ Co) of 55 %, C less than 0.08 % and Mn less than 0.5 %, a specific weight of 8.25 and Vickers hardness of about 240 was used as a starting specimen. A stress is applied using a stepping motor and a ball-screw motion controller. The stress is measured using a load cell unit. The output voltage from the load cell is amplified by an amplifier and transferred to 16-bit AD board built in a PC. A pair of magnetizing coils with 600 turns and a detecting coil with 500 turns were directly wound over the specimen to

observe Barkhausen noise only from the sample itself [5]. The load of the detecting coil was 10 kΩ.The magnetic field was swept from -0.02 T to 0.02 T (=200 Oe) in sinusoidal wave form with a frequency of 0.5 Hz. The Barkhausen noise voltage was amplified by a low-noise preamplifier followed by a band-pass filter with a frequency range from 1 kHz to 100 kHz, and transferred to 16-bit AD board built in an another PC. Examples of one-shot and rms voltage profiles of Barkhausen noise from a starting specimen of a rolled 45-permalloy plate at stress levels of 0 and 150 MPa are shown in Fig.1. The profiles of externally applied magnetic fields are also shown.

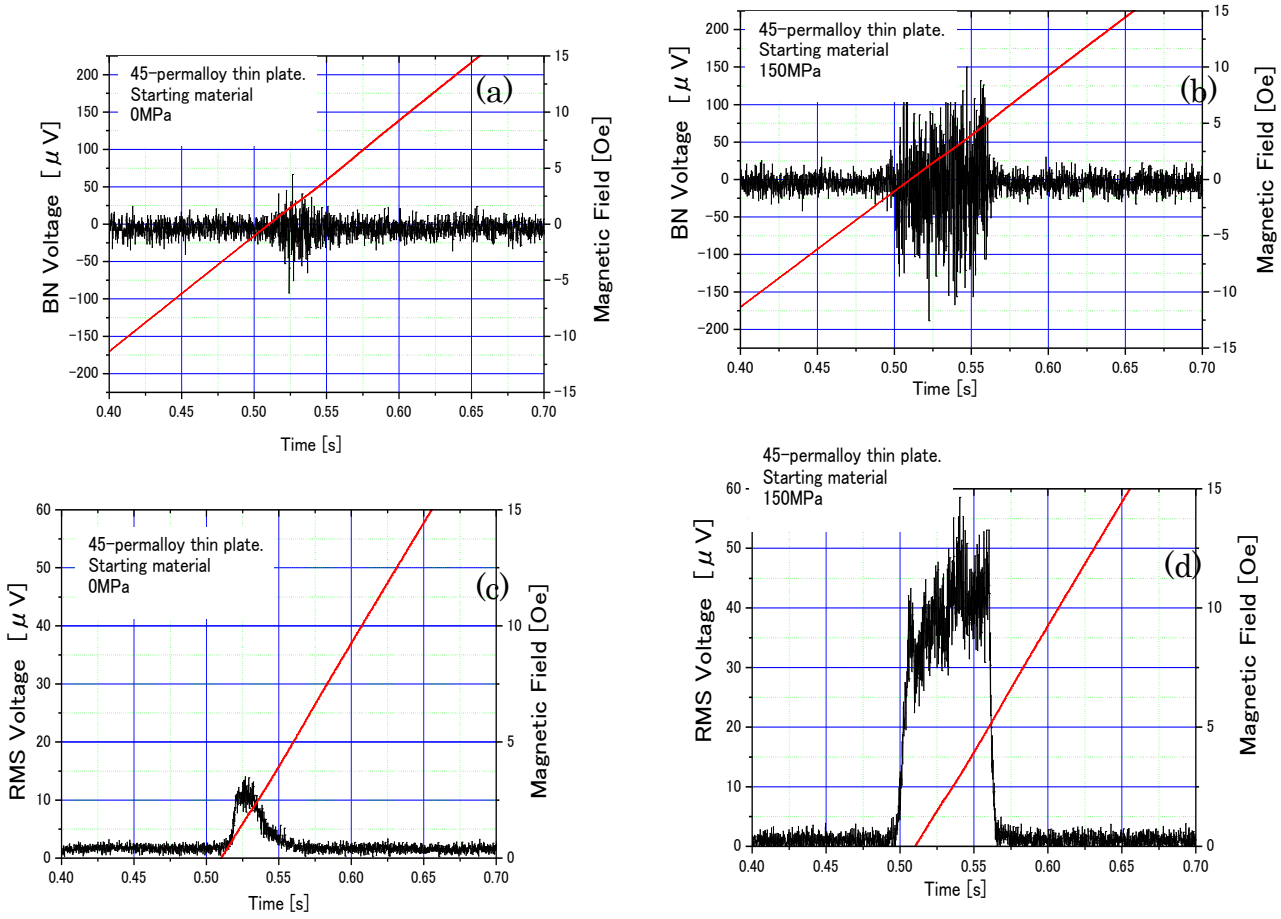

Fig.1. Examples of one-shot and rms voltage profiles of Barkhausen noise from a rolled 45-permalloy plate at stress levels of 0 and 150 MPa are shown; (a) one-shot, 0 MPa, (b) one-shot, 150 MPa, (c) rms, 0 MPa, (d) rms, 150 MPa. The profiles of externally applied magnetic fields are also shown.

One-shot voltage profile is different in every run because the Barkhausen noise is essentially a noise, and root-mean-square (rms) voltage profiles averaged over 100 times are shown in Fig.1. The effect of the tensile stress to this material is apparently an increase of the Barkhausen noise as in XC10 French steel. The starting specimen of the rolled 45-permalloy plate is annealed at 400, 500, 600, 700, 800, 900 and 1000 K for 1 hour in a temperature-controlled furnace and cooled slowly down to room temperature in the furnace. A parameter, the Barkhausen noise energy (BNE), which is defined as the total electric energy integrated over a single sweep of externally applied field for a 10 kΩ resistance load on a detecting coil, is proposed [6]. Each specimen was given a constant stress step by step, rms Barkhausen noise profile was measured in each step, and the magnitude of the BNE was calculated. The magnitude of BNE is shown in Fig.2 as a function of nominal stress

for the rolled 45-permalloy plates of the starting material and specimens annealed at various temperatures. It is seen that the Barkhausen noise energy increases linearly with nominal stress for all specimens. The larger the annealing temperature, the less the rate of increase is observed.

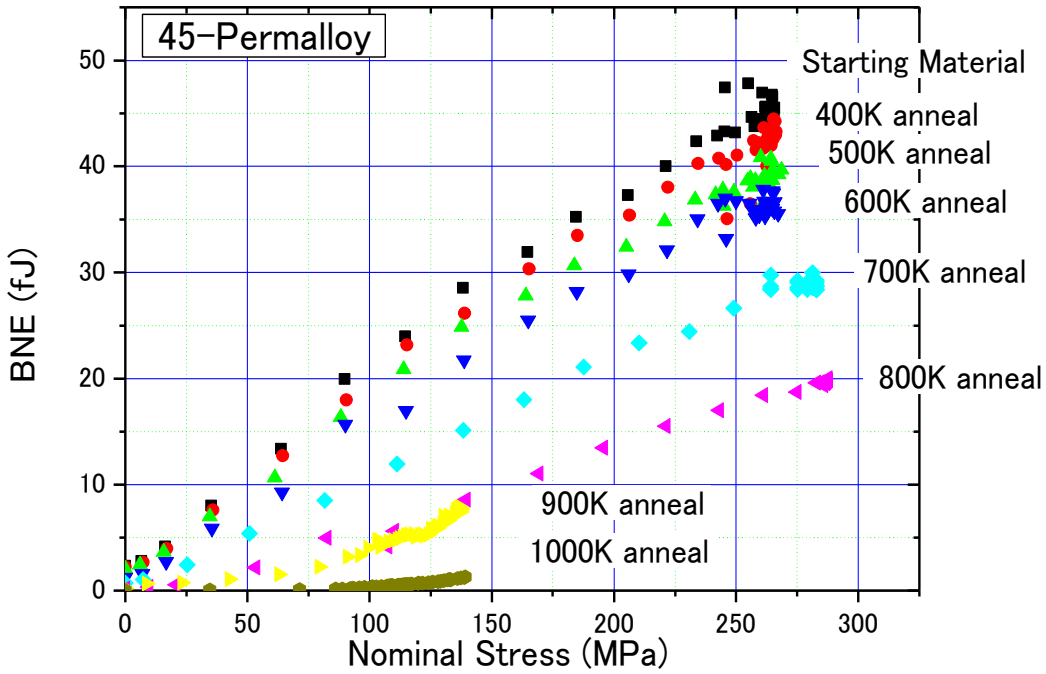

Fig.2. Barkhausen noise energy (BNE) is shown as a function of nominal stress for the rolled 45-permalloy plates of the starting material and specimens annealed at various temperatures.

The magnetic permeability μ was measured with a handy apparatus, Doctor μ, produced by Aichi Steel Corporation, during the tension test for the rolled 45-permalloy plates of the starting material. The magnitude of the magnetic permeability is shown in Fig.3 as a function of nominal stress for this specimen. The magnitude of the permeability decreases linearly in a small stress range, which is confirmed to be in an elastic range from a tension test, in a just opposite way against the BNE. This indicates that the tensile stress makes the material magnetically harder. This effect due to the tensile stress was confirmed also by a measurement of a coercive force H_c before and after the tensile test, where H_c of about 35 Oe in the starting material decreased to about 25 after annealing with temperatures higher than 800 K, which recovered to about 35 after the fracture due to the tension test. The Vickers hardness H_V of the 45-permalloy plate was also measured and it was found that H_V remains constant with a value of about 240 up to the annealing temperature of 800 K, which is considered to be a recrystallization temperature, while it decreased to 180 and 140 when the specimen is annealed at 900 and 1000 K, respectively. The values of H_V of 180 and 140 were increased to 190 and 175, respectively, after the fracture due to the tension test. From these features, the experimental results in Fig.2 are interpreted qualitatively as follows. The tensile stress distorts the local crystal structure of the polycrystalline material. The distortion makes the local crystal magnetically anisotropic and the easy axis of the magnetization is not continuous anymore near crystal defects or grain boundaries. Thus, activation energy is necessary for the motion of magnetic domain wall to overcome the difference of the anisotropy energy across the pinning sites such as crystal defects or grain boundary. This discontinuous domain wall motion induces the magnetic Barkhausen noise in a pickup coil. The number of effective pinning sites which have sufficient

activation energy to make discontinuous motion increase with the tensile stress. The annealing process makes just the number of defects and grain boundaries less. This seems to be the origin of the experimental result that BNE is proportional to nominal stress. It seems to be possible to know the internal stress from the measurements of the Barkhausen noise in this kind of magnetically soft material like 45-permally.
On the other hand, the stress dependence of BNE in nickel plate, where BNE was found generally to decrease with nominal stress, was interpreted by a newly proposed model of "existing of preferable conditions for Barkhausen noise observation" [5]. If the specimen becomes magnetically too hard, tensile stress pull out the Barkhausen jumps from observable conditions of the apparatus and makes BNE less.

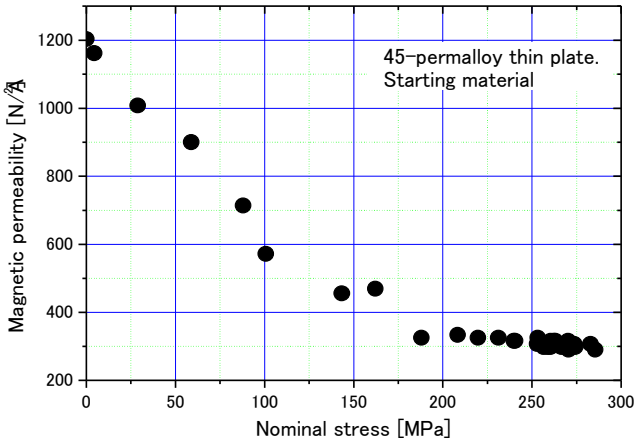

Fig.3. Magnetic permeability as a function of nominal stress for the starting specimen of 45-permalloy.

Acknowledgements
This work was partially supported by a grant based on the High-Tech Research Centre Program for private universities from the Japan Ministry of Education, Culture, Sports, Science and Technology. This work was also supported in part by the sabbatical program at Ryukoku University in 2007.

References

[1] O. Sundstrom and K. Torronen, Materials Evaluation Vol. 37 (1979), p. 51.

[2] D.C. Jiles, NDT International Vol. 21 (1988), p. 311.

[3] M.J. Sablik and B. Augustyniak, J. Appl. Phys. Vol. 79 (1996), p. 963, and references cited therein.

[4] R. Rautioaho, J. Kivimaa and M. Moilanen, J. Mag. Mag. Mater. Vol. 129 (1994), p. 217.

[5] H. Nishihara, S. Taniguchi, H. Maeda, I. Oguro, M. Harada, T. Ogino, S. Matsumoto, Y. Shindo and N. Ohtsuka, reported orally at 12th APCNDT 2006 (Asia-Pacific Conference on NDT) 5-10 Nov. 2006, Auckland, New Zealand.

[6] H. Nishihara, T. Ogino, I. Oguro, M. Harada, Y. Shindo, N. Ohtsuka, and T. Sagae, Electromagnetic Nondestructive Evaluation Vol. VII (2006), p. 259.

Key Engineering Materials Vols. 385-387 (2008) pp 361-364
© (2008) Trans Tech Publications, Switzerland
doi:10.4028/www.scientific.net/KEM.385-387.361

Real-Time Measurements on Crack-tip Deformation Fields of LY12 Samples under Impact Tension

Siying Chen[a] Tian Lan[b] Xiaomei Chen[c] Weiguo Kong[d] Guoqiang Ni[e]

Department of Optoelectronic Engineering, Beijing Institute of Technology, Beijing, 100081, China

[a]csy@bit.edu.cn, [b]lantian@bit.edu.cn,[c]cxiaomei@bit.edu.cn, [d]kongwg@bit.edu.cn, [e]nigq01@sina.com

Keywords: SHTB, optical measurement, digital correlation method, failure evolution, Damage Mechanics

Abstract: In this paper, the deformation fields of LY12 crack samples loaded by an SHTB are real-time investigated with the time interval of 10 μs by an optical system, which consists of a high-speed camera, a flash light, a frame grabber and a synchronization device with the delay-time less than microsecond. The cracks are preset by using the three-points bending method in a MTS fatigue machine. The crack is 2mm long with a flare angle of 60 degree. During the experiments, the dynamic deformation images are captured by the high speed camera and analyzed by newly developed software based on Digital Correlation theory. And the displacements fields near crack-tips according to the changes of the flare angle and radius during the impact process are obtained. Experimental results acquired in this paper are proofed, by compared with the theoretical calculations.

Introduction

In the study of dynamic behaviors of materials, the real-time observation on the evolution of flaws is always a key issue to disclosure the principle of the failure mechanism. Most of the research work on damage mechanism of crack samples is focused on theoretical analysis and numerical simulations. There are few reports on the real-time and in-situ experimental investigation on the crack expansion under impact loading. As we know, the crack-tip region may be subjected to large deformation gradients under impact loading, and typical experimental methods, most of which can only acquire the discrete surface deformations, instead of the in-situ deformation details in this region. Especially, acquiring crack expansion fields becomes even more complicated in harsh environmental conditions such as high-stain-ratio tensile process. Now, some optical testing methods have been used in the investigation of dynamic performance of materials. Moiré interferometry method is a representative one, and it has been used in in-plane deformation measurements at elevated temperatures [1-4].However, most of uses of moiré interferometry methofs are related to statistic and quasistaitc measurements because the testing precision will be severely affected by the rough environment when it's applied under high-speed impact loading.

In this paper, an optical system, combined with digital correlation method, is used to detect the real-time and in-situ displacements of LY-12 samples under high-speed tensile process. It provides a new angle and an experimental evidence for the study of materials properties when the crack tip extends under impact loading.

Basic Theory and Measurement System

From the reference book [5], it is known that if we can record the differences of the surface gray-scale map during the impact process at two different times, the deformation field can be

deduced by the correlation method through the following equation:

$$C\left(u,v,\frac{\partial u}{\partial x},\frac{\partial u}{\partial y},\frac{\partial v}{\partial x},\frac{\partial v}{\partial y}\right)=\frac{\sum\left[F(x,y)\cdot G\left(x^*,y^*\right)\right]}{\left[\sum\left(F(x,y)^2\right)\cdot\sum\left(G\left(x^*,y^*\right)^2\right)\right]^{\frac{1}{2}}}=\frac{\langle F\cdot G\rangle}{\left[\left\langle F^2\right\rangle\cdot\left\langle G^2\right\rangle\right]^{\frac{1}{2}}} \tag{1}$$

Where, $f(x,y)$ is the gray function of the first image while $G(x^*,y^*)$ denotes that after deformation. The measuring system, shown in Fig.1, consists of a high-speed camera, a He-Ne laser and synchronization and recording devices.

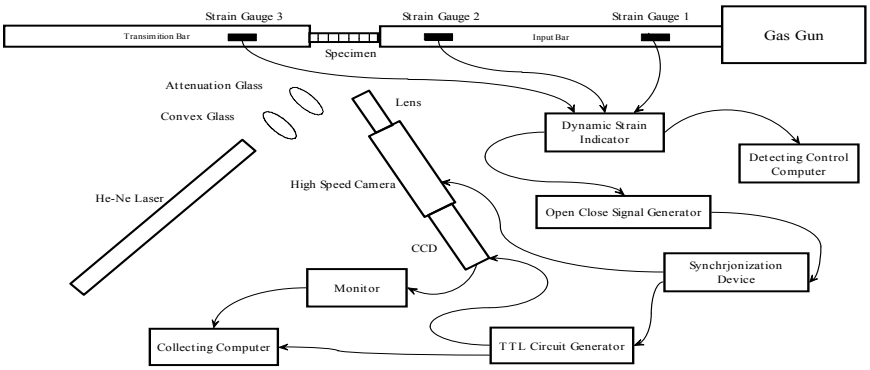

Fig.1 Sketch of measuring system

A picture obtained by the high-speed camera is divided into 8 subgraphs with the sequence depicted in Fig.2, with the time interval of 10 μs .Synchronizing control is very important and complicated in dynamic tests. The strain signal, which comes from a strain gauge attached to the input bar, is used as the trigger source. A three-channel synchronization device with accurate time-delay is designed to trigger the flash, high-speed camera and frame grabber in turn. The sketch map of synchronizing control is shown in Fig.3.

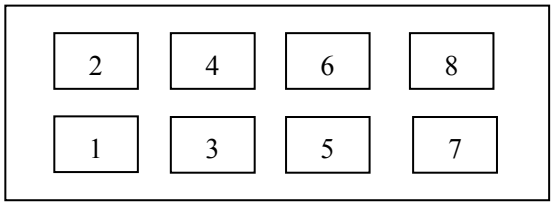

Fig.2 High-speed camera imaging sequence

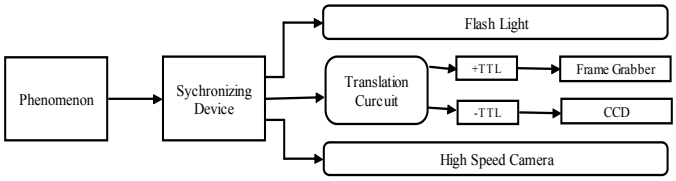

Fig. 3 Synchronizing contral

Besides, to satisfy the exposure requirements the camera is not perpendicular to the sample surface hence the slope angle has to be adjusted in image processing. The image resolution ratio is about 50 μm and the accuracy of measurement displacement is 0.5 μm . The accuracy of measuring displacement is determined by the image-processing code design. The correlation algorithm we use can reach the accuracy of 0.5 μm . While the image resolution is determined by the structure of the image-forming system (the high-speed camera and the CCD) and our system can only reach 50 μm .

The image processing includes mainly three steps, as follows,

1. Image cutting. Because each CCD photograph consists of 8 small subgraphs, which depict the object at different times, a method must be employed to divide the photograph accurately. In this paper, a method based on correlation calculation is presented, and it is used in a specially written code with MATLAB v7.0. When we select an interesting region in the first small picture, the other 7 pictures can be obtained automatically and saved as different files. Because the successive pictures are defined by the codes based on Statistic Correlation Method, it can be considered that the rigid displacement has been erased in the area selection.
2. Image pre-processing. In this step, the gray-degree difference and rigid motion among 8 small

pictures resulted from measuring system error can be removed.

3. Displacement calculating. The calculation is based on the correlation iteration, as depicted in the above equations.

Experimental Results and Discussions

The samples for experiments are made of LY12. A groove with a flare angle of 60° and the length of 4mm is precut at the middle-bottom of the sample. After that, the sample surface is polished and placed on the MTS machine to generate a crack by using three-point bending method. After all, the dimension of LY12 samples under tensile process is shown in Fig.4. And the Fig. 5 shows the map of typical I type crack.

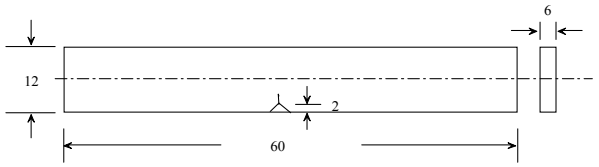

Fig.4 The dimension of LY12 samples

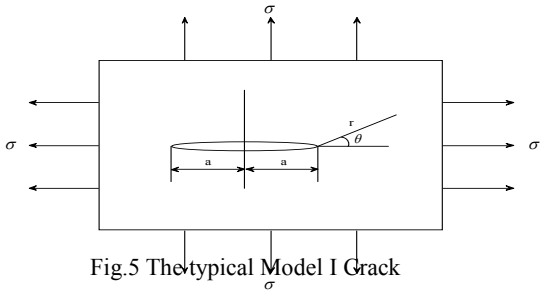

Fig.5 The typical Model I Crack

When the cracks are two-way stretched, the deformation fields around the crack tip will be:

$$u=\sqrt{\frac{K_I}{2G}}\sqrt{\frac{r}{2\pi}}\cos\frac{\theta}{2}\left(\kappa-1+2\sin^2\frac{\theta}{2}\right) \qquad v=\sqrt{\frac{K_I}{2G}}\sqrt{\frac{r}{2\pi}}\sin\frac{\theta}{2}\left(\kappa+1-2\cos^2\frac{\theta}{2}\right) \qquad (2)$$

For plane state of stress, $\kappa=(3-\upsilon)/(1+\upsilon)$. K_I is the stress intensity factor.

We can compare the experimental results with the theoretical ones then mark them in the same picture. The resolution of the image is 47.6 μm and the ratio of precision is 0.5 μm .

The real-time deformation image of crack samples under tensile process is shown in figure 6(b) with the shooting speed of $10^5 fr/s$, and the static one before loading is shown in Fig. 6(a).

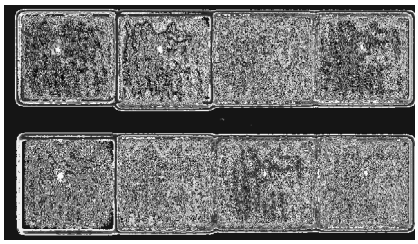

Fig. 6(a) The sample image before loading

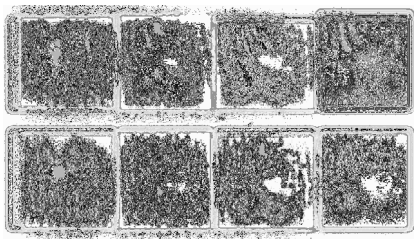

Fig. 6 (b) The sample image after loading

The displacement fields around the crack tip in the time-interval of 10 μs ~20 μs after the tensile process begins is shown in Fig. 7 and Fig. 8, and the theoretical calculation values are also shown in the same figure for comparisons. The u displacements field with a distance of 0.6mm to the crack tip according to the variations of the angle is shown in Fig. 7. When θ=33.7°, the relationship between the displacement and the variation of the radius is shown in Fig. 8. In Fig. 8, the actual line presents the theoretical results and the discrete spots denote the measured values. Especially, in the above figures, only the tendency of the theoretical result and the experimental one can be compared because in the theoretical calculation, the coefficients in E.q 1 are not strictly defined according to the practical loading conditions and the plastic deformation is not considered, either.

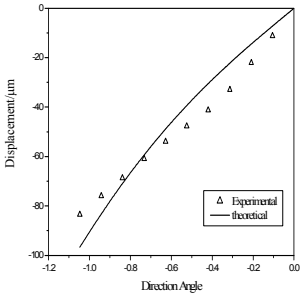

Fig. 7 The u displacements 0.6mm away from the crack-tip

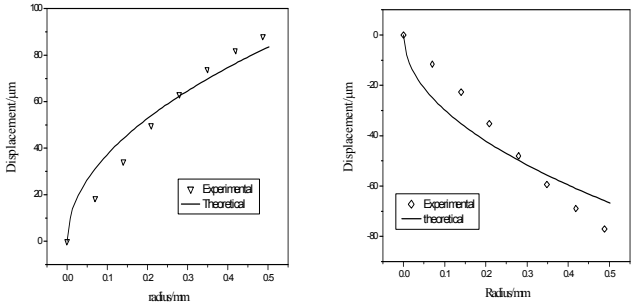

Fig. 8 The u and v displacements when θ=33.7°

Similarly, the deformation fields around the crack tip during the time-interval of 20 μs ~30 μs is shown in Fig. 9 and Fig. 10. Fig. 9 presents the dependency of the displacements u, with a distance of 0.5mm to the crack tip. And in Fig. 10, it can be found that when θ=52°, the relationship between the displacement component v and the distance away from the crack tip. In the same way, during the time-interval of 30 μs ~40 μs , the u and v displacements , combined with the theoretical calculation values when θ=49°are shown in Fig. 11. From the above figures, it can be found that the experimental results of the deformation fields around the crack tip are reasonable.

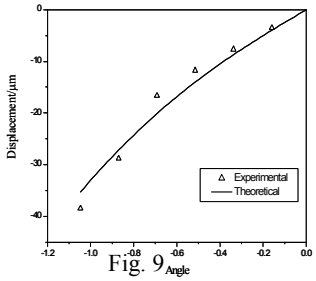

Fig. 9

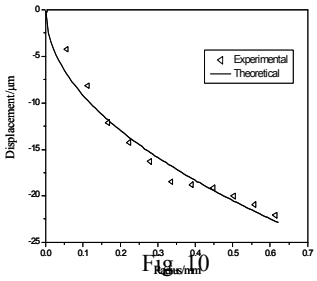

Fig. 10

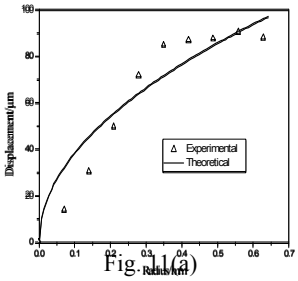

Fig. 11(a)

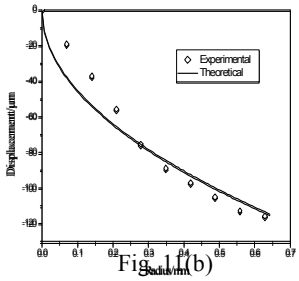

Fig. 11(b)

Fig. 9 The u displacements 0.5mm away from the crack-tip Fig. 10 The v displacements when θ=52°; Fig. 11 The u and v displacements when θ=49°;

From the comparisons of the experimental results and the theoretical values (based on the linear elastic theory), it could be found that the alterations of deformation fields resulted from the variations of r and θ obtained by the experiments are credible and effective. And it shows that the digital speckle correlation method is an effective way to acquire the in-situ deformation fields under impact loading.

Conclusions

In this paper, the real-time measurements of deformation fields around the crack-tip with high resolution and precision ratio under impact loading are presented, by using a high-speed camera and digital correlation method. Through the comparison of the experimental testing values and the theoretical ones in different time-intervals, the relationship between the dependence of the displacements around the crack tips on r and θ seems reasonable. And it's a good proof to show that digital speckle correlation method, combined with SHTB, is an effective and valid method to study the dynamic failure mechanism of flaw samples.

Acknowledgement

Authors thank a lot for the National Natural Science Foundation (10602009) for financial support.

References:

1. Kang, B.S.J, Zhang, G.Z, Development of moiré-interferometry for in-situ material surface deformation measurement at high temperature, SEM Spring Conference on Experimental Mechanics, Dearborn, Michigan, 1993, 964-976
2. Wang,F.X, Idju,P, High temperature moiré interferometry using zero-thickness grating, SEM Spring Conference on Experimental Mechanics, Las Vegas, Nevada, 1992, 727-731
3. Kang, B.S, J,Yao, Investigation on environmental assisted fracture behavior of iron aluminides using moiré interferometry, Mat.Sci.Eng., 1997, A239-240
4. Carpenter, W., Kang, B.S.J,SAGBO Mechanism on high temperature cracking behavior of Ni-base superallays, TMS international Symposium on superallays , 718,625,706 and Various Derivatives, Pittsburgh, Pennsylvanis, 1997, 679-688
5. Jin Guanchan, Computer-aided optical metrology. (1997) pp 148

Key Engineering Materials Vols. 385-387 (2008) pp 365-368
© (2008) Trans Tech Publications, Switzerland
doi:10.4028/www.scientific.net/KEM.385-387.365

Stress Analysis of Composite Plates with Non-circular Cutout

J. Rezaeepazhand [1, a] and M. Jafari[2,b]

[1,2] Department of Mechanical Engineering, Ferdowsi University of Mashhad, Mashhad, Iran

[a] *jrezaeep@ferdowsi.um.ac.ir* , [b] *mojaf2001@yahoo.com*

Keywords: Composite, Perforated Plate, Stress, Non-circular Cutout.

Abstract. The high stress concentration at the edge of a non-circular shaped cutout is of practical importance in designing of the engineering structures. These types of cutout usually are evaluated either experimentally or numerically. In this paper an attempt is made to formulate a simple analytical method for stress analysis in perforated composite plates with non-circular cutouts. The stress concentration of isotropic and composite perforated plates with variety of centrally located non-circular cutout was investigated. Numerical evaluation using commercial finite element code, were conducted to evaluate the analytical results. Parametric studies were conducted to investigate the effects of variation in cutout shape, bluntness, and material properties on the location and the value of the maximum stress in plates subjected to uni-axial tension load. The results presented herein, indicated that the maximum stress in perforated isotropic/composite plates can be significantly change by using proper material properties, cutout shapes and bluntness.

Introduction

It is well known that the presence of a cutout in a stressed member creates highly localized stresses at the vicinity of the cutout. The ratio of the maximum stress at the cutout edge to the nominal stress is known as stress concentration factor (SCF). Many researchers have investigated the stress concentration factor around cutouts in isotropic and composite materials. Using conformal mapping Savin [1] presented the stress function for a plate with a central cutout. Circular and elliptical cutouts were presented for anisotropic materials by Lekhnitskii [2]. Stress distribution around an equilateral triangle cutout and square cutout were presented by Theocaris[3] and Naik[4]. Daoust [5] present the case of circular and triangular cutouts and investigated the influence of blunt curvature and material properties on the state of stress around a triangular cutout in an infinite composite plate. Most of these works are based on the theory developed by Savin and Lekhnitskii for anisotropic perforated plates. In our previous works, stresses in perforated metallic and composite [6,7] plates with circular, rectangular, and triangular shaped cutouts are investigated.
This study investigates problems associated with the stress concentration in perforated composite plates with polygonal shaped cutouts. Analytical solution, based on Lekhnitskii's solution, for stress analysis of composite plates with various shape central cutout is presented. The main objective of this paper is to investigate the influence of bluntness on the maximum stress cutout boundary. In the present studies, the material behavior is assumed to be linearly elastic.

Problem description

Consider an infinite plate with a central cutout of diameter D as presented in Fig.1. Different non-circular cutout shapes are considered. For noncircular cutouts, D is the diameter of the circumscribe circle of the cutout. Since the cutout is small, its effect will be negligible at a distance of a few diameters from its edge. Thus point at such distance may be regarded as at infinity. The material properties used in this analysis are given in Table 1.

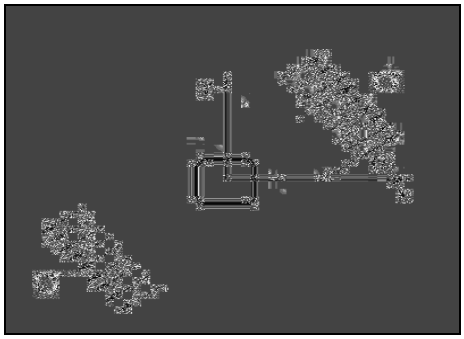

Figure 1: A plate with a central cutout under uniaxial tension.

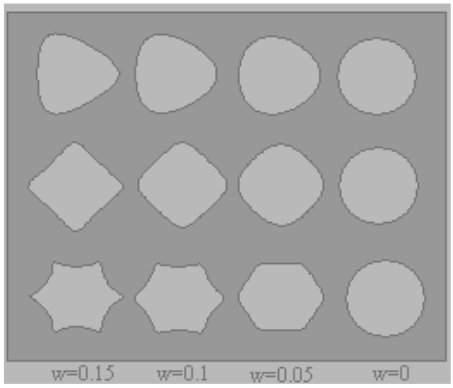

Figure 2: Effect of bluntness parameter (w) on different shaped cutouts.

Table 1: Material properties [6].

Material	E_1(GPa)	E_2(GPa)	G_{12}(GPa)	ν_{12}
Isotropic	**207**	**207**	**79.3**	**0.3**
CE9000 Glass/Epoxy	**47.4**	**16.2**	**7**	**0.26**
Woven Glass/Epoxy(7781/5245C)	**29.7**	**29.7**	**5.3**	**0.17**
Graphite/Epoxy	**181**	**10.3**	**7.2**	**0.28**
Plywood	**11.8**	**5. 9**	**0.7**	**0.3**

Basic relations

Non-circular Shaped Cutouts. The following simple mapping function is used to represent the geometry of different-shaped cutouts [6].

$$x = \lambda(\cos\theta + w\cos(n\theta)) \quad , \quad y = -\lambda(c\sin\theta + w\sin(n\theta)) \tag{1}$$

The cutout size is controlled by λ, which is a positive and real number. The shape of the cutout is determined by integer **n** and parameter **c.** Parameter **w** is the bluntness factor which changes the radius of curvature at the corner of the cutout. Fig. 2 presents different cutout shapes generated using these equations.

Stress Analysis. Based on the theory of anisotropic elasticity presented by Savin [1] and Lekhnitskii [2], the in plane stresses around cutout in an anisotropic plate can be expressed as function of two complex stress potentials as below:

$$\begin{aligned}\sigma_x &= 2\,\mathrm{Re}\left[\mu_1^2 f_1''(z_1) + \mu_2^2 f_2''(z_2)\right],\\ \sigma_y &= 2\,\mathrm{Re}\left[f_1''(z_1) + f_2''(z_2)\right]\\ \tau_{xy} &= -2\,\mathrm{Re}\left[\mu_1 f_1''(z_1) + \mu_2 f_2''(z_2)\right]\end{aligned} \tag{2}$$

f_1 and f_2 are arbitrary function which defines the stress function $F(x,y)$ in terms of complex variable $z_k = x + \mu_k y$ for k=1,2.

$$F(x,y) = 2\,\mathrm{Re}\left[f_1(z_1) + f_2(z_2)\right] \tag{3}$$

For an orthotropic plate, μ_k are the roots of the following characteristic equation and depend on the plate elastic constants.

$$\mu^4 + \left(\frac{E_{11}}{G_{12}} - 2\nu_{xy}\right)\mu^2 + \frac{E_{12}}{E_{22}} = 0 \tag{4}$$

With this approach, the problem is reduced to finding two complex functions f_1 and f_2 such that the boundary conditions on the cutout edge are satisfied.

Results and Discussions

In the following sections, effect of each parameter on maximum normalized stress of non-circular shaped cutouts is presented. The results presented for CE 9000 Glass/Epoxy composite.

Validation. Numerical evaluation using commercial finite element code, were conducted to evaluate the present analytical results. Both isotropic and composite materials are considered. Fig. 3 presents this comparison for isotropic plate with triangular cutout. Similar results are presented for composite plate with hexagonal cutout in Fig.4. As shown in Fig. 3 and 4 analytical solution is in good agreement with the finite element solution. As was expected, SCF for circular cutout(w=0) made of isotropic material(Fig. 3) is equal 3 which is equal to its theoretical value.

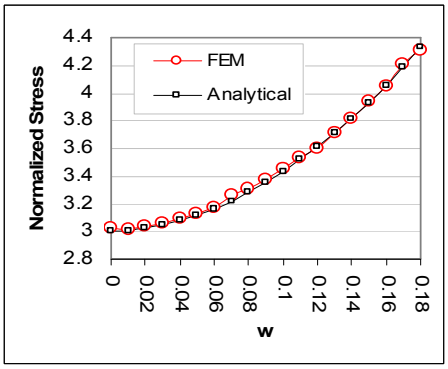

Figure 3: Comparison between present study and FE results for isotropic plates with triangular cutout.

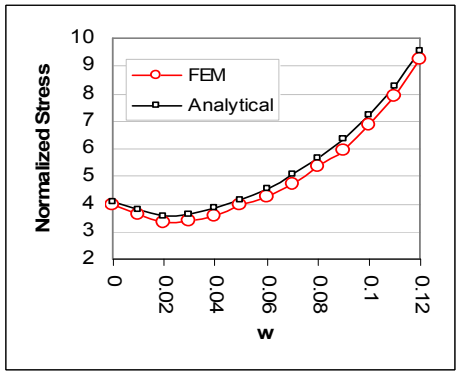

Figure 4: Comparison between present study and FE results for composite plate with hexagonal cutout.

The normalized stresses are the σ_x or σ_θ stress divided by the nominal or applied stress σ_n. In isotropic cases, this normalized stresses represent theoretical stress concentration factor of the plate. There are two values of maximum normalized stress for each cutout which are very important in design, desirable and undesirable one. The desirable maximum normalized stress (desirable stress) of a specific shaped cutout is the one which yields to lower maximum stress in plates.

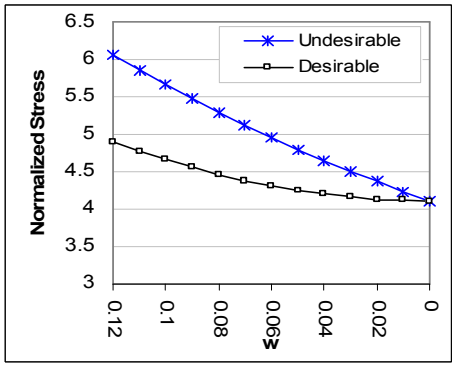

Figure 5: Variation of normalized stresses for composite plates with Triangular cutout.

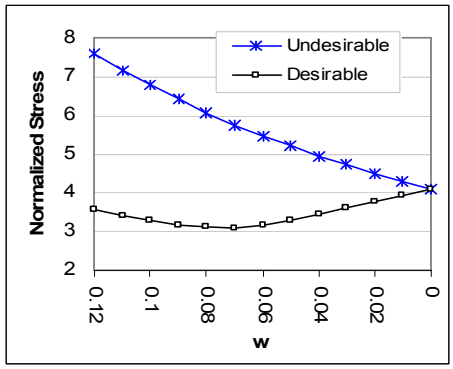

Figure 6: Variation of normalized stresses for composite plates with square cutout.

Triangular Cutouts. Fig. 5 shows the variation of desirable and undesirable stress in composite plates with triangular cutout with respect to variation of cutout bluntness. It is clear, for a triangular cutout both desirable and undesirable stresses are reduced when bluntness decreases. For w=0 which represent a circular cutout, both stresses are the same and equal 4 as it was expected.

Square Cutouts. As shown in Fig. 6, unlike triangular cutout, a global minimum desirable stress is happened in particular bluntness (w). For w<0.12 minimum desirable stress is less than desirable stress of a circular cutout in the same composite plate. For square cutouts, by choosing w = 0.073, the maximum normalized stress of 3.1 is achieved which is less than this stress for a circular cutout in a composite plate with the same material properties (CE Glass/Epoxy).
Fig. 7 illustrates the effect of material properties on normalized stress for square cutouts. It is clear that, the bluntness which produced the minimum desirable stress varies with material properties.

Polygonal Cutouts. In this section effect of bluntness on desirable stress for polygonal shaped cutouts is presented. Pentagonal and Heptagonal shaped cutouts are similar to triangular cutout and the minimum stress is happened for w=0. However, for hexagonal and octagonal shaped cutouts, similar to square cutout, there is a bluntness which has lower maximum stress than circular cutout.

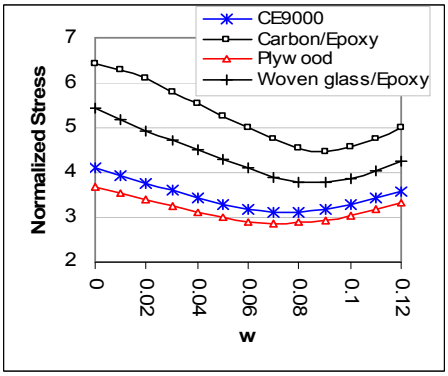

Figure 7: Effect of material properties on stress of plates with square cutout.

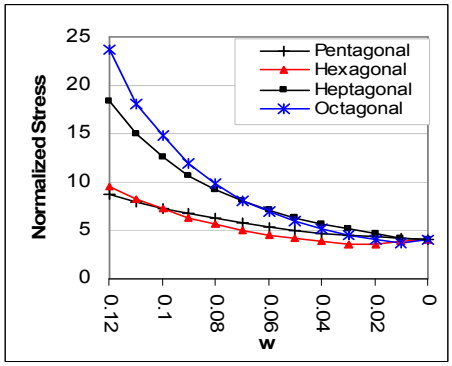

Figure 8: Variation of normalized stresses for composite plates with polygonal cutout.

Conclusion

The stress concentration of isotropic and composite perforated infinite plates with variety of centrally located non-circular cutout was presented. The Lekhnitskii's solution for circular and elliptical cutout is expanded to other polygonal shape cutout. Analytical and numerical studies were conducted to investigate the effects of variation in cutout shape, bluntness, and material properties on the location and the value of the maximum stress. The results presented herein, indicated that the maximum stress in perforated isotropic/composite plates can be significantly change by using proper material properties, cutout shapes and bluntness.

References

[1] G.N. Savin , *Stress concentration around holes,* Pergamon Press,New York(1961).
[2] S.G. Lekhnitskii, *Anisotropic Plates*, Gordon & Breach Science Publishers, New York, USA(1968).
[3] P.S. Theocaris, and L.Petrou: Int J Fract, 31,271–89(1986).
[4] N.K. Naik: *Proceedings of the International Conference on Computational Mechanics (ICCM-86),* Tokyo, (1986).
[5] J. Daoust and S.V. Hoa : Composite Structures, 19,107–30(1991).
[6] J. Rezaeepazhand, and M. Jafari: Composite Structures, Vol.71, 463-468(2005).
[7] J. Rezaeepazhand, and M. Jafari: *Proceeding of 12th ECCM*, Biarritz, France(2006).

Key Engineering Materials Vols. 385-387 (2008) pp 369-372
© (2008) Trans Tech Publications, Switzerland
doi:10.4028/www.scientific.net/KEM.385-387.369

Numerical and experimental analysis of crack closure

P. Lopez-Crespo[1, a], D. Camas-Peña[2,b], A. Gonzalez-Herrera[2,c], J. R. Yates[1,d], E. A. Patterson[3,e] and J. Zapatero[2,f]

[1]Mechanical Engineering Department, University of Sheffield, Mappin Street, Sheffield S1 3JD, UK

[2]Department of Civil and Materials Engineering, University of Malaga, Plaza El Ejido, s/n 29071 Malaga, Spain

[3]Department of Mechanical Engineering Department, Michigan State University, 2555 Engineering Building, East Lansing, MI 48824-1226, USA

[a]p.lopezcrespo@sheffield.ac.uk, [b]danicamas@gmail.com, [c]agh@uma.es, [d]j.yates@sheffield.ac.uk, [e]eann@egr.msu.edu, [f]jzapatero@uma.es

Keywords: crack closure, finite element method, digital image correlation

Abstract. The fatigue life of metallic materials is strongly influenced by crack closure effects. Finite element (FE) methods allow the study of crack closure with great detail and can provide valuable information about phenomena occurring in the bulk of the material. In this work the distribution of stresses through the thickness of a cracked specimen has been studied using 3D FE simulations. It was found that the transition between the interior of the specimen (plane strain) and the surface (plane stress) differs from that predicted by 2D plane stress models. In addition, an attempt is presented to experimentally validate the results at the surface level. For this purpose full-field image correlation technique was utilized. This allowed direct comparison between the displacement field predicted by the numerical simulations and the experimental results measured by digital image correlation.

Introduction

History effects inherited from plastic deformation greatly affect the fatigue life of structural components. Amongst them, plasticity-induced crack closure has a major importance, since it can decelerate considerably the crack propagation, thus enhancing the residual life of structures [1]. Nevertheless there are still many unresolved issues which demand further research on the topic [1]. One of them is the transition between the bulk of the material and the surface, i.e. the transition between plane strain and plane stress conditions.

The 3D FE model provides interesting information of the real crack behaviour along the thickness regarding crack closure [2] and the plastic zone size [3]. Plasticity-induced crack closure has been found to be mainly present on the external zone of the specimen. In addition, it was found that the transition between plane strain and plane stress conditions depends strongly on the thickness and loading conditions of the specimen.

The FE method allows phenomena occurring in the interior of the material to be explored. However, the computational complexity of the model demands validations with experimental observations. This work presents an attempt to validate numerical results with experimental data measured optically with digital image correlation.

Experimental procedure

A wedge opening loaded specimen [4] was employed. This geometry is similar to the compact tension, but with longer ligament, thus allowing more growth of the crack before complete fracture. The specimen was machined from 10 mm thick Al 2024 T351 alloy plate. In addition, it was fatigue pre-cracked with SIF range of approximately 10 MPa$\sqrt{m}$ and load ratio of 0.1, at a frequency of 10 Hz, until the crack length was 24 mm.

Digital image correlation was used to analyze experimentally the specimens. The technique provides full-field measurements of in-plane displacements of an object. It works by comparing two digital images acquired at different states, one before and another one after deformation. The initial image is divided in sub-images or subsets, and their location is then identified in the deformed image, by means of a correlation algorithm [5]. The calculation of each displacement vector is based on correlating subsets of 32 × 32 pixels, overlapped by 50%. By doing so the signal to noise ratio was improved and the spatial resolution was increased.

Images were captured using a 1600 × 1200 CCD with 14-bit dynamic range. The camera was equipped with a 55 mm macro lens. The features needed for best performance of the correlation algorithm were introduced by scratching the surface with 120 grade SiC grit paper.

The samples were mounted on a 50 kN servo-hydraulic machine. Digital images of the area surrounding the crack tip, of about 15 × 11 mm, were captured before and after loads were applied. Two loads of 24.0 and 3.8 MPa√m were applied. The displacement field associated to each loading was measured and stored in order to compare with simulated results.

Numerical model

The same specimen and material tested experimentally was simulated with the commercial FE code ANSYS. The material was assumed to follow an isotropic hardening behaviour. The two loading cases analyzed experimentally were simulated, i.e. K_{max} = 24.0 and 3.8 MPa√m. Fig. 1 illustrates a typical 3D mesh employed in the simulations, where a homogeneous and uniform undistorted mesh is made around the crack tip. A mesh transition is necessary in order to capture properly the effect of the plastic zone around the crack tip where the smaller elements are placed. Due to symmetry, only one quarter of the specimen was modelled. The plastic zone size is the scale reference to relate to the minimum element size. In this work, Dugdale's plastic zone size (expressed as $r_{pD} = (\pi/8)(K_I/\sigma_y)^2$) has been used. The minimum element size has been established following a recommendation proposed previously [6] adapted to reduce the computational cost, as the crack opening load was not required and the plastic wake did not need to be simulated. So a requirement of a number of divisions of the plastic zone above 30 (in plane stress) is adopted.

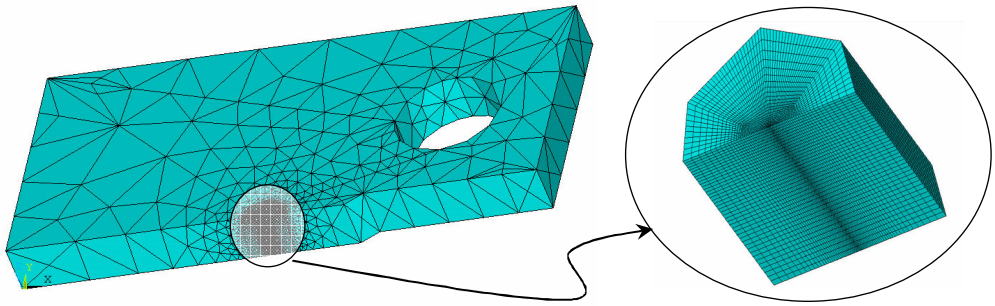

Fig. 1: Finite element model

In order to keep an acceptable element shape ratio, no dimension was 6 times greater than other dimension. This implied that the minimum number of thickness divisions was not smaller than 30 in the region close to the crack tip. Outside this region the number of through-thickness divisions was reduced to speed up the simulations. Accordingly a transition in the through-thickness mesh has been done (see detail in Fig. 1). A good compromise between accuracy and computational cost was achieved by employing hexahedral prism shaped elements within the plastic zone and 8-node tetrahedral elements outside [2]. In addition, the use of 8-node tetrahedral elements facilitated the transition between both zones.

In Fig. 2 the plastic zone of a model is shown and the behaviour of the crack along the thickness is illustrated. It can be appreciated that the plastic zone size shows an unexpected evolution from plane strain condition at the mid-plane of the specimen, growing up to a maximum close to the

surface and then dropping to a smaller value at the surface differing from those results predicted by 2D models.

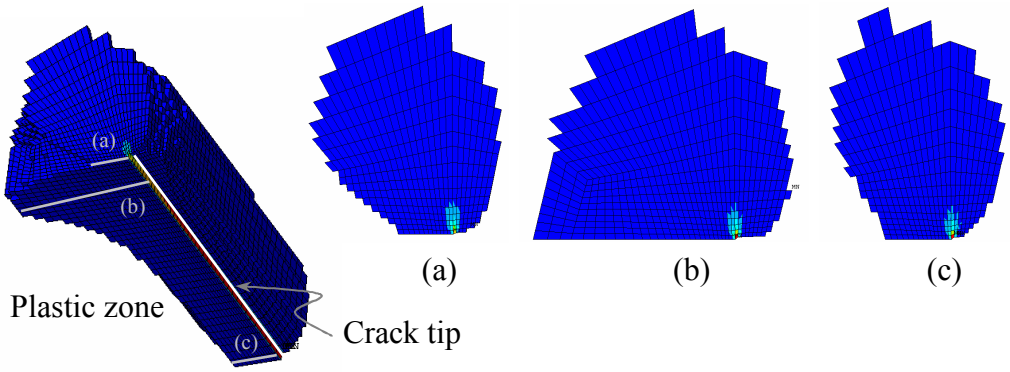

Fig.2: Plastic zone, (a) exterior surface (b) maximum (c) mid-plane.

Comparison between experiments and numerical simulation

The results obtained by 3D FEM were compared with experimental results obtained by digital image correlation. The comparison was established through the displacement fields at the surface, in the area surrounding the crack tip. Rigid body motion needed to be removed from image correlation results in order to compare directly experimental and numerical data. Figs. 3 and 4 show the profile of vertical displacements, v, at three different distances 1, 3 and 7 mm above the symmetry plane, for two different loads. The plastic zone was evaluated and all data employed in the comparison were sampled from outside the plastic zone. In Figs. 3 and 4 the crack tip is located at the origin, and the ligament corresponds to the positive values of the x-coordinate. The direction of crack propagation is parallel to the x-coordinate.

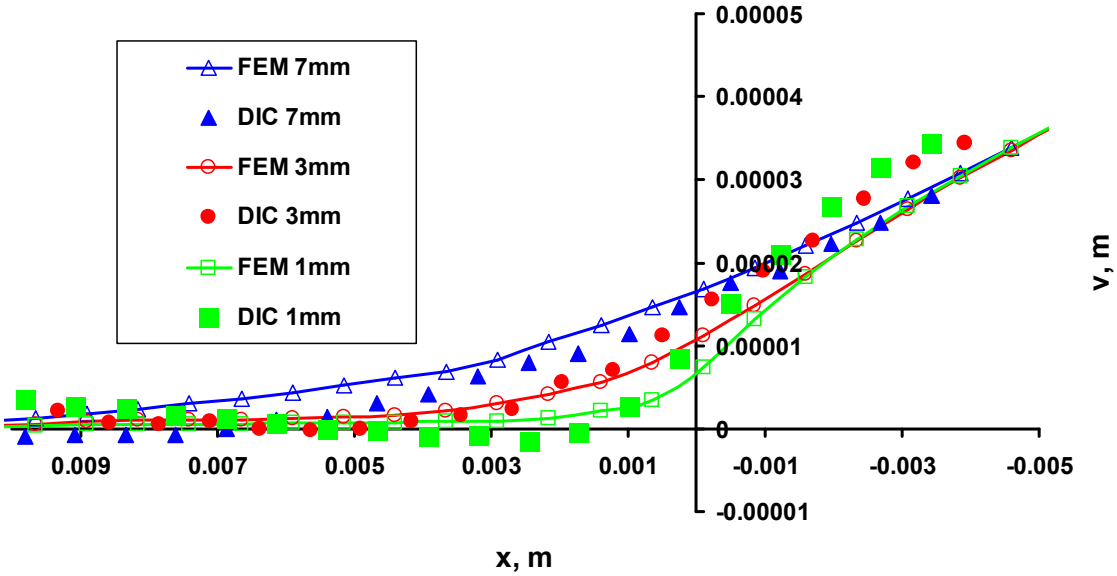

Fig. 3: Comparison between vertical displacements, v, obtained by finite element model (FEM) and digital image correlation (DIC), at 3 distances from the symmetry plane, namely 7, 3 and 1 mm. Results obtained for $K_I = 24.0$ MPa$\sqrt{m}$.

Overall good agreement between experimental and numerical results is observed in both Figs. 3 and 4. It can also be appreciated that there is greater scatter away from the crack tip and above the cracked area, that is x-coordinate between -0.003 and -0.005 m. These small discrepancies are probably caused by the crack wake existing in the real crack but not considered in the model.

Perhaps unsurprisingly, it can be seen that this difference is more accentuated in the 1-mm curve, i.e. data located closer to the crack flank. In addition, the agreement is slightly worse for lower K_I case (Fig. 4). The reason for this can be the poorer signal to noise ratio of the results obtained at lower load, compared to those obtained at higher load. Similar agreement was also found in the horizontal displacement data.

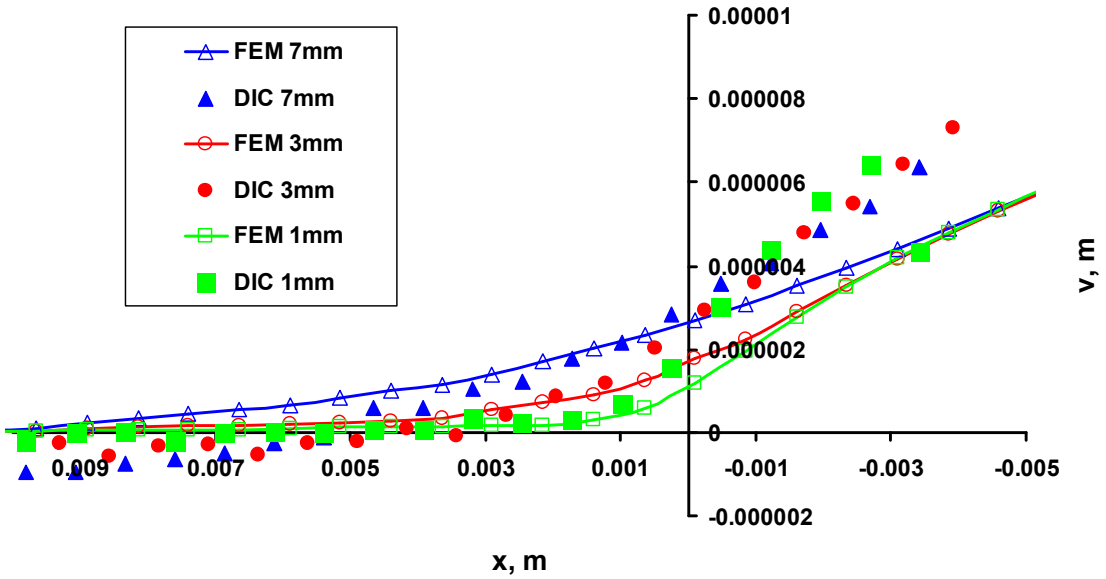

Fig. 4: Comparison between vertical displacements, v, obtained by finite element model (FEM) and digital image correlation (DIC), at 3 distances from the symmetry plane, namely 7, 3 and 1 mm. Results obtained for $K_I = 3.8$ MPa$\sqrt{m}$.

Conclusions and perspectives

3D FE modelling of a cracked specimen allowed the visualization of the plastic zone shape through the thickness. A complex transition between plane strain and plane stress conditions was observed, and was in agreement with previous simulations performed in 3D. The model was validated successfully with experimental data measured by digital image correlation. A more thorough comparison would be desirable, in order to check the validity of the simulations with different geometries. It is also expected to extend the analysis to general mixed-mode (I+II) conditions.

References

[1] M.N. James, in: *Advance in Fracture Research*, edited by B.L. Karihaloo (1996).

[2] A. Gonzalez-Herrera and J. Zapatero: Tri-dimensional numerical modelling of plasticity induced fatigue crack closure, submitted to Eng. Fract, Mech.

[3] A. Gonzalez-Herrera, J. Garcia-Manrique, A. Cordero and J. Zapatero: Key Eng. Mat. v.334-335 (2006) p.555.

[4] Y. Murakami ed.: *Stress Intensity Factors Handbook* (Pergamon Press, Oxford 1987).

[5] M.A. Sutton, S.R. McNeill, J.D. Helm and Y.J. Chao, in: *Photomechanics, Topics in Applied Physics*, edited by P.K. Rastogi (2000).

[6] A. Gonzalez-Herrera and J. Zapatero: Eng. Fract. Mech. v.72 (2005) p.337.

Key Engineering Materials Vols. 385-387 (2008) pp 373-376
© (2008) Trans Tech Publications, Switzerland
doi:10.4028/www.scientific.net/KEM.385-387.373

Dynamic Damage Analysis of SRC Frame Structure under Earthquake Action

Shansuo ZHENG[a], Bin WANG[b], Liang Zhang[c], Lei LI[d] , and Wei WANG[e]

School of Civil Engineering, Xi'an University of Architecture and Technology, Xi'an 710055, China

[a]zhengshansuo@263.net, [b]wangbin1853@163.com, [c]gztrzl@126.com,
[d]lilei1004@163.com, [e]wangwei@126.com

Key words: SRC frame structure; Damage variable; Dynamic balance equation; Numerical analysis

Abstract: Structures may enter into nonlinear stage under strong earthquake, so precise prediction of nonlinear behavior for building structure in earthquake is important which can assess the earthquake resistance safety of structures accurately. The exact numerical analysis model is required in actual engineering. In this paper the concept of nonlinear dynamic damage is introduced in steel reinforced concrete (SRC) composite structure, based on the theory of continuous damage mechanics. The damage variable is defined and computed by effective plastic strain of material, furthermore, concrete dynamic constitutive model is derived which considered plastic strain of material. Finally, the damage dynamic balance equation is established. Via comparison with test results of a three-story, two-bay SRC frame model which is tested on a shaking table, it is shown that the results of numerical analysis agree well with test results, indicating that the nonlinear dynamic balance equation is capable of describing the dynamic response of SRC frame structure with satisfactory accuracy. The research supplies theoretical basis for the seismic behavior analysis of SRC high-rise buildings.

Introduction

As one of important composite structure systems, steel reinforcement concrete (SRC) composite structure have been widely used in high and super-high building in recent decades. In order to assess the safety and serviceability of SRC structure in seismic resistant design for structural engineers accurately, it is necessary to develop reliable numerical methods and models. Owing to the inelasticity of materials, stiffness degradation, pinching effects, strength degradation, SRC frame structures exhibit obvious nonlinear relation under dynamic loading. There are many models to simulate the nonlinear analysis of SRC frame structures, nevertheless, all of these models based on the moment-curve relation are still limited in terms of simulating exact structural behavior, because they exclude the internal force variation according to the loading history. In this paper, the damage variable is defined, which can describe the process of structural damage. The dynamic constitutive model and damage dynamic balance equation are established based on some assumption: (1) Bond-slip effect between steel and surrounding concrete is neglected. (2) The strain distribution of steel and concrete agrees with the plane section assumption.

Concrete Damage Constitutive Model

Strain tensor ε_{ij} can be separated into elastic part ε_{ij}^{e} and plastic part ε_{ij}^{p}, which can be expressed as

$$\varepsilon_{ij} = \varepsilon_{ij}^{e} + \varepsilon_{ij}^{p} \tag{1}$$

According to Hooke's law, the elastic part can be given by

$$\varepsilon_{ij}^{e} = D_{ijkl}^{e}\sigma_{kl} \tag{2}$$

where, D^e_{ijkl} and σ_{kl} are tetradic and second order tensor, respectively. According to Eq. 1, effective stress $\bar{\sigma}_{ij}$ can be defined by nondestructive elastic stiffness as following

$$\bar{\sigma}_{ij} = D^0_{ijkl}\left(\varepsilon_{kl} - \varepsilon^p_{kl}\right) \tag{3}$$

where, D^0_{ijkl} is the initial elastic stiffness tensor. As similar to the concept of degradation damage in damage mechanics, stress can be separated into stiffness degradation and effective stress as following

$$\sigma_{ij} = (1-\omega)\bar{\sigma}_{ij} = (1-\omega)D^0_{ijkl}\left(\varepsilon_{kl} - \varepsilon^p_{kl}\right) \tag{4}$$

where, ω is a scalar damage variable, the value range is from 0 to 1.

The tension damage evolution equation which is presented by Mazars (1986) is used in this paper

$$\omega(\bar{\varepsilon}) = 1 - \frac{(1-A_T)\varepsilon_{D0}}{\bar{\varepsilon}^p} - \frac{A_T}{\exp\left[B_T\left(\bar{\varepsilon}^p - \varepsilon_{D0}\right)\right]} \tag{5}$$

where, A_T and B_T are characteristic parameters of material which are constant; ε_{D0} is the threshold value of initial damage; $\bar{\varepsilon}^p$ is effective plastic strain which can be obtained by following

$$\bar{\varepsilon}^p = \sqrt{\frac{2}{3}\varepsilon^p_{ij}\varepsilon^p_{ij}} \tag{6}$$

SRC frame structure reciprocating cycle test exhibits obvious stiffness degradation of material with strain increase and tension crack appearance. When crack changes from tension state to compression state, elastic stiffness of material can be restored by closure of opening crack. Parameter s and tension damage ω_t are introduced to express the degree of stiffness degradation, damage variable is given by

$$\omega = (1-s)\omega_t \tag{7}$$

The value range of s is from 0 to 1 which can be used to express restoration degree of material stiffness, when crack is compression completely, s is equal to 1; in contrast, when crack is tension completely, s is equal to 0, the value of s can be computed by effective stress when microcracks occurs in material .

Substituting Eq. 7 into Eq. 4 yields

$$\sigma_{ij} = \left[1-(1-s)\omega_t\right]D^0_{ijkl}\left(\varepsilon_{kl} - \varepsilon^p_{kl}\right) \tag{8}$$

After multiple opening and closure of microcracks, lots of microcracks changes macro-crack in crack zone. It can be difficult for classical inelasticity strain evolution to express macro-crack. In this paper, when cumulative strain of microcracks reaches a definite value, macro-crack is thought about appearance.

Steel Constitutive Model

For the cyclic constitutive model of steel, Brown and Jirsa's model (1971), which addresses the Bauschinger effect, is used in this paper (see Fig.1). A simplified displacement control method developed by Ramm (1980) is used as the nonlinear numerical method for analyzing the softening behavior of SRC structures or members.

Damage Dynamic Balance Equation

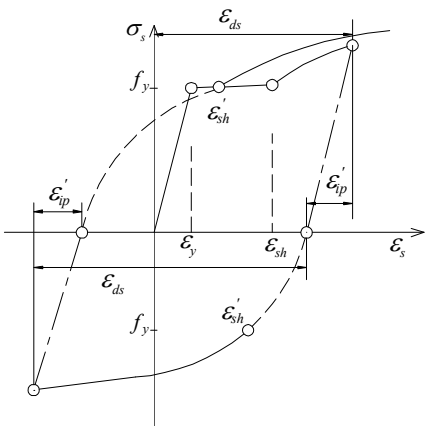

— $\sigma_s = \left[\dfrac{112(\varepsilon_s - \varepsilon_{sh}) + 2}{60(\varepsilon_s - \varepsilon_{sh}) + 2} + \dfrac{\varepsilon_s - \varepsilon_{sh}}{\varepsilon_u - \varepsilon_{sh}}\left(\dfrac{f_u}{f_y} - 1.7\right)\right]$

--- $\sigma_s = f_y\left[1 - \exp\left(\dfrac{-2.05\varepsilon_s}{\varepsilon'_{sh}}\right) + \dfrac{0.129\varepsilon_s}{\varepsilon'_{sh}}\right]$

—·— Unloading with degraded constant stiffness

$$\varepsilon'_{ip} = 0.2\varepsilon_{ds}$$

$$\varepsilon'_{sh} = \frac{\varepsilon_{sh}}{1.38}\ln\left(\frac{0.8\varepsilon_{ds}}{\varepsilon_y}\right)$$

Fig.1 Cyclic stress-strain relationship of steel

When a structure is subjected to ground acceleration $\ddot{u}_g$, according to constitutive model of material mentioned above and Galerkin equation of nondestructive material, the increment equation of damage dynamic balance equation can be written as

$$[M]\{\Delta\ddot{u}(t)\} + [C^*(\omega)]\{\Delta\dot{u}(t)\} + [K^*(\omega)]\{\Delta u(t)\} = -[M]\{\Delta\ddot{u}_g(t)\} \tag{9}$$

where, $[M]$ is the mass matrix assumed a constant in this paper; $[C^*(\omega)]$, $[K^*(\omega)]$ are damping and stiffness matrices of damage structure at t hour, respectively; $\{\Delta\ddot{u}(t)\}$, $\{\Delta\dot{u}(t)\}$ and $\{\Delta u(t)\}$ are increment acceleration, velocity and displacement vector matrices at t hour, respectively.

Damage damping of Material is defined by following

$$[C^*(\omega)] = \alpha^*[M] + \beta^*[K^*(\omega)] \tag{10}$$

where, α^* and β^* are Rayleigh damping parameters of damage material. The stiffness matrix of damage structure $[K^*(\omega)]$ can be expressed as following

$$[K^*(\omega)] = \int_V [B]^{\mathrm{T}}[D^*][B]dV \tag{11}$$

where, $[B]$ is deformation transition matrix which is a constant. $[D^*] = [D](1-\omega)$ is effective damage elasticity matrix; $[D]$ is nondestructive elasticity matrix.

Numerical Analysis

In order to testify the calculation method mentioned above, a three-story, two-bay SRC frame model, which has been tested on a shaking table by Xue Jianyang, is used in this paper. The material properties of steel and concrete are given as following: concrete strength grade is C35; steel yield strength is 273MPa; the damping ratio is assumed to be 5% and 0.53g El-Centro (1940N.S) is adopted during the test. Furthermore, Wilson θ-method is employed to solute damage dynamic equation,

because when $\theta \geq 1.37$, the solution of the equation is unconditional stabilization, in this paper, θ is equal to 1.4. The physical dimensions of model members are given in table 1.

Table 1 Dimensions of model members

Member	Longitudinal steel/ mm	Section size/ mm	Steel size/ mm
SRC Beam	4ϕ18	600×320	H 320×160×16×16
Bottom SRC Column	4ϕ18	480×480	H 288×320×16×24
2nd ,3rd storey SRC Column	4ϕ18	480×480	H 272×240×16×16

The comparison of the numerical calculation results which are obtained on the basis of the proposed concrete damage constitutive model in this paper and experiment results are shown in Fig.2 and Fig.3. The results from the proposed model show very good agreement with the experimental results. But there is small difference between numerical calculation results and experiment results, the main reason is bond-slip effect of material is neglected.

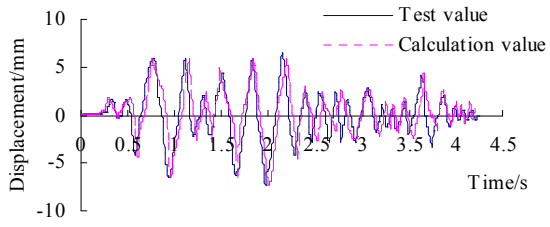

Fig.2 Top displacement responses

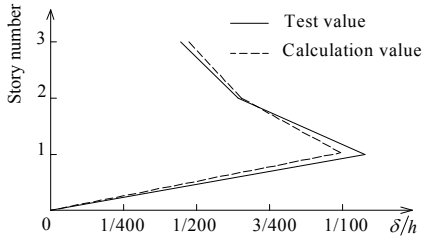

Fig.3 Story drift

Conclusions

In this paper, based on the theory of continuous damage mechanics, material stiffness degradation caused by material damage is considered. Mazars's tension damage evolution equation is introduced to compute the value of damage. Furthermore, the concrete dynamic constitutive model and increment equation of damage dynamic equilibrium are obtained. A three-story, two-bay SRC frame model is analyzed again by numerical method. Comparison of numerical calculation results and test results shows that the numerical analysis results agree with test results well, which indicate that the above method is scientific and reasonable. The method introduced in this paper is also valuable for the nonlinear analysis of other steel-concrete composite structures. The bond-slip effect of material is neglected in this paper and will be studied in future. This project is sponsored by National Natural Science Foundation of China (Grant No. 50378080) and the Educational Office of Shaan'xi Province in China (Grant No. 06JK263).

References

[1] Xue Jianyang, Zhao Hongtie. *Experiment on the Elastoplastic Seismic Responses for Steel Reinforced Concrete Frame*. J. of Xi'an Univ. of Arch. & Tech.. Vol. 29 (1997), No. 4, p.360

[2] Mazars J.. *A Description of Micro-and Macro-scale Damage of Concrete Structures*. J. of Engineering Fracture Mechanics. Vol. 25 (1986), No. 5, p.729

[3] Brown, R. H. and Jirsa, J. O.. *Reinforced Concrete Beams under Load Reversals*. J. Am. Concr. Inst.. Vol. 68 (1971), No. 5, p.380

[4] Ramm, E.. *Strategies for Tracing Nonlinear Response near Limit Point*. Nonlinear Finite Element Analysis in Structural Mechanics: Pro., Europe-US Workshop, Springer, Berlin, p.63

Key Engineering Materials Vols. 385-387 (2008) pp 377-380
© (2008) Trans Tech Publications, Switzerland
doi:10.4028/www.scientific.net/KEM.385-387.377

Buckling of Perforated Plates Repaired with Composite Patches

J. Rezaeepazhand [1, a] and H. Sabori[2,b]

[1]Department of Mechanical Engineering, Ferdowsi University of Mashhad, Mashhad, Iran
[2]Department of Mechanical Engineering, Tarbiat Modares University, Tehran, Iran
[a] *jrezaeep@ferdowsi.um.ac.ir* , [b] *h_sabouri@modares.ac.ir*

Keywords: Buckling, Laminated Composites, Perforated plates, Patch, Repair.

Abstract. Performance level and life span of existing structural elements can be increased by repair and strengthening of these structural elements using advanced composite materials.The performance of damaged metallic plates reinforced with fiber-reinforced polymer composite materials (composite patch) are presented in this study. A square aluminum plate with a central circular cutout is considered as a damaged structural element. Numerical studies using commercial finite element code were conducted to investigate the effects of variation in patch geometries and lamination parameters on buckling responses of repaired plates. The varying laminate parameters such as, fiber angles and stacking sequences are considered in this study. A quantitative measure for the effectiveness of the composite patches is taken to be the relative change in buckling loads of the reinforced plates compare to those of the perfect one. The results presented herein indicated that, for buckling response of a repaired metallic plate with central cutout, a set of laminated composite patches with different shape and stacking sequences can be found which improve load carrying capacity of damaged plates.

Introduction

Structural elements are at the risk of being damaged during their service life. In this case, usually, the damage area/material is removed by cutting a circular or elliptical shape cutout and then the cutout area is repaired using composite patches. One of the most practical and easy to apply type of patches is adhesively bonded external composite patches. In some cases which, cutout is a part of initial design of the structures, composite patches can be applied around the cutout to reinforce or strengthening the perforated structure. These types of patches must have a cutout area similar to the one in the structure. The correct and effective use of advanced composite materials requires complex analyses in order to achieve good understanding of the system response characteristics to external causes. With a view to better understanding the applicability of composites patches in repair and strengthening of existing structures, a numerical investigation was undertaken to assess the feasibility of their use. The procedure consists of systematically observing the effect of important parameters.

In this study application of external patches for repair and strengthening of metallic plates with circular central cutout is presented. Particular emphasis is placed on the case of buckling of square aluminum plates. In the present studies, the material behavior is assumed to be linearly elastic. It is assumed that the plate and patches are without imperfections and the adhesive layer perfectly bonded between the base plate and composite patches. In order to achieve a symmetric laminated plate, only double sided patches (symmetric patches) were considered in this study (Fig. 1).

Baker and Jones [1] presented most of the work on developing the adhesively bonded repairs up to 1988. Chue and Liu [2] investigated the effect of stacking sequences of laminated composite patch for a plate with an inclined central cracked under biaxial loads. Pai et al. [3] presented the effect of debonding on dynamic response and buckling of cracked aluminum plates repaired with a

composite laminate. Engels and Becker [4] presented a closed-form solution analysis of a laminated plate with an elliptical cutout repaired by elliptical patches. In pervious works, Rezaeepazhand et. al [5-7], vibration behavior of metallic plates repaired and strengthening with composite single sided and double sided patches are investigated. Furthermore, the effect of patch parameters on buckling behavior of perforated metallic plates subjected to shear load was presented [8]. Few works has reported in retrofit and changing buckling behavior of perforated panels or shells with composite patches.

This study investigates problems associated with the performance of damaged metallic plates reinforced with fiber reinforced polymer composite materials (composite patches). A square aluminum plate with a central circular cutout is considered as a damaged structural element. Numerical studies using commercial finite element code were conducted to investigate the effects of variation in patch geometries and lamination parameters on buckling responses of repaired/ reinforced plates.

Materials and Methods

The original plate is a simply supported square aluminum plate subject to uniaxial compression. The dimensions of the plate are 200×200×1mm. A circular hole of diameter *d* at the center of plate is considered as a cutout(Fig. 1). The Aspect Ratio (*AR*) of cutout is defined as the ratio of cutout diameter to the plate width (*d/a*). Perforated plates with the cutout aspect ratios of 0.2, 0.4 and 0.6 are considered in this study. The linear buckling analysis is performed for two different types of patches (Fig. 1), square and annular symmetric (double sided).

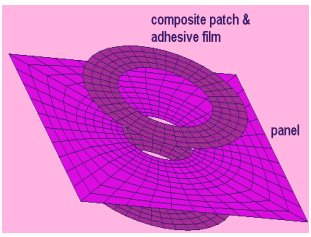

a- Symmetric Patch

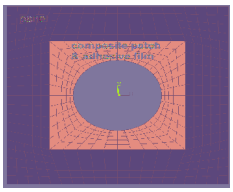

b- Square Patch

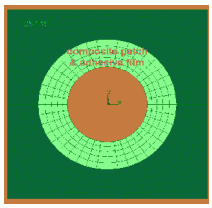

c- Annular Patch

Figure 1: Repair of perforated plate with a- Symmetric, b-Square, and c-Annular patch.

Boron/epoxy and graphite/epoxy have been the main composite materials used for bonding to metallic structures with epoxy based adhesive. In this study, a square, 100×100 mm, Boron/Epoxy (B5.6/5505) laminate was considered as composite patches. The adhesive layer thickness is 0.1 mm. The thickness of each layer of composite patch is 0.1 mm. The material properties used in this analysis are shown in Table 1.

Table 1. *Material properties.*

Al 2024-T6	Epoxy	Boron/Epoxy 5.6/5505
E = 70 GPa	E = 2.6 GPa	E_1 = 201 GPa
ν = 0.32	ν = 0.32	$E_2 = E_3$ =21.7 GPa
		G_{12} = 5.4 GPa
		ν_{12} = 0.17

Finite Element Models. Due to complexity of the model with cutout and partial patches, all buckling loads are calculated using finite element models. The results for these cases are presented here. A finite element model is created for each case. The Shell91 layered element is used to model the base plate, adhesive film and composite patches. This element has 8 nodes with 6 DOF at each node. Subspace solver was chosen for solution of eigenvalue system of equations. For each case mesh sensitivity is investigated and acceptable mesh is chosen. Validation study for the finite element modeling is carried out by comparing the analytical buckling loads of perfect and

perforated aluminum and boron/epoxy square plates with those results from FEM and good agreement was achieved [9-10].
To demonstrate the effect of cutout size on the buckling load of perforated plates, the buckling load of the perfect plate is compared to that of perforated one. To demonstrate the effect of composite patch on the buckling load of perforated plates, the buckling load of the perfect plate is compared to those of patched one. Buckling load factor (*BLF*), is defined as the ratio of buckling load of a perforated or patched plate to the buckling load of perfect plate ($BLF = N_{cr}^{Patched} / N_{cr}^{Perfect}$).

Results and Discussion

Buckling of two different cases of repaired plates was investigated. The varying laminate parameters such as, fiber angles, and stacking sequences could allow the designer to modify the load carrying capacity of damaged plates. For this reason, three different, two plies laminated composite patches, for each side of the base plate, are considered. These laminate are: *(2θ)*, *(0/θ)* and *(±θ)*. For each case, different fiber angles are considered.
Figures 2 presents buckling load factor (BLF) for perforated plates reinforced with square unidirectional (2*θ*) composite patches (Fig. 1b) for different fiber angles (*θ*). For all three cutout sizes which considered, load carrying capacity increases (BLF >1) for small fiber angles (θ <45). For the same number of plies, all of these patches with *θ=0* have greater influence on buckling loads of plates. In all cases with small and intermediate aspect ratios (AR=0.2 and 0.4), BLF reaches its minimum values at *θ=90*.

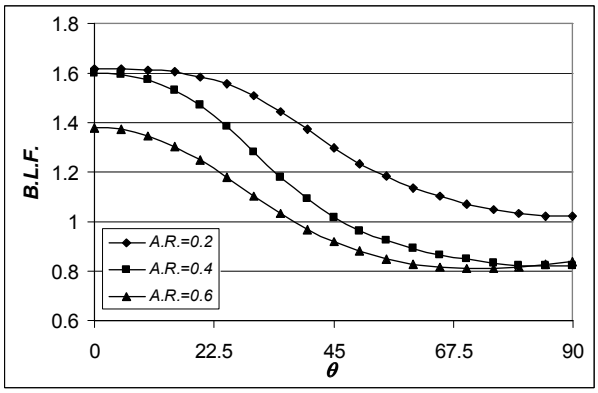

Figure 2: Effect of unidirectional **(2**θ**)** square patches on BLF of perforated plates.

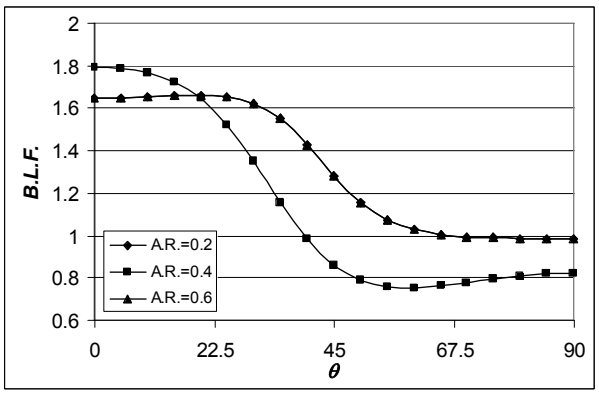

Figure 3: Effect of unidirectional **(2**θ**)** annular patches on BLF of perforated plates.

Similar results are presented in Fig. 3 for annular (Fig. 1c) unidirectional patches. In these cases, variations of BLF with respect to fiber angles are similar to square patches. As it shows, for unidirectional patches *(2θ)* the BLF reduces with fiber angle and has its minimum value about 55 degree. Higher buckling load factors are achieved using annular patches compare to square patches.
Two other stacking sequences, angle ply (±*θ*), and (*θ/0*) are also considered in this study. Figures 4 and 5 present BLF of perforated plates with square and annular composite patches. In these cases, the BLF is less sensitive to fiber angles than other lay ups. For all aspect ratios which considered, BLF>1 are achieved for any fiber angles.

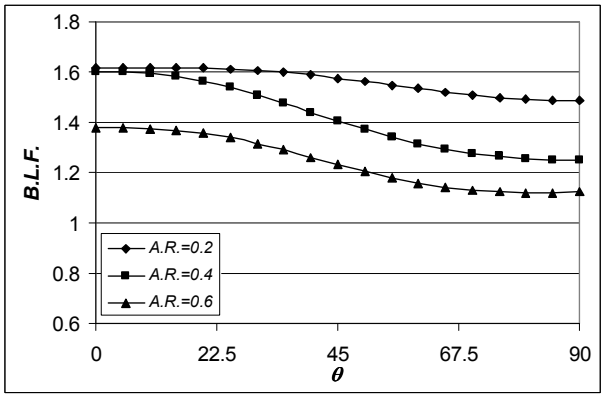

Figure 4: Effect of **(θ /0)** square patches on BLF of perforated plates.

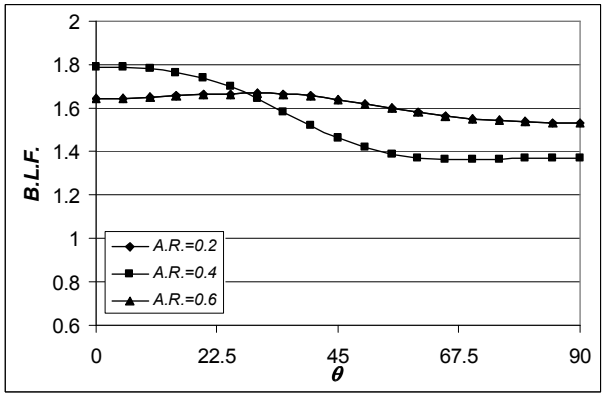

Figure 5: Effect of **(θ /0)** annular patches on BLF of perforated plates.

Conclusions

The main goal of repair/strengthening with composite patches is to restore the damaged structures to its original performance condition and increasing the load carrying capacity of an existing structure. The use of advanced composite materials for changing the buckling load of reinforced aluminum plates has been studied. Numerical results show that buckling load of perforated plates can be significantly change by using proper composite patches.

Buckling behavior of aluminum plates with variety of composite patches were evaluated in order to investigate the effective of composite patches properties in changing the buckling load of repaired systems. Then acceptable intervals and limitations for these parameters are presented. In each case, a set of composites patches that accurately satisfy the design criteria was introduced. The results presented herein indicate that, for buckling of a perforated plate, a set of laminated composite patches can be found which increase load carrying capacity of repaired plates.

References

[1] AA. Baker, R. Jones, *Bonded Repair of Aircraft Structures*, Mart. Nijhoff Pub. (1988).
[2] C. Chue, and J. Liu, Composite Engineering, Vol. (5) 223-230 (1995).
[3] Pai, P.F., Naghshineh-Pour, A.H., Schulz, M.J. and Chung, J., Finite Element in Analysis and Design, Vol. (28) 55-275(1998).
[4] Engels, H and Becker, W, *Composite Structures*, Vol. (56) 259-268(2002).
[5] Rezaeepazhand, J. and Sabouri, H., *Proceeding of the ACCM4*, Sydney Australia (2004).
[6] Rezaeepazhand, J. and Sabouri, H., *Proceeding of the ECCM12*, Biarritz, France (2006).
[7] Rezaeepazhand, J. and Sabouri, H., Modarres Technical and Eng. J., Vol.(17) 65-74(2004).
[8] Rezaeepazhand, J. and Sabouri, H., *Proceeding of the ICMSAO1*, Sharjah, UAE(2005).
[9] Moein Darbari, A. *Buckling Analysis of Plates with Central Cutouts*, MSc. Thesis, Ferdowsi University of Mashhad, Iran(2003).
[10] Sabouri, H. *Modal Behavior of Repaired and Reinforced Structural Elements with PMC*, MSc. Thesis, Ferdowsi University of Mashhad, Iran(2004).

Key Engineering Materials Vols. 385-387 (2008) pp 381-384
© (2008) Trans Tech Publications, Switzerland
doi:10.4028/www.scientific.net/KEM.385-387.381

Experimental Study on Compressive Strength of Recycled Aggregate Concrete

WANG Wei [1, a], LING Hua[2, b], WANG Xiaoni[3, c], XIA Tian[4, d],

WANG Dazhi [5, e] and JIANG Yibo[6, f]

[1] Department of Civil Engineering, Shaoxing College of Art and Science, Shaoxing, 312000, China

[2] Department of Civil Engineering, Nanjing Hydraulic Research Institute, Nanjing 210024, China

[3] Zijin College, Nanjing University of Science and Technology, Nanjing 210046, China

[4] Jiangsu Maritime Institute, Nanjing 211170, China

[5] Department of Civil Engineering, Shaoxing College of Art and Science, Shaoxing, 312000, China

[6] Department of Civil Engineering, Shaoxing College of Art and Science, Shaoxing, 312000, China

[a] wellsking.wang@gmail.com, [b] linghua@tom.com, [c] wangxiaoni@tom.com,

[d] xiatian@tom.com, [e] wells.wk@gmail.com, [f] ybjiang@163.com

Keywords: recycled aggregate concrete, stress, strain, strength, solidification age.

Abstract. With the increase in the use of recycled aggregate concrete (RAC), it is necessary to clearly understand its behavior and characteristics. In this paper, experimental study on compressive strength of RAC with same water/cement ratio is conducted. Firstly, influence of recycled coarse aggregate contents on cube compressive strength of RAC is studied. Secondly, experiment on time-dependent strength developing process of RAC is conducted with different solidification ages. Finally, based on above experimental investigations, empirical formula for compress strengths of RAC with different ages is presented. The result of this paper is helpful to theoretical analysis and practical engineering design of RAC structures.

Introduction

In recent years, there has been a great promotion of environmental management and sustainable development in China and elsewhere in the world. Due to the scarcity of natural resources coupled with the increase in aggregate requirement for construction, construction by nature is not an environmentally friendly activity and the use of recycled aggregate to partially replace the virgin aggregate has become more common [1,2].

As a result, the properties and behaviors of recycled aggregate need to be explored and fully understood. Unlike ordinary aggregate, recycled aggregate is coated with patches of cement mortar remains that increase water absorption, prolong the mixing time and affect the strength of the recycled aggregate concrete [3]. The most important mechanical properties of RAC are the compressive strength, the tensile and the flexural strengths, the bond strength and the elastic modulus of such concrete [4-5]. These properties strongly depend on coarse aggregate replacement percentages (ARP) and solidification ages. In particular, the time-dependent and ARP-related compressive strength of RAC is especially significant in theoretical and numerical analysis as well as engineering practice.

Most of the work on RAC has focused on its durability and traditional compressive strength, and the corresponding results have been used to many designs of engineering structures [5-7]. However, work on finding ARP-strength relationship and age-strength relationship is not found in details. The objective of this study is to conduct the experimental study on time-dependent and ARP-related compressive strength of RAC and find corresponding empirical formula to describe them. The results presented in this paper are significant to efficiently use the RAC in practical applications.

Experimental Descriptions

Ordinary Portland cement with a 28d compressive strength of 32.5 MPa was used in this investigation [2]. The fine aggregate used was river sand from Yangtze River, PR China. The used natural coarse aggregate was with 5-13 mm diameter. The used recycled coarse aggregate (7–17 mm accounting for 57%, and 17–25 mm accounting for 33% in weight) was obtained from the waste concrete brought from the concrete dike of Yangtze River. The physical properties of the natural coarse aggregates and the recycled coarse aggregates are shown in Table 1.

Table 1 Physical properties of he natural coarse aggregates and the recycled coarse aggregates

Coarse aggregates	Grading (mm)	Density (kg/m^3)	Water absorption (%)	Crush index (%)
Nature	5-13	1500	0.5	5
Recycled	5-25	1310	8	12

The water/cement ratio was kept constant as 0.45. The mixtures were divided into six groups. The main difference between these six groups is the ARP, which is 0%, 20%, 40%, 60%, 80% and 100%, respectively. In which, ARP=0% denotes that the concrete is the nature concrete, and ARP=100% means that the concrete is fully RAC.

At the same time, 9 solidification ages were taken into accounted to investigate the time-dependent compressive strength of RAC with ARP=60%, which is 0, 3, 5, 7, 14, 28, 42, 56 and 90 d, respectively.

Test Result

The stress-strain curves (SSC) of RAC with different ARP are shown as in Fig. 1. Fig. 1 illustrates that the ARP has great influences on the SSC of RAC. However, the shape of the SSC for all the recycled aggregate concrete was similar to that of the natural aggregate concrete, irrespective of the ARP. The compressive strength, f_u, is the peak stress of the test specimens of RAC, which decreases deeply with the increase of ARP, shown as in Fig. 2.

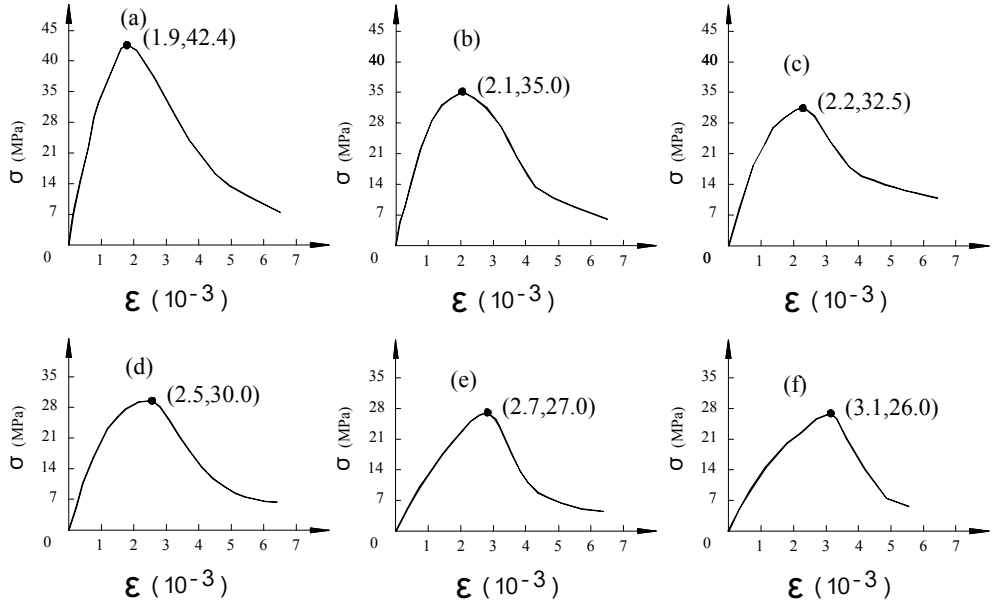

Fig.1. Experimented SSCs of RAC with different ARP
(a) ARP=0%; (b) ARP=20%; (c) ARP=40%; (d) ARP=60%; (e) ARP=80%; (f) ARP=100%.

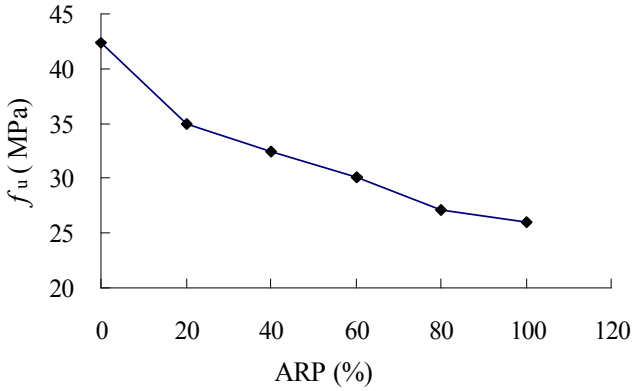

Fig. 2. Experimented $ARP - f_u$ relationships of RAC

The peak strain is the strain corresponding to the peak stress. The peak strains of the RAC with different ARPs are shown in table 2. From table 2, it can be seen that the value of the peak strain, denoted by ε^*, increases as the ARP increases, which can be described as

$$\varepsilon^* = 0.012ARP + 1.838 \quad (1)$$

Table 2 Relationship between ARP and peak strain of RAC

ARP (%)	0	20	40	60	80	100
Peak strain	1.9	2.1	2.2	2.5	2.7	3.1

Fig. 3 demonstrates the increase process of compressive strength, f_u, with solidification age, t. From Fig.3, it can be seen that the value of the compressive strength increases as the ARP increases. At the early ages, the compressive strength increases quickly. After 14 days, the increase becomes slowly with the tendency to one constant value.

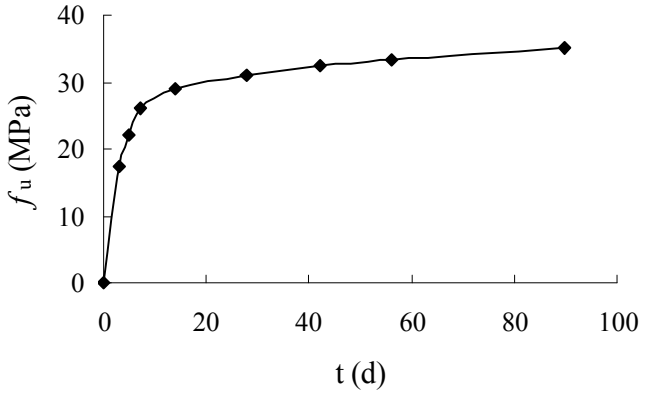

Fig. 3. Experimented $t - f_u$ relationships of RAC

A mathematical expression for the time-dependent compressive strength of RAC is desirable for the structural analysis and design in many practical engineering applications. Based on the experimentally obtained compressive strength with different ages, we find that solidification age is linear to the ratio of solidification age to compressive strength, shown as in Fig. 4. Then, we can obtain

$$\frac{t}{f_u} = 0.029t + 0.086 \quad (2)$$

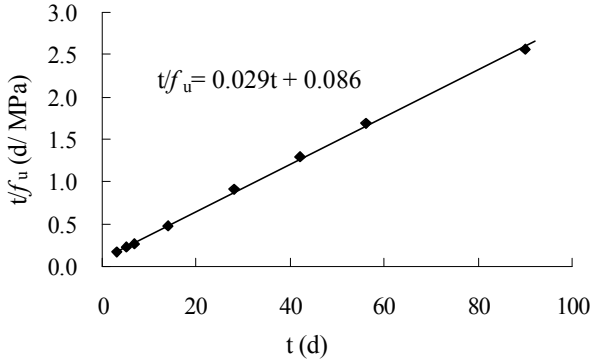

Fig. 4. Experimented $t-t/f_u$ relationships of RAC

So the relationship between solidification age and compressive strength of this series experiments can be empirically expressed as

$$f_u = \frac{1000t}{29t+86} \tag{3}$$

Generally, the relationship between solidification age and compressive strength of RAC can be empirically determined as hyperbolic model

$$f_u = \frac{t}{a+bt} \tag{4}$$

Where a and b are two parameters corresponding to RAC property.

Conclusions

In this paper, experimental results for the mechanical properties of recycled aggregate concrete under compression loading are presented and discussed. From this experimented data, the following conclusions can be drawn.

(1) The shape of the SSC for all the recycled aggregate concrete was similar to that of the natural aggregate concrete, irrespective of the ARP. However, the compressive strength of RAC decreases deeply with the increase of ARP

(2) The peak strains of the RAC increases almost linearly as the ARP increases.

(3) The relationship between solidification age and compressive strength of RAC can be empirically determined as hyperbolic model.

References

[1] W.Y. Vivian, X. F. Gao, C. M. Tam: Constr. Build. Mater. Vol.22 (2008), p. 364

[2] J. Z. Xiao, J. B. Lia, Ch. Zhang: Cement Concrete Res. Vol. 35 (2005), p.1187

[3] J. S. Ryu: J. Mater. Sci. Lett. Vol. 21 (2002), p. 1565

[4] B. G. Fontebo, F. M. Abella: Constr. Build. Mater. Vol.21 (2007), p. 887

[5] W. Wang, B. X. Sun, T. H. Lu: Key Eng. Mat. Vol. 384-385 (2007), p. 881

[6] G. Y. Cheng: Concrete Vol. 19(2005), p.67

[7] W. Xu: Concrete Vol. 20(2006), p.45

Key Engineering Materials Vols. 385-387 (2008) pp 385-388
© (2008) Trans Tech Publications, Switzerland
doi:10.4028/www.scientific.net/KEM.385-387.385

Corrosion Behavior and Mechanism of a Cu-Ni Alloy in Marine Environment

Li Qing-fen [1,2,a], Li Chun-hui [1,b], Qiao Ying-jie [1,c]

[1]College of Material Science and Chemical Engineering, Harbin Engineering University,

[2]College of Mechanical and Electrical Engineering, Harbin Engineering University,

Harbin 150001, China

[a]qingfli@yahoo.com.cn, [b]lichunhui@hrbeu.cn, [c]qiaoyingjie@hrbeu.cn

Keywords: Corrosion; Cu-NI alloy; marine environment; microbiological influenced corrosion (MIC)

Abstract. The microbiological influenced corrosion (MIC) behavior of a marine pipeline Cu-Ni alloy in the sterile seawater and sulfate-reducing bacteria (SRB) solution was investigated. Results show that severe pitting corrosion appeared on the specimens in the SRB solution. The corrosion potential of specimen in the SRB solution was much lower than that in the sterile seawater and the polarization resistance of specimen in the SRB solution decreased quickly after a period immersion and became much lower than that in the sterile seawater. Besides, the results of EDS and XRD show that the content of element Ni and Fe of the Cu-Ni alloy decreased greatly and the high content of element S appeared after 30 days immersion in the SRB solution. It was concluded that the SRB accelerated the corrosion process of the Cu-Ni alloy greatly. The MIC mechanism of the alloy in marine environment is discussed.

Introduction

There are lots of microorganisms in seawater. When immersed in seawater, many metals would suffer serious microbiological influenced corrosion damage, and the cost of such damage may reach billions of dollars annually. Among them, the SRB influenced corrosion is one of the most severe one in marine environment [1-2].

Cu-Ni alloy is widely used in the marine pipeline system which is often attacked by the SRB influenced corrosion. Corrosion behavior of some Cu-Ni alloy in marine environment has not been investigated in detail and the corrosion mechanism is not totally clear yet, although many research studies of MIC caused by SRB have been carried out [3-5].

In the present work, the corrosion behavior of marine pipeline material Cu-Ni alloy in the sterile seawater and SRB solution was investigated and the mechanism of MIC was discussed.

Experimental

The chemical composition of the Cu-Ni alloy used in the present investigation is shown in Table 1. The size of test sample is Φ11.3 mm x 6 mm with working area of 1 cm^2. A copper wire was soldered to the lower surface of the test sample for potential measurements. Samples were polished up to grit 400 and then cleaned with deionized water. All samples were sterilized under UV for 3 hours before test.

Tests were carried out in two solutions: the sterilized seawater and the SRB solution. The SRB strains were isolated from the sea-mud in Qingdao seashore. The composition of the sterile seawater

and SRB solution is given in table 2.

MIC behavior of sample in different media was investigated with electrochemical impedance spectroscopy (EIS), energy dispersive spectroscopy (EDS), X-ray diffraction (XRD) and scanning electron microscopy (SEM).

Table 1 Chemical Composition of the Cu-Ni alloy [wt %]

Cu	Ni	Fe	C	O
60.32	28.81	1.11	6.67	3.09

Table 2 Composition of Solutions [g/L]

	Sea water	SRB	PH	K_2HPO_4 $3H_2O$	$MgSO_4$ $7H_2O$	$CaCl_2$	Na_2SO_4	NH_4Cl	Sodium lactate	Vc	Yeast
sterile seawater	1L	0	7.00	0.50	2.00	0.10	0.50	1.00	3.50	0.10	1.00
SRB solution	1L	0.06L	7.00	0.50	2.00	0.10	0.50	1.00	3.50	0.10	1.00

Results and discussion

The variation of corrosion potential over time of the Cu-Ni alloy samples in different test solutions is given in Fig.1. Fig.2 gives the variation of charge reaction resistance which came from the data of equivalent electrical circuits (EEC) in the electrochemical impedance Nyquist plots and Bode plots (Fig.3 and 4). Results of EDS and XRD of samples original and after 30 days exposure in different solutions are given in Fig. 5 and 6 respectively. Fig.7 gives the surface micrographs of samples.

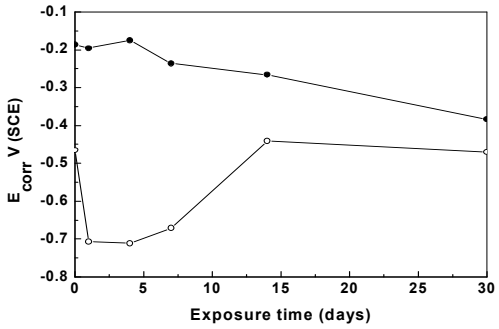

(•) Sterile seawater (○) SRB solution

Fig.1 Variation of corrosion potential over time

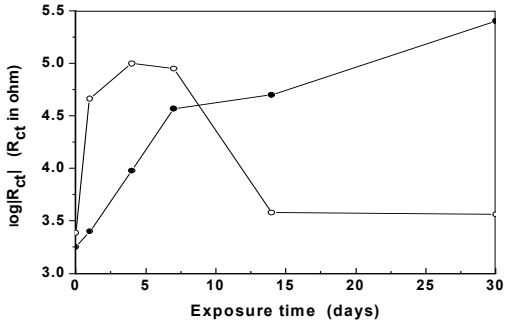

(•) Sterile seawater (○) SRB solution

Fig.2 Variation of charge reaction resistance over time

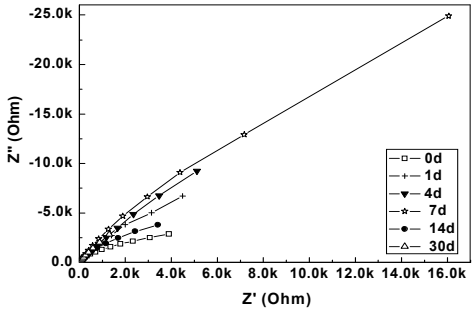

(a) Sterile seawater

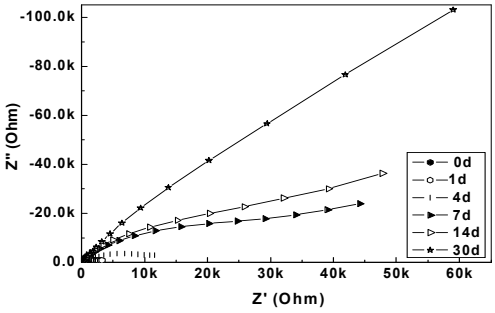

(b) SRB solution

Fig.3 Nyquist plots

From Fig.1 and 2, we see that the corrosion potential of the sample in the SRB solution was much lower than that in the sterile seawater. The polarization resistance of specimen at the first several days in the SRB solution was higher than that in the sterile seawater, and then it decreased

quickly after a period immersion and became much lower than that in the sterile seawater in which the polarization resistance of specimen increased continuously. It was concluded that the SRB accelerated the process of corrosion greatly for the B30 Cu-Ni alloy samples.

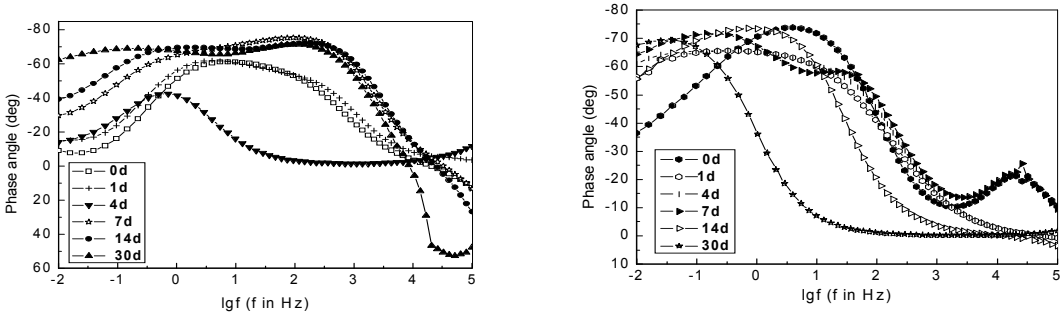

(a) Sterile seawater (b) SRB solution

Fig.4 Bode plots

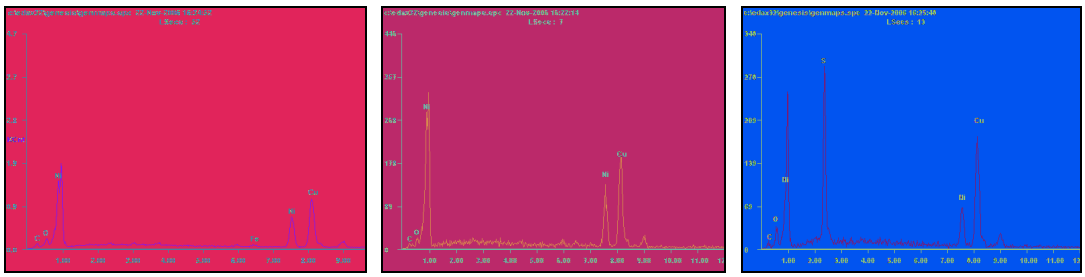

(a) Original (b) in sterile seawater (c) in SRB solution

Fig.5 EDS of samples original and after 30 days immersion in different solutions

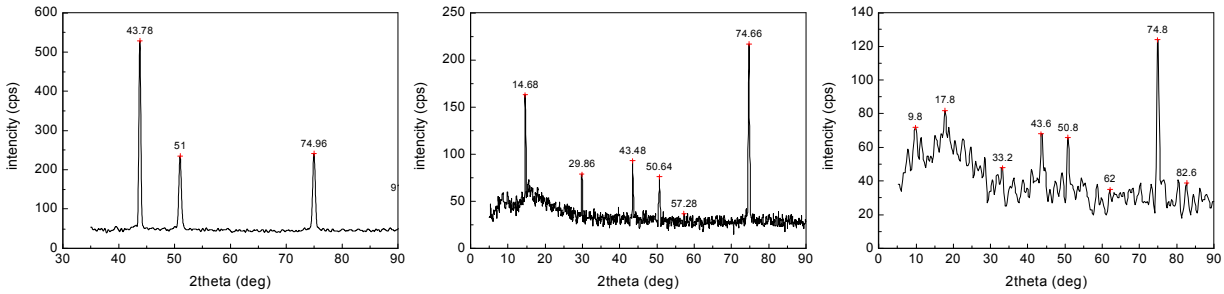

(a) Original (b) in sterile seawater (c) in SRB solution

Fig.6 XRD of samples original and after 30 days immersion in different solutions

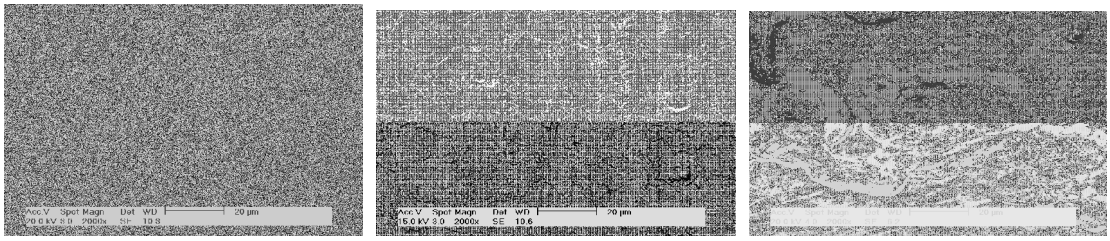

(a) Original (b) in sterile seawater (c) in SRB solution

Fig. 7 Surface micrographs of samples original and after 30 days immersion in different solutions

Results of energy dispersive spectroscopy (EDS) gave the same conclusion. From Fig.5, we can see that, comparing with the original sample, the content of element Fe, C and O of the Cu-Ni alloy decreased, and the content of element Cu and Ni increased in the sterile seawater. The content of element Ni and Fe of the Cu-Ni alloy decreased greatly and the high content of element S appeared after 30 days immersion in the SRB solution. It suggests that the de-alloy corrosion may have

happened in SRB solution. From the results of XRD (Fig.6), we can see that the Cu_2S appeared after 30 days immersion in the SRB solution. It suggests that the SRB promoted the dissolution of the Cu-Ni alloy

Micrographs of samples (Fig.7) show that severe pitting corrosion appeared on the specimens in the SRB solution.

The mechanism of corrosion in the sterile seawater and SRB solutions is analyzed.

In both sterile seawater and SRB solutions, the anodic reaction is

$$Cu \rightarrow Cu^{+} + e^{-}$$

In the sterile seawater, the content of Cl^- is very high，the main reaction is as follow:

$$Cu + 2C1^{-} \rightarrow CuC1^{-}_{2} + e^{-}$$

SRB is anaerobic bacteria and it gets energy from the reduction process of $SO_4^{2-} \rightarrow S^{2-}$. SRB biofilm restrained the corrosion process in the early stage of the test, but the corrosion process was promoted with the increasing amount of SRB then.

The reaction of cathodic depolarization in SRB is as follow:

$$8H_2O \rightarrow 8H^{+} + 8OH^{-} \qquad \text{(cathodic reaction)}$$

$$8H^{+} + 8e \rightarrow 8H$$

$$SO_4^{2-} + 8H \rightarrow S^{2-} + 4H_2O \qquad \text{(cathodic reaction caused by bacteria)}$$

The corrosion product came from the follow reaction:

$$2Cu + S^{2-} \rightarrow Cu_2S + 2e \qquad \text{(corrosion product)}$$

The corrosion process was controlled by both bacteria and corrosion products. The corrosion process would be more restrained when thicker biofilm and more corrosion products accumulated on the specimen surface with increasing bacteria. However the thick film will give a more corrosive environment between the film and the alloy surface. The small anodic area where the elements of $C1^-$ and S^- enriched ceaselessly will accelerate the corrosion and results in the serious pitting over the specimens surface.

Summary

Experimental results of the marine pipeline Cu-Ni alloy in the sterile seawater and SRB solution show that the SRB accelerated the process of corrosion greatly since the SRB promoted the dissolution of the Cu-Ni alloy and the de-alloy corrosion may have happened in SRB solution. The small anodic area formed under the thick precipitates or biofilm accelerated the corrosion and resulted in the serious pitting over the specimens surface.

References

[1] S. L. Zhu, B. R. Hou, and J. L. Zhang: Marine Environment Science Vol. 19 (2000), p. 27.
[2] B. Haluk and L. Zbigniew: Water Research Vol. 38 (2004): p. 2726.
[3] S. Z. Song, L. H. Yin, and J. Wu: Journal of Chemical Industry and Engineering Vol. 56 (2005): p.121-125.
[4] G. F. Cui, N. Li, D. Y. Li, J. Zheng, and Q. L. Wu: Surface & Coatings Technology Vol. 200 (2006), P. 6808–6814.
[5] B. Haluk and L. Zbigniew: Water Research Vol. 38 (2004), p. 2726–2736.

Key Engineering Materials Vols. 385-387 (2008) pp 389-392
© (2008) Trans Tech Publications, Switzerland
doi:10.4028/www.scientific.net/KEM.385-387.389

Dynamic Anti-plane Behaviors of a Semi-infinite piezoelectric Medium with a Circular Cavity and a Crack near the Surface

Tianshu Song[1,a], Dong Li[1,b], Xinwang Wang[1,c]and Shengli Dong[2,d]

[1] School of Civil Engineering, Harbin Engineering University, Harbin, 150001, P.R. China

[2] Department of Civil Engineering, Heilongjiang Engineering College, Harbin, 150001, P.R. China

[a]songts@126.com, [b]lidong242@163.com, [c]wangxinwang740@163.com, [d]dsl8000@163.com

Keywords: Semi-infinite piezoelectric medium; Green's function; Dynamic stress concentration factor; Dynamic stress intensity factor; Interacting crack and circular cavity near the surface

Abstract. Dynamic interaction is investigated theoretically between a circular cavity and a crack near the surface in a semi-infinite piezoelectric medium subjected to time-harmonic incident anti-plane shearing in this paper. The formulations are based on the method of complex variable and Green's function. Dynamic stress concentration factors at the edge of the circular cavity and dynamic stress intensity factors at the crack tip are obtained by solving boundary value problems with the method of orthogonal function expansion. The calculating results are plotted to show how the frequencies and the orientation of incident wave, piezoelectric characteristic parameters of the material and the structural geometries influence upon the dynamic stress concentration factor (DSCF) and dynamic stress intensity factor (DSIF).

1. Introduction

It is well known that the coupling behavior of piezoelectric materials has led to their wide applications in smart materials. Failure or fracture often occurs in newly developed piezoelectric materials because of their brittleness and presence of faults or flaws during the manufacturing and the polling process. So the investigation of the failure behaviors caused by stress concentrations has become more important. It should be noted that most of the published papers on piezoelectric materials with flaws are about infinite medium [1, 2, 3]. In recent years, Chen and Worswick investigated dynamic fracture behavior of a cracked piezoelectric half space under anti-plane mechanical and in-plane electric impact [4]. Studies about infinite piezoelectric medium with the same detects have been more reported, but the dynamic interaction between two kinds of defects have been reported not too many, especially in a semi-infinite piezoelectric medium.

Therefore the objective of this paper is to provide a theoretical study on dynamic anti-plane interaction between a crack and a circular cavity near the surface in a semi-infinite piezoelectric medium. The emphasis is placed on stress intensity factors and stress concentration factors. The boundary conditions of both the cavity and the crack are assumed to be traction free and electrically permeable. And the surface of the semi-infinite medium is assumed to be traction free but electrically impermeable.

2. The Governing Equations

Consider a semi-infinite piezoelectric medium containing a circular cavity and a crack near the

surface subjected to time harmonic out-plane elastic displacement field and in-plane electric potential field directed at an incident angle α_0 with the positive x-axis, as show in Fig.1. The medium is assumed to have been poled along the z-axis normal to the xy-plane. In the absence of body forces and free charges, the governing equations of linear piezoelectricity for dynamic anti-plane shearing with the exponential time harmonic factor exp(-$i\omega t$) are given by

$$c_{44}\nabla^2 w + e_{15}\nabla^2\phi + \rho\omega^2 w = 0 \ , \ e_{15}\nabla^2 w - \kappa_{11}\nabla^2\phi = 0 \tag{1}$$

in which, c_{44}, e_{15} and κ_{11} are shear elastic modulus, piezoelectric constant and dielectric constant of the medium, respectively; while w, ϕ, ρ and ω are anti-plane displacement, electric potential, mass density and frequency of the incident wave, respectively.

The constitutive relations can be written in complex variable $\eta = x + iy = re^{i\theta}$, $\overline{\eta} = x - iy = re^{-i\theta}$

$$\begin{aligned} &\tau_{rz} = (c_{44} + \frac{e_{15}^2}{\kappa_{11}})(\frac{\partial w}{\partial \eta}e^{i\theta} + \frac{\partial w}{\partial \overline{\eta}}e^{-i\theta}) + \frac{e_{15}^2}{\kappa_{11}}(\frac{\partial f}{\partial \eta}e^{i\theta} + \frac{\partial f}{\partial \overline{\eta}}e^{-i\theta}), \quad \tau_{\theta z} = (c_{44} + \frac{e_{15}^2}{\kappa_{11}})i(\frac{\partial w}{\partial \eta}e^{i\theta} - \frac{\partial w}{\partial \overline{\eta}}e^{-i\theta}) + \frac{e_{15}^2}{\kappa_{11}}i(\frac{\partial f}{\partial \eta}e^{i\theta} - \frac{\partial f}{\partial \overline{\eta}}e^{-i\theta}) \\ &D_r = -e_{15}(\frac{\partial f}{\partial \eta}e^{i\theta} + \frac{\partial f}{\partial \overline{\eta}}e^{-i\theta}), \quad D_\theta = -e_{15}i(\frac{\partial f}{\partial \eta}e^{i\theta} - \frac{\partial f}{\partial \overline{\eta}}e^{-i\theta}) \end{aligned} \tag{2}$$

where τ_{rz}, $\tau_{\theta z}$, D_r and D_θ are two shear stress components and two electric displacement components, respectively. Equation1 can be simplified further

$$\frac{\partial^2 w}{\partial \eta \partial \overline{\eta}} + \frac{1}{4}k^2 w = 0 \ , \ \phi = \frac{e_{15}}{\kappa_{11}}(w + f) \ , \ 4\frac{\partial^2 f}{\partial \eta \partial \overline{\eta}} = 0 \tag{3}$$

in which $k^2 = \rho\omega^2 / c^*$ with $c^* = c_{44}(1+\lambda)$ and $\lambda = \frac{e_{15}^2}{c_{44}\kappa_{11}}$.

3. Green's functions and boundary value problem

Firstly, consider the problem of single circular cavity in a semi-piezoelectric medium subjected to an incident elastic wave (see fig.1 without the crack). The boundary conditions at the circular edge and at the impermeable surface can be written as:

$$\begin{aligned} &\tau_{rz} = 0 \ , \ D_r = D_r^c \ , \ \phi = \phi^c \ , \ |\eta| = R \\ &\tau_{yz} = 0 \ , \ D_y = 0 \ , \qquad\qquad y = h_1 \end{aligned} \tag{4}$$

in which, superscript "c" expresses the variable in the cavity, same in the follows. This problem has the solutions of the following form

$$\begin{aligned} &w = w_0 e^{i\frac{k}{2}[(\eta - ih_1)e^{-i\alpha_0} + (\overline{\eta} + ih_1)e^{i\alpha_0}]} + w_0 e^{i\frac{k}{2}[(\eta - ih_1)e^{i\alpha_0} + (\overline{\eta} + ih_1)e^{-i\alpha_0}]} + w^{(s)} + w_0 \sum_{n=-\infty}^{+\infty} A_n \{H_n^{(1)}(k|\eta|)(\frac{\eta}{|\eta|})^n + H_n^{(1)}(k|\eta - 2h_1 i|)(\frac{\eta - 2h_1 i}{|\eta - 2h_1 i|})^{-n}\} \\ &\varphi = \frac{e_{15}}{\kappa_{11}}w + \frac{e_{15}}{\kappa_{11}}w_0 \sum_{n=1}^{+\infty}\{D_n[\eta^{-n} + (\overline{\eta} + 2h_1 i)^{-n}] + E_n[(\overline{\eta})^{-n} + (\eta - 2h_1 i)^{-n}]\} \end{aligned} \tag{5}$$

where $H_n^{(1)}$ expresses Hankel function of the first kind; unknown constants A_n, D_n and E_n can be obtained, see [5] in details.

Secondly, construct a couple of Green's Functions G_w and G_φ, which are fundamental solutions of elastic displacement and electric potential respectively for a semi-infinite piezoelectric medium with a circular cavity under a time harmonic anti-plane line force at an arbitrary point $\eta_0 = r_0 e^{i\theta_0}$ in the medium. So Green's functions of the current paper should satisfy the following equations

$$\nabla^2 G_w + k^2 G_w = 0, \quad G_\phi = \frac{e_{15}}{\kappa_{11}}G_w + g, \quad \nabla^2 g = 0, \quad \tau_{\theta z} = \delta(\eta - \eta_0) \tag{6}$$

and (4), in which δ indicates Dirac-δ function. G_w can be solved and have the following form

$$G_w(\eta,\eta_0'') = \frac{i}{4c_{44}(1+\lambda)}[H_0^{(1)}\left(k\left|\eta-\eta_0''e^{i\beta_0}+ih_2e^{i\beta_0}\right|\right)+H_0^{(1)}\left(k\left|\eta-\overline{\eta}_0''e^{-i\beta_0}-ih_2e^{-i\beta_0}-2ih_1\right|\right)]$$
$$+\frac{i}{4c_{44}(1+\lambda)}\sum_{n=-\infty}^{\infty}B_n[H_n^{(1)}\left(k|\eta|\right)\left(\frac{\eta}{|\eta|}\right)^n+H_n^{(1)}\left(k|\eta-2ih_1|\right)\left(\frac{\eta-2ih_1}{|\eta-2ih_1|}\right)^{-n}] \quad (7)$$

where $\eta_0'' = \eta e^{-i\beta_0} + ih_2$, $\overline{\eta}_0'' = \overline{\eta}e^{i\beta_0} - ih_2$; B_n can be obtained by solving boundary value problem.

Finally, reverse shear stress -$\tau_{\theta z}$ based on (5) and (2) is applied to the crack's location and along its surface. This can result $\tau_{\theta z}$=0 as well as continued electric potential and continued normal electric displacement at the above location, namely a traction free and an electrically permeable crack. Thus the total electromechanical field can be given by

$$w^{(t)} = w - \int_{(b,0)}^{(2c+b,0)} \tau_{\theta''z''}\Big|_{\eta''=\eta_0''} \times G_w(\eta,\eta_0'')d\eta_0''$$
$$\phi^{(t)} = \frac{e_{15}}{\kappa_{11}}w + w_0\frac{e_{15}}{\kappa_{11}}\sum_{n=1}^{+\infty}\{D_n[\eta^{-n}+(\overline{\eta}+2ih_1)^{-n}]+E_n[\overline{\eta}^{-n}+(\eta-2ih_1)^{-n}]\} \quad (8)$$

Thus, DSCF $\tau_{\theta z}^*$ at the cavity's edge and DSIF k_{III} at the left tip of the crack can be expressed as

$$\tau_{\theta z}^* = \left|\frac{\tau_{\theta z}^{(t)}}{\tau_0}\right|,\ k_{III} = \frac{\left|\tau_{rz}^{(t)}\right|_{\eta\to\eta_1}}{\tau_0 Q},\ \tau_0 = kc_{44}w_0 \quad (9)$$

in which $\tau_{\theta z}^{(t)}$ and $\tau_{rz}^{(t)}$ are governed by (8) and (2), respectively; Q is characteristic length of the crack; η_1 denotes coordinate of the left tip of the crack.

4. Calculating Cases and Discussion

Some calculating cases based on (9) are obtained and plotted to show the sensitivity of piezoelectric medium to material constants under vertical incidence. Fig.2 shows DSIFs at the crack's tip near the cavity; while Fig.3 shows DSCFs at the cavity's edge at the same situation. And Fig.4 shows that DSIFs vary from the ratio h_1/R.

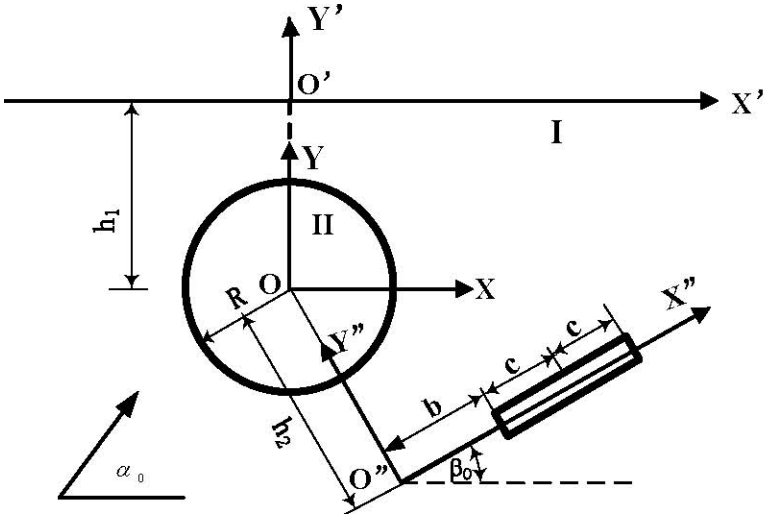

Fig.1 Interacting circular cavity and crack near the surface

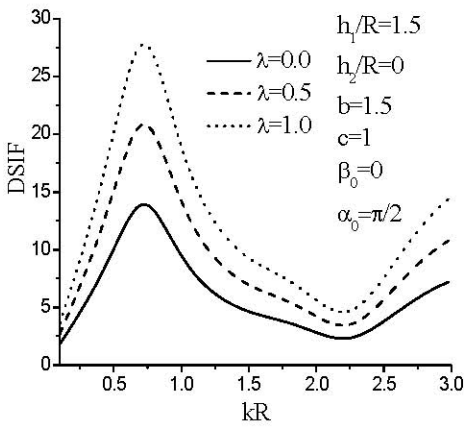

Fig. 2 DSIFs at the crack's tip under vertical incidence

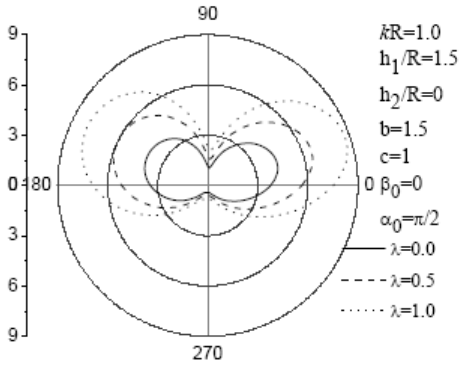

Fig. 3 DSCFs and the cavity's edge under vertical incidence

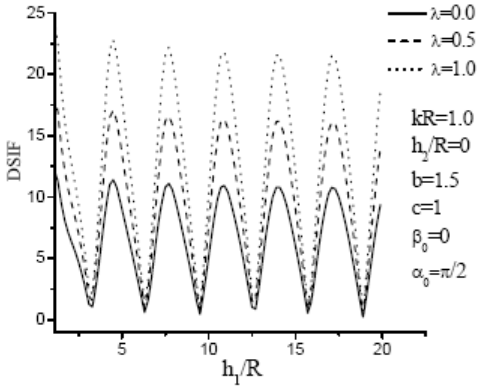

Fig. 4 Oscillation of DSIFs under vertical incidence

It can be seen through the asymmetry of Fig.3 that the influence of a crack and a surface on DSCFs at the cavity's edge at higher frequencies is quite obvious. The calculating results indicate when b/R and h_1/R reach 8 or more and 6 or more respectively, the interaction between the cavity and the crack as well as the interaction between the surface and defects can be ignored, respectively. The maximal DSIF as well as the maximal DSCF appears at lower frequency kR=0.6~0.8 shown in Fig.2. In addition, periodical oscillating phenomenon depending on the ratio h_1/R can be seen through Fig.4. And the oscillation is more obvious with the increment of incident wave frequency.

5. Summary

Dynamic strength is one of the properties of piezoelectric materials used as sensors and actuators in smart materials and structure technology. The method of electro-elastic mechanics is developed in the present paper to solve the problem of dynamic anti-plane interaction between two kinds of defects and the surface for a semi-infinite piezoelectric medium. Dynamic analyses are very important to the interaction between a crack and a circular cavity near the surface in a semi-infinite piezoelectric medium at lower frequencies and larger piezoelectric characteristic parameters especially. The method used in present paper can serve as a useful reference for modeling of piezoelectric media with other defects near the surface.

Acknowledgments

The work is supported by the Natural Science Foundation of Heilongjiang Province of China (A00-10) and the Basis Research Foundation of Harbin Engineering University (HEUF04008).

References

[1] X.D.Wang, S.A.Meguid: Modeling and analysis of a cavity or a crack in a piezoelectric material. Int. J. Solids Structures, 38, 2803-2820 (2001).

[2] X.Wang, S.Yu: Scattering of SH waves by an arc-shaped crack between a cylindrical piezoelectric inclusion and matrix-II: Far fields. Int. J. Fracture, 100(4), 35-40 (1999).

[3] S.A,Meguid, X.D.Wang: Dynamic anti-plane behavior of interacting cracks in a piezoelectric medium. Int. J. Fracture, 91, 391-403 (1998).

[4] Z.T.Chen,M.J.Worswick:Dynamic fracture behavior of a cracked piezoelectric half space under anti-plane mechanical and in-plane electric impact.Archive of Applied Mechanics, 1-12 (2002).

[5] T.S.Song, S.L.Wang: Dynamic stress concentration on a semi-infinite piezoelectric medium with a circular cavity near the surface. Proceedings of ASME IDETC/CIE, (2007).

Key Engineering Materials Vols. 385-387 (2008) pp 393-396
© (2008) Trans Tech Publications, Switzerland
doi:10.4028/www.scientific.net/KEM.385-387.393

Blade failure in second stage turbine

K. Mohammadi [a] , A. K. Haghi [b]
University of Guilan , P. O. Box 3756, Rasht, Iran
[a] kmohammadi@guilan.ac.ir
[b] Haghi@guilan.ac.ir

Abstract

The present paper reports the investigation of a sudden blade fracture leading to a fatal engine failure. The blade sample was subjected to a series of examinations, including visual examination and photographic documentation, optical microscopy, scanning electron microscopy (SEM), using both energy dispersive spectroscopy (EDS) and X-ray mapping. Analysis of all elements show that loss of aluminum from coating due to oxidation and coating phases changing; decreasing of alloy ductility and toughness due to carbides precipitation in grain boundaries; degradation of the alloy gamma prime γ' phase (aging and coarsening) and micro cavities. These were found on fracture surfaces which served as an origin of creeping failure mechanism and are the most important factor for failure of this blade.

Keywords: blade, corrosion, creep, fatigue

Introduction

There has recently been considerable interest in the analysis of gas turbine failure [1]. Three probable damage mechanisms affect turbine blades, these being mechanical damage through either creep or fatigue and high temperature corrosion .However, materials used for turbine blades must be suitable in these conditions. The most common materials for turbine blade manufacture are the nickel-based ‘‘super-alloy’’ materials. these alloys are able to withstand the very aggressive environment of high temperature and high stress found within the hot gas path of a turbine engine [2]. Nevertheless turbine blades are exposed to strongly oxidising conditions and the gaseous combustion products contain elements such as sulphur, vanadium or even lead and bromine from the fuel at very high temperatures. Meanwhile corrosion damage to compressor blades occurs mainly through ingested atmospheric pollutants mixing with the water vapour inevitably present [3]. To modify corrosion resistance and high temperature strength, these alloys sustained an especial heat treatment for example with aluminium additions, Al2O3 diffusion surface layers can be a highly oxidation- resistant at very high temperature [4]. With additions such as chromium to confer oxidation resistance, into which is precipitated a second γ' phase with the general form of Ni(Al,Ti)3 formed through alloying with aluminium and titanium [5]. The γ' phase shows an unusual property in that it tends to increase in strength with increasing temperature, at least at lower temperatures below about 973ºK. The precipitation of the γ' phase is carefully controlled during manufacture to give a controlled size and morphology, resulting in a fine, ordered quasi-cubic precipitate to optimize high temperature strength by maximizing resistance to both diffusion creep at lower temperatures and power-law creep at higher temperatures [6].

Experiment

The investigation of the failure was carried out by providing samples from different zones of fractured and un fractured blades which their chemical analysis mentioned in Table 1.

Table1.Chemical composition of blade

Element	P	S	Zr	Mg	C	Fe	Nb	Mo	W	Ti	Al	Co	Cr	Ni
Wt% in Alloy	0.003	0.004	0.02	0.05	0.09	0.44	.0.99	1.94	3.2	3.7	4	8.18	15.92	bal

First of all, optical microscopy was performed on specimens removed from the blade, followed by mechanical polishing with up to 0.1 μm grade alumina, and subsequent chemical etching. Then metallographic observations were performed with optical microscopy and scanning electron microscopy equipped with an energy dispersive X-ray (EDX) phase analyzer, as well as X-Ray diffraction (XRD) and X-Ray fluorescence (XRF) tests .The results from longitudinal microanalysis through both sides of blade as well as SEM photographs were sued for explanation of source of blade failure.

Discussion of Results

The micro structural investigation of pholished samples of the blade airfoil revealed the presence of continuous film of carbides Fig.1. These carbide films in grain boundaries are tested by EDX. They are Cr-rich and include 80% Cr while the other regions have around 17% Cr. These continuous networks of carbides reduce ductility and toughness of the and facilitate crack initiation and propagation which leads to reduced lifetime .According to results from XRD&XRF the presence of a continuous film of carbides in grain boundaries is a result of transformation of carbides of MC type to carbides of $M_{23}C_6$ or M_6Ctype due to high temperature operation of the blade.
Fig.2. shows micro-cavities that served as the origin of a creep failure mechanism. On the other hand the sliding of grain boundaries continued to generate initial cracks.
The coating crack initiation was probably due to a thermal fatigue mechanism as a result of high thermal transient loads (trips, start-ups and slow-downs), and crack grain boundary initiation and propagation in the substrate by a creep mechanism (high steady state load) shown in Fig.3..

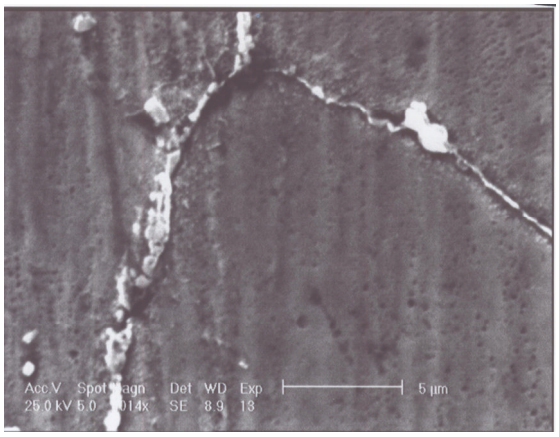

Fig.1. precipitation carbide on grain boundary inter granular fracture

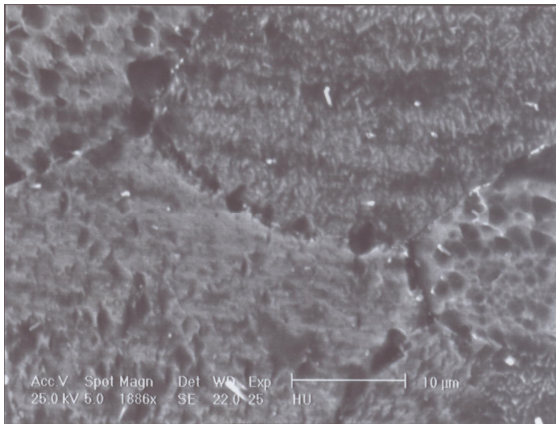

Fig.2.Microvoide on the grain boundary Caused shows creep at high temperature

The degradation of coatings resistant to high temperature proceeds in two ways:
1. Loss of coating constituents due to oxidation and corrosion, which results in loss of Al from coating to create a thin protective layer of Al2O3 on the surface.
2. Inter diffusion of coating-substrate, which results in diffusion of alloy elements into the coating.

Using an electron beam micro analyzer, it is found that discrete sulfide particles of chromium and titanium are present in a region; the sulfur diffuses inward and then reacts with chromium from the substrate to form chromium sulphides. As corrosion proceeds, and phase stability adjusts to changing chemistry, the sulphides are converted to complex unstable metal oxides and the sulfure thus released diffuses more deeply into the substrate where it forms more sulphides [7].
After measuring and comparing the Al content of coating through the longitudinal section of blade results to compare the damage condition of the coating layers, it was found that concave side of blade, which suffered more severe surface discoloration, had a thickness reduction and necking more than convex side of blade(Fig. 4). The reason that the coating layer on the concave side peeled off more than that on the convex side was the concave side suffered longer from the effects of high temperature air flow. At the same time Al% shows higher reduction on the tip of blade because of higher temperature [8].

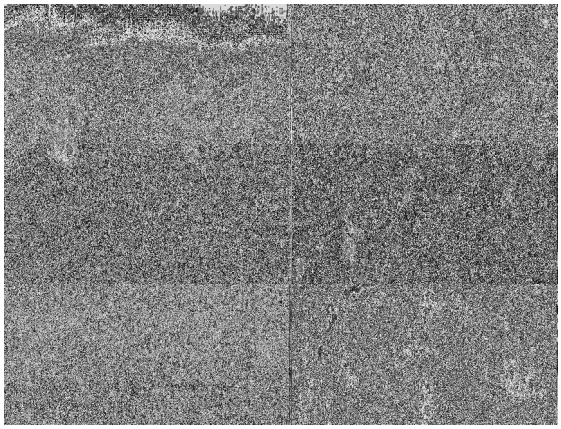

Fig.3.surface crake on the Al coat of blade diffusion and brittle grain boundary

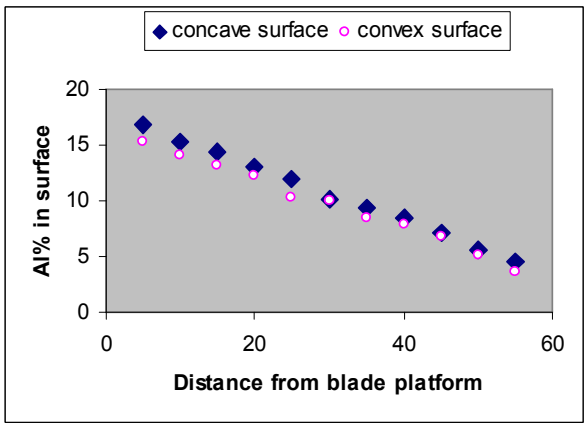

Fig. 4.Al% in coat of blade via distance Caused S from platform

Conclusion

On the basis of the analysis of the results of the second stage blade metallographic examination, it can be concluded that the type of damage which occurs in gas turbine blades can be divided into:
1-External and internal surfaces damage (corrosion, oxidation, crack formation, erosion, foreign object damage and fretting).
2-Internal damage of microstructure as γ'[Ni3(Al,Ti)] phase aging (rafting), grain growth, grain boundary creep voiding, carbides precipitation and brittle phases formation.
The pollutants entering with the inlet air depend on the turbine location, but include sodium, sulfur, chlorine and calcium. These impurities in the fuel and the air can lead to the deposition of alkali.
metal sulfates on the blade, resulting in the hot corrosion attack When the salt arrives on a surface already covered with a protective oxide, there is initially no reaction. In order for accelerated oxidation to occur, the protective oxide must be destroyed. This can happen in four distinct ways. The first is the mechanical disruption of the oxide by erosion, thermal cycling, and by elastic strain of the substrate putting the oxide in tension. A second method is by diffusion of sulfur through the oxide until chromium-rich sulfides form within the metal; later development of the external oxide, or its reformation if it is mechanically removed, is inhibited. The third method is dissolution (or fluxing) of the protective oxide by the salts, and finally during ignition, a local reducing environment may form due to incomplete burning of fuel. Such a reducing atmosphere can damage the protective surface oxide layer, especially in the presence of contaminants such as Na2SO4 and

cause initiate crack on the surface of blade. The sulfur diffuses inward and then reacts with chromium from the substrate to form chromium sulphides. As corrosion proceeds, and phase stability adjusts to changing chemistry, the sulphides are converted to complex unstable metal oxides and the sulfure thus released diffuses more deeply into the substrate where it forms more sulphides. This type features intergranular attack, sulfide particles and a denuded zone of base metal. Using an electron beam microanalyzer, it is found that discrete sulfide particles of chromium and titanium are present in a region depleted in these elements, below the scale. The surface scales consist of chromium oxide [9].

The SEM photograph of blade very clearly indicates high stresses along the blade axis resulting in a high density of 'w-cracks'. The sliding of grain boundaries continued to generate initial cracks. In the blades studied, the subsequent propagation of cracks is controlled by cyclic stresses. The region that has undergone these two phenomena 1-grain boundary sliding and 2-fatigue propagation is clearly visible.

Finally the presence of rafted γ' phase on the grain boundary under aging phenomena and diffuse elements such as S via surface crake are most important factor to failure of blade.

References

[1] Z. Mazur, Rafael Garcia-Illescas, Jorge Aguirre-Romano, Norberto Perez-Rodriguez, Steam turbine blade failure analysis, Engineering Failure Analysis 15 (2008) 129–141

[2] J. Safari, S. Nategh, On the heat treatment of Rene-80 nickel-base superalloy, Journal of Materials Processing Technology 176 (2006) 240–250

[3] T. Carter, Common failures in gas turbine blades, Engineering Failure Analysis 12 (2005) 237–247

[4] J.S. Houa, J.T. Guo, L.Z. Zhou, C. Yuan, H.Q. Ye, Microstructure and mechanical properties of cast Ni-base superalloy K44, Materials Science and Engineering A 374 (2004) 327–334

[5] M. Marx, H. Vehoff, Propagation of microcracks in single crystalline nickel-based superalloys: size effects on the crack opening, Materials Science and Engineering A 387–389 (2004) 511–515

[6] Z. Mazur, A. Luna-Ramı´rez, J.A. Jua´rez-Islas, A. Campos-Amezcua , Failure analysis of a gas turbine blade made of Inconel 738LC alloy, Engineering Failure Analysis 12 (2005) 474–486

[7] M.R. Khajavi, M.H. Shariat, Failure of first stage gas turbine blades, Engineering Failure Analysis 11 (2004) 589–597

[8] K.Mohammadi, A.K.Haghi, Journal of Material Processing Technology, In press, DOI:10.1016/j.jmatprotec.2007.11.273

[9] R.Viswanathan,An investigation of blade failure in combustion turbines,Engineering Failure Analysis 8(2001)493-511

Key Engineering Materials Vols. 385-387 (2008) pp 397-400
© (2008) Trans Tech Publications, Switzerland
doi:10.4028/www.scientific.net/KEM.385-387.397

Effect of Humidity on Fatigue Strength of Squeeze Cast Al Alloy

Y. Sofuku[1,a], N. Kawagoishi[1,b], M. Adachi[2],
K. Okutani[2] and Y. Maeda[1,c]

[1]Kagoshima University, 1-21-40 Korimoto, Kagoshima 890-0065, Japan

[2]Ube Industries LTD, 1978-96 Kogushi, Ube, Yamaguchi, 755-8633, Japan

[a]m0781032@mech.kagoshima-u.ac.jp, [b]hiro@mech.kagoshima-u.ac.jp,mail,mail,

[c]maro@mech.kagoshima-u.ac.jpmail

Keywords: Fatigue, Aluminum Alloy, Squeeze Cast, Humidity, Crack Initiation, Crack Propagation.

Abstract. Fatigue properties of a squeeze cast Al-Si-Mg alloy were examined under rotating bending and the effect of humidity on the crack initiation and propagation behavior was investigated in controlled humidity. The fatigue strength was decreased in high humidity (RH85%) in comparison with the one in low humidity (RH25%). Cracks initiated at the early stage of fatigue life from slip bands and eutectic Si particles in many cases and partially casting defects, and most of fatigue life was occupied by the growth life of a small crack regardless of humidity. The propagation of a crack were promoted by humidity, especially the growth rate of a crack larger than about 100 μm, which propagated in tensile mode, was strongly accelerated.

Introduction

Recently, aluminum die casting products have been widely used in engineering structures and mechanical components, including industrial machines, airplanes and automobiles, because of their excellent qualities such as high productivity, cost efficiency, recyclability and being light in weight. Moreover, aluminum die casting technology has been dramatically improved to produce high-quality castings, among which squeeze casting can achieve superb mechanical properties, derived from its capability to suppress porosity and refine microstructure [1, 2]. Application of squeeze cast has been increasing to a wide variety of products, which include large automobile parts such as cross members or heavy duty large wheels, which rapidly increased to achieve low fuel consumption.

In the present study, fatigue properties for squeeze cast Al alloy, Al-Si-Mg alloy were examined under rotating bending and the effect of humidity on the crack initiation and propagation behavior was investigated in controlled humidity.

Material and experimental procedures

Material used was an aluminum-silicon-magnesium casting alloy (JIS AC4CH). The chemical composition (wt. %) was 7.02 Si, 0.08 Fe, 0.37 Mg, 0.12 Ti and remainder Al. Material was squeeze cast by a vertical squeeze casting machine under the following conditions: (1) molten metal at temperature of 1050K and (2) injection speed between 50 mm/sec and 80 mm/sec. Then the castings were heat treated under T6 conditions (solution and aging treatment).

The microstructure of the alloy was shown in Fig.1, where the dendrite arm spacing (DAS) was about 20 μm. The mechanical properties of the alloy were 0.2% proof stress of 219.9MPa, tensile strength of 310.5MPa and reduction of area of 15.2%, respectively.

Fig. 2 shows the fatigue specimen. The fatigue test specimen was machined as shown in the figure, then slightly electro-polished by 40 μm to secure the direct surface observation using the plastic-replica method. The crack length was observed by the replica and measured in the circumferential direction of the specimen. The fatigue tests were carried out using the ONO type

rotating bending machine with 15 N·m capacity under 50 Hz repetition in controlled humidity of 25 and 85 % (RH, relative humidity).

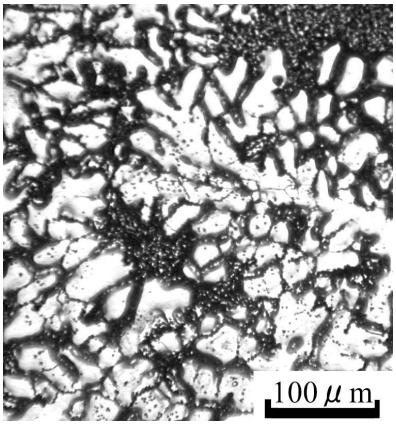

Fig.1 Microstructure

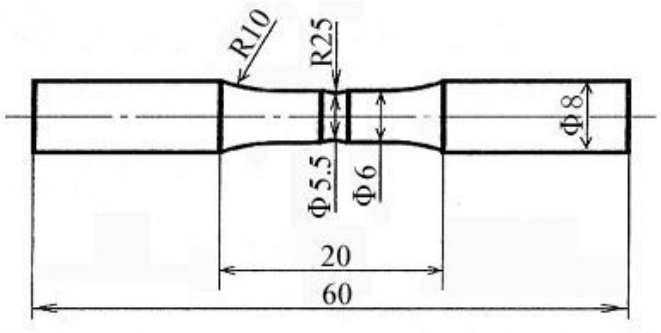

Fig.2 Fatigue specimen

Results and discussion

Fig. 3 shows the *S*-N_f curves (N_f: number of cycles to failure). Fatigue life was decreased obviously in high humidity.

Fig. 4 shows the typical crack propagation curves. In each stress level, fatigue cracks were found to start at the early stages of the fatigue cycle and many cracks joined in the propagation process regardless of humidity. The crack growth rate is higher in the crack smaller than about 100μm, which propagates in shear mode, in comparison with the larger crack, which propagates in tensile mode. As seen from the figure, in the process of propagation in tensile mode, the relation between the logarithm of crack length and the number of cycle was approximated by a straight line, meaning that the crack growth rate is proportional to the crack length. The effect of humidity on the fatigue life was marked in the crack propagation process, but not large in the crack initiation one. Therefore, it is important to know the crack growth rate for evaluation of fatigue life. In the following, the effect of humidity on the crack growth rate will be investigated by small crack growth law ($\mathrm{d}\ell/\mathrm{d}N \propto \sigma_a{}^n \ell$, n: constant) [3, 4], which is valid for evaluating the growth rate of a crack propagated under high stress levels. Because a crack in plain specimen propagates under high stress levels, the condition of small scale yielding is not satisfied, meaning stress intensity factor is not valid.

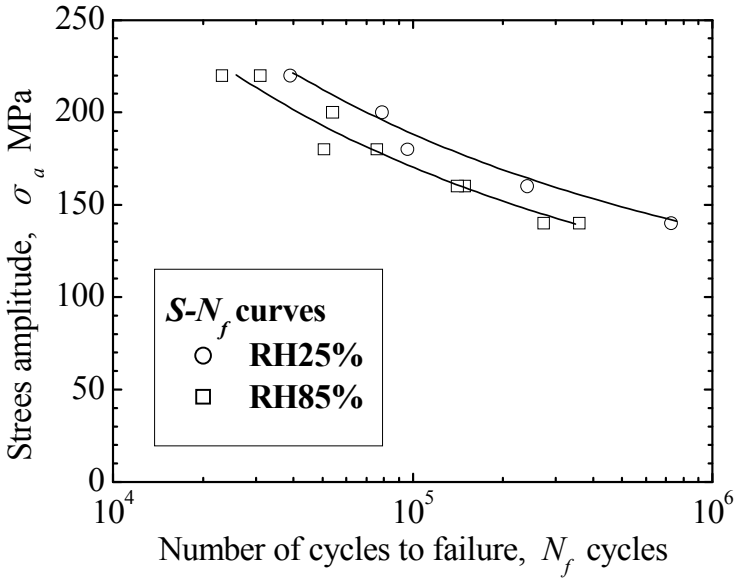

Fig.3 *S*-N_f curves

Fig. 5 shows the crack growth rate against for the term $\sigma_a{}^n\ell$. The crack growth rate can be evaluated by the law ($n \cong 5$) in both environments. The crack growth rate is higher about ~2 times in high humidity than in low one, corresponding to the decreasing rate of fatigue life due to high humidity. This large acceleration of crack growth is very significant, because the humidity of 85% is not a special case in practical use, especially in case of car wheels.

Fig. 6 shows the examples of crack morphology of specimens in both environments. Marks ↑ and ⇧ mean the fronts and the initiation site of a crack, respectively. In general, a crack initiated at not only slip bands in α phase but also the boundary between base metal and eutectic Si particles, segregated Si and small defects, though a crack initiated from surface slip bands in α phase in the figure. It is reported that, cracks initiated from corrosive pits in high humidity in many aluminum alloys [5]. However, no crack originated from corrosive pits and there is no difference in the morphology of a crack in both environments. The reason may be explained from that a crack of the present alloy initiated at the early stage of fatigue life even in low humidity as mentioned above, consequently the effect of humidity on the crack initiation was very small.

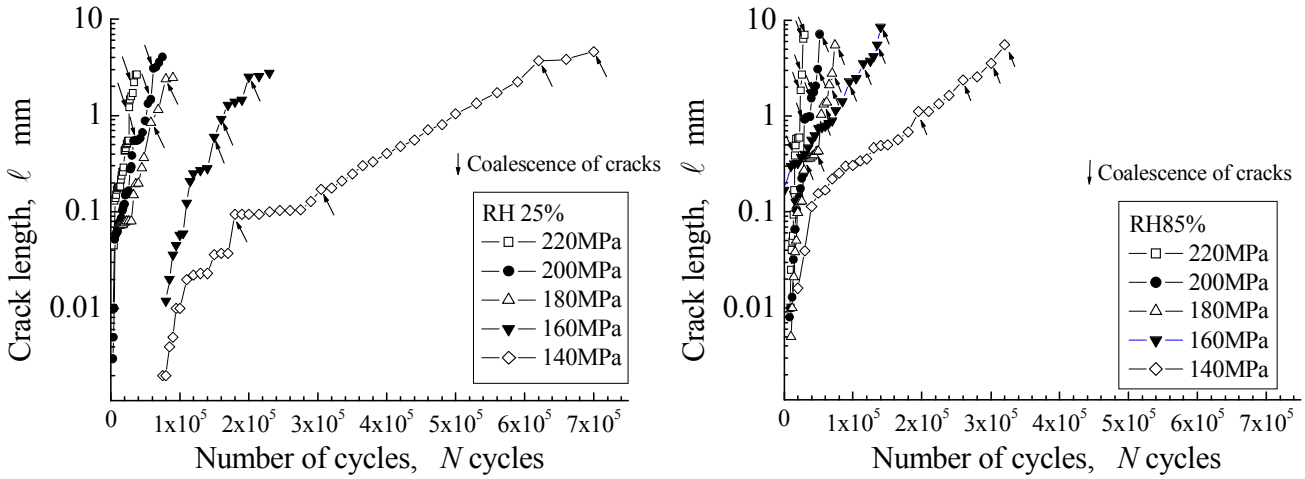

(a) RH25% (b) RH85%

Fig.4 Crack propagation curves

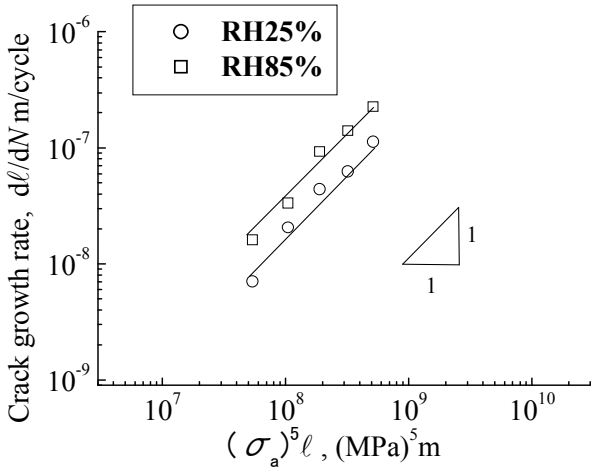

Fig.5 Crack growth rate against for the term $\sigma_a{}^n\ell$

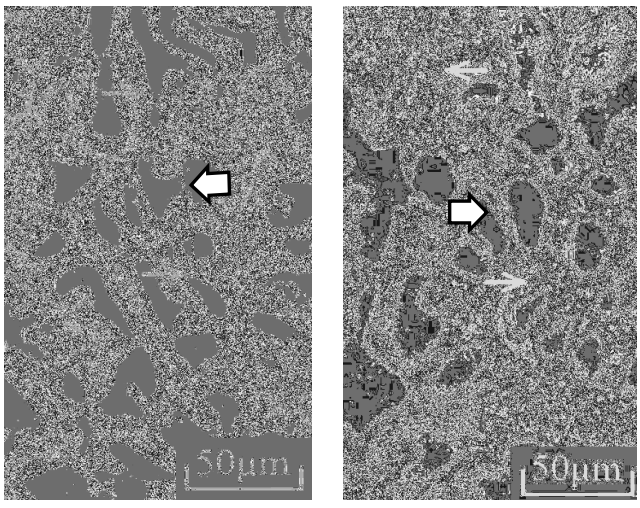

(a) RH25% (σ_a=180MPa) (b) RH85% (σ_a=200MPa)

(↑: Fronts of crack, ⇧: Initiation site of crack)

Fig.6 Morphology of crack (⟷ Axial direction)

Fig.7 shows the examples of fracture surfaces in both environments. Fracture surface was smoother in the high humidity than in the low one. However, intergranular cracks were not confirmed on the fracture surface even in the high humidity, though they were observed in many aluminum alloys, when humidity was high [5, 6]. These facts mean that the acceleration of crack growth in high humidity was caused by the decrease in the effect of roughness-induced crack closure. The reason for the smoothed fracture surface in high humidity can be explained as follows; A crack propagates in zigzag manner being affected by microstructures like a eutectic Si, segregated Si particles, grain boundary, etc, in the present alloy in general. On the other hand, when humidity is high, a crack propagates under large effect of tensile stress because of active-path corrosion type stress corrosion cracking, consequently the crack path becomes smoother.

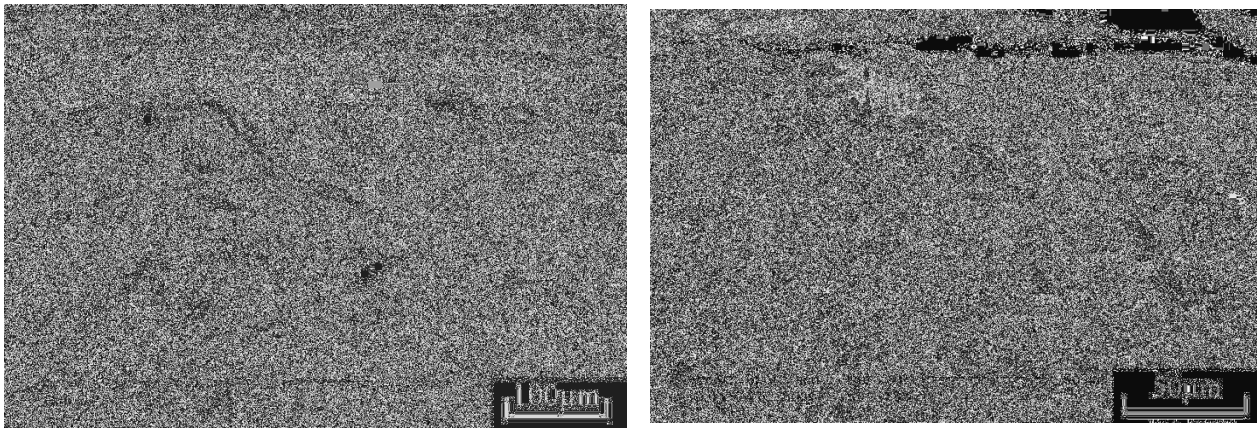

(a) RH25%

(σ_a=200MPa, N_f=7.9×10^{4}cycles)

(b) RH85%

(σ_a=220MPa, N_f=3.1×10^{4}cycles)

Fig.7 Fracture surfaces

Conclusions

Fatigue properties for squeeze cast Al alloy, Al-Si-Mg alloy were examined under rotating bending and the effect of humidity on the crack initiation and propagation behavior was investigated in controlled humidity (Relative humidity: 25%, 85%). Most of fatigue life was occupied by the growth life of a small crack regardless of humidity. Fatigue life was largely decreased by high humidity, though corrosive pits on specimen surface and intergranular cracks on fracture surface were not observed even in high humidity. Fracture surface was smooth when humidity was high.

Acknowledgement

The authors would like to acknowledge Mr. K. Susukino, for their generous support on experiment.

References

[1] N.Kawagoishi, H.Nisitani and T.Tsuno, Trans. Japan Soc. Mech. Eng., Vol.55 (1989), p.1733

[2] M. Adachi, Y. Waku, H. Iwai, T. Nishi and A. Yoshida, Jour. of Japan Institute of Light Metals, Vol.39 (1989), p.487

[3] Nisitani, Mechanics of Fatigue, ASME-AMD, Vol. 47, edited by T. Mura (1981), p.151

[4] N.Kawagoishi, H.Nisitani, T.Toyohiro, N. Yamamoto and T. Tsuno, Trans. Japan Soc. Mech. Eng., Vol.60 (1994), p.358

[5] J.A. Dunsby and W. Wiebe, Mater. Research Standard, Vol.8 (1969), p.15

[6] Haftirman, S. Hattori and T. Okada, Trans. Japan Soc. Mech. Eng., Vol.62 (1996), p.1140

Key Engineering Materials Vols. 385-387 (2008) pp 401-404
© (2008) Trans Tech Publications, Switzerland
doi:10.4028/www.scientific.net/KEM.385-387.401

Numerical Simulation and Experimental Investigation of the Failure of a Gas Turbine Compressor Blade

N. Nourbakshnia[1,a], S. Ziaei-Rad[1,b], A. Kermanpur[2,c], H. Sepehri-Amin[2,d]

[1] Department of Mechanical Engineering, Isfahan University of Technology, Isfahan 84156-83111, Iran
[2] Department of Materials Engineering, Isfahan University of Technology, Isfahan 84156-83111, Iran

a) nasibeh.n@nus.edu.sg , b) szrad@cc.iut.ac.ir, c) ahmad_k@cc.iut.ac.ir, d) navidsepehri@yahoo.com

Keywords: fracture, finite element method, fretting fatigue, stress intensity factor, compressor blade

Abstract

This paper is concerned with the premature failures occurred in the high pressure compressor section of the gas turbine of HESA power plant in Iran. Metallurgical and mechanical properties of the blade alloy were evaluated. Fractography investigations were carried out on the fracture surface of the blade roots using scanning electron microscopy. Stress and fracture simulations were conducted using ANSYS software in both 2D and 3D dimensions under centrifugal, aerodynamic and contact forces. The aerodynamic forces were evaluated using FLUENT software.

The results showed no metallurgical and mechanical deviations for the blade material from standards. SEM fractography showed different aspects of fretting fatigue including multiple crack initiation sites, fatigue beach marks, debris particles, and a high surface roughness on the edge of contact (EOC). The simulation results showed that there was a high stress gradient at the EOC of the blade which is one of the most significant characteristics of the fretting fatigue. Another analysis was performed to simulate the fracture by creating an initial crack on the EOC. The stress fields and stress intensity factors for modes I, II and III were evaluated along the crack front. The results indicated a strong stress intensity factor for mode I at the EOC.

Introduction

Fretting fatigue is responsible for a large number of service failures across a wide range of applications. For example wherever two or more turbine components are in tight contact, fretting fatigue becomes a relevant failure mechanism. Yoshimura and his co-workers evaluated the fretting fatigue life of titanium alloy dovetails by using stress singularity parameters [1]. They also used the finite element method analysis to show that there exists stress concentration and high stress gradient in the zone of crack initiation under work condition. Arrieta and his co-workers focused on identifying the driving factors for fretting damage on blade-disk attachment under real engine conditions and used a two-dimensional finite element contact model. They showed the high influence of contact pressure on the fretting fatigue fracture [2]. Bramhall was the first to investigate the size effect on the fretting fatigue and showed that there was a clear variation in fatigue life with contact size [3]. Nowell reviewed a number of recent developments, starting with attempts to apply multi axial initiation criteria to the fretting problem [4]. Golden and Calcaterra evaluated a fracture mechanics based crack growth life prediction methodology for dovetail fretting fatigue laboratory experiments. They considered contact loads and bulk stress calculated from finite element method as input to the stress and life analysis [5].

Experimental Materials and Procedures

The materials of the disk and blade were a low alloy steel and titanium alloy Ti-6%V-4%Al, respectively. Fractography investigations were carried out on the fracture surface of the blade roots by using scanning electron microscopy (SEM).

In order to evaluate the force conditions of the broken blades, finite element method and the commercial software ANSYS was used in both 2D and 3D. To consider the centrifugal force, the origin of coordinate system was located at the disk center and an angular velocity of 8500 rpm was applied to disk-blade structure. The contact forces were also simulated by using surface-to-surface contact elements at the edge of contact (EOC) between blade root and disk. The aerodynamic force applied on the blade was evaluated by software FLUENT. In this part of simulation, the vane movement was assumed zero and the blade velocity was considered as rω, where ω was the compressor rotating speed and r was the average distance of blade from disk center. The fluid was assumed to be compressible and viscose, and k-ε turbulence equation was applied for simulating its turbulence behavior.

Results and Discussion

Results of the macro- and micro-fractography for different broken blades are shown in figures 1 and 2, respectively. The position of the main crack initiation in the fracture surface and three distinct regions are shown in figure 1. The initiation point is located at the EOC between the blade and the disc in the dovetail region. Figure 2 shows details of the multiple cracks formed on the EOC, beach marks and radial lines in the region1 of the fracture surface. Also, many debris particles as an indication of wear were found on the EOC and in the mouth of cracks [6]. These are the main features of the fretting fatigue mechanism that is due to the bad contact condition. According to the beach marks, it can be concluded that the initiated micro cracks has propagated by the fatigue mechanism until the blade has fractured (region 3 in figure 1).

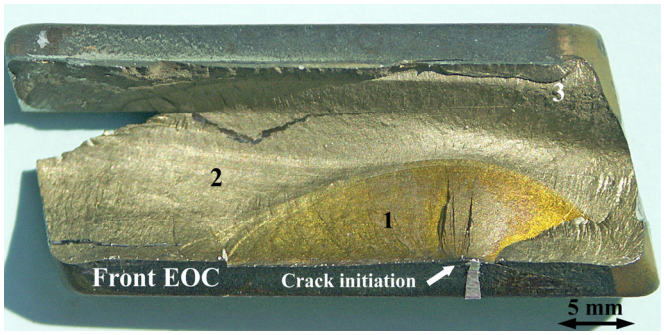

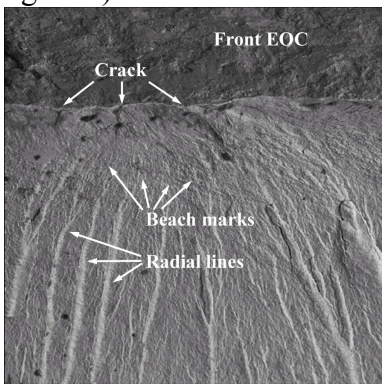

Fig.1 Macro-fractography of fracture surface of the blade. Fig.2 Micro-fractography of fracture surface

The stress distribution on the dovetail at 2D and 3D are shown in figures 3 and 4, respectively, where the stress results are in kPa. It can be easily seen that the stress value in the contact zone is more than the fretting fatigue stress threshold of Ti-6%V-4%Al which was reported about 200MPa [4], and can lead to the crack initiation at the point of most stress concentration. This point exactly corresponds to the point of crack initiation in the real blades.

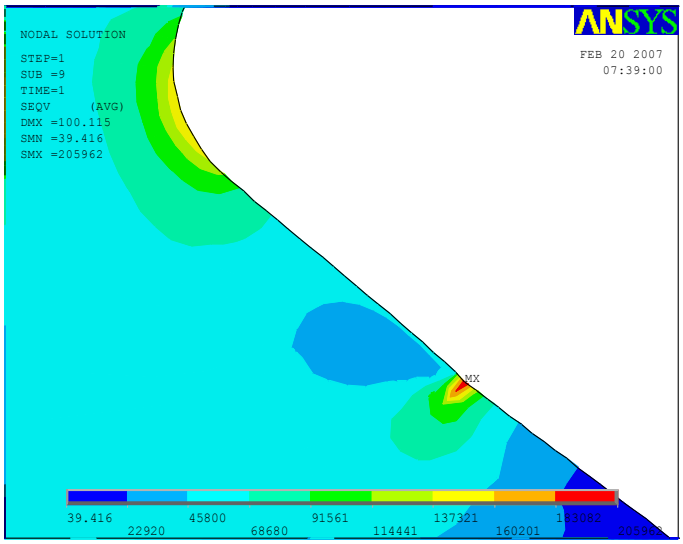

Fig.3 Simulated stress distribution at the EOC in 2D analysis

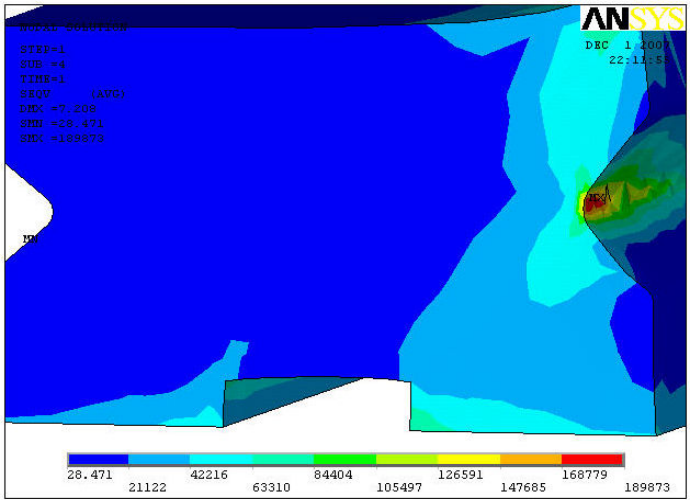

Fig.4 Simulated stress distribution at the EOC in 3D analysis

For fracture analysis, an initial crack was created at the EOC of the blade root and intensity factors were evaluated with the material toughness which was reported as $130MPa\sqrt{mm}$ by Yoshimura [1]. It must be mentioned that in fracture analysis, the elements at the crack tip must be singular elements to simulate the singular behavior of stress at the crack tip. Figure 5 shows the initial crack and singular mesh around the crack tip. Figure 6 illustrates the stress field around the crack. The length of crack was assumed to be 0.95 mm. The stress intensity factors calculated by the analysis are tabulated in Table 1. It can be noted that the stress intensity factor KI in Table 1 is more than the threshold stress intensity factor for Ti-6V-4Al.

Table .1 The values of KI, KII and KIII received from ANSYS

Stress intensity factor	**KI**	**KII**	**KIII**
Present calculated value	140.910	4.160	0.000
Test (Ref. [6])	130		

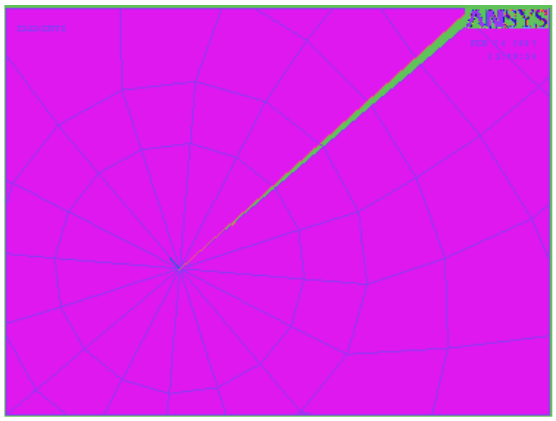

Fig.5 Singular elements around the initial crack.

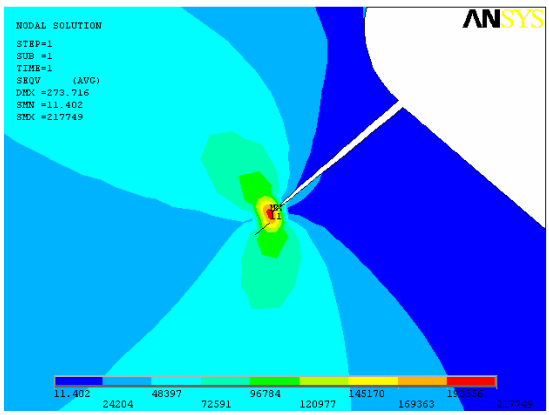

Fig.6 Simulated stress distribution around the crack at the EOC of the blade

It can therefore be concluded from the analysis that if a crack initiated at the dovetail of blade, it will propagate under the assumed force condition. Thus, one can estimate the stable fatigue fracture propagation by use of Paris law according to [7]:

$$\frac{da}{dN} = c(\Delta k)^m \ (mm/cycle) \qquad (1)$$

Where c and m are the empirical constants (c=2.66e-12 and m=4.23 for Ti-6%Al-4%V [7]). Substituting the numerical values in equation (1), and considering the angular velocity of the rotor, it can be predicted that the blade is broken about 4000 hour after crack initiation. This prediction is in a good agreement with the real life of the broken blades.

Conclusion

A finite element analysis was applied to find out the fracture mechanism of a compressor blade. All forces acting on the blade were simulated in 2D and 3D. It was shown that a high stress gradient and concentration at the EOC between the blade root and disk can lead to the crack initiation under fretting mechanism. A fracture analysis was also performed to predicting the blades life. The results showed no metallurgical and mechanical deviations for the blade material from standards. SEM fractography showed different aspects of fretting fatigue including multiple crack initiation sites, fatigue beach marks, debris particles, and a high surface roughness on the EOC. All of these experimental and simulation results introduces the *fretting fatigue* as the failure mechanism for the compressor blades, which is a direct result of unsuitable contact between the blade root and disk.

Refrences

[1] Yoshimura Toshihiko, Tao Hiroaki, Fukunaga Hideharu and Hattori Toshiko, Evaluating Fretting Fatigue Life of Titanium Alloy Dovetails by Using Stress Singularity Parameters, J. of Material Science Society of Japan , vol.40, No.6 ,41-46, 2003.

[2] Arrieta Hernan V., Wackers Patrick ,Van Ky Dang , Constantinescu Andrei , Maitournam Habibou, Modelling attempts to predict Fretting-Fatigue life on turbine components .

[3] Bramhall, R., Studies in Fretting Fatigue, D.Phil. thesis, University of Oxford, 1973.

[4] Nowell D., Recent Developments in the Understanding of Fretting Fatigue, Department of Engineering Science University of oxford.

[5] Golden P.J., Calcaterra J.R., A fracture mechanics life prediction methodology applied.

[6] Mazur Z., Hernandez-Rossette A., Garcia-Illescas R., Investigation of the failure of the L-0 blades, Engineering Failure Analysis 13,1338-1350, 2006.

[7] A. Kermanpur, H. Sepehri Amin, S. Ziaei-Rad, N. Nourbakhshnia, M. Mosaddeghfar, Failure Analysis of Ti6Al4V Gas Turbine Compressor Blades, Eng. Fail. Anal., (2008), doi:10.1016/j.engfailanal.2007.11.018.

Key Engineering Materials Vols. 385-387 (2008) pp 405-408
© (2008) Trans Tech Publications, Switzerland
doi:10.4028/www.scientific.net/KEM.385-387.405

Thermal Fatigue of Thermal Barrier Coatings by Atmospheric Plasma Spraying

Qi Hongyu[1,a], Ma Haiquan[2,b] , Li Xu [1,c] , Yang Xiaoguang [1,d], Shi Duoqi[1,e]

[1] School of Jet Propulsion, BeiHang University, Beijing China 100083

[2] China Academy of Space Technology, Beijing China 100094

[a]qhy@buaa.edu.cn, [b]mahaiquan@sina.com, [c]lixu0124@163.com, [d]yxg@buaa.edu.cn, [e]shidq@buaa.edu.cn

Keywords: Thermal barrier Coatings; Young's modulus; Thermal fatigue; Life prediction

Abstract. Turbine vanes and blades are the most intensively loaded elements in that they are subjected to a large variety of mechanical and high temperature loads. The thermal barrier coatings (TBCs) are widely used on different hot components of gas turbines, as blades and vanes, for both, power engineering as well as aeronautical applications. Currently, two methods are used for depositing TBCs on substrate, which are plasma spray (PS) and electron beam-physical vapor deposition (EB-PVD). A typical TBCs system consists of two thin coatings, including a ceramic coating and a metallic bond coat. Despite considerable efforts, the highly desirable prediction of their life time is still a demanding task. The PS coating was focused on in this work. Firstly, the TBCs systems are multiplayer material systems. The material properties are not easily determined, such as Young's modulus of the top-coating of TBCs. Using the resonant frequency and the composite beam theory, the Young's modulus of APS TBCs was gotten under from room temperature to 1150°C. Then using a commercial finite-element program, the model geometry is that of a cylinder specimen. The interface region between bond coat and top coating is modeled and meshed with a sinusoidal geometry. The temperature was designed and cycled over a range from room temperature to 1050°C. The force-air-cooling was designed to form temperature gradient across the thickness of TBCs. Finally, the fatigue life of TBCs was predicated. The maximum relative error is 20.1%.

Introduction

Nowadays, the main turbine-producing manufacturers provide an initial gas temperature level of 960-1100°C for basic service and 1065-1300°C for peak service. In military aircraft turbine, the temperature of gas rises to 1600°C [1]. The application of thermal barrier coatings (TBCs) is an effective way to protect aero-engine blades from hot gas. Over the last 5-8 years, the failure mechanisms of atmospheric plasma spraying (APS) manufactured domestically have been analyzed. The spallation and the buckling are the main failure mode. But the potential of TBCs cannot be fully used due to the lack of a reliable life prediction method. Most of life prediction models are based on NASA's initial works on phenomenological and macroscopic approaches [2]. The parameters of the model are fitted from data generated in a macroscopic way. The stress-strain data at the bond-coat/top-coating interface are obtained from the numerical calculation. There are many material data of TBCs system to be tested. One of the most important parameters is the Young's modulus of the top coating.

Many methods of testing Young's modulus such as nano-indentation, direct tension and beam-bend testing have not ability to test the Young modulus under elevated temperature [3, 4]. The frequency-response testing is chosen to test it under high temperature in this work.

The work reported here is arranged as follows. First, one method is chosen to test the Young's modulus of the top coating under high temperatures. Using the materials data, the stress-strain at the interface are obtained by finite element method. Finally, the predictive results of APS-TBC are demonstrated against existing APS-TBC thermal fatigue life data.

Materials and methods

There are many methods of testing the Young's modulus of TBCs system under room temperature, such as nano-indentation, beam-bending testing. Because of the thin and brittle of the top coating, it is difficult to measure the Young's modulus under elevated temperature *in situ*.

According to the resonant frequency and the composite beam theory, the equipment was manufactured to test the resonant frequency of the TBC system. Then the Young's modulus of the top coating was calculated. The schematic figure of the device was shown in Fig.1. The substrate is a Cr18Ni9Ti stainless steel and was prepared by 120*mm*×10*mm*×1*mm*. The bond coat is a CoNiCrAlY material, about 150*um* thick. The TBCs comprises an air-plasma-sprayed (APS) yttria-stabilized zirconia about 250*um* thick. The specimens were manufactured by METCO-7M equipment.

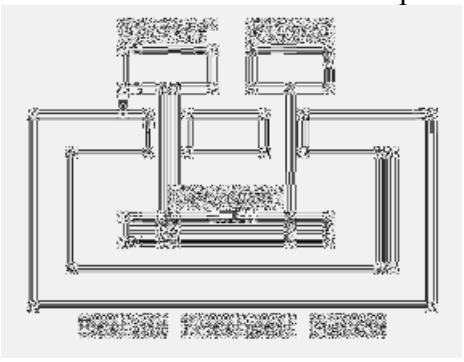

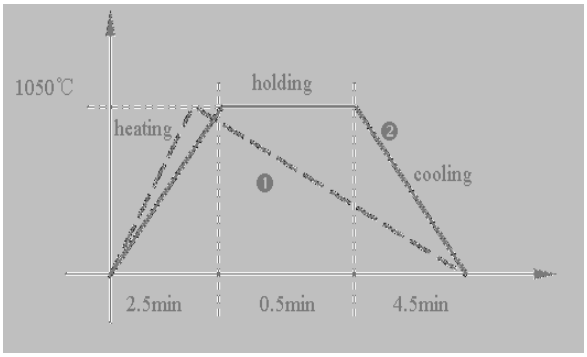

Fig.1 A schematic of equipment for Young's modulus Fig.2 Thermal cycle used in experiment and simulation

Three specimens with TBCs were fabricated. The resonance frequencies of specimens were obtained under room temperature to 1150°C .The average Young's modulus of top coating was showed in Table1.

Table 1 Young's modulus under different temperatures for top coating

Temperature/°C	20	100	200	300	400
Young's modulus/GPa	62.5	59.6	55.7	50.3	44.9
Temperature/°C	600	800	900	1050	1150
Young's modulus/GPa	29.8	22.2	21.5	19.8	18.6

In order to simulate the structure of the vane and take into account of the curvature, the cylindrical specimens were chosen which the force-air-cooling was designed to form temperature gradient across the thickness of TBCs. The substrate of the specimen is a directional solidification alloy DZ40M. Atmospheric Plasma Spraying TBCs, in which the bond coating is made up of Ni22Cr10A11.0Y, and top coating is 8%Y_2O_3-ZrO_2, with 0.115*mm* and 0.25*mm* in thickness respectively .

The oxidation of bond coat and thermal cyclic load play an important role in failure of TBCs. To take into account of oxidation, the thermal load should include suitable holding time. The thermal cycle was shown in Fig.2. There are two kinds of load case. The first load-case has 2*min* heating and 240*min* cooling. The second load-case consists of a 2.5*min* heating from room temperature to 1150°C, a holding time of 0.5*min*, and a cool-down period 4.5*min*.The research includes 3 specimens and the thermal fatigue life are 430,350,and 330 cycles respectively

Thermal Fatigue Life Analyses

The numerical simulation in this work has been made cylindrical geometry with an internal diameter of 14*mm* and external inner diameter of 16*mm*. The length of specimen is 80*mm*.In order to simulate the interface of TGO and analyze accurately the stress-stain of TBCs system under cyclic load, the sinusoidal interface was designed and meshed.

Establishing the axial symmetry FEM model, the finite element mesh used is shown in Fig.3. It consists of 2142 nodes and 2020 axially symmetric elements. The meshing is very fine in the region of TGO (bond coat/top coating-interface) with element sizes of about 1*um*.The FEM model is

constrained in the *y*-direction on axis in order to simulate a full cylinder. The nodes at *x*=0 are constrained in the *y*-direction, nodes on top of model at *x*=2*mm* are allowed to move, but the movement is constrained such that all modes must have the same displacement.

The material properties of top coating used in the simulation were mostly taken from literature. But the Young's modulus was taken from the measurement in this work. The classic elasticity-plasticity theory was used. According to the literature on TBCs, the cooling stage of specimen was paid great attention. The failure mechanism of TBCs results from the heat-mismatch. During cooling stage, the residual stress of TBCs occurs. The stress state of interface (peak, off-peak, valley) was analyzed to obtain the parameters of thermal fatigue life model.

The TBCs under thermal cyclic load can lead to distinctly different failure modes, but it is generally acknowledged that TBCs life is governed by a sequence of crack nucleation, propagation and coalescence that occurs prior to final failure by large-scale buckling and spallation. For failure modes of the buckling and spallation, the axial stress is compressive stress and the radial stress is tensile stress [6, 7]. For the FEM simulation of TBCs under thermal fatigue shown in Fig.5, the compressive stress at axial direction result at "peak" during cooling. The tensile stress at radial direction results at "peak". For at "off-peak" and "valley", the stress state can't lead to the failure. So the stress-strain state at "peak" should be considered as the important data for predicted life of thermal fatigue

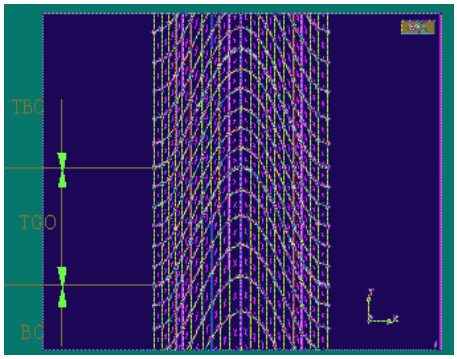

Fig.3 Geometry and meshing of the used FEM model

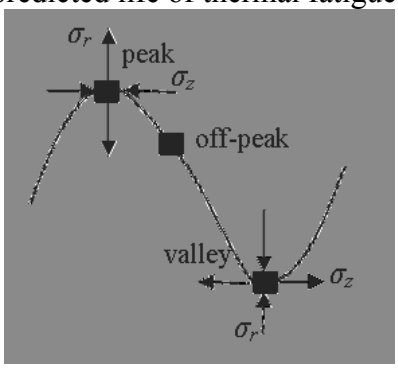

Fig.4 A stress state at the sinusoidal interface

According to the NASA report on TBCs, the following fatigue life model was chosen:

$$N = \left[\left(\Delta\varepsilon_{f0} / \Delta\varepsilon \right) \left(1 - \delta / \delta_c \right)^c + \left(\delta / \delta_c \right)^c \right]^b \tag{1}$$

The b is 7.64, and $\Delta\varepsilon_{f0}$ was a constant, with its value is 0.016mm/mm, c is 1.0, the calculated width of oxidation coating δ_c was 23.28um [8].

According to the analysis of some literatures, the location of the TBCs failure lies in the interface between the bond coating and top coating. The location of failure also occurs at interface in this work. In other words, the buckling and spallation is at the "peak" of the sinusoidal interface. On the other hand, the strain range in Eq.1 was taken as axial strain. For the effect of the radial strain range, that the existence of the radial strain can accelerate the tendency of failure.

Above all, the parameters of the Eq.1 for the TBCs life model have been obtained. Using the Eq.1, the fatigue life can be calculated under constant thermal-cyclic load. To predict the fatigue life under multi-level thermal load, cumulative damage theory was chosen.

The thermal fatigue life was predicted by the cumulative damage model. The thermal lives were listed in Table.2, testing and predicted lives respectively. The maximum relative error is only 20.1%. But the number of data is not enough. The reliability of the fatigue model needs to be tested in the future work

Table 2 the testing data and predicated life

Testing data	Predicated life	Relative error
430	358	20.1%
350	358	2.26%
330	358	7.82%

Conclusion

The thermal fatigue life model was experimentally and theoretically investigated. The APS coating was chosen. The material data under high temperature of top coating were measured and the stress-strain state at interface of TBCs was simulated. The following conclusions were gotten:

Using the resonant frequency and the composite beam theory, the Young's modulus of top coating for under the temperatures from room temperature to 1150°C were gotten, from 62.5GPa to 18.6GPa.

The cylindrical specimens with TBCs were manufactured. The sinusoidal interface was modeled by FEM. The stress-strain at interface of TBCs was simulated under the transient temperature load as the boundary condition. The experiment and predicated lives of the coating were analyzed. The maximum relative error is only 20.1%.

Reference

[1] J. Rosler, M. Baker: Acta Mater. Vol.49 (2001),p.3659

[2] F. Traeger, M. Ahrens.: Materials Science and Engineering.A358 (2003),p.255

[3] J.A. Thompson: Acta. Mater. Vol.49 (2001),p.1565.

[4] Qian Lihe. Shijie Zhu:Surface and Coatings Technology. Vol. 173 (2003), p.178

[5] Zhou Lizhu: *Measurement of Young's modulus and damage inspection techolongy for Thermal Barrier Coatings*. (BeiHang University Thesis 2007)

[6] M. Caliez, J.-L. Chaboche:Acta Materialia. Vol.51 (2003),p.1133

[7] A.G. Evan,D.R. Mumm:Progress in Materials Science.Vol.46 (2001),p.505

[8] Qi Hongyu: *Mechanical properties and thermal fatigue for thermal barrier coatings*. (BeiHang University Thesis 2004)

Key Engineering Materials Vols. 385-387 (2008) pp 409-412
© (2008) Trans Tech Publications, Switzerland
doi:10.4028/www.scientific.net/KEM.385-387.409

A comparison of two direct methods of generalized stress intensity factor calculations of bi-material notches

Jan Klusák [1,a], Tomáš Profant [2,b] and Michal Kotoul [2,c]

[1] Institute of Physics of Materials, Academy of Sciences of the Czech Republic, Žižkova 22, 616 62, Brno, Czech Republic

[2] Institute of Solid Mechanics, Mechatronics and Biomechanics, Faculty of Mechanical Engineering, Brno University of Technology, Technická 2, 616 69, Brno, Czech Republic

[a]klusak@ipm.cz, [b]profant@fme.vutbr.cz, [c]kotoul@fme.vutbr.cz

Keywords: Generalized stress intensity factor, numerical calculation, bi-material notch.

Abstract. The study of bi-material notches is becoming a topical problem as they can model geometrical or material discontinuities efficiently. Assessing the conditions for crack initiation in bi-material notches makes it necessary to calculate the generalized stress intensity factors *H*. In contrast to the determination of the *K* factor for a crack in an isotropic homogeneous medium, for the ascertainment of a generalized stress intensity factor (GSIF) there is no procedure incorporated in the calculation systems. The calculation of these fracture mechanics parameters is not trivial and requires certain experience. Nevertheless, the accuracy of the *H*-factor calculation directly influences the reliability of the assessment of the singular stress concentrators. Direct methods of the estimation of *H* factors usually require choosing the length parameter entering into the calculation. Two types of direct methods of calculating the GSIFs are presented, tested and mutually compared. Recommendations for reliable estimation of *H* factors are suggested.

Introduction

Failures in constructions usually start in the vicinity of a geometrical or material discontinuity. The existence of such places leads to high stress concentrations and consequently to crack initiation. Especially if material properties change in step or the geometry contains sharp notches, the stress field around such concentrators exhibits singular distribution. Generally, by using the model of a bi-material wedge it is possible to analyse many construction points such as sharp notches in both homogeneous and non-homogeneous materials, the edges of protective coatings, sharp notches with their vertex at the bi-material interface, free edge stress singularity or sharp material inclusions. The basic assumptions of the paper are the validity of linear elastic fracture mechanics, a sharp notch radius $R \to 0$, and the interface of a welded type (ideal adhesion).

Assessing the conditions for crack initiation in bi-material notches makes it necessary to calculate the generalized stress intensity factors *H*. In contrast to the determination of the *K* factor for a crack in an isotropic homogeneous medium, for the ascertainment of a generalized stress intensity factor GSIF there is no procedure incorporated in the calculation systems. The calculation of these fracture mechanics parameters is not trivial and requires certain experience. Nevertheless, the accuracy of the *H*-factor calculation directly influences the reliability of the assessment of the stress concentrators.

Bi-material notch

The model of a bi-material notch is suitable to simulate a number of construction points from which a failure is initiated. In the case of layered or fibre composite locations where the layers or fibres touch the surface of the composite body the singular stress concentrations occur. The singular stress distribution can be derived on the basis of Airy stress functions in the form of Williams` expansion

[1]. In most of the geometrical and material configurations of a bi-material notch there are two terms of the expansion with the real stress singularity exponents p_1 and p_2 in the interval (0; 1). Contrary to a crack in a homogeneous material, the exponents differ from ½ and, furthermore, each singular term includes both normal and shear mode of loading, see [2] for detail. Then the singular stress components can be written in the polar coordinates:

$$\sigma_{mij} = \frac{H_1}{\sqrt{2\pi}} r^{-p_1} F_{ij1m} + \frac{H_2}{\sqrt{2\pi}} r^{-p2} F_{ij2m}\,, \tag{1}$$

where for $\{i, j\} = \{r, \theta\}$ and for each singular term $k = 1, 2$:

$$F_{rrkm} = (2-p_k)(-a_{mk}\sin((2-p_k)\theta) - b_{mk}\cos((2-p_k)\theta) + 3c_{mk}\sin(-p_k\theta) + 3d_{mk}\cos(-p_k\theta))$$

$$F_{\theta\theta km} = (p_k^2 - 3p_k + 2)(a_{mk}\sin((2-p_k)\theta) + b_{mk}\cos((2-p_k)\theta) + c_{mk}\sin(-p_k\theta) + d_{mk}\cos(-p_k\theta))$$

$$F_{r\theta km} = (2-p_k)(-a_{mk}\cos((2-p_k)\theta) + b_{mk}\sin((2-p_k)\theta) + c_{mk}\cos(-p_k\theta) - d_{mk}\sin(-p_k\theta))$$

The subscript m differentiates the materials 1 and 2 where the stresses are determined. The values H_k are the generalized stress intensity factors that follow from the numerical solution of the studied geometry with given materials and boundary conditions [2], [4]. Numerical approaches to the calculation of GSIFs have a varying level of difficulty and accuracy. In the following paragraphs the direct methods based on the mean value of the tangential stress and the mean value of the generalized strain energy density factor are described.

Direct methods

Direct methods compare the results of some appropriate variable from a numerical solution with its analytical representation.

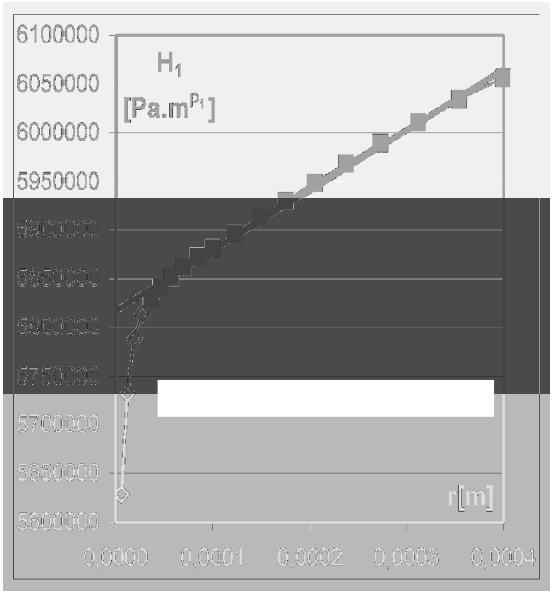

Fig.1 Extrapolation of H_1 into the tip of the notch ($r = 0$)

Tangential stress. The tangential stress $\sigma_{\theta\theta}$ is used here as the appropriate variable for comparison. If the stress distribution is described by a combination of H_1 and H_2, it is necessary to solve the system of two equations. To achieve this, the values of $\sigma_{\theta\theta}$ following from the finite element method are determined for two different angles θ_1, θ_2. Then knowing the analytical relations for $\sigma_{\theta\theta}$ (1) we solve the system of equations for H_1 and H_2:

$$\begin{bmatrix} r^{-p_1}F_{\theta\theta 1m}(\theta=\theta_1) & r^{-p_2}F_{\theta\theta 2m}(\theta=\theta_1) \\ r^{-p_1}F_{\theta\theta 1m}(\theta=\theta_2) & r^{-p_2}F_{\theta\theta 2m}(\theta=\theta_2) \end{bmatrix} \begin{bmatrix} H_1 \\ H_2 \end{bmatrix} = \begin{bmatrix} \sigma_{m\theta\theta}(r,\theta_1) \\ \sigma_{m\theta\theta}(r,\theta_2) \end{bmatrix} \tag{2}$$

The valid values of H_1, H_2 are then determined by an extrapolation of the solutions (2) into r=0, see Fig. 1 illustrating the extrapolation of the value H_1.

Strain energy density factor. Similarly, the values H_1 and H_2 can be determined from the mean value of the strain energy density factor (SEDF). The mean value is evaluated over a distance d as:

$$\overline{\Sigma_m} = \frac{1}{d}\int_0^d \Sigma_m \mathrm{d}r = \frac{1}{8d\mu_m} H_1^2 \left(\frac{d^{2-2p_1}}{2-2p_1} U_{1m} + \frac{d^{2-2p_2}}{2-2p_2} \Gamma_{21}^2 U_{2m} + \frac{d^{2-p_1-p_2}}{2-p_1-p_2} 2\Gamma_{21} U_{12m} \right), \tag{3}$$

and is used in order to eliminate the dependence of SEDF on the polar coordinate r which occurs in the case of the bi-material notch. The value of d has to be chosen considering the failure mechanism. For example, for the brittle fracture d relates to a grain size, while for the fatigue loading d can be chosen as the plastic zone size. The functions U are defined as follows:

$$U_{1m} = [(F_{rr1m}^2 + F_{\theta\theta 1m}^2)(k_m + 1) + 4F_{r\theta 1m}^2 + 2F_{\theta\theta 1m}F_{rr1m}(k_m - 1)]$$
$$U_{2m} = [(F_{rr2m}^2 + F_{\theta\theta 2m}^2)(k_m + 1) + 4F_{r\theta 2m}^2 + 2F_{\theta\theta 2m}F_{rr2m}(k_m - 1)]$$
$$U_{12m} = [(F_{rr1m}F_{rr2m} + F_{\theta\theta 1m}F_{\theta\theta 2m})(k_m + 1) + 4F_{r\theta 1m}F_{r\theta 2m} + (F_{\theta\theta 1m}F_{rr2m} + F_{\theta\theta 2m}F_{rr1m})(k_m - 1)]$$

where $k_m = (1-\nu_m)/(1+\nu_m)$ holds for plane stress and $k_m = (1-2\nu_m)$ for plane strain, μ_{m} is the shear modulus.

Here the two unknown parameters are calculated from the two following conditions. First the ratio $\Gamma_{21}=H_2/H_1$ is gained from the numerically ascertained angle θ_0 of the minimum of the mean value of the SEDF $\overline{\Sigma_m}$. For the minimum of $\overline{\Sigma_m}$ the condition of the first derivation equal to zero must be satisfied:

$$\frac{d^{2-2p_1}}{2-2p_1}\frac{\partial U_{1m}}{\partial\theta} + \frac{d^{2-2p_2}}{2-2p_2}\Gamma_{21}^2\frac{\partial U_{2m}}{\partial\theta} + \frac{d^{2-p_1-p_2}}{2-p_1-p_2}2\Gamma_{21}\frac{\partial U_{12m}}{\partial\theta} = 0\,. \tag{4}$$

From the two possible solutions Γ_{21} to the quadratic equation (4) we take only one that returns positive value of the second derivation, and thus it implies the minimum.

Finally, knowing the ratio $\Gamma_{21}=H_2/H_1$ the value of GSIF H_1 is determined as:

$$H_1 = \left[\frac{1}{\overline{\Sigma_m}8d\mu_m}\left(\frac{d^{2-2p_1}}{2-2p_1}U_{1m} + \frac{d^{2-2p_2}}{2-2p_2}\Gamma_{21}^2U_{2m} + \frac{d^{2-p_1-p_2}}{2-p_1-p_2}2\Gamma_{21}U_{12m}\right)\right]^{\frac{-1}{2}}. \tag{5}$$

The value $\overline{\Sigma_m}$ results from the numerical solution. The value of the coefficient H_2 is determined reciprocally from: $H_2=\Gamma_{21}H_1$.

Numerical example

The numerical study is performed on the rectangular bi-material notch loaded as shown in figure 2.

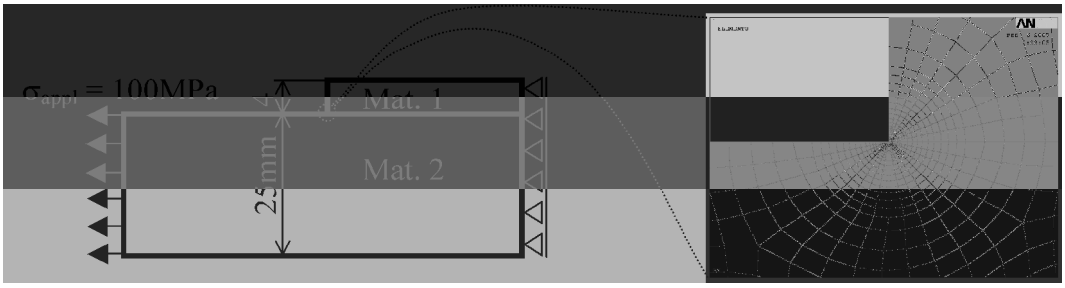

Fig.2: Rectangular bi-material wedge used in the numerical example, a detail of a FEM mesh.

Within the numerical study the methods of the calculation of GSIF were tested for a varying combination of the material components expressed by Young`s moduli. The results of both presented methods are compared. Figure 3 shows the dependence of the values of GSIFs H_1 and H_2 on the ratio of the moduli $E_1/E_2 \in \langle 0.0125;\ 10\rangle$. Note that for the ratios E_1/E_2 greater than 12 there is no singularity for the studied geometry, i.e. only non-singular terms occur in the stress distribution relations.

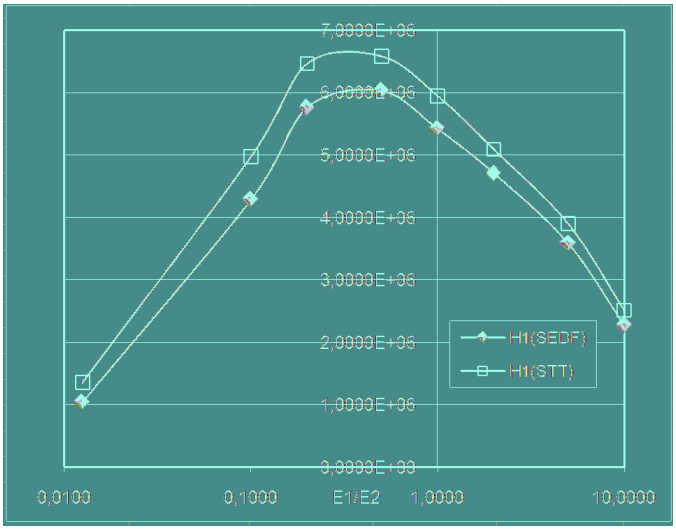

Fig. 3: Values of the generalized stress intensity factors H_1, H_2 gained from the mean value of the generalized strain energy density factor (SEDF) and tangential stress (STT).

Conclusions

The results of GSIFs ascertained by means of the two presented direct methods on the basis of two variables match well each other. Both methods provide reliable input parameters for the assessment of composite structures. The advantage of the direct methods is that they can be easily used with the standard finite element calculation systems. The method gaining GSIFs in two steps – from the supposed angle of potential crack initiation and from the mean value of the particular variable – can be easily programmed and thus automated. The two-step approach described here by means of the mean value of the generalized SEDF can be analogically derived for the mean value of tangential stress as well. The length parameters entering into the calculations as averaging distances are connected with the plastic zone size (in case of fatigue) or with a grain size of material (in case of brittle fracture). Further ahead, this distance will be specified by means of the method combining the application of the reciprocal theorem (Ψ-integral) and FEM that does not require entering any length parameter and is capable to extract the near-tip information directly from the far-field deformation where the numerical fields are more accurate. The latter method can be readily applied to bi-materials composed of orthotropic materials components. Note that for the final evaluation of the bi-material notch it is further necessary to determine the critical applied stress on the basis of critical values of the generalized stress intensity factors. These approaches are described within the suggestion of the stability criteria, see e.g. [2].

Acknowledgements

The authors are grateful for support through the Research project of the Academy of Sciences of the Czech Republic AVOZ20410507 and the project of the Czech Science Foundation 101/08/0994.

References

[1] M.L. Williams: Bull. Seismol. Soc.Amer., 49 (1959), p. 199–204.

[2] J. Klusák, Z. Knésl, L. Náhlík: Engineering Mechanics, No. 6 (2007) p. 409–422.

[3] P.D. Hilton, G.S. Sih: In: *Mechanics of Fracture – Methods of Analysis and Solutions of Crack Problems*, by G. C. Sih, Noordhoff International Publishing, Leyden, p. 426-477, (1973).

[4] D.R.J. Owen, A.J. Fawkes: *Engineering Fracture Mechanics: Numerical Methods and Applications*. Pineridge Press Ltd, Swansea, (1983).

Key Engineering Materials Vols. 385-387 (2008) pp 413-416
© (2008) Trans Tech Publications, Switzerland
doi:10.4028/www.scientific.net/KEM.385-387.413

Welding behavior analysis of stiffened stainless steel structure

Hong LI [1,a] and Huilong REN [2,b]

[1]School of Civil Engineering, Harbin Engineering University, Harbin 150001,China

[2]School of Shipbuilding Engineering, Harbin Engineering University, Harbin 150001,China

[a]leeh2005@sohu.com, [b]renhuilong@263.net

Keywords: elastic-plastic-model, temperature field, residual strains and stresses, fatigue analysis, FEM

Abstract. Welding residual plastic strains and residual stresses are the product of complicated nonlinear behaviors of the structures during welding. The residual strains and stresses for stiffened stainless steel structure and welding fatigue analysis are studied in this paper. The three-dimensional transient temperature field is analyzed by FEM first. Doing the welding experiment for fundamental model is to verify the numerical results, the infrared thermograph is used to follow and record the whole process. The results of FEM are supported by experimental data. Then, the elastic-plastic-model is established to analyze the residual strains and stresses. Based on the stresses, loading and fatigue factors, according to Miner fatigue damage law, some fatigue behaviors such as fatigue life and remaining life are obtained.

Introduction

Welding is a fundamental manufacturing technique used to join metal components. The welding process has always played a major role in industrial production, especially in the automotive, maritime and aerospace industries. Due to highly localized transient heat input, considerable welding residual stresses and deformations (welding distortion, welding shrinkage, welding warpage) occur during and after welding[1]. Despite many advantages, welding has some process-specific disadvantages: thermal expansion and shrinkage, micros structural transformations, residual stresses and component distortions developed. All, of which, need to be controlled. Furthermore, based on the nonuniform welding operations and the inner lacunas of the materials, some tiny cracks maybe come forth in the welded region. They can lead the welded structure to fatigue failure under cycle loads. So the study on welding behavior is essential.

The distribution of the temperature field in the welded region must be calculated first. According to the results of temperature, welding residual plastic strains and stresses of stiffened stainless steel structure are analyzed by thermal-elastic –plastic FEM in this study. Then, some fatigue behaviors such as fatigue life and remaining life are obtained.

Experiment and Temperature Field Simulation

A fillet welding experiment followed by infrared thermograph is done, and a three-dimensional transient temperature field is analyzed by FEM. The heat source is modeled as a moving heat flux

with a Gaussian distribution [2]. The material is Avesta2205 double phase stainless steel. In the process of analysis, the temperature-dependent properties of stainless steel and enthalpy are considered. When it is assumed that the heat source moves at a constant speed along a straight line, the temperature profile seen from the heat source will become quasi-stationary [3]. The comparison of calculation results with experimental data is shown as Fig.1.

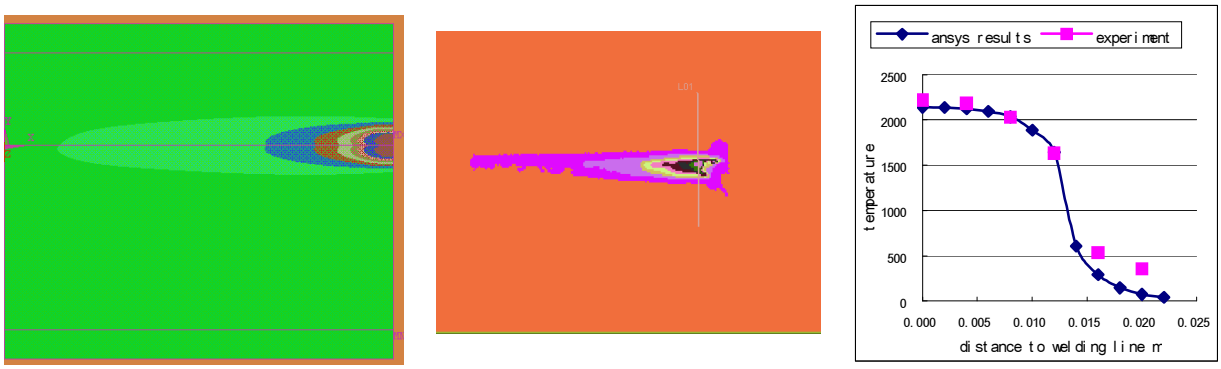

(a) result of ansys (b) result of experiment (c) comparison of temperature

Fig.1 Comparison between ansys and experiment

In the Fig.1(c), the path along transverse coordinate is following the straight line perpendicular to welding line in Fig.1 (b). The simulation results have been supported by the experimental data that are got by infrared thermograph.

Welding-induced Residual Strains

The model of complicated stainless steel structure is shown as Fig.2. The welding conditions are the same as the experiment of the fillet welding. The residual strains and stresses of the structure are calculated by thermal-elastic –plastic FEM.

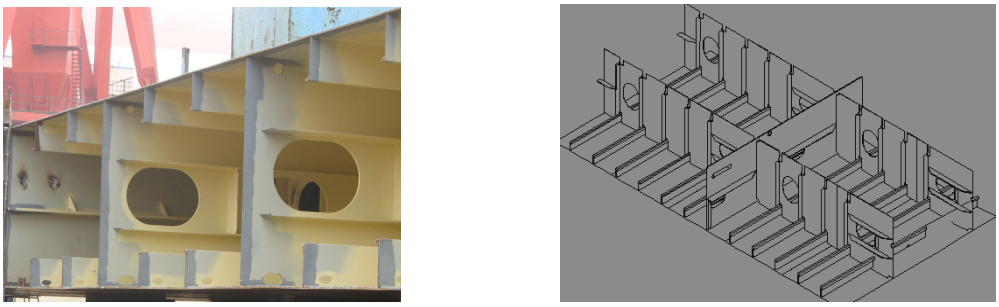

(a) actual model (b) simulation model

Fig.2 The models of ship sides

Furthermore, the distortions of the stiffened stainless steel structure are simulated. The shrinkages of ship sides are shown as Fig.3.

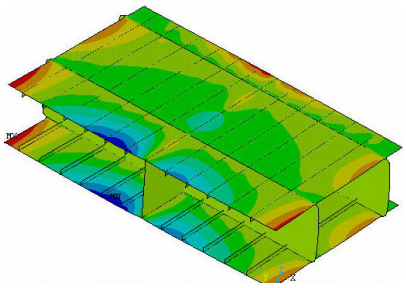

(a) longitudinal shrinkage

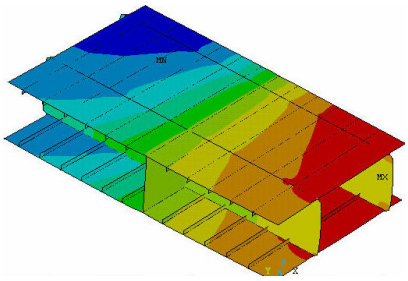

(b) transverse shrinkage

Fig.3 The deformation of ship sides

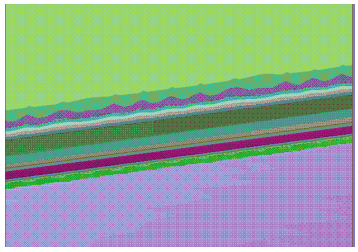

Fig.4 Stress field near welding line

It is got that at the edge of the structure the deformation is distinct, and it is repressed where there is stiffened plate.

Residual Stresses and Fatigue Analysis

The distribution of stress and strain field in the structure is changed following the moving of heat source. The relationship between stress and strain is nonlinear [4, 5]. In the process of analysis, the properties of material, such as Young's module and yield stress, are variable with temperature. The yield properties of material obey the Mises yield rule.

The equilibrium equation of forces in the welded region is satisfied

$$\sigma_{ij,j} = 0 \tag{1}$$

Where, σ_{ij} are the components of stresses, which include thermal stresses.

The thermal strains are expressed as

$$\varepsilon_{ij}^{T} = \alpha_{ij}\left(T - T_0\right)\delta_{ij} \tag{2}$$

Where, ε_{ij}^{T} is the thermal strain tenser, α_{ij} is the coefficient of thermal expansion, T_0 is the reference temperature.

The relationship between stress and strain is expressed as

$$d\sigma_{ij} = D_{ijkl}\left(d\varepsilon_{kl} - d\varepsilon_{kl}^{p} - d\varepsilon_{kl}^{T}\right) \tag{3}$$

Where, D_{ijkl} is the elastic coefficient tenser, $d\varepsilon_{kl}$ is total strain, $d\varepsilon_{kl}^{p}$ is plastic strain, $d\varepsilon_{kl}^{T}$ is thermal strain.

The stress field of the stiffened structure is shown as Fig.4. The maximum of residual stress at the welding line is much larger than those at other parts. The residual stresses near welding line are residual tension stresses, and they .are attenuated rapidly far away from the welding line.

Based on the residual stress field, according to Miner fatigue damage law [6], assuming the type of fatigue loading is cycle vibration loading (sinusoid) and the design life of the stiffened structure is 10^7 cycle periods, it is calculated that the minimum of the safety factors is 0.3357 and the lowest

fatigue life of the welded structure is $10^{4.037}$. The most danger position is along the welding line.

Summary

In the production of welded structures the expenses for rework are an important part of the production costs. It is attractive to quantify the thermal deformations and stresses by mathematical models. The prediction of fatigue life and remaining life of the welded structures is essential. The results of temperature field in this paper are supported by the experiment data very well. And the residual stresses and strains based on thermal elastic plastic analysis are valuable for the design office. When influence from the welding, i.e. the thermal process, is described and quantified it is possible to simulate the mechanism of the welding process in a computer-based product model.

References

[1] D.Radaj: Heat Effects of Welding(Springer-Verlag Berlin Heidelberg 1997).

[2] LI Hong, REN Huilong, ZENG Ji: Prediction of Welding Deformations of Stiffened Plate Based on Inherent Strain. Journal of Harbin Engineering University , Vol. 27, No. 1, Feb.2006,pp. 57-60(in Chinese)

[3] J-B. Roelens, Numerical Simulation of Multi-pass Submerged Arc Welding Determination of Residual Stresses and Comparison with Experimental Measurements, Welding in the World, Vol. 35, No. 2, pp.110-117, 1995.

[4] Karlsson RI, Josefson BL. Three-dimensional Finite Element Analysis of Temperatures and Stresses in a Single-pass Butt-welded Pipe. ASME Journal of Pressure Vessel Technology, 1990 , 112 (2):76-84.

[5] NI Hongfang,LING Xiang,TU Shandong. Simulation of 3D Residual Stresses Field of Multi-pass Welding by FEM. Journal of Mechanical Strength. 2004 ,26(2) :218 ~ 222 (in Chinese)

[6] Zhang Xiaoming,Zhao Liangzhi.Application of Fatigue Analysis by Ansys in Fixed Mould Plate of Injection Machine. China Plastics Industry.Vol.34,No.1, 2006(1).

Key Engineering Materials Vols. 385-387 (2008) pp 417-420
© (2008) Trans Tech Publications, Switzerland
doi:10.4028/www.scientific.net/KEM.385-387.417

A Numerical Analysis of Double Notch on Stress Distribution in Single Lap Aluminium Joints

Xiaoling Zheng [a], Zhi Li, Min You [b], Shan Yu and Meirong Zhao

College of Mechanical and Material Engineering, China Three Gorges University

Yichang 443002, China

[a] zhengxiaoling@ctgu.edu.cn, [b] youmin@ctgu.edu.cn

Key words: epoxy; aluminium alloy; double notch; stress distribution; single lap joint; FEA

Abstract. The stress distributed in the mid-bondline of the joints made of aluminium alloy and an epoxy adhesive was determined with the ANSYS software. The results from the FEA showed that the values of the peak stresses of the all the stress components (including the longitudinal stress *Sx*, the peel stress *Sy*, the shear stress *Sxy*, the 1st principal stress *S1* and the von Mises equivalent stress *Seqv*) distributed in the mid-bondline are changed a little as the notch distance *L* was increased while the notch depth *d* was not great than 0.6mm. But the evidently changes occurred when the notch depth *d* was great than 0.9 mm for the stress *Sx*, *Sy* and *S1* distributed in both the mid-bondline and the interface of the lap zone. When taken the stress distributed in the middle part of the lap zone into account, the peak stress at the point in the mid-bondline corresponding to the edge of the notch decreased firstly and then increased again as the notch distance *L* was increased from 0 mm to 8 mm. The proper geometry of the notch in the specimen was chosen by finite element analysis.

Introduction

In the procedure of the shear strength testing of the single lap joint, the peel stress plays a great part in the failure of the specimen because it is geometrically nonlinear due to the non-collinear load path. Avila and Bueno [1] showed that the stress distribution was more uniform by using a wavy-lap bonded joint, giving a higher strength from their experiments and numerical simulation. Oterkus et al [2] investigated the effect of tapered edges on the performance of the joint. Belingardi et al. [3] discussed the results from the finite element analysis about the effect of inner chamfering angle in the unloaded adherend ends. Sancaktare and Simmons [4] reported that a top and bottom notch at the ends of the lap zone increased the strength of the joint. Shokrieh and Lessard [5] verified the double-notch test method with the finite element technique. Pettersson and Neumeister [6] reported they developed the inclined double notch shear (IDNS) test further and achieved accurate interlaminar shear strength values. In our earlier work [7], the authors studied the effect of the parallel slots in the middle of the lap zone and found the stress concentrations decreased. The object of this work is to study the effect of depth and the distance of two parallel slots in lap zone on the stress distribution of adhesively bonded single lap joints using the elastic finite element method.

Finite element model and mesh

The model and mesh were built using the ANSYS finite element software as shown in Fig.1. The load applied was taken as 3kN and the constraint of the model is also shown in Fig.1. The properties of the materials used in this study are chosen as follows: 71 GPa or 2.875 GPa (elastic modulus) and 0.37 or 0.33 (Poisson's ratio) for aluminium or epoxy respectively. The dimensions of the aluminium adherend were in accordance with the Chinese standard GB 7124 (equivalent to ISO

4587) with a length of 100mm, width of 25mm, and a thickness of 2mm. In the outside of the joint there were two parallel slots in the lap zone and symbols ‘D’, ‘W’ and ‘L’ presented the depth, width (2mm) and distance of the slots respectively. The thickness of the bondline was 0.2mm and divided into four layers through the direction of the thickness.

Fig.1 Finite element model

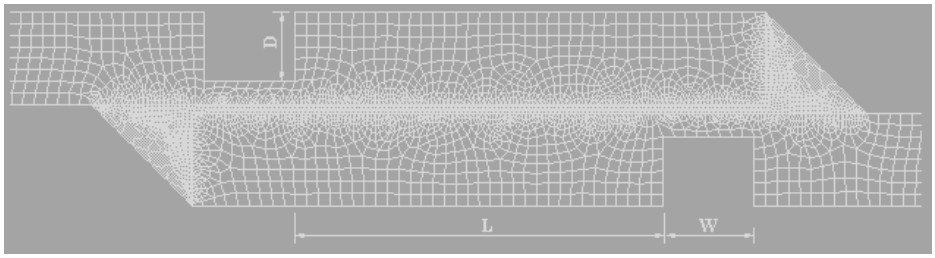

Results and discussion

When the parallel slot depth was kept constant at 0.9mm, the distance between two parallel slots L was set as 0mm, 2mm, 4mm, 6mm and 8 mm respectively and the effect of the slot distance on the stress distribution in mid-bondline (y = - 0.1 mm) is presented in Fig.2.The results from the finite element analysis showed that the effect of the distance between two parallel slots was very small when the slot depth was not great than 0.9 mm except for peel stress *Sxy.* For the longitudinal stress

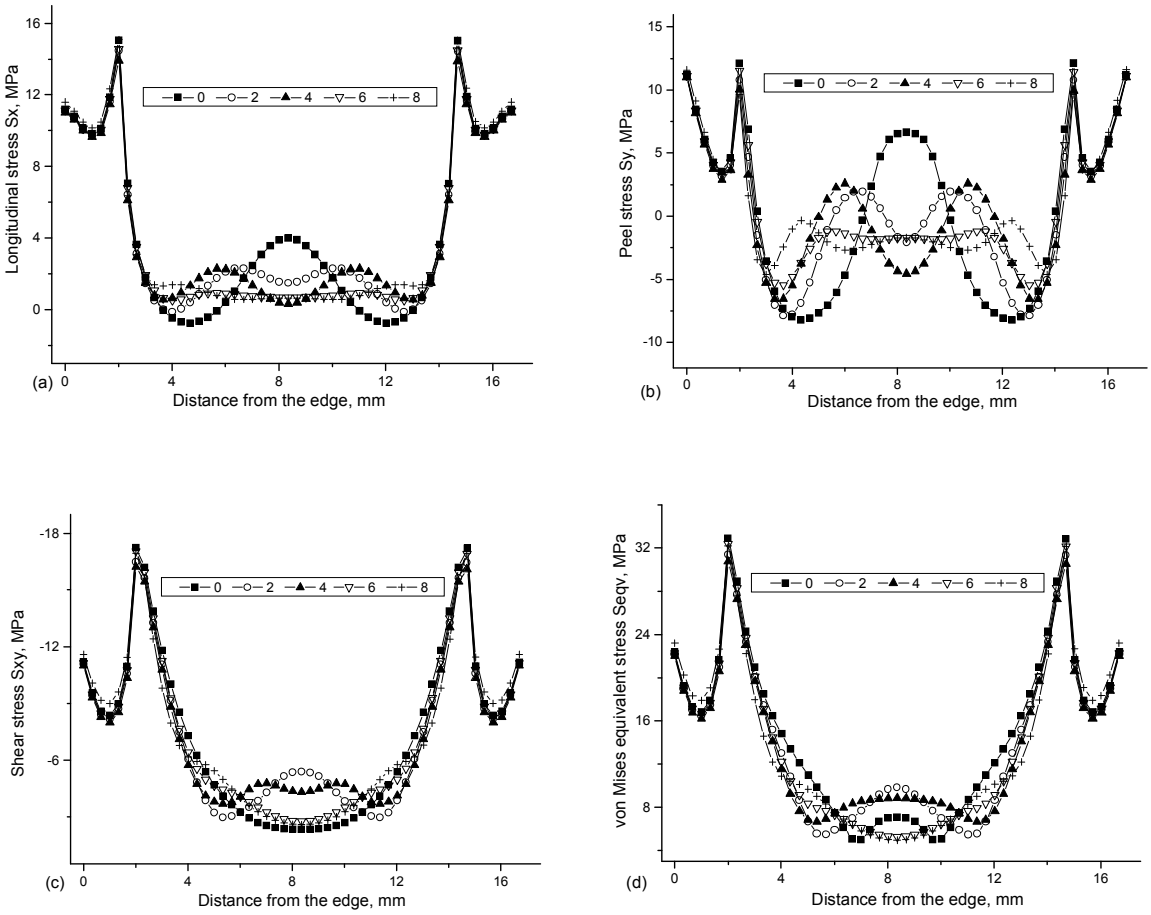

Fig.2 Effect of the distance between two parallel slots on the Stress distribution along the mid-bondline: (a) longitudinal stress Sx; (b) peel stress Sy; (c) shear stress Sxy and (d) von Mises equivalent stress Seqv

Sx, the peak stress near the fillet decreased first as the distance L increased to 4 mm and then increased again. The minimum value of the peak stress is achieved when the distance was equal to 4mm (in Fig. 2a, from about 15.1 MPa to 13.9 MPa). The distribution tendency of the peel stress *Sy* (Fig. 2b) was similar to that of the longitudinal stress *Sx* (Fig. 2a) as the distance between two parallel slots was increased and the peak stress occurred at the middle part of the lap zone changed markedly from positive to negative, the valley point occurred under the condition of L= 4 mm, which was beneficial and improved the load bearing ability of the joint [13]. The distribution of the shear stress *Sxy* (Fig. 2c) is also similar to that of the von Mises equivalent stress *Seqv* (Fig. 2d).

The effect of the slot depth on the stress distribution of the joint in the mid-bondline (y= -0.1 mm) along the length of the lap zone is shown in Fig.3 when the distance between two parallel slots was kept constant at 4 mm and the parallel slot depth was taken as 0.3 mm, 0.6 mm, 0.9 mm, 1.2 mm and 1.5 mm respectively. As the parallel slot depth increased, the peak value of the longitudinal stress *Sx* in the mid-bondline occurred at the points corresponding to the middle part of the slots in the adherend increased (Fig. 3a). For the peel stress *Sy,* the peak stress at the point corresponding to the edge of the parallel slot increases greatly as the depth of the slot increases, but the stresses in the middle zone got a relatively great valley point (Fig. 3b). The stress distribution of the shear stress *Sxy* (Fig. 3c), 1st principal stress *S1* (Fig. 3d) and the von Mises equivalent stress *Seqv* (Fig. 3e) are also similar to that of the longitudinal stress *Sx* (Fig. 3a).

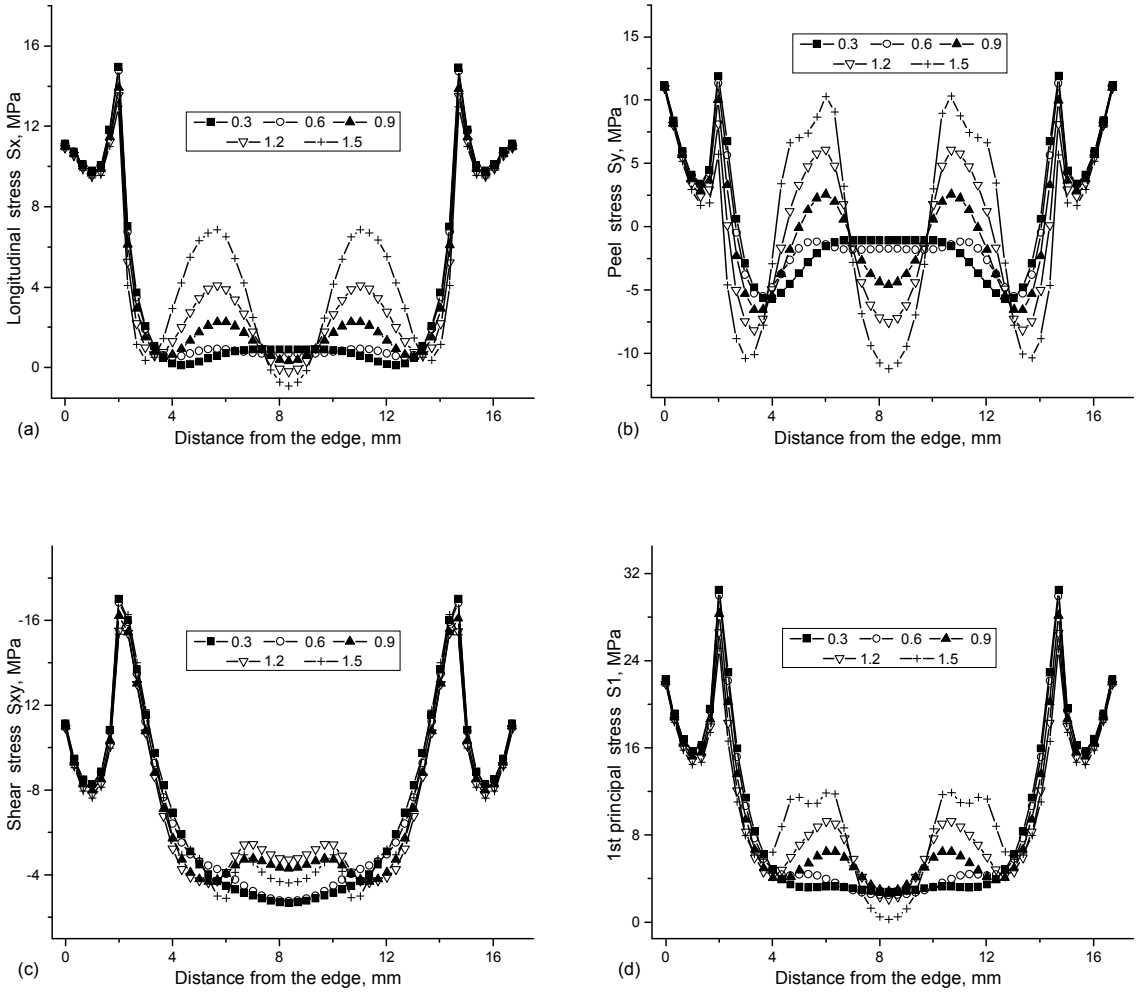

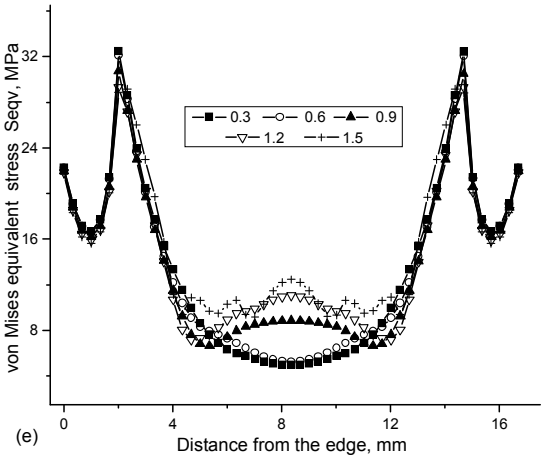

Fig.3 Effect of the slot depth on the stresses distribution in the mid-bondline of the joint: (a) longitudinal stress Sx; (b) peel stress Sy; (c) shear stress Sxy; (d) 1st principal stress S1 and (e) von Mises equivalent stress Seqv.

Summary

When the two 2 mm wide slots were arranged in the lap zone of the adherend, the peak values of the longitudinal stress *Sx*, the shear stress *Sxy*, the 1st principal stress *S1* and the von Mises equivalent stress *Seqv* in the mid-bondline decreased as the distance between two slots increased while the stress level increased in the middle part of the overlap zone. For the peel stress *Sy,* the peak stress changed markedly from positive to negative at the left end of the lap zone and it is of benefit to restrict the harmful effect of the peel stress on the joint.

The values of the peak stresses in the mid-bondline decrease when the distance between two parallel slots is increased, except that the peak peel stress *Sy* decreases all the time. As the parallel slot depth was increased, the stress in the mid-bondline at the point near the end of the lap zone decreases gradually while the stress in the middle part of the lap zone corresponding to the parallel slot also increases. The stress in the adherend with the parallel slot increases gradually as the parallel slot depth increases.

Acknowledgements

The authors would like to acknowledge the financial supported by the Major Research Programs of Science and Technology of Hubei Provincial Department of Education (2003Z001), China.

References

[1] A.F. Avila, P. O. Bueno. *Int J of Adhesion and Adhesives,* 2004, 24: 407–414
[2] E. Oterkus, A. Barut, E. Madenci, et al. *Int J of Solids and Structures,* 2006, 43: 1459-1489
[3] G. Belingardi, L. Goglio, A. Tarditi. *Int J of Adhesion and Adhesives*, 2002, 22: 273–282
[4] E. Sancaktar, S. Simmons. *J Adhesion Sci. Techno.* 2000, 14: 1363–1404
[5] M. M. Shokrieh and L. B. Lessard. *Applied Composite Materials* 1998, 5: 289–304.
[6] K. B. Pettersson, and J. M. Neumeister. *Composites: Part A*, 2006, 37: 229–242
[7] Z. M. Yan, M. You, X. S. Yi, et al. *Int J of Adhesion and Adhesives*, 2007, 27: 687-695

Key Engineering Materials Vols. 385-387 (2008) pp 421-424
© (2008) Trans Tech Publications, Switzerland
doi:10.4028/www.scientific.net/KEM.385-387.421

Study on Enhancement of Mechanical Strength by Knotted Shape Memory Alloy Fiber in TiNi Fiber Composites

Yongli Zhao[1, a], Jie Li[1, b] and Ming Jin[1, c]

[1]Institute of Mechanics, Beijing Jiaotong University, Beijing 100044, China

[a]yglizhao@tom.com, [b]lijie8282@126.com, [c]mjin@bjtu.edu.cn

Keywords: shape memory alloy; fiber composites; prestrain; knotted fiber; epoxy matrix; stress transfer

Abstract. In this paper, the experimental investigation into the enhancement of mechanical strength in shape memory alloy (SMA) fiber composites is made by using knotted fiber at the two ends instead of straight fiber. TiNi SMA fiber with both ends knotted is used for purpose of better ensuring stress transfer from the matrix to the fiber than straight fiber. Tension test is carried out above the austenitic finish temperature in air. Specimens are heated by means of electrical resistive lamplight heating. The results indicate that the mechanical strength is larger in the knotted fiber composite than in the straight fiber composite. Knotted fiber exerts the superiority of TiNi SMA fiber composite.

1. Introduction

Shape memory alloy (SMA) fiber reinforced composite materials are now an important class of engineering materials. They offer outstanding mechanical properties, unique flexibility in design capabilities, and ease of fabrication. Hence, studying the SMA fiber composites is very necessary. Some relevant studies were made. For example, Taya et al. [1-3] studied the use of intelligent materials in a passive function. They utilized the SMA to improve the mechanical properties of the materials without supplying energy externally. Umezaki [4] investigated crack closure in epoxy resin plates with an embedded spiral SMA wire using a method for generating heat via the current supplied. Shimamoto et al. [5] developed the new design concept that improved the material strength. It uses SMA to actively control the material strength. Poon et al. [6] reported the experimental results on the interfacial bonding properties of SMA composites in which prestrained SMA wires were embedded into epoxy cylinder to form the composites.

In the present work, experiment is performed as a preliminary one to reduce the degree of fiber debonding and enhance the mechanical strength of SMA fiber composite. Such composite material specimen is made using knotted fiber at the two ends instead of straight fiber. This fiber is expected to enable good stress transfer from the matrix to the fiber, so that it can enhance the mechanical strength of the composite material.

2. Experiment

2.1 TiNi SMA fiber reinforced epoxy resin matrix composite

The SMA used is a TiNi fiber 0.65 mm in diameter, with 7.8% shape recovery and $55^{\circ}\mathrm{C}$ austenitic finish temperature, A_f, and 310 MPa maximum recovery stress at $80^{\circ}\mathrm{C}$. The TiNi SMA fiber has 16.1 GPa Young's modulus at room temperature. TiNi SMA fibers are heated to shape-memorize their initial length at higher temperatures ($> A_f$). Then, they are quenched to room temperature. Tensile prestrain 6% is given on them.

The specimen is made of a TiNi SMA fiber-reinforced epoxy resin matrix composite developed by the authors. Two kinds of specimens are made: straight fiber composite and knotted fiber composite. As for knotted fiber composite specimen, TiNi fiber is tied two knots by hand. Basic geometrical shape of knot of TiNi fiber is shown in Fig. 1.

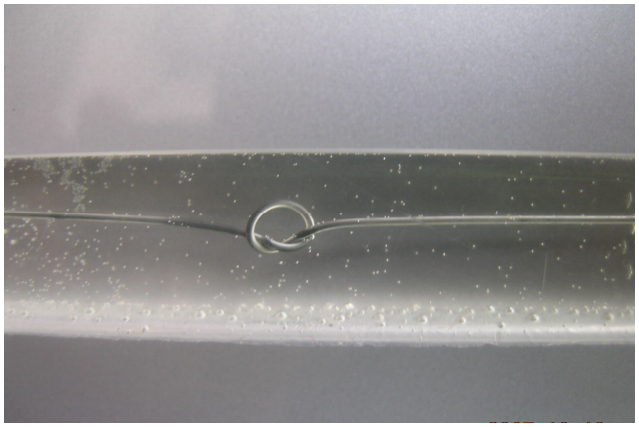

Fig. 1 Basic geometrical shape of knot of TiNi fiber

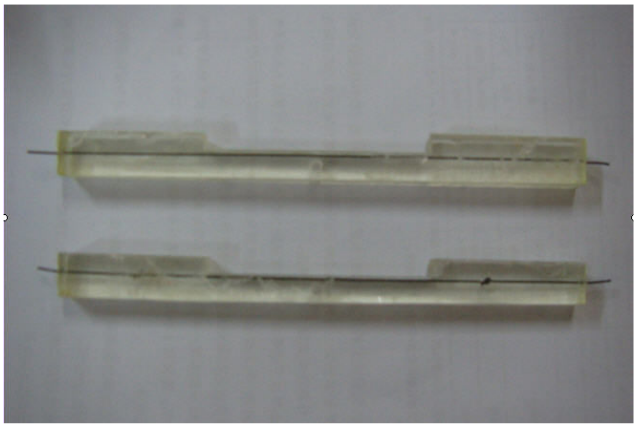

Fig. 2 Straight fiber and knotted fiber reinforced epoxy resin matrix composite specimens

All fibers are aligned along the longest axis of plastic mould by the hand layup process. The two terminals of every TiNi fiber are fixed by fasteners in order to prevent the compression of TiNi fiber caused by the temperature rise which might exceed A_f. The plastic moulds are laid into thermostated container at constant temperature $90^\circ\mathrm{C}$ for 12 hours to finish solidification. After some machining, the straight fiber reinforced and knotted fiber reinforced epoxy resin matrix composite specimens are given in Fig. 2. The actual design for enhancing the mechanical strength of the TiNi SMA fiber composite is schematically illustrated in Fig. 3. The specimen shape and size are shown in Fig. 4 and the mechanical properties are given in Table 1.

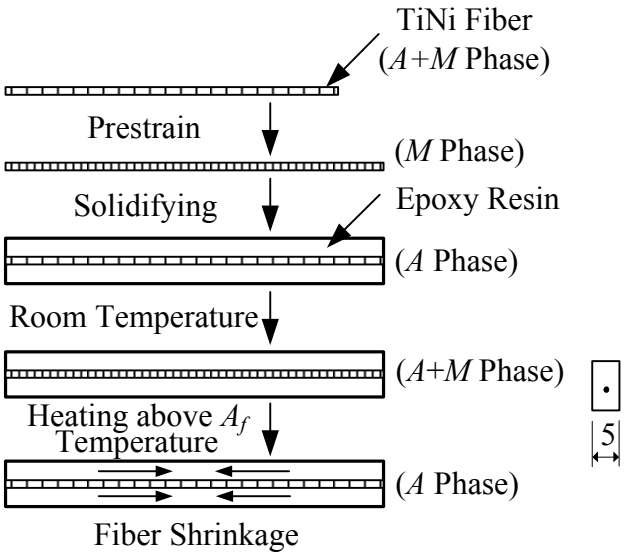

Fig. 3 Schematic illustration for enhancing the mechanical strength of the SMA fiber composite

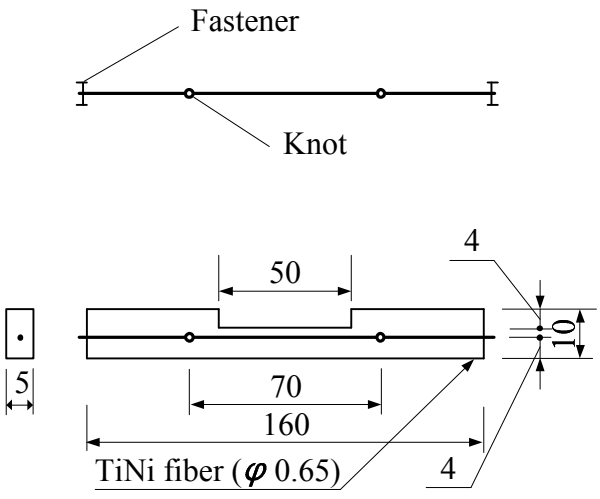

Fig. 4 Geometry of knotted TiNi/epoxy resin composite specimen

Table 1 Mechanical Properties of constituents ($80^\circ\mathrm{C}$)

Material	Young's modulus (GPa)	Poisson's ratio	Yield stress (MPa)
Epoxy resin	5.9	0.43	23
TiNi fiber	83	0.33	690

2.2 Experimental method

The WDW-100D electronic universal testing machine is used to test the fracture strength of specimens, shown in Fig. 5. The specimens are heated to above the A_f temperature ($80^\circ\mathrm{C}$) by

electrical resistive lamplight heating, shown in Fig. 6. Then the temperatures on the surface of the test specimens are confirmed after 10 minutes of heating. Crosshead movement is held constant at 1.0 mm/min throughout the experiment.

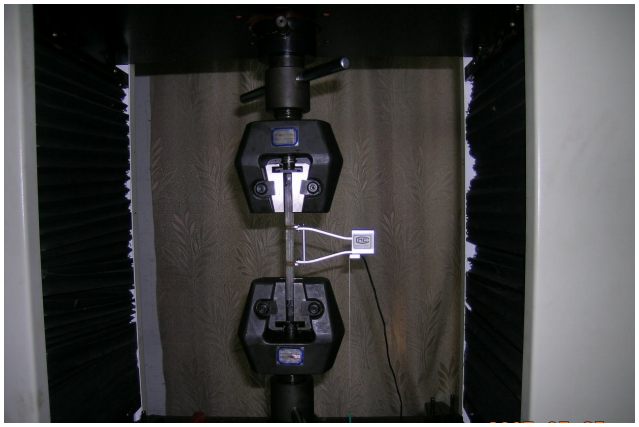

Fig. 5 Tension experiment on a WDW-100D electronic universal testing machine

Fig. 6 Electrical resistive lamplight heating

3. Results and discussion

For the composite reinforced with straight fiber, load increases with increasing displacement toward the maximum load. A sudden load drops just after the maximum load corresponding to catastrophic fracture of the epoxy matrix at the center of the specimen. When the matrix is fractured, the TiNi SMA fiber and, therefore, the composite does not separate away. Then, fiber is pulled out from the matrix and bridges the fracture pieces of the epoxy matrix by the frictional force between the fiber and the matrix. Typical fiber composite specimen fracture is shown in Fig. 7.

The composite with knotted fiber reinforced shows little pullout of fiber and, meanwhile, fiber firmly bridges the two fracture pieces of the matrix. From the experimental data of 36 groups of specimens, it can be obviously found that the fracture strength of knotted fiber composite specimens is larger than that of straight fiber composite specimens, shown in Fig. 8.

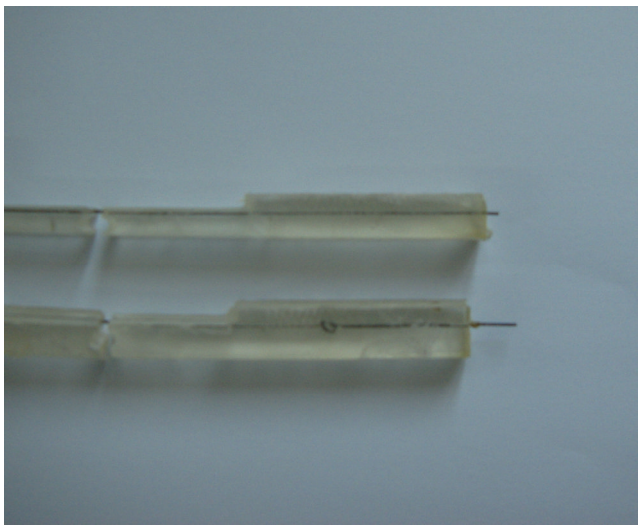

Fig. 7 Typical fiber composite specimen fracture

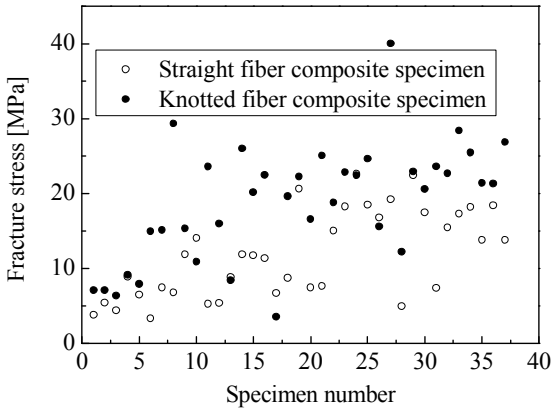

Fig. 8 Comparison of fracture strength among of straight and knotted fiber composite specimen

Stress transfer from the matrix to knotted fiber is made possible due to the peculiar geometrical shape of the fiber. The two knots are regarded as two fixed terminals which effectively restricts the behavior of the fiber debonding so that knotted SMA fiber exerted the superiority of fiber reinforced composites.

4. Conclusions

The mechanical strength of both types of fiber composites differs in detail depending on their fiber geometry. The mechanical strength is larger in the knotted fiber composite than in the straight fiber composite. This is due to the fact that the stress transfer effect between the matrix and the fiber is better for the knotted fiber composite than for the straight fiber composite. Knotted fiber can effectively reduce fiber debonding, thus it can create more recovery stress than that of straight fiber.

It has been considered that it is possible to control the fracture process of epoxy resin by knotted TiNi SMA fiber even when the interface is very weak and stress transfer is impossible in the straight fiber composite.

Knotted fiber exerts the superiority of TiNi SMA fiber composite and enhances the mechanical strength of shape memory TiNi fiber reinforced composite.

Acknowledgement

This work is supported by the National Science Foundation of China, No. 90205007.

References

[1] Y. Furuya, A. Sasaki and M. Taya: Mater. Trans. JIM Vol. 34 (3) (1993); p. 224

[2] A. Shimamoto, Y. Furuya and M. Taya: JSME Spring-Annual Meeting (1994)

[3] M. Taya et al.: Proc. Smart Mater. SPIE 1916 (1993); p. 373

[4] E. Umezaki: Mater. Sci. Eng. Part A Vol. 285 (2000); p. 363

[5] A. Shimamoto, H. Ohkawara and F. Nogata: Eng. Fract. Mech. Vol. 71 (2004); p. 737

[6] C. K. Poon, K. T. Lau and L. M. Zhou: Composites Part B Vol. 36 (2005); p. 25

Key Engineering Materials Vols. 385-387 (2008) pp 425-428
© (2008) Trans Tech Publications, Switzerland
doi:10.4028/www.scientific.net/KEM.385-387.425

Effect of Nitrogen on Creep Properties of 22Cr-25Ni Austenitic Heat-Resistant Steels

Yong Uk Kim[1,a], Woo Sang Jung[2,b] , Young Hoon Chung[2,c] , S.I. Kwun[1,d]

[1]Department of Materials Science and Engineering, Korea University, Seoul 136-713, Korea

[2]Materials Science and Technology Research Division, Korea Institute of Science and Technology, Seoul 136-791, Korea

[a]yonguck80@ korea.ac.kr, [b]wsjung@ kist.re.kr, [c]yhchung@ kist.re.kr, [d]sookkwun@ korea.ac.kr

Keywords: Austenitic heat resistant steels; Nitrogen effect; Creep properties; Precipitate

Abstract. The effect of nitrogen on creep properties of 22Cr-25Ni austenitic heat-resistant steels with different nitrogen content was studied. The tensile and creep strength increased with increasing nitrogen content. The tensile strength increased due to grain refinement by Nb-rich carbonitride. The creep strength increased with increasing nitrogen content because nitrogen retarded the formation and growth rate of Cr-rich carbide and the growth rate of Nb-rich carbonitride during creep.

Introduction.

Energy saving and lower emissions of carbon dioxide are increasingly seen as key factors in protecting the global environment. Research and development of heat resistant steels and alloys for high-efficient USC power plants at 973K are being now promoted in Europe [1]. If the operating temperature of coal fired power plant increases from the current 863K to 973K, thermal efficiency increases from 41 to 54 percent. For this reason, it is crucial to develop heat resistant steels having improved creep strength over 973K. Many researchers focused on the development of the austenitic heat-resistant steels which have better creep strength than ferritic heat resistant steels. In austenitic heat-resistant steels, the precipitation of Cr-rich carbides at grain boundary results in Cr depletion in the vicinity of the grain boundary. This Cr depleted area around the grain boundary reduces resistance to intergranular embrittlement during creep. However, the decreasing Cr content to suppress the precipitation of Cr-rich carbides, would decrease corrosion resistance at high temperatures. On the other hand, decreasing C content would decrease precipitation strengthening and thereby reduce the tensile and creep strength. It is reported [2] that the addition of nitrogen, which is an austenite stabilizer, suppresses the precipitation of Cr-rich carbide and improves creep strength by forming nitrides. However, the effects of nitrogen on the creep strength in austenitic heat-resistant steels are not clearly understood. The present study aims to gain a better understanding of the effects of nitrogen on the creep strength of 22Cr-25Ni austenitic heat-resistant steels.

Experimental Procedure

The 6.2 kg ingot of 22Cr-25Ni austenitic heat-resistant steel used in this study was made by vacuum induction melting. The chemical composition of this steels is given in Table 1. Hot forging and rolling were performed to make plate of 8 mm thickness and the plate was solution treatment at 1473 K for two hours. Creep and tensile specimen of 25 mm gauge length and 4 mm gauge diameter were machined in the rolling direction. All samples were tempered at 973 K for one hour. Tensile tests were conducted in air in the temperature range between 773 K and 1023 K. Creep tests were conducted in air at 973 K. The microstructures of the creep fractured specimen were observed using a field emission scanning electron microscope (FE-SEM) equipped with energy dispersive x-ray spectroscopy (EDS).

Table 1. Chemical composition of 22Cr-25Ni austenitic heat-resistant steels in this study[wt.%].

Alloy	C	Si	Mn	Cr	Ni	Co	W	Cu	Nb	N	Fe
N08	0.11	0.27	0.93	22.44	25.31	1.53	3.5	3.1	0.68	0.08	Bal.
N12	0.11	0.3	0.95	22.47	25.20	1.53	3.5	3.02	0.67	0.12	Bal.

Results and discussion

Fig. 1 shows high temperature tensile and creep rupture test results in the 22Cr-25Ni austenitic heat-resistant steels with different nitrogen content. The tensile strength decreased with increasing temperature. The tensile and creep strength increased with increasing nitrogen content. Fig. 2(a) and (b) shows SEM micrograph of the N08 and N12 steel, respectively, after solution treatment. Coarse precipitates, 1-2 μm, were observed in both steels. Fig. 2(c) shows EDS analysis result of coarse precipitates observed in Fig. 2(a) and (b). The coarse precipitates are Nb-rich carbonitrides. The amount of coarse Nb-rich carbonitride in the N12 steel as shown Fig. 2(a) and (b) was higher than that of the N08 steel, but the mean particle size of the N08 and N12 steels was similar.

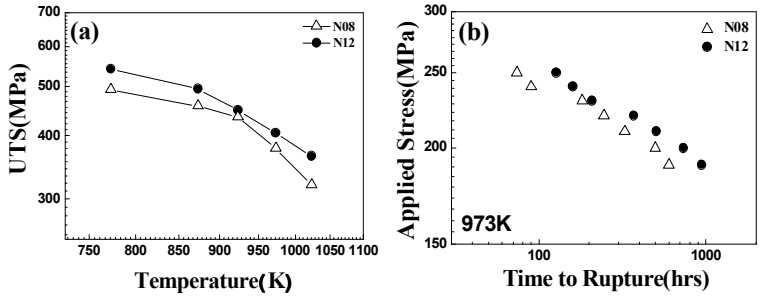

Fig. 1 Variation of (a) tensile strength with temperature and (b) applied stress with time to rupture.

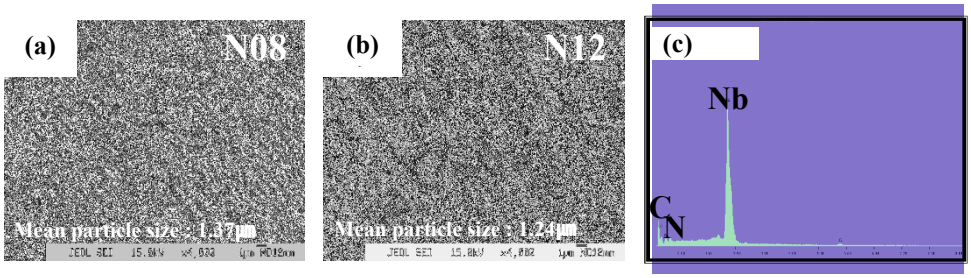

Fig. 2. The SEM micrograph and EDS result after solution treatment.
(a) N08 (b) N12 (c) Nb-rich carbonitride

Fig. 3 shows optical micrograph in the N08 and N12 steels after tempering. The grain size decreases with increasing nitrogen content. The mean grain size of the N08 and N12 steels is 112 μm and 81 μm, respectively. The higher amount of precipitates in N12 steel is able to suppress grain growth resulting in its relatively smaller grain size. This finer grain size increases the high temperature strength of N12 as also reported in ref. [3,4].

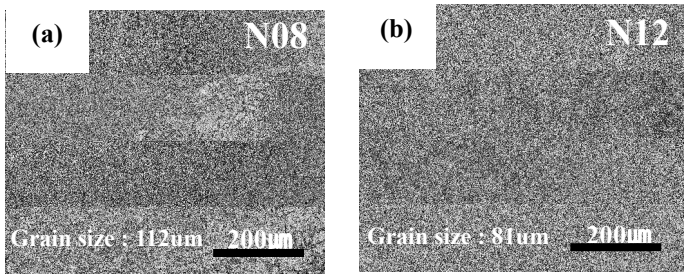

Fig. 3 The optical micrograph after tempering treatment. : (a) N08 (b) N12

Fig. 4 shows SEM micrograph for the N08 and N12 steels after creep test at 973 K under 190 MPa. It can be seen that the amount of plate shaped precipitate in the N12 steel at grain boundary is relatively lower than that of the N08 steel. Also, the amount of globular shaped precipitate in the

N12 steel in the grain is relatively higher than that of the N08 steel. Fig. 5 shows EDS analysis result of precipitates at (a) grain boundary and (b) inside grain shown in Fig. 4. The grain boundary precipitate is Cr-rich carbide (Fig. 4(a), (b)) and precipitate inside grain is Nb-rich carbonitride(Fig. 4(c), (d)). Fig. 5(c) shows mean particle size of Cr-rich carbide and Nb-rich carbonitride for the N08 and N12. The mean particle size of Cr-rich carbide at grain boundary decreased with increasing nitrogen content as shown Fig. 4(a) and (b). Also, the mean particle size of Nb-rich carbonitride in the grain was smaller with increasing nitrogen content as shown Fig. 4(c) and (d). These results indicate that increasing the nitrogen content retards the formation and growth rate of Cr-rich carbide and the growth rate of Nb-rich carbonitride.

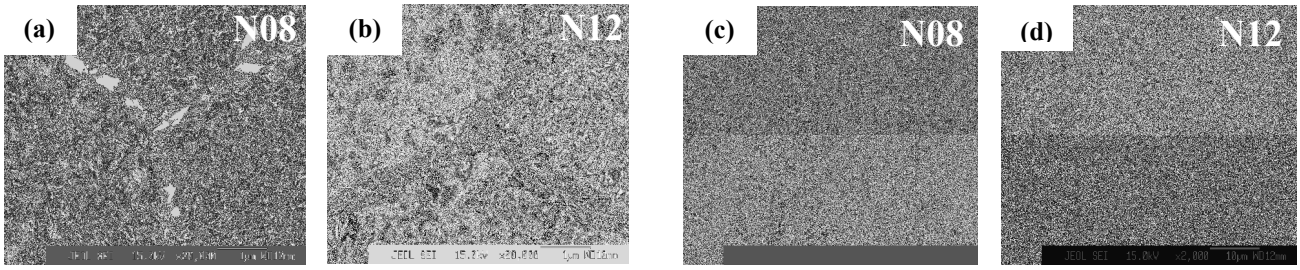

Fig. 4 SEM micrograph after creep test at 973K under 190MPa. : (a)(c) N08 steel (b)(d) N12 steel

Mozhi et al. [5] and Briant [6] reported that the nitrogen retarded Cr diffusion from matrix to grain boundary. Also, Satsko et al. [7] reported that the increase of nitrogen content increased coarsening resistance of Nb-rich carbonitride. These results are consistent with the results of this study. Therefore, the creep strength increased with increasing nitrogen contents as shown Fig. 1(b) because nitrogen retards the formation and growth rate of Cr-rich carbide and the growth rate of Nb-rich carbonitride during creep.

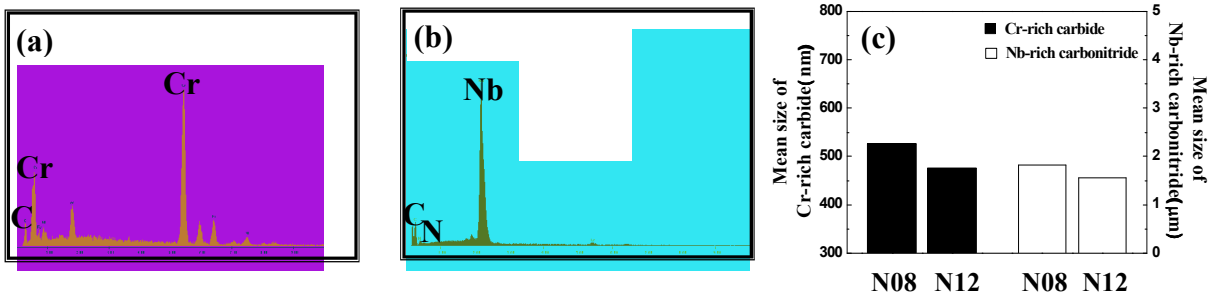

Fig. 5 EDS Results and mean particle size after creep test at 973K under 190MPa.
(a) Cr-rich carbide(at the grain boundary) (b) Nb-rich carbonitride(inside grain) (c) Mean particle size

Fig. 6 shows the relationship between the applied stress and Larson Miller Parameter (LMP) for N08 and N12 steels at 973K. For comparison, the creep data of Sanicro25 steel [8] is also included in this figure. It can be seen that Sanicro25 has longer creep rupture life compared to N08 and N12 steels. The carbon content of N08 and N12 steels is higher and nitrogen content of these steels is lower than those of Sanicro25. Therefore, it is thought that the formation and growth rate of Cr-rich carbide in N08 and N12 steels are relatively higher than those of Sanicro25 because of the increased activity of carbon. Also, the Cr-rich carbide and Nb-rich carbonitride in N08 and N12 steels have higher growth rate than those in Sanicro25 due to the difference in nitrogen contents. For these reasons, it is thought that N08 and N12 steels have lower creep rupture life than Sanicro25.

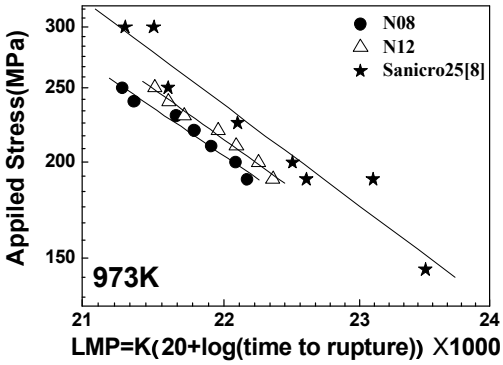

Fig.6 Variation with applied stress of N08 and N12 steels.

Summary

1. Higher tensile strength was obtained when nitrogen content was increased, because the grain growth was suppressed by the increased amount of Nb-rich carbonitride.

2. Higher creep strength was obtained when nitrogen content was increased, because nitrogen retarded the formation and growth rate of Cr-rich carbide and the growth rate of Nb-rich carbonitride during creep.

References

[1] F. Abe, M. Taneike and K. Sawada: Int. J. Pres. Ves. Pip. Vol.84 (2007), p. 3

[2] J.W. Simmons: Mater. Sci. Eng. A Vol.207 (1996), p. 159

[3] E. Werner: Mater. Sci. Eng. A Vol.101 (1988), p. 93

[4] M.L.G. Byrnes, M. Grujicic and W.S. Owen: Acta metall. Vol.35 (1987), p. 1853

[5] T.A. Mozhi, H.S. Betrabet, V. Jagannathan, B.E. Wilde and W.A.T. Clark: Scripta Metall. Vol.20 (1986), p. 723

[6] C.L. Briant: Scripta Metall. Vol.21 (1987), p. 71

[7] R. Stasko, H. Adrian, A. Adrian: Mater. Charact. Vol.56 (2006), p. 340

[8] R. Rautio, S. Bruce: proceeding at Conference on Advances in Materials Technology for Fossil Power Plants, edtied by R. Viswanathan, D. Gandy and K. Coleman (2004), p. 394

Key Engineering Materials Vols. 385-387 (2008) pp 429-432
© (2008) Trans Tech Publications, Switzerland
doi:10.4028/www.scientific.net/KEM.385-387.429

Comparison of Impact Properties of Sn-9Zn and Sn-3Ag-0.5Cu Lead-free Solder Ball Joints

Ikuo Shohji[1, a], Satoshi Shimoyama[1], Hisao Ishikawa[2] and Masao Kojima[3]

[1]Graduate School of Engineering, Gunma University, Tenjin-cho, Kiryu, 376-8515, Japan

[2]Nippon Joint Co., Ltd., 475-2 Tsuruta, Mooka, 321-4302, Japan

[3]KOJIMA SOLDER Co., Ltd., 129-2 Matsudoshinden, Matsudo, 270-2241, Japan

[a]shohji@me.gunma-u.ac.jp

Keywords: Sn-9mass%Zn, Sn-3mass%Ag-0.5mass%Cu, Impact properties, Fracture, Ball shear impact test, Lead-free solder

Abstract. Impact properties of solder ball joints with Sn-9mass%Zn and Sn-3mass%Ag-0.5mass%Cu lead-free solders were investigated under aging at 423 K. In the case of the joints with Cu electrodes, both Sn-9Zn and Sn-3Ag-0.5Cu joints have similar impact forces before aging. For the Sn-3Ag-0.5Cu joint, fracture occurred in an intermetallic compound (IMC) layer formed in a joint interface regardless of aging, and thus the impact force was stable upon aging at 423 K for 500 h. For the Sn-9Zn joint, fracture mode changed from solder fracture to other fracture upon aging and thus this change led a decrease in the impact force.

In the Sn-9Zn joint with an electroless Ni/Au plated electrode, fracture occurred in the solder regardless of aging, and thus impact properties improved compared with the joint using the Cu electrode. The impact properties are superior to those of the Sn-3Ag-0.5Cu joints with the Cu and the electroless Ni/Au electrodes.

Introduction

Lead-free soldering has become widely spread in electronic assemblies due to legislation such as the restriction of the use of certain hazardous substances (RoHS). Recently, ternary Sn-Ag-Cu solders are used in various applications as a major lead-free solder. A Sn-Zn lead-free solder has been expected to be low-melting lead-free solder, because the melting temperature is much closer to that of the conventional Sn-Pb eutectic solder compared with other lead-free solders such as Sn-Ag-Cu. Thus, some studies on solder ball joints with the Sn-Zn solder have been reported [1-4]. For solder ball joints, the impact reliability is one of the crucial issues. Although some studies on impact properties of the Sn-Ag-Cu solder ball joint have been performed [5-7], those of the Sn-Zn solder ball joint are a little [1]. The purpose of this study is to investigate the impact properties of the Sn-Zn solder ball joints in aging conditions and to compare them with those of the Sn-Ag-Cu joints.

Experimental

Sn-9mass%Zn and Sn-3mass%Ag-0.5mass%Cu solder balls with 0.45 mm diameter were prepared. The solder ball was joined on a Cu electrode and an electroless Ni/Au plated Cu electrode on an FR-4 substrate by reflow soldering with non-clean flux using a hot plate. The diameter of the Cu electrode was 0.3 mm. The thicknesses of the Ni layer and the Au layer were 3 μm and 0.04 μm, respectively. The composition of the Ni layer was Ni-6mass%P. Fig. 1 shows temperature profiles in reflow soldering. After reflow soldering, the subsequent aging treatment were conducted at 423 K for 100 h, 250 h and 500 h. For the cross-sections of the joints before and after aging, microstructural observation was conducted using an electron probe X-ray microanalyzer (EPMA).

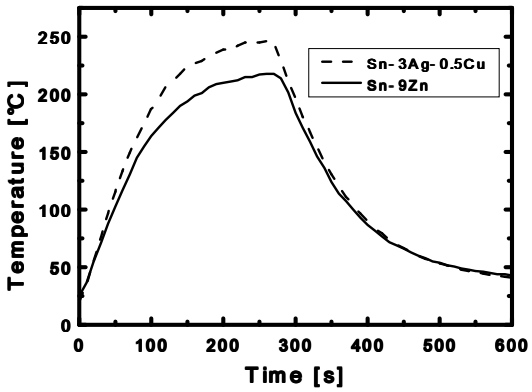

Fig. 1 Temperature profiles in reflow soldering.

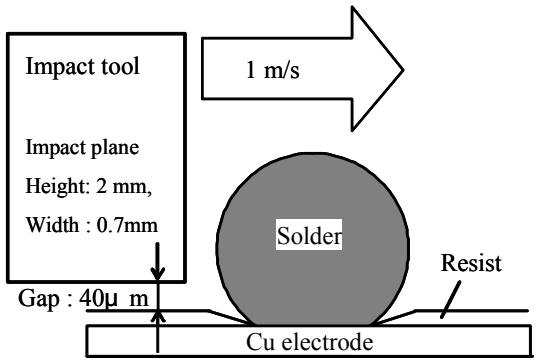

Fig. 2 Schematic of the impact test.

The impact test of the solder ball joint was conducted at room temperature using Instron Micro Impactor [7]. Fig. 2 shows a schematic of the impact test. The thickness of the resist was 10 μm. The velocity before impact was set at 1 m/s. Fig. 3 indicates an example of the result of the impact test with a Sn-9Zn solder ball joint. In this study, energy to peak load was defined as E_p, and thus the ball impact force (peak load) and the impact toughness (E_p) were investigated. Eight joints were tested under each condition, and the averages of the peak load and E_p were evaluated by the data except maximum and minimum values. Fracture surfaces after the impact test were observed with the EPMA to investigate the fracture mode.

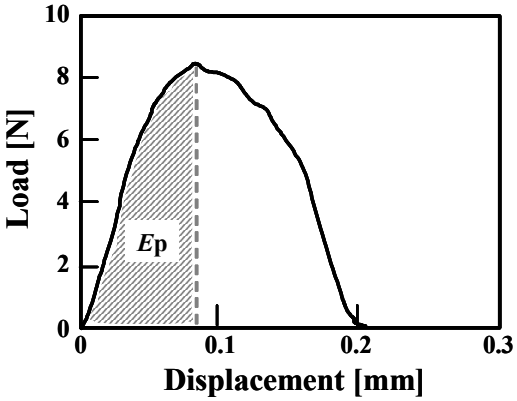

Fig. 3 Example of a result of impact test with a Sn-9Zn solder ball joint (Cu electrode, without aging).

Results and discussion

Microstructures. Fig. 4 shows microstructures of joint interfaces before and after aging. In the Sn-9Zn joint with Cu, a Cu-Zn IMC layer, which thickness is approximately 1 μm, forms in the as-reflowed joint interface. Cu-Sn compounds form between the Cu-Zn layer and Cu upon aging.

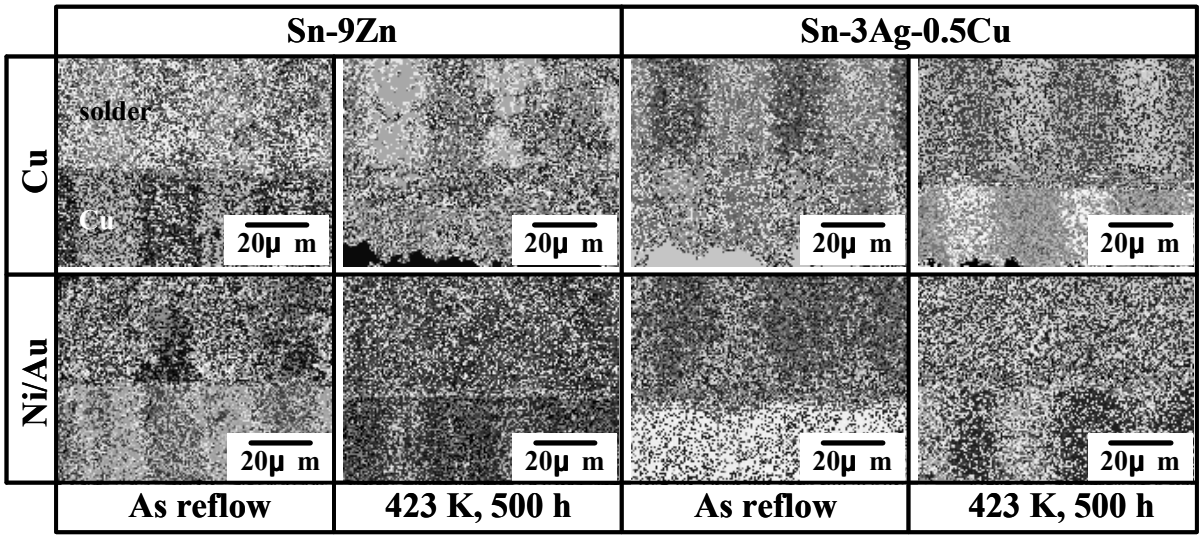

Fig. 4 Microstructures of joint interfaces.

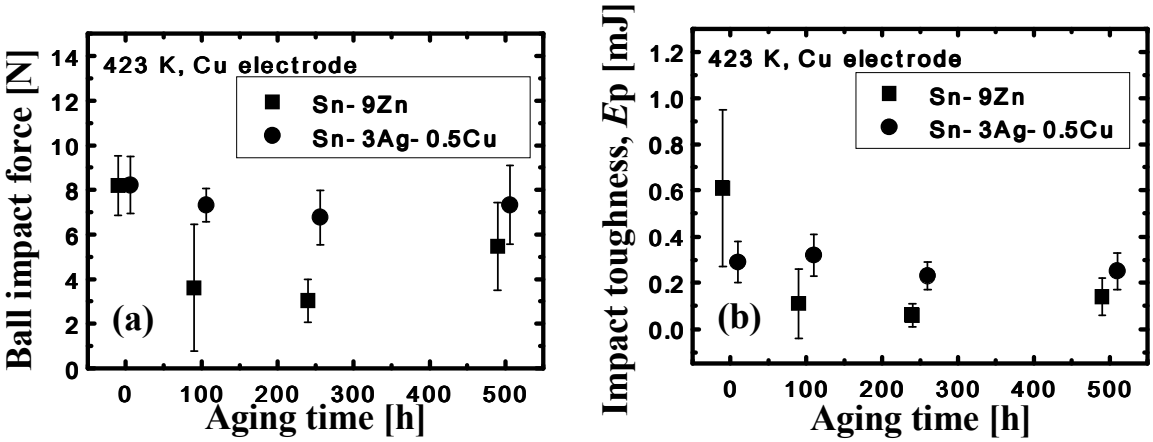

Fig. 5 Impact properties of solder ball joints with Cu electrodes. (a) ball impact force, (b) impact toughness (*E*p).

This formation was observed after aging at 423 K for 100 h. Further aging treatment causes growth of a Cu-Sn IMC layer into Cu and disappearance of the Cu-Zn layer as shown in Fig. 4. This microstructural change has been reported in the previous report [8]. In the Sn-3Ag-0.5Cu joint with Cu, a scallop-shape Cu-Sn IMC layer approximately 2 μm thick forms in the as-reflowed joint interface. The Cu-Sn IMC layer grows up to approximately 7 μm by aging at 423 K for 500 h.

In the case of joints with electroless Ni/Au plated electrodes, reaction layers formed in the joint interfaces scarcely grow upon aging in both Sn-9Zn and Sn-3Ag-0.5Cu joints. The thicknesses of the layers were at most 1 μm and 6 μm in the Sn-9Zn joint and the Sn-3Ag-0.5Cu joint, respectively.

Impact properties of solder ball joints.

Cu electrodes. Fig. 5 shows impact test results of solder ball joints with Cu electrodes. In this study, three fracture modes were observed in fracture surfaces after the impact test. Those are solder fracture, IMC fracture and their complex fracture.

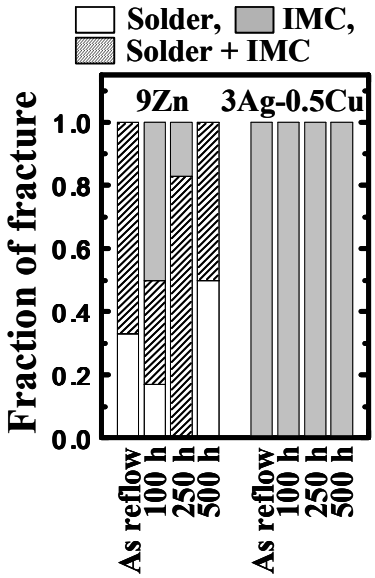

Fig. 6 Fraction of fracture (Cu electrodes).

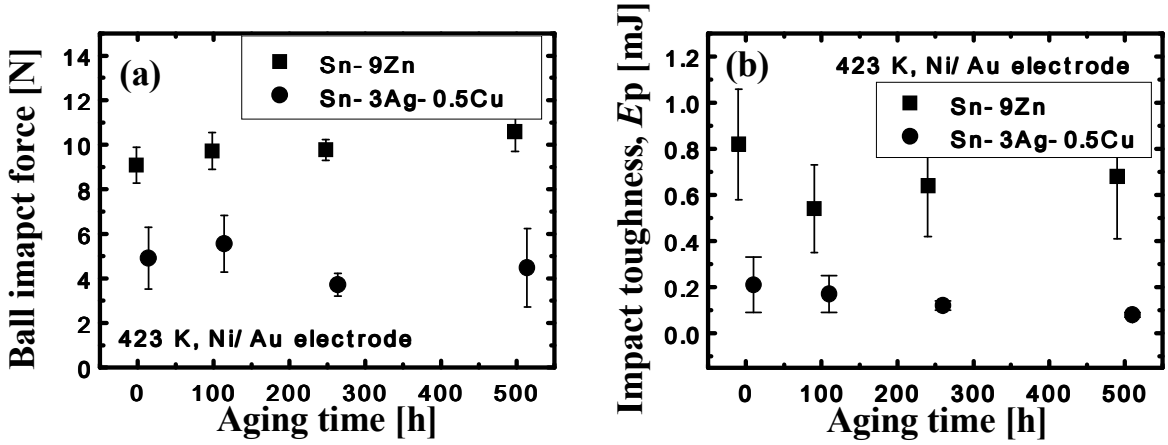

Fig. 7 Impact properties of solder ball joints with electroless Ni/Au plated electrodes. (a) ball impact force, (b) impact toughness (*E*p).

Fig. 6 shows the change of the fraction of fracture mode upon aging for each solder joint. In the Sn-3Ag-0.5Cu joint, fracture mode does not change upon aging, and thus the impact properties are

also relatively stable. In contrast, impact properties of the Sn-9Zn joint degraded upon aging, although they were similar to those of the as-reflowed Sn-3Ag-0.5Cu joint. This is caused by the increase of IMC fracture upon aging. After aging at 423 K for 500 h, the solder fracture mode is dominant and thus impact properties of the Sn-9Zn joint slightly improve.

Electroless Ni/Au plated electrodes. Fig. 7 shows impact properties of the solder ball joints with electroless Ni/Au plated electrodes. Solder fracture and IMC fracture were observed in all the Sn-9Zn joints and all the Sn-3Ag-0.5Cu joints, respectively. The fracture modes did not change upon aging in both joints. Thus, impact properties of each joint are relatively stable regardless of aging time. In particular, impact properties of the Sn-9Zn joint are superior to those of the Sn-3Ag-0.5Cu joints with Cu and electroless Ni/Au plated electrodes. This means the use of the electroless Ni/Au plated electrode is very effective to improve the impact properties of the Sn-9Zn solder ball joint.

Summary

Impact properties of Sn-9Zn and Sn-3Ag-0.5Cu solder ball joints were investigated in aging at 423 K, and those were compared. The results obtained are summarized as follows.

(1) In the joints with Cu electrodes, although similar impact properties were observed in as-reflowed Sn-9Zn and Sn-3Ag-0.5Cu joints, the impact properties of the Sn-9Zn joint degraded with increasing aging time.
(2) The use of an electroless Ni/Au plated electrode improves impact properties of the Sn-9Zn joint due to fracture mode change from complex fracture of IMC and solder to solder fracture.
(3) The impact properties of the Sn-9Zn joint with the electroless Ni/Au plated electrode are superior to those of the Sn-3Ag-0.5Cu joints with Cu and electroless Ni/Au plated electrodes.

Acknowledgement

The authors would like to thank Instron Ltd. for conducting the impact test for solder ball joints.

References

[1] M. Date, T. Shoji, M. Fujiyoshi, K. Sato and K. N. Tu: Scr. Mater., Vol. 51 (2004), p. 641

[2] K. S. Kim, J. M. Yang, C. H. Yu, I. O. Jung and H. H. Kim: J. Alloys Compd., Vol. 379 (2004), p. 314

[3] K. S. Kim, K. W. Ryu, C. H. Yu and J. M. Kim: Microelectron. Reliab., Vol. 45 (2005), p. 647

[4] I. Shohji, S. Shimoyama, H. Ishikawa and M. Kojima: Smart Processing Technology, Vol. 2 (2008) in press

[5] T. Morita, R. Kajiwara, I. Ueno and S. Okabe: Proc. of Mate (Microjoining and Assembly Technology in Electronics) 2003 (Japan Welding Society, 2003) p. 157

[6] K. Yamamoto, H. Akahoshi, T. Kato, T. Kawamura, R. Kimoto and R. Sato: Proc. of Mate (Microjoining and Assembly Technology in Electronics) 2006 (Japan Welding Society, 2006) p. 311

[7] E. H. Wong, Y-W. Mai, R. Rajoo, K. T. Tsai, F. Liu, S. K. W. Seah and C-L. Yeh: Proc. of 2006 Electronic Components and Technology Conference (IEEE, 2006) p. 64

[8] I. Shohji, T. Nakamura, F. Mori and S. Fujiuchi: Mater. Trans., Vol. 43 (2002), p. 1797

Key Engineering Materials Vols. 385-387 (2008) pp 433-436
© (2008) Trans Tech Publications, Switzerland
doi:10.4028/www.scientific.net/KEM.385-387.433

Effect of Thermal Cycle Conditions on Thermal Fatigue Life of Chip Size Package Solder Joint

Ikuo Shohji[1, a], Tomotake Tohei[1], Keisuke Yoshizawa[1], Masaharu Nishimoto[2], Yasushi Ogawa[2] and Takayuki Kawano[2]

[1]Graduate School of Engineering, Gunma University, Tenjin-cho, Kiryu, 376-8515, Japan

[2]Somar corporation, 5-19-1 Inari-cho, Soka, 340-8686, Japan

[a]shohji@me.gunma-u.ac.jp

Keywords: Thermal fatigue life, Chip size package, Coffin-Manson's relation, Lead-free solder, Sn-Ag-Cu

Abstract. Accelerated thermal cycling (ATC) tests were conducted to investigate an effect of thermal cycle conditions on thermal fatigue life of a chip size package (CSP) lead-free solder joint. A ternary Sn-Ag-Cu alloy was used as a lead-free solder material. For frequency of thermal cycle (1~3 cycles/h) and maximum (388~423 K) and minimum (223~273 K) temperatures investigated, the effects of them on thermal fatigue life of the solder joint were slight. On the contrary, correlation was recognized between temperature amplitude and thermal fatigue life of the solder joint. The thermal fatigue life increased with decreasing temperature amplitude. The relationship obeyed the Coffin-Manson's type equation.

Introduction

ATC test is usually performed to evaluate the thermal fatigue reliability of the solder joint. The modified Coffin-Manson's type equation has been used to predict thermal fatigue life of the conventional Sn-Pb solder joint [1, 2]. For lead-free solder joints, although a number of studies on reliability evaluation by ATC have been reported [3-8], the Coffin-Manson's type equation for thermal fatigue life prediction has not been completely elucidated yet. In this study, several ATC tests were conducted to evaluate thermal fatigue lives of CSP joints with a Sn-Ag-Cu solder under various thermal cycle conditions. Using the obtained data, the effects of frequency, maximum temperature and temperature amplitude in ATC on thermal fatigue lives of CSP lead-free solder joints were investigated. From the results, the Coffin-Manson's type equation for the CSP lead-free solder joint was examined.

Experimental

CSP with 12 x 12 mm size, 228 electrodes and a 0.5 mm electrode pitch was prepared. A Sn-4mass%Ag-0.5mass%Cu solder ball with 0.3 mm diameter, was attached on each electrode of CSP. The CSP was joined on a FR-4 substrate with Sn-3mass%Ag-0.5mass%Cu solder paste by reflow soldering. Fig. 1 shows a cross sectional view of a CSP solder joint. Detailed specifications of CSP, the substrate and reflow soldering have been described in the previous report [9]. The chemical composition of the solder in the CSP joint was approximately Sn-3.5mass%Ag-0.75mass%Cu [9]. ATC tests were conducted under eight conditions as shown in Table 1. The ramp time was approximately 5 min in all tests. Measurements of electric resistance in the joint were performed by the four-wire method every 100 cycles until 1000 cycles, and after that, every 500 cycles. The failure was determined as a cycle at which a 10% increase in electric resistance occurred by joint cracking. Five CSPs were tested for each ATC condition to examine the mean thermal fatigue life. The cross sections of fractured joints were observed using an electron probe X-ray microanalyzer (EPMA) after ATC tests.

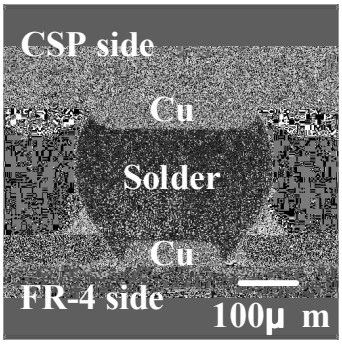

Fig. 1 Cross sectional view of CSP solder joint [9].

Table 1 ATC test conditions.

Test No.	Temperature range (K)	Frequency (cycles/h)	Δ *T* (K)
1	233 – 398	1	165
2	233 – 398	2	165
3	233 – 398	3	165
4	258 – 423	2	165
5	253 – 398	2	145
6	243 – 408	2	165
7	223 – 388	2	165
8	273 – 398	2	125

Table 2 Summary of ATC test results.

Test No.	Mean life (cycles)
1	1980
2	1760
3	2130
4	2080
5	2280
6	1440
7	1520
8	>2960

Results and discussion

ATC test results. Fig. 2 shows Weibull plot of the ATC test results. The mean life of each ATC condition was estimated as the cycle at which the cumulative failure rate becomes 0.5. Table 2 summarizes the ATC test results. For the No. 8 test, one joint have not been failed yet after 4000 thermal cycles. Therefore, mean life possibly improves above 2960 cycles in the joint. Fig. 3 shows an example of a fractured joint. In this study, most of fracture occurred in the solder in the FR-4 side as shown in Fig. 3. To evaluate the thermal fatigue life of the solder joint, the modified Coffin-Manson equation expressed in Eq. 1 has been used [1, 2].

$$N_f = C \cdot F^m \cdot (\Delta T)^{-n} \exp(Q / RT\max). \quad (1)$$

N_f: thermal fatigue life, C: constant, F: frequency, ΔT: temperature range, Q: apparent activation energy, R: gas constant, Tmax: maximum temperature, m, n: exponential constant.

In following section, m, n and Q in Eq. 1 are examined using ATC test results shown in Table 2.

Effects of thermal cycle conditions on thermal fatigue life. Fig. 4 shows relationship between N_f and F. The slope of the line in the figure corresponds to m value. The m value was estimated as 0.04. This value is very smaller than the conventional value of 0.33, which has been used for the Sn-Pb solder. This means that effect of frequency on thermal fatigue life of the Sn-Ag-Cu lead-free solder is negligible. Since the ramp time was fixed approximately at 5 min in this study, the difference of

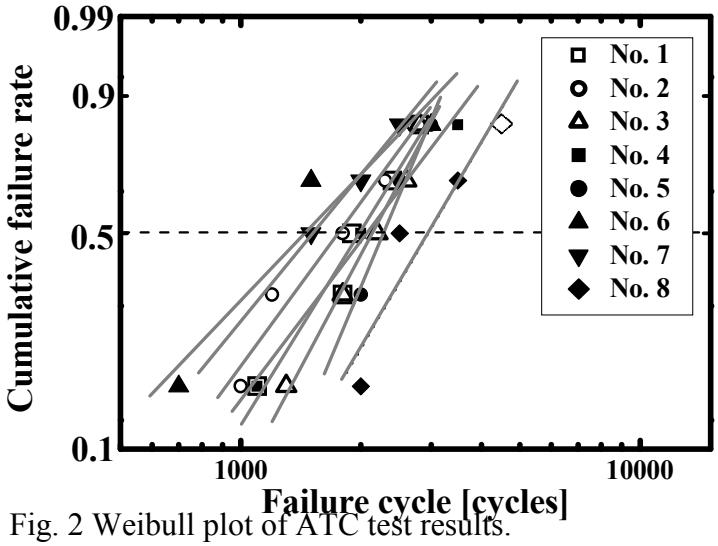

Fig. 2 Weibull plot of ATC test results.

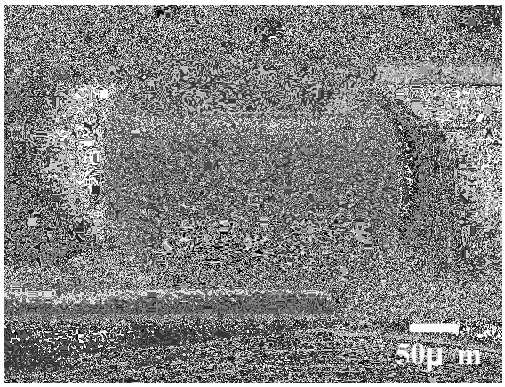

Fig. 3 Fractured solder joint after 1300 cycles (Test No.1).

frequency corresponds to that of dwell time. In the No. 1, 2 and 3 ATC tests, dwell time were 25, 10 and 5 min, respectively. Therefore, the effect of frequency on thermal fatigue life of the solder joint depends on creep properties of the solder at dwell temperature. Fig. 5 shows stress relaxation curves of the solder joints [10]. The figure shows stress relaxation curves at 373 K when shear strain of 0.05 was applied to the Cu lap joint with the solder and the shear strain was hold for 60 min. In the Sn-37Pb joint, stress relaxation occurs rapidly with increasing relaxation time. In contrast, stress relaxation negligibly occurs in time ranging from 5 min to 60 min in the Sn-3.5Ag joint. The effect of dwell time on stress relaxation of the lead-free solder is slight under the conditions investigated, and thus the effect of frequency on thermal fatigue life of the lead-free solder joint is negligible.

Fig. 6 shows Arrhenius plot result for Q. Since the slope of the regression line shown in the figure is a minus value, Q can not be estimated. As listed in Table 1, four Tmax, from 388 K to 423 K, were selected in this study. In such temperature range, creep properties of the lead-free solder have been reported to be stable [11]. Since mechanical properties of the lead-free solder scarcely change at maximum temperatures investigated, the dependance of thermal fatigue life on Tmax was not recognised.

Fig. 7 shows relationship between N_f and ΔT. The n value was estimated as 1.9 from the slope of the line shown in the figure, although the value may become a little larger by the results of test No. 8.

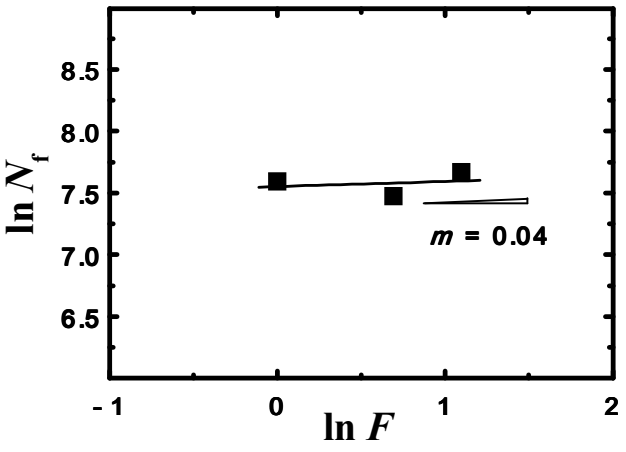

Fig. 4 Relationship between N_f and F.

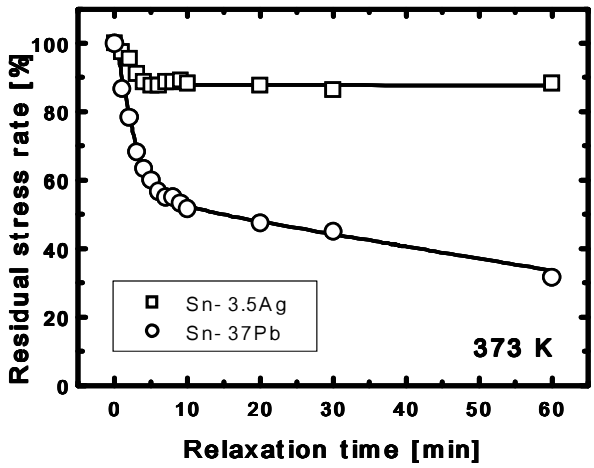

Fig. 5 Stress relaxation curves of Sn-37Pb and Sn-3.5Ag solder joints.

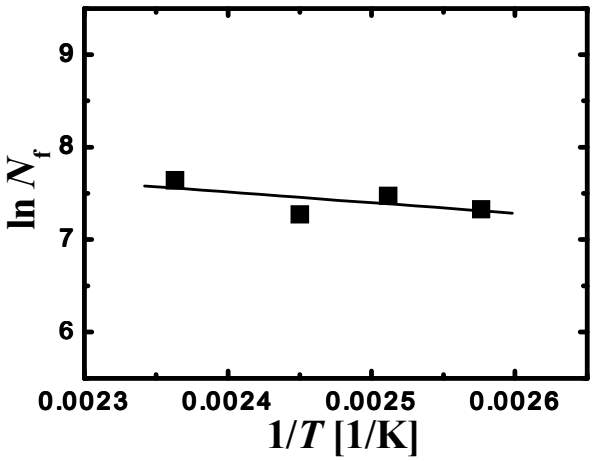

Fig. 6 Arrhenius plot for Q.

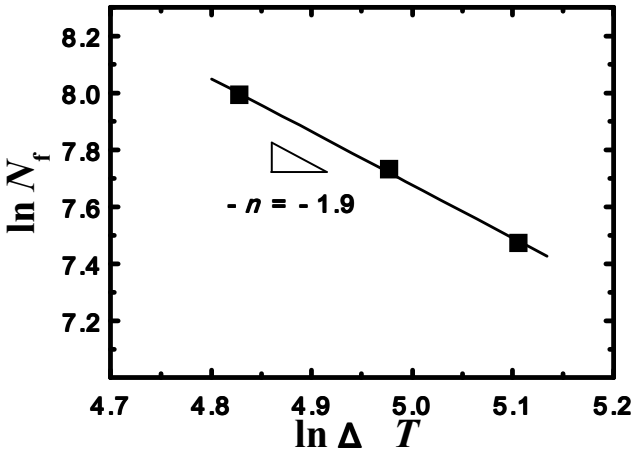

Fig. 7 Relationship between N_f and ΔT.

This is very close to the conventional value used for Sn-Pb solder joints [1, 2]. Similar n values have been reported in lead-free solder joints encapsulated with epoxy based underfill materials [12] and the

lead-free solder joint of the ceramic ball grid array (CBGA) package [13]. When the ceramic package is joined on the epoxy based substrate such as FR-4, mismatch of the coefficient of thermal expansion (CTE) between package and substrate materials is relatively larger compared with that in the joint using epoxy based package. On increasing the CTE mismatch, the effect of ΔT and Tmax on thermal fatigue life of the solder joint becomes larger. In this study, both CSP and substrate materials were epoxy based ones, and thus the CTE mismatch was relatively low. This means that thermal stress and strain introduced in the solder joint are relatively low. Therefore, the effect of ΔT on thermal fatigue life of the solder joint seems to be slight in this study due to low thermal strain. For n value, it is clarified that the conventional value used for Sn-Pb solder joints is also effective for the Sn-3.5Ag-0.75Cu lead-free solder joint.

Summary

ATC tests were conducted to investigate effects of thermal cycle conditions on thermal fatigue lives of CSP lead-free solder joints and to examine the Coffin-Manson's type equation for the joints. Effects of frequency and maximum temperature in ATC test on thermal fatigue life of the Sn-Ag-Cu lead-free solder joint were slight in ATC conditions investigated. The main reason why such a result was obtained is that the lead-free solder has excellent creep resistance compared with the Sn-Pb solder. The n value in the modified Coffin-Manson equation was estimated as 1.9 for the joint. This value is very close to the conventional value used for Sn-Pb solder joints.

References

[1] K. C. Norris, A. H. Landzberg: IBM J. Res. Develop., Vol. 13 (1969), p. 266

[2] I. Shohji, H. Mori and Y. Orii: Microelectron. Reliab., Vol. 44 (2004), p. 269

[3] S. K. Kang, P. Lauro, D. Y. Shih, D. W. Henderson, J. Bartelo, T. Gosselin, S. R. Cain, C. Goldsmith, K. Puttlitz, T. K. Hwang and W. K. Choi: Mater. Trans., Vol. 45 (2004), p. 695

[4] A. G. Gracia, E. Woirgard and C. Zardini: Microelectron. Reliab., Vol. 45 (2005), p. 1652

[5] T. Y. Tee, H. S. Ng and Z. Zhong: Microelectron. Reliab., Vol. 46 (2006), p. 2131

[6] M. Spraul, W. Nuchter, A. Moller, B. Wunderle and B. Michel: Microelectron. Reliab., Vol. 47 (2007), p. 252

[7] B. Vandevelde, M. Gonzalez, P. Limaye, P. Ratchev and E. Beyne: Microelectron. Reliab., Vol. 47 (2007), p. 259

[8] A. R. Zbrzezny, P. Snugovsky and D. D. Perovic: Microelectron. Reliab., Vol. 47 (2007), p. 220

[9] I. Shohji, K. Yoshizawa, M. Nishimoto and T. Kawano: Smart Processing Technology, Vol. 1 (2006), p. 175

[10] I. Shohji: Doctoral Dissertation of Osaka University (1998)

[11] I. Shohji, T. Yoshida, T. Takahashi and S. Hioki: Mater. Sci. Eng., Vol. A366 (2004), p.50

[12] I. Shohji, T. Tohei, K. Yoshizawa, M. Nishimoto, Y. Ogawa and T. Kawano: Smart Processing Technology, Vol. 2 (2008) in press

[13] K. Shimizu, S. Sakuyama and T. Yamamoto: Proc. of 14th Symposium on Microjoining and Assembly Technology in Electronics (The Japan Welding Society, 2008) p. 145

Key Engineering Materials Vols. 385-387 (2008) pp 437-440
© (2008) Trans Tech Publications, Switzerland
doi:10.4028/www.scientific.net/KEM.385-387.437

Approximate method for predicting inelastic displacement of SDF systems

Mun-Su Bae[1, a], Jong-Bo Kim[1,b] and Sang-Whan Han[2,c]

[1]Graduate Student, Dept. of Architectural Engineering, Hanyang University, Seoul 133-791, Korea

[2]Professor, Ph.D., Dept. of Architectural Engineering, Hanyang University, Seoul 133-791, Korea

[a]bms79@hanmail.net, [b]jong_bok@hotmail.com, [c]swhan82@hotmail.com

Keywords: inelastic displacement; bilinear SDF systems; ground motions; regression analysis.

Abstract. The objective of this study is to develop inelastic displacement ratio for calculating peak inelastic displacement of SDF systems. The inelastic displacement ratio is defined as the ratio of peak displacement of inelastic SDF system to the peak displacement of corresponding elastic SDF system. Statistical studies are carried out to estimate median inelastic displacement ratios and those dispersion of bilinear SDF systems with given yield-strength reduction factors, natural periods, post-yield stiffness ratios and damping ratios ranging from 1 to 20% when subjected to 60 earthquake ground motions recorded on stiff soil sites. This study shows that equal displacement rule overestimates the peak inelastic displacement of the system which has a fundamental period ranging from the intermediate to long period. It is also observed that no significant difference was observed in the value of median inelastic displacement ratio across site classes.

Introduction

To avoid extremely effort of nonlinear response history analysis, simplified and approximate method has been developed in recent provisions by applying the nonlinear static procedure or pushover analysis [1, 2]. Peak inelastic displacement demands of single degree of freedom (SDF) system during earthquake excitation are needed for these methods.

Miranda [3] was shown that *R*-μ-*T* relationship for calculating peak inelastic displacements leads to underestimations comparing with inelastic displacement ratio which is derived form statistical studies. *Equal displacement rule* which is traditional method to predict peak inelastic displacements in the intermediate and long period range is only appropriate for elasto-perfectly-plastic systems [4]. Thus this study investigates inelastic displacement ratio for various range of post-yield stiffness ratio and damping ratio and proposes equations to predict inelastic displacement ratio for bilinear systems.

Inelastic Displacement Ratios C_R in Bilinear System

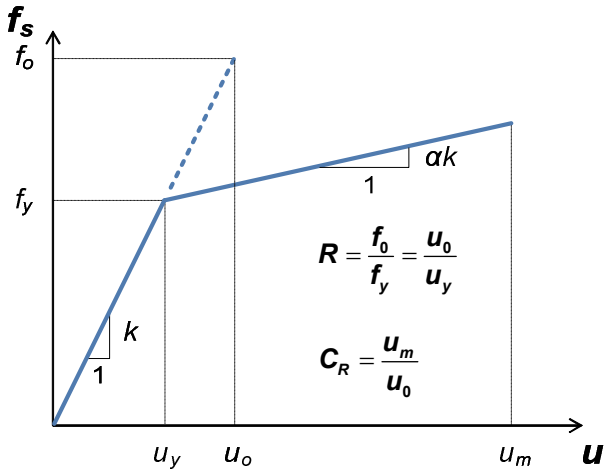

Fig. 1 Force-displacement relationship in a bilinear system

The inelastic displacement ratio, C_R is defined as u_m from the inelastic SDF system divided by u_o from the corresponding elastic SDF system, which has the same structural properties. Yield-strength reduction factor, R is the ratio of elastic strength, f_o of the elastic SDF system to yield strength, f_y. Figure 1 shows force-displacement relationship for bilinear system having post-yield stiffness ratio, α.

Statistical Studies for Inelastic Displacement Ratios

To conduct statistical study of C_R, it uses 60 ground motions recorded at firm sites, used in Chopra and Chintanapakdee [5]. This study conducts linear and nonlinear RHA with combinations of the variables shown in Table 1 and uses the geometric mean as the median value of C_R.

Table 1 Variables for statistical studies for C_R

Variable	Range	Number
T_n	0.1~5.0 (ΔT_n=0.1)	50
α	0~0.10 ($\Delta\alpha$=0.01), 0.15, 0.20	13
R	1.5, 2~8 (ΔR=1)	8
ζ	0.01~0.10 ($\Delta\zeta$=0.01), 0.12~0.20 ($\Delta\zeta$=0.02)	15

Effects of Soil Conditions. Ruiz-García and Miranda [4] reported that, at firm soil sites, the effect of ground motions on C_R in elasto-perfectly-plastic system is small. The maximum difference in C_R was less than 20%. In this study, no significant difference was observed in the values of median C_R across site classes. The ratio of $C_{R,D}$ to $C_{R,BCD}$ for a system having post-yield stiffness of 10%, and damping ratios of 2, 5 and 20% was between 0.9 and 1.1. But this data is not present here.

Acceleration Sensitive Ranges. In short period systems (0.2sec), the median C_R becomes larger with increasing R [Fig. 2(a), (b)]. As shown in Fig. 2(a), the median C_R decreases with increasing α. A more significant reduction in the median C_R is observed in short period systems having small α [Fig. 2(a), 3(a)]. In short period systems having small α (3%), the influence of ζ on C_R is greater than long period [Fig. 2(b), 3(b)]. This phenomenon is more obvious for larger R.

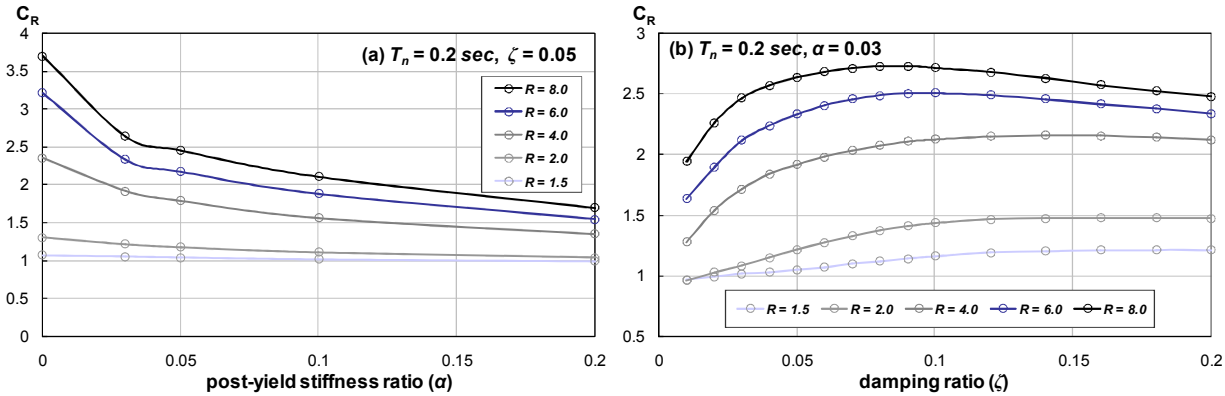

Fig. 2 C_R factor with respect to (a) post-yield stiffness (b) damping ratio at short period

Velocity and Displacement Sensitive Ranges. As shown in Fig. 3, the effect of α and ζ is not obvious in long period systems (1.0sec). Equal displacement rule can not apply having small ζ and large α and R. However, it is noted that in systems with high damping ratio (20%), the median C_R is approximately 1, regardless of the value of α and R [Fig. 3(b)].

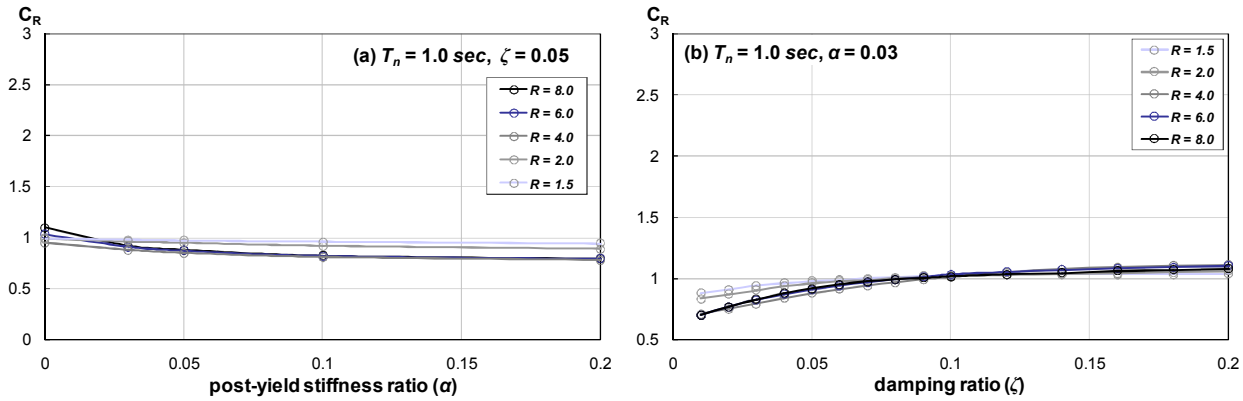

Fig. 3 C_R factor with respect to (a) post-yield stiffness (b) damping ratio at intermediate period

Nonlinear Regression Analyses

In this study, equations for calculating median displacement ratio, $\tilde{C}_{R,\zeta}$ are proposed:

$$\tilde{C}_{R,\zeta} = \tilde{C}_{R,\zeta=0.05} \times \tilde{C}_{\zeta} \tag{1}$$

where $\tilde{C}_{R,\zeta=0.05}$ is the median C_R for a damping ratio of 5%, and $\tilde{C}_{\zeta}$ is the calibration factor to account for different damping ratios. Equations are established as follows. The coefficients used in Eq.2 are summarized in Table 2:

$$\tilde{C}_{R,\zeta=0.05} = a^{(R-1)^b} + \frac{c\cdot(R-1)^d}{T^e \cdot R^f \cdot \left[g+(100\alpha)^h\right]} \tag{2}$$

Table 2 Coefficients of $\tilde{C}_{R,\zeta=0.05}$

	a	*b*	*c*	*d*	*e*	*f*	*g*	*h*
$T_n \le 0.8$	*1.00*	*0.50*	*0.34*	*2.82*	*2.19*	*2.76*	*3.12*	*0.75*
$T_n > 0.8$	*0.82*	*0.64*	*0.62*	*0.13*	*0.12*	*-0.65*	*4.85*	*0.50*

$$\tilde{C}_{\zeta} = \frac{\gamma_1 \ln(\gamma_2\zeta+\gamma_3)}{(1-\alpha)^{\gamma_4}} \frac{T^{0.2}}{R^{0.1}} + (\gamma_5\zeta^2+\gamma_6\zeta+\gamma_7) \qquad T_n < 0.2 \tag{3-a}$$

$$\tilde{C}_{C} = 1 + \frac{\gamma_8 \ln\zeta + \gamma_9}{T^{0.3}} R^{0.3} \qquad T_n \ge 0.2 \tag{3-b}$$

$\gamma_1 = 3.01$, $\gamma_2 = 9.75$, $\gamma_3 = 0.56$, $\gamma_4 = 0.39$, $\gamma_5 = 25.32$, $\gamma_6 = -17.12$, $\gamma_7 = 1.70$, $\gamma_8 = 0.06$, $\gamma_9 = 0.18$

This study also proposed an equation for calculating the dispersion, $\sigma_{\ln C_R}$, which is represented by the standard deviation of the natural log of C_R, follows:

$$\tilde{\sigma}_{\ln C_R} = \theta_1 \cdot \left(\frac{1}{\exp(\theta_2\cdot\zeta)} + \frac{1}{T^{0.5}}\right) \cdot \left(1-\exp(\theta_3\cdot(R-1)^{0.3})\right) / \left(\theta_4+\alpha^{0.5}\right) \tag{4}$$

$\theta_1 = -0.60$, $\theta_2 = 3.84$, $\theta_3 = 0.25$, $\theta_4 = 1.16$

The fractiles of C_R $\left(C_{R,p\%}\right)$ can be calculated using Eqs.1-4. As shown in Figure. 4, proposed equations predict actual data accurately.

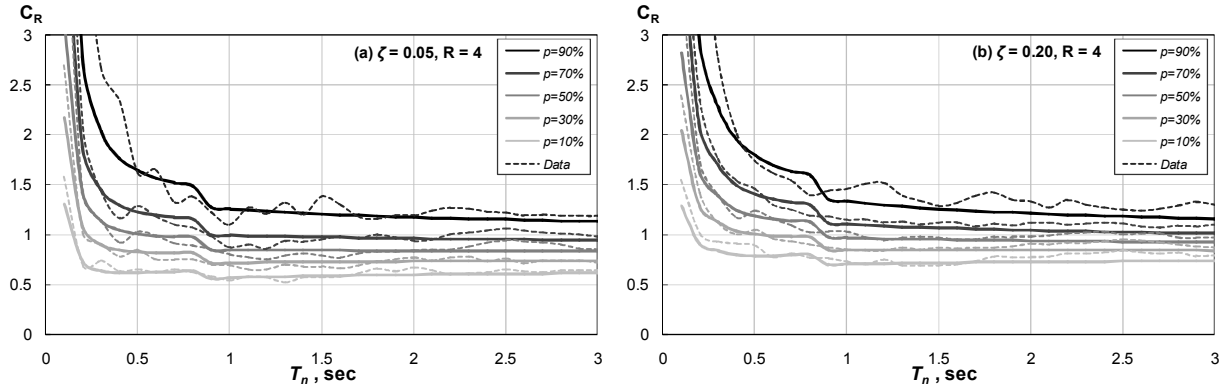

Fig. 4 Actual and predicted C_R factor ($\alpha = 10\%$)

Summary

The primary purpose of this study is to develop the equations for estimating median C_R and dispersion of C_R in various probabilistic ranges. Statistical studies were carried out under an ensemble of 60 ground motions collected at stiff soil sites. No significant difference was observed in median C_R across site classes B, C and D. Thus it constructed equations to calculate median C_R and dispersion of C_R without dependence upon site classifications.

This study observed that the median C_R is significantly influenced by the change in post-yield stiffness ratio, damping ratios (≤5%) and yield-strength reduction factor in short period systems. Equal displacement rule overestimates peak inelastic displacement in bilinear SDF systems, particularly in long period systems having a small damping ratio.

Using nonlinear regression analysis, equations of median inelastic displacement, C_R and the dispersion, $\sigma_{\ln C_R}$, in bilinear SDF systems were proposed. The fractile of C_R predicted accurately using the proposed equations.

Acknowledgements

This study was supported by a grant 07-UR-B04 (High-tech Urban development program) and SRC/ERC R11-2005-056-04002-2.

References

[1] Applied Technology Council: *Seismic evaluation and retrofit of concrete buildings*, *Report ATC-40*, Redwood City, Calif., 1996

[2] BSSC: *NEHRP guidelines for the seismic rehabilitation of buildings, Report FEMA 273(Guidelines) and Report. 274 (Commentary)*, Federal Emergency Management Agency Washington, D.C., 1997

[3] Miranda, E.: *Estimation of inelastic deformation demands of SDOF systems*, J. Struct. Engrg., ASCE, 127(9), 1005-1012, 2001

[4] Ruiz-García, J. and Miranda, E.: *Performance-based assessment of existing structures accounting for residual displacement, Report TR-153*, The John A. Blume Earthquake Engineering Center, Stanford University, Stanford, CA, 2005

[5] Chopra, A.K. and Chintanapakdee, C.: *Inelastic deformation ratios for design and evaluation of structures: single-degree-of-freedom bilinear system*, J. Struct. Engrg., ASCE, 130(9), 1309-1319, 2004

Key Engineering Materials Vols. 385-387 (2008) pp 441-444
© (2008) Trans Tech Publications, Switzerland
doi:10.4028/www.scientific.net/KEM.385-387.441

Mechanical Properties of Scandia Stabilised Zirconia with Alumina Addition

Wakako Araki[1,a], Hiroyuki Norigoe[2,b], and Tadaharu Adachi[2,c]

[1]Dept Mechanical Engineering, Saitama University

405 Bldg Mech Eng, 255 Shimo-Okubo, Sakura-ku, Saitama-shi, Saitama 3388570, JAPAN

[2]Dept Mechanical Sciences and Engineering, Tokyo Institute of Technology

2-12-1 O-okayama, Meguro-ku, Tokyo 1528550, JAPAN

[a]araki@mech.saitama-u.ac.jp, [b]norigoe@stu.mech.titech.ac.jp, [c]adachi@mech.titech.ac.jp

Keywords: Solid Oxide Fuel Cell, Zirconia, Mechanical Property

Abstract. Zirconium oxide doped with scandium oxide is one of the most promising materials for electrolytes of solid oxide fuel cells because of its high ionic conductivity. In this study, temperature dependence of mechanical property, especially strength, of 9 mol% scandia doped zirconia polycrystalline samples with 0 to 30 wt% of alumina additions was examined at temperatures from 293 to 1273 K. Ionic conductivity was also measured by AC impedance analysis. From both mechanical and electrical standpoints, the experimental results were discussed in terms of alumina addition.

Introduction

Zirconium oxides doped with trivalent rare-earths are one of most promising materials for electrolytes of solid oxide fuel cells because it has a high oxygen ionic conductivity through oxygen -ion vacancies. 8 mol% yttria doped zirconia is the most common electrolytes today because of its high ionic conductivity, mechanical properties, and phase stability under oxidation/reduction atmospheres. Amongst the zirconia system, it is well known that scandium oxide is the best dopant because scandium has a very close ionic radius to the one of zirconium, which can make the association enthalpy small [1].

Recently, composites of stabilised zirconia and alumina particles have been proved to improve ionic conductivity because added alumina could work to scavenge grain boundaries [2]. Also, alumina addition is expected to work to strengthen materials and improve mechanical properties. Although a lot of work has been devoted to crystal structures and conductivities of zirconia electrolytes, mechanical properties and fracture behaviours of these materials have not been fully understood, especially considering correlation to ionic conductivity at high temperatures.

In this study, mechanical strength of scandia-stabilised zirconia with various contents of alumina addition is examined. Also, relationships between mechanical strength and ionic conductivity are investigated. Based on experimental results, a useful property diagram for selecting appropriate electrolytes of SOFC is proposed.

Experimental Procedure

Zirconium oxides (ZrO_2) doped with 9 mol% of scandium oxide (Sc_2O_3) added with alumina (Al_2O_3) were prepared by a standard solid-state reaction in this study. Powders of ZrO_2, Sc_2O_3, and Al_2O_3 were mixed with addition of some acetone by a ball-milling for 24 h. The weight ratio of Al_2O_3 varied from 0 to 30 wt%. The mixture powders were dried at room temperature to remove the acetone, and then they were pressed into discs with a diameter of about 26 mm and a thickness of 2 mm followed by sintering at 1873K for 10 hours in air. The mixture ratios of prepared samples are summarized in Table

X-ray powder diffraction analysis (XRD) was conducted to determine crystal structures. Observation by scanning electron microscope (SEM) was performed to investigate grain structures. Three-point bending test was performed at 293, 973, and 1273 K in a furnace with a universal testing machine in order to measure the mechanical bending strength. Each sample was cut into 1 mm wide and 20 mm long. The fracture surfaces were observed by SEM. To examine ionic conductivity from 873 K to 1273 K in air, alternative current (AC) impedance measurements were performed. A four-probe technique was employed by using platinum paste electrodes with platinum meshes and wires.

Experimental Results and Discussion

Crystal and Grain Structure. The XRD confirmed cubic and tetragonal phases for 9ScSZ and additional rhombohedral phase of alumina for 1 to 30A9ScSZ. The alumina addition caused no change in the crystal structure of 9ScSZ. The intensity of alumina increased with its content. Some unidentifiable peaks could represent a very small amount of solid solution of 9ScSZ and alumina.

The SEM observation showed that 9ScSZ had a densified grain structure and the average grain size of about 8 μm. The grain size increased with 10wt% of alumina but decreased from 10 to 30 wt%. Alumina prevents the grain growth of zirconia due to the difference of their surface energies whereas a small amount of alumina works as a sintering aid. There were some pores observed for 1 to 20A9ScSZ but not for 30A9ScSZ probably because the pore size and the grain size were very close for 30A9ScSZ.

The crystal and grain structures are summarised in Table 1.

Table 1 Crystal and Grain Structure of Prepared Sample

Sample Name	Sc_2O_3 [mol%]*	Al_2O_3 [wt%]	Crystal structure		Grain size
			$Sc_{0.09}Zr_{0.91}O_x$	Al_2O_3	[μm]
9ScSZ	9	0	cubic, tetragonal	rhombohedral	8.5
1A9ScSZ	9	1	cubic, tetragonal	rhombohedral	14
10A9ScSZ	9	10	cubic, tetragonal	rhombohedral	12
20A9ScSZ	9	20	cubic, tetragonal	rhombohedral	3.6
30A9ScSZ	9	30	cubic, tetragonal	rhombohedral	2.7

* proportional to ZrO_2

Bending Strength. Figure 1(a) shows the effect of the alumina content on the bending strength of 9ScSZ and 10 to 30A9ScSZ measured by the three-point bending test at room temperature (293 K). The bending strength showed an increase with the alumina content. Figure 1(b) shows the temperature dependence of the bending strength of 9ScSZ and 30A9ScSZ with 8YSZ. As well as the modulus, the strength had a small value at 973 K especially for 9ScSZ, where the value was less than half of that at 293 K, but showed a small increase at 1273 K.

Figure 2 shows the SEM pictures of the fracture surfaces of 9ScSZ and 30A9ScSZ tested at 973 K. It clearly illustrated the transgranular fracture for 9ScSZ and the intergranular fracture for 30A9ScSZ. In the fractography by SEM, 9ScSZ and 10A9ScSZ generally showed the transgranular fracture mode at any test temperatures while 20A9ScSZ and 30A9ScSZ showed the intergranular fracture, although a little bit of intergranular fracture was observed for 9ScSZ fractured at 1273 K.

Figure 3 shows the average strength of each sample at each temperature with deviation and also with Hall-Petch model; $\sigma_f = \sigma_y + kR^{-1}$, where σ_f and σ_y are strength, k is and R are constant and grain size, respectively, for the results at 293 K. It is well known that the small grains generally improve mechanical strength because it fractures in the intergranular mode [3]. This explains well the high strength of 30A9ScSZ and 20A9ScSZ. In addition, the tetragonal phase is known to improve the strength due to stress-induced phase transition mechanism, however, its effect decreases with temperature because the tetragonal phase becomes more stable at high temperature. This explains the decrease of the strength at 973 K. The recovery of the strength at 1273 K will be discussed somewhere else.

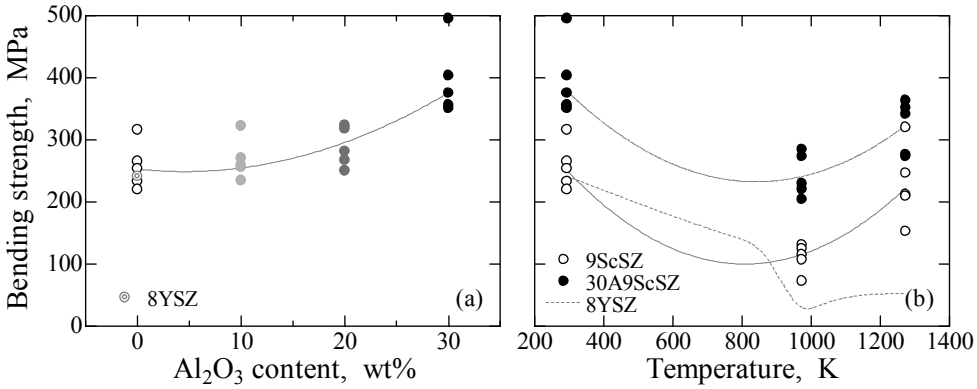

Figure 1 Bending Strength

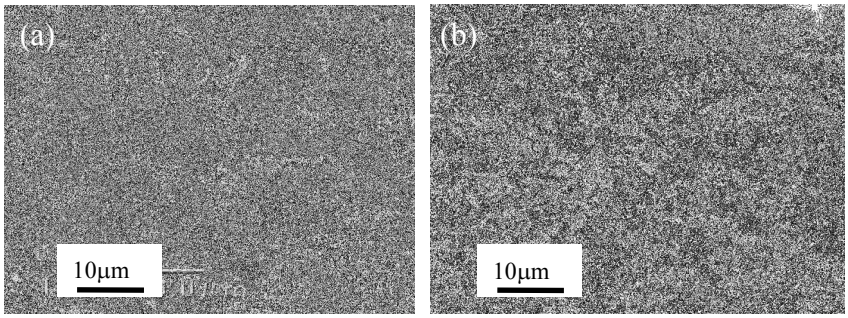

Figure 2 Fractography

Ionic Conductivity. The ionic conductivity at any temperature decreased with the alumina content, even with 1 wt% of alumina addition. The small drop was seen with 1 wt% of alumina addition and the conductivity monotonically decreased up to 30 wt% of alumina content. At 1273 K, for instance, the conductivity of 9ScSZ was about 3.1 S/cm while the one of 30A9ScSZ was 0.070 S/cm.

The decrease in the conductivity could be mainly attributed to the increase in volume of the non-conductive alumina phase; however, the decrease in the conductivity of the samples with alumina was much larger than the expected value from the volume ratio. The very small amount of second phase which was identified by the XRD and also the increase of grain boundary could have also contributed to the decrease in the conductivity. The improvement in the conductivity by the scavenge effect reported in several studies [*] was not observed in the present study.

Property diagram. The alumina addition definitely increased mechanical strength whereas it decreased the ionic conductivity. Figure 4 shows a property diagram of bending strength and ionic conductivity from 973 K to 1273 K. This kind of diagram illustrating relationships between mechanical properties and conductivity can be a useful tool to select materials and design of electrolytes.

Conclusion

In this study, the mechanical strength and ionic conductivity of 9 mol%-scandium-doped zirconium oxide added with 0 to 30 wt% of alumina was investigated at various temperatures. The alumina addition decreased grain size and increased strength at expenses of ionic conductivity. A property diagram for material selection was suggested based on the results.

References

[1] Y. Arachi et al.: Solid State Ionics Vol. 121 (1999), 121, p. 133.

[2] V.V. Kharton et al: Solid State Ionics Vol. 174 (2004), p. 135.

[3] R.W. Rice: *Mechanical properties of ceramics and compositess* (Marcel Dekker Inc, New York 2000).

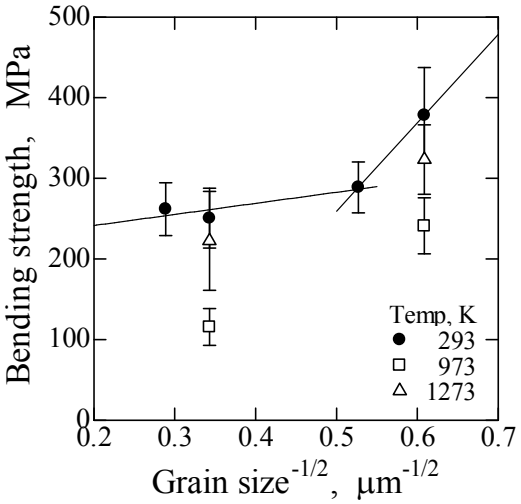

Figure 3 Grain size effect on strength

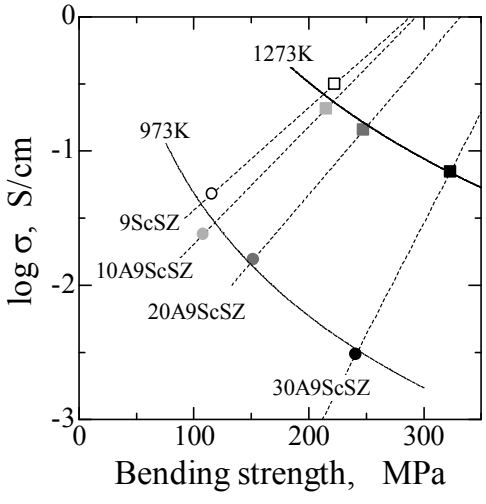

Figure 4 Property diagram

Key Engineering Materials Vols. 385-387 (2008) pp 445-448
© (2008) Trans Tech Publications, Switzerland
doi:10.4028/www.scientific.net/KEM.385-387.445

Wood fibre reinforced cement matrix: a micromechanical based approach

M.G. Sierra Beltran[1, a], E. Schlangen[1,b]

[1]Microlab, M & E, Faculty of Civil Engineering and Geosciences, Delft University of Technology, P.O. Box 5048, 2600 GA Delft, The Netherlands

[a]m.g.sierrabeltran@tudelft.nl, [b]h.e.j.g.schlangen@tudelft.nl

Keywords: Wood fibre, cement matrix, micromechanics, microcracking, ductility.

Abstract

In this paper a micromechanics-based design is proposed for the development of a material with enhanced ductility and flexural strength combined with low production cost. The composite performance is described by 11 micromechanical properties of the system consisting of cement matrix, fibres and fibre-matrix interface. Most of these properties are defined through laboratory tests. A strain-hardening behaviour with multiple microcracks prior to failure is is the goal for the composite with enhanced ductility. The amount and size of the fibres needed for bridging the microcracks as well as the composition of the cement matrix will be determined in order to achieve this behaviour.

Introduction

Natural fibres such as wood are a lightweight and low-cost replacement for synthetic fibres. Compared with synthetic flexible fibres currently used as reinforcement for cement matrixes wood fibres have similar values of modulus of elasticity but 50% lower tensile strength. However, the price of wood fibres is only about 10% of the price of synthetic fibres. Furthermore wood fibres are a renewable resource and the amount of energy needed to produce them is just one third of the energy needed to produce synthetic fibres. Most of the research about wood fibres in cement composites has been done for thin sheet products and other non structural applications. This article proposes a different approach in order to achieve reasonable compressive and tensile strength and enhanced ductility: through micromechanics. A material with such characteristics could be use for cast-in-place or prefabricated elements for seismic design, retaining walls, piles, foundations and other structural applications were flexural capacity and ductility are needed. In order to accomplish these objectives the experience of tailoring a cementitious material called Engineered Cementitious Composite (ECC) with short synthetic fibres will be taken into account [1].

Materials

Wood fibres. For this project fibres from softwood trees were selected. The two main species of trees are gymnosperms, another name for softwood or conyferous trees and angiosperms, also known as hardwood or broadleaf trees. Softwood was the choice to work with for several reasons. Since the cells in softwood have a more simple form and there are no vessels, the percentage of fibres is higher than in hardwood, up to 90%, and the fibres tend to be more uniform. Furthermore the softwood fibres are longer (3 to 5 mm average) and thicker (up to 45 μm) than hardwood.

Three types of softwood fibres are being studied as possible reinforcement for a cement matrix: Fibres from larch, spruce and pine. Lumber pieces of larch and spruce are cut into small blocks of 1x1x2 cm. These blocks are cooked following a neutral sulphite semichemical (NSSC) pulping procedure after which the bundles of fibres are manually taken apart. Each bundle have about 65 fibres. The fibres from pine are prepared out of a veneer sheet. The veneer is first cut into pieces of about 2x3 cm and then bundles of fibres are cut using a microtome. These bundles have about 160

fibres. The bundles were cut at length 10 mm. The bundles of fibres will now be referred to as fibres. The fibres were tested under direct tensile strength at the Microlab, using a micro tension-compression testing device (developed by Kammrath & Weiss) with a setup adapted for it (Fig. 1). The results from the tests are shown in Table 1.

Table 1. Average measured dimensional and mechanical properties of the wood fibres investigated

Fibre	Tensile strength σ_f [MPa]	Young´s modulus E_f [GPa]	Area [mm^2]
Spruce	663	39	0.055
Larch	708	34	0.041
Pine	730	29	0.113

Cement matrix. The proposed cement matrix has the following weight ratios: cement:fly ash:sand:water and superplasticiser (SP) = 1:1.2:0.8:0.6. The cement is type CEM I 52.5 and the sand size ranges from 0.125 – 0.25 mm. This mixture will be optimised during the design to fulfill the requirements of strength, toughness and flaw size.

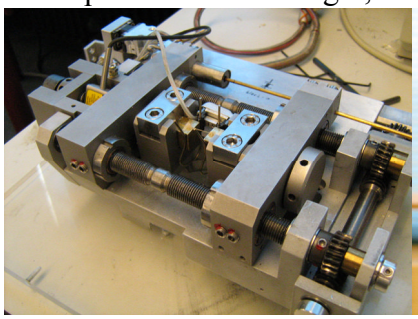
Fig. 1 Single fibre tensile test setup

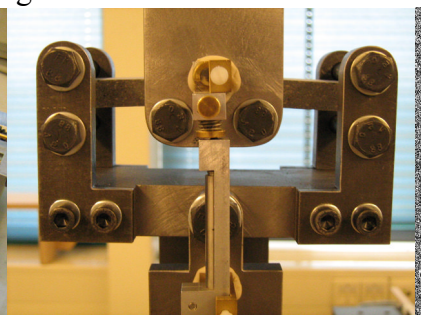
Fig. 2 Four point bending test setup

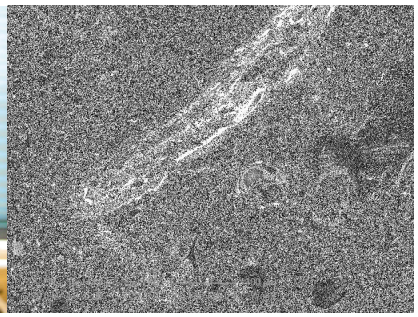
Fig. 3 Wood fibre in cement matrix

Micromechanics based design

Micromechanical Model. Micromechanical models based on fracture mechanics and deformation mechanisms make it possible to tailor the material by controlling the failure mode, the tensile strength and the ultimate tensile strain [1]. In fibre cement composite the model will predict the tensile strength by calculating the maximum bridging stress. As mentioned before, the composite performance is described by 11 micromechanical properties of the fibre-matrix system [2]:

- Fibre parameters: fibre length (L_f), fibre diameter (d_f), fibre stiffness (E_f), fibre strength (σ_f), fibre volume fraction (V_f)
- Matrix parameters: matrix stiffness (E_m), matrix fracture toughness (K_m), initial flaw size (c).
- Fibre-matrix interaction parameters: interfacial frictional bond (τ_o), interfacial chemical bond (G_d), snubbing coeficient(f)

K_m is measured from three or four point bending tests (Fig. 2) The fibre matrix interface properties are measured from single fibre pullout tests: a fibre with a controlled embedment length is pulled out from a block of matrix while the load vs displacement relation is recorded [3]. The data interpretation and calculation of the interface parameters will be done according to reference [4].

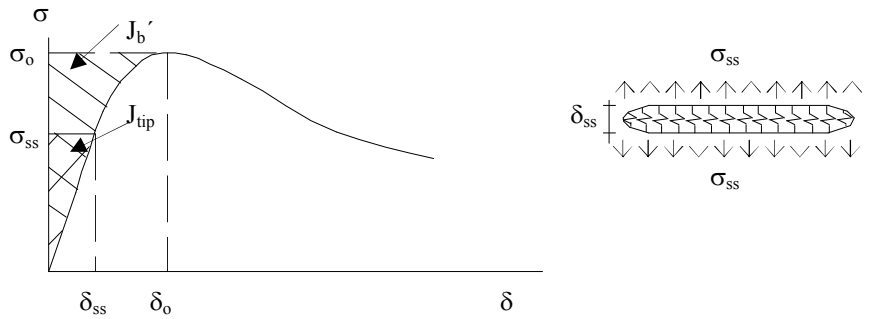

Fig. 4 Typical σ(δ) curve for strain-hardening composite

A material that shows a strain-hardening behaviour with multiple microcracking prior to failure develops enhanced ductility. Two criteria must be satified in order to achieve strain-hardening behaviour: steady state cracking criterion and first-crack stress criterion. To clarify these criteria, the composite bridging law, also known as the σ(δ) relation, is plotted in Fig.4. This relation describes the fundamental material property that rules the mechanical performance of fibre reinforced composites beyond the first crack. σ(δ) can be formulated (Eq. 1) by integrating the contributing effects of the individual fibres bridging the crack. It takes into account probabilistic density functions, random orientation of fibres, fibre rupture, slip hardening and matrix spalling.

The pullout load-displacement relation P(δ) is modeled at a single fibre level. P(δ) has two regions; first the debonding and after that the slip. The debonding process can be modeled as a tunneling crack with a characteristic interface fracture energy G_d. After debonding the interface is dominated by a constant frictional stress τ_o.

$$\sigma(\delta) = \frac{4V_f}{\pi {d_f}^2} \int_{\varphi=0}^{\pi/2} \int_{z=0}^{(L_f/2)\cos\varphi} P(\delta)\, p(\varphi)\, p(z)\, dz\, d\varphi \tag{1}$$

The steady state crack criterion will assure the presence of multiple cracking if the complementary energy J_b' is equal to, or greater than the matrix crack tip toughness J_{tip} (Eq. 2). The steady state crack stress σ_{ss} can be expressed as Eq. 3. J_{tip} is estimated as K_m^2/E_m [5] while J_b'depends on the fibre and fibre matrix interface parameters. After some simplifications [5] this relation can then be derived as in Eq. 4.

$$J_{tip} \le \sigma_0 \delta_0 - \int_0^{\delta_0} \sigma(\delta)\, d\delta \equiv J_b' \tag{2}$$

$$\sigma_{ss}\delta_{ss} - \int_0^{\delta_{ss}} \sigma(\delta)\, d\delta = J_{tip} \tag{3}$$

$$J_b' = V_f \frac{L_f}{d_f}\left(\frac{{\tau_0}^2 {L_f}^2}{6 d_f E_f} - 2G_d\right) \tag{4}$$

The first-crack stress criterion states that the first crack strength σ_{fc} should not exceed the maximum bridging strength σ_o [6].

Application to wood fibre cement composite. It is known that a strong chemical bond promotes fibre rupture: the fracture energy is reduced while the tensile strength of the composite increases, hence the material becomes strong but brittle. Since cement is an alkaline inorganic material (pH>12.5) containing surface hydroxyl groups [7,8] and wood fibres contain covalent hydroxyl groups from either residual lignin or both the cellulose component and the oxidation of end groups [7] the chemical bond is believed to be either hydrogen bonds or hydroxide bridges between fibres or between the fibres and the cement matrix. This can be a strong chemical bond, so high values of G_d are expected (G_d>2). The fiber-matrix interface has been investigated with an Environmental Scanning Electron Microscope (ESEM) (Fig. 3). G_d will be calculated after performing single fibre pullout tests. For the proposed cement matrix J_{tip} =15 J/m^2 [5]. From Eq. 4 with the fibre properties mentioned in Table 1 and the assumed value of G_d>2 to assure a strain hardening behaviour (J_b'>J_{tip}) calculations show that the minimum values for τ_o should be as shown in Table 2.

The fibre diameter has a strong influence in the estimation of J_b' A logical first assumption would be to lower the diameter of the fibres in order to be able to develop a ductile behaviour, but this may not be possible due to production contraints. Fibre volume fraction and fibre length also have a strong impact in J_b' but high fibre percentage or longer fibres will decrease the reology of the composite, affecting the workability and the uniform dispersions of the fibres. Since the fibre aspect

ratio is low (<100) there may be end effects on the total debonding load. The properties G_d and τ_o should be carefully studied as high values of τ_o suggest fibre rupture. The matrix contribution J_{tip} could be made lower by increasing the water to binder ratio, reducing the size of sand particles or by the use of inert filler.

Table 2. Predicted values of τ_o and σ_o

	Spruce fibres		Larch fibres		Pine fibres	
Fibre vol. fraction	2%	4%	2%	4%	2%	4%
τ_o (Mpa) >	3.84	2.94	3.14	2.42	4.63	3.47
σ_o (MPa)	2.99	4.65	2.83	4.46	2.49	3.79

Table 2 presents rough estimates of the bridging strength calculated with equations derived in reference 5 (for specific optimal conditions) and with the values of G_d and τ_o above mentioned. From direct tensile test on notched specimens (dimension: 170x35x10mm) performed at the Microlab the σ_{fc} for a composite with 2% larch fibres is 3.4 MPa. During that test and in 4 point bending tests (Fig. 2) this composite did not develop strain hardening behaviour nor ductility. From Table 2 the σ_o for this composite is lower than σ_{fc} which means that after the first crack no more load is transfered, the load drops due to fibre rupture or pullout. To prevent this to happen the matrix strength should be lowered.

Conclusions and future work

By relating microstructure to composite performance a micromechanics based design will help develop ductile wood fibres cementitious composites. The first steps in developing this material are described in this paper. Future work in this ongoing project includes the development of new equations for the micromechanical model in which the shape of the fibres (not circular) will be taken into account. Single fibre pullout tests and more direct tensile tests for wood fibre composites will be done in the future.

Acknowledgements

Financial support for this research from the National Council of Science and Technology (CONACYT), Mexico (Grant # 206108) is gratefully acknowledged. Furthermore the authors thank Prof. V. C. Li and Prof. K. Van Breugel for valuable discussions on the subject.

References

[1] V.C. Li, in: Engineered cementitious composites – Tailored composites through micromechanical modeling, edited by N. Banthia, A. Bentur, A. Mufti, Canad. Soc. of Civ. Eng.(1998).

[2] Z. Lin, T. Kanda, V.C. Li: Concr. Sci. Eng. Vol. 1 (1999), pp. 173-184.

[3] V.C. Li, C. Wu, S. Wang, A. Ogawa, T. Saito: ACI Mater. J. Vol. 99 (2002), pp. 463-472.

[4] C. Rendon, V.C. Li, C. Wu, H. Hoshiro, T. Saito, A. Ogawa: J. Mater. Civ. Eng. Vol. 13 (2001), pp. 399-406.

[5] S. Wang, V. Li: ACI Mater.J. Vol. 104 (2007), pp 233-241.

[6] C. Wu, in: Micromechanical tailoring of PVA-ECC for structural applications, PhD Thesis, University of Michigan, Ann Arbor, USA (2001)

[7] R.S.P. Coutts, P. Kightly: J. Mater. Sci. Vol 19 (1984) pp. 3355-3359.

[8] J.L. Pehanich, P.R. Blankenhorn, M.R. Silsbee: Cem. Concr. Res. Vol. 34 (2004), pp 59-65.

Key Engineering Materials Vols. 385-387 (2008) pp 449-452
© (2008) Trans Tech Publications, Switzerland
doi:10.4028/www.scientific.net/KEM.385-387.449

Crack Size Dependency of Shear-mode Fatigue Crack Threshold in Bearing Steel

Satoshi Muramoto[1, a], Hisao Matsunaga[1, b], Shigeaki Moriyama[1, c] and Masahiro Endo[1, d]

[1]Department of Mechanical Engineering, Fukuoka University,
8-19-1 Nanakuma, Jonan-ku, Fukuoka, 814-0180, Japan

[a]td070011@cis.fukuoka-u.ac.jp, [b]hm@fukuoka-u.ac.jp, [c]moriyama@fukuoka-u.ac.jp, [d]endo@fukuoka-u.ac.jp

Keywords: Shear-mode Fatigue Crack, Bearing Steel, Small Crack, Torsional Fatigue Test, ΔK_{IIth}, $\Delta K_{\mathrm{IIIth}}$

Abstract. Semi-elliptical shear-mode fatigue cracks were promoted in the axial direction of round specimens of SAE52100 bearing steel by fully-reversed cyclic torsion tests under a static axial compressive stress. Non-propagating cracks smaller than 1 mm were obtained in two ways; (i) stress amplitude decreasing tests of notched specimens, or (ii) constant stress amplitude tests of smooth specimens. The threshold stress intensity factor ranges, ΔK_{IIth} and $\Delta K_{\mathrm{IIIth}}$, showed a crack size dependency.

Introduction

Rolling-contact fatigue failures, such as flaking-type failure in bearings and shelling-type failure in railroad rails, are intimately related to the shear-mode (Modes II and III) fatigue crack-growth [1, 2]. For the quantitative evaluation of such problems, the behaviour of the crack-growth and its threshold must be clarified. However, their properties have not been well understood either qualitatively or from a quantitative fracture mechanics point of view, though there has been some significant progresses in recent years. For example, with respect to the Mode II threshold stress intensity factor range for bearing steel SAE52100, Otsuka *et al.* [3] made use of a decreasing, fully-reversed Mode II testing method which prevented contact of the opposing crack face. They found the Mode II threshold to be approximately 3 MPa·m$^{1/2}$. In contrast, Murakami *et al.* [4] found in decreasing ΔK_{II} tests that when the opposing crack faces were allowed to contact and if the friction coefficient was hypothesized to be 1.0, ΔK_{IIth} was 13 ~ 15 MPa·m$^{1/2}$. There is a large discrepancy between these results but the cause has yet to be clarified.

In the present study, semi-elliptical shear-mode fatigue cracks were promoted in the axial direction of round specimens of SAE52100 bearing steel by fully-reversed cyclic torsion tests under a static axial compressive stress. The threshold stress intensity factor ranges, ΔK_{IIth} and $\Delta K_{\mathrm{IIIth}}$, were estimated for cracks smaller than 1 mm.

Material and experimental methods

The studies were carried out on a commercial grade SAE52100 bearing steel. The chemical composition in wt. % was 0.98 C, 0.16 Si, 0.38 Mn, 0.12 P, 0.06 S, 0.12 Cu, 0.07 Ni, 1.39 Cr, 0.02 Mo and bal. Fe. The steel had been heat treated at 840°C for 30 minutes in a deoxiding gas followed by oil-quenching and tempered at 170°C for 2 hours. The average Vickers hardness *HV* measured with a load of 9.8 N was 753.

Fig.1 shows the shape and dimensions of the specimen. The specimen surfaces were finished by polishing with an emery paper and then buffing with an alumina paste. In some cases, three adjacent small holes aligned with the specimen axis were introduced. Fig.2 shows the shape and dimensions of the holes. They have crack-like thin slits made by the focused ion beam (FIB) technique at the both ends to facilitate crack initiation. The total length of the defects ranged

240~440 μm and their depths ranged 80 ~ 200 μm. In the following, these defects are termed defect A and B, respectively.

Cyclic torsion tests were carried out using a biaxial servo-hydraulic fatigue testing machine with a test frequency of 14 ~ 28 Hz and a stress ratio R of −1. To further reduce any tendency for Mode I cracking, an axial static compressive stress σ_m of −1200 or −1000 MPa was superposed on the torsional cyclic loading.

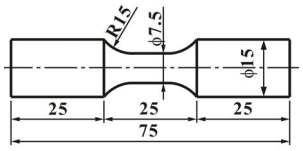

Fig.1 Shape and dimensions of fatigue test specimen (mm)

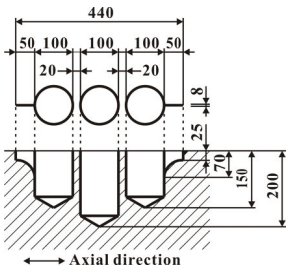

(a) Defect A

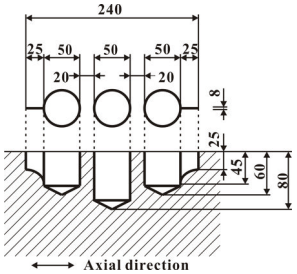

(a) Defect B

Fig.2 Shape and dimensions of holes having crack-like thin slits at the both ends (μm)

Results and discussion

Shear-mode crack-growth in axial direction. The fatigue tests were started at a τ_a of 540 ~ 600 MPa, where τ_a is the shear stress amplitude at specimen surface. In specimens having a defect A or B, shear-mode cracks were initiated from the crack-like slits and propagated in the axial direction. To obtain non-propagating cracks, τ_a was gradually decreased by 10 ~ 40 MPa with every increment in crack length $2a$ of 10 ~ 30 μm. If the crack stopped propagating for 10^7 cycles the test was finished. Fig.3 (a) and (b) show the non-propagating cracks emanating from the defects A and B. The crack-growth rate, da/dN, was less than 1×10^{-11} m/cycle for all stress levels, the extremely slow growth rate subsequently became even slower before complete arrest.

Smooth specimens without defect were also tested at a constant stress amplitude τ_a of 600 MPa. A number of cracks initiated from elongated MnS inclusions on the specimen surface. Most of the cracks became non-propagating crack before N =10^7 cycles without decreasing the stress amplitude, whereas a few cracks continued to propagate. Thus, it was assumed that the fatigue limit of smooth specimen was close to τ_a = 600 MPa. Fig.3 (c) shows an example of the non-propagating cracks in a smooth specimen.

Threshold of shear-mode crack-growth. Fig.4 shows the shape and dimensions of the non-propagating cracks shown in Fig.3, which were obtained by a successive polishing. The threshold stress intensity factor ranges, ΔK_{IIth} and ΔK_{IIIth}, were estimated from these results.

In the shear-mode surface crack such as the cracks in Fig.4, the propagation mode is Mode III at the crack bottom. On the other hand, the propagation is mainly dominated in a Mode II fashion in the vicinity of free surface. However, it is known that the nature of the crack tip singularity changes in the vicinity of a corner point where a crack front intersects a free surface [5-7]. Besides, it has been pointed out that the crack front edge of a propagating crack should terminate at the surface obliquely [7]. For such difficulties, stress intensity factor cannot be determined definitely in the vicinity of the corner point. Therefore, stress intensity factor ranges, ΔK_{II} and ΔK_{III}, were estimated approximately by use of Kassir and Sih's solution for an elliptical crack in an infinite body under uniform shear [8]. Poisson's ratio was assumed to be 0.3.

Fig.5 shows the relationship between crack sizes and the threshold values. ΔK_{IIth} was plotted for half crack length a and ΔK_{IIIth} for crack depth b, respectively. It is noted that the aspect ratio b/a of the non-propagating cracks emanating from inclusions ranged from 0.2 to 0.4. The relatively shallow crack shape implied that the crack-growth threshold was mainly determined by the growth in the internal direction. For this reason, the threshold values in smooth specimens

were estimated only for Mode III propagation. It appeared that the threshold values showed a crack size dependency for cracks less than 1 mm in size.

Microstructural change along shear-mode crack. Fig.6 shows an etched microstructure at the section A-A′ of the crack shown in Fig.4(b). A white structure was observed along shear mode cracks. Such microstructural changes are the typical characteristics in contact fatigue problems related to the shear-mode fatigue crack-growth. They have also been reported in a rail steel [4] and a medium carbon steel [9].

Summary

Semi-elliptical shear-mode fatigue cracks were promoted in round specimens of SAE52100 bearing steel. The threshold stress intensity factor ranges, ΔK_{IIth} and $\Delta K_{\mathrm{IIIth}}$, showed a crack size dependency for cracks less than 1 mm in size.

References

[1] Y. Murakami, Transactions of the Japan Society of Mechanical Engineers, Series A, Vol. 59 (1993), pp. 283-290

[2] S. Beretta, M. Boniardi, M. Carboni and H. Desimone, Engineering Failure Analysis, Vol. 12 (2005), pp. 157-165

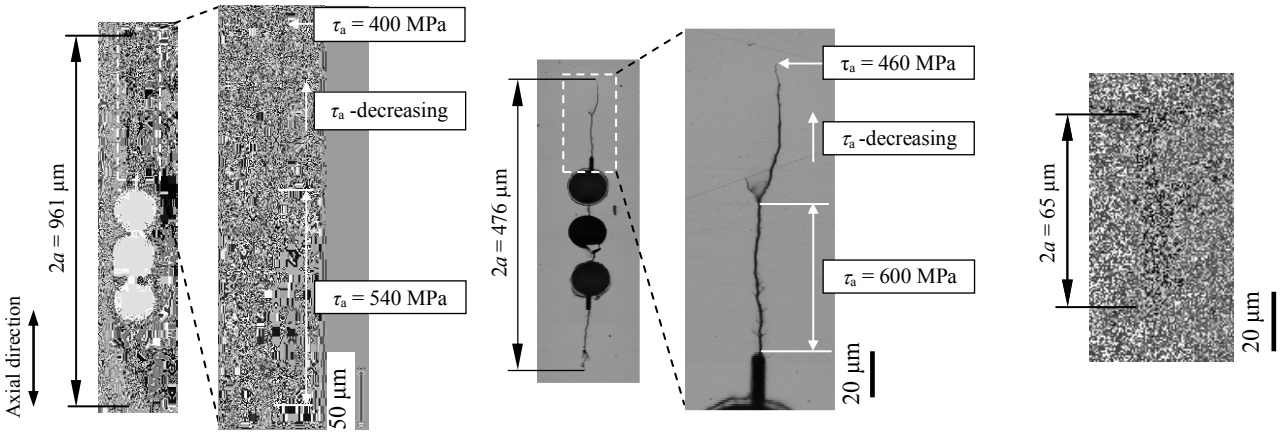

(a) Defect A

τ_a =540 MPa → 400 MPa,
σ_m = –1200 MPa, $N = 9.84\times10^7$

(b) Defect B

τ_a =600 MPa → 460 MPa,
σ_m = –1200 MPa, $N = 5.28\times10^7$

(c) Smooth specimen

τ_a = 600 MPa (constant),
σ_m = –1000 MPa, $N = 1\times10^7$

Fig.3 Non-propagating cracks

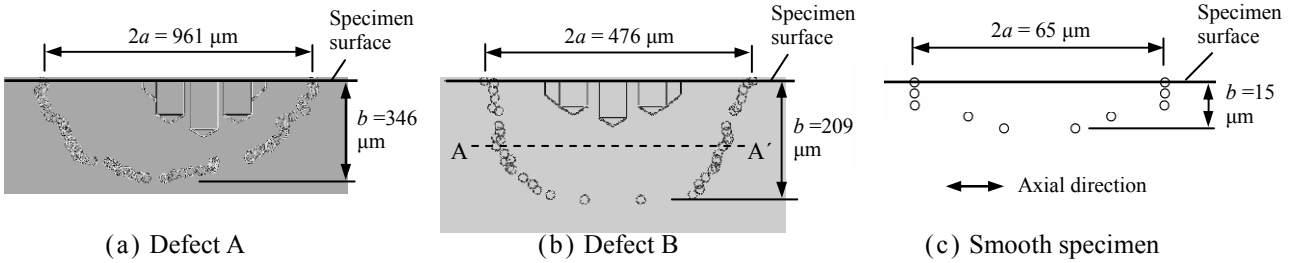

(a) Defect A (b) Defect B (c) Smooth specimen

Fig. 4 Shape and dimensions of non-propagating crack obtained by successive polishing

[3] A. Otsuka, Y. Fujii and K. Maeda, FFEMS, Vol. 27 (2004), pp. 203-212

[4] Y. Murakami, T. Fukuhara and S. Hamada, Journal of the Society of Materials Science, Japan, Vol. 51 (2002), pp. 918-925

[5] Y. Murakami and H. Natsume, Transactions of the Japan Society of Mechanical Engineers, Series A, Vol. 66 (2000), pp. 2211-2217

[6] L.P. Pook, Engineering Fracture Mechanics, Vol. 48 (1994), pp. 367-378

[7] Z.P. Bažant and L.F. Estenssoro, Int. J. Solids and Structures, Vol. 15 (1979), pp. 405-426

[8] M.K. Kassir and G.C. Sih, Journal of Applied Mechanics, Vol. 33 (1966), pp. 601-611

[9] K. Toyama, Y. Fukushima and Y. Murakami, Journal of the Society of Materials Science, Japan, Vol. 55 (2006), pp. 719-725

Acknowledgement

This work was partially supported by funds from the Central Research Institute of Fukuoka University (No. 081501).

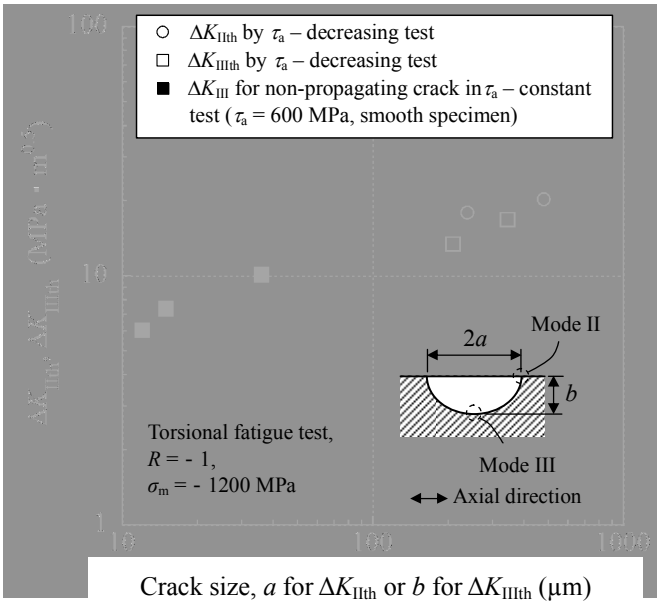

Fig. 5 Relationship between crack sizes and crack-growth thresholds

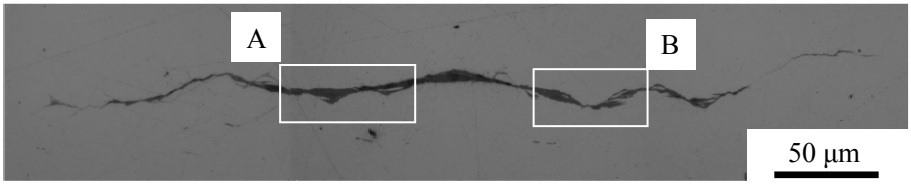

(a) Shear-mode fatigue crack at A−A' in Fig. 4(b)

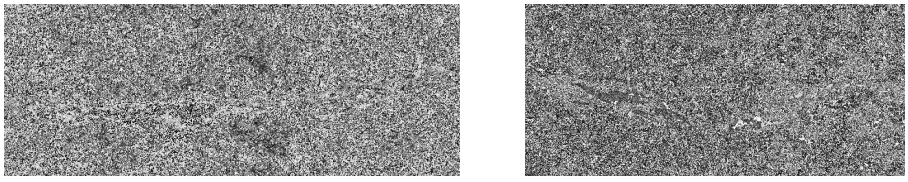

(b) Etched microstructure (Area A) (c) Etched microstructure (Area B)

Fig.6 Microstructural change along shear-mode fatigue crack

Key Engineering Materials Vols. 385-387 (2008) pp 453-456
© (2008) Trans Tech Publications, Switzerland
doi:10.4028/www.scientific.net/KEM.385-387.453

A Study of Crack Propagation in BCC Iron by Molecular Dynamics Method

Yuan Gao[1, a], Cheng Lu[1,b], Guillaume Michal[1,c] and Anh Kiet Tieu[1,d]

[1]School of Mechanical, Material & Mechatronic Engineering, University of Wollongong, Australia

[a]yg984@uow.edu.au, [b]chenglu@uow.edu.au, [c] gmichal@uow.edu.au and [d]ktieu@uow.edu.au

Keywords: molecular dynamics simulation, crack propagation, bcc iron, lattice orientation.

Abstract. In this paper, molecular dynamics method has been employed to model mode I crack propagation in body center cubic (BCC) single iron crystal. To maximize the simulation efficiency the parallel computing was performed. Six cases with different lattice orientations have been simulated to investigate the crack propagation behaviors at atomic level. The strain distributions have been calculated to indicate the density of dislocation. It has been found that the lattice orientation significantly affects the propagation behaviors. The crack in BCC iron propagates more readily along the direction <111> on the plane {1-10}.

Introduction

Molecular dynamics (MD) method has been widely used to investigate the fundamental mechanism of material fracture behaviors [1-4]. It has been known that the fracture process was accompanied by emission of edge dislocations, twin generation from the crack tip and generation of extrinsic stacking faults [5,6]. However, few reports have been on crack behaviors on different lattice planes, which are fairly important to understand the basic mechanism of the crack propagation.

To accurately simulate fracture in the atomic scale, embedded-atom method (EAM) has been adopted to describe the many-body atomic interaction. It was developed by Daw & Baskes [7,8] and has become a powerful potential function for metallic materials. With EAM, many researchers have studied the fracture processes, ductile-brittle behaviors and void or dislocation growth in a crystalline material [9-11]. However, there are still some problems that may affect simulation results. Firstly, the simulation size is limited in the number of atoms one can simulate. Typically, a larger size can eliminate the local imperfections and become close to the nature of the material. But it will take much longer time to achieve final results. Currently, the fastest supercomputer can simulate up to billions atoms [12] with the simple LJ potential function. Secondly, longer computing time are needed to calculate the interaction between atoms at each time step. Ideally one would like to use the largest time step size possible. However the MD integration algorithm becomes unstable at large time steps. So researchers must balance between the largest time step and the conservation of energy to enhance convergence.

In this paper, we studied the crack propagation behaviors in the bcc iron crystals with six different lattice orientations, using EAM potential [10] with Mode I tensile applied. The MD model with parallel computing ability has been developed based on the MD software XMD [13] and run on two supercomputers. A self-adaptive time step algorithm has been developed to increase the stability of the simulations. The propagation behaviors and strain distributions are discussed in this paper.

Molecular Dynamics Model

EAM Potencial. The EAM potential [7,8,10] used in this paper is semi-empirical potential, which is energy functions and governs the interaction among the neighboring atoms. The total energy of a metal system can be written as the sum of a function of the total electron density and a short-range pair-wise potential, as

$$E_{tot} = \sum_i F_i(\rho_{h,i}) + \frac{1}{2}\sum_{i\neq j} V(r_{ij}) \quad (1)$$

$$\rho_{h,i} = \sum_{i\neq j} \rho_j^a(r_{ij}),\ V(r) = \frac{Z_i(r)Z_j(r)}{r} \quad (2)$$

where $F_i(\rho_{h,i})$ is the embedding energy of atom i to the background electron density ρ, $\rho_{h,i}$ is the host electron density at atom i., $V(r_{ij})$ is the repulsive central force between the atoms i and j separated by r_{ij} and $Z_i(r)$ is the effective charge of atom i at distance r.

Parallel Computing. As MD simulation consumes large amount of computing time [14], we have conducted MD parallel computing on two supercomputers: Australian AC3's beowulf cluster "Barossa" and our own cluster "Eukles. The assignment of the atoms to processors plays an important role on calculation efficiency of parallel computing. A method called "spatial decomposition" has been applied in our simulations, which decomposes the simulation domain into small sub-blocks and assigns each sub-block to each processor as shown in Fig.1. Each processor runs calculations for atoms in its block and tracks atoms as they enter and exit its block. Each processor only needs communicate with a few surrounding blocks at each time step within finite potential range.

A time step self-adaptive method has been proposed to enhance the stability of the simulation [15]. Since the changes of the temperature and energy are mainly depended on the atom speeds, we can constrain the time step by using $dt=\alpha\times ds/v_{max}$, where ds is the average movement of the atoms, v_{max} is the maximum velocity of all atoms, α is a factor, which was set to be 1 in this study.

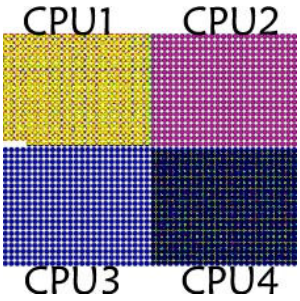

Fig 1 Spacial decomposition of parallel computing

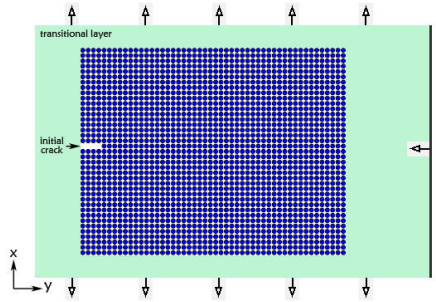

Fig 2 Schematic of the simulation model

Table Lattice orientations in six cases

Direction	Case 1	Case 2	Case 3	Case 4	Case 5	Case 6
Axis x	[1-10]	[111]	[-1-12]	[111]	[1-10]	[-1-12]
Axis y	[111]	[1-10]	[111]	[-1-12]	[-1-12]	[1-10]
Axis z	[-1-12]	[-1-12]	[1-10]	[1-10]	[111]	[111]

Simulation Model. In the paper, we assumed that the initial α–Fe plates were perfect single crystal lattice, having bcc structures. The schematic of the MD simulation is shown in Fig. 2. The simulations were performed on the two major slip planes of bcc iron, {1 1 0} and {1 1 2}. Six cases with different orientations have been studied. The details of the lattice orientations in six cases are shown in Table 1. The simulation volume was 10.4nm×28.7nm×1.15nm (x, y, z directions, respectively) with periodic boundary conditions, which consisted of over 25000 atoms. There were 10-20 layers of transitional regions around the simulation domain, which were used to alleviate the effect of the boundaries. Uniform Mode I loads were applied on the top and bottom boundaries to keep the crack faces apart. In all simulations, the initial crack with the length of about 10nm was inserted in the midpoint of the left side of the simulation lattice. All the simulation data including time step, coordinates, velocities, displacements, forces, stresses, strains, temperatures etc. were saved for further analysis.

Results and Discussion

The simulation results at time step 10000 are shown in Fig. 3. The same loading conditions, boundary conditions and initial crack length have been applied to all the cases. It has been observed that the behavior of the crack propagation is different for different cases. The crack in Case 1 propagates much faster then other cases. At time step 10000 the crack in Case 1 has already reached the right side of the simulation domain, while the cracks in other cases just moved a short distance. This indicates that the crack in BCC iron prefers to move along the direction <111> on the plane {1-10}. The nearest distance between two neighbor atoms along [1-10] direction is $\sqrt{2}\times a_0$, where a_0 is the lattice constant. This distance is larger than the nearest atom distances in other directions ($(\sqrt{3}/2)\times a_0$ along [111] and $(\sqrt{3}/2)\times a_0$ along [-1-12]), indicating the weakest atoms absorption between planes {1-10}. In addition, [111] direction is the slip direction in BCC iron. If the initial crack aligns along [111] direction, the dislocations tend to emit from the crack tip along the crack propagation direction. This will also weaken the atom interaction. The crack in Case 1 is set along [111] direction on the plane (1-10). Since [111] direction is the easy slip direction and the plane (1-10) is the weak-connection plane as discussed above, the crack in Case 1 propagates more readily than other cases.

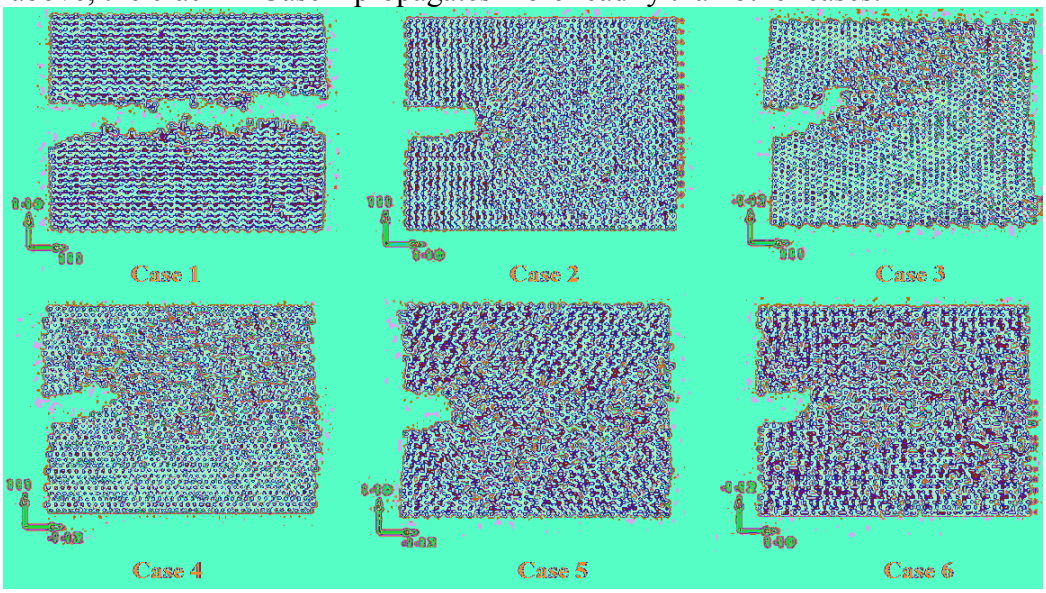

Fig. 3: Snapshot of simulation domain at time step 10000

It has been found that the total energy and internal stress increases gradually at the beginning stage of simulation of Case 1 (time step less than 6000). The crack tip just vibrated around the original position without any propagation. When the internal stress reached a certain level the cracks started to propagate. Consequently the energy was released to form new free surfaces and the propagation speed was increased. And then the stress was reduced. With the movement of the crack toward the right boundary, the crack propagation slowed down and the system energy and stress accumulated again until they reached the next critical point. According to the calculation, the critical stress intensity factor was $K_{IC} = 0.7707\,\mathrm{MPam}^{1/2}$ and the maximum velocity was about 1000m/s for Case 1. In addition, some phenomenon, such as emission of edge dislocations, twin generation from the crack tip, generation of extrinsic stacking faults and vacancies caused by the emission of dislocation, can be observed. The detailed analysis will be published in a separate paper.

Fig. 4 shows the strain distributions at simulation time step 7000. It has been observed that there is a high-strain region in front of the crack of Case 1. High strain indicates high dislocation density, which assists the movement of the crack. Therefore, the crack tends to propagate through the high strain region. There is also a high-strain region in Case 2 although its magnitude is less than Case 1. This leads to a slow propagation speed of crack. The strain in Cases 3 and 4 are relatively small, while the high-strain regions in Cases 5 and 6 could not be observed. Therefore, the cracks in Cases 5 and 6 hardly move.

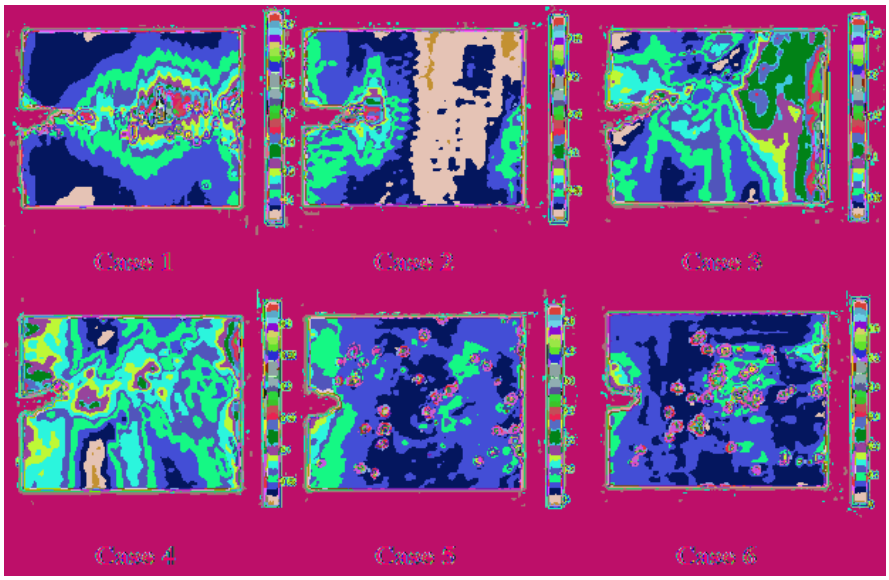

Fig. 4: Strain distributions at step 7000

Summary

In this paper molecular dynamic simulations of crack propagation in body centre cubic (bcc) single crystal have been performed. Spatial decomposition technique has been applied to the parallel computing to improve the simulation efficiency. A self-adaptive time step algorithm has also been developed to increase the stability of the simulations. Six cases with different lattice orientations were carried out to study the crack propagation behaviors at atomic level. The strain distributions have been calculated to indicate the density of dislocation. It has been found that the lattice orientation significantly affects the propagation behaviors. The crack in BCC iron likes to move along the direction <111> on the plane {1-10}.

References

[1] F. F. Abraham, D. Brodbeck, W. E. Rudge and X. Xu, J. Mech. Phys. Solids, Vol. 45, No. 9, 1595 (1997).
[2] A. Latapie and D. Farkas, Physical Review, B 69, 134110 (2004).
[3] M. J. Buehler, H. Gao and Y. Huang, Theo. & App. Frac. Mech., 41 (2004) 21-42.
[4] A. Machova and G. E. Beltz, Materials Sci. and Eng., A 387 (2004) 414-418.
[5] V. Pelikan, P. Hora, A. Machova and A. Spielmannova, Czechoslovak Journal of Physics, Vol. 55 (2005), No.10.
[6] K. Nishimura and N. Miyazaki, Computational Materials Science 31 (2004) 269-278.
[7] M. S. Daw, M. I. Baskes, Phy. Rev. Vol 29, No. 12 (1984).
[8] M. S. Daw, S. M. Foiles and M. I. Baskes, Mater. Sci. Rep. 9 (1993) 251.
[9] V. Shastry and D. Fankas, Model. Simul. Mater. Sci. Eng. 4 (1996) 473-492.
[10] V. Shastry and D. Fankas, Proceedings of the Symposium (1996) 75-80
[11] S. J. Zhou, P. S. Lomdahl, A. F. Voter, B. L. Holian, Eng. Frac. Mech. 61 (1998) 173-187.
[12] M. J. Buehler, A. Hartmaier, H. Gao, M. Duchaineau and F. F. Abraham, Comput. Methods Appl. Mech. Engrg. 193 (2004) 5257-5282.
[13] XMD – Molecular Dynamics for Metal and Ceramics, 2005. Retrived Feb. 2006, from website: http://xmd.sourceforge.net/.
[14] X. Liu, H. Liu, J. Dong and X. Xie, Scripta Mater. 42 (2000) 189-195.
[15] Y. Gao, C. Lu and A. K. Tieu, Molecular Dynamics Simulation of Crack Propagation on Different Slip Plane of BCC Iron, ICONN 2008 (submitted)

Key Engineering Materials Vols. 385-387 (2008) pp 457-460
© (2008) Trans Tech Publications, Switzerland
doi:10.4028/www.scientific.net/KEM.385-387.457

Atomic Simulation of Effect of Stacking Fault and Dislocation on Fracture Behavior in Fe Crystal

Cheng Lu[1, a], Yuan Gao[1,b], Hongtao Zhu[1,c] and Anh Kiet Tieu[1,d]

[1] School of Mechanical, Materials & Mechatronic Engineering, University of Wollongong, Australia

[a] chenglu@uow.edu.au, [b] yg984@uow.edu.au, [c] hongtao@uow.edu.au and [d] ktieu@uow.edu.au

Keywords: Facture behavior, Stacking fault, Edge dislocation, Molecular dynamics.

Abstract. The defects in crystalline materials significantly affect the fracture behaviors. In this paper molecular dynamics (MD) model using a potential of embedded atom method (EAM) has been developed to investigate the effect of the major crystalline defects, stacking fault and edge dislocation, on the crack propagation in Fe crystal. Six cases with different locations of stacking fault and edge dislocation have been studied. The strain distribution in lattice aggregate was heterogeneous. The dislocations were observed slipping along directions [100] and [-100] on the plane (100). Simulation results showed that the location of the stacking fault and edge dislocation significantly influenced the crack propagation speed.

Introduction

Fracture strength of crystalline materials depends on the dislocation emission from the crack tip. The phenomena of dislocation emission have been widely investigated by molecular dynamics (MD) method [1-3]. It has been known that the fracture behavior and dislocation emission are significantly affected by the defects surrounding the crack tip. The effects of point defect (impurity cluster) and surface defect (grain boundary) have been studied [4-6]. However, the influence by other major defects, such as stacking fault and concomitant edge dislocation, still remains unclear.

In this paper MD simulations using a potential of embedded atom method (EAM) have been conducted to investigate the effect of stacking fault and edge dislocation on crack propagation in Fe crystal. The stacking fault and edge dislocation were created by inserting a plate of atoms in the perfect iron lattice aggregate. Six cases with different locations of stacking fault and edge dislocation have been studied. It has been found that the location of the stacking fault and edge dislocation significantly affected the crack propagation speed.

Molecular dynamic analysis

In molecular dynamic simulation the motion of a large number of atoms is described by Newton's law:

$$\mathbf{f}_i = m\mathbf{a}_i = \frac{\partial^2 \mathbf{r}_i}{\partial t} \tag{1}$$

where **f** is the force on the atom, m the mass, **a** the acceleration, **r** the position of the atom, t the time and i represents the i^{th} atom.

The force $\mathbf{f}_i$ is calculated by the differentiating the potential function (E), namely

$$\mathbf{f}_i = -\frac{\partial E(\mathbf{r}_1, \mathbf{r}_2, \cdots, \mathbf{r}_N)}{\partial \mathbf{r}_i} \tag{2}$$

where N is the number of the atoms. The potential function describes the interaction between atoms and it determines the properties of the materials. The embedded-atom method (EAM) potential function proposed by Daw and Baskes [7] has considered the many body interaction effects. It has

been proved to be more accurate than traditional pair potential functions in metals. The EAM potential function can be expressed by

$$E_{tot} = \frac{1}{2}\sum_{\substack{i,j \\ i\neq j}} V(r_{ij}) + \sum_{i} F_i(\rho_i) \tag{3}$$

where $V(r_{ij})$ is the pair potential, $F_i(\rho_i)$ is the embedding energy of atom i to the background electron density ρ and ρ_i is the host electron density at atom i. The electron density at the site of atom i is calculated by:

$$\rho_i = \sum_{j\neq i} \rho_j(r_{ij}), \tag{4}$$

where ρ_j is the electron density of atom j at the position of atom i, r_{ij} is the distance between atom i and atom j.

In this paper, the Newton's equation of motion (Eqn.(1)) was solved by the Gear predictor corrector algorithm, which used up to the 5'th time derivative of the particle positions. The system temperature was initiated to be 300K. To control the temperature, the velocity scaling method was used to maintain the temperature approximate constant. The position of each atom could be determined by solving Eqn.(1). The strain was calculated according to the displacement of the atoms.

Three dimensional lattice with about 12250 Fe atoms was simualated as shown in Fig. 1. The x-axis and y-axis represent the lattice direction [110] and [1-10], respcetively. The initial crack located at the centre of the left side (AC) and its direction lied along the x directioin. The displacement boundaries along y and –y directions were applied to the top and bottom sides (AB and CD). The moving velocity was 0.1nm/ps. The right side (BD) correspondingly moved to the left to avoid tearing the right side. The stacking fault and edge dislocation were created by inserting a plate of atoms in the lattice. The inserted atom plate positions along the x-axis for Cases I, II and III and along the y-axis for Cases IV, V and VI. The corresponding Burger vector of the created edge dislocation was along the y-axis for Cases I, II and III and along the x-axis for Cases IV, V and VI. The locations of the inserted atom plate for six cases are shown in Fig.1.

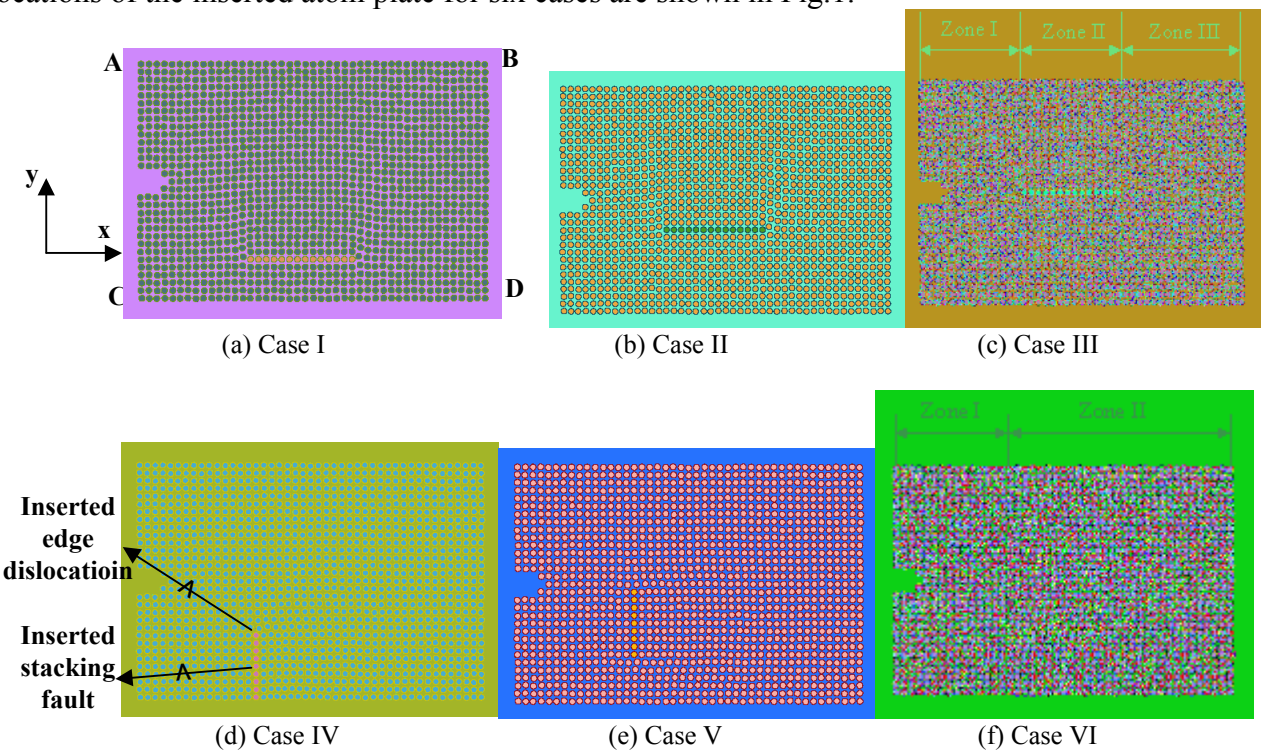

(a) Case I (b) Case II (c) Case III

(d) Case IV (e) Case V (f) Case VI

Fig. 1 Six simulation cases with different locations of stacking fault and edge dislocation

Results and Discussion

Fig.2 shows the strain distribution for all the cases at the early stage of the simulation (time step 500). It is clear that the distribution of strain is non-uniform. There are four high-strain regions locating around the middle plane along the y-axis. High strains near the left side and right side of the simulation aggregate are caused by the boundaries, while strains in two middle high-strain regions are mainly induced by the dislocation slip. The stacking fault and edge dislocation affect the strain distributions. They release the strains in the lower part of domain in Cases I-V and those in the upper part in Case VI. The streaks lying along 45°C and 135°C to the x-axis can be observed in the middle high-strain regions. They indicate the slip directions of dislocation on the displayed plane (100) are [100] and [-100]. One of the principle slip direction in BCC is [111], which can be decomposed into four imperfect dislocations: a/2[111]→a/8[110]+a/8[101]+a/8[011]+a/4[111]. [100] dislocation is the projection of [101] dislocation on the displayed plane, while [-100] dislocation is the projection of [-101] dislocation decomposed from [-111] dislocation.

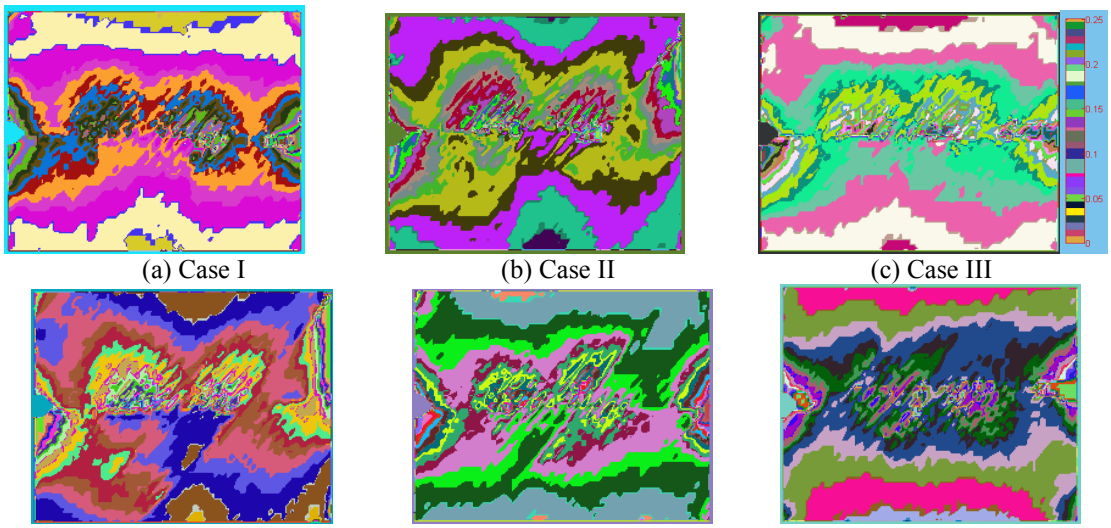

(a) Case I (b) Case II (c) Case III

(d) Case IV; (e) Case V (f) Case VI

Fig. 2 Strain distribution in six cases at time step 500

The MD simulation snapshots for six cases at time step 8500 are shown in Figs. 3. It can be observed that the lengths of the cracks are different. This indicates that the locations of the inserted stacking fault and edge dislocation influence the cracking propagation. Case II has the shortest crack length, while Case IV has the longest crack length. It can be seen from Fig. 3 that the dislocations are emitted from the crack tips. They locate along 45°C and 135°C to axis x, namely [100] and [-100] directions.

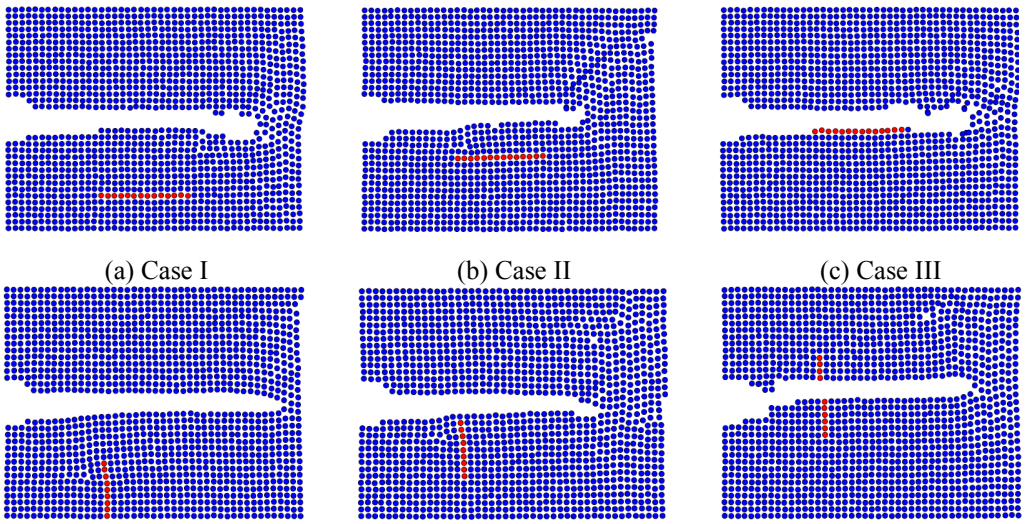

(a) Case I (b) Case II (c) Case III

(d) Case IV (e) Case V (f) Case VI

Fig. 3 Snapshots of MD simulation for six cases at time step 8500

To quantitatively analyze the effect of the inserted stacking fault and edge dislocation on the speed of the crack propagation, the lattice aggregate is divided into several zones as shown in Fig.1. There are three zones for cases I, II and III and two zones for cases IV, V and VI. The speeds of the crack propagation are calculated for each zone. The speed results are shown in Fig. 4(a) and Fig. 4(b). It can be seen that the location of the defects (inserted stacking fault and edge dislocation) profoundly affects the crack propagation speed. The speeds in Cases III and IV have small variation. Their values are around 300m/s. In Case I the existence of stacking fault and dislocation significantly reduces the crack propagation speed, while Case II accelerates the crack propagation before the crack passes through the inserted defect area and then it reduce the crack speed. Case V has a little higher speed than Case IV before the crack reaches the defect area and the speed is significantly decreased after the crack move through this area. Case VI shows an opposite trend to Case V.

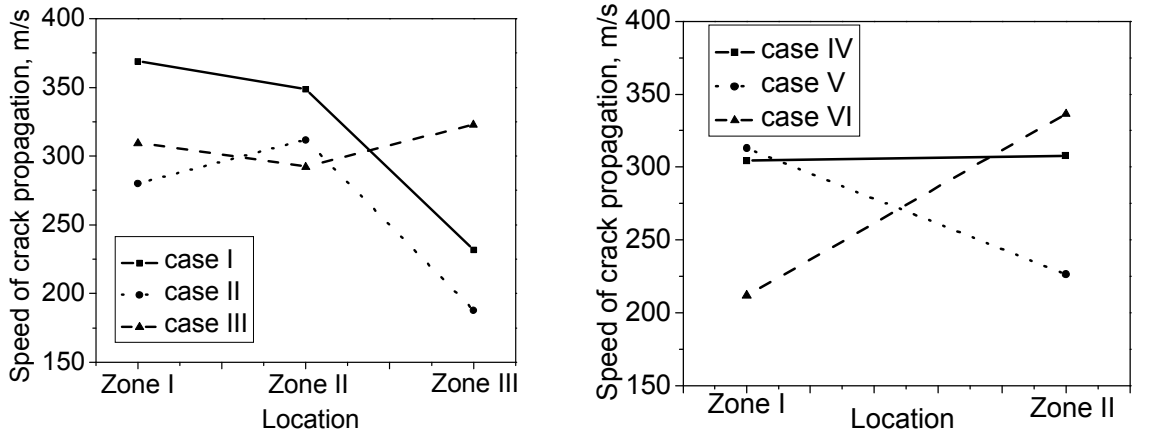

(a) Horizontal inserted atom plates (Cases I, II, III) (b) Vertical inserted atom plates (Cases IV, V, VI)

Fig. 4 Crack propagation speeds in six cases

Summary

Molecular dynamics (MD) model using a potential of embedded atom method (EAM) has been developed to investigate the effect of major crystalline defects, stacking fault and edge dislocation, on the crack propagation in Fe lattice. The stacking fault and edge dislocation were created by inserting a plate of atoms in the perfect iron lattice aggregate. Six cases with different locations of the stacking fault and edge dislocation have been studied. The strain distribution in lattice aggregate was heterogeneous. The dislocations were observed slipping along directions [100] and [-100] on the plane (100). It has also been found that the crack propagation speed depended on the location of the stacking fault and edge dislocation.

Acknowledgment

The authors acknowledge the financial support from an Australia Research Council Discovery Grant.

References

[1] F. Abraham, D. Brodeck, W. E. Rudge, X. Xu, J. Mech. Phys. Solids 45(1997) 1595.
[2] Q. H. Tang, T. C. Wang, Computational Materials Science 12 (1998) 73.
[3] K. Nishimura and N. Miyazaki, Computational Materials Science 31 (2004) 269.
[4] H. Rafii-Taba, H.M. Shodja, M. Darabi, A. Dahi, Mechanics of Materials 38 (2006) 243.
[5] V. Yamakov, E. Saether, D.R. Phillips, E.H. Glaessgen, Journal of the Mechanics and Physics of Solid, 54 (2006) 1899
[6] M. de Koning, R.J. Kurtz, V.V. Bulatov et al., Journal of Nuclear Materials 323 (2003) 281.
[7] M. S. Daw, M. I. Baskes, Phy. Rev. 29(1984) 6443

Key Engineering Materials Vols. 385-387 (2008) pp 461-464
© (2008) Trans Tech Publications, Switzerland
doi:10.4028/www.scientific.net/KEM.385-387.461

Pore Properties of Eco-material for Erosion Control of Slope and Its Fractal Features

WANG Ji[1,a] , HU Zai-liang[2,b] , ZHANG Ji-ru[1,c] , ZHANG Ming-zhong[1,d]

[1]Senior Engineer, The Design and Research Institute, Wuhan University of Technology, No.122, Luoshi Road, Wuhan, 430070, China.

[2]Engineer, China Academy of RailWay Sciences, No.2, Daliushu Road, Xizhimenwai Beijing, 100081, China.

[3]Professor, School of Civil Engineering and Architecture, Wuhan University of Technology, No.122, Luoshi Road, Wuhan, 430070, China.

[4]Postgraduate, School of Civil Engineering and Architecture, Wuhan University of Technology, No.122, Luoshi Road, Wuhan, 430070, China.

[a]hmywj@263.net, [b]hzl_bj@126.com, [c]zhangjr@whut.edu.cn, [d]zmzfj@126.com

Key words: eco-material for erosion control of slope; soil; pore volume-size distribution; fractal dimension; range of pore-size

Abstract: The pore properties of the porous material are important factors influencing the vegetation to grow. The pore properties of an artificial planting material and soil were studied by a mercury intrusion test. Based on the fractal concept of Menger-sponge, the fractal dimensions characterizing pore volume-size distribution of planting material and soil are obtained from the experimental data, and the different of both of the fractal dimensions is compared. The testing results show that the total porosity of planting material varies from 30.27 % to 32.11%, and the total porosity of soil is 24.87%. The law of their pore volume-size distribution in different range of pore-size is identical. The fractal research exhibits that the fractal dimensions have a different value in all the range of pore-size for planting material or soil, and small fractal dimension corresponds to small pore-size. As compared with soil, the fractal dimension of planting material is larger slightly in range of small pore, and is same basically in range of micro and medium pore. These results indicate that the fractal dimension is a useful measure of pore grading, which divides the pore into four groups with micro pore, small pore, medium pore and large pore. And the pore properties of eco-material for erosion control of slope are helpful to the vegetation growth.

1 Introduction

With the construction of highway, railway, hydraulic and electric engineering, etc., natural vegetation is often destroyed and unable to recover rapidly, which results in the soil erosion. So, how to protect and recover the vegetation is becoming the hotspot research of Geotechnical Engineering. Since eighties of the 20th century, a new technology for erosion control of cutting slopes has developed, which has been used in China for nearly ten years[1]. Recent years, a kind of eco-material obtained from clay mixing with natural mineral, cement and sand, etc., was successfully developed and deeply researched by authors of this paper [2]. Because of heterogeneous and asymmetric properties of artificial planting material, similar to soil, researches on how to measure pore-size and how to divide pore-size into different ranges, etc., are extremely complicated. And the description of pore structure is quite difficult with traditional geometry method. However, as a data, the pore structure of soil has obvious fractal characteristics. And fractal theory is effective to analyze the pore structure [3]. Compared with soil, the structure of artificial planting material is also similar to that of Menger sponge, the process of which is similar to the pore fractal measure

with the method of mercury injection. In the paper, based on the mercury injection experiment and the fractal concept of Menger-sponge, the fractal dimensions characterizing pore volume-size distribution of artificial planting material and soil are obtained from the experimental data. And the differences of both of the fractal dimensions are compared.

2 Materials and Method

2.1 Experimental Equipment

The experimental samples are provided by the planting and experimental area of eco-material for erosion control of slope. Two group samples of artificial planting material (each serial number is PM1 and PM2) are chosen by concrete core machine. At the same time, a group sample of soil (serial number is S1) from slope nearby is chosen to have comparison. According to the mercury injection experiment, samples are air-dried and putted into drying cabinet to drying to clear the remaining moisture in the pore completely, and prevent mercury from invasion. Then round samples diameter of which is about 5mm are made and stored in special test tube.

2.2 Mercury Injection Experiment

Mercury injection experiment is carried out on the auto mercury injection instrument, the range of pore-size of which is from 0.007 to 400μm. The working pressure of low tension system is from 3.5 to 350kPa. And that of high tension system is from 0.140 to 231Mpa. Before the experiment, mercury injection instrument is connected with vacuum pump and computer. The experimental parameter is chosen by analytical software of PoreMaster. In the experiment, the samples are putted into the dilatometer, which is vacuumized to 0.3Mpa, to ensure the air pressure of pore is close to vacuum. Then, the analysis of low pressure mercury injection is accomplished. After these, the samples are putted into high pressure system. And the analysis of high pressure system is accomplished until the pressure is at 210Mpa. In the experiment, wetting angel between mercury and sample is 140°, and surface tension is 0.48 N/m. Based on the experiment, the pore-size, pore volume-size and porosity, etc., are obtained.

3 Results and Discussion

Fig.1 (a) and (b) are the statistic frequence histograms between pore volume-size and pore-size distribution of samples PM1 and PM2, which are exported from the analysis software of PoreMaster. The results indicate the figures of pore-size distribution look as a camel, having two peaks and valley. The distance between two peaks is large. Larger the difference of pore volume-size between two peaks, larger the difference of volume-size between peak and valley. Pore-size of sample PM1 and PM2 are identical. The values are 0.02 μm and 0.80 μm. However, the pore volume-sizes of them are different. For sample PM1, the top value of lower pore-size (0.2μm) is larger than that of higher pore-size (0.80μm). Compared to sample PM1, the law of pore volume-size distribution of PM2 is contrary.

Fig.2 is the statistic frequence histograms between pore volume-size and pore-size distribution of sample S1. The figure of pore-size distribution also looks as a camel. The pore-size of the peaks are about 0.02μm and 0.30μm. Compared to Fig.1, the distance between two peaks is less, volume-size is identical and the value of two peaks is close. The results of mercury injection test indicate the maximum pore-size of sample PM1 PM2 and S1 are 8.75μm 7.01μm and 7.86μm. The minimum pore-sizes of them are 7.90×10^{-3}μm 7.88×10^{-3}μm and 7.65×10^{-3}μm. The testing results show pore-size is basically not greater than 8μm. The data obtained from test is very limited. It is considered to be the result that at the beginning of mercury injection test the first pressure of mercury injection is too big, which leads some pore with big size can't be detected. It also shows that pore with big size is difficult to be detected by mercury injection test. If the pressure of

mercury injection is small, mercury can be easy to enter into the big pore. Thus there small mercury won't be exactly detected by instrument.

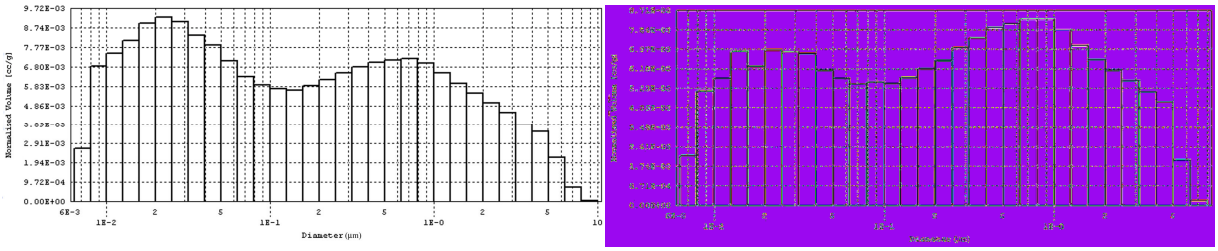

(a) Sample PM1 (b) Sample PM2

Fig. 1 Statistic frequence histograms of pore-size distribution of sample PM1 and PM 2

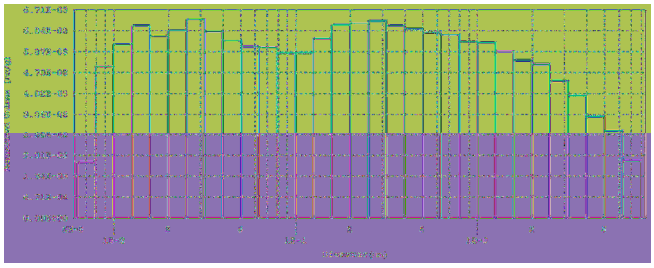

Fig. 2 Statistic frequence histograms of pore-size distribution of sample S1

4 Fractal Research

4.1 Fractal Model

The shape of Menger sponge made from a square body is regular. The square body is divided into 27 partitions. The mid 7 partitions are taken out and the other 20 partitions are remained. Thus the first conformation is produced. According to the same method, the first conformation is divided into 27 partitions, taking out the mid partitions. Then the second conformation is produced. Repeating the above work for many times, the sponge structure full of interspacing with different size is finally produced. It is given in Fig.3.

4.2 Fractal Dimension

According to the data of pore-size distribution of planting material and soil, obtained from mercury injection test, the logarithm relation between $-\mathrm{d}V_p/\mathrm{d}\delta$ and δ is developed. And the linear fitting curve between $-\mathrm{d}V_p/\mathrm{d}\delta$ and $\ln\delta$ is described as Fig.4. Fig.4 shows the curve is divided into three different regions and fractal dimension is different in the different regions of pore-size.

The different fractal dimensions corresponding to different pore-size regions are listed in Table 1. The results indicate the fractal dimensions of sample PM1, PM2 and S1 are basically identical in the range of micro pore (d <0.04μm) and small pore ($0.04 \le d < 0.30$μm). However, the fractal dimensions of them are different in the range of medium pore ($0.30 \le d < 8$μm). Because the data is too few, the fractal dimensions of them in large pore ($d \ge 8$μm) aren't analyzed.

It can also be seen from Table 1, the fractal dimensions are different in all the range of pore-size for planting material or soil. Small fractal dimension corresponds to small pore-size and large fractal dimension corresponds to large pore-size. Compared with soil, the fractal dimension of planting material is larger slightly in range of small pore, and is same basically in range of micro and medium pore. From fig. 4, it can be seen, the linear relation between $-\mathrm{d}V_p/\mathrm{d}\delta$ and $\ln\delta$ is more perfect in range of small pore and medium pore than that in range of micro pore. The reasons for this are analyzed as follows. Because of high mercury injection pressure which is larger than 50MPa, the pore structure in range of micro pore is destroyed. And there are many irregular pores and cracks in it. The testing data is up-and-down. The results also indicate mercury injection test is

very suitable for pore structure, the pore-size of which is from 0.04 μm to 8 μm.

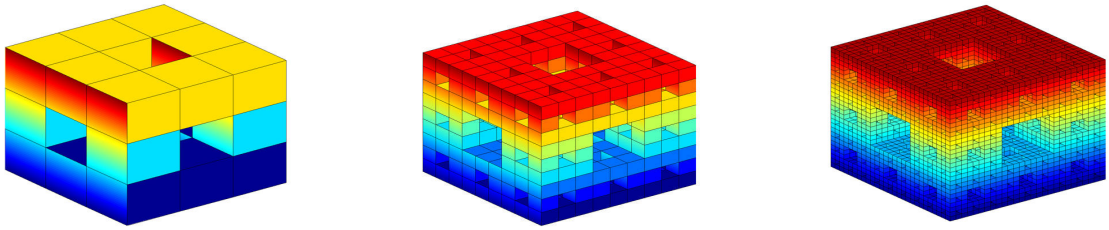

(a) The first conformation (b) The second conformation (c) The third conformation

Fig.3 Fractal structure of Menger sponge

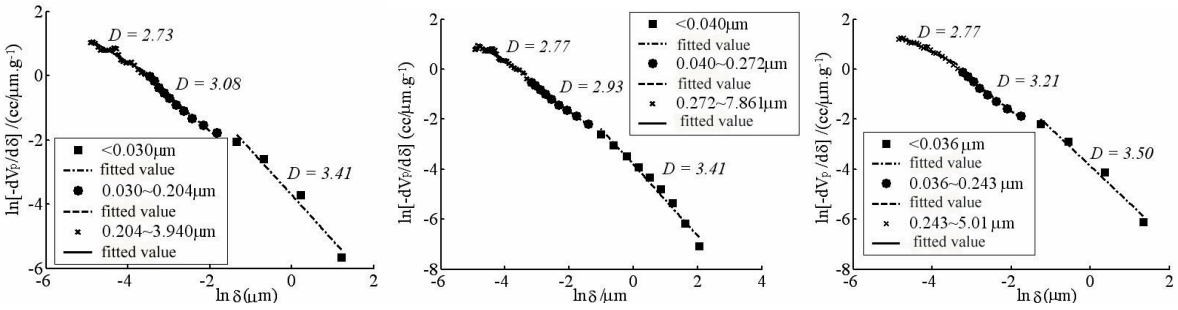

(a) Sample PM1 (b) Sample PM2 (c) Sample S1

Fig.4 Fractal dimension of pore volume-size distribution

4.3 Division of Different Pore-size

In China, the pore-size of soil is usually divide into four areas, such as micro pore (d < 0.04 μm), small pore (0.04 ≤ d < 0. 4 μm), medium pore (0.4 ≤ d < 4 μm) and large pore (d ≥ 4 μm). This division accord with the results of this paper, which also testify the division of pore-size according to fractal dimensions, is relatively reasonable.

Table 1 Fractal dimension in range of different pore-size

Samples number	Range of pore-size /μm	Fractal dimension D
Sample PM1	0.243~5.010	3.50
	0.036~0.243	3.21
	< 0.036	2.77
Sample PM2	0.204~3.940	3.41
	0.030~0.204	3.08
	< 0.030	2.73
Sample S1	0.272~7.861	3.41
	0.040~0.272	2.93
	< 0.040	2.77

5 Conclusions

a) For eco-material for erosion control of slope and soil, mercury injection test is suitable for pore structure, whose pore-size is from 0.03 μm to 8 μm. The total porosity of planting material varies from 30.27 % to 32.11%, and the total porosity of soil is 24.87%. The law of their pore volume-size distribution in different range of pore-size is identical.

b) The fractal dimensions have a different value in all the range of pore-size for planting material or soil, and small fractal dimension corresponds to small pore-size. Compared with soil, the fractal dimension of planting material is larger slightly in range of small pore, and is same basically in range of micro and medium pore.

c) According to the fractal dimensions, the pore-size of soil is usually divide into four areas, such as micro pore (d < 0.04 μm), small pore (0.04 ≤ d < 0. 4 μm), medium pore (0.4 ≤ d < 4 μm) and large pore (d ≥ 4 μm). This division accord with the results of this paper. The fractal dimension is a useful measure of pore grading, which divides the pore into different groups

References

[1] Zhang Junyun, Zhou Depei: submitted to Bulletion of Soil and Water Conservation (2001).
[2] Zhang Jiru: submitted to Journal of Wuhan University of Technology-Mater. Sci. Ed., (2004).
[3] KATZ A J, THOMPSON A H: submitted to Physical Review Letters (1985).

Key Engineering Materials Vols. 385-387 (2008) pp 465-468
© (2008) Trans Tech Publications, Switzerland
doi:10.4028/www.scientific.net/KEM.385-387.465

Stability maps of a cracked Timoshenko beam resting on elastic soils under sub-tangential forces

Erasmo Viola[1,a], Alessandro Marzani[1,b] and Walid Hasan[2,c]

[1]DISTART Department, University of Bologna, viale del Risorgimento 2, 40132 Bologna, Italy

[2]Civil Engineering Department, Al-Isra Private University-Jordan

[a]erasmo.viola@unibo.it, [b]alessandro.marzani@unibo.it, [c]walid.hasan@isra.edu.jo

Keywords: dynamic stability maps, nonconservative forces, Timoshenko beam, Pasternak soil, cracked beam, finite element method.

Abstract. The goal of this paper is to generate the stability maps for an elastic cracked beam resting on elastic soils and loaded by a constant distribution of sub-tangential forces. The soil behavior is simulated by a two-parameter Pasternak model.
Firstly, the extend version of the Hamilton principle is used to formulate the weak form of the governing equation for the undamaged beam problem. Secondly, a finite element procedure, in which the effect of an open surface crack is computed via the Line-spring model, leads to the discrete governing equation for the cracked beam. Finally, the effect of several parameters on divergence or flutter instability, such as the crack depth and location, the non-conservativeness of the applied load as well as the stiffness of the two soil parameters, is highlighted.

Introduction. Slope dependent forces, frequently involved in the analysis of structures, are non-conservative. As is it well known, slender systems subjected to compressive slope dependent forces, may lose stability for divergence or flutter. While divergence instability can be characterized by a static approach, flutter instability can be noticed only by studying the dynamic of the problem.
Sub-tangential forces, a combination of slope dependent (nonconservative) and slope independent (conservative) compressive forces, have been largely adopted in the literature to explore the stability regions of divergence and flutter phenomena. In sub-tangential forces the amount of nonconservative loads is usually given by means of the non-conservativeness parameter α that sets the slope of the sub-tangential forces in respect to the slope of the system.
The peculiarity of the governing equations of nonconservative problems is their unsymmetrical nature that might yield divergence or flutter. Among the several analytical and numerical approaches the Finite Element method (FEM) has been shown to be well suited to study the unsymmetrical nature of nonconservative stability problems [1].
As far as the effect of a surface crack on the stability of non-conservative systems is concerned, only few authors have studied this problem despite its relevance. The presence of a crack, in fact, introducing a discontinuity in the deformed shape of the beam, may change its instability form as well as its critical load [2], [3].
It should be noted that, the existing literature regarding nonconservative problems reveals no studies on the effect of an open crack on the stability of beams involving elastic foundations. Cracks in foundation beams can easily develop due to the differential compliance of the soil that causes unforeseen tensions on both the beam top and bottom surfaces.
In this study the effect of an open crack on the stability of Timoshenko beams, loaded by a constant distribution of sub-tangential forces and resting on a bi-parameter soil is investigated. The extended Hamilton's principle is used to derive the equations of motion in weak form. The finite element formulation is then employed to discretize the differential governing equation as a system of algebraic equations in which the crack is accounted by means of the line-spring model [4]. The versatility of the proposed formulation allows computing the effect of several factors on the stability of the system. Here, attention will focus on how the stiffness of the soil, the crack depth and location can effect the transition from divergence to flutter, or from flutter to divergence.

Governing equation for the cracked system. A Timoshenko prismatic beam of length L and constant cross-section of area A is considered resting along its all length on a two-parameter soil: a Winkler-type soil with constant modulus k_1 and a shear layer with constant modulus k_2. The beam is loaded by a uniform distribution of sub-tangential loads q_α, as indicated in Fig. 1a. The non-conservativeness parameter α, that sets the angle $\vartheta(x,t)$ between the x-axis and the force q_α, is introduced as shown in Fig. 1b. For $\alpha = 0$ the force remaining parallel to the *x*-axis for any beam deformed configuration is conservative, while for $\alpha \neq 0$ the force presents a slope-dependent nonconservative component. A surface open crack, located at $x = lc$, is considered.

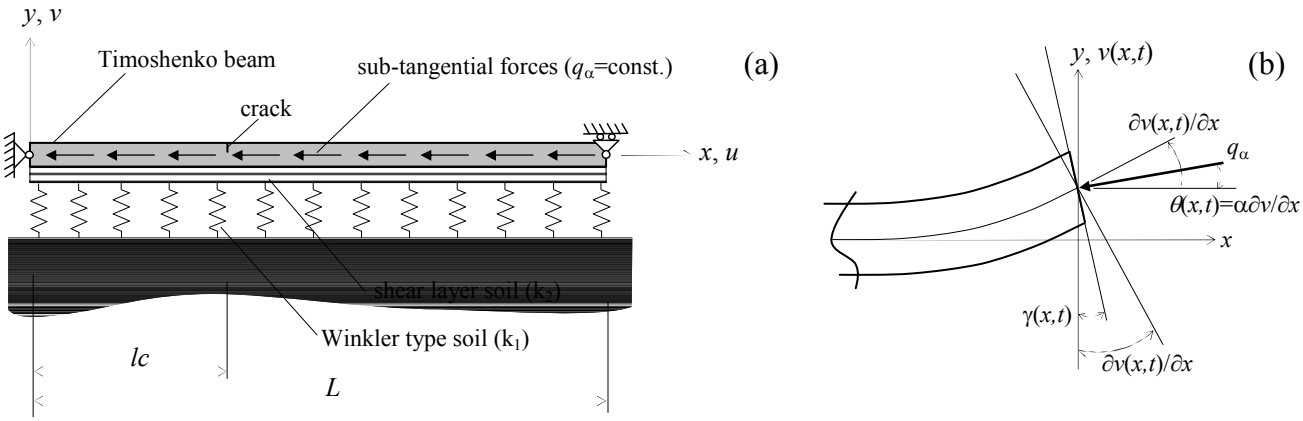

Fig. 1. a) Cracked beam at $x = lc$ on a two-parameter soil. b) Scheme of a deformed configuration.

The weak form of the governing equation for the undamaged beam can be derived from the extended form of the Hamilton's principle. The foundation is divided into ne elements of equal length l and the local coordinate $\bar{x} = x - (i-1)l$ is introduced where i represents the generic i-th element (the $i = 1$ element has its first node at $x = 0$). The Hamilton's principle reads:

$$\delta \int_{t_1}^{t_2} \sum_{i=1}^{ne} \left(T^i - \Phi^i + {W_C}^i \right) dt + \int_{t_1}^{t_2} \sum_{i=1}^{ne} \left(\delta {W_{NC}}^i \right) = 0 \tag{1}$$

where T^i is the element kinetic energy, Φ^i is the sum of all the elastic potential energies of the element, ${W_C}^i$ and $\delta {W_{NC}}^i$ are the element conservative work and the non-conservative virtual work, respectively. Limiting the discussion to beam deflection in the $(x-y)$ plane, the only non-zero displacement components for the Timoshenko beam element are the deflection $v = v(\bar{x},t)$, along the y-axis, and the cross-section rotation $\varphi = \varphi(\bar{x},t)$. Using a two-node super-convergent locking-free beam element [5] with two degrees of freedom per node $\mathbf{q} = [v_1 \quad \varphi_1 \quad v_2 \quad \varphi_2]^{\mathbf{T}}$, the direct stiffness method leads to the discrete equations of motion for the whole structure as:

$$\mathbf{M}\mathbf{Q}_{,tt} + [\mathbf{K}_e - \mathbf{K}_g(q_\alpha) + \mathbf{K}_{nc}(\alpha, q_\alpha)]\mathbf{Q} = \mathbf{0} \tag{2}$$

where the global matrices $\mathbf{M}$, $\mathbf{K}_e$, $\mathbf{K}_g$ and $\mathbf{K}_{nc}$ have dimension $n \times n$, $n = 2(ne+1)$, while $\mathbf{Q}$ is the $n \times 1$ global vector of nodal displacements. In Eq.(2) $\mathbf{M}$ is the consistent mass matrix, $\mathbf{K}_e$ is the elastic stiffness matrix, $\mathbf{K}_g$ is the geometric stiffness matrix and $\mathbf{K}_{nc}$, also known in literature as the load correction matrix, represents the contribute of the nonconservative forces.

The line-spring model is used to account for the crack in the beam. This approach models the crack via a two-node zero-length finite element, where each node of the element is thought on one side of the crack edges, with two degrees of freedom per node. The element nodal displacements are put in relation to shear force T and bending moment M at the nodes by the line-spring matrix $\mathbf{s}$:

$$\mathbf{s}=\begin{bmatrix} 1/\lambda_{tt} & 0 & -1/\lambda_{tt} & 0 \\ 0 & 1/\lambda_{mm} & 0 & -1/\lambda_{mm} \\ -1/\lambda_{tt} & 0 & 1/\lambda_{tt} & 0 \\ 0 & -1/\lambda_{mm} & 0 & 1/\lambda_{mm} \end{bmatrix} \quad \text{where} \quad \begin{aligned} \lambda_{mm} &= \frac{2(1-\nu^2)}{E}\int_0^{A_C}\left(\frac{K_{1b}}{M}\right)^2 dA_C \\ \lambda_{tt} &= \frac{2(1-\nu^2)}{E}\int_0^{A_C}\left(\frac{K_{\mathrm{II}s}}{T}\right)^2 dA_C \end{aligned} \tag{3}$$

In Eq. (3) ν is the Poisson's ratio, E is the Young's modulus, K_{1b} is Mode I stress intensity factor caused by bending moment M, $K_{\mathrm{II}s}$ is Mode II stress intensity factor caused by shear force T and dA_C is an infinitesimal increment of the cracked area [4]. Assuming the crack located in correspondence to a node of the finite element mesh of the uncracked system, the inclusion of the line-spring matrix requires the addition of one extra node within the FE mesh. Expanding the global matrices the equation of motion for the cracked structure may be derived as:

$$\bar{\mathbf{M}}\bar{\mathbf{Q}}_{,tt}+\left(\bar{\mathbf{K}}_e-\bar{\mathbf{K}}_g(q_\alpha)+\bar{\mathbf{K}}_{nc}(\alpha,q_\alpha)+\mathbf{L}^{\mathrm{T}}\mathbf{s}\mathbf{L}\right)\bar{\mathbf{Q}}=\bar{\mathbf{0}} \tag{4}$$

where the overbar indicates that the matrices in Eq.(4) have now a $m\times m$ dimension, $m=2(ne+2)$, $\bar{\mathbf{Q}}$ is the $m\times 1$ global vector of nodal displacements, and $\mathbf{L}$ is a $4\times m$ Boolean collocation operator that depends on the distance of the crack from zero of the reference axis, i.e. lc. Assuming the displacement vector varying with time as $\bar{\mathbf{Q}}(t)=\mathbf{V}e^{i\omega t}$, the governing equation yields:

$$\left[\left(\bar{\mathbf{K}}_e-\bar{\mathbf{K}}_g(q_\alpha)+\bar{\mathbf{K}}_{nc}(\alpha,q_\alpha)+\mathbf{L}^{\mathrm{T}}\mathbf{s}\mathbf{L}\right)-\omega^2\bar{\mathbf{M}}\right]\mathbf{V}=\bar{\mathbf{0}} \tag{5}$$

The m non-trivial solutions of Eq.(5) are the square of the frequencies of vibration for the damaged system. The system is stable if all the eigenfrequencies are real and $\omega_i>0$; loses its stability for divergence when the smallest $\omega_i=0$; undergoes to flutter if two of the eigenfrequencies become complex conjugate $\omega_{1,2}=\omega_{\mathrm{Re}}\pm i\omega_{\mathrm{Im}}$ and their real part is a positive quantity.

Numerical results. A cantilever beam clamped at $x=0$ can be modelled by imposing zero nodal displacement at the two degrees of freedom of the first finite element of the mesh. Different boundary conditions follow straightforwardly from similar considerations. Stability maps are given in terms of the eigenfrequency curves that represent the system frequencies of vibration versus the applied load. The numerical results, obtained by considering $ne=20$, are presented in terms of the following dimensionless parameters: frequency $\Omega^2=\omega^2(\rho AL^4/EI)$, sub-tangential force $\mathrm{Q}=q_\alpha L^3/(EI)$, Winkler soil stiffness $\mathrm{K}_1=k_1L^4/(EI)$, shear soil stiffness $\mathrm{K}_2=k_2L^2/(EI)$, where ρ is the material density, I is the second moment of inertia of the cross-section.

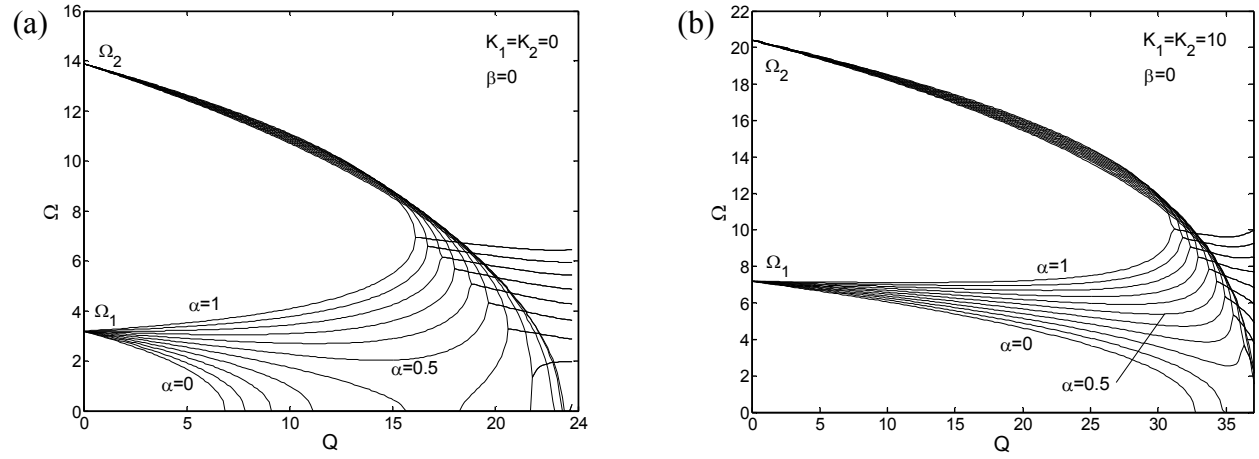

Fig. 2. Eigenfrequency curves for an undamaged cantilever Timoshenko beam for non-conservativeness parameter $0\le\alpha\le 1$ (step 0.1). (a) free beam, (b) effect of the elastic foundation.

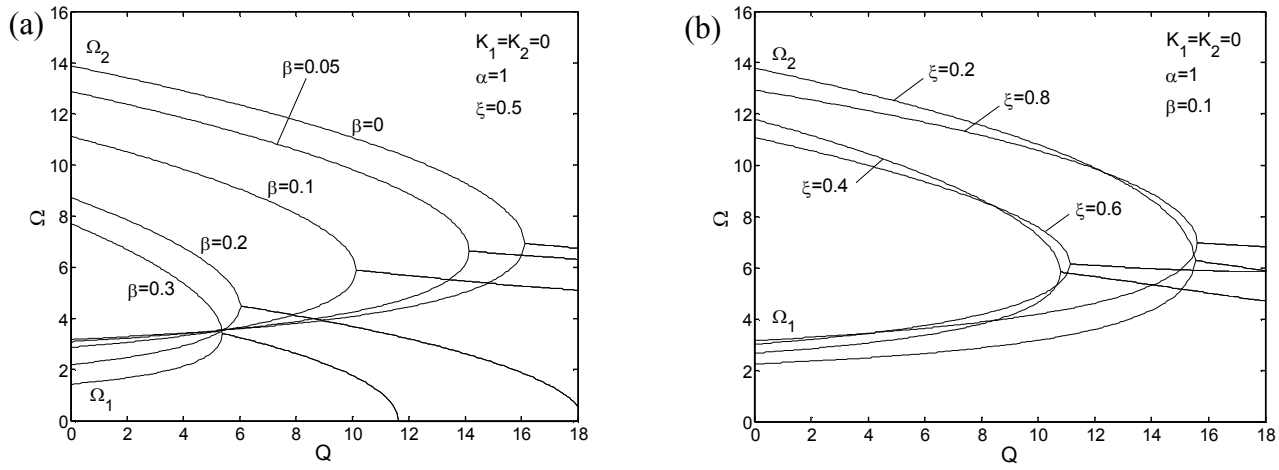

Fig. 3. Eigenfrequency curves for a cantilever Timoshenko beam for $\alpha = 1$. (a) effect of the crack depth β for a crack located at $\xi = 0.5$. (b) effect of the crack location for a crack depth $\beta = 0.1$.

The eigenfrequency curves represented in Fig. 2 for $0.0 \le \alpha \le 1.0$ (step 0.1) have been obtained for $v = 0.25$, cross-section shear correction factor $\kappa = 2/3$ and $L/(I/A)^{1/2} = 10$ [6]. For $Q = 0$ both $\Omega_1 = 3.1888$ and $\Omega_2 = 13.8850$ in Fig. 2a approximate extremely well the exact solution given in [6]. For an increasing magnitude of the applied loads while the second eigenfrequency always decreases, the first one decreases or increases depending on the amount of nonconservativeness of the load. In particular, the system is unstable for divergence for $\alpha \le 0.4$, for which the first eigenfrequency branch cross the $\Omega = 0$ axis, while results to be flutter unstable for $\alpha \ge 0.5$. The maximum critical load is reached in this case for $\alpha = 0.5$. As it can be seen in Fig. 2b the elastic soil defined as $K_1 = K_2 = 10$ increases the frequencies of vibration and approximately doubles the system critical loads. For $\alpha = 0.2, 0.3, 0.4$ the stiffness of the soil changes the instability form from divergence to flutter. In the end, assuming a rectangular cross-section beam, of width b and height h, in Fig. 3 the effect of the crack depth (a) and location (lc) on the stability of the beam is investigated for $\alpha = 1$. In particular Fig. 3a shows the eigenfrequency curves for different crack depths $\beta = a/h$ when the crack is located at the mid-length of the beam, while in Fig. 3b for an assumed crack depth $\beta = 0.1$ the curves are traced for different crack locations $\xi = lc/L$. It can be noted that in this case the system is always flutter unstable.

References

[1] A. Marzani, E. Viola: Effect of boundary conditions on the stability of beams under conservative and non-conservative forces, Struct. Eng. and Mech., Vol. 16, pp. 195-217, (2003).

[2] N. Anifantis, A. Dimaragonas: Stability of columns with a single crack subjected to follower and vertical loads, International Journal Solids and Structures, Vol. 19, pp. 281-291, (1985).

[3] E. Viola, A. Marzani: Crack effect on dynamic stability of beams under conservative and nonconservative forces, Engineering Fracture Mechanics, Vol. 71, pp. 699-718, (2004).

[4] T. Yokoyama, M.C. Chen: Vibration analysis of edge-cracked beams using a line-spring model, Engineering Fracture Mechanics, Vol. 59(3), pp. 403-409, (1998).

[5] J.B. Kosmatka: An improved two-node finite element for stability and natural frequencies of axial-loaded Timoshenko beams, Computers and Structures, Vol. 57(1), pp. 141-149, (1995).

[6] T. Yokoyama: Vibration analysis of Timoshenko beam-columns on two-parameter elastic foundations, Computers and Structures, Vol. 61(6), pp. 995-1007, (1996).

Key Engineering Materials Vols. 385-387 (2008) pp 469-472
© (2008) Trans Tech Publications, Switzerland
doi:10.4028/www.scientific.net/KEM.385-387.469

Investigation of Static and Dynamic Response of graphite and carbon fiber modified conductive asphalt-based composite

Ning LI [1, a], Shaopeng WU[2, b], Conghui LIU [3, c],

[1] Key Laboratory of Silicate Materials Science and Engineering

(Wuhan University of Technology), Ministry of Education, Wuhan 430070, China

[2] Key Laboratory of Silicate Materials Science and Engineering

(Wuhan University of Technology), Ministry of Education, Wuhan 430070, China

[3] Key Laboratory of Silicate Materials Science and Engineering

(Wuhan University of Technology), Ministry of Education, Wuhan 430070, China

[a]lin@whut.edu.cn, [b]wusp@whut.edu.cn, [c]chlaw@whut.edu.cn

Keywords: conductive asphalt-based composite, indirect tensile strength, fatigue property.

Abstract. The conductive behavior of asphalt concrete can be improved with the addition of conductive materials, thus a multifunctional asphalt-based composite can be obtained. The conductive asphalt-based composite modified by graphite was studied extensively. Conductive materials percentages may have influences on performance of asphalt mixture. The performance of an asphalt pavement is significantly affected by its resistance to permanent deformation and its fatigue performance. The paper presents the results of a project aimed at investigating static and dynamic response as cracking and fatigue behaviors of conductive asphalt-based composite using the ITT. In particular ITT were performed in which the graphite percentages, loading mode was varied. As test results indicate that the addition of graphite shows positive influence on the indirect tensile strength, failure stiffness modulus in static loading test, especially in high loading speed. The number of load cycles to fatigue failure presents a bit decrease with graphite percentages in dynamic loading test. After adding discontinuous carbon fibers, conductive asphalt-based composite shows good fatigue property, which can prevent crack propagation. It can be concluded that the combined modification brings reinforcement effect to asphalt concrete and improves its mechanical and fatigue properties.

Introduction

Adding appropriate conductive material to asphalt mixture, its electrical conductivity will improve markedly and the interior structure will convert from insulator to conductor [1]. Conductive asphalt concrete would potentially make many technologies applicable to pavement. Examples of potential applications of conductive asphalt concrete include thermal electric de-icing, Self-monitoring of pavement damage and so on. However, conductive asphalt has found little application in the highway industry. The main reason for this is due to the fact that traditional carbon-based additives have to be applied in significant quantity in order to increase the electrical conductivity of asphalt concrete.The presence of graphite in large quantity consequently compromises the normal performance of asphalt concrete. The indirect tensile tests (ITT) are considered the most promising for their fundamental performance of asphalt concrete mixtures [2-4]. The object of this paper is to study the influence of addition of conductive fillers on indirect tensile strength, failure stiffness modulus and fatigue life to analysis the cracking properties of the neat and conductive asphalt concrete.

Experimental

Materials. The asphalt used was AH-70 made from Koch Asphalt Co. Ltd (Hubei Province, China), with penetration of 65 (0.1 mm at 25 °C, 100 g and 5 s), ductility of 167.3 cm (at 5 °C) and softening

point of 51.5 °C. Fresh basalt mineral aggregate was obtained from Jingshan Aggregate Plant (Hubei Province, China), with density of 2.93 g/cm3. Limestone powders were applied as mineral filler, with a density of 2.83 g/cm3, major chemical compounds: CaO 51.5% and SiO2 1.76%. Microcrystal graphite powders and chopped carbon fibers were selected as conductive fillers. The graphite was obtained from Xingtai Graphite Ore Factory in Hebei province, China. Its particle size <150μm, carbon content 98.9% by weight, the electrical resistivity 10-4 Ω·cm. The carbon fiber was supplied by An Shan Eastern Asia Carbon Fiber Co. Ltd. in China. Its tensile strength 1.68 GPa, tensile modulus 752 GPa, fiber diameter 10-14μm, and average filament length 5 mm, the electrical resistivity 10-3 Ω ·cm. Conductive asphalt concrete was obtained with a 12.5 mm Superpave gradation. Table 1 presents the particle size distribution.

Table 1 selected mix gradation

Sieves [mm]	16	12.5	9.5	4.75	2.36	1.18	0.6	0.3	0.15	0.075
Passing [%]	100	95.6	77.3	49.5	29.7	21.7	15.7	10.5	7.9	5.7

Test methods. Graphite can replace some limestone powders due to its smaller size than mineral fillers. Graphite powders in the amount of 0%, 12%, and 18 % by volume of asphalt were used for the test specimens. Moreover, Graphite content of 12% and 18 % added with 0.3% carbon fibers by total of aggregate weight were used to contrast against the concrete with single conductive filler. The asphalt dosage increases with the increasing graphite content. The aggregates were preheated at temperatures with a range of 180°C~220°C. The asphalt was heated at 160°C and the mixer was controlled at 170°C. Filler was dried, not preheated. First, carbon fibers and aggregates were blended for 180 seconds (180s). Asphalt of required amount was then added and blended for another 90s. Finally, filler and graphite powders was added and blended for 90s. The total mixing time was 360s [1]. Mixtures were stored in a Marshall mold to compaction for the tests. The air voids and other volumetric properties of the test specimens were matched with the design requisition.

The indirect tensile test can be used for determining the tensile strength, modulus of elasticity, Poisson s ratio, and tensile failure strain of asphalt concrete mixes. Some of these parameters are required for fatigue potential analysis.

The fatigue test was carried out by a repeated haversine load of 2Hz frequency (0.1s loading and 0.4 s unloading) at 20°C, which was implemented in UTM-25 with an environment conditioner. First, tensile strength was tested by the loading speed of 50mm/min, and then stress levels of 0.4, 0.5, and 0.6 are employed to measure the fatigue life of these mixtures including conductive asphalt mixture with graphite, conductive asphalt mixture without carbon fiber and neat mixture.

Results and discussions

Indirect tensile strength. Figure 1 shows the experimental curves of static indirect tensile test. Asphalt material, a kind of visco-elastic material, expresses its unique nonlinear stress-strain response as shown in Fig. 1.

The maximum stress of each stress-strain curve is defined as Indirect Tensile Strength (ITS). Fig. 1 shows the comparison of ITS of each group of asphalt mixtures at 20°C. Compared to different test conditions, the ITS increases sharply with the loading speed from 1mm/min to 50 mm/min. For example, ITS of neat asphalt mixture increases more than three times, from 0.43 MPa at 1 mm/min to 1.37 MPa at 50 mm/min, as shown in Fig. 1. It is illustrated that asphalt materials exhibited high stress resistance in high loading speed. Compared with groups of asphalt materials at low loading speed, the neat asphalt concrete tend to show the lowest ITS than the others. This trend becomes clearer when applied a high loading speed. Conductive asphalt concrete presents higher stiffness compared with the neat one, moreover the value will rise with the increase in graphite content because of the sclerous effect of graphite in the asphalt. Especially the group of asphalt mixture added carbon fiber shows

highest strength over two test conditions, because the addition of carbon fiber can reinforce the toughness of concrete.

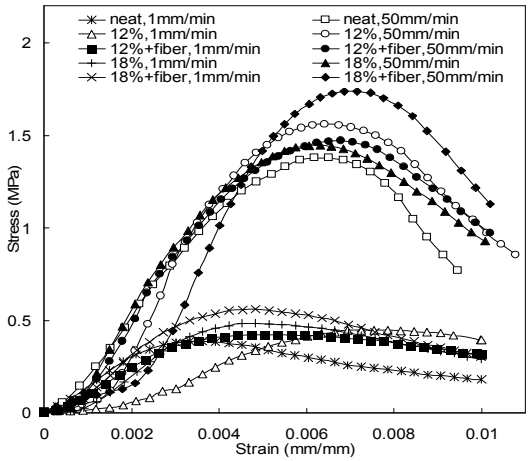

Figure1 Experimental result of static test

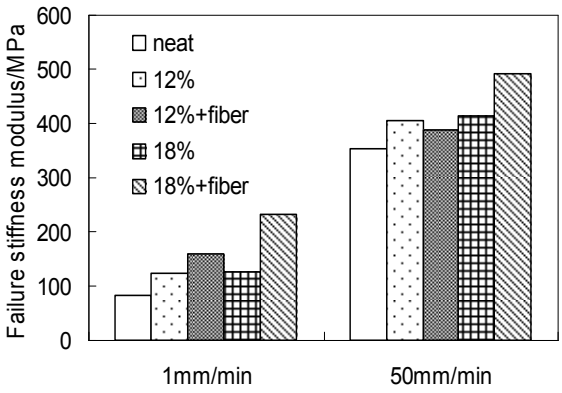

Figure2 Failure stiffness modulus

Failure Stiffness Modulus. Figure 2 illustrates the failure stiffness modulus (E_{sp}) of groups of asphalt mixtures and presents the loading-dependency of five groups of mixtures.

Fig. 2 trends are similar to Fig. 1 that asphalt materials shows high modulus in high loading speed. For example, neat asphalt mixture presents 81.3MPa and 354MPa at 20 °C, 1mm/min and 50mm/min, respectively. At these two loading conditions E_{sp} of conductive concrete is higher than that of neat one. It can be observed from figure 2 that the value of stiffness modulus increases from 81.3 MPa to 127.3 MPa at 1 mm/min when the graphite content varies from 0 to 18%. These data mean that the failure stiffness modulus was influenced remarkably by the addition of graphite powder. As also shown in Fig. 2, mixture with 18% graphite added carbon fiber shows the highest E_{sp}, 490MPa, compared to the others when applied high loading speed. It can be seen that, with the same dosage of graphite, graphite and carbon fiber modified asphalt concrete has a higher E_{sp} than that of asphalt concrete only containing graphite powder. Stiffness modulus is an elastic index in material mechanics measurement. Asphalt mixture is a visco-elastic body, which can be described by Burgers body. When adding graphite, the viscous component of asphalt binder decreases sharply. Asphalt binder could be transferred from ideal Burgers body to a more elastic-like body, a non-Newton liquid. Thus, asphalt mixture with conductive material shows more elastic modulus compared with neat mixtures. In particular, elasticity of conductive concrete is more sensitive to high loading speed [6-9].

Fatigue life. Table 2 summarizes the results from the ITT in the form of tensile stress plotted against the number of load cycles to failure. An empirical relationship of the following form was used during the regression analysis:

$$N_f = K\,(\sigma_T)^{-n}. \quad (1)$$

Where N_f = number of cycles to failure; σ_T= indirect tensile tress, MPa; and K and n = material coefficients, listed in Table 2.

Table 2 Calculated regression coefficients for ITT

Graphite content (%)	n	K
neat	2.9736	2337.3
12%	3.1899	1640.7
18%	3.8764	3189.5
12% (with carbon fiber)	2.9332	1444.7
18% (with carbon fiber)	3.6335	2181.8

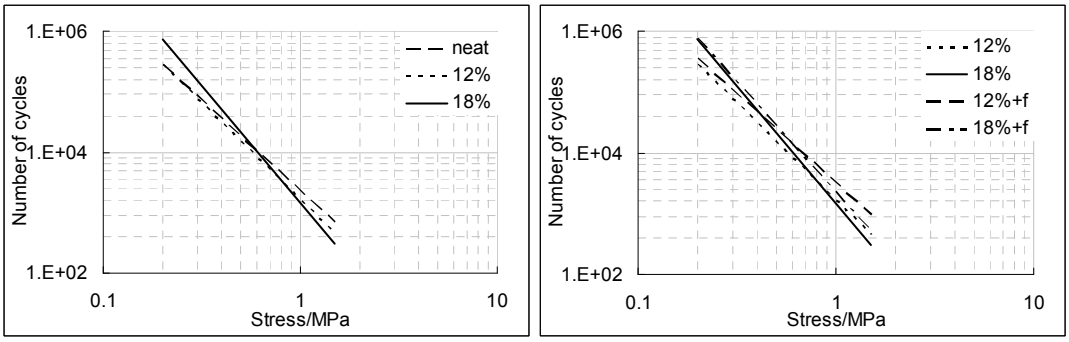

(a) (b)

Figure 3 fatigue life of asphalt mixture

Figure 3 depicts the predicted fatigue life curves of five groups of mixtures observed in the experiments. Compared the trends of five groups of curves after peak, it can be seen that the fatigue lives of these groups of mixtures show stable decrease with the increase of stress level. Compared with the slopes of mixtures shown in Fig. 3, group of conductive asphalt mixture without carbon fiber shows the largest decreasing rate. In addition, neat mixture and conductive asphalt mixture with carbon fiber show similar decreasing rate. When applied a high stress, conductive asphalt materials seem perform better fatigue properties.

It can be observed from Fig.3 (a) that three fatigue curves intersect each other at stress level of 0.7MPa. At low stress level below 0.7MPa, conductive asphalt mixture shows relatively high fatigue life, but just the reverse is true when stress level is high. Under low stress level such as 0.2MPa, concrete with 18 vol.% graphite shows fatigue life of about 7.4×105 at 0.2MPa and 3.1×102 at 1.5 MPa, while neat mixture presents fatigue life of 2.8 ×106 at 0.2MPa and 7.3×102 at 1.5 MPa, respectively. Fig. 3(b) compared the fatigue property of the concrete containing single conductive filler with that of the mixed-fillers modified concrete. It can be concluded that mixed conductive fillers have appreciable advantages in fatigue life over single powder filler at the same total content significantly.

Conclusion

(1) Under a same temperature, the indirect tensile strength and show significant increase with graphite percentages in static loading test using ITT, especially in high loading speed.

(2) The mixed-fillers modified Conductive concrete shows high failure stiffness modulus, which can prevent crack propagation.

(3) The number of load cycles to fatigue failure presents a bit decrease with graphite percentages at high stress levels in dynamic loading. The fatigue property of conductive asphalt concrete is susceptible to the stress level.

(4) The addition of 0.3% carbon fibers can further improve the fatigue property of conductive concrete, especially under both high and low stress levels.

References

[1] S. P. Wu, L. T. Mo, Z. H. Shui, Chen Zheng: Investigation of the conductivity of asphalt concrete containing conductive fillers, Carbon Vol. 43 (2005), p.1358-1363.

[2] D. W. Christensen and R. F. Bonaquist: NCHRP Report, No.530, Trans Research Board, 2004.

[3] P. Paulo: The International Journal of Pavement Engineering, Vol. 5 (4) (2004), p. 211.

[4] P. S. Kandhal, S. S. Rao, D. E. Watson and B. Young: NCAT Report, No.95-1

Key Engineering Materials Vols. 385-387 (2008) pp 473-476
© (2008) Trans Tech Publications, Switzerland
doi:10.4028/www.scientific.net/KEM.385-387.473

Temperature sensitivity of Asphalt-aggregate Adhesion via Dynamic Mechanical Analysis

WU Shao-peng[1, a], XIAO Yue[2, b], LIU Quan-tao[3, c] and CAO Ting-Wei[4, d]

[1] Key Laboratory of Silicate Materials Science and Engineering of Ministry of Education,

[1] Wuhan University of Technology, Wuhan, CHINA

[2] Key Laboratory of Silicate Materials Science and Engineering of Ministry of Education,

[2] Wuhan University of Technology, Wuhan, CHINA

[3] Key Laboratory of Silicate Materials Science and Engineering of Ministry of Education,

[3] Wuhan University of Technology, Wuhan, CHINA

[4] Key Laboratory of Silicate Materials Science and Engineering of Ministry of Education,

[4] Wuhan University of Technology, Wuhan, CHINA

[a]wusp@whut.edu.cn, [b]xiaoy@whut.edu.cn, [c]liuqt@whut.edu.cn, [d]caotw@whut.edu.cn

Keywords: Asphalt-stone adhesion; temperature sensitivity; dynamic mechanical analysis; dynamic tension stress test;

Abstract. It is known that the properties of asphalt-aggregate adhesion show great effect on the performance of asphalt pavement, while the temperature plays an important role in determining the fundamental properties of asphalt binder between single aggregate-aggregate contacts surfaces. The temperature sensitivity is considered to be very important on understanding the failures of asphalt pavement, especially on the asphalt-aggregate adhesion. Knowledge the temperature sensitivity of asphalt-aggregate adhesion is very important in asphalt mixture design. The purpose of this paper was to quantify the effect of temperature on the adhesion and cohesion of asphalt film between aggregate and asphalt. The adhesive/cohesive failure of asphalt film between single aggregate-aggregate contacts was investigated using dynamic mechanical analyzer under dynamic tension stress test with force-control mode, then fracture surface were analysis by a Polarizing Microscope. Contrastive experiments were conducted on SBS modified asphalt under different temperatures. Experimental results indicate that the area percentage of adhesive failure was decreased with the increase of test temperature. And the adhesive failure percentage is enhancing with the increase of loading max-stress level.

Introduction

The strength and lifespan of asphalt pavement are determined mainly by the properties of asphalt-aggregate adhesion. The condition temperature can affect the adhesion strength significantly. Some failures of asphalt pavement, such as rut in hot days and crack in low temperature, have a strong relationship with temperature sensitivity of asphalt-aggregate adhesion [1, 2].

The adhesion properties of bituminous materials have been studied mainly in the mechanic field [4, 5], however, temperature sensitivity of asphalt-aggregate adhesion has not been included. Thus, the adhesion strength and failure mode between asphalt and aggregate was investigated in this paper with force-controlled tension tests using SBS modified asphalt, at 0°C, 10°C and 20°C. And then the area percentage of adhesive failure was observed by Image analysis. Above all, this work was further aimed at finding an exact relationship between asphalt-aggregate adhesion properties and temperature to supervise the asphalt pavement design and predict the serving time according to the variety of environmental temperature.

Materials and experimental method

Materials. The asphalt binder tested was PG70-28 SBS modified asphalt supplied by Shell Asphalt Co. Ltd. in Hubei province, China, whose specifications was showed in table 1.

Table 1 specifications SBS modified asphalt

Item	Results	Index	Specification
Penetration/0.1mm	76	60-80 (25°C)	ASTM D5-06e1
softening point/	56.8	≥55	ASTM D2398-82
Viscosity/	1.3	≤39(°C)	ASTM D2170-07

Basalt stone with specific density of 2.924 g/cm^3 was used for the experiment tests, whose main chemical components were SiO_2 content of 44.23%, CaO content of 10.45%, MgO content of 11.28%, Al_2O_3 content of 8.79%, Fe_2O_3 content of 10.02%, FeO content of 6.46%, K_2O content of 1.87% and Na_2O_4 content of 1.03%.

Test-specimen preparation. Fig. 1 shows the schematic illustration of the process of test-specimen preparation. The geometry and dimensions of test specimen which consists of a double layered sandwich was also showed in Fig. 1. Two small columnar stones of 10 mm height and 2.8 mm diameter are required.

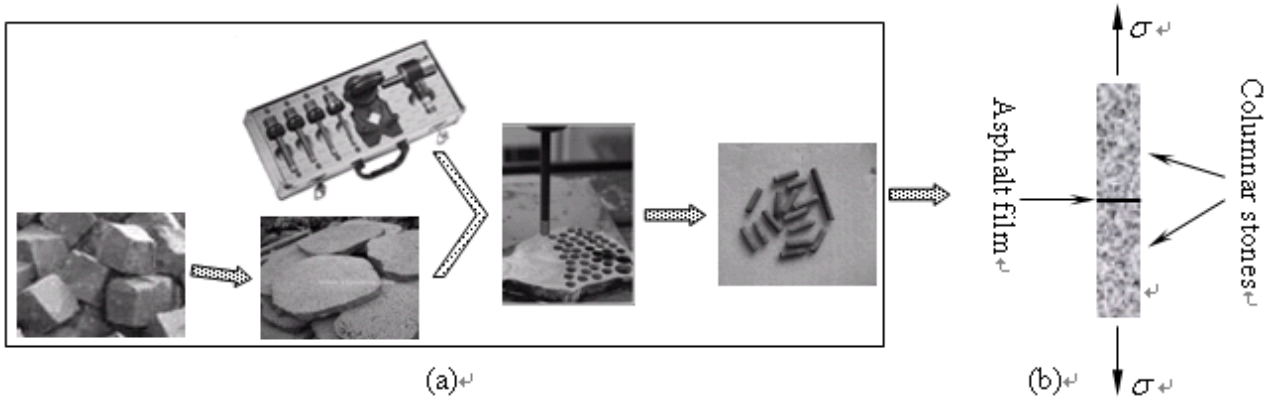

Fig. 1 preparation process of Test-specimen

The small columnar stones are gained by a special way, as can be seen in Fig. 1(a). First, cleaning the stones and then cut them into slices. After we got the slices we have to polish the surface with successively finer grit metallographic papers down to provide a rough surface finish for adhesion of the asphalt binder. Third, drill columnar stones from slices and make final inspection. At the last, in order to clean up the dust and other useless powder from the columnar stones` surface, stones were cleaned carefully in boiling distilled water for at least 30 min and then dry at temperature 165°C for another 3h. Finally it is ready for assembling stone samples.

As fig. 1(b) shows, the test-specimen was glued by a thin binder film between two columnar stones. The thickness of the binder film was controlled by DSR (Dynamic Shear Rheometer), a precise instrument that can be used for micro-thickness setting. Specimens were manufactured by coating hot, molten bitumen upon each bonding surface using DSR, and get it out from camp stove of DSR after it already cool down to ensure good alignment.

Testing method. All the samples were performed using Dynamic Thermal Mechanics Analyzer (Model: DMA Q800, TA Instruments Company, US). Before applied force, the samples were held for 30 min in a thermostated working chamber at the test temperatures, 0°C, 10°C and 20°C respectively. The dynamic tension stress tests were performed under force controlled mode, with the max-stress ranged from 0.4 to 0.8 Mpa.

Both adhesive and cohesive failure modes will occur in these tests. To be able to distinguish them, the failure surface after each test is inspected using Axioskop 40 Pol (Car Zeiss Far East Co., Ltd.).

From this inspection, the area percentage of adhesive failure is determined by an image analysis software.

3. Results and discussion

An important characteristic of tension bond test on the asphalt-aggregate adhesive zone is its failure mode. Usually distinction is made between adhesive failure and cohesive failure. In the case of adhesive failure the pure interface is failing, resulting in bare stone after failure, as shown in fig. 2(a), a micro-image of failure surface in 0°C. Cohesive failure implies that failure occurs within the mastic. In such a case the stone will still be covered with bituminous material after failure, just like fig. 2(b), a micro-image of failure surface in 20°C.

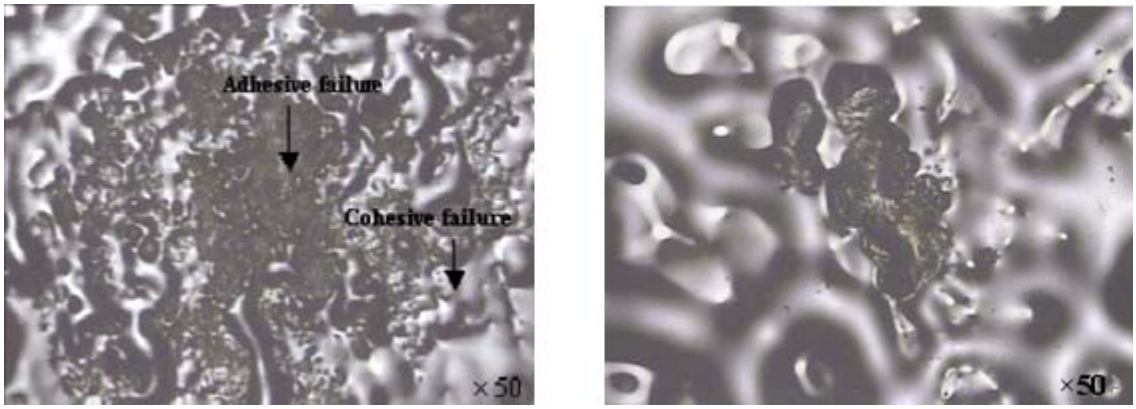

(a) (b)

Fig.2 micro-images of failure surface at 0° C and 20° C

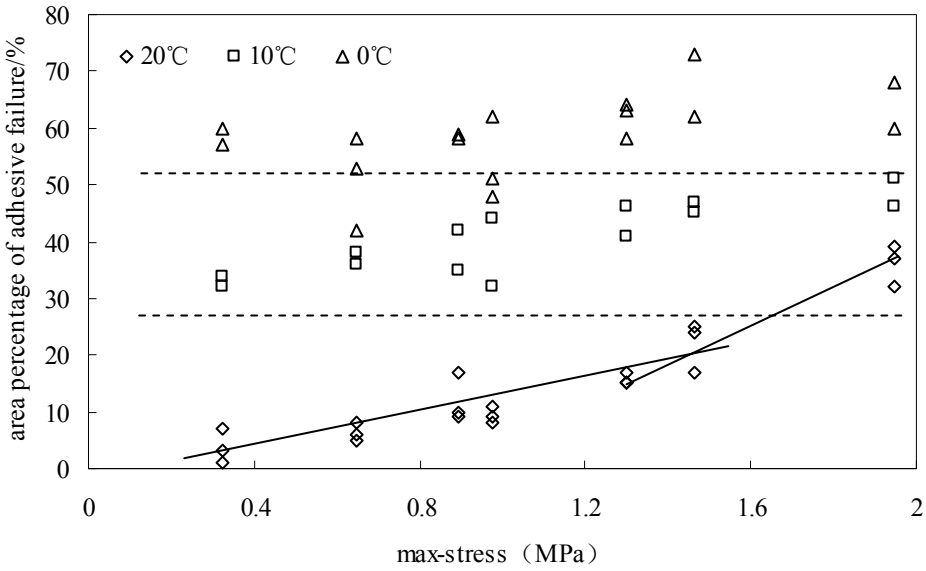

Fig.3 area percentage of adhesive failure in different temperature

According to the image analysis software, the area percentage of adhesive failure for SBS modified asphalt in different temperature was shown in fig. 3. At the room temperature, 20°C, the area percentage is lower than 50 percent. This illustrates that at room temperature, resistance property of adhesion strength to fatigue fracture in the surface is better than cohesion strength in asphalt binder. The percentage is enhancing with the increase of loading max-stress level, but the trend is not same. In the low max-stress area, the increase of adhesive failure percentage is slowly but at higher max-stress it is much remarkably. This is because the creep and self-healing of asphalt film play significant effects on

asphalt-aggregate adhesion at low max-stress condition, while at higher max-stress loading enviroment the stiffness and strength of asphalt film become larger, results in more adhesive failure between surfaces.

At 0°C, the area percentage of adhesive failure is much higher than 50 percent, this indicates adhesive failure play a prominent role, while at 10°C the percentage is right around 50 percent. This result illustrates that adhesion strength between asphalt and aggregate is quite close to cohesion strength in asphalt binder at 10°C, but at low temperature the cohesion strength is greater than adhesion strength. These analysis shows that cohesive failure is the main failure mode in high temperature and adhesive failure in low temperature.

It is probably because asphalt is a typical viscoelastic material at room temperature. When stress was applied to the sample, stress was totally loaded to asphalt film and translated to film strain. Cyclical stress loading will cause final failure in asphalt film. But at the lower temperature, asphalt is characterized as high stiffness and low elasticity. When a certain stress was applied on this asphalt film, it cannot offer enough strain, at the same time the resistance tension strength of asphalt film is higher than adhesion strength in surface, so adhesive failure occurred mainly.

Conclusions

Asphalt film is sensitive to temperature. The asphalt-aggregate adhesive zone has two failure mode, adhesive failure and cohesive failure. At high temperature, the elastic contribution to viscoelastic response was more pronounced, and cohesive failure is the main part. But at lower temperature, such as 0°C, the adhesive failure is the maily failure mode. The adhesive failure percentage is enhancing with the increase of loading max-stress level because of the self-healing of asphalt binder is significantly in small max-stress loading level.

References

[1] L.T. Mo, S.P. Wu, M. Huurman and A.A.A. Molenaar: Theoretical and Applied Fracture Mechanics, Vol. 46-2(2006), p.140-147

[2] Isacsson, U. and Zeng, H.: Construction and Building Materials, Vol. 11-2(1997), p.83-91

[3] Kanitpong, Kunnawee and Bahia, Hussain: Transportation Research Record, n1901(2005), p.33-43

[4] Khattak, Mohammad J., Baladi, Gilbert Y. and Drzal, Lawrence T.: Journal of Materials in Civil Engineering, Vol. 19-5(2007), p.411-422

[5] El Hussein, H Mohamed, El Halim and A.O. ABD: Canadian Journal of Civil Engineering, Vol. 20- 3(1993), p.366-373

[6] There are two failure modes in asphalt mix fracture, cohesive failure in the asphalt film or mastic mortar and adhesive failure in the adhesive zone between aggregate and asphalt [3].

Key Engineering Materials Vols. 385-387 (2008) pp 477-480
© (2008) Trans Tech Publications, Switzerland
doi:10.4028/www.scientific.net/KEM.385-387.477

Thin Liquid Crystal Film For Corrosion Sensing.

F. Kossivas[1,a], A. Kyprianou[1,b].
[1] 75 Kallipoleos, P.O.Box 20537, 1678 Nicosia, Cyprus.
[a] mep6kf1@ucy.ac.cy,[b] akyp@ucy.ac.cy.

Abstract.
The anchoring energy of Liquid Crystals (LCs) is influenced by several parameters. Many scientists have exploited LCs anchoring in order to develop several LC based optical sensors. This paper proposes and proves a new principle of operation for corrosion sensing based on the anchoring energy of liquid crystals. For the work of this paper 5CB (4-cyano-4-n-pentylbiphenyl) nematic LCs were used to coat iron substrates forming films of about 7μm thickness. Both corroded and non-corroded iron substrates were coated and the differences in LC anchoring between the two substrates are reported. These differences were studied experimentally using the atomic force microscope (AFM) and the laser profilometer.

Introduction

Through the displays of the modern televisions and computers the liquid crystalline phase of matter had permeated our everyday life as much as the other better known, gaseous, liquid and solid, phases of matter. The physics and chemistry that this phase manifests when interacts with its surroundings motivated scientists and engineers to exploit liquid crystals in other areas of technology and research [1].
In sensor technology for example the correlation of a) LCs birefringement with external pressure had lead to a hydrostatic pressure sensor development [2], b) the director of the nematic liquid crystal to external electric field to an elecromangetic field sensor [3] and c) the ordinary and extraordinary refractive indices to temperature variations to temperature sensor [4]. An important aspect of LCs is their interaction with the surface of their substrate and the nature of this interaction is dictated by the LC anchoring energy [5]. This interaction had been utilized in detecting surface abnormalities [6] and to discriminate malignant tissue from normal [7].
This paper presents the first steps taken to evaluate the potential of applying the liquid crystals as the primary sensing element for corrosion. Optical based corrosion sensor based on evanescent fields, Bragg grading, spectroscopy and optical fibers had been developed and they are described [8,9] and references therein. The work described in this paper is a part of a bigger endeavor which aspires to develop an integrated liquid crystal based optical corrosion sensor.

Experimental Results and discussion.

An iron (pearlite steel) surface was coated with a thick film of LCs in an area where a corrosion spot had been initiated by a 0.1M NaCl solution. AFM in wave mode had been used, for in this mode the tip does not contact the substrate and hence does not disturb the LC alignment, to measure the LC topography. AFM had also been used to measure the surface roughness of the iron. Finally optical profilometer was used to discriminate the LC anchoring on the corroded part from the non corroded.

Substrate Preparation: The iron sample was firstly polished in order to achieve a nano roughness finish. A dual preparation 3 Allied polisher was used in a seven stage polishing process. Grinding was done by p180c, c320, c600 and 1200(p-4000) grinding papers together with diamond (6μm), alumina (0.3μm) and colloidal silica (0.05μm) solutions. The sample was then cleaned with ethanol in clean room paper and stored in a nylon bag containing nitrogen gas. This ensured that no corrosion occurred until that stage of the experiment. Finally an AFM image as shown in Figure 1, using the Quescant Q-scope, of the targeted to corrode area had been taken from which the values of 115nm for the average height 36.26nm for the mean deviations were extracted.

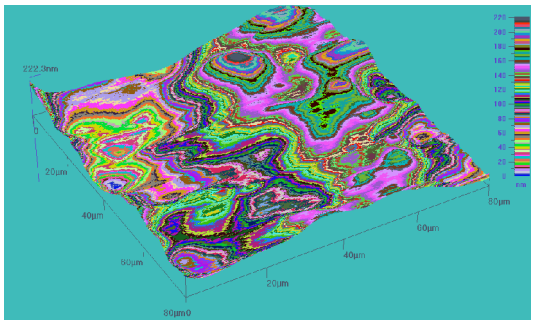

Figure 1: AFM topological image of the polished iron substrate

Corrosion spot initiation: A corrosion spot was initiated upon the evaporation of a single drop of 0.1M NaCl solution over the substrate. This drop had been deposited on the sample's surface using a micropipette. Subsequently the sample had been cleaned with ethanol and dried with nitrogen in order to remove the remaining products from the evaporation of solution. An image 10x with optical microscope of the corrosion spot is shown in figure 2. This part of the experiment, and what follows, were executed in a clean room in order to avoid dust and particles disturbances. The temperature was also kept constant at 22°C.

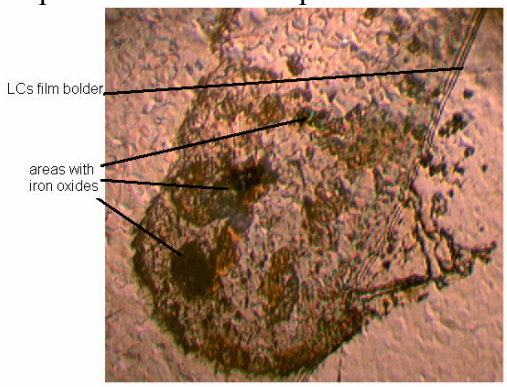

Figure 2: Optical image of the corrosion spot.

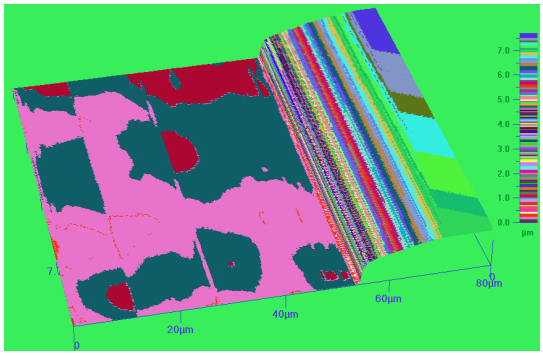

Figure 3: AFM image of LCs film over the iron substrate.

LCs Film Deposition: 5CB nematic LCs (Aldrich) were deposited over the substrate. A 10μL drop was deposited, using a micropipette, over the corrosion spot and then the sample positioned in a vertical position for approximately one day. The drop flow due to the gravity and only a thin film remain in the area of the corrosion spot. The sample was then positioned in horizontal position for another day, so the LCs film reached an equilibrium stage with homogenous thickness. The value, 7.356μm, for the film thickness was exacted from an AFM topological image of the sample, figure 3.

LCs anchoring: The differences in anchoring due to corrosion were imaged using the Ambios Xi-100 optical profilometer. Figure 4 shows that LCs surface is flat even in eroded but not oxidized area of the sample. In the three areas where iron oxides remained, there is a significant change of the topology, figure 5. This is because the anchoring energy of LCs at the oxide boundaries is different than at the oxide free iron boundaries and hence LC molecules anchor with different orientation.

It also of great interest in the way light reflects from the LC film. Excluding some disturbances due to surface imperfection as viewed at the upper right corner of Figure 4, homogenous formation of linear fringes in the iron substrate occurs contrary to the cyclic fringes occurring in the oxidized area. This is more evident in Figure 5.

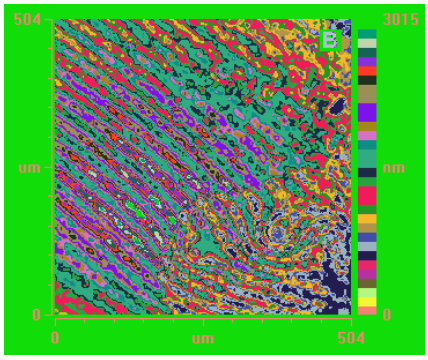

Figure 4: Optical fringes at the LC coated corrosion spot

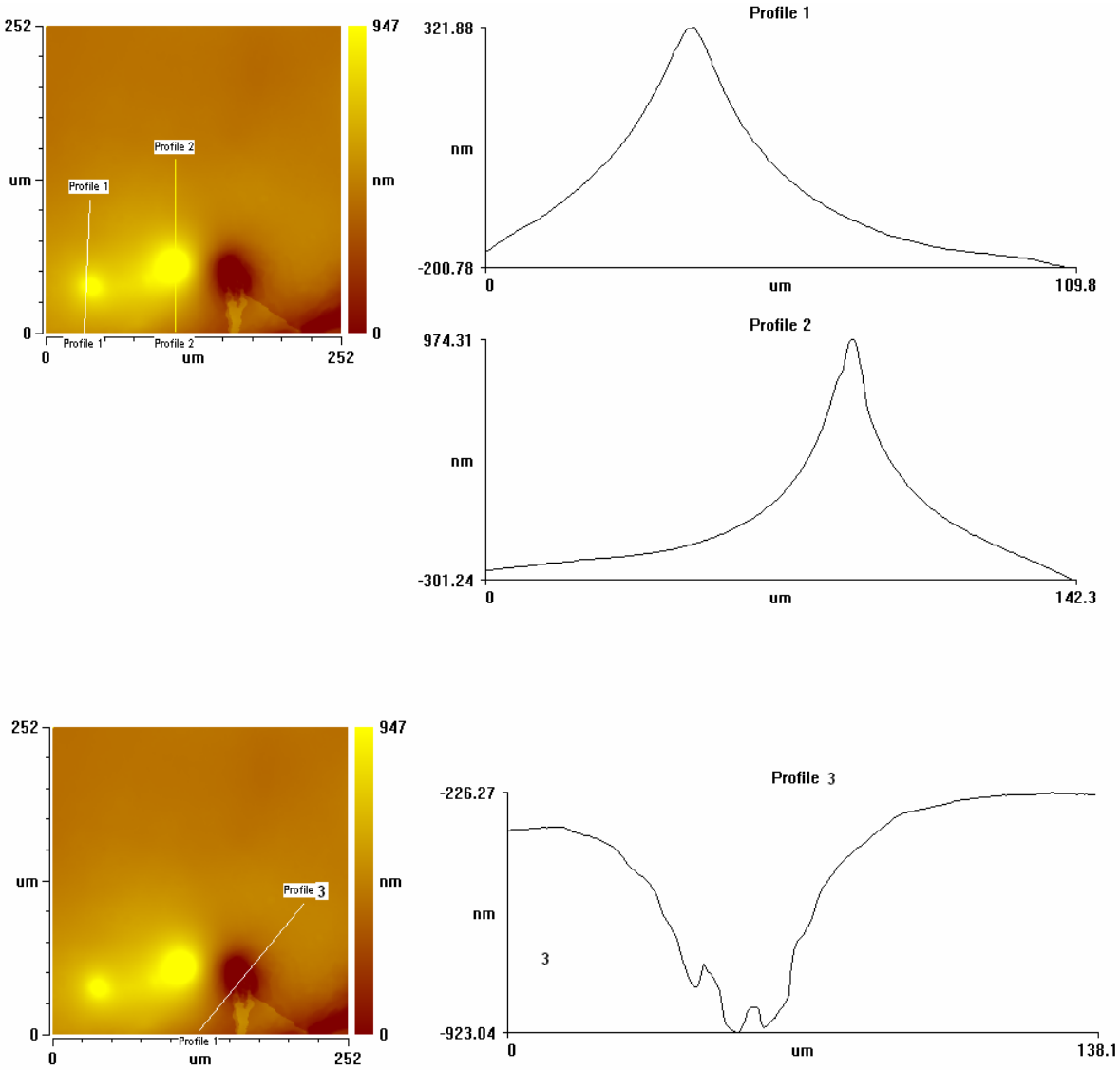

Figure 5: Optical profiler images of the areas in corrosion spot with iron oxides.

Conclusion.

The work featured in this paper aimed to demonstrate the capability of liquid crystal to sense corroded areas. A film of 5CB nematic LCs was deposited on a corroded spot and was shown through a profilometer and AFM measurements that LCs anchor differently on a corroded lesion than on a non-oxidized one. These results proposed and proved a new principle of operation for corrosion sensing. Future studies will refine this technique and from the results that will be obtained an innovative LCs based optical sensor for corrosion detection will be developed.

References.

[1] Peter J. Collings and Michael Hird, "Introduction to Liquid Crystals, Chemistry and Physics" Taylor and Francis, Third Edition, 2004.

[2] Tomasz R. Woli´nski, Aleksandra Jarmolik, and Wojtek J. Bock, "Development of Fiber Optic Liquid Crystal Sensor for Pressure Measurement", IEEE Transactions on Instrumentation and Measurement, 48(1), 1999, 1-6.

[3] Byoungho Lee, Yoonchan Jeong, Seungin Baek, Hak-Rin Kim, Yonghyun Kim, Yong Wook Lee, and Sin-Doo Lee, "Electromagnetic Field Sensing Using Liquid Crystal Optical Fibers", Optical Fiber Sensors Conference Technical Digest, 2, 2002**,** 403-406.

[4] Hak-Rin Kim, Eunje Jang, and Sin-Doo Lee*,* "Electrooptic Temperature Sensor Based on a Fabry–Pérot Resonator With a Liquid Crystal Film", IEEE Photonics Technology Letters, vol. 18, 2006, no. 8.

[5] T. J. Sluckin "Anchoring transitions at liquid crystal intrerfaces", Physica A, 213, 1995, p. 105-109.

[6] Y. Hayashi, M. Masuda, J. Lee, M. Kojima, "Study on corrosion properties of sputter coating of oxides on stainless steels", Materials Science and Engineering, A 198,1995, 71-74.

[7] M. G. Tomilin, S. A. Povzun, A. F. Kurmashev, E. V Gribaniva and T. A. Efimova, "The application of nematic liquid crystals for objective microscopic diagnosis of cancer", Liquid Crystals Today, 10(2), 2001, 3-5.

[8] M. Benounis, N. Jaffrezic, "Elaboration of an optical fibre corrosion sensor for aircraft applications", Sensors and Actuators B 100, 2004, 1–8.

[9] S.A. Wade, C.D. Wallbrink, G. McAdam, S. Galea, B.R.W. Hinton, R. Jones, "A fibre optic corrosion fuse sensor using stressed metal-coated optical fibres", Sensors and Actuators B , Article in press, 2008.

Key Engineering Materials Vols. 385-387 (2008) pp 481-484
© (2008) Trans Tech Publications, Switzerland
doi:10.4028/www.scientific.net/KEM.385-387.481

The Effect of Ageing on Rheological Properties and Chemical Conversions of Asphalts

Shaopeng WU [1, a], Ling PANG [2, b] and Guojun ZHU [3, c]

[1] Key Laboratory of Silicate Materials Science and Engineering

(Wuhan University of Technology), Ministry of Education, Wuhan 430070, China

[2] Key Laboratory of Silicate Materials Science and Engineering

(Wuhan University of Technology), Ministry of Education, Wuhan 430070, China

[3] Key Laboratory of Silicate Materials Science and Engineering

(Wuhan University of Technology), Ministry of Education, Wuhan 430070, China

[a]wusp@whut.edu.cn, [b]lingpang@whut.edu.cn, [c]guojunzhu@whut.edu.cn

Keywords: asphalt, ageing, ultraviolet, dynamic shear rheology.

Abstract. Asphalt ageing induced by heat, oxidation and ultraviolet (*UV*) radiation was investigated using various laboratory simulation ageing methods and outdoor ageing. One normal 70 penetration asphalt and its styrene-butadiene-styrene (*SBS*) modified asphalt were employed to assess the changes in chemical and rheological properties by infrared spectroscopy and dynamic shear rheometer under various ageing conditions, thus the relationship among rolling thin-film oven(*RTFO*), pressurized ageing vessel (*PAV*) and *UV* radiation ageing was distinguished. Experimental results showed that photodegradation caused by outdoor exposure *UV* ageing of 50~200μm thin films for a month, was found to be the most severe, following by *PAV* and then *RTFO* with respects to rehological and chemical changes. Photodegradation effect decreased as the thickness of asphalt film increases. Dynamic shear tests indicated that polymer networks were gradually destroyed during ageing, but the aged *SBS* modified asphalts still displayed better rheological properties than the corresponding base asphalt. The weight percent of oxygen as carbonyl increased and of *SBS* as butadiene decreased after ageing based on infrared spectrums. However, chemical and rheological changes were not generally consistent, and ageing susceptibility may be ranked differently when different evaluation methods were used.

Introduction

Due to the effect of heat, air, and ultraviolet (*UV*) radiation during asphalt mixture construction (short-term ageing) and in the service (long-term ageing), the chemical and mechanical properties of road asphalt is changed [1]. The loss of volatile components and oxidation of the asphalt cause hardening of the mixture, which may make the deterioration of asphalt pavements [2, 3]. The conditions at different ageing stages vary continually. In laboratory tests, rolling thin film oven (*RTFO*) test is used for examining the thermal degradation during short-term ageing, and the pressure ageing vessel (*PAV*) test is used for simulating long-term ageing [4]. Besides heating and oxidation, the effects of *UV* radiation on asphalt pavement materials, which are relative close to conditions in service, have gained attention in recent years [5]. Our objective is to study the evolution of the asphalt at different ageing conditions, especially photodegradation of asphalt. In this paper, two standard methods, *RTFO* and *PAV* were used to age asphalt. The results of both artificial types of ageing are compared to those observed from outdoor exposure *UV* radiation during the summer time. The effects of ageing on asphalt chemical and rheological properties were investigated using Fourier transform infrared spectroscopy (*FTIR)* and dynamic shear rheometer (*DSR*). Furthermore, the correlation between chemical and physical changes is examined.

Materials and Experimental

Materials. The base asphalt AH70 with 60/80 penetration and its styrene-butadiene-styrene (*SBS*) modified asphalt PG76 were obtained from Koch Asphalt Co.Ltd in Hubei province, China. For AH70, with penetration of 65 dmm at 25°C, viscosity of 0.4 Pa·s at 135°C, and softening point of 48°C; for PG76, with penetration of 55 dmm at 25°C, viscosity of 2.9 Pa·s at 135°C, and softening point of 85.5°C. In order to prepare thin films 50μm to 200μm in thickness, 5g of asphalt sample, by using samples after *RTFO*, was diluted with carbon disulfide to form a 15g to 25g mixture, then deposited onto a glass plate with suitable size respectively, with the evaporation of the organic solvent at room temperature, asphalt thin films were obtained.

Ageing Procedures. *RTFO* (75 min, 163°C and air flow at 4 L/min) test was conducted according to ASTM D2872. The *RTFO*-aged samples were subsequently aged in *PAV* (20h, 100°C, and air pressure at 2.1 MPa) according to AASHTO PP1.

Thin films (50μm to 200μm in thickness) of the asphalts were flatly mounted on the roof of a building in Wuhan City located in Hubei province, China (Location: latitude 30° 35' North, Longitude 114° 19' East; Temperature: 20 ± 15 °C), and were exposed to outdoor *UV* radiation and atmospheric conditions in August 2006. A glass plate having *UV* transmittance of 70% in the 300–400 nm region was set with a 5 mm interspace above the specimen to prevent contamination from dirt and water. The maximum surface *UV* intensity (W/m^2) of the specimens was around 12 W/m^2.

Experimental. A Thermo Nicolet Model Nexus FT-IR-Raman spectrophotometer loaded with Omnic 6.2 software was used to acquire *FTIR* spectra. Five percent by weight solutions of asphalt were prepared in carbon disulfide. All samples were obtained using a 0.1-mm path length sample KBr cell. Spectra were recorded using the following settings: number of scans 32; gain 1; apodization weak; and resolution 4. The carbonyle index (around $1700cm^{-1}$), and the butadiene double bonds (around $985cm^{-1}$) can be calculated with the following equations [6]:

$$I_{C=O} = \frac{Area\ of\ the\ carbonyle\ band\ centered\ around\ 1700\ cm^{-1}}{\sum Area\ of\ the\ spectral\ bands\ between\ 2000\ and\ 600\ cm^{-1}} \quad (1)$$

$$I_{SBS} = \frac{Area\ of\ the\ butadiene\ band\ centered\ around\ 985\ cm^{-1}}{\sum Area\ of\ the\ spectral\ bands\ between\ 2000\ and\ 600\ cm^{-1}} \quad (2)$$

The rheological properties of base asphalt and its *SBS* modified asphalt were measured by a dynamic shear rheometer. Frequency sweeps were applied at 10 rad s^{-1}, and temperature sweeps with 2°C increments from 10°C to 80°C were performed. For tests at 35°C or higher, a 1-mm gap and a 25-mm diameter plate were used. For tests below 35°C, a 2-mm gap and an 8-mm diameter plate were used. Viscoelastic properties at different temperatures and frequency at 10 rad s^{-1} were obtained. The strain was kept low enough so that all tests were performed within the linear viscoelastic range.

Results and Discussion

Chemical Structure Evolutions of AH70 and PG76. Table 1 reveals the *FTIR* changes of AH70 and PG76 before and after ageing. The peaks absorbance at 1700 cm^{-1} strengthen during *RTFO*, *PAV*, outdoor exposure *UV* ageing, on the contrary, the peaks at 985 cm^{-1} in PG76 weaken. Obviously, more carbonyl groups were generated while chain segments of butadiene decomposed after ageing, the sharpest changes occurred after outdoor exposure *UV* ageing. Table 1 also indicates the influence of film thickness on the changes of the peaks absorbance at 1700 cm^{-1} in asphalt AH70 during the outdoor exposure *UV* ageing. The carbonyl peak at 1700 cm^{-1} increases with the sample thickness decreasing from 200μm to 50μm, which means more oxidation reaction happened in asphalt samples with relatively thin thickness during the outdoor exposure *UV* ageing. For the *SBS* modified asphalt, the evolution of the carbonyl group shows a similar tendency to that of base asphalt. But its carbonyl

absorbance is smaller than those of base asphalt after the introduction of *SBS*. This result means that the modification of asphalt can restrict the formation of carbonyl group during ageing.

Table 1 Functional group indices of asphalt and its *SBS* modified asphalt before and after ageing

Asphalt	Carbony1index	*SBS* modified asphalt	Carbony1 index	Butadiene index
AH70	0	PG76	0	0.0354
AH70-*RTFO*	0.0146	PG76-*RTFO*	0.0127	0.0351
AH70-*PAV*	0.0479	PG76-*PAV*	0.0137	0.0310
AH70-*UV*(50μm)	0.3194	PG76-*UV*(50μm)	0.2602	0.0079
AH70-*UV*(100μm)	0.2905	-	-	-
AH70- *UV*(200μm)	0.0511	-	-	-

Rheological Properties Changes of AH70 and PG76. Fig.1 display the curves of complex modulus G* versus temperature for the base asphalt and its *SBS* modified binder before and after ageing. As can be seen, the modified binder indicates a distinct increase in the complex modulus G* at high temperature and a slight decrease in the complex modulus G* at low temperature when compared with base asphalt, which means that modification makes the asphalt binder less temperature sensitive in G*. And after ageing, the temperature sensitive of modified asphalt is still less than unmodified asphalt. Fig. 1 shows the effect of various ageing process, and it can be observed that the change order of G* values after different ageing conditions is the same as the change order of *FTIR* above. The outdoor exposure *UV* ageing is severer than *PAV* ageing and the degree of ageing worsens toward the surface of the asphalt layer after the outdoor exposure *UV* ageing.

Fig. 1 also reveals that the curves of phase angle versus temperature for the base asphalt and its *SBS* modified binders. The addition of *SBS* decreases the phase angle value significantly, and ageing results in a significant shift of the entire phase angle curve in the direction of more elastic behavior. When ageing is performed on the modified binders, large decrease in phase angle is observed at low temperatures, and consequently, a plateau region moves gradually to higher temperature range and then disappears after *UV* ageing, indicating that polymer networks are almost destroyed.

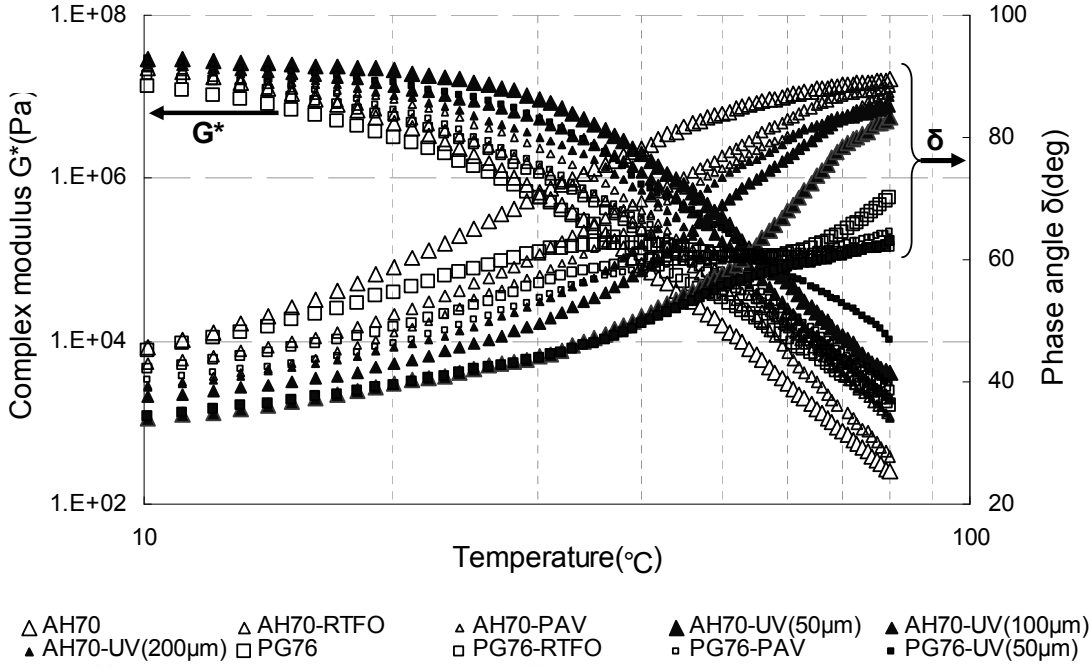

Figure 1 G* and δas function of temperature for base and *SBS* modified binders

Table 2 Ageing indices of asphalt and its *SBS* modified asphalt

Ageing indices	AH-70			PG76		
	RTFO	*PAV*	*UV*	*RTFO*	*PAV*	*UV*
Carbonyls ratio	1	3.28	21.88	1	1.08	20.49
*G** ratio (25°C, 10rad/s)	1	1.60	5.24	1	1.24	3.82
*G** ratio (60°C, 10rad/s)	1	1.96	7.42	1	1.37	4.14

Ageing Index. Ageing indices are defined as the ratio of a chemical or physical parameter of the aged asphalt to that of the original asphalt, which can be used to evaluate ageing degree of asphalt. Chemical and rheological ageing indices of AH70 and PG76 are listed in Table 2. It can be observed from Table 2 that *UV* ageing is found to be the severest among the different oxidation condition. The addition of *SBS* decreases the ageing indices of base asphalt, especially in complex modulus G* ratio at 60°C. It is also found that very weak correlation exists between chemical and rheological ageing indices. This observation suggests that ageing susceptibility may be ranked differently when different evaluation methods are used.

Conclusions

In this paper, *FTIR* and *DSR* were applied to characterize the ageing of base asphalt AH70 and its *SBS* modified asphalt PG76 after *RTFO*, *PAV* and outdoor exposure *UV* ageing test. As for *SBS* modified asphalt, oxidation of asphalt and the degradation of *SBS* happened at the same time, and modification of asphalt with *SBS* can inhibit the formation of asphalt carbonyl compounds. For the base and *SBS* modified asphalt, complex modulus was increased markedly at high temperatures and phase angle was reduced after ageing. The rheological properties of the aged polymer-modified binders also indicated that polymer networks were gradually destroyed, but the aged *SBS* modified asphalts still displayed better rheological properties than the corresponding base asphalt. Compared with *RTFO* and *PAV*, more oxidation degradation happened after outdoor exposure *UV* ageing. Photodegradation effect decreased as the thickness of asphalt film increase by *DSR* and *FTIR* analysis. It was also found from ageing indices that very weak correlation existed between chemical changes and rheological properties, and ageing susceptibility may be ranked differently when different evaluation methods were used.

References

[1] O.Whiteoak: Handbook of Shell Asphalts (London Shell Asphalt UK, 1991).

[2] YH Ruan, RR Davison, CJ Glover: Energy Fuel, Vol. 17(4) (2003), P.991-998

[3] M.N.Siddiqui, M.F.Ali: Fuel, Vol.78 (1999), P.1005-1015

[4] G.D.Airey: The International Journal of Pavement Engineering, Vol. 4(3) (2003), P.165-176

[5] Françoise Durrieu, Fabienne Farcas, Virginie Mouillet: Fuel, Vol. 86 (2007), P.1446-1451

[6] J.Lamontagnea, P.Dumas, V.Mouillet, J.Kister: Fuel, Vol. 81 (2001), P.483-488

Key Engineering Materials Vols. 385-387 (2008) pp 485-488
© (2008) Trans Tech Publications, Switzerland
doi:10.4028/www.scientific.net/KEM.385-387.485

Contributions in the Study of Hybrid Layered Composites under Static and Variable Loads

Nicolae Constantin[a], Viorel Anghel[b], Mircea Găvan[c], Ştefan Sorohan[d]

Laboratory for integrity evaluation of composite structures

The University "Politehnica" of Bucharest, Romania

[a]email: naec@form.resist.pub.ro , [b]email: anghel@form.resist.pub.ro ,

[c]email: mirceag@form.resist.pub.ro , [d]email: sorohan@form.resist.pub.ro

Keywords : hybrid layered composites, static and fatigue behavior, impact loading, residual strength, Lockin thermography

Abstract. The research work behind this paper focused a rather extensive assessment of hybrid composites made of pure aluminium sheets, alternating with GFRP and CFRP layers. Static, fatigue and low velocity impact tests were performed, combined with NDI on damaged samples, using Lockin thermography, on specimens obtained from the two hybrid laminates and from genuine GFRP and CFRP laminates, all having five layers. The static and fatigue tests were made on parallel specimens, un-notched and having a central 5 mm drilled hole, with various failure modes. The low velocity impact tests were followed by CAI tests, meant to evaluate residual mechanical performance and damage tolerance. Lockin thermography was used for prior assessment of damage.

Introduction

Hybrid composites or fibre-metal laminates (FML) were developed decades ago, the most common being those created at the University of Delft under the name of GLARE and ARALL, consisting of alternating FRP and Al layers. Improved behaviour under various loads was expected and indeed recorded in a number of applications, especially in aeronautical structures.

Mechanical behaviour of this special type of composites was reported a number of published papers [1,2,3,4,5], covering a wide range of aspects in the field. As mentioned in a comprehensive overview [6], behaviour under certain loading conditions has to be still investigated in order to prevent in service damage and/or evaluate structural reliability when using such composites in a variety of lay-up architectures and material combinations. The methods used in the evaluation of the structural integrity of these materials and results obtained were reviewed in [7], the literature on this important aspect, highly needed for keeping a good in-service reliability of hybrid composites used in sensitive structures, being quite scarce.

The research work presented in this paper was aimed to evaluate the properties of hybrid composites made of pure aluminium sheets alternating GFRP and CFRP layers, as the efficiency of IRT for assessing the damage produced after invasive loading. The composites were intended to be used for parts undergoing impact events, but a broader property assessment was finally performed.

Behaviour under static and fatigue loading

The static and fatigue tensile tests were made on parallel specimens, un-notched and having a central 5 mm drilled hole. All specimens were made of five layers, three, including the external ones, made of pure Al and two of GFRP and CFRP. The Al layers had 0.35 mm and 0.5 mm averaged thickness. The interleafing GFRP were made of epoxy resin reinforced with satin type glass fibre fabrics, each layer having 0.3 mm averaged thickness. The interleafing CFRP were made of epoxy resin reinforced with plain weave carbon fibre fabrics with 200g/m^2 and 300g/m^2, each layer having 0.35 mm averaged thickness in the first case and 0.4 mm averaged thickness in the second case. The thickness of the wet moulded FRP layers was bigger than in an all polymeric composite, as part of the epoxy matrix had the role of bonding layer with the Al layers.

The UTS values for the components and the hybrid composites are mentioned in Table 1 and Table 2. The numbers correspond to recorded maximum values on the stress/strain curve, and the machine was programmed to stop after an over 20 % drop of the tensile force. In some cases, this meant a breaking failure, in others, irreversible damaging of the material. In fact, the braking failure was observed only in the Al sheets in FML samples. For un-notched specimens, it happened when the ratio of UTS values of the two components was too high, as it is the case for Al/CFRP (Fig. 1, bottom). The Al/GFRP un-notched samples failed due to yielding of the Al sheets, the phenomenon being completed by delamination and severe buckling at sudden unloading (Fig. 1, top). The notched samples failed due to cracks propagating from the central hole in the Al sheets (Fig. 2).

Table 1. Failure values of the components used for the hybrid composites.

Material	Al		GFRP		CFRP (reinforced with 200 g/m^2 fabric)		CFRP (reinforced with 300 g/m^2 fabric)	
Sample type	Un-notched	Notched	Un-notched	Notched	Un-notched	Notched	Un-notched	Notched
UTS [MPa]	96	85	172	133	454	302	547	351

Table 2. Failure values of the hybrid composites.

Material	Al/GFRP		Al/CFRP (thin plates)		Al/CFRP (thick plates)	
Sample type	Un-notched	Notched	Un-notched	Notched	Un-notched	Notched
UTS [MPa]	132	108	166	109	200	190

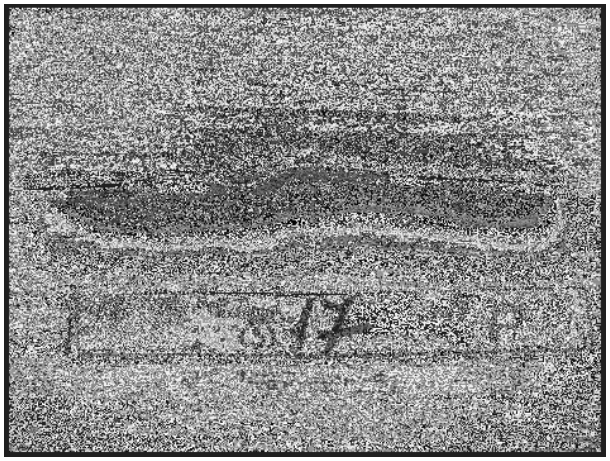

Fig. 1. Failed un-notched FML samples; top – Al/GFRP, bottom – Al/CFRP.

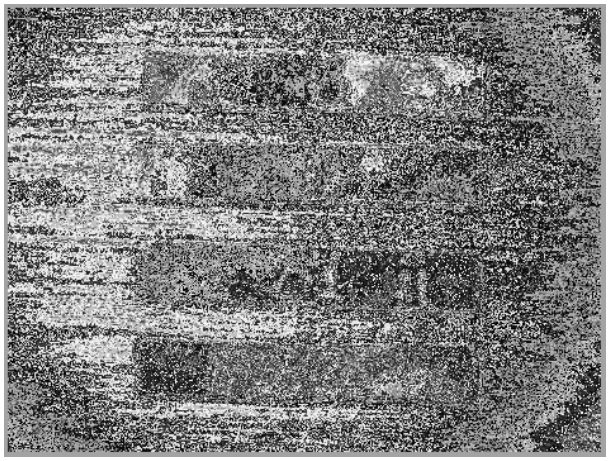

Fig. 2. Failed notched FML samples.

Concerning the reduction in strength produced by the presence of a notch, there are two aspects to retain:

1. The reduction is less severe when the high plasticity of Al sheets, obviously favourable to lower notch sensitivity, is supported by a low stiffness of the FRP material – see Al/GFRP;
2. *The reduction of notch sensitivity is boosted by the increase of Al volume fraction* – see Al/CFRP, thick plates; for such materials, the failure of notched samples was produced in a similar way as observed for un-notched Al/GFRP, with less severe buckling of the Al sheets when unloading, due to the stiffer CFRP sheets (Fig. 3).

As it was observed in [6], it is difficult to predict tensile failure by simply using the Al volume fraction, proposed in [8], due to the generally long excursion in the plastic behaviour domain of that metal, in any forms. A FEM approach could lead to more realistic results, for that reason a static nonlinear analysis, with large displacements and a bilinear model with Bauschinger effect for the Al sheets, was performed with ANSYS, for an un-notched Al/GFRP sample.

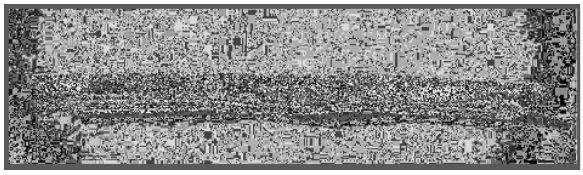

Fig. 3. Failed notched Al/CFRP specimen, thick plate.

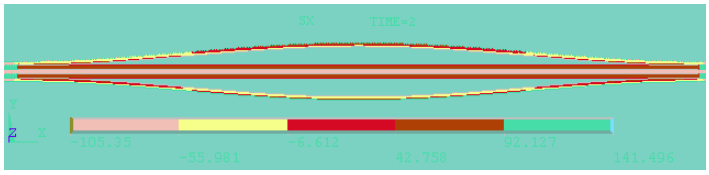

Fig. 4. Deformed model of an Al/GFRP un-notched specimen, static nonlinear analysis.

The mechanical characteristics used in the FE model followed closely the real ones, for Al being considered the yield point at 90 MPa and a 700 MPa modulus of plasticity. The loading was driven to 150 MPa stress limit in 10 steps, and equally 10 steps for unloading. For putting in evidence the buckling, it was used a slight perturbation, created by a lateral pressure of 0,002 MPa.

The fatigue tests were performed on notched specimens, using an Amsler vibrophore. The zero-to-peak cycles, topping 0.4 UTS, in average, were applied at around 80 Hz working frequency. In most of the cases, for all types of FML samples, the Al sheets only presented transverse cracks at the limit of low cycle fatigue range (~ 10^5 cycles) as can be seen in figure 5, the top force dropping to approx. 60% of the initial value. From that moment, the samples, in which only the two FRP layers were still working, deeply entered in the high cycle fatigue domain. Tests performed in similar conditions on samples with 5 layers of FRP ended quickly (< 5×10^4 cycles), due to excessive heating of the material.

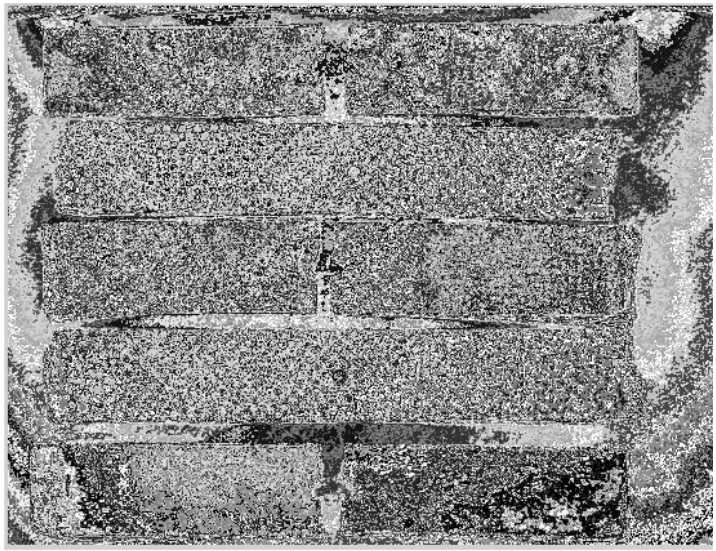

Fig. 5. State of layers in an Al/CFRP notched sample loaded in high cycle fatigue range.

Behaviour at low velocity impact

Low velocity impact was produced with a modified Charpy hammer, at 5 J, 10 J and 15 J, on all three types of FRM material and on 5 layer GFRP and CFRP material. The impact tests were made on 100 × 150 mm samples, clamped on all sides, and was followed by CAI tests. The damages produced in FML ranged from bumps with various amplitudes (Fig. 6) to almost penetration (Fig. 7). At visual inspection, GFRP samples behaved better than CFRP samples.

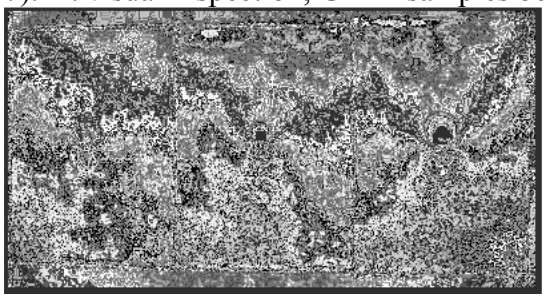

Fig. 6. Al/CFRP thick plate samples impacted with 5J, 10 J and 15 J energy.

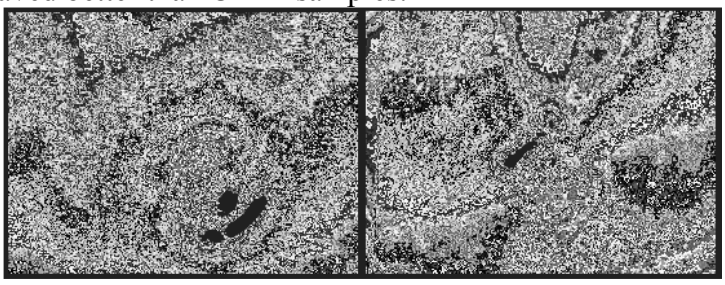

Fig. 7. Al/CFRP thin plate sample impacted with 15 J energy; top face (left) and bottom face (right).

The CAI tests revealed that the residual compression strength for all FML samples was more or less constant, the failure occurring on the top edge, in the form of edge delamination and kinking. On the reverse, the same property droped significantly with the impact energy for the FRP samples.

Structural integrity assessment with Lockin thermography

The inspection was made using a Flir A 40 M camera and a Lockin inspection package – lamps + software, with harmonic approximation analysis. Adequate setting had to be made for the FRP impacted samples and the FML ones, due to the quite different thermal behaviour of the two materials. For FML samples, a higher frequency had to be combined with a black painting of the exposed face. Some results, with the mention of the set parameters, are presented in figures 8 and 9.

Fig. 8. Lockin inspection of CFRP sample impacted at 15 J (period: 20 s; number of periods: 4; camera frequency: 50 Hz).

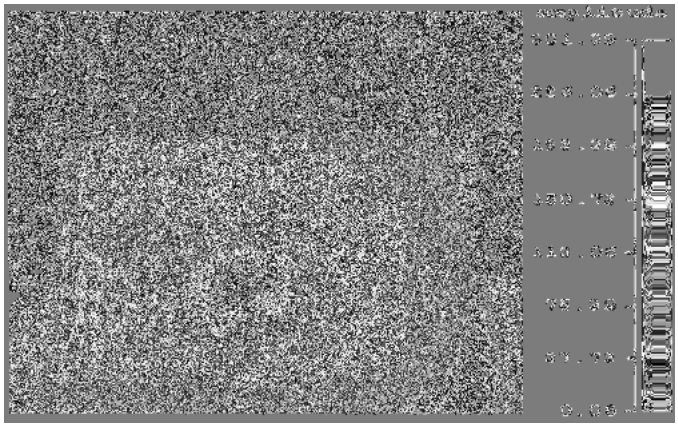

Fig. 9. Lockin inspection of thick Al/CFRP sample impacted at 15 J (period: 10 s; number of periods: 4; camera frequency: 50 Hz).

The damage produced by the 15 J impact on the CFRP sample is more localized and severe, explaining so the important drop in residual compressive strength for this type of material.

Conclusions

The research work performed so far and the results presented here indicate that the use of pure Al in FML assures a lower notch and impact sensitivity for the material *when the metal volume ratio exceeds 60 %*. The price consists in a considerable lower tensile and compressive strength, compared with the properties of the embedded FRPs. *Behaviour at high frequency pulsating fatigue is remarkably over that of the same reference materials, irrespective of the presence of notches*.

Acknowledgment: The research work was financed by Sure2Grip CRAFT project, run in FP6 programme under COOP-CT-2004-513266 contract, and DALEISC project, run in CEEX M4 programme of A.N.C.S., under 252/10.08.2006 contract.

References

[1] A. Vlot, E. Kroon and G.L. Rocca: Key Eng. Mater., Vol. 141-143(1998), p. 235.
[2] J.J. Homan: Report B2v-98-11, Delft University of Technology, December (1998).
[3] R. K. Govindan Potti, B. Nageswararao and V.K. Srivastava: Adv. Comp. Mater., Vol. 9, No. 3 (2000), p. 187.
[4] M. Hangenbeek et al.: Appl. Comp. Mater., Vol. 10 (2003), p. 207.
[5] R.C. Alderliesten et al.: Appl. Comp. Mater., Vol. 10 (2003), p. 223.
[6] G. Wu and J.-M. Yang: JOM, Vol. 57, No. 1 (2005), p. 72.
[7] A. Fahr et al.: Polymer Comp., Vol. 21 (2000), p. 568.
[8] H.F. Wu: J. of Mater. Sci., Vol. 29 (1994), p. 4583.

Key Engineering Materials Vols. 385-387 (2008) pp 489-492
© (2008) Trans Tech Publications, Switzerland
doi:10.4028/www.scientific.net/KEM.385-387.489

Experimental Investigation on Fracture and Tensile Characteristics of Micro-surfacing Containing Crumb Rubber

CHEN Zheng[1, a], WU Shaopeng[1, b], ZHANG Tao[1, c], PANG Ling[1, d]

[1] Key Laboratory of Silicate Materials Science and Engineering of Ministry of Education

Wuhan University of Technology, Wuhan 430070, Hubei, P.R China

[a]chenz@whut.edu.cn, [b]wusp@whut.edu.cn, [c]370218zt@163.com, [d]lingpang@whut.edu.cn

Keywords: fracture, tensile, Micro-surfacing, crumb rubber

Abstract: The major objective of this research was to evaluate the tensile and fracture properties of micro-surfacing, which as a preventive maintenance surface treatment on asphalt pavement, that formed the basis for the ISSA recommendation of an optimum micro-surfacing design incorporating crumb rubber. The research involved a full-factorial experiment with different rubber contents (0, 2 and 5%) and different polymer modified asphalt emulsion contents ranged from 10 to 13% by total weight of crushed aggregate in micro-surfacing. Fracture and indirect tension tests were performed on micro-surfacing beams and Marshall test samples, respectively, at two different test temperatures of 25 and -10°C. The variables studied were indirect tensile strength, peak center-point load carried, and load-point displacement. The results show that higher mean values of indirect tensile strength were obtained corresponding to the highest modified asphalt emulsion content (13%), irrespective of rubber contents, particularly at lower temperatures. A statistical analysis of the test results reveals that there are no significant differences among the means of most of the variables studied corresponding to different rubber contents. However, the differences are significant for different asphalt emulsion contents.

1. Introduction

In accordance with the statistic data in China, 80 million scrap tires were produced in 2002, and with 12% of growth rate every year, the total number of abandoned tires will be expected to reach 120 million in 2005 and 200 million in 2010 [1]. How to deal with the huge number of waste tires has become an urgent problem of environment. The disposal of waste tires in the world primarily has three ways to deal with such as landfill, burning and recycling. Recycled tire rubber applied to pavement may be the best way to reduce waste tires in large quantities and, at the same time, improve some engineering properties of asphalt mixtures. Crumb rubber can be incorporate by a wet process or dry process. Wet process refers to modification of asphalt cement binder with 5–25wt% of fine tire rubber crumb modifier (CRM) at an elevated temperature. The dry process includes mixing the rubber particles with aggregates prior to addition to asphalt. The main differences between the two processes consist in rubber particle size, rubber amount, rubber function, and incorporation facility [2].

As a preventive maintenance surface treatment on asphalt pavement, micro-surfacing is a mixture of polymer-modified asphalt emulsion, mineral aggregate, mineral filler, water, and other additives, properly proportioned and mixed. It has a liquid consistency, and spread over a prepared surface can be used as a sealant layer that waterproofs the area, acting as a renovating agent or an antiskid layer for the paving [3].

The objective of this project was to study the fracture and tensile properties of crumb rubber modified micro-surfacing mixtures using dry process to formulate an optimum mixture design. The mixture variables studied include binder content and rubber contents. The response parameters were the maximum load carried, LPD obtained in the fracture test, and the indirect tensile strength in the indirect tension test. The results were compared and analyzed statistically.

2. Test materials

Crushed basalts were used for coarse aggregate and fine aggregate. Table 1 showed the values of aggregate tests. And Table 2 showed the values of tests performed on modified asphalt emulsion and its residue. Specifications of aggregates and asphalt emulsion for micro-surfacing were normalized according to the International Slurry Surfacing Association (ISSA) Guidelines A143. Mineral filler was any recognized brand of non-air entrained Portland cement that was free from lumps. The recycled tires rubber was free of wire and fabric. The rubber particle size was 80 meshes.

Table 1 Values of the tests performed on the aggregates

Properties	Results	Specifications
Sand equivalent, %	78.5	Min. 65%
Soundness, %	5.6	Max. 15%
Los Angeles abrasion, %	17.8	Max. 30%

Table 2 Values of the modified asphalt emulsion tests

Properties	Results	Specifications
Settlement, %	1.5	Max. 5%
Particle charge	Positive	-
Residue by distillation, %	63.7	Min. 62%
Softening point, °C	65	Min. 57°C
Penetration (25°C), 0.1mm	58	40~90

The appropriate percentages of these materials incorporated in the mix were blended in an appropriate gradation to satisfy the grading requirements for gradation III recommended by International Slurry Surfacing Association (ISSA) to restore the paving surface layer. The gradation of the combined aggregates was listed in Table 3.

Table 3 Gradation of the combined aggregates

Sieve size (mm)	9.5	4.75	2.36	1.18	0.6	0.3	0.15	0.075
Scope	100	90~70	70~45	50~28	34~19	25~12	18~7	15~5
Gradation	100	77.6	57.4	42.4	30.3	21.2	11.8	7.1

3. Experimental program

The experimental program was divided into two parts: (1) Fracture tests on beam specimens and (2) indirect tension tests on Marshall test specimens. A full-factorial experiment was used with three different rubber contents (0, 2 and 5%), and three different modified asphalt emulsion contents (10, 11, and 13%). Two test temperatures, 25 and -10°C, were selected to represent the average and low in-service pavement temperature conditions. Marshall test samples of 101.6 mm diameter and approximately 63.5 mm height, and beams of (35±2) mm height × (30±2) mm wide × (250±2) mm length were fabricated. Fracture tests were conducted with a servohydraulic closed-loop testing machine, and indirect tension tests were performed on the Marshall test samples with diametral loading on a universal testing machine. Besides the rate of loading for the indirect tension tests was 1 mm/min at -10°C, the rates of loading for other tests were taken as 50 mm/min following the recommendations [4].

4. Results and discussions

4.1 Fracture test

Fig.1 and 2 illustrated the results for the peak center-point loads carried and LPDs at both -10 and 25°C, respectively. The values shown were the mean of two test results. Excellent agreements were observed for the results of tests on replicates.

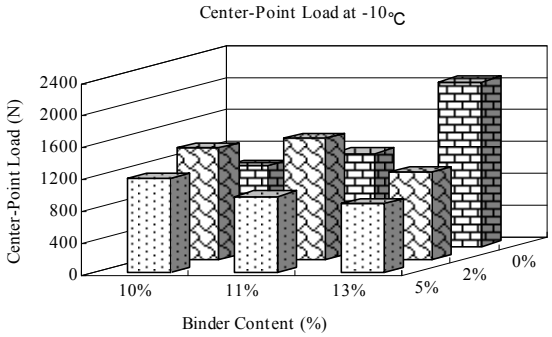

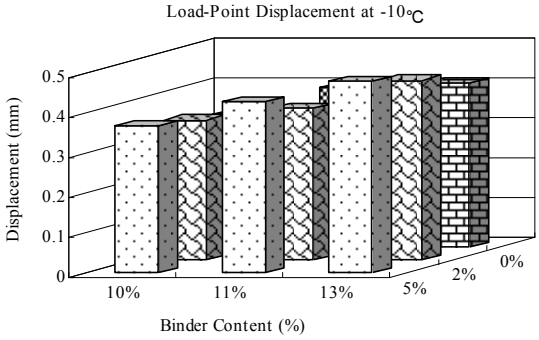

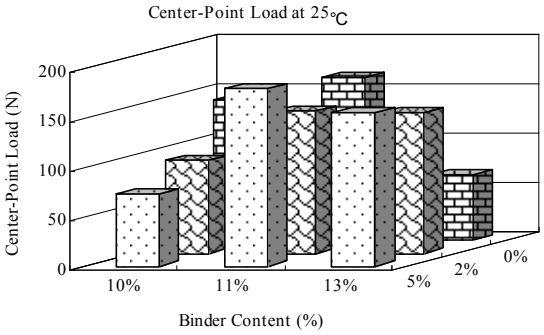

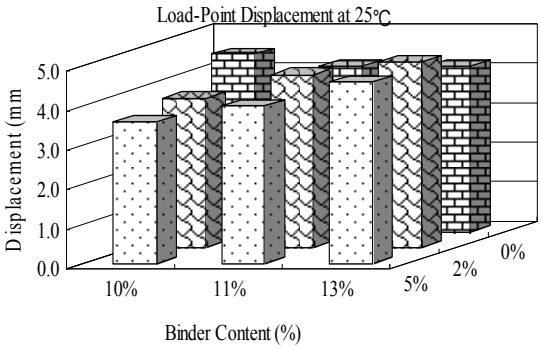

Fig.1 Peak Center-Point Loads at -10 and 25°C

Fig.2 Center-Point Displacements at -10 and 25°C

At 25°C, the highest center-point load were obtained for 11% modified asphalt emulsion content. At this temperature, modified asphalt emulsion content was the only significant factor affecting the LPD of micro-surfacing mixtures. Results of the statistical analysis also showed that there were no significant differences between the mean values of center-point load at 11 and 13% modified asphalt emulsion contents, but significant differences exist between 10 and 13%. And the LPD corresponding to 13% modified asphalt emulsion content was the highest. This showed that at an average service temperature, micro-surfacing mixtures with more modified asphalt emulsion content should be able to withstand more deformation before failure. At -10°C, the results showed that there were no significant differences in the mean values of center-point loads and LPDs for different binder contents. However, 2% rubber tended to produce the highest mean peak center-point load, and 0% rubber produced the lowest displacement before failure; although rubber content was not statistically significant for either the peak center-point loads carried or the resulting LPDs of the micro-surfacing samples.

4.2 Indirect tensile test

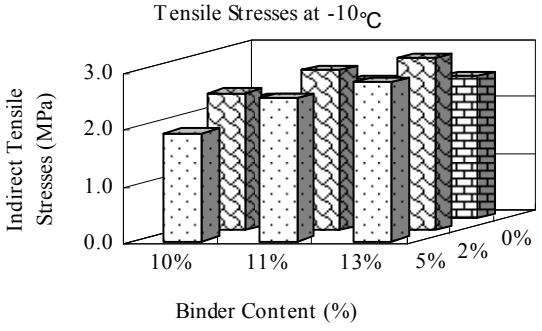

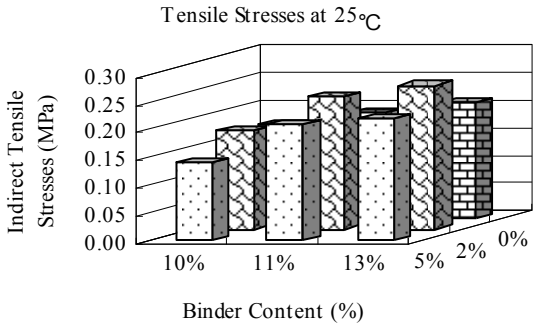

Fig.3 Indirect Tensile Strengths at -10 and 25°C

Fig.3 illustrated the results for the indirect tensile strengths at both -10 and 25°C, respectively. The indirect tensile strengths of the micro-surfacing samples increased with the increase in modified asphalt emulsion content at either -10 or 25°C. Micro-surfacing samples with a 13% modified asphalt emulsion content showed the highest tensile strength. However, 2% rubber tended to produce the highest mean indirect tensile strength values, and neither the modified asphalt

emulsion content nor the test temperature was found to affect the trend significantly.

5. Conclusions

Results of this study show that at average temperatures (25°C), micro-surfacing mixtures with more asphalt emulsion content should be able to withstand more deformation. Statistical analysis shows that except for the LPD, there are no significant differences in peak center-point loads carried for all three rubber contents. At a low temperature (-10°C), there are no significant differences in the center-point loads carried by the micro-surfacing mixtures corresponding to different binder contents. However, the rubber contents did not appear to affect this outcome.

At a low temperature (-10°C), micro-surfacing with higher asphalt emulsion contents showed higher indirect tensile strengths, irrespective of the rubber content. And 2% rubber tended to produce the highest indirect tensile strengths, and the asphalt emulsion content was not found to affect the trend significantly. These were also observed for the indirect tensile strength values at the average service temperature (25°C).

References

[1]. Jiang Zhi-Yun: *The Status and Development of Waste Tire Resources Recycling in China*. Chinaire Resource Recycling, 2005. p. 6–8 [in Chinese].

[2]. Roberts FL, Kandhal PS, Brown ER, Dunning RL: *Investigation and Evaluation of Ground Tire Rubber in Hot Mix Asphalt*. NCAT Report No. 83-3.

[3]. *Recommended Performance Guidelines for Micro-Surfacing,* International Slurry Surfacing Association (ISSA), A143 (revised), May 2005.

[4]. Ministry of Communications of P.R.China: *Standard Test Methods of Bitumen and Bituminous Mixtures for Highway Engineering*, People's Communication Press, Beijing, 2000.

Key Engineering Materials Vols. 385-387 (2008) pp 493-496
© (2008) Trans Tech Publications, Switzerland
doi:10.4028/www.scientific.net/KEM.385-387.493

Influences of Aging History on Low Temperature Performance of Asphalt Concrete

Wu, S. P[1, a], ZHu, G. J[2, b,] Pang, L[3, c], Liu, C.H[4, d]

[1]Key Laboratory of Silicate Materials Science and Engineering of Ministry of Education, Wuhan University of Technology, Wuhan, Hubei 430070, China

[2]Key Laboratory of Silicate Materials Science and Engineering of Ministry of Education, Wuhan University of Technology, Wuhan, Hubei 430070, China

[3]Key Laboratory of Silicate Materials Science and Engineering of Ministry of Education, Wuhan University of Technology, Wuhan, Hubei 430070, China

[4]Key Laboratory of Silicate Materials Science and Engineering of Ministry of Education, Wuhan University of Technology, Wuhan, Hubei 430070, China

[a]wusp@wuht.edu.cn, [b]guojunzhu@whut.edu.cn, [c]lingpang@whut.edu.cn ,[d]chlaw@whut.edu.cn

Keywords: SMA; low temperature performance; three-point bending; aging

Abstract: According to three-point bending test, this paper explores the influence of low temperature on the flexural strength, the tensile strain and bending stiffness modulus of the aged Stone Mastic Asphalt (SMA-13) concrete. The asphalt mixtures are aged according to the short-term aging (at 135°C, 4 hours), and long-term aging (asphalt concrete at 85°C, 120 hours) and natural aging (3 months, 6 months and 9 months). The result shows that, with the same loading rate, the tensile strain of specimens at -30°C are smaller than those at -10°C; but when temperature is certain, the tensile strain of specimens lager than those of aged specimens. The longer the aging time lasts, the more flexural strength differences between high and low temperatures can be found. A pretty well index variation can be found between the tensile strain and temperature. The same trend also appears between the bending stiffness modulus and temperature of SMA-13 asphalt concrete.

Introduction

Stone mastic asphalt (SMA)pavement is featured with gap gradation with much coarse aggregate, litter fine aggregate, much breeze as well as asphalt. SMA structure has aroused wide interest of many countries owing to its good stability at a high temperature, durability and surface [1-2]. Influenced by light, heat, oxygen and water, as cementing material, asphalt keeps aging in the process of long-term use so that the performance of SMA pavement becomes increasingly poorer. Especially at low temperature, temperature exerts greater impact on the flexural strength and tensile strain of asphalt mixtures. Focused on flexural property at extremely low temperature, this paper is intended to conduct beam bending experiment on SMA-13 asphalt concrete at -10°C and -30°C respectively, to analyze regularities of impacts of low temperature and aging time on SMA-13 asphalt concrete, and in the meanwhile to make a comparison of the bending strain energy of SMA-13 beam specimens at two different low temperatures.

Experimental works

Materials. Modified asphalt (Penetration is 55; Softening point is 83°C; Ductility (cm) is 32 (5°C); Viscosity (Pa.s) is 2.27 (135°C) from Ezhou Koch co.ltd, Hubei Province, the limestone breeze made by Jinzhou in Hubei Province and polyester fiber provided by Wuhan Tianhui Fiber co.ltd in Hubei province. Technical norms of this experiment are shown by the following Table 1 and 2.

Table.1 Properties of polyester fiber

Color	Average length /mm	Average diameter /mm	Specific gravity g/cm^3	Melting point /°C	Burning point/°C	Tensile strength / Mpa
White	6	0.02	1.32~1.40	248	538	520

Table.2 The gradation of SMA-13asphalt concrete

Particle size / mm	16	13.2	9.5	4.75	2.36	1.18	0.6	0.3	0.15	0.075	asphalt	fiber
Passage rate / %	100	94.1	64	27.7	18.3	16.4	14.3	13.3	12.5	10.5	6.1	0.25

Experimental plan. Firstly, mix asphalt and aggregate at 175°C for 90 seconds (referring to 1995 American AASHTO PP2-1994 norms), then place the loose asphalt mixture in the dryer at 135°C and heat it for 4 hours under the condition of forced ventilation. Later, stir it once every hour, which is the short-term aging of asphalt mixture. Then place the short-term aged loose asphalt mixture in the dryer at 85°C and heat it for 120 hours successively. Finally, cool it naturally for over 16 hours. Natural aging comes into being after short-term aging. Place the asphalt mixture outdoors and age naturally for three, six or nine months.

The selected equipment is UTM-25 test machine system. Specimens are prism-shaped beams with the standard size being (250±2.0) mm × (30±2.0) mm × (35±2.0) mm and the span being 200 ± 0.5mm in JTJ052-2000. Before the experiment, put the cut beam in the environment box for over four hours. The experimental temperatures are -10°C and -30°C. The way of loading is constant strain loading and the loading rate is 50mm/min. In the process of this experiment, when the flexural strength reaches the maximum, specimens can be regarded. If the load is further added, tensile strain would decrease. By Acc specimen size, flexural strength R_B, tensile strain ε_B and the bending stiffness modulus S_B [3-4] can be obtained respectively when the beam is damaged.

Results and Discussion

The influence of temperature, aging time on flexural strength when damaging. Fig.1 and Fig.2 demonstrate regularities of changes in flexural strengths of damaged beam in the process of the test at -10°Cand -30°C when indoor simulate aging and outdoor natural aging are happening. From the Figures, corresponding flexural strengths of two ways of aging both have a tendency to increase at first and decrease later with an increase in aging time. At low temperature, there is a relatively slow tendency to decrease. Besides, corresponding flexural strengths of two different temperatures are close. While within the range of temperature, aging time has salient impacts on aging degree with an increase in short-term aging degree first and then the flexural strength decreases with aging time increasing By comparison, changes in flexural strength are more salient with aging time at -30°C than those at -10°C. At the same aging degree, the flexural strength at -30°C is larger than that at -10°C.

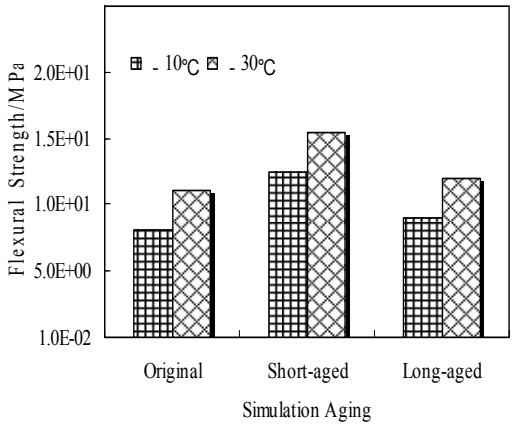

Fig.1 Flexural strength of simulation aging specimens

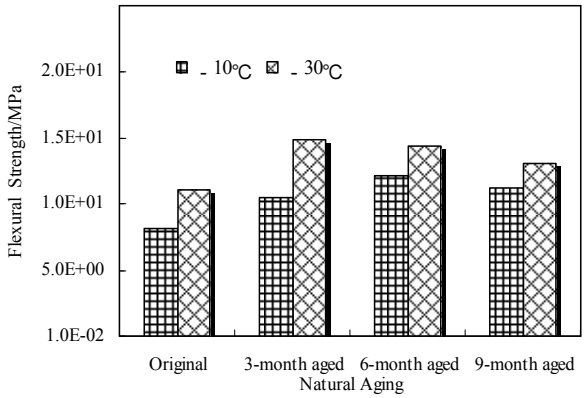

Fig.2 Flexural strength of natural aging specimens

The influence of temperature, aging time on tensile strain when damaging. Fig.3 and Fig.4 illustrate the variation law of loaded tensile strain as aging time changing. Under the condition of aging time, It also shows that, in the same aging degree, the tensile train at -10°C is larger than that at -30°C. At the same temperature, the tensile strain at -10°C is 1.9~2.5 times as that at -30°C. The decrease of tensile strain of specimens under aging condition is probably related with the asphalt aging. In the aging environment, the viscous decline and elasticity increase of asphalt; the brittleness increases under the condition of low temperature; with the outside loading, its loading capacity is quite limited; and what's more, the anti-flexural strength and the shear performance is comparatively poor. The asphalt fractures as a result of its aging and the decline in cohesive fore of stone materials. The damaged tensile strain also has a tendency of decline after aging.

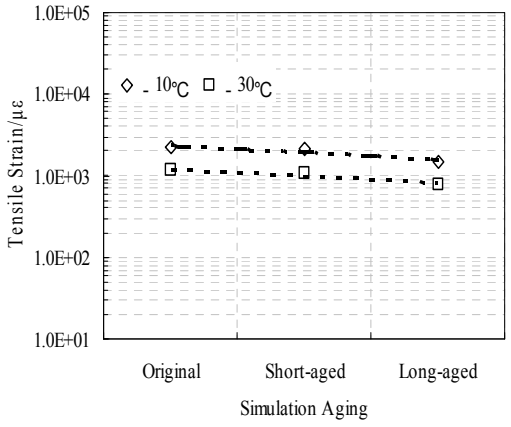

Fig.3Flexural strain of simulation aging specimens

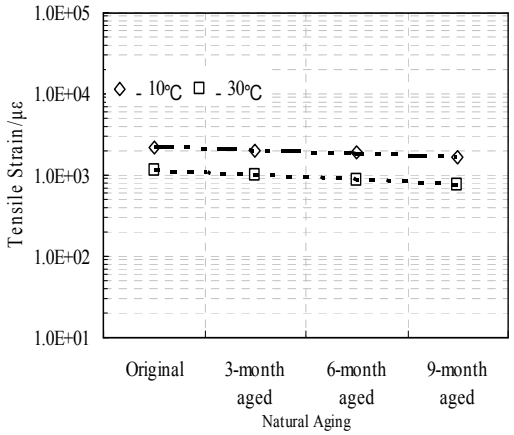

Fig.4 Flexural strain of natural aging specimens

The influence of temperature and aging time on bending stiffness modulus. Fig.5 and Fig.6 demonstrates the bending stiffness modulus - aging time curves corresponding with two aging

models. The bending stiffness modulus of aged one is bigger than those without aging. The curves show there is an obvious index variation between the bending stiffness modulus and aging period. The index b in the regression equation

$$S=a\times e^{bt} \tag{1}$$

in two aging models and two temperatures is between 0.15 and 0.3. The bending stiffness modulus of these two different aging models has a similar variation tendency towards temperature.

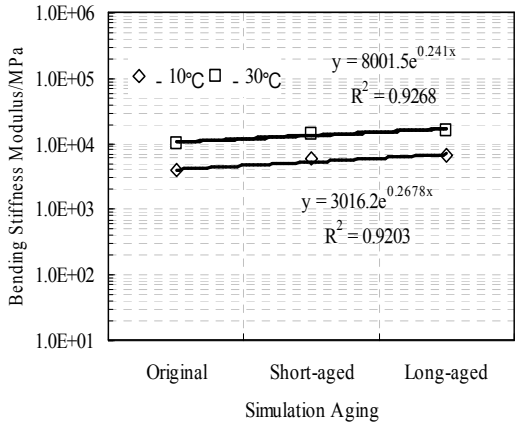

Fig.5 Bending stiffness modulus of simulation aging specimens

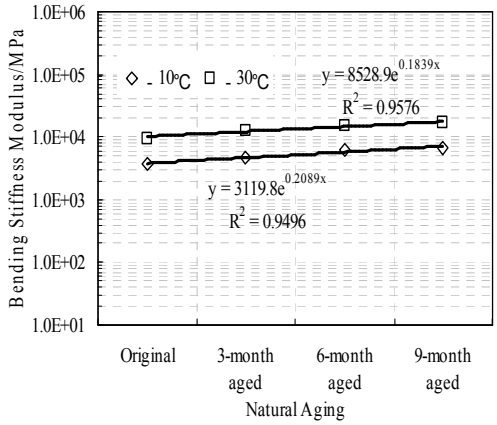

Fig.6 Bending stiffness modulus of natural aging specimens

Summary

The longer the aging time lasts, the largerer the decrease extent is. In the same aging period, the flexural strength at -30°C is stronger than that at -10°C. With the same loading rate, the peak appears both in these two aging models. There is a good index variation between the tensile strain of SMA-13 asphalt mixture and temperature in these two aging models. In the same aging environment, the tensile strain at -30°C is smaller than that at -10°C. The variation tendency between bending stiffness modulus of those two aging models and aging time is almost the same.

References

[1] Shen. JA. Modified Asphalt and SMA Pavement [M]. Beijing: China Communications Press, 1999.260-265

[2] Huang. XM, Wu. SP, Zhao. YL. Asphalt and Asphalt Mixtures [M].Nanjing: Southeast University Press, 2002. 7

[3] JTJ052-2000, Standard Test Methods of Bitumen and Bituminous Mixtures for Highway Engineering[S]

[4] XUE LI. Investigation of the fracture resistance of asphalt mixtures at low temperatures with a semi circular bend (SBC) test [D]. 2005, 8: 43-44.

Key Engineering Materials Vols. 385-387 (2008) pp 497-500
© (2008) Trans Tech Publications, Switzerland
doi:10.4028/www.scientific.net/KEM.385-387.497

Preparation of amido modified silicone in microemulsion

Liu jiesheng[1], a, Huang shiqiang[2], b, Wu shaopeng[3], c

1. Key Laboratory of Silicate Materials Science and Engineering of Ministry of Education, Wuhan University of Technology, Wuhan 430070, China,

2. Faculty of Material Science and Engineering, Hubei University, Key Laboratory of Polymer Materials, Wuhan 430062, China,

3. Key Laboratory of Silicate Materials Science and Engineering of Ministry of Education, Wuhan University of Technology, Wuhan 430070, China,

[a]wsljs628@yahoo.com, [b]huangsq@hubu.edu.cn, [c]wusp@mail.whut.edu.cn

Abstract: A translucent amido modified microemulsion was synthesized by the adding of amido silane coupling agent. Transmission electron microscope (TEM), Fourier Transform Infrared Spectra (FT-IR), Photon Correlation Spectroscopy (PCS) were used to characterize the structures and properties of amido microemulsion, respectively. IR spectroscopy confirmed that amido group was successfully introduced into the polysiloxane microemulsion. TEM images indicated that the granules agglomerated heavily when the coupling agent was in a larger content. The effects of PH values, amount of coupling agent on the size and the configuration of the amido microemulsion were investigated. The results indicated that the properties of amido microemulsion were stable when the microemulsion was under weak acid condition (pH=3-7). When the amount of coupling agent increased, the particles size of microemulsion increased and the particle size distribution became narrow.

Key words: polysiloxane ring-opening modified microemulsion amido

1 Introduction

Amido functional polymers play an important part in the textile finishing, cosmetic and leather fields. It mainly exists as the form of emulsion, which consists of oil, water and surfactant and haves particles size of hundreds nanometers.

For the past few years, microemulsions are more and more widely researched due to the smaller particle size than that in emulsions. Microemulsions consist of oil, water, surfactant and coemulsifier, have a particle size of less than 140nm, preferably less than 100nm, and visually appear translucent to transparent [1]. It is well known that certain physical and mechanical properties of material considerably change as their grain size is reduced [2]. In microemulsion polymerization, the kinetics and mechanism have been studied extensively. As reported in the previous researches, the mechanism of microemulsions mainly ranged over radical polymerization initiated by initiator [3, 4].

In this paper, it pertains to a method for producing aminosiloxane microemulsion wherein said method comprises the emulsion polymerization of a mixture comprising cyclosiloxanes and an aminosilane coupling agent, basing on the reaction mechanism of condensation of active centers. Series of amido functional polysiloxane microemulsions were prepared by the grafting of amido modifier onto polysiloxanes without coemulsifier

2 Experimental

2.1Materials

Octamethylcyclotetrasiloxane (D_4), purchased from Xinghuo organicsilicone Plant in China; distilled; used to obtained silicone polymer by the ring opening polymerization; mp 16-19°C; b.p.

175°C/760mmHg; n_D^{20} 1.3960; d_4^{20} 0.955. A nonionic surfactant, (OP-10), used without any further purification, >95%; pH=5.0~7.0. Dodecyl benzenesulfonic acid, ($C_{12}H_25C_6H_4SO_3$) purchased from Henan province in China, industrial material; pH=0.4; mp 16.3°C; bp 286°C/760mmHg. Water was distilled and deionized before using, pH=5.0~7.0; electrical conductivity≤0.5μs/cm (25°C); 2MΩ. Amido silane coupling agent, ($C_8H_{22}N_2O_3Si$), commercial grade, ≥98.0%; d_4^{20} 0.955-0.975; used as modifier of silicone polymer.

2.2 Preparation of amino modified silicone microemulsion

Catalyst, non-ionic emulsifier and distilled water were filled into a four-neck round bottom flask, which was equipped with condenser pipe, thermometer, Nitrogen gas inlet, and stirrer system. D_4 monomer was dropped into the flask and heated to 80°C. The ring opening of D_4 reacted for hours, and the flask was purged with nitrogen. Buffer solution was added into the flask to adjust pH values of the aqueous medium. Then, the amino silane coupling agent was dropped into four-neck round bottom flask when the emulsion appears blue. The polymerization was continued thereafter in batch for 4 hours and the amido microemulisons formed.

2.3 Identification and characterization methods

IR Spectra was recorded on an M-80 SPECORD spectrophotometer using KBr tablets. The particle size and size distribution were characterized by PCS, which was made in Malvern Company in U.K. The particle configuration was exhibited by TEM, made in Japan. UV-visible Spectrophotometer, made in perkin-Elmer in USA, showed the transparency of silicone microemulsions. The pH values were exhibited by acidometer, made in China. Mechanical stability and chemical stability of the final latexes were studied. Mechanical and storage stabilities were determined at room temperature with a high speed (3000rpm) stirrer for 30 minutes. Chemical stabilities were determined at the conditions of alkaline and Ca^{2+} solutions for 48 hours.

3 Results and discussion

3.1 IR analysis of product

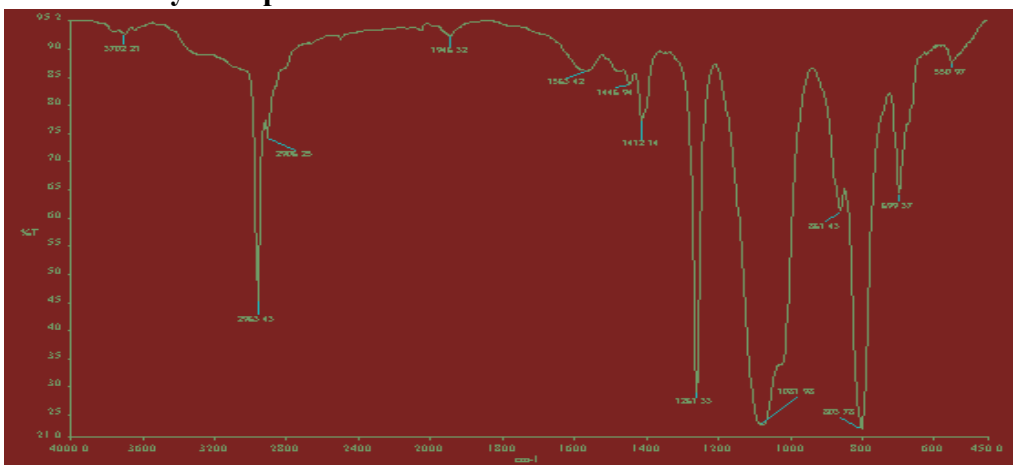

Fig.1 IR spectra of the amido modified polysiloxane polymer

The results of infrared transmittance of multipolymer were shown in Fig 1. The band at 1081.98 cm^{-1} is believed to correspond to Si-O species. The band at 3702.21 cm^{-1} is only associated with Si-OH species. A weak band centered at 1563.42 cm^{-1} was detected obviously, which indicated that the amino group was successfully introduced into the polysiloxane.

3.2 The effect of pH values on the amido modified microemulsion

Table 1 the effect of pH on the amido modified microemulsion

pH range	pH=0.5-2.0	pH=2.0-3.0	pH=3.5-4.5	pH=4.5-5.0
stability of amido microemulsion	unstable	unstable	stable	stable
appearance of amido polisiloxane microemulsion	layered	layered	opaque	semitransparent

By carefully controlling the pH values, a series of the amido modified microemulsions are obtained. The stability and the appearance of the amido microemulsions with different pH ranges are discussed after 48 hours of the formation of the microemulsions. As shown in Table 1, amido polysiloxane microemulsions were stable when the microemulsions formed at the weak acid conditions (pH=3.0-7.0), and the microemulsions exhibited semitransparent. It is possible that the hydrolysis and condensation rate of the polymerization are pH-dependent. At the strong acid conditions, the rate of hydrolysis and condensation of coupling agent became faster, more active centers of coupling agent are produced in a shorter time. As the pH values decreased, the active centers of amido coupling agents are more easily to self-condense and are less condensed with active silicone polymer, which caused the microemulsions to present two phases and showed unstable properties.

3.3 The effect of the amount of amido silane coupling agent on the microemulsion

Table 3 the effect of the amounts of the silane coupling agent on the particle size and size distribution

wt% amido silane coupling agent	0.2	0.5	1.0	1.5
particle size (nm)	47.83	53.14	62.14	66.63
size distribution index	0.618	0.605	0.584	0.472

An increase of amount of the amido silane coupling agent leads to an increase of the particle sizes and a decrease of the particle size distribution index as shown in Table 3. When the coupling agent was dropped into the polysiloxane, there were two main types of reactions in the microemulsion: self-condensation of coupling agent, reaction between coupling agent and active polysiloxane. As the amount of amido silane coupling agent increase, more cross linking between amido coupling agent and polysiloxane happen, and the particle size grows. On the other hand, amido coupling agents are inclined to be self-condensed because of their good hydrolysable property. The proportion of self-condensation rises with the increase of the amount of amido silane coupling agent, which results the narrower size distribution.

Comparing 0.5% and 1.0% weight fraction of coupling agent, one can see that there are more large particles and gelatins with larger amount of amido coupling agent,as shown in Fig 3. It can be seen that such comparison made with different amount of amido coupling agent is in a good agreement with the results of discussion of transparency and stability. This agreement proves that less amount of coupling agent helps the formation of microemulsions. It can be concluded that the microemulsion have good properties when the amido coupling agent is less than 1.0 wt % of the microemulsion.

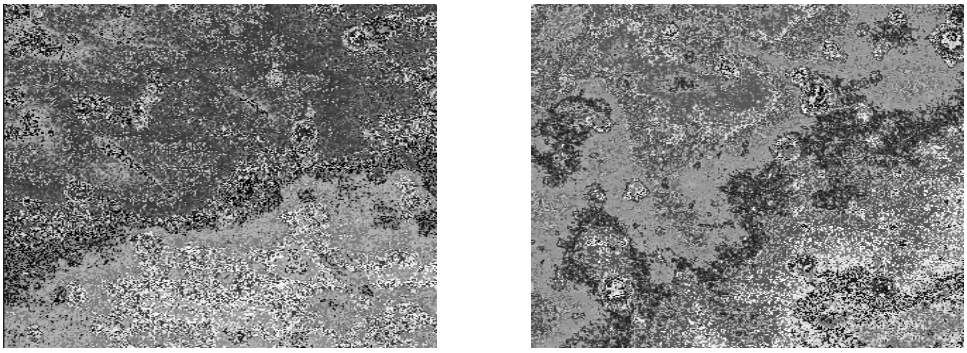

a. 0.5 wt% amido silane coupling agent b. 1 wt% amido silane coupling agent

Fig.3 TEM imagesof microemulsions with different amount of amido silane coupling agent

4. Conclusions

1. IR Spectra indicated that the amido group was successfully introduced into the polysiloxane.

2. The transparency of the microemulsions decreases with the increasing amount of the amido silane coupling agent.

3. An increase of amount of the amido silane coupling agent leads to an increase of the particle sizes and a decrease of the particle size distribution.

4. TEM photos show that there are more large particles and gelatins with larger amount of amido coupling agent.

References

[1] Ronald Paul Gee, U.S.Patent 5,852,110 (1998)

[2] M.Bonini, U.Bardi., A New Way to Prepare Nanostructured Materials: Flame Spraying of Microemulsions J.Phys. Chem.B (2002),106, p.6178

[3]Atik, S.S and Thomas, J.K., I. Radical Polymerization in Disperse Systems. J.Am.Chem.Soc, (1981).

[4]Capek On the free-radical microemulsion polymerization of alkyl methacrylates

Eur. Polym.J Vol. 34, No. 5/6, pp. 783~788, (1998).

Key Engineering Materials Vols. 385-387 (2008) pp 501-504
© (2008) Trans Tech Publications, Switzerland
doi:10.4028/www.scientific.net/KEM.385-387.501

Investigation of Flow Instability in High Temperature Deformation of INCONEL Alloy 783 using Processing Map Approach

Jong Taek Yeom[1,2,a], Eun Jeoung Jung[1,b], Jeoung Han Kim[1,c], Jae-Keun Hong[1,d], Nho-Kwang Park[1,e], Seung Sik Choi[3,f], and Chong Soo Lee[2,g]

[1]Korea Institute of Materials Science, 531 Changwondaero, Changwon 641-831, South Korea

[2]Department of Materials Science and Engineering, Pohang University of Science and Technology, Pohang 790-784, South Korea

[3]Taewoong Co., Busan 618-270, South Korea

[a]yjt96@kims.re.kr, [b]euny012@nate.com, [c]kjh1754@kims.re.kr, [d]jkhong@kims.re.kr, [e]pnk@kims.re.kr, [f]seungsik.choi@taewoong.com, [g]cslee@postech.ac.kr

Keywords: Alloy 783, Flow Instability, High Temperature Deformation, Processing Map, FEM simulation.

Abstract. The high temperature deformation behavior and flow instabilities of Ni-Fe-Co base superalloy, INCONEL alloy 783 during hot working process were investigated with process maps consisting of a power dissipation of dynamic materials model (DMM) and various flow instability criteria. In order to establish the processing map of INCONEL alloy 783, hot compression tests were carried out under different temperature and strain rate conditions, with true strain up to 0.7. On the basis of the comparison between processing maps and microstructural analysis, the reliability of various flow instability criteria was estimated. Finally the useful instability criterion for predicting the forming defects was suggested through the compression test results and experimental observations of actual ring rolling process of INCONEL alloy 783.

Introduction

INCONEL alloy 783 was developed for gas turbine applications due to its low coefficient of thermal expansion [1]. However, this alloy is rater difficult to form into a complex shape and uniform microstructure during hot forming processes because of its poor workability and large variation of microstructure with temperature, strain, strain rate, etc. The hot formability of this alloy is normally limited by the generation of various deformation defects such as shear bands, crack and other non-uniformities, etc [2]. Moreover, the study on hot workability of INCONEL alloy 783 during hot working processes was not accomplished yet. In this work, a useful tool for the prediction of forming defects occurred during hot deformation was established and the processing map of INCONEL alloy 783 indicating the optimum forming condition was generated based on the quantitative understanding of the dynamic deformation behavior. The accurate method among various instability criteria was selected by the comparison between the experimental data obtained from compression tests and prediction results. The actual ring rolling process of INCONEL alloy 783 was carried out to evaluate the process map approach.

Experimental Procedures

The materials used in this work was the forged INCONEL alloy 783 billet with a diameter 203mm. The chemical composition of the alloy is 0.01C, 0.03Mn, 24.98Fe, 0.001S, 0.06Si, 0.04Cu, 3.28Cr, 5.36Al, 0.2Ti, 34.81Co, 2.99Nb, 0.006Ta, 0.005P and balance Ni (in wt.%). Microstructure of the billet showed numerous inter and intragranular β particles (NiAl-type) in γ austenite matrix. The

average grain size of as-produced material was ASTM 7~8. In order to analyze the deformation behavior and forming defects during hot working, compression tests were carried out at the temperature ranges between 800°C and 1200°C at 50°C intervals and at the strain rate ranges between 10^{-3} and $10s^{-1}$. The cylindrical specimens of 12mm in height and 8mm in diameter were induction-heated to the test temperature at a heating rate of $5^{o}Cs^{-1}$, and quenched by purged N_2 gas as soon as the compression tests were completed. In order to identify the optimum forming condition obtained from the the processing map approach, actual ring rolling process of INCONEL alloy 783 was carried out. The heating temperature of workpiece and feed rate of the mandrel were selected by considering the optimum conditions obtained from the processing map approach.

Results and Discussions

Dynamic materials model(DMM) and Instability Criteria. Dynamic Materials Model (DMM) [3] and various stability or instability criteria were applied to construct processing maps for INCONEL alloy 783. The DMM includes an important dimensionless parameter called the efficiency of power dissipation (η).

$$\eta = \frac{2m}{m+1}, \quad m = \left(\frac{\partial \log \sigma}{\partial \log \dot{\varepsilon}} \right)_{T,\varepsilon}$$

Where, m is stain rate sensitivity. The parameter η represents the dissipating ability of the workpiece as normalized by the total power absorbed by the system. For an ideal linear dissipater, m=1 and η=1. Besides, the evaluation of forming defects such as flow localization, shear band, cracking, etc was investigated with various forming stability or instability criteria, that is, Ziegler's instability criterion [4], the four stability criteria based on a Liapunov function [5] and Rao's instability criterion [6]. The stable condition of four stability criteria are given by the strain rate sensiticity (m) and temperature sensitivity (s) as

$$0 < m \le 1, \quad m' = \left(\frac{\partial m}{\partial (\log \dot{\varepsilon})} \right) < 0, \quad s = \frac{1}{T} \left[\frac{\partial (\ln \sigma)}{d(1/T)} \right] \varepsilon, \dot{\varepsilon} \ge 1, \quad s' = \frac{\partial s}{\partial (\log \dot{\varepsilon})} < 0.$$

Ziegler's instability criterion is based on the
continuum principle as applied to large plastic flow. In the unstable deformation regime, the instability criterion is defined by the following equation.

$$\xi(\dot{\varepsilon}) = \frac{\partial \ln(m/m+1)}{\partial \ln \dot{\varepsilon}} + m < 0$$

Murty and Rao[6] suggested the following condition for the unstable material flow.

$$\varsigma = \frac{2m}{\eta} - 1 < 0 \quad or \quad \eta < 2m$$

If the σ-$\dot{\varepsilon}$ behavior follows the power law, the instability parameter ς becomes m and the condition for flow instability becomes $m < 0$.

Processing Map and Instability Analysis of INCONEL Alloy 783. In order to establish the processing maps and instability regimes during hot deformation, flow stress curves and microsturctural analysis results generated from the compression tests were used. Fig. 1 shows the power dissipation contour map and the various instability contour maps obtained at the strain of 0.6. The microstructures observed at the several test conditions are shown in Fig. 2. The power dissipation contour map shows a peak efficiency of 0.423 at the temperature range between 1100°C and 1200°C, and strain rate range between 10^{-2} and $10^{0}s^{-1}$, indicating that the region is an optimum condition for thermomechanical processing of this alloy.

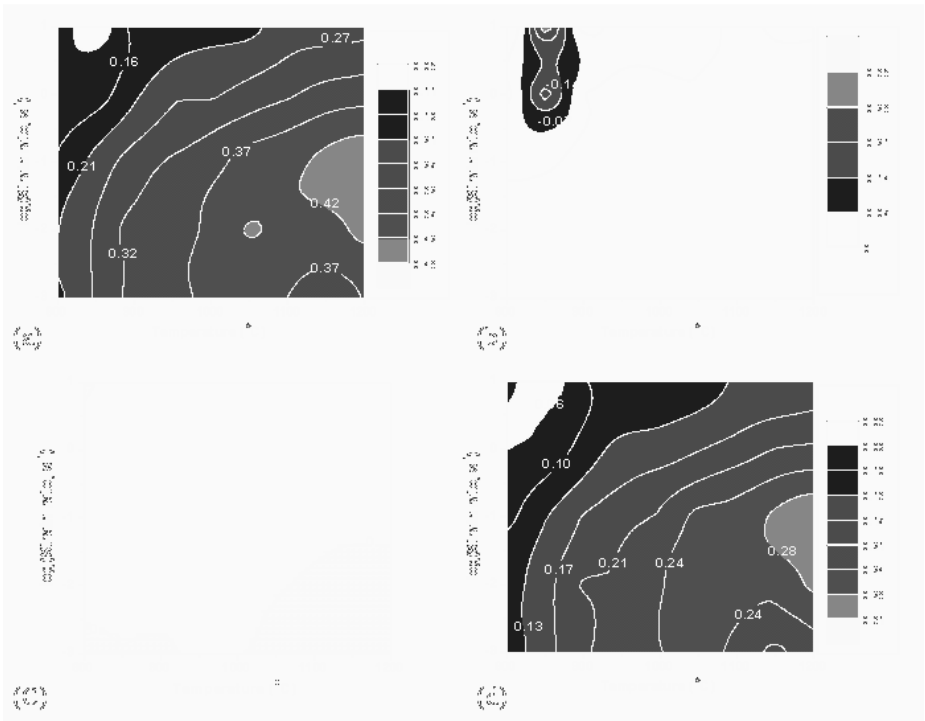

Fig. 1. (a)Power dissipation efficiency map of INCONEL Alloy 783 at a strain of 0.6 and instability maps by (b) Ziegler's instability criterion, (c) the four stability criteria and (d) Rao's instability criterion.

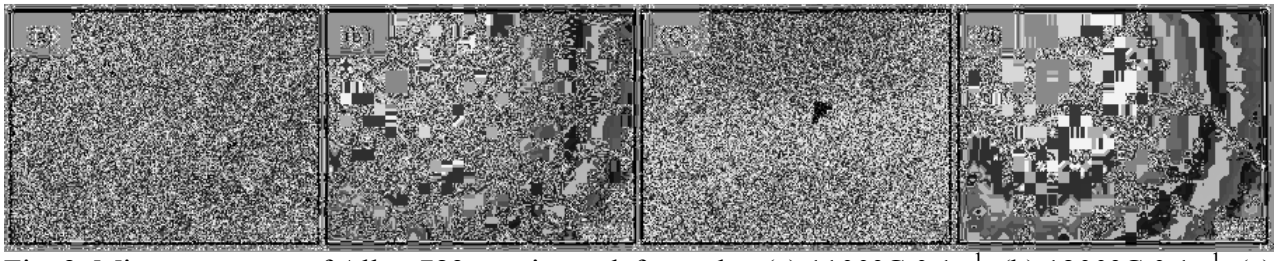

Fig. 2. Microstructures of Alloy 783 specimen deformed at (a) 1100°C $0.1s^{-1}$, (b) 1200°C $0.1s^{-1}$, (c) 850°C $10s^{-1}$, (d) 1200°C $0.001s^{-1}$

The microstructures observed at these peak efficiency area exhibit fine-grain structure formed by dynamic recrystallization behavior. Rao's instability criterion represents that stable flow zone is formed at all regions for a given test conditions. However, the micrographs of specimen deformed at high strain rate regions and high temperature and low strain rate regions showed flow localization band and dynamic grain growth, respectively. Ziegler's instability criterion is adequate to predict the flow localization band formed at high strain rate, but leads to a significant error in the prediction of dynamic grain growth occurred at high temperature and low strain rate regions. The instability map developed using the four stability criteria based on Liapunov function shows that a large regime of flow instability occurs at low strain rate regions. The microstructures observed at these regions reveals that dynamic grain growth is developed. However, the stability criteria didn't predict the flow localization band formed at high strain rate regions. From a comparison of various flow stability or instability criteria, it was summarized that the coupling approach of Ziegler's instability criterion and

four stability criteria based on a Liapunov function was suggested as the optimum method for predicting the forming defects during hot working.

Ring Rolling Process of INCONEL Alloy 783 Ring.

The ring rolling condition was obtained by considering optimum condition of the processing map and grain growth during hot forming process. The initial heating temperature of the blank was selected as 1100°C. The angular velocity of the main roll was 26 rpm and average feed rate of the mandrel was selected as 0.5 mm/s. Also, the dimension design for calculating the rolled dimension, blank size and billet size was carried out by applying the calculation method to prevent the surface defects such as fishtail and fold. The detailed calculation method has been presented elsewhere [7]. Fig. 3 shows expremental observation of rolled INCONEL alloy 783 ring performed in optimum process condition. Note that the actual ring indicates a relatively uniform shape without forming defects such as fishtail, fold, crack, etc.

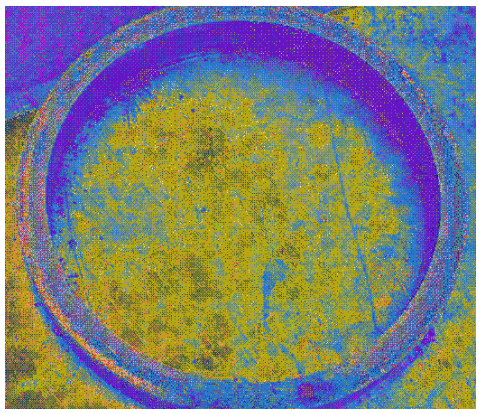

Fig. 3. Rolled INCONEL Alloy 783 ring in optimum process condition.

Summary

The metal forming behavior of alloy 783 during hot working was investigated with various forming stabilities or instabilities criteria, that is, Ziegler's instability criterion, four stability criteria based on a Liapunov function and Rao's instability criterion. These criteria were validated with compression tests performed at different temperatures and strain rates conditions and actual ring rolling process of INCONEL alloy 783. In a comparison of three criteria for predicting the forming defects, the coupling approach of Ziegler's instability and the four stability criteria was suggested as the useful method to predict the forming defects occurred in a large range of hot forming process conditions.

References

[1] K.A. Heck, J.S. Smith, R. Smith: J. Engineering for Gas Turbines and Power, Vol. 120 (1998), p. 363

[2] D.U. Furrer and S.L. Semiatin, in: *Metalworking: Bulk Forming,* edited by S. L. Semiatin, volume 14A of ASM Handbook, Forging of Nickel-Base Alloys, AMS International (2005).

[3] Y.V.R.K. Prasad, et al.: Metall. Trans. A, Vol. 15A (1984), p. 1883

[4] H. Ziegler, in: *Prog. Solid Mech*. edited by I. N. Sneddon and R. Hill, Vol. 4, John Willey and Sons, New York (1965)

[5] J.C. Malas and V. Seetharaman: JOM, June (1992), p. 8

[6] S.V.S. Narayana Murty and B.N. Rao: Materials Science and Technology, Vol. 14 (1998), p.835

[7] J.T. Yeom, J.H. Kim, N.K. Park, S.S. Choi and C.S. Lee, J. Materials Processing Technology, Vols 187-188 (2007), p.747

Key Engineering Materials Vols. 385-387 (2008) pp 505-508
© (2008) Trans Tech Publications, Switzerland
doi:10.4028/www.scientific.net/KEM.385-387.505

Effect of Strain-induced Martensitic Transformation on Coaxing Effect of Austenitic Stainless Steels

Jae Woong Jung [1], Masaki Makajima [2,a],
Yoshihiko Uematsu [3], Keiro Tokaji [3] and Masayuki Akita [3]

[1] LS Industrial Systems, Songjung-Dong, Chongju, Chungbuk, Korea

[2] Toyota National College of Technology, 2-1 Eisei-cho, Toyota 471-8525, Japan

[3] Faculty of Engineering, Gifu University, 1-1 Yanagido, Gifu 501-1193, Japan

[a] nakajima@toyota-ct.ac.jp

Keywords: Fatigue, Coaxing effect, Austenitic stainless steel, Martensitic transformation.

Abstract. The effects of martensitic transformation on the coaxing behavior were studied in austenitic stainless steels. The materials used were austenitic stainless steels, type 304 and 316. Conventional fatigue tests and stress-incremental fatigue tests were performed using specimens subjected to several tensile prestrains from 5% to 60%. Under conventional tests, the fatigue strengths of both steels increased with increasing prestrain. Under stress-incremental tests, 304 steel showed a marked coaxing effect, where the failure stress significantly increased irrespective of prestrain level. On the other hand, the coaxing effect in 316 steel decreased with increasing prestrain up to 15%, where the failure stresses were nearly the same. Above this prestrain level, the coaxing effect increased with increasing prestrain. In 304 steel, the coaxing effect is primarily dominated by work hardening at low prestrains, while the effect of strain-induced martensitic transformation increases with increasing prestrain. The coaxing effect in 316 steel is dominated by both work hardening and strain aging at low prestrains, but strain-induced martensitic transformation could play a significant role at high prestrains.

Introduction

Machine components are generally subjected to some plastic deformation during manufacturing process. Since austenitic stainless steels exhibit a marked work hardening under plastic deformation, the prestrained materials would be expected to show a different behavior from the unprestrained ones under cyclic loading. Therefore, it is important to evaluate the effect of prestraining on fatigue behavior of austenitic stainless steels.

Fatigue damage is usually developed and accumulated with cyclic loading. However, when metals are subjected to understressing followed by a small step-wise increment of stress amplitude, they are strengthened. This behavior is known as coaxing effect [1]. As possible mechanisms of the coaxing effect, strain aging [1], work hardening [2] and strengthening at the tip of non-propagating cracks [3] have been indicated, but the mechanisms in austenitic stainless steels have not been fully understood. Moreover, the effect of prestrain on the coaxing effect in austenitic stainless steels, which may be influenced by work-hardening and martensitic transformation due to prestrain [4], is not identified.

The purpose of the present study is to clarify the effect of prestrain on the coaxing effect in austenitic stainless steels, type 304 and 316. Special attention was paid on the strain-induced martensitic transformation of the prestrained specimen under cyclic loading.

Experimental procedures

Materials. The materials used in the present study were austenitic stainless steels, type 304 and SUS316, whose austenite phase is metastable and stable, respectively. Both materials were solution

treated at 1353 K for 1 hr. The mechanical properties after heat treatment are listed in Table 1. After solution treatment, several tensile prestrains from 5% to 60% were subjected to the materials. Hourglass-shape fatigue specimens with a minimum diameter of 5~5.5 mm were machined and then mechanically polished by emery paper. Hereafter, the specimen not subjected to prestrain is denoted as the unprestrained specimen and the specimens subjected to prestrain are designated as the prestrained specimens, *e.g.* the 15% prestrained specimen for 15% prestrain.

Procedure. Fatigue tests were performed using cantilever-type rotating bending fatigue testing machines operating at a stress ratio of -1 and a frequency of 53 Hz. Stress-incremental tests were started from a stress level just below the fatigue limit. If no failure occurred after 10^7 cycles, then the stress level was increased by a small increment of 20 MPa. This procedure was repeated until fatigue failure took place. Crack initiation was monitored by replication technique just before the stress level was increased. After experiment, fracture surfaces were examined using a scanning electron microscope (SEM). Martensitic transformation was detected by either X-ray diffraction method or EBSD analysis.

Results and discussions

Fatigue strength. The *S-N* diagram is shown in Fig.1. As seen in the figure, the fatigue limits of the unprestrained specimens in both steels are the same, 300MPa, and fatigue strength increases with increasing prestrain. In particular, the specimens subjected to more than 25/30% prestrain exhibit a marked increase in fatigue strength. The fatigue limits for the 58/60% prestrained specimens, corresponding to tensile strength, are 470 MPa and 460 MPa in 304 and 316 steels, respectively, which are more than 50% increase in comparison to the fatigue limit of the unprestrained specimens. In the run-out specimens of both steels, non-propagating cracks were not detected.

Coaxing behavior. The results of stress-incremental tests in 304 and 316 steels are shown in Fig.2 (a) and (b), respectively. In 304 steel (Fig.2 (a)), the failure stress of all prestrained specimens increases compared with each fatigue limit, indicating that the coaxing effect occurs remarkably irrespective of prestrain level. On the other hand, 316 steel shows a different behavior between less than 15% prestrain and more than 25% prestrain, as can be seen in Fig.2 (b). The coaxing effect decreases with increasing prestrain up to 15%, where the failure stresses are nearly the same, 360MPa~380MPa. Above this prestrain level, the coaxing effect increases with increasing prestrain. The failure stresses of the 25% and 58% prestrained specimens are 460 MPa and 540 MPa, respectively. Based on these experimental results, it is suggested that mechanisms of the coaxing effect in 316 steel would change below and above the prestrain level of 15%. Crack initiation was monitored when the stress level was increased, but cracks were not detected in both steels.

Hardness measurement. After experiment, Vickers hardness of the failed specimens was measured. The results are given in Table 2. As can be seen in the table, a marked increase of hardness is observed in both steels, while the increased ratio of hardness in both steels decreases

Table 1 Mechanical properties.

Material	0.2% proof stress $\sigma_{0.2}$(MPa)	Tensile strength σ_B (MPa)	Elongation δ(%)	Vickers hardness *HV*
SUS304	298	594	69	192
SUS316	211	560	66	134

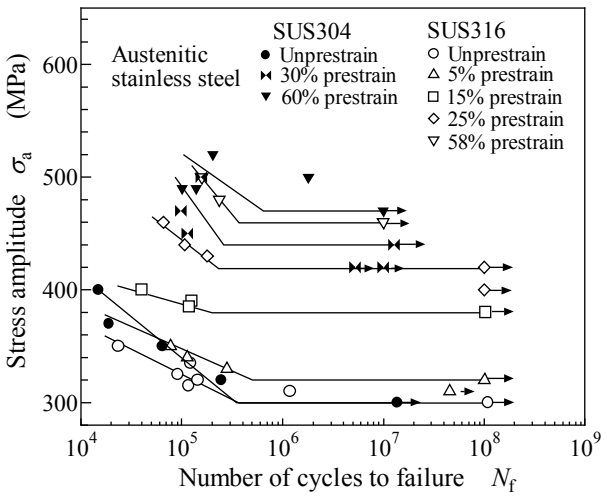

Fig.1 *S-N* diagram.

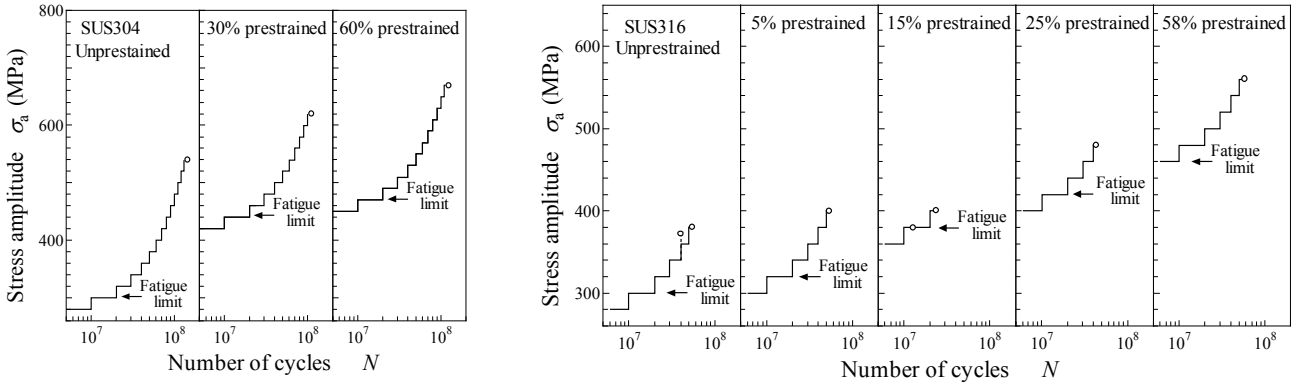

(a) Type 304 (b) Type 316

Fig.2 Stress-incremental test results in austenitic stainless steels: (a) Type 304, (b) Type316.

with increasing prestrain. By the way, in 304 steel, the increased ratios of failure stress in stress-incremental tests were 73%, 36% and 38% for the unprestrained, 30% and 60% prestrained specimens, respectively. Also in 316 steel, the ratios were 20%, 19%, 0%, 10% and 17% for the unprestrained, 5%, 15%, 25%, 58% prestrained specimens, respectively. Therefore, it is indicated that the change of the increased ratio in hardness is consistent with the qualitative tendency of the increased fatigue limit due to coaxing effect.

Strain aging ability. It is known that coaxing effect is caused by strain aging [1]. Hence, strain aging ability in both steels was evaluated by tensile tests. The material subjected to a prestrain of about 10% was aged at 383 K for 5 hour, and then reloaded in tension. The stress-strain curves before and after aging for 304 and 316 steels are represented in Fig.3 (a) and (b), respectively. In 304 steel (Fig.3 (a)), the increase of proof stress was not observed, while in 316 steel (Fig.3 (b)) significantly increased after aging. This result suggests that 316 steel has much larger strain aging ability than 304 steel. However, the increase of proof stress was not observed for 316 steel subjected to a prestrain of about 22%. This means that the coaxing effect of 316 steel subjected to a prestrain of more than 25% is not affected by strain aging.

Strain-induced martensitic transformation. It is well known that 304 steel shows the strain-induced martensitic transformation [4, 5]. The amount of transformed martensite phase was measured by X-ray diffraction method. Figure 4 shows the variation in martensite volume fraction

Table 2 Vickers hardness before and after stress-incremental test.

SUS304	Unprestrained	30% prestrained	60% prestrained	SUS316	Unprestrained	5% prestrained	15% prestrained	25% prestrained	58% prestrained
Before test	192	247	335	Before test	137	177	214	251	302
After test	307	323	357	After test	228	282	237	321	335
Increased ratio (%)	60	31	7	Increased ratio (%)	66	59	11	28	11

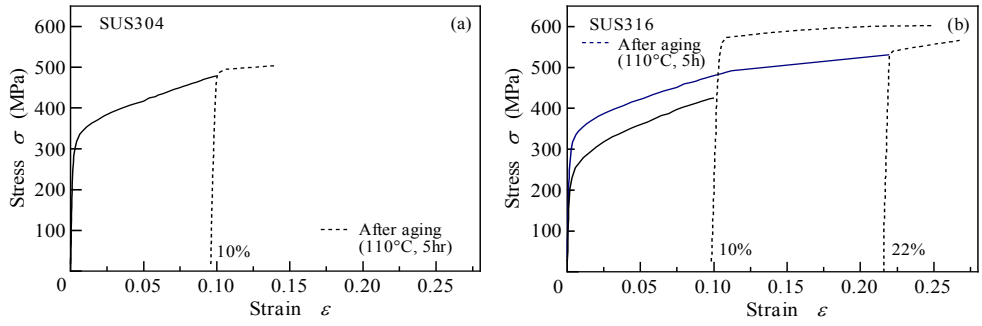

(a) Type 304 (b) Type 316

Fig.3 Stress-strain curves showing strain aging ability: (a) Type304, (b) Type316.

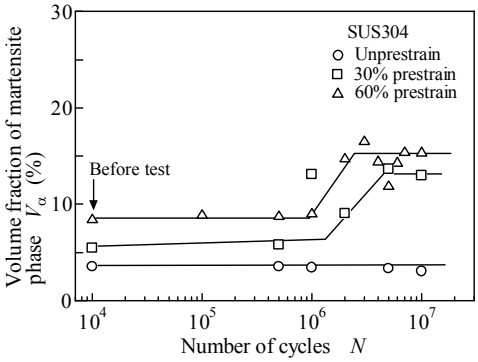

Fig.4 Variation in volume fraction of martensite phase with cyclic loading in 304 steel.

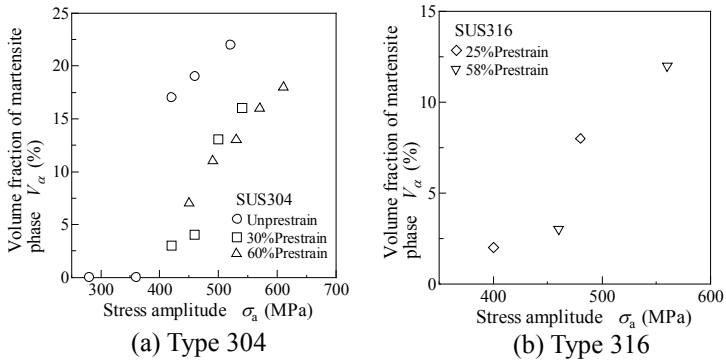

(a) Type 304 (b) Type 316

Fig.5 Variation in volume fraction of martensite phase with loading amplitude under stress-incremental test: (a) Type304, (b) Type316.

for 304 steel as a function of number of cycles under constant amplitude loading at a stress level of fatigue limit. The martensite volume fraction of the unprestrained specimen is constant during cyclic loading, while the 30% and 60% prestrained specimens show a marked increase of martensite volume fraction in the region of $N > 10^6$ cycles. Figure 5 shows the variation in martensite volume fraction for both steels with stress amplitude under stress-incremental test. As can be seen in the figure, the martensite volume fraction significantly increases in the range of σ_a>400 MPa for 304 steel and 450 MPa for 316 steel. For 316 steel, however, in the specimens subjected to prestrains below 15%, no martensite phase was detected. The extent of martensitic transformation is larger for 304 steel than 316 steel, because of the higher stability of austenite phase in 316 steel.

Factors of influence. Based on the results, the coaxing effect in austenitic stainless steels is influenced by work hardening, strain aging and martensitic transformation [4, 5]. As shown in Table 2, the increased ratios of hardness before and after experiment decreased with increasing prestrain, indicating that work hardening abilities in both steels decreased with increasing prestrain. Therefore, it is considered that the coaxing effect depends on work hardening ability. However, the coaxing effect was still recognized in the specimens subjected to high prestrains in 316 steel.

As a possible mechanism, martensitic transformation should be taken into account. Fig.5 (b) indicates that martensitic transformation in 316 steel might affect the coaxing effect only at high prestrains, because the austenite phase of 316 steel is relatively stable. On the other hand, in 304 steel for which the austenite phase is metastable, the coaxing effect could be attributed to martensitic transformation during cyclic loading as seen in Figs.4 and 5 (a). Strain aging also should be considered as a possible mechanism. However, 304 steel showed little strain aging ability (Fig.3 (a)), thus the coaxing effect of this steel was not affected by strain aging. In 316 steel, the coaxing effect in the specimens subjected to low prestrains is due to strain aging, but not in high prestrains (Fig.3 (b)).

Conclusions

(1) In 304 steel, the coaxing effect is primarily dominated by work hardening at low prestrains, while the effect of strain-induced martensitic transformation increases with increasing prestrain.
(2) The coaxing effect in 316 steel is dominated by both work hardening and strain aging at low prestrains, but strain-induced martensitic transformation could play a significant role at high prestrains.

References

[1] G.M. Sinclair: Proc. ASTM, **52** (1952), p. 743-758.
[2] H. Nisitani and S. Nishida: Transactions of the JSME, **39**-321 (1973), p. 1385-1394.
[3] H. Nisitani and Y. Yamaguchi: Transactions of the JSME, **45**-391 (1979), p. 260-266.
[4] A. Oda: J. Soc. Mater. Sci., Japan, **23**-247 (1974), p. 279-285.
[5] T. Ogawa and K. Tokaji: Proceedings of the VHCF-3, Kusatsu, Japan, (2004), p. 366-373.

Key Engineering Materials Vols. 385-387 (2008) pp 509-512
© (2008) Trans Tech Publications, Switzerland
doi:10.4028/www.scientific.net/KEM.385-387.509

Characteristics of Deformation-induced Transformation in Steel 2.25Cr1Mo

Li Qing-fen[1, 2,a] Chen Hong-bin [3,b]

[1]College of Material Science and Chemical Engineering, Harbin Engineering University,

[2]College of Mechanical and Electrical Engineering, Harbin Engineering University,

Harbin 150001, China

[3]College of Material Science and Engineering, Harbin University of Science and Technology,

Harbin 150040, China

[a]qingfli@yahoo.com.cn, hrbust@sohu.com

Keywords: Deformation-induced Transformation; steel 2.25Cr1Mo; controlled - rolling; controlled - cooling

Abstract. Characteristics of deformation-induced transformation (DIT) in the refractory low alloy steel 2.25Cr1Mo were experimentally studied. Effect of different controlled-rolling and controlled-cooling process on the steel microstructure and mechanical properties were investigated and the mechanism was discussed. Results show that the grain size and the ferrite volume fraction were obviously affected by the rolling and cooling processes. Proper DIT technique may significantly accelerate the transformation of austenite to ferrite in the steel and improve the steel strength.

Introduction

Steels with fine grain size have favorable mechanical properties such as strength, toughness and fatigue strength. Therefore, grain refinement has been an important item among research studies. With the development of new generation steels, the deformation-induced transformation (DIT) is known as a new method to refine grain in steels. In the past decades, many researchers have been developing the technique that can produce steel with ferrite grain size smaller than 5 μm. Some of them have produced 1 μm ultrafine grained ferrite steel through the DTT. Hot deformation causes considerable austenite microstructure change, such as the increase in dislocation density and grain refinement of austenite grain which will affect the ferrite transformation. However, the mechanism is not very clear yet, and most of the previous works about DIT technique were used in low carbon steels. Only a few were in low alloy steels [1-5].

In the present work, grain refinement technique by deformation induced phase transformation in the refractory low-alloy steel, 2.25Gr1Mo, was investigated. Effect of different controlled-rolling and controlled-cooling process on the steel microstructure and mechanical properties was experimentally studied and the mechanism was discussed.

Experimental procedures

Experimental study was carried out on steel 2.25Cr1Mo. The compositions are listed in Table 1 and the critical temperatures are given in table 2. Specimens were of Φ8 mm x 15 mm. Simulation experiments of hot deformation were carried out with Gleeble-1500 system. Specimens were

deformed compressively by single-pass and multi-pass hot rolling process with different rolling temperature, strain rate, cooling rate and deformation reduction. The rolling and cooling schedule was different in different process. For example, it was as follow: specimen was heated at 20°C/s to 1150°C, held for 4 min, after that it was cooled to rolling temperature (860°C) at 5°C/s, when rolling temperature was 860°C, deformation reduction was 50%, strain rate was 1/s. Optical microscope, scanning electron microscopy (SEM) and transmission electron microscopy (TEM) were used to investigate the microstructure evolution and mechanisms of grain refinement during the deformation.

Table 1 Chemical Compositions of Steel 2.25Cr1Mo [wt. %]

C	P	Mn	Si	Cr	Mo	V	S	Ni	W
0.13	0.0072	0.56	0.20	2.14	1.10	0.01	0.015	0.08	0.06

Table 2 Critical temperature of Steel 2.25Cr1Mo

Critical point	A_{c1}	A_{c3}	A_{r1}	A_{r3}
°C	804	870	720	820

Experimental results and discussion

Effects of deforming temperature, strain reduction, cooling rate and rolling pass on the ferrite grain size and ferrite volume fraction are shown in Fig. 1-4 respectively. Fracture microstructures of steel 2.25Cr1Mo at various rolling schedule are given in Fig.5. Effect of deforming temperature on the stress-strain curves of steel 2.25Cr1Mo is given in Fig. 6.

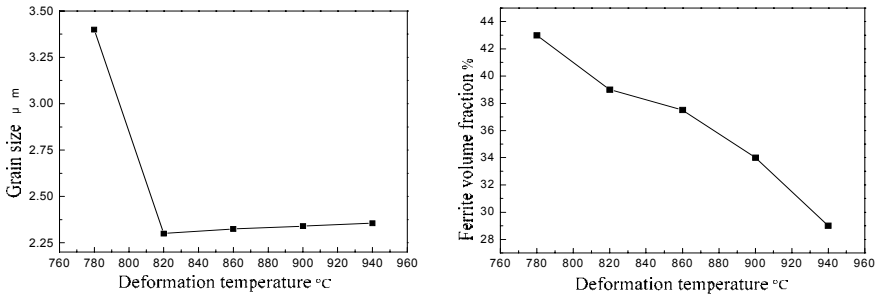

(a) (b)

Fig. 1 Effect of deforming temperatures on grain size and ferrite volume fraction

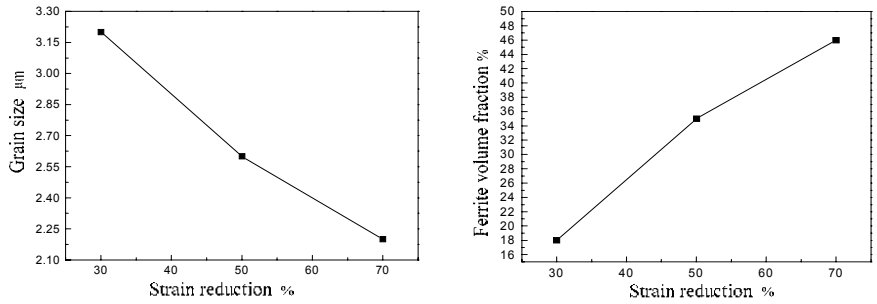

(a) (b)

Fig. 2 Effect of strain reductions on grain size and ferrite volume fraction

From Fig. 1, we see that the grain size of the test steel decreased with decreasing deforming temperature above A_{r3} and was about 2.30μm at 820°C, the ferrite volume fraction increased with decreasing deforming temperature and reached a maximum about 43% at 780°C. It suggests that lower deforming temperature accelerates austenite to ferrite transformation and is beneficial to grain refinement around A_{r3}.

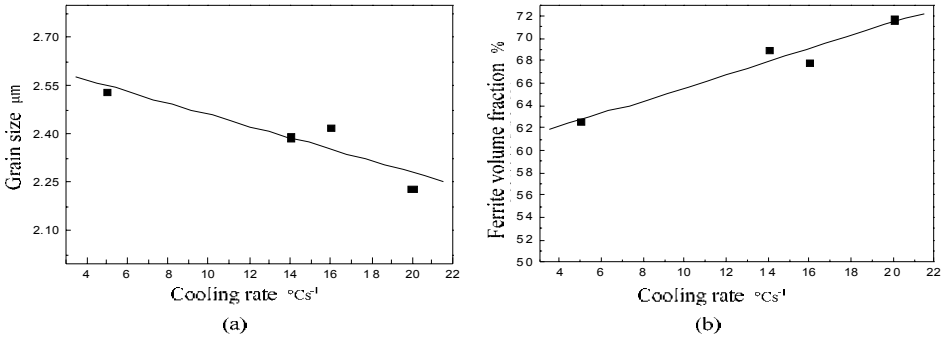

Fig. 3 Effect of cooling rate on grain size and ferrite volume fraction

Fig.2 and 3 showed that the grain size decreased and the ferrite volume fraction increased with increasing strain reduction and cooling rate. Suggest that higher strain reduction and higher cooling rate are helpful to grain refinement and ferrite transformation. Since heavy deformation may cause more deforming strips, twins, and higher dislocation density which provide more energy and position for ferrite crystal formation in the test material. Cooling rate is one of the most important factors affecting the initial γ→α phase transformation temperature. The higher the cooling rate, the lower the initial transformation temperature is. Lower initial transformation temperature may constrain the growth of grain size and is therefore helpful to grain refinement.

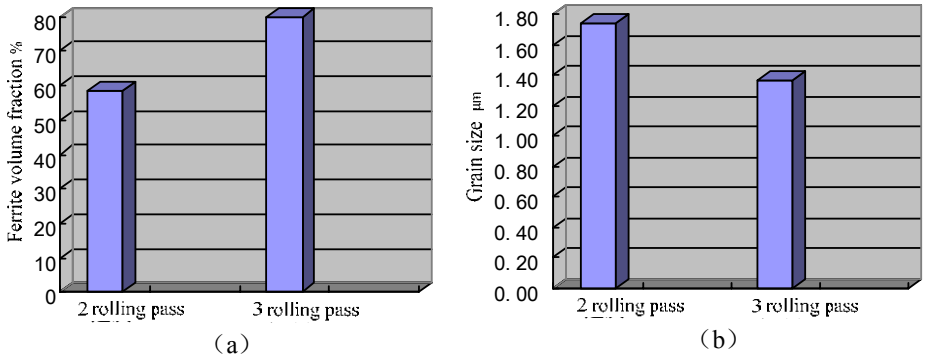

Fig. 4 Effect of rolling passes on grain size and ferrite volume fraction

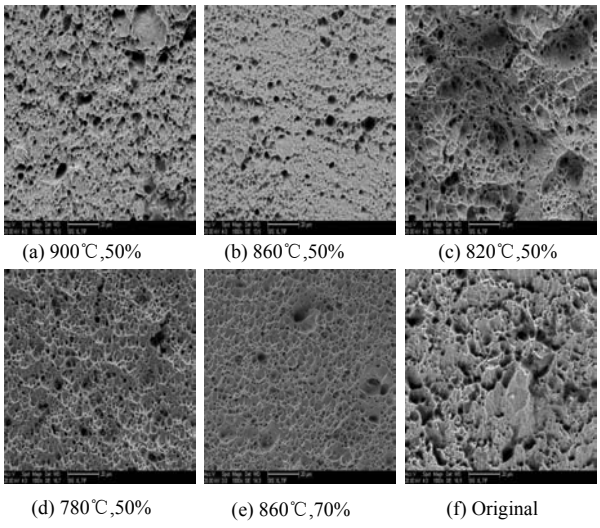

Fig. 5 Fracture microstructure of steel at various rolling schedule

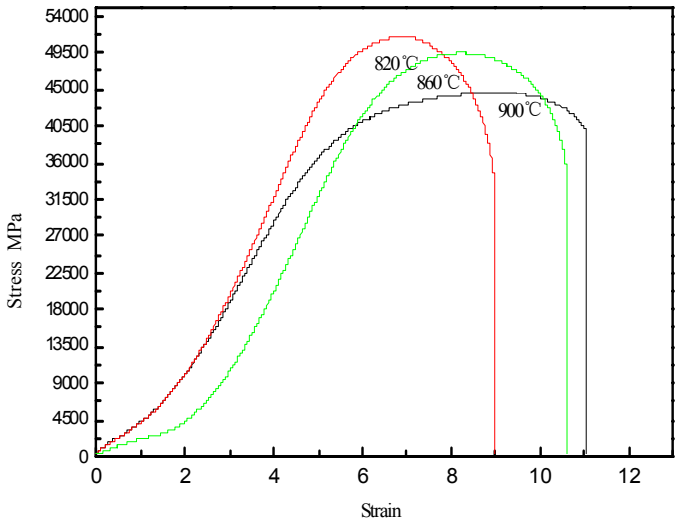

Fig. 6 Effect of deformation temperature on stress-strain curve

The grain size and the ferrite volume fraction were improved more by three-passes than two-passes rolling (Fig. 4). It is known that ferrite phase transformation and ferrite re-crystallization dynamic mainly induced by deformation at the boundary of austenite crystal and deforming strips. The accumulative effect of multi-passes rolling may induce more ferrite transformation, re-crystallization, and finer ferrite grains.

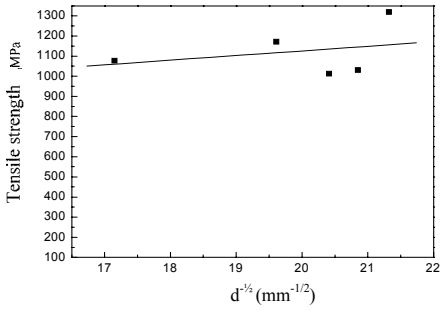

Fig. 7 Effect of grain size on tensile strength

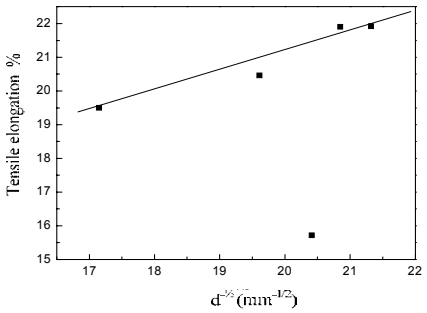

Fig. 8 Effect of grain size on tensile elongation

It can be seen from the SEM fractographs (Fig.5) that the grain size is smaller and the microstructure is more uniform when deforming temperature is lower. From Fig. 5 (b) and (e), we see that finer grain size and more uniform microstructure may be obtained when strain reduction is higher.

Fig. 6 shows that the strength is obviously improved when deforming temperature decreased, because lower deforming temperature is beneficial to grain refinement.

From Fig. 7 and 8, we see that both the tensile strength and elongation of the steel are improved when the grain size decreased. Thus, we may conclude that strength and toughness of steels may be controlled and improved by grain refinement technique. Since grain boundaries may constrain the dislocation and increase the strength of steel. The finer the grain size is, the more the grain-boundary areas are, and the higher the strength of steel will be.

It is obvious from the above results that the grain sizes and ferrite volume fraction were affected by the deforming temperature, strain reduction, cooling rate and rolling passes. The properties of steel were improved by DIT technique.

Summary

Experimental results show that lower deforming temperature accelerates austenite to ferrite transformation and is beneficial to grain refinement around A_{r3}. The grain size decreased and the ferrite volume fraction increased with increasing strain reduction and cooling rate. It suggests that higher strain reduction and higher cooling rate are helpful to grain refinement and ferrite transformation. The strength is obviously improved when deforming temperature decreased, because lower deforming temperature is beneficial to grain refinement. Both the tensile strength and elongation of the steel are improved when the grain size decreased. It is obvious from the results that the properties of steel were improved by DIT technique.

References

[1] X. C. Li, G. Chen, K. H. Zhang: J. Review Hot Working Technology, Vol. 6(2002), p.22
[2] Y. B. Xu, Y. M. Yu, X. H. Liu, G. D.Wang: J. Mater. Sci. Technol., Vol. 20(2004), p. 487
[3] V. M. Khlestov, E. V. Konopleva, H. J. McQueen: J. Material Science & Technology, Vol. 14(1998), p783.
[4] B. Yun, H. Pan, C. F. Yang, J. C. Shen, H. Su: J. Iron & Steel Research, Vol. 6 (2003), p. 59
[5] Q. Y. Liu, H. R. Hou, H. J. Chen, etc: J. Iron & Steel, Vol. 36 (2001), p.38

Key Engineering Materials Vols. 385-387 (2008) pp 513-516
© (2008) Trans Tech Publications, Switzerland
doi:10.4028/www.scientific.net/KEM.385-387.513

Stress Analysis for Shrink fitting System used for Ceramics Conveying Rollers

HENDRA [1,a], Masakazu TSUYUNARU [1,b], Nao-Aki NODA [1,c], Yasushi TAKASE[1,d]

[1]Department of Mechanical Engineering Kyushu Institute of Technology

Sensui-Cho 1-1 Tobata-Ku, Kitakyushu-Shi, Fukuoka, Japan

[a]*mpe2_boy@yahoo.com,* [b]*f344128m@tobata.isc.kyutech.ac.jp,* [c]*noda@mech.kyutech.ac.jp,* [d]*takase@mech.kyutech.ac.jp*

Keywords: Finite element method, Elasticity, Bending and Maximum tensile stress.

Abstract. Cast iron and steel conveying rollers used in hot rolling mills must be changed very frequently because conveyed strips with high temperature induces wear on the roller surface in short periods. This failure automatically stops the production line for repair and maintenance of conveying rollers. In this study a new type of roller is considered where a ceramics sleeve is connected with two short shafts at both ends by shrink fitting. Here, a ceramics sleeve provides longer life and therefore reduces the cost for the maintenance. However, for the hollow ceramics rollers, care should be taken for maximum tensile stresses appearing at both edges of the sleeve. In particular, because fracture toughness is extremely smaller compared with the value of steel, stress analysis for the roller is necessary for ceramics sleeve. In this study FEM analysis is applied to the structure, and the maximum stress has been investigated with varying the dimensions of the structure. It is found that the maximum tensile stress appearing at the end of sleeves takes a minimum value at a certain amount of shrink fitting ratio.

Introduction

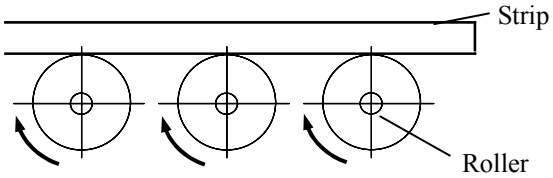

Fig.1 Layout of Conveying Rollers

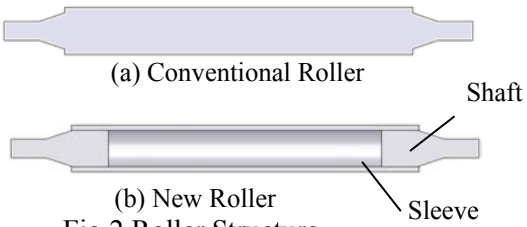

Fig.2 Roller Structure

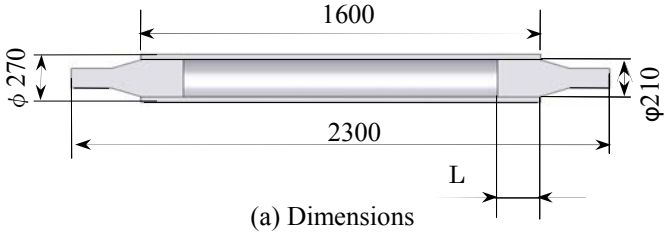

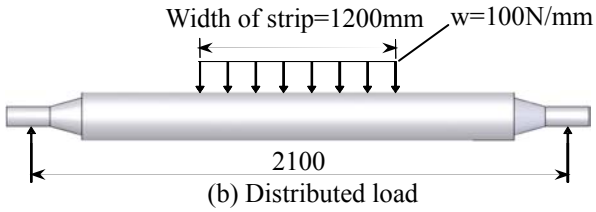

Fig.3 Models considered (mm)

Cast iron and steel conveying rollers used in hot rolling mills (see Fig.1) must be changed very frequently because conveyed strips with high temperature induces wear on the roller surface in short period. The damage portions have been repaired with the flame spray coating [1]. Use of ceramics and cemented carbide has been also promoted [2] because they have high temperature resistance and high abrasion resistance.

Figure 2(a) shows the structure of the conventional rollers. For conventional rollers material consumptions are large and the exchange cost of roller is high because we have to change whole

Table 1 Material Properties

	Young's modulus [GPa]	Poisson's ratio	Tensile strength [MPa]	Fracture toughness [MPa$\sqrt{m}$]
Ceramics	300	0.28	500	7.7
Cemented Carbide	500	0.24	1000	20
Steel	210	0.3	600	100

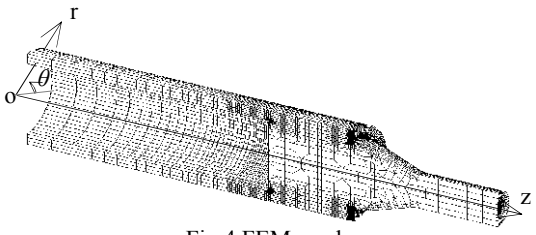

Fig.4 FEM mesh

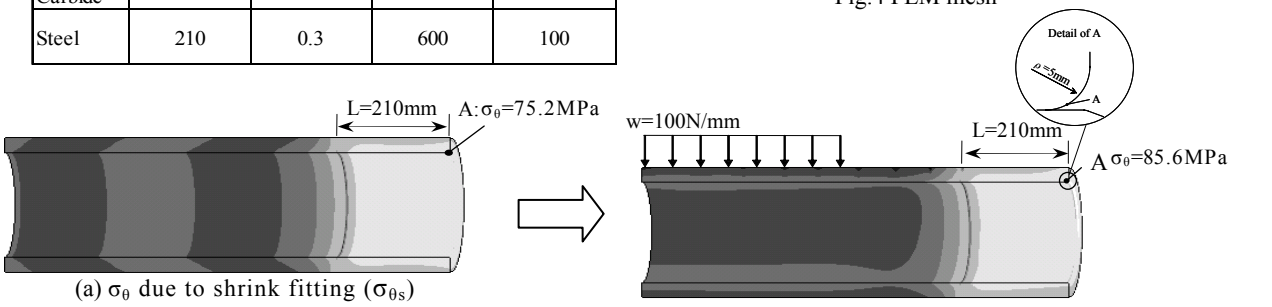

Fig.5 Stress distribution σ_θ when $\delta/d=3.0\times10^{-4}$

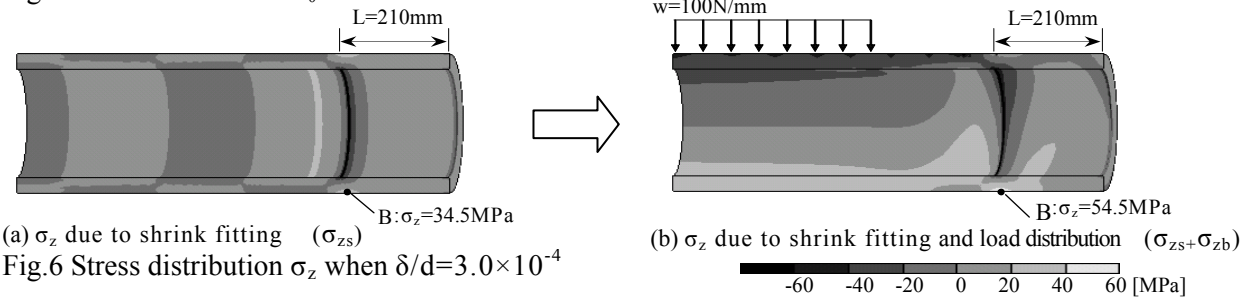

Fig.6 Stress distribution σ_z when $\delta/d=3.0\times10^{-4}$

roller. In this study, we will focus on the roller structure where a sleeve and two short shafts are connected by shrink fitting at both ends as shown in Fig.2 (b).

The new roller is suitable for maintenance and reducing the cost because we can exchange the sleeve only. In addition, the running speed of the steel strip can be changed smoothly due to the light weight. Moreover, further cost reduction can be realized if ceramics are used as the sleeve because they offer high temperature resistance and high abrasion resistance. However, for the hollow rollers, care should be taken for maximum tensile stresses appearing at the edge of the sleeve. Especially, because fracture toughness of ceramics is extremely smaller compared with the values of steel, stress analysis for the roller becomes important. Therefore, in this study FEM analysis is applied to the structure as shown in Fig.2 (b).

Analytical Conditions

Define the shrink fitting ratio as δ/d, where δ is the diameter difference with the diameter d=210mm. Assume that the roller is subject to distributed load w=100N/mm and simply supported at both ends (see Fig.3). The friction coefficient between sleeve and shafts is assumed as 0.3.

Table 1 shows the material properties of steel, ceramics and cemented carbide. Stainless steel is usually used for conventional rollers but ceramics and cemented carbide rollers may provide a longer maintenance span due to their high temperature resistance and high abrasion resistance.

Fig. 4 shows the finite element mesh model of the conveying rollers. The total number of elements is 22,340 and the total number of nodes is 26,751. The model of 1/4 of the roller is considered due to symmetry.

Results and Discussion

Maximum Tensile Stress

Figure 5 shows stress distribution σ_θ at the shrink fitting ratio $\delta/d = 3.0\times10^{-4}$. Figure 5(a) shows the stress $\sigma_{\theta s}$ due to shrink fitting and Fig.5(b) shows maximum stress distribution $\sigma_{\theta max}(=\sigma_{\theta s}+\sigma_{\theta b})$ due to load distribution w=100N/mm after shrink fitting. As shown in Fig.5, the maximum tensile stress at point A is 75.2 MPa while shrink fitting. It becomes 85.6 MPa by applying the distribution load after shrink fitting, that is, $\sigma_{\theta b}$=10.4 MPa.

Figure 6 shows stress distribution σ_z at the shrink fitting ratio $\delta/d = 3.0\times10^{-4}$. Figure 6(a) shows the stress due to shrink fitting σ_{zs} and Fig.6(b) shows maximum stress distribution $\sigma_{zmax}(=\sigma_{zs}+\sigma_{zb})$ due to load distribution w=100N/mm after shrink fitting. As shown in Fig.6, the maximum tensile stress at point B is 34.5 MPa while shrink fitting. It becomes 54.5 MPa by applying the distribution

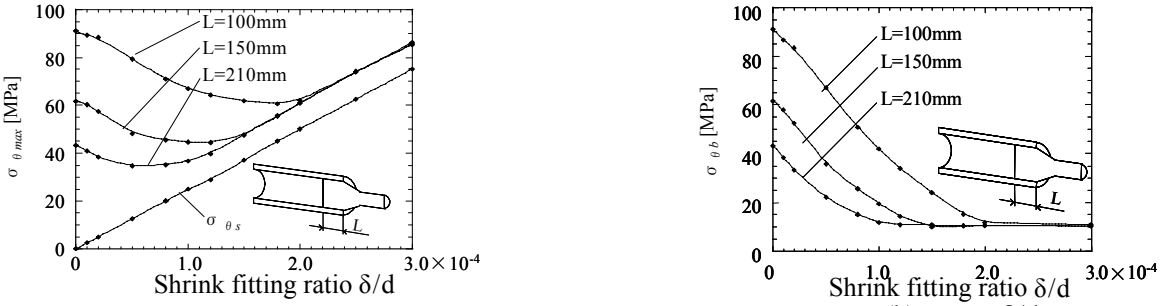

Fig.7 σ_θ vs. δ/d when L=100, 150, 210mm ($\sigma_{\theta s}$: Stress due to shrink fitting, $\sigma_{\theta b}$: Stress due to load distribution)

load after shrink fitting, that is, σ_{zb}=20.0 MPa.

It is found understood that the maximum tensile stress appears at point A as σ_θ. In this study we will focus on the maximum tensile stress σ_θ at A with varying geometrical conditions.

Effect of Shrink Fitting Ratio and Bending Moment upon the Maximum Tensile Stress $\sigma_{\theta max}$

Figure 7 shows effects of Shrink Fitting Ratio and Bending Moment upon the Maximum Tensile Stress $\sigma_{\theta max}$. Figure 7 (a) shows $\sigma_{\theta s}$ vs. δ/d and $\sigma_{\theta max}(=\sigma_{\theta s}+\sigma_{\theta b})$ vs. δ/d relations when the load distribution w=100N/mm is applied after shrink fitting. In Fig.7(b) shows $\sigma_{\theta b}$ vs. δ/d relations when the load distribution w=100N/mm applied. When shrink fitting ratio $\delta/d \geqq 2.0\times10^{-4}$, $\sigma_{\theta b}$ becomes constant and independent of δ/d. When $\delta/d \geqq 2.0\times10^{-4}$, the shafts and sleeve can be treated as a unit body.

The Effect of Fitted Length L on $\sigma_{\theta max}$ and $\sigma_{\theta b}$

If possible, small value of L is suitable for repairing and maintenance because the exchanges of the sleeve is easier for smaller L. Assume fitted length L=100mm, 150mm, 210mm. As shown in Fig.7 (a), $\sigma_{\theta s}$ is proportional to δ/d, and independent of L. When the fitted length L becomes smaller, $\sigma_{\theta max}$ increases. From Fig.7 (a), it is found that $\sigma_{\theta max}$ has a minimum value 60.5MPa at $\delta/d = 1.8\times10^{-4}$ when L=100mm. Similarly, it is found that the optimum shrink fitting ratio is $\delta/d = 1.2\times10^{-4}$ when L=150mm, and also $\delta/d = 5.0\times10^{-5}$ when L=210mm. When shrink fitting ratio $\delta/d \geqq 2.0\times10^{-4}$, $\sigma_{\theta b}$ becomes constant 10.5MPa independent of δ/d.

The Effect of Sleeve Materials on $\sigma_{\theta max}$ and $\sigma_{\theta b}$

Figure 8 shows $\sigma_{\theta max}$ vs. δ/d and $\sigma_{\theta b}$ vs. δ/d relations for different materials of conveying roller. As shown in Fig.8 (a), the maximum tensile stress of cemented carbide is larger than that of ceramics and steel because the Young's modulus E=500MPa is larger that the ones of ceramics and steel E=300MPa, E=210MPa.

The Effect Radius Curvature ρ on $\sigma_{\theta max}$ and $\sigma_{\theta b}$

Figure 9 shows $\sigma_{\theta max}$ vs. δ/d and $\sigma_{\theta b}$ vs. δ/d relations when the radius at the end of sleeve is changed as ρ=5, 10, 20, 30. From Fig.9(a), it is found that the maximum stress $\sigma_{\theta max}$ increases with decreasing the radius ρ. The stress $\sigma_{\theta b}$ becomes constant at the same value of δ/d independent of ρ.

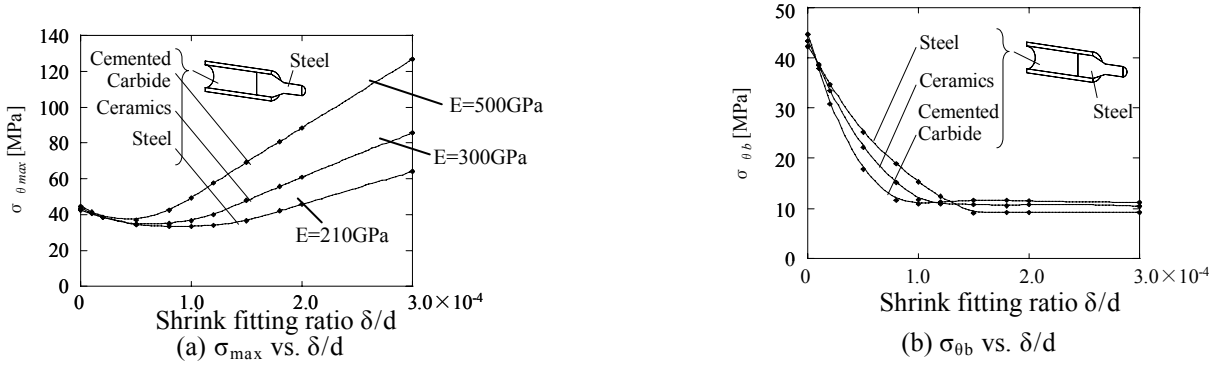

(a) σ_{max} vs. δ/d (b) $\sigma_{\theta b}$ vs. δ/d

Fig.8 σ_θ vs δ/d when Steel, Ceramics, Tungsten Carbide ($\sigma_{\theta max} = \sigma_{\theta s}+\sigma_{\theta b}$, $\sigma_{\theta s}$: Stress due to shrink fitting, $\sigma_{\theta b}$: Stress due to load distribution)

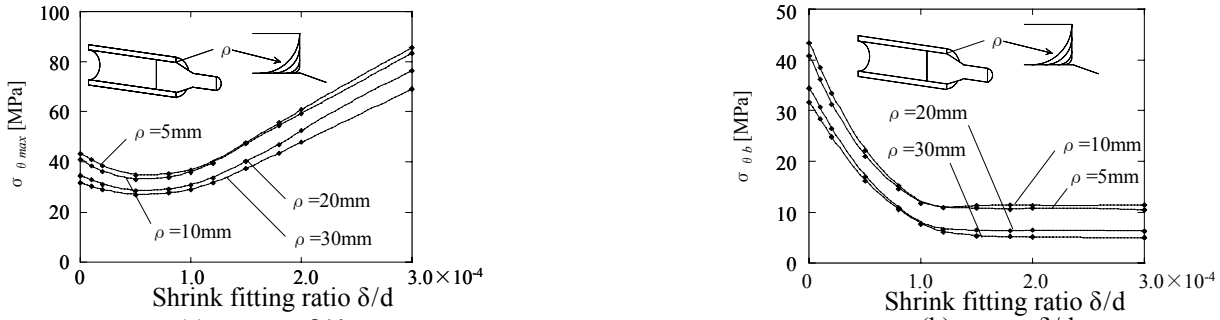

(a) σ_{max} vs. δ/d (b) $\sigma_{\theta b}$ vs. δ/d

Fig. 9 σ_θ vs δ/d when ρ=5, 10, 20, 30 ($\sigma_{\theta max} = \sigma_{\theta s}+\sigma_{\theta b}$, $\sigma_{\theta s}$: Stress due to shrink fitting, $\sigma_{\theta b}$: Stress due to load distribution)

Conclusions

Conveyed strips with high temperature induce wear on the roller surface in short periods and maintenance cost increases by exchange the rollers. In this study, a ceramics sleeve connected with short steel shafts at both ends is considered. Stress analysis was performed with the application of the finite element method and the effects of fitted length L, sleeve materials, radius curvature □ at the contact region were investigated. The conclusions can be made in the following way.

1. The value of maximum tensile stress is 85.6MPa when shrink fitting ratio $\delta/d = 3.0\times10^{-4}$ and the load w=100N/mm distribution is applied after shrink fitting.
2. When shrink fitting ratio $\delta/d \geqq 2.0\times10^{-4}$, $\sigma_{\theta b}$ becomes constant and independent of δ/d. When $\delta/d \geqq 2.0\times10^{-4}$, the shafts and sleeve can be treated as a unit body.
3. The maximum stress $\sigma_{\theta max}$ increases with decreasing the radius at the end of sleeve ρ. The stress $\sigma_{\theta b}$ becomes constant at the same value of δ/d independent of ρ.

References

[1] Miki, E., "High Corrosion Resistance and Cost Reduction by Spraying Methods", *Plant Engineer*, Vol.21, No.1 (1989), pp.8-12 (in Japanese).

[2] Iwata, T. and Mori, H., "Material Choice for Hot Run Table Roller", *Plant Engineer*, Vol.15, No.6 (1983), pp.55-59 (in Japanese).

[3] S. Harada, N. Noda, O. Uehara and M. Nagano, "Tensile strength of hot isostatic pressed silicon nitride and effect of specimen dimension", Journal of the Japan society of mechanical engineering, Vol.57, No.539 (1991).

[4] H. Kobayashi and T. Kawakubo, "Fatigue –Difference between ceramics and metal-", Journal of the Japan institute of metals, Vol.27, No.10 (1988).

[5] Editorial Committee of Ceramic Society of Japan, "Material properties of ceramics", pp.34-36 (1979), Ceramic Society of Japan.

Key Engineering Materials Vols. 385-387 (2008) pp 517-520
© (2008) Trans Tech Publications, Switzerland
doi:10.4028/www.scientific.net/KEM.385-387.517

A study of residual stresses in Al/SiC_p linear friction weldment by energy-dispersive neutron diffraction

Tea-Sung Jun[1, a], Fabio Rotundo[2, b], Lorella Ceschini[2, c], Alexander M. Korsunsky[1, d]

[1]Department of Engineering Science, University of Oxford, Parks Rd, Oxford OX1 3PJ, UK

[2]SMETEC, University of Bologna, Viale Risorgimento 4, I-40136 Bologna, Italy

[a]tea.jun@eng.ox.ac.uk, [b]fabio.rotundo@studio.unibo.it, [c]ceschini@bomet.fci.unibo.it, [d]alexander.korsunsky@eng.ox.ac.uk

Keywords: residual stress, linear friction welding, metal matrix composite, neutron diffraction, eigenstrain

Abstract. Linear friction welding (LFW) is a solid state joining process for bonding of two flat-edged, complex geometry components through relative reciprocating motion under axial (compressive) forces. Although the proof of principle has been obtained some time ago, recently a number of studies have been published aimed at optimising the joining operations to obtain best joint strength and reduced distortion and residual stress. The present paper is devoted to the study of linear friction welds between components made from aluminium alloy 2124 matrix composite (AMC) reinforced with 25vol% particulate silicon carbide (SiC_p). Neutron diffraction was used to measure interplanar lattice spacings in the matrix and reinforcement, and to deduce residual elastic strains and stresses as a function of distance from the bond line. Significant asymmetry is observed in the residual stress distribution within the two components being joined, that may be associated with the difference in the microstructure and texture.

Introduction

Aluminium matrix composites (AMCs) form a class of attractive light-weight materials possessing a good combination of high stiffness and strength. The incorporation of stiff and hard (usually ceramic) reinforcement in the form of fibres or particles leads to a significant increase in the overall elastic modulus. Strength is also improved due to a variety of mechanisms, including grain refinement, creation of additional obstacles to dislocation movement, etc. Based on these advantages over conventional base alloys, AMCs have recently been considered for application in aerospace, motor sport and automotive industries [1]. However, a significant limitation to industrial application of AMC's arises from the problems arising in conventional fusion welding methods, such as segregation and degradation of the reinforcement phase. Consequently, friction welding processes (friction stir welding or linear friction welding) is seen as a promising candidate for joining AMCs materials, since no melting is involved and the formation of brittle solidification products is reduced [2-3]. In the case of friction stir welding, additional difficulty arises because of the significant tool wear caused by the presence of highly abrasive ceramic particles within the bulk of material. In the case of linear friction welding, published studies of the process has been limited to components of relatively simple geometry, e.g. jet engine blades to discs.

Linear Friction Welding (LFW) is a solid state joining process in which the bonding of two flat edged, complex geometry components is completed with their relative reciprocating motion under axial compressive force. During the process, significant heat is generated by friction at the component interface, resulting in continued plastification and the displacement of plastically deformed material [4-5]. After fusion and cooling down from the processing temperature some misfit strains (eigenstrains) are generated, and the attendant process of elastic re-equilibration ultimately results in the generation of residual stresses.

Residual stresses in AMC's exist on a variety of scales, from microscopic (at the characteristic length scale of alloy crystallites and diameters of particles or fibres) to macroscopic, associated with the overall deformation and/or thermal history of the entire sample or component [6]. It is crucially important for industrial applications to develop improved understanding of these

residual stresses in order to modify and control them by deformation and thermal processing, and to be able to predict their performance in service.

Among a variety of residual stress measurements, neutron diffraction from pulsed sources provides a particularly attractive approach for truly non-destructive spatial mapping of residual elastic strains. Pulsed sources are particularly well-suited for energy-dispersive diffraction experiments due to the fact that the neutrons are created over a wide energy range, and their wavelength (energy) is easily determined by the time-of-flight (TOF) technique. Although LFW has seen significant development over the last decade, little or no data on residual stress characterisation has been published. Publications found in the literature focused in particular on joining of titanium alloys for application in the aircraft engine manufacturing industry [4]. In the present study residual stress measurements by neutron diffraction have been carried out on AMC linear friction weldments.

Experimental and data analysis

The material used in this research was an aluminium alloy matrix composite AMC225xe, high quality aerospace grade aluminium alloy reinforced with 25% by volume of ultra-fine particles of silicon carbide, manufactured by Aerospace Metal Composites Ltd (Farnborough, UK). The matrix material was aluminium alloy AA2124, with the nominal composition (in wt %): Cu – 3.8, Mn – 0.5, Mg – 1.4, Zn < 0.25, Al balance. Reinforcement consisted of fine (<3μm) particles of SiC. Composite was produced by the powder route consisting of mixing, followed by de-gassing and consolidation by hot iso-static pressing, and extrusion. The addition of finely dispersed reinforcement provides significant improvement in stiffness (E_{Al} = 73GPa, E_{SiC} = 415GPa, E_{comp} = 115GPa) and strength (composite σ_Y of 487MPa, UTS of 690MPa) without an appreciable change in density (ρ_{Al}=2.78gcm^{-3}, ρ_{SiC}=3.22gcm^{-3}).

Figure 1 illustrates the linear reciprocal motion of the welding process and dimensions of each component. Initial settings for the process corresponded to the amplitude of 2mm, frequency of 50Hz, the compressive welding force perpendicular to the weld line of 100kN and the burn-off of 2mm. The variation of welding parameters as a function of time is shown in Figure 2. The frictional heat generated by reciprocal motion under pressure softens the material in the vicinity of the weld interface, thus leading to plastification of the interface. Interface rubbing removes the oxide layer and creates fresh surfaces suitable for bonding, creating large extrusions known as “flash” of different shape depending on the material(s) being bonded and extruded. In the present linear friction welding process the total upset was 9.37mm. The heat affected zone extends from the bond line into the bulk of material.

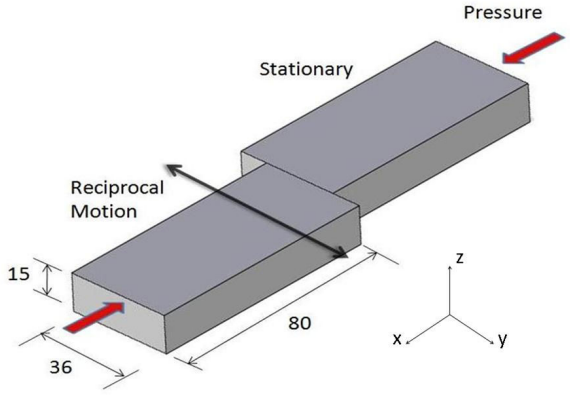

Fig. 1. Schematic of the linear friction welding process

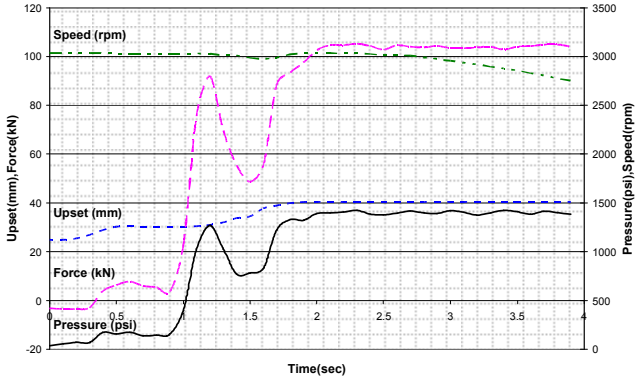

Fig. 2. Variation of the weld parameters with time

Neutron diffraction measurements were carried out on the ENGIN-X instrument (ISIS, Rutherford Appleton Laboratory, UK). Figures 3 and 4 show the schematic diagram of the ENGIN-X diffractometer and the illustration of the experimental setup, respectively. The diffraction patterns were collected as time-of-flight data by two detectors mounted perpendicularly to the incident beam. The results are converted into lattice *d*-spacing by combining the de Broglie’s equation ($\lambda = h/mv = ht/mL$) and Bragg’s equation ($\lambda = 2d_{hkl}\sin\theta_B$):

$$d_{hkl} = \frac{ht}{(2mL\sin\theta_B)}, \tag{1}$$

where $2\theta_B$ is the neutron scattering angle, d_{hkl} is the lattice spacing between the family of planes with *hkl* Miller indices, λ the neutron wavelength, *h* Planck's constant, *m* neutron mass, *L* the flight path, *t* the time-of-flight of the neutron and *v* its velocity. The elastic strain is determined from the change in the atomic interplanar distances d_{hkl}, as compared with the value d^0_{hkl} measured in the unstressed (or reference) condition, $\varepsilon_{hkl} = \left(d_{hkl} - d^0_{hkl}\right)/d^0_{hkl}$ [7]. In the absence of reference strain-free samples, the unstrained lattice parameters d^0_{hkl} were obtained from pattern collected by placing the beam at the very corner of the plate, which was assumed to carry no or little residual macroscopic strain. A different reference was used for each half of the component, due to the fact that different parts came from slightly different production routes. The reference at central point (x=0) was taken to be the average value of the two far-field references.

The data analysis was carried out on the entire diffraction spectra obtained at each measurement position, using the Open Genie software for the display and analysis of data from the neutron scattering instruments at the ISIS facility [8]. The stresses of Al and SiC in the component were computed using Hooke's low for triaxial stress, i.e.,

$$\sigma_{xx} = \frac{\mathrm{E}}{(1+\nu)(1-2\nu)}\left[(1-\nu)\varepsilon_{xx} + \nu\left(\varepsilon_{yy} + \varepsilon_{zz}\right)\right] \tag{2}$$

$$\sigma_{yy} = \frac{\mathrm{E}}{(1+\nu)(1-2\nu)}\left[(1-\nu)\varepsilon_{yy} + \nu\left(\varepsilon_{xx} + \varepsilon_{zz}\right)\right] \tag{3}$$

$$\sigma_{zz} = \frac{\mathrm{E}}{(1+\nu)(1-2\nu)}\left[(1-\nu)\varepsilon_{zz} + \nu\left(\varepsilon_{yy} + \varepsilon_{xx}\right)\right] \tag{4}$$

Finally, macroscopic residual stresses were computed using the rule of mixtures:

$$\sigma_{Macro} = f\sigma^{SiC}_{tot} + (1-f)\sigma^{Al}_{tot} = 0.25\sigma^{SiC}_{tot} + 0.75\sigma^{Al}_{tot} \tag{5}$$

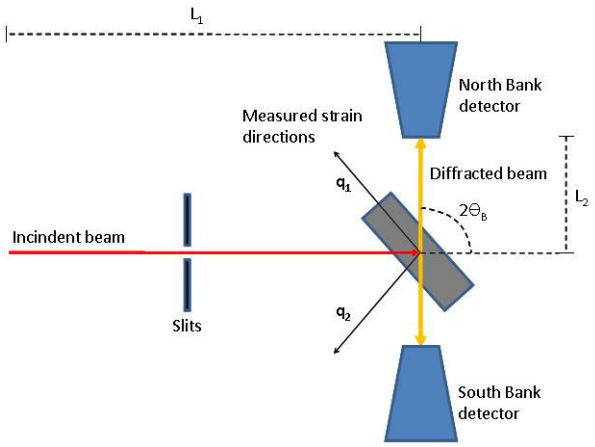

Fig. 3. Schematic of the ENGIN-X diffractometer at ISIS

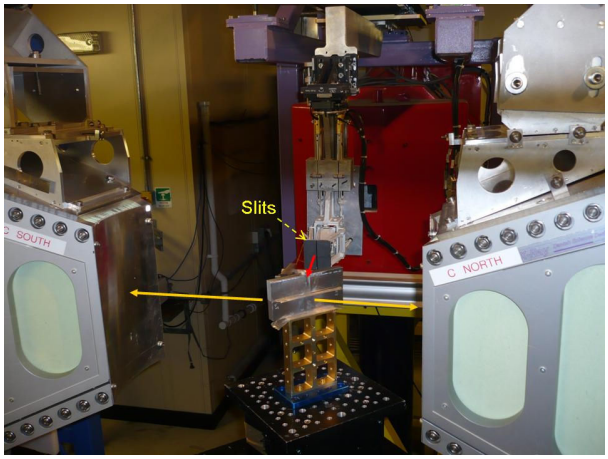

Fig. 4. Illustration of the experimental setup at ISIS

Results and discussion

Figure 5 and 6 shows the computed stress distributions as a function of the x position across the bond line for Al alloy matrix and SiC reinforcement respectively, for three components: x, normal to the bond plane (longitudinal), y, along the bond line (transverse), and z, through the thickness. Figure 7 shows the macroscopic residual stress variation computed using the rule-of-mixtures, equation (5). It is interesting to note that significant asymmetry of residual stress is observed across the bond line. It is surmised that this asymmetry may be associated with the presence of different texture in the two pieces being joined. Since aluminium alloy crystals possess a relatively low level of elastic anisotropy, the presence of texture has little effect on macroscopic strain computation from diffraction patterns. However, texture may be expected to exert significant influence over

plastic flow, resulting in different strength of the components being joined, that serves as the primary cause of residual stress asymmetry in weldments. Further experimental investigation of bulk texture is envisaged to verify this hypothesis.

Compared with previous LFW studies involving Ti [4] and Ni [9] alloys that have relatively higher thermal resistance, larger amounts of plastic flow are observed in Al-based materials. It is noted that *y*-strain is tensile in weld zone and compressive in the heat affected zone, while the spatial variation trend for the *z*-strain component is opposite to that for the *y*-strain.

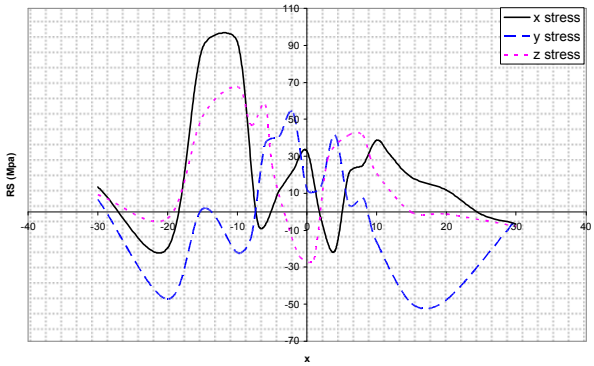

Fig. 5. Stress (Al) as a function of *x*-axis position

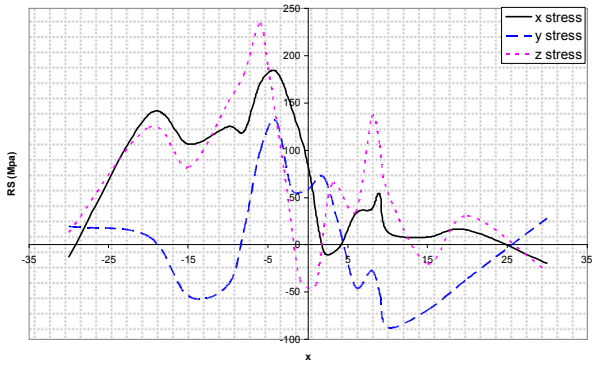

Fig. 6. Stress (SiC) as a function of *x*-axis position

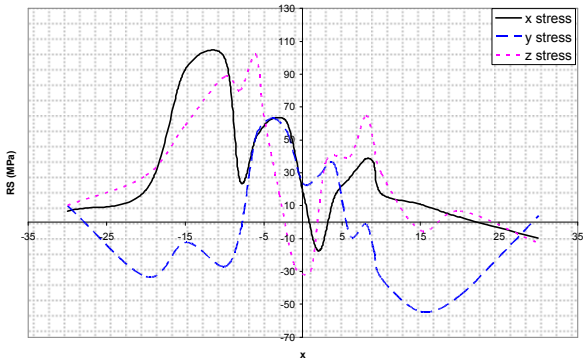

Fig. 7. Residual macroscopic stress (AlSiC) as a function of *x*-axis position

Conclusion

The study described in this paper was devoted to the analysis of residual stresses in linear friction weldments between aluminium alloy matrix – SiC particulate reinforced composite material. It has been demonstrated that neutron diffraction provides a powerful means of evaluating the residual stress variation around LFW joints. Modelling of macroscopic residual stress using inverse eigenstrain modelling should be carried out in order to improve process characterisation. The observed asymmetry of residual stress is likely to be associated with the difference in the microstructure and texture of the two components.

References

[1] S. Xu, S. Chardonnet, G. Savini, S.Y. Zhang, W.J.J. Voster and A.M. Korsunsky: Mater. Sci. Forum 571-572 (2008), p.277-282
[2] H. Uzun: Materials and Design 28 (2007) p.1440-1446
[3] J.A. Wert: Scripta Materialia 49(2003) p.607-612
[4] M.R. Daymond and N.W. Bonner: Physica B 325 (2003) p.130-137
[5] P. Wanjara, M. Jahazi: Metallurgical and Material Transactions A 36A (2005) p.2149-2164
[6] A.M. Korsunsky and K.E. Wells: Matls. Sci. Forum 321-323 (2000) p.218-223
[7] J.R. Santisteban, M.R. Daymond, J.A. James, L. Edwards: J. Appl. Cryst. 39 (2006) p.812-825
[8] F.A. Akeroyd, R.L. Ashworth, S.D. Johnston, J.M. Martin, C.M. Moreton-Smith and D.S. Sivia: OPEN GENIE User Manual
[9] M. Preuss, J. Quinta da Fonseca, A. Steuwer, L. Wang, P.J. Withers, S. Bray: J. Neutron Research 12(1-3) (2004) p.165-173

Key Engineering Materials Vols. 385-387 (2008) pp 521-524
© (2008) Trans Tech Publications, Switzerland
doi:10.4028/www.scientific.net/KEM.385-387.521

Mathematical Model for Compressive Stress-strain Curve of Recycled Aggregate Concrete

WANG Wei [1, a], YANG Lijun[2, b] and WANG Xiaoni[3, c]

[1] Department of Civil Engineering, Shaoxing College of Art and Science, Shaoxing, 312000, China

[2] Department of Civil Engineering, Shaoxing College of Art and Science, Shaoxing, 312000, China

[3] Zijin College, Nanjing University of Science and Technology, Nanjing 210046, China

[a] wellsking.wang@gmail.com, [b] lijunyoung@tom.com, [c] wangxiaoni@tom.com

Keywords: recycled aggregate concrete, stress, differential governing equation, strength.

Abstract. For the effective utilization of recycled aggregate concrete (RAC), it is necessary to correctly describe its compressive stress-strain curve (SSC) in theoretical and numerical analysis as well as engineering design of RAC structures. The objective of this study is to establish a good mathematical model for SSC of RAC. Based on energy dissipation theory, the differential governing equation of SSC is deduced and a new mathematical model is obtained. The new model can well describe both hardening type SSC and softening type SSC. It can overcome the shortcoming of the traditional model. Finally, good agreements have been found between the new model and the experimental investigations.

Introduction

Large quantities of crushed concrete and wasted concrete are produced annually in China and elsewhere in the world. Due to the scarcity of natural resources coupled with the increase in aggregate requirement for construction, the use of recycled aggregate to partially replace the virgin aggregate has become more common [1,2]. Therefore, recycling of waste concrete is beneficial and necessary from the viewpoint of environmental preservation and effective utilization of resources. To make this technology feasible, many experimental works have been engaged in the processing of demolished concrete, the mixture design, the physical and the mechanical properties as well as the durability aspects [3, 4]. The most important mechanical properties of RAC are the compressive strength, the tensile and the flexural strengths, the bond strength and the elastic modulus of such concrete [1]. In particular, the SSC model of RAC is especially significant in theoretical and numerical analysis as well as engineering design of RAC structures [5].

Most of the work on the SSC model of the RAC has focused on finding mathematical models with same shapes to experimental investigations [6,7], but theses models have no enough theory bases and have some limitations. So, good analytical expression for the SSC of RAC is desirable for the structural analysis and design in many practical engineering applications. The objective of this study is to construct a reasonable SSC model of the RAC based on energy dissipating theory. The results presented in this paper are significant to efficiently use the RAC in practical applications.

Traditional Exponent Model

According to the experimental results, Cheng and Xu has proposed a exponent model to describe relationship between the compressive strain, ε, and the compressive stress, σ, during compressive process of RAC. The model is written as

$$\sigma = A(1-e^{-B\varepsilon}) \tag{1}$$

Where A and B are two undetermined parameters. In Eq. 1 there is a limit to the compressive stress , $\sigma(\infty) = A$; while the strain is equal to zero, the initial compressive modulus, E(0)= AB.

Thus the two parameters A and B are directly related to the limiting compressive stress and the initial compressive modulus, respectively. However, many experimental investigations show that exponent model can well describe the hardening type SSC of RAC but can not describe the softening type SSC of RAC accurately. A good SSC model of RAC should be established according to theory bases and well describe both hardening type SSC and softening type SSC.

Establishing of New SSC Model

Under fixed mix proportion, replacing portion and solidification age, the compressive stress-strain behavior of RAC depends strongly on its compressive resistance energy which is closed to friction angle and cohesion force. In fact, the compressive fracture process of RAC can be considered as the dissipating process of compressive resistance energy. During the process, some particles of aggregate are rearranged from one place to another, which often gives rise to the softening type SSC of RAC. Establishing of the SSC model should take above analysis into accounted.

Basic postulates of new model. In the further study, following basic postulates are given to deduce the new SSC model of RAC.

(a) Under fixed mix proportion, replacing portion and solidification age, the compressive resistance energy of RAC, $U(\sigma)$, is changed with compressive stress, σ. At initial state, it is constant, denoted by $U(0)$.

(b) During compressive process, the dissipated compressive resistance energy is proportionate to compressive general stress, ϕ, and the general compressive modulus is proportionate to compressive general strain.

$$\Delta U(\phi) = k_1\phi; \quad \frac{d\phi}{d\varepsilon} = k_2(U(0) - \Delta U(\phi)) \tag{2}$$

where k_1 and k_2 are two parameters corresponding to mix proportion, replacing portion and solidification age. At initial state, $\varepsilon = 0$ and $\phi = 0$, so we can obtain

$$\phi = \frac{U(0)}{k_1}(1 - e^{-k_1 k_2 \varepsilon}) \tag{3}$$

$$\frac{d\phi}{d\varepsilon} = k_2 U(0) e^{-k_1 k_2 \varepsilon} \tag{4}$$

(c) During compressive process, the general stress, ϕ, can be divided into two parts. One part is stress for strain development and the other part is stress for particle rearrangement. They are denoted by σ and θ, respectively.

$$\phi = \sigma + \theta \tag{5}$$

(d) During compressive process, the ratio of the particle rearrangement stress increment to strain increment is proportionate to the stress for strain development.

$$\frac{d\theta}{d\varepsilon} = \beta\sigma \tag{6}$$

Differential governing equation of new model. Differentiating Eq. 5 with ε, we obtain

$$\frac{d\sigma}{d\varepsilon} = \frac{d\phi}{d\varepsilon} - \frac{d\theta}{d\varepsilon} \tag{7}$$

Substitute for Eq. 4 and Eq. 6 into Eq. 7, we get

$$\frac{d\sigma}{d\varepsilon} = k_2 U(0) e^{-k_1 k_2 \varepsilon} - \beta\sigma \tag{8}$$

Eq. 8 is the differential governing equation of new SSC model of RAC.

New SSC model. Integrating Eq. 8, the new SSC model of RAC is determined as

$$\sigma = \frac{k_2 U(0)}{\beta - k_1 k_2}(e^{-k_1 k_2 \varepsilon} - e^{-\beta\varepsilon}) \tag{9}$$

It is obvious that, whether $\beta > k_1 k_2$ or $\beta < k_1 k_2$, the value of σ is always positive. Following discussion is under the relationship that $\beta > k_1 k_2$. So we can simplify the Eq. 9 as

$$\sigma = s(e^{-\alpha\varepsilon} - e^{-\beta\varepsilon}) \tag{10}$$

Where $s = k_2 U(0)/(\beta - k_1 k_2)$, $\alpha = k_1 k_2$ and $\alpha < \beta$. All the parameters above mentioned are positive.

Mathematical Property of the New SSC Model of RAC

Peak point. Differentiating Eq. 10 with ε, we obtain its first order derivative

$$\frac{d\sigma}{d\varepsilon} = s(-\alpha e^{-\alpha\varepsilon} + \beta e^{-\beta\varepsilon}) \tag{11}$$

Let its first order derivative be zero, we can determine the corresponding strain ε^*

$$\varepsilon^* = \frac{\ln\beta - \ln\alpha}{\beta - \alpha} \tag{12}$$

Eq. 11 and Eq. 12 indicate that the curve of the new SSC model only has one peak point. Value of this peak point is on behalf of the compressive strength of RAC, denoted by f_c.

Inflection point. Differentiating Eq. 11 with ε, we obtain the second order derivative

$$\frac{d^2\sigma}{d\varepsilon^2} = \frac{s\alpha}{\beta - \alpha}(\alpha^2 e^{-\alpha\varepsilon} - \beta^2 e^{-\beta\varepsilon}) \tag{13}$$

Let the second order derivative be zero, we can determine the corresponding strain ε^{**}

$$\varepsilon^{**} = \frac{2\ln\beta - 2\ln\alpha}{\beta - \alpha} \tag{14}$$

Eq. 13 and Eq. 14 show that the curve of the new SSC model only has one inflection point.

Form Eq. 10, Eq. 12 and Eq. 14, we can make a conclusion that the new SSC model has dromedary shape, as shown in Fig. 1.

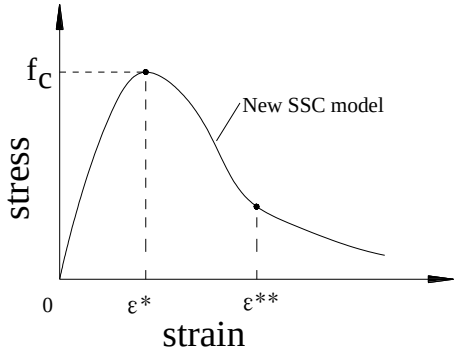

Fig. 1 Mathematical property of the new SSC model

If α is equal to zero, Eq. 10 can be rewritten as

$$\sigma = s(1 - e^{-\beta\varepsilon}) \tag{15}$$

Eq. 15 is equal to Eq. 1from mathematical angle, so the exponent model is one degraded type of the new SSC model of RAC. Because the Eq. 1 is for hardening type SSC and Fig. 1 is for softening type SSC, the new model of Eq. 10 can well describe both hardening type SSC and softening type SSC of RAC.

Comparison with Laboratory Tests

In order to verify the accuracy of the new SSC model, experimental study on RAC was conducted using laboratory. The fine aggregate used was river sand from Yangtze River, PR China. The used natural coarse aggregate was with 5-13 mm diameter. The used recycled coarse aggregate (7–17 mm accounting for 57%, and 17–25 mm accounting for 33% in weight) was obtained from the waste concrete brought from the concrete dike of Yangtze River. Two replacement percentages (RP) of coarse aggregate are designed, namely20% and 40%. The solidification age of tested RCA is 28 d.

In Fig. 2, comparisons between the experimentally investigated and the fitted SSCs provided by Eq. 10 are shown for different values of the replacement percentages. The fitted SSCs agree quite well with those investigated experimentally.

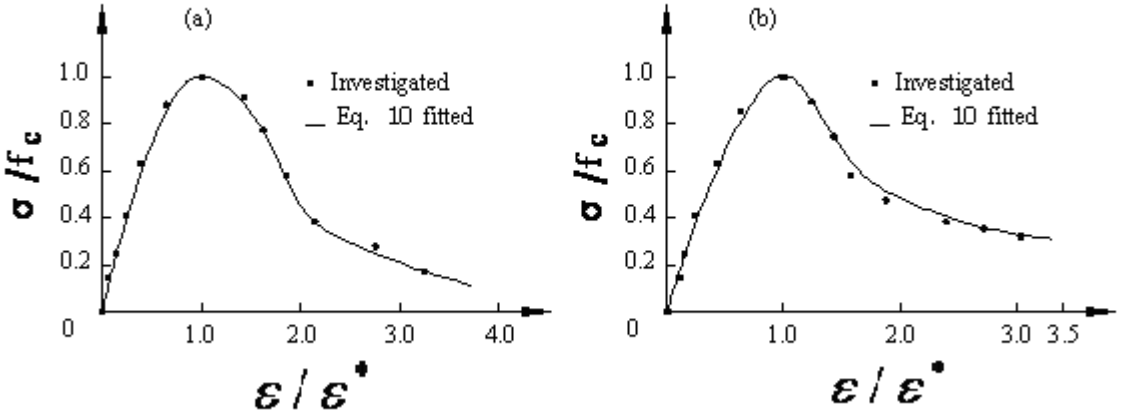

Fig. 2. Comparison of the normalized SSC of RCA. (a) . RP=20%; (b) RP=40%

Conclusions

Mathematical model for SSC of RAC is studied in details. The basic conclusions are as fellows:

(1) Exponent model of can describe the hardening type SSC of RAC but can not describe the softening type SSC of RAC accurately.

(2) A new SSC model of RAC is established and proposed based on energy dissipating theory. The proposed model has good mathematical behaviors and it can well describe both hardening type SSC and softening type SSC. The exponent model is one degraded type of it.

(3) The fitted results of the new proposed SSC model have the good agreements with laboratory investigations.

References

[1] J. M. Khatib: Cement Concrete Res. Vol. 35 (2005), p. 763
[2] J. Z. Xiao, J. B. Lia, Ch. Zhang: Cement Concrete Res. Vol. 35 (2005), p.1187
[3] J. S. Ryu: J. Mater. Sci. Lett. Vol. 21 (2002), p. 1565
[4] B. G. Fontebo, F. M. Abella: Constr. Build. Mater. Vol.21 (2007), p. 887
[5] W. Wang, B. X. Sun, T. H. Lu: Key Eng. Mat. Vol. 384-385 (2007), p. 881
[6] G. Y. Cheng: Concrete Vol. 19(2005), p.67
[7] W. Xu: Concrete Vol. 20(2006), p.45

Key Engineering Materials Vols. 385-387 (2008) pp 525-528
© (2008) Trans Tech Publications, Switzerland
doi:10.4028/www.scientific.net/KEM.385-387.525

Equivalent Stress Intensity Factor of Pre-Northridge Connections

Ding Lin[1,a], Liu Hongbo[1,2,b], Shao Yongsong[2,c] , Zhai Changhai[2,d]

[1] College of Civil Engineering and Architecture, Heilongjiang University, Harbin 150080, China

[2]School of Civil Engineering, Harbin Institute of Technology, Harbin 150001, China

[a]interdage@163.com, [b]HDLiuHB@yahoo.com.cn, [c]hitsys@163.com, [d]zch-hit@hit.edu.cn

Key words: fracture mechanics; finite element; steel frame; stress intensity factor

Abstract: The objective was to quantify the variation of stress intensity factor to weld root flaw sizes in steel frame connections. Finite-element analyses were used to study fracture toughness in welded beam-column connections. Investigations of fracture behavior mainly focused on the standard pre-Northridge connection geometry. Finite element analysis was performed using the ANSYS computer program. Stress intensity factor was calculated through a J-integral approach. The parametric study was conducted to quantify elastic fracture demands as a function of beam geometries. Results show that stress intensity factor is not uniform and is the largest in the middle of beam flange. The breadth of beam flange has primary effect on ratio of equivalent stress intensity factors to average. The ratio is nearly linear with the increase of the breadth, and it increases with the increase of breadth of beam flange.

Introduction

Following the 1994 Northridge earthquake, widespread damages were discovered in welded moment frames of steel buildings. Detailed inspections indicated that most of the structural damages occurred at the weld connections between the beam and column flanges [1]. In particular, the weld joints between the bottom beam flange and the column face suffered the most severe damage. Cracks were mostly initiated at the weld root and propagated with very little indication of plastic deformation. The desired plastic hinges were not formed in the weaker beam away from the weld joint. Instead, brittle weld fracture was identified as the dominant failure mechanism. In devising improved connection details and material toughness requirement, one needs an accurate means to determine fracture toughness demands in the connection. The other one is to quantify fracture toughness demands due to varied connection detail [2].

Since 1994, many studies have focused on investigating the load transfer characteristics of connections in steel frames and the potential sources of observed failures [3,4,5]. Liu Hongbo, etc.[6,7,8] performed extensive 3-D finite element analyses of the full joint using models with pre-existing cracks for seismic loading in recent years. Results showed that stress intensity factor is not uniform and is the largest in the middle of beam flange. The connection geometry was separately investigated in terms of the beam and column properties. Formulas for average stress intensity factors were deduced. These researches were based on the assumption of equal defect size. In fact, the weld root defect size generally varies across the flange width and is usually largest in bottom flange beneath the beam web where welding access is limited and weld passes terminate. So, the crack must propagate from the middle of bottom flange to the edge of bottom flange. Before the crack propagates to the edge of bottom flange, it is stable. On the contrary, after the crack propagates to the edge of bottom flange, it is unstable. When the crack propagates to the edge of bottom flange, stress intensity factors are all equal to fracture toughness across the flange. Equivalent stress intensity factors are defined if the defect size is equal to the critical crack size across the flange. This research focuses on variation of equivalent stress intensity factors as a function of average stress intensity factors. Finite element analysis is performed using the ANSYS computer program. Fracture toughness demands are evaluated in terms of the mode I stress intensity factor K_I. Stress intensity factor is calculated through a J-integral approach.

Finite element model

The geometries of the analysis configurations utilized in this research are derived from the geometry of Berkeley specimen SAC-PN3 tested during Phase I of the SAC Steel Project. The material properties are shown in Table 1. The weld defect size is designated as a_0 in Fig. 1. The elastic modulus and Posson's ratio are assumed as E=220,000MPa and ν=0.3. SAC-PN3 consisted of W36×150 beam connected to W14×257column (Fig. 2). This specimen had no doubler plates. The web was connected through a bolted shear tab with supplementary welding, and the flanges were joined using field groove welds. The flange welds were made by using the flux core arc welding procedure with E70-T4 electrodes.

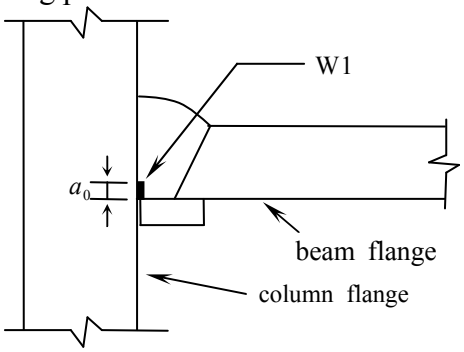

Fig. 1 Location most often defined for W1

Table 1 Material properties of SAC-PN3

Members		Grade	Yield stress (MPa)	Ultimate strength (MPa)
Column	Web	A572 Gr.50	310	525
	Flange		333	467
Beam	Web	A36	276	419
	Flange		345	396
Weld		E70T-4	415	495

The models are analyzed using ANSYS, as shown in Fig. 3. The finite element model utilized in this study is comprised of Solid45, Solid95, Targe170, Conta173 and Prets179. Solid45 is used for the 3-D modeling of solid structures. The element is defined by eight nodes having three degrees of freedom at each node. Solid45 has plasticity, creep, swelling, stress stiffening, large deflection and large strain capabilities. Solid95 is a higher order version of the 3-D 8-node solid element Solid45. It can tolerate irregular shapes without as much loss of accuracy. Contact problems are highly nonlinear and require significant computer resources to solve. Contact problems between shear tab and beam web are considered. Pretension problems of bolts are also considered [9].

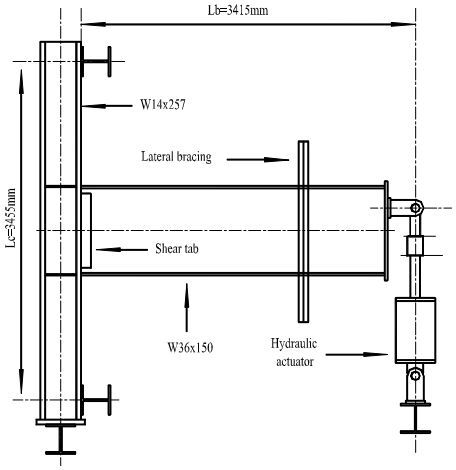

Fig.2 Test setup for specimen SAC-PN3

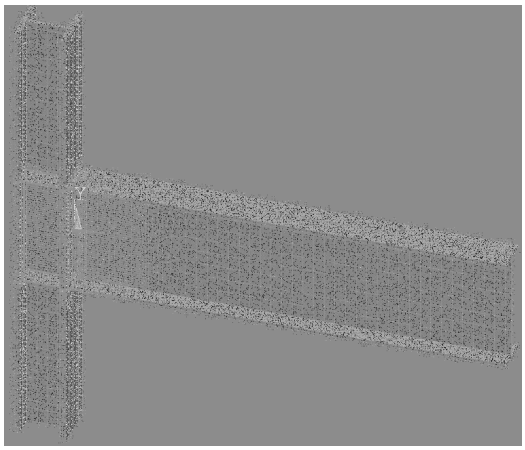

Fig. 3 Finite element model

Crack propagation

The finite-element method is used to simulate the crack propagation in bottom beam flange. The crack propagation is shown in Fig. 4, where K_I is average stress intensity factors. For defect size a_0 = 0 and material toughness of K_{IC}=66 $MPa\sqrt{m}$, the analyses predict initial fracture at K_I/σ_n =0.207. The fracture origin is at the middle of bottom flange.

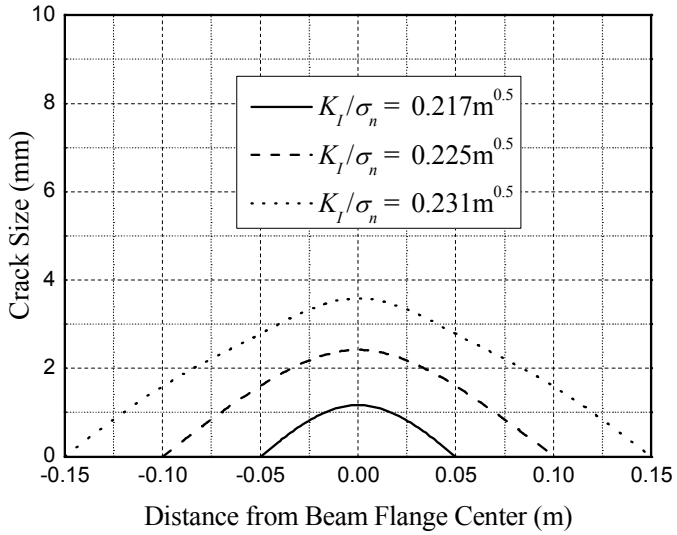

Fig. 4 Crack propagation

Variation in K_{Ieq} /K_I with breadth of beam flange

K_{Ieq} is calculated when the defect size is equal to the critical defect size across the flange, where K_{Ieq} is equivalent stress intensity factors. K_I is calculated when the defect size is all equal to 0 across the flange. The connection geometry is separately investigated in terms of the beam and column properties. Results show that the breadth of beam flange has primary effect on K_{Ieq}/K_I. Variation in K_{Ieq}/K_I with breadth of beam flange is shown in Fig. 5, where b_b is the breadth of beam flange. K_{Ieq}/K_I increases with the increase of depth of beam and width of beam. Other parameters have little effect on K_{Ieq}/K_I. Because of space limitation, this paper only includes breadth of beam flange. Base on the results shown in Fig. 4, the calibration equation for estimating the equivalent stress intensity factors for breadth of beam flange is proposed as Equation (1). Formulas for average stress intensity factors are deduced in paper [7]. Based on average stress intensity factors equations, equivalent stress intensity factors may be obtained.

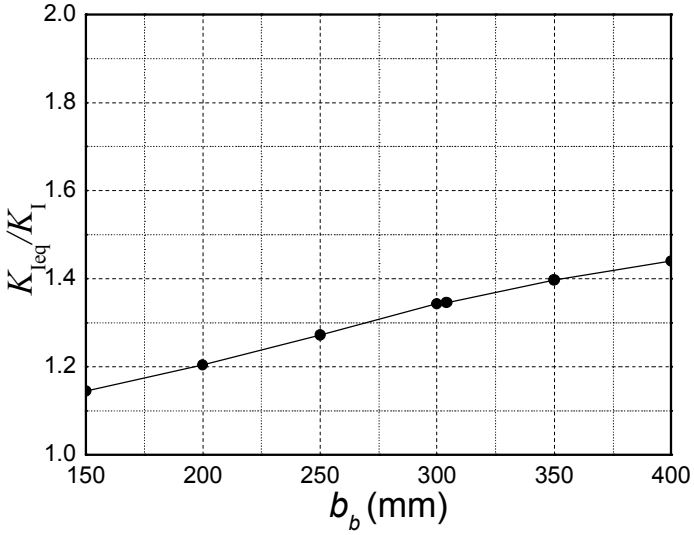

Fig. 5 Influence of breadth of beam flange on K_{Ieq}/K_I

$$\frac{K_{Ieq}}{K_I} = 1.027 + 0.41(b_b - 0.15), \qquad 0.15\,\text{m} \le b_b \le 0.4\,\text{m}. \tag{1}$$

Summary

A method that combined fracture mechanics and finite element is applied to study weld fracture in steel frame connections. The finite-element method is used to simulate the crack propagation in bottom beam flange. This research focuses on variation of equivalent stress intensity factors as a function of average stress intensity factors. Results show that the fracture origin is at the middle of bottom flange. The breadth of beam flange has primary effect on K_{Ieq}/K_I. K_{Ieq}/K_I increases with the increase of depth of beam and width of beam.

Acknowledges

The work presented in this paper is supported by National Natural Science Foundation of China (50538050) and Foundation of Heilongjiang Educational Committee (11521210).

References

[1] Terrence F. Paret.: Journal of structural engineering. Vol. 126(2000), P. 10

[2] Binnur G. K., Secil E.: Engineering Structures. Vol. 27(2005), P. 760

[3] Zhang J., Dong P.: Journal of structural engineering. Vol. 126(2000), P. 307

[4] Matos C. G., Dodds Jr.: Engineering structures. Vol. 23(2001), P. 1011

[5] Chi W. M., Gregory G. D., P. E.: Journal of structural engineering. Vol. 126(2000), P. 88

[6] Liu H. B., Zhai Z. H., Shao Y. S., Xie L. L.: Key Engineering Material. Vol. 325(2006), P. 1007

[7] Liu H. B., Xie L. L., Shao Y. S.: Journal of Zhejiang University. Vol. 41(2007), P. 40

[8] Liu H. B., Zhai Z. H., Shao Y. S., Xie L. L.: Key Engineering Material. Vol. 325(2006), P. 1007

[9] Zhao J. S.: Fracture mechanics and fracture physics (Huazhong University of Science and Technology Press 2003).

Key Engineering Materials Vols. 385-387 (2008) pp 529-532
© (2008) Trans Tech Publications, Switzerland
doi:10.4028/www.scientific.net/KEM.385-387.529

Fast Analytical Algorithm for Fatigue Crack Life Estimations of Integrally Stiffened Metallic Panels

Sascha Marc Häusler[1, a] and Peter Horst[1,b]

[1]Institute of Aircraft Design and Lightweight Structures, Technische Universität Braunschweig, Hermann-Blenk-Straße 35, D-38108 Braunschweig, Germany

[a] s.haeusler@tu-bs.de, [b] p.horst@tu-bs.de

Keywords: fatigue crack propagation, residual stresses, integral structures

Abstract. This work presents the enhancement of a pseudo-numerical tool for fatigue crack growth investigations on integrally stiffened metallic panels. The model is based on an analytical approach that demands compatibility of displacement between skin sheet and stiffener. Since the basis model was presented before, the focus of the present work is on the incorporation of residual stress effects in order to improve simulation results of welded panel configurations that are manufactured by laser beam welding or friction stir welding and exhibit a significant amount of residual stresses. The necessary input parameters for the developed residual stress module are determined from experimental residual stress field measurements. Simulation results using the presented approach are compared with results from finite element simulations on a two stringer panel which show the good accordance of the base model as well as the capability of the tool enhancements to account for the crack retarding effect caused by residual stresses.

Introduction

Increasing trends to utilise composite materials for fuselage structures of commercial aircrafts, intensify the competition for metallic structures. Innovative manufacturing technologies face this competition with potential advantages with respect to manufacturing time and costs and savings with respect to resulting structural weight. However, these benefits are opposed by the detrimental fatigue crack growth behaviour of integral structures which consequently requires more elaborate simulation methods compared to conventional riveted designs. With respect to innovative welding techniques like laser beam welding (LBW) and friction stir welding (FSW) an adequate consideration of residual stress effects is essential since these techniques introduce a significant amount of residual stresses into the structure which will influence the propagation behaviour of approaching cracks. A weight function approach is adopted to determine the stress intensity factor due to the presence of residual stresses which can be combined with the stress intensity factor resulting from global loading. An integrally stiffened two stringer panel is used to evaluate the implementation by result comparisons between the presented pseudo-numerical simulation tool and finite element simulations.

Simulation Model

The developed pseudo-numerical method enables fast estimations on the crack growth behaviour of integrally stiffened metallic panels and is based on analytical, two-dimensional approaches, originally developed for riveted structures by Swift [1] and Nishimura [2]. The developed method merges the features of both approaches and adapts them to the characteristics of integrally stiffened structures and was already presented in detail by the authors [3]. The present work will therefore focus on the latest model implementations which enable the consideration of residual stress effects on fatigue crack growth.

Implementation of Residual Stress Effects. The use of laser beam welding (LBW) and friction stir welding (FSW) introduces a significant amount of residual stresses into the stiffened panel which will influence the propagation behaviour of occurring cracks. Herein the analytical approach only considers the case of cracks perpendicularly approaching the stiffener. This scenario is highly relevant for damage tolerance investigations on stiffened panels and is primarily influenced by the longitudinal residual stress field along the welded stiffener. Following model implementations are consequently limited to this kind of residual stress.

Terada and Nakajima [4] and Tada and Paris [5] presented empirical formulations which are capable to characterise the longitudinal residual stress field along butt welds. Following [4] the stress intensity factor (SIF) for a perpendicular crack being located directly at the welding line can be determined using the following weight function

$$K_{res,\pm a} = \frac{1}{\sqrt{\pi a}} \int_{-a}^{+a} F_i(\xi) \frac{\sqrt{a \pm \xi}}{\sqrt{a \mp \xi}} d\xi \tag{1}$$

which can be evaluated using numerical integration available in [6]. $F_i(\xi)$ characterises the residual stress field that results from the welding process. For cases where the crack is located at a distance L away from the welding line the following adapted expressions for $F_i(\xi)$ are given in [4].

$$F_{Terada} = \sigma_0 \cdot e^{-0.5(\xi+L)^2} \left(1-(\xi+L)^2\right) \quad ; \quad F_{Tada} = \sigma_0 \frac{\left(1-(\xi+L)^2\right)}{\left(1+(\xi+L)^4\right)} \tag{2}$$

Since the residual stress field along a welded stringer is qualitatively comparable to the one resulting along a butt weld, the presented weight function approach represents a possibility to assess the stress intensity factors K_{res} for cracks within residual stress fields of welded stringer configurations. Superposition of K_{res} with the stress intensity factor K_{nom}, resulting from globally applied loads, gives the absolute stress intensity factor acting on the skin crack. Different crack growth laws (*Paris*, *Forman* and *NASGRO*) are available to determine the crack growth increment da/dN, which all use the stress intensity factor range ΔK and a varying number of additional parameters depending on the applied law.

$$\begin{aligned} \Delta K &= K_{max} - K_{min} = \left(K_{nom,max} + K_{res}\right) - \left(K_{nom,min} + K_{res}\right) \\ &= K_{nom,max} + K_{res} - K_{nom,min} - K_{res} = K_{nom,max} - K_{nom,min} \end{aligned} \tag{3}$$

$$R_{eff} = \frac{K_{min}}{K_{max}} = \frac{K_{nom,min} + K_{res}}{K_{nom,max} + K_{res}} \tag{4}$$

As can be seen from eq. 3 the use of ΔK is not sufficient to incorporate residual stresses into the crack growth calculation since K_{res} cancels out. Therefore the effective R-ratio R_{eff}, given in eq. 4, is required to account for residual stresses. Consequently the use of the above mentioned *Paris* law is not suitable here since it does not include the stress ratio R.

Integral two stringer panel

In order to validate the simulation model and the implemented residual stress module, simulation results for an integral two stringer panel, depicted in Fig. 1, are compared with results from finite element simulations of a detailed 3D solid model that uses degenerated quarter point elements (Barsoum type) to discretise the crack tip region (cmp. Fig. 1).

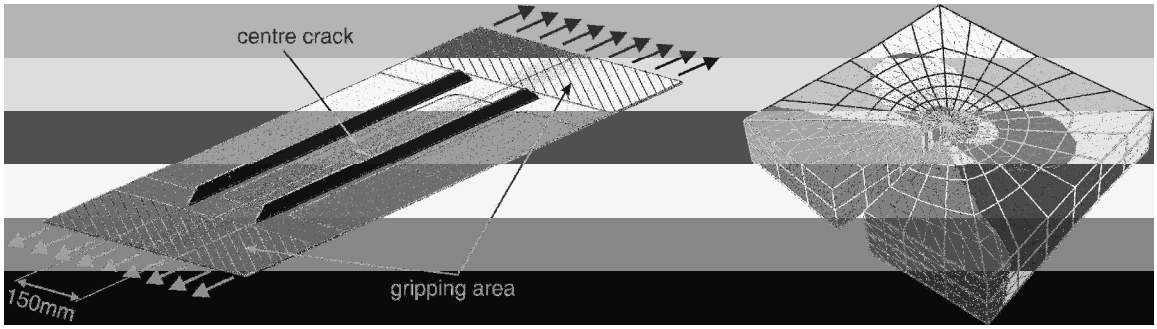

Figure 1: investigated two stringer panel (left) and FE representation of crack tip region (right)

Residual Stresses. The input parameters for the residual stress module are determined via curve fitting of experimentally determined residual stress fields. In Fig. 2 the longitudinal residual stress distributions for a LBW and FSW configuration of the two stringer panel are given. For each configuration the experimentally determined residual stress field and the best approximations using the above presented empirical approaches are shown, which yield the input parameters to be used for the residual stress module of the simulation tool.

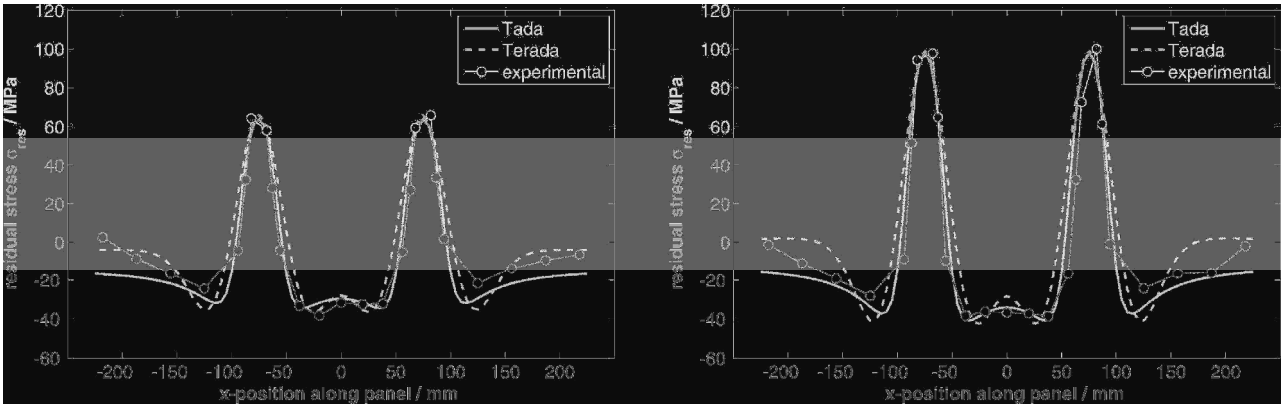

Figure 2: experimental and empirical residual stress fields for LBW (left) and FSW (right)

Result comparison. For evaluation purposes the results attained from the pseudo-numerical tool and the finite element model are compared. Whereas residual stresses are not included in the FE model, simulations for the presented simulation tool are performed with and without consideration of residual stress effects. Stress intensity factor (SIF) results and resulting crack growth curves are depicted in Fig. 3. The SIF solutions without residual stresses show good accordance between developed routine and finite element method for cracks approaching the stiffener ($a \leq 75mm$) with increasing deviations for the case of the cracking stiffener (branched crack in skin and stiffener) and the broken stiffener case. The deviations for the broken stiffener case can be attributed to the redistribution of load that occurs when the stiffener fails, which significantly perturbs the simulations.

The residual stress effect can be observed for the SIF solutions and the resulting crack growth curves. For crack lengths up to approximately $60mm$ the SIFs for the welded configurations are well below the configuration without residual stresses. For larger crack lengths this difference vanishes and the SIF solutions correlate. This can be explained by the residual stress field solutions in Fig. 2 which show a change from compressive to tensile residual stresses for both configurations at about $60mm$. As a consequence of the reduced SIFs, the resulting crack growth curves for the welded configurations clearly show a retardation effect with an increased number of bearable load cycles. An interesting observation is that the differences between the experimental residual stress

fields in Fig. 2, do not have such a significant influence on the resulting SIF solutions and crack growth curves.

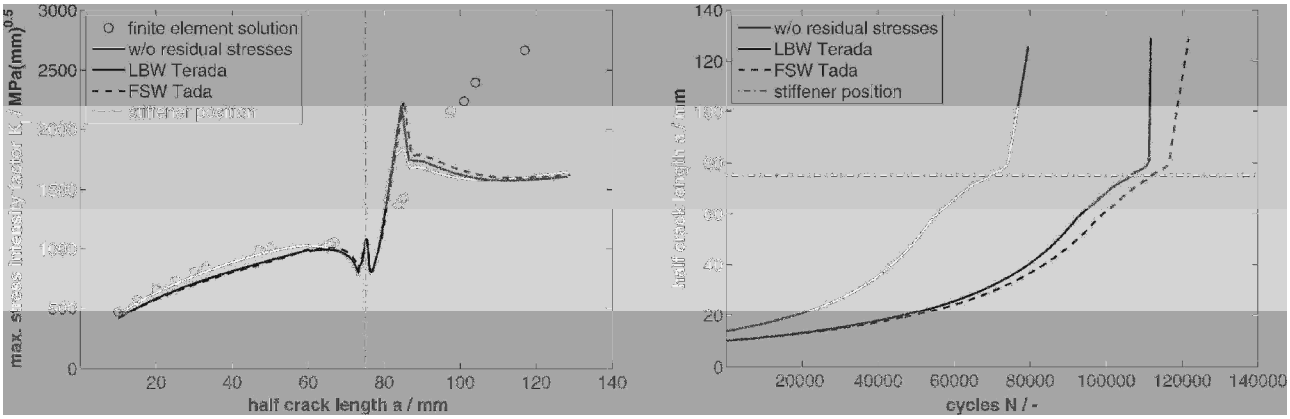

Figure 3: stress intensity factor solutions (left) and resulting fatigue crack growth curves (right)

Summary

A pseudo-numerical simulation tool was presented which enables fast estimations on the stress intensity factors and fatigue crack growth behaviour of integrally stiffened panels based on an analytical approach. Herein this work focuses on the latest enhancement of the tool which incorporates residual stress effects in order to improve crack growth estimations for welded configurations that exhibit a significant amount of residual stresses due to manufacturing. This is realised by using empirical formulations to assess the stress intensity factor for cracks in residual stress fields which are then combined with the SIF resulting from global loading. Simulation results for a two stringer panel were presented and show the good accordance of the base model with finite element solutions, as well as the crack retarding effects of residual stresses which can be simulated with the presented approach.

Acknowledgements

Parts of the presented work were developed within the project DaToN which is funded by the European Commission within the 6th Framework Program. The authors would also like to thank L. Lazzeri, A. Lanciotti and C. Polese for providing the experimental residual stress measurements which were recorded by them at the University of Pisa.

References

[1] T. Swift. Damage tolerance analysis of redundant structures. In *Fracture Mechanics Design Methodology, AGARD-LS-97*, 1979.

[2] T. Nishimura. Stress intensity factors for a cracked stiffened sheet with cracked stiffeners. *Journal of Engineering Materials and Technology*, 113:119–124, 1991.

[3] S. M. Häusler, A. D. Reim, and P. Horst. Fatigue crack growth - a challenge for new integrally stiffened aircraft structures. In *Proceedings of the 24th ICAF Symposium*, Naples, 2007.

[4] H. Terada and T. Nakajima. Analysis of stress intensity factor of a crack approaching welding bead. *International Journal of Fracture*, 27:83–90, 1985.

[5] H. Tada and P.C. Paris. The stress intensity factor for a crack perpendicular to the welding bead. *International Journal of Fracture*, 21:279–284, 1983.

[6] P. J. Davis and I. Polonsky. *Handbook of mathematical functions*, chapter 25, page 890. Dover Publications, Inc., New York, 1965.

Key Engineering Materials Vols. 385-387 (2008) pp 533-536
© (2008) Trans Tech Publications, Switzerland
doi:10.4028/www.scientific.net/KEM.385-387.533

Application of artificial neural network to forecast the tensile fatigue life of carbon material

Xiaoling Liao[a], Wenfeng Xu[b], Zhiqiang Gao[c]

Chemistry and Environment Science Department, Chongqing University of Arts and Sciences, Chongqing 402160, China

[a]zxc_228@163.com; [b]xwf_228@163.com; [c]gzq@cqwu.net

Keywords: Artificial neural network, carbon materials, tensile fatigue life, forecast

Abstract: Artificial neural network (ANN) is widely applied to the modeling of complex systems, which has become a common modeling method in the study of materials science. As the ideal candidates for high temperature structural materials, carbon materials are no doubt involved in fatigue loads, so the study on forecasting fatigue life is meaningful. In this paper, the electrical resistance at various fatigue cycles and level of applied stress of the materials under tensile fatigue loading has been detected, and regarded the fracture or fatigue cycles equal to 106 as fatigue life of carbon materials. On the basis of the electrical resistance value, the fatigue life has been forecasted by applied the ANN. The results indicated that the ANN could forecast the fatigue life of carbon materials well; finally, the applications of ANN in the study of material, such as properties prediction, damage prediction and failure detection were reviewed.

1. Introduction

Carbon materials have been considered as the most promising candidate for high temperature structural material for various purposes, duo to the high-temperature resistance. As preferred high-temperature structural materials, the potential applications for carbon materials are bound to involve fatigue loading. The fatigue loading can make carbon matrix prone to cracking, and these cracks may be the root of damage for any material. Therefore, there is a need for monitoring the condition or health of a carbon material structure while the structure is in use, in order to minimize hazards. This monitoring is conventionally conducted by acoustic emission, which is capable of detecting substantial cracking, but not slight crack. WANG and D. D. L mentioned using the increase in electrical resistivity as a measure of the irreversible carbon material damage, even extremely slight damage. So we may indirect monitor the evolution of structure damage for fatigued carbon materials composites by measuring the change of electrical resistivity.

At the same time, artificial neural network (ANN) is widely applied to the modeling of complex systems, and now it has become a common modeling method in the study of materials science, but the reports using ANN to forecast the fatigue life of material are few. In this paper, the electrical resistance at various fatigue cycles and level of applied stress of the composite under tensile fatigue loading has been detected, and regarded the fracture or fatigue cycles equal to 10^6 as fatigue life of carbon materials. On the basis of the electrical resistance value, the fatigue life has been forecasted by applied the ANN.

2. Experimental methods

In this study, the carbon materials and the data of test measure provided by Research Center of Carbon/Carbon Composites (National Key Laboratory of Ultrahigh Temperature Composites, Northwestern Polytechnical University). For the carbon materials, the carbon fibers were braided into a rectangular strip (with width of 6.5mm and thickness of 3.5mm) as a reinforcement perform by a four-step method using 1K PAN based T-300 carbon fibers, in which the braided angle was 22° and the fiber volume fraction was 45%. The carbon materials were fabricated by an isothermal chemical vapor infiltration (CVI) process at temperatures from 900 to 1200°C in low vacuum (10^4 Pa), using propylene (C_3H_6) as the organic feed gas and nitrogen (N_2) as the diluent. Several densification cycles were carried out until the density reached 1.72±0.03 g/cm^3.

The load-controlled fatigue tests were conducted with stress ratio R = 0.1 under ambient laboratory conditions in tensile and flexural mode, respectively. Loads on the specimen followed a sinusoidal waveform at frequency 10 Hz.

The specimens for the tensile fatigue or static tests were cut 100×6.5×3.5 mm^3 along the carbon fiber length direction. To avoid damage at the grip portions, aluminum tabs (thickness-1.0mm) were attached to the grip areas using an epoxy resin adhesive. The tensile fatigue loading direction was set parallel to the fiber length direction in the specimens. The fatigue tests were performed using a servo hydraulic Instron 8871 testing machine with an automated data-acquisition system.

The electrical resistance R was measured in the direction of the intertexture of fiber bundles with a four-probe method while cyclic and static test until failure was applied in the same direction. The four- probes consisted of two outer current probes and two inner voltage probes. The resistance R refers to the sample DC resistance between the inner probes. The two outer probe collets were nipped the samples with space between 20mm, as shown in Fig.1. The electrical resistances of un-fatigued samples were marked as the initialization, Ro, the electrical resistances of fatigued samples at various cycles, R, $\Delta R = R - Ro$.

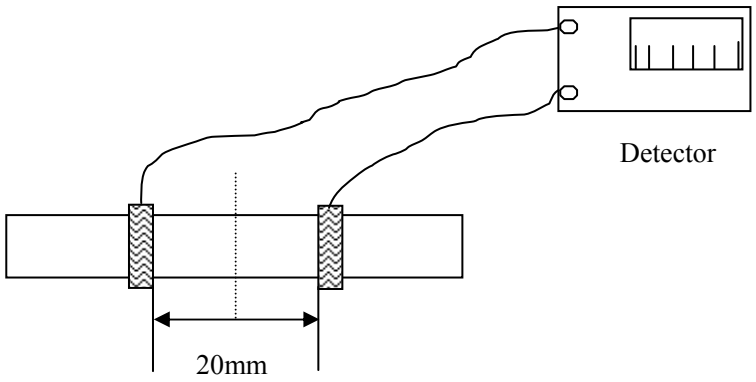

Fig.1 The schematic diagram of the measure in electrical resistance test

3. Forecast the tensile fatigue life

As we known, C/C composites are prepared by using carbon fibers or their basketwork as reinforced framework and pyrocarbon as matrix. The microstructures are very complex, and entirely differ from the metal materials. The fatigue damage modes and mechanism of fatigue for composites are diversiform, such as severe cracks and delamination of matrix, weakening of the fiber-matrix interface and the fracture of reinforced fibers, etc. Therefore, the conventional fatigue life forecast by accounting the spread speed of single crack was not applicable, and there is very

difficult for fatigue life forecast. But the ANN possess powerful abilities of character pick-up, mode identify and clustering, so it can been used to forecast the fatigue life by collecting the change of information (such as sound, frequency, electrical resistances) from whole or part of the composites, and training the ANN.

As we know, C/C composites consisted of carbon fibers, carbon matrix, remnant pores and interface between fiber and matrix. If we ignore the effect of pores, the C/C composites can looked as a parallel connection electrocircuit, the relation of total electrical resistance R of C/C and that of fiber, matrix and interface as following:

$$\frac{1}{R}=\frac{1}{R_f}+\frac{1}{R_m}+\frac{1}{R_i} \qquad (1)$$

The R_f, R_m and R_i represent the electrical resistance of fiber, matrix and interface, respectively, which changed with the change of microstructure of them, and then led to the change of total electrical resistance R of C/C. The change of $\Delta R/Ro$ was correlated to the irreversible damage extent of C/C composites during fatigue loading. So the damage extent of the C/C composites was to sense through changes in its DC electrical resistance after fatigue loading at various cycles and applied stress level.

The ANN is kinds of new information manage and account system, which has been developed by math abstracting, predigesting and imitating the structure and function of bio-nerve. It has is widely applied to the modeling of complex systems, and now it has become a common modeling method in the study of materials science due to its self-study, high tolerate fault function and high nonlinear characterization function. Especially, the error reverse transmit multilayer feedback network, the BP (Back-Propagation) network, the characteristic of BP network is showing in Fig.2:

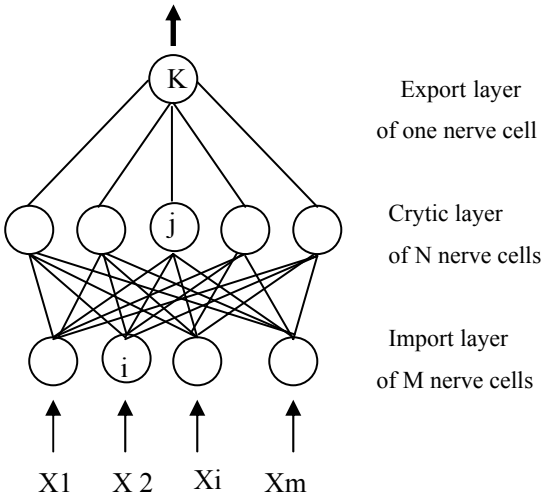

Fig.2 The sketch of BP-ANN

1) The network makes up of three layers, the import layer is on the bottom, the crytic layer is in the middle and the export layer is on the top of the BP network, every layer contains multi-nerve cells, which connect with one another. 2) Nonlinear manage function of nerve cells can be come true by using the S model compress function:

$$f(x)=1/(1+e^{-x}) \qquad (2)$$

3)The method of training network introduces error reverse transmit, the study process is showing in Fig.3.

In the paper, the value of Δ R/Ro and applied stress looked as import layer, the fatigue cycle as export layer. The Fig.3 showed the results of network trainrecord by using the BP network to forecast the tensile fatigue life for C/C composites. It is clear that the fatigue life of C/C composites changed regularly with the value of Δ R/Ro and applied stress, and imple that ANN can apply to

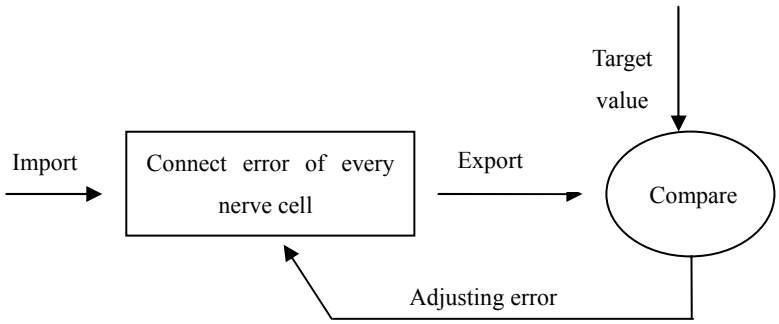

Fig.3 The study sketch of ANN

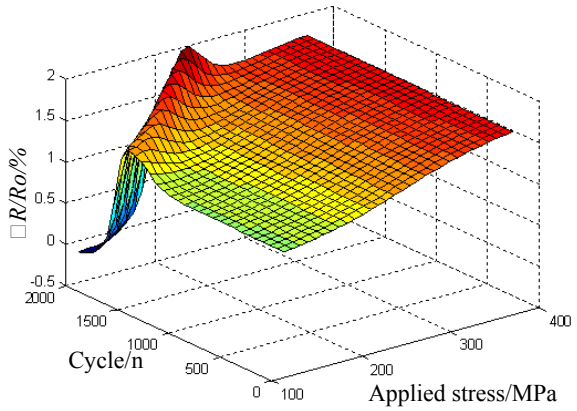

Fig.4 The network trainrecord of forecast

forecast the fatigue life of materials science. But the astringency of ANN need betterment, and the veracity of estimation can not predict, it will limit the application of ANN.

Acknowledgements

The research was supported by the Science and Technic Study Foundation of Chongqing municipal education commission of China under Grant No. KJ081205 and the Startup Foundation of Chongqing University of Arts and Sciences of China.

References

[1] Hejun Li, Xinghui Hou, Yixi Chen. Densification of unidirectional carbon/carbon composites by isothermal chemical vapor infiltration. Carbon, 2000, 38(3): 423-427.

[2] A Ozturk. The influence of cyclic fatigue damage on the fracture toughness of carbon/carbon composites.Compoties Part A, 1996, 27A:641-646

[3] Ken Goto, Hiroshi Hatta, Daisuke Katsu, Terufumi Machida.Tensile fatigue of a laminated carbon–carbon composite at room temperature. Carbon, 2003, (41): 1249-1255

[4] H Hatta, Y Kogo, T Tanimoto, T Morii. Static and fatigue fracture behavior of C/C composites. In: Proc of 4th Japan Int SAMPE Symposium, 1995:368-373.

[5] C Tallaron, D Rouby, P Reynaud, G Fantozzi. Improvement of cyclic fatigue analysis by the use of a tensile master curve in carbon/carbon composites. Key Eng Mater, 1999, 164-165:329-332

[6] Y Z Pappas, Markopoulos, V Kostopoulos.Failure mechanisms analysis of 2D carbon/carbon using acoustic emission monitoring, NDT & International, 2001, 31(3):157-163

[7] S Wang and D D L Cheng. Self-monitoring of strain and damage by a carbon-carbon composite.Carbon, 1997, 35(5):621-630

[8] Cai A H, Shun G X.The forecast of property of materials by using ANN. Foundry, 2003, 152 (4): 269-271

[9] Liu Y L, Zhong Q P, Zhang Z. The forecast of fatigue damage degree of aluminum alloy by using ANN.J of Aviation, 2001,22(2):135-139

[10] Valoor M T, Chandrashekhara K. A thick composite-beam model for delamination prediction by the use of neural networks. Composites Science and Technology, 2000, (60):1773-1779

[11] Qian Hancheng, Xia Bocai, Li Shangzheng, et al .Fuzzy neural network modeling of material properties. Journal of Materials Processing Technology, 2002,(122):196-200

Key Engineering Materials Vols. 385-387 (2008) pp 537-540
© (2008) Trans Tech Publications, Switzerland
doi:10.4028/www.scientific.net/KEM.385-387.537

Study on the Fatigue Behavior of Carbon/Carbon Composites

Xiaoling Liao[a], Wenfeng Xu[b], Zhiqiang Gao[c]

Chemistry and Environment Science Department, Chongqing University of Arts and Sciences, Chongqing 402160, China

[a]zxc_228@163.com; [b]xwf_228@163.com; [c]gzq@cqwu.net

Key words: carbon/carbon composites; fatigue behavior; fatigue mechanism

Abstract: As the ideal candidates for high temperature structural materials, carbon/carbon (C/C) composites are no doubt involved in fatigue loading. Therefore, the study on fatigue behavior is meaningful. In this paper, the research on fatigue behavior of C/C composites was reviewed and the characteristic of fatigue behavior was summarized. Some viewpoints for further investigations for the study on the fatigue behavior of C/C composites are also made in this paper.

1. Introduction

C/C composites have been considered as the most promising candidate for high temperature structural material for various purposes [1-3]. As preferred high-temperature structural materials, the potential applications for C/C composites are bound to involve fatigue loads. Therefore, a clear understanding of the behavior of these composites under fatigue loads is necessary. However, research studies on the fatigue behavior of C/C composites were still insufficient [4-6]. In particular, the evolution of microstructure in C/C composites under the fatigue loading is not well understood.

In the recent years, research studies on the fatigue behavior of C/C composites have been performed [7-14]; it is currently understood that fatigue limit of C/C composites is about 80-90% of the static tensile strength, and residual tensile strength after fatigue loads is not degraded from its original value, and is improved. However, the results of these studies were still few; these were insufficient to establish the design criteria for load-bearing structures. Thus, the usage of C/C composites was limited to heat resistant components of spacecraft, rocket nozzles and nuclear reactors, etc.

In present work, the research of fatigue behavior of C/C composites was reviewed and the characteristic of fatigue behavior was summarized. The positive effect of fatigue loading on the reinforcing behavior of fatigue was proposed as well, which could provide a basis for further studies on the fatigue mechanisms of C/C composites.

2. The fatigue behavior of C/C composites

The results of fatigue test showed: the fatigue limit of C/C composites can reach above 80% of the static strength, Ken Goto [6] had measured the fatigue limit of 2D C/C composites in tensile fatigue test, and the tensile fatigue limit was 210MPa, which was 91% of static tensile strength; Yasuhiro Tanabe [11] considered the bend fatigue limit of C/C composites as above 80% of static strength. It shows that C/C composites are provided with high fatigue properties, which indicate the long fatigue life, and it is one of welcome reasons for C/C composites.

Furthermore, researcher also find the singularity fatigue phenomenon: the fatigue loading not only did not reduce the strength of C/C composites, but also enhance the strength, and has the

notable enhancement effect, which was not explain by using fatigue theory of conventional material.

Han H M [16] reviewed the change of tensile strength of 3D C/C composites before the fatigue cycles of 6×10^4 by using the alternant test of fatigue tensile loading and static tensile, and compared the relationship curve of tensile loading and displacement, as shown in Fig.1. From seeing the Fig., it is clear that the tensile strength of C/C composites was enhanced with increasing in fatigue cycles, and the residual strength can increase 50% of original tensile strength when the cycles reach to 6×10^4. At the same time, the fatigue enhancement is not boundless for C/C composites, and that enhancement degree will appear degressive trend, it implies that the enhancement of strength has limit. Liao[15], Ozturk[3,7] and Ken Goto[6] also find the same fatigue enhancement phenomenon in the fatigue test of 2D C/C composites, and find the increase of residual tensile strength can reach to 117% of static strength. Yasuhiro Tanabe [11] measured the residual strength of C/C composites in bend model with the stress ratio of 0.8 and 0.9, and found the fatigue enhancement phenomenon, the bend strength reach to 250MPa, but the original strength is 235MPa. A. Ozturk [3,7] also found the fatigued samples did not fracture at the fatigue cycles up to10^4, the sample will can not fracture at the stress level.

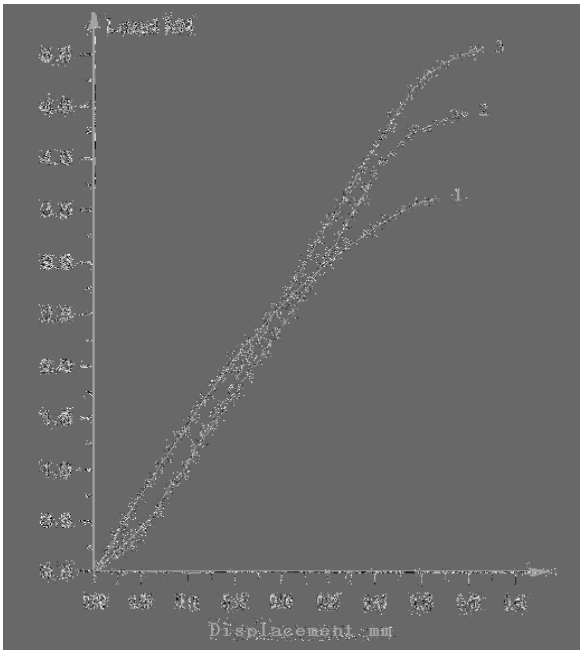

Fig.1 Effect of tension-tension cyclic loading on tensile load-displacement curve of 3D C/C

Curve 1: static tension of original sample; Curve 2: static tension after 3×10^4;

Based on the tensile strength of the carbon fiber used in C/C composites (about 2000 MPa), the simple rule of mixture predicts the tensile strength of the C/C to be 685MPa. However, the experimentally obtained tensile strength of C/C composites was about 200~400MPa, which was about 1/3 of the expected value. The main source of degradation of the tensile strength is considered to be the fiber damage caused by matrix cracking. This means that if the fibers can be protected from damage caused by matrix cracks, the tensile strength of C/C can be potentially increased. This protection might occur when the fiber damaged.

A.Ozturk[3,7], Ken Goto[6] found many cracks running along the interface of C/C composites after fatigue loading, but few interfacial cracks were observed in the original C/C. The strength-enhancing mechanism resulting from the cracks generated at the fiber–matrix interface is

illustrated in Fig. 2. As this figure shows, the matrix cracks can easily penetrate into the fibers in the original C/C due to its strong interfaces. On the other hand, the matrix cracks might be deflected in fatigued C/Cs when the cracks reach the interface, because of the damaged weak interface. Then, cracks should proceed along the interface as shown in Fig. 2(b).

The present authors [15] also found clear cracks between fiber bundles of fatigued 3D C/C composites and the phenomenon of delamination in interface and matrix of fatigued 2D C/C composites. In addition, the fracture fashion had been changed from brittle to ductile fracture pattern after fatigue loading. Observations of the fatigue-loaded specimens revealed that these fatigue behavior is related to weakening interface, which aroused by evolution of pores. The evolution of microstructure under fatigue loading must induce unusual fatigue behavior, and it is also reported that residual strength of C/C composites after fatigue loading is not degraded from its original value, and is improved, which is not discovered in other material.

Fig. 2 Schematic of the strength-enhancement mechanism involving the fiber-matrix interface cracks generated by fatigue loading

3. Summary

It has been accepted widely that C/C composites has high fatigue limit and fatigue enhancement function, but the study of fatigue behavior and enhancement mechanism were still insufficient, such as the fatigue behavior at the various fatigue cycles and stress level, and that the micro-structure of C/C composites is complex, C/C composites are made of the carbon fiber, carbon matrix, interface between fiber and matrix and pores. It is clear that the mechanism responsible for the fatigue behavior was insufficient, mainly due to the lack of information regarding changes in the microstructures induced by fatigue loads.

Acknowledgements

The research was supported by the Science and Technic Study Foundation of Chongqing municipal education commission of China under Grant No. KJ081205 and the Startup Foundation of Chongqing University of Arts and Sciences of China.

References

[1] Xianghui Hou, Hejun Li, Can Wang, Zhengang Zhu, Jian Shen. Internal friction behavior of carbon-carbon composites. Carbon, 2000, 38:2095-2101

[2] R. Si, G. Hu, H. Li, et al. Interfacial Microstructures of Intrabundle in as-Received Carbon/Carbon Composites Prepared by CVI. Carbon, 1998, 36(9): 1331

[3] A Ozturk. The influence of cyclic fatigue damage on the fracture toughness of carbon/carbon composites.Compoties Part A, 1996, 27A:641-646

[4] H Mahfuz, M Maniruzzaman, J Krishagopalan, A Haque, M Ismail, S Jeelani. Effects of stress ratio on fatigue life of carbon/carbon composites.Theoretical and Applied Fracture Mechanics, 1995, 24:21-31

[5] T Fend, J Goering. Strength and fatigue behavior of 2D-carbon/carbon composites under shear conditions. Ceram Trans, 1994, 46:165-76

[6] Ken Goto, Hiroshi Hatta, Daisuke Katsu, Terufumi Machida.Tensile fatigue of a laminated carbon–carbon composite at room temperature. Carbon, 2003, (41): 1249-1255

[7] A Ozturk, R E Moore. Tensile fatigue behaviour of tightly woven carbon/carbon composites. Composites, 1992, 23:39-46

[8] D Surya, Pandita, Ignaas Verpoest. Tension–tension fatigue behaviour of knitted fabric composites.Composits Structure, 2004, (64):199-209

[9] F Namiki, T W Chou. Tensile behavior of a quasi-isotropic carbon–carbon composite. J Am Ceram Soc, 1998, 81(1):113-120

[10] C Tallaron, D Rouby, P Reynaud, G Fantozzi. Improvement of cyclic fatigue analysis by the use of a tensile master curve in carbon/carbon composites. Key Eng Mater, 1999, 164-165:329-332

[11] Yasuhiro Tanabe, Takuya Yoshimura, et al. Fatigue of C/C composites in bending and shear modes. Carbon, 2004, (42):1-6

[12] A Ozturk, R E Moore. Tensile fatigue behavior of tightly woven carbon–carbon composites. Composites, 1992, 23:39-46

[14] O Siron, J Lamon. Damage and failure mechanisms of a 3D carbon/carbon composite under uniaxial tensile and shear loads. Acta Mater, 1998, 46(18): 6631-6643

[15] Xiao-Ling Liao, He-Jun Li, Ke-Zhi Li, Qian-Gang Fu. Effects of tensile fatigue cycle on the flexural strength of 3-D C/C composites, Carbon2005, Gyeongju, Korea, 2005.7

[16] Zhang Meizhong, Li Hejun, Li Kezhi. Progressing in the study on mechanical properties of 3D composites. Materials Engineering, 2004, 2:44-48

Key Engineering Materials Vols. 385-387 (2008) pp 541-544
© (2008) Trans Tech Publications, Switzerland
doi:10.4028/www.scientific.net/KEM.385-387.541

On the inclined surface crack terminating at the orthotropic bimaterial interface

Tomas Profant[1, a], Michal Kotoul[1,b]

[1] Institute of Solid Mechanics, Mechatronics and Biomechanics, Faculty of Mechanical Engineering, Brno University of Technology, Technická 2, 616 69, Brno, Czech Republic

[a]profant@fme.vutbr.cz, [b] kotoul@fme.vutbr.cz

Keywords: Inclined crack, bimaterial interface, matched asymptotic expansions, reciprocal theorem, finite element method.

Abstract. The evaluation of the stress singularities and generalised stress intensity factor (GSIF) for the case of an inclined surface crack terminating perpendicular to the interface between two orthotropic materials is considered. The knowledge of the regular and auxiliary solution allows evaluating the GSIF using the reciprocal theorem (Ψ-integral). A co-operating effect of a stronger and a weaker singular stress field for a crack impinging a bimaterial interface is investigated.

Introduction

The aim is to investigate a co-operating effect of a stronger and a weaker singular stress field for a crack impinging a bimaterial interface between two orthotropic materials. For many combinations of the materials and the impinging angle, the two modes of the singular stress field have unequal real exponents. The impinging crack may either penetrate across, or debond the interface. The concept of matched asymptotic expansions together with the contour integral based upon reciprocal theorem becomes very useful to derive the formula for the energy release rate in terms of the crack length l, the singularity exponent δ and the generalized stress intensity factors.

Analysis of crack tip singularity

The singular stress field of inclined crack impinging a bimaterial interface between two orthotropic materials is analyzed by means of continuously distributed edge dislocations technique for semi-infinite crack. It is assumed that the principal axes of both materials are aligned and the bimaterial interface is parallel or perpendicular to the principal axes. Since both of the materials' principal axes in the out of plane direction are assumed to be parallel with the z-axis, the anti-plane deformation can be decoupled from the in-plane deformation. Two coordinate systems are introduced: the primary coordinate system x_1,x_2,x_3 aligned with the material principal axes and the coordinate system x_1',x_2',x_3 rotated around the x_3 axis with x_2' coinciding with the inclined crack. For plane deformation, the elastic field can be represented in terms of complex potential functions $\Phi_1(z_1)$, $\Phi_2(z_2)$, $\Phi_3(z_3)$, each of which is holomorphic in its arguments $z_\alpha = x_1 + p_\alpha x_2$. Here, p_α are three distinct complex numbers with positive imaginary parts, which are obtained as the roots of the characteristic equation

$$\det\left[c_{i1k1} + p\left(c_{i1k2} + c_{i2k1}\right) + p^2 c_{i2k2}\right] = 0\,, \tag{1}$$

where c_{ijkl} is the tensor of elastic constants. With these holomorphic functions, the representation for the displacements u_i and stresses σ_{ij} is

$$u_i = 2\,\mathrm{Re}\left[\sum_{\alpha=1}^{3} A_{i\alpha}\Phi_\alpha\left(z_\alpha\right)\right],\quad \sigma_{2i} = 2\,\mathrm{Re}\left[\sum_{\alpha=1}^{3} L_{i\alpha}\Phi'_\alpha\left(z_\alpha\right)\right],\quad \sigma_{1i} = -2\,\mathrm{Re}\left[\sum_{\alpha=1}^{3} L_{i\alpha}p_\alpha\Phi'_\alpha\left(z_\alpha\right)\right]. \tag{2}$$

A and **L** are matrices given by $L_{i\alpha} = A_{k\alpha}\left(c_{i2k1} + p_\alpha c_{i2k2}\right)$, where $A_{k\alpha}$ denotes the eigenvector corresponding to the eigenvalue p_α above. The matrices and potential functions are expressed in the primary coordinate system. The asymptotic stress field near the crack tip is modelled as a continuous distribution of dislocations along the x_2'axis of the coordinate system connected to the crack with density function $f_k\left(x'_{2o}\right) = Hg_k\left(-x'_{2o}\right)^{\delta-1}$, $x'_{2o} < 0$, where δ is the stress singularity exponent, which is yet unknown, g_k are the components of corresponding eigenvector, and H is the generalized stress intensity factor (GSIF). The resulting eigenvalue problem can be written as follows

$$\mathbf{D}'(\delta)\mathbf{g} = 0, \text{where } D'_{ik}(\delta) = \sum_\alpha \sum_\beta L''^{II}_{i\alpha} G'_{\alpha\beta} \bar{M}'^{II}_{\beta k} \left(-\frac{\bar{p}'^{II}_\beta}{p'^{II}_\alpha}\right)^{-\delta} \csc\left(\pi(1-\delta)\right) - \delta_{ik}\cot\left(\pi(1-\delta)\right), \tag{3}$$

where superscripts I and II refer to the materials I and II respectively. All matrices and eigenvalues $p_{\alpha(\beta)}$ are expressed in the rotated coordinate system connected to the crack. Specifically,

$$\begin{aligned} &p'_{\alpha(\beta)} = \frac{p_{\alpha(\beta)}\cos\omega - \sin\omega}{p_{\alpha(\beta)}\sin\omega + \cos\omega},\ \mathbf{A}'=\mathbf{\Omega A},\ \mathbf{L}' = \mathbf{\Omega L},\ \mathbf{G}' = \mathbf{G} \text{ where} \\ &\mathbf{G} = -i\mathbf{M}^{II}\bar{\mathbf{H}}^{-1}\left(\bar{\mathbf{A}}^{II}\bar{\mathbf{M}}^{II} - \bar{\mathbf{A}}^{I}\bar{\mathbf{M}}^{I}\right)\bar{\mathbf{L}}^{II},\ \mathbf{H} = i\left(\mathbf{A}^{I}\mathbf{M}^{I} - \bar{\mathbf{A}}^{II}\bar{\mathbf{M}}^{II}\right),\ \mathbf{M} = \mathbf{L}^{-1},\ \mathbf{\Omega} = \begin{bmatrix} \cos\omega & \sin\omega \\ -\sin\omega & \cos\omega \end{bmatrix}, \end{aligned} \tag{4}$$

where ω is the angle formed by the crack and the interface normal. The parameter δ is calculated from the characteristic equation $\mathrm{Det}\left[\mathbf{D}'(\delta)\right] = 0$ and the eigenvector **g** is determined from Eq. (3) up to a multiplicative constant. For an inclined crack impinging a bimaterial interface there exist generally two exponents of singularity: the stronger singularity exponent denoted by δ_1 and the weaker singularity exponent denoted by δ_2. The corresponding displacement fields are $r^{\delta_1}\mathbf{u}_1(\theta)$ and $r^{\delta_2}\mathbf{u}_2(\theta)$, and the generalized stress intensity factors are denoted by H_1 and H_2 respectively. It can be proved that if δ is a root of Eq. (3), then -δ also verifies this equation.

Matched asymptotic analysis

Matched asymptotic procedure [1] is used to derive the change of potential energy. Consider a perturbation of the domain Ω with crack impinging the interface; the perturbation is a deflected (double) crack extension of length a_d or penetrating crack extension of length a_p with the small perturbation parameter τ defined as $\tau = a/L \ll 1$, where $a = a_d$ or a_p respectively, and L is the characteristic length of Ω. A second scale to the problem can be introduced, represented by the scaled-up coordinates $y = x/\tau$, or $(y_1, y_2) = (x_1/\tau, x_2/\tau)$ which provides a zoomed-in view into the region surrounding the crack. The displacement $\mathbf{U}^\tau$ of the perturbed elasticity problem due to the crack extension can now be expressed in terms of the regular coordinate x and the scaled-up coordinate y as $\mathbf{U}^\tau(x) = \mathbf{U}^\tau(\tau y) = \mathbf{V}^\tau(y)$, where the definition of the function $\mathbf{V}^\tau$ has been introduced, simply by a change of variable from x to y. Consider now the asymptotic expansion for $\mathbf{U}^\tau$ (which is also known as the ''outer expansion'') and for $\mathbf{V}^\tau$ (which is also known as the ''inner expansion''),

$$\mathbf{U}^\tau(x) = f_0(\tau)\mathcal{U}_0(x) + f_1(\tau)\mathcal{U}_1(x) + \ldots = \sum_{i=0}^{\infty} f_i(\tau)\mathcal{U}_i(x), \text{ outer expansion}, \tag{5}$$

where $\lim_{\tau\to 0} f_{i+1}(\tau)/f_i(\tau)=0,\ \ \forall i=1,2,...$ and $\{\mathcal{U}_1,\mathcal{U}_2,...\}$ form a set of linearly independent basis functions, and

$$\mathbf{V}^{\tau}(y)=F_0(\tau)\mathcal{V}_0(y)+F_1(\tau)\mathcal{V}_1(y)+...=\sum_{i=0}^{\infty}F_i(\tau)\mathcal{V}_i(y),\ \text{ inner expansion},\tag{6}$$

where $\lim_{\tau\to 0} F_{i+1}(\tau)/F_i(\tau)=0,\ \ \forall i=1,2,...$ and $\{\mathcal{V}_1,\mathcal{V}_2,...\}$ form a set of linearly independent basis functions. The basis functions $\{\mathcal{U}_i\}$ satisfy the elasticity problem on the same domain $\Omega\approx\Omega^{\tau}$ but with zero body force and with homogeneous boundary conditions. Asymptotic expansion for the primary inclined crack before the perturbation inception takes place reads

$$\mathbf{U}^0(x)=\mathbf{U}^0(0)+H_1r^{\delta_1}\mathbf{u}_1(\theta)+H_2r^{\delta_2}\mathbf{u}_2(\theta)+..\tag{7}$$

The outer expansion for the perturbed domain Ω^{τ} is

$$\mathbf{U}^{\tau}(x)=\mathbf{U}^0(x)+f_1(\tau)K_{1d(p)}r^{-\delta_1}\mathbf{u}_{-1}(\theta)+f_2(\tau)K_{2d(p)}r^{-\delta_2}\mathbf{u}_{-2}(\theta)+...\tag{8}$$

The inner expansion for the perturbed domain Ω^{τ} reads

$$\begin{aligned}&\mathbf{V}^{\tau}(y)=F_1(\tau)\left[\rho^{\delta_1}\mathbf{u}_1(\theta)+K_{1d(p)}\rho^{-\delta_1}\mathbf{u}_{-1}(\theta)+K_{2d(p)}\rho^{-\delta_2}\mathbf{u}_{-2}(\theta)+...\right]+F_2(\tau)\times\\&\times\left[\rho^{\delta_2}\mathbf{u}_2(\theta)+K'_{1d(p)}\rho^{-\delta_1}\mathbf{u}_{-1}(\theta)+K'_{2d(p)}\rho^{-\delta_2}\mathbf{u}_{-2}(\theta)+....\right]+...,\ \ (F_0(\tau)=1,\ \mathcal{V}_0(y)=\mathbf{U}^0(0)=0,\rho=\frac{r}{\tau}).\end{aligned}\tag{9}$$

The first terms in the brackets on the right-hand side of Eq.(9) describe the behaviour of functions $\mathcal{V}_i$ for $\rho\to\infty$. $\mathbf{u}_{-1}(\theta),\mathbf{u}_{-2}(\theta)$ are dual solutions to $\mathbf{u}_1(\theta),\mathbf{u}_2(\theta)$, see above.

In the absence of body forces the reciprocal theorem states that the following integral is path independent

$$\Psi(\mathbf{u},\mathbf{v})=\int_{\Gamma}\left[\sigma_{kl}(\mathbf{u})n_kv_l-\sigma_{kl}(\mathbf{v})n_ku_l\right]\mathrm{d}s,\ \ k,l=1,2,\tag{10}$$

where Γ is any contour surrounding the crack tip and **u**, **v** are two admissible displacement fields. If the following displacement fields are considered $\mathbf{u}=r^{\delta_i}\mathbf{u}_i(\theta),\ \ \mathbf{v}=r^{\delta_j}\mathbf{u}_j(\theta)$, one can show that the contour integral Ψ is equal to zero for $\delta_i \neq -\delta_j$ and non-zero if $\delta_i = -\delta_j$. Since the basis functions corresponding to the coefficients H_1, H_2 in the asymptotic expansion for $\mathbf{U}^{\tau}$ are $r^{\delta_1}\mathbf{u}_1(\theta),r^{\delta_2}\mathbf{u}_2(\theta)$, due to the former orthogonality conditions the GSIFs H_1 and H_2 can be computed as follows:

$$H_1=\frac{\Psi\left(\mathbf{U}^{\tau},r^{-\delta_1}\mathbf{u}_{-1}\right)}{\Psi\left(r^{\delta_1}\mathbf{u}_1,r^{-\delta_1}\mathbf{u}_{-1}\right)},\ H_2=\frac{\Psi\left(\mathbf{U}^{\tau},r^{-\delta_2}\mathbf{u}_{-2}\right)}{\Psi\left(r^{\delta_2}\mathbf{u}_2,r^{-\delta_2}\mathbf{u}_{-2}\right)}\ .\tag{11}$$

Since the exact solution $\mathbf{U}^{\tau}$ is not known, a finite element solution $\mathbf{U}^h$ can be used as an approximation for $\mathbf{U}^{\tau}$ so to obtain an approximation for H_1, H_2. The determination of the coefficients $K_{1d(p)},K_{2d(p)},K'_{1d(p)},K'_{2d(p)}$, proceeds in a similar fashion as for H_1, H_2. $K_{1d(p)},K_{2d(p)}$ are calculated in the inner domain whose remote boundary $\partial\Omega_{\text{in}}$ is subjected to the boundary condition $\mathbf{U}\big|_{\partial\Omega_{in}}=\rho^{\delta_1}\mathbf{u}_1(\theta)$

$$K_{1d(p)}=\frac{\Psi\left(\mathcal{V}_1^h(y),\rho^{\delta_1}\mathbf{u}_1\right)}{\Psi\left(\rho^{-\delta_1}\mathbf{u}_{-1},\rho^{\delta_1}\mathbf{u}_1\right)},\ K_{2d(p)}=\frac{\Psi\left(\mathcal{V}_1^h(y),\rho^{\delta_2}\mathbf{u}_2\right)}{\Psi\left(\rho^{-\delta_2}\mathbf{u}_{-2},\rho^{\delta_2}\mathbf{u}_2\right)},\ \mathcal{V}_1^h\text{-FEM approximation to }\mathbf{V}^\tau. \tag{12}$$

Similarly, the coefficients $K'_{1d(p)}, K'_{2d(p)}$ are calculated in the inner domain whose remote boundary $\partial\Omega_{\text{in}}$ is subjected to the boundary condition $\mathbf{U}\big|_{\partial\Omega_{in}}=\rho^{\delta_2}\mathbf{u}_2(\theta)$

$$K'_{1d(p)}=\frac{\Psi\left(\mathcal{V}_2^h(y),\rho^{\delta_1}\mathbf{u}_1\right)}{\Psi\left(\rho^{-\delta_1}\mathbf{u}_{-1},\rho^{\delta_1}\mathbf{u}_1\right)},\ K'_{2d(p)}=\frac{\Psi\left(\mathcal{V}_2^h(y),\rho^{\delta_2}\mathbf{u}_2\right)}{\Psi\left(\rho^{-\delta_2}\mathbf{u}_{-2},\rho^{\delta_2}\mathbf{u}_2\right)},\ \mathcal{V}_2^h-\text{FEM approximation to }\mathbf{V}^\tau. \tag{13}$$

$f_1(\tau), f_2(\tau), F_1(\tau), F_2(\tau)$ are found from the matching conditions of the outer and the inner asymptotic expansions. The incremental energy release rate (ERR) $G_{d(p)}$ is

$$\begin{aligned}
&G_{d(p)}=-\frac{\delta W}{\tau_{d(p)}L}=-\frac{W^\tau-W^0}{\tau_{d(p)}L}=-\frac{1}{2\tau_{d(p)}L}\int_\Gamma\left(\sigma_{kl}\left(\mathbf{U}^\tau\right)n_kU_l^0-\sigma_{kl}\left(\mathbf{U}^0\right)n_kU_l^\tau\right)ds=-\frac{1}{2\tau_{d(p)}L}\Psi\left(\mathbf{U}^\tau,\mathbf{U}^0\right)=\\
&=\frac{1}{2L}H_1^2K_{1d(p)}\tau_{d(p)}^{2\delta_1-1}\Psi\left(\rho^{\delta_1}\mathbf{u}_1(\theta),\rho^{-\delta_1}\mathbf{u}_{-1}(\theta)\right)+\frac{1}{2L}H_1H_2K'_{1d(p)}\tau_{d(p)}^{\delta_1+d_2-1}\Psi\left(\rho^{\delta_1}\mathbf{u}_1(\theta),\rho^{-\delta_1}\mathbf{u}_{-1}(\theta)\right)+\\
&+\frac{1}{2L}H_1H_2K_{2d(p)}\tau_{d(p)}^{\delta_1+d_2-1}\Psi\left(\rho^{\delta_2}\mathbf{u}_2(\theta),\rho^{-\delta_2}\mathbf{u}_{-2}(\theta)\right)+\frac{1}{2L}H_2^2K'_{2d(p)}\tau_{d(p)}^{2\delta_2-1}\Psi\left(\rho^{\delta_2}\mathbf{u}_2(\theta),\rho^{-\delta_2}\mathbf{u}_{-2}(\theta)\right)+..
\end{aligned} \tag{14}$$

where $\tau_{d(p)}=a_{d(p)}/L$. The ratio of the debonding to the penetrating ERR follows from Eq.(14) as

$$\begin{aligned}
&\frac{G_d}{G_p}=\frac{K_{1d}\Psi_1+\left(K'_{1d}\Psi_1+K_{2d}\Psi_2\right)\eta_d+K'_{2d}\Psi_2\eta_d^2}{K_{1p}\Psi_1+\left(K'_{1p}\Psi_1+K_{2p}\Psi_2\right)\eta_p+K'_{2p}\Psi_2\eta_p^2}\left(\frac{a_d}{a_p}\right)^{2\delta_1-1},\ \eta_d=\frac{H_2}{H_1}\left(\frac{a_d}{L}\right)^{\delta_2-\delta_1},\ \eta_p=\frac{H_2}{H_1}\left(\frac{a_p}{L}\right)^{\delta_2-\delta_1}\\
&\Psi_1\equiv\Psi\left(\rho^{\delta_1}\mathbf{u}_1(\theta),\rho^{-\delta_1}\mathbf{u}_{-1}(\theta)\right),\ \ \Psi_2\equiv\Psi\left(\rho^{\delta_2}\mathbf{u}_2(\theta),\rho^{-\delta_2}\mathbf{u}_{-2}(\theta)\right),
\end{aligned} \tag{15}$$

which corresponds to the relation obtained by authors [2] in different way, see their Eq. (18). An ERR based phase angle ψ_G for deflected crack is defined as

$$\begin{aligned}
&\tan^2\psi_G=\frac{G_{dII}(a_d)}{G_{dI}(a_d)}\ \text{ where }\ G_{dII}=-\frac{1}{2a_d}\int_\Gamma\left(\sigma_{kl}\left(\mathbf{U}^\tau\right)n_kt_lt_jU_j^0-\sigma_{kl}\left(\mathbf{U}^0\right)n_kt_lt_jU_j^\tau\right)ds,\\
&G_{dI}=-\frac{1}{2a_d}\int_\Gamma\left(\sigma_{kl}\left(\mathbf{U}^\tau\right)n_kn_ln_jU_j^0-\sigma_{kl}\left(\mathbf{U}^0\right)n_kn_ln_jU_j^\tau\right)ds,\ \ t_l\text{ - unit tangential vector of }\Gamma.
\end{aligned} \tag{16}$$

Note that the ERR and the SIF based measures of mode mixity for an interface crack, phase angle ψ_G and ψ_K, are related by

$$\cos(2\psi_G)=\sqrt{\frac{\sinh(2\pi\varepsilon)}{2\pi\varepsilon(1+4\varepsilon^2)}}\cos\left[2\psi_K+2\varepsilon\ln\frac{a_d}{2L}+\arg\left[\frac{\Gamma(1/2+i\varepsilon)}{\Gamma(1+i\varepsilon)}\right]-\arctan(2\varepsilon)\right],\ \varepsilon-\text{oscillation index}$$

References

[1] D. Leguillon, C. Lacroix and E. Martin: Int. J. Solids and Struct. 38 (2001), p. 7445.

[2] Z. Zang and Z. Suo: Int. J. Solids and Struct. 44 (2007), p. 4559.

Acknowledgments: The support through the grant GACR 106/06/0724 is gratefully acknowledged

Key Engineering Materials Vols. 385-387 (2008) pp 545-548
© (2008) Trans Tech Publications, Switzerland
doi:10.4028/www.scientific.net/KEM.385-387.545

Fatigue behavior of non-crimp fabrics

Peter Horst and Stephan Adden

Institute of Aircraft Design and Lightweight Structures

TU Braunschweig, Hermann-Blenk-Str. 35, D-38108 Braunschweig, Germany

p.horst@tu-bs.de

Keywords: Composite fatigue, Glass fibre, Experiments, Biaxiality

Abstract. The fatigue behavior of non-crimp-fabrics under different multi-axial loading conditions is presented, using a beneficial characteristic of the material, i.e. the fact that cracks may be detected by using an optical microscope. This allows to compare two different damage parameters, the crack density and the stiffness reduction over the life of the specimens.

Introduction

The fatigue behavior of non-crimp-fabrics (NCF) tube specimens under multiaxial loading is tested. Special emphasis is put on the development of damage parameters and the difference of these parameters under different loading conditions.

Non-crimp–fabrics (NCF) consist of several sub-layers with different orientations, all stitched together by a stitching yarn. The specimens used in the experiments are tube specimens made of E-Glass-fiber non-crimped-fabric and a common resin material using resin transfer moulding (RTM). The NCF has been provided by SAERTEX^{R} and consists of 4 sub-layers, whose lay-up can is given in TAB1. The sub-layers are tied together using a tricot-type of stitching. The material of the stitching yarn is PES (poly-ether-sulfone), with a mass per unit area of about 12g/m². The roving used during manufacturing of the NCF is OC111A from Owens-Corning. The resin/ hardener-combination used for manufacturing the specimens is L135i/ H137/ H134 from MGS, which has been certified by the Germanische Lloyd for use in wind-energy industry.

Experiments

The experimental work was performed with a servo-hydraulic testing machine MTS 319.25, which allows to apply tensional as well as torsional loading. The maximum forces that can be applied are ±250 kN in tension and compression and a torsional moment of ±2200 Nm. Because of the possibility to equip the machine with circular clamping supports this machine is capable of testing tube-specimens. All fatigue tests reported here were performed in a force-controlled manner under R=-1. Different biaxial loading ratios were introduced by using different ratios of tension force (introducing normal stress σ) and torsional moments (introducing shear stress τ). During the mechanical testing a so-called characterization step was followed by a fatigue step. In order to distinguish the different loading directions of the tube specimen a parameter β is introduced, which is the angle calculated by $\beta = atan(\tau/\sigma)$, i.e. $\beta = 0°$ means pure tension/compression and $\beta = 90°$ pure shear. Calculations were performed for the load ratios β=0°, 30°, 60° and 90°. For all load ratios three different load amplitudes were chosen on the basis of static test results. Three specimens were tested per load-amplitude.

As mentioned above, the crack density is one of the most interesting parameters, because it may be interpreted as a true internal state variable, which helps describing the material behavior. Due to the fact that the refraction index of fiber and resin are nearly similar, the material is, apart from the

stitching yarn, transparent, which allows monitoring the crack density by means of a light microscope. The fatigue tests were stopped after several steps; the specimen was taken out of the testing machine and observed per light microscope. Photos were taken over several (up to 15) different areas of the specimen which were used for the crack counting. All data presented here were derived after analyzing each area. Results are therefore average values, sometimes with additional standard deviation, from the different areas.

Experimental Results

This section shows a few results on the fatigue behaviour of the tube specimens. In Figure 1 the development of cracks in one tube specimen under pure shear loading is presented. Cracks are visibly developing. It is clear that cracks under 45° develop first in a considerable number, while cracks of other orientations are developing later. The axial, i.e. the 0°-direction is the horizontal direction in the photographs. It is easily possible to identify that certain cracks develop quite fast and do not extend over a certain size, while others seem to propagate as far as possible almost immediately. Although it is not possible to detect this in the almost transparent continuum, it is clear that the cracks occur in the layers of the same fibre orientation along or within the rovings. For more information on the experimental set-up, see [1, 2].

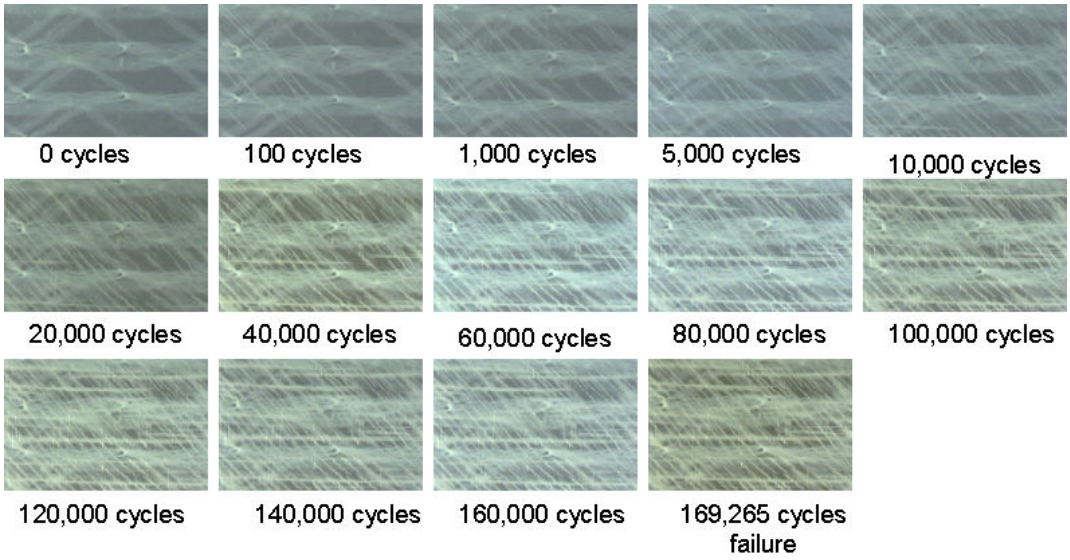

FIG1: crack development under pure shear fatigue loading

As stated already, it is now possible to count the number of cracks of different orientation, in order to define a damage parameter for each layer. In Figure 2 this is done without distinguishing between the sizes of the cracks. The crack densities are plotted versus the normalized life of the specimen. Just for comparison, Figure 3 shows the crack densities plotted versus the normalized life of a specimen under pure tension. The development of the cracks in Figure 3 is quite in line with observations found in composites, which are not NCFs under tension loading (see e.g. [3] for almost classical developments).

The other damage parameter, the stiffness degradation with respect to the Young's modulus is shown in Figure 4 for several loading directions β. The $\beta = 0°$ curve shows the typical behaviour of a rapid decrease of the Young's modulus in the first 10 – 15% again and, after something like 80 - 90% of the life, a further rapid decrease, which ends in the final failure. Between these two phases, there is a phase with a slow, almost linear decrease. A similar behaviour is visible in Figure 5 for the decrease of the shear modulus. The similarities between Figures 2 to Figure 5 suggest to look for a link between stiffness decrease and crack density as a first step, before trying to predict fatigue life itself. Finally we can see that the increase of the crack density and the decrease of the stiffness are different for different load ratios.

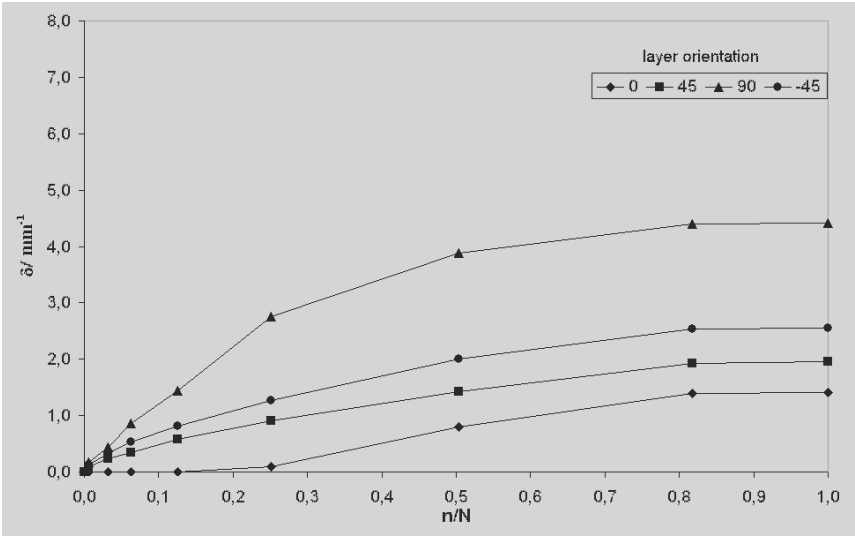

FIG2: crack densities of different orientation under pure shear loading

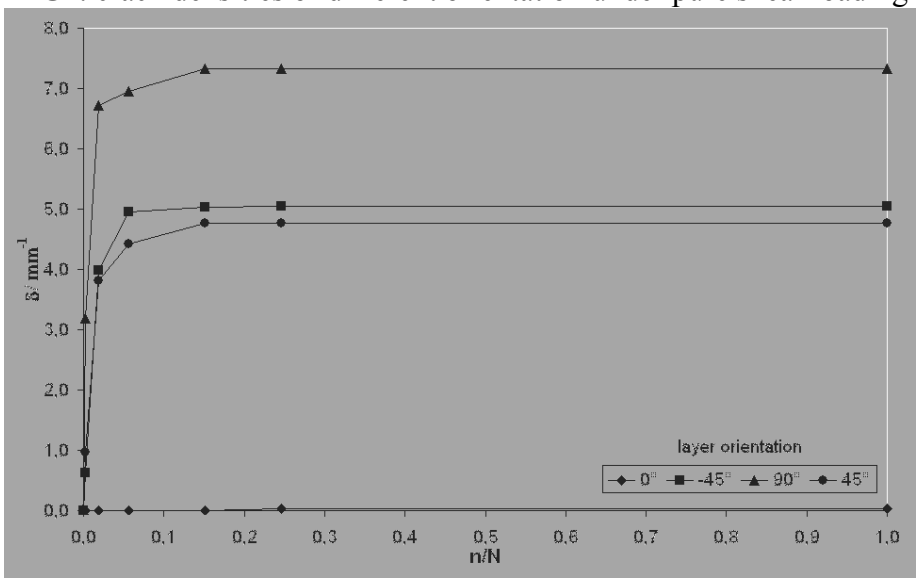

FIG3: crack densities of different orientation under pure tension loading

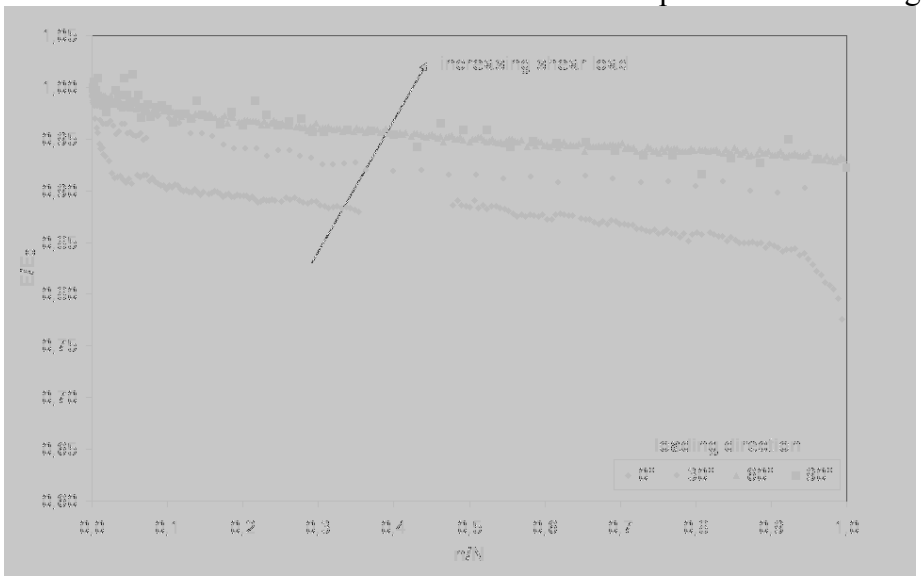

FIG4: Young's modulus versus normalized life for different loading directions β

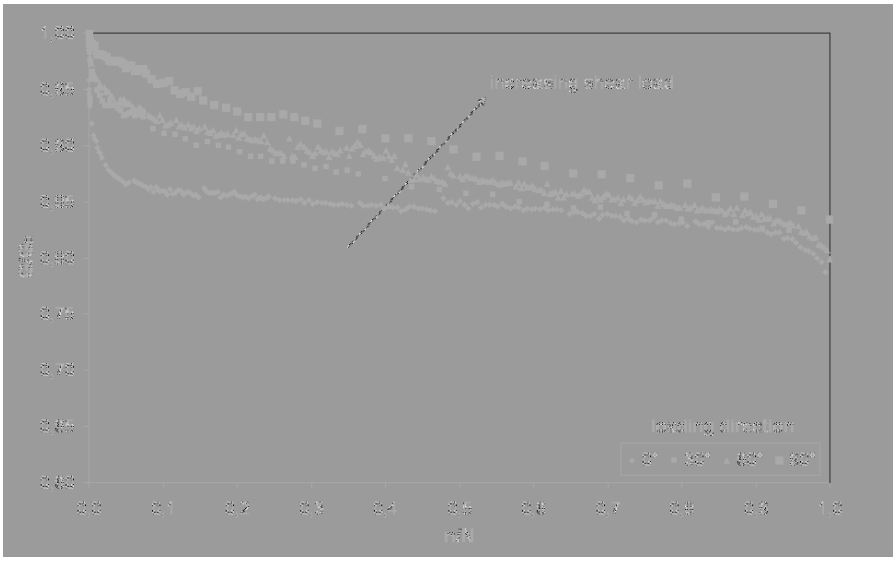

FIG5: Shear modulus versus normalized life for different loading directions β

SAERTEX V92402-01310-01270-000000	
Orientation	mass per unit area
0 [°]	638 [g/m²]
-45 [°]	301 [g/m²]
90 [°]	63 [g/m²]
45 [°]	301 [g/m²]

TAB1: Lay-up of the NCF

What is visible from Figures 4 and 5 is the fact that the development of the stiffness degradation is not exactly the same for all loading conditions. It therefore seems to be dangerous to conclude from measurements made under pure tension loading on the more realistic multi-axial loading. Both, slope of the degradation and life may be totally different.

Acknowledgement

The data presented here have been obtained in the frame of the German Research Foundation (DFG) Focus Project SPP1123 “Textile Composites” under the grant number HO2122/6-3

References

[1] S. Adden, P. Horst, “Damage propagation in non-crimp fabrics under bi-axial static and fatigue loading”, Composite Science and Technology, Vol. 66, pp. 626-633, 2006

[2] Adden, S., Horst, P., Fatigue in multiaxially loaded non-crimped fabrics, in revision: *Journal of Fatigue*, 2008

[3] Reifsnider, K.L., “Damage and Damage Mechanics”, in: “Fatigue of Composite Materials”, editor: K.L. Reifsnider, pp. 11-77, Elsevier, 1991

Key Engineering Materials Vols. 385-387 (2008) pp 549-552
© (2008) Trans Tech Publications, Switzerland
doi:10.4028/www.scientific.net/KEM.385-387.549

Fatigue Analysis on a Full Scale Fuselage Panel

Alfonso Apicella[1,a], Enrico Armentani[2,b], Stefano Priore[2,c]

[1]Alenia Finmeccanica, Viale dell'Aeronautica, 80038 Pomigliano d'Arco, Naples, Italy

[2]Department of Industrial Design and Management, University of Naples, P.le Tecchio 80, 80125 Naples, Italy

[a]aapicella@aeronautica.alenia.it, [b]enrico.armentani@unina.it, [c]stefano.priore@inwind.it

Keywords: fatigue test, full scale panel, Sines criterion

Abstract. Fatigue test on a full scale panel with complex loading and geometry has been carried out using a tri-axial test machine specifically designed, built and located in the laboratory of the University of Naples. The aeronautical test panel was designed and manufactured by Alenia. The demonstrator is made up of two skins which are linked by a transversal butt-joint that is parallel to the stringer direction. A fatigue load was applied in the direction normal to the longitudinal joint, while a constant load was applied in the longitudinal joint direction. The demonstrator broke up after about 177000 cycles. Subsequently, a finite element analysis was carried out in order to correlate failure events; due to the biaxial nature of the fatigue loads, Sines criterion was used. The analysis was performed taking into account the different materials of which the panel is composed. The output shows good correlation between experimental data and numerical results, predicting the location on the panel exactly where the failure occurred.

Introduction

The Sines criterion is a common method of evaluation of the fatigue life of a structure [1] and is widely used provided that structural load conditions respect two main assumptions:

- the structure is subject to alternating proportional loads,
- the directions of the principal stresses are fixed during the application of the loads.

The criterion was developed on the basis of an extensive collection of experimental data. It linearly relates the octahedral shear stress of the alternating component of the principal stresses to the fatigue strength for uniaxial alternating load by means of the sum of the mean component of the principal stresses. Thus, defining

$$\sigma_S = \sqrt{\sigma_{1a}^2 + \sigma_{2a}^2 + \sigma_{3a}^2 - \sigma_{1a}\sigma_{2a} - \sigma_{2a}\sigma_{3a} - \sigma_{3a}\sigma_{1a}}\,,$$

the Sines criterion is:

$$\sigma_S + k\left(\sigma_{1m} + \sigma_{2m} + \sigma_{3m}\right) \le \frac{\sigma_{fa}}{n} \quad \text{with}$$

$$k = \frac{\sigma_{fa} - \sigma_{fp}}{\sigma_{fp}} = \tan\alpha \quad \text{where:}$$

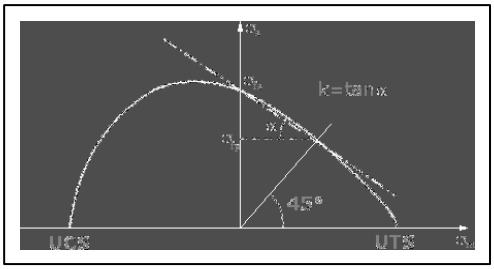

Fig. 1 - Definition of k on the Haigh diagram

k is a coefficient which depends on the material and may be computed using the corresponding Haigh diagram as in Fig. 1.

$\sigma_{(1,2,3)a}$ are the principal stresses of the alternate part of the load,

$\sigma_{(1,2,3)m}$ are the principal stresses of the mean part of the load,

σ_{fa} is the fatigue strength for alternating load,

σ_{fp} is the fatigue strength for pulsating load,

n is a safety factor.

If the fatigue limit for pulsating loads is not available, it is acceptable to determine it by using the modified Goodman linearized law. Experimental research on the full scale panel was carried out using the tri-axial test machine located at the University of Naples [2]. A fatigue test on the full scale panel has shown that the panel breaks after 177000 cycles at the middle-lower bay, near the third frame (Fig. 2) [3].

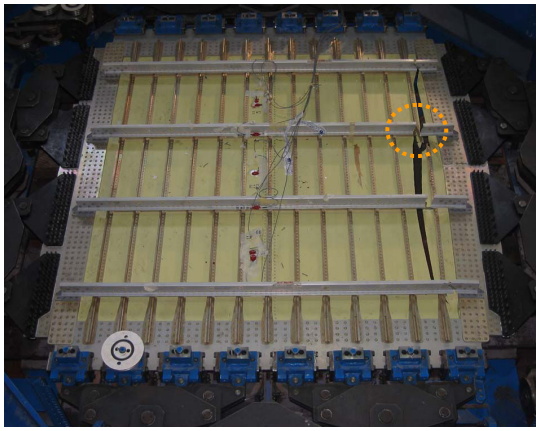

Fig. 2 - Broken panel after 177000 cycles

Finite Element Model

Finite elements analysis of the demonstrator was performed using ANSYS commercial code. The complete model is made of 64432 elements and 205664 nodes (Fig. 3). The SHELL91 element was used to model the skins, the stringers and the other components of the panel; two material models (Al2024 T3 and Al7075 T6) and fifteen different sets of "real constants" were employed to simulate the different thicknesses of the panel. The presence of the rivets was taken into account when defining the proper number and location of constraint points (CP).

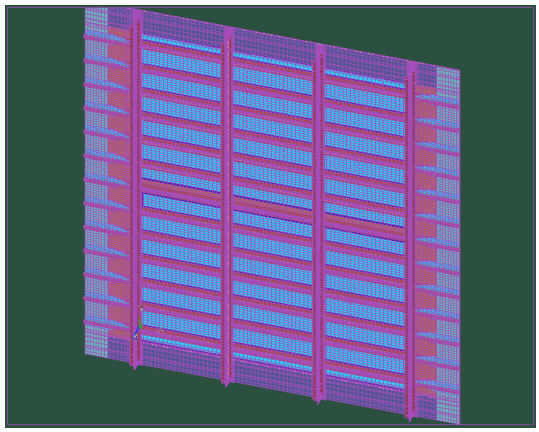

Fig. 3 - FE model of the panel

The algorithm ran four times: in each run, the aforementioned fatigue strengths were set to evaluate a fatigue life respectively of 10^4, 10^5, 10^6 and 10^7 cycles. A fifth run was performed at the failure cycle number (177000). The fatigue strengths were collected from the Haigh diagrams for the considered materials (Fig. 4). Table 1 summarizes the fatigue limits that define the Haigh diagram for each number of cycles.

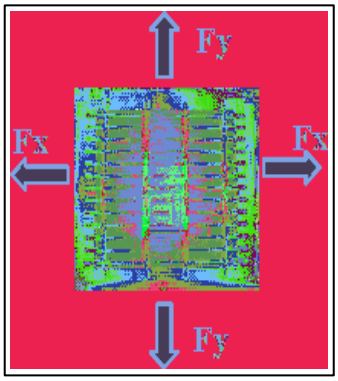

Fig. 5 - Loading scheme of the panel

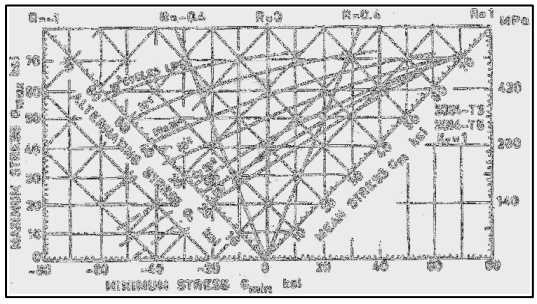

Fig. 4 - Haigh diagram of AL2024 T3 [4]

The panel was loaded by a constant traction force (F_x) of 200 kN along the stringers' direction and an alternating sinusoidal force varying between 2.4 kN and 400 kN along the frames' direction (F_y) (Fig. 5), with a frequency of 1 Hz. The static analysis previously performed showed a good correlation between numerical and experimental results [3].

Tab. 1 - Fatigue properties of the materials

	10^4 Cycles		10^5 Cycles		$1.77 \cdot 10^5$ Cycles		10^6 Cycles		10^7 Cycles	
	σ_{fa} [MPa]	σ_{fp} [MPa]	σ_{fa} [MPa]	σ_{fp} [MPa]	σ_{fa} [MPa]	σ_{fp} [MPa]	σ_{fa} [MPa]	σ_{fp} [MPa]	σ_{fa} [MPa]	σ_{fp} [MPa]
Al2024 T3	341	214	238	166	225	162	162	124	138	110
Al7075 T6	345	286	222	224	236	183	179	172	155	145

Results

The ratio $\rho = \left[\sigma_S + k\left(\sigma_{1m} + \sigma_{2m} + \sigma_{3m}\right)\right] \Big/ \frac{\sigma_{fa}}{n}$ ($n = 1$ is assumed) is calculated and mapped upon the structure: values equal or greater than 1 are indicative of critical points; the higher the value, the higher the possibility of failure. Values less than 1 are typical of locations that are not critical fatigue-wise.

The resulting contour plots present a consistent pattern, showing that the highest Sines ratio is always located at the bottom of the panel (marked by a circle), near the third frame, on the rear side. As shown in Fig. 6, there are no critical points after 10000 cycles (ρ_{max} = 0.8); critical zones begin to appear just before 100000 cycles (ρ_{max} = 1.015) (Fig. 7). The extension of the critical zones increases at the locations near the lower bay, extending along the lower stringer. As the number of cycles goes up, more zones interested by the fatigue crisis appear on the left side of the panel (Fig. 8, 9, 10). At 177000 cycles (Fig. 8) numerical results predict panel failure at an applied load level 1.033 times the experimental one.

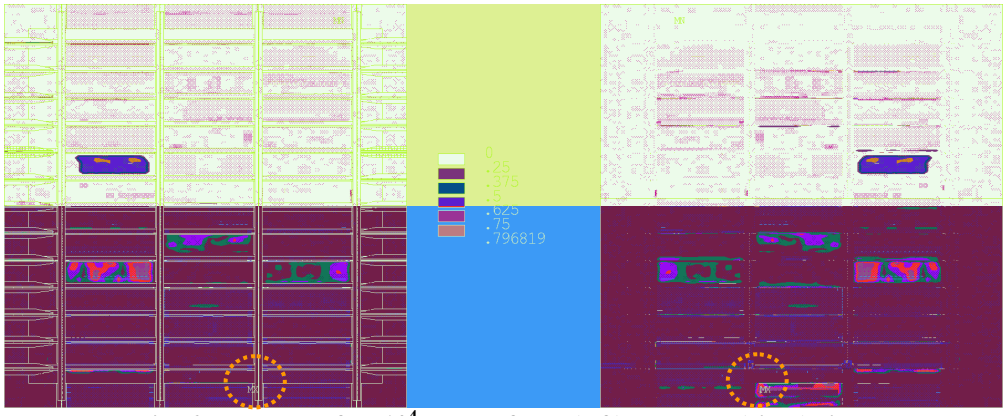

Fig. 6 - ρ values after 10^4 cycles: front (left) and rear (right) sides

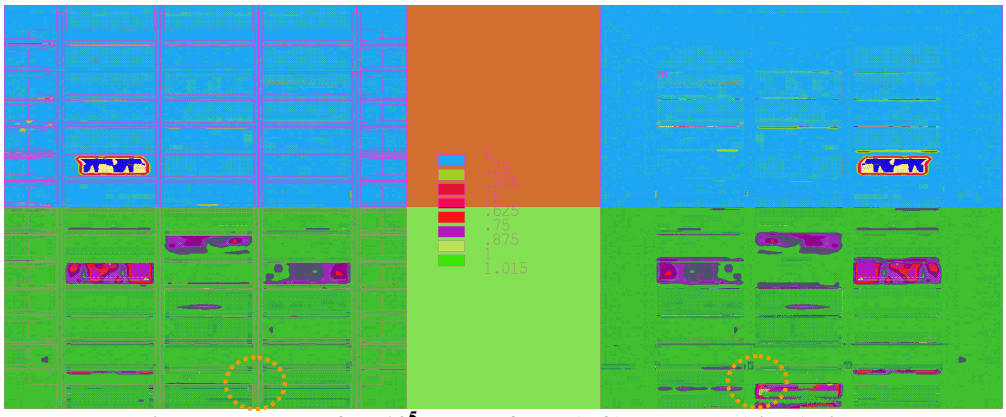

Fig. 7 - ρ values after 10^5 cycles: front (left) and rear (right) sides

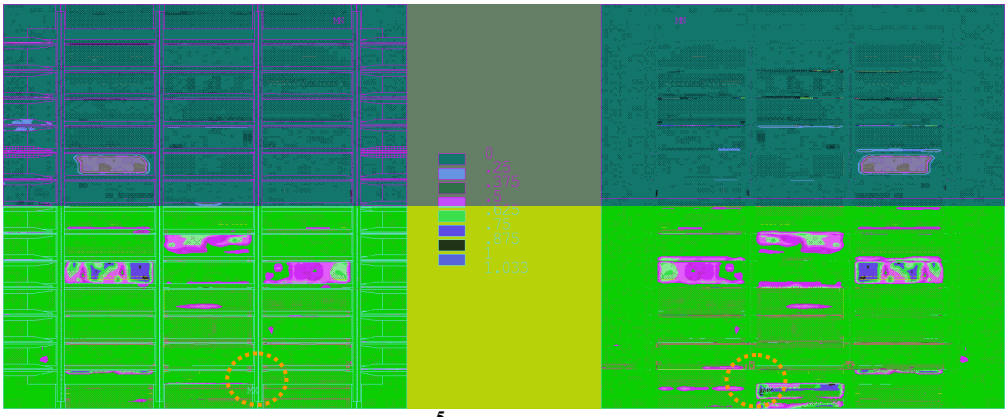

Fig. 8 - ρ values after $1.77 \cdot 10^5$ cycles: front (left) and rear (right) sides

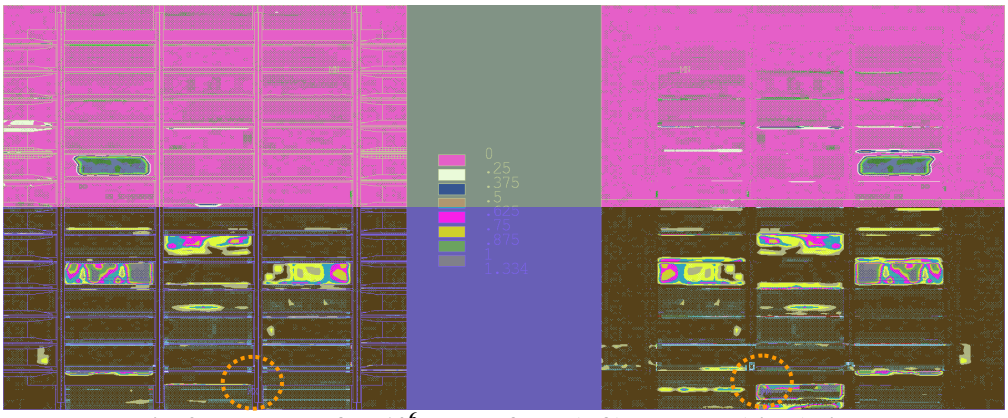

Fig. 9 - ρ values after 10^6 cycles: front (left) and rear (right) sides

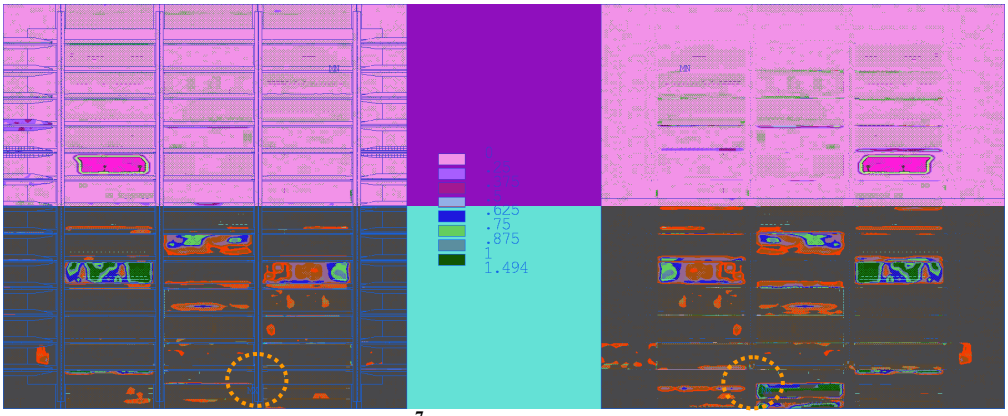

Fig. 10 - ρ values after 10^7 cycles: front (left) and rear (right) sides

Conclusions

The results of the numerical analysis are in good agreement with the experimental analysis data collected by the tests on the full scale panel: the latter broke due to fatigue after 177000 cycles, while the model had predicted the initiation of the fatigue crisis at about 100000 cycles. At 177000 cycles the difference between numerical evaluation of the critical fatigue load and experimental data may be determined in terms of 3.3%.

The position of the failure is predicted approximately in the same zone, located on the skin. Overall, these results show that the Sines criterion can be an effective method to rapidly evaluate the initiation of fatigue crisis. The method hereby proposed has the additional advantage of providing, with a single analysis, a description that is both qualitative and quantitative of the fatigue status of a structure.

References

[1] Sines G., Waismann J. L., Metal Fatigue, McGraw Hill, New York, 1959

[2] Armentani E, Caputo F., Esposito R., Godono G., A New Three Loading Axes Machine for Static and Fatigue tests, Proceedings of the Sixth International Conference on Biaxial/Multiaxial Fatigue & Fracture, Lisboa, Portugal, June 25-28, 2001, Vol. 1, pp. 323-330

[3] Apicella A., Armentani E., Esposito R., Fatigue test on a full scale panel, Key Engineeering Materials, Vols. 324-325, pp. 719-722, 2006

[4] Buch A., Fatigue Strength Calculation, Trans Tech Publications, Switzerland, 1988

Key Engineering Materials Vols. 385-387 (2008) pp 553-556
© (2008) Trans Tech Publications, Switzerland
doi:10.4028/www.scientific.net/KEM.385-387.553

Fatigue Properties Improvement of Notched Structural Steel Sheets

Nobusuke Hattori[1,a], Kazuhiko Nakayama[2], Mian Zhang[2,b], Shin-ichi Nishida[3,c]

[1]Department of Mechanical Engineering, Faculty of Science and Engineering, Saga University, Honjo-machi 1, Saga 840-8502, Japan

[2]Graduate School of Science and Engineering, Saga University, ibid

[3]Professor Emeritus, Saga University

[a] hattori@me.saga-u.ac.jp, [b] zhangwango@hotmail.com, [c] nishida@me.saga-u.ac.jp

Keywords: Fatigue properties, Pulsating fatigue, Plastic working, Notched part, Structural steel

Abstract. Nearly 90% of failures of machines and mechanical parts are caused at the area of stress concentrated in the structural components. Hence, it is important to investigate the method of improving fatigue strength for notched parts. In this paper, the fatigue tests have been performed to investigate the effect of the plastic-working on fatigue strength of specimens with notch. The main results obtained in this study are as follows: (1) The fatigue limit of notched specimen chamfered by the plastic-working increases by 45% than that of specimen without chamfer. (2) The reason of enhancing the fatigue strength may be to attributed to the work-hardening and compressive residual stress which suppress the fatigue crack initiation and propagation in early stage.

Introduction

According to the statistical analysis results of the failures cause of the machine & the mechanical parts, as more than 90% of the failures are caused by the fatigue. Moreover, about 90 % of the fatigue crack initiated from the stress concentrated parts of structural component [1]. Therefore it is considered that improving fatigue strength of notched parts is very useful practically.

As generally known for the plain specimen, the surface chemical treatment and the surface heat treatment are pretty effective to increase the fatigue strength. But for the notched specimen, it is almost ineffective or may become the opposite effect, due to the notch sensitivity of the notched parts also becomes high, as the stress concentration factor of the notch becomes larger by above the methods[2]. Then authors have reported improvement of the fatigue strength of round bar specimen with annular V notch, by roller-working[3]. The fatigue strength of the notched specimen by roller working is enhanced 120% in comparison with that of plain specimen.

Herein, the specimen with stop-hole is used, and fatigue tests have been carried out, in order to examine effect of the chamfering by the die-pressing to the hole edge, on the fatigue strength. The cause of the improving the fatigue strength is investigated through hardness distribution, surface state successively observation by replica-taken method and fracture graph by SEM.

Experimental Procedure

The material used in this study is structural steel (JIS SM400A). The chemical compositions and mechanical properties are listed in Tables 1 and 2, respectively. Fig.1 the details of pulsating fatigue test specimen. After machining, the specimens were polished with emery paper # 400 to # 3000. In addition, about 50 μm of surface layer was removed by electro-polishing. Finally, to observe the surface state during fatigue test, they were etched in some solution of distilled water and sulfuric acid. The specimens are identified to two types as follows.

(1) Non-pressed specimen : Type 1 has drilled circular stop-holes as the notch.

(2) Pressed specimen : Type 2 is chamfered C1 by die-pressing after drilling the stop-hole.

The pulsating fatigue test were conducted by tensile-compressive fatigue testing machine under the frequency of 10 Hz and a constant stress ratio of R=0.1, respectively. The hardness distribution was evaluated with a Vickers hardness tester. Moreover, the fatigue crack initiation and propagation behavior was observed by the method of the successive taken-replica and the fracture surfaces were observed by SEM..

Table 1 Chemical composition (mass %)

Material	C	Si	Mn	Cr	P	S
SM400A	0.14	0.19	0.77	-	0.0018	0.004

Table 2 Mechanical properties

Materials	σ_y, MPa	σ_B, MPa	El %
SM400A	299	441	28

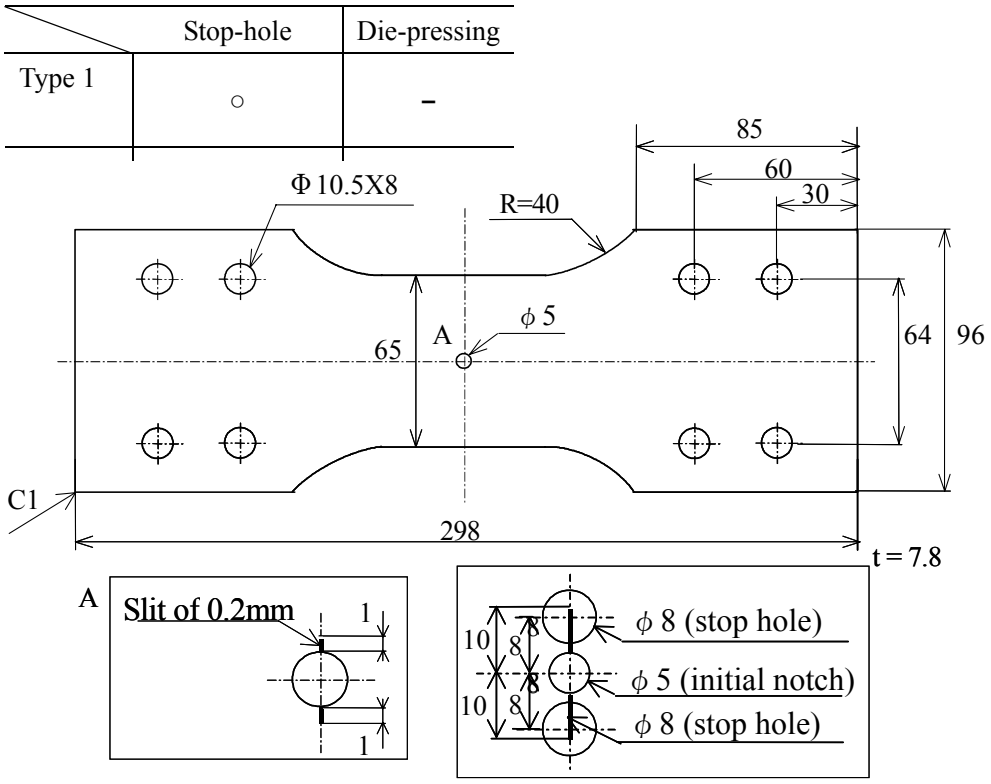

Fig.1 Shape and dimensions of fatigue specimen

Results and discussion

Fig.3 shows the S-N curves. The fatigue limit of specimens Type 1 and Type 2 are 49.5 and 72MPa, respectively. The fatigue limit of Type 2 is enhanced 22.5MPa from that of Type 1. It may be concluded that the method of die-pressing chamfer is very effective to improve the fatigue limit of the notched specimen with hole.

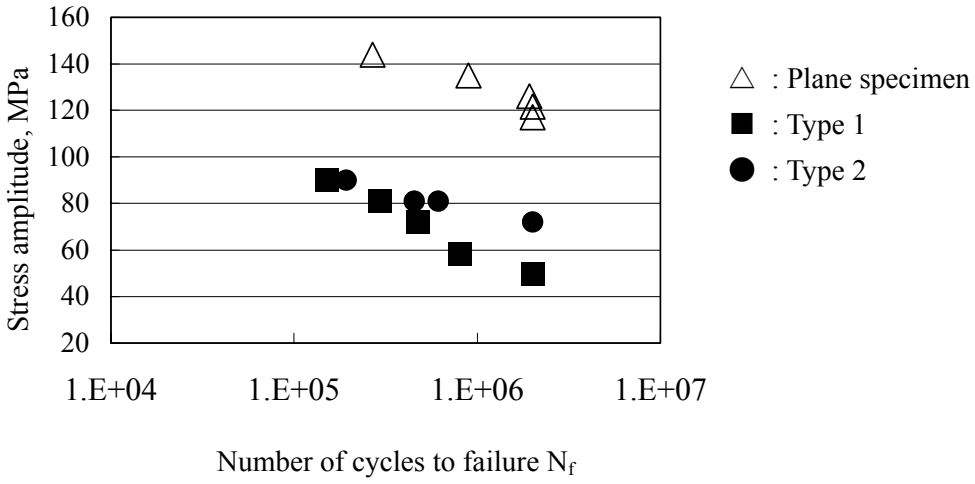

Fig.3 S-N curves

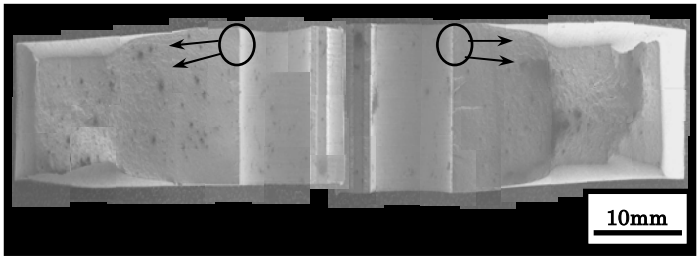

(a) Type 1 (σ_a=81MPa, N_f=2.9×10^{5}cycles)

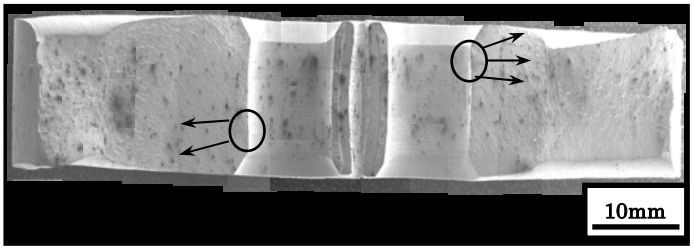

(b) Type 2 (σ_a=81MPa, N_f=6.1×10^{5}cycles)

Fig. 4 Fracture surface

Fig.4 shows the fractographs of the plate specimens observed by SEM. The fatigue crack initiated from the hole-edge in Type1. On the other hand, the crack initiation area in Type 2 has observed at the surface where leaving from the hole-edge.

Fig.5 shows the distribution of micro-Vickers hardness numbers, from the edge of hole to the end direction on the upper surface of the specimen, and from the edge of hole to the depth direction on cross section of the specimen, for Type 1 and Type 2 specimens respectively. In both the results of Type 1 and Type 2 specimens, the hardness numbers substantially increased within 1 mm from the edge of the hole on the upper surface of specimens, and within 2 mm from the edge of the hole to the depth direction of the specimens.

It is considered that the reason of improvement of the fatigue strength of the pressed-specimen is due to work-hardening and compression residual stress.

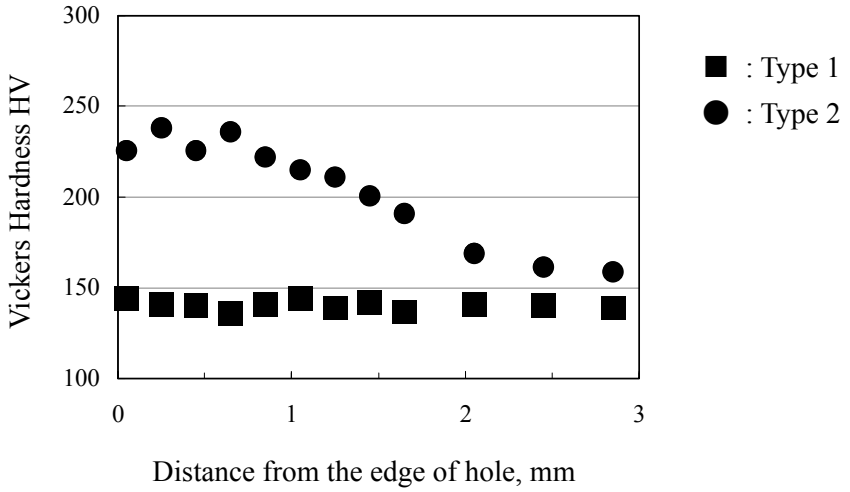

Fig.5 Distribution of micro-Vickers hardness from the edge of hole

Conclusions

The main results obtained in this study are as follows:

(1) The fatigue limit of the notched specimen, which chamfered by the die-pressing to the edge of the stop-hole, increases by 45% than that of specimen without chamfer.

(2) It is considered that the work-hardening and compression residual stress improve fatigue strength notched specimen.

References

[1] S.Nishida: Failure analysis in engineering applications. Butterworth Heinemann Co. Ltd; 1992, p. 4.

[2] For example, H.KANESHIRO, Y.SHIMOJI, T.MAKABE and T.MAKISHI: Fatigue Properties and Dislocation Structure of Nitrided SS400, Proc. of the 1998 Annual Meeting of JSME & MMD, 11, (1998), p.53

[3] S.NISHIDA, S.WANG, N.HATTORI: Fatigue Strength Improvement by Roller-Working and Fatigue Design'98, 1, (1998) p.107

Key Engineering Materials Vols. 385-387 (2008) pp 557-560
© (2008) Trans Tech Publications, Switzerland
doi:10.4028/www.scientific.net/KEM.385-387.557

Sensitivity of Fatigue Crack Growth Data to Specimen Geometry

Seitl Stanislav[1, a], Hutař Pavel[1,b] and Knésl Zdeněk[1,c]

[1]Institute of Physics of Materials, Academy of Sciences of the Czech Republic

Zizkova 22, 616 62 Brno, Czech Republic

[a]seitl@ipm.cz, [b]hutar@ipm.cz, [c]knesl@ipm.cz

Keywords: Fatigue crack, Paris law, threshold values.

Abstract. The formulations of fatigue crack growth prediction are still mostly based on phenomenological models. A commonly used formula in the field of high cycle fatigue is the Paris-Erdogan law. For given experimental conditions (such as temperature, stress ratio or environmental conditions) the parameters C and m have to be experimentally determined and considered as material constants. Thus, for a given material, the fatigue crack growth rate (FCGR) depends only on the applied range of the stress intensity factor. In a threshold region a significant shift in the data of the fatigue crack propagation rate can be observed. The shift is induced by different test specimen geometry. To analyses it the authors will present their own laboratory fatigue crack growth rate test data measured on two different specimens with different levels of constraint and for different steels. It is demonstrated that fatigue characteristics (i.e. C, m and K_{th}) obtained from different specimen geometries are not only properties of the materials but depends on the specimen geometry.

Introduction

A commonly used formula in the field of high cycle fatigue is the Paris-Erdogan law:

$$\frac{da}{dN} = C(\Delta K)^m \tag{1}$$

where C and m are experimentally obtained, and are considered to be a constant for a particular material and environment [1]. For damage tolerant design, it is important to be able to accurately determine the threshold stress intensity range, ΔK_{th}, as the value of the stress intensity factor, when fatigue damage caused by fatigue crack growth is not expected. Therefore, the threshold region is from the practical point of view the most important part of the v-K curve.

The objective of this paper contains a description and analysis of a experimental results involving geometry effects observed between the C(T) and M(T) specimens in two different steels. The authors will present their own laboratory fatigue crack growth rate test data measured on two different specimens with different levels of constraint and for different steels. It is demonstrated that fatigue characteristics (i.e. C, m and ΔK_{th}) obtained from measurement different specimen geometries are not only properties of the material, but also depend on the geometry of the structure as well. It is of paramount importance for damage tolerant design applications to have a deep understanding of the mechanism of the fatigue crack propagation in the threshold region in order to prevent unexpected failure of the structural components.

Experimental Details

Materials and Specimen Detail

The materials used in this investigation were steel 12050 and steel 15313, see Table 1. The material properties corresponding to the cyclic strain-stress curve are: Young's modulus E=2.1×10^5 MPa, Poisson ratio v =0.3, cyclic yield stress σ_0 = 350 MPa and hardening exponent n = 0.314, for steel 15313 are Young's modulus E=2×10^5 MPa, Poisson ratio v =0.3, cyclic yield stress σ_0 = 330 MPa and hardening exponent n = 0.426.

Table 1. Steels composition (wt %)

	C	Mn	Si	P	S	Cr	Ni	Cu	Mo
12050	0.50	0.80	0.30	0.04	0.04	0.25	0.30	0.30	0
15313	0.10	0.60	0.40	0.035	0.035	2.3	0.60	0	1.05

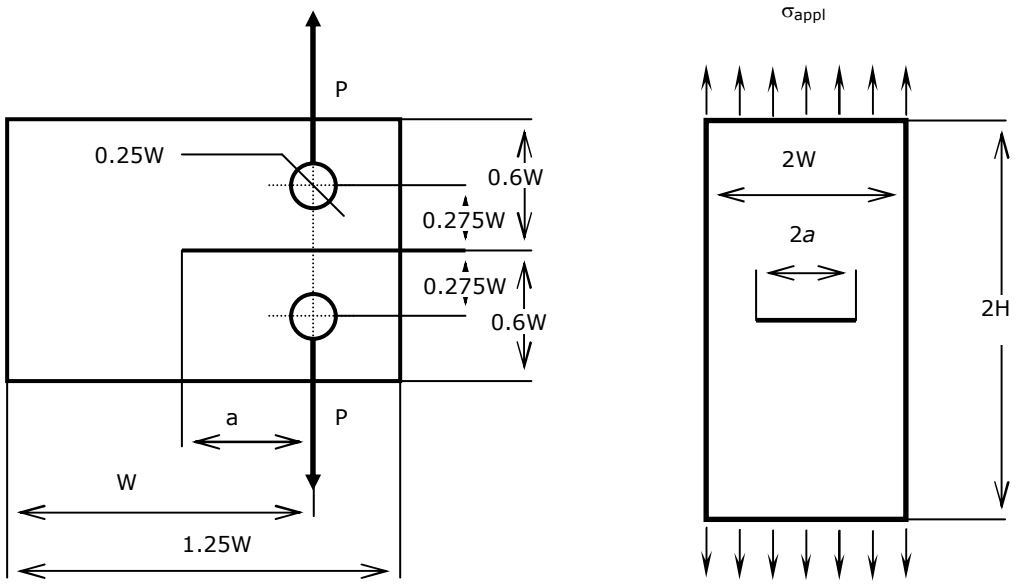

Fig. 1. Schematic of C(T) and M(T) specimen geometries. (W=50, H=150 and thickness =10 dimensions in mm). $a/W \in (0.3; 0.7)$.

Experimental procedure

To define the threshold regime constant R=0.1 load reduction tests were performed at room temperature in laboratory air in accordance to ASTM E647 [2] using the above mentioned specimens C(T) and M(T), see Fig.1. The tests were performed using computer controlled high-frequency resonating machines AMSLER and SCHENCK. Threshold conditions are achieved for long fatigue cracks by K decreasing test by stepped shedding, ΔK, as the crack propagates. The FCG threshold is reached when the crack stops growing. Because load reduction occurs gradually as the crack grows, no true threshold is reached in a practical amount of time. Instead, a working definition for ΔK_{th} is used as very low FCG rates are achieved (10^{-10} m/cycle has been suggested) [2]. Frequencies in the threshold region were in the range of 60 Hz to 90 Hz, which had no influence on fatigue crack behaviour. Crack length was monitored using an optical microscope marked in increments of 0.01 mm.

Discussion of the results and conclusions

The result of the fatigue crack growth tests performed at R=0.1 using the two specimen geometries for the steel 12050 are presented in Figure 2.

For steel 12050, at an intermediate ΔK value of approximately 12 MPa $m^{1/2}$ or greater (Paris region), the nominal crack growth rates observed for the both specimen geometries from engineering view were comparable (Figure 2). The values of Paris parameters for C(T) and M(T) specimens are C=6.92 $\times 10^{-11}$, m=4.33 and C=6.86$\times 10^{-10}$ m= 3.67, respectively. However, as ΔK values approached the threshold, the C(T) specimen exhibited lower nominal crack growth rates and a higher nominal threshold value (ΔK_{th}= 9 $MPam^{1/2}$) than observed for the M(T) specimen (ΔK_{th}= 6 $MPam^{1/2}$).

The similar fatigue crack growth tests performed at the same stress ratio R=0.1 using the two different specimen geometries were performed for the second steel 15313 and presented in Figure 3. The trends of the fatigue crack rate curve for this material are the same.

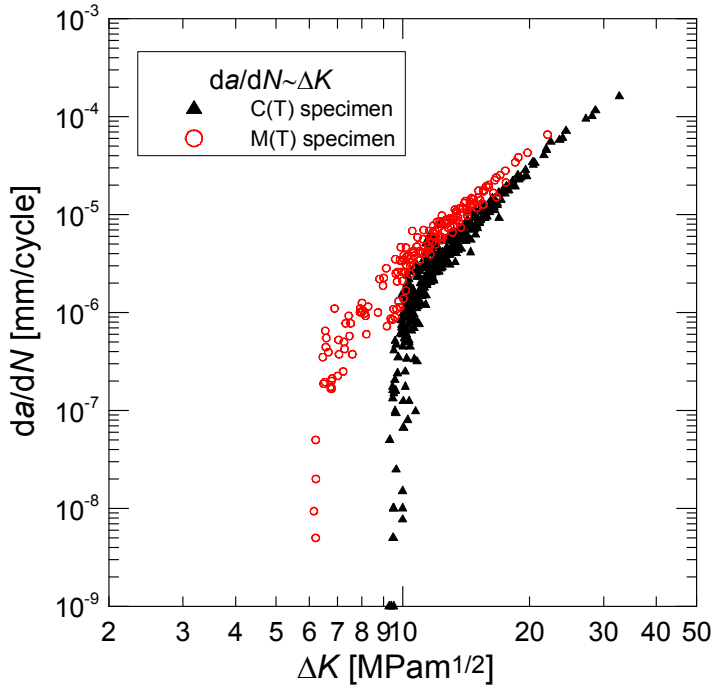

Fig. 2. Fatigue crack behavior of steel 12050 for R=0.1.

At an intermediate ΔK value of approximately 10 MPa $m^{1/2}$ or greater (Paris region), the crack growth rates observed for the both specimen geometries from engineering view were comparable, see Fig. 3. The values of Paris parameters for C(T) and M(T) specimens are $C= 1.6\times10^{-10}$, m=4.06 and C=2.11×10^{-9} m=3.28 , respectively. As the ΔK values approached the threshold, the C(T) specimen exhibited lower crack growth rates and a higher threshold value (ΔK_{th}= 8 $MPam^{1/2}$) than observed for the M(T) specimen (ΔK_{th}= 4.5 $MPam^{1/2}$). Therefore, it can be concluded that the fatigue crack growth rate is higher for M(T) specimen than for the C(T) for intermediate ΔK values, but from the point of view of residual life time its estimation is not very important.

Due to the strong difference in fatigue crack propagation rates in the threshold region obtained for C(T) and M(T) specimens, it is not appropriate to make an fitting of all experimental data by the same material curve, which is independent of the outer geometry of the specimen, as is usually presented in the literature [3].

The level of constraint induced by the different geometry of the specimen has to be considered. Structures with a low level of the constraint (e.g. M(T) specimen) produce a bigger plastic zone near the crack tip than structures with a high level of the constraint (e.g. C(T) specimen, see [4], and consequently fatigue crack growth rates increase with a decrease in constraint level. The difference between FCGR for intermediate ΔK values can be explained by this phenomenon, but discrepancies in threshold values are much larger [5].

Fatigue crack growth close to the threshold is usually influenced by crack closure effects, especially in cases of crack closure induced by roughness. With the decreasing of the ΔK values the size of the cyclic plastic zone also decreases and becomes comparable with the microstructure of the material. For this reason, in the threshold region fatigue crack growth is microstructure sensitive and roughness induced by crack closure induced by roughness occurs. A different constraint level can influence the intensity of crack closure. Experimental measurements [6] of the crack closure effect for different levels of the stress intensity factor range confirm this ideas and indicate a much larger closure effect in the threshold area for specimens with a high level of the constraint (C(T)) than for specimens with a low level of the constraint (M(T)). Therefore, transferability of experimentally obtained threshold values between different specimens is only possible assuming of the same

constraint level. For a conservative estimation of the residual fatigue life time of the structures it is better to use specimens with low level of the constraint.

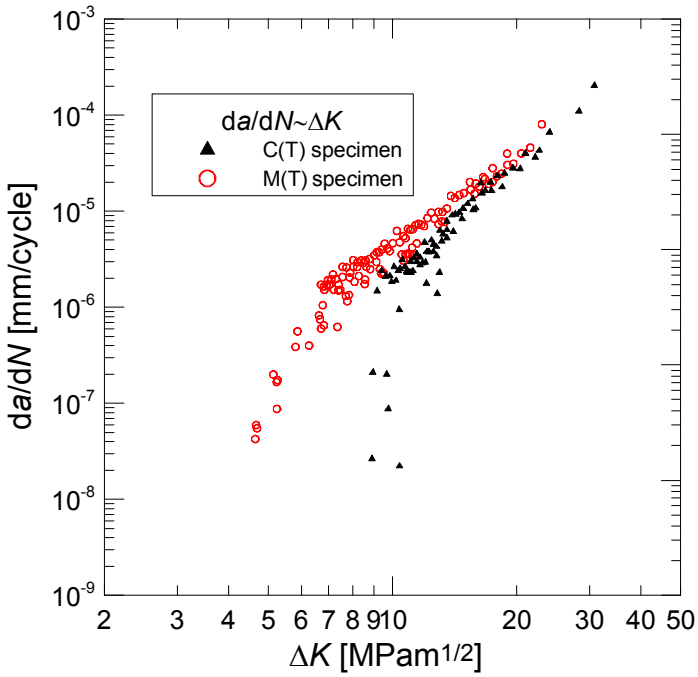

Fig. 3. Fatigue crack behavior of steel 15313 for R=0.1.

Acknowledgments

This investigation was supported by grants No. 101/08/1623 and 106/06/P239 of the Czech Science Foundation.

References

[1] P Paris and F Erdogan, A critical analysis of crack propagation laws, Journal of Basic Engineering, Transactions of the American Society of Mechanical Engineers, 1963, pp.528-534.

[2] ASTM Standard E647-00, Standard Method for Measurement of Fatigue Crack Growth Rates, ASTM 03.01, 2004

[3] Klesnil M., Lukáš P. Fatigue of metallic materials, Elsevier 1992

[4] Anderson, T. L. F*racture Mechanics Fundamentals and Applications*, Second Edition, 1995, CRC Press

[5] Hutař, P., Seitl, S., Knésl, Z., Effect of constraint on fatigue crack propagation near threshold in medium carbon steel, *Computational Materials Science*, Vol. 37, 51-57, 2006 Dj.M. Maric, P.F. Meier and S.K. Estreicher: Mater. Sci. Forum Vol. 83-87 (1992), p. 119

[6] Garr K.R., Hresko G.C. III. A Size effect on the fatigue crack rate threshold of Alloy 718, ASTM STP 1372, pp. 155-174

Key Engineering Materials Vols. 385-387 (2008) pp 561-564
© (2008) Trans Tech Publications, Switzerland
doi:10.4028/www.scientific.net/KEM.385-387.561

Electro-mechanical admittance-based damage detection using extreme value statistics

C P Providakis

Department of Applied Science, Technical University of Crete

GR-73100 Chania, Greece

email: cpprov@mred.tuc.gr

Keywords: Damage detection, Piezoelectric patch, FEM, Electromechanical admittance, Extreme values.

Abstract. This paper presents the use of statistically rigorous algorithms combined with electromechanical (E/M) impedance approach for health monitoring of engineering structures. In particular, a statistical pattern recognition procedure is developed, based on frequency domain data of electromechanical impedance, to establish a decision boundary for damage identification. In order to diagnose damage with statistical confidence, health monitoring is cast in the context of outlier detection framework. Inappropriate modeling of tail distribution of outliers imposes potentially misleading behavior associated with damage. The present paper attempts to address the problem of establishing decision boundaries based on extreme value statistics so that the extreme values of outliers associated with tail distribution can be properly modeled. The validity of the proposed method is demonstrated using finite element method (FEM) simulated data while a comparison is performed for the extreme value analysis results contrasted with the standard approach where it is assumed that the damage-sensitive features are normally distributed.

Introduction

As structures experience damage, they will no longer behave as they were designed to, which could pose safety and reliability risk. Thus, the interest in the ability to monitor a structure and diagnose damage at the earliest possible stage is pervasive thought the civil, mechanical and aerospace engineering communities. This helps engineer to ensure that the structure is in good health, and if necessary, to apply prompt measures to repair any damage.

Many visual or localized experimental damage detection methods have been developed and are routinely employed to a variety of structures [1]. However, all of these experimental techniques require that the vicinity of the damage be known a priori and that the portion of the structure being inspected is readily accessible. As structures become larger and more complex those techniques become unfeasible and more efficient methods have to be developed.

In the aspect of the structural health monitoring using active piezoelectric materials, the electromechanical (E/M) impedance technique is recently used as a promising approach in finding minor changes in structural integrity [2]. The basic concept of this approach is to use high-frequency structural excitations to inspect the local portion of a structure for changes in (E/M) impedance (or its inverse admittance) that would indicate imminent damage. The attractive features of the (E/M) impedance technique include its capability of capturing a wide range of structural damage from small to large scale, availability of continuous on-line monitoring, ease of practical application, and cost effectiveness. Implementations of the (E/M) impedance technique have been successfully performed on a number of structures [3].

While the above cited references propose many different methods for extracting damage-sensitive features from (E/M) impedance measurements, few of these works use a statistical approach to quantifying the observed changes in these features. However, because all those measurements rely on date with inherent uncertainties, statistical analysis procedures are necessary

if one is to state in a quantifiable manner that changes in the (E/M) impedance of a structure are indicative of damage as opposed to operational and/or environmental variability.

The focus of this paper is to demonstrate the feasibility of using a frequency-domain auto-regressive system identification model with exogenous inputs (ARX) for detecting damage in structures. This approach uses coefficients from frequency domain model developed in FDIDENT [4] toolbox of MATLAB. The residual error, which is the difference between the (E/M) impedance (admittance) signatures numerically resulted from a finite element analysis and the prediction obtained from the ARX model developed from the undamaged model (E/M) impedance (admittance) reference signature, is defined as the damage-sensitive feature. This feature is then analyzed using a statistical methodology known as extreme value statistics (EVS) to develop a robust damage classifier. Although EVS has been widely applied there has been little application of this technique to damage identification. Recently, a number of works proposed the use of EVS methodology to structural damage identification and health monitoring [5].

The present paper investigates the effectiveness of the combine use of EVS with (E/M) admittance approach in damage diagnosis and identification process. The proposed methodology is tested on a numerical example of a concrete sample where the integration of EVS is explored into damage detection comparing the thresholds of the outliers estimated using Gaussian normal distribution with those estimated using the present EVS approach.

Electro-mechanical admittance

Consider a structural component with a PZT patch of length $2\ell_{PZT}$ and thickness h_{PZT} bonded on it. When a harmonic voltage $V=V_0e^{j\omega t}$ with $j=\sqrt{-1}$ is applied in the z-direction, producing an electric field $E=E_0e^{j\omega t}$, an in-plane vibration is induced in both x and y directions. Then the electric current passing through the PZT patch, can be considered to be given by

$$I = j\omega \int_{-\frac{\ell_{PZT}}{2}}^{\frac{\ell_{PZT}}{2}} \int_{-\frac{\ell_{PZT}}{2}}^{\frac{\ell_{PZT}}{2}} D\,dx\,dy \tag{1}$$

where D is the electric displacement. Considering that the electric field is defined by

$$E = \frac{V}{h_{PZT}} \tag{2}$$

and that the input voltage V is an AC voltage of 1 V (rms) magnitude the electromechanical admittance of the PZT patch can be expressed as:

$$Y = \frac{I}{V} = j\,\omega\,\Sigma Q_i \tag{3}$$

where ΣQ_i is the total charge over the whole surface of the PZT patch.

ARX parametric modeling

The conventional electro-mechanical admittance–based damage detection technique first begins by obtaining input, output and noise signals. In the present case, input is coming from the unit applied voltage at the PZT patch surface while output is obtained from the resulted admittance signal. In the so called system identification process the second step is the data cleansing, filtering and averaging. The cleansed signals are then used to produce parametric mathematical models, which in turn evaluate the current state of health of the system and predict future states of health.

Parametric models are based on ordinary or partial differential equations that describe the dynamic system. Usually ready-made models such as autoregressive (AR) models with exogenous (ARX) inputs are chosen since they are cost-effective and convenient to use.

The frequency-domain ARX parametric model produced from the use of FDIDENT toolbox of MATLAB is then employed to predict the response of a newly measured signal. If this new signal is measured under a structural condition different from the condition where baseline signal was

obtained, the predicted model would not reproduce the new signal well and there would be a residual error. Then, the feature for damage is related to this relative error which if exceeds a predefined threshold value it referred as outlier. A statistically significant number of outliers will indicate damaged situation. When analyzing outliers, EVS approach of Statistical Toolbox of MATLAB [6] is employed in the present work. According to the pivotal theorem of EVS, in the limit as the number of samples data tends to infinity there are only three EVS distributions (Gumbel, Weibull and Frechet distributions[5]) to choose from, regardless the distribution of the parent data points. Then, by giving the vector of sample data for maximum or minimum data from a number of n-data populations, it is possible to select the appropriate EVS distribution and fix a parametric model for the tails of data. Once the parametric model is established, effective threshold limits for the outliers analysis can be accurately computed by using EVS analysis of Statistical Toolbox of MATLAB and (E/M) admittance signals measured for the undamaged structure.

Numerical results

In the present paper, the test structure is a concrete beam 500 mm in length, 100 mm in width and 100 mm in thickness. A PZT patch is considered to be bonded to the upper surface of the monitored beam in a distance of 40 mm away from the left end (Fig. 1). Damages were then simulated on the upper surface of the beam specimen by considering cross-width notches 5 mm in depth. The first simulated damage was considered at a distance of 400 mm from the PZT patch.

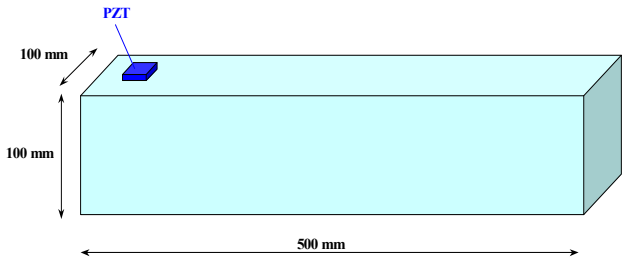

Fig.1. Beam specimen with a PZT patch

The finite element model was generated in COMSOL 3.4 [7] using 2633 finite elements and then a frequency response analysis was performed over a frequency range of 200-500 kHz at an interval of 1 kHz producing 300 data point measurements. In the damaged state, the real part of the admittance (conductance) was acquired and compared to the pristine (undamaged) state. The pristine (undamaged) state was acquired before the first crack was simulated.

Once the ARX model is estimated, the residual errors are extracted as a damage-sensitive feature by subtracting the FEM computed impedance from the predicted output of the ARX model. The upper and lower threshold limits of the confidence interval are produced based on probability of a type I error that we intends to tolerate the structure in the present paper. Once, type error I is specified with a probability p (0<= p<= 1), a percentage of 100x(1-p)% of the measured data points from a Gaussian normal condition should be cast within the confidence interval and 100xp% of the data will be outliers. If we assume that the F-1(p) is the inverse CDF of the known parent distribution then the upper and lower limits of the confidence inrerval can be evaluated at F-1(a-p/2) and F-1(p/2), respectively. Thus for a type I error of 0.5% which corresponds to a 99.5% confidence interval the expected number of outliers is 1 to 2 out of 300 data points. The 99.5 % confidence interval is chosen in our work because it provides acceptable risk.

Figure 2 presents the detrended residual error as well as the associated 99.5% EVS confidence interval for undamaged and damaged structural conditions. It can be seen that results from the undamaged condition are excellent showing no false positive indications of damage while for the damaged condition it returns 3 outliers which leads to correct damage diagnosis of the structural condition.

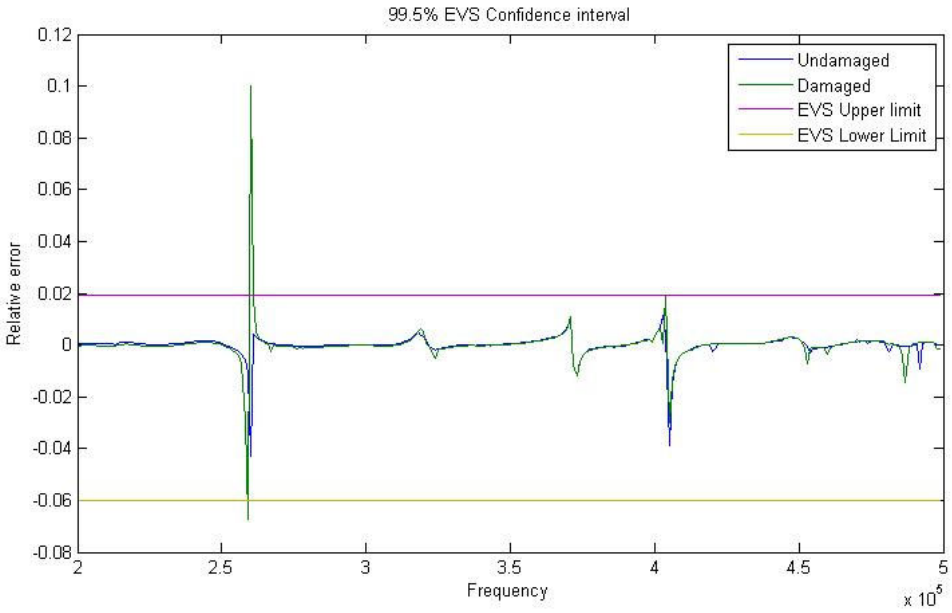

Fig.2. 99.5% EVS confidence interval for residual errors for undamaged and damaged state

Conclusions

With the combination of finite element method and EVS statistical approach, parametric estimation was greatly simplified and the process of system and damage identification was made efficient. Having an accurate parametric model of a system is important in analyzing a structure's current state of health and predicting structural behavior in various conditions. The health monitoring process proposed here that capitalizes the feature of electro-mechanical impedance signals in combination with the extraction of outliers in the associated prediction error can be efficiently used in determining the damage state of a structure over the traditional SHM approaches.

References

[1] J.E. Doherty: *Handbook of Experimental Mechanics, Chapt. 12, Society for experimental Mechanics, Inc,* Bethel, CT, USA, 1987.

[2] G. Park, H.H. Cudney and D.J. Inman: *Impedance-based health monitoring of civil structural components*, J. Infrastuctures Systems 6, (2000), pp. 153-160.

[3] K.K. Tseng and L. Wang: *Impedance-based method for nondestructive damage identification*, J. Engng. Mech., 131(1), (2005), pp. 58-64.

[4] FDIDENT, *Frequency Domain System Identification toolbox*, Gamax Ltd, http://elecwww.vub.ac.be/fdident/index.html

[5] H. Sohn, D.W. Allen, K. Worden and C.R. Farrar: *Structural damage classification using extreme value statistics*, J. Dynamic Systems Measurements and Control ASME, 127, (2005), pp. 125-132.

[6] MATLAB, *The Mathworks Inc. Users Guide*, www.mathworks.com, U.S. (2005)

[7] COMSOL, Ltd, London, COMSOL Multiphysics Modelling 3.4, www.comsol.com, 2007, Users Guide.

Key Engineering Materials Vols. 385-387 (2008) pp 565-568
© (2008) Trans Tech Publications, Switzerland
doi:10.4028/www.scientific.net/KEM.385-387.565

Evolution of relevant parameters on fretting fatigue tests

M. Buciumeanu[1,a], A. S. Miranda[1,b] and F. S. Silva[1,c]

[1]Department of Mechanical Engineering, University of Minho,

Azurem, 4800-058 Guimaraes, Portugal

[a]mihaela@dem.uminho.pt, [b]asm@dem.uminho.pt, [c]fsamuel@dem.uminho.pt

Keywords: fretting fatigue, normal load, tangential load, relative displacement, aluminum alloy

Abstract. The degradation process in fretting fatigue is due to mechanical and chemical attack between two contacting surfaces, being directly related to wear, corrosion and fatigue. There are many parameters that influence the fretting fatigue phenomenon out of which relative displacement, δ, normal load, F_n, and tangential load F_t, are the most important and consequently the most studied ones. This paper describes the fretting fatigue phenomenon occurring on a high strength aluminium alloy, Al7175. The aim of this study is to achieve a better understanding of the fretting fatigue behaviour by observing the evolution of the fatigue life of the specimen with the normal load, the tangential load and the relative displacement amplitude.

Introduction

As it is well known fretting occurs at the interface between two contacting bodies that are pressed against each other in the presence of cyclic load that give rise to a small relative displacement. Directly or indirectly the reduction in fretting fatigue life is caused by several parameters. Among these, the mechanical loading conditions (normal load, F_n, tangential load, F_t and axial load, σ) and indirectly the relative displacement amplitude, δ, are the most important variables that influence fretting fatigue. It is important to observe the variation of these parameters during the fretting process (in an ongoing test), using different testing procedures and apparatus, in order to achieve a better understanding of the effect of the testing apparatus on the results.

In relation to the *normal load*, F_n, Jin and Mall showed that it decreased during a test from 1334 N to 750 N [1]. In another test Jin kept the normal load approximately constant by increasing it after each drop of 10% (for gross slip regime). It was observed that the fretting fatigue life of the specimens with constant normal load (approx.) was shorter than in the ones where the normal load decreased during the test. Ramalho and co-authors [2] used a set of springs in order to overcome the previously mentioned phenomena, and to maintain the normal load constant during the fretting test. In relation to *tangential load,* F_t, Jin and Mall [3] showed that the maximum tangential load in some situations continuously increased, or increased and suddenly dropped. The sudden drop in tangential load was explained by the decrease in applied normal contact load, which resulted from material removal of both specimen and pad. Regarding the evolution of the tangential load amplitude during a fretting test, some research [4,5] stated that it initially increased and then stabilized after about 100 cycles. Regarding the *relative displacement amplitude, δ,* many studies showed [3-7] that it is a key variable in fretting fatigue life, because it seems to be the main reason of the damage. Much attention has been given to the average or maximum value of the relative displacement amplitude with total fatigue life, but very little attention has been given to its evolution during a test. Vingsbo and Soderberg [7] showed that there is a value of the relative displacement amplitude below which fretting fatigue life decreases and above which fretting fatigue life increases. Favrow and Anton [8] observed that relative displacement amplitude has a much bigger effect on the fretting fatigue life on Ti-6Al-4V alloy that the normal contact load. A study of the effect of the relative displacement amplitude on fretting fatigue life of an automotive formed suspension component showed an increase in fatigue life by increasing relative displacement amplitude (above 30 μm) [9].

This paper describes the fretting fatigue phenomenon occurring during a test with an aluminium alloy, Al7175 (specimen), in contact with a 34CrNiMo6 steel (pad). The aim of the study was to achieve a better understanding of the fretting fatigue behaviour with the particular testing apparatus used by observing the evolution of minimum, maximum and amplitude of the normal and the tangential load, and the relative displacement amplitude.

Experimental procedure

The specimens used for fretting fatigue tests were machined from an Al7175 alloy rod and the pads from a 34CrNiMo6 steel rod. Their mechanical properties are given in Table 1. The fretting fatigue experiments were carried out using the specimen and pad shown in Fig. 1. Fig. 2 shows a picture of the fretting fatigue device [10] along with the servo hydraulic DARTEC uniaxial testing machine. Fig. 3 shows schematically the test configuration for fretting fatigue tests. Two series of fretting fatigue tests were carried out at a stress ratio $R=0,1$. All tests were conduced at ambient temperature, in a laboratory environment, and at a cyclic frequency of 4 Hz. The surface of specimens and pads were polished with abrasive paper, finished with diamond spray (1 μm), and then cleaned with alcohol as to provide a standard surface. Load conditions for the test described in this paper are shown in Table2.

Table 1 Mechanical properties and the approximate grain size of the materials

Material	Mechanical properties					
	Young modulus [GPa]	0.2% Yield strength[MPa]	Tensile strength[MPa]	Rupture strain [%]	Grain size [μm]	Hardness HV
Al 7175	74	461	535	13.8	4,5	185
34CrNiMo6	210	1100	1250	10.0	15,6	-

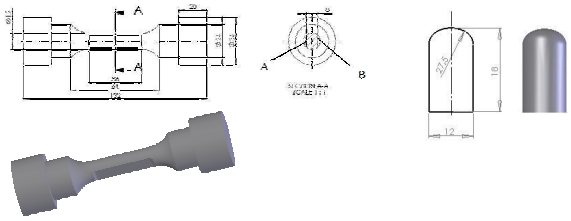

Fig. 1 Geometry of the specimen and pad

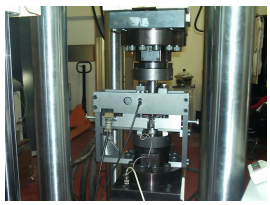

Fig. 2 Experimental test set-up

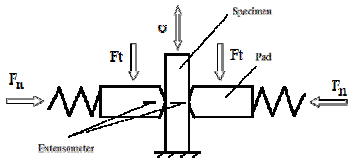

Fig. 3 Schematic test configuration

Table 2 Load conditions for the fretting fatigue test

Axial load (kN)	Normal load (N)	Tangential load (N)
1.9-19.0	750	800

Results and discussions

Fig. 4 shows the evolution of the minimum and maximum normal load, F_n, and tangential load, F_t, during the test. The evolution of the amplitudes of normal load, tangential load and relative displacement are shown in Fig. 5. In Table 3 are presented the macroscopic photographs of the fretted surfaces. Fig. 6 shows the high resolution image of a sample surface obtained with the scanning electron microscope (SEM) and a schematic evolution of profiles during the test and the real profile at the end of the test.

Normal load, Fn. In the present study the minimum and the maximum normal loads decrease with increasing number of cycles (Fig. 4a). This can be explained by the roughness (peaks) breakage at the initial stage followed by the hole formation effect (Table3 and Fig. 6). Due to wear of the specimen and pads the peaks break up and the normal load start to decrease. After a few hundred cycles, a hole (damaged area) develops at the specimen, allowing the pad to approach the specimen, decreasing the normal load till the final rupture of the specimen. At the end of the test the normal load slightly increases due to the bigger local deformation of the specimen after the crack reaches a certain length. Regarding the variation along the test, the maximum normal load changed

from 750 N to 738 N. This is very small change (about 0.02%) and it is expected that it did not have a substantial influence in fatigue life. The reason for this small variation of the normal load relies on the use of the two springs (see Figs. 2,3,4). Jin and Mall [1] observed that is important to keep the normal load constant because the life of the specimen is shorter in this situation. Regarding the normal load amplitude, it changed at the beginning of the test and then continuously decreased. This small initial variation can be explained by the roughness effect, the continuous decrease along the test being explained by the hole effect.

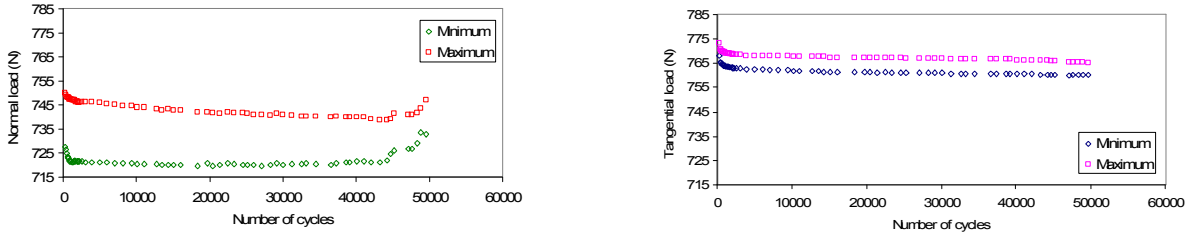

a b

Fig. 4 Evolution of minimum and maximum of: a. normal load and b. tangential load

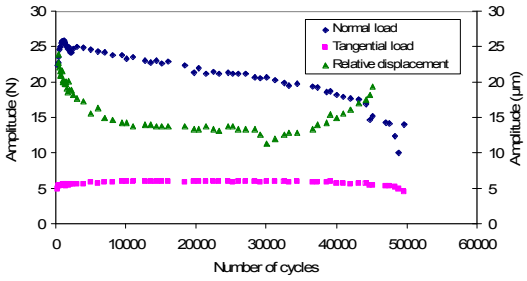

Fig. 5 Evolution of normal load, tangential load and relative displacement amplitude

Table 3 Macroscopic photographs of the fretted surfaces with number of cycles and the roughness

Cycles	0	5	100	500	66199
macroscopic photographs					
R_a	0.07	0.13	0.14	0.20	1.2

A b

Fig. 6 a. High resolution image of a sample surface obtained with the scanning electron microscope (SEM): Al7175 (66.199 cycles), b. Evolution of profiles and the real profile

Tangential load, Ft. The tangential load is a consequence of the contact friction between pads and specimen. The minimum and the maximum values of the tangential load were expected to increase in the beginning of the test due to the roughness formation then due to the hole formation. This variation was observed by Jin and Mall [3]. Initial roughness as well as the hole should not allow the pad to slip, therefore making the pad to move along with the specimen, causing an increase of the tangential load. In this study the minimum and maximum tangential loads decreased in the beginning of the test. This is explained by the initial roughness formation originating a more difficult slipping of the pad along the specimen. However it is interesting to observe that the hole geometrical evolution (Fig. 6 and Table3). The surface profiles changed with the fatigue cycles. It can be observed the stick and the slip zone evolution and the hole asymmetrical formation. This

effect is due to the different wear sensitivity of the specimen to different stress states. The specimen changed its stress condition in each cycle, being the wear resistance sensitive to the specimen stress state. A similar variation of the tangential load was obtained by Yongqing Fu and co-authors [12]. Regarding the tangential load variation along the test, changed from 793 N to 765 N. This small variation (about 0.04%) is not expected to have any influence on fatigue life. Regarding the tangential load amplitude (Fig. 5) it slightly increased during the initial stage of fretting fatigue life, remaining constant afterwards. It reached a stabilized value after a certain number of cycles (approx. 20000 cycles). There is a variation (decrease) at around 40 000 cycles when a crack is supposed to exist already. After that the amplitude seems to decrease till fracture of the specimen occurs. The increasing of the tangential load amplitude in the beginning may result from the initial surface roughness (Table 3). This variation of the tangetial load amplitude along the test (Fig. 5) is a typical variation of the partial slip regime when the region has two zones, stick and slip [4,5,11].

Relative displacement amplitude, δ. In the present study the relative displacement amplitude decreased with increasing number of cycles up to 30000 cycles and then decreased (Fig. 5). The relative displacement amplitude decreases because the stick zone increases with fatigue life (see Table 3). As the stick zone increases the pad movement becomes more difficult. Furthermore, as the hole becomes deeper the pad tends to become confined to the hole and slipping also becomes more difficult. The increase at the end of the test is due to the propagation of the crack. Regarding the variation along the test the relative displacement amplitude changes from 25μm to 12μm, a variation of about 52%. Special attention should be give to this variation during a test because fretting fatigue life is significantly dependent on relative displacement [7].

Conclusions

The normal load, tangential load and relative displacement during a fretting fatigue test were investigated for the apparatus developed. The following conclusions can be drawn:
- the maximum and minimum normal load slightly decrease during the test. This may be attributed to the hole formation and its evolution. This slight variation is not expected to influence fatigue life;
- the minimum and the maximum tangential load slightly decrease during the test. This is attributed to the stick and slip zones evolution and to the hole asymmetrical formation. However it is not expected that it may have any influence on fatigue life;
- the relative displacement amplitude substantially decreases with increasing number of cycles. Special attention must be paid to this variable during a test because fretting fatigue life it is very sensitive to the relative displacement.

Acknowledgement

The research was supported by “Fundação para a Ciência e a Tecnologia” (Portugal) through the PhD grant with the reference SFRH / BD / 19555 / 2004.

References

[1]. O. Jin, S. Mall, Wear 256 (2004) 671-684.
[2]. A. Ramalho, L. M. Correia, J.D. Costa, Tribology International 33 (2000) 761-768.
[3]. O. Jin, S. Mall, Wear 253 (2002) 585-596.
[4]. O. Jin, S. Mall, O. Sahan, International Journal of Fatigue 27 (2005) 395-401.
[5]. O. Jin, S. Mall, J. H. Sanders, S. K. Sharma, Surface&Coatings Techn. 201 (2006) 1704-1710.
[6]. O. Jin, S. Mall, O. Sahan, International Journal of Fatigue 27 (2005) 395-401.
[7]. O. Vingsbo, S. Soderberg, Wear 126 (1988) 131–147.
[8]. H. Lee, S. Mall, Wear 260 (2006) 642-651.
[9]. M. Buciumeanu, A.S. Miranda, A.C.M. Pinho and F.S. Silva, Engineering Failure Analysis 14, (2007) 810-821.
[10]. M. Buciumeanu, A.S Miranda, F.S. Silva, XXIII Encuentro del Grupo Español de Fractura, Albarracín, Spain, March 29-31, 2006.
[11]. O. Jin, S. Mall, International Journal of Fatigu 24 (2002) 1243-1253.
[12]. Y. Fu, J. Wei, A. W. Batchelor, Journal of Materials Processing Techn. 99 (2000) 231-245.

Key Engineering Materials Vols. 385-387 (2008) pp 569-572
© (2008) Trans Tech Publications, Switzerland
doi:10.4028/www.scientific.net/KEM.385-387.569

The thermoelectromechanical J-integral and the thermal permeability of cracks

Andreas Ricoeur[a] and Meinhard Kuna[b]

TU Bergakademie Freiberg, Institute of Mechanics and Fluid Dynamics
09596 Freiberg, Germany
[a]Andreas.Ricoeur@imfd.tu-freiberg.de, [b]Meinhard.Kuna@imfd.tu-freiberg.de

Keywords: J-integral, thermopiezoelectric ceramics, fracture mechanics, crack permeability

Abstract. The J-integral for cracks in structures storing elastic, dielectric and thermal energies is derived from thermodynamical fundamentals. The FEM is applied to solve thermoelectromechanical boundary value problems, accounting for piezoelectric coupling, thermoelasticity and the pyroelectric effect. Examples demonstrate the influence of the thermal conductivity of cracks on the loading of the crack tip.

Introduction

As an important class of functional materials piezoelectric ceramics find a wide-spread application in smart structures and have to be subject to strength evaluations. The extension of piezoelectric fracture mechanics taking into account thermal effects is motivated by the manufacturing and operating conditions, where the material is exposed to temperature gradients. However, little numerical work has been done in this field to evaluate the fracture mechanics of arbitrary crack configurations [1]. In this paper, the J-integral for thermopiezoelectric material behavior is derived from thermodynamical fundamentals. Results of fracture mechanical calculations are presented, where the focus is on thermal and dielectric crack permeabilities.

Thermodynamics and the J-integral

The local energy balance in a body is governed by the First Law of thermodynamics

$$\delta u = \delta q + \delta w^{\mathrm{rev}} + \delta \psi \ , \tag{1}$$

where δu, δq and δw^{rev} are the change of the specific intrinsic energy, the exchange of specific heat and work related to an infinitesimal control volume dV. Whereas δw^{rev} comprises the reversible part of work, all irreversibilities going along with the change of state are expressed by the dissipative work $\delta\psi$. Considering e.g. the migration of a dislocation or point defect described by the displacement δz_k, all the variables in Eq. (1) represent the associated changes. If the dislocation is within the finite volume V, the total dissipative work $\delta\Psi$ is

$$\delta\Psi = \int\limits_V \delta\psi \, dV = J_k \, \delta z_k = \mathcal{G} \, \delta A \ . \tag{2}$$

Here, J_k is a generalized or configurational force acting on the defect, thermodynamically constituting the energy available for the irreversible displacement δz_k. Considering a crack, $\delta\Psi$ is related to the total energy rate $\mathcal{G}$ released from the system during a virtual crack extension by δA. Applying a Legendre transformation, the electric enthalpy density $h(\epsilon_{ij}, E_i, s)$ and the Gibbs energy density $g(\epsilon_{ij}, E_i, T)$ are introduced, being thermodynamical potentials as functions of the strain ϵ_{ij}, electric field E_i, specific entropy s and temperature T, respectively

$$u = h + E_i \, D_i = g + s \, T + E_i \, D_i \ , \tag{3}$$

where D_i is the electric displacement. If all dissipative processes are included in $\delta\psi$, the reversible specific electromechanical work and the specific heat are

$$\delta w^{\mathrm{rev}} = \sigma_{ij}\,\delta\epsilon_{ij} + E_i\,\delta D_i \quad , \quad \delta q = T\,\delta s \ . \tag{4}$$

Inserting Eqs. (2) to (4) in Eq. (1) and integrating yields the global energy balance in V:

$$J_k \delta z_k = \int_V (\delta g - \sigma_{ij}\,\delta\epsilon_{ij} + D_i\,\delta E_i + s\,\delta T)\,dV \ . \tag{5}$$

Next, the changes of state variables are expressed in terms of the virtual displacement δz_k, e.g.

$$\begin{aligned} &\int_V \delta g\,dV = \delta G = \frac{d\,G}{d\,x_k}\,\delta z_k = \int_V (g\,\delta_{kj})_{,j}\,dV\,\delta z_k \quad , \quad s\,\delta T = s\,T_{,k}\,\delta z_k \ , \\ &\sigma_{ij}\,\delta\epsilon_{ij} = \sigma_{ij}\,u_{i,kj}\,\delta z_k = (\sigma_{ij}\,u_{i,k})_{,j}\,\delta z_k \ , \end{aligned} \tag{6}$$

where volume forces have been omitted, i.e. $\sigma_{ij,j} = 0$. Inserting into Eq. (5) and applying Gauss's Theorem to a domain surrounded by the contour S with the normal n_j, the generalized force or – applied to cracks – the thermoelectromechanical J-integral finally comes out to be

$$J_k = \oint_S (g\,\delta_{kj} - \sigma_{ij}\,u_{i,k} + D_j\,E_k)\,n_j\,dS + \int_V s\,T_{,k}\,dV \ . \tag{7}$$

Solution of the coupled boundary value problem

The weak formulation of the electromechanical boundary value problem is derived form the principle of virtual work

$$\delta W^i + \delta W^a = 0 \quad \Rightarrow \quad \delta W^a - \delta G = 0 \ , \tag{8}$$

where the virtual work of external forces and charges acting on the Neumann boundaries S_t and S_ω as well as volume loads b_i and ω_V

$$\delta W^a = \int_{S_t} \bar{t}_i\,\delta u_i\,dS - \int_{S_\omega} \bar{\omega}_S\,\delta\phi\,dS + \int_V b_i\,\delta u_i\,dV + \int_V \omega_V\,\delta\phi\,dV \tag{9}$$

and the virtual work of internal forces and charges in terms of the change of the Gibbs potential for $\delta T = 0$, i.e. $\delta g = \sigma_{ij}\delta\epsilon_{ij} - D_i\delta E_i$ are balanced. Thus, the weak formulation is obtained as

$$\int_V (\sigma_{ij} + b_i)\ \delta u_i\,dV + \oint_S (\bar{t}_i - \sigma_{ij}\,n_j)\ \delta u_i\,dS + \int_V (D_{i,i} - \omega_V)\ \delta\phi\,dV - \oint_S (D_i\,n_i + \bar{\omega}_S)\ \delta\phi\,dS = 0 \tag{10}$$

The thermal heat conduction problem is governed by Fouriers Law

$$h_i = -\lambda_{ij}\,T_{,j} \ , \tag{11}$$

with h_i as the heat flux per unit area. The heat balance in the domain V yields

$$h_{i,i} = -\lambda_{ij}\,T_{,ij} = \dot{q}_V - T\,\dot{s} \tag{12}$$

and on the surface ($\dot{q}_V, \dot{q}_S$: heat sources in V and on S, $\dot{(..)}$: time derivative)

$$\dot{q}_i \, n_i = -\dot{q}_S \ . \tag{13}$$

Applying the "principle of virtual temperature" taking into accounting Eqs. (12) and (13), the weak formulation for the thermal problem is

$$\delta W_T = \int\limits_V \left(\dot{q}_{i,i} + T\,\dot{s} - \dot{q}_V\right)\,\delta T\,dV - \oint\limits_S \left(\dot{q}_S + \dot{q}_i\,n_i\right)\,\delta T\,dS = 0 \ . \tag{14}$$

The thermopiezoelectric material behavior is governed by the linear constitutive equations:

$$\begin{aligned} \sigma_{ij} &= C_{ijkl}\,\epsilon_{kl} - e_{kij}\,E_k - \beta_{ij}\,\theta \\ D_i &= e_{ijk}\,\epsilon_{jk} + \kappa_{ik}\,E_k + k_i\,\theta \\ \eta &= \beta_{ij}\,\epsilon_{ij} + k_i\,E_i + \gamma\,\theta \end{aligned} \quad . \tag{15}$$

The material tensors C_{ijkl}, κ_{ij} and γ represent elastic, dielectric and caloric properties. The coupling phenomena are comprised by the tensors e_{ijk}, β_{ij} and k_i of piezoelectric, thermal stress and pyroelectric constants. The relative temperature $\theta = T - T_0$ and entropy $\eta = s - s_0$ have been introduced referring to homogeneous constant reference states T_0 and s_0. The time derivative $\dot{s} = \dot{\eta}$ in Eq. (14) is zero, if a steady state is considered, i.e. $\dot{\epsilon}_{ij}, \dot{E}_i, \dot{\theta} = 0$. Introducing element shape functions for displacement, electric potential and temperature, Eqs. (10) and (14) are discretisized leading to an algebraic system of equations with the respective nodal values $\hat{u}$, $\hat{\phi}$, $\hat{\theta}$ as unknowns:

$$\begin{aligned} \begin{pmatrix} [K_{uu}] & [K_{u\phi}] \\ [K_{\phi u}] & [K_{\phi\phi}] \end{pmatrix} \begin{pmatrix} \{\hat{u}\} \\ \{\hat{\phi}\} \end{pmatrix} &= \begin{pmatrix} \{\hat{F}_V\} + \{\hat{F}_S\} \\ \{\hat{\Omega}_V\} + \{\hat{\Omega}_S\} \end{pmatrix} - \begin{pmatrix} [K_{u\theta}] \\ [K_{\phi\theta}] \end{pmatrix} \{\hat{\theta}\} \\ [K_{\theta\theta}]\ \{\hat{\theta}\} &= \{\hat{Q}_V\} + \{\hat{Q}_S\} \end{aligned} \tag{16}$$

The generalized stiffness matrices containing material constants according to Eq. (15) are written in square brackets. Nodal loads in terms of forces $\hat{F}$, charges $\hat{\Omega}$ and heat flux $\hat{Q}$ are on the right hand sides. The piezoelectric and thermal boundary value problems are decoupled, thus the thermomechanical and thermoelectrical effects are incorporated as volume loads.

Cracks in thermopiezoelectric materials

The streamlines of the heat flux near a crack exhibit similar characteristics as e.g. those of the electric field, leading to a crack tip singularity. Thus, the thermal conductivity of the crack interior plays an important role, controlling the gradients of mechanical, electrical and thermal fields. The model applied is akin to the capacitor analogy model by Hao and Shen in electrostatics, assuming the crack to be a parallel alignment of one-dimensional heat conduction elements. The local flux within the crack is given by Eq. (11) with $\lambda_{ij} = \lambda\,\delta_{ij}$ (δ_{ij} : unit tensor):

$$\dot{q}_n^C = -\lambda^C\,\frac{\Delta\theta}{\Delta u_n} \ . \tag{17}$$

Numerically, the normal heat flux $\dot{q}_n^C$ is treated as external load on the crack faces. Eq. (17) is satisfied applying an iterative procedure in connection with the numerical calculation of the jump of temperature $\Delta\theta$ and normal displacement Δu_n across the crack faces. Thus, the crack is considered to be thermally semi-permeable. Similar as with dielectric permeability models, the limiting cases of impermeable and fully permeable cracks are represented by the boundary

conditions $\dot{q}_n^C = 0$ and $\Delta\theta = 0$ (dielectric :$D_n^C = 0$ and $\Delta\phi = 0$). If the J-integral Eq. (7) is calculated for crack surface loads D_2^C and $\dot{q}_n^C$, the contour S has to be extended along the crack faces. For a straight virtual crack extension in the x_1-direction, the J_1-component as the relevant crack tip loading quantity is equal to the energy release rate. Due to $n_1 = 0$ the crack surface integral is reduced as

$$J_1^C = -\int_{S^C} D_2^C \, \phi_{,1} \, dS \;\approx\; \frac{\kappa^C \, \Delta\phi^2}{\Delta u_n} \; . \tag{18}$$

The crack faces are assumed to be free of mechanical tractions. According to Eq. (18), J_1^C is replaced by a jump of displacements and electric potentials across the crack with a dielectric permittivity κ^C [3]. The thermal loads $\dot{q}_n^C$ do not appear in the crack surface integral, their influence is incorporated in the volume integral in Eq. (7).

Results

First, the influence of the heat conductivities λ of the material on the thermal permittivity of the crack are investigated. Assuming air inside the crack, $\lambda^C = 0.026$ W/(mK). In Fig. 1 the heat fluxes at the crack faces $\dot{q}_n^C$ (normalized with respect to the thermal load $\dot{q}_S = \dot{q}^\infty$) are presented for the model of a Griffith crack of length $2a = 4.8$ mm. The abscissa shows the mechanical load in terms of the normalized stress intensity factor K_I/K_{IC}. The heat conductivities λ^{Cu}, λ^{Fe} and λ^{Cer} are those of copper, steel and ceramics. The fracture toughnesses K_{IC} are those of the respective materials. According to Fig. 1, increasing values of λ and K_I foster the impermeability of the crack. i.e. $\dot{q}_n^C \to 0$. For ceramics, the crack may be considered as fully permeable. In Fig. 2, J_1 from the equivalent domain integral formulation of Eqs. (7) and (18) is presented for an edge crack with different thermal boundary conditions and external heat fluxes ($\dot{q}_S > 0$: in poling direction). The crack is additionally loaded by tractions $\bar{t}_n$ and charges $\bar{\omega}_S$. The thermal loading has a large influence on the enrgy release rate, whereas the choice of thermal crack boundary conditions manifests itself by only a few percent in the example.

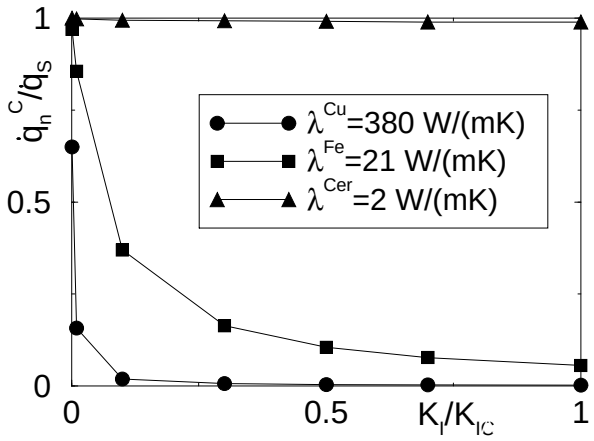

Figure 1: Crack surface heat flux $\dot{q}_n^C$ for 3 materials under mech. and therm. loading

edge crack	$\dot{q}_S$ [W/m^2]	J_1 [N/m]
thermally semipermeable	0	10
	-10^3	16
	$+10^3$	5.3
thermally impermeable	-10^3	16.7
	$+10^3$	5.1

Figure 2: J_1-integral for edge crack of length $a = 2.4$ mm; $\bar{t}_n = 11.5$ MPa, $\bar{\omega}_S = 10^{-2}$ N/(Vm), different therm. loadings $\dot{q}_S$

References

[1] M. Kuna, in: *IUTAM Symposium on Mechanics and Reliability of Actuating Materials*, ed. by W. Yang, Springer, 131-143 (2006).

[2] T.H. Hao and Z.Y. Shen: Engineering Fracture Mechanics Vol. 47 (1994), p. 793.

[3] A. Ricoeur, M. Enderlein and M. Kuna: Archive of Applied Mechanics 74 (2005), p. 536.

Key Engineering Materials Vols. 385-387 (2008) pp 573-576
© (2008) Trans Tech Publications, Switzerland
doi:10.4028/www.scientific.net/KEM.385-387.573

Stress Singularity of Thermal Stresses in Three-Dimensional Bonded Structures with An Interlayer

Hideo KOGUCHI[1, a] and Akira TANIGUCHI[2,b]

[1]Nagaoka University of Technology, 1903-1Kamitomioka, Nagaoka, Niigata, 940-2188 Japan

[2]Graduate School, Nagaoka University of Technology, 1903-1Kamitomioka, Nagaoka, Niigata, 940-2188 Japan

[a]koguchi@mech.nagaokaut.ac.jp, [b]taniguti@stn.nagaokaut.ac.jp

Keywords: Stress singularity, Three-dimensional joint, Residual thermal stresses, BEM, Eigen analysis

Abstract. In the present paper, singular stress field at the vertex on the interface in three-dimensional bonded joints is analyzed using BEM and eigen analysis. The order of stress singularity is determined solving an eigen equation based on FEM formulation and the stress distribution is expressed using the result of the eigen-value analysis. A relationship between the thickness of interlayer and residual thermal stresses is presented. Then, a three-dimensional intensity of singularity is determined.

Introduction

It is well known that stress singularity occurs at a vertex on an interface in joints under mechanical and thermal loadings [1,2]. Stress distribution in the stress singular region can be usually expressed as $\sigma_{ij}(\boldsymbol{r},\theta,\phi)=\sum_{m}\boldsymbol{K}_{ij}^{m}\boldsymbol{r}^{-\lambda_m}\boldsymbol{f}_{ij}^{m}(\theta,\phi)$. In the present paper, singular fields in residual thermal stresses at the vertex on the interface in three-dimensional bonded joints are analyzed using BEM. The order of stress singularity is determined through eigen-value analysis based on FEM formulation, and the expression for stress distribution is presented. The intensity of singularity at the vertex in the joint is determined considering the influence of stress singular line. The dependence of the intensity of singularity on the thickness of joint is investigated for various thicknesses of interlayer.

Method for analysis

The stress distribution in three-dimensional bonded joints is obtained using BEM described as follows.

$$\boldsymbol{c}_{ij}(\boldsymbol{P})\boldsymbol{u}_j(\boldsymbol{P})=\int_{\Gamma}\boldsymbol{U}_{ij}^{*}(\boldsymbol{P},\boldsymbol{Q})\boldsymbol{t}_j d\boldsymbol{S}(\boldsymbol{Q})-\int_{\Gamma}\boldsymbol{T}_{ij}^{*}(\boldsymbol{P},\boldsymbol{Q})\boldsymbol{u}_j d\boldsymbol{S}(\boldsymbol{Q}). \tag{1}$$

where $\boldsymbol{U}_{ij}^{*}$ and $\boldsymbol{T}_{ij}^{*}$ are fundamental solutions for displacement and traction. Observation point, P and source point, Q, are located on the boundary of domain for analysis. t_j and u_j are traction and displacement vectors, respectively. Using the fundamental solution of Rongved's two-phase materials, mesh division on the interface is not needed.

In this analysis, the order of stress singularity is determined using an eigen analysis of FEM. The characteristic solution, p, has the relationship of λ=1-p with the order of stress singularity λ. p is determined from the following eigen equation in Ref. [3].

$$\left(\boldsymbol{p}^2[\boldsymbol{A}]+\boldsymbol{p}[\boldsymbol{B}]+[\boldsymbol{C}]\right)\{\boldsymbol{u}\}=0. \tag{2}$$

where $[A]$, $[B]$ and $[C]$ are matrices composed of elastic moduli, and $\{u\}$ represents the

displacement vector. Material property is expressed by Hooke's law shown below.

$$\sigma_{ij} = \frac{\boldsymbol{E}}{1+\nu}\left(\varepsilon_{ij} + \frac{\nu}{1-2\nu}\varepsilon_{kk}\delta_{ij}\right) - \frac{\boldsymbol{E}}{1-2\nu}\alpha\Delta\boldsymbol{T}\delta_{ij}\,. \tag{3}$$

where E represents Young's modulus, ν Poisson's ratio, α the coefficient of thermal expansion, ΔT temperature change and δ_{ij} Kronecker's delta.

Residual thermal stresses in joints can be calculated following Duhamel theorem. External traction, $-\boldsymbol{E}\alpha\Delta\boldsymbol{T}/(1-2\nu)$, for materials constituting a joint is applied to the side surface of the joint. After that, the applied stresses are removed from calculated stresses.

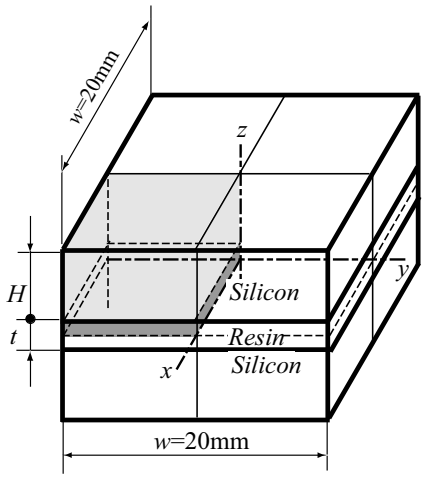

Fig.1 Model for analysis

Analysis and Results

Figure 1 represents the model for analysis, where silicon of thickness H is bonded with resin of thickness t. Two models are prepared for comparing the effect of thicknesses on the intensity of singularity at a vertex in joints. In model A, the thickness of resin is fixed at t=0.02mm, and that of silicon is varied from H=0.005 to 25.6mm. In model B, the thickness of silicon is fixed at H=10mm, and that of resin is varied from t=0.05 to 3.2mm. Material properties used in the analysis are presented here. Young's modulus, Poisson's ratios and a thermal expansion coefficient are (E, ν, α)=(166.0GPa, 0.26, 0.3) for silicon and (E, ν, α)=(2.74GPa, 0.38, 3.3) for resin. Here, ΔT is -155K. Then, the applied external forces are -161MPa for silicon and -58.4MPa for resin.

In the present paper, stress components are transformed from rectangular coordinate system to spherical coordinate system with an origin located at the vertex as shown in Fig.2. An example of stress distribution for spherical coordinate systems is shown in Fig.3. Distribution of stress, $\sigma_{\theta\theta}$, at θ=90deg and ϕ=45deg is demonstrated against the distance r shown in

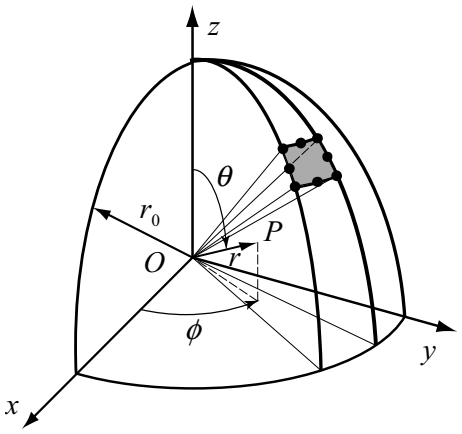

Fig.2 Spherical coordinate system

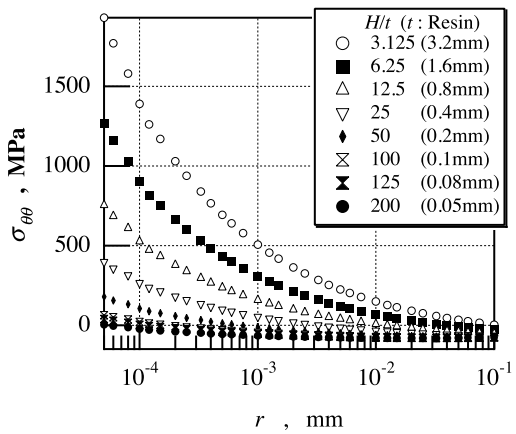

(*a*) Distribution for distance r

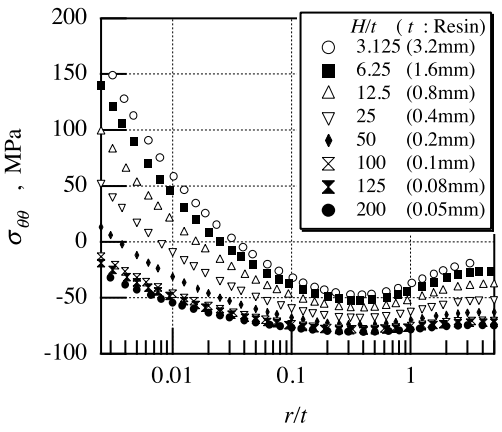

(*b*) Distribution for dimensionless distance r/t

Fig.3 Stress distribution against r (Model B) at θ=90deg and ϕ=45deg

Table 1 Order of stress singularity

Order of singularity				
	ϕ = 90deg		ϕ = 180deg	
	p_{vertex}	λ_{vertex}	p_{side}	λ_{side}
1	1.000	0.000	1.000	0.000
2	1.000	0.000	1.000	0.000
3	1.000	0.000	1.000	0.000
4	0.605	0.395	1.000	0.000
5	-	-	1.000	0.000
6	-	-	0.682	0.318

Fig.2. Figures 3(*a*) and 3(*b*) represent the stress distributions against the distance *r* and against a dimensionless distance *r*/*t*, respectively. It is found from Fig.3(*b*) that the minimum value of $\sigma_{\theta\theta}$ for different thickness of resin occurs around *r*/*t*=0.3.

The order of stress singularity, λ, obtained from eigen analysis is shown in Table 1. The value for ϕ=90deg shows the one for vertex and that for ϕ=180deg the one for stress singularity line. Stress distribution in the stress singular region from the result of eigen analysis can be expressed as follows.

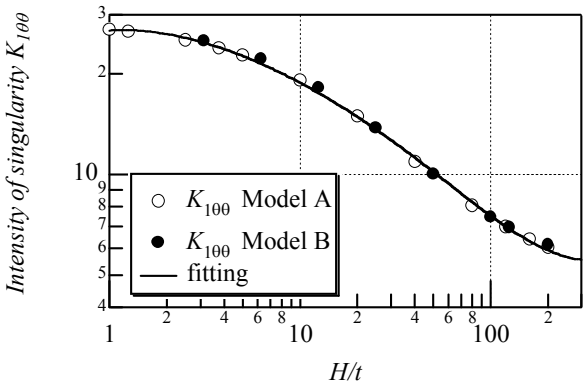

Fig.4 A relationship between $K_{1\theta\theta}$ and *H*/*t*

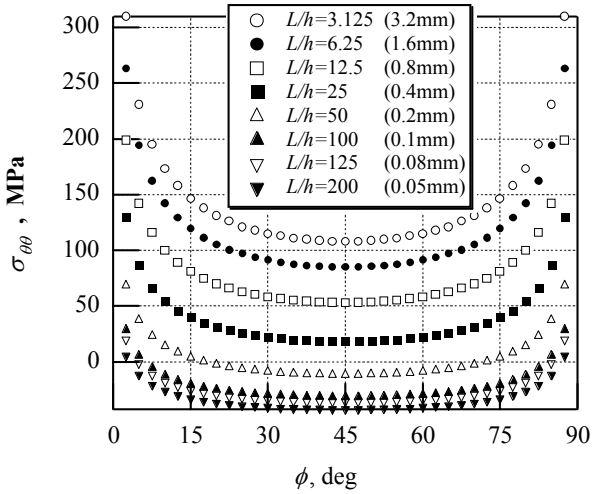

Fig.5 Stress distribution for angle ϕ

$$\sigma_{ij}\left(\bar{\boldsymbol{r}},\frac{\pi}{2},\frac{\pi}{4}\right)=\boldsymbol{K}_{1ij}\bar{\boldsymbol{r}}^{-0.395}+\boldsymbol{K}_{2ij}+\boldsymbol{K}_{3ij}\ln\bar{\boldsymbol{r}}+\boldsymbol{K}_{4ij}\left(\ln\bar{\boldsymbol{r}}\right)^2 \tag{4}$$

where $\bar{r}=r/t$.

Coefficients in Eq.(4) are determined from the stress distribution shown in Fig.3(*b*), and the values of $K_{1\theta\theta}$ in models *A* and *B* are plotted in Fig.4 against *H*/*t*. The distributions are approximated using a least square method as

$$\boldsymbol{K}_{1\theta\theta}=-66.46\left(\boldsymbol{H}/\boldsymbol{t}\right)^{-0.395}+93.4-25.2\ln\left(\boldsymbol{H}/\boldsymbol{t}\right)+1.94\left\{\boldsymbol{n}\left(\boldsymbol{H}/\boldsymbol{t}\right)\right\}^2 \tag{5}$$

Distributions of $\sigma_{\theta\theta}$ on the interface against angle ϕ for model *B* are shown in Fig.5. It is found that the stress increases as approaching to the side surfaces, which are referred to as stress singularity lines. In the present study, it is supposed that the stress distribution near the vertex is affected by the stress singularity line. Here, the distance from the stress singularity line to a point *P* is introduced as shown in Fig.6. Considering the result of eigen analysis on the stress singularity line, the angular function of

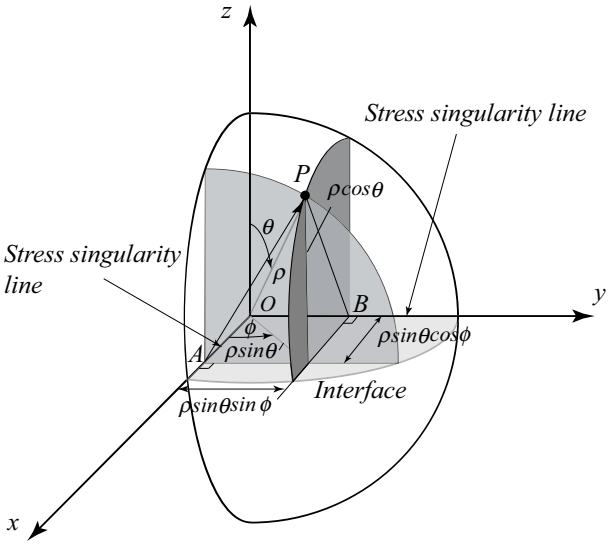

Fig.6 Distance from stress singularity line and vertex

the stress distribution is expressed as

$$f_{\theta\theta}(\rho_A,\rho_B,\pi/2,\phi)=L^A_{1\theta\theta}\rho_A^{-0.318}+L^B_{1\theta\theta}\rho_B^{-0.318}+L_{2\theta\theta}+\sum_{k=1}^{4}L^A_{(k+2)\theta\theta}(\ln\rho_A)^k+\sum_{k=1}^{4}L^B_{(k+2)\theta\theta}(\ln\rho_B)^k \quad (6)$$

where $\rho_A=\rho\sqrt{1-\sin^2\theta\cos^2\phi}$ and $\rho_B=\rho\sqrt{1-\sin^2\theta\sin^2\phi}$. Here, $L^A_{1\theta\theta}=L^B_{1\theta\theta}$ and ρ=1.

The coefficients in Eq.(6) are determined from Fig.5 and shown in Fig.7. The coefficient, $L_{1\theta\theta}$, is approximated using a least square method as follows.

$$L^A_{1\theta\theta}=-5.49(H/t)^{-0.318}+6.93-1.71\ln(H/t)+0.12\{\ln(H/t)\}^2. \quad (7)$$

Finally, the intensity of singularity at the vertex in three-dimensional bonded joints is determined. The distribution of stress, $\sigma_{\theta\theta}$, can be expressed considering stress singularity line

$$\sigma_{\theta\theta}(\bar{r},\rho_A,\rho_B,\pi/2,\phi)=K^{3D}_{1\theta\theta}\left(\rho_A^{-0.318}+\rho_B^{-0.318}+L_{2\theta\theta}/L_{1\theta\theta}\right)\bar{r}^{-0.395}+K_{2\theta\theta}f_{2\theta\theta}(\theta,\phi) \quad (8)$$

where $K^{3D}_{1\theta\theta}=K_{1\theta\theta}L_{1\theta\theta}$ and is called as the intensity of singularity at the vertex. Figure 8 shows a relationship between $K^{3D}_{1\theta\theta}$ and H/t. The solid line plotted represents the following expression.

$$K^{3D}_{1\theta\theta}=-70.66(H/t)^{-0.713}+109.38-47.83\ln(H/t)+7.13\{\ln(H/t)\}^2-0.36\{\ln(H/t)\}^3 \quad (9)$$

It is noted that the power terms in the expressions of $K_{1\theta\theta}$ and $L_{1\theta\theta}$ have the same value as the order of singularity, and the value of power term in $K^{3D}_{1\theta\theta}$ is a sum of the values of the order of singularity for the vertex and the singularity line.

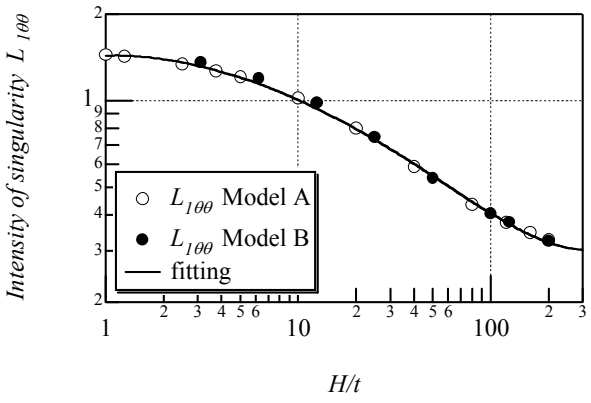

Fig.7 A relationship between $L_{1\theta\theta}$ and H/t

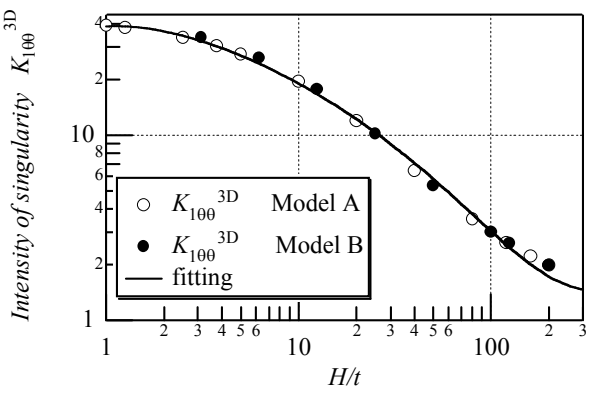

Fig.8 A relationship between $K^{3D}_{1\theta\theta}$ and H/t

Summary

In the present paper, the intensity of singularity at the vertex in three-dimensional bonded joints with varying the thicknesses of silicon and resin was investigated. The intensity of singularity was expressed with a function of H/t, where H is the thickness of silicon and t that of resin.

References

[1] H. Koguchi, Trans. Japan Soc. Mech. Eng., Vol.72 (2006), p.2058.

[2] H. Koguchi and S. Nakamura, Trans. Japan Soc. Mech. Eng., Vol.73 (2007), p.883.

[3] S.S. Pageau and Jr S.B. Bigger, Int. J. Numer. Methods Eng., Vol.38 (1995), p. 2225.

Key Engineering Materials Vols. 385-387 (2008) pp 577-580
© (2008) Trans Tech Publications, Switzerland
doi:10.4028/www.scientific.net/KEM.385-387.577

Generalized Quasi-variational Principles and Application in Nonlinear Non-conservative Elasto-dynamics

Tao Fan[1,a], HaiYan Song[1,b]

[1] School of Civil Engineering, Harbin Engineering University, Harbin, 150001,China

[a]fantao19812005@yahoo.com.cn, [b]songhaiyan@hrbeu.edu.cn

Keywords: nonlinear; non-conservative system; elasto-dynamics ;quasi-variational principle

Abstract. The generalized quasi-variational principles with two kinds of variables of time initial value problem were established in nonlinear non-conservative elasto-dynamics. Then, the analytic solution of time initial value problem of a typical non-conservative elasto-dynamics was studied by applying the obtained quasi-complementary variational principle.

Introduction

The research of generalized variational principles in nonlinear non-conservative is very vital, which consists of many subjects. However, studies on this aspect have been only a few, due to the double-difficulty of establishing generalized variational principles in nonlinear non-conservative system and applying them to practical and engineering problems.

The generalized variational principles of time initial value problem in nonlinear non-conservative elasto-dynamics are investigated in this paper, based on the relevant researches [1-4]. Taking the method in reference [5], the generalized quasi-variational principles with two kinds of variables were established in nonlinear non-conservative elasto-dynamics. Furthermore, the analytic solution of time initial value problem of a typical non-conservative elasto-dynamics was studied by the obtained quasi-complementary variational principle.

Basic Equations

$$[(\delta_{IJ}+U_{I,J})S_{JK}]_{,K}+\bar{F}_I-\dot{R}_I=0. \quad (\text{in } V) \tag{1}$$

$$(\delta_{IJ}+U_{I,J})S_{JK}N_K-\bar{P}_I=0. \quad (\text{on } S_\sigma) \tag{2}$$

$$E_{JK}-\frac{1}{2}U_{J,K}-\frac{1}{2}U_{K,J}-\frac{1}{2}U_{I,J}U_{I,K}=0. \quad (\text{in } V) \tag{3}$$

$$U_I-\bar{U}_I=0. \quad (\text{on } S_u) \tag{4}$$

$$S_{JK}-\frac{\partial A(E_{JK})}{\partial E_{JK}}=0. \quad (\text{in } V) \tag{5}$$

$$E_{JK}-\frac{\partial B(S_{JK})}{\partial S_{JK}}=0. \quad (\text{in } V) \tag{6}$$

$$\dot{U}_I-V_I=0. \tag{7}$$

$$R_I-\rho_0 V_I=0. \tag{8}$$

$$V_I-\frac{1}{\rho_0}R_I=0. \tag{9}$$

$$U_I(0)-\bar{U}_I(0)=0. \tag{10}$$

$$V_I(0)-\bar{V}_I(0)=0. \tag{11}$$

$$R_I(0)-\bar{R}_I(0)=0. \tag{12}$$

where : S_{JK} ——Kirchhoff stress tensor, E_{JK} ——Green strain tensor, U_I ——displacement component in initial configuration, $\bar{F}_I$ ——body force component, $\bar{P}_I$ ——surface force component, R_I ——momentum component, V_I ——velocity component, ρ_0 ——mass density

before deformation, $A(E_{JK})$ —— density function of strain energy, $B(S_{JK})$ —— density function of strain complementary energy, N_K —— normal vector, "," ——derivative to space-coordinate variables, S_σ —— force boundary, S_u ——displacement boundary, V ——spatial domain.

The Generalized Quasi-variational Principles with Two Kinds of Variables

According to the corresponding relations between generalized forces and generalized displacements, Eqs.(1)~(4) and (7) are convol-multiplied by corresponding virtual quantities respectively, integrated with volume and area, then added algebraically, we get

$$\iiint_V \{[(\delta_{IJ}+U_{I,J})S_{JK}],_K+\bar{F}_I-\dot{R}_I\}*\delta U_I dV+\iiint_V\{(E_{JK}-\frac{1}{2}U_{J,K}-\frac{1}{2}U_{K,J}-\frac{1}{2}U_{I,J}U_{I,K})*\delta S_{JK}-(\dot{U}_I-V_I)*\delta R_I-[U_I(0)-$$
$$\bar{U}_I(0)]\delta R_I-[R_I(0)-\bar{R}_I(0)]\delta U_I\}dV-\iint_{S_\sigma}[(\delta_{IJ}+U_{I,J})S_{JK}N_K-\bar{P}_I]*\delta U_I dS+\iint_{S_u}(U_I-\bar{U}_I)*\delta[(\delta_{IJ}+U_{I,J})S_{JK}N_K]dS=0\ .(13)$$

Using the convolution theory of Laplace transform, and Green theorem,

$$-\dot{U}_I*\delta R_I=-U_I*\delta\dot{R}_I+U_I(0)\delta R_I\ . \tag{14}$$
$$-\iiint_V U_{J,K}*\delta S_{JK}dV=-\iint_{S_\sigma+S_u}U_I*\delta(S_{IK}N_K)dS+\iiint_V U_I*\delta S_{IK,K}dV\ . \tag{15}$$

According to the idea of restricted variation[3,4], there are the following two equations

$$\delta(\frac{1}{2}U_{I,J}U_{I,K})=0\ . \tag{16}$$
$$\delta(U_{I,J}S_{JK})=0\ . \tag{17}$$

Substituting Eqs.(14)、(15), and material constitutive relation (6) and momentum constitutive relation (9) into Eq.(13), and substituting Eqs.(16)、(17) into Eq.(13) by transformation of naught addition, finishing it, we get

$$\delta\Gamma_{G21}-\delta Q_G-\delta P_G=0\ . \tag{18}$$

Where

$$\Gamma_{G21}=\iiint_V\{[(\delta_{IJ}+U_{I,J})S_{JK}],_K+\bar{F}_I-\dot{R}_I\}*U_I dV+\iiint_V\{\frac{1}{2}\frac{1}{\rho_0}R_I*R_I+B^*(S_{JK})-(\frac{1}{2}U_{I,J}U_{I,K})*S_{JK}+\bar{U}_I(0)R_I-$$
$$[R_I(0)-\bar{R}_I(0)]U_I\}dV-\iint_{S_\sigma}[(\delta_{IJ}+U_{I,J})S_{JK}N_K-\bar{P}_I]*U_I dS-\iint_{S_u}\bar{U}_I*[(\delta_{IJ}+U_{I,J})S_{JK}N_K]dS\ .$$
$$\delta Q_G=\iiint_V U_I*\delta\bar{F}_I dV\ .\qquad \delta P_G=\iint_{S_\sigma}U_I*\delta\bar{P}_I dS\ .$$

Eq.(18) is called convolution-type generalized quasi-complementary energy principle with two kinds of variables in nonlinear non-conservative elasto-dynamics.

If using the convolution theory of Laplace transform, and Green theorem,

$$-\dot{R}_I*\delta U_I=-R_I*\delta\dot{U}_I+R_I(0)\delta U_I\ . \tag{19}$$
$$\iiint_V[(\delta_{IJ}+U_{I,J})S_{JK}],_K*\delta U_I dV=\iint_{S_\sigma+S_u}(\delta_{IJ}+U_{I,J})S_{JK}N_K*\delta U_I dS-\iiint_V(\delta_{IJ}+U_{I,J})S_{JK}*\delta U_{I,K}dV\ . \tag{20}$$

Substituting Eqs.(19)、(20), and material constitutive relation (6) and momentum constitutive

relation (9) into Eq.(13), and substituting Eqs.(16)、(17) into Eq.(13) by transformation of naught addition, then changing the signs of Eq.(13), finishing it, we get

$$\delta \Pi_{G21} + \delta Q_G + \delta P_G = 0 . \tag{21}$$

Where

$$\Pi_{G21} = \iiint_V \{R_I * \dot{U}_I - \frac{1}{2}\frac{1}{\rho_0} R_I * R_I - B^*(S_{JK}) + (\frac{1}{2}U_{J,K} + \frac{1}{2}U_{K,J} + \frac{1}{2}U_{I,J}U_{I,K}) * S_{JK} + (U_{I,J}S_{JK}) * U_{I,K} -$$
$$\bar{F}_I * U_I - \bar{R}_I(0)U_I + [U_I(0) - \bar{U}_I(0)]R_I\}dV - \iint_{S_\sigma} \bar{P}_I * U_I dS - \iint_{S_u} (U_I - \bar{U}_I) * [(\delta_{IJ} + U_{I,J})S_{JK}N_K]dS .$$

$$\delta Q_G = \iiint_V U_I * \delta \bar{F}_I dV . \quad \delta P_G = \iint_{S_\sigma} U_I * \delta \bar{P}_I dS .$$

Eq.(21) is called convolution-type generalized quasi-potential energy principle with two kinds of variables in nonlinear non-conservative elasto-dynamics.

Example

In aerocraft structural mechanics, there are many cases of multi-cell thin walled cantilever beam. The extended part of the aerofoil can be simplified as a model of free bending and torsion problem of the cantilever beam. Aerodynamic forces on the aerofoil can make it turn an angle. Conversely, the torsional angle can also change the aerodynamic forces. Thus, this is a non-conservative mechanics problem. We can solve the problem by generalized quasi-complementary energy principle with two kinds of variables.

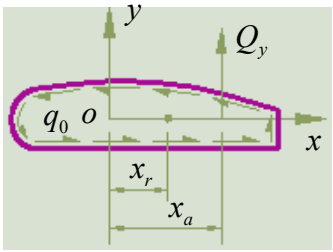

Fig.1 section view of the aerofoil

Consider the section view of the aerofoil with single closed cell shown in Fig.1, the shear force of section is Q_y, the coordinate of air-powered center is x_a, let the cross section of the aerofoil is symmetrical, its mass center and rigid center are coincident, so the vibration of bending and torsion aren't coupling, we only consider torsion in this paper. Let the coordinate of rigid center is x_r. By "cutting" the single closed cell of the section imaginarily, the shear flow of open section is vanish, while the unknown value of shear flow of the single closed section is q_0.

In this concrete problem,let the initial condition of relative angles is $\varphi(0) = \bar{\varphi}(0)$,while without considering the initial condition of moment of momentum, and based on finite deformation theory of beam[6,7], convolution-type generalized quasi-complementary energy principle with two kinds of variables is expressed as

$$\delta \Gamma_{G2} - \delta Q_G - \delta P_G = \dot{L} * \delta\varphi + \varphi * \delta\dot{L} + \bar{\varphi}(0)L - \int \frac{q_0}{Gt} dS * \delta q_0 - \frac{1}{I_c} L * \delta L + M_z * \delta\varphi - \Omega q_0 * \delta\varphi - \Omega\varphi * \delta q_0 dt = 0 . \tag{22}$$

where, I_c ——moment of inertia about centroidal axis, G ——shear modulus, t ——thickness of wall, φ ——relative torsional angle of per unit length of section of the aerofoil, M_z ——the external moment, L ——moment of momentum about rigid center.

The Laplace tramform of Eq.(22) is

$$\delta \tilde{\Gamma}_{G2} - \delta \tilde{Q}_G - \delta \tilde{P}_G = [p\tilde{L} - L(0)]\delta\tilde{\varphi} + \tilde{\varphi}\delta[p\tilde{L} - L(0)] + \bar{\varphi}(0)\delta L - \int \frac{\tilde{q}_0}{Gt} dS\delta\tilde{q}_0 - \frac{1}{I_c}\tilde{L}\delta\tilde{L} + \tilde{M}_z\delta\tilde{\varphi} - \Omega\tilde{q}_0\delta\tilde{\varphi} - \Omega\tilde{\varphi}\delta\tilde{q}_0)dt = 0 . \tag{23}$$

Eq.(23) can be dealt with into the following

$$\delta\tilde{\Gamma}_{G2}-\delta\tilde{Q}_G-\delta\tilde{P}_G=[p\tilde{\varphi}-\frac{1}{I_c}\tilde{L}+\bar{\varphi}(0)]\delta\tilde{L}+[p\tilde{L}-L(0)+\tilde{M}_z-\Omega\tilde{q}_0]\delta\tilde{\varphi}-[\int\frac{\tilde{q}_0}{Gt}dS+\Omega\tilde{\varphi}]\delta\tilde{q}_0=0\,. \tag{24}$$

Considering the arbitrariness of $\delta\tilde{L}$、$\delta\tilde{\varphi}$ and $\delta\tilde{q}_0$, and $L(0)=I_c\dot{\varphi}(0)$, let $Q_y=qAC_y^{\alpha}(\alpha-\varphi)$, where, q——dynamic pressure，A——aera of wing surface，C_y^{α}——derivative to lift coefficient，α——attack angle of aera，we get

$$p^2\tilde{\varphi}+p\bar{\varphi}(0)-\dot{\varphi}(0)+\omega_n^2\tilde{\varphi}=\frac{F_0}{p}\,. \tag{25}$$

where

$$\omega_n=\sqrt{\frac{1}{I_c}\left[\frac{\Omega^2}{\int\frac{dS}{Gt}}-(x_a-x_r)qAC_{\alpha}^{y}\right]}\,.\quad\text{And}\quad F_0=-\frac{(x_a-x_r)qAC_{\alpha}^{y}\alpha}{I_c}\,.$$

Finishing Eq.(25), we get

$$\varphi=-[\bar{\varphi}(0)+\frac{F_0}{\omega_n^2}]\cos\omega_n t+\frac{\dot{\varphi}(0)}{\omega_n}\sin\omega_n t+\frac{F_0}{\omega_n^2}\,. \tag{26}$$

$$q_0=\frac{\Omega}{\int\frac{dS}{Gt}}\{-[\bar{\varphi}(0)+\frac{F_0}{\omega_n^2}]\cos\omega_n t+\frac{\dot{\varphi}(0)}{\omega_n}\sin\omega_n t+\frac{F_0}{\omega_n^2}\}\,. \tag{27}$$

Summary

In this paper, the convolution-type generalized quasi-variational principles with two kinds of variables of time initial value problem in nonlinear non-conservative elasto-dynamics are given, and its application is discussed. The method in the paper could be used to study some other correlative problems.

References

[1] Hu Haichang. Variational principles and application in elasticity. Beijing：Sciences Press，1981.

[2] Liang Lifu. Variational principles and application. Harbin Engineering University Press and other 4 associated Presses，2005.

[3] Luo En, Zhu Huijian. Gurtin-type variational principles for finite deformation elastodynamics. Acta Mechanica Solida Sinica, 2003, 24(1):1-7.

[4] Finlayson B A, Scriven L. On the search for variational principles. Int J HeatMassTransfer, 1967, 10: 799.

[5] Liang Lifu, Liu Diankui, Song Haiyan . Generalized quasi-variational principles with two kinds of variables in non-conservative system. Science in China(Series G),2005,35(2): 201-212

[6] Li Mingrui. The geometric large deformation of beam, plate an shell - from the approximate non-linear theory to the finite deformation theory. Mechanics and practice, 2003,25(3):1-8.

[7] Li Jinjing, Li Mingrui, Li Xin. Exact and approximate finite deformation theories of 2-D beam. Journal of China Agricultural university, 1999,4(2):36-42.

Key Engineering Materials Vols. 385-387 (2008) pp 581-584
© (2008) Trans Tech Publications, Switzerland
doi:10.4028/www.scientific.net/KEM.385-387.581

Low cycle fatigue of cast superalloy Inconel 738LC at high temperature

Karel Obrtlík [1,a], Alice Chlupová[1,b], Martin Petrenec [1,c] and Jaroslav Polák[1,d]

[1] Institute of Physics of Materials AS CR, Žižkova 22, 616 62 Brno, Czech Republic

[a] obrtlik@ipm.cz, [b] chlupova@ipm.cz, [c] petrenec@ipm.cz, [d] polak@ipm.cz

Keywords: Low cycle fatigue, Inconel 738LC, hardening/softening curves, cyclic stress-strain curve, fatigue life curve, strain localization, slip marking.

Abstract. Cylindrical specimens of cast polycrystalline nickel base superalloy Inconel 738LC were cyclically strained under total strain control at 23 and 800 °C to fracture. Cyclic hardening/softening curves, cyclic stress-strain curves, and fatigue life curves were obtained at both temperatures. Surface relief was studied in specimens fatigued to failure using scanning electron microscopy. Cyclic hardening/softening behaviour depends both on temperature and strain amplitude. Low amplitude straining was characterized by saturation of the stress amplitude. In high amplitude straining a pronounced hardening was found which was followed by saturation at room temperature and by cyclic softening at 800 °C. The cyclic stress-strain curves can be fitted by power law. They are shifted to lower stresses with increasing temperature. Fatigue life curves can be approximated by the Manson-Coffin and Basquin laws. The Manson-Coffin and Basquin curves are shifted to lower lives with increasing temperature. Slip markings were detected on specimen surface at all test temperatures. When temperature grows the density of slip markings is reduced.

Introduction

Inconel 738LC (IN 738LC) is a precipitation strengthened nickel base superalloy with excellent high temperature strength and hot corrosion resistance. It is widely used for the production of blades and disks of gas turbine engines [1]. The critical turbine parts are subjected to repeated elastic-plastic straining as a result of heating and cooling during start-up and shut-down periods. Therefore, low cycle fatigue is an important factor in the design of the components and cyclic stress-strain and fatigue life data up to high temperatures are needed.

Fatigue behavior of Inconel 738LC is reported rarely [2-6]. Fatigue hardening was obtained at room temperature cycling [3] while the material gradually softens in the course of the fatigue life at 900 °C. Cyclic stress-strain curves based on the data at the half life agree well with the power law [3,4]. Fatigue life curves were obtained both in the Manson-Coffin and Basquin representation. The absolute value of the fatigue ductility exponent in the Manson-Coffin law is higher at 900 °C than that obtained at room temperature [3,4]. Strain localization is a very important phenomenon in the fatigue damage of crystalline solids [7]. Transmission electron microscopy investigation shows that planar slip bands cutting the γ' particles are present from room temperature up to 600 °C [2]. Localized deformation in narrow slip bands is observed even at 950 °C [6].

The purpose of the present work is to study the effect of temperature on the low cycle fatigue characteristics of cast polycrystalline Inconel 738LC in symmetrical total strain cycling. Strain localization was observed at the specimen surface.

Experimental details

Inconel 738LC polycrystals were provided by PSB Turbo, Velká Bíteš a.s. as conventionally cast rods in fully heat treated condition. Chemical composition of the superalloy is 16.22 Cr, 8.78 Co, 3.37 Ti, 3.35 Al, 2.63 W, 1.71 Mo, 0.2 Fe, 0.84 Nb, 0.1 C, 0.04 Zr, 0.008 B, the rest Ni (all in wt. %). Polished sections of the material reveal coarse grains with dendrites, carbides and shrinkage pores being rarely up to 0.16 mm in diameter. Rugged grain boundaries due to the complex

dendritic structure are apparent. The average grain size, found using the linear intercept method, was 1.3 mm. After the heat treatment γ′ precipitates are formed with near-cuboidal shape. They have an average diameter of 670 nm (see Fig. 1). TEM study revealed the presence of 61 % volume fraction of the γ′ precipitates. The low cycle fatigue tests were performed on button-end specimens having gauge length and diameter of 15 mm and 6 mm, respectively. Specimens were machined parallel to the rod axis and their gauge length was mechanically ground. The gauge section of some specimens was electrolytically polished to facilitate the observation of surface relief. Surface relief observations were performed in JEOL 6460 SEM (scanning electron microscope). Specimens were fatigued in a computer controlled electrohydraulic testing system in a symmetrical push-pull cycle in strain control. The strain was measured and controlled using a sensitive extensometer with a 12 mm base. The strain rate of $2x10^{-3}$ s^{-1} and total strain amplitude were kept constant in each test. The tests were conducted at room temperature (23 °C) and at 800 °C in air. Plastic strain amplitude was derived from the half of the loop width.

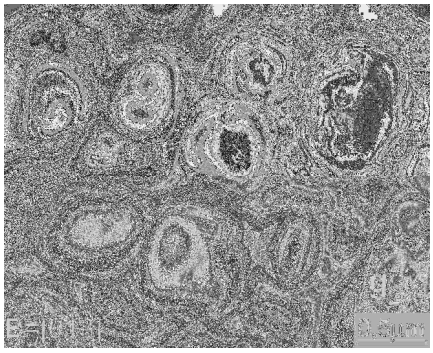

Fig. 1. Microstructure of IN 738LC in the dark field (TEM).

Results and discussion

Fig. 3 shows the dependence of the stress amplitude σ_a on the number of cycles N obtained at two temperatures for different total strain amplitudes. The character of these hardening/softening curves varies with strain amplitude and temperature. For room temperature cycling, the saturated stress response is observed until failure for low amplitudes – see Fig. 3a. The continuous hardening that becomes more pronounced with increasing strain amplitudes is typical for high amplitudes. For middle amplitudes the initial hardening is followed by the slow softening which changes into the secondary hardening – see Fig. 3a. The material exhibits different hardening/softening behaviour at elevated temperature of 800 °C - see Fig. 3b. The superalloy cyclically hardens in the early cycles and after that slowly softens up to the end of the fatigue life for higher amplitudes whilst the saturated behaviour can be seen in the low amplitude domain – see Fig. 3b.

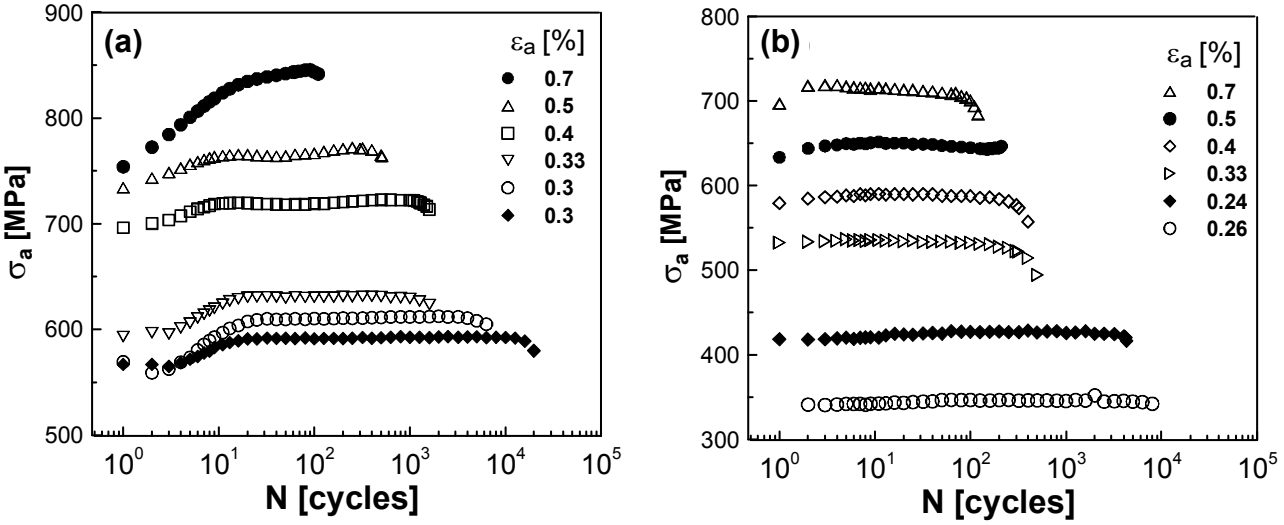

Fig. 3. Cyclic hardening/softening curves of IN 738LC at temperatures: (a) 23 °C and (b) 800 °C.

Inconel 738LC used in the present study is characterized by the coarse grain size – see Fig. 1. Thus, only several grains are present in the volume of a specimen corresponding to the gauge length. Therefore, the measured elastic modulus on individual specimens differed appreciably. The difference in the moduli of specimens strained with similar total strain amplitude results in great

difference of their stress response (Fig. 3b). Namely, the stress response of a specimen strained at 800 °C with $\varepsilon_a = 0.24$ % is about 80 MPa higher than that of a specimen strained with $\varepsilon_a = 0.26$ %.

Cyclic stress-strain curves (CSSCs) of the material are shown in Fig. 4 for both temperatures. The stress amplitude is plotted vs. the plastic strain amplitude at half-life. Experimental data were approximated by the power law

$$\log \sigma_a = \log K' + n' \log \varepsilon_{ap}. \quad (1)$$

Fatigue hardening coefficient K´ and fatigue hardening exponent n´ were evaluated using regression analysis and are shown for both temperatures in Table 2. It can be seen that both parameters of the CSSC strongly depend on temperature. Their values increase with temperature growth.

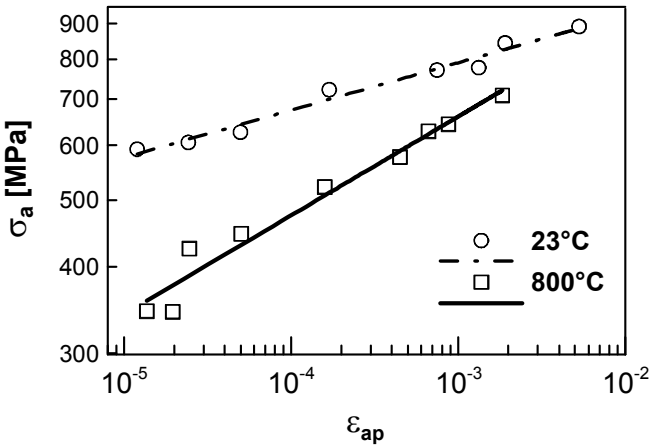

Fig. 4. Cyclic stress-strain curves of IN 738LC at both temperatures.

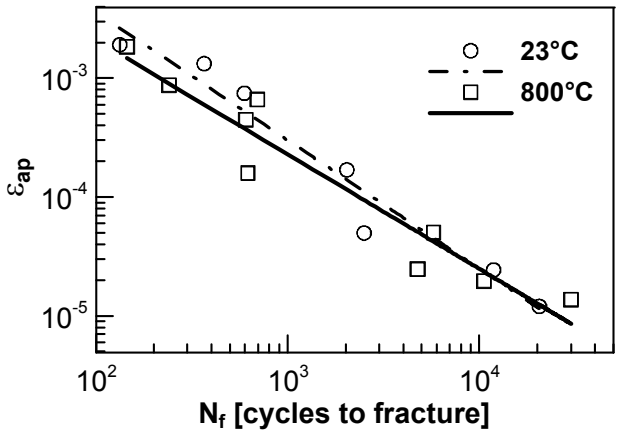

Fig. 5. Manson-Coffin curves of IN 738LC at both temperatures.

Fatigue life curves are plotted for two temperatures in Fig. 5 and 6. Figure 5 shows the plastic strain amplitude ε_{ap} at half life vs. the number of cycles to fracture N_f in the bilogarithmic representation. Experimental data are fitted by the Manson-Coffin law

$$\log 2N_f = (1/c) \log \varepsilon_{ap} - (1/c) \log \varepsilon_f'. \quad (2)$$

The fatigue ductility coefficient, ε_f', and the fatigue ductility exponent, c, were evaluated using regression analysis and are shown in Table 2. No temperature effect is apparent on the Manson-Coffin curve – see Fig. 5.

Fatigue life curves in the representation of the stress amplitude σ_a at half life vs. the number of cycles to fracture N_f are shown in Fig. 6. Experimental data are fitted by the Basquin law

$$\log 2N_f = (1/b) \log \sigma_a - (1/b) \log \sigma_f' \quad (3)$$

and the fatigue strength coefficient, σ_f', and the fatigue strength exponent, b, are evaluated using regression analysis and are shown in Table 2. The Basquin curve depends strongly on temperature.

Table 2. Parameters of cyclic stress-strain, Manson-Coffin and Basquin curves of IN 738LC.

Temperature [°C]	K´ [MPa]	n´	ε_f'	c	σ_f' [MPa]	b
23	1 270	0.068	1.70	- 1.13	1 330	- 0.079
800	1 780	0.140	0.66	- 1.04	1 700	- 0.152

Surface topography of selected specimens cycled to fracture at four temperatures has been studied in the scanning electron microscope. Figure 7 shows the surface relief of a specimen cycled with the high strain amplitude (ε_a = 0.5%, ε_{ap} = 0.087% at half life) at 800 °C. Parallel slip markings in Fig. 7 witness inhomogeneous deformation in the material. The right corner of Fig. 7 shows the surface relief within the box area in detail. An extrusion with intrusions on its both sides are apparent. Slip markings were observed on the specimen surface at all tested temperatures. However, the density of slip markings decreases with increasing temperature at specimens cycled with the same plastic strain amplitude. Extrusions are observed at all temperatures.

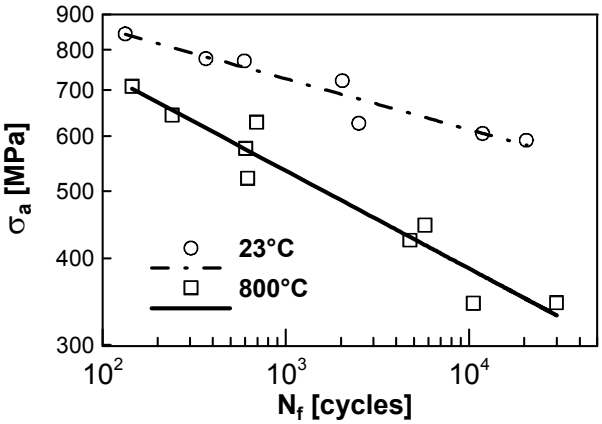

Fig. 6. Fatigue endurance curves of IN 738LC at both temperatures.

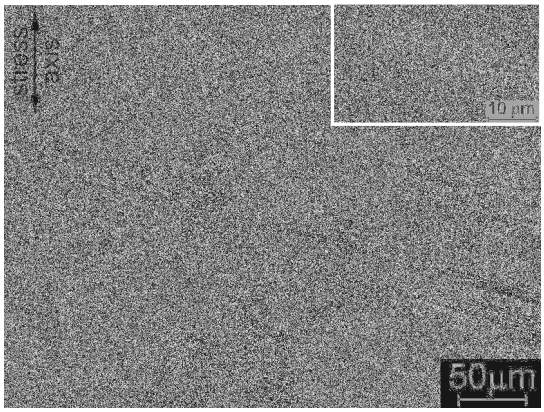

Fig. 7. SEM micrograph of surface relief at 800 °C (test to failure with ε_a = 0.5 %).

Conclusions

The results of total strain controlled fatigue tests performed on cast Inconel 738LC polycrystals at symmetrical strain cycle at room temperature and 800 °C can be summarized as follows:

(i) High amplitude straining is characterized by hardening that is followed by saturation at 23 °C. Sustained weak softening is shown at 800 °C. Low amplitude cycling results in the stable stress response.

(ii) The cyclic stress-strain curve depends on temperature. Fatigue hardening coefficient and fatigue hardening exponent increase with growing temperature.

(iii) The Basquin curve depends strongly on temperature. No temperature effect is apparent on the Manson-Coffin curve.

(iv) Cyclic strain localization into slip bands was observed at both temperatures. Slip markings with extrusions and intrusions were found at both temperatures.

Acknowledgements: this research was supported by the grants No. AV0Z 204 10507 and 1QS200410502 of the Academy of Sciences of the Czech Republic and Nos. 106/07/1507 and 106/08/1631 of the Czech Science Foundation.

References

[1] M.J. Donachie and S.J. Donachie: *Superalloys: A Technical Guide.* (ASM International, Materials Park 2002).

[2] D. Bettge, W. Österle and J. Ziebs: Scr. Metall. Mater. Vol. 32 (1995), p. 1601.

[3] G. Jianting and D. Ranucci: Int. J. Fatigue Vol. 5 (1983), p. 95.

[4] G. Jianting, D. Ranucci and E. Picco: Mater. Sci. Eng. Vol. 58 (1983), p. 127.

[5] L. Lindé and P.J. Henderson, in: *Low Cycle Fatigue and Elasto-Plastic Behaviour of Materials 4*, edited by K.-T. Rie and P.D. Portella, Elsevier, Amsterdam (1998), p. 143.

[6] F. Jiao, J. Zhu, R.P. Wahi, H. Chen, W. Chen and H. Wever, in: *Low Cycle Fatigue and Elasto-Plastic Behaviour of Materials 3*, edited by K.-T. Rie, Elsevier, London (1992), p. 298.

[7] J. Polák: *Cyclic Plasticity and Low Cycle Fatigue Life of Metals*. Elsevier, Amsterdam(1991).

Key Engineering Materials Vols. 385-387 (2008) pp 585-588
© (2008) Trans Tech Publications, Switzerland
doi:10.4028/www.scientific.net/KEM.385-387.585

Stress Fields near Mode II Interface Crack Tip of Two Dissimilar Orthotropic Composite Materials

Zhang Shaoqin[1,2, a] , Yao Hesheng [1,2, b] and Li Junlin[1, c]

[1]School of Applied science, Taiyuan University of Science and Technology, Taiyuan 030024, P. R. China

[2]Department of Engineering Mechanics, Beijing University of Aeronautics and Astronautics, Beijing, 100083,P R China

[a]zhangshaoqin@sina.com,[b]icemoonyao4@163.com, [c]lijunlin9726@yahoo.com.cn

Keywords: Orthotropic, Interface Crack, Crack Tip, Stress Fields

Abstract: Orthotropic bi-materials interfacial crack was studied, by constructing new stress function and using composite complex function method of material fracture. When secular equations' discriminant $\Delta_1 < 0$ and $\Delta_2 < 0$, the theoretical solutions of stress fields without oscillation singularity and displacement fields without embedding of upper and lower sides are derived.

Mechanical Model

In paper [1-3], studied stress field near interface crack tip of composite material, the expressions of stress fields near interface crack tip. But, their results exist irrational phenomenon of oscillation the stresses near crack tip and the embedding of the displacements of the upper and lower sides of the crack. This paper skillfully constructs special functions, the theoretical solutions to the stress fields and the displacements fields of double dissimilar orthotropic composite materials near the crack tip are obtained. These results do not exist that phenomenon.

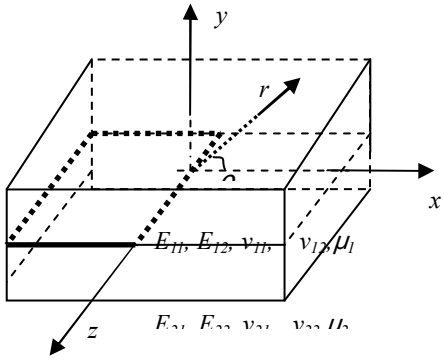

Fig. 1 Interface Crack Tip of Two Dissimilar Orthotropic

The plane $x \le 0,\ y=0$ is interface crack and $x > 0,\ y=0$ is a bonded surface of two dissimilar materials as shown in Fig.1. From the theory of elasticity, the governing equations and the boundary conditions can be expressed as follows

$$(b_{22})_j \frac{\partial^4 U_j}{\partial x^4} + [2(b_{12})_j + (b_{66})_j] \frac{\partial^4 U_j}{\partial x^2 \partial y^2} + (b_{11})_j \frac{\partial^4 U_j}{\partial y^4} = 0, \qquad (j = 1,2) \tag{1}$$

and

$$(\sigma_\theta)_1 = (\sigma_\theta)_2 = 0, \quad (\tau_{r\theta})_1 = (\tau_{r\theta})_2 = 0, \qquad \theta = \pm\pi \tag{2}$$

$$(\sigma_\theta)_1 = (\sigma_\theta)_2 \qquad (\tau_{r\theta})_1 = (\tau_{r\theta})_2, \qquad \theta = 0 \tag{3}$$

$$(u_r)_1 = (u_r)_2, \qquad (u_\theta)_1 = (u_\theta)_2, \qquad \theta = 0 \tag{4}$$

Based on the theory of elasticity, the formulae for the stress components and for the strain components are given as

$$(\sigma_r)_j = \frac{1}{r^2}\frac{\partial^2 U_j}{\partial\theta^2} + \frac{1}{r}\frac{\partial U_j}{\partial r}, (\sigma_\theta)_j = \frac{\partial^2 U_j}{\partial r^2}, (\tau_{r\theta})_j = -\frac{1}{r}\frac{\partial^2 U_j}{\partial r\partial\theta} + \frac{1}{r^2}\frac{\partial U_j}{\partial\theta}, (j=1,2) \tag{5}$$

$$(\varepsilon_r)_j = (b_{11})_j(\sigma_r)_j + (b_{12})_j(\sigma_\theta)_j, (\varepsilon_\theta)_j = (b_{21})_j(\sigma_r)_j + (b_{22})_j(\sigma_\theta)_j, (\gamma_{r\theta})_j = (b_{66})_j(\tau_{r\theta})_j, (j=1,2) \tag{6}$$

$$(\varepsilon_r)_j = \frac{\partial(u_r)_j}{\partial r}, (\varepsilon_\theta)_j = \frac{1}{r}\frac{\partial(u_\theta)_j}{\partial\theta} + \frac{(u_r)_j}{r}, (\gamma_{r\theta})_j = \frac{1}{r}\frac{\partial(u_r)_j}{\partial\theta} + \frac{\partial(u_\theta)_j}{\partial r} - \frac{(u_\theta)_j}{r}, (j=1,2) \tag{7}$$

in while the constants $(b_{11})_j$, $(b_{12})_j$, $(b_{22})_j$, $(b_{66})_j$ satisfy

$$(b_{11})_j = \frac{1}{E_{j1}}, \quad (b_{12})_j = -\frac{v_{j1}}{E_{j1}} = -\frac{v_{j2}}{E_{j2}} = (b_{21})_j, \quad (b_{22})_j = \frac{1}{E_{j2}}, \quad (b_{66})_j = \frac{1}{\mu_j}, \quad (j=1,2) \tag{8}$$

Stress Functions

Let s_{jk} satisfied the following biquadratic equations

$$(b_{11})_j s_j^4 + \left[2(b_{12})_j + (b_{66})_j\right] s_j^2 + (b_{22})_j = 0, \quad (j=1,2) \tag{9}$$

define

$$\Delta_j = \left[\frac{2(b_{12})_j + (b_{66})_j}{(b_{11})_j}\right]^2 - 4\frac{(b_{22})_j}{(b_{11})_j}, \quad (j=1,2) \tag{10}$$

In this paper, the case $\Delta_1 < 0$ and $\Delta_2 < 0$ will just be discussed. The equations (9) has following roots

$$s_{jk} = (-1)^{k+1}\alpha_j + i\beta_j, \quad s_{j(k+2)} = \overline{s}_{jk}, \beta_j > \alpha_j > 0, (j=1,2, k=1,2) \tag{11}$$

$$2\alpha_j^2 = \sqrt{\frac{(b_{22})_j}{(b_{11})_j}} - \frac{2(b_{12})_j + (b_{66})_j}{2(b_{11})_j}, 2\beta_j^2 = \sqrt{\frac{(b_{22})_j}{(b_{11})_j}} + \frac{2(b_{12})_j + (b_{66})_j}{2(b_{11})_j} \quad (\beta_j > \alpha_j > 0), \quad \text{j=1,2} \tag{12}$$

From equations (1), the special stress functions are chosen as

$$\begin{aligned} U_j(r,\theta) = \sum_{k=1}^{2}\frac{1}{2}\Bigg[& \frac{1}{(\lambda_1+2)(\lambda_1+1)}\left(\frac{z_{jk}^{\lambda_1+2} + \overline{z}_{jk}^{\lambda_1+2}}{2}a_{jk} + \frac{z_{jk}^{\lambda_1+2} - \overline{z}_{jk}^{\lambda_1+2}}{2i}b_{jk}\right) \\ & + \frac{1}{(\lambda_2+2)(\lambda_2+1)}\left(\frac{z_{jk}^{\lambda_2+2} + \overline{z}_{jk}^{\lambda_2+2}}{2}c_{jk} + \frac{z_{jk}^{\lambda_2+2} - \overline{z}_{jk}^{\lambda_2+2}}{2i}d_{jk}\right)\Bigg] \end{aligned} \tag{13}$$

$$\begin{cases} z_{jk} = x + s_{jk}y = r(\cos\theta + s_{jk}\sin\theta) \\ \overline{z}_{jk} = x + \overline{s}_{jk}y = r(\cos\theta + \overline{s}_{jk}\sin\theta) \end{cases} \qquad (j=1,2; k=1,2) \tag{14}$$

Substituting (13), (14) into(5) - (7), the expressions for $(\sigma_\theta)_j$, $(\sigma_r)_j$, $(\tau_{r\theta})_j$, $(u_r)_j$ and $(u_\theta)_j$ *(j=1,2)* can be obtained respectively. Putting them all into the conditions (2) - (4), it gives two systems of

eight racks equations about $(a_{11}, a_{12}, b_{11}, b_{12}, a_{21}, a_{22}, b_{21}, b_{22})$ and $(c_{11}, c_{12}, d_{11}, d_{12}, c_{21}, c_{22}, d_{21}, d_{22})$.

In order to make homogeneous system of linear equations have nonzero solution, that the determinant of coefficient must be zero, we have

$$\sin^4 \lambda\pi \cdot \left\{ \lambda \left[c_1^2 + c_2 c_4 \cot^2 \lambda\pi \right] + c_1 c_3 \right\} = 0 \tag{15}$$

where $c_1 = \frac{\alpha_1^2 + \beta_1^2 - \nu_{11}}{E_{11}} - \frac{\alpha_2^2 + \beta_2^2 - \nu_{21}}{E_{21}}$, $c_2 = 4(\frac{\beta_1}{E_{11}} + \frac{\beta_2}{E_{21}})$,

$$c_3 = \left(\frac{2(\nu_{11}+1)}{E_{11}} - \frac{1}{\mu_1} \right) - \left(\frac{2(\nu_{21}+1)}{E_{21}} - \frac{1}{\mu_2} \right), \quad c_4 = \frac{\beta_1(\alpha_1^2 + \beta_1^2)}{E_{11}} + \frac{\beta_2(\alpha_2^2 + \beta_2^2)}{E_{21}} \tag{16}$$

Let $\lambda = -\frac{1}{2} + \varepsilon$, when $|\varepsilon| << 1$, omit the third-order and above hands of ε, then (15) may be turned as

$$c_2 c_4 \pi^2 \varepsilon^2 - 2c_1^2 \varepsilon + c_1^2 - 2c_1 c_3 = 0 \tag{17}$$

Solving equation (17), when $\Delta = 4c_1^4 - 4c_1^2 c_2 c_4 \pi^2 + 8c_1 c_2 c_3 c_4 \pi^2 > 0$, have

$$\varepsilon_1 = \frac{c_1^2}{\pi^2 c_2 c_4} + \frac{\sqrt{c_1^4 - c_1^2 c_2 c_4 \pi^2 + 2c_1 c_2 c_3 c_4 \pi^2}}{\pi^2 c_2 c_4}, \quad \varepsilon_2 = \frac{c_1^2}{\pi^2 c_2 c_4} - \frac{\sqrt{c_1^4 - c_1^2 c_2 c_4 \pi^2 + 2c_1 c_2 c_3 c_4 \pi^2}}{\pi^2 c_2 c_4} \tag{18}$$

as $\lambda_1 = -\frac{1}{2} + \varepsilon_1$ $\lambda_2 = -\frac{1}{2} + \varepsilon_2$.

When λ satisfy (18), unknown numbers of homogeneous system of linear equations a_{jk}, b_{jk} $(j=1,2;\ k=1,2)$ are linear independence, they can be expressed in term of a_{22}, and as c_{jk}, d_{jk} $(j=1,2;\ k=1,2)$ can be expressed in term of c_{22}.

Noting

$$f_{11} = \frac{-\beta_1^2 - 2\beta_1\beta_2 + \nu_{11} - \alpha_1^2}{E_{11}} - \frac{\beta_2^2 + \nu_{21} - \alpha_2^2}{E_{21}}, \quad f_{12} = 2\alpha_2(\frac{\beta_1}{E_{11}} + \frac{\beta_2}{E_{21}}) \tag{19}$$

then $a_{jk} = A_{jk} a_{22}, \quad b_{jk} = B_{jk} a_{22}; \quad c_{jk} = C_{jk} c_{22}, \quad d_{jk} = D_{jk} c_{22}$ (20)

The stress function (13) can be rewritten as follows

$$U_j(x,y) = 2\,\mathrm{Re}\left[U_{j1}(z_{j1}) + U_{j2}(z_{j2}) \right] \tag{21}$$

noting $\frac{dU_{jk}}{dz_{jk}} = \Phi_{jk}(z_{jk}), \quad \Phi'_{jk}(z_{jk}) = \frac{d\Phi_{jk}(z_{jk})}{dz_{jk}}$

$$\Phi'_{jk}(z_{jk}) = \frac{1}{4}(a_{jk} - ib_{jk}) z_{jk}^{\lambda_1} + \frac{1}{4}(c_{jk} - id_{jk}) z_{jk}^{\lambda_2} \tag{22}$$

Stress Fields and Displacement Fields of Model I Crack Tip

τ symmetrical loading, II crack interface in addition to the boundary condition (2) - (4), the need to be added:

$$(\sigma_y)_j = 0, \qquad (\tau_{xy})_j = \tau, \qquad |y| \to \infty \tag{23}$$

$$(\tau_{xy})_j = \tau, \qquad |x| \to \infty \tag{24}$$

The crack length is 2a, through the coordinate transformation z = z* + a combination of complex function series expansion theory and boundary conditions (23), (24), the expression of (22) in the new coordinate system as follows

$$\Phi'_{jk}(z_{jk}) = \frac{a_{jk} - ib_{jk}}{4} M_{jk}(z_{jk}) + \frac{c_{jk} - id_{jk}}{4} N_{jk}(z_{jk}), \qquad (j = 1,2; k = 1,2) \tag{25}$$

where $M_{jk}(z_{jk}) = \dfrac{z_{jk}^{1-2\varepsilon_1}}{(z_{jk}^2 - a^2)^{\frac{1}{2}-\varepsilon_1}}\tau, \qquad N_{jk}(z_{jk}) = \dfrac{z_{jk}^{1-2\varepsilon_2}}{(z_{jk}^2 - a^2)^{\frac{1}{2}-\varepsilon_2}}\tau$

By (23), (24), when $|z_{jk}| \to \infty$, solving equations, have

$$a_{22} = -\frac{\tan \pi\varepsilon_2}{2(\alpha_2 f_{11} + \beta_2 f_{12})(\tan \pi\varepsilon_1 - \tan \pi\varepsilon_2)}, \quad c_{22} = \frac{\tan \pi\varepsilon_1}{2(\alpha_2 f_{11} + \beta_2 f_{12})(\tan \pi\varepsilon_1 - \tan \pi\varepsilon_2)} \tag{26}$$

Define stress intensity factors of mode I crack tip

$$K_{II1} = \lim_{z_{jk} \to a} \left[2(z_{jk} - a)\right]^{\frac{1}{2}-\varepsilon_1} M_{jk}(z_{jk}) = a^{\frac{1}{2}-\varepsilon_1}\tau, \quad K_{II2} = \lim_{z_{jk} \to a} \left[2(z_{jk} - a)\right]^{\frac{1}{2}-\varepsilon_2} N_{jk}(z_{jk}) = a^{\frac{1}{2}-\varepsilon_2}\tau \tag{27}$$

Stress fields near mode II and Displacement fields interface crack tip of two dissimilar orthotropic composite materials can be obtained.

Conclusions

The results as follows: (1) there is $r^{-\frac{1}{2}+\varepsilon_1}$ and $r^{-\frac{1}{2}+\varepsilon_2}$ singularity at interfacial crack tip of double dissimilar orthotropic composite materials(ε_1, ε_2 is material parameter); (2) when the upper and lower half-plane with the same parameters, using the derivation of the text, will be orthotropic composite material stress field and displacement field, and the results are the same as [4]; (3) there does not exist the oscillation of stress field near crack tip and the embedding of the displacements of the upper and lower sides of the crack; (4) stress fields and displacement fields of two dissimilar orthotropic composite materials near the mode I or I+II interfacial crack tip can be obtained similarly.

Acknowledgement

Authors are grateful for the support of the Natural Science Foundation of Shanxi Province (No. 200740)

Reference

[1] Williams M. L. The Stresses Around a Fault or Crack in Dissimilar Media[J]. Bulletin of the Seismological Socity of America. 1959, 49(2): 199-204

[2] Suo. Z. G. Singularities, interfaces and cracks in dissimilar anisotropic media [J]. Proc. R. Soc. Lond, 1990, A 427: 331-358

[3] Xu Jinquan. Interface Mechanics[M]. Beijing: Science Press, 2006

[4] Yang Weiyang, Li Junlin, Zhang Xuexia. Composite material complex function method[M]. Beijing: Science Press, 2006

[5] Li Junlin. Theoretical Studies and Experiment Analysis on Interfacial Fracture Between Dissimilar Orthotropic Composite Materials[D]. Beijing: Beijing University of Aeronautics and Astronautics, 2007

Key Engineering Materials Vols. 385-387 (2008) pp 589-592
© (2008) Trans Tech Publications, Switzerland
doi:10.4028/www.scientific.net/KEM.385-387.589

Damage Evaluation Based on Electrical Resistance Measurement

Lijun Yang[1, a], Binxiang Sun[2, b] and Yimu Guo[3, c]

[1]Department of Civil Engineering, Shaoxing College of Arts and Sciences, Shaoxing 312000, China

[2]Department of Civil Engineering, Shaoxing College of Arts and Sciences, Shaoxing 312000, China

[3]Department of Mechanics, Zhejiang University, Hangzhou 310027, China

[a]yanglj@zscas.edu.cn, [b]sbinxiang@yahoo.com.cn, [c]guoyimu@cmee.zju.edu.cn

Keywords: damage evaluation, low electrical resistance measurement, metal

Abstract. The formulae between electrical resistance change and damage in metals were studied on the basis of different damage mechanisms. This DC electrical resistance is a more sensitive parameter to the initiation of microcracks during the irreversible damage accumulation process. Measurement of low electrical resistance due to accumulative damage is discussed. Agreement between evaluations of ductile damage via electrical resistance change and elasticity modulus measurement is good.

Introduction

During the past three decades, continuum damage mechanics has been applied to study ductile plastic damage, brittle damage, fatigue damage, creep damage, etc [1-7]. Determination of parameters that can be more sensitive to irreversible damage and easier to be tested is a key to successful application. Among them, the potential drop and electrical resistance methods are one of the best nondestructive testing ones [8-14]. Under the hypothesis of conducting-loading area equivalence [9, 10], the damage variable based on DC electrical resistance changes can represent the fatigue damage evolution process in metals. Especially this DC electrical resistance approach is much more sensitive to the initiation of microcracks during the damage evolution and a good nondestructive measuring technique [8-14]. In this study, the formulae between electrical resistance change and damage in metals were studied on the basis of different damage mechanisms. Agreement between evaluations of ductile damage through electrical resistance change and elasticity modulus measurement is good.

Electrical Resistance Change Representation of Damage

The definition of an isotropic damage based on global mechanical measurements can result naturally from the concept of effective stress. Usually, the macroscopic damage variable D is defined by [2-4]

$$D = 1 - \frac{\tilde{A}}{A}, \tag{1}$$

where A is the apparent cross-sectional area of the damaged specimen, $\tilde{A}$ is the effective area which effectively carries the load. The overall damage variable is a non-decreasing function of time [2-4].

Usually, directly measuring the total area of the defects in metals is very difficult, even inaccurate. The practical damage measurement is performed by the indirect methods [3-6]. Damage measurement is linked to modification of the mechanical properties and the electrical properties caused by damage. Electrical resistance changes are more sensitive to damage in metals [3]. However, besides effective area due to damage, the phenomenological change of electrical resistance may also be caused by the specimen length change, the temperature change, the electrical resistivity change, and the area change of other factors. This problem can be simplified by assuming the influence of damage to be distributed uniformly on the electrical resistance. Now, we introduce the hypothesis of conducting-loading area equivalence, i.e. the current-conducting cross-sectional area equal to the load-bearing cross-sectional area in the specimen. In other words, area variables A and $\tilde{A}$ in Eq. 1, which represent the load-bearing

cross-sectional areas, are identical to the current-conducting cross-sectional areas. Hence, the damage variable based on electrical resistance changes can be rewritten as [9]

$$D = 1 - \frac{(1+\varepsilon_p)}{(1-\varepsilon_p)} \frac{\rho'}{\rho} \frac{R}{R'}, \tag{2}$$

where R and R' are the electrical resistance of the virgin specimen and the damaged specimen, ρ and ρ' are the electrical resistivity of the virgin metal specimen and the damaged metal specimen, ε_p is the plastic strain of the damaged specimen, respectively.

From a physical point of view, the electrical resistivity increases with increasing of dislocations and other defects of inclusion and vacancy. For small damage, the electrical resistivity change induced by damage may be negligible [9]. Therefore, the definition of global damage based on the electrical resistance change can be simplified as

$$D = 1 - \frac{(1+\varepsilon_p)}{(1-\varepsilon_p)} \frac{R}{R'}. \tag{3}$$

We assume that the damaged metal specimen occurs without noticeable overall plastic deformations. As a result, Eq. 3 is neglected the plastic deformation may be expressed as the common definition of damage based on the electrical resistance change, that is

$$D = 1 - \frac{R}{R'}. \tag{4}$$

$R' = R$ implies $D = 0$, that is, the initial state is the undamaged one. $R' = R'_c \le \infty$ corresponds to damage failure of metals. R'_c is called the critical electrical resistance value of the damaged specimen [9, 10].

Damage due to Different Damage Mechanisms

Damage mainly concerns the initiation of brittle, ductile, creep and fatigue cracks in metals [3]. These different phenomena correspond to different physical mechanisms. Micro-defects imply microcracks or microcavities of any kind, whatever is the physical mechanism brittle or ductile, low- or high-cycle fatigue damage [6]. Eq. 2 can be simplified in view of the impact of different physical mechanisms of damage evolution on the overall plastic deformation and electrical resistivity.

Ductile Damage. Damage is of a ductile type when overall plastic strain exists at the mesoscale, that is in the nucleation, growth and coalescence of microcavities induced by noticeable large plastic strains. The variation of electrical resistivity at the microscopic stage may be negligible.

For tensile or compressive ductile damage, its large plastic strain may be expressed as $\varepsilon_p = \ln L'/L$. Then, the formula of damage measurement based on electrical resistance changes is written as

$$D = 1 - \frac{(1+\ln L'/L)}{(1-\ln L'/L)} \frac{R}{R'}. \tag{5}$$

For low-cycle fatigue damage, its plastic strain in common structural steels may be approximately expressed as $\varepsilon_p = 0.0325(\sigma_a/\sigma_u)^{6.25}$, where σ_a and σ_u are the cyclic stress amplitude and static ultimate stress in tension. Then, the formula of damage measurement in Eq. 3 is written as

$$D = 1 - \frac{1+0.0325(\sigma_a/\sigma_u)^{6.25}}{1-0.0325(\sigma_a/\sigma_u)^{6.25}} \frac{R}{R'}. \tag{6}$$

Brittle Damage. Damage is called brittle when plastic strain is negligible at the mesoscale, that is damage governed only by microplastic at the microscale with practically no influence on the behavior at the mesoscale [3]. From a microscopic point of view, the electrical resistivity change induced by damage needs to be considered. As a result, Eq. 2 neglected the plastic strain may be written as

$$D = 1 - \frac{\rho'}{\rho}\frac{R}{R'}. \tag{7}$$

For high-cycle fatigue, materials exhibit quasi-brittle behaviors. In alternate tension-compression fatigue testing, damage is assumed to be uniformly distributed in the specimen. Then, the formula of evaluating fatigue damage via measurement of electrical resistance changes can be expressed as [9]

$$\frac{R'}{R} = \frac{1 + 2D^{3/2}}{1 - D}. \tag{8}$$

For rotating pure-bending fatigue test, electrical resistance changes caused by high-cycle fatigue damage present uneven electrical properties. At the mesoscale, the damaged specimen regarded as a homogenous electrical resistance and neglected the electrical resistivity change is good approximate for high-cycle fatigue. Hence, the damage variable can be expressed as Eq. 4 [9, 10].

Measurement of Damage Based on Electrical Resistance Change

In this work tensile damage testing was conducted at room temperature. Typical unnotched specimens with a diameter 10 mm for ductile damage measurement were prepared. The ductile damage studies were carried out by monitoring the electrical resistance changes of the specimen with increasing of load by interrupting the tests at pre-selected loading intervals. Removed from the testing machine, the relevant electrical resistance of the specimen from the sequence as a function of the plastic strains was measured. DC electrical resistance measurement was made in the gauge length of metal specimens, using a direct current double bridge for four-probe, in which brass screws in conjunction with short and thick copper wires served as electrical contacts, as shown in Fig. 1. This testing method is more reliable than the two-probe method, due to the essential elimination of the contact electrical resistance and lead electrical resistance from the measured electrical resistances [10].

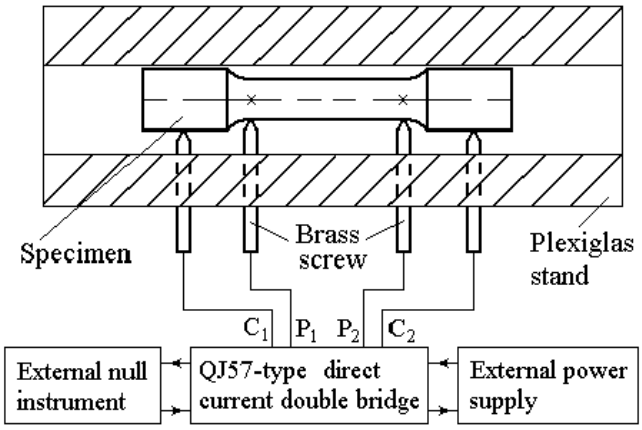

Fig. 1 Schematic diagram of the apparatus for electrical resistance measurement

In order to demonstrate the validity of evaluating damage described in this study, measurement of damage based on elasticity modulus was also performed [3]. For the mild steel specimens, damage evolution curves with a plastic strain ε_p were evaluated through the electrical resistance and elasticity

modulus measurement, as shown in Fig. 2. Good agreement has been obtained. This implies that the electrical resistance is a suitable parameter using measurement of damage.

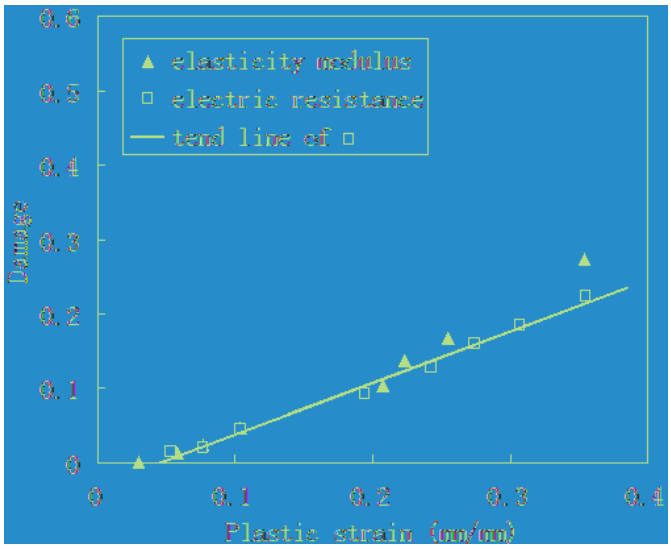

Fig. 2 Damage evaluation for mild steel by electrical resistance and elasticity modulus measurements

Conclusions

The formulae between electrical resistance change and damage in metals were studied on the basis of different damage mechanisms. Measurement of low electrical resistance due to accumulative damage is discussed. Agreement between evaluations of damage through the electrical resistance change and elasticity modulus measurement is good. Thus, the approach to evaluating damage in metals through electrical resistance measurement proposed in the work is a good nondestructive measuring technique.

References

[1] G.X. Cheng and A. Plumtree: Int. J. Fat. Vol. 20(7) (1998), p. 495

[2] Y.C. Xiao, S. Li and Z. Gao: Int. J. Fat. Vol. 20(7) (1998), p. 503

[3] J. Lemaitre and J.L. Chaboche: *Mechanics of solid materials* (Cambridge University Press, England 1990).

[4] J. Lemaitre and J. Dufailly: Engng. Fract. Mech. Vol. 28(5/6) (1987), p. 643

[5] M. Alves, J.L. Yu and N. Jones: Computer & Structures Vol. 76 (2000), p. 703

[6] J. Lemaitre and J.P. Sermage: Comp. Mech. Vol. 20 (1997), p. 84

[7] Z.X. Wu: Int. J. Fat. Vol. 23 (2001), p. 363

[8] N. Tada, Y. Hayashi, T. Kitamura and R. Ohtani: Int. J. Fract. Vol. 85 (1997), p. 1

[9] B.X. Sun and Y.M. Guo: Int. J. Fat. Vol. 26(5) (2004), p. 457

[10] B.X. Sun, L.J. Yang and Y.M. Guo: Fatigue Fract. Engng Mater. Struct. Vol. 30 (2007), p. 1052

[11] M. Schelp and D. Eifler: Mater. Sci. Eng. A Vol. 319/321 (2001), p. 652

[12] J.H. Constable and C. Sahay: Trans. Compon. Hybr. Manuf. Technol. Vol. 15 (1992), p. 1138

[13] P. Starke, F. Walther and D. Eifler: Int. J. Fatigue Vol. 28 (2006), p. 1028

[14] F. Walther and D. Eifler: Int. J. Fatigue Vol. 29 (2007), p. 1885

Key Engineering Materials Vols. 385-387 (2008) pp 593-596
© (2008) Trans Tech Publications, Switzerland
doi:10.4028/www.scientific.net/KEM.385-387.593

An Experimental Study on the Fatigue of Structural Steels with Various Welding Details

B. C. Goo[1, a]

[1]Korea Railroad Research Institute, Woulam-Dong 360-1, Uiwang-City, Gyeonggi-Do, 437-757, Korea

[a]bcgoo@krri.re.kr

Keywords: Fatigue, Residual Stress, SM 490 A, S-N Curves, Welded Joint

Abstract. A structural steel should satisfy various properties under varied conditions. Fatigue strength is one of them. When structural steels are used in the form of welded joints, fatigue strength is one of the key characteristics that should be considered. In this study, comprehensive fatigue tests of a structural steel with yielding strength of about 350 MPa and tensile strength of about 520 MPa were carried out. First, a lot of specimens: parent material plates, butt welded specimens with reinforcement removed, as-welded plates, plates with weld toe ground, load-carrying cruciform, non load-carrying cruciform, plates with transverse fillet welded rib, etc were prepared and tested. S-N curves for the above specimens were compared and analyzed. Secondly, some life-size rectangular beams were fabricated by welding and tested. It is found that annealing is detrimental to fatigue strength rather than beneficial. The experimental data and results may be used usefully by engineers.

Introduction

Welding joints are widely used for structures. Though welding is a convenient joining method, the fatigue life evaluation of welded structures is one of the challenging problems. In particular, the role of residual stresses due to welding is very complicate and remains to be studied. A lot of study on the effect of weld bead shapes and weld details on fatigue has been performed and many phenomena were clarified[1-5]. For fatigue design and assessment of steel structures there are well-known codes [6-8]. In this study, to quantify the effects of residual stresses, annealing, weld details, etc on fatigue strength, various specimens were made and tested.

S-N Curves of Welded Joints

Specimens and Welding Conditions. Fig. 1 shows the shapes and dimensions of the specimens used in this study. Figs. 1 (a)-(f) are small scale specimens for tensile fatigue tests. Figs. 1 (g), (h) are life-size specimens for three-points bending fatigue tests. All specimens were made of SMA 490A (JIS G 3114) plates with thickness of 10 mm. For annealing, holding time: three hours at 590±20 °C; cooling rate: 120 °C/hour. Similar welding conditions used in industry were applied. In case of AAN, AAY, GAN, RNN, RNY, GAN and GAY, GMAW semi-automatic 1-pass welding in 300 A, 30 V was done. In case of TN, CN and NCN, 1-pass welding in 270 A, 28 V. In case of life-size beams, 280 A, 29V for the first pass and 280 A, 29 V for the second pass. AWS ER 70S-6 welding wire, ϕ1.2 was used. Ar 80%+Co_2 20% protection gas was used.

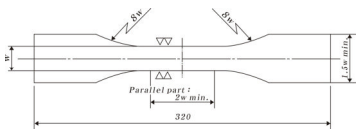

(a) Base material (BM)

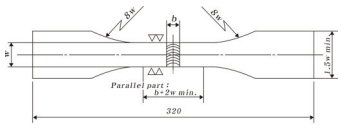

(b) Butt weld, AAN=as-welded, AAY=annealed, GAN=weld toe ground, GAY=weld toe ground and annealed.

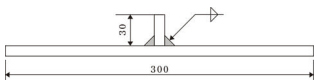

(c) Plate with fillet welded rib (TN) , width 25

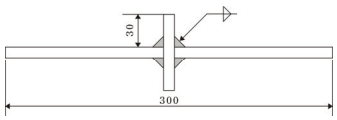

(d) Load-carrying cruciform, fillet weld (CN) , width 25

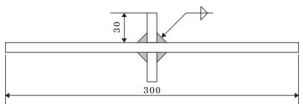

(e) Non load-carrying cruciform (NCN) , width 25

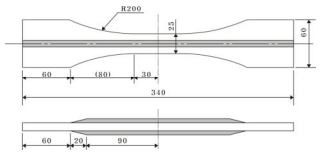

(f) Longitudinal X-groove butt weld (LN)

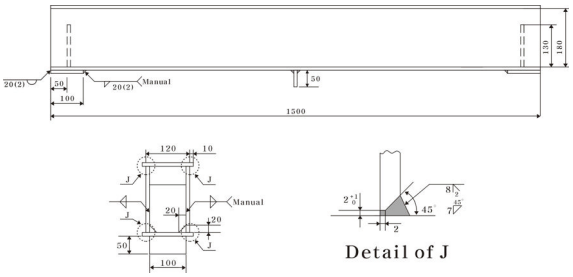

(g) Box-beam V with a vertical plate, not annealed

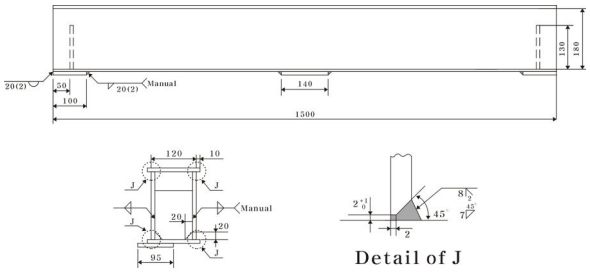

(h) Box-beam H with a horizontal plate, not annealed

Fig. 1 Shapes of the specimens

Fatigue Tests and S-N Curves. Fatigue testes were carried out according to ASTM E 466 by using an Instron model 8802 (25 ton) or 8503 (50 ton). Before the fatigue tests, three tensile tests were carried out on an Instron Model 8802 (25ton) at the speed of 1 mm/min according to ASTM E8-01. A 25 mm extensometer was used. The shape and surface condition of the test specimens are similar to the fatigue specimens shown in Fig. 1 (b). The yield strength is 347 MPa and the tensile strength is 519 MPa. The obtained S-N curves for the base material, reinforcement removed, as-welded, weld toe ground specimens, etc are shown in Figs. 2-11. AAY specimens were as-welded and annealed (post-weld heat treatment). AAN specimens were as-welded but not annealed. After annealing, weld toes of GAY specimens were ground by an aluminum oxide grinder with diameter of 3 mm. GAN specimens were ground by the same sort of grinder but not annealed. Almost all the tests were carried out at $R = \sigma_{\min} / \sigma_{\max} = 0.1$ and frequency of 20 Hz. We can observe several characteristics in the S-N curves. First, in the long life, the fatigue strength of AAY is higher than that of AAN, but in short life, vice verse. Second, the fatigue strength of GAN is higher than that of GAY in all life range. Third, the fatigue strength reversal observed in AAY and AAN is not examined in GAY and GAN. These phenomena seem to be related mainly to residual stresses[5]. The tensile fatigue limits of the specimens are defined at 2×10^6 cycles and shown in Table 1. The fatigue limit of the CN specimen is lowest. The magnitudes of the fatigue limits are in the order of BM, RN, AAY, GAN, GAY, AAN, TN, NCN, CN. It is found that removing the welding reinforcement is effective for improving the fatigue strength of butt-welded joints. GAN and GAY have nearly the same fatigue strength. Grinding by an aluminum oxide grinder is not so effective. The effect of stress ratio to fatigue strength is important as shown in Figs. 8-10. Fig. 11 shows the S-N curves of the life-size specimens with/without attached plates. The fatigue strength of the annealed specimen is lower than that of the as-welded specimen which has high welding residual stresses. In case of the annealed specimen, the hardness is lower than the base material so that the fatigue strength becomes lower. But removal of the tensile residual stresses increases the fatigue strength. Therefore, the fatigue strength of the annealed specimen will be decided by these two combined effect. It is found the box beam H with a plat plate welded horizontally has lowest fatigue strength.

Table 1. The tensile fatigue limits of the specimens, R=0.1

	BM	AAN	AAY	RN	GAN	GAY	TN	NCN	CN
Fatigue limit	135.1	78.3	90.8	106.7	82.4	81.9	74.1	48.7	41.3
Normalized by BM (%)	100	58	67	79	61	61	55	36	31

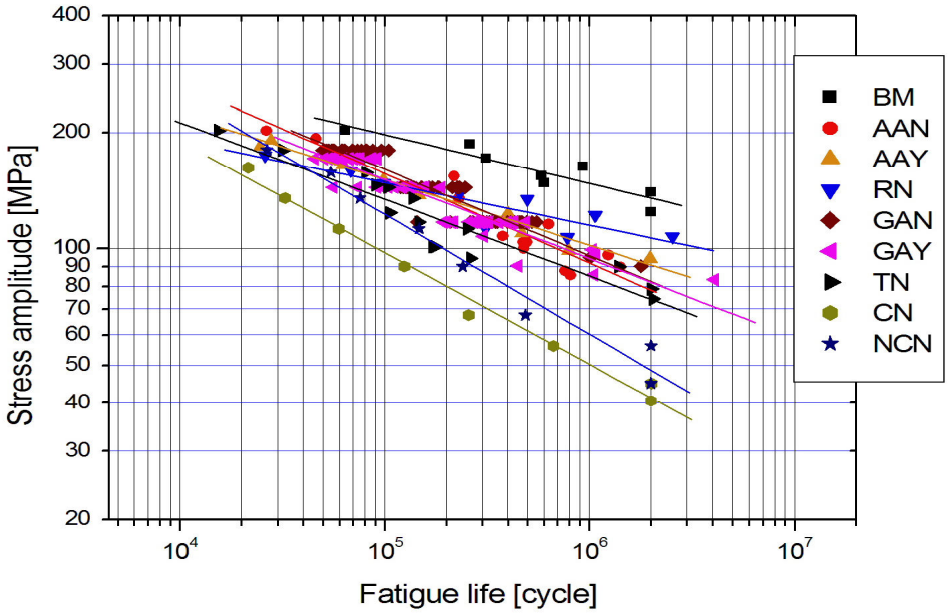

Fig. 2 S-N curves of the specimens, R=0.1

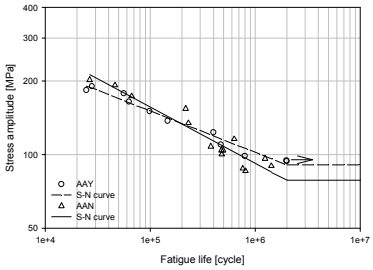

Fig. 3 S-N curves of AAY and AAN

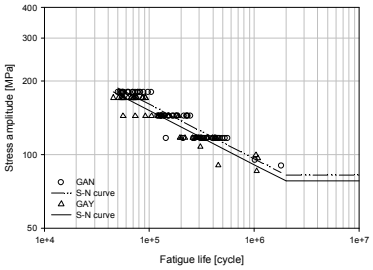

Fig. 4 S-N curves of GAY and GAN

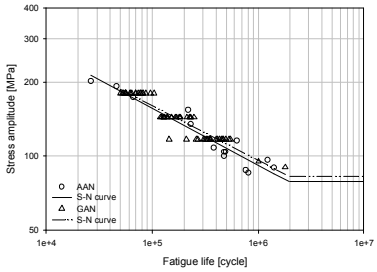

Fig. 5 S-N curves of AAN and GAN

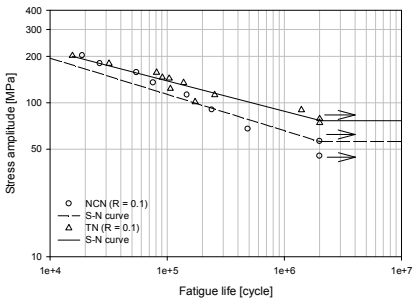

Fig. 6 S-N curves of NCN and TN (R=0.1)

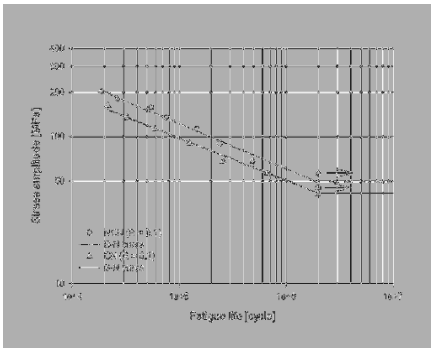

Fig. 7 S-N curves of CN and NCN (R=0.1)

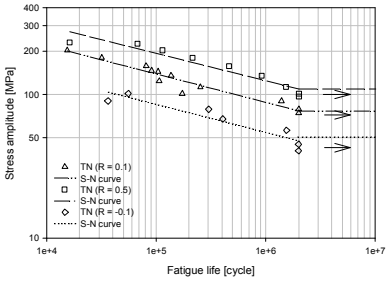

Fig. 8 SN curves of TN (R=0.1, 0.5, -0.1)

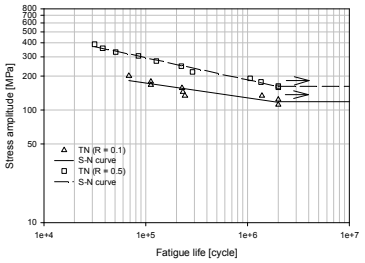

Fig. 9 S-N curves of T bending (R=0.1, 0.5)

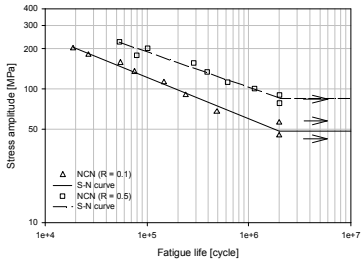

Fig. 10 S-N curves of NCN (R=0.1, 0.5)

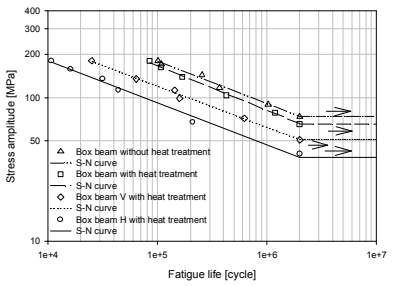

Fig. 11 S-N curves of the box beam specimens, bending, (R=0.1)

Summary

To quantify the fatigue strength of welded specimens, fatigue tests of several kinds of welded specimens were carried out. Some interesting results are obtained.

1) Annealing of the weldments is not so effective for the improvement of the fatigue strength. In case of the life-size specimens the as-welded specimens have higher fatigue strength than the annealed specimens.
2) Removing weld reinforcement is effective for the improvement of the fatigue strength.
3) Grinding weld toes by an aluminum oxide grinder is not so effective.
4) The effect of stress ratio on the S-N curves is significant.
5) Cruciform weldments have relatively lower fatigue strength.

References

[1] R. P. Newman and T. R. Gurney, British Welding Journal, (1959), p. 569.

[2] K. Takahashi and A. Ito, Japanese J. of Welding, Vol. 40, No. 8 (1971), p. 723.

[3] S. Yoshida, M. Inagaki, M. Kanao, E. Sasaki, M. Nihei and M. Kamakura, Japanese J. of Welding, Vol. 47, No. 9 (1978), p. 5.

[4] W. Fricke and A. Muller-Schmerl, Journal of Offshore Mechanics and Arctic Engineering, Vol. 120 (1998), p. 97.

[5] B.C. Goo, J.H. Kim, J.W. Seo and C.S. Seok, Key Engineering Materials, Vol. 270-273 (2004), p.2302

[6] BS 7608, 1993, Code of Practice for Fatigue Design and Assessment of Steel Structures

[7] Japanese Society of Steel Structures, 1993, Fatigue Design Guide of Steel Structures

[8] ENV 1993-1-1, Eurocode 3: Design of Steel Structures

Key Engineering Materials Vols. 385-387 (2008) pp 597-600
© (2008) Trans Tech Publications, Switzerland
doi:10.4028/www.scientific.net/KEM.385-387.597

Numerical Simulation of Temperature Stress on Asphalt Pavement of Concrete Bridge Deck in Cold Region

Hong WANG[1, a], Shaopeng WU[2, b], Bo LI[3, c], and Conghui LIU[4, d]

[1] Key Laboratory of Silicate Materials Science and Engineering

(Wuhan University of Technology), Ministry of Education, Wuhan 430070, China

[2] Key Laboratory of Silicate Materials Science and Engineering

(Wuhan University of Technology), Ministry of Education, Wuhan 430070, China

[3] Key Laboratory of Silicate Materials Science and Engineering

(Wuhan University of Technology), Ministry of Education, Wuhan 430070, China

[4] Key Laboratory of Silicate Materials Science and Engineering

(Wuhan University of Technology), Ministry of Education, Wuhan 430070, China

[a]wanghong@whut.edu.cn, [b]wusp@whut.edu.cn, [c]lip@whut.edu.cn, [d]liuconghui666@126.com

Keywords: asphalt pavement, concrete bridge, cold region, temperature stress

Abstract: Flexible pavement plays an important role in the primary concrete bridges at present. However, climate environment, to which pavement is exposed, significantly impact pavement stability and long-term performance. Especially, low temperature cracking of asphalt pavement in cold region is a common existing problem. In order to improve the pavement's crack resistance it is necessary to predict the temperature stress distribution within the asphalt layers. A two-dimensional finite element model of a concrete bridge in thermal and thermal-structural couple analysis is developed to predict temperature and temperature stress variation of asphalt layers in cold region. The temperature stress variation is analyzed at seasonal temperature, different cooling rate and the different thickness of asphalt layers. The model considers a set of primary thermal environmental conditions. Ultimately, the model is aimed at providing pavement engineers with an efficient computational tool that attempts to increase the prediction accuracy of temperature in asphaltic pavement of cold region for more reliable pavement design.

1. Introduction

Climate environment, to which pavement is exposed, significantly impact pavement stability and long-term performance[1]. Especially, low temperature cracking of asphalt pavement in cold region is a common existing problem. Asphalt concrete is not good at thermal conductivity. The temperature distribution in asphalt pavement is directly affected by the climate conditions to which it is exposed[3]. When outside temperature changes, the inside temperature's distribution of asphalt concrete is uneven, and the temperature gradient will grow. To predict the temperature stress of the pavement it is necessary to analyze the temperature fluctuation of bridge deck pavement.

This paper proposes a method to predict transient temperature stress distribution at seasonal temperature, different lower temperature speed and different asphalt pavement's thickness using a transient finite element model of a pavement section. The model considers a set of primary thermal environmental conditions. Ultimately, the model is aimed at providing pavement engineers with an efficient computational tool that attempts to increase the prediction accuracy of temperature in asphaltic pavement of cold region for more reliable pavement design.

2. Methodology

2.1 Basic assumptions

Combined the actual situation, the model is simulated following some assumptions:
1. Every layers of asphalt pavements and the concrete bridge is uniform completely, isotropic and elastic.
2. Asphalt pavement's temperature and stress fluctuation are even along the vertical.
3. The contact between every layer is close, the temperature and heat flux between layers are continuous completely, and heat resistance of the contact is not considered.

2.2 Finite element mesh

A concrete bridge of box-beam with asphalt pavement is modeled in Sinkiang, P.R.China where the winter is very cold and far-flung from first November to next May, especially the average temperature in January is almost -20°C. Representation of the two- dimension finite element mesh used in the model is shown in Fig. 1. A uniform square nodal spacing of 2.5cm in the x and z directions has been used in the asphalt pavement. The maximal size of other element is 5cm in the concrete bridge.

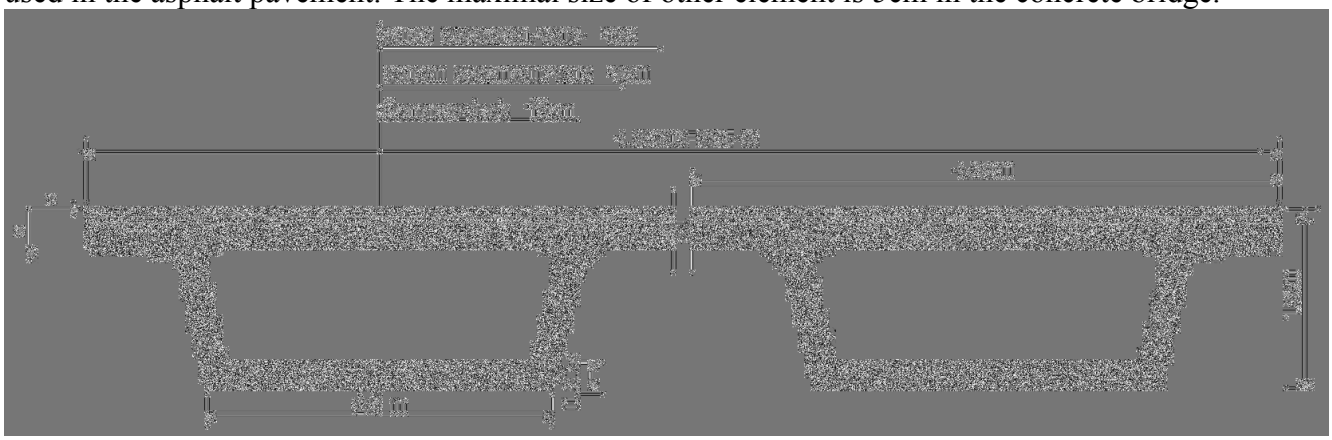

Fig.1 Finite-element nodal network

2.3 Calculational parameters

Some basic parameters about the concrete bridge system are listed in table 1.

Table 1 Material parameters

	Thermal conductivity [W/(m•°C)]	Specific heat[J/Kg•°C]	Density[kg/m^3]	Elastic modulus[MPa]	Linear contraction factor(10^{-5})	Poisson's ratio
AC 13	1.504	946	2100	1800	1.58	0.25
AC 16	1.826	1013	2100	1800	1.58	0.25
Concrete bridge deck	1.54	840	2500	30000	1.0	0.2

2.4 Boundary conditions

2.4.1 Thermal boundary condition

Conjugating the first law of the thermodynamics, which states that thermal energy is conserved, and Fourier's law, that relates the heat flux with the thermal gradient, the problem of heat transfer by conduction within the pavement is solved. Using an energy balance approach, heat flux at each top and bottom surface node is given by equation 1-2[2][4]:

$$q = q_s + q_{tr} + q_c \qquad [1]$$

Where: q =total gained heat flux; q_s =solar radiation heat flux; q_{tr} =thermal radiation heat flux; q_c =convection heat flux;

Then q can be expressed by equation 2:

$$q = \alpha_s I_t + B(T_a - T_s) \qquad [2]$$

Where: α_s = absorption coefficient of asphalt mixtures; I_t =solar radiation incident on the pavement surface; T_a =atmosphere temperature; T_s =pavement surface temperature; B = multiplex coefficient of heat transfer.

The first type of thermodynamic boundary conditions is applied in the model. Therefore, the boundary condition of the pavement surface and the boundary condition of the concrete box-beam's bottom surface are applied as equation 3-4:

$$q = \alpha_s I_t + B(T_a - T_s\big|_{z=0}) \qquad [3]$$

$$q = \alpha_f I_f + h(T_a - T_s\Big|_{z=\sum_{i=1}^{n}\delta_i}) \qquad [4]$$

Where: α_f = absorption coefficient of concrete; and I_f = ground reflection incident on the bottom surface. In the model α_s, B, α_f and h is suggested to be 0.9, 22.45, 0.65 and 21.5 respectively[5].

2.4.2 Structural boundary condition

In the structural boundary condition, some constraints are applied as boundary condition. In the model the bridge is freely-supported, which is just that the leftmost and rightmost nodes are free in x direction and not free in z direction.

2.5 Weather data

Typical meteorological weather data of winter times in Sinkiang, P.R.China were used in the model. The weather data on 16-Janurary-2007 was selected for specific analysis. The minimum and the maximum temperature of the whole day respectively appear at 11:00 AM and 02:00 PM, which is -17.8°C and -9.1°C.

3. Results and discussion

3.1 Daily temperature and temperature stress's variation of asphalt pavement

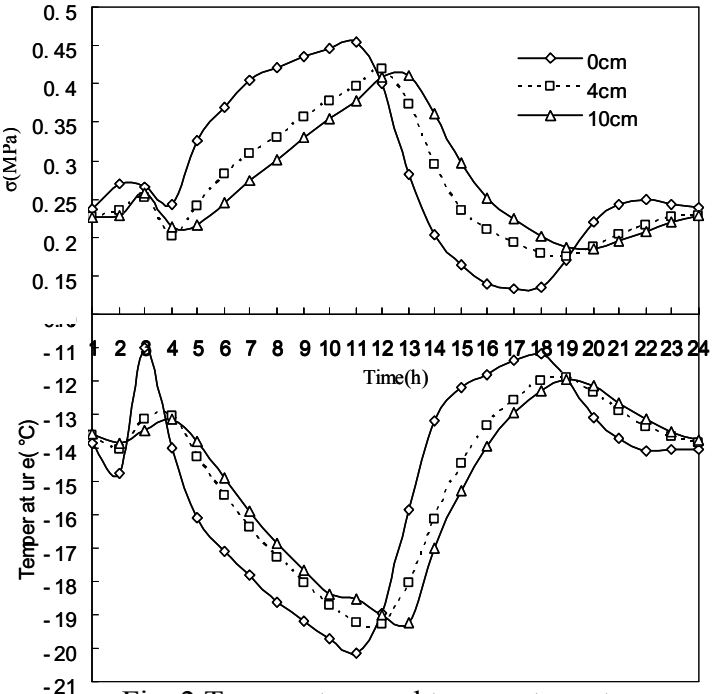

Fig. 2 Temperature and temperature stress distributions of 0cm, 4cm and 10cm depth

Fig. 2 presents the daily temperature and temperature stress's distributions of asphalt pavement at different depths on 16-Janurary-2007. It indicates that the maximum temperature stress decrease with the increase of depths along z direction while the minimum temperature increases at the same time. The rangeability of the temperature stress decreases gradually with the depths' increasing from the top down. From fig.2 the maximal tensile stress may not achieve the ultimate tension of the asphalt pavement, but the long time of the large stress level can make the asphalt mix reach its ultimate tension and finally the cracking of the asphalt pavement happens.

3.2 Temperature stress's variation on different cooling rates

Fig.3 presents the temperature stress distribution at different cooling rates. The bigger the cooling rate is, the bigger the temperature stress is.
The cooling rate has important effect on the surface temperature stress. The bigger the cooling rate is, the more difficultly the stress relaxation behaved and the bigger the accumulative temperature stress. All these can accelerate the cracking of the asphalt pavement.

3.3 Temperature stress's variation on different pavement thickness

The analysis about temperature stress is done on different surface pavement's thickness-4cm, 5cm and 6cm. The result indicates that the rangeability of the surface temperature stress is very small with the variety of pavement thickness. However, the bottom is on the contrary. Fig.4 presents the temperature stress's variation of bottom pavement on different pavement thickness. It shows that the temperature stress at the bottom is degressive gradually with the increasing of the pavement thickness. In addition, the maximum daytime temperature stress at the bottom is observed at 11:00 AM. And it has been delayed to be 12:00 AM due to the addition of the thickness.
Adding the thickness of the asphalt pavement is propitious to reduce the temperature stress of the pavement and avoid the asphalt mix's cracking.

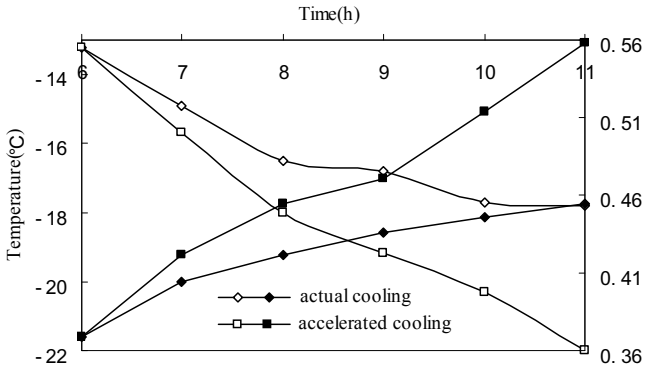

Fig. 3 Surface temperature stress distribution on different cooling rates

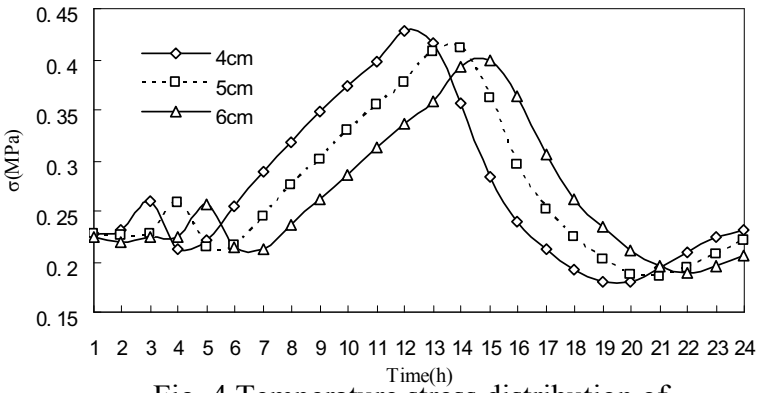

Fig. 4 Temperature stress distribution of bottom pavement on different asphalt thickness

4. Conclusions

(1) The maximum temperature stress of the asphalt pavement decreases from the top town along z direction while the minimum temperature increases at the same time.
(2)The bigger the cooling rate is, the bigger the temperature stress of the asphalt pavement is, and the bigger the accumulative temperature stress in the asphalt mix.
(3)With the increasing of the asphalt pavement's thickness, the temperature stress at the bottom pavement is degressive gradually.

References

[1] C. Yavuzturk, K. Ksaibati, P.E., and A. D: Chiasson, P.E. Journal of Materials in Civil Engineering, Vol. 17(2005), p. 465-475.
[2] Manuel J. C. Minhoto, Jorge C. Pais and Paulo A. A. Pereira etc: Transportation Research Record, Vol. 1919(2005), p. 96-110.
[3] H. I. Al-Abdul Wahhab, and F. A. Balghunaim: Journal of Materials in Civil Engineering, Vol. 6(1994), p. 5282-5296.
[4] Andrew D. Chiasson, Ph.D., P.E., and Cenk Yavuzturk etc: Journal of Materials in Civil Engineering, Vol. 20(2008), p. 118-127.
[5]Barber, E. S: Highway Research Board Bulletin, Vol. 168(1957), p. 1–8.

Key Engineering Materials Vols. 385-387 (2008) pp 601-604
© (2008) Trans Tech Publications, Switzerland
doi:10.4028/www.scientific.net/KEM.385-387.601

Investigating Vibration Sources of Faulty Gear Units

Ales Belsak[1, a], Joze Flasker[2, b]

[1, 2]University of Maribor, Faculty of Mechanical Engineering,

Smetanova 17, 2000 Maribor, Slovenia

[a] ales.belsak@uni-mb.si, [b] joze.flasker@uni-mb.si

Keywords: Gear, Fatigue Crack, Vibrations, Wavelet Signal Analysis.

Abstract. A crack in the tooth root is the least desirable damage of gear units, which often leads to failure of gear unit operation. A possible damage can be identified by monitoring vibrations. The influences that a crack in the tooth root of a single-stage gear unit has upon vibrations are dealt with. Changes in tooth stiffness are much more expressed in relation to a fatigue crack in the tooth root, whereas in relation to other faults, changes of other dynamic parameters are more expressed. Signal analysis has been performed in relation to a non-stationary signal, by means of the Time Frequency Analysis tool, such as Wavelets. Typical scalogram patterns resulting from reactions to faults or damages indicate the presence of faults or damages with a very high degree of reliability.

Introduction

The aim of maintenance is to keep a technical system (gear-unit) in the most suitable working condition; its purpose is to discover, to diagnose, to foresee, to prevent and to eliminate damages. The purpose of modern maintenance, however, is not only to eliminate failures but also to define the stage of a potential danger of a sudden failure of system operation. The aim of diagnostics is to define the current condition of a system and the location, shape and reason of damage formation. With the purpose to define incorrect operation, the possibility and the location of damages and the possibility of elimination of these damages, the following diagnostic values are used: different signals, condition parameters and other indirect signs.

A gear unit is a complex dynamic model; it contains elements that enable transmission of rotating movement; its movement is usually periodical. Faults and damages represent a disturbing quantity or impulse [1]. On the basis of disturbance local and time changes occur in vibration signals. As a result, time-frequency changes can be expected [2,3]. This idea is based on kinematics and operating characteristics.

Wavelet Analysis

The continuous wavelet transform of function $x(t) \in L^2(\Re)$ at the time and scale is expressed as follows [4]:

$$W\ x(u,s) = \left\langle x, \psi_{u,s} \right\rangle = \int_{-\infty}^{+\infty} x(t) \cdot \frac{1}{\sqrt{s}} \cdot \psi^* \left(\frac{t-u}{s} \right) \cdot dt = x(t) \otimes \overline{\psi}_s(t) \tag{1}$$

$$\overline{\psi}_s(t) = \frac{1}{\sqrt{s}} \cdot \psi^* \left(\frac{-t}{s} \right) \tag{2}$$

$$\overline{\Psi}_s(\omega) = \sqrt{s} \cdot \Psi^*(s \cdot \omega) \tag{3}$$

where the transform is presented as the product of convolution; in the equation (2), the expression of an average wavelet function and the corresponding Fourier integral transform, equation (3), is expressed.

In relation to the continuous wavelet transform, the observed function *x(t)* is multiplied by a group of shifted and scaled wavelet functions; thereby their time and frequency dissemination changes; time and frequency dissemination of the continuous wavelet transform are changed at the same time. Wavelets are locally limited functions and as such they are used to analyse the observed function *x(t)*. The sensitivity of the continuous wavelet transform to local non-stationarities is very much expressed.

Gabor wavelet function is a representative of an approximately analytical wavelet function; it is acquired by means of a frequency modulation of the Gauss window function [4]:

$$\psi_{Gabor}(t,\sigma,\eta)=\frac{1}{\sqrt[4]{\sigma^2\cdot\pi}}\cdot e^{-\frac{t^2}{2\cdot\sigma^2}}\cdot e^{i\cdot\eta\cdot t} \tag{4}$$

Practical Example

All the measurements were carried out, using the test plant of the Computer Aided Design Laboratory of the Faculty of Mechanical Engineering, University of Maribor. The test plant is presented in Fig. 1. A one-stage helical gear unit is located at the spot where vibrations were measured. A helical gear unit with straight teeth was integrated into the gear unit. Tests were performed under constant loads; vibrations were measured directly, using accelometers, which were fixed on the housings. Each gear unit contained a carburised spur gear pair of module 4 mm, the pinion had 19 and the wheel 34 teeth. The results presented in this paper are related to a nominal pinion torque of 20 Nm and nominal pinion speed of 1200 rpm (20 Hz), which is a very typical load condition for this type of gear units in industrial applications.

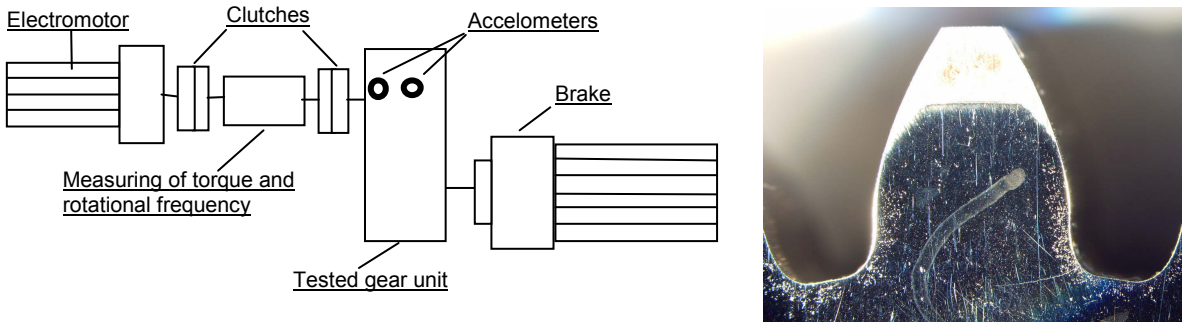

Figure 1: Test plant and a pinion with a crack in the tooth root

Measurements of a gear unit with a fatigue crack in the tooth root of a pinion were performed; the operating conditions were such as are usually associated with this type of a gear unit [5]. A ground gear pair with the teeth quality 6 was used a standard gear pair; however, a crack in the tooth root of a pinion was present; this pinion is shown in Fig. 1.

The crack on one of the teeth is 4.8 mm long; it is presented in Fig. 1. The measurement process and the preparations for analysis are presented in detail in [6].

The length of the signal of measured values was 1 s; on an average, it was composed of 12500 measuring points. The rotational frequency was 20 Hz during measurement.

A scalogram of analytical wavelet transform with Gabor wavelet function represents normalised and square values of amplitudes of wavelet coefficients. Due to the connection between the scale

and frequency, the representation is carried out in a time-frequency domain. It is much simpler to find adequate characteristics in time-frequency domain (frequency scalogram) than in time-scale domain (scalogram). This is very appropriate in relation to technical diagnostics. Based on normalization, the transform matches the Parseval characterstic of energy preservation. This means that the energy of wavelet transform equals the energy of the original signal in time domain [7].

For analysis, the analytical continuous wavelet transform, with parameters $\eta = 6$ and $\sigma = 1$, was applied. The highest frequency in the signal (6250 Hz) was acquired on the basis of Nyquist frequency and the frequency of sampling the measured time signal. For analysis, only a part of the signal, which represents one whole rotation of the tooth, i.e. of a pinion with a crack, of 50 ms, was used.

The figures in the frequency scalogram show that, in relation to the faultless gear, no particularities in expressed components that would indicate local changes are noted, which applies to a square representation (Fig. 2) of wavelet coefficients. In respect to the analysis of the signal produced by a gear with a crack the case is quite different: in concern to this signal a local change in wavelet coefficients, in time at the value of 11 ms, is clearly evident in frequency scalograms (Fig. 3). In relation to the spot where there is the tooth with the crack in its root it is possible to observe local changes, i.e. the presence of transients. If the wavelet is 50 ms long, which is one rotation of the pinion, and 19 teeth are along the circumference, the increased amplitude is located at 11 ms and belongs to the fourth tooth in the direction of rotation from the reference positional point of the gear unit.

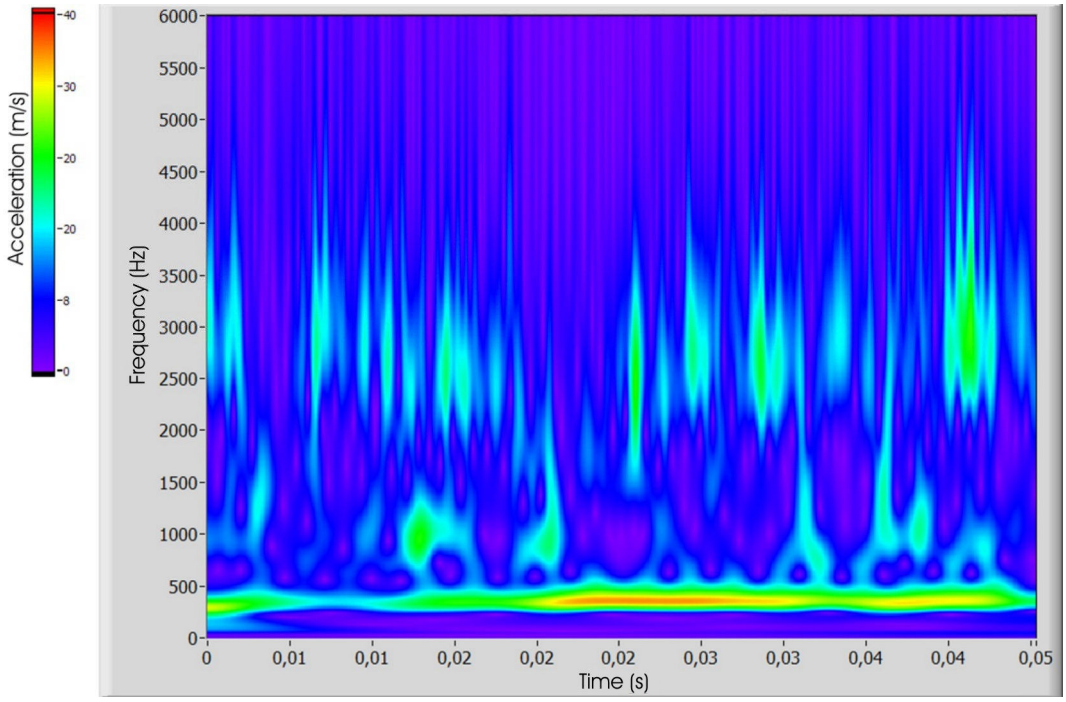

Figure 2: Average twodimensional Gabor frequency scalogram of square wavelet coefficient of the reference gear unit

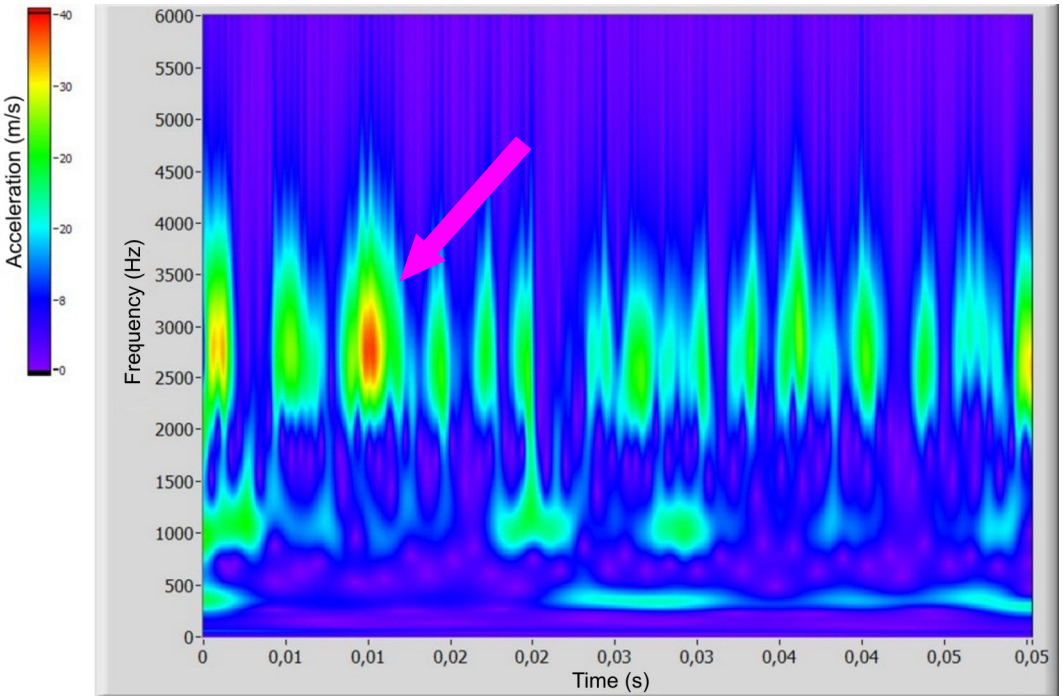

Figure 3: Average twodimensional Gabor frequency scalogram of square wavelet coefficient of the gear unit with a gear with a crack in a tooth root

Conclusion

Vibration analysis aimed at fault detection in reference to industrial gear units is presented in this paper. It is possible to improve the safety of operation on the basis of the methods described; consequently, the reliability of monitoring operational capabilities can be increased as well. By means of wavelet transform changes can be identified in a very short time and the presence of a damage can be defined at the level of an individual tooth.

In view of this it is possible to monitor, in relation to life cycle design, the actual condition of a device and its vital component parts. This can, by means of an adequate method or criterion, influence the operational capability in a considerable way. The reliability of operation is controlled to a great extent if faults and damages are detected in time.

References

[1] Fladrin P., Time-Frequency/Time-Scale Analysis, Academic Press, San Diego, 1999

[2] Qian S., Chen D., Joint Time-Frequency Analysis, Prentice Hall, Upper Saddle River1996

[3] Victor C. Chen, Hao Ling, Time-Frequency Transforms, Artech Hause Publishers, Boston, 2002

[4] Mallat S., A Wavelet Tour of Signal Processing, Academic Press, San Diego, 1999

[5] Suresh S., Fatigue of Materials, Cambridge University Press, Cambrige, 1998.

[6] Belsak A., Time-Frequency Analysis of the Condition of Gear Units (Abstract in English), Doctoral Thesis, University of Maribor, Faculty of Mechanical Enginerinng, 2006.

[7] Adewusi S. in AI-Bedoor B., Wavelet analysis of vibration signals of an overhang rotor with a propagating transverse crack, Journal of Sound and Vibration, 246(5), 777–793, 2001

Key Engineering Materials Vols. 385-387 (2008) pp 605-608
© (2008) Trans Tech Publications, Switzerland
doi:10.4028/www.scientific.net/KEM.385-387.605

Experimental Study on the Development of New Corrosion Inhibitor contained a lot of $Ca(No_2)_2$ using Concrete Structure

Byung Chul Moon[1, a], Hanseung Lee[1, b], Youngjin, Kim[2c]

[1]School of Architecture & Environmental Engineering, Hanyang University, Ansan, 425-791, Korea
[2] Land & Urban Research Institute, Korea Land Corporation, Yusung-gu, Taejon, Korea

[a]patrick1@hanyang.ac.kr, [b]ercleehs@hanyang.ac.kr, [c]yjkim016@dreamwiz.com

Keywords: hydration, pH value, cement, admixture

Abstract. The purpose of this research is to evaluate the effectiveness of nitrate as a corrosion inhibitor in mortar containing chloride. In the experiment, test specimens of mortar to which chloride and nitrite had been added, were subjected to accelerated corrosion by means of repeated drying and wetting on condition of high temperature. This study concerns the assessment of the inhibition effect of nitrite-based corrosion inhibitor using a polarization method and its influence on the chloride transport, compressive strength and setting time of concrete. From the results of the experiments, it was confirmed that the lithium, calcium nitrite corrosion inhibitor and new corrosion inhibitor over dosage 0.6 (NO_2-/Cl^-) molar ratio is very effective in protecting reinforcement from corrosion in mortar in which chloride ions have contained.

Introduction

Use of the nitrous acid rust preventive is one of countermeasure to prevent various reinforcing rod corrosion that occur in the reinforced concrete structure. There is lithium and calcium in representative the nitrous acid corrosion inhibitor. Two kinds of corrosion inhibitor are good to prevent concrete corrosion. However, time of coagulation quickens rapidly in case contain the nitrous acid calcium corrosion inhibitor more than 3%. With the reason the nitrous acid calcium is acting role of accelerator in the concrete coagulation speed. The other side, in the case of the nitrous acid lithium, the mixing amount does not influence in the setting time increase but because price is high, use of the nitrous acid calcium is more. The concrete coagulation speed developed new the nitrous acid calcium corrosion inhibitor because influence concrete constructability and durability. Therefore, do by purpose that mix retardant of concrete agent in this research and develop new corrosion inhibitor because delaying the setting time.

Experiment program

In this study, experimental method: Setting time test of mortar test piece is each variable setting time measurement and testing method for setting time of concrete mixture by penetration resistance by KS F 2436 and corrosion protection effect with Electrochemical. Table 1, 2 and 3 shows experimental factors and levels of this experiment.

Table 1 Experimental factor and levels for corrosion setting time

Name	Cement	C/S	W/C	Corrosion inhibitor
OPC	3000 g	40%	45%	-
C 1%				1%
C 3%				3%
C 5%				5%
C 7%				7%

Table 2 Experimental factor and levels for new corrosion inhibitor setting time

Name	C	C/S	W/C	Corrosion inhibitor	Retarder
C3%-S0.1%	3000g	40%	45%	3%	0.1%
C5%-S0.1%				5%	
C7%-S0.1%				7%	
C3%-S0.13%				3%	0.13%
C5%-S0.13%				5%	
C7%-S0.13%				7%	
C3%-S0.15%				3%	0.15%
C5%-S0.15%				5%	
C7%-S0.15%				7%	

Table 3 Experimental factor and levels for potentiostat experiment

An aqueous solution.		saturated calcium hydration	NaCl	Corrosion inhibitor
non corrosion inhibitor and non Cl^-anion		1000g	0g	-
Cl^- anion 0.3kg/m³			2.7g	
Cl^- anion 0.6kg/m³			5.4g	
Cl^- anion 1.2kg/m³			10.7g	
Cl^- anion 1.8kg/m³			16g	
Cl^- anion 2.4kg/m³			21.4g	
Cl^- anion 1.2kg/m³	mol ration $(NO_2^-)/(Cl^-)$ 0.3		10.7 g	9.3g
	mol ration $(NO_2^-)/(Cl^-)$ 0.45			13.8g
	mol ration $(NO_2^-)/(Cl^-)$ 0.6			18.3g
	mol ration $(NO_2^-)/(Cl^-)$ 0.75			22.9g
	mol ration $(NO_2^-)/(Cl^-)$ 0.9			27.5g
	mol ration $(NO_2^-)/(Cl^-)$ 1.2			36.55g
	mol ration $(NO_2^-)/(Cl^-)$ 1.5			45.58g

Result and Discussion

Setting time result of corrosion inhibitor and normal mortar

The mixing amount of the coagulation speed of mortar that mix calcium increases, the coagulation speed happened fast. For these reasons, Concrete construction is some problem when the calcium nitrite corrosion inhibitor in large quantities mixes.

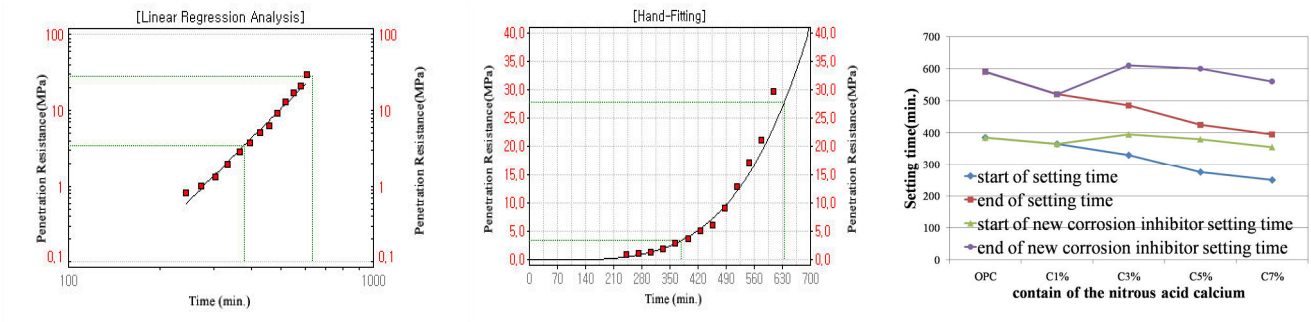

(a) Hand- Fitting (b) Linear Regression Analysis (c) each for corrosion inhibitor

Fig. 1 Result of corrosion inhibitor setting time

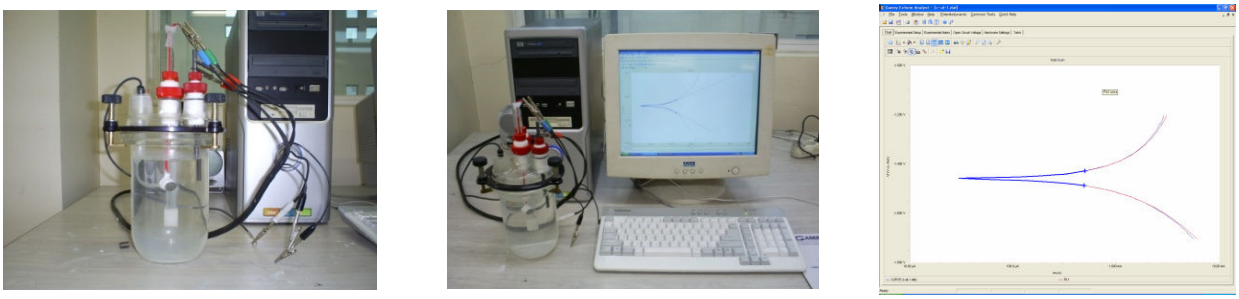

Fig. 2 corrosion protection effect of electrochemical by potentiostats

Mortar setting time result new corrosion inhibitor

Table 2 of experiments the results are as shown as follows.

Figure 3 is the nitrous acid calcium 3%, 5%, 7% and retarder Sodium Gluconate mixes each 0.1%, 0.13%, 0.15%. The start setting time of the nitrous acid calcium 3%, 5%, 7% are fast more than opc to 60~120minute. However, contain retarder in corrosion inhibitor, it delay can be setting time than opc.

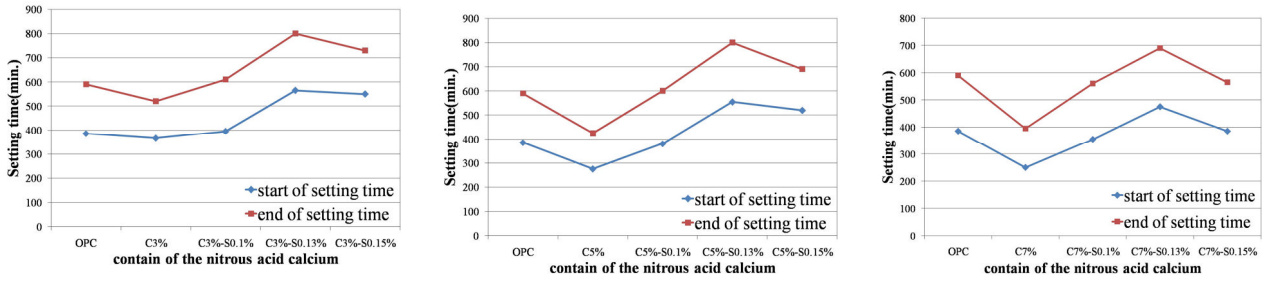

(a) corrosion inhibitor 3% (b) corrosion inhibitor 5% (c) corrosion inhibitor 7%

Fig. 3 Result of new corrosion inhibitor content by percentage

Figure 4 is retarder content by percentage. Retarder SG contains 0.1% than contain 0.13% to 0.15% is delay setting time. The coagulation speed appeared as effect of delay according to calcium nitrous content is different as result that mix retardant Sodium Gluconate 0.15% to calcium nitrous 3%, 5%, 7%. However, it decline strength when SG has much content by percentage. So content is the more appropriate of 0.1%.

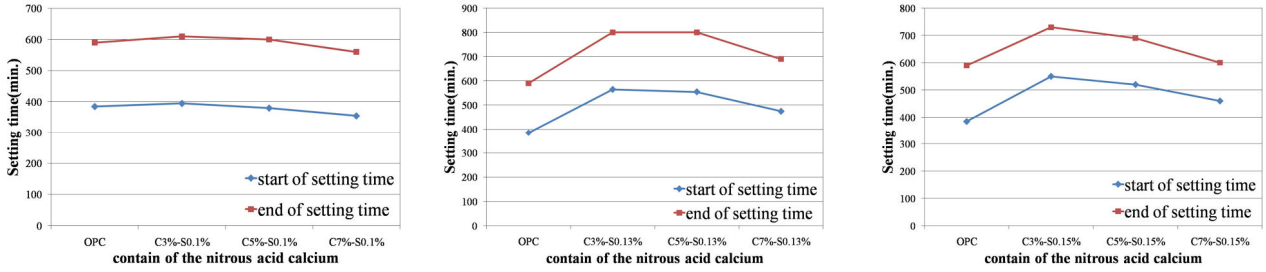

(a) corrosion inhibitor 3% (b) corrosion inhibitor 5% (c) corrosion inhibitor 7%

Fig. 4 Result of retarder content by percentage

An aqueous solution on the corrosion rate by mol ration

Corrosion rates are shown in Figure 5, it is Cl^- anion quantity by an increases mol ration of corrosion inhibitor of a tendency to represent. This applied in the study of the corrosion rate units (mpy) by corrosion and erosion that sided diminution mil (10^{-3} = 1mil inch) will be represented by

the unit. 1mpy is $2.54*10^{-2}$mm/yr, and within 100 years of this study, the corrosion of rebar sided loss of more than 10 percent to avoid a corrosion inhibitor mol ration excellent protection against corrosion with corrosion inhibitor mol ration to calculate. According to Figure 6 for Chloride 0.6% in the mol ration corrosion rate can be measured in less than 0.5mpy. This is 0.6% more than in mol ration chloride for securing buildings, the life expectancy of 100 against corrosion caused by the one-sided loss of 10% within a means to restrain the mol ration exceed 0.6% of the performance improvements are even approach because it does not increase significantly 0.6% is the most economical.

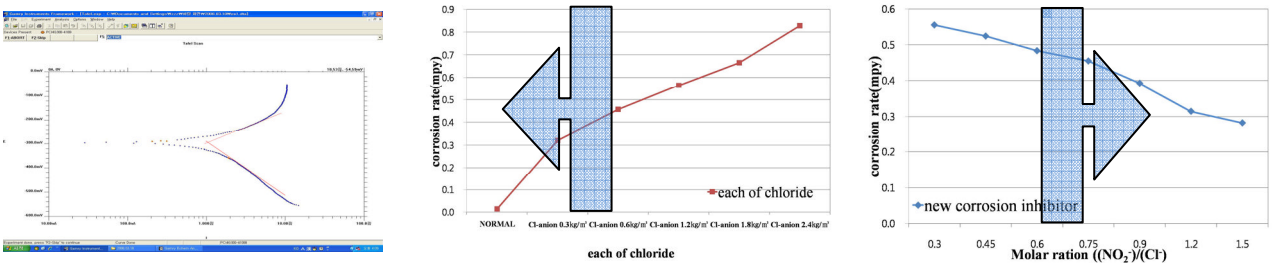

(a) electrochemical plots (b) effect of chloride contents (c) effect of molar ratio

Fig. 5 corrosion rate of electrochemical by potentiostats

Conclusions

The purposes of this study as following if summarize the result measured setting time of mortar about the nitrous acid calcium large quantity mixing.

[1] The mixing amount of the coagulation speed of mortar that mix calcium increases, the coagulation speed happened fast.

[2] When I was use retarder of 0.1%, nomal mortar use setting time similarly to make a success of the new corrosion inhibitor.

[3] The corrosion rate is late to more than 0.6 mol ration for economy or construction that can be secure.

Acknowledgements

This work was supported by Sustainable Building Research Center Hanyang University which was supported the SRC/ERC program of MOST (#R11-2005-056-04003-0) and the Center for Concrete Corea (05-CCT-D11), supported by Korea Institute of Construction and Transportation Technology Evaluation and Planning (KICTTEP) under the (MOCT)

References

[1] K.Y. Ann, H.S. Jung, H.S Kim, S.S. Kim, and H.Y. Moon, Effect of calcium nitrite-based corrosion inhibitor in preventing corrosion of embedded steel in concrete (2007)

[2] Ha-Won Song and Velu Saraswathy, Analysis of Corrosion Resistance Behavior of Inhibitors in Concrete using Electrochemical Techniques (2006)

[3] A. Bentur, S. Diamond and N.S. Berke, Steel Corrosion in Concrete, Chapman & Hall, London, UK 1997.

[4] B. Borgard, C. Warren, S. Somayaji and R. Heidersbach, Corrosion Rates of Steel in Concrete, p. 174, STP 1065, ASTM 1990.

Key Engineering Materials Vols. 385-387 (2008) pp 609-612
© (2008) Trans Tech Publications, Switzerland
doi:10.4028/www.scientific.net/KEM.385-387.609

Structural Similitude for Buckling of Delaminated Beams

Jalil Rezaeepazhand

Department of Mechanical Engineering
Ferdowsi University of Mashhad
P.O. Box 91775-1111,
Mashhad, Iran

jrezaeep@ferdowsi.um.ac.ir

Keywords: Buckling, Delamination, Scaling Laws, Similitude

Abstract. A significant amount of research has been conducted on the buckling behavior of delaminated composite laminates. However, none of the investigations has been focused on establishing similarity and scaling laws for buckling response of composite laminated with delamination. The main objective of this study is to demonstrate the applicability of similitude theory in designing scaled down models for predicting the buckling behavior of delaminated laminated beam subjected to uni-axial compression. The results presented herein indicate that, for buckling response of delaminated beam-plates, based on structural similitude, a set of scaling laws can be found which use to develop design rules for small scale models. For models with the same material properties and stacking sequence as prototype, distorted models with different number of delaminations, delamination length and depth than those of the prototype can predict the behavior of the prototypes with good accuracy.

Introduction

Damage tolerance and residual strength after impact of composite structures are very important issues in aerospace engineering. Delamination buckling theory and equivalent inclusions are two residual strength models which are used for assessing damage of impacted composite structures. It has been shown [1] that, for various low impact energy levels, thicknesses and stacking sequences, delamination buckling theory is in good agreement with experimental data.

Using numerical, experimental and analytical methods a significant amount of research has been conducted on the buckling behavior of delaminated composite laminates. A brief description and a historical review of this subject are presented by Simitses[2]. In these studies the effect of different parameters, such as delamination shape, location, and number of delaminations on buckling of delaminated beams, plates and shells has been presented. To the author's knowledge, none of the investigations has been focused on establishing similarity and scaling for the buckling response of composite laminates with embedded delaminations.

The main objective of this study is to demonstrate the applicability of similitude theory in designing scaled down models for predicting the buckling behavior of delaminated laminated beams/plates subjected to uni-axial compression. In this study, we consider the procedure that is based on the direct use of the governing equations of the systems. The method presented herein has already been shown to be effective in the design of scaled down models for buckling and vibration response of laminated composite shells[3-4] and panels[5]. Scaling laws provide a relationship among similar structures and can be used to extrapolate the available experimental/computed data of one structure, herein called the *model*, into design information for another similar structure which is called the *prototype*. In the present studies, the material behavior is assumed to be linearly elastic. Therefore, scale effects due to damage or other forms of non-linearity are not present or they have similar effect on both the prototype and the scaled models.

Governing equation and Corresponding Scaling laws

For a conventional one-dimensional model of a delaminated beams, the governing differential equation for each sublaminate is expressed as Eq.1[6]. This model assumes the plates are homogeneous and orthotropic, the material behavior is linearly elastic, and delaminations exists and grow along a plane parallel to the reference plane. Delaminations are symmetric about the longitudinal centerline of the beam. The plate is fixed or simply supported along its loaded edges, and has length 2*L*, thickness *H=2h* and width W(Fig. 1). Thin local delamination buckling occurs when the instability is initiated by the buckling of the delaminated layer.

$$D_{11i}^2 \frac{d^4 w_i}{dx_i^4} + 4P_i L^2 \frac{d^2 w_i}{dx_i^2} = 0 \tag{1}$$

Where i =1,2,3,… are the regions in the delaminated beam, D_{11} is the stiffness matrixes of each sublaminate and P_i the buckling load of each sublaminate, expressed as a fraction of applied compressive load.

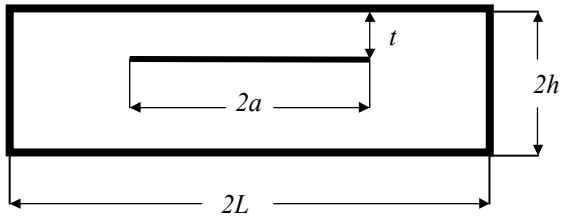

Figure 1: Configuration of a beam with one delamination.

Eq. 1 represents the response behavior of both the prototype and its models. Performing the necessary transformation [5], and applying similitude theory, yields the following scaling law of applied compressive load *P* for orthotropic laminated beam.

$$\lambda_P = \lambda_t^2 \lambda_a^{-2} \lambda_L^{-2} \lambda_h \lambda_{\bar{Q}_{ii}} \tag{2}$$

where $\lambda_x=(x_{\text{prototype}} / x_{\text{model}})$ denotes the scale factor of parameter *x*.

Results

The necessary scaling laws for buckling of delaminated beam have been established in previous section. Now, the possibility of the existence of different models can be investigated. The procedure consists of systematically observing the effect of each parameter and corresponding scaling laws. Then acceptable intervals and limitations for these parameters and scaling factor are discussed. In each case, a set of valid scaling factors that accurately predict the response of prototypes from models is introduced. Scaling laws provide a relationship among similar structures and are used to extrapolate the available computed/experimental data of one delaminated composite model to predict the response of similar prototypes. Numerical results are obtained using published work of Lee[7].

The definition of the computed values for the prototype or models, are the computed buckling loads which are given by Lee [7]. However, the predicted values of buckling loads of the prototype are those given by projecting the computed buckling load of the model using the resulting scaling law (Eq. 2). The presented normalized buckling load is the buckling load of the delaminated plate divided by that of the undelaminated case. Model and prototype have the same material properties or $\lambda_{Qii}=1$.

The necessary condition for complete similarity between the model and its prototype is that all scaling laws are satisfied simultaneously [5]. Note that this condition is a necessary but not a sufficient condition for complete similarity. In order to achieve complete similarity, models and prototypes must buckle in a similar mode shape.

In the present case, for thin delaminations (t_i < 0.25h) and for long delaminations (a_i > 0.4L), the buckling modes are usually symmetric mode[7]. Hence, complete similarity can be achieved even for laminates with different delamination lengths if the model and prototype have the same buckling mode.

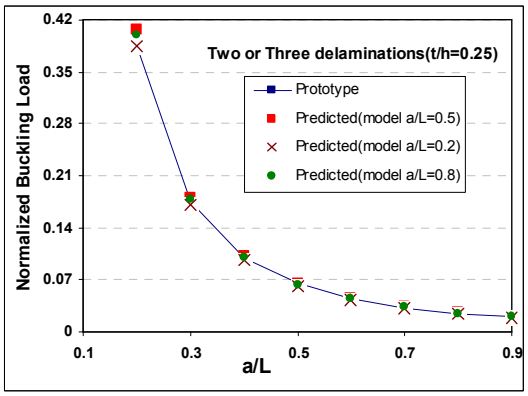

Figure 2: Predicted and directly computed buckling loads of prototype using models with different a/L and similar t/h=0.25.

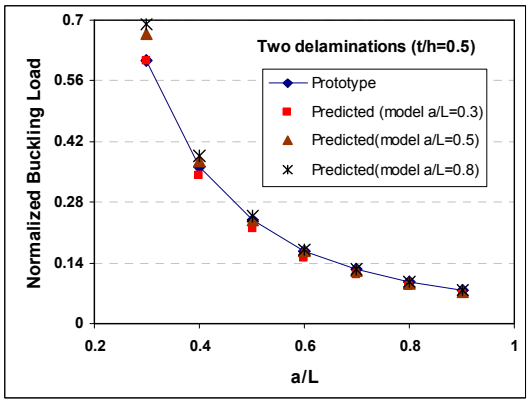

Figure 3: Predicted and directly computed buckling loads of prototype with two delamination t/h=0.5.

Fig. 2 presents the normalized buckling load predicted using Eq. 2 for a model with the same number of plies, material properties, dimensions, and delamination position(h/H=0.25) as the prototypes compared with the directly computed results. Three different delamination lengths, short $(a/L)_m$=0.2, intermediate 0.5, and large 0.8 are considered for the models. However, a wide range of delamination length are considered for the prototypes (0.2< $(a/L)_p$ <0.9). It is clear that the behavior of all range of prototype delamination lengths can be accurately predicted from the scaling equation using these three models. This particular result can be attributed to the similarity of buckling mode shapes of the model and prototype. Both models and prototypes are buckled in a symmetric mode. This behavior presents the complete similarity conditions.

Fig. 3 illustrate the accuracy of the models in predicting the buckling loads of prototypes with two equal length delaminations locate at t_1/h=0.5, and 1.5. with different a/L. In this case, model with intermediate delamination length can predict the prototype buckling load better than two other models. For prototype with short delamination length $(a/L)_p$ <0.3, models with intermediate and large a/L, overestimate the prototype buckling load. In this case, both model and prototype are buckled in a local symmetric mode. Therefore, the complete similarity is achieved.

Similar results are presented in Fig. 4 for beams with three equal length delaminations locate at t_1/h=0.5, 1, 1.5. Models with intermediate and large a/L are capable of predicting buckling load of prototype with $(a/L)_p$ <0.4 with good accuracy. However model with short delamination $(a/L)_m$=0.3 underestimate buckling load of the prototype. Again this behavior may be attributed to dissimilarity between the model and prototype buckling mode shapes. When additional delamination is located at the mid-plane of the laminate, the mode is more likely to be influenced by global antisymmetric rather than local buckling, and the change in mode shape means that the complete similarity is not achieved. Based on results presented by Lee[7], for the case of a composite bream with three delamination, the antisymmetric global mode governs buckling in the range of (0.1< a/L <0.4). For other values of a/L, the beam is buckled in its symmetric local mode. This explains the weakness of models with intermediate and large delamination on predicting the response of a prototype with short delamination (a/L=0.3 in Fig.3).

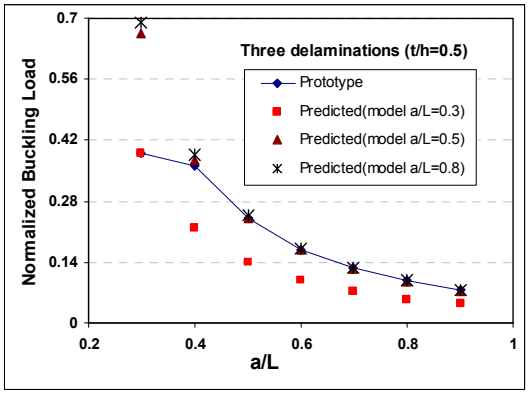

Figure 4: Predicted and directly computed buckling loads of prototype with three delamination t/h=0.5.

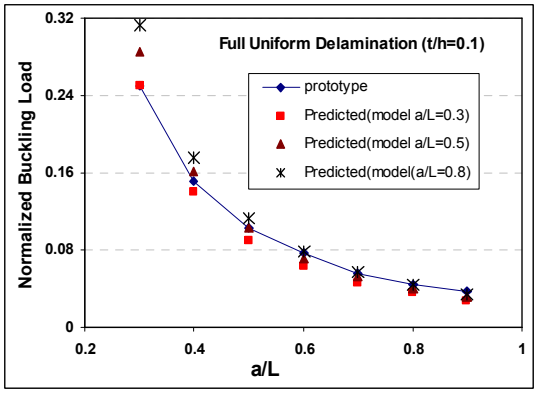

Figure 5: Predicted and directly computed buckling loads of prototype with full uniform delamination t/h=0.1.

Predicted and directly computed buckling loads of prototype with full uniform delamination are presented in Fig. 5. Similar to the case of beam with three delamination, the difference in buckling mode shapes of the model and prototype influence the accuracy of the models with intermediate and large delamination length in predicting the buckling loads of prototypes with short delamination(a/L <0.3).

Discussion

An analytical study has been presented to investigate the applicability of similitude theory to buckling response of delaminated composite beams. The results presented herein indicate that for buckling response of delaminated beams, based on structural similitude a set of scaling laws can be found. The accuracy of predicted prototype buckling load by using various models is investigated. Models with different delamination length are capable of accurately predicting the prototype buckling load.

References

[1] T. Nyman, A. Bredberg, and J. Schon: J. Reinforced Plastics and Comp. Vol. 19(6) 428-448(2000).
[2] GJ. Simitses, in: *Buckling and Post Buckling of Composite Plates,* edited by I.H. Marshal and G.J. Turvey, Chapman & Hall, London, (1994).
[3] GJ. Simitses, J. Rezaeepazhand, and RL. Sierakowski: Mechanics of Composite Materials and structures Vol. 4, 267 - 280(1997).
[4] J. Rezaeepazhand, GJ. Simitses, and JH. Starnes Jr: Composite Structures Vol. 34(4), 361 - 369(1996).
[5] J. Rezaeepazhand, GJ. Simitses, JH. Starnes Jr: AIAA Journal Vol. 33(3), 515-519(1995).
[6] KS. Numayer, and RH. Hadda: Mechanics of Composite Materials and Structures Vol. 8 283-297(2001).
[7] J. Lee, Z. Gurdal, and H. Griffin Jr: AIAA Journal Vol. 31(2), 331-337(1993).

Key Engineering Materials Vols. 385-387 (2008) pp 613-616
© (2008) Trans Tech Publications, Switzerland
doi:10.4028/www.scientific.net/KEM.385-387.613

Experimental study on the adhesion properties of Zn-Al metal spray method for steel structures

Jooho Jin[1, a], Hanseung Lee[1, b]

[1]School of Architecture & Environmental Engineering, Hanyang University, Ansan, 425-791, Korea

[a]jinjooho@hanyang.ac.kr, [b]ercleehs@hanyang.ac.kr

Keywords : Metal Spray, Anticorrosion, Surface Roughness, Adhesion Strength

Abstact. Examination about sticking intensity security way of normal temperature metal spraying covering is required compulsorily accordingly with quantitative assessment about steel plate's surface roughness to secure adhesive power of steel materials and metal membrane stably at application of way method of construction by normal temperature metal spraying. In case of metal spraying, Sticking strength of metal spraying way finish is influenced greatly, and it is judged that is desirable that manages Sm/Rz by 6 lows to secure more than sticking intensity 20kgf/cm^2 by Sm/Rz that evaluate that is rough of nature surface. The purpose of this study was to analyze an adhesion strength of metal spraying finish layer with the surface conditions of steel plate. For the purpose the experimental factors such as anticorrosive finish method and surface treatment method were selected.

Introduction

In the application of the normal temperature metal spraying method at the present time, it has been reported that it is possible to guarantee bond strength on the surface of steel structures by processing the surface as a rough surface through applying a type of two liquid type epoxy resin with ceramic particles.[1] However, the surface roughness in base materials can be significantly varied according to the preprocessing method of steel structures and the amount of rough surface forming agent and these conditions represent a large difference in the bond strength of metal layers.[2]
Thus, this study performed the quantitative evaluation of the surface roughness of steel structures and investigated a method that guarantees the bond strength of metal layers in a normal temperature metal spraying method in order to stably establish the bond strength between steel structures and metal layers in a corrosion resistant process using the normal temperature metal spraying method.
This study evaluated the bond performance of the Zn-Al normal temperature metal spraying layer through applying a steel base treatment method and the thickness of the metal spraying layer.

Experiment

Table 1 shows the factors and levels in this experiment to evaluate the bond strength of the corrosion resistant finish using a normal temperature metal spraying method according to the steel base treatment methods and conditions.[3]

Table 1. Experimental factors and level

Finish work	Surface preparation method and level		Levels
Sand blast	Sand blast	#40,#80, #100	17
	Sanding+Rough surface forming (g/m^2)	20, 50-T50, 50-T100, 50-T200, 70	
Grinding	Grinding	T-100	
	Grinding+rough Surface forming (g/m^2)	20, 50-T50, 50-T100, 50-T200, 70	
Heavy-duty coating	Sand blast	#40	2

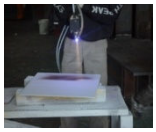
1. Sand blast

2. Grinding

3. Rough surface forming

4.Roughness measurement

Fig 1. Specimen production process

Result

Surfaces based on applied base treatment methods

Fig. 2 illustrates the relationship between the average roughness and the coefficient of variance based on R_z. Also, Fig. 3 shows the relationship between the roughness and the coefficient of variance based on S_m/R_z. Whereas, the factor of R_z in the S-80 that represents the sum of the average values of peaks and troughs in jagged structures showed higher value than that of the S-100, but the S-40 showed higher value than the S-80. In the case of the application of rough surface forming agent after grinding the surface, it showed higher values according to the increase in the amount of the application of rough surface forming agent.

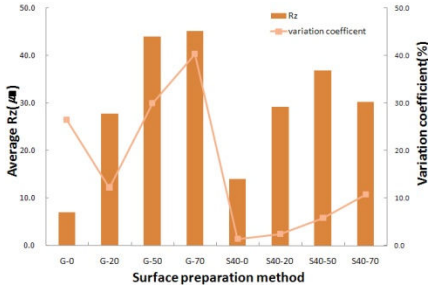

Fig. 2 Average Rz and the coefficient of variance according to the base treatment methods

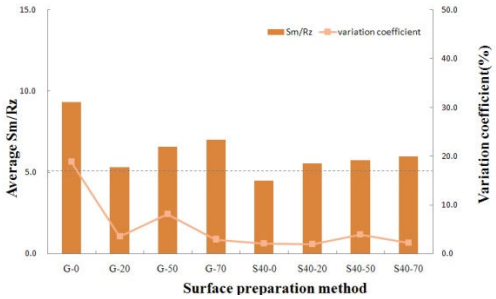

Fig. 3 Sm/Rz and the coefficient of variance according to the base treatment methods

Although there were no specific differences in the value of Sm/Rz obtained by dividing the average distance of the peaks in jagged surfaces by the average depth of troughs, it demonstrated a little decrease according to the increase in the amount of rough surface forming agent.

In addition, the value of the coefficient of variance in R_z and S_m/R_z according to the base treatment methods showed a significant decrease according to the increase in the amount of rough surface forming agent that showed stable results in the measurement. Also, in the case of the application of a 70g/cm^2 of rough surface forming agent after applying grinding and sand blast treatments, the coefficient of variance showed almost same results.

Bond strength according to the steel base treatment methods

Fig. 4, Fig. 5, and Fig. 6 show the results of the measurement of bond strength for each corrosion resistant finish according to the base treatment methods.

In the case of the bond strength in corrosion resistant finish, it showed almost similar values. The bond strength showed the highest value in the finish of sand blast+rough surface forming agent treatments whereas the bond strength increased according to the increase in the amount of rough surface forming agent.

In particular, it is evident that the bond strength showed significantly high values in the application of rough surface forming agent rather than without based on the comparison of Fig. 6 and Fig. 8

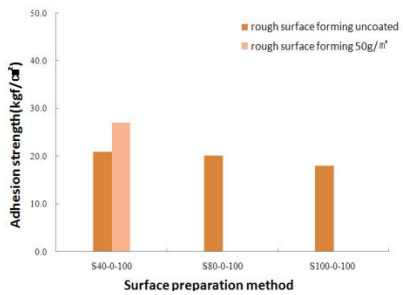

Fig. 4 Bond strength in the sand blast treatment among base treatment methods

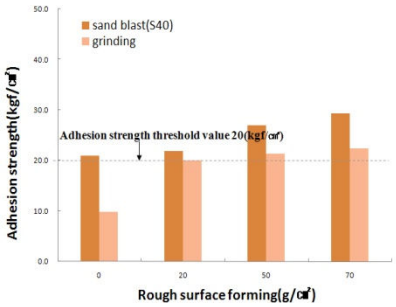

Fig. 5 Bond strength according to the amount of rough surface forming agent

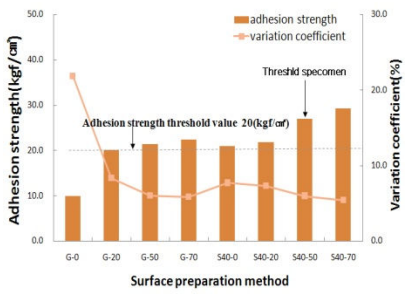

Fig. 6 Bond strength and the coefficient of variance according to the base treatment of steel structures

In addition, the treatments of grinding+rough surface forming agent showed almost same bond strength compared to that of the sand blast treatment. Fig. 6 illustrates the bond strength according

to the base treatment methods and its coefficient of variance. The base treatment methods that investigate changes in the coefficient of variance when the bond strength increased according to the increase in the amount of rough surface forming agent for the treatments of sand blast and grinding in which the coefficient of variance in the sand blast treatment represented lower value than that of the grinding. Also, it showed a significant decrease according to the increase in the amount of rough surface forming agent. Thus, the surface treatment using the rough surface forming agent that provides an easy construction process is a very effective way in a metal spraying method because the application of rough surface forming agent largely affects the bond strength and coefficient of variance.

Changes in the bond strength according to the roughness of steel structures

Fig. 7 and 8 show the change in the bond strength of corrosion resistant finish according to the factors of R_z and S_m/R_z. It is considered that the bond strength of corrosion resistant finish increased according to the increase in the peak of jagged surface (R_z). In the case of the metal spraying process, however, the bond strength of the metal spraying layer increased a little according to the increase in R_z. Also, changes in the bond strength caused by the value of S_m/R_z that represents the ratio of the average distance and peak in jagged surface showed a decrease in the bond strength of corrosion resistant finish according to the increase in S_m/R_z as demonstrated in Fig. 12. In particular, it showed more significant changes in the values using a metal spraying finish method.

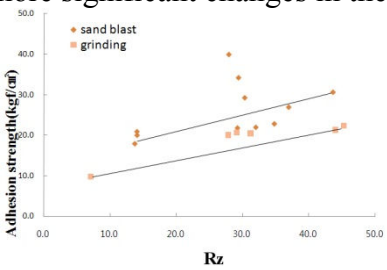

Fig. 7 Relationship of the bond strength between the Rz (+point average roughness) and the corrosion resistant finish

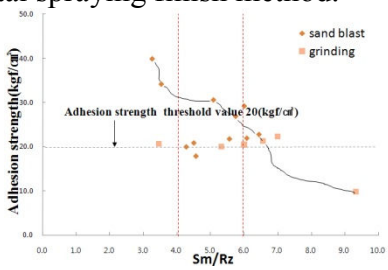

Fig. 8 Relationship of the bond strength between the ratio of S_m/R_z and the corrosion resistant finish

In addition, it is considered that the grinding treatment showed excellent results compared to a heavy duty coating process and the bond strength of the metal spraying finish according to the application of rough surface forming agent was required more than 20kgf/cm^2 in order to obtain the same or excellent bond strength as the sand blast treatment. Thus, it is necessary to manage the factor of S_m/R_z less than 4~6 as marked in the dotted line produced by the rough surface forming agent.

Bond strength according to the thickness of coating layers

As shown in Table 1 and Fig. 11, the coating layer thickness of 100 μm represented the highest bond strength in the treatments of sand blast and grinding under the reference that applied a 50g/m^2 of rough surface forming agent. However, the bond strength showed no increases due to the increase in the thickness of coating layers and no decreases due to the decrease in the thickness. It showed similar values according to the change in such thickness.

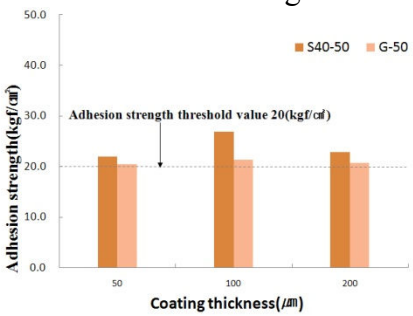

Fig. 10 Bond strength based on the thickness of coating layers according to the base treatment methods

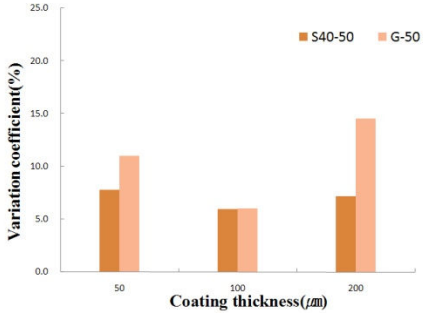

Fig. 11 Coefficient of variance based on the thickness of coating layers according to the base treatment methods

Fig. 11 shows the coefficient of variance based on the thickness of coating layers according to the base treatment methods. In the comparison of Fig. 10 and 11, the coefficient of variance decreased according to the increase in bond strength. Thus, it is considered that the most desirable bond performance can be obtained by constructing the coating layer with the thickness of 100 μm that shows the highest values in the coefficient of variance and bond strength.

Summary

[1] In the mentioned corrosion resistant finish methods, the bond strength of the Zn-Al metal spraying method with the sand blast treatment represented higher values than that of the treatments of grinding or heavy duty coating. Also, the bond strength of the application of rough surface forming agent after applying the grinding treatment showed higher values than that of the heavy duty coating.
[2] The bond strength of metal spray finish can be largely affected by the factor of S_m/R_z that is used to evaluate the roughness of base surface. It is necessary to control the factor of S_m/R_z less than 4~6 in order to guarantee the bond strength more than 20kgf/cm^2.
[3] The process obtained the same level of bond strength as the application of rough surface forming agent with a 20~70g/m^2 of scale.
[4] The most desirable bond performance can be obtained by constructing the coating layer with the thickness of 100 μm in which the bond strength maintained similar results according to the increase or decrease in the thickness of coating layers.

Acknowledgements

This work was supported by Sustainable Building Research Center Hanyang University which was supported the SRC/ERC program of MOST (#R11-2005-056-04003-0) and the Center for Concrete Corea (05-CCT-D11), supported by Korea Institute of Construction and Transportation Technology Evaluation and Planning (KICTTEP) under the (MOCT)

References

[1] J. S. Kim, H. S. Lee, “Evaluation of the corrosion resistant performance in a normal temperature metal spraying method using a CASS test”, Spring Conference in the Architectural Institute of Korea, No. 21, #1, 2001.4, pp.237~240.
[2] H. S. Lee, T. Y. Jang, “Corrosion resistant technology using a normal temperature metal spraying system in architecture", the 12th metal spraying workshop, the Korea Thermal Spray Association, 2000.
[3] T, Kondo , "The surface roughness of metal spraying technology and quality stability in normal temperature", Spring conference in the Japan society for finishing technology, 1999, p147
[4] S, Kenji, Practical material coating guideline, Nikkan Kogyo Shimbun, LTD. 1998
[5] H, Hamaki, Quality control of metal spraying technology, Architect Institute of Japan 1999, p.995

Key Engineering Materials Vols. 385-387 (2008) pp 617-620
© (2008) Trans Tech Publications, Switzerland
doi:10.4028/www.scientific.net/KEM.385-387.617

The Analytical Trial Function Method (ATFM) for Finite Element Analysis of Plane Crack/Notch Problems

Xiang-Rong Fu[1, a], Song Cen[2, 3, b], Yu-Qiu Long[4, c], Xiu-Gen Jiang[1], Jin-San Ju[1]

[1]Department of Civil Engineering, China Agricultural University, Beijing 100083, China

[2]School of Aerospace, Tsinghua University, Beijing 100084, China

[3]Failure Mechanics Laboratory, Tsinghua University, Beijing 100084, China

[4]Department of Civil Engineering, Tsinghua University, Beijing 100084, China

[a]fuxr@cau.edu.cn, [b]censong@tsinghua.edu.cn, [c]longyq@tsinghua.edu.cn

Keywords: analytical trial function method (ATFM); crack/notch problem; finite element; stress singularity; the sub-region accelerated Müller method; fracture mechanics

Abstract. A new technique, Analytical Trial Function Method (ATFM), is proposed to formulate new finite element models for analysis of plane crack/notch problems. A new analytical finite element, named ATFM-CN, is successfully constructed. Furthermore, in order to determine the eigenvalues of the crack/notch problems, which utilized in above analytical trial functions, a modified sub-region accelerated Müller method is also suggested. Numerical examples show the present approach exhibits excellent performance in the analysis of stress-singularity problems.

Introduction

In the past 40 years, many researchers have put significant effort into the numerical methods that are valid for the analysis of fracture problems. Numerous approaches have been proposed, such as traditional finite element method [1], sub-region mixed finite element method [2], extended finite element method [3], boundary element method [4], mesh-free method [5], and so on.

Here, a new technique, *Analytical Trial Function Method* (*ATFM*), is presented to formulate new finite element models for analysis of plane crack/notch problems. Firstly, the basic analytical solutions of the stress fields at the tips of cracks/notches are derived out by the Williams stress functions. Secondly, these solutions are used as trial functions to formulate a stress-based finite element model. Thirdly, by using the sub-region mixed energy principle, the stiffness matrix of a mixed element with crack/notch and variable degrees of freedom is established. Following this procedure, a new analytical finite element, named ATFM-CN, is successfully constructed. Furthermore, in order to determine the eigenvalues of the crack/notch problems which utilized in above analytical trial functions, a modified sub-region accelerated Müller method is also suggested. Numerical examples show the present approach exhibits excellent performance in the analysis of stress-singularity problems.

The formulations of the new analytical finite element model ATFM-CN

The basic analytical stress solutions nearby a tip of the plane crack/notch, which are usually composed of symmetry part and anti-symmetry part, were given by Williams [6]. The symmetry part, also called the mode I stress field, can be expressed by,

$$\begin{Bmatrix}\sigma_r\\ \sigma_\theta\\ \tau_{r\theta}\end{Bmatrix}=\begin{Bmatrix}r^{\lambda-1}\lambda[(3-\lambda)\cos(\lambda-1)\theta+(\lambda\cos\alpha+\cos\lambda\alpha).\cos(\lambda+1)\theta]\\ r^{\lambda-1}\lambda[(\lambda+1)\cos(\lambda-1)\theta-(\lambda\cos\alpha+\cos\lambda\alpha)\cdot\cos(\lambda+1)\theta]\\ r^{\lambda-1}\lambda[(\lambda-1)\sin(\lambda-1)\theta-(\lambda\cos\alpha+\cos\lambda\alpha)\sin(\lambda+1)\theta]\end{Bmatrix}, \tag{1}$$

The anti-symmetry part, also called the mode II stress field, is expressed by

$$\begin{Bmatrix}\sigma_r\\ \sigma_\theta\\ \tau_{r\theta}\end{Bmatrix}=\begin{Bmatrix}-r^{\lambda-1}\cdot\lambda[(3-\lambda)\sin(\lambda-1)\theta+(\lambda\cos\alpha-\cos\lambda\alpha)\sin(\lambda+1)\theta]\\ -r^{\lambda-1}\cdot\lambda[(\lambda+1)\sin(\lambda-1)\theta-(\lambda\cos\alpha-\cos\lambda\alpha)\sin(\lambda+1)\theta]\\ -r^{\lambda-1}\cdot\lambda[(1-\lambda)\cos(\lambda-1)\theta+(\lambda\cos\alpha-\cos\lambda\alpha)\cos(\lambda+1)\theta]\end{Bmatrix}, \tag{2}$$

In which λ is an unknown complex number, representing the eigenvalues for a notch problem with arbitrary open angle α. Since these complex eigenvalues always appear in the form of conjugate pairs, the real part and the imaginary part of the stress solutions can be treated as independent stress solutions, respectively. After selecting a set of rational basic analytical solutions corresponding to the low order eigenvalues, a stress field sub-space with stress parameters can be obtained as follows

$$\{\sigma_r \quad \sigma_\theta \quad \tau_{r\theta}\}^{\mathrm{T}}=[\boldsymbol{S}]\{\boldsymbol{\beta}\}=[\boldsymbol{S}]\{\beta_1 \quad \cdots \quad \beta_m\}^{\mathrm{T}}, \tag{3}$$

where $\{\boldsymbol{\beta}\}$ includes m unknown parameters β_i of the assumed stress field, i.e., m represents the number of the analytical stress trial functions, and $[\boldsymbol{S}]$ is the stress matrix determined by the analytical trial functions given by equations (1) and (2).

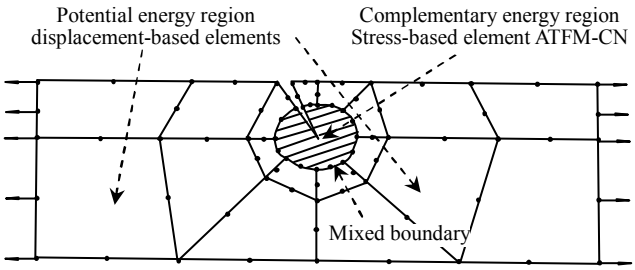

Fig.1 Sub-region mixed meshes

As shown in Fig. 1, the present analytical element ATFM-CN (stress-based element) should be located around the tip of a crack/notch (complementary energy region). Its size, shape, and node number can be varied according to outer mesh divided by conventional isoparametric displacement-based elements (potential energy region). Based on the sub-region mixed energy principle [2], the mixed energy functional of this problem can be written as

$$\Pi=\frac{1}{2}\{\boldsymbol{w}\}^{\mathrm{T}}[\boldsymbol{K}_0]\{\boldsymbol{w}\}-\{\boldsymbol{w}\}^{\mathrm{T}}\{\boldsymbol{P}\}-\frac{1}{2}\{\boldsymbol{\beta}\}^{\mathrm{T}}[\boldsymbol{V}]\{\boldsymbol{\beta}\}+\{\boldsymbol{\beta}\}^{\mathrm{T}}[\boldsymbol{H}]\{\hat{\boldsymbol{w}}\}, \tag{4}$$

where $\{\boldsymbol{w}\}$ is the nodal displacement vector of the structure except for those on the mixed boundary, $[\boldsymbol{K}_0]$ is the stiffness matrix derived from displacement elements of the potential region, $\{\boldsymbol{P}\}$ is the nodal force vector, $[\boldsymbol{V}]$ is the new element flexible matrix derived from $[\boldsymbol{S}]$ in equation (3), $[\boldsymbol{H}]$ is the additional energy matrix and derived from the interpolations of tractions and displacements along the mixed boundary, $\{\hat{\boldsymbol{w}}\}$ is the displacements of the nodes on the mixed boundary. From $\delta\Pi=0$, the relationship between $\{\boldsymbol{\beta}\}$ and $\{\hat{\boldsymbol{w}}\}$ can be established. Thus, the 'stiffness' of the element ATFM-CN associated with its nodal displacement vector $\{\hat{\boldsymbol{w}}\}$ can be obtained,

$$[\boldsymbol{K}]^e=[\boldsymbol{H}]^{\mathrm{T}}[\boldsymbol{V}]^{-1}[\boldsymbol{H}]. \tag{5}$$

Then other calculations can be performed following the standard finite element solution procedure.

Calculation of the eigenvalues – the sub-region accelerated Müller method

The Williams's eigen-equations of the plane notch problem are as follows [6]

$$f(\lambda)=\pm\lambda\sin(\alpha)+\sin(\lambda\alpha)=0 \tag{6}$$

For the plane crack problems, $\alpha = 2\pi$, so the eigenvalues are simply $\lambda=K/2$, where K is an arbitrary integer. But for the plane notch problem with arbitrary angle α, the eigenvalues must be evaluated by the nonlinear iteration method. One of the usual schemes is Müller iteration method. But it is not

always stable. So in order to make the iteration more stable and quickly, equation (6) is replaced by a modified form

$$f^*(\lambda)=\frac{f(\lambda)}{(\lambda-a)(b-\lambda)(\lambda-\lambda_1)(z-\lambda_2)\cdots(z-\lambda_n)}=0, \tag{7}$$

where a and b are the lower and upper bounds of the solution region for the real part of λ respectively, which can be obtained by analysis of $f(\lambda)$; λ_i (i=1…n) are those eigenvalues that have been found out. This modified iteration procedure is named *Sub-Region Accelerated Müller Method (SRAMM)*.

As an example, a Williams eigen-equation $f(\lambda)$=-λsin(α)+sin($\lambda\alpha$)=0 (α = 300°) is solved by the normal Müller method and SRAMM. All results are listed in Table I. It can be seen that the correct convergent solutions can always be obtained by SRAMM within a limited iteration number.

Table I. Comparison of the two kinds of Müller method

a	b	λ by normal Müller method		Iter.	λ by SRAMM		Iter.
		Real part	Imaginary part		Real part	Imaginary part	
0.6	0.9	0.730900742	0	8	0.730900742	0	7
1.8	2.1	1.89349155*	0*	101*	2.07482620	0.229425800	30
3.0	3.3	3.01938419*	0*	101*	3.27976709	-0.326690313	16
4.2	4.5	3.27976709*	-0.32669031*	19*	4.48290004	-0.388983761	17
5.4	5.7	3.01938419*	6.21124E-13*	101*	5.68509375	-0.435407938	20
6.6	6.9	6.88672925	0.472546839	87	6.88672925	-0.472546839	25

*can not converge after 100 iterations or can not converge to correct values.

Numerical examples

Example 1. Fig. 2 shows a cracked plate subjected to uniform tension load q=1. The Young's modulus E and Poisson's ratio μ are assumed to be 0.21×10^7 and 0.3, respectively. And the geometrical sizes are L=1 and h=0.5. Two angle cases are considered: α = 360° for the crack problem and α = 300° for the notch problem.

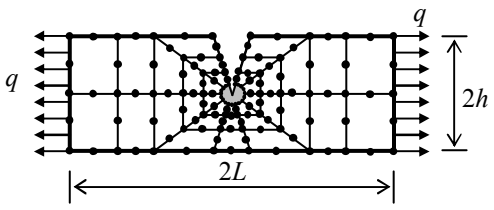

Fig.2 Mesh, loads and geometry for example 1

In this example, the shape of the element ATFM-CN is circle, and its radius R is changeable. Fig.3 to Fig.6 illustrate the variation of the percentage errors of the stress intensity factor K_I with different R and the number m of the analytical stress trial functions.

Example 2. Fig.7 shows a specimen subjected to an anti-symmetry load. The resultant force of this load P=1. The material properties are the same as those in previous example. And the geometrical sizes of this crack/notch plate are as follows: a=1, h=1 and w=3. Four angle α cases (330°, 340°, 350° and 360°) are considered. Fig.8 plots the percentage errors of the stress intensity factor K_{II} with different α and the number m of the analytical stress trial functions.

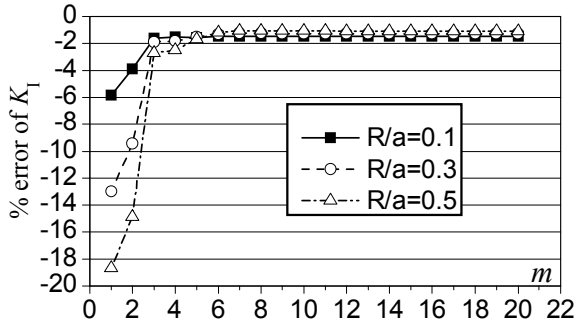

Fig.3 The % errors of K_I with different m (α = 360°)

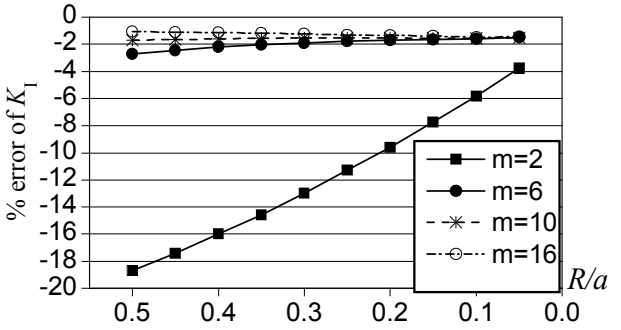

Fig.4 The % errors of K_I with different R/a (α = 360°)

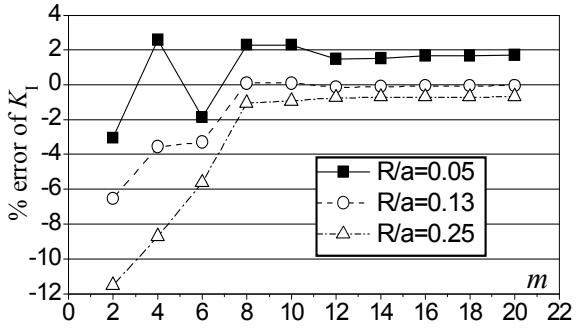

Fig.5 The % errors of K_I with different m ($\alpha = 300°$)

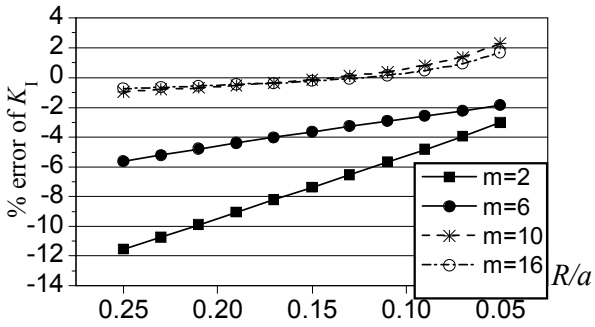

Fig.6 The % errors of K_I with different R/a ($\alpha = 300°$)

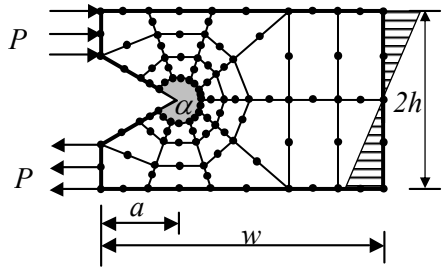

Fig. 7 Anti-symmetry crack/notch problems

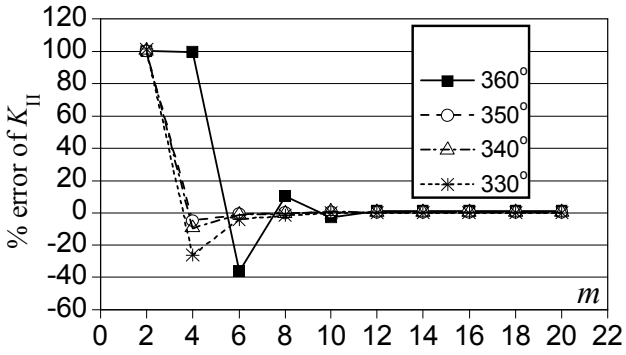

Fig.8 The % errors of K_{II} with different α and m

Conclusions

This paper develops a new type of finite element model, ATFM-CN, for the analysis of plane crack/notch problems. It exhibits obvious *h-p* version convergence in the numerical tests. The presented solution strategy possesses the advantages of both analytical method and discrete method. And it can be generalized to other stress-singularity calculations of fracture mechanics.

Acknowledgement

This study was supported by the National Natural Science Foundation of China (Project no. 10502028), the Foundation for the Author of National Excellent Doctoral Dissertation of PR China (200242), and the Science Research Foundation of China Agricultural University (2004016).

References

[1] *ABAQUS/Standard User's Manual*, *Version 6.5* (Hibbitt, Karlsson & Sorensen, Inc.: Rawtucket, Rhode Island, USA 2005).

[2] Z. Fan, Y. Q. Long: International Journal of Fracture Vol. 56 (1992), p. 333-344.

[3] N. Moës, J. Dolbow and T. Belytschko: International Journal for Numerical and Analytical Methods in Geomechanics Vol. 46 (1999), p. 131-150.

[4] K. Xu, S. T. Lie and Z. Cen: International Journal for Numerical and Analytical Methods in Geomechanics Vol. 28 (2004), p. 421-435.

[5] W. K. Liu, S. Hao and T. Belytschko: Computational Material Science Vol. 16 (1999), p. 197 -205.

[6] M. L. Williams: J. App. Mech. Vol. 14 (1952), p. 526-528.

[7] B. Gross, A. Mendelson: Int. J. Fract. Mech. Vol. 8 (1972), p. 267-276.

Key Engineering Materials Vols. 385-387 (2008) pp 621-624
© (2008) Trans Tech Publications, Switzerland
doi:10.4028/www.scientific.net/KEM.385-387.621

Reliability Assessment of Corrosion Initiation of Harbor Concrete Structure using FOSM

Sang-Hun Han[1, a], and Woo-Sun Park[1,b]

[1]Coastal & Harbor Engineering Research Center, Korea Ocean Research & Development Institute, 1270 Sa2dong Ansan, Kyunggido 426-744, Republic of Korea

[a]shhan@kordi.re.kr, [b]wspark@kordi.re.kr

Keywords: Reliability, Corrosion, Durability, FOSM

Abstract. Due to the uncertainty of variables in durability model, the probabilistic approach is increasing. Monte Carlo Simulation (MCS) is an easily accessible method, but requires a lot of repeated operations. This paper evaluated the effectiveness of First Order Second Moment method (FOSM), which is more convenient and time saving method than MCS, to predict the corrosion initiation in harbor concrete structure. Mean Value First Order Second Moment method (MV FOSM) and Advanced First Order Second Moment method (AFOSM) are applied to the error function solution of Fick's second law modeling chloride diffusion. Reliability index and failure probability based on MV FOSM and AFOSM are compared with the results by MCS. The comparison showed that AFOSM and MCS predict similar reliability indexes and MV FOSM underestimates the probability of corrosion initiation by chloride attack. Also, the sensitivity of variables in durability model to failure probability was evaluated on the basis of AFOSM. The results showed that AFOSM is a simple and efficient method to estimate the possibility of corrosion initiation in harbor concrete structures.

Introduction

The adoption of probabilistic approach is increasing because of the uncertainty of variables in durability model. Monte Carlo simulation (MCS), an ordinary method, is an easily accessible method, but requires a lot of repeated operations [1,2]. The objective of this paper is to evaluate the effectiveness of First Order Second Moment method (FOSM), which is more convenient and time saving method than MCS, to predict the corrosion initiation in harbor concrete structure and investigate the influence of variables in durability model on corrosion initiation.

Durability Analysis in Harbor Concrete Structure

Model of Analysis. The corrosion initiation of harbor concrete structure is assessed on the basis of chloride ion concentration in the location of reinforced steel. Because the general process of chloride ion penetration occurs in response to concentration gradient between surface and inner concrete, Fick's second law estimating diffusion phenomenon can be used to describe this movement as follows.

$$\frac{\partial C}{\partial t} = D_d\left[\frac{\partial^2 C}{\partial x^2} + \frac{\partial^2 C}{\partial y^2} + \frac{\partial^2 C}{\partial z^2}\right] = D_d \nabla^2 C \tag{1}$$

where C is the chloride ion concentration, D_d is the diffusion coefficient, t is the time. If chloride ion diffusion occurs in one-direction and an averaged diffusion coefficient can be obtained during diffusion process, the following equation is an available solution of Eq. (1).

$$C = C_o\left[1 - erf\left(\frac{x}{2\sqrt{D_d t}}\right)\right] \tag{2}$$

where C_o is the surface chloride ion concentration, x is the cover depth. In Korea, in order to analyze the durability of harbor concrete structure, Eq. (2) including error function is generally used for convenience and promptitude.

FOSM. Because limit state occurs at the condition that the chloride concentration at the steel location is larger than the critical chloride concentration, C_d, from which the steel is corroded, the limit state equation can be formulated as follows.

$$Z(C_d, C_o, x, D_d) = C_d - C_o\left[1 - erf\left(\frac{x}{2\sqrt{D_d t}}\right)\right] \tag{3}$$

To obtain the failure probability of Eq. (3) on the basis of MV FOSM, it is necessary to linearize Eq. (3). The Taylor series to first order of Eq. (3) at mean values is Eq. (4) and the reliability index or failure probability by MV FOSM can be calculated on the basis of mean value and standard deviation of Eq. (4).

$$Z(C_d, C_o, x, D_d) \approx \left.\frac{\partial Z}{\partial C_d}\right|_{mean} C_d + \left.\frac{\partial Z}{\partial C_o}\right|_{mean} C_o + \left.\frac{\partial Z}{\partial x}\right|_{mean} x + \left.\frac{\partial Z}{\partial D_d}\right|_{mean} D_d + C_{d,\mu} - C_{o,\mu}\left[1 - erf\left(\frac{x_\mu}{2\sqrt{D_{d,\mu} t}}\right)\right]$$

$$- C_{d,\mu}\left.\frac{\partial Z}{\partial C_d}\right|_{mean} - C_{o,\mu}\left.\frac{\partial Z}{\partial C_o}\right|_{mean} - x_{,\mu}\left.\frac{\partial Z}{\partial x}\right|_{mean} - D_{d,\mu}\left.\frac{\partial Z}{\partial D_d}\right|_{mean} \tag{4}$$

Reliability index in AFOSM is the distace from the origin to the most probable failure point(MPFP) geometrically. Hasofer and Lind [3] proposed the convient process calulating MPFP and reliability index in terms of AFOSM as follows.

$$u^{k+1} = \frac{P_u^{kT} u^k - Z(u^k)}{P_u^{kT} P_u^k} P_u^k \qquad P_u^k = \left\{\frac{\partial Z}{\partial u_1}, \frac{\partial Z}{\partial u_2}, \cdots, \frac{\partial Z}{\partial u_n}\right\}^T \qquad \text{at} \quad u = u^k \tag{5}$$

$$\beta = \sqrt{u^{*T} u^*} = -\frac{P_u^{*T} u^*}{\sqrt{P_u^{*T} P_u^*}} \qquad \alpha = -\frac{P_u^{*T}}{\sqrt{P_u^{*T} P_u^*}} \tag{6}$$

where u is variables modified in terms of standard normal distribution, β is the reliability index, α is the sensitivity of variable.

Comparison of MCS and FOSM. The availability of FOSM is assessed on the basis of comparison between Monte Carlo Simulation and FOSM. To conduct the comparison, generally used or specification proposing values about Eq. (3) are adopted. C_d, C_o , x, and D_d , is 1.2 kg/m^3, 13 kg/m^3, 5 to 12 cm, and 0.2 x 10^{-8} cm^2/s, respectively, and the coefficient of variation of all variables is 0.1. As shown in Fig. 1, the difference of MCS, whose results are obtained by iteration more than 300,000, and AFOSM estimating failure probability is smaller than 0.1 %. But, MV FOSM underestimates the failure probability in the range less than 50%. Therefore, it can be concluded that the accuracy of AFOSM is similar to that of MCS and can be used as an alternative method estimating the probability of corrosion initiation for harbor concrete structure but MV FOSM does not give a good results because of the nonlinearity of limit state equation evaluating corrosion initiation.

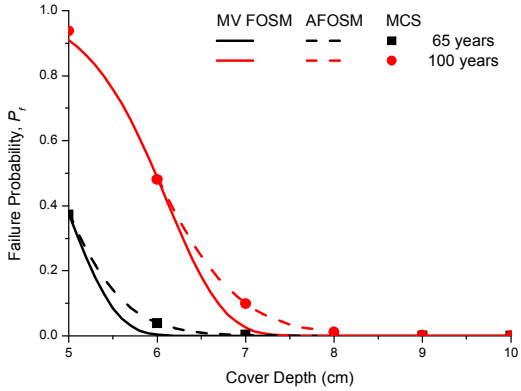

Fig. 1 Comparison of MV FOSM, AFOSM, and MCS

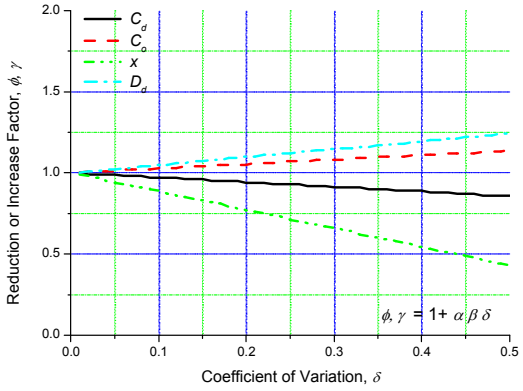

Fig. 2 Partial safety factors

Influence of variables on durability failure

Partial safety factors of variables AFOSM is a convenient method estimating the sensitivity as well as the failure probability. If the sensitivity is calculated, the partial safety factor, which is used as resistance reduction or load amplification factors in Load and Resistance Factor Design (LRFD), can be obtained. Investigating the change of these factors with coefficient of variation, the influence of each variable on failure probability is quantified. Fig. 2 shows the relationship between coefficient of variation and partial safety factor. In this analysis, the target reliability index is 1.29 and values of variables are the same as previous calculation for comparison of MCS and FOSM. As shown in Fig. 2, the slope of cover depth is steepest and the cover depth is the most dominant factor on corrosion initiation in terms of coefficient of variation. Diffusion coefficient, critical chloride concentration, and surface chloride concentration have an influence on durability failure in sequence. Therefore, an effective way reducing the possibility of corrosion initiation increases the level of quality control of concrete and reinforcing bar and reduces the coefficient of variation of cover depth and diffusion coefficient.

Cover depth The in-situ observation on steel corrosion in harbor concrete structure showed that many cases of durability failure were due to inadequate arrangement of steel bar less than designed cover depth. Fig. 3 confirms this investigation in terms of probability failure. As shown in the figure, the rise of coefficient of variation from 0.1 to 0.3 requires the increase of cover depth from 5.6 cm to 7.9 cm to maintain the failure probability of 10 percent. Therefore, the reduction of difference between designed and in-situ cover depth is an important factor to decrease the possibility of corrosion initiation.

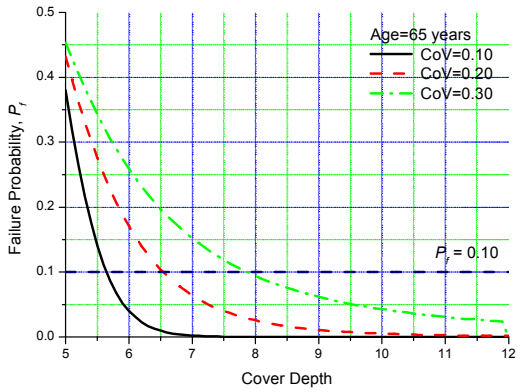

Fig. 3 Influence of cover depth

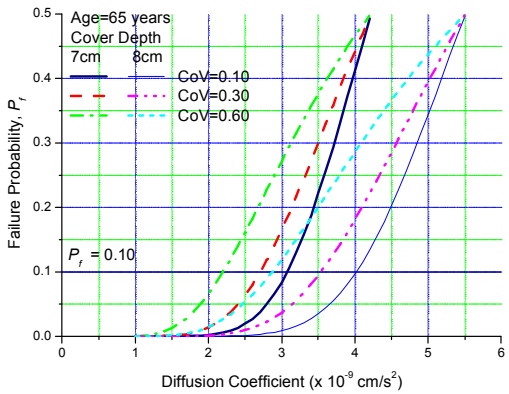

Fig. 4 Influence of diffusion coefficient

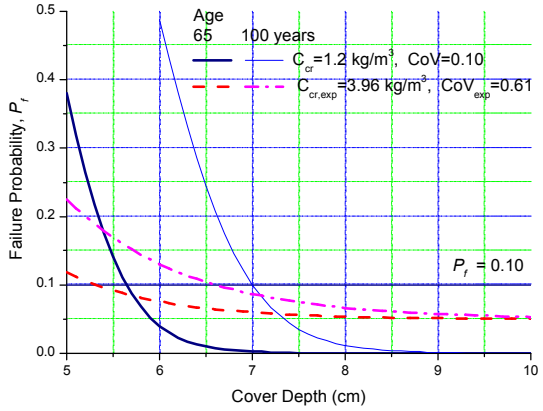

Fig. 5 Influence of critical chloride concentration

Diffusion coefficient The diffusion coefficient is the main element to control the corrosion initiation in reinforced concrete structure. As the diffusion coefficient changes with test method as well as material properties such as water-cement ratio, mineral and chemical admixture, etc, the estimation of diffusion coefficient in design level includes much uncertainty. The probabilistic approach is a good method to consider the influence of the uncertainty on failure probability. As shown Fig. 4, the rise of coefficient of variation from 0.1 to 0.6 in 7 cm cover depth requires the decrease of diffusion coefficient from 3.1 x 10^{-9} cm^2/s to 2.2 x 10^{-9} cm^2/s to maintain the failure probability of 10 percent. This decrease of diffusion coefficient can be obtained by the adjustment of mixture proportion and type.

Critical chloride concentration The designer or analyzer of harbor concrete structure uses the critical chloride concentration suggested by design code and specification. The critical chloride concentration, 1.2 kg/m^3, proposed in Korea concrete standard specification is based on hundreds of experimental data and is adopted to guarantee failure probability less than 10 percent. The average and coefficient of variation of the experimental results are 3.96 kg/m^3 and 0.61. This paper investigated the failure probability by the critical chloride concentration, 1.2 kg/m^3, and the coefficient of variation, 0.1 used in ordinary probabilistic analysis and by the experimental results. As shown in Fig. 5, the cover depth on the basis of experimental data is 4 to 6 mm smaller than that based on ordinary values. It seems that ordinary probabilistic analysis of durability using the critical chloride concentration recommended by design code and specification has the safety margin.

Summary

This paper investigated the possibility of First Order Second Moment method (FOSM) as a probabilistic method for durability analysis. The investigation showed that AFOSM is more convenient and time saving method than MCS to predict the corrosion initiation in harbor concrete structure. Based the examination of the influence of variables in durability model on corrosion initiation, it was found that an effective way reducing the possibility of corrosion initiation increases the level of quality control of concrete and reinforcing bar and reduces the coefficient of variation of cover depth and diffusion coefficient.

Acknowledgements

The authors acknowledge the financial support of the Infrastructures Assessment Research Center (ISARC) funded by Korea Ministry of Land, Transportation and Maritime Affairs.

References

[1] D. V. Val and M. G. Stewart: *Structural Safety*, Vol. 25 (2003), p.343.
[2] A. Sarja and E. Vesikari: *Durability Design of Concrete Structures*, (1996).
[3] A. M. Hasofer and L. C., Lind: *J. Eng. Mech. ASCE,* Vol. 100 No.1 (1974), p.111.

Key Engineering Materials Vols. 385-387 (2008) pp 625-628
© (2008) Trans Tech Publications, Switzerland
doi:10.4028/www.scientific.net/KEM.385-387.625

A Study on the pH Value Changes of Blended Cement Paste according to the carbonation

Sanghyun Lee[1,a] Hanseung,Lee[1,b]

[1]School of Architecture & Environmental Engineering, Hanyang University, Ansan, 425-791, Korea

[a]behappy@hanyang.ac.kr [b]ercleehs@hanyang.ac.kr

Keywords: Carbonation, $Ca(OH)_2$, quantitative analysis, blast furnace slag, pH value

Abstract. Life span of structures made with concrete was shortened by carbonation. This phenomenon makes pH in concrete lower. If pH value in concrete become below 10, rebar in concrete begin to be corroded. This pH value was effected by quantity of $Ca(OH)_2$ that depends on cement types, hydration reaction and carbonation time. In this study, pH value and quantity of $Ca(OH)_2$ in mortar which has blast furnace slag were tested according to hydration and carbonation time. As a test result, the more cement has blast furnace slag (BFS) and the longer carbonation time last, the lower pH value in mortar has. And using this quantitative analysis result of pH and $Ca(OH)_2$, it may be used effectively when service life considering carbonation is predicted using FEMA.

Introduction

A carbonation is a phenomenon that reaction between $Ca(OH)_2$ that is a product from hydration reaction and CO_2 that penetrate into concrete from the air reduce quantity of $Ca(OH)_2$ in the concrete. As a result, pH of solution in the concrete pore became low from pH>12 and then rebar in the concrete begin to be corroded when pH in the concrete is under 10. Under that condition, a volume of corroded rebar becomes bigger and this causes crack in the concrete. A series of these phenomenons makes durability of concrete poor. In carbonation phenomenon, it is important to know relation between carbonated depth and beginning time of rebar corrosion. Especially, a lowering pH that causes a rebar corrosion is affected by quantity of $Ca(OH)_2$ in the concrete. So the quantity of $Ca(OH)_2$ is a critical factor in carbonation. From this reason, in the former study, a carbonated depth was evaluated in that place where tested quantity (concentration) of $Ca(OH)_2$ become 40%~70% compared to initial concentration of $Ca(OH)_2$.[1] In this study, the object is to put the relation data between carbonated depth and quantity of $Ca(OH)_2$ from the surface into the concrete (1,2,3cm) using accelerating carbonation experiment. And this datum will be used effectively in making analyzing model that estimates service life of structure considering carbonation in the next study.

Methods and scope of study

In this study, mortar specimens were used as a preceding research before using concrete. There are six kinds of specimens. Three specimens were made with ordinary portland cement (OPC) in different W/C ratio (40, 50, 60%), and the others were made with OPC and BFS that was replaced with OPC in different amount(30, 50, 70%). After molding those specimens, they were cured for 1 month in water and 1 month in the air. The scope in this study is to measure pH value and quantitative analyses of $Ca(OH)_2$ according to accelerated carbonation time and find out relation between them.

Introduction of experiment and methods

Introduction of experiment Measuring pH value and quantity of $Ca(OH)_2$ were conducted to find out relation between pH value and quantity of $Ca(OH)_2$ for six specimens in different depth from the surface(1,2,3cm) according to carbonation time.

Molding and factor of specimens Size of specimens is 5cm×5cm×5cm, mix table according to specimens are like table 1. Mortar was mixed with cement and sand whose ratio is 1:2.45 in accordance with KS L 5109. The molds were removed after pouring concrete into the mold in 24 hours. And then the specimens were cured 1 day in a water and 1 day in the air(20°C, RH=60%).

Table 1 Test factors

	Index of specimen	W/C ratio (%)	OPC ratio in cement	BFS ratio in cement	Curing/measurement day	Measurement item
1	OPC-40	40	100%	0%	1 month in water 1 month in air : Curing day 1, 2, 4, 8 week after carbonation : measurement day	1. Carbonated depth 2. pH value 3. quantity of $Ca(OH)_2$
2	OPC-50	50				
3	OPC-60	60				
4	BS-50-30	50	70%	30%		
5	BS-50-50		50%	50%		
6	BS-50-70		30%	70%		

Accelerated carbonation test of concrete. According to defined in the KS F 2584, specimens are to be aged in water for 28 days. Then, the specimen is dried in the air at 20°C and 60% relative humidity for 28 days. In addition, the CO_2 concentration of the specimen is configured to 5%. Although all conditions were configured according to standard conditions, the relative humidity and CO_2 concentration applied in this study were reconfigured to 40% and 20%, respectively, to accelerate the carbonation process. And measurement items were measured according to measurement time like table 1.

Measurement of carbonated depth. An accelerated carbonation process applied to the specimen was fractured based on the KS F 2596. Then, a 1% of phenolphthalein solution was spread on the fractured face to measure the distance from the concrete surface to the pink colored section. And fig. 1 shows introduction of test.

a) Making specimen

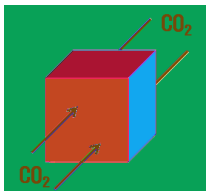

b) Accelerated carbonation test

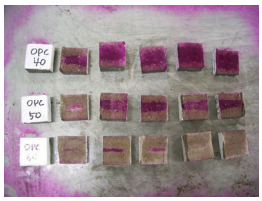

c) Measurement of carbonated depth

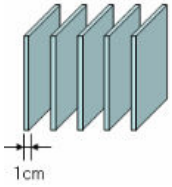

d) Cutting specimens

e) Measurement of pH value

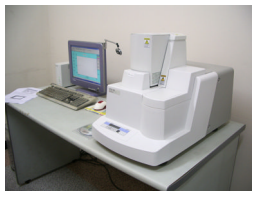

f) Measurement of $Ca(OH)_2$ quantity using TG/DTA

Fig. 1 An introduction of test

Results and analysis

Measurement of pH for the specimens after curing. Fig. 2 show pH value of each specimens after curing time (1 month in water, 1month in air). In case of OPC, the higher W/C ratio has the higher pH value appear. But in case of BFS, the higher substitution rate has the lower pH value appear. Before the test, in case of OPC, if W/C ratio is low, pH value was predicted to be high because of high unit cement quantity and high $Ca(OH)_2$ quantity. But in fig. 2, pH value is the

highest in OPC-60. This is the why although sufficient curing time in water is required over 3 months [2], but in this study, curing time in water lasted only 1 month. In situation of insufficient curing time, the higher W/C ratio has, the faster hydration reaction progress because of more unit water content. And in case of BFS, pH value is the lowest in BS-50-70. This is the why while OPC has much more CaO which produce $Ca(OH)_2$ than BFS(it has SiO_2 over 90% in constitution) after hydration. And another reason is a possolanic reaction that consume $Ca(OH)_2$ in concrete during hydration time. From these reason, the higher BFS has, the lower pH value appear like fig. 2. [3]

Measurement of carbonated depth according to carbonation time. Fig. 3 shows carbonated depth according to carbonation time. In case of OPC, OPC-60 has the most carbonated depth while OPC-40 begin to be carbonated 2 weeks later in carbonation time. Because a pore structures in mortar with high W/C are bigger than that in mortar with low W/C. It is easy for CO_2 to penetrate into the mortar. And another reason is that although OPC-60 has the highest pH value after curing, that has the most carbonated depth in carbonation time.(fig. 3) Fig. 4 shows a carbonated depth of mortar using BFS. 4 weeks later in carbonation time, BS-50-30 has the lowest carbonated depth, BS-50-70 has the most carbonated depth. This is the why BFS has lower pH value than OPC after curing like fig. 2.

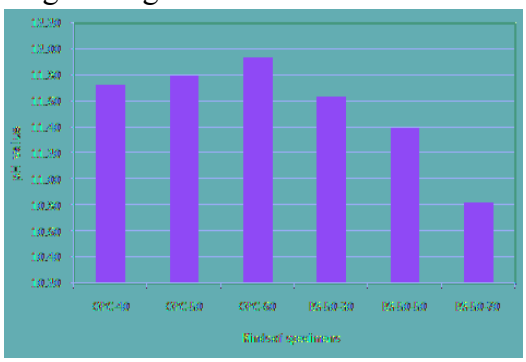

Fig. 2 pH value of each specimen.

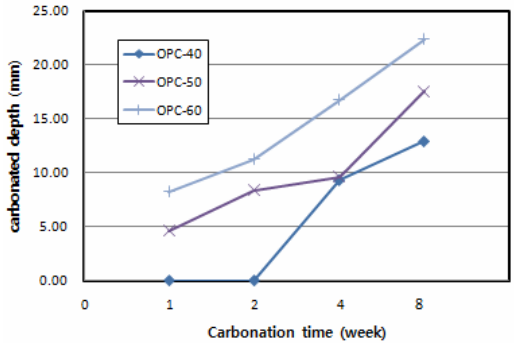

Fig. 3 Carbonated depth according to W/C in carbonation time

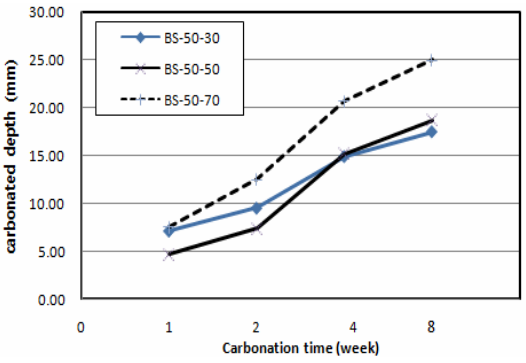

Fig. 4 Carbonated depth according to BFS substitution rate in carbonation time

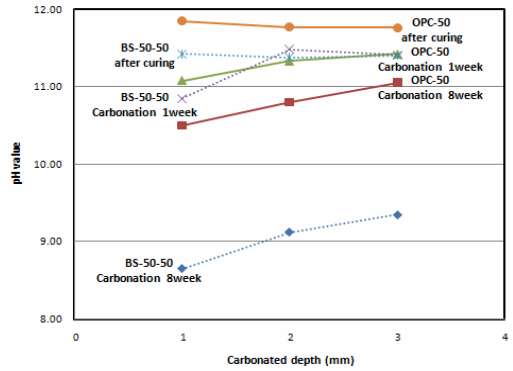

Fig. 5 pH value of each specimens in carbonation time

Changes of pH value according to depth in carbonation time. Table 2 shows pH value according to time and depth from the surface. In case of OPC, pH values were predicted to be low in longer carbonation time and in the nearest place from the surface because of reducing $Ca(OH)_2$ through carbonation. In case of BFS, decreasing tendency of pH values is clear according to increasing amount of BFS. Although it is not clear according to carbonation time and each depth, this tendency is confirmed clearly by comparing datum 1week with 8week. Fig. 5 shows difference of pH value compared OPC-50 with BS-50-50 according to carbonation time and each depths. The pH value of OPC-50 is higher than that of BFS-50-50 in every carbonation time, especially in 8 week carbonation time, the pH value of BFS-50-50 became much lower than that of OPC-50. This

is the why BFS produce less $Ca(OH)_2$ than OPC after hydration and it consume $Ca(OH)_2$ during hydration.

Table 2. pH value and $Ca(OH)_2$ quantity according to each specimen in carbonation time(sample:20mg)

item / time / cnt / specimens	pH value according to each depth in carbonation time												$Ca(OH)_2$ quantity according to each depth in carbonation time (mg)								
	1week			2week			4week			8week			1week			2week			4week		
	1	2	3	1	2	3	1	2	3	1	2	3	1	2	3	1	2	3	1	2	3
OPC-40	11,24	11,4	11,45	12,35	12,34	12,42	11,87	12,23	12,25	10,58	10,91	11,05	1,13	2,0	2,27	0,84	1,75	1,78	0,68	1,79	2,22
OPC-50	11,08	11,33	11,42	12,10	12,27	12,38	11,28	12,15	12,17	10,5	10,8	11,05	0,93	2,07	2,03	0,75	1,15	2,16	0,79	1,61	2,29
OPC-60	11,11	11,85	11,98	11,87	12,36	12,39	11,22	11,90	12,22	10,01	9,54	9,45	1,12	1,46	2,70	0,92	2,21	2,71	0,97	0,65	1,90
BS-50-30	10,75	11,60	11,66	10,38	11,85	12,06	11,43	12,35	12,01	8,50	8,33	8,20	1,67	1,79	1,87	1,86	1,56	1,94	1,21	0,92	0,92
BS-50-50	10,85	11,48	11,41	10,97	11,96	12,03	10,07	11,44	11,86	8,65	9,12	9,35	2,06	1,27	1,59	2,25	2,23	1,70	1,74	1,19	0,98
BS-50-70	9,68	10,77	11,04	10,11	10,83	11,73	9,13	9,18	10,77	9,02	9,65	9,91	1,887	0,939	1,20	1,87	1,50	1,19	1,17	1,43	0,94

Quantitative analysis of $Ca(OH)_2$ according to specimens in carbonation time. Table 2 shows quantitative result of $Ca(OH)_2$ by using TG./DTA.[4 and 5] In case of OPC, decreasing tendency of $Ca(OH)_2$ was confirmed according to carbonation time and each depth from deeper place to surface. But that is not clear in terms of increasing W/C ratio. This result is estimated that specimen has insufficient hydration time. So a further research is needed to have good datum considering sufficient hydration time in the future.

Summary

This study measured pH value and quantitative analysis of $Ca(OH)_2$ in mortars that has different W/C ratio in OPC and different substitution rate in BFS. Based on the results of this experiment, conclusions for this study can be summarized as follows:

1) In case of BFS, it is estimated that decreasing amount of $Ca(OH)_2$ in deeper place from the surface in time is caused by a possolanic reaction.
2) In same W/B ratio, in case of BS-50-50, a carbonated depth progressed deeper and pH value became lower than those of OPC-50. This is the why a possolanic reaction makes $Ca(OH)_2$ quantity reduce in mortar with BFS.

Acknowledgement

This work was supported by Sustainable Building Research Center Hanyang University which was supported the SRC/ERC program of MOST (#R11-2005-056-04003-0) and a grant (06-CIT-A02: Standardization Research for Construction Materials) from Construction Infrastructure Technology Program funded by Ministry of Land, Transport and Maritime Affairs.

Reference

[1] Yosihiro Masude et, Mathematical model on progress of carbonation of concrete, Concrete Research and Technology, Japan Concrete Institute, pp.125~133, Vol.2, No.1, 1991

[2] Vagelis.G.Papadakis et. Experimental investigation and mathematical modeling of the concrete carbonation problem, Chemical Engineering Science, Vol.46, No.5/6, pp.1333-1338, 1991

[3] Song,H.S et. Relation between rebar corrosion and concrete carbonation that has blast furnace slag, Korea Concrete Institute, proceeding, Vol. 13, pp.1193-1198, 2001

[4] Lee,J.G et, Prediction model of service life for concrete using measurement carbonation, Korea Concrete Institute, Vol.15, No.4, pp.529-540, 2003

[5] Cheng-Feng Chang et, The experimental investigation of concrete carbonation depth, Cement and Concrete Research, vol.36, pp.1760-1767, 2006

Key Engineering Materials Vols. 385-387 (2008) pp 629-632
© (2008) Trans Tech Publications, Switzerland
doi:10.4028/www.scientific.net/KEM.385-387.629

Numerical Simulation of Autogenous Shrinkage in High-Performance Cement Paste Based on a Multi-Component Hydration Model

Seung-Min Lim[1,a], Han-Seung Lee[1,b] and Xiao-Yong Wang[1,c]

[1]School of Architecture & Environmental Engineering, Hanyang University, Ansan, 425-791, Korea
[a]crayoner9@hotmail.com, [b]ercleehs@hanyang.ac.kr, [c]wxbrave@hotmail.com

Keywords: high-performance cement paste, autogenous shrinkage, multi-components hydration model, numerical simulation

Abstract. Autogenous shrinkage is the term for the bulk deformation of a closed, isothermal, cement-based material system not subjected to external forces. It is associated with the internal volume reduction of cement/water mixture in the course of the hydration process.

However, addition of blended components to cement, especially such as fly ash or silica fume, for the high-performance concrete will lead to a densification of the microstructure. The autogenous shrinkage deformation will increase and the following autogenous shrinkage crack will do harm to durability of concrete structure. In this paper, numerical simulation is suggested to predict autogenous shrinkage of high performance cement paste. The simulation is originated from a multi-component hydration model. The numerical program considers the influence of water to cement ratio, curing temperature, particle size distribution, cement mineral components on hydration process and autogenous shrinkage. The prediction result agrees well with experiment result.

Introduction

Recently trends in concrete technology have been towards so-called high-performance concrete with blended components such as silica fume or fly ash and the low water/binder ratio. However, these cause a considerable drop in the internal relative humidity in the cement paste during sealed hydration. Because autogenous shrinkage is closely related to this relative humidity change, so the cement paste go through autogenous shrinkage.

In concrete, autogenous shrinkage results in tesile stresse in the cement paste due to restraint from aggregates. Auto genous shrinkage should be limited because it may induce micocracking of macrocraking and impair the concret quality. In this paper, based on the multi-component hydration model, a numerical program is built to predict autogenous shrinkage high-performace cement paste. The prediction result agrees well with experiment result.

Multi-Component Hydration Model

In this paper, a multi-component hydration model is built to describe the evolution of cement hydration and formation of microstructure. Figure 1 and figure 2 show basic concept of this proposed model. Cement particles are cast randomly in the representative unit cell space, as shown in Figure 1. The length of edge of representative unit cell is 100*um*. Cement hydration process will start since cement contacts with water. The degree of hydration of cement paste can be regarded as a weighted sum of all cement particles and four major mineral components, C_3S, C_2S, C_3A, and C_4AF,as shown in figure 2. More details about this model are described in reference 1. The basic hydration equation of each mineral composition in cement particles can be described as following equation (1), which is originally built by Tomosawa [2] to describe hydration process of single cement particle:

$$\frac{d\alpha_i^j}{dt} = \frac{3C_{W\infty}}{(v_i+w_{agi})r_0^j\rho_i}\frac{1}{\left(\frac{1}{K_d}-\frac{r_0^j}{D_{ei}}\right)+\frac{r_0^j}{D_{ei}}(1-\alpha_i^j)^{-\frac{1}{3}}+\frac{1}{K_{ri}}(1-\alpha_i^j)^{-\frac{2}{3}}} \quad (1)$$

The meaning of variables in equation 1 can be found from reference 1. During hydration process, The solid cement paste volume is determined by systematic point sampling method [3]. Using a 100*100*100 point gird in cell volume, the solid volume can be obtained. The porosity of hydrating cement paste can be obtained as following equation (2):

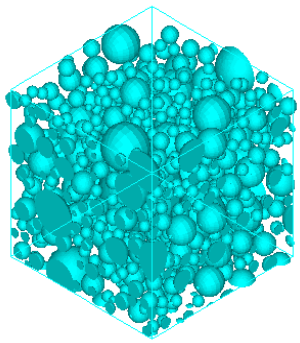

Figure 1 cement particles distribute randomly in cell space.

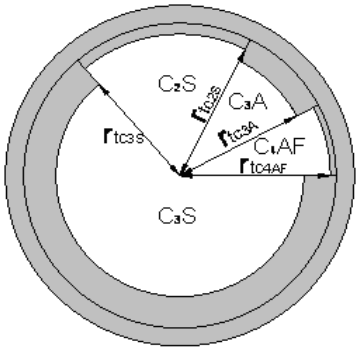

Figure 2 the schematic of multi-component hydration model.

$$\mathbf{poro} = \frac{V_{cell} - V_{solid}}{V_{cell}} \tag{2}$$

As proposed by reference 4, the pore size distribution of hydrating cement paste can be simplified as following equation (3):

$$V_{poro} = a\ln\left(\frac{\emptyset}{\emptyset_0}\right) \tag{3}$$

Where a is pore structure constant and $\emptyset_0$=0.002um. The pore structure constant can be determined by equal area projection method proposed in reference 5 or can be regressed from experiment result. A bigger value of pore structure constant means much finer pore structure.

The Prediction of Autogenous Shrinkage of Hydrating Cement Paste

When cement is mixed with water, the pressure of the part which is occupied by air is 1 atmospheric pressure. However, with progress of the hydration process the total volume of hydration product is smaller than the initial volume of cement and water, the reduced volume is called air pore volume and it will be filled with air. Due to the increase of the air volume the gas pressure in the air pore decreases. Under such circumstance, the air pore water will be partly consumed in the hydration process and therefore the relative humidity in the vapor filled pores gradually decreases. This phenomenon is called self-desiccation and it is the mechanism for autogenous shrinkage in cement paste.

After initial setting time, capillary microstructures are partly filled with water. The empty pore volume is filled with air. A thin layer of water molecules is adsorbed against the pore wall area. Based on first principle of thermodynamics, the surface free energy (J/m^2) in adsorption layer can be determined by following equation (4):

$$\gamma_s = -\frac{RT}{V_m}\int_{p_0}^{p} td\left(ln\left(\frac{p}{p_0}\right)\right) \tag{4}$$

And adsorption layer thickness can be determined Badmann equation, as equation (5):

$$t = 0.395 - 0.185ln\left(-ln\left(\frac{p}{p_0}\right)\right) \tag{5}$$

Where p is vapour pressure in capillary pore and p_0 is 1 atmosphere pressure. p is less than p_0.

Meanwhile, based on the Kelvin-Laplace equation, the relative humidity in hydrating cement paste can be determined as following equation (6)

$$\ln\left(\frac{p}{p_o}\right) = \frac{-2}{\gamma}\frac{V_m\gamma_s}{RT} \tag{6}$$

Where V_m is molar volume of water, T is absolute temperature, R is the universal gas constant, r is the widest radius of pore that is still filled with water.

Based on equation (4)-(6) and aforementioned hydration model, the internal relative humidity can be obtained by iteration algorithm. The hydrostatic pressure or capillary tension in the capillary-condensed water can be determined as following equation (7).

$$\sigma_{cap} = \frac{-2\gamma_s}{\gamma} \tag{7}$$

Where σ_{cap} is capillary tension stress of adsorption layer and r is the widest radius of pore that is still filled with water.

The evolution of elastic modulus can be determined from reference 6. The autogenous shrinkage deformation can be determined as following equation (8):

$$d(\varepsilon_{lin}) = \frac{S}{3}\left(\frac{1}{K} - \frac{1}{K_S}\right) d(\sigma_{cap}) \tag{8}$$

$$S = \frac{V_{ew}(\alpha)}{V_p(\alpha)} \tag{9}$$

$$K = \frac{E}{3(1-2v)} \tag{10}$$

Where S is saturation fraction, which equals to the ratio between evaporable water volume and whole pore volume, as shown in figure 9. K is the modulus of the whole porous body (MPa), which can be calculated as equation 10. based on equation 8-10, the autogenous shrinkage can be determined by increment method.

Verified of Proposed Model

When capillary pore size distribution, water saturation condition in capillary pore and meachnical property of hydrating cement are determined, the autogenous shrinkage can be obtained by increment method, step by step. The calcation flow chart is shown in figure 3. This calculation procedure can be used to both ordinary Portland cement and blended cement.

In this paper, experiment result in reference 4 is used to verify proposed model. Under sealing curing condition, due to limitation of available water for hydration, when water to cement ratio increases from 0.3 to 0.5, as shown in figure 5, the maximum degree of hydration increases from 0.5 to 0.9. To each mix proposition, with hydration process going on, the internal relative humidity decreases from 100% to almost 80%. This is consistent with experment result in reference 4. As shown in figure 6, based on proposed method in reference 6, the prediction result of elastic modulus of cement paste overall agrees well with experiment result. As shown in figure 7, experimental result of two kinds of cement, with water to cement ratio 0.3 and water to binder ratio 0.285(w/c=0.3, blended with 5% silica fume), are adopted. Both of sepcimen are cured under sealing condition. As shown in figure 5, prediction result agrees well with experiment result and this proves the relability of proposed model.

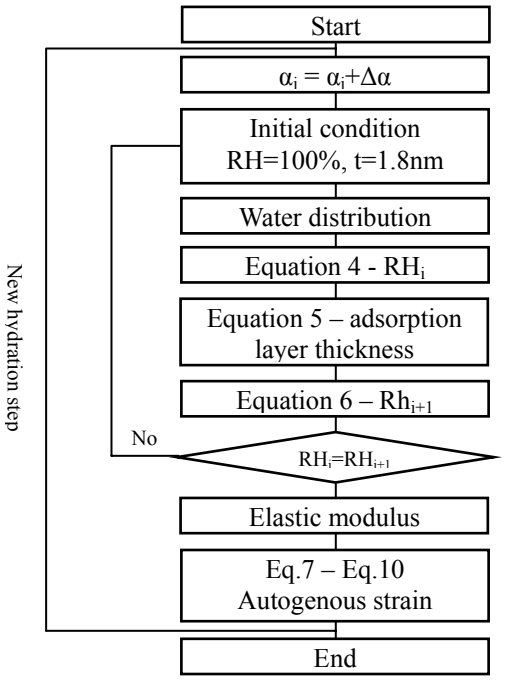

Figure 3 flow chart of calculation prcedure of autogenous deformation

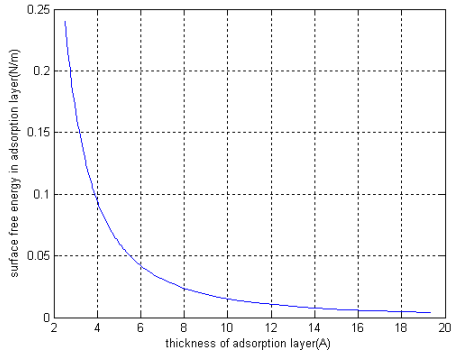

Figure 4 surface free energy in adsorption layer as function of thickness

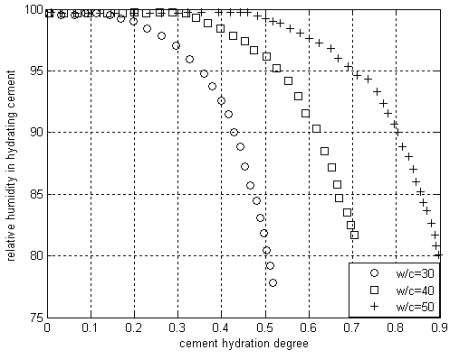

Figure 5 relative humidity as function of hydraton dgree

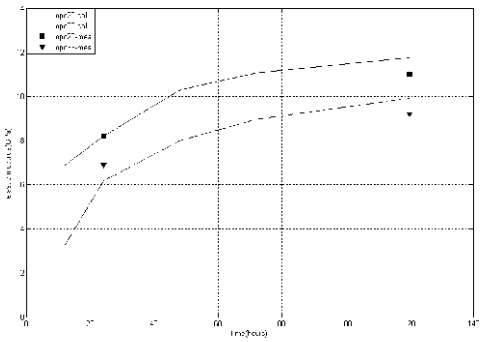

Figure 6 the evolution of elastic modulus as function of time

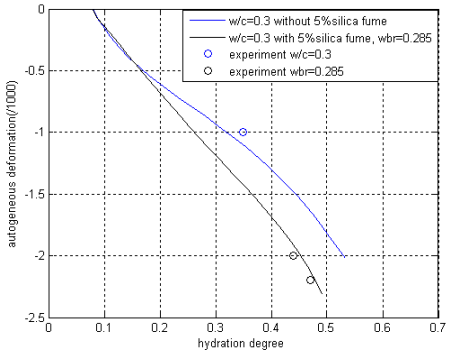

Figure 7 autogenous shrinkage as function of hydration degree

Summary

Based on the multi-component hydration model and thermodynamic mechanism, a numerical program is built to describe capillary pore size distribution, water saturation condition in pore space of hydrating cement paste, and the evolution of mechanic property (such as elastic modulus). By using increment method in time field, the autogenous shrinkage of ordinary Portland cement and blended Portland cement is calculated step by step. The prediction result overall agrees well with experiment result and prove the reliability of proposed model. Furthermore, the autogenous crack in early-age concrete structure in real construction site can be a potential result of proposed model.

Acknowledgement

This work was supported by Sustainable Building Research Center Hanyang University which was supported the SRC/ERC program of MOST (#R11-2005-056-04003-0) and a grant(06-CIT-A02: Standardization Research for Construction Materials) from Construction Infrastructure Technology Program funded by Ministry of Land, Transport and Maritime Affairs.

Reference:

[1]. Xiaoyong Wang, Hanseung Lee, Kibong Park, numerical simulation of heat evolution of eco-friendly blended portland cements using a multi-component hydration model, *submitted to ISEPD 2008*, Chang won,Korea,
[2]. F.Tomosawa, Proceeding of 10th International Congress Chemistry Of Cement, 1997, Sweden
[3]. Bentz, E.J.Gaboczi, Cement and Concrete Research, Vol,24, 1994,pp.25-37,
[4]. E.A.B. Koenders, *simulation of volume changes in hardening cement-based materials*, PhD thesis of Delft University, 1997
[5]. Snyder.J.P. [J].Cartographica,1992,29(1):10-21
[6]. Ki-Bong Park, *Prediction of cracking in high strength concrete using a hydration model*, PhD thesis, The University of Tokyo, Japan, 2001.

Key Engineering Materials Vols. 385-387 (2008) pp 633-636
© (2008) Trans Tech Publications, Switzerland
doi:10.4028/www.scientific.net/KEM.385-387.633

Prediction of the carbonation depth of concrete with a mortar finish

Xiao-Yong Wang [1,a], Han-Seung Lee [1,b]

[1]School of Architecture & Architectural Engineering, Hanyang University, Ansan, 425-791, Korea

[a]wxbrave@hotmail.com, [b]ercleehs@hanyang.ac.kr

Keywords: Carbonation, Hydration, Mortar, Surface finishing

Abstract: It is well known that carbonation will result corrosion of steel reinforcement in reinforced concrete structures. To reduce the rate of carbonation, the surface coatings, such as mortar finish, has been used widely to concrete. This paper presents a numerical procedure about carbonation of the coating-concrete system. This numerical procedure starts with a multi-component hydration model. By hydration model which considers both and Portland cement and pozzolanic reaction, the amount of hydration products which are susceptible to carbonate as well as porosity is obtained as function of age. Furthermore, the diffusivity of CO_2 is determined and carbonation depth of concrete is predicted. Parameter studies are performed to show the influence of composition and application time of mortar finish on carbonation depth of substrate concrete.

Introduction

It is well known that carbonation will result corrosion of steel reinforcement in reinforced concrete structures. To reduce the rate of carbonation, a supplementary protective method is the application of anti-carbonation coatings. Most of them were constituted of organic coating using volatile organic compound [1-3]. The results revealed that the use of protective coating reduced significantly corrosion of rebars and carbonation depth of concrete. However, such organic coatings could have decisive shortcoming of being air-polluting during manufacturing process as well as during coating works. So the inorganic coating which exhibits composition similar to cement, was adopted to compensate this disadvantage [4, 5]. In case of concrete without surface finish, carbonation depth is proportional to square root of exposure period to surrounding carbon dioxide. However, when concrete is coated with inorganic material, the carbonation depth can not be determined by this method [6].

This paper presents a numerical procedure about carbonation of the coating-concrete system. This procedure includes two parts as hydration model and carbonation model. Using a hydration model, the hydration products that are susceptible to carbonate as well as porosity are obtained as accompanied by the results of the proposed model. Furthermore, by carbonation model, the carbonation depths are predicted.

Hydration model

The proposed hydration model considers both Portland cement hydration and pozzolanic reaction. The details of hydration model are introduced in reference [7, 8] and this paper only shows the main procedure of hydration model.

1) hydration model of Portland cement

The basic hydration equation of each mineral composition in cement particles can be described as following equation (1):

$$\frac{d\alpha_i^j}{dt}=\frac{3C_{w\infty}}{(v_i+w_{ag})r_0^j\rho_i}\frac{1}{(\frac{1}{k_d}-\frac{r_0^j}{D_{ei}})+\frac{r_0^j}{D_{ei}}(1-\alpha_i^j)^{\frac{-1}{3}}+\frac{1}{k_{ri}}(1-\alpha_i^j)^{\frac{-2}{3}}} \tag{1}$$

2)hydration model of cement blended with supplementary cementing materials (SCM)

The hydration equation of active (glass) part in SCM can be written as equation (2):

$$\frac{d\alpha_{reacted}}{dt}=\frac{m_{CH}}{P}\frac{3}{v_{FL}r_{FL0}\rho_{FL}}\frac{1}{(\frac{1}{k_{dFL}}-\frac{r_{FL0}}{D_{eFL}})+\frac{r_{FL0}}{D_{eFL}}(1-\alpha_{reacted})^{\frac{-1}{3}}+\frac{1}{k_{rFL}}(1-\alpha_{reacted})^{\frac{-2}{3}}} \tag{2}$$

During hydration period the amount of calcium hydroxide and CSH can be written as following equation (3):

$$CH=(1.5g_{c3s}\alpha_{c3s}+0.5g_{c2s}\alpha_{c2s}-2g_{c4af}\alpha_{c4af})*74.1*Ce_0-(1.85*\gamma_S*f_{S,P}+2.907*\gamma_A*f_{A,P})*\alpha_{reacted}*P \tag{3-1}$$

$$CSH=(1.5g_{c3s}\alpha_{c3s}+0.5g_{c2s}\alpha_{c2s})*342.1*Ce_0+2.85*f_{S,P}*\gamma_S*\alpha_{reacted}*P \tag{3-2}$$

The porosity of hydrating blends is reduced due to the Portland cement hydration and pozzolanic activity during hydration period. The porosity can be determined as equation (4):

$$\varepsilon_c=\frac{w_0}{\rho_w}-\Delta\varepsilon_h-\Delta\varepsilon_p \tag{4}$$

where $\Delta\varepsilon_h$ is the porosity reduction due to the hydration of Portland cement. Also, $\Delta\varepsilon_p$ is the porosity reduction due to the pozzolanic activity.

Carbonation model

1)carbonation of concrete without surface coating

For the usual range of parameters, certain simplifying assumptions can be made and that lead to the formation of a carbonation front. For one-dimensional geometry, the evolution of the carbonation depth $x_c(m)$ with time $t(s)$, is given by the analytical expression as following equations (5) and

$$x_c=\sqrt{\frac{2D_e[CO_2]_0t}{0.33CH+0.214CSH}} \tag{5}$$

where $[CO_2]_0$ is the CO_2 content in the ambient air at the concrete surface. Papadakis [9] performed accelerated carbonation experiments of the concrete containing low-calcium fly ash. The comparison between the prediction results and the experiment results is shown in Figure 1.

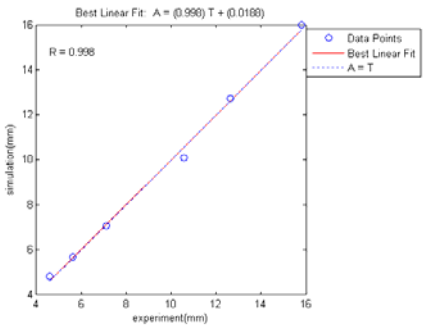

Fig.1. The comparison between experiment and prediction result of carbonation depth.

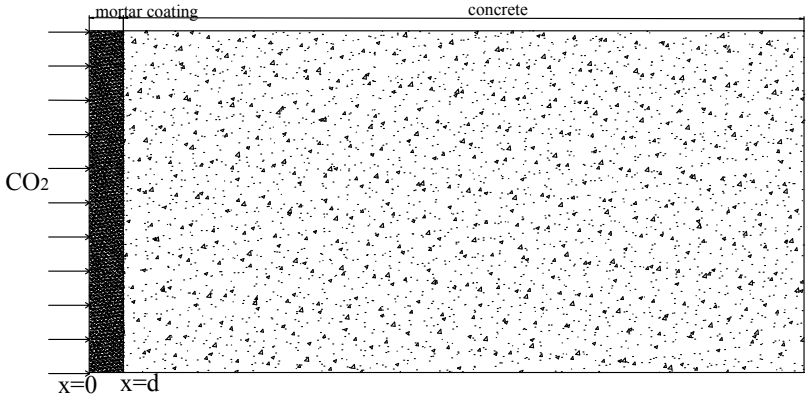

Fig.2 schematic illustration of concrete carbonation in presence of a mortar coating

2)carbonation of concrete with mortar coating

Furthermore, based on boundary condition and initial condition, the carbonation depth is given as following equation (6):

$$x = d + \left(\frac{2D_e^{(2)}[CO2]^0}{0.33CH^{(2)} + 0.214CSH^{(2)}}(t - t_d) + d^2\left(\frac{D_e^{(2)}}{D_e^{(1)}}\right)^2 \right)^{1/2} - d\frac{D_e^{(2)}}{D_e^{(1)}} \qquad (t > t_d) \qquad (6)$$

Where x is carbonation depth; $CH^{(2)}$ and $CSH^{(2)}$ is CH and CSH amount in concrete, respectively.

In practice, the concrete surface may be left initially uncoated, and after several years it may be decided to apply the finish, for reasons of architecture appearance, or for maintenance and protection from further deterioration. During the period of time, denoted by t_a, in which the concrete remains exposed to the environment, the concrete is left to carbonate and carbonation depth reaches a depth x_a.The carbonation depth in concrete can be determined as following equation (7):

$$x = \left[\frac{2D_e^{(2)}[CO2]^0}{0.33CH^{(2)} + 0.214CSH^{(2)}}(t - t_d) + (d\frac{D_e^{(2)}}{D_e^{(1)}} + x_a)^2 \right]^{1/2} - d\frac{D_e^{(2)}}{D_e^{(1)}} \qquad (7)$$

By aforementioned carbonation model, the parameter analysis of effect of mortar coating composition on carbonation of substrate concrete is done and shown in figure 3. In control specimen, water to cement ratio (w/c), aggregate to cement ratio (a/c) of mortar coating is 0.45 and 3, respectively. The thickness of mortar coating is 20mm. The surrounding CO_2 concentration is 3% and relative humidity is 0.6. The mixture proportion of substrate concrete is same as control specimen listed in reference [9].

As shown in figure 3, we can see that 1) with decreasing of w/c in mortar coating, the initiation of carbonation in concrete become later and given a certain exposure time carbonation depths are also reduced. 2) the influence of a/c on carbonation depth is similar with w/c. however, the influence of w/c is much more significant than a/c. This is in that cement amount in unit volume varies obviously with variation of w/c. Moon[4] also found that carbonation depth of coated-concrete decreased with reducing of w/c and a/c. 3) the addition of mineral admixture has obvious influence on carbonation depth. When aggregate is replaced by low-calcium fly ash with10% ratio, initiation of carbonation is significantly longer. Correspondingly, given a certain exposure time, carbonation depth is much smaller. By addition of mineral admixture, the pore structure becomes finer and more carbonatable components are made from pozzolanic reaction. So give a certain exposure time, carbonation depth decreases. 4) the latter mortar coating is applied on concrete surface, given a certain exposure time, the bigger carbonation depth will be made.

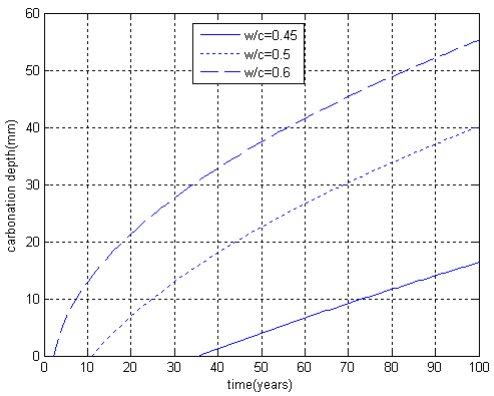

(a) the influence of w/c of mortar coating on carbonation depth of substrate concrete

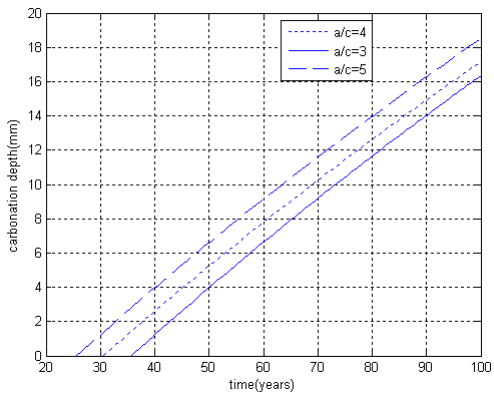

(b) the influence of a/c of mortar coating on carbonation depth of substrate concrete

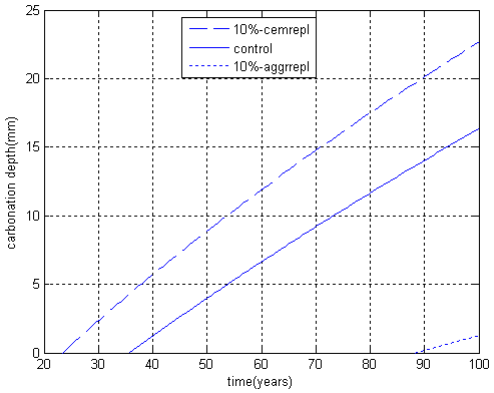

(c) the influence of mineral admixture addition of mortar coating on carbonation depth of substrate concrete

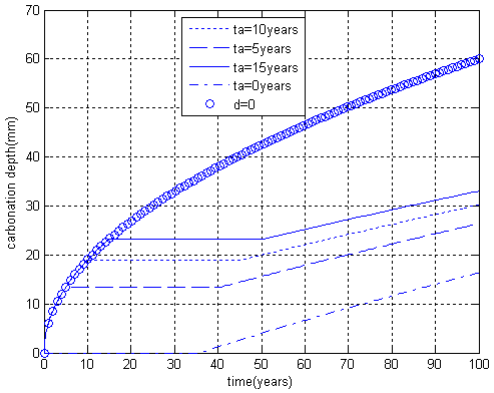

(d) the influence of application time of mortar coating on carbonation depth of substrate concrete

Fig.3 parameter analysis of the effect of mortar coating composition on carbonation of substrate concrete

Conclusion

This paper presents a numerical procedure about carbonation of the coating-concrete system. This procedure includes two parts as hydration model and carbonation model. Using a hydration model, the hydration products as well as porosity are obtained as accompanied by the results of the proposed model. Furthermore, by carbonation model, the carbonation depths are predicted.

Acknowledgements

This work was supported by Sustainable Building Research Center of Hanyang University which was supported by ERC program of Ministry of Education, Science Technology (#R11-2005-056-04003-0) and Standard Technology Improvement Project supported by Ministry of Knowledge Economy(#2007-000-0000-6365).

References

[1].A.M.G.Seneviratne, G.Sergi, C.L.Page, performance characteristic of surface coatings applied to concrete for control of reinforcement corrosion, construction and building materials, vol.14,2000,pp.55-59

[2]. D.C.Park, carbonation of concrete in relation to CO2 permeability and degradation of coatings, construction and building materials, 2007,doi:10.1016/j.conbuildmat.2007.07.032

[3].G.Batis, N.Kouloumbi,P.Pantazopoulou, corrosion protection of steel in pumice lightweight mortar by coatings, cement and concrete composites, vol.27, 2005,pp.261-267

[4]. Han Young Moon, Dong Gu Shin, Doo Sun Choi, evaluation of the durability of mortar and concrete applied with inorganic coating material and surface treatment system, Constr. Buil.Mat., vol.27, 2007,pp.362-369

[5]. Miguel Angel Sanjuan, Cesar del Olmo, carbonation resistance of one industrial mortar used as a concrete coating, building and environment, vol.36, 2001,pp.949-953

[6].V.G.Papadakis, M.N.Fardis, C.G.Vayens, effect of composition, environmental factors and cement-lime mortar coating on concrete carbonation, materials and structures, 1992, vol.25, 293-304

[7]. Xiaoyong Wang, Hanseung Lee, Kibong Park, Numerical simulation of heat evolution of eco-friendly blended portland cements using a multi-component hydration model, Materials Science Forum Vol. 569(2008)pp.257-260

[8]. Xiao-Yong Wang, Han-Seung Lee, Seung-Min Lim. Numerical Simulation of Autogenous Shrinkage of Eco-friendly Blended Portland Cements Using A Multi-Component Hydration Model Materials Science Forum Vol. 569 (2008) pp. 261-264

[9]. Vagelis G. Papadakis, S.Tsimas. Effect of supplementary cementing materials on concrete resistance against carbonation and chloride ingress. Cem Concr Res 2000;30(2): 291-299

Key Engineering Materials Vols. 385-387 (2008) pp 637-640
© (2008) Trans Tech Publications, Switzerland
doi:10.4028/www.scientific.net/KEM.385-387.637

Mechanical Property of Porous Titanium Produced by Spark Plasma Sintering

Yuki Sakamoto[1,a], Shigeaki Moriyama[1,b], Masahiro Endo[1,c] and Yuji Kawakami[2,d]

[1]Department of Mechanical Engineering, Fukuoka University, 8-19-1 Nanakuma, Jonan-ku, Fukuoka, 814-0180, Japan

[2]Industrial Technology Center of Saga, 114 Yaemizo, Nabeshima, Saga, 848-0932, Japan

[a]ysak@fukuoka-u.ac.jp, [b]moriyama@fukuoka-u.ac.jp,

[c]endo@fukuoka-u.ac.jp, [d]Kawakami@saga-itc.go.jp

Keywords: Titanium powder, Mechanical properties, SPS (Spark plasma sintering), Biomaterial

Abstract. Titanium has widely been used as a biomaterial because of its excellent corrosion resistance and biocompatibility. However, problems with respect to biological reaction and fitness of elastic modulus for human bone or tooth have yet to be solved. Porous titanium is expected to be a promising material to solve these problems. The aim of this study is to clarify the effect of the porous structure of this material on the biomechanical compatibility. The spherical pure titanium powder, with an average particle size of 100 μm, was sintered by spark plasma sintering. The sintered porous titanium compacts had a porosity of 33 %. The specimens were machined from the sintered compacts for the evaluation of the mechanical properties. The elastic modulus indicated a value close to human bone, while the tensile and compressive strengths showed lower values than those of human bone.

Introduction

Metallic materials used for biomaterials such as artificial bones and dental implants require higher corrosion resistance and biocompatibility. Titanium (Ti) and its alloys are possible candidate metals that can fulfill such requirements and over the years they have specifically been developed to be used in orthopedic surgery and implant dentistry [1, 2]. However, Ti is a bioinert material that will not be integrated directly with the surrounding tissue and its elastic modulus is extremely high compared with that of human bone or tooth, having a bad influence on the bone remodeling. As a method for solving these problems, coating of calcium phosphate (apatite) on the Ti surface has been studied by many researchers. Another method is to fabricate a porous structure by which the fixation with bone tissue is expected to be promoted by the ingrowth of bone into the pores and in addition the elastic modulus can be reduced to a value equal to human bone. The former contributes an improvement of biological compatibility and the latter does that of biomechanical compatibility. In general porous Ti compacts have been fabricated by means of the sintering method by transforming the space between powdery particles into pores [3]. The conventional sintering methods such as HP, HIP and PLS need a high sintering temperature of about 1400 ^{o}C and a long keeping time for over 24 h, whereas the spark plasma sintering (SPS) method accomplishes the sintering for only 5-20 min at 1000 ^{o}C in a low vacuum environment [4].

In this study, as a first step, the porosity of the porous material, and its mechanical properties, such as tensile strength, compressive strength, elastic modulus and the Vickers hardness, were measured. The present paper focuses on the clarification of the optimized conditions of SPS and the effects of the porous structure on the biomechanical compatibility of Ti.

Materials Production and Experimental Methods

Commercial spherical pure Ti powders with the particle diameter less than 150 μm were sieved using a 100-μm screen. The impurity chemical component of pure Ti powders was: 0.099% O, 0.033% Fe, 0.029% N, 0.009% H, and 0.008% C. The powders were packed in a carbon die (50 mm dia. x 160 mm length) with a longitudinal through-hole of 17 mm in diameter. The die is equipped with a port to insert a thermocouple for the measurement of the temperature in the die center. The powders were pre-compacted by applying a pressure of 20 MPa before sintering. The compressed powders were sintered in a vacuum of 4 Pa using an SPS system. Sintering was carried out with a pressure of 25 MPa at 570 ^{o}C for 30 min. To prevent the dispersion of heat, a carbon felt was wrapped around the die. The above sintering conditions were determined through trial and error.

The weight (0.1mg in accuracy) and the external dimensions of porous compacts were measured and thereafter the apparent porosity was calculated from the Ti density of 4.53g/cm^3 and the apparent volume. The surface morphology of the compacts was observed by scanning electron microscopy (SEM). To evaluate the mechanical properties, the sintered compacts were machined by a lathe to the shape of dumbbell shown in Fig. 1. Tensile strength, compressive strength, and elastic modulus were measured using as-machined specimens by a universal testing machine with the capacity of 250 kN. The elastic modulus was measures by the offset method. The Vickers hardness were the avarage value of 20 point values measured by a micro-hardness tester with a load of 9.81 N.

Results and Discussion

Characteristics of SPS processing. Fig. 2 indicates the temperature and the change in sample length as a function of time during SPS processing. The change in sample length increases with the sintering temperature and finally it reaches a constant of 14 mm at the end of sintering, corresponding to a 15% contraction. The hunting of temperature is seen in the stage of maintaining a constant temperature. This phenomenon has frequently been observed also in the HIP processing and this is appeared to be due to the temperature difference between the pressing edge and the central part in a slender die. It is known that the temperature fluctuation has only a small influence on the production of sintered compact, though it is more controllable in SPS compared with HIP.

The sintered compacts were smoothly machined to the dumbbell specimens. There was no sample damage in working. The porous Ti produced under the present conditions has a good workability and therefore it can be machined into the various shapes of specimens required for mechanical and biological tests.

Fig. 3 shows the SEM micrographs of the surface of a porous titanium compact. Open pores are confirmed that have a geometry of openings of spherical Ti particles connecting to the outside of the material. A number of particles smaller than 100 μm in diameter were observed though the powders were sieved with a screen with a 100 μm mesh. They may be the residual particles that were not sieved completely mainly because of static electricity.

Mechanical properties. The porosity and the mechanical properties of tensile strength, compressive strength, elastic modulus and the Vickers hardness are shown in Table 1. Porous compacts having a porosity of 33 % are successfully obtained under the present SPS conditions. The scatter of porosity among batches was very small, so that a stable production of porous materials can be expected. The average value of the Vickers hardness was 77 HV, which is a 30 % reduction from 110 HV for dense CP (commercially pure) Ti, because of the presence of pores.

Figs. 4 indicates stress-strain curves obtained in tensile and compressive tests. The tensile strength of SPS-processed materials was 42 MPa, which is lower than half the value ranging 80-160 MPa for human cortical bone [5], while the compressive strength was 90 MPa, a value somewhat close to 110-170 MPa for human cortical bone [5]. The absolute value of compressive strength was about twice as much as the tensile strength. The elastic modulus is a crucial factor in considering the biomechanical compatibility with human cortical bone from the viewpoint of bone remodeling. The

elastic modulus, *E*, was 16 GPa, which is quite close to the values of 17-20 GPa reported for human cortical bone [5]. The reduction in apparent *E* value compared with dense CP Ti with *E* of 105-110 GPa is about 85% and very sensitive to the porosity. The porous Ti produced in this study has the *E* value suitable for bone remodeling but an insufficient strength. Fig. 5 shows the fracture surface of specimen broken in tension. It is seen that the bonded areas are of the order of 10μm. The lack of strength may be due to the incomplete bonding of Ti perticles.

Porosity, pore shapes, pore size may affect the mechanical properties of propous materials. It is considered that the elastic modulus may be able to controlled by porosity. Porosity and bonded area of perticles is considered the major factors controlling the strength. It is known that the porous materials can be strengthened by additional heat treatment such as annealing performed after SPS processing. The resistance against impact load and fatigue is important as a biomaterial used for bone and tooth. Also, the *in vivo* measurement of mechanical properties must be made in the future works.

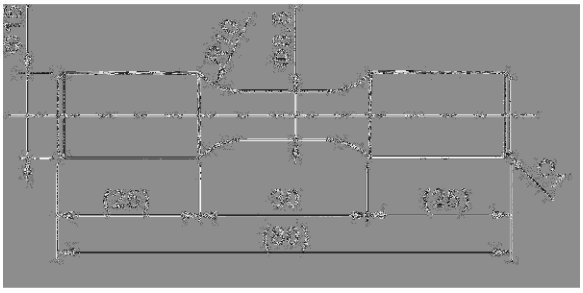

Fig.1 Shape and dimensions of porous titanium specimen, in mm.

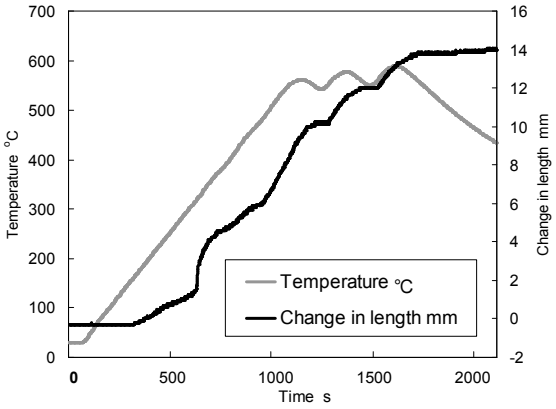

Fig.2 Relationship between sintering temperature and change in sample length.

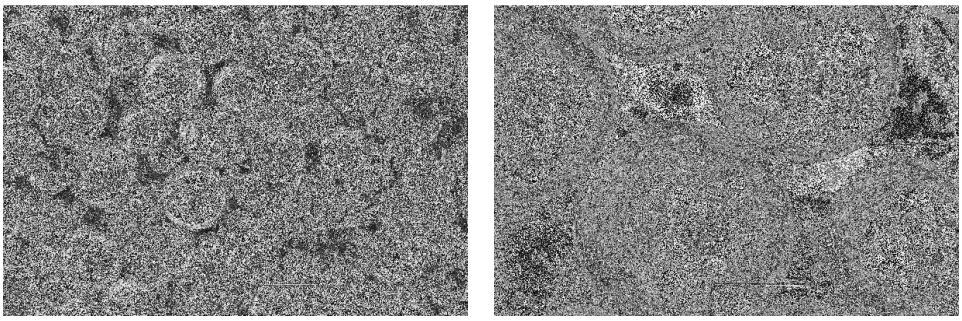

Fig.3 SEM micrographs of porous titanium compact after SPS processing.

Table 1. Mechanical properties of porous titanium specimen.

Porosity %	32.9
Vickers hardness	79.6
Tensile strength MPa	41.7
Compressive strength MPa	90.1
Elastic modulus GPa	15.5

Conclusions

The mechanical properties of the porous Ti material sintered by SPS were measured to investigate the effects of the porous structure of this material on the biomechanical compatibility. The following conclusions were derived from the results and discussion.

1. An SPS processing condition was presented to manufacture stably the porous materials of 33 % porosity from spherical pure Ti powders of about 100 μm in particle diameter.

2. The apparent elastic modulus of the porous material was almost equal to that of human bone. The fracture strengths in tension and compression were lower than those of human bone. Improvement of the strength may be achieved by annealing.

Acknowledgements

This work was supported by funds (No. : 081501) from the Central Research Institute of Fukuoka University.

References

[1] R. Van Noort: J. Mater. Sci. Vol. 22 (1987), pp. 3801-3811.

[2] J. L. Nilles, M. T. Karagian and K.R. Wheeler: J. Biomed. Mater. Res Vol. 8 (1974), pp. 319-328.

[3] D.C. Dunand: Adv. Eng. Mater. Vol. 6 (2004), pp. 369-375.

[4] K. Ishizaki, S. Komarneni and M. Nanko, in: Porous Materials: Process Technology and Applications, Kluwer Academic Publishers (1998).

[5] W.G. Billotte, in: The biomedical Engineering Handbook, edited by JD. Bronzino, CRC Press LLC (2000).

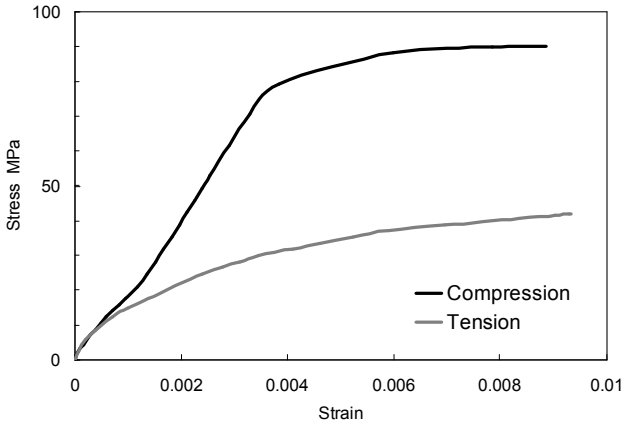

Fig. 4 Stress-strain curves in tensile and compressive tests.

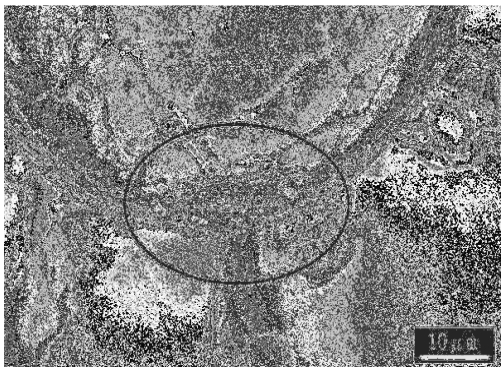

Fig. 5 Fracture surface of a Ti particle in a specimen broken in tension.

Key Engineering Materials Vols. 385-387 (2008) pp 641-644
© (2008) Trans Tech Publications, Switzerland
doi:10.4028/www.scientific.net/KEM.385-387.641

An Analysis of the Behavior of Small Fatigue Cracks Emanating from Stress Concentrators

Satoshi Ikeda[1,a], Daisuke Koyanagi[1,b], Masahiro Endo[1,c] and Yuki Sakamoto[1,d]

[1]Department of Mechanical Engineering, Fukuoka University,
8-19-1 Nanakuma, Jonan-ku, Fukuoka 814-0180, Japan

[a]td070001@cis.fukuoka-u.ac.jp, [b]tm040036@cis.fukuoka-u.ac.jp,

[c]endo@fukuoka-u.ac.jp, [d]ysak@fukuoka-u.ac.jp

Keywords: Stress Concentration, Notch effects, Non-propagating Cracks, Plastic Zone Sizes, Dugdale Model, McEvily Method.

Abstract. The plastic zone size (PZS) at the tip of a crack emanating from stress concentrators subjected to uniform tension was calculated based upon the Dugdale model. A method was proposed for the prediction of fatigue notch effects in terms of the McEvily method that has widely been used for the analysis of small fatigue crack growth. In modifying this method, the elastic-plastic effects due to stress concentration were taken into account using the values of PZS calculated in this study. The results predicted by this method accounted successfully for the behavior of small fatigue cracks near the threshold levels observed in the fatigue tests conducted using notched steel specimens.

Introduction

Geometrical discontinuities in the engineering components, such as holes, fillets, grooves, and keyways, are unavoidable in design. They act as a stress concentrator that causes fatigue cracks to initiate under cyclic loading and frequently a significant reduction in fatigue strength. It is known that the fatigue limit of notched components is determined by the critical condition for either initiation or propagation of a small crack at the root of a notch [1]. The behavior of such a small crack cannot be described only by linear-elastic fracture mechanics (LEFM) because the elastic-plastic effects and the crack closure are involved. The purpose of the present study is to give a rational interpretation for the notch effect in fatigue by use of the method of modified LEFM proposed by McEvily et al. [2]. The plastic zone sizes (PZS) of a crack emanating from a notch in a plate subjected to uniform tension will be calculated based upon the Dugdale model [3] to account for the elastic-plastic behavior of a crack propagating in the stress field generated by a notch.

Method of Analysis: Application of the McEvily Method to Fatigue Notch Effect Problems

The McEvily method. McEvily et al. [2] proposed the basic equation of fatigue crack growth law as

$$\frac{\mathrm{d}a}{\mathrm{d}N} = A(\Delta K_{\mathrm{eff}} - \Delta K_{\mathrm{effth}})^2 \tag{1}$$

where a is the crack length; N is the number of load cycles; A is a constant which depends upon the material and the environment; ΔK_{eff} is the effective range of stress intensity factor (SIF) given by $K_{\max} - K_{\mathrm{op}}$, where $K_{\max}$ is the maximum value of SIF in a cycle and K_{op} is the value of SIF at the crack opening level; and $\Delta K_{\mathrm{effth}}$ is the ΔK_{eff} at threshold level, a material constant.

They modified Eq. (1) [2] to deal with aspects of short fatigue crack growth as the LEFM approach as

$$\frac{\mathrm{d}a}{\mathrm{d}N} = AM^2 \tag{2}$$

where

$$M = \left[\sqrt{2\pi r_e F} + Y\sqrt{\pi a F}\right]\Delta\sigma - (1-e^{-k\lambda})(K_{\text{opmax}} - K_{\min}) - \Delta K_{\text{effth}} \quad (3)$$

where $\Delta\sigma$ is the range of applied stress; r_e, a material constant of the order of 1 μm, is the inherent crack length which accounts for the Kitagawa effect; F, the modification factor of crack length to include the elastic-plastic behavior of a crack, is defined as $aF = a + PZS / 2$ according to Irwin's crack length correction [4]; k is a material constant which determines the rate of crack closure development; Y is the geometrical correction factor of SIF; λ is the length of the newly formed fatigue crack measured from the tip of an initial crack; K_{opmax} is the crack opening level for a macroscopic crack; and $K_{\min}$ is the minimum value of SIF in a cycle.

Extensions. It was assumed that when a crack is present at a notch root, only Y and F in Eq. (3) are affected by the stress field generated by the notch. The Y for a crack emanating from a notch was obtained from the handbook [5] for holed plates and V-notched plates in this study. In order to attain a smooth connection of unnotched with notched specimens, it was modified in this study that the value of r_e is zero.

The values of *PZS* were calculated based upon the Dugdale model [3]. Fig. 1 illustrates a hole with cracks in a plate under uniform tension as an example of notched components. In calculating *PZS*, we consider an fictitious crack of b in length that is longer than the physical crack of a in length and that the crack faces are subjected to a negative pressure of the yield stress, σ_Y, over a distance, ω. The unknown *PZS* is determined from the condition that the stress singularity at the tip of the fictitious crack, i.e., at the tip of the plastic zone, must vanish. This condition is written by means of SIF in the form of

$$K_A + K_B = 0 \quad (4)$$

where K_A is the SIF of a fictitious crack subjected to remote tensile stress, $\sigma_{y\infty}$, and K_B is the SIF of a fictitious crack which a negative pressure of σ_Y is applied along its faces over a distance of ω, a minus. The value of ω that satisfies Eq. (4) is the PZS to be determined.

In order to provide a generalized procedure for the calculation of *PZS*, in this study, a crack at the root of a notch was approximated to be an edge crack in a semi-infinite plate to which the remote stress with the same distribution as generated by the notch is applied. The basic solution of SIF for an edge crack opened by a pair splitting forces [6] is hereby available to calculate the values of K_A and K_B. The respective equations are expressed as

$$K_A = \int_0^b \left[\frac{2\sigma_{yy}\sqrt{\pi b}}{\pi\sqrt{b^2 - x^2}}\{1 + f(\chi)\}\right]dx \quad \text{and} \quad K_B = -\int_a^b \left[\frac{2\sigma_Y\sqrt{\pi b}}{\pi\sqrt{b^2 - x^2}}\{1 + f(\chi)\}\right]dx \quad (5)$$

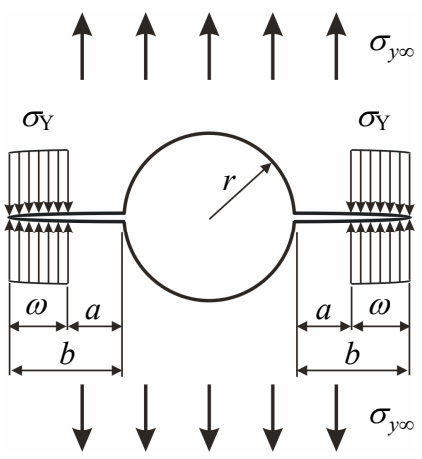

Fig. 1 The Dugdale model for a crack emanating from a hole

Table. 1 Material constants used in the analysis

	El Haddad et al.	Frost
Material	G40.11 Steel	Mild Steel
σ_Y [MPa]	376	334
σ_{w0} [MPa]	276	198
k [m^{-1}]	6000	6000
K_{opmax} [MPa $m^{1/2}$]	5.5	4.5
ΔK_{effth} [MPa $m^{1/2}$]	3.0	3.0

where

$$f(\chi)=\left(1-\chi^2\right)\left(0.2945-0.3912\chi^2+0.7685\chi^4-0.9942\chi^6+0.5094\chi^8\right) \quad (7)$$

where $\chi = x / b$; x is the distance from the notch root; b is the fictitious crack length; a is the physical crack length; σ_{yy} is the stress distributed near the root of a notch having no crack, as a function of x; and σ_Y is the yield stress.

Results and Discussion

Calculated PZS. Table 1 shows the material constants used in the analysis The notch geometries investigated in the present analysis were coincided with those of the specimens used in the experiments conducted by El Haddad et al. [7] and Frost [8] The values of *PZS* at the tip of a crack emanating from a hole with cracks in a plate under uniform tension are shown in Fig. 2. In this figure, lines indicate the results of the present analysis and open symbols indicate Rich et al.'s accurate values [9]. The results calculated by the proposed method were further modified considering the extreme cases for short and long cracks [10] . The agreement is quite good.

Fig. 3 shows an example of the calculated values of *PZS* at the tip of a crack emanating from an edge V-notch in a finite-width plate under uniform tension. The stress distribution generated by a notch with no crack was calculated by FEM using the same shapes and dimensions as those of Frost's specimens.

Comparison of the predicted with experimental results of notch effects. The behavior of a fatigue crack emanating from a notch under cyclic loading at an R of –1 was analyzed. The threshold stress range, $\Delta\sigma_{th}$, for crack propagation was calculated as a function of the crack length, c, under the condition that M in Eq. 3 equals zero. The length of an initial crack, a_0, was derived by setting the driving force, $1.12(2\sigma_{w0})\sqrt{\pi a_0 F}$, at the fatigue limit of unnotched specimen, σ_{w0}, equal to ΔK_{effth}. The calculated values of a_0 were 3.9 μm for a G40.11 steel and 10.2 μm for a mild steel.

The relationships between $\Delta\sigma_{th}$ and c are shown in Fig. 4 that were calculated using El Haddad et al.'s data observed in tension-compression fatigue tests of G40.11 steel plates having a hole of the radius, r, of 0.2 mm, 0.48 mm or 4.8 mm. The stresses at the left ends of lines in Fig. 4 indicate the threshold levels that a crack starts propagation from an initial crack, σ_{w1}. The maxima of lines indicate the threshold levels for macro-crack propagation, σ_{w2}. In Fig. 4, the lengths of non-propagation cracks are also shown that were observed by El Haddad et al. Solid symbols indicate that a crack was not arrested, while open symbols indicate the crack lengths at which a crack was arrested. The results of the present analysis predict well the experimental results obtained by El Haddad et al.

Fig, 5 shows the relationship between fatigue limit, σ_w, and elastic stress concentration factor, K_t. The experimental data was obtained by Frost. The behavior of a crack emanating from a V-notched plate under uniform tension was analyzed in the same way. Fig. 5 compares the present calculations with Frost's data. The predicted curves are a little lower than Frost's experimental results, although the notch effect in fatigue is reasonably characterized.

Concluding Remarks

1. A generalized method was proposed for the calculation of the plastic zone size (PZS) at the tip of a crack emanating from a notch.
2. By use of the calculated PZS, the McEvily method was modified to analyze the notch effect in fatigue. The predicted results were in reasonable agreement with the experimental results observed by El Haddad et al. and Frost

.

Acknowledgements

This work was supported by funds (No. : 081501) from the Central Research Institute of Fukuoka University.

References

[1] T. Isibasi: *Prevention of Fatigue and Fracture of Metals*, (Yokendo, Tokyo 1954).
[2] A.J. McEvily, D. Eifler and E. Mscerauch: *Engng. Fract. Mech.,* Vol. 40 (1991), 571-584
[3] D.S. Dugdale: *J. Mech. Phys. Solids,* Vol. 8 (1960), 100-104
[4] G.R. Irwin, D: *Naval Research Laboratory Report No.5486,* (Washington DC 1960).
[5] Y. Murakami et al.: *Stress Intensity Factors Handbook,* (Pergamon Press, Oxford 1987).
[6] R.J. Hartranft and G.C. Sih: *Mech. of Fract.,* Vol. 1 (1973), p. 56
[7] M.H. El Haddad, T.H. Topper and K.N. Smith: *Engng. Fract. Mech.,* Vol. 28 (1979), 573-584
[8] N.E. Frost: *Proc. Inst. Mech. Engrs.,* Vol. 173 No. 35 (1959), 811-827
[9] T. Rich and R. Roberts: *Engng. Fract. Mech,* Vol. 1 (1968), 167-173
[10] S. Ikeda and M. Endo: *Fukuoka Univ. Review of Technological Sciences,* Vol. 80 (2008), 1-9

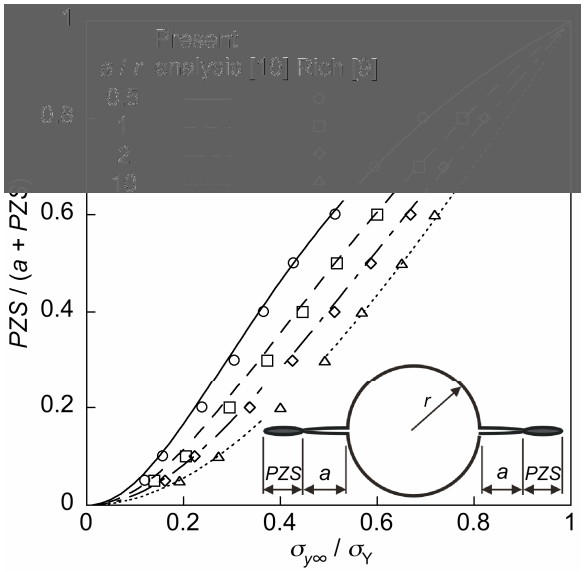

Fig. 2 PZS of a crack emanating from a hole

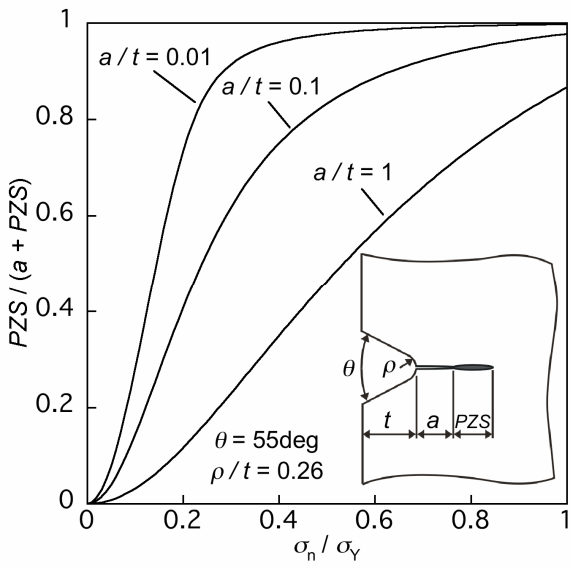

Fig. 3 PZS of a crack emanating from a V-notch

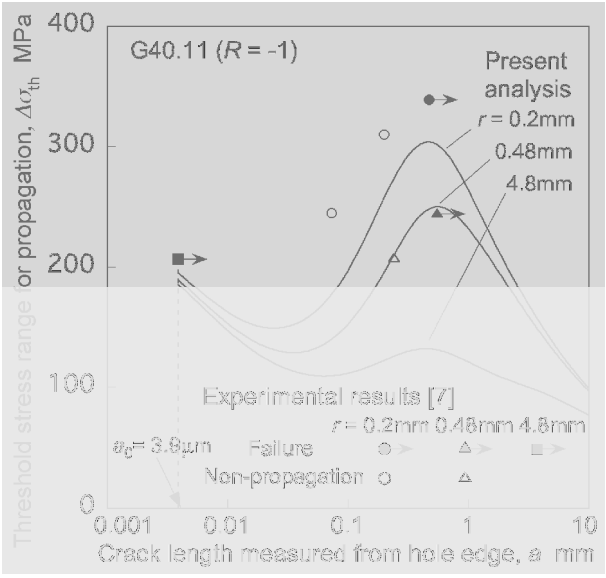

Fig. 4 Relation between $\Delta\sigma_{th}$ and a of holed G40.11 plates

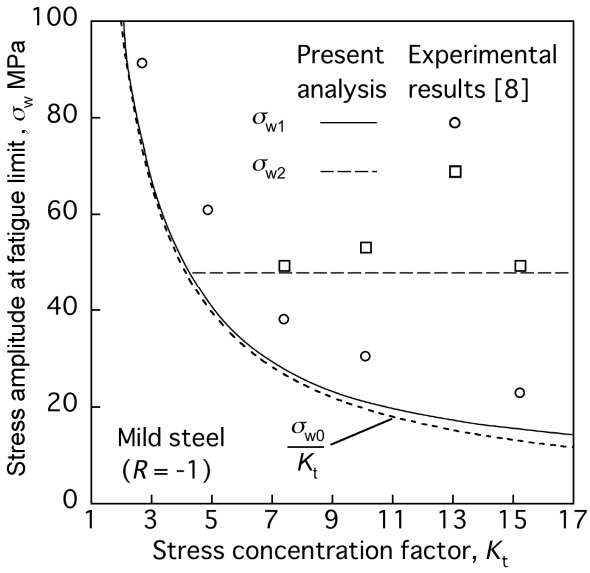

Fig. 5 Relation between σ_w and K_t of V-notched mild steel plates

Key Engineering Materials Vols. 385-387 (2008) pp 645-648
© (2008) Trans Tech Publications, Switzerland
doi:10.4028/www.scientific.net/KEM.385-387.645

A Study on the Fatigue Test of Bogie Frame by Stress Measurement

Sung-Cheol Yoon [1,a], Chang-Sung Jeon [1,b], Won-Kyung Kim [1,c], Jeongguk Kim [1,d] and Sang-Hoon Chang [1,e]

[1] Korea Railroad Research Institute, 360-1, Woulam, Uiwang, Kyunggi, South Korea 437-718

[a]scyoon1@krri.re.kr, [b]csjeon@krri.re.kr, [c]wkkim@krri.re.kr, [d]jkim@krri.re.kr kr, [e]shchang@krri.re.kr

Keywords: Bogie frame, Finite element method, Stress analysis, Load test, Fatigue limit

Abstract. This paper describes the results of structural analysis and loading test of a bogie frame. The purpose of the analysis and test is to evaluate the safety and functionality of the bogie frame under maximum load. The bogie system consist of the bogie frame, suspensions, wheel-sets, a brake system and a transmission system. Of these components, the bogie frame is the major component subjected to the vehicle and passenger loads. The evaluation method used the JIS E 4207 specifications throughout the FEM analysis and static load test. The test results have shown the bogie frame to be safe and stable under design load conditions.

Introduction

The bogie frame, which is a running system for railway rolling stock, is a key structural part that supports the car body's load, and significantly influences the safety of the passengers and the railway vehicle, running performance, and riding comfort. The running system mainly consists of the bogie frame, wheel, axle, primary and secondary suspension systems, braking system, motor, and transmission gear. The bogie frame, which designates the structure of the bogie, has a complex configuration, directly supports the loads. It involves complex application of both static and dynamic loads, and is subject to the static load due to the car body's empty weight and passenger weight, the dynamic load due to irregular rail tracks, and the motion mode of the car body, running system, and wheel axle [1]. First, a structural analysis was conducted for the bogie frame, a major component of the running system, and then structural safety was evaluated. The characteristics of the bogie were analyzed by confirming its strength through a load test based on this structural analysis. The structural analysis was conducted for the test loads of the vertical load, twist load, longitudinal load, lateral load, driving gear load, traction motor load, and brake load, primarily in accordance with the Standard for conducting performance tests for urban railway rolling stocks. The performance test was conducted by installing the strain gauge where high stress is expected under each load condition, based on the result of the structural analysis in accordance with the standard for conducting performance tests for urban railway rolling stocks [2-4].

1. Structural analysis of the body structure

Strength analysis was conducted for the bogie frame with a bolster-less welding structure, the roll rubber spring of the primary suspension system, and the air spring of the secondary suspension system by using the finite element method. Shell and solid elements were used for analysis, and the spring element was used for the roll rubber spring. The analysis model is shown in Fig. 1. The calculated weight of the bogie of the electrical multiple unit is shown in Table 1, and each test load, including the vertical load, is calculated in Table 1.

The loads applied on the bogie frame are calculated based on the bogie test in the performance test, and are as follows. The structural analysis and the load test were conducted by applying the load conditions in Table 3 [2-4].

The strength of the bogie must be less than the yield stress of the materials for each part of the bogie frame in Table 2.

The stress distributions of each load condition are shown in Table 4, and are shown in Figs. 2 and 3.

Table 1. Weight of the bogie frame

No.	Type	Weight	Remarks (unit: kg)
1	Empty weight	33,463	

Table 2. Mechanical property of the bogie frame

Material	Yield stress	Tensile stress	Fatigue Limit			Remarks (unit: kgf/mm^2)
			Base metal	Welding and grinding	Welding	

2	Max. passenger weight	24,000		SWS490A	33	50	16	11	7	side frame, transom support bracket, T/M bracket
3	Bogie weight	13,600	2 sets	STKM18B	32	50	14			transom pipe
4	Spring bottom weight	6,347	2 sets	SS400	25	41	14			stiffener, seat
5	Weight per bogie	25,558	[①+②-④]/2							

Table 3. Load conditions of the bogie frame

No.	Load condition	Load	Direction of the Load	Remarks
1	Vertical load	25,558 kg	Down	Static load (1.0 g)
		33,225 kg	Down	Dynamic load (1.3 g)
2	Twist load	25,558 kg	Down	
		25,558 kg	Down	
3	Longitudinal load	7,667 kg	Forward	
		7,667 kg	Backward	
4	Lateral load	7,667 kg	Left	
		7,667 kg	Right	
5	Driving gear load	3,382 kg	Up and down (Forward)	
		3,382 kg	Up and down (Backward)	
6	Traction motor load	3,673 kg	Down (5.0g)	
		2,373 kg	Up (3.0g)	
7	Brake load	5,097+ 1,274 kg	Forward Backward	
		5,097+ 1,274 kg	Forward Backward	

In Table 4, the maximum stress was 14.8 kgf/mm^2 at the brake hanger bracket when it was subject to the vertical load, and was within the yield stress, 33.0 kgf/mm^2, of the material used for this part, SWS490A

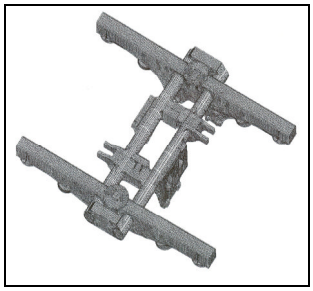

Fig. 1 Analysis model of the bogie frame

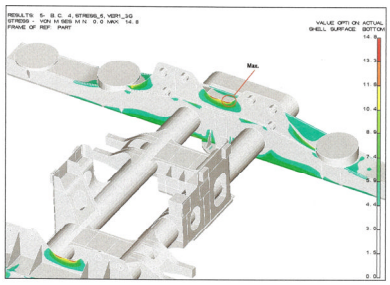

Fig. 2 Stress diagram of the vertical load

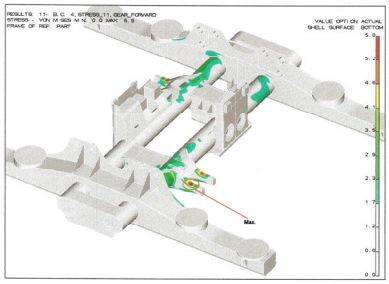

Fig. 3 Stress diagram of the driving gear load

Table 4. Maximum stress of the load condition (unit: kgf/mm^2)

No.	Load condition	Max. stress	Yield stress	Material	Remarks
1	Vertical load	14.8	33.0	SWS490A	Brake hanger bracket
2	Twist load	12.0	33.0	SWS490A	Brake hanger bracket
3	Longitudinal load	10.0	33.0	SWS490A	T/M mount bracket
4	Lateral load	7.3	33.0	SWS490A	Transom support bracket
5	Driving gear load	5.8	25.0	SS400	Gear hanger bracket
6	Traction motor load	8.1	32.0	STKM188	Transom
7	Brake load	4.1	25.0	SS400	Brake hanger bracket

2. Load tests of the bogie

The vertical load, twist load, longitudinal load, lateral load, driving gear load, etc. were measured by installing strain gauges where high stress is expected under each load condition, and where stress concentration is expected due to configuration changes, etc., based on the result of the structural analysis. Strain gauges were installed intensively on the half of the bogie frame, considering the symmetry of the bogie frame [4]. Its weights are shown in Table 1.

2.1 Vertical load

The measurement points with 14.1 kgf/mm^2 or more stress measured in the vertical load test are as shown in Table 5. Maximum stress was developed at the air spring seat (strain gauge no. 6), and its value was -14.86 kgf/mm^2.

Table 5. Vertical load

S/G No.	Load step (kg)			
	0	25,558	33,225	0
6	-0.02	-11.44	-14.86	0.06
52	0.02	11.02	14.31	0.12
5	0.00	-10.93	-14.13	0.10

Table 6. Twist load

S/G No.	Load step (kg)			
	0	19,169	25,558	0
6	0.00	-9.39	-12.29	0.10
52	-0.06	8.51	11.27	0.20
5	-0.02	-7.77	-10.36	0.06

Table 7. Longitudinal load

S/G No.	Load step (kg)			
	0	5,751	7,667	0
24	0.00	-5.51	-7.17	0.00
30	0.00	-5.13	-6.73	0.04
29	-0.02	-4.86	-6.38	0.02

2.2 Twist load

The measurement points with 10.3 kgf/mm^2 or more stress measured in the twist load test are as shown in Table 6. Maximum stress was developed at the air spring seat (strain gauge no. 6) of the side frame, based on the second and third positions, and its value was -12.29 kgf/mm^2.

2.3 Longitudinal load

The measurement points with 6.3 kgf/mm^2 or more stress measured in the longitudinal load test are as shown in Table 7. Maximum stress was developed at the mono link bracket (strain gauge no. 24) during the backward movement test, and its value was -7.17 kgf/mm^2.

2.4 Lateral load

The measurement points with 1.3 kgf/mm^2 or more stress measured in the lateral load test are as shown in Table 8. Maximum stress was developed at the transom support bracket (strain gauge no. 10) during the left load test, and its value was -4.58 kgf/mm^2.

Table 8. Lateral load

S/G No.	Load step (kg)			
	0	5,751	7,667	0
10	0.02	-3.39	-4.58	0.08
8	0.02	1.80	2.17	0.06
14	0.02	1.10	1.32	0.08

Table 9. Driving gear load

S/G No.	Load step (kg)			
	0	2,537	3,382	0
27	0.00	5.27	6.79	0.16
7	0.00	4.34	5.70	0.16
50	0.04	-4.09	-5.33	0.16

Table 10. Traction motor load

S/G No.	Load step (kg)			
	0	2,755	3,673	0
25	0.02	5.85	7.78	0.02
12	0.00	5.17	6.89	0.04
36	0.02	4.74	6.34	0.08

2.5 Driving gear load

The measurement points with 5.3 kgf/mm^2 or more stress measured in the driving gear load test are as shown in Table 9. Maximum stress was developed at the gear hanger bracket (strain gauge no. 27) during the forward moving test, and its value was 6.79 kgf/mm^2.

2.6 Traction motor load

The measurement points with 6.3 kgf/mm^2 or more stress measured in the traction motor load test are as shown in Table 10. Maximum stress was developed at the transom support bracket(strain gauge no. 25) during the load down test, and its value was 7.78 kgf/mm^2.

2.7 Brake load

Maximum stress was developed at the brake hanger bracket (strain gauge no. 57) during the backward moving test, and its value was -6.44 kgf/ mm^2.

We found out that the results of the 7 loading tests conducted were all within the yield stress of 33 kgf/mm^2 of used materials(SWS490A).

2.8 Combined stress

We obtained the combined stress and the Goodman diagram, in reference to the results of the loading tests. The Tables 11 and 12 show the measured points whose average stresses reached more

Table 11. Combined stress result

S/G No.	Combined stress (driving)		Combined stress (braking)		Remarks
	Mean stress	Stress amplitude	Mean stress	Stress amplitude	
6	-11.62	4.74	-11.35	4.19	Welding
5	-11.29	4.05	-10.83	4.06	Welding
52	11.22	4.07	7.35	3.76	Base metal

Table 12. Combined stress result

S/G No.	Combined stress (driving)		Combined stress (braking)		Remarks
	Mean stress	Stress amplitude	Mean stress	Stress amplitude	
24	-0.52	7.38	-0.40	7.26	Grinding
30	0.40	7.06	0.45	7.06	Base metal
43	-0.06	6.89	-0.06	6.84	Base metal

than 11.2 kgf/mm^2 and the measured points whose stress amplitude reached more than 6.8 kgf/mm^2. The Figures 9 and 10 show the results of the calculation of the combined stress using the Goodman diagram. Looking into these results, concerning the combined stress, we determined that in the area where the average stress was highly distributed, the maximum compressive stress was found in the air spring seat (Welding Area - Strain Gauge No. 6) whereas the maximum tensile stress was found in the frame (Base Metal - Strain Gauge No. 52) where the brake was installed. In the area where the stress amplitude was highly distributed, the stress was maximal in the mono link bracket (Grinding – Strain Gauge No. 24) when the vehicle was running. As shown in the Fig. 9 and 10, those areas were located in the safe margin by the individual areas showing the welding limit, the grinding limit and the base metal limit.

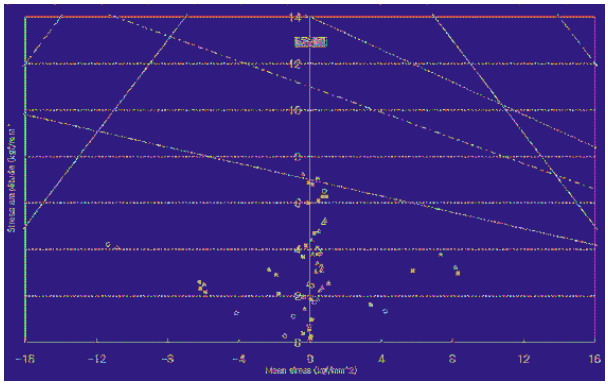

Fig. 9. Fatigue endurance diagram for driving mode

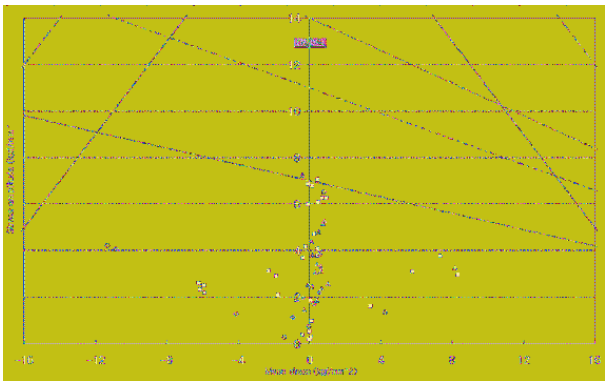

Fig. 10. Fatigue endurance diagram for braking mode

3. Conclusions

In this study, vertical load, twist load, longitudinal load, lateral load, driving gear load, traction motor load, and brake load tests were performed to evaluate the structural safety of the rail transit's bogie frame. The results obtained were based on the above seven tests, which were included in this paper and are as follows:

(1) According to the result of the structural analysis, the maximum stress under vertical load was 14.8 kgf/mm^2 at the brake hanger bracket, the maximum stress under twist load was 12.0 kgf/mm^2 at the brake hanger bracket , the maximum stress under longitudinal load was 10.0 kgf/mm^2 at the traction mount bracket, and the maximum stress under traction motor load was 8.1 kgf/mm^2 at the transom.

(2) According to the result of the load test, the maximum stress in the vertical load was -14.86 kgf/mm^2 at the air spring seat (strain gauge no. 6), the maximum stress in the twist load was –12.29 kgf/mm^2 at the air spring seat (strain gauge no. 6), the maximum stress in the longitudinal load was -7.17 kgf/mm^2 at the mono link (strain gauge no. 24), and the maximum stress in the traction motor load was 7.78 kgf/mm^2 at the transom support bracket (strain gauge no. 25).

(3) The maximum stress of the bogie frame based on the result of the structural analysis was at the brake hanger bracket under vertical load, whereas the maximum stress of the bogie frame based on the result of the load test was at the air spring seat under vertical load. Both were within the yield stress and are considered safe in terms of strength.

(4) All combined stresses were within the safety zone in the fatigue endurance diagram.

Based on the results, it was found that the bogie frame of the electrical multiple unit had sufficient static strength and fatigue strength.

References

[1] Kijun Park, Hoyong Lee, et al, *Evaluation of fatigue strength of the bogie frame of the standard electrical multiple unit*, Journal of the Korean Society for Railways, Vol. 3, No. 3 (2000), pp.170-176.

[2] MOCT, Standard for performance tests for urban railway rolling stocks, load tests for the bogie (2000).

[3] Japanese Industrial Standards, Truck Frames for Railway Rolling Stock-General Rules for Design, E 4207 (1992).

[4] Japanese Industrial Standards, Test Methods of Static Load for Truck Frames and Truck Bolsters of Railway Rolling Stock, E 4208 (1988).

Key Engineering Materials Vols. 385-387 (2008) pp 649-652
© (2008) Trans Tech Publications, Switzerland
doi:10.4028/www.scientific.net/KEM.385-387.649

Fatigue Life Evaluation of Automotive Engine Mount Insulator

Chang-Su Woo[1, a], Wan-Doo Kim[1,b], Shin Hur[1,c]

[1]Korea Institute of Machinery & Materials, 171, Jang-Dong, Yuseong-Gu, Daejeon, Korea.

[a]cswoo@kimm.re.kr, [b]wandoo@kimm.re.kr, [c]shur@kimm.re.kr

Keywords: Rubber engine mount, Fatigue life prediction, Finite element analysis, Fatigue test, Maximum Green-Lagrange strain, Fatigue Damage parameter

Abstract. Fatigue life of automotive engine mount insulator made of natural rubber was evaluated. In order to develop an appropriate fatigue damage parameter of the rubber material, a series of displacement controlled fatigue tests was conducted using 3-dimensional dumbbell specimens with different levels of mean displacement. It was shown that the maximum Green-Lagrange strain was a proper damage parameter, taking the mean displacement effects into account. Nonlinear finite element analyses of the rubber engine mount insulator and 3D dumbbell specimen were performed based on a hyper-elastic material model determined from the simple and equi-biaxial tension tests. Fatigue life prediction of the engine mount insulator was made by incorporating the maximum Green-Lagrange strain values, which was evaluated from the finite element analysis and fatigue tests, respectively. Predicted fatigue lives of the engine mount insulator showed a fairly good agreement with the experimental fatigue lives.

Introduction

The fatigue life prediction on the rubber components was increasing according to the extension of warranty period of the automotive components. A design of rubber components against fatigue failure is one of the critical issues to prevent the failures during the operation [1,2]. Therefore, fatigue life prediction and evaluation are the key technologies to assure the safety and reliability of mechanical rubber components [3]. In this paper, the fatigue lifetime prediction methodology of rubber components is developed by incorporating the finite element analysis with material characterization of the rubber material and fatigue damage parameter determined from fatigue tests. The methodology is applied to the fatigue life estimation of a rubber engine mount used for automobile in order to assure the durability of the rubber components at the design stage. Predicted fatigue lives of the engine mount insulator showed a fairly good agreement with the experimental fatigue lives.

Finite Element Analysis

Simple and equi-biaxial tension tests were conducted to determine the nonlinear material constants of the engine mount rubber. Displacement - maximum Green-Lagrange strain relationships of the 3D dumbbell specimen and engine mount were obtained from the nonlinear FEA using the hyper-elastic material model determined from the material tests [4,5]. The 3D dumbbell specimen, made with the same manufacturing process as the engine mount, has an elliptical cross-section and parting lines are located on the minor axis of the specimen to avoid undesirable failure at the surface discontinuities [6]. Fig. 1 shows the Green-Lagrange strain distribution of the dumbbell specimen under a tensile displacement. The maximum Green-Lagrange strain was found at the surface of the major axis in the dumbbell specimen. The Green-Lagrange strain at the critical location determined from the finite element analysis was used for evaluating the fatigue damage parameter of the natural rubber. Finite element model and Green-Lagrange strain distribution of an engine mount under a tensile and compression loading are shown in Fig. 2. A maximum Green-Lagrange strain occurred at the edge location as indicated in Fig. 2, and fatigue cracking at the critical location was observed during the fatigue test of the engine mount.

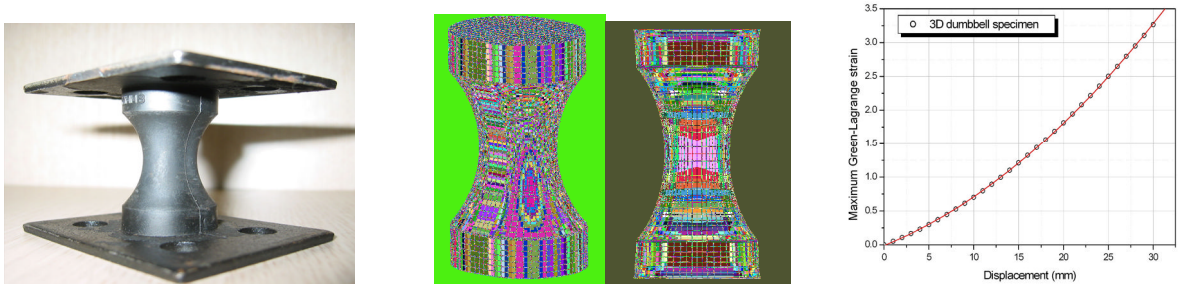

(a) 3D dumbbell specimen (b) Finite element analysis (c) Displacement vs G-L strain

Fig. 1 Finite element analysis of 3D dumbbell specimen

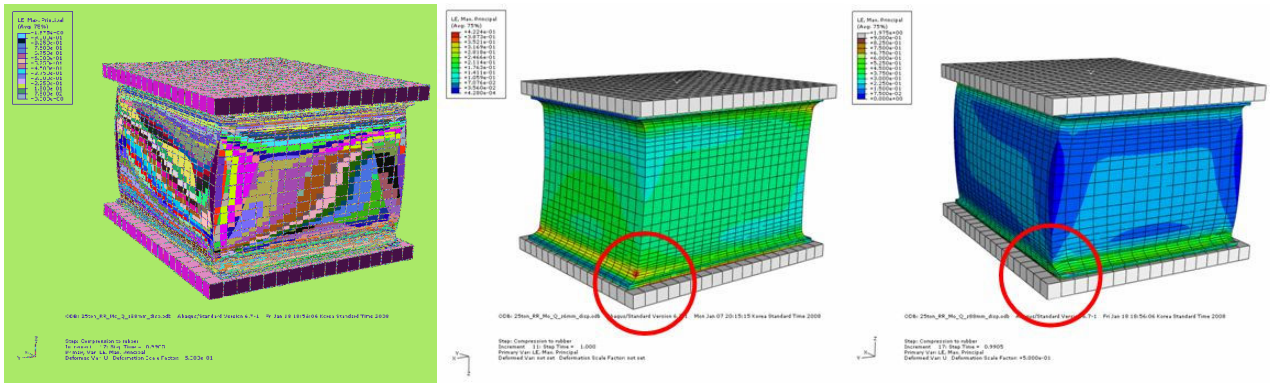

(a) Engine mount (b) Tension (c) Compression

Fig. 2 Finite element analysis of engine mount insulator

Fatigue Test of 3D dumbbell Specimen

The test piece has the basic shape of the 3D dumbbell specimen with a metal fitting cure bonded to each end. The test piece should be capable of compression and tensile deformation without developing slackness under cyclic deformation. Fatigue tests of 3D dumbbell specimen were performed using the fatigue testing system under the stroke-controlled condition with a sine waveform of 5 Hz and the mean displacement is 0, 3, 4, 5, 6, 8mm at the maximum displacement range is 8~17mm as shown Fig. 3. Crack initiation was occurred at the surface of the major axis in the dumbbell specimen in both compression and tension. As increasing the cycles in initial phase, the maximum load decreased little by little. When the crack grew over the critical size, the maximum load decreased suddenly and the final failure reached. The fatigue failure was defined as a number of cycles at which the maximum load dropped by 20 percent.

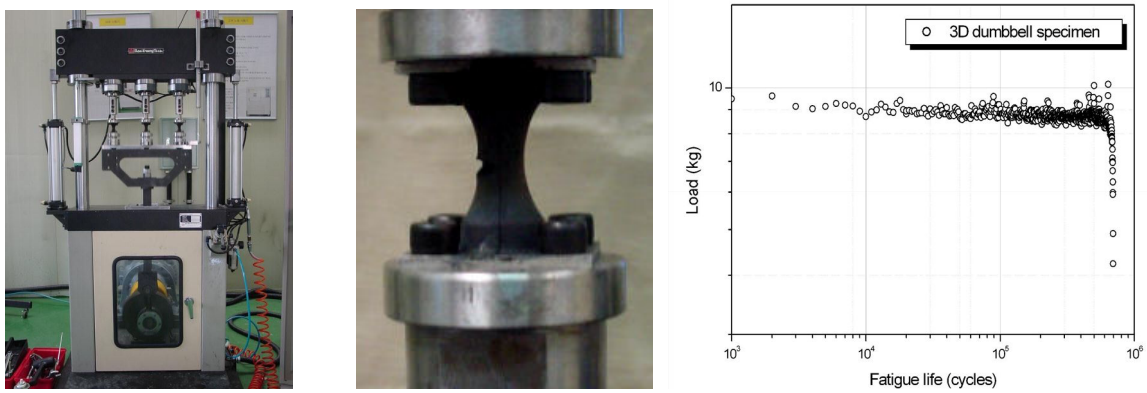

(a) Fatigue test (b) Crack initiation (c) Load vs Fatigue life

Fig. 3 Fatigue test of 3D dumbbell specimen

Fatigue Life Prediction and Evaluation

Fatigue process begins with the accumulation of damage at a localized region due to alternating loads, leading to crack nucleation, growth, and final fracture. The crack nucleation life of a component may be defined as the number of cycles required for the appearance of a crack to a certain size. Therefore, the crack nucleation life of the component can be related to the life of a smooth specimen that is cycled to the same stresses or strains as the material at the critical region of the component. Fig. 4(a) shows the relationship between the maximum displacement amplitude and the fatigue life of 3D dumbbell specimens. The fatigue life decreased as the maximum tension displacement increases. It is possible to express the fatigue life with the maximum tension displacement fairly good. Fig. 4(b) shows relation of maximum Green-Lagrange strain and fatigue life. It was observed that the maximum Green-Lagrange strain was a good parameter to account for the hardness, mean strain, amplitude effects [5]. Fatigue live of the 3D dumbbell specimen represented by the maximum Green-Lagrange strain parameter was shown in equation (1), where the Green-Lagrange strain for 3D dumbbell specimen is calculated from the displacement versus Green-Lagrange strain.

$$N_f = 357{,}272 \cdot [\varepsilon_{G-L}]^{-3.546} \tag{1}$$

Where, ε_{G-L} : Green-Lagrange strain

Fatigue test of the engine mount insulator was performed by using a servo-hydraulic fatigue testing system of 10 kN load capacity. Test loading are 1G ± 2.5G (1.60 ± 4.0 kN) in room temperature. Fatigue life has been defined as the number of cycles when the deformation increased to 20 mm above the reference deformation. The change of deformations was determined from the deformation at 100 cycles as a reference, since the desired load of the hydraulic testing system was achieved after 10 to 20 cycles from the start and the deformation of the rubber specimen varied considerably during the initial period. Fatigue failure occurred at the edge location of engine mount as indicated in Fig. 5. Experimental fatigue life of engine mount is 562,746 cycles. Predicted fatigue life of the engine mount was calculated from Equation (1) using the Maximum Green-Lagrange strain of the engine mount at maximum load. Predicted fatigue of engine mount is 436,634 cycles. Predicted fatigue life of the engine mount insulator showed a fairly good agreement with the experimental fatigue life. Therefore, fatigue life estimation procedure employed in this study could be used approximately for the fatigue design of the rubber components at the early design stage.

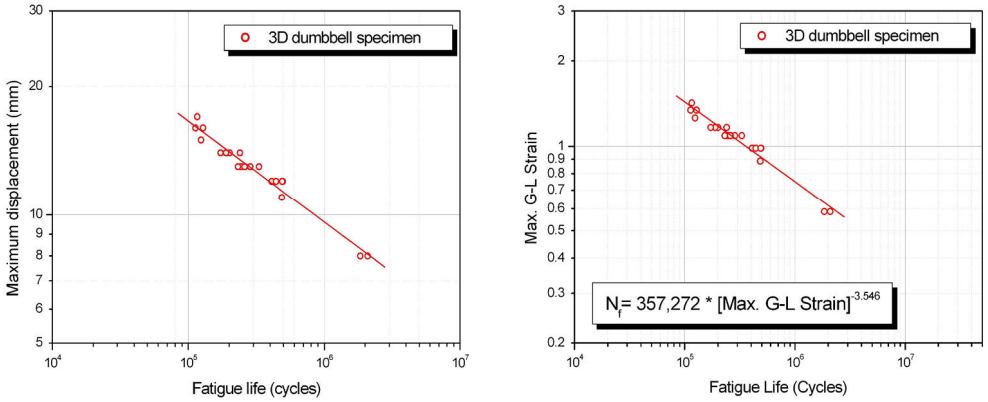

(a) Max. displacement vs fatigue life (b) Max. G-L strain vs fatigue life

Fig. 4 Fatigue life prediction of 3D dumbbell specimen

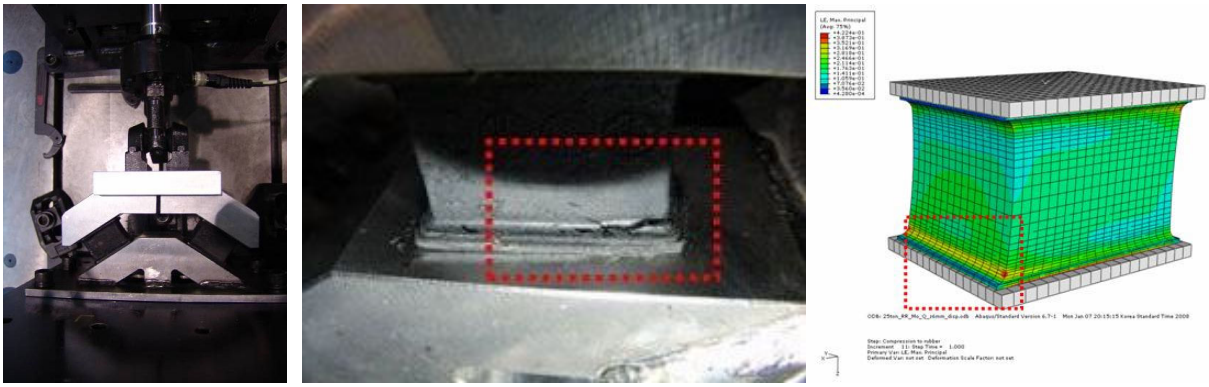

(a) Fatigue test (b) Fatigue crack (c) Critical location

Fig. 5 Fatigue test of rubber engine mount insulator

Summary

A procedure to predict the fatigue life of the engine mount at the initial design stage was proposed. Nonlinear finite element analyses for the engine mount and 3D dumbbell specimen were performed based on the hyper-elastic material model determined from the tensile and biaxial tension tests. Displacement versus maximum Green-Lagrange strain relationships of the engine mount and the 3D dumbbell specimen were obtained from the nonlinear FEA. Fatigue tests of the 3D dumbbell specimen with various loading conditions were performed, and the maximum Green-Lagrange strain vs. fatigue life relation was obtained. Fatigue lives of the engine mount were predicted by using the displacement vs. maximum Green-Lagrange strain of engine mount and maximum Green-Lagrange strain vs. fatigue life of 3D dumbbell specimen. Predicted fatigue life was in a fairly good agreement with the experimental life. Further researches on the applications of the fatigue life prediction and the construction of databases for rubber material properties and 3D dumbbell specimen fatigue properties are in progress.

Acknowledgement

This research has been supported by Development of materials and Component program of Ministry Commerce Industry & Energy, Korea.

References

[1] Hirakawa H, Urano F, Kida M. “Analysis of fatigue process of rubber vulcanizates”, Rubber Chemistry and Technology, (1978), p. 201-214.

[2] Mars WV, Fatemi A., “A literature Survey on fatigue analysis approaches for rubber”, International Journal of Fatigue, Vol. 24(2002), p. 949-961.

[3] Lake GJ., “Fatigue and fracture of elastomers”, Rubber Chemistry and Technology, vol. 68(1995), p.435-460.

[4] Morman KH, Pan TY., “Application of finite-element analysis in the design of automotive elastomeric components”,, Rubber Chemistry and Technology, (1988), p.503-533.

[5] Kim, W., “Application of FEA to design of Rubber Component”, KSME, vol. 38(2005), p. 42.

[6] Yamaguchi, H. & Nakagawa M., “Fatigue Test Technique for Rubber materials of Vibration Insulator”, International polymer Science and Technology, vol. 20 (1993), p 64-69.

Key Engineering Materials Vols. 385-387 (2008) pp 653-656
© (2008) Trans Tech Publications, Switzerland
doi:10.4028/www.scientific.net/KEM.385-387.653

Structural Safety Assessment of Railway Freight Car during Static Loading

Jeongguk Kim[1, a], Sung-Cheol Yoon [1, b], Jung-Won Seo[1,c] and Sung-Tae Kwon[1,d]

Railroad Safety Research and Testing Center, Korea Railroad Research Institute,adder 360-1 Woulam, Uiwang, Kyunggi, South Korea 437-757

[a]jkim@krri.re.kr, [b]scyoon@krri.re.kr, [c]jwseo@krri.re.kr, [d]stkwon@krri.re.kr

Keywords: Structural strength, Freight car, Railway application, FEM analysis

Abstract. The structural strength during static loadings for a carbody of railway container freight car was evaluated to verify the structural strength of newly manufactured carbody. The carbody of freight car was designed with SM490YA steel and stainless steel for the general railway transportation. Prior to the assessment of structural strength, finite element method (FEM) characterization was used for the stress and structural analyses on stress distribution in a carbody of container freight car. The strain gages were attached on the carbody based on the FEM results in order to measure structural strength during static loadings such as vertical and compression loadings. The actual vertical loading test and horizontal compression loading test were conducted, and the results were compared with the previous FEM results. In this investigation, the evaluation method for the structural strength in a structural component has been introduced using several engineering techniques, and experimental and theoretical results were compared.

Introduction

In Korea, recently, the freight container transportation using railroad has been a convenient way as compared with any other transportation methods, such as marine or road transport due to mass transportation of railway, on-time delivery, environment-friendly railroad system, etc. [1-3]. The freight car in this research was designed with SM490YA steel plate for the transportation of freight container for the purpose of general commercial transportation. Therefore, it is required to verify design and manufacturing assurance of freight car for safety concerns during operation.

The main objectives of the current investigation are to introduce the evaluation method of the structural strength of carbody in a freight car, to apply loading tests for the structural safety evaluation of carbody of freight car, to conduct loading test of freight car carbody to verify design and manufacturing assurance for safety concerns, and to verify the structural strength of newly manufactured carbody of a freight car.

The Freight Car and Experimental Procedures

The Freight Car and Carbody. Figure 1 shows a photo of freight container car with the loading of 40 ft container. The freight car is composed of 2 bogies and carbody with firm underframe for loading the freight container. The freight car needs to possess enough strength to endure the weight of freight container. The material properties data can be found in Table 1.

Loading Conditions. Several different loading conditions, e.g., vertical and compressive loadings and loading condition for an actual operation, were considered to reflect the actual loading condition during commercial operation of freight car. The vertical loading condition means to consider vertical loading component when either two 20 ft-long containers or one 40 ft-long freight container is loaded, while the compressive loading condition is for considering a horizontal load transfer component between cars, which were connected each other. Also, the actual loading test condition is the loading

condition that the freight car is running on the commercial lines with loading either two 20 ft-long containers or one 40 ft-long freight container.

Figure 1. A photo of freight container car on the testing stand.

Table 1. The Material properties of the freight container car

Materials	Yield Strength (MPa)	Tensile Strength (MPa)
SM490YA (Underframe)	363	490
SS400 (Other Part)	245	402

Evaluation Criteria. From the static loading tests, the following evaluation criteria should meet to guarantee the safety of freight car carobdy during commercial operation according to Koran Industrial Standards guideline [4]. Table 2 summaries the static loading evaluation criteria [4].

Table 2. Static loading evaluation criteria

Testing Condition	Measurement Items	Criterion
Vertical Loading	Stress	Within Yield Strength
	Amount of Slack	Within Camber Value
Horizontal Compressive Loading	Stress	Within Yield Strength
Loading Test with Operation Condition	Stress	Within Yield Strength
	Amount of Slack	Within Camber Value
Natural Frequency	Bending Natural Frequency	Over 10.0 Hz

Structural Analysis of Freight Car Carbody. Structural analysis with I-DEAS 11 NX, which is a commercial finite element analysis package, was performed for the analysis of load transfer of car body to under frame during static loading. Also, the distribution of stress concentration was obtained through the stress analysis [5].

Attachment of Strain Gages and Displacement Sensors. Since the carbody is symmetric in all direction, the strain gages were attached for a quarter area, where the major stress concentration occurred. A bridge circuit was constituted using total 34 channels with 31 strain gages and a rosette gage. Furthermore, in order to measure the amount of slack in carbody during loading, 8 dial gages, displacement sensors, were installed under carbody.

Natural frequency measurements. With the same testing condition of vertical loading, 1 ton weight was applied at the center of carbody under the frame. The instant removal of the weight made possible to measure the natural frequency of carbody with an accelerometer. In general, the natural frequency measurements were conducted twice.

Results and Discussion

Structural Analysis. The main purpose of this structural analysis was to identify the load transfer passages to car body structure and to understand the stress distribution in the car body during static loading. The structural analysis for car body was performed with various applied loading conditions, and the modeling was achieved for a half considering the width and length directions. The shell elements were used in the most of elements in structural analysis and the shell and solid elements were used for the under frame analysis. Total numbers of elements and nodes were 40,630 and 40,853,

repectively, the HP Workstation was used as a hardware, and I-DEAS 11 NX analysis package was used for this investigation.

Figure 2 shows FEM analysis results. Based on FEM analysis results, the max stress value was obtained at intersection of side sill and bolster for vertical loading, the intersection between bolster and center sill for compressive loading, and the intersection between bolster and center sill for composition loading condition, as shown in Figs. 2 (a) and (b).

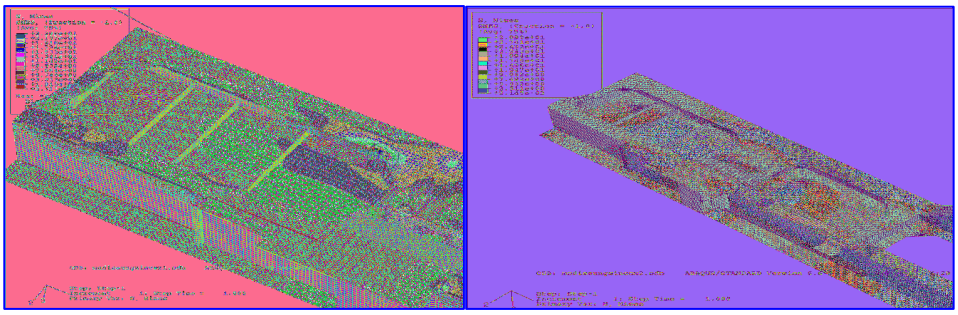

Figure 2. Max stress areas obtained from FEM analysis in (a) vertical loading condition and (b) compressive loading condition

The loading condition. As mentioned in previous section, several different loading conditions were applied to verity the safety analysis of the freight car carbody according to Korean Industrial Standards guideline, and each loading condition and loading amount are as follows,

(1) Vertical Loading Test (20 ft Container 2 ct.): 67.4 ton

① *Equally Distributed Vertical Load*

= (Carbody Weight - Bare Frame Weight) × (Vibrate Acceleration)

= (10,520 – 6,679) × 1.3 = 5,000 kg

② *Container Vertical Load*

= (20 ft Container Weight) × (Vibrate Acceleration)

= 24,000 × 2 × 1.3 = 62,400 kg (1)

(2) Vertical Loading Test (40 ft Container): 44.6 ton

① *Equally Distributed Vertical Load*

= (Carbody Weight - Bare Frame Weight) × (Vibrate Acceleration)

= (10,520 – 6,679) × 1.3 = 5,000 kg

② *Container Vertical Load*

= (40 ft Container Weight) × (Vibrate Acceleration)

= 30,480 × 1 × 1.3 = 39,624 kg (2)

(3) Horizontal Compressive Loading Test: 220 ton

① *Equally Distributed Vertical Load*

= (Carbody Weight - Bare Frame Weight) × (Vibrate Acceleration)

= (10,520 – 6,679) × 1.3 = 5,000 kg

② *Coupler Compressive Load*

= 220,000 kg (3)

(4) Loading Test with Operation Condition: 63 ton

① *Equally Distributed Vertical Load*

= (Carbody Weight - Bare Frame Weight) × (Vibrate Acceleration)

= (10,520 – 6,679) × 1.2 = 4,609 kg

② *Container Vertical Load*

= 24,000 × 2 × 1.2 = 57,600 kg (4)

Natural Frequency Measurements. With the same testing condition of vertical loading, 1 ton weight was applied at the center of carbody under the frame. From the results of natural frequency measurement, and 10.5 Hz was obtained as natural frequency of the freight car carbody. The results satisfied with the desired requirement according to the guideline.

Calculation of Composition Stress. In order to determine the composition stress components, which mean the combined loading of vertical and compressive conditions in freight car carbody, the following steps were applied. First, assume the simultaneous application of vertical loading and horizontal loading, and check out the applied stress as compared with the yield strength of materials. Finally, the summation of vertical stress and horizontal stress was accomplished.

Summary of Vertical/Horizontal Loading Tests. Table 5 presents the summary of vertical and horizontal loading tests results. From the results the areas occurring max stress were determined, and the max stress values of individual loading conditions were provided. Moreover, the max stress occurred areas were found. As compared with the previous FEM simulation, a good agreement was obtained in terms of stress distribution and max stress regions.

Conclusions

The current research on stress and safety analysis of freight container carbody leads the following summaries.

From the vertical loading and compressive loading test results, it was found that the stress values in the carbody of freight car under max loading condition showed within the yield strength of carbody materials. The FEM analysis results showed a good agreement with experimental results. The max stress of -256 MPa during static loading test occurred at the intersection of side sill and bolster. The max stress of -179 MPa during horizontal compressive loading test occurred at the curvature area of bolster. The max stress of -259 MPa for the combined composition stress, occurred at the intersection of center sill and bolster, and they were within the yield strength of carbody materials. The amount of slack, for the determination of camber amount, in carbody was obtained at the center of side sill, and they were within the optimal camber range. The measurement results of natural frequency in carbody showed 10.7 Hz, and satisfied with design criteria.

Table 5. The results showing vertical and horizontal loading tests

Items		Max Stress (MPa)		Criterion (MPa)	Max Stress Occurred
		Tensile	Compression		
Stress	Vertical (20 ft)	85	-132	Under 363	Intersection of Side Sill and Bolster
	Vertical (40 ft)	62	-256	Under 363	Intersection of Side Sill and Bolster
	Compressive	48	-179	Under 363	Curvature Area of Bolster
	Composition (20 ft)	64	-271	Under 363	Curvature Area of Bolster
	Composition (40 ft)	96	-259	Under 363	Intersection of Center Sill and Bolster
Slack	Vertical	9.90 mm		Under Camber Limit	Center Area of Side Sill
	Compressive	3.85 mm		Under Camber Limit	Center Area of Side Sill
Natural Frequency		10.7 Hz		Over 10	

References

[1] S.C. Yoon, W.K. Kim, and J. Kim: Key Engineering Materials, Vols. 326-328 (2006), p. 1087.

[2] J.D. Chung, J. Kim, and D.S. Bae: Key Engineering Materials, Vols. 297-300 (2005), p. 1876.

[3] S.C. Yoon, C.S. Jeon, and J. Kim: Key Engineering Materials, Vols. 353-358 (2007), p. 2728.

[4] Korean Industrial Standards, KS A ISO 668 (2002).

[5] V. Esslinger, et al.: Engr. Failure Analysis Vol. 11 (2004), p. 515.

Key Engineering Materials Vols. 385-387 (2008) pp 657-660
© (2008) Trans Tech Publications, Switzerland
doi:10.4028/www.scientific.net/KEM.385-387.657

An integrated approach to durability design of steel structures against atmospheric corrosion

L. Cascini[a] , R. Landolfo[b] and F. Portioli[c]

Department of Constructions and Mathematical Methods in Architecture

University of Naples "Federico II"

Via Forno Vecchio 36, 80129, Naples, Italy

[a]lucrezia.cascini@unina.it, [b]landolfo@unina.it, [c]fportiol@unina.it

Keywords: Metallic materials, sustainable steel structures, durability design, corrosion, lifetime safety factor method.

Abstract. To develop a durability design procedure based on lifetime safety factor method, different dose-response functions based on both ISO standards and the literature are presented for the prediction of the thickness loss due to atmospheric corrosion in metal structures. Finally, serviceability and ultimate limit states are defined for the durability design against corrosion.

Introduction

Durability design of new and existing steel structures is a key issue for the sustainable development of built-up environment. Durability is strongly influenced by damage due to atmospheric corrosion, whose control is a key aspect for the design and the maintenance of both new constructions and historical buildings. In terms of structural effects, the atmospheric corrosion results in the thickness loss of the cross section leading to a smaller resistant area. The loading capacity of the element itself is reduced and the safety margin rapidly decreases.

Besides the effects on coatings, which could modify the exterior appearance of constructions reducing their aesthetic and economic value, corrosion represents an additional critical load which is able to lead the structures to collapse, specially when it is associated with high stress rates and cyclic loads, such as in the cases of stress and fatigue corrosion.

With regard to life duration, even if international standards and codes provide general recommendations for preventing early ageing of constructions, the durability design of metal structures has still to be fully defined and codified. In particular, a procedure for the evaluation of original and residual service life should be developed for each material under assigned environmental loads on the basis of available degradation models.

This paper represents a first attempt to propose and develop a durability design procedure for both new and existing metal structures with the aim of evaluating the residual service life of constructions with respect to corrosion degradation.

Durability criteria in standards and codes

The main European standards and codes on constructions give only few qualitative and common provisions for durability of metal structures, that are mainly concerned with corrosion of coating systems or with general recommendations on structural material redundancy. In EN 1993-1-1 it is stated that steel structures should be designed against corrosion by means of surface protection system and the use of stainless and/or weathering steel [1], referring to EN 1990 for durability criteria to be fulfilled [2]. A definition of durability with respect to corrosion can be found in EN ISO 8044:1999 where *durability* is the capability of corrosion system, that is the metal itself or the coating, to fulfil the serviceability requirements for a specific period of time, when adequate maintenance actions are performed [3]. Many other references can be found in international

standards and literature as discussed elsewhere but no specific design procedure is provided for the evaluation of design life time of constructions under the identified environmental loads [4]. Taking into account the lack of codified durability design procedures, the application of the life time safety factor method to metal structures is discussed in the following.

Durability analysis based on lifetime safety factor method

The lifetime safety factor method in durability design was first time presented in the RILEM Report on concrete structures [5] and then developed within the framework of the EU Project LIFECON [6].

The method is used for the calculation of design life of constructions and it is based on probabilistic degradation models, which consider the decrease of structural resistance caused by different classes of environmental loads. It is so called because of the safety factor applied to the average or the characteristic value of design life. The latter is calculated by degradation models, taking into account the statistical values of resistance and loads and it is calibrated on the maximum allowable failure probability related to the considered limit states.

The theoretical background of the procedure is as for the static limit state design, but in this case the resistance R is considered as a time dependant variable. The procedure is organized into different steps as specified in the following.

First, in order to perform the durability calculation a reference period has to be specified as a basis for assessing statistically variable actions and evaluating the reliability with respect to durability. This reference value is assumed to be the target service life t_g, the period of time during which a structure or part of it is to be used for its intended purpose with anticipated maintenance but without major repair being necessary [2]. The numerical reference values are selected according to both common standards, regulations and codes and the requirements of mechanical design.

Once the reference period has been stated, it is possible to characterize the project scenario by selecting the environmental loads S that will likely act onto structure. With regard to atmospheric corrosion of metal structures climatic conditions (average temperature, rainfall, condensation of moisture, freezing, solar radiation and air pollution), together with geological conditions (such as the location of ground water, possible contact with sea water, contamination of the soil by aggressive agents like sulphates and chlorides) have to be provided.

On the basis of the identified environmental loads, the degradation factors and mechanisms are quantified in terms of damage curves in the form:

$$D_m(t) = \alpha * t^n \quad (1)$$

where: $D_m(t)$ is the mean value of degradation; α is a constant coefficient; t time; n degradation mode coefficient.

For the calculation of durability parameters, serviceability limit states as well as ultimate limit states have to be defined on the basis of the performance requirements to be fulfilled. That could be achieved by selecting a maximum allowable value of degradation D_{max}. The durability requirements are thus fulfilled if the failure event, corresponding to $D(t_{max})=D_{max}$, occurs after the design service life had expired, with a proper safety margin according to Eq. 2.

$$t_d = t_{max}/ \gamma_{t0} \geq t_g \quad (2)$$

where: t_d is the design service life; t_{max} is the calculated mean value of the service life; γ_{t0} is the central lifetime safety factor; t_g is the target service life.

The numerical values of the partial safety factors are calculated on the basis of the maximum allowable failure probability defined for the selected limit state and the degradation function corresponding to the deterioration mechanism acting onto the structure, as reported elsewhere [5,6].

Degradation models

As far as corrosion modelling is concerned, it is possible to distinguish different modelling approaches. Models suitable for engineering applications express the deteriorations over time by means of thickness loss of the materials and they are usually based on short and/or long term field test exposures. The corrosion of metals is strongly affected by the climatic conditions (average temperature, relative humidity…) and pollutants in the atmosphere. The relation between corrosion rate and the relevant environmental parameters is usually expressed according to Eq.3:

$$D\,(t) = \alpha\, t^{n} \tag{3}$$

where $D(t)$ is the corrosion depth at time t [μm; g/m^2]; α is the first year of exposure corrosion rate, t is the time and n is the degradation mode coefficient.

Table 1. Corrosion models.

$D(t) = r_{av} \cdot t$	(3.1)
$D(t) = r_{av} \cdot 10 + r_{lin}\,(t-10)$	(3.2)
$D(t) = 34[SO_2]^{0.33}\exp\{0.020Rh + f(T)\}t^{0.33}$	(3.3)
$D(t) = A \cdot t^{B}\left(\frac{TOW}{C}\right)^{D} \cdot \left(1+\frac{SO_2}{E}\right)^{F}\left(1+\frac{Cl}{G}\right)^{H} e^{J(T+T_0)}$	(3.4)

Some simplified models have been proposed which take into account the environmental effects influencing the corrosion rate by means of constant values of coefficients α and n. Such models express the thickness loss only as a function of time and are usually calibrated on data obtained from short and long term field test exposure. As a consequence, if they are used for environments which differ from the one where the model has been calibrated, the predicted value of the corrosion rate is often inaccurate.

A first attempt to develop general models has been provided by International Standard ISO 9224. Such model expresses the thickness loss over time by means of average corrosion rate for the first 10 years of exposure and steady state corrosion rates in the next years, according to Eqs.3.1 and 3.2 [7]. Recently, as for Eq. 3.3 and 3.4 in Table 1, different models have been developed with the aim to generalize the corrosion loss over time for different environments, reporting the climate and pollutants variables as independent factors as discussed elsewhere [8, 9]. At this stage of the study, it should be noted that the largest part of corrosion models are calibrated on the basis of local field test exposure data. Since the empirical coefficients that characterize each model are strongly influenced by the exposure location, condition and duration, such models can be used just for similar environmental conditions. Of course, the scattering of results influences the reliability of models and the value of related safety factors in a durability design procedure.

The probabilistic characterization of the corrosion development over time, relating the average value of the corrosion depth with the standard deviation, represents the further step of this study

Durability limit states

In order to complete the development of a durability design procedure based on the partial safety factor method, both serviceability and ultimate limit states related to basic requirements have to be defined, such as functionality in use and structural safety.

Serviceability and ultimate limit states in durability design can be referred to the thickness loss of coating and structural material respectively. In particular, serviceability limit states are related to

changes in functionality or aesthetics and they are based on maintainability, economy and environmental impacts. As a consequence, such limit states can be ascribed to the attainment of partial or total loss of coating thickness. On the contrary, ultimate limit states are related to the thickness loss of structural material which compromises the mechanical safety of constructions.

With regard to serviceability limit states (SLS) different limit states should be defined depending on the possibility of a building component to be inspected. According to [10], in case of galvanized steel sections, the limit state is reached when 50% of the weight of zinc has been lost if the use conditions do not allow regular inspections, otherwise the limit state is defined as the 80% of the weight of zinc loss.

As far as ultimate limit states (ULS) are concerned, the safety of constructions at the end of their life-time should be evaluated by considering the possibility that base material of structural members is damaged by corrosion when the protective coating is ineffective. In this case, thickness loss of structural material during the residual service life has to be computed. Such thickness should be added to the one obtained from mechanical calculation in design phase of new constructions, increasing the structural redundancy, or should be used for evaluating the actual safety factor and the residual service life in existing ones.

Concluding remarks

In this paper different dose-response functions for the modelling of atmospheric corrosion have been presented for durability design of metal structures. A first proposal of the different phases of the design procedure against corrosion damage have been discussed according to life-time safety factor method. Further developments are devoted to the probabilistic characterization of the deterioration mechanism, including also pitting corrosion and fatigue, and the quantitative definition of relevant limit states.

References

[1] CEN 2004. EN 1993-1-1. Eurocode3: Design of steel structures. Part 1-1.

[2] CEN 2001. EN 1990. Eurocode. Basis of structural design

[3] CEN 1999. EN ISO 8044. Corrosion of metals and alloys. Basic terms and definitions.

[4] Landolfo R., Cascini L, Portioli F. (2007). Modelling of corrosion damage for metal structures. In: Proc. of the First Workshop COST C25 on "Sustainability of Constructions" PORTUGAL.

[5] Sarja, A. & Vesikari, E. 1996. Durability design of concrete structures. RILEM Report of TC 130-CSL.RILEM Report Series 14.

[6] Sarja, A. 2004. Lifecon deliverable D2.1. Reliability based methodology for lifetime management of structures. Finland

[7] CEN 1992. EN ISO 9224. Corrosion of metals and alloys. Corrosivity of atmospheres. Guiding values for the corrosivity categories.

[8] Kucera V. 2004. Mapping effects on materials in Manual mapping critical load. ICP Materials Coordination Centre, Sweden.

[9] Klinesmith, D.E. & McCuen R. & Albrecht P. 2007. Effect of environmental condition on corrosion rate. Journal of Materials in Civil Engineering.

[10] Popo-Ola, S.O.& Biddle, A.R. & Lawson R.M.2000. Durability of light steel framing in residential buildings. SCI Publication P262.Ascot:The Steel Construction Institute.

Key Engineering Materials Vols. 385-387 (2008) pp 661-664
© (2008) Trans Tech Publications, Switzerland
doi:10.4028/www.scientific.net/KEM.385-387.661

Analysis of Chloride Diffusion in Cracked Concrete

Xiao-Yong Wang [1, a], Han-Seung Lee [1, b]

[1]School of Architecture & Environmental Engineering, Hanyang University, Ansan, 425-791, Korea

[a]wxbrave@hotmail.com, [b]ercleehs@hanyang.ac.kr

Keywords: Chloride, Hydration, Diffusion, Concrete, Crack

Abstract. This paper presents a model for chloride diffusion in cracked concrete. This numerical model includes two parts: hydration model and chloride diffusion model. The hydration model starts with mix proportion of concrete and considers both Portland cement hydration and pozzolanic activity. By hydration model, the evolution of properties of cement paste is described as function of curing age. Furthermore, based on general effective media theory and composite spheres assemblage model, the effective diffusivity of chloride ions in concrete without crack is obtained. Finally based on crack distribution in cracked concrete and finite element methods, the diffusion of chloride ions in cracked concrete is predicted. The prediction results agree well with experiment results.

Introduction

Reinforced and plain concrete structures are often subjected to various solicitations, such as thermal or moisture gradients, mechanical loads. When these solicitations exceed locally the tensile strength of the material, crack will be generated and subsequently affect the transport properties of concrete.

In recent years, the effect of cracking on durability of concrete has been the subject of numerous investigations. By using feedback controlled splitting tests to generate crack width-controlled concrete specimens, Wang [1] evaluated water permeability of cracked concrete. The preliminary results indicate that cracks openings generally accelerate water flow rate in concrete. Aldea [2] studied the effect of cracking on water and chloride permeability. The crack width varies from 50 to 400μm. The results show that the chloride permeability increased with increasing crack width and that the water permeability was significantly more sensitive than the chloride permeability. Olg a[3] studied the influence of crack width(the cracks are artificially created with widths ranging from 0.08 to 0.68mm) and crack wall surface roughness on chloride ingress. Based on the results, it was concluded that chloride diffusion in concrete was independent of either crack with or the crack wall roughness for the ranges studied. Gerard [4] proposed a simple method to predict the effect of cracking on the concrete diffusivity. Predictions are made on the basis of crack density and mean crack aperture. Djebri [5] studied the effects of traversing crack on chloride diffusion into concrete. The diffusion coefficient through the crack was not dependent of material parameters and becomes constant when the crack width is higher than 80μm, where the value obtained was the diffusion coefficient in free solution. From references [1-5], we can see that the presence of cracks could contribute to permeability of concrete.

A model about chloride diffusion in cracked concrete is proposed in this paper. This numerical procedure starts with mixing proportion of concrete. The prediction results agree well with experiment results.

Hydration model

The proposed hydration model considers both Portland cement hydration and pozzolanic reaction. The details of hydration model are introduced in reference [6, 7] and this paper only shows the main

procedure of hydration model (the meaning of variables is available in reference [6-7]).

1) hydration model of Portland cement

On Park' s model [8], some improvements are done to consider cement particle size distribution and cement mineral component, including C_3S,C_2S,C_3A and C_4AF. The basic hydration equation of each mineral composition in cement particles can be described as following eq. (1):

$$\frac{d\alpha_i^j}{dt} = \frac{3C_{w\infty}}{(v_i + w_{ag})r_0^j \rho_i} \frac{1}{(\frac{1}{k_d} - \frac{r_0^j}{D_{ei}}) + \frac{r_0^j}{D_{ei}}(1-\alpha_i^j)^{\frac{-1}{3}} + \frac{1}{k_{ri}}(1-\alpha_i^j)^{\frac{-2}{3}}} \tag{1}$$

2) hydration model of cement blended with supplementary cementing materials (SCM)

The hydration equation of active (glass) part in SCM can be written as equation (2):

$$\frac{d\alpha_{reacted}}{dt} = \frac{m_{CH}}{P} \frac{3}{v_{FL} r_{FL0} \rho_{FL}} \frac{1}{(\frac{1}{k_{dFL}} - \frac{r_{FL0}}{D_{eFL}}) + \frac{r_{FL0}}{D_{eFL}}(1-\alpha_{reacted})^{\frac{-1}{3}} + \frac{1}{k_{rFL}}(1-\alpha_{reacted})^{\frac{-2}{3}}} \tag{2}$$

The reacted ratio of total SCM (both active part and inert part), can be obtained as following:

$$\alpha_{flyash} = (\gamma_s * f_{S,P} + \gamma_A * f_{A,P}) * \alpha_{reacted} \tag{3}$$

The volume of evaporable water volume can be estimated as following:

$$\omega_e = w_g + \omega_c = \omega_{g-cement} + w_{g-scm} + \omega_c \tag{4-1}$$

$$\phi_{cap} = (w_0 - 0.38 * \alpha * Ce_0 - w_{g-scm})/1000 \tag{4-2}$$

Where ω_e is the volume of evaporable water; w_g and ω_c are the volume of gel water and capillary water, respectively; ϕ_{cap} is capillary porosity in cement-SCM paste.

Prediction of chloride ions diffusion

1) *effective diffusivity of chloride ions in concrete*

The GEM equation[9] is able to account for a nonzero solid phase conductivity (or diffusion) problem and allows the prediction of conductivity even near the percolation threshold. The GEM equation is written as following equation:

$$\frac{D_c}{D_0} = \left(m_\phi + \sqrt{m_\phi^2 + \frac{\phi_c}{1-\phi_c}\left(\frac{D_s}{D_0}\right)^{\frac{1}{n}}} \right)^n \tag{5-1}$$

$$m_\phi = \frac{1}{2}\left[\left(\frac{D_s}{D_0}\right)^{\frac{1}{n}} + \frac{\phi_{cap}}{1-\phi_c}\left(1 - \left(\frac{D_s}{D_0}\right)^{\frac{1}{n}}\right) - \frac{\phi_c}{1-\phi_c} \right] \tag{5-2}$$

Where D_c is the effective diffusion coefficient of paste, D_0 is diffusivity of ions in continuum, such as bulk water; D_s is diffusivity of ions in solid phase; ϕ_c is percolation threshold (the critical porosity that the pore network first percolates); n is percolation exponent of the pore network. The diffusivity of concrete can be determined as following:

$$\frac{D_e}{D_c} = 1 + \frac{V_a}{\frac{1}{2(D_i/D_c)\varepsilon - 1} + \frac{1-V_a}{3}} \tag{6}$$

Where D_e is effective diffusivity of chloride in concrete; D_i is diffusivity in ITZ. V_a is

aggregate volume ;The chloride diffusion process is treated as two-dimensional diffusion [10].

2) chloride penetration depth in cracked concrete

Schutter[11] investigated the influence of crack width and crack depth on chloride penetration in mortar. In the experiment program chloride penetration tests were performed on mortar specimens of size 40mm*40mm*160mm, provided with different sizes of artificial cracks with a width up to 0.5mm and a depth up to 10mm. The profile of specimens is shown in figure 1. Finite element model is shown in figure 2. The comparison of chloride penetration depth between simulation results and experiment results is shown in figure 3.

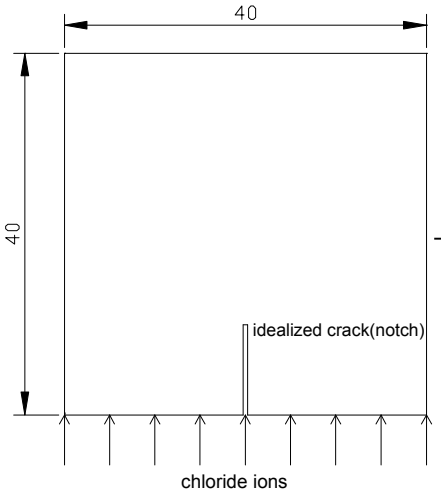

Figure 1. profile of mortar specimen

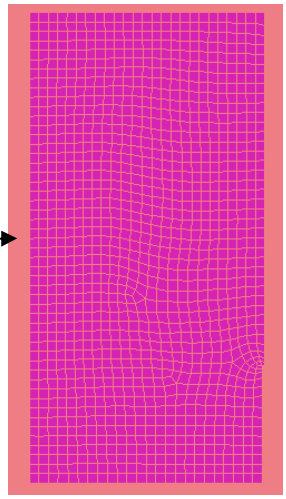

Figure 2. finite element model of specimen

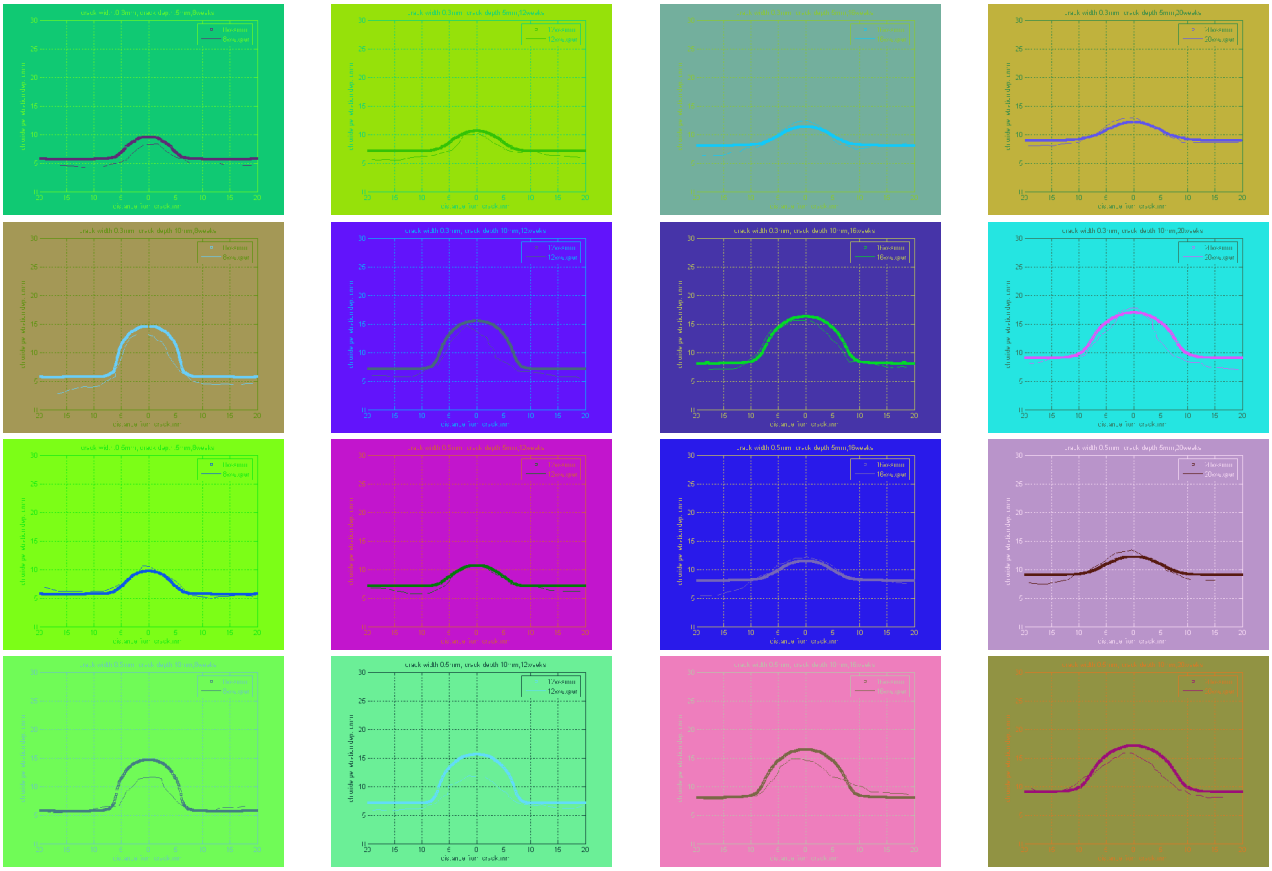

Figure 3. the comparison of chloride penetration depth between simulation results and experiment results

As shown in figure 3, the simulation results generally agree well with experiment result. The chloride penetration depths are overall symmetrical with crack. With increasing of crack width and crack depth, chloride penetration depth increases. At initial age of immersion, cracks significantly contribute to chloride penetration depth. Given a certain crack width and depth, with time elapsing, the difference of chloride penetration depth between cracked zone and uncracked zone gradually decreases. The shape of chloride penetration contour changes from convex curve line in early age to horizontal straight line in late age.

Conclusions

This paper presents a model about chloride penetration in cracked concrete when the cracks were artificially realized as notches. Based on hydration model, the diffusivity of concrete without crack is obtained. Furthermore, based on cracks distribution in cracked concrete and finite element methods, the penetration depth of chloride ions in cracked concrete is predicted.

Acknowledgements

This work was supported by Sustainable Building Research Center of Hanyang University which was supported by ERC program of Ministry of Education, Science Technology (#R11-2005-056-04003-0) and Standard Technology Improvement Project supported by Ministry of Knowledge Economy(#2007-000-0000-6365).

References

[1]Kejin Wang, Daniel C.Jansen, Surendra P.Shah, permeability study of cracked concrete, cement and concrete research, Vol.27, 1997, pp.381-393

[2]Corina-Maria Aldea, Surendra P.Shah, Alan Karr, effect of cracking on water and chloride permeability of conrete, journal of materials in civil engineering, vol.11,1999,pp.181-186

[3]Olga Garces Rodriguez, R.Doug Hooton, influence of cracks on chloride ingress into concrete, ACI materials journal, vol.100, 2003, pp.120-126

[4]B.Gerard, J.Marchand, influence of cracking on the diffusion properties of cement-based materials Part I: influence of continuous cracks on the steady-state regime, cement and concrete research, vol.30, 2000, pp.37-43

[5] influence of traversing crack on chloride diffusion into concrete, A.Djerbi, S.Bonnet, A.Khelidj, V.Baroghel-bouny, cement and concrete research, doi:10.1016/j.cemconres,2007.10.007

[6] Xiaoyong Wang, Hanseung Lee, Kibong Park, Numerical simulation of heat evolution of eco-friendly blended portland cements using a multi-component hydration model, Materials Science Forum Vol. 569(2008)pp.257-260

[7] Xiao-Yong Wang, Han-Seung Lee, Seung-Min Lim. Numerical Simulation of Autogenous Shrinkage of Eco-friendly Blended Portland Cements Using A Multi-Component Hydration Model Materials Science Forum Vol. 569 (2008) pp. 261-264

[8] Ki-Bong Park, Takafumi Noguchib, Joel Plawsky.Cem Concr Res 2005;35(9):1676– 1684

[9]Byung Hwan Oh, Seung Yup Jang, cement and concrete research, 2000, Vol.34, 2004, 463-480

[10]Sang-Hun Han, construction and building materials, 2007, Vol.21, 370-378

[11]G.De Schutter, magazine of concrete research, 1999, pp.427-435

Key Engineering Materials Vols. 385-387 (2008) pp 665-668
© (2008) Trans Tech Publications, Switzerland
doi:10.4028/www.scientific.net/KEM.385-387.665

An Experimental Study on the Application of Cathodic Protection Method Applying Zn-Al Metal Spray on the RC structure

Manhae Han[1,a], Hanseung Lee[1,b]

[1]School of Architecture & Environmental Engineering, Hanyang University, Ansan, 425-791, Korea

[a]hide8945@hanyang.ac.kr, [b]ercleehs@hanyang.ac.kr

Keywords: Cathodic Protection Method, Metal spray, Half-cell potential

Abstract. Cathodic Protection Method was introduced as a corrosion protection method of metals under the ground or sea. Since 1970, it was applied to corrosion protection method of reinforced concrete structures. After 1990, this method has been used around the world, and its usability was proved. But this method has some problems on the aspect of construction and economy. In order to solve these problems, Cathodic Protection Method by using high durable metal spray was developed. First, the specimen was covered with anodic materials (Zn, Al) by using metal spray. And a performance of corrosion protection was confirmed by measuring corrosion current and half-cell potential of specimen. Through the result of experiment, it is possible to know that Cathodic Protection Method by using high metal spray is good protect to corrosion on reinforced concrete structures.

Introduction

Steel and concrete have become the most common materials for man-made structures over the last hundred or so years with the use of the composite material, concrete reinforced with steel, becoming one of the most popular methods for construction. Until the 1950s it was assumed that when steel was encased in the alkaline concrete matrix, neither would suffer from any degradation for the indefinite future. However, evidence of degradation was noted as early as 1907 where it was observed that chlorides added to concrete could allow sufficient corrosion of the steel to crack the concrete. The implicit assumption to this day by many engineers of reinforced concrete's virtually infinite durability has proven to be true in several cases, with structures reaching their design lives without any evidence of structural degradation. However, it is now evident that in areas where there is an aggressive atmosphere, the concrete can be damaged or the steel can corrode in a dramatically shorter time period than that specified as a design life.[1]

The traditional use of cathodic protection has been to prevent corrosion of steel objects in the ground or water and this is still its most common application. It is now almost universally adopted on ships, oil rigs and oil and gas pipelines. Over the last 50 years cathodic protection has advanced from being a black art to something approaching a science for these applications. Over the past 30 or so many years there has been a steady increase in the use of cathodic protection for the rehabilitation of reinforced concrete structures which are exhibiting signs of distress. The most common damage mechanism is chloride-induced corrosion of the steel reinforcement and this is normally what cathodic protection systems are intended to stop.[1]

In this study, electrode formation method through Zn-Al metal spraying was presented to assure constructional and economic performance of cathodic protection method.

Principle of Cathodic protection (sacrificial anode method)

Sacrificial anode method is natural method of cathodic protection that protect to reinforced rebar through corroding another metal (Its potential is lower than steel) instead of reinforced rebar. Fig. 1

is overview of sacrificial anode method. If reinforced steel is connected with sacrificial anode that is installed on the concrete surface, then as current passes naturally by potential difference between two metals, and the electron is supplied to reinforced steel. Fig. 2 is polarization of sacrificial anode method. When there is no sacrificial anode (Zn-Al), point B move to point C by anode-polarization. In a part of reinforced rebar surface, point A move to point C by cathode-polarization. It is a corrosion potential (Ecorr, Fe) and current density(Icorr, Fe) of reinforced rebar. When there is sacrificial anode (Zn-Al), point E move to point D by anode-polarization. And corrosion potential in point C move to point D. On the surface of metal Zn, very strong current was passed. On the surface of rebar, point C move to point B by depolarization. So corrosion current was reduced and then corrosion was stopped.[2]

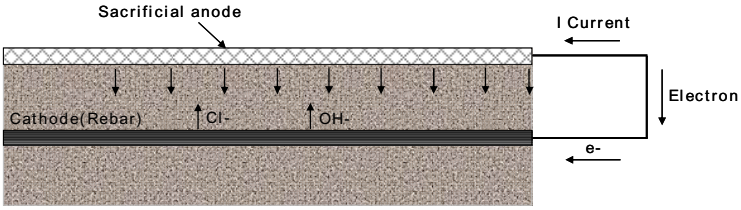

Fig. 1 Overview of sacrificial anode method

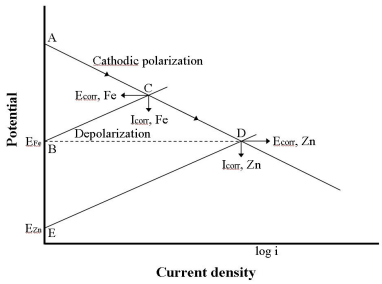

Fig. 2 Polarization of sacrificial anode method

Zn-Al metal spray

A number of cathodic protection systems have used metal spray method (Al, Zn, Ni and Ti) as the anode material. To achieve electrical connection between the DC positive cables and the anode, primary anodes are required. The earlier primary anodes were brass or copper stud plates fixed to the concrete surface using an epoxy bedding layer which acted as an electrical barrier to prevent current dumping and consumption of the plates. The metallized spray was applied directly onto the stud plate primary anode and the abrasively blast-cleaned concrete surface.

Of the metallized coatings tried, zinc (Zn) proved to have the best adhesion characteristics and appears to be the most appropriate metallized anode material. So in this study, Zn-Al metal was selected as a material of metal spray.

Metallizing is a technique which utilizes a metal or metal alloy in the form of a wire or powder, melting it into a liquid form, which is then sprayed onto the surface by compressed air. Flame spray is a method using a hand-held gun through which feeds a metal wire. The wire is melted by an oxygen acetylene gas flame and blown onto the concrete surface by compressed air where it solidifies into a continuous metallized film.[1]

Fig. 3 Zn-Al metal spray.

Experiment

Overview of experiment. To confirm corrosion protection performance of Zn-Al metal spraying method on the RC structure, make specimens and measured half-cell potential and corrosion current.

Specimen's condition and method of experiment. Table 1 shows composition of experiment by variable of each specimen. Covering depth of specimens is 15, 30 and 40mm. It is to confirm corrosion protection performance by covering depth of reinforced rebar. Also, metal spraying and chloride ion inclusion are variable of experiment. Size of specimen is 100×100(90)×180mm. Height does changelessly under reinforced rebar, and covering depth differed. Specimen did water curing during 28 days after placing. And then it coated by epoxy over whole surface except metal spraying side and the opponent side. After spraying pre-former, did metal spraying. Attach metal for connect electric wire, and then did air dried curing during 1 day. After make specimens, and moisturizing by 3% NaCl solution. And then take out from the solution, measure a half-cell potential and corrosion current density.

Table 1 Composition of experiment by variable of each specimen

Name	Cover depth	Metal spray	Cl^- ion	Name	Cover depth	Metal spray	Cl^- ion
N10	10cm	X	0 kg/m^3	NS10	10cm	○	1.2kg/m^3
N20	20cm	X	0 kg/m^3	NS20	20cm	○	1.2kg/m^3
N40	40cm	X	0 kg/m^3	NS40	40cm	○	1.2kg/m^3
C40	40cm	X	0 kg/m^3	C4S0	40cm	○	1.2kg/m^3

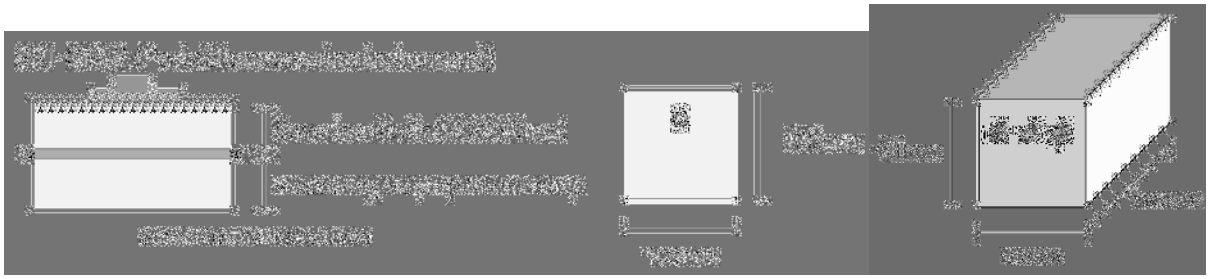

Fig. 4 Shape of specimen

Result and discussion

To confirm corrosion protection performance of Zn-Al metal spraying method, planed an experiment. Make specimens, and moisturizing by 3% NaCl solution, measure a half-cell potential and corrosion current density. But it is impossible to measure a half-cell potential because of effect of Zn-Al metal. On the table 2, it is very wrong data in case of specimen which is executed metal spraying. So, to confirm corrosion protection performance of Zn-Al metal spraying method, compare a current density on each condition.(moisture, dry)

Table 2 Half-cell potential

Name	Half-cell potential(mV)
N10	-231
N20	-204.2
N40	-173
C40	-212.6
NS10	-769.4
NS20	-694.0
NS40	-949.4
CS40	-870.8

Table 3 Current density by measuring condition

Data	Dry condition	Moisture condition
Voltage (V)	0.018	0.111
Resistance (Ω)	100	100
Current (A)	0.00018	0.00111
Current density (μA/㎠)	1	6.17

On the table 3 and fig. 5, current density in moisture condition is higher than in case of dry. It is a result that water of concrete inside is used as electrolyte. Because of this electrolyte, current of concrete inside is flowed well. Thus, metal spray cathodic protection method is good to apply to seaside structure.

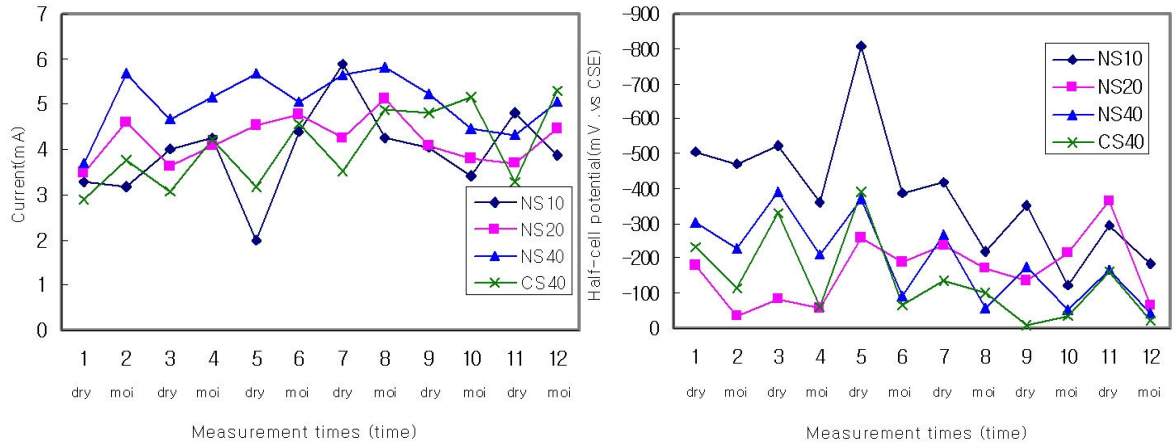

Fig. 5 Corrosion current and Half-cell potential on the different condition

Summary

Existent corrosion protection method has some problems on the aspect of construction and economy. In order to solve these problems, cathodic protection method by using high durable metal spray was developed. Make specimens, and measure a half-cell potential and corrosion current density. But it is impossible to measure a half-cell potential because of effect of Zn-Al metal. Accordingly, another method is necessary for confirm to corrosion condition.

In the meantime, to confirm corrosion protection performance of Zn-Al metal spraying method, measured corrosion current. And confirm difference of current density on each condition (moisture, dry). Thus, it is possible to know that metal spray method can apply on reinforced concrete structure. Also, because of high current density on moisture condition, metal spray cathodic protection method is good to apply to seaside structure.

Acknowledgement

This work was supported by Sustainable Building Research Center Hanyang University which was supported the SRC/ERC program of MOST (#R11-2005-056-04003-0) and the Center for Concrete Corea (05-CCT-D11), supported by Korea Institute of Construction and Transportation Technology Evaluation and Planning (KICTTEP) under the (MOCT).

Reference

[1] Chess Paul, 1998. “Cathodic protection of steel in concrete”, London U. K., E & FN Spon.
[2] Kim, K.J., Lee, M.H. and Moon K.M., 2006. “Principle and Application of Cathodic Protection for Concrete structures”, September, Korea Concrete Institute(KCI) journal.

Key Engineering Materials Vols. 385-387 (2008) pp 669-672
© (2008) Trans Tech Publications, Switzerland
doi:10.4028/www.scientific.net/KEM.385-387.669

Thermographic Investigation of Hot Spots in Railway Brake Discs

Jeongguk Kim[1, a], Byeong-Choon Goo[1, b], Sung-Cheol Yoon[1,c] and Sung-Tae Kwon[1,d]

Railroad Safety Research and Testing Center, Korea Railroad Research Institute,adder

360-1 Woulam, Uiwang, Kyunggi, South Korea 437-757

[a]jkim@krri.re.kr, [b]bcgoo@krri.re.kr, [c]scyoon@krri.re.kr, [d]stkwon@krri.re.kr

Keywords: Hot spots, Railway brake disc, Infrared thermography

Abstract. Damage evolution due to generation of hot spots on railway brake disc was investigated using the infrared thermography method. A brake disc with gray cast iron, which is currently used in Korea, was employed for this investigation. A high-speed infrared camera was used to measure the surface temperature of brake disc as well as for in-situ monitoring of hot spot evolution. From the thermographic images, the observed hot spots and thermal damage of railway brake disc during braking operation were qualitatively analyzed. Moreover, in this investigation, the previous experimental and theoretical studies on hot spots phenomenon were reviewed, and the current experimental results were introduced and compared with theoretical prediction.

Introduction

As increases in the speed of train, the brake system has been recognized as a critical and important part for modern railway applications. In general, several types of braking methods could be possible for commercial applications; tread brake and disc brake, which utilizes the adhesive power between wheel and rail; hydrokinetic brake, rheostatic brake, regenerative brake, magnetic brake, and linear eddy current brake, which are operated by hydraulic cylinder or other electrical methods. Generally, the cutting edge technologies for brake system include system design and control, performance analysis and testing and/or evaluation of brake system, and materials related technologies, such as brake disc and pads.

In this investigation, the disc brake system is considered, and the system is composed of several components, such as brake disc, brake pad, brake cylinders, etc. Among those parts, the brake disc plays an important role in terms of enhancement of the brake ability. However, damage evolution due to generation of hot spots on railway brake disc has been considered the main degradation mechanism in brake disc. Therefore, the understanding of hot spots, also called 'hot judder,' which is undesirable low frequency vibrations developed by non-uniform contact area between brake pad material and brake disc, is important for a better understanding of material design as well as enhancement of materials properties in railway brake disc [1,2]. Although there is an important aspect to understand hot spot phenomena in railway brake system, so far, not much attention has been given to the research of this field.

Infrared (IR) Thermography is a powerful NDE technique for the characterization of thermal phenomenon in engineering components and/or systems including engineering materials. The use of an infrared (IR) camera can provide rapid, non-contact scanning of surfaces, components, or assemblies [3]. The high-speed IR camera provided the measurement of temperature change during brake operation as well as the images of temperature contour on the brake disc surface in this investigation.

Therefore, the main objectives of this investigation are to understand the hot spot phenomenon on the railway brake disc, provide the previous research and study on hot spot of railway brake disc, and investigate the temperature evolution during brake operation in railway brake disc, which is currently employed for Korean railway operation.

Previous Research Activities and Experimental Procedures

The Hot Spot Phenomenon on Brake Disc. The hot spot phenomenon has extensively investigated mainly in the field of automotive research [1,2,4]. Normally, a sliding system operates under uniform pressure and temperature distribution on the friction surface [1,4]. However, when sliding speed reaches a certain critical value called *critical speed*, the contact load is concentrated in one or more small regions of the friction surface. This leads to the forming of localized high temperature contact regions known as *hot spots*. The resulting interaction of frictional heat generation, thermoelastic distortion, and elastic contact, is known as frictionally excited thermoelastic instability or TEI [5]. This phenomenon is observed in many practical sliding systems and, in particular, many experimental studies have been conducted on the hot spot formation in automotive and industrial disk brakes [6]. Severe hot spotting may cause the harmful martensitic transformation [6] and induce the low frequency vibration called brake judder in automotives [4,6].

Current research activities include theoretical studies to predict the critical speed of the automotive disk brake systems [1,2], finite element techniques to perform a stability analysis of a disk [2], and simulation research on a nonlinear transient behavior of a disk [1,2].

Based on leading research on hot spot phenomena in automotive rotors, recently, an eminent research advancement in railway areas has been accomplished [7-9]. Painer Et al. have investigated on an experimental research of hot spots in railway disc brakes [7]. In their research, high-speed infrared camera was employed to investigate detailed damaging thermal gradients, called macroscopic hot spots (MHS). Moreover, a scenario of hot spots occurrence was suggested step by step, and the influence of parameters including pad stiffness and pad contact length on hot spots development was quantitatively studied. Figure 1 presents thermographic image showing the high thermal gradients, and Painer Et al. have suggested that this stage was considered as major in the mechanisms of disc failure [7]. Generally, at a MHS site could be a crack initiation site, which shows the craystalline structure change with martensite formation. Martensite usually may produce severe local strains due to a specific volume change. Therefore the control of hot spots in brake disc during brake operation is an important stage to avoid premature failure of brake discs.

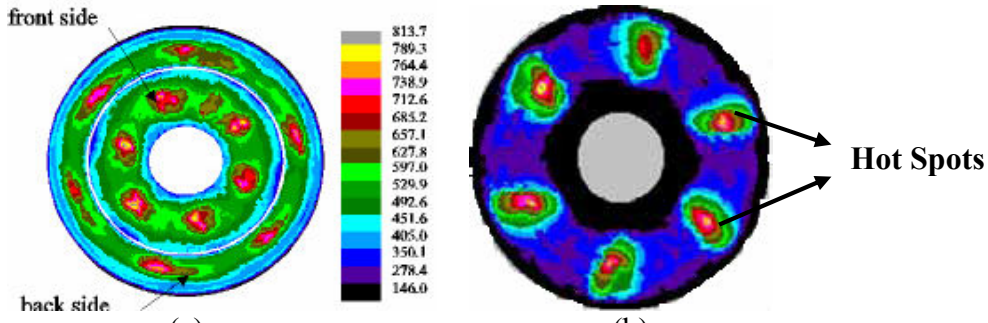

Figure 1. Thermographic images of brake discs (a) simultaneous thermographic images of the two sides of the disc and (b) thermographic image showing macroscopic hot spots [7].

Experimental Procedures. Thermal evaluation has been conducted with state of the art infrared camera, as well as single point detectors, to observe the non-uniform temperature distributions on the brake disc sureface during braking operation. Conventional thermal image cameras are not capable of resolving the hot spots occurring on an operating brake system. Special modifications to a relatively recent technology, thermographic imaging, allows observation of the operating brake system and provides confirmation of temperature fields which correlate with torque variation during test.

The braking tests were performed with a full-scale (860 mm in diameter) dynamomer available at Korea Railroad Research Institute (KRRI) as shown in Figure 2. A brake disc with gray cast iron, which is currently used in Korea commercially, was employed for this investigation. In front of

dynamometer, a high-speed infrared camera was used to measure the surface temperature of brake disc as well as for in-situ monitoring of hot spot evolution.

The characteristics of IR camera for the current investigation include the maximum speed of 400 Hz full frame maximum frame rate. The focal plane arrays show up to 320×256 pixels, the spatial resolution is about 5.4 μm, and the temperature resolution is as sensitive as 0.015°C at 24°C . The calibration of the IR camera was achieved before dynamometer tests. The brake disc was heated up to 90°C using a heat gun, and then, cooled in air. A thermocouple was attached on the brake disc, and measured the surface temperature of the brake disc when the disc was cooling down from heated condition. Different temperatures with every 5°C were read from the thermocouple during cooling. The calibrated intensities of the IR camera were used to generate temperature maps. For IR camera calibration of this investigation, the IR camera was used at a speed of 100 Hz.

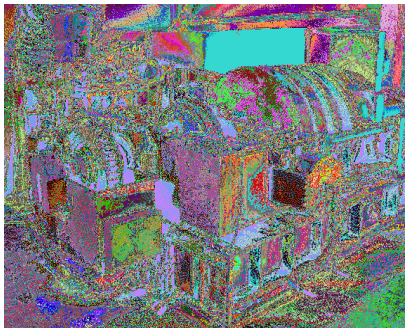

Figure 2. The full scale brake dynamometer available at KRRI.

Current Activities on Hot Spot Investigation during Brake Operation

Figure 3 exhibits the infrared thermographic views of brake disc surface showing hot spots or thermal band (a) with clear view and (b) with reference index. The braking operation was achieved at 150 km/h, and the IR images were taken to analyze the temperature evolution.

From the thermographic image, Fig. 3(a), the analysis of temperature evolution during braking operation was performed. Figure 3(b) shows the temperature evolution during braking operation with 5 interesting positions.

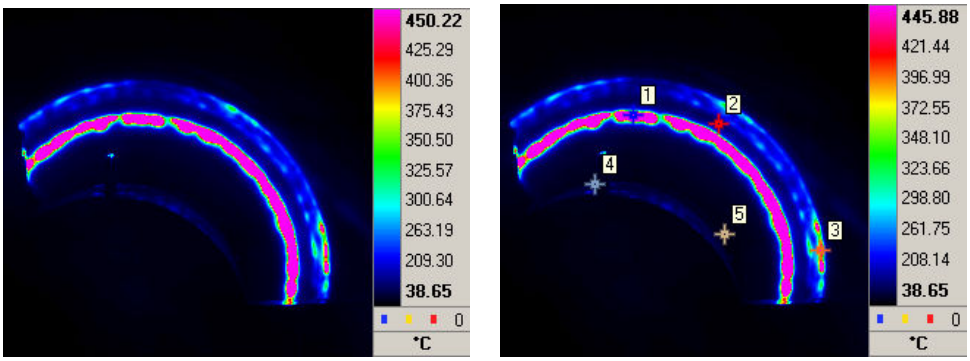

(a) (b)

Figure 3. Infrared thermography views of brake disc surface showing hot spots or thermal band (a) with clear view and (b) with reference index

In Figure 4, the temperature evolution during braking operation was obtained from 5 interesting positions. As expected from Fig. 3(b), the points 1 and 3 showed much higher values of temperature distribution as compared with any other points, which were located at out of hot spot or thermal band, as shown in Fig. 3(b). Moreover, temperature evolution in terms of elapsed time during brake operation was clearly presented with minor temperature changes on disc. Although this preliminary results show very limited information of quantitative analysis in hot spot, it could be understood that

infrared thermographic detection of hot spot images might be a powerful technique for further investigation of hot spots phenomenon in railway brake disc.

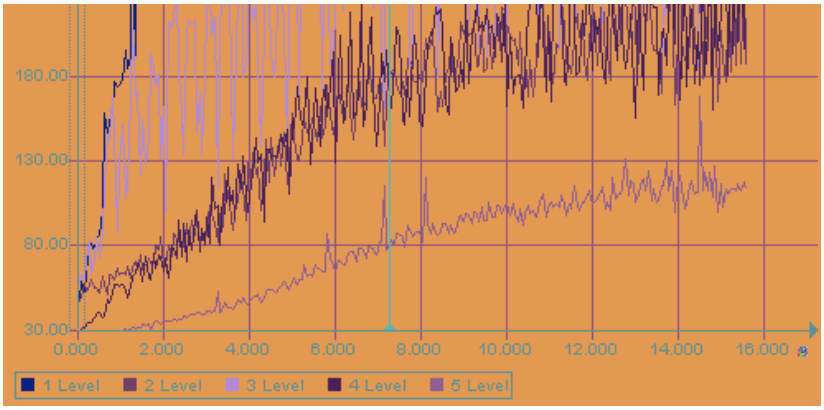

Figure 4. The temperature evolution during braking operation with 5 difference positions on brake disc obtained from Fig. 3. Note that the color indexes indicate the 5 interesting positions with the temperature ranges of 30°C to 250°C.

Summary

The current research on thermographic investigation of hot spots in railway brake disc leads to the following conclusions; Infrared thermography could be an effective way for the investigation of railway brake disc hot spot phenomena since high-speed infrared camera could provide rapid and non-contact scanning of railway brake disc surfaces. The previous research and study on railway brake disc were briefly introduced in addition to the current research on automotives. The temperature evolution during brake operation in brake disc, which is currently employed for Korean railway operation, was introduced, and it was confirmed that the necessity of infrared thermographic images for the investigation of hot spot phenomenon in railway brake disc.

References

[1] K. Lee and F.W. Brooks, Journal of Tribology, Vol. 125, 44-51, 2003.

[2] Y. Lee, H. Cho, C. Cho, C.B. Kim, ATEM'07, JSME-MMD, Sep. 12-14, 2007. (a CD ROM).

[3] J. Kim and P.K. Liaw: J. Eng. Mater. Technol, 2005, vol. 127, pp. 8–15.

[4] K. Lee and R.B. Dinwiddie, SAE 98PC-392, 1998.

[5] J.R. Barber, "Thermoelastic Instabilities in the Sliding of Conforming Solids," Proc. R. Soc. London, Ser. A, 312, pp. 381-394, 1969.

[6] Anderson, A. E., and Knapp, R. A., 1990, ''Hot Spotting in Automotive Friction Systems,'' Wear, **135**, pp. 319–337.

[7] S. Panier, P. Dufrenoy, D. Weichert, An experimental investigation of hot spots in railway disc brakes, Wear 256 (2004) 764-773.

[8] P. Dufrenoy, Two-/three-dimensional hybrid model of the thermomechanical behavior of disc brakes, Proc. Instn Mech. Engrs Vol. 218 Part F: J. Rail and Rapid Transit, 17-30 (2004).

[9] G.Degalaix, P. Dufrenoy, J. Wong, P. Wicker, and F. Bumbieler, Failure Mechanisms of TGV Brake Discs, Key Engineering Materials, Vols. 345-346 (2007) pp. 697-700.

Key Engineering Materials Vols. 385-387 (2008) pp 673-676
© (2008) Trans Tech Publications, Switzerland
doi:10.4028/www.scientific.net/KEM.385-387.673

Experimental Study on the Flexural Fatigue Damage Evolution of Layered Fiber Reinforced Concrete

WANG Ji[1,a] , ZHANG Ming-zhong[2,b] , FAN Xiao-chun[3,c]

[1]Senior Engineer, The Design and Research Institute, Wuhan University of Technology, No.122, Luoshi Road, Wuhan, 430070, China.

[2]Postgraduate, School of Civil Engineering and Architecture, Wuhan University of Technology, No.122, Luoshi Road, Wuhan, 430070, China.

[3]Doctor, School of Civil Engineering and Architecture, Wuhan University of Technology, No.122, Luoshi Road, Wuhan, 430070, China.

[a]hmywj@263.net, [b]zmzfj@126.com, [c]fxc-free@whut.edu.cn

Key words: layered steel fiber reinforced concrete(LSFRC); layered hybrid fiber reinforced concrete(LHFRC); flexural fatigue; damage

Abstract: In order to study the damage evolution law for layered fiber reinforced concrete subjected to flexural fatigue, the flexural fatigue tests were carried out on both layered steel fiber reinforced concrete(LSFRC) and layered hybrid fiber reinforced concrete(LHFRC) beams of which the type of steel fiber was uniform on the same concrete mix. At the same time the flexural fatigue tests with original concrete(OC) were carried out. Based on the experiments, both flexural fatigue life and damage characteristic of LSFRC LHFRC and OC were compared and analyzed. The results indicated that the fatigue life of LHFRC was a little larger than that of LSFRC under the stress level, which was more than an order of magnitude of OC. And the fatigue distortion of LSFRC, LHFRC and OC were similar. They all followed three-phase law. However, the proportion of every phase was different, which proved that layered steel fibers and polypropylene fibers could effectively restrain the degradation of concrete.

1 introduction

In recent years, steel fiber reinforced concrete which was made through mixing short steel fiber in concrete, were getting in-depth research and extensive application[1]. However, integral steel fiber reinforced concrete had many problems, such as difficult agitation uniform, easy cohering, large dosage, high cost and so on, which had limited the development of steel fiber concrete. LSFRC was made by artifical symmetrical sprinkling the determinate number of steel fiber at the area 2cm away from the top and bottom of the panel. Thus mixing a few of steel fiber not only improved the flexural intensity, toughness and fatigue performance but also enhanced the utilization ratio of material and reduces the cost at the same time[2]. Layered hybrid fiber reinforced concrete(LHFRC) was made by adding organic fibers with uniform distribution into steel fiber reinforced concrete. So, it was the improvement of layered steel fiber reinforced concrete.

For civil engineering, such as road surface, bridge surface, railway sleeper and so on, steel fiber reinforce concrete mainly supported flexural fatigue load. Therefore, research on the fatigue property was very important. At present, the research relating to fatigue life and damage characteristic of LSFRC and LHFRC under flexural fatigue load was rare. So, in this paper, based on flexural fatigue tests, the fatigue life and damage characteristic of LSFRC and LHFRC under different stress levels was studied. And the results were compared with those of original concrete(OC).

2 Fatigue Test

2.1 Tests Materials

The cement(C) was employed the 42.5# ordinary Portland cement. The coarse aggregate(CA) was composed of the continuously graded fine stone whose grain diameter was 5~31.5mm.; the fine aggregate(FA) was composed of medium sand and coarse sand whose fineness modulus was 2.6 and sand ratio(SR) was 34%; The water(W) content and modified polyacrylonitrile(MP) content was 152 and 1.18. The concrete mix proportion is shown in Table 1. The experimental steel fiber was arch fiber produced by WuHan DongZhou Co., Ltd, which was made of sheared steel wire. The length/diameter ratio of steel fiber was 80. Its young modulus was 200GPa and its tensile strength was 630Mpa. The main parameters of modified polyacrylonitrile produced by the Shenzhen Development Co., Ltd, were shown in table 2.

Table 1 Concrete Mix Proportion

*C*42.5# / $kg \cdot m^{-3}$	*CA* / $kg \cdot m^{-3}$	*FA* / $kg \cdot m^{-3}$	*W* / $kg \cdot m^{-3}$	*MP* / $kg \cdot m^{-3}$	*W/C*	*C* : *FA* : *CA*	*SR* /%
330	1300	671	152	1.18	0.46	1:2.03 : 3.94	34.0

Table2 Main Parameters of Polyacrylonitrile Fiber

Diameter/μm	13~21	*Length/mm*	6±
Proportion/ $g \cdot m^{-3}$	1.18~1.2	*Color*	Light yellow
Tensile Strength/ MPa	≥950	*Crack Extending Rate*	8~20%
Young Modulus/ GPa	≥17	*Lightfastness*	well

2.2 Test Setup and Test Procedure

Groups of needed materials were calculated and weighed up according to the designed mix proportion. The mixture of stone, aggregate and 10% water was poured into revolving-drum concrete mixer and mixed round in it for 30s; then the cement was added in and mixed with them for another 30s; then the remanent water and polyacralonitrile were added in the above mixture and mixed together for 3min. After these processes, the mixed synthetical fiber concrete was produced. It was filled into the steel test mold for three times. The size of steel test mold was 150mm×150mm×550mm. The steel fibers whose volume ratio was converted with 2cm width were respectively sprinkled at the upper and lower level by hand; the mix ratios of steel fibers for upper and lower level were 1.0% and 1.5%. The position of mixed steel fibers was respectively 2cm away from the bottom and jaws of the mold. Subsequently, the specimens were vibrated on shake table; the thick liquid was charged and the mortar was striked off. Thus the tested specimens were set up after stripping. They were unified in serial number and maintained in the standard curing room for 90 days.

2.3 Test Method

According to test method used for steel fiber reinforced concrete(CECS13:89), the machine used for this test was electric liquid servo omnipotent testing machine(Instron1341) produced by the British Instron corporation. The loading rate of Instron1341 was 0.2mm/min. The three point loading test method was used to measure the flexural intensity of tested specimens; in the fatigue test, the flexural intensity of static loading was regarded as a consulting value for the tests of four different stress levels. The four stress levels were 0.90, 0.85, 0.80 and 0.75. In the test, the loading characteristic value of circulation ρ was 0.1.

3 Test Results and Analysis

3.1 Test Results

The average fatigue life of LSFRC, LHFRC and OC under different stress level were listed in Table 3. And the relation curves of maximum strain were listed in Fig.1 and Fig.2.

Table3 Fatigue life of LSFRC, LHFRC and OC under different stress levels

S / Fatigue number	0.75	0.80	0.85	0.90
LSFRC (1)	485280	89728	11006	411
LHFRC (2)	506466	125568	11382	488
OC	45801	15475	872	121
(2)/ (1)	1.04	1.40	1.03	1.19

3.2 Results Analysis

3.2.1 Analysis of Fatigue Life

From Table 3, it could be seen the fatigue life of LSFRC and LHFRC was more than an order magnitude of OC under the same stress level. This showed that the fatigue property of LSFRC and LHFRC were obviously better than that of OC. With the same of mix proportion, steel fiber content and length-diameter rate, the average fatigue life of LHFRC was longer than that of LSFRC under all fatigue stress levels. That was the result of the hybrid composites effects of polyacrylonitrile fiber. This result was according with the former, which indicated organic fiber could improve flexural toughness resistance and fatigue properties of layered reinforce concrete.

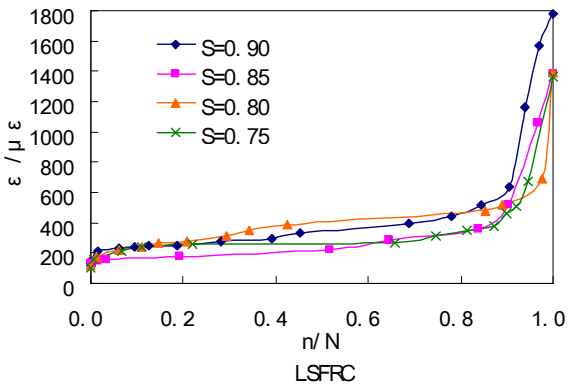

Fig. 1 Relation curve of LSFRC

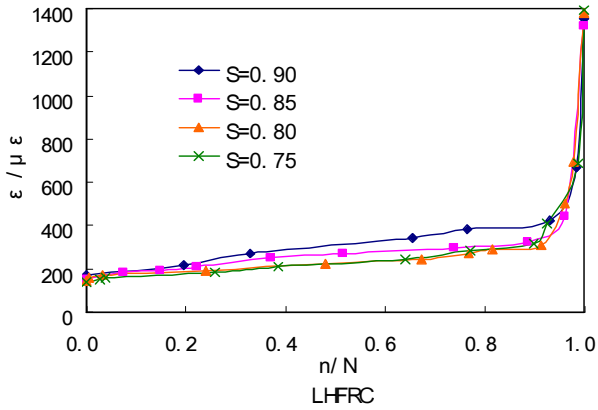

Fig. 2 Relation curve of LHFRC

3.2.2 Damage Analysis

The strain of general engineering material changing with circle times followed three-phase law under circle load. As shown in Fig 3, the three phases were: I. formative phase of inner damage; II. stable crack growth phase of inner damage; III. instability development of inner damage. In Fig 3, at the end of first phase, the ratio between circle number nA corresponding to point A and total circle number N was k_1. At the end of second phase, the ratio between circle number nB corresponding to point B and total circle number N was k_2.

As to OC, k_1 was about 0.1 and k_2 was about 0.9. The second stable crack growth phase was about 80% of total fatigue life. For traditional steel fiber reinforced concrete, k_1 was about 0.05 to 0.1, k_2 was about 0.9 to 0.95[3]. According to literature [4] about compress fatigue test result of SFRC, steel fiber had crack-resistant function. And steel fiber prolonged damage evolution phase of inner damage and the second phase. So k_1 was about 0.2 to 0.22 and k_2 was about 0.9 to 0.95.

From Fig.1 and Fig.2, it could be seen, fatigue evolution law of LSFRC under fatigue load

could be divided into three phases. In the first phase, fatigue strain increased rapidly, the speed of increase reduced gradually. And this phase was about 5% of total fatigue life. In the second phase, the increase of fatigue strain with fatigue life was almost uniform. And this phase was about 85% of total fatigue life. After coming into the third phase, fatigue strain increased quickly. As a result, it finally led to the instable failure. This phase was about 10% of total fatigue life. Compared with LSFRC, fatigue evolution law of LHFRC was different. In the first phase, the fatigue strain was about 5% of total fatigue, which was smaller than LSFRC. And fatigue strain increase rapidly. The second phase was about 90%. In the third phase, the fatigue strain increased fast, which eventually resulted in the destruction of specimens. And it was about 5%.

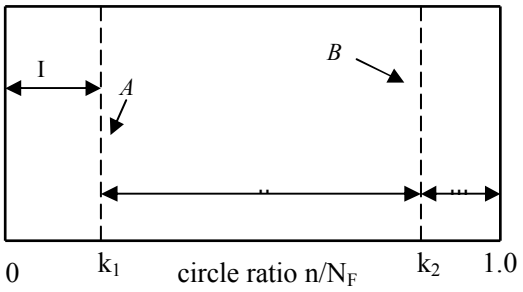

Fig.3 The three-phase development curve of strain along with circle ratio

Compared LSFRC with LHFRC, it could be seen that fatigue strain phases of LSFRC were more obvious, and fatigue strain curve in the first phase of LHFRC was not obvious. The proportion of the second phase of total fatigue life was bigger than the LSFRC. This phase curve was a more gentle line, and proportion of the line was bigger than that of LSFRC. In this phase, the most of energy was absorbed by the steel fiber and organic fiber in the micro-cracks. Because organic fiber and steel fiber had excellent ductility, the line of second phase was longer and more straight. During this period, the performance of the specimen was without any macro-cracks. With the increase of the cycle number, synthetic and steel fibers among the cracks were gradually pulled out or fatigue damage, for having reached the limit of fatigue. And then, the micro-cracks were rapidly extended and run-through. With the appearance and expansion of macro-cracks, the specimens were quickly destroyed.

4 Conclusions

In this paper, based on the flexural fatigue experiments, fatigue damage properties of LSFRC, LHFRC and OC were studied. The following conclusions were gained.

(1) Compared with OC, the fatigue life of LSFRC and LHFRC were more than an order of magnitude under the same stress level. And fatigue properties of LSFRC and LHFRC were better.

(2) Compared with LSFRC, the fatigue life of LHFRC was a little larger under the stress level, which indicated layered steel fibers and polypropylene fibers played positive hybrid effect.

(3) The fatigue distortion of LSFRC, LHFRC and OC were similar. They all followed three-phase law. However, the proportion of every phase was different.

(4)Layered steel fibers and polypropylene fibers could effectively restrain the degradation of concrete.

References

1 Zhao Guofan, Peng Shaomin, Huang Chengkui, in: *Steel Fiber Reinforced Concrete Structure*,edited by China Architecture and Building (1999), in press.

2 Yuan Haiqing, Chen Jingtao, Zhu Jidong:submitted to Journal of Wuhan University of Technology-Materials Science (2003)

3 Byung Hwan Oh: submitted to ACI, (1992)

4 Yi Cheng, Shen Shizhao, Xie Heping: submitted to Engineering Mechanics (2002)

Key Engineering Materials Vols. 385-387 (2008) pp 677-680
© (2008) Trans Tech Publications, Switzerland
doi:10.4028/www.scientific.net/KEM.385-387.677

Analytical Study on the Chloride Ion Permeation of Reinforced Concrete Repaired by Finishing Material

Sunyoung Yun[1, a], Sangheon Shin[1, b], Hanseung Lee[1, c]

[1]School of Architecture & Environmental Engineering, Hanyang University, Ansan, 425-791, Korea

[a]heath83@hanyang.ac.kr, [b]ssh8065@hanyang.ac.kr, [c]ercleehs@hanyang.ac.kr

Keywords: Diffusion coefficient, Chloride ion, Concrete repair material, Durability design

Abstract. When the RC structure degraded in sea environment, chloride ion is one of the most important factors of degradation. Therefore, the purpose of this analytical study is measuring diffusion coefficient of patching repair material and the structure which repaired with patching repair material by RCPT. Also with this experimental result, Finite Element Method (FEM) is used for determining service year of building and concentration of chloride ion in the structure material. As the result of RCPT, diffusion coefficient of patching repair material is $0.44\times10^{-8}cm^2/sec$, which is 18.7% of concrete ($3.18\times10^{-8}cm^2/sec$). Meanwhile, as the result of FEM, patching repair material is effective for prevent chloride ion. When service year of normal concrete structure is 16years, on the other hand, the structure recovered 10mm of patching repair material will take 49 years to its service year. Furthermore, the result derived from equation given from JSCE predicts service year of the structure is little bit less than FEM.

Introduction

For rational construction of patching repair method which removes degraded area before fills with patching repair material, it is necessary to figure out diffusion coefficient of material or structure. However, these fields are still in the lack of research.[1 and 2] Therefore, in this study, diffusion coefficient of patching repair material is determined by experimental method: rapid chloride permeability test (RCPT). With this experimental results of material diffusion coefficient, chloride concentration by depth from structure surface is determined by finite element method (FEM) and equation suggested by Japan society of civil engineers (JSCE). Consequently, Purpose of estimation of chloride ion diffusion coefficient is to predict a risk when the rebar erode. So it is possible to figure out exact concentration of chloride ion by depth from surface to use diffusion coefficient.

Experiment

In this study, experimental method: RCPT (Rapid Chloride Permeability Test) [3] which proposed by Tang & Nilsson was done to determine diffusion coefficient of chloride ion. Table 1 shows experimental factors and levels of this experiment.

Table 1 Experimental factors and levels

Factor	Level		Voltage[V]	Name
	Thickness[mm]	Time[hr]		
Thickness of patching repair material	0	72	30	R-0-72
	10			R-10-72
	20			R-20-72
	50			R-50-72

In this experiment, 0.3M NaOH (sodium hydroxide) water solution is in anode side of experiment tool, also 3% NaCl (sodium chloride) water solution is in cathode side. 30V of voltage was applied during 72hours. Concentration depth of chloride ion was measured 3 times by vernier calipers after splitting the experimental body and spraying 0.1N $AgNO_3$ (silver nitrate). Fig. 1 shows experimental procedure.

(1) Making experimental bodies (2) RCPT (3) Spraying $AgNO_3$ (4) Measuring permeated depth

Fig. 1 Experimental procedure

Also diffusion coefficient of chloride ion was estimated by Eq. (1).

$$D = \frac{RTL}{zFU} \cdot \frac{x_d - a\sqrt{x_d}}{t} \quad [\, a = 2\sqrt{\frac{RTL}{zFU}} \cdot erf^{-1}(1 - \frac{2c_d}{c_0}) \,] \tag{1}$$

The result of RCPT was in table 2. As the result, diffusion coefficient of simple concrete body was determined as 3.18×10-8cm^2/sec, which was in the range of established data standard error. On the other side, diffusion coefficient of patching repair material was determined as 0.44×10-8cm^2/sec and this is only 18.7% of simple concrete. Furthermore, concrete body recovered 10mm of patching repair material's result was 1.45×10-8cm^2/sec; also, this is 54.4% of simple concrete. And 20mm of patching repaired concrete result was 1.02×10-8cm^2/sec, 67.9% of simple concrete.

Table 2 Result of RCPT

Name	Time[hr]	Diffusion coefficient[cm^2/sec]	Permeated depth[mm]
R-0	72	3.18×10^{-8}	39.75
R-10		1.45×10^{-8}	24.75
R-20		1.02×10^{-8}	20.80
R-50		0.44×10^{-8}	14.98

Analysis by finite element method (FEM)

To evaluate durability of RC structure, finite element method (FEM) program: Total-CPS was used. Also table 5 is description of analytical factor. When the expected service year was 30, 50, 75 and 100 years, chloride concentration was assumed as 11.0kg/m^3. At this time, diffusion coefficient was experimental result, thickness of patching repair material were 0, 10, 20 and 50mm.

Table 3 Analytical factor for FEM

Factor	Name	Patching repair material [mm]	Concrete [mm]	Diffusion coefficient[cm^2/sec]	
				Patching repair material	Concrete
Thickness of patching repair material	R-0-72	0	60	0.44×10^{-8}	3.18×10^{-8}
	R-10-72	10	50		
	R-20-72	20	40		
	R-50-72	50	10		

Fig. 2 to Fig. 5 is result of analysis by FEM. As the result, if covering depth is 3cm, point of rebar in concrete, it will take 16years to become 1.2kg/m^3(limitation quantity) of chloride ion concentration in case of simple concrete(R-0). If structure recovered by 10mm of patching repair material(R-10), service year will be 49years which is triple of simple concrete. Moreover, if thickness of patching repair material is 20mm(R-20), then 99years, patching material is 50mm(R-50), then concentration will be only 0.9kg/m^3 at the point of rebar in 100th year.

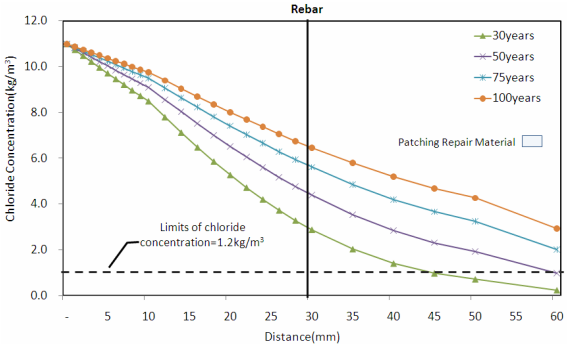

Fig. 2 Result of FEM(R=0mm)

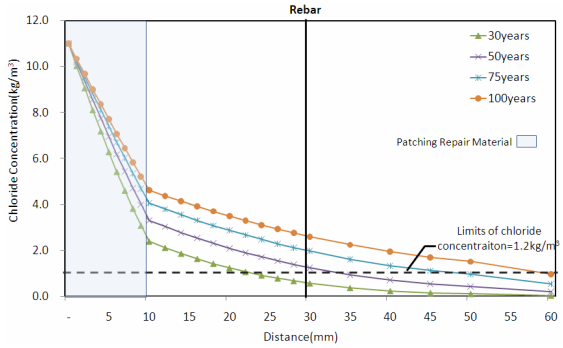

Fig. 3 Result of FEM(R=10mm)

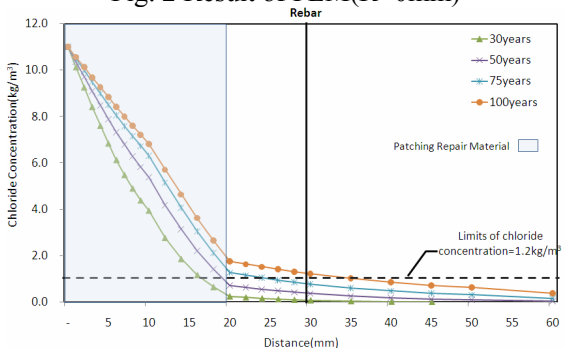

Fig. 4 Result of FEM(R=20mm)

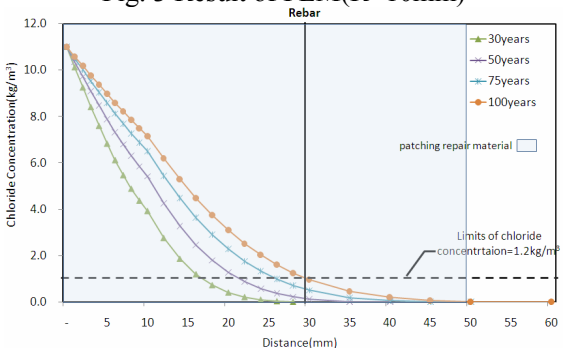

Fig. 5 Result of FEM(R=50mm)

Discussion

Eq. (2) is proposed by Japan society of Civil Engineers (JSCE).[4]

$$C(x,t) = c_0\left(1 - erf\left(\frac{0.1}{2\sqrt{t}}\right)\left(\frac{x}{\sqrt{D_c}} + \frac{c_s}{\sqrt{D_s}} + \frac{c_{b(p)}}{\sqrt{D_{b(p)}}}\right)\right) + C(x,0) \qquad (2)$$

Where, C(x,t) :Chloride ion concentration at depth of (x) and time of (t)[kg/m^3]

C_0 : Chloride ion amount at depth of (x) and time of 0

erf : Error function

c_s : Thickness of patching repair material[mm]

D_c : Diffusion coefficient of concrete[cm^2/sec]

D_s : Diffusion coefficient of patching repair material[cm^2/sec]

Results of calculation by Eq. (2) and FEM were compared with their results. According to the result, their movements were almost similar between two ways, but, concentration calculated by Eq. (2) was a little bit larger than FEM result. (Fig. 6, Fig. 7) Thus the reason of gap between two ways is occurred by different way to treat diffusion coefficient. FEM considers time effect; regarding to diffusion coefficient, it is variable and decreased by time spends. On the other hand, a diffusion coefficient is constant regardless of time effect in case of Eq. (2).

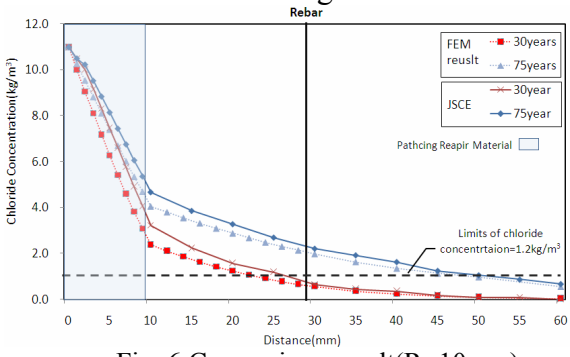

Fig. 6 Comparison result(R=10mm)

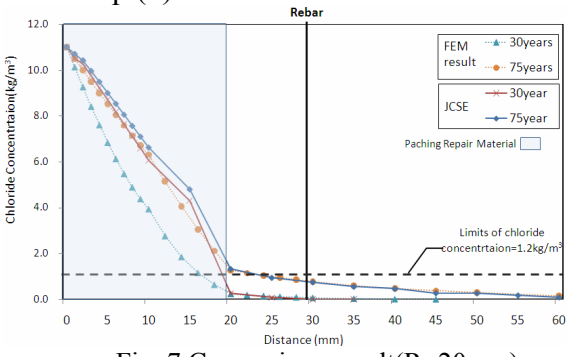

Fig. 7 Comparison result(R=20mm)

Case study

With this analytical result, practical case study was done. There were two cases, first is 19mm of patching repair material with 1mm of water paint and the other is 18mm of patching repair material and 2mm of bontile. Those two results of FEM and Eq. (2) were compared with patching repair material 0mm and 20mm cases in 50years. Also, diffusion coefficient of bontile is $0.11\times10^{-8}cm^2/sec$ and water paint is $4.95\times10^{-8}cm^2/sec$ which is according to ref. [1]. Fig. 8 is a Comparison among those FEM results. According to this, bontile was more efficient than paint. In case of painted structure, it was same or larger than patching repair material 20mm. Also Fig. 9 is comparison between FEM and Eq. (2). Regarding this, result of FEM has two inflection points at material's boundary. But result of Eq. (2) doesn't consider two different surface material, bontile (or paint) and patching repair material. However, there is only small difference at rebar point. Therefore, Eq. (2) is hard to guess diffusion of two different surface materials, but it will be possible to guess chloride concentration at rebar point.

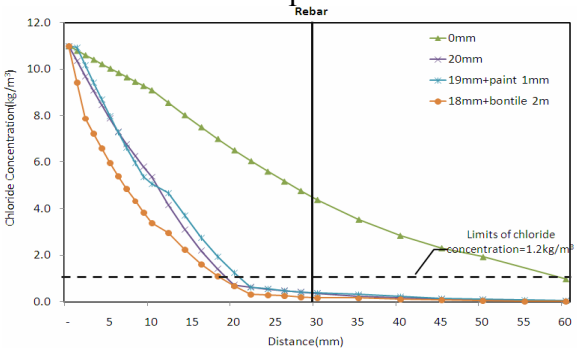

Fig. 8 Comparison result of FEM
(R=0mm, 20mm, 19mm+paint 1mm, 18mm+bontile 2mm)

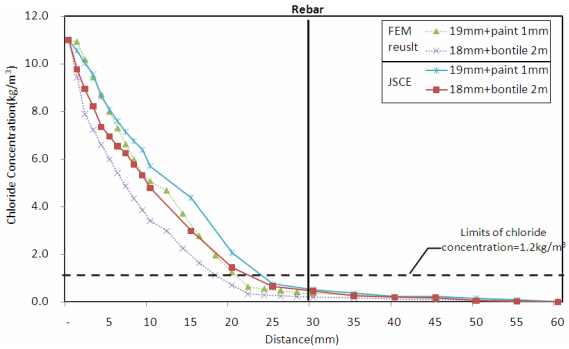

Fig. 9 Comparison result between FEM and Eq. (2)
(R=19mm+paint 1mm, 18mm+bontile 2mm)

Summary

According to the result of RCPT, diffusion coefficient of patching repair material was determined, also, concentration of chloride ion was predicted by FEM and equation with the result.

[1] Diffusion coefficient of polymer mortar cement: patching repair material is $0.44\times10\text{-}8cm^2/sec$ and this is 18.7% compared with concrete.

[2] Result of comparison between FEM result and calculated by equation which proposed by JSCE, FEM result was smaller than equation calculation. This is caused by equation does not consider time effects of diffusion coefficient.

Acknowledgements

This work was supported by Sustainable Building Research Center of Hanyang University which was supported by ERC program of Ministry of Education, Science Technology (#R11-2005-056-04003-0) and Standard Technology Improvement Project supported by Ministry of Knowledge Economy(#2007-000-0000-6365).

References

[1] W.J. Lee, D.S. Kim and H.S. Lee: *A study on the effect of resistance to the chloride ion penetration with various surface finishing materials,* Architectural Institute of Korea(AIK) 60th anniversary forum Vol. 25(1) (2005), p.p. 341-344

[2] H.S. Lee and W.J. Lee: *A Prediction of the Durability life at RC Structure with Surface Finishing Materials in Marine Environment,* AIK Journal, Vol. 22(1) (2006), p.p. 119-126

[3] L.Tang and L.O.Nilsson: *Rapid Determination of the Chloride Diffusivity in Concrete byApplying an Electrical Field,* ACI MATERIALS Journal, Jan.-Feb., (1992), p.p.49-53

[4] Japan Society of Civil Engineers(JSCE): *Construction guideline of surface protection method,* JSCE publishing, Japan, Tokyo (2005), p.p. 113-114

Key Engineering Materials Vols. 385-387 (2008) pp 681-684
© (2008) Trans Tech Publications, Switzerland
doi:10.4028/www.scientific.net/KEM.385-387.681

Experimental Study on the Water Penetration into Mortar under Water Pressure Condition

Johyeong Yoo[1, a], Hanseung Lee[1,b] ,Youngjin, Kim[2,c]

[1]School of Architecture & Environmental Engineering, Hanyang University, Ansan, 425-791, Korea
[2] Land & Urban Research Institute, Korea Land Corporation, Yusung-gu, Taejon, Korea

[a]johyeong@hanyang.ac.kr, [b]ercleehs@hanyang.ac.kr , [c]yjkim016@dreamwiz.com

Keywords: The Darcy's Law, Coefficient of seepage, Average penetration Depth, Water Penetration of Mortar

Abstract. Concrete is a type of porous materials and is physically and chemically damaged due to exposure to various environments from the placing to the service life. These reactions affect the corrosion of steel bars applied in concrete and that decreases the durability life and strength of such steel bars. Thus, it is very important to insert rust inhibitors into steel bars in the case of a deterioration element that exceeds the critical amount of corrosion in the location of steel bars. However, it is very difficult to guarantee corrosion resistance at the location of steel bars using conventional technology that applies corrosion inhibitors only on the surface of concrete. This study attempts to develop a method that penetrates corrosion inhibitors up to the location of steel bars and investigate the penetration depth of corrosion inhibitors by verifying moisture migration in concrete under an applied pressure.

Introduction

Concrete is a type of porous materials and is physically and chemically damaged due to exposure to various environments from the placing to the service life. These reactions affect the corrosion of steel bars applied in concrete and that decreases the durability life and strength of such steel bars. Thus, it is very important to insert rust inhibitors into steel bars in the case of a deterioration element that exceeds the critical amount of corrosion in the location of steel bars. However, it is very difficult to guarantee corrosion resistance at the location of steel bars using conventional technology that applies corrosion inhibitors only on the surface of concrete. This study attempts to develop a method that penetrates corrosion inhibitors up to the location of steel bars and investigate the penetration depth of corrosion inhibitors by verifying moisture migration in concrete under an applied pressure. In the penetration of water in concrete, the penetration depth according to the passage of time can be estimated using Darcy's law, which is also applicable to the migration of sand stratums under low pressure conditions, Meanwhile, it is necessary to analyze the penetrative diffusion flow accompanied by internal deformation under high pressure conditions [1]. Therefore, this study attempts an experiment evaluation of the moisture migration in mortar by applying time and pressure as variables using average mortar accompanied by water forced penetration based on the water flow in mortar with consideration to existing literature.

Confining seepage flow (Darcy's seepage flow)

Because Darcy's flow speed is constant for time and space, the hydraulic gradient can be determined as a linear shape. Therefore, Darcy's equation can be re-expressed as Eq. (1).

$$u = \frac{d\chi}{dt} = k\frac{P}{\omega_0}\chi \tag{1}$$

P = Pressure applied on the upper section of concrete ;
χ = seepage depth
$\chi d\chi$ = $(kP)/(\omega_0)dt$

Regarding the initial condition, $t = 0, \chi = 0$, the integration of Eq. (1) becomes Eq. (2).

$$\frac{\chi^2}{2} = \frac{kP}{\omega_0}t \quad , \quad \chi = \sqrt{\frac{kP}{\omega_0}t} \tag{2}$$

dm is defined as the measured average seepage depth, and k redefined as K . Then, Eq. (2) can be expressed as Eq. (3). [2]

$$K = \frac{\omega_0}{2Pt}dm^2 \tag{3}$$

where, K : seepage coefficient, mm/s
dm : average penetration depth, mm
P : water pressure, MPa
ω_0 : water density, 9.8×10^{-6} N/mm^3
t : pressuring time, s

Test outline and method

Test outline. This test measures the water penetration quantity and depth in hardened mortar by applying time and pressure. Fig. 1 illustrates cylinder shaped specimen (10×20cm, each 5cm) fabricated to apply a seepage depth test. It was aged in water for 28 days and dried at 20□ and 65% humidity for 14 days. Then, it was applied to the average water seepage depth test as illustrated in Fig. 2 using a pressured permeability tester by controlling time and pressure.

Table 1 Mix Proportion (Mortar)

Item	W/C(%)	Water	Cement	Sand	A.D	Remark
M-1	55	163	326	935	1.63	-

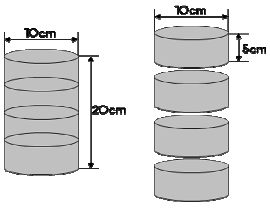

(a) Specimen size

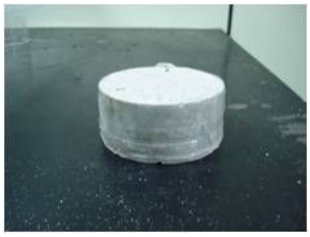

(b) Specimen

Fig.1 cylinder specimen (10×20cm, each 5cm)

(a) Permeability Tester

(b) Set the specimen

Fig.2 Permeability Tester

Test Method. Fig. 3 illustrates the measurement of average seepage depth using a pressured permeability tester according to water pressure and pressuring time. The process of this test can be summarized as follows:

(a) Seal the side and bottom face

(b) Apply pressure until the desired time and separate the specimen from tester

(c) Measure the seepage quantity

(d) Fracture the separated specimen using an UTM and measure the average seepage depth

(a) (b) (c) (d)

Fig.3 Test Method

Test Result and Analysis

Result of the average seepage quantity and depth. Table 2 shows the results of the measurement of seepage quantity and average seepage depth in accordance with test factors. Fig. 4 shows the water penetration configuration by water pressure.

Table 2 Test Result

Water pressure (MPa)	Pressuring time (hour)						Remark
	24 hour		48 hour		96 hour		
	Seepage quantity(g)	Seepage depth(mm)	Seepage quantity(g)	Seepage depth(mm)	Seepage quantity(g)	Seepage depth(mm)	
0	10	8	11.6	9.5	12	21.2	average value of three specimens
0.1	14	12	20	26	30	35	
0.3	25	20	33	34	49	43	

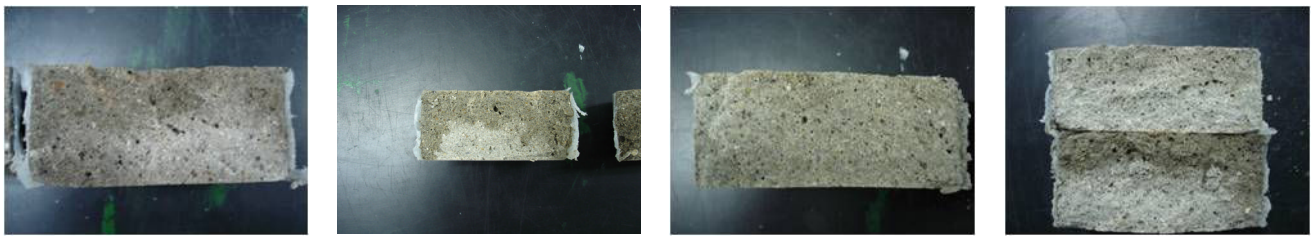

(a) 0.3 MPa (b) 0.1 MPa (c) 0Mpa (d) comparison

Fig.4 Water Penetration Configuration

Analysis. Fig. 5 shows the average seepage depth produced from the test based on the analysis of Darcy's seepage flow. The comparison of the results between the estimation with Darcy seepage

coefficient, , and the value obtained in this test. As shown in Fig. 5, the estimation value is similar to the value obtained in the test. Fig. 6 shows the penetration quantity produced from the test based on the water pressure.

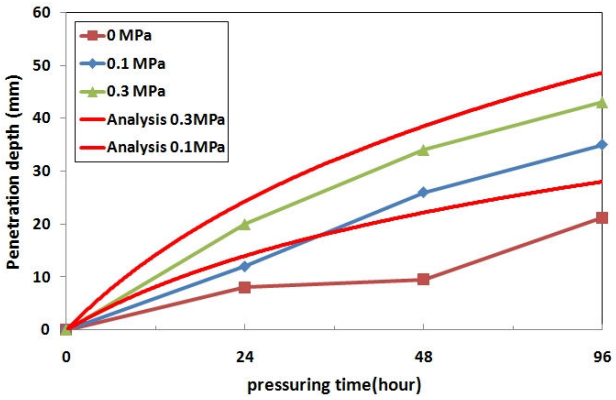

Fig. 5 Analysis of Darcy seepage flow

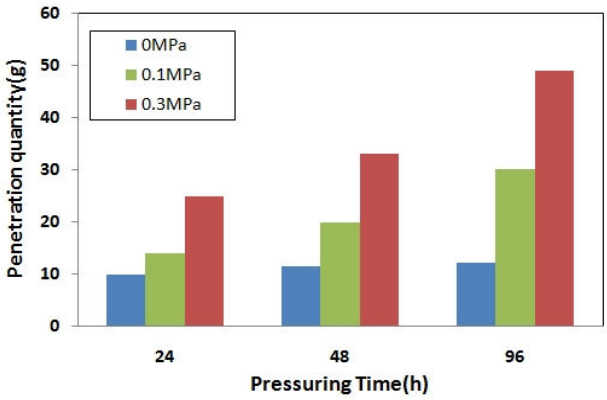

Fig. 6 Penetration quantity by water pressure

Conclusions

This study obtained and analyzed results using a seepage quantity and depth as follows:

(1) In the comparison of Darcy's seepage for the confining seepage flow using the average seepage depth, it was evident that the analysis applied by the Darcy's seepage flow was a method to analyze the migration of water in mortar under pressured water.
(2) In capillary penetration it did not increase almost in case, pressuring to percentage case the possibility the fact that the penetration quantity which it follows with a graph together at hour increases plentifully there was penetration quantity which it follows in water pressure.
(3) This study attempted to verify the water penetration mechanism by the comparison of penetration depth and penetration quantity. However, it is necessary to conduct more advanced studies in the future.

Acknowledgements

This work was supported by Sustainable Building Research Center Hanyang University which was supported the SRC/ERC program of MOST (#R11-2005-056-04003-0) and the Center for Concrete Corea (05-CCT-D11), supported by Korea Institute of Construction and Transportation Technology Evaluation and Planning (KICTTEP) under the (MOCT)

References

[1] Johyeong Yoo, et. al. " Study on the water Penetration and Diffusion into Concrete under water Pressure, Korea Architecture Institute / Vol. 23 No. 9 September 2007

[2] Jiro Murata, et. al. „Study on Watertightness of Concrete", ACI Journal / March-April 2004

[3] Ruettgers, A., Vidal, E.N. and Wing, S.P, ACI Journal, Vol. 31, Mar.-Apr., 1935

[4] B. H. Oh et. al. "A study on the measurement of permeability and development of concrete with ultra low permeability concrete". J. of the Korea Concrete Institute. Vol. 8. No. 5. 1996

Key Engineering Materials Vols. 385-387 (2008) pp 685-688
© (2008) Trans Tech Publications, Switzerland
doi:10.4028/www.scientific.net/KEM.385-387.685

Crash Tests of Tension Bolts in Light Safety Collision Devices

Jin Sung Kim[1, a], Hoon Huh[1,b], Won Mog Choi[2,c] and Tae Soo Kwon[2,d]

[1] School of Mechanical, Aerospace and Systems Engineering, KAIST, Daedoek Science Town, Gwahangno 335, Daejeon, 305-701, Korea

[2] Railway Systems and Safety Research Department, Korea Railroad Research Institute, 360-1, Woulam-Dong, Uiwang-City, Gyonggi-Do, 437-757, Korea

[a]soitgoes@kaist.ac.kr, [b]hhuh@kaist.ac.kr, [c]wmchoi@krri.re.kr, [c]tskwon@krri.re.kr

Keywords: Tension bolt, Light weight collision safety devices, Dynamic failure, Crash test, Finite element analysis

Abstract. This paper demonstrates the jig set for the crash test and the crash test results of the tension bolts with respect to an applied pre-tension. The tension and shear bolts are adopted at Light Collision Safety Devices as a mechanical fuse when tension bolts reach designed failure load. The kinetic energy due to the crash is absorbed by secondary energy absorbing devices after the fracture of tension bolts. One tension bolt was designed to be failed at the load of 375 kN. The jig set was designed to convert a compressive loading to a tensile loading and installed at the high speed crash tester. The strain gauges were attached at the parallel section of the tension bolts to measure the level of the pre-tension acting on the tension bolts. Crash tests were performed with a barrier whose mass was 250 kg and initial speed of the barrier was 9.5 m/sec. The result includes the load response of the tension bolts during both the crash tests and finite element analysis.

Introduction

Crashworthiness of trains is now a major concern since the crash accident of the train leads to enormous disaster accompanying a loss of lives and property even if the train accident is not frequently reported than a car accident. It is now widely recognized that a more systematic approach is needed where crashworthiness standards will be established forming the basis on which improved energy management concepts are adopted and new design will be implemented, involving new structural arrangements with the capacity to absorb higher levels of energy in a controlled manner and minimize passenger injuries and fatalities. Light Collision Safety Devices is adopted as an energy absorber for energy absorption in low speed collision. Repairing charges can remarkably decrease and passenger safety is also secured by absorbing most crash energy in Light Collision Safety Devices. Single tension bolt sustains the tensile load of 375 kN respectively since four tension bolts are designed to carry the load of 1,500 kN. The maximum load of the designed tension bolt is verified in dynamic loading conditions both experimentally and numerically. The load responses are measured by strain gauges attached on the specimens and calibrated to a reference load cell. Since the designed tension bolt experiences dynamic tension, the dynamic material properties of the base material, SCM440H, should be considered in finite element analysis of the tension bolts. This paper demonstrates the maximum load of tension bolts obtained from both crash tests and numerical analysis with dynamic material properties of the base material.

Specimen preparation

The designed tension bolt has central diameter of 21 mm, gage length of 30 mm and total length of 190 mm as shown in Fig. 1. The material of tension bolt is SCM440H after heat treatment. The stress-strain curves of SCM440H are shown in Fig. 2 and SCM440H shows lower strain rate sensitivity than that of conventional steels. Strain gauges are attached on the parallel region which is machined intentionally for load measurement. The load signal is calculated from the strain gauge

signal by synchronizing with the load signal from a quasi-static universal testing machine. Strain gauges are located oppositely to each other in order to compensate a bending effect by constructing half bridge.

Fig. 1 Designed tension bolt(diameter: 21 mm)

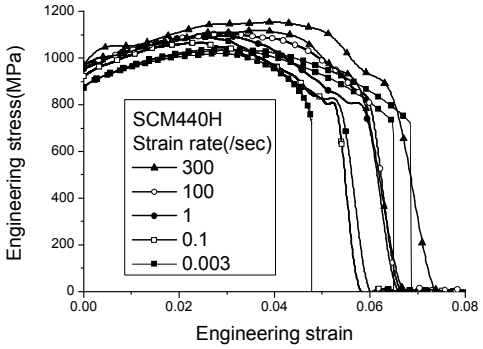

Fig. 2 Stress-strain curves of SCM440H

Experimental apparatus

Maximum carrying load of the designed tension bolt should be investigated by impact testing since the designed tension bolt undergoes high speed deformation during the train crash. For the reason High Speed Crash Tester is needed to perform crash tests of the tension bolts as shown in Fig. 3. The maximum speed of High Speed Crash Tester is 17 m/sec and the mass of a barrier is 250 kg. Crash speed is adjusted to 9.5 m/sec(34.2 km/h) which is almost same with the targeting train speed. Tension type jig system shown in Fig. 4 converts compressive loading condition to tensile loading condition since the tension bolts experience tensile loading suddenly. The jig system consists of two parts, fixed frame and movable frame. Fixed frame of the jig system is fixed on the wall by bolting as shown in Fig. 4 and has four main columns which sustain crash loads. Movable frame slides smoothly on the four holes bored in the fixed frame. The tension bolt specimen locates between the fixed frame and the movable frame and is fastened by a spanner. Cylindrical buckles are inserted into four columns between two thick plates to sustain pre-tension. Pre-tension of the tension bolt is continuously monitored by checking the strain signal from a signal conditioning amplifier. After applying designated amount of pre-tension, main controller of High Speed Crash Tester triggers the barrier with a speed of 9.5 /sec. Maximum carrying load of tension bolts are designed to be 375 kN for each tension bolt and the strain gauges attached on the both sides of specimen measure the load signal accurately. The deformed shapes are continuously taken at 7000 frames/sec by high speed camera.

Fig. 3 High Speed Crash Tester

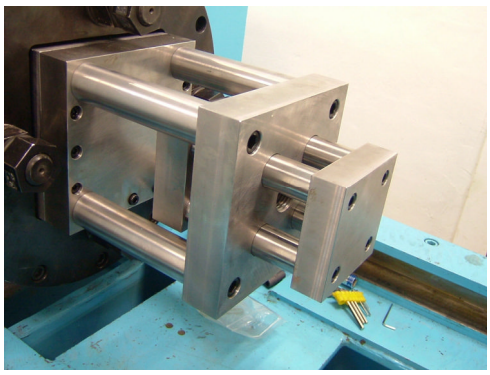

Fig. 4 Tension type jig system for crash tests

Experimental results

Six testing results are shown in Fig. 5 with respect to an applied pre-tension. Pre-tension denotes tension force applied during fastening tension bolts. Load curve of specimen #1 starts from 55 kN since the pre-tension is 55 kN in this case. Crash test results of specimens without pre-tension are shown in Fig. 5 (e) and (f). The load response shows elastic region, yield point, ultimate tensile strength, necking and fracture finally. The load at the yield point of the tension bolt is about 350 kN for all cases and averaged maximum load is 410.4 kN as shown in Table 1. The amount of pre-tension has effect on neither maximum loads nor impact durations of the tension bolt. Total displacements of specimens are about 11 mm, i.e. total elongation of 0.33. Necking occurs at between 0.5 msec and 1.0 msec from sequential deformed shapes Fig. 6. The maximum load in crash tests is 9.4% higher than originally designed maximum load and an acceptable range for application to light collision safety devices.

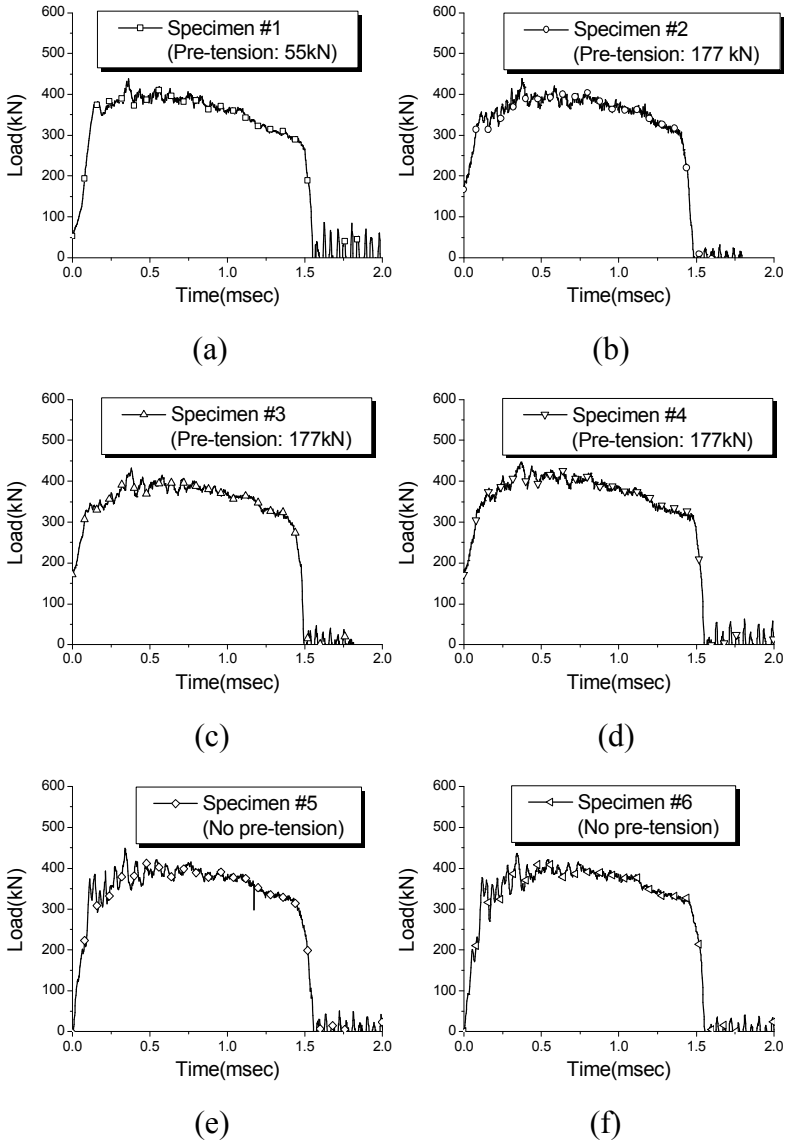

Fig. 5 Load-time curves in the crash tests of tension bolts: (a) specimen #1(pre-tension: 55 kN); (b) specimen #2(pre-tension: 177 kN); (c) specimen #3(pre-tension: 177 kN) ; (d) specimen #4(pre-tension: 177 kN) ; (e) specimen #5(no pre-tension) ; (f) specimen #3(no pre-tension)

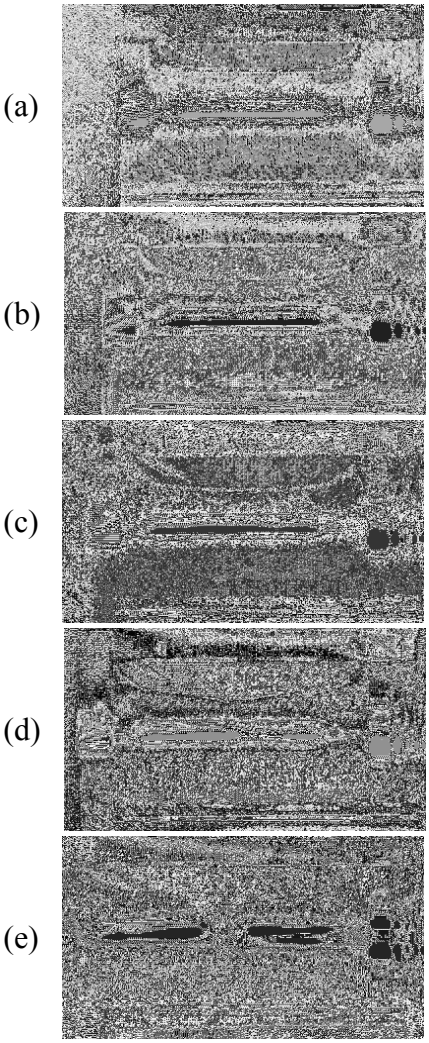

Fig. 6 Deformed shapes during crash test of a tension bolt: (a) 0 msec; (b) 0.5 msec; (c) 1.0 msec; (d) 1.5 msec; (e) after fracture

Table 1 Crash testing results of tension bolts

Specimen Number	Pre-tension(kN)	Maximum Load(kN)	Duration(msec)
1	55	413.9	1.55
2	177	407.9	1.49
3	177	406.4	1.49
4	177	427.5	1.55
5	0	401.2	1.55
6	0	405.3	1.55
Average		410.4	1.53

Numerical simulation

Finite element analysis of the tension bolt was performed to verify crash test results. The material properties used are dynamic stress-strain relations for SCM440H after heat treatment as shown in Fig. 2. Finite element mesh system has 18,186 nodes and 16,644 brick elements as shown in Fig. 7. Finite element simulation was carried out using LS-DYNA 3D. Fig. 8 shows the load response and energy absorption of both the numerical analysis and the experiment. Load response in the numerical analysis coincides with the experimental result closely.

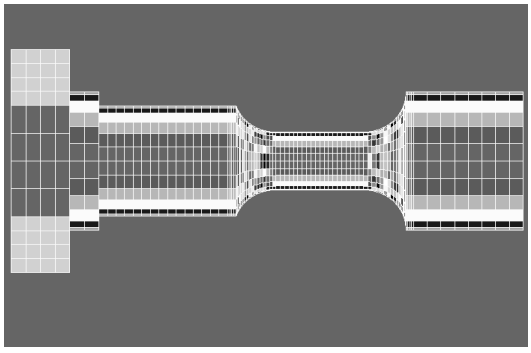

Fig. 7 Finite element model of the tension bolt

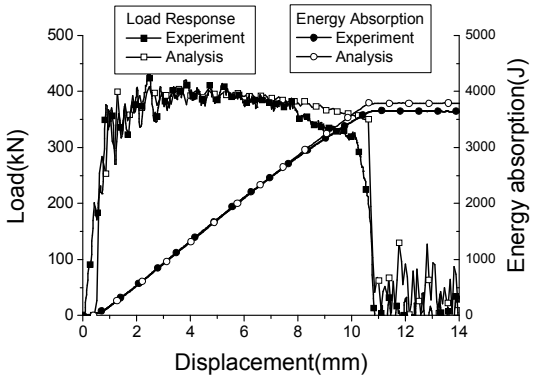

Fig. 8 Comparison of load responses and energy absorption between experiment and analysis

Conclusion

Crash test result of the designed tension bolt showed maximum load of 410.5 kN and absorbed energy of 3785.3 J while the target load was 375 kN. The tensile testing devices were designed to perform the crash tests of tension bolts at High Speed Crash Tester. Load measuring system using strain gauges was calibrated and carried out measurement of load responses successfully. Amount of applied pre-tension had no effects on the maximum load. The numerical simulation with dynamic material properties of SCM440H approximated the experimental results closely.

References

[1] W. M. Choi, H. S. Jung, W. H. Yu, J. S. Ku and T. S. Kwon: proc. of Korean Society for Railway(2006), p. 26

[2] J. H. Lewis: proc. of WCRR ’94(1994), p. 893

[3] SAFETRAIN, BRITE/EURAM Project n.BE-3092, *Dynamic tests*, SAFETRAIN Technical Report T8.2-F, Deutsche Bann, Berlin, Germany, 2001

Key Engineering Materials Vols. 385-387 (2008) pp 689-692
© (2008) Trans Tech Publications, Switzerland
doi:10.4028/www.scientific.net/KEM.385-387.689

Analysis of Heat Generation during Fracture in Ceramic Matrix Composites

Jeongguk Kim

Railroad Safety Research and Testing Center, Korea Railroad Research Institute,adder

360-1 Woulam, Uiwang, Kyunggi, South Korea 437-757

jkim@krri.re.kr

Keywords: Ceramic matrix composites, Infrared thermography, Microstructural characterization

Abstract. Ceramic matrix composites (CMCs) have evolved as potential candidate materials for high-temperature structural applications due to lightweight, high-temperature strength and excellent corrosion and wear resistance. In this investigation, damage evolution and heat generation of CMCs during monotonic loadings were investigated using different types of nondestructive evaluation (NDE) techniques, such as acoustic emission (AE) and infrared (IR) thermography and microstructural characterization. IR camera was used for in-situ monitoring of temperature evolution, and the temperature changes during testing were measured. A significant temperature increase has been observed at the time of failure. Microstructural characterizations using scanning electron microscopy (SEM) were performed to investigate fracture behavior of CMC samples. In this investigation, the NDE technique and SEM characterization were employed to analyze damage evolution and progress of ceramic matrix composites during monotonic loading.

Introduction

Ceramic matrix composites (CMCs) have been identified as promising materials for high-temperature structural applications because of their high-temperature strength, light weight, and excellent corrosion and wear resistance [1]. Due to those advantages, CMCs have been widely used for high-temperature structural and aerospace applications, such as heat exchangers, gas turbines, and space shuttle engine components. In order to encourage the expanded application of engineering ceramics, the use of appropriate nondestructive evaluation (NDE) approaches is critical to effective process control and the assurance of high-quality products and reliable performance in service [2-5]. NDE techniques, such as acoustic emission (AE) and infrared (IR) imaging, are powerful methods to investigate the fracture behavior and defect distribution in the composite [2-8].

The objectives of the current research are to introduce and apply NDE techniques to assure the quality and structural integrity of CMCs, perform NDE using AE and IR thermography methods for the analyses of defect distributions that may affect mechanical properties, and investigate tension behavior of CMC samples with the aid of NDE methods.

Materials and Experimental Procedures

Ceramic Matrix Composites (CMCs). In this investigation, several different types of continuous fiber reinforced ceramic matrix composites (CFCCs) were used for the understanding of structural performance during tensile testing with NDE signatures, i.e., continuous Nicalon (manufactured by Nippon Carbon Co. Ltd., Japan) fiber-reinforced silicon carbide (SiC) matrix composites designated as Nicalon/SiC, continuous Nicalon fiber-reinforced calcium aluminosilicate glass-ceramic matrix composites, designated as Nicalon/CAS, and continuous Nextel (manufactured by 3M) fiber-reinforced Blackglas matrix composites, designated as Nextel/Blackglas.

Nondestructive Evaluation (NDE) Techniques for CMCs. Several NDE techniques are available for assessing the integrity of composite materials [5-8]. In particular, AE can be a very

powerful NDE technique for the in-situ monitoring of damage evolution during mechanical testing [8]. When a material is subjected to stress, it experiences plastic deformation, the formation of flaws, or fracture; these conditions produce small stresses or ultrasonic waves in the material and acoustic emissions are generated. For ceramics, an increase in acoustic emissions occurs before fracture, providing a potential means of either detecting crack initiation or predicting when failure is imminent.

The infrared (IR) thermography is another possible NDE method for characterizing of CMCs. This technique is based on the concept that after applying a uniform heat pulse to the sample surface, a localized disruption of the heat flow will occur when defects and/or flaws are present [6,7]. In this study, the IR thermography was used to measure the temperature changes of CMC samples during mechanical tests.

Results and Discussion

Structural Performance during Tensile Testing. Monotonic tensile tests were conducted using a computer-controlled Material Test System (MTS) 810 servohydraulic frame equipped with hydraulic grips. The tensile tests were performed at room temperature under displacement control at a cross-head speed of 0.5 mm per minute. In this study, dog-bone type flat specimens were used to investigate the damage evolution during the tests.

Figure 1 shows the tensile behavior of different types of CMC samples. The ultimate tensile strength (UTS) values were determined about 290 MPa, 197 MPa, and 89 MPa for Nicalon/SiC, Nicalon/CAS, and Nextel/Blackglas, respectively, as shown in Fig. 1. The tensile stress-strain behavior for the composites exhibits very similar except showing different UTS values. After proportional limit, the stress-strain behavior of both Nicalon/CAS and Nicalon/SiC composites shows plastic deformation-like behavior due to the subsequent fiber breakage and fiber pullout, and presents enhanced fracture toughness as compared with monolithic ceramics, which show only linear elastic behavior followed by catastrophic failure.

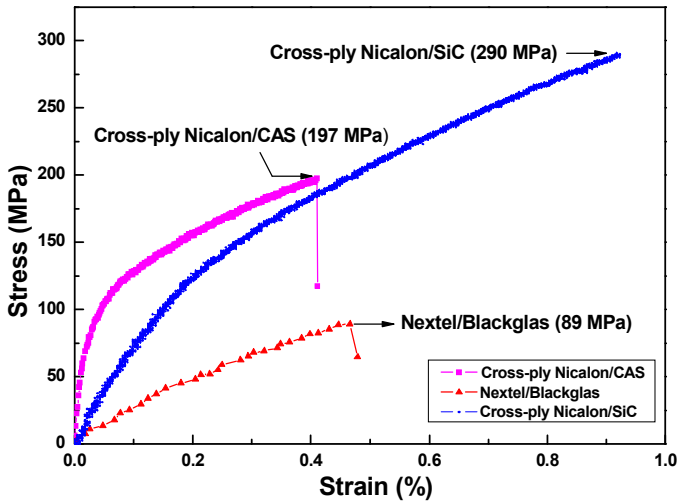

Figure 1. The stress-strain behavior of several CMC specimens with values of ultimate tensile strength

IR Thermography during Tensile Testing. Figure 2 shows a direct comparison between the stress-strain behavior and temperature evolution behavior during monotonic tensile testing. The speed of the IR camera was 7 Hz for both samples, and the individual data points in Figure 2 indicate one frame of IR image, i.e., every frame was obtained every 1/7 second (about 0.143 sec). The number of frames at the time of failure shows more than 6 frames. This means that the failures of the Nicalon/CAS composites were achieved by more fiber pullout and breakage at the time of failure, which indicates the toughening mechanisms in the composites. The sample exhibits the temperature peaks, especially, at the time of failure. From these results, it is understandable that the main

temperature changes for the composites during tensile testing seem to result from the final fiber pullout and breakage. The fiber pullout and breakage at the final moment of failure generate severe heating between the fiber and matrix, and the temperature increases seem to be developed from the final fractures of fibers.

Acoustic Emission (AE) Investigation. Figure 3 shows another evidence of failure mode in a Nextel/Blackglas composite using AE methods. Figure 3 presents the cumulative acoustic emission (AE) energy-time relationship during tensile testing, and also, stress-strain curves are juxtaposed with AE results. Only one significant peak has been found during the tensile testing, which indicates instant failure of the composite specimen. The main purpose of the use of AE method for this investigation is to detect and investigate damage initiation and the associated evolution process. The failure mode was instant brittle failure right after crack initiation in Nextel/Blackglas samples.

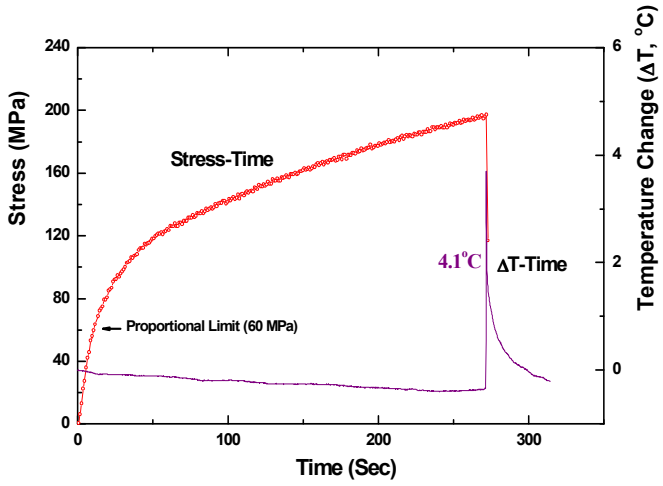

Figure 2. Stress vs. temperature evolution during tensile testing for a cross-ply Nicalon/CAS composite.

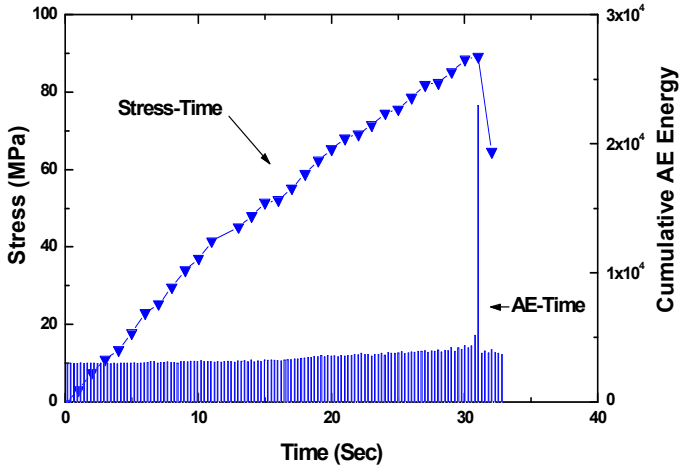

Figure 3. Stress responses vs. AE energy during tensile testing for a Nextel/Blackglas composite.

SEM Characterization of Structural Performance in CMCs. After mechanical testing, microstructural characterization was conducted to investigate fracture mechanisms in CMC samples using scanning electron microscopy (SEM). Figure 4(a) presents the entire cross-sectional view of failure area in a Nextel/Blackglas composite. The SEM micrograph shows that initial cracks/damages start at 0° fiber bundle and propagated with debonding at the interface between fiber and matrix. The 90° fiber bundle plays a role to retard the crack propagation, and the bundle provides a toughening mechanism of Nextel/Blackglas composites.

Figure 4(b) presents the summary of the failure mechanisms in Nextel/Blackglas composites showing the fracture surface. The initial cracks start from the intersection of 0° and 90° fiber bundles due to the stress concentration, and crack propagates along 0° fiber bundle and matrix region, and final rupture occurs at 90° fiber bundle with fiber/matrix debonding and fiber pullout. Figure 4(b) also shows limited fiber pullout.

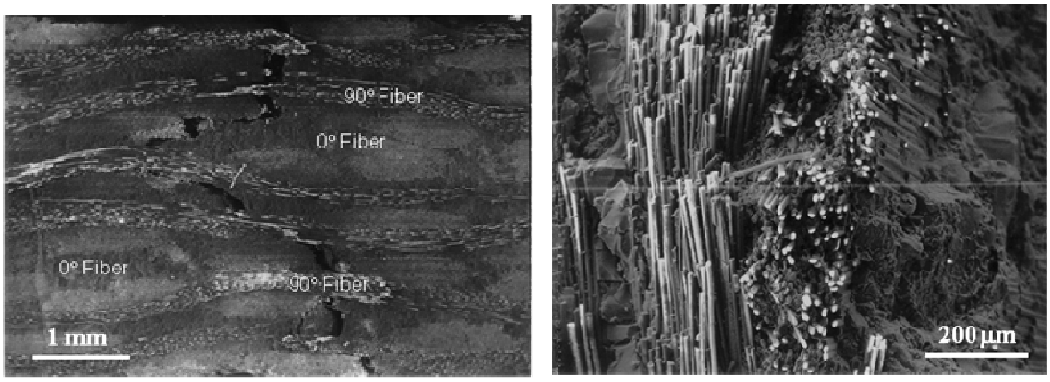

(a) (b)

Figure 4. The micrographs showing (a) the cross-sectional view of fracture area, and (b) fracture surface of Nextel/Blackglas composite.

Summary

The tensile behavior of CMCs was investigated with the aid of several NDE techniques, such as acoustic emission and infrared thermography methods. Various types of NDE methods provided the possible ways to predict and interpret structural performances of CMCs. The combination of several NDE techniques could assure greater level of reliability for ceramic composites evaluation to investigate the fracture behavior of CMCs.

The failure mode (mechanism) of CMCs was provided through the microstructural characterizaion with SEM micrographs. The fractures of CMC samples were shown brittle failure manners for all testing samples. The strong interfaces between continuous fibers and ceramic matrices provides brittle fracture modes with extensive fiber pullout.

References

[1] K. K. Chawla, Ceramic Matrix Composites, Chapman & Hall, London, 4 (1993).

[2] ASM Handbook, vol. 17, ASM International, 284 (1992).

[3] Nondestructive Testing Handbook, 2nd ed., vol. 10, Nondestructive Testing Overview, American Society for Nondestructive Testing, Inc., (1996).

[4] P.K. Liaw, JOM, 38 (1995).

[5] J. Kim and P.K. Liaw, JOM, 50,11 (1998).

[6] J. Kim and P.K. Liaw, Met Transactions A, 38A(13), 2203 (2007).

[7] J. Kim and P.K. Liaw, MSE A, Vol. 409,302 (2005).

[8] J. Luo, S. Wooh, and I.M. Daniel, Journal of Composite Materials, 29(15), 1946 (1995).

Key Engineering Materials Vols. 385-387 (2008) pp 693-696
© (2008) Trans Tech Publications, Switzerland
doi:10.4028/www.scientific.net/KEM.385-387.693

Modeling of a Long-term Creep Curve of Alloy 617 for a High Temperature Gas-cooled Reactor

Woo Gon Kim[1,a], Song Nan Yin[1,b], Ik-Hee Jung[2,c], and Yong Wan Kim[1,d]

[1] KAERI, 150 Deogjin-dong, Yuseong-gu, Daejeon, 305-353, Korea

[2] Pukyoung National University, 599-1 Daeyon-dong, Nam-gu, Busan, Korea

[a]wgkim@kaeri.re.kr, [b]yjsongnam@kaeri.re.kr, [c] jih2000@hanmail.net, [d]ywkim@kaeri.re.kr

Keywords: Alloy 617, Creep Curve, High Temperature Gas-cooled Reactor (HTGR), Nonlinear Least Square Fitting (NLSF), Monkman-Grant (M-G) Strain, Minimum Creep Rate

Abstract. This study aimed to model the long-term creep curves above 10^5 hours by implementing a nonlinear least square fitting (NLSF) of the Kachanov-Rabotnov (K-R) model. For this purpose, the short-term creep curves obtained from a series of creep tests at 950°C were used. In the NLSF of their full creep curves, the K-R model represented a poor match to the experimental curves, but the modified K-R one revealed a good agreement to them. The Monkman-Grant (M-G) strain represented the behavior of a stress dependency, but the λ parameter was constant with a stress independency. The λ value in the modified K-R model was 2.78. Long-term creep curves above 10^5 hours from short-term creep data were modeled by the modified K-R model.

Introduction

Alloy 617 is the principle candidate alloy for the high temperature gas-cooled reactor (HTGR) components, such as the hot gas ducts, intermediate heat exchanger (IHX) tubes because of its high creep rupture strength coupled with its good corrosion behavior in simulated HTGR-helium and its sufficient workability [1]. Since the HTGR components are designed for a lifetime of 40 years at 950°C, one of the most important properties for the components is the long-term creep behavior [2].

Over the past several decades, typical constitutive equations to well describe a creep strain-time curve have been developed by Kachanov-Rabotnov[3], Andrade[4], Garofalo[4,5], Evans [6] and Maruyama[7], et al.. Among them, the K-R model has been used frequently, because a secondary creep resulting from a balance between a softening and a hardening of materials and a tertiary creep resulting from an appearance and acceleration of the internal or external damage processes are adequately considered. In the case of nickel-base alloys, it has been reported that a tertiary creep at a low strain range may be generated, and this tertiary stage may govern the total creep deformation [2]. Therefore, a creep curve for nickel-based Alloy 617 can be modeled appropriately by using the K-R model that reflects a tertiary creep.

In this paper, the long-term creep curves for Alloy 617 were modeled by using the NLSF method in the K-R model. The modified K-R model was also introduced to fit the full creep curves. Optimum values for the λ and K parameters in the modified K-R model were obtained with stresses. Relationships between the M-G strain and a stress were investigated and discussed.

Results and Discussion

Creep behavior. Alloy 617 (Inconel 617) used in this study is a commercial type hot-rolled plate with a thickness of 15.875mm (5/8 inch). Creep specimens were a cylindrical form of a 30 mm gauge length and 6 mm diameter. Creep tests were carried out with different stress levels, 35MPa, 30MPa, 25MPa, 22MPa, 20MPa and 18MPa at 950°C. Typical creep curves at 950°C are shown in Fig. 1. A well-defined secondary creep stage, which is obtained for austenitic materials in the temperature range 500-600°C, is not obtained, and the onset of a tertiary creep is unclear. Also, a primary creep strain is not generated, and a tertiary creep stage is started from a low strain level. A creep deformation is mainly controlled by the tertiary creep stage. The relationship between a minimum

creep rate (MCR) and a stress shows a good linearity, as in Fig. 2. The constants of Norton's law, $\dot{\varepsilon}_{MCR} = A\sigma^n$ were obtained. The A value was 7.29x10^{-14} (MPa^{-n} h^{-1}) and the n value was 6.50.

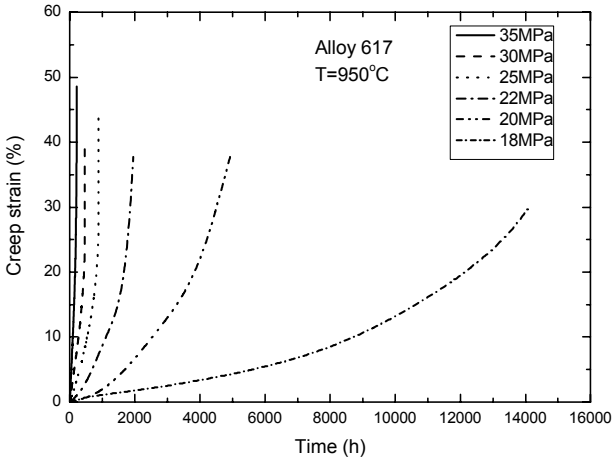

Fig. 1 Creep curves for Alloy 617 at 950°C

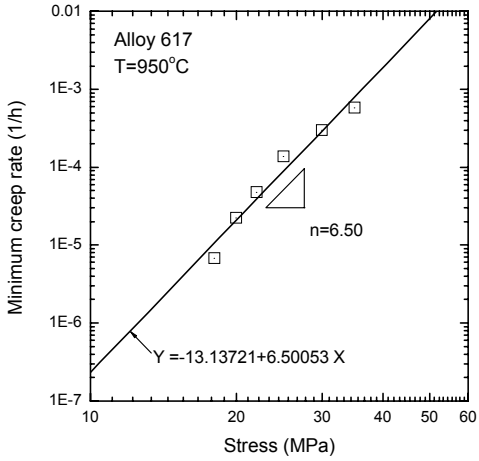

Fig. 2 Minimum creep rate vs. stress

Nonlinear fitting of the full creep curves. Using the experimental creep data, full creep curves were nonlinearly fitted by the K-R model. The K-R model can be written as follows [2,3],

$$\frac{\varepsilon}{\varepsilon^*} = \lambda \left[1 - \left(1 - \frac{t}{t_r} \right)^{1/\lambda} \right] \tag{1}$$

$$\varepsilon^* = \dot{\varepsilon}_o \cdot t_r \ (= \varepsilon_r / \lambda \ ) \tag{2}$$

where, ε_r and t_r are the rupture strain and the rupture time, and λ is a material parameter as a constant. Also, $\dot{\varepsilon}_o$ is the creep strain rate for a range of stresses and ε^* is the M-G strain.

In the K-R model, the λ parameter is an important constant which is regarded as a creep resistant feature of a material, because the shapes of a creep curve depend on its value. In order to properly obtain the λ value, the NLSF method is employed. An optimum λ value is determined by using a nonlinear regression of Eq. 1 for the experimental creep curve. A calculating process was carried out by using the "Nonlinear Curve Fit" and the "Advanced Fitting Tool" in the Origin program 7.5 version. Because the NLSF method can be fitted by an iterative regression to obtain the best value against a full creep curve, this method is superior in its description of a full creep curve.

Fig. 3 shows a typical NLSF result by the K-R model of Eq.1 for the full creep curve at 35MPa. The square symbols indicate the experimental creep curves, and the solid lines indicate the result of the NLSF curve. The NLSF curve between a strain fraction ($\varepsilon/\varepsilon^*$) and a life fraction ($t/t_r$) reveals a poor agreement with R^2=0.97 to the experimental curve. Where, R^2 is a coefficient of determination as a statistic parameter.

On the other hand, to obtain a closer match to the experimental creep curves, this study has introduced a modified K-R model, as follows,

$$\frac{\varepsilon}{\varepsilon^*} = K, \lambda \left[1 - \left(1 - \frac{t}{t_r} \right)^{1/\lambda} \right] \tag{3}$$

where, K is a correction coefficient. Because Eq.3 has another variable, K in Eq.1, it will be better for a description of the creep curves than the K-R one.

Fig. 4 shows a typical NLSF result by the modified K-R model at 35MPa. The NLSF result for the modified one reveals a better agreement with R^2=0.997 to the experimental curves. It is identified that the modified K-R model has a superior agreement to those of the K-R one. In addition, for the average value of the R^2 for all the stress levels, the modified K-R model was higher with 0.988 than 0.963 in the K-R one, as shown in Fig. 5. Thus, in this study, the modified K-R one was employed to model the long-term creep curves. The creep muster curves for each stress level were obtained by the NLSF of the modified K-R model. The average values for λ and K in the modified K-R model were 2.78 and 1.24, respectively. These parameters can be considered as constant parameters regardless of stress variations, as shown in Fig. 6.

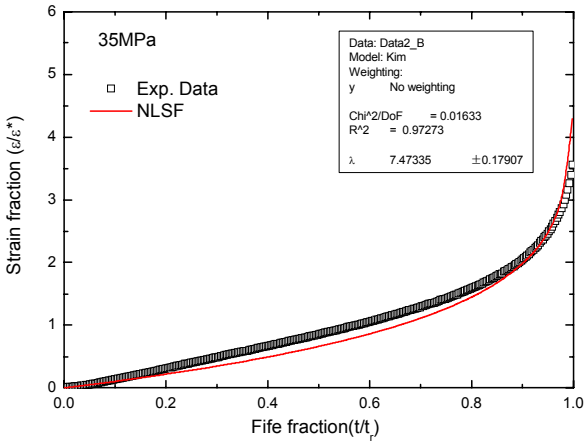

Fig. 3 NLSF of the K-R model at 35MPa

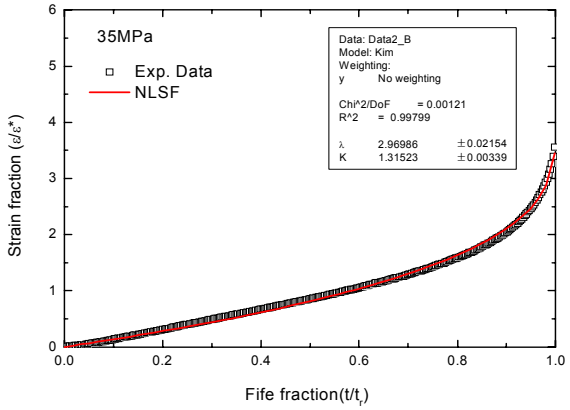

Fig. 4 NLSF of the modified K-R model at 35MPa

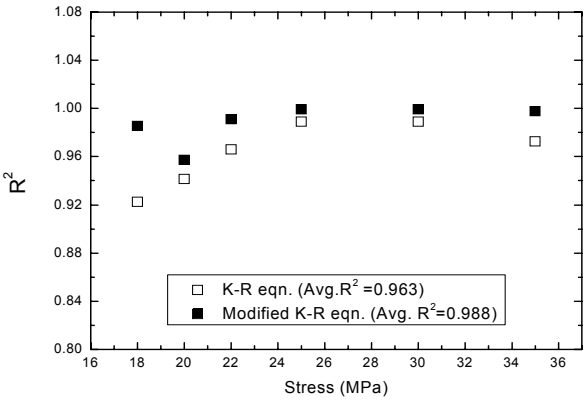

Fig. 5 Comparison of R^2 values between the K-R and modified K-R models

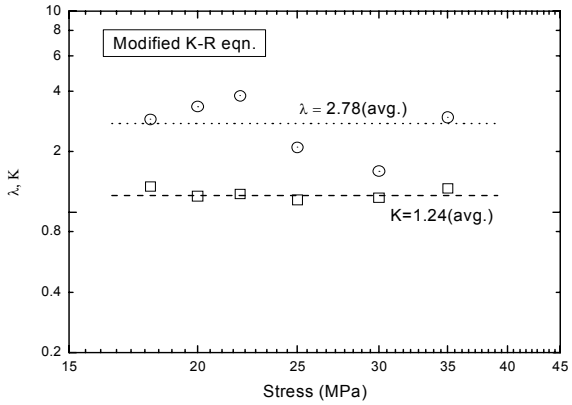

Fig. 6 A stress independency of the K and λ in the modified K-R model

Modeling of the long-term creep curves. To model the long-term creep curves by using the modified K-R Eq. 3, it is necessary to know the K, λ and ε^* values. The K and λ values have already been obtained by the NLSF, as described above, but the M-G strain, ε^* has not been determined. The M-G strain can be written as Eq.4, and the M-G relationship is defined as Eq.5.

$$\log \varepsilon^* = \log t_r + \log \dot{\varepsilon}_{MCR} \tag{4}$$

$$\log t_r + m \log \dot{\varepsilon}_{MCR} = C \tag{5}$$

Combining Eq.4 and Eq.5, Eq.6 is obtained. Also, Norton's power law is given as Eq.7.

$$\log \varepsilon^* = C + \log \dot{\varepsilon}_{MCR}(1-m) \tag{6}$$

$$\dot{\varepsilon}_{MCR} = A\sigma^n \tag{7}$$

Substituting Eq.7 into Eq.6, ε^* is derived as

$$\log\varepsilon^* = C + (1-m)(\log A + n\log\sigma) \tag{8}$$

$$\log\varepsilon^* = C_1 + (1-m)\, n\log\sigma \tag{9}$$

Hence, in Eq. 8, it is used as $C + (1-m)\log A = C_1$. In Eq.9, when m =1, ε^* is constant, but when $m \neq 1$, log ε^* becomes a function of $\log\sigma$.

It is clearly seen that the ε^* values for Alloy 617 at 950°C increased with an increasing stress, as a function of a stress, as shown in Fig. 7. From this linear relation, the ε^* value at a given stress level is predicted, and a creep rate at a given stress level is obtained by Norton's law of Fig. 2. Then, a long-term rupture time can be predicted by using the M-G relation of Eq.2. Finally, the long-term creep curves at a given rupture time can be modeled mathematically by Eq. 3. The results of the modeled creep curves for up to 500,000 hours are shown in Fig. 8.

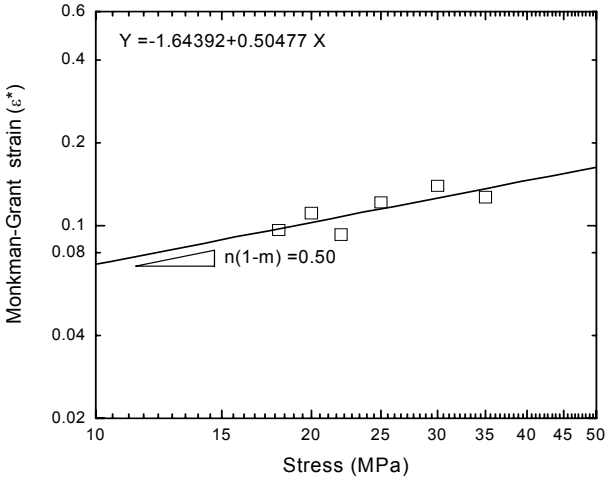

Fig. 7 A stress dependency of the M-G strain

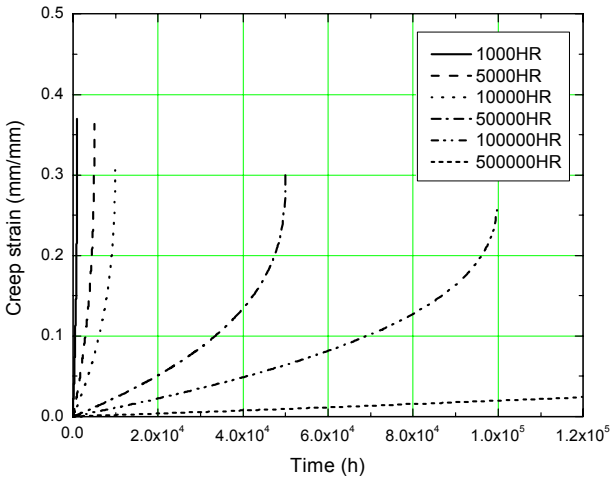

Fig. 8 Prediction of the long-term creep curves

Conclusion

The modified K-R model for the NLSF of full creep curves revealed a better agreement than the K-R one. The λ and K parameters of the modified model were constant regardless of the stress variations, and the λ value was obtained at 2.78. For the M-G strain, ε^* increased with an increasing stress, as a function of a stress. Long-term creep curves above 10^5 hour from short-term creep data were plotted by the modified K-R model, which can be utilized for a creep design of Alloy 617 at 950°C.

References

[1] H.Nickel, F.Schubert, H.J. Penkalla and H.H. Over: Nucl. Eng. and Design, Vol. 76 (1983), p. 197.
[2] W.G. Kim, S.N. Yin, W.S. Ryu, Y.W. Kim and Won Yi: Key Eng. Materials, Vols. 345-346 (2007), p. 589.
[3] R.K. Penny and D.L. Marriott: *Design for Creep*, Chapman & Hall (1995).
[4] F. Garofalo: *Fundamentals of Creep and Creep Rupture in Metals*, Macmillan Co., NY(1966).
[5] L.D. Blackburn: American Society of Mechanical Engineers, NY(1972), p. 14.
[6] R.W. Evans, J. D. Parker and B. Wilshire: Int. J. of PVP, Vol. 50 (1992), p. 147.
[7] K.Maruyama, C. Harada and H. Oikawa: J. Soc. Mater. Sci., Japan, Vol. 34(1985), p. 1289.

Key Engineering Materials Vols. 385-387 (2008) pp 697-700
© (2008) Trans Tech Publications, Switzerland
doi:10.4028/www.scientific.net/KEM.385-387.697

Mechanical Properties of Ductile Fiber Reinforced Cementitious Composites for Rehabilitation on concrete Structures

Gum-Sung Ryu[1,a], Kyung-Taek Koh[1,b], Su-Tae Kang[1,c]and Jung-Jun Park[1,d]

[1]Structural Material Research Division, Korea Institute of Construction Technology, 2311 Daehwa-Dong, Ilsanseo-Gu, Goyang-Si Gyeonggi-Do, 411-712 Republic of Korea

[a]ryu0505@kict.re.kr, [b]ktgo@kict.re.kr, [c]alphard@kict.re.kr, [d]jjpark@kict.re.kr

Keywords: repair, rehabilitation, PVA Fiber reinforced cementitious composites, ductility,

Abstract.

This paper present the results of an experimental study on the performance of PVA fiber reinforced cementitious composites as a repair material. The test of results is that the PVA fiber reinforced cementitious composites showed not only a significant improvement of in the load bearing capacity compared to exiting restorative materials but also enhanced the ductility without the occurrence of interfacial failure or brittle fracture.

Introduction

Various fiber reinforced cementitious composites including large quantities of PVA or steel fiber have been developed recently and studies to find application in diverse domains are currently conducted actively[1-4]. Regard to economical efficiency, high toughness fiber reinforced cementitious composites becomes competitive when applied as repair material with small quantities rather than the casting of large volume for the main body of structures in field. The authors have developed a wet spraying technique using PVA fiber reinforced cementitious composites and attempt to exploit it for rehabilitation[5-6]. Differently from previous polymer-type or epoxy-type restorative materials, the coefficient of thermal expansion and the elastic modulus of the PVA fiber reinforced cementitious composites are similar to those of concrete, which allows it to behave similarly to the concrete members. However, inadequate attention has been devoted by the Korean researchers to examine systematically the extent of the improvement brought by such fiber-reinforced ductile cementitious composites comparing with existing restorative materials and techniques. Therefore, this study investigates the repair effects of the sprayed PVA fiber reinforced cementitious composites through estimation of its physical properties and flexural performance of beam in order to secure its stability for use on field.

Materials

The PVA fiber reinforced cementitious composites is characterized by the admixing of

1.2%(by volume) of PVA fiber to the cementitious composites composed of cement, fly-ash and CSA-type expansion agents. The existing product R composed the natural cellulose fiber in the mortar composed of polymer and carbon fiber sheet has the depth of 0.11㎜, tensile strength of 3,550MPa, and Elastic modulus of 235GPa.

Flexural Test method

Specimens with dimensions of 300×300×2,400mm were manufactured as shown in Figure 1 in order to examine the flexural load bearing capacity of the repaired structure with the PVA fiber reinforced cementitious composites. Repaired structures were made by applying the matrix after removing the area to be repaired. Table 1 summarizes the details of the specimens and the applied techniques. Two non-reinforced specimens(plain) were manufactured. Three specimens were fabricated with the PVA fiber reinforced cementitious composites to possess a reinforcement thickness of 30mm and 50mm with proportions of PVA fiber set to 1.2% and 1.5%, respectively. Specimens with used polymer-type repair mortar and one layer of carbon fiber sheet, widely used for rehabilitation purpose, were also manufactured for the comparison with the PVA fiber reinforced cementitious composites. The concrete used for the specimens used coarse aggregates with the maximum dimension of 25mm and exhibited a design strength of 24MPa. Steel rebars of 13mm diameter with yield strength of 350MPa were also used.

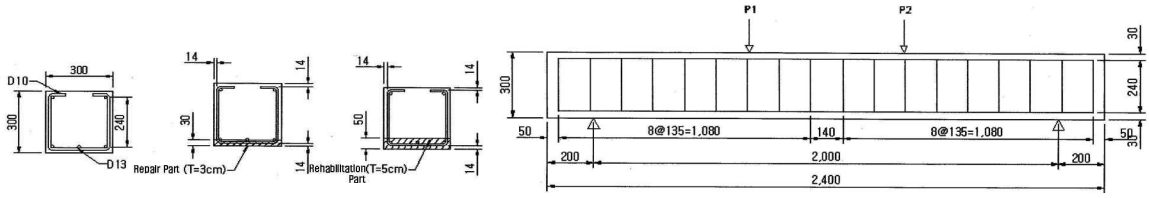

Fig. 1 Specimen for flexural Test

Table 1 Features of the tested repair materials

Classification		Notation	Number of specimens	Dimensions	Volume fraction of fiber (Vf)
Standard specimen		Plain	2	Standard specimen	–
Repairing	PVA fiber reinforced mortar	VF1.5-T30	1	T = 30mm	1.5 %
		VF1.2-T50	1	T = 50mm	1.2 %
		VF1.5-T50	1	T = 50mm	1.5 %
	The existing	Product R	1	T = 50mm	–
Reinforcement	The existing	Carbon fiber sheet	1	1 layer reinforced	–

Flexural Performance

The compressive strength of normal concrete was 26.4MPa. The PVA fiber reinforced

cementitious composites and product R has compressive strength of 68.6MPa and 31.2MPa, respectively. Table 2 summarizes the results of the load-displacement relationship of the beam specimen and the strain of the tension rebar. Figure 2 and Figure 3 plot the corresponding curves. Assuming that the yield strength of fy = 350MPa for the main rebar of 13mm diameter, the yield load of the main rebar is defined as the load Py for which the yield strain μ_ϵ is equal to 1,750. In addition, the yield load of the reinforced specimen is expressed in terms of the ratio of the yield loads of the carbon reinforced specimen (Py) to those of the specimen without the reinforcement.

Table 2 Results of Flexural Test

Specimen	Load-displacement results			At yielding of tension rebar		
	Max. load (kN)	Yield load (kN)	Yield displ. (mm)	Py (kN, mean)	Reinforced/ Non-reinforced	Reinforced/ Carbon fiber sheet
plain 1	133.58	98.6	3.99	98.2	1.00	0.77
plain 2	129.89	97.9	4.19			
VF1.5-T30	140.89	121.7	5.04	121.7	1.24	0.95
VF1.2-T50	148.95	117.9	4.57	117.9	1.20	0.92
VF1.5-T50	151.87	121.0	4.27	121.0	1.23	0.95
Product R	125.09	99.3	4.57	99.3	1.01	0.78
carbon fiber sheet	201.35	127.6	4.52	127.6	1.30	1.00

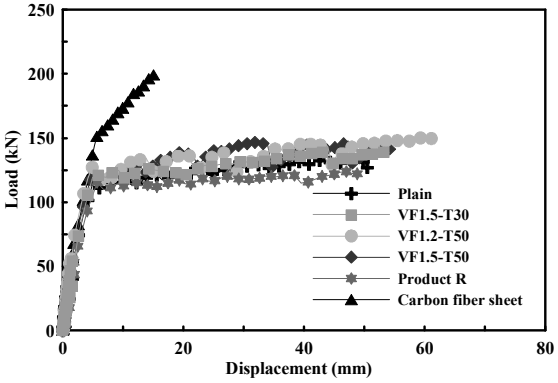

Fig. 2 Load-displacement relationships

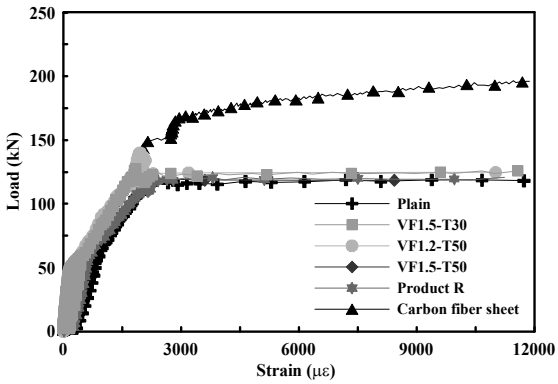

Fig. 3 Relationships of Load versus strain of the rebar

Since both the strength and the stiffness of the specimens using existing repair materials are not exhibiting any increase compared to the reference non-reinforced specimen, it is likely that no reinforcement effect should be expected for the specimens using existing repair materials. The specimen bonded with one layer of carbon fiber sheet, which corresponds to a the reinforcement methods widely selected recently, is showing a reinforcement effect with an increase of 50.7% in the maximum strength compared to the reference specimen. However, debonding of the sheet occurs suddenly at a displacement of 15.6mm, which reveals a significant reduction in the ductility. Accordingly, even if the carbon fiber sheet

reinforcement technique is results in a reinforcement effect with respect to the load bearing capacity at early construction, a careful attention should be paid to the sudden failure at the interface between the sheet and concrete that eventually leads to a brittle fracture at failure. The increase in the maximum strength and stiffness was verified for all of the three specimens using the PVA fiber reinforced cementitious composites. Among these specimens, the one with admixing of 1.5% fiber in the 50mm-thickness reinforcement manifested the largest increase of in the maximum strength, corresponding to an augmentation of about 15% compared to the reference specimen as well as an approximately 17% increase in the yield strength. In addition, the yield strain increased by 1.2 times compared to the reference specimen regardless of the type of the specimens and the proportion of fiber and reinforcement thickness. Consequently, regarding the fact that PVA fiber reinforced cementitious composites also exhibits reinforcement effect and considering the durability and the load bearing capacity globally, PVA fiber reinforced cementitious composites is evaluated to be sufficiently effective as a material combining both rehabilitation and reinforcement effects.

Conclusions

In order to explore the use of high-toughness fiber-reinforced cementitious composites mixed with PVA fiber as a repair material, the flexural performance of beam specimens were compared with those of existing repair materials, the results are summarized in the following. The PVA fiber reinforced cementitious composites showed not only a significant improvement of in the load bearing capacity compared to exiting restorative materials but also enhanced the ductility without the occurrence of interfacial failure or brittle fracture. The PVA fiber reinforced cementitious composites also exhibited a reinforcement effect nearly similar to an existing reinforcement method (95% of the reinforcement effect of 1 one layer of carbon fiber sheet).

References

1. JSCE Concrete Committee: Evaluation and Using of High Performance Fiber Reinforced Cementitious Composites, Concrete Engineering Series 64, JSCE, 2005.
2. Naaman, A. E., and Reinhardt, H. W.: High Performance Fiber Reinforced Cement Composites 2 (HPFRCC2), E&FN SPON, 1995.
3. Li, V. C.: High Performance Applications of Fibers in Civil Engineering, Journal of Applied Polymer Science, Vol. 83, 2002.
4. Koh, K. T. et al.: Development of the Advanced Technology of Durability in Concrete Bridges, Korea Institute of Construction Technology (KICT), 2005.
5. Lee, G. C. et al.: Fundamental Properties of Fiber Composite Spray Mortar, Proceedings of the Korea Concrete Institute, Vol. 18, No. 2, 2006, pp. 305-308.
6. Ryu, G. S. et al.: A Study on the Evaluation for Durability Performance of the Repair Method Using Fiber Reinforced Mortar, Proceedings of the Korea Concrete Institute, Vol. 18, No. 2, 2006, pp.291-314.

Key Engineering Materials Vols. 385-387 (2008) pp 701-704
© (2008) Trans Tech Publications, Switzerland
doi:10.4028/www.scientific.net/KEM.385-387.701

The influence of the amount of silica fume on the mechanical property of ultra-high performance concrete

Jung-Jun Park[1, a], Gum-Sung Ryu[1,b], Su-Tae Kang[1,c] and Sung-Wook Kim[1,d]

[1] Structure Material Research Division, Korea Institute of Construction Technology, Goyang, 411-712, Korea

[a]jjpark@kict.re.kr, [b]ryu0505@kict.re.kr, [c]alphard@kict.re.kr, [d]swkim@kict.re.kr

Keywords: Ultra High performance, Silica Fume, Micro Structure

Abstract. Silica fume constitutes an element of extreme importance in improving the strength and fluidity of UHPC. The adopted amount of silica fume generally is generally exceeding 25% of cement in weight but the influence of this amount on the properties of UHPC is still remaining as a domain to be investigated. Accordingly, this paper investigates the effects of the amount of silica fume on the mechanical characteristics of the fluidity, compressive strength, elastic modulus and flexural strength and on the micro structure of UHPC by means of SEM and MIP. Results revealed that adequate amount of silica fume is improving the fluidity and strength. MIP tests demonstrated that such improvement is brought by the increase of hydrates due to the pozzolan reaction and the effective densification inside concrete due to the filler. It seemed also that similar mechanical characteristics can be obtained for a volumetric ratio to cement ranging between 10 and 25%.

Introduction

Concrete presents the problem of experiencing brittle failure with larger compressive strength. Therefore, fiber reinforcement is introduced to overcome the defect and problem of such concrete and resulted in the adoption of diversified fiber reinforced cements with improved toughness. Especially, RPC (Reactive Powder Concrete) has gained interest and is today actively studied in USA and Japan. RPC is an ultra-high strength cement compound with remarkably improved toughness by securing early strength through high-temperature curing and admixing of steel fibers. With large reduction of the W/B ratio down to about 0.2% and the absence of coarse aggregates, RPC is composed of cement, silica fume, sand with grain size below 0.5mm and superplasticizer, which secure homogeneity and fluidity of the cement matrix[1]. In Korea, researches on RPC have been completely neglected until the Seonyu pedestrian bridge constructed with the support of French technology. Recently, a RPC-type ultra-high performance concrete (UHPC) with compressive strength of 200MPa and flexural strength of 30MPa developed has been developed by our research team and attracted keen interest[2].

Besides, silica fume stands among the materials used in UHPC, which plays the role of filler filling the pores between the cement particles, increases the strength and the fluidity of the cement paste by generating hydrates through pozzolan reaction during hydration. Silica fume represents thus an extremely important constituent for the improvement of the strength and fluidity of UHPC and is introduced in relatively large quantity being exceeding 25% in weight ratio to cement[3]. However, the whole volume of silica fume in Korea relies unilaterally on importation. Therefore, in an economical point of view, need is to endeavor efforts in searching for solutions replacing silica fume or reducing the amount of silica fume considering the mechanical effects of silica fume on UHPC.

Accordingly, this study intends to derive the adequate amount of silica fume enabling to develop performances equivalent to former UHPC in terms of mechanical properties like the strength while reducing this amount. To that goal, UHPC was manufactured and the mechanical properties of the

compressive strength and flexural strength as well as the effects of the amount of silica fume on the fluidity of UHPC were examined. In addition, SEM photography and MIP (Mercury Intrusion Porosimetry) tests were conducted to observe the micro structure of UHPC so as to provide basic database to be exploited for the development of economically efficient UHPC.

Materials

The cement used in this study was ordinary Portland cement. Silica fume presenting specific surface of about 200,000cm^2/g was used as admixture. Sand with grain size below 0.5mm was used as fine aggregates. Coarse aggregates were discarded. Fine aggregates presented density of 2.62g/cm^3 with characteristics corresponding to approximately 98% of SiO_2. The filler exhibited mean particle size of about 2 μm and was composed of material with density of 2.65g/cm^3 and content of SiO_2 larger than 99%. Polycarbonate-based superplasticizer in dark brown liquid form with density of 1.01g/cm^3 was used. Highly elastic steel fibers with tensile strength of 2,500MPa, diameter of 0.2mm, length of 13mm and shape coefficient of 65 were introduced.

Mix design and test method

Table 1 arranges the mix design of UHPC in terms of the relative ratio of each constituent to the amount of cement. The fluidity of the so-mixed UHPC was measured in compliance with the flow test method proposed by KS L 5105. The specimens were stripped from the molds after 1 day of wet curing at temperature of 20°C and relative humidity of 65%. Thereafter, high temperature curing was performed during 3 days at temperature of 90±2°C. The compressive strength of UHPC was measured with respect to KS L 2405 on Φ100×200mm specimens. The value for the compressive strength corresponds to the mean of 6 specimens. The flexural strength of UHPC was measured by means of 4-point loading test on beam specimens notched at their center. The value for the flexural strength corresponds to the mean of 5 specimens. The samples for SEM and MIP measurements were sampled with dimensions of 5 to 10mm, immersed in acetone during 1 day and dried during about 1 day at 40°C prior to being treated suitably to each of the test purposes.

Table 1. Mix design of concrete (relative ratios[*])

Cement	Water	Silica fume	Fine aggregates	Filler	Superplasticizer	Steel fiber
1.00	0.25	0.05~0.30	1.10	0.30	0.018	2% vol.

([*]) Relative ratios: weight ratio to cement, except steel fiber expressed as volumetric ratio to the whole volume.

Experimental results and discussion

Fluidity. Figure 1 plots the fluidity of UHPC according to the amount of silica fume. Test results reveal that increasing amount of silica fume up to 25% in weight ratio to cement increases the fluidity to reach a maximum fluidity of approximately 230mm. Amount of silica fume larger than 25% is seen to increase the viscosity of UHPC and degrade its fluidity. This shows the existence of an appropriate amount of silica fume improving the fluidity of UHPC.

Mechanical property. Figure 2 and Figure 3 plot respectively the compressive strength and the elastic modulus of UHPC according to the amount of silica fume. An observation of the measured compressive strength reveals that the compressive strengths of SF10 to SF25 are similar with a value of about 200MPa. In addition, the elastic modulus decreases with larger amount of silica fume but remains within a range of 43.6 to 45.4GPa for weight ratio to cement of approximately 10 to 25%. Accordingly, an amount of silica fume between 10 to 25% in weight ratio to cement is securing compressive strength of about 200MPa with quasi constant value of the elastic modulus.

Figure 4 plots the flexural strength of UHPC according to the amount of silica fume. It is seen that the flexural strength remains nearly constant with value of about 33Mpa for SF10 to SF25. However, SF05 develops a flexural strength of about 30MPa, which shows that the contribution of the steel fiber

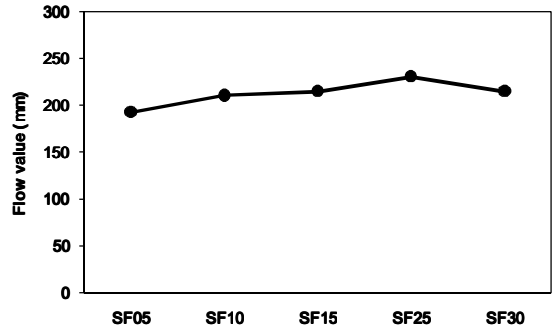

Fig. 1 Fludity of UHPC

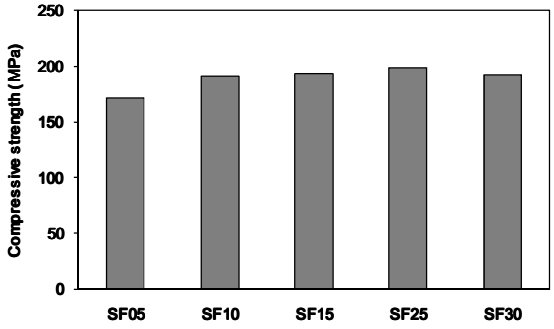

Fig. 2 Compressive strength of UHPC

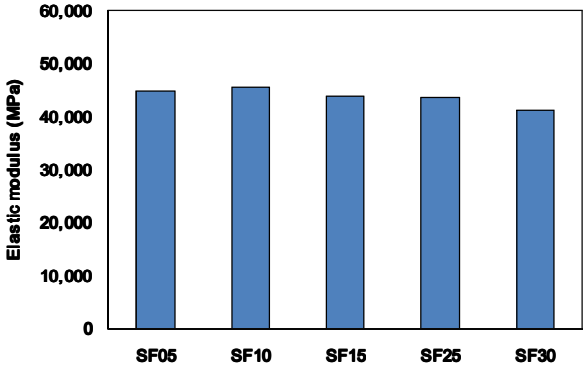

Fig. 3 Elastic modulus of UHPC

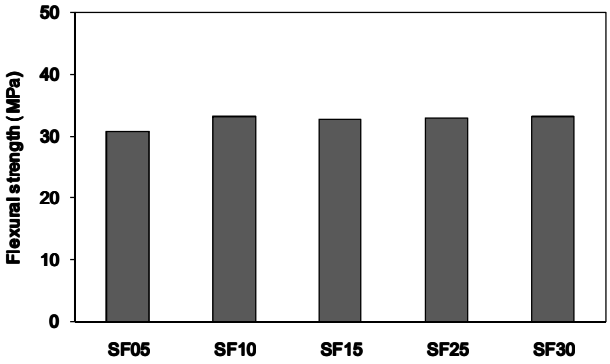

Fig. 4 Flexural strength of UHPC

content to the flexural strength of UHPC is more important than that of silica fume. Accordingly, the maximum fluidity of UHPC appeared when using up to 20% of silica fume in weight ratio, while an amount of silica fume ranging between 10 to 25% in weight ratio to cement provides similar mechanical characteristics regard to the compressive and flexural strengths. Therefore, it seems that the amount of silica fume can be reduced to 15% compared to former mix designs when fabricating UHPC. This allows more economical fabrication of UHPC through the adoption of other mineral admixtures considering the durability or fluidity.

Micro structure. Figure 5 illustrates the SEM measurements of UHPC according to the amount of silica fume. Quartz crystals with SiO_2 content can be mostly observed owing to the effect of the sand and filler included in UHPC. Even if the existence of hydrates like $Ca(OH)_2$ cannot be clearly assessed, it can be seen that the pores of the internal structure are filled with larger contents making the structure denser. In order to evaluate the effect of the hydrates according to the amount of silica fume, it seems that observation should be done on a paste mixed uniquely with cement and silica fume.

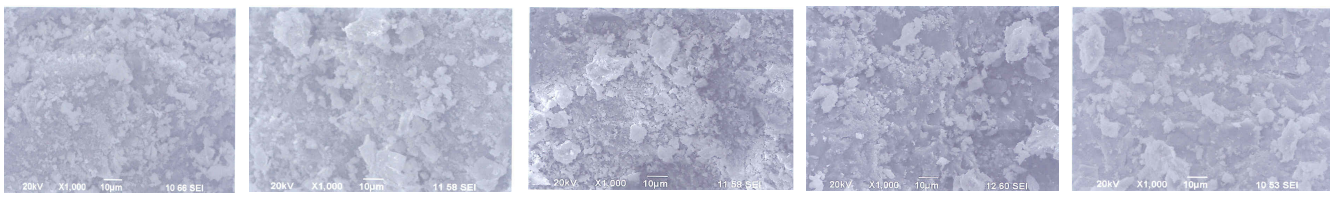

SF 05 SF 10 SF 15 SF 25 SF 30

Fig 5. SEM photographs (×1000)

Figure 6 depicts the pore distribution of UHPC according to the amount of silica fume by means of MIP measurements. The larger porosity exhibited by SF05 compared to the other specimens can be seen as the reason for the loss of its strength. Besides, Figure 7 illustrates the relationship between the compressive strength and the porosity within a range of 0.03 and 10 μm corresponding to the capillary

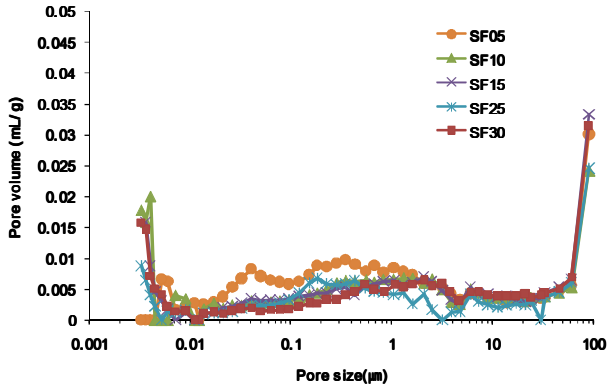

Fig. 6 Pore distribution of UHPC provided MIP

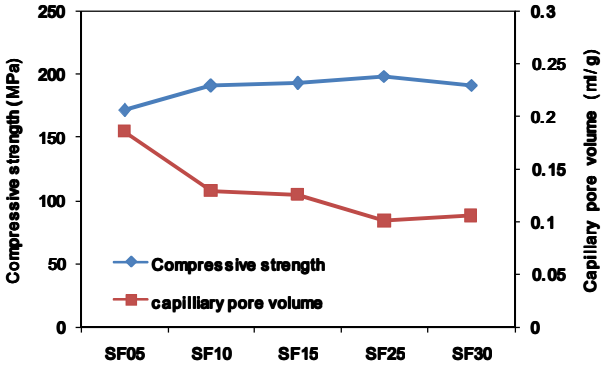

Fig. 7 Relation between compressive strength and capilary pore

pore range affecting the durability of concrete[2]. The porosity reduces up to an amount of silica fume of 25% leading to increased compressive strength. This is due to the augmentation of hydrates through pozzolan reaction of which filler action densifies effectively the internal structure of concrete and, subsequently, increases the strength and improves the durability.

Conclusions

This study investigated the effects of the amount of silica fume on the fluidity and developed compressive and flexural strengths in order to derive the appropriate amount of silica fume enabling to develop performances equivalent to former UHPC regard to the mechanical properties like strength while reducing the amount of silica fume to be adopted in the fabrication of UHPC. The corresponding results revealed that an amount of silica fume ranging between 10 to 25% in weight ratio to cement secured a flow larger than 210mm without significant differences in the strength characteristics with compressive strength, elastic modulus and flexural strength of about 200MPa, 43.6 to 45.4GPa and 33MPa, respectively. The MIP test showed that such range corresponded to the augmentation of hydrates through pozzolan reaction of which filler action densified effectively the internal structure of concrete and, subsequently, increased the strength of UHPC. Accordingly, the amount of silica fume can be reduced by a maximum of 15% compared to previous mix designs of UHPC so as to allow more economical fabrication of UHPC through the adoption of other mineral admixtures considering the durability or fluidity.

Acknowledgements

This study was carried out as a partial research of the “Development of UHPC for hybrid cable-stayed bridges” in the Korea Institute of Construction Technology. The authors express their gratitude for the support.

References

[1] Pierre Richard; Marcel Cheyrezy: COMPOSITION OF REACTIVE POWDER CONCRETES, Cement and Concrete Research, Vol.25, No.7(1995), p.1501-1511.

[2] KICT: Development of the advanced technology of durability in concrete bridges(2006).

[3] Park, J.J.; Koh, K.T.; Kang, S.T.; Ryu, G.S.; Kim, S.W.; Lee, J.H.: The effect of material factors on the compressive strength of ultra-high strength Steel Fiber Reinforced Cementitious Composites”, Proceedings of the Korean Concrete of Institude, Vol.16, No.1(2004), p.288-291.

Key Engineering Materials Vols. 385-387 (2008) pp 705-708
© (2008) Trans Tech Publications, Switzerland
doi:10.4028/www.scientific.net/KEM.385-387.705

Creep Curve Modeling to Generate the Isochronous Stress-Strain Curve of Type 316LN Stainless Steel

Song-Nan Yin[1,a], Woo-Gon Kim[1,b], Ik-Hee Jung [2,c], Yong-Wan Kim[1,d] and Seon-Jin Kim [2,e]

[1] KAERI, 150 Deogjin-dong, Yuseong-gu, Daejeon, 305-353, Korea

[2] Pukyong National University, 599-1 Daeyon-dong, Nam-gu, Busan, Korea

[a] yjsongnam@kaeri.re.kr, [b] wgkim@kaeri.re.kr, [c] jih2000@hanmail.net,

[d] ywkim@kaeri.re.kr, [e] sjkim@pknu.ac.kr

Keywords: Type 316LN Stainless Steel (316LN SS), Isochronous Stress-Strain Curve (ISSC), Creep Curve, Garofalo Model, Nonlinear Least Square Fitting (NLSF)

Abstract. An isochronous stress-strain curve (ISSC) needs to be generated for a creep design application for high-temperature materials. To generate the ISSC for type 316LN stainless steel (SS), a series of creep data, which was obtained from creep tests with different stress levels at 600°C, was used. Creep curves were modeled by means of a nonlinear least square fitting (NLSF) of the Garofalo model. In the fitting of the creep curve, a secondary creep region was separated into first and second phases, and its fitting range was suitable to use for the first phase. The Garofalo model revealed a good agreement with the experimental creep data, and its parameters, P_1, P_2 and P_3 revealed a good linear relationship as a function of a stress. The ISSCs for type 316LN SS at 600°C were successfully generated up to 300,000 hours.

Introduction

Type 316LN SS (nitrogen added 'LN' grade) is a candidate material for the major structural components of a liquid metal reactor (LMR) because of its good high-temperature mechanical properties. Since these LMR components are used for 30 to 40 years at 550°C, one of the most critical factors in their design is their time-dependent creep behavior [1,2].

In the design application of high temperature materials, the ISSC needs to avoid an excessive deformation of the materials during an intended service life, because they are designed with a target life based on a specified amount of allowable strain and stress. However, for an intended life over 30 to 40 years, to obtain the ISSC is not only very difficult, but also very time-consuming work. So, it is necessary to accurately predict long-term creep curves from short-term creep data.

To describe a creep strain-time curve well, typical constitute equations have been proposed by Garofalo[3], Kachanov-Rabotnov(K-R)[4], Blackburn [5], Evans[6~8] and Maruyama [9, 10], et al. Among them, the Garofalo model was used by Blackburn to generate the ISSC for austenitic stainless steel of type 304 and type 316 SS, because it is considered as the simplest one of all the constitutive equation forms. However, the ISSC data for type 316LN SS is not available yet in the ASME BPV NH code, but it has been reported for 304SS, 316SS, Alloy 800H, 2.25Cr-1Mo, and 9Cr-1Mo steels [11].

In this paper, long-term creep curves from short-term creep data for type 316LN SS at 600°C were modeled by means of the NLSF of the Garofalo model. The ISSCs for type 316LN SS were drawn successfully up to 300,000 hours.

Experimental procedure

Laboratory ingots of type 316LN SS were manufactured by a vacuum induction melting, and their chemical compositions are given in Table 1. They contain around 0.1wt.% nitrogen

instead of 0.03wt.% low carbon. The ingots were annealed for 2 hours at 1150°C in an argon atmosphere and reduced to 15mm by a hot rolling process. After, they were solution annealed for 1 hour at 1100°C and water quenched.

The creep test specimens were taken in the rolling direction and machined to a cylindrical shape with a 30mm gauge length and 6mm diameter. The creep tests were conducted with various stress levels of 210MPa~280MPa at 600°C. Creep strain data with elapsed times was taken automatically by a PC. Tensile specimens were also machined with a rectangular cross section of a 1mm thickness and 3.5mm width, and with a 25mm gauge length. Tensile tests were carried out under a strain control mode at 600°C. The creep curves obtained with different stress levels at 600°C are shown in Fig. 1.

Table 1 Chemical composition of type 316LN SS (wt.%)

Fe	C	Si	Mn	P	S	Cr	Ni	Mo	N	B
Bal.	0.022	0.7	1.01	0.029	0.005	17.15	12.3	2.35	0.094	0.003

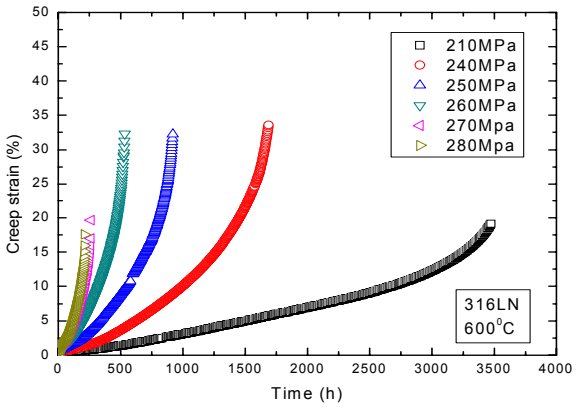

Fig. 1 Creep curves for type 316LN SS for 210MPa ~280MPa at 600°C

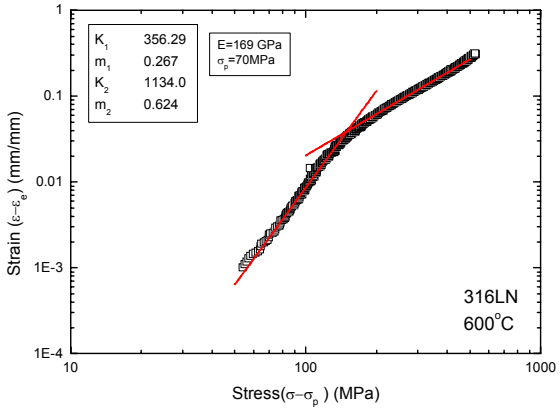

Fig. 2 True stress-strain curve for type 316LN SS at 600°C

Results and Discussion

Tensile property. The basic equations for time-independent elastic plus plastic strain are

$$\varepsilon_L = \frac{\sigma}{E} \quad for\ \sigma \le \sigma_p \tag{1}$$

$$\varepsilon_L = \frac{\sigma}{E} + \left[\frac{\sigma - \sigma_p}{K_1}\right]^{1/m_1} \quad or \quad \frac{\sigma}{E} + \left[\frac{\sigma - \sigma_p}{K_2}\right]^{1/m_2} \quad for\ \sigma > \sigma_p \tag{2}$$

Where, E, σ_p, K_1, m_1, K_2 and m_2 are material constants and are evaluated by the least square fitting method for the tensile test data. The E and σ_p are the elastic modulus and elastic limit stress. A numerical result of Eq.2 for a true plastic strain region of type 316LN SS was separated into two phases, as shown in Fig. 2. It is emphasized that Eq. 2 is derived in terms of a true stress and a true strain, while the equations for a creep strain are all in engineering strain units. Thus, when significant plastic strains are involved, it is necessary to convert the stress and strain values from Eq. 2 to engineering units before combining ε_L with the creep strains [3].

Creep property. The equation for a time-dependent creep strain proposed by Garofalo is given by the following form [3],

$$\varepsilon = \varepsilon_L + \alpha[1 - e^{-\beta t}] + \dot{\varepsilon}_m t \tag{3}$$

Where ε is the total strain, ε_L is the instantaneous strain, α is the limiting magnitude of a transient creep strain, β is a constant related to the rate of an exhaustion of a transient creep, and $\dot{\varepsilon}_m$ is a secondary creep or minimum creep rate, and t is the time.

To avoid an initial strain effect in the modeling process of a creep strain, Eq. 3 can be rewritten as Eq.4, where ε_c is a pure creep strain, P_1, P_2 and P_3 are the equation parameters corresponding to α, β and $\dot{\varepsilon}_m$, and a stress dependency for each parameter is given as Eq. 5.

$$\varepsilon_c = (\varepsilon - \varepsilon_L) = P_1\left[1 - e^{-P_2 t}\right] + P_3 t \tag{4}$$

$$\log P_i = a_i + b_i \sigma \tag{5}$$

Fig. 3 shows the creep curve result tested under 240MPa at 600°C. The creep curve was separated into three regions: primary, secondary and tertiary creep stages. Also, it is clearly observed that the secondary creep region was separated into first and second phases. Thus, the fitting range is suitable to use for the first phase to accurately describe the secondary creep stages in the NLSF process, because a creep design is generally carried out within the 1% strain limit.

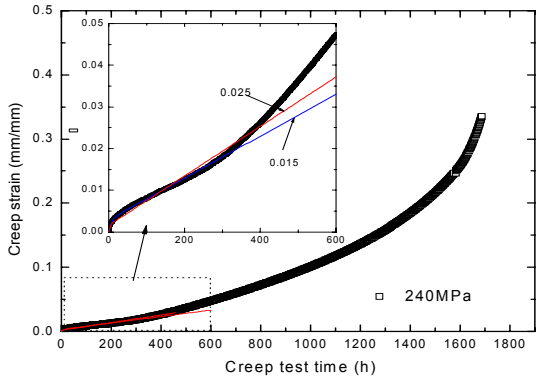

Fig. 3 Effect of the fitting range for a 0.025 and a 0.015 strain in the creep curve

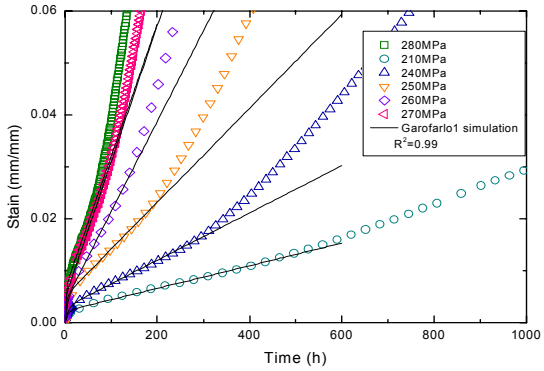

Fig. 4 Creep strain-time curve for type 316LN SS at 600℃

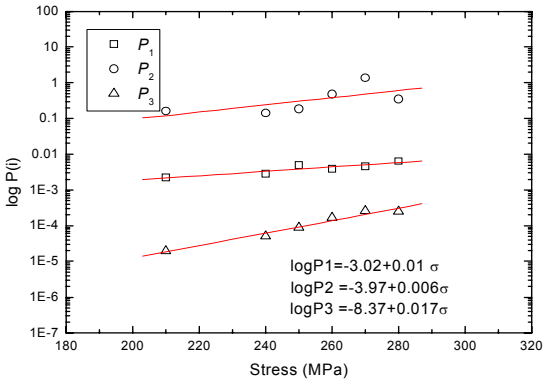

Fig. 5 A stress dependency of parameter P_i in the Garofalo model

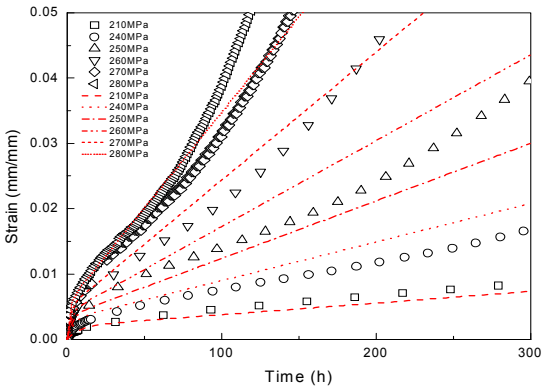

Fig. 6 Comparison between the estimated and experimental creep curves

Fig. 4 shows the fitting result of the experimental creep curves for 210MPa ~280MPa at 600°C. When the NLSF was carried out up to the first phase of the secondary creep stage, it was quite similar to the experimental creep data, and the correlation factor (R^2) was above 0.99 for all of the regression analysis. Also, the behavior of the stress dependency for the equation parameters, P_i is shown well in Fig. 5. The P_1, P_2 and P_3 parameters increased linearly with an increasing stress, as a function of the stresses. From this linear relation, the values for the three parameters can be predicted up to a given low-stress level.

Fig. 6 shows the comparison results between the modeled creep curves and the experimental data.

The modeled curves were predicted by calculating the three parameters obtained in Fig 5. Although the fitting results were not matched perfectly with the individual creep data, they are able to properly describe the creep curves for wide ranges of stresses. Thus, from the three determined parameters of P_1, P_2 and P_3, the ISSCs for an extended period can be generated by using Eq. 3.

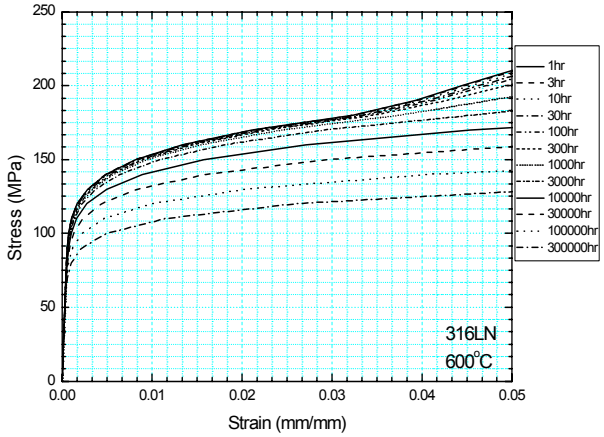

Fig. 7 The ISSC obtained for type 316LN at 600°C

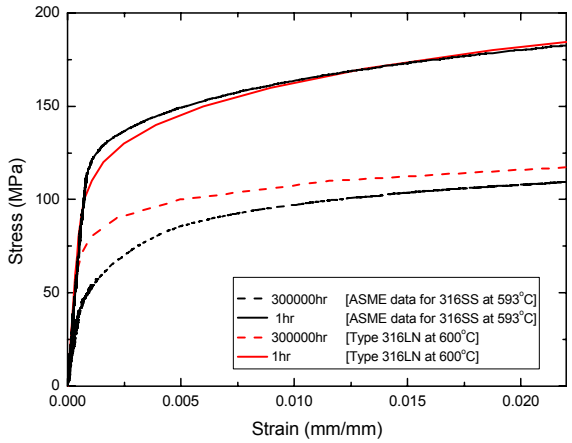

Fig. 8 The ISSC comparison of type 316LN SS and 316SS in 1hr and 300,000hr

The ISSC generation for type 316LN SS. The ISSCs for 1 hour to 300,000 hours were generated successfully for type 316LN SS at 600°C, as shown in Fig. 7. These ISSCs were obtained by directly computing Eq. 3. The ISSC for 1hour, which indicates a conventional tensile test, reveals a steep change in the slope at the 3%~4% strain range. The reason for this change is due to the transition from Eq. 1 to Eq. 2 when computing the ISSC.

Fig. 8 shows the comparisons of the ISSC results for type 316LN and 316 SS at 600°C. The ISSCs for type 316 SS is the reported data in ASME BPV NH Code [11]. For 1 hour of the ISSC, the two materials were almost similar, but for 300,000 hours, the materials revealed a significant difference. Thus, it is clearly confirmed that type 316LN SS is superior for its long-term creep strength when compared to type 316SS.

Conclusion

In the NLSF of the creep curves for type 316LN SS, a secondary creep region was separated into first and second phases, and its fitting range was suitable to use for the first phase. The Garofalo model revealed a good agreement with the experimental creep data, and the P_1, P_2 and P_3 parameters revealed a good linear relationship as a function of a stress. From this result, the ISSC for type 316LN SS at 600°C was successfully drawn for up to 300,000 hours.

References

[1] W. G. Kim, S. N. Yin, W. S. Ryu and W. Yi: Key Eng. Mater., Vol. 326 (2006), p. 1313.
[2] S.N. Yin, W.G. Kim, W.S. Ryu and W. Yi: Trans. of the KSME A, Vol.31, (2007), p. 160.
[3] F. Garofalo: *Fundamentals of Creep and Creep Rupture in Metals*, Macmillan Co., NY (1966).
[4] R. K. Penny and D. L. Marriott: *Design for Creep*, Chapman & Hall, (1995), p. 206.
[5] L. D. Blackburn: ASME, NY (1972), p. 14.
[6] R. W. Evans, J. D. Parker and B. Wilshier: Int. J. of PVP, Vol. 50 (1992), p. 147.
[7] S. G. R. Brown, R. W. Evans and B. Wilshire: Int. J. of PVP, Vol. 24 (1986), p. 251.
[8] M. D. Mathew, S. L. Mannan and P. Rodriguez: Mater. Sci. and Eng., Vol. A159 (1992), p. 199.
[9] K. Maruyama, C. Harada and H. Oikawa: J. Soc. Mater. Sci., Vol. 34 (1985), p.1289.
[10] K. Maruyama and H. Oikawa: Scripta Metallurgica, Vol. 21 (1987), p. 233.
[11] ASME BPV Code III-Division–Subsection NH, *Rules for Construction of Nuclear Facility Components*, (2007), p. 129.

Key Engineering Materials Vols. 385-387 (2008) pp 709-712
© (2008) Trans Tech Publications, Switzerland
doi:10.4028/www.scientific.net/KEM.385-387.709

Fracture Model for PT Flat Plate Connections under Seismic Loading

Ki-Hoon Moon [1, a], Jin Hwang-Bo[2,b] and Sang-Whan Han[3,c]

[1,2,3]Architectural Engineering, Hanyang University, Seoul, 133-791, Korea

[a]acttr@hanmail.net, [b]breadjin@naver.com, [c]swhan@hanyang.ac.kr

Keywords: PT flat plate, connection, nonlinear behavior, pushover.

Abstract. Post-tensioned (PT) flat plate frames are commonly used to support gravity load in connections in high seismic regions. But test results of many studies indicated that PT flat plate connections were possessed of later-resisting capacity for lateral load though this capacity is not enough to be used by itself in high seismic regions. So this study evaluated the cyclic behavior of PT flat plate connections and developed an analytical model for predicting nonlinear behavior of those to estimate the seismic performance of PT flat plate frames accurately. For this purpose, the test results of static pushover test and shaking table test of 2 story PT flat plate frame were used to evaluate the characters of failure mode for PT flat plate connections and to compare with analysis results. The test results indicated two failure modes which are classified the shear failure mode or the moment failure mode as for shear strength of PT connections to resist lateral loads acted on the specimens. So the analytical model was designed to consider these failure modes of PT connections and the results of comparing with test results predict the nonlinear behavior of PT connections.

Introduction

Post-tensioned flat plate frames (PT flat plate) have been generally used to support gravity loads, which should be constructed with lateral resisting system such as shear walls or moment frames. However PT flat plate frames that resist the gravity loads without collapse are evaluated the lateral displacements by lateral resisting system. And PT flat plate frames that resist to lateral loads are permitted to construct to the intermediate moment frame (IMF) with special conditions by ACI 318-05 [1]. For evaluating seismic performance the PT flat plate frames exactly, the connection of PT flat plate frame has to reflect lateral deformation capacity.

Prior to slab-column connection analytical model, this is used to equivalent beam section model. But prior analytical models do not reveal exactly punching shear failures in PT flat plate slab-column connection. According to ACI 318-05 [1], minimum top bonded reinforcement is required to the PT gravity flat plate system, however, for these PT gravity systems, minimum bottom reinforcement is usually not required in the connection regions. But prior researches [2, 3, 4, 5] indicate that slab bottom reinforcements influenced to lateral drift. The positive slab moment eventually develops on one side of the slab-column connection as the seismic demand is increased, therefore, sufficient bottom reinforcement should be provided to avoid the formation of large cracks. So, this study developed to correspond to with and without slab bottom reinforcement as well as punching shear. And this analytical model compare to analytical model and connection experimental results by Han et al [3, 4, 5] and frame results by Kang and Wallace[6, 7].

Slab-Column connection

In this study, analytical model that are developed P-Delta effect use OpenSees program. [6, 7, 8, 9]

As more lateral load being induced, rotational angle of connection of PT flat Plate systems became significance and flexural cracks which occurred at slab surface and in the vicinity of connection become wider. After that, strain of slab reinforcement reach to yield and system shows inelastic behavior.

Punching failures are expected to occur either when the shear capacity of the slab critical section is reached or when drift capacities of the slab-column connections are reached for a given gravity shear

ratio. Punching failure prior to yielding of slab reinforcement occur when the sum of unbalanced moment of direct gravity shear stress and of shear stress induced by the fraction of unbalanced moment transferred by eccentric shear reaches the shear stress capacity on the slab critical section.

$$M_{unb,s} = (v_c - \frac{V_u}{b_o d})\frac{J_c}{c\gamma_v} \quad (1)$$

$$M_{unb} = \frac{(M^{\pm}_{y,c_2+3h} + M^{\mp}_{y,c_2+3h})}{\gamma_f} \quad \text{(Interior)} \quad (2)$$

$$M_{unb} = \frac{M^{\pm}_{y,c_2+3h}}{\gamma_f} \quad \text{(Exterior)} \quad (3)$$

where V_g is the gravity force to be transferred from the slab to the column, b_0 is the perimeter of critical section, d is the effective slab depth, γ_v is the fraction of unbalanced moment transferred by eccentric shear, $M_{unb,s}$ is the unbalanced moment, c is the distance from the centroid of the critical section to the perimeter of the critical section that results in $M_{unb,s}$, J is the polar moment of inertia of the critical section, and v_n is the nominal shear capacity at the connection. $M^{\pm}_{y,c_2+3h} + M^{\mp}_{y,c_2+3h}$ is the yield moment of the slabs framing into a connection over a transfer width of $c_2 + 3h$, c_2 is the column width, h is the slab thickness.

In the case of M_{unb} derived by equations (2) and (3) is greater than $M_{unb,s}$ derived from equation (1), punching failure occurred before slab reinforcement and strands experience the yield. For this case, the capacity of the connection spring drops suddenly prior to reaching yield of slab reinforcement as like failure mode 1 in Fig. 1.

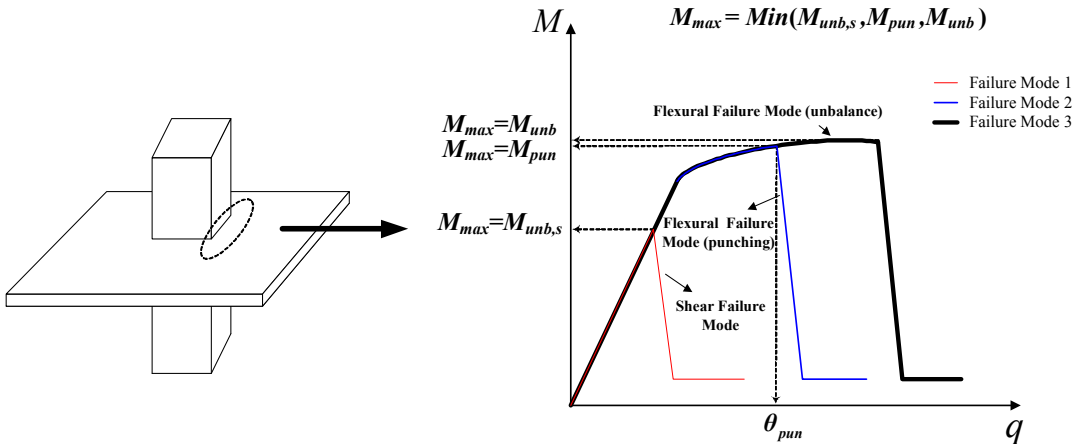

Fig. 1 Slab-Column connection

In the case of $M_{unb,s}$ derived by eq. (1) less than M_{unb} derived by eq. (2), (3), punching shear would occur after yielding of flexural reinforcement.

The flexure failures are yielding of slab reinforcement followed by punching failure (failure mode 2 in Fig. 1) and punching failure after flexural yielding within the column strip (failure mode 3 in Fig. 1).

The drift ratio at punching is determined by regression analysis of drift ratio data which are occurred at punching shear failure of flat plate slab-column connection according to gravity shear ratio as shown in the fig. 2.

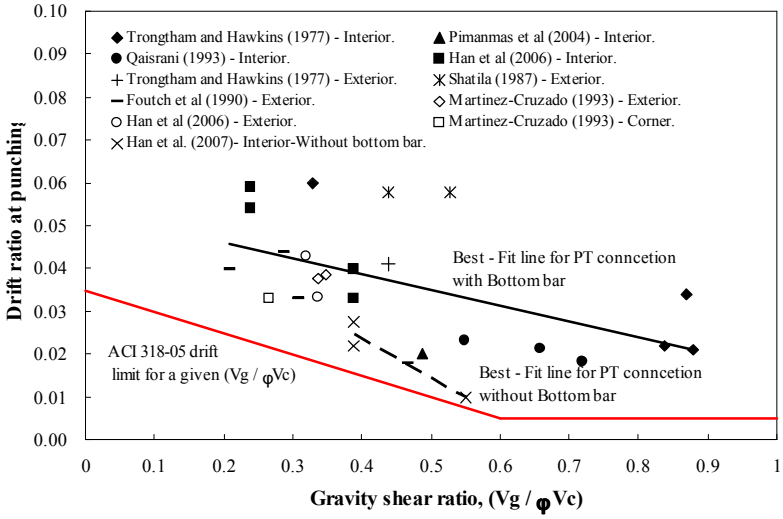

Fig. 2 Lateral Drift Capacity of flat plate

The slab analytical model was assumed elastic beam sections. The thickness of beam is assumed to be equal to the thickness of slab. The width of beam is used to the effective slab width model by Banchick[7], the stiffness reduction factor is used 0.33. The column was fiber model selected because this relatively simple model accurately captures nonlinear flexure-axial load behavior of column.

Comparison to experiment results and analytical results

This study compares to the analytical slab-column connection model results and the prior experimental PT connection results in Fig 2. PI-D30 and PI-D50 specimens are interior connections that gravity shear are 0.3 and 0.5. PI-D50X is a without slab bottom reinforcement, PE-E50 is a exterior connection. The variables of the PT flat plate connection permissions are gravity load, with and without slab reinforcement, location of connections that are equal gravity load and quasi-static cyclic loading (Han et al). Fig. 3 shows that the analytical results are similar to prior experimental results.

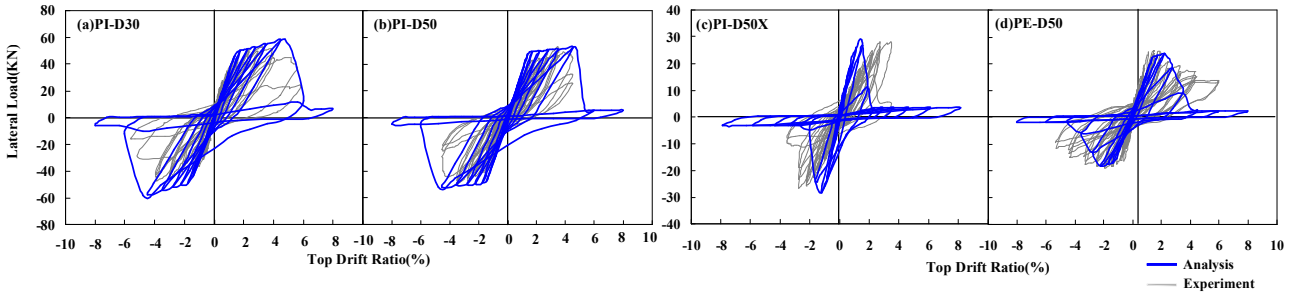

Fig. 3 Measured and experiment and analysis results

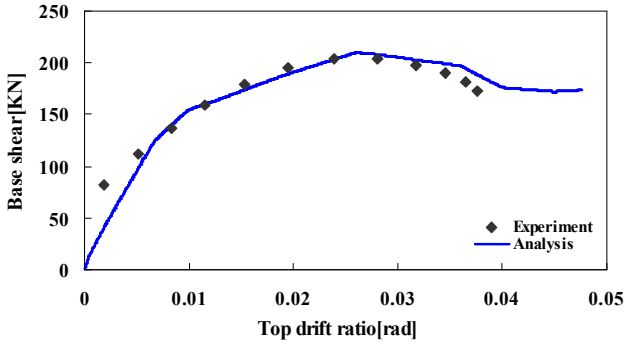

Fig. 4 Measured and pushover analysis

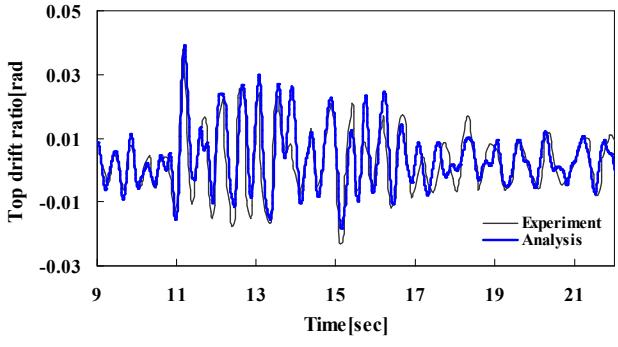

Fig. 5 Measured and dynamic analysis

And this study compare with the shaking table results of PT flat plate 2-frame that have conducted by Kang and Wallace [6, 7] used Chi-Chi earthquake(PGA=0.136g) acceleration in 1999. The static pushover analysis result in Fig. 4. are estimated well the base shear and the roof drift that were experimtal result. And in Fig . 5, the reult of nonlinear response history analysis are approximately 2% diffrennce to experimatal results.

Summary

This study develops the analytical model that reflects various PT flat plate connection behaviors and failure modes. Especially, this analytical model reflects a variety of punching failures of with and without slab bottom reinforcement. The analytical results are evaluated to experimental results.

Acknowledgements

The work presented in this paper was sponsored by Hanyang University, MOST R01-2006-000-10722-0 and SRC/ERC R11-2005-056-04002-0. The views expressed are those of authors and do not necessarily represent those of the sponsor.

References

[1] ACI Committee 318, "Building Code Requirements for Reinforced Concrete(ACI 318-02)", American Concrete Institute, Detroit, 2002.

[2]. Martinez-Cruzado, Jose Antonio, "Experimental study of post-tensioned flat plate exterior slab-column connections subjected to gravity and biaxial loading, "Ph D Thesis, Department of Civil Engineering, University of Berkeley, CA, 1993.

[3] Han, et all, "Hysteretic behavior of exterior post-tensioned flat plate connections", Engineering Structures, Elsevier, 28 (2006) 1983–1996

[4] S.W. Han, S.-H.Kee, T.H.-K.Kang, S.-S.Ha, J.W.Wallace,L-H.Lee "Cyclic behaviour of interior post-tensioned flat plate connections", Magazine of Concrete Research, Vol 58, p699~711 2006

[5] S.W. Han, S.-H.Kee, S.-S.Ha, J. W. Wallace, " Effects of Bottom Reinforcement on Hysteretic Behavior of Post-Tensioned Flat Plate Connections" submitted to Journal of Structural Engineering, ASCE, 2007.

[6] KANG T. H.-K., "Shake Table Tests and Analytical Studies of Reinforced and Post-Tensioned Concrete Flat Plate Frames," Ph.D. Thesis, UCLA, Sept. 2004, 309 pp.

[7] Thomas H.-K. Kang and John W. Wallace, "Punching of Reinforcedand Post-Tensioned Concrete Slab-Column Connections" ACI Structural Journal, V. 103, No. 4, July-August 2006.

[8] Mary Beth D. Hueste and James K. Wight "NONLINEAR PUNCHING SHEAR FAILURE MODEL FOR INTERIORSLAB-COLUMN CONNECTIONS," JOURNAL OF STRUCTURAL ENGINEERING, V. 125, No. 9 SEPTEMBER 1999.

[9] OpenSees Development Team (2006). "OpenSees: Open System for Earthquake Engineering Simulations," Version 1.7.3, Berkeley, CA

Key Engineering Materials Vols. 385-387 (2008) pp 713-716
© (2008) Trans Tech Publications, Switzerland
doi:10.4028/www.scientific.net/KEM.385-387.713

Study on Calculation Method of Fracture Parameters of the Tubular Based on 3D VCCT

Qingyuan Wang[1,a] Yongjie Liu[1,b] Xiangguo Zeng[1,c] Huayan Chen[1,d],

[1.] Dept of Civil Eng & Mechanics, Sichuan University, Chengdu, P.R. China, 610065

[a] wangqy@scu.edu.cn , [b] liuyongjie_2002@163.com, [c] xiangguo_zeng@yahoo.com.cn, [d] kay_chy@126.com

Keywords: tubular specimen; single-variable; 3D VCCT; fracture parameter; FEM.

Abstract: The stress intensity factor (SIF) for tubular specimens were calculated based on virtual crack closure technique （VCCT）. The effects of geometrical factors (inner radius, wall thickness and relative crack length) and external loads on the SIF were analyzed, respectively, by use of the single-variable approach. Finally, an approximate formula for SIF of compact-tensile tubular specimens was obtained as all factors mentioned were considered, which was presented as a reference for the tubular engineering design.

Introduction

The macro flaws produced during machining. When the integrality was evaluated by using the method of fracture mechanics, the important parameter used is the SIF. Up to now, the calculation method that SIF of tubular specimens was calculated has been unresolved. Because the SIF is related to the geometry configuration with crack body and external load, it can not be measured directly and just calculated according to state of crack body. Due to mathematical difficulty, only a few closed analytical solutions exist for some specific problems of infinite body and anti-plane problems. For practical engineering problems, the mode is finite body with complex stress state and constitutive relationship. It is very difficult for engineer to find the solution of SIF for complex situation. In this paper, by use of the single-variable approach, the effects of geometrical factors (inner radius, wall thickness and relative crack length) and external loads on the SIF were analyzed. Finally, an approximate formula for SIF of compact-tensile tubular specimens was obtained as all factors were considered, which was presented as a reference for the tubular engineering design.

Finite element model for tubular component with crack

The sketch of sample with side crack as shown as Fig. 1. The dimension of sample was shown as table 1.

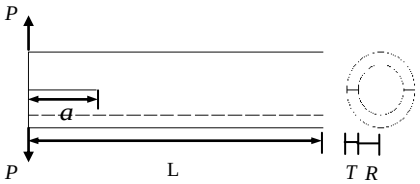

Fig. 1 Sample with side crack

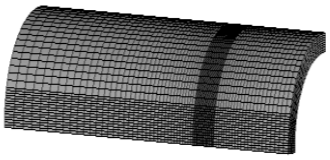

Fig. 2 Finite model

Table 1 the dimension of model

T(mm)	R(mm)	L(mm)	a(mm)
3	15	50	15

Structural analysis code ANSYS 10.0 is employed. Element type SOLID182 is selected. The material property is linear elastic isotropic. Young's modulus of steel is 142.4 GPa, and Poisson's ratio is set as 0.25, respectively. Due to the symmetry of the model, the 1/4 calculation model was adopted. Fig. 2 shows the finite element model that contains 60978 nodes and 13050 elements. The minimum dimension of the element in front of crack is almost 0.01 mm.

The calculations of energy released rate and SIF based on VCCT

The VCCT was first proposed for 2D crack configurations by Rybicki and Kanninen [1], and was extended to three dimensions (3D-VCCT) by Shivakumar et al. [2]. Because the plane strain exist in front zone of crack, the expression of SIF, proposed by Bakker[3], is given as

$$K = \sqrt{EG/(1-\upsilon^2)} \qquad (1)$$

where E is Young's modulus, ν is Poisson's ratio, G is energy release rate and K stands for SIF, respectively.

When a body, with a crack length a, is subjected to loads, the energy release rate is defined as follow:

$$G = \partial U / \partial a \tag{2}$$

where U is total strain energy of structure, a is crack length.

In terms of Eq. 2., the strain energy release rates can be calculated for the 3D configuration using virtual crack closure technique [4] by calculating the work required to close the crack from ($a+\Delta$) to (a) for mixed-mode situation. The nodal forces at nodes c_3, c_4, c_5, d_2 and d_3 and the relative displacements at nodes a_3, a_4, a_5, b_2 and b_3 behind the crack front are used to calculate G-values, i.e. G^e as:

$$G_I^e = -\frac{1}{2\Delta b_j}\left\{C_1\left[Z_{c_3}\left(w_{a_3}-w_{A_3}\right)+Z_{d_2}\left(w_{b_2}-w_{B_2}\right)\right]+C_2\left[Z_{c_5}\left(w_{a_5}-w_{A_5}\right)+Z_{d_3}\left(w_{b_3}-w_{B_3}\right)\right]+Z_{c_4}\left(w_{a_4}-w_{A_4}\right)\right\}$$

$$G_{II}^e = -\frac{1}{2\Delta b_j}\left\{C_1\left[X_{c_3}\left(u_{a_3}-u_{A_3}\right)+X_{d_2}\left(u_{b_2}-u_{B_2}\right)\right]+C_2\left[X_{c_5}\left(u_{a_5}-u_{A_5}\right)+X_{d_3}\left(u_{b_3}-u_{B_3}\right)\right]+X_{c_4}\left(u_{a_4}-u_{A_4}\right)\right\} \tag{3.1}$$

$$G_{III}^e = -\frac{1}{2\Delta b_j}\left\{C_1\left[Y_{c_3}\left(w_{a_3}-w_{A_3}\right)+Y_{d_2}\left(u_{b_2}-u_{B_2}\right)\right]+C_2\left[Y_{c_5}\left(w_{a_5}-w_{A_5}\right)+Y_{d_3}\left(w_{b_3}-w_{B_3}\right)\right]+Y_{c_4}\left(w_{a_4}-w_{A_4}\right)\right\} \tag{3.2}$$

(3.3)

where $C_1 = \dfrac{b_j}{b_{j-1}+b_j}$, $C_2 = \dfrac{b_j}{b_{j+1}+b_j}$. For first layer, $C_1 = 1$, for last layer, $C_2 = 1$. The expresses of total energy released rates of element and structure are given by

$$G^e = G_I^e + G_{II}^e + G_{III}^e \quad , \quad G = \sum G^e \tag{4}$$

The forces X, Y, Z in Eq. (3) are the forces calculated only from elements in the J th layer and above the crack plane. u, v, w in Eq. (3) are the displacements of x, y, z directions. Width b_{j-1}, b_j, b_{j+1} are separately the widths of ($J-1$)th layer, J th layer, ($J+1$)th layer, as shown as Fig. 3.

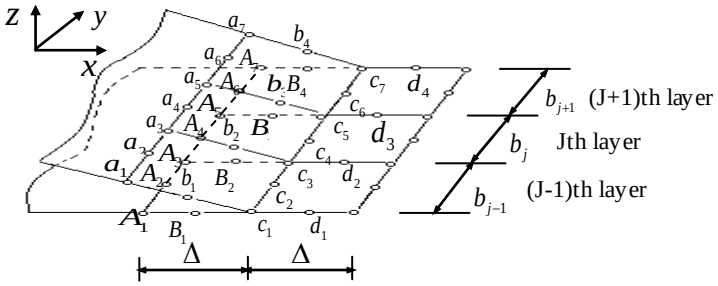

Fig. 3 Elements and nodes in the G calculation by the VCCT method

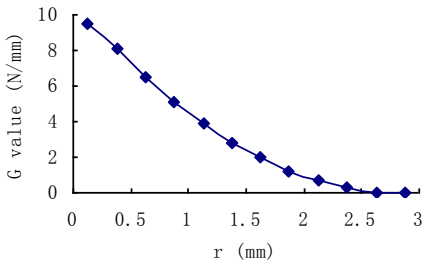

Fig.4 G-value distribution in ahead of crack

The G-values calculated from Eq. (3) are assigned to the J th layer and are assumed to be the G-values at the middle node on the crack front in the J th layer, i.e. at node c_4 in Fig.3. Eq.(3) is applied to each layer in the model to calculate the G-values throughout the width. Thus these values along the crack front yield the G - distribution for the crack configuration.

G-value distribution in front of crack

Considering the external load P=2 KN, the nodal force at ahead of crack and nodal displacement at behind of crack are evaluated by using the VCCT. In Eq.(5), the G-value of each element can be gotten along radial direction in front of crack. And then the G-values of each element are assumed as the nodal ones in front of crack. G-value distribution in front of crack is shown as Fig.4. In Fig.4, the G-values are decreasing along radial direction and the maximum G-value are located the cross position between the front of component crack and inner surface. The G-values are assumed as cube polynomial distribution, i.e. $G = ar^3 + br^2 + cr + d$, r represents radial distance, when $r \to 0$, it means the G-value at cross position between ahead of component crack and inner surface, respectively. In this paper, the SIF is evaluated by using the maximum G-value in Eq.(1).

The effect of load magnitude on the SIF

The inner radius R, thickness T and relative depth α are constant, the SIF is evaluated by changing the magnitude of load P,as shown in Fig.5. In Fig.5, the SIF increases with the increasing of load P, and the SIF is proportional to external load P.

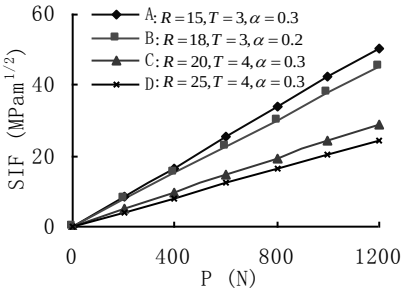

Fig.5 Change of SIF with the increasing of external load

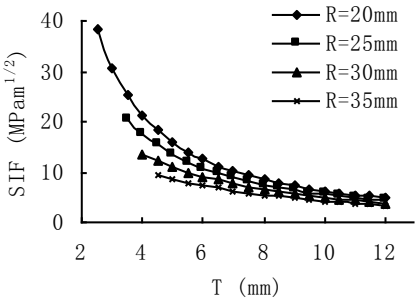

Fig.6 Change of SIF with the increasing of thickness

The effect of thickness on the SIF

Considering load P=1 KN and relative crack depth α=0.3, the SIF is evaluated by changing the magnitude of thickness T, as shown in Fig.6.In Fig.6,the SIF is decreasing with increasing of thickness T.With the same thickness, the less the radius, the bigger the SIF. Under the bigger thickness, as shown in Fig.6 the thickness T is over 10mm, the effect of radius R on SIF is decreasing. Based on the tendency of curves, the power function was adopted to fit the curves, respectively.

The effect of radius on the SIF

When load P is 1 KN and relative crack depth α is 0.3, the SIF is evaluated by changing of the radius of component, the results are shown as Fig. 7. In Fig.7, the SIF is decreasing with increasing of radius R. At the same radius R, the bigger the thickness, the smaller the SIF. Based on the tendency of curves, the power function was adopted to fit the curves, respectively.

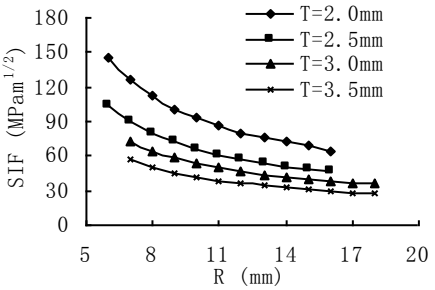

Fig.7 Change of SIF with the increasing of radius

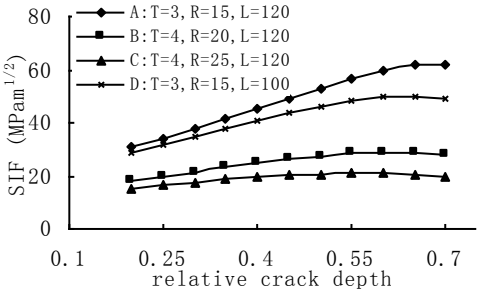

Fig.8 Change of SIF with the increasing of relative crack length

The effect of relative crack depth on the SIF

When load P is 1 KN, the SIF is evaluated by changing of the relative crack depth of component, the results are shown as Fig. 8. In Fig.8, in the beginning of the curves, with the increasing of crack length, the stress intensity is proportional with crack length. When the relative crack depth reaches a specific value (e.g., the relative crack depth is 0.5 on curve C), the SIF almost does not change, respectively.

The fitting of expression and certification

The effects of extender load P, inner radius R, thickness T and relative crack length α on the SIF were made. Under the range of $2T < R < 5T$,the curves were fitted by using data of finite element. By means of controlling of single variable, the power functions for radius R and thickness T were adopted by $K = C / R^{2/3}$ and $K = C / T^{4/3}$ as fitting functions and liner functions for external load P and relative crack depth α were adopted by $K = CP$ and $K = C_1\alpha + C_2$ as fitting functions. The changes of the SIF with the thickness T （ R=25mm, α=0.3 , P=1 KN） and inner radius R

（T=5mm, α=0.3 , P =1 KN）were fitted as Fig.9.

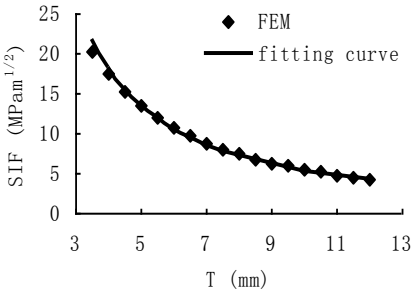

（a） Fitting curve $K=114.8185/T^{4/3}$

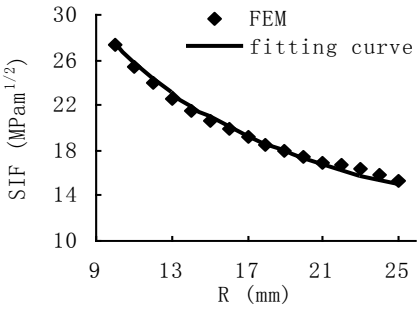

（b）Fitting curve $K=127.344/R^{2/3}$

Fig.9 Curves of the fitting

The factors that mentioned ahead were considered, the SIF can be nearly expressed as:

$$K = I \times \frac{P}{T^{4/3}R^{2/3}}\left(C_1\alpha + C_2\right) \qquad (5)$$

where I is non-dimensional constant, C_1 and C_2 are constants. When α and T meet $0.2 \le \alpha \le 0.4$ and $4mm \le T \le 6mm$,substituting the results of finite calculation into Eq.(5),the C_1 and C_2 are evaluated by using least squared method and the results were shown as follows:

$$K = I \times \frac{P}{T^{4/3}R^{2/3}}\left(1.4857\alpha + 0.6144\right) \qquad (6)$$

where K is SIF（MPam$^{1/2}$）, I is unite variable with dimension of m$^{1/2}$; P is extender force (N); R is the inner radius (mm); T is the thickness (mm); α is relative crack length.

The comparison between results from finite calculation and ones by using the Eq. (6) are shown at table 2. It shows good agreement.

Table 2 The comparison between results from finite calculation and ones by using the Eq. (6)

$\alpha = 0.2$											
T=4mm				T=5mm				T=6mm			
R(mm)	K_E	K_F	（%）	R(mm)	K_E	K_F	（%）	R(mm)	K_E	K_F	（%）
8	33.985	35.890	5.60	10	21.534	22.969	6.66	12	15.071	15.951	5.84
10	29.348	30.929	5.39	12	19.386	20.341	5.86	14	13.921	14.393	4.63
12	26.305	27.389	4.11	14	17.851	18.354	2.82	16	13.046	13.167	0.93

Acknowledgments

Financial support from the Chinese National Science Foundation through the contracts of 10776023 and 10772125 is appreciated.

References

[1] Rybicki, E.F. and Kanninen, M.F. A finite element calculation of stress intensity factors by a modified crack closure integral. *Engineering Fracture Mechanics*.1977,9:931–938.

[2] Shivakumar KN, Tan PW, Newman Jr JC. A virtual crack-closure technique for calculating stress intensity factors for cracked three dimensional bodies. *Int J Fract* 1988;36:R43–50.

[3]Bakker,A.. Three-dimensional constraint effects on stress intensity distributions in plate geometries with through-thickness cracks. *Fatigue and Fracture of Engineering Materials and Structures*.1992,15(11): 1051–1069.

[4] I.S.Raju,R.Sistla and T.Krishnamurthy. Fracture mechanics analyses for skin-stiffener debonding. *Engineering Fracture Mechanics*. 1996,54(3):317-385.

Key Engineering Materials Vols. 385-387 (2008) pp 717-720
© (2008) Trans Tech Publications, Switzerland
doi:10.4028/www.scientific.net/KEM.385-387.717

Study on the optimum mixing condition for control of spalling in high strength concrete by a orthogonal array

Mun-Hwan Lee[a], Young-Hun, Kim[b], Jong-Chan Lee[c]

[abc]Building Structure & Material Research Division, Korea Institute of Construction Technology, 2311, Daehwa-dong, Ilsan-gu, Koyang, Kyonggi-do, 411-712, Korea

[a]mhlee@kict.re.kr, [b]youngkh7@kict.re.kr, [c]mcljc@korea.com

Keywords: Spalling, High strength concrete, Fire resistance, Orthogonal array, Meta-kaolin

Abstract. This study proceeded to find the optimum mixing rate of a high strength concrete with 80MPa of compressive strength using meta-kaolin, waste tire chips, polypropylene, and steel fiber together for improvement of fire resistance performance.
To estimate of optimum mixing rate, the orthogonal array method was used to plan the factors (slump flow, air content, compressive and flexural strength, steel bar temperature and concrete spalling volume) of high strength concretes and experiment was executed. Then the functional relationship of each factor was valuated by general linear model of ANOVA and functional relation between the factors and the data was estimated using response surface analysis. The optimum mixing rate was computed as 80% replacement of silica fume volume by meta-kaolin, 3% replacement of fine aggregates volume by waste tire chips and 0.2% additive rate of polypropylene fiber without steel fiber to the total mixed volume with this modeling of the functional relationship.

1. Introduction

The high temperature caused by fire is provoking defects of the cement matrix and aggregates of high-strength concrete and is also standing as the main cause of spalling. Numerous researches have been conducted to develop material reinforcement and techniques to improve the fire-resistance performance of high-strength concrete but these researches remained limited to concrete with compressive strength below 60MPa or faced limitations due to the increase of costs required to improve the relevant performances. Accordingly, a new approach is today being adopted to enhance fundamentally the material characteristics of high-strength concrete through the improvement of its material properties so as to strengthen the fire-resistance performance over a higher range of strength.

Securing improved fire resistance characteristics of concrete by means of the material itself requires the contribution of multi-functional materials. This study focused primarily on securing fire resistance performance of concrete by replacing silica fume, a major admixture used in high-strength concrete, by meta-kaolin[1], known to exhibit remarkable fire-resistance, so as to find out the optimal material combination improving the fire resistance performance of 80MPa-class high-strength concrete. Moreover, waste tire chips were mixed with polypropylene fibers. Former polypropylene fibers are providing a percolated network mechanism exhausting the vapor inside the concrete matrix. The mixing of waste tire chips enables to obtain synergy effect between these two different fibers by dispersing the vapor through the creation of terminal pores in the network mechanism and inducing the development of micro-cracks at these pores. Steel fibers[2] were introduced to exploit their functions preventing spalling through the bridging effect and toughness of fiber pull-out on the stress transfer between the cracks occurring at the spalling-induced defects of the matrix. Finally, the contribution and composite effect on the resistance to fire of the fibers were analyzed and the corresponding results were exploited to derive practical mix proportions.

2. Research method

The orthogonal array table is a test schedule enabling to reduce dramatically the number of tests by sacrificing information related to high order interactions and interactions between two variables of which correlation is technically of poor importance so as to extract the major effects among the huge number of variables to be considered in a given study. Accordingly, this study planned the test variables according to the orthogonal array table and the contribution of each of the variables was assessed using the general linear model of ANOVA. The research was conducted by estimating the functional relationship between the factors for fire resistance increment and the measured data using

response surface analysis and determining the optimal reactive conditions (optimal mix design) through prediction and analysis of the responses after modeling of the functional relationship mentioned before.

3. Experimental plan and method

3.1 Experimental plan

Meta-kaolin, waste tire chip, polypropylene fiber and steel fiber were selected as the main materials for the strengthening of the fire resistance performance of high strength concrete. These 4 materials were arranged in 3 levels and mixed as shown in Table 1 and Table 2 for test purpose. Considering the interaction between the tests, $L_{27}(3^{13})$ orthogonal array tables were designed as shown in Table 3 so as to prevent disturbance of the interactions and test factors to be assessed. The level of each of the factors was composed with correspondence to the volumetric replacement ratio of silica fume by meta-kaolin, the volumetric replacement ratio of fine aggregates by tire waste chips, the volumetric ratio of polypropylene fibers to the total volume and the replacement ratio of steel fibers to the total volume.

Table 1 Mix proportions of concrete mixture (kg/m^3)

W	B(binder)			Fine aggregate	Coarse aggregate	A.D (B×1.7)	W/B (%)	S/a (%)	Air (%)
	Blast furnace slag cement	Fly ash	Silica fume	Sea Sand	Lime stone				
160.0	557.2	32.4	51.0	702.5	874.3	12.2	25	44	1.5

Table 2 Parameters and levels (vol %)

Factors	Levels			Tests
	1	2	3	
A: Metakaolin[1)]	0	50	100	-slump flow
B: Waste Tire Chip[2)]	0	5	10	-air content -compressive strength
C: Polypropylene Fiber[3)]	0	0.1	0.2	-frexural strength
D: Steel Fiber[4)]	0	0.5	1	-max. rebar temp. -spalling area

1) Volume replacement of silica fume 2) Volume replacement of fine aggregate
3) Adaptive rate to total volume 4) Replacement rate of total volume

Fig. 1 fire-resistance test apparatus

Table 3 Layout using orthogonal array ($L_{27}(3^{13})$)

No.	Factor				Mix condition
	A	B	C	D	
1	1	1	1	1	A1B1C1D1
2	1	1	2	2	A1B1C2D2
3	1	1	3	3	A1B1C3D3
4	1	2	1	2	A1B2C1D2
5	1	2	2	3	A1B2C2D3
6	1	2	3	1	A1B2C3D1
7	1	3	1	3	A1B3C1D3
8	1	3	2	1	A1B3C2D1
9	1	3	3	2	A1B3C3D2
10	2	3	1	1	A2B3C1D1
11	2	3	2	2	A2B3C2D2
12	2	3	3	3	A2B3C3D3
13	2	1	1	2	A2B1C1D2
14	2	1	2	3	A2B1C2D3
15	2	1	3	1	A2B1C3D1
16	2	2	1	3	A2B2C1D3
17	2	2	2	1	A2B2C2D1
18	2	2	3	2	A2B2C3D2
19	3	2	1	1	A3B2C1D1
20	3	2	2	2	A3B2C2D2
21	3	2	3	3	A3B2C3D3
22	3	3	1	2	A3B3C1D2
23	3	3	2	3	A3B3C2D3
24	3	3	3	1	A3B3C3D1
25	3	1	1	3	A3B1C1D3
26	3	1	2	1	A3B1C2D1
27	3	1	3	2	A3B1C3D2

3.2 Experimental method

In order to derive the optimal conditions of fire resistive high strength concrete, the evaluation criteria were obtained through tests on basic characteristics and tests on member characteristics under high temperature condition. The test criteria selected for the basic characteristics were the compressive strength, flexural strength, slump flow and air content. For the high temperature member characteristics, specimens with dimensions of 500mm×500mm×150mm reinforced with rebar and cover thickness of 40mm were manufactured. Measurements were performed on the temperature of rebar in the specimens heated at high temperature as well as on the volumetric loss of the specimens due to spalling. The heating equipment used in the fire resistance test is illustrated in Fig. 1 to allow heating in one side in order to analyze the spalling characteristics of members and evaluate the temperature of the main rebar. The high temperature heating furnace for the concrete test has been manufactured so as to simulate the standard temperature heating curve of ISO 834-1 as shown in Fig. 2. The schematic of manufactured specimens is shown in Fig. 3.

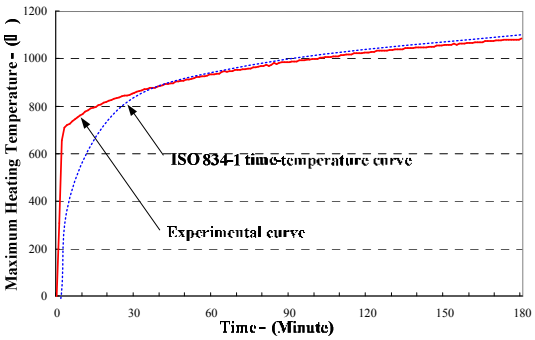

Fig. 2 Experimental and standard time- temperature curves.

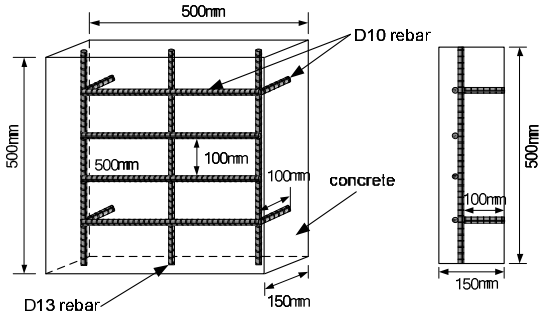

Fig. 3 Schematic of specimen

Table 4 ANOVA analysis results using adjust SS(Sum of Squre) *C(%): contribution rate

	Slumpflow		Air content		Compressive strength		Flexural strength		Max. rebar temperature'		Spalling volume	
R-Sq(%)	94.03		84.36		89.78		88.99		55.69		80.15	
	C(%)	p	C(%)	p	C(%)	P	C(%)	p	C(%)	p	C(%)	p
Metakaolin	10.31	0.000	9.36	0.015	5.58	0.020	5.35	0.028	1.88	0.682	1.38	0.547
Wast tire chip	26.56	0.000	64.61	0.000	79.80	0.000	26.98	0.000	4.74	0.393	7.56	0.055
PP fiber	35.10	0.000	5.04	0.081	0.01	0.920	7.66	0.009	39.52	0.003	70.45	0.000
Steel fiber	23.38	0.000	5.35	0.071	4.39	0.040	49.00	0.000	10.55	0.140	0.77	0.711

Fig. 4 Surface spalling by the expansion of aggregates

Fig. 5 Spalling of concrete using steel fibers

Fig. 6 Spalling of concrete using waste tire chip

4. Analysis of experimental results

Fig 4, 5 and 6 are representative forms of concrete surface after fire resistance test. The contribution of the independent factors was computed using the coefficient of determination (R^2) obtained by means of ANOVA analysis for the experimental values of the orthogonal array table. The contribution (R_{xi}^2) of each of the independent facotors was calculated by dividing the coefficient of determination (SSR_{xi}) of each independent factor by the global coefficient of determination (SST). In addition, the overall coefficient of determination was calculated as $R^2=SSR/SST$. This coefficient being the variance ratio of the error, larger value of this coefficient has been treated as giving higher explanatory power of the specimen. Table 4 and Fig. 7 arranges the contribution analysis results related to the effects of the independent variables that are meta-kaolin, tire waste chip, polypropylene fiber and steel fiber on the dependent variables that are slump flow, air content, compressive strength, flexural strength, maximum temperature of main rebar and spalling volume.

Response surface analysis being expressing the relation between the fireproof reinforcing variables and each experimental data as an unknown function, the appropriate response surface can be formulated using the method of least squares. Expressing it in matrix form makes it possible to determine the optimal response conditions. Table 5 summarizes the results of the response surface analysis. Fig. 8 plots the optimization analysis results of each variable as 2nd order response surface equations. In view of the analysis results, the polypropylene fiber and meta-kaolin are exhibiting high levels with respective levels of about 3 and 2.6, while the tire waste shows a level of 1.6 steel fiber was discarded owing to the resulting level of 1. Taking only the fireproof characteristics into consideration, the steel fibers developed the expected performance but with relatively poor effects compared to the other materials. The unfavorable results observed in the basic characteristics test for practicability seemed to have been missing during the optimization stage.

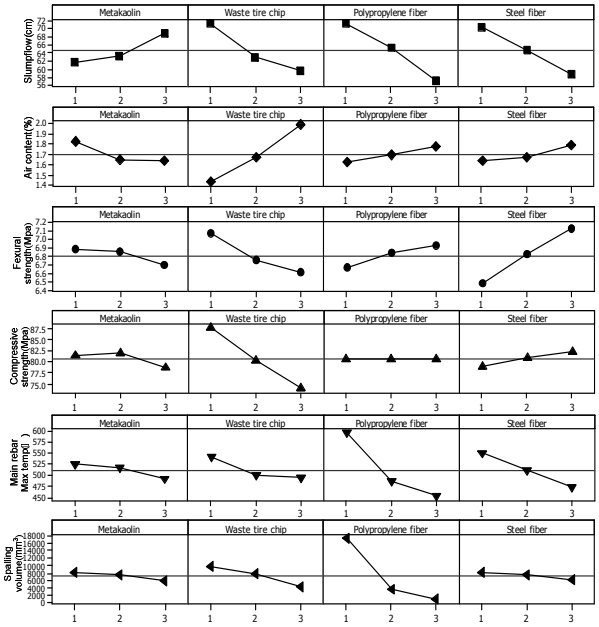

Fig. 7 Main effect plot for independent variables

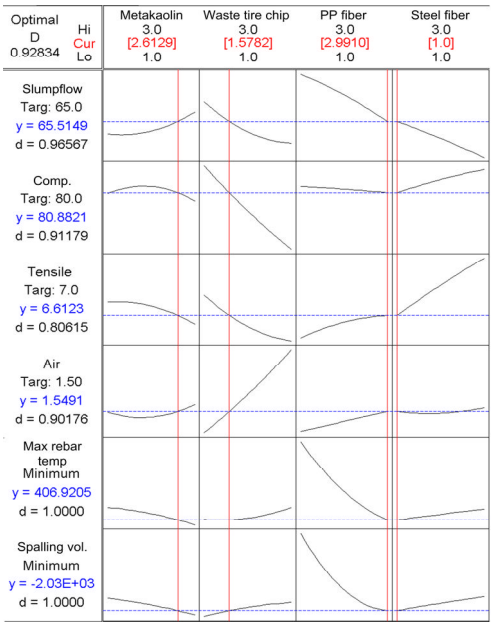

Fig. 8 Results of response optimization

Table 5 Response surface modeling analysis

Term	Slump flow	Air content	Compressive strength	Flexural strength	Max. rebar temperature	Spalling volume
constant	102.800	1.73556	88.0456	6.97222	1509.81	75503.1
x_1	-9.367	-0.39222	8.3356	0.09611	-43.58	-3743.8
x_2	-11.811	-0.02000	-7.5061	-0.89667	-227.95	-8310.7
x_3	-1.311	-0.22000	-1.7894	0.23611	-424.91	-40987.6
x_4	-2.922	0.15778	1.3372	0.30889	-184.73	-4788.1
x_1^2	2.056	0.08333	-1.9378	-0.06611	-9.38	-504.0
x_2^2	2.389	0.03333	1.1221	0.08222	17.02	-605.3
x_3^2	-0.778	0.00000	-0.0928	-0.04278	38.80	5436.4
x_4^2	-0.278	0.03333	-0.2628	-0.01444	-0.15	-124.8
x_1x_2	1.400	-0.01778	0.8195	0.06556	19.64	1537.7
x_1x_3	0.378	0.06222	0.2362	-0.00511	2.55	26.1
x_1x_4	0.600	-0.06222	-0.0296	-0.02600	10.71	721.6
x_2x_3	-1.733	0.11556	0.2449	0.03733	41.24	3222.8
x_2x_4	-1.511	-0.01556	0.1184	0.06378	7.15	-818.3

*x_1: metakaolin, x_2: waste tire chip, x_3: polypropylene fiber, x_4: steel fiber

5. Conclusions

The following conclusions could be drawn from the experimental results.

1. Meta-kaolin, tire waste chips, polypropylene fibers and steel fibers have been selected as factors in order to improve the fire resistance performance of 80MPa-class high-strength concrete by means of the involved materials. Accordingly, ANOVA analysis has been conducted using orthogonal array table with 4 variables and 3 levels. The analysis results verified the reciprocal interaction between the basic properties and the fireproof characteristics in terms of contribution.
2. The optimal conditions of the factors derived from response surface analysis revealed that the case with volumetric replacement ratio of silica fume by meta-kaolin of about 80% and the volumetric replacement ratio of fine aggregates by tire waste chips of about 3%, and the case where polypropylene fibers are admixed at a ratio of 0.2% to the total volume without addition of steel fibers were advantageous. It has been seen that in such cases the basic characteristics of high-strength concrete as well as its fire resistance characteristics can be evenly satisfied.
3. The analysis of the fire resistance performance verified that steel fiber is a variable to be carefully considered. In terms of constructability, steel fiber exhibits drawbacks compared to the other variables. In terms of economic efficiency, a mix design adopting only the other variables was seen to be able to develop equivalent or superior performance.

References

[1] C.S.Poon, Salman Azhar, Mike Anson, Yuk-Lung Wong. Performance of metakaolin concrete at elevated temperatures. Cement & Concrete Composites 2003;25:83-9

[2] Kutzing, L.: Fire Resistance of High Performance Concrete with Fibre Cocktails. LACER NO 4. 1999.

Key Engineering Materials Vols. 385-387 (2008) pp 721-724
© (2008) Trans Tech Publications, Switzerland
doi:10.4028/www.scientific.net/KEM.385-387.721

Effects of Equal Channel Angular Pressing and Heat Treatment on Low Cycle Fatigue Properties of 6005 Al Alloy

W.H.Kim[1,a], H.H.Cho[2,b], J.H.Cha[1,c], S.I.Kwun[1,d], D.H.Shin[2,e]

[1]Department of Materials Science and Engineering, Korea University, Seoul, South Korea

[2]Department of Metallurgy and Materials Science, Hanyang University, South Korea

[a]croach@korea.ac.kr, [b]cmusic81@hanyang.ac.kr, [c]nanjooho@korea.ac.kr,

[d]sookkwun@korea.ac.kr, [e]dhshin@hanyang.ac.kr

Keywords: 6005 Al alloy, ECAP, ultra fine grained material, low cycle fatigue, heat treatment

Abstract. The effects of equal channel angular pressing (ECAP) and subsequent heat treatment on the low cycle fatigue properties of 6005 Al alloy were investigated. The ECAPed specimens showed cyclic softening, whereas the peak aged specimens showed cyclic hardening at all strain amplitudes. After ECAP, artificial aging was performed at 175°C to observe the change of the low cycle fatigue properties due to precipitation. The fatigue life and behavior of the unECAPed and ECAPed 6005 Al alloys were discussed in terms of the microstructural changes and aging conditions.

Introduction

Materials with a fine-grained microstructure exhibit enhanced mechanical properties as compared to the conventional bulk materials. Therefore, a new processing route, namely the severe plastic deformation (SPD) technique, has been developed to produce materials with fine grained microstructures. Equal channel angular pressing (ECAP) is one of the most efficient SPD processes, which allows a grain size of about 1μm to be achieved [1]. While there has been considerable emphasis on the mechanical properties of ECAPed materials, there have been relatively few studies on their fatigue behavior [2]. Therefore, it is indispensable to study the fatigue behavior of ECAPed materials in order to obtain an accurate understanding of their properties and applications. In this study, the mechanical properties, especially the low cycle fatigue properties, of a 6005 Al alloy fabricated by ECAP were investigated.

Experimental procedure

The chemical composition of the 6005 Al alloy is given in Table 1. The 6005 Al alloy was solid-solution treated at 530°C for 90 min and then quenched in water. After quenching, one group of specimens was aged at 175°C for 8h to achieve peak aging (SS+AA). The other group consisted of the solution treated alloy subjected to subsequent ECAP (SS+ECAP). The ECAP was conducted using a solid die with an angle of $\Phi = 90^{o}$, $\Psi = 40^{o}$, and speed of 3 mm/s at 150°C. After the 4 Passes of ECAP, some of the specimens were aged at 175°C for 8h (SS+ECAP+AA). The low cycle fatigue test was conducted at constant total strain amplitudes in the range of ±0.4%~1.0% using a symmetrical triangular waveform at a constant strain rate of 3×10^{-3}/s.

Table 1. Chemical composition of 6005 Al alloy [Wt. %].

Material	Elements								
	Si	Fe	Cu	Mn	Mg	Cr	Zn	Ti	Al
6005 Al	0.9	0.13	0.008	0.008	0.52	0.01	0.005	0.005	Bal.

Results and discussion

The micrographs of the 6005 Al alloy peak aged (175°C for 8h) after solid-solution treatment (SS+AA) are shown in Fig. 1(a). The results of the EBSD analysis indicated that the average grain size and misorientation angle are about 120μm and 21°, respectively. Fig. 1(b) is the dark field TEM image of the precipitates. Precipitates having a needle shape with a length of about 30nm were reported to be the main strengthening phase in Al-Mg-Si alloy. The bright field TEM image of the 6005 Al alloy subjected to 4 passes of ECAP after the solid-solution treatment is shown in Fig. 1(c). Many dislocations are visible inside the grain. The subgrain structure seems to be formed owing to the dislocation rearrangement and the rotation of the grain induced by repetitive shear deformation during ECAP. The grain size and subgrain size were measured to be about 1μm and 200nm, respectively. Fig. 1(d) is the bright field TEM image of the 6005 Al alloy subjected to 4 passes of ECAP followed by artificial aging at 175°C for 8h. The sizes of the grain and subgrain did not change significantly and the dislocation density inside the grain remained high.

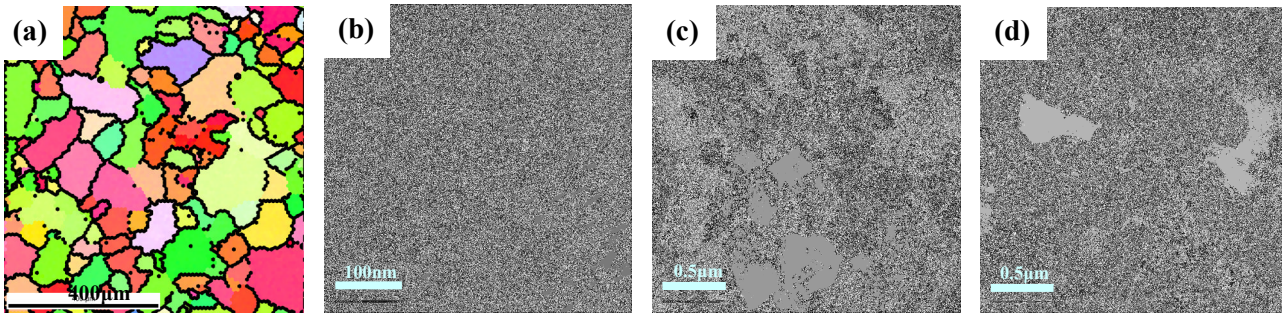

Fig. 1 Microstructure of 6005 Al alloy. : (a) EBSD of SS+AA (175°C for 8h) (b) precipitates morphology (dark field image in TEM) (c) SS+ ECAP 4 passes (d) SS + ECAP 4 passes +AA (175°C for 8h)

Fig. 2 shows the variation of the hardness and tensile strength of the 6005 Al alloy under various conditions. To compare the aging effect of the precipitates before and after ECAP, some specimens were annealed at 415°C for 150 min, in which case all of the precipitates were assumed to be stable. The change of the hardness and strength of the annealed specimens is also presented. In the case of the specimens aged at 175°C after solid solution treatment, the peak hardness was observed after aging for 8h, following which the hardness decreased due to the over-aging of the precipitates. A continuous decrease of the hardness with increasing aging time was observed in the specimens subjected to 4 passes of ECAP. A previous publication reported that the hardness of materials having an SPD history deceased due to grain growth and the reduction of the dislocation density during aging [3]. However, it seems that the decrease of the hardness was caused by over-aging, as the grain growth and the decrease in the amount of dislocations were not distinctly observed in this study, as shown in Fig. 1(d). There are two pieces of evidence which confirm this. First, the hardness of the solid solution treated specimens was greatly increased after 1 pass of ECAP. Fig. 2(a) presents the change of the hardness with the number of passes of ECAP in the specimens subjected to ECAP after solid solution processing, and annealing treatment. The significant increase in hardness observed in the specimens subjected to 1 pass of ECAP after solid solution treatment cannot be explained without taking into consideration the precipitation hardening effect in addition to the increased number of dislocations. Subjecting the annealed specimen to the ECAP process only had the effect of increasing the number of dislocations, which led to a smaller increase in the hardness than that observed in the solid solution treated specimen. Consequently, even though the time of ECAP was short, it can be concluded that the precipitation process progressed rapidly during ECAP, due to the acceleration of the precipitation rate induced by the severe plastic deformation. Therefore, it is thought that the peak aging condition imposed on the solid-solution treated specimens subjected to 4 passes of ECAP was over-aged

condition in this case, as considerable precipitation had occurred already. Fig. 2(b) presents the change of the hardness with the aging time in the specimens subjected to ECAP after solid solution processing. The second piece of evidence confirming the existence of over-aging is the decrease in the elongation of the specimens aged at 175°C for 8h after 4 passes of ECAP in the tensile test. Fig. 2 (c) shows that both the strength and elongation decreased after this aging process. This kind of result was also observed in age-hardened alloys which have been over-aged [4].

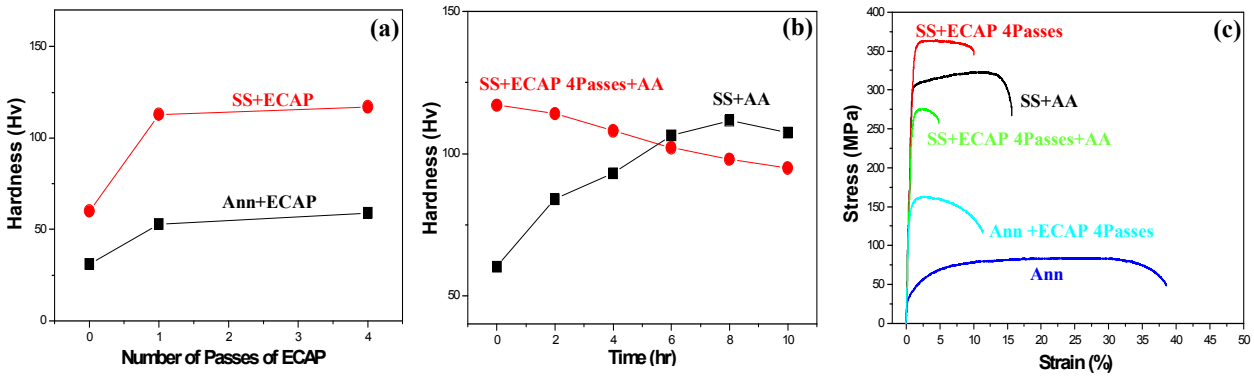

Fig. 2 The change of the mechanical properties due to ECAP and heat treatment. : (a) The change of the hardness with the number of passes of ECAP (b) The change of the hardness with the aging time (c) Stress-strain curves under the various conditions

The cyclic stress response curves of the 6005 Al alloy under the various conditions are presented in Fig. 3. Fig. 3(a) shows that the continuous cyclic hardening occurred at strain amplitudes ranging from 0.4 to 0.8%, and both the cyclic hardening and saturation occurred at strain amplitude of 1.0% in the specimens that were aged at 175°C for 8h after solid solution treatment. It is believed that the continuous cyclic hardening occurred because the dislocations were not able to shear the precipitates easily at strain amplitudes ranging from 0.4 to 0.8% owing to the low strain amplitude. The dislocation density might increase with cycle during the low cycle fatigue when the precipitates impeded the movement of dislocations. The saturation of cyclic stress response curves after initial hardening at strain amplitude of 1.0% can be explained by the fact that the precipitates which act obstacles to moving dislocations initially are sheared eventually by repeated shutting of dislocations. There was a report that the dislocations were able to shear the precipitates during fatigue under high strain amplitudes [5]. Therefore, the softening effects resulting from the shear of the precipitates and the hardening effects resulting from the increased dislocation density seem to balance each other to result in the saturation stress. Fig. 3(b) and (c) show the cyclic stress response curves of the specimens subjected to 4passes of ECAP without and with subsequent aging (175°C, 8 h). Cyclic softening was observed in both specimens. However, the specimen aged after ECAP softened faster due to the increased mean free path for dislocations than that without aging. These cyclic softenings are similar to those observed in previous studies, in which materials having an SPD history showed cyclic softening [6]. In the current study, it is believed that the reason for the cyclic softening of the specimens which had an ECAP history was that the dislocations with a high density after ECAP were rearranged during fatigue due to the dynamic recovery effect. Fig. 3(d) presents the Coffin-Manson plot, which shows that the specimens subjected to 4 passes of ECAP after solid solution treatment had a superior fatigue life to those in other conditions at all strain amplitudes applied in this study.

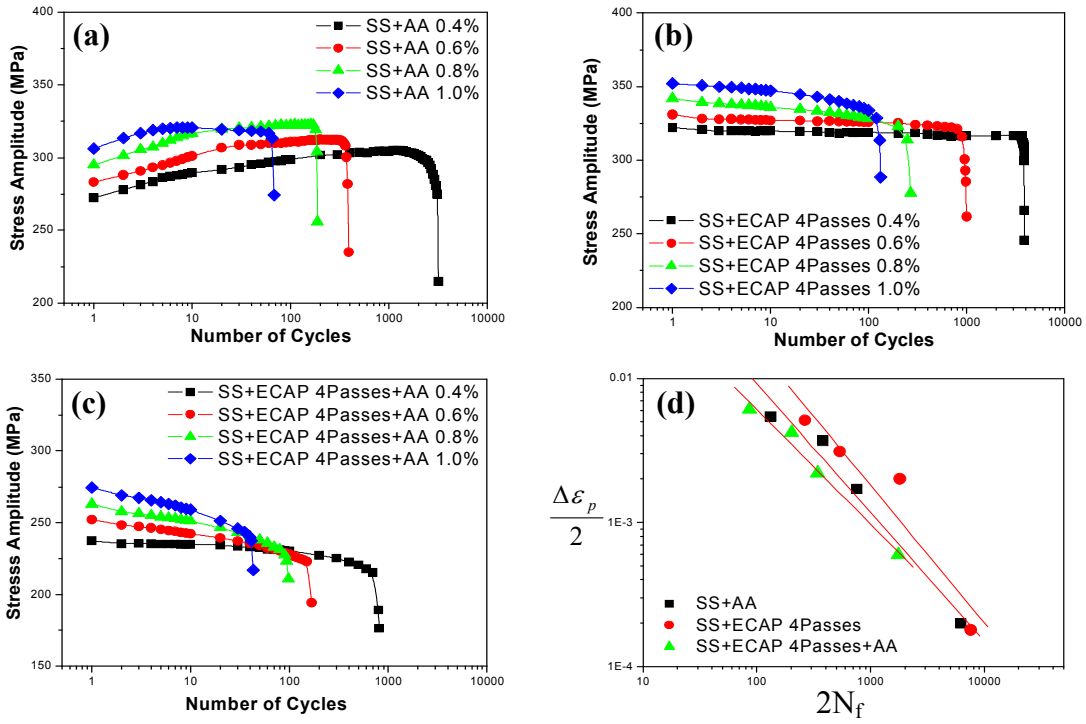

Fig. 3 The cyclic stress response curves for the 6005 Al alloy. : (a) SS + AA, (b) SS + 4 passes of ECAP, (c) SS + 4 passes of ECAP +AA, (d) Coffin–Manson plot

Summary

a. The decrease in the hardness and tensile strength of the specimens subjected to 4 passes of ECAP and subsequent aging was due to the over-aging of the precipitates.

b. The cyclic hardening during low cycle fatigue in the peak aged specimen (SS+AA) was due to the interaction between the dislocations and coherent precipitates.

c. The cyclic softening in the ECAPed specimen was due to rearrangement of the dislocations resulting from the dynamic recovery.

References

[1] C. S. Chung, J. K. Kim, H. K. Kim and W. J. Kim: Mater. Sci. Eng. Vol.A337 (2002), p. 39

[2] A. Vinogradov, Y. Kaneko, K. Kitazawa, S. Hashimoto, V. Stolyarov and R. Valiev: Scripta Mater. Vol.36 (1997), p. 1345

[3] J. K. Kim, H. G. Jeong, S. I. Hong, Y. S. Kim and W. J. Kim: Scripta Mater. Vol.45 (2001), p. 901

[4] A. H. Busby, L. Edwards and J. W. Martin, in: Cyclic Hardening of Al-Mg-Si Alloys with Coherent and Incoherent Phases, edited by C. J. Beever, Volume1 of Proceedings of the 2nd International Conference on Fatigue Thresholds, UK(1984)

[5] J. S. Cho, S. I. Kwun and M. C. Shin: J. Kor. Inst. Met. & Mater. Vol.27 (1989), p.463

[6] A. Vinogradov and S. Hashimoto: Adv. Eng. Mater. Vol.5 (2003), p.351

Key Engineering Materials Vols. 385-387 (2008) pp 725-728
© (2008) Trans Tech Publications, Switzerland
doi:10.4028/www.scientific.net/KEM.385-387.725

The Low Cycle Fatigue Behavior of Equal-Channel Angular Pressed Al 5052 Alloy

J.H. Cha[1a], H.H. Cho[2b], W.H. Kim[1c], S.I. Kwun[1d], and D.H. Shin[2e]

[1]Department of Materials Science and Engineering, Korea University, Seoul, 138-713, South Korea

[2]Department of Metallurgy and Materials, Hanyang University, Ansan, Kyunggi-do 425-791, South Korea

[a]nanjooho@korea.ac.kr, [b]cmusic81@hanyang.ac.kr, [c]croach@korea.ac.kr, [d]sookkwun@korea.ac.kr, [e]dhshin@hanyang.ac.kr

Keywords: Al 5052 alloy, low cycle fatigue, ECAP, annealing, ultrafine grain

Abstract. The low cycle fatigue(LCF) test was performed to characterize the influences of the equal channel angular pressing(ECAP) and subsequent annealing of Al 5052 alloy. In the present research, one group of Al 5052 alloy specimens was directly subjected to ECAP, while another was subjected to ECAP and subsequent annealing. It was found that the tensile strength of the Al 5052 alloy increased, while its elongation decreased, with increasing number of ECAP passes. The LCF test was conducted at constant total strain amplitudes of 0.5%, 0.7%, 0.9% and 1.1%. Only cyclic hardening was observed as the number of fatigue cycles increased at all strain amplitudes in the specimen without ECAP. However, the ECAPed specimens showed a slight amount of cyclic hardening in the beginning and then saturation until fracture.

Introduction

At present, the ECAP technique is especially attractive for obtaining ultrafine grained(UFG) materials, and has been widely applied to various metals and alloys by many investigators throughout the world[1]. Until now, many investigations have focused on the static mechanical properties of UFG materials, such as by conducting uniaxial tensile tests, however, studies of their fatigue properties are quite rare. In this study, the LCF test was performed to characterize the influences of ECAP and subsequent annealing on the fatigue behavior of Al 5052 alloy.

Table 1. Chemical composition of the Al 5052 alloy [wt. %].

Material	Elements							
	Si	Fe	Cu	Mn	Mg	Cr	Zn	Al
Al 5052	0.04	0.15	0.006	0.04	2.2	0.16	0.01	Bal.

Experimental procedure

The chemical composition of the Al 5052 alloy is given in Table 1. Cylindrical samples 18mm in diameter × 140mm in length were prepared from the extruded bar. The material was solid solution treated at 500°C for 1 hr, followed by water quenching. This alloy was ECAPed with a die angle of $\Phi = 90^{o}$, $\Psi = 40^{o}$, and speed of 3 mm/s at 150°C and subsequently annealed at 150°C for 1hr. One or four passes of ECAP were carried out using route Bc(rotation of sample by 90° in same direction after every pass). Before ECAP, the samples were coated with MoS_2 as a lubricant. A small piece was cut from each sample for the hardness test. Tensile tests were carried out using tensile specimens with a gauge length of 15mm at strain rates of 1×10^{-4} s^{-1}, 1×10^{-6} s^{-1} and 1×10^{-7} s^{-1} at room temperature. The LCF test was carried out in accordance with the procedure defined in ASTM standard E606-92[2], using a computer controlled servo hydraulic testing machine. A plate-type specimen with a gauge length of 14mm was used for the LCF test under fully reversed total strain amplitude control in air.

The strain amplitude was varied from 0.5 to 1.1% and the strain rate was 4×10^{-3} s^{-1}. The microstructure observations were performed by electron backscatter diffraction(EBSD) and transmission electron microscopy(TEM). The specimen surfaces were prepared for EBSD by electrochemical polishing in a 5% perchloric acid solution in methanol at -20°C and 10 V. The TEM specimens were prepared by twin-jet polishing 3 mm discs in a solution of 25% nitric acid and 75% methanol at -20°C and 25 V. The Vickers hardness test was carried out with a load of 200 gf and holding time of 10 sec.

Results and discussion

Fig. 1(a) shows the microstructure obtained in the specimen of the Al 5052 alloy with 0 passes (i.e., without ECAP). Its mean grain size was about 86μm. The ECAP processing provides an important procedure for obtaining a UFG microstructure in the materials studied. Figs. 1(b-d) show the TEM micrographs of the various specimens. Fig. 1(b) shows that the microstructure after 1 pass of ECAP mostly consisted of an elongated band structure and a high dislocation density within the grains. The sample subjected to 4 ECAP passes consisted of equiaxed grains with a diameter of 0.3 ~ 0.5μm, as shown in Fig. 1(c). Fig. 1(d) shows that the dislocations partly disappeared inside some of the grains after annealing, but no grain growth was observed. This is due to the relatively low annealing temperature.

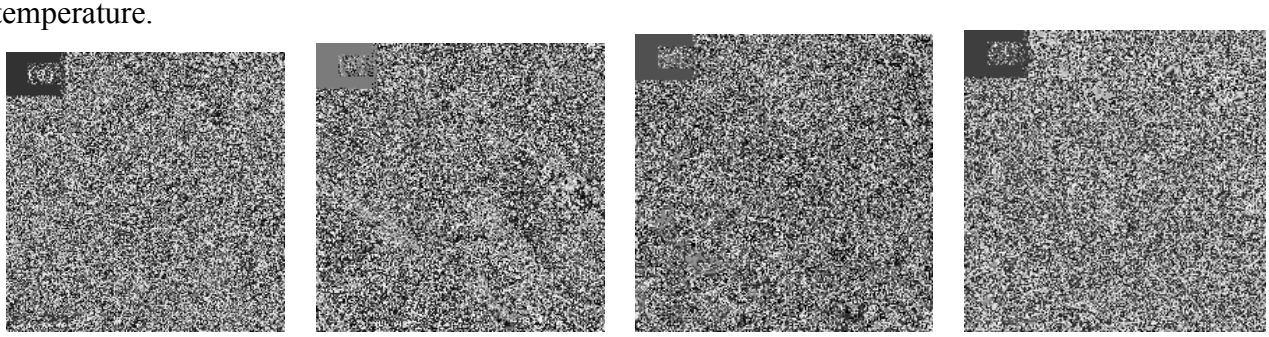

Fig. 1 (a) EBSD image showing grain structures, (b) TEM image of specimens after 1 pass of ECAP, (c) 4 passes, (d) 4 passes + annealing at 150 °C for 1hr.

The tensile stress–strain curves obtained for the as-ECAPed Al 5052 alloy are shown in Fig. 2. It was found that the tensile strength of the Al 5052 alloy increased, while its elongation decreased, with increasing number of ECAP passes, due to grain refinement and the continuous increase in the dislocation density[3]. However, the strength of the sample subjected to 4 passes and subsequent annealing at 150 °C for 1hr decreased slightly, while its elongation increased. The increase of the elongation is due to the decreased dislocation density inside the grains caused by the subsequent annealing. A serration on the flow curve of the specimen without ECAP was noticed, as shown in Figs. 2(a-c). As shown in Figs. 2(b) and (c), the amplitude of the serration increased as the strain rate decreased. This is reported to be related to mobile dislocation[4]. The effect of the serration on the low cycle fatigue will be investigated later in this study.

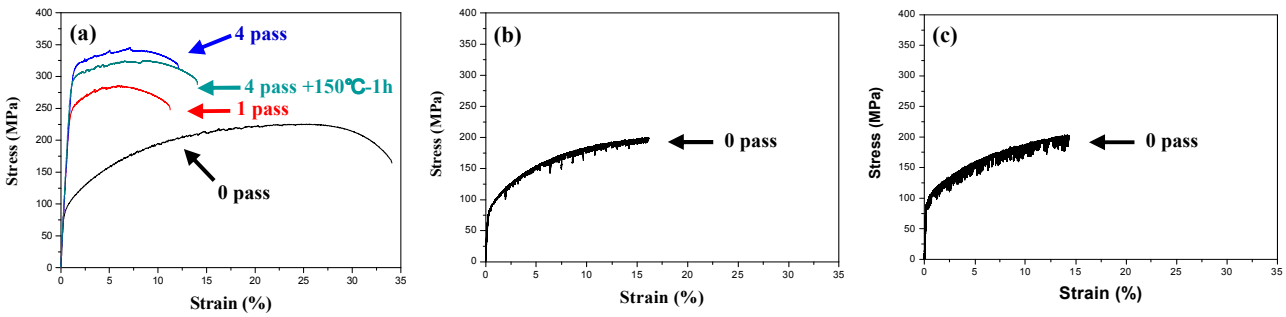

Fig. 2 Tensile stress-strain curves at strain rates of (a) 1×10^{-4} s^{-1}, (b) 1×10^{-6} s^{-1}, and (c) 1×10^{-7} s^{-1}.

As shown in Fig. 3, the Vickers hardness increased as the number of passes increased. This result is similar to that of the tensile test.

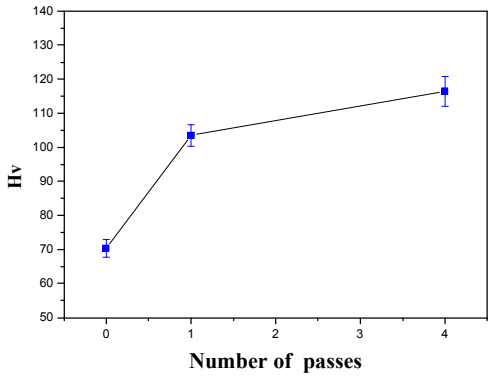

Fig. 3 Variation of Vickers hardness after 0, 1 and 4 passes of ECAP.

Fig. 4 shows the cyclic stress response curves (i.e., stress amplitude vs. number of cycles) of the Al 5052 alloy before and after ECAP at four different total strain amplitudes. The number of fatigue cycles to failure decreased with increasing strain amplitude in all cases. As shown in Fig. 4(a), the stress amplitude of the specimen without ECAP increased gradually as the number of cycles increased at all test strain amplitudes. This result was caused by the increase of the dislocation density caused by the repeated loading of the annealed alloy. The ECAPed only and 4 pass + annealing alloys showed a very small amount of hardening in the beginning, and then saturation until fracture at all strain amplitudes.

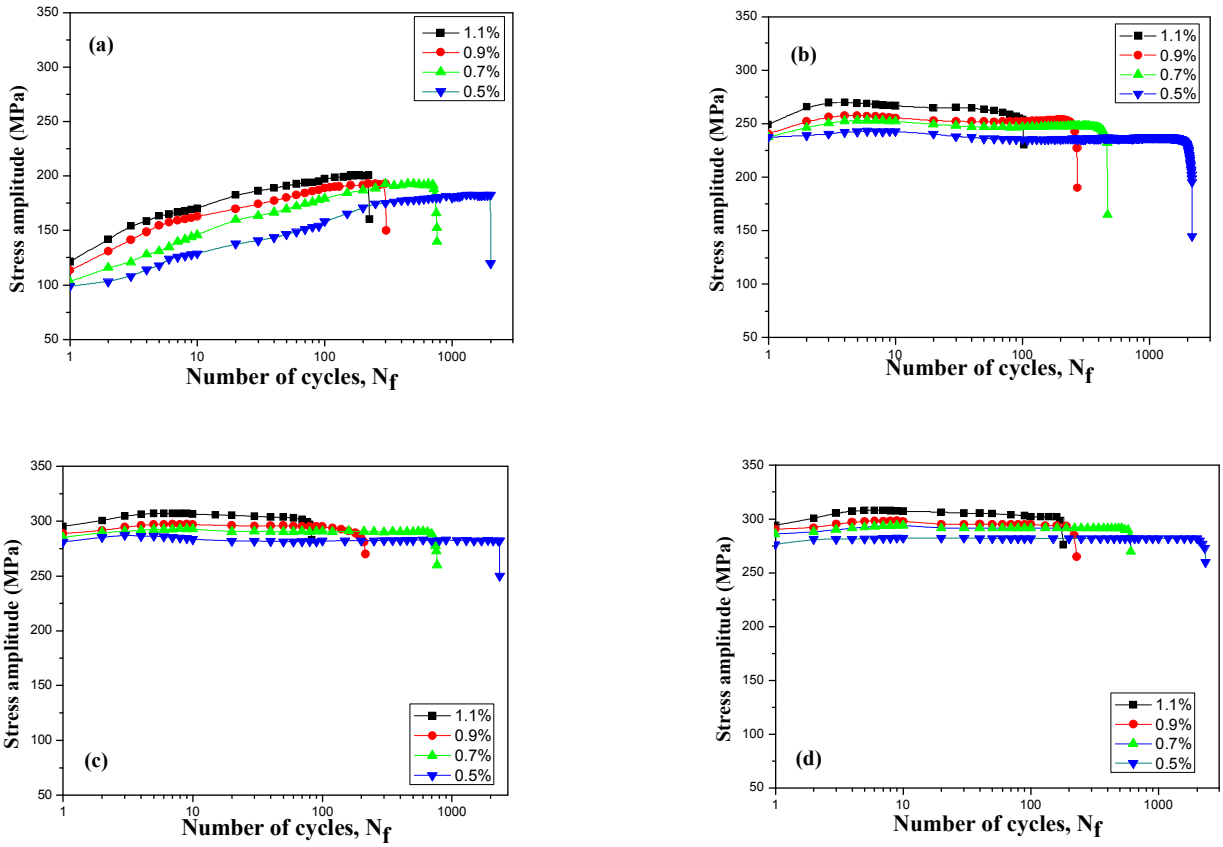

Fig. 4 Cyclic stress response curves under various strain amplitudes for the specimens (a) without ECAP (b) 1 pass of ECAP (c) 4 passes (d) 4 passes + annealing at 150°C for 1hr.

Fig. 5 shows the Coffin-Manson plot of the alloys studied. At the given plastic amplitudes, the fatigue life of the specimen without ECAP was longer than those of the ECAPed ones. This result is similar to that reported in the literature[5].

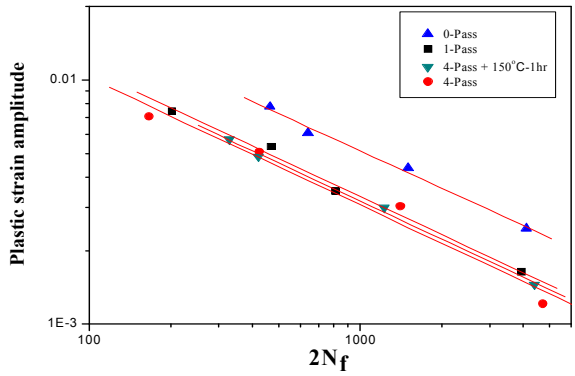

Fig. 5 Coffin-Manson plot of the Al 5052 alloy before and after ECAP.

Summary

As the number of ECAP passes increased, the tensile strength increased and the elongation decreased. However, the tensile strength was decreased, while the elongation was increased, by annealing after 4 passes of ECAP. It was noted that the serration amplitude increased as the strain rate decreased in the tensile test. Only cyclic hardening was observed as the number of fatigue cycles increased at all strain amplitudes in the specimen without ECAP. However, the ECAPed specimens showed a small amount of cyclic hardening in the beginning and then saturation until fracture. The plastic strain amplitude after a certain number of fatigue cycles was much higher in the specimen without ECAP than in the ECAPed ones, even though the fatigue life was almost the same in both cases.

References

[1] Z.F. Zhang, S.D. Wu, Y.J. Li, S.M. Liu and Z.G. Wang: Mater. Sci. Eng. Vol. A 412 (2005), p. 279

[2] ASTM E606-92. Standard Practice for Strain-Controlled Fatigue Testing. Annual book of ASTM standards. ASTM(1998)

[3] D.R. Fang, Q.Q. Duan, N.Q. Zhao, J.J. Li, S.D. Wu and Z.F. Zhang: Mater. Sci. Eng. Vol. A 459 (2007), p. 137

[4] J.M. Reed and M.E. Walter: Mater. Sci. Eng. Vol. A359 (2003), p. 1

[5] V. Patlan, A. Vinogradov, K. Higashi and K. Kitagawa: Mater. Sci. Eng. Vol. A300 (2001), p. 171

Key Engineering Materials Vols. 385-387 (2008) pp 729-732
© (2008) Trans Tech Publications, Switzerland
doi:10.4028/www.scientific.net/KEM.385-387.729

Application technique of PZT sensors to detect structural damage

Yong Hong[1, a], Seungho Hwang[1,b], Gaoping Wang[1,c], Dongpyo Hong[1,d]

[1]Department of Precision Mechanical Engineering, Chonbuk National University, Jeonjusi Jeonbuk, 561-756, South Korea

[a]hongyong@chonbuk.ac.kr, [b]shhwang@chonbuk.ac.kr, [c]gpwang@chonbuk.ac.kr, [d]hongdp@chonbuk.ac.kr

Keywords: PZT sensors, Impedance analysis, Guided wave, Mode Switching Algorithm.

Abstract. This paper presents a primary study for a method of measurement using PZT sensors which is widely used for SHM. PZT sensor has many advantages when using smart material. It is easy to be shaped to various forms and can be embedded on the materials more conveniently. The development for a practical and quantitative technique for assessment of the structural health condition by PZT sensor associated with wave propagation is investigated. Two aluminum specimens bonded with PZT sensors tested for estimating characteristics of the wave propagate on specimens change by various damage condition *cf. line crack, bolt loosening.* To estimate condition of the specimens numerically, we suggest impedance and guided wave method in this paper.

Introduction

As society base facilities and building, structure etc becomes bigger, study for structure health monitoring (SHM) system that measure health of these facilities is developed as important field. Specially, a lot of measure methods are studied because nondestructive testing is convenient of testing, chip cost charge of maintenance and is used in industry field actually. Non-destructive test that use piezoelectric sensor has a lot of advantages. Can achieve sensor and Actuator at the same time. Therefore, instruments are simple and construction is available as is inexpensive. Specially, need high efficiency instrument and professional manpower to measure structure which becomes bigger gradually precisely. Studied for development of efficient large structure monitoring algorithm that can use several measure arts that has been studied about damage measure of small structure

Damage Detect Technique

E/m impedance method

The interaction between a PZT and its host structure can be described by using a simple 1-D model, as shown in Figure 1. The PZT is normally bonded directly to the surface of the structure with using a high-strength adhesive to ensure a better mechanical interaction. The bonded PZT is considered as a thin bar that is undergoing axial vibration in response to an applied alternating voltage. One end of the bar is fixed and the other end is connected to the host structure, which is represented by a single-degree-of-freedom system. This assumption regarding the interaction at two discrete points is consistent with the mechanism of force transfer from the bonded PZT sensor to the structure

Guided Wave Technique

In order to find the damage location, a time domain approach using multiple piezoelectric sensors and actuators is investigated. Our idea is from the pulse-echo method which is often used in ultrasonic inspection. Instead of ultrasonic transducers, multiple piezoelectric sensors and actuators are used for the feasibility study on identifying damage location. The piezoelectric sensor-actuator is basically a thin PZT patch. In this case, we have to be careful about the wave form generated by the PZT. The wave speed can be calculated from the length of the test piece and the time difference between the initial echo and the back echo. Thus, we can assess the damage location by tracking the flaw echo. However, this method can apply only 1-Dimensional model. The manner of reflections will be complicated if the wave propagation can't be considered one-dimensional [1]

Waves in one-dimensional longitudinal strain are not the only type of wave motion for a purely longitudinal disturbance. The second type is provided by wave motion in one-dimensional stress, whereby the longitudinal normal stress, say τ_x, which is a function of x and t only, is the one non-vanishing stress component. All other stress components vanish. For the case of one-dimensional stress τ_x and ε_x are related by $\tau_x = E\varepsilon_x$. [2] So, the longitudinal wave equation can be expressed as :

$$\frac{\partial^2 u(x,t)}{\partial t^2} = c_b^{\,2} \frac{\partial^2 u(x,t)}{\partial x^2}, \qquad c_b = \sqrt{E/\rho} \tag{1}$$

where $u(x, t)$ is the displacement at position x and time t, c_b is the longitudinal wave speed(usually called the bar velocity), E is the Young's modulus, and $\boldsymbol{\rho}$ is the mass density. The longitudinal wave speed calculated c_b can be used to check the validity of the wave speed obtained by the experiment.

Experimental

Impedance Analysis

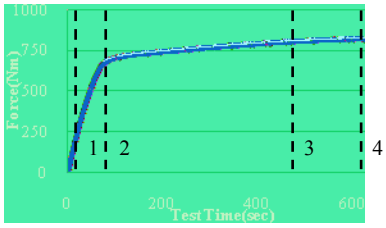

Test Spec	1	2	3	4
Force(Nm)	214.99	745.85	772.48	820.33
Time(sec)	20.2	84.4	464.4	605.4
Extended length(mm)	0.505	2.110	11.610	15.135

Figure 1. Load Input of tensile test

We extend the specimen by tensile machine and measure the impedance response in four regions where the failure is occurred as shown in Figure 1, i.e. the elastic deformation, started deformation through the yield point, that just before sheared by tensile force.

The impedance wave form is very different by cyclic load test which is made damage in local specimen with tensile load test which is applied with stress and deformation in whole specimen. The result which is analyzed based on statistical method data of cyclic load test is not made a quantitative data, so it is impossible to know the growth of the damage and the condition through the result. Figure 2 shows the impedance peak frequency shift quantity.

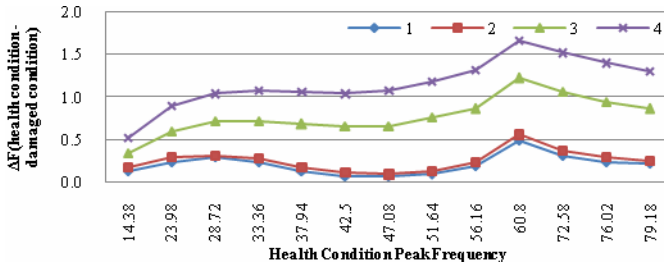

Figure 2. Impedance peak frequency shifting value

Specimens 3, 4 which are of large change of length by tensile force are less than specimens 1, 2 which are of small change of length. Also, once the extension is started, the shift of peak is prominently grown, but the width of change is small until the change of shape is large through the yield point. The tendency of change of impedance in the frequency domain is shown same in all specimens, and we can realize the fact that the width of change is small in 35~50kHz and the width of change is large in 55~75kHz. We can know that magnitude of tension applied to the specimen and the force is over the yield point or not by observing the peak shift variation.

SHM by impedance measurement give the proper result which we can judge the damage. The method of analyze the data is used two method, the one is using quantity of the peak frequency shifting and the other is using the statistical analyze method by choosing the particular frequency band. Using the

method of peak frequency shifting is suitable for detecting local damage. If natural frequency of structure alters by influence of concentration stress that occur in the structure by damage, frequency value that peak of impedance response happens is changed. Method that analyze impedance using statistical indices can bring good sequence if use in detection of damage that produce on whole structure. According as structure damage propagated, each indices change quantitatively. Embodiment of algorithm is easy if use statistical indices, and we can reduce time to analyze impedance data. Therefore, statistical analysis index is suitable in real-time monitoring.

Guided Wave Analysis

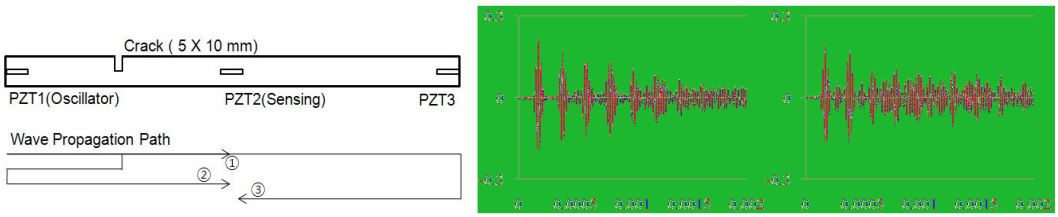

Figure 3. Guided wave propagation path and time signals (health / damaged condition)

The following shows sequence of Calculating damage location:
Theoretical equation using first echo time (t_1) gives the following

$$c_{Al-meas.} = L / t_1 = 500 / 0.122 \times 10^{-3} = 4098\,[m/s] \tag{5}$$

Next, we considered that wave propagation path help us to find damage location, damage location can be obtained by the following equation.

$$L - l - d = \frac{c(t_2 - t_1)}{2}, \quad d = L - l - \frac{c(t_2 - t_1)}{2}, \quad d = 1000 - 500 - \frac{4098 \times (0.243 - 0.122)}{2} = 252.1\,[mm] \tag{8}$$

Where, L is total length of specimen and l is location of PZT2(sensing) from PZT1(oscillator), d is distance to PZT1 from crack, t_1 is time when first echo arrives at PZT2 and t_2 is time when reflection echo arrives at PZT2.
Now, we think about instrument resolution. Wave speed using first echo time t_1 is 4098[m/s] and signal acquisition re-sampling frequency of Digitizer is 1MS/s. Finally, resolution, Δd, is :

$$\Delta d = 4098 \times 10^{-3} \times 1.00 \times 10^{-6} = 4.10[mm] \tag{9}$$

It is possible to detect damage location by analysis of guided wave propagation path changed by damage with time domain data. This analysis method can grasp position of damage by high accuracy. If apply sensor networking technique, there are advantage that grasping of damage shape and extent is possible theoretically. Also, in a repeat a short time experiment several times can prove reliability of analysis result

Mode Switching Algorithm

We wrote the program by LabVIEW to execute the SHM efficiently. LabVIEW is powerful to write the algorithm separately. When we develop the hardware to embody the switching algorithm, it is easier to modify and apply. When the program is worked at first, it recognizes the conditions of structure as healthy condition. The program gathers the response of impedance and guided wave data as it is Healthy condition to compare with the damaged conditions. The measured data is saved as spreadsheet format or LabVIEW data file format. When program gather the data of healthy condition, it gather the impedance data at regular interval, and monitor the healthy condition of structure. The respond of impedance is proper method, because it grasp the property of structure in wide range. The

program judge the condition as damaged, it switch the structural monitoring mode as measuring the guided wave. And the program grasp accurately the location of damaged, by guided wave mode.

Advantage of Mode Switching Algorithm

These merits of mode switching algorithm are advantage in complex or large structure. It is hard to accurately measure using the small number of sensors, because these structures are complex shape. To overcome these demerits, we study the sensory networking method to measure the accurate damage in wide range by connect the sensors organically. Because the method of sensory networking is generated many data, we need the high specification H/W and complex algorithm to process the data. It is possible to reduce the quantity of data by using the impedance method of mode switching method in wide structure. So, it can reduce the H/W specification to process the data efficiently. Using the traveling straight of the method of impedance measurement, it divide the large structure into several section, and then it track the damage by guided wave and monitoring by impedance measurement used the one sensor each section. It's possible to measure accurately the condition of object by using the small number of sensors in wide range.

Conclusions

We researched the efficient measurement algorithm for SHM by this study. It was possible to search the damage by impedance measurement and to measure the damage location efficiently by guided wave. Through the programming of measurement program and experiment by LabVIEW, we know that the detection and tracking is executed efficiently.

To develop the method of multi-mode switching more efficiently, we will study about the measurement module which can simultaneously execute the measurement of impedance and guided wave, and the miniaturization of module, the increase the reliability.

Acknowledgments

This work was supported by the Korea Science and Engineering Foundation (KOSEF) grant funded by the Korea government(MOST) (No. R01-2007-000-10941-0)

References

1. Kazuhisa K., Faculty of Virginia Polytechnic Institute, April (1998)

2. J. D. Achenbach, North-Holland Publishing company (1975).

3. Y. Hong, B.J. Kim, D.P. Hong, Y.M. King, Damage Detection and Quantitative Assessment for the cracked beam structures, Key Engineering Materials(2007)

4. G.P. Wang, Y. Hong, J.J. Lee, D.P. Hong, Y.M. Kim, J.Y. Kim, Quantitative Estimation of the Fastening Condition of a Bolt with Using Piezoceramic(PZT) Sensors, Key Engineering Materials(2007)

5. Victor G., Andrei N. Z. and Jing J. B., Sage Publications (2002)

Key Engineering Materials Vols. 385-387 (2008) pp 733-736
© (2008) Trans Tech Publications, Switzerland
doi:10.4028/www.scientific.net/KEM.385-387.733

FRACTURE ANALYSIS OF AN OBLIQUE CRACK PROPAGATION IN A PRE-STRESSED GLASS-EPOXY COMPOSITE

Eduard-Marius Craciun[1,a], Adrian Carabineanu[2,b], Niculae Peride[1,c]

[1]"Ovidius" University Constanta, Bdul Mamaia 124, 900527, Constanta, Romania
[2]University of Bucharest, Academiei str. 14, 010014, Bucharest, Romania

[a]mcraciun@univ-ovidius.ro,[b]acara@fmi.unibuc.ro,[c]nperide@univ-ovidius.ro

Keywords: oblique crack, pre-stressed Glass-Epoxy composite, resonance, numerical analysis.

Abstract. We consider a pre-stressed material containing an oblique crack of a length $2a$ situated in x_1x_3 plane. We supposed that the material is unbounded and the crack faces are acted by constant normal incremental stresses p. The initial applied stress $\overset{\circ}{\sigma}$ is in direction of the crack. Our first aim is to determine the elastic state produced in the body using Guz's representation theorem. Our second aim is to determine the critical values of the incremental stresses and the direction of crack propagation. To do this, we use Sih's generalised fracture criterion for an orthotropic elastic composite. In the last part we find the critical values of the initial applied stress $\overset{\circ}{\sigma}$ for which the phenomenon of resonance can appear in a pre-stressed Glass-Epoxy composite.

Guz's representation theorem for incremental fields

We consider a pre-stressed, orthotropic, linear elastic material. We take the symmetric planes of the material as coordinate planes. We assume that the material is unbounded and contains a right crack of length $2a$, situated in a plane making an angle β with x_2x_3. We suppose that the material is pre-stressed by an initial applied stress $\overset{\circ}{\sigma}$ acting in the direction of x_1 - axis.

We assume that the magnitude of the initial applied stress $\overset{\circ}{\sigma}$ is sufficiently small and it produces only infinitesimal initial deformations. We suppose that the upper and lower faces of the crack are acted by distributed incremental stress having a constant value $p > 0$. Finally, we consider that the initial deformed equilibrium configuration of the body is locally stable.

As it was shown by Guz [1] - [2] the incremental elastic state of the body can be expressed by two analytical complex potentials $\Psi_j(z_j)$ defined in two complex planes z_j, $j = 1, 2$. We denote by u_1, u_2 and respectively by $\theta_{11}, \theta_{12}, \theta_{21}$ and θ_{22} the involved components of incremental displacements, respectively incremental stresses. According Guz's representation formulae we have:

$$u_1 = 2Re\{b_1\Phi_1(z_1) + b_2\Phi_2(z_2)\}, \quad u_2 = 2Re\{c_1\Phi_1(z_1) + c_2\Phi_2(z_2)\}, \tag{1}$$

$$\theta_{11} = 2Re\{a_1\mu_1^2\Psi_1(z_1) + a_2\mu_2^2\Psi_2(z_2)\}, \quad \theta_{12} = -2Re\{\mu_1\Psi_1(z_1) + \mu_2\Psi_2(z_2)\}, \tag{2}$$

$$\theta_{21} = -2Re\{a_1\mu_1\Psi_1(z_1) + a_2\mu_2\Psi_2(z_2)\}, \quad \theta_{22} = 2Re\{\Psi_1(z_1) + \Psi_2(z_2)\}, \tag{3}$$

In above relations μ_k, are the root of factorized incremental equation and a_k, b_k, c_k, $k = 1, 2$ are coefficients depending by instantaneous elasticities of the body and by initial applied stress.

The expressions of the complex potentials $\Psi_j(z_j),\ j = 1, 2$ corresponding to our incremental boundary value problem have the following equations

$$\Psi_j(z_j) = \frac{(-1)^j}{\chi_j(\varphi)} \cdot \frac{a_j\mu_j K_I + K_{II}}{2\Delta\sqrt{2\pi r}}, \tag{4}$$

with $\Delta = a_2\mu_2 - a_1\mu_1$ and $\chi_j(\varphi) = (\cos\varphi + \mu_j \sin\varphi)^{1/2},\ \ j = 1, 2.$
The stress intensity factors corresponding to the first respectively second modes of fracture for an applied incremental stress $p > 0$ are

$$K_I = p\sin^2\beta\sqrt{\pi a},\quad K_{II} = p\sin\beta\cos\beta\sqrt{\pi a}. \tag{5}$$

Sih's energetically criterion in a mixed fracture mode

We denote by W the incremental strain energy density

$$W = \frac{1}{2}\theta_{kl}u_{l,k},\quad u_{l,k} = \frac{\partial u_l}{\partial x_k}\ \ k, l = 1, 2. \tag{6}$$

The expressions (4) of the complex potentials $\Psi_j(z_j),\ j = 1, 2$ show that near a crack tip the incremental strain energy density W has a singular part as well a regular part. We design by r and φ the radial distance from considered crack tip and the angle between radial direction and the line ahead the crack. Using the expressions (4) of complex potentials and Guz's formulae (1) - (3) after long but elementary calculus we obtain that near, the considered crack tip the strain energy density have the following structure

$$W(r, \varphi) = \frac{S(\varphi)}{r} + \ a\,regular\,part. \tag{7}$$

Here $S(\varphi)$ is Sih's incremental strain energy density factor and is given by the following equation

$$S(\varphi) = \frac{(a_1\mu_1 K_I + K_{II})(a_2\mu_2 K_I + K_{II})}{4\pi} s_m(\varphi), \tag{8}$$

where the function $s_m(\varphi)$ depends by the elastic constants of the material and by the initial applied stress.

We extend the validity of Sih's fracture criterion, for orthotropic or isotropic pre-stressed elastic materials. The assumed Sih's generalised fracture criterion is based on local density of the incremental strain energy near the crack tip and requires no apriori assumptions concerning the direction in which energy is released by separating crack surfaces. Using the equation (8) we obtain the incremental stress p_c for which crack propagation starts at critical direction φ_c

$$ap_c^2 = 4S_c/s_m(\varphi_c). \tag{9}$$

In above relation S_c is Sih's new material parameter, which takes the place of Griffith's specific surface energy γ in the new theory of brittle fracture. Once S_c is known, the relation (9) can be used to get p_c.

Crack propagation for unpre-stressed orthotropic materials

In this section we suppose that our material is not initially deformed *i.e.* $\overset{\circ}{\sigma}= 0$.

Obviously, the relation (8) giving Sih's strain energy factor $S(\varphi)$ rest valuable, but now the function $s_m(\varphi)$ will have a simplified form. In the following we present the results of our numerical analysis concerning the possible values of critical angle φ_c versus angle β for a Glass/Epoxy fiber reinforced orthotropic composite material, characterized by the following technical constants: $E_1 = 41.55GPa,\ E_2 = E_3 = 9.90GPa,\ G_{12} = 4.05GPa,\ G_{13} = G_{23} = 6GPa,\ \nu_{12} = 0.46,\ \nu_{13} = \nu_{23} = 0.2, \nu_{21} = 0.11,\ \nu_{31} = 0.05,\ \nu_{32} = 0.2$.

The dependence of the crack propagation angle φ, versus angle β is presented in Fig.1.

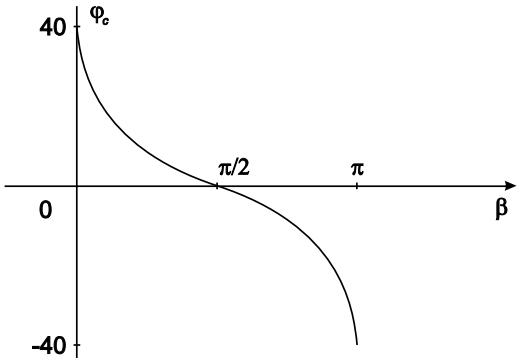

Fig. 1: Angle φ_c versus angle β

We observe that critical angle φ_c decreases when crack's angle β increases. Also, a remarkable result is obtained in the case when $\beta = \pi/2$, which corresponds to the first mode of fracture.

Resonance phenomenon for an inclined crack

As Guz [2] shows the phenomenon of internal stability or resonance has a well-defined physical meaning and can be elucidated taking into account the fact that all materials have an internal structure. The phenomenon concerns the loss of stability of the structure and depends on the geometrical and mechanical characteristics of the body as a whole. A rigorous study of this phenomenon has to take into account explicitly the parameters describing the internal structure of the body. Taking into account that such phenomenon can take place arise the following question: may exist a critical value σ^c of the initial applied stress σ such that when σ starting from zero converges σ^c, the incremental stress p_c converges to zero?

For a fiber reinforced composite the answer to this question was given by Guz and it is positive. The critical compressive stress $\overset{\circ}{\sigma}{}^{ci}_{11}$, respectivelly $\overset{\circ}{\sigma}{}^{cs}_{11}$ acting in the fibers direction, producing internal (structural), respectivelly superficial instability, of the material have the following values $\overset{\circ}{\sigma}{}^{ci}_{11} = -4.05GPa$, $\overset{\circ}{\sigma}{}^{cs}_{11} = -3.89GPa$. Consequently, superficial instability occurs *before* internal instability and the compressive stress leading to superficial instability produces only infinitesimal deformations.

Using equation (9) we obtain for the critical incremental stress following expression:

$$p_c = 2\sqrt{\frac{S_c}{as_m(\varphi_c)}}. \tag{10}$$

How Sih's parameter S_c and the fracture's length are constant we shall study the variation of the new stress function $\pi_c = \pi_c(\sigma)$ given by

$$\pi_c = \frac{p_c}{2}\sqrt{\frac{a}{S_c}}. \tag{11}$$

Table 1 presents the dependence of the incremental stress φ_c and of critical fracture angle φ_c versus the incremental stress $\overset{\circ}{\sigma}$.

Table 1. The values of π_c and φ_c versus $\overset{\circ}{\sigma}$

$\overset{\circ}{\sigma}$ (*GPa*)	-3.5	-3.0	-2.5	-2.0	-1.5	-1.0	-0.5	0
π_c (*GPa*)	0.08	0.39	0.57	0.75	0.91	1.04	1.16	1.25
φ_c (°)	44.5	43.7	43.1	42.5	41.9	41.4	40.9	40.5

Conclusions

From our numerical analysis we conclude that:
- critical fracture angle φ_c decreases when crack's angle β increases;
- when crack's angle β is equal with $\pi/2$, case corresponding to the first classical fracture mode, we obtain a well-known result, that $\varphi_c = 0$, *i.e.* the crack propagates along its line, see Sih [3];
- when $\overset{\circ}{\sigma}$ decreases to the critical value $\overset{\circ}{\sigma}^{ci}$ also the incremental stress p_c decreases. When $\overset{\circ}{\sigma}$ converges to $\overset{\circ}{\sigma}^{ci}$ we observe that p_c converges to zero, *i.e* the crack will start to propagate even that φ_c is approximately zero. In this case resonance phenomenon occurs;
- critical fracture angle φ_c, decreases when incremental stress $\overset{\circ}{\sigma}$ decreases. In the case $\beta = \pi/2$, which corresponds to the first classical fracture mode for pre-stressed materials we obtain that critical fracture angle φ_c is in a vicinity of 40°, see Craciun [4].

References

[1] A.N. Guz: *Fracture mechanics of composites acted by compression* (N. Dumka, Kiev, 1989)

[2] A.N. Guz: *Mechanics of brittle fracture of prestressed materials* (Visha Schola, Kiev, 1983)

[3] G.C. Sih: *Mechanics of Fracture* Vol I, pp. XXI-XLV, (Norhoof Int. Leyden, 1973)

[4] E.M. Craciun: Rev. Roum. Sci. Techn.-Méc. Appl., **44**, (1999), p. 533.

Key Engineering Materials Vols. 385-387 (2008) pp 741-744
© (2008) Trans Tech Publications, Switzerland
doi:10.4028/www.scientific.net/KEM.385-387.741

Computational Fracture Analyses of a Compact Tension Shear (CTS) Specimen With an Inclined Crack Plane

Li Qing-fen[1,a], Qi Gui-ying[1,b], Yan Sheng-yuan[1,c], Buchholz, F.-G.[2,d]

[1]College of Mechanical & Electrical Engineering, Harbin Engineering University, Harbin 150001, PR China

[2]retired from Institute of Applied Mechanics, University of Paderborn, D-33098 Paderborn, Germany

[a]qingfli@yahoo.com.cn [b]qiguiying@163.com [c]yanshycncn@yahoo.com.cn [d]fus.buchholz@t-online.de

Keywords: computational fracture analysis, 3D mixed-mode fracture, modified virtual crack closure integral method.

Abstract. In this paper some results of 3D-finite element analyses of a modified CTS-specimen with an inclined crack plane are presented. It will be shown, that through the inclination of the crack plane, even under pure tension loading of the specimen, a superposition of all fracture modes I, II and III can be generated along the straight crack front of the inclined crack plane. Furthermore, mixed-mode I, II and III loading conditions can also be generated if this modified CTS-specimen is subject to an in-plane tension/shear loading. The computational fracture analysis is based on the calculation of separated energy release rates GI, GII and GIII along the crack front by the numerically highly effective modified virtual crack closure integral(MVCCI)-method and for the finite element(FE)-modelling the commercially available FE-code ANSYS is utilized.

Introduction

Among the various kinds of specimens which are in use for experimental and computational mixed-mode fracture investigations the Compact Tension Shear(CTS)-specimen, proposed by Richard [1], offers some particular advantages. By the CTS-specimen the entire range of in-plane mixed-mode loading conditions can be generated on a standard tensile testing machine together with the special loading device [2]. Hereby the loading conditions generated locally at the crack tip (2D-case) or locally along the straight crack front of the CTS-specimen (3D-case) reach from pure tension (mode I) via in-plane tension/shear (mixed-mode I and II) to pure in-plane shear (mode II).

In this paper some results of 3D-finite element analyses are presented of a modified CTS-specimen with an inclined crack plane, for which an inclination angle of γ=45° has been chosen here. The new results will show, that through the inclination of the crack plane a superposition of all fracture modes I, II and III can be generated along the straight crack front of the inclined crack plane , even under pure tension loading of the specimen. Furthermore, mixed-mode I, II and III loading conditions can also be generated along the straight crack front of the inclined crack plane, if this modified CTS-specimen is not loaded by pure tension or pure in-plane shear, but an in-plane tension/shear loading is applied, e.g. with a loading angle of α=45° as considered here.

The computational fracture analysis is performed by the numerically highly effective modified virtual crack closure integral(MVCCI)-method [3,4], which can provide simultaneously the separated strain energy release rates(SERRs) $G_i(a, z/t)$, i=I, II and III, for all nodal points along the crack front of the specimen. For the Finite Element(FE)-modelling of the specimen the commercially available FE-code ANSYS is utilized.

Compact Tension Shear (CTS)-specimen and 3D FE-model of the modified specimen

In Fig. 1 the CTS specimen and the loading device are displayed as mounted together in a standard tensile testing machine. By aid of the special loading device various in-plane loading conditions can

be created [1, 2], reaching from pure tension (α=0°) via in-plane tension/shear (0<α<90°) to pure in-plane shear loading (α=90°).

The geometrical parameters of the specimen (Fig. 1) are as follows: width w=90mm, height h=145mm, thickness t=10mmm, crack length a=50mm (straight crack front). For the analysis the material parameters are chosen as follows: Young's modulus E=80.000N/mm^2 and Poisson's ratio ν=0.3 (Al-alloy AlCuMg). The specimen is subject to a static loading of F=40kN.

Some parts of the 3D FE-model of the CTS specimen are shown in Fig. 1c. The model is assembled from low order volume elements (8-node solid 45 elements in ANSYS). Away from the crack front the model contains two elements through the thickness (0≤z/t≤±0.5), whereas mesh refinements are incorporated next to the straight crack front (β=90°) or next to the crack front of the inclined crack plane (γ=45°) and adjacent to the free side surfaces (z/t→±0.5) of the specimen.

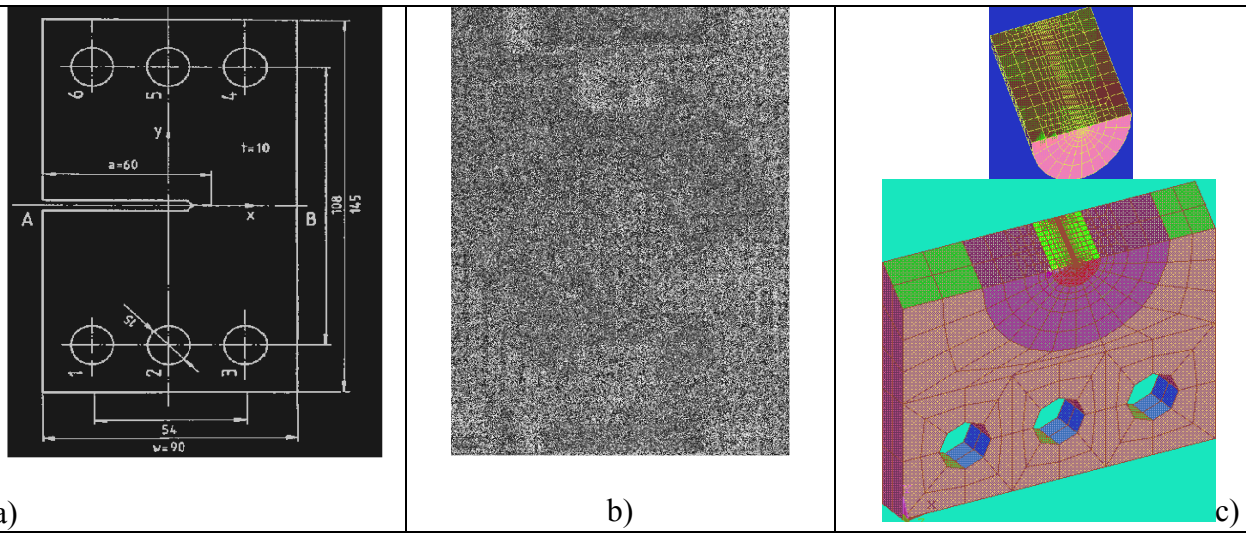

a) b) c)

Figure 1. a) CTS-specimen, b) CTS-specimen and loading device mounted together in a standard testing machine (loading angle α), c) Un-deformed FE-model (one half) of the modified CTS-specimen with an inclined crack plane (inclination angle γ=45°) and mesh detail of crack front

3D Computational fracture analysis and discussion of results

The computational fracture analysis is performed by the numerically highly effective and accurate modified virtual crack closure integral(MVCCI)-method [3,4], which provides simultaneously the separated strain energy release rates(SERRs) G_i(a, z/t), i=I, II and III, for all nodal points along the crack front of the specimen. In order to find a common basis for the comparison of the results the SERRs calculated by the MVCCI method are converted into stress intensity factors (SIFs) by the aid of Irwin´s well known equations relating SERRs and SIFs. All SIFs are normalised as follows: $K_{in}= K_i/\sigma_0$ sqrt(πa), i=I,II and III with σ_0=F/wt.

In Figs. 2 and 3 the quantitative results of the computational fracture analysis of the CTS-specimen with a straight crack front (a=50mm, β=90°) are given in form of the normalised SIFs for pure tension loading and for pure in-plane shear loading, respectively. From Fig. 2 we see that for pure tension loading (α=0°) of the CTS-specimen only mode I loading is generated locally along the straight crack front through the thickness of the specimen (0≤z/t≤±0.5). The KIn-3D curve is symmetric with respect to the mid plane of the specimen and the KIn-3D values are about constant for 0≤z/t≤±0.4, but show distinctly decreasing values adjacent to the free side surfaces of the specimen, which are intersected by the crack front at z/t=±0.5. This result qualitatively corresponds well with 3D fracture analysis results for CT-specimens to be found in the literature.

In the case of pure in-plane shear loading (α=90°) of the CTS-specimen we see from Fig. 3 that not only a dominant mode II loading is generated locally along the straight crack front, but also a small amount of mode III is analysed. The KIIn-3D curve is symmetric again with respect to the

mid plane of the specimen and rather constant for $0 \le z/t \le \pm 0.4$, whereas the KIIIn-3D curve changes the sign at z/t=0 and is found to be skew-symmetric. In contrast to KIn-3D in Fig. 2 the KIIn-3D values show increasing values adjacent to the free side surfaces of the specimen. The local mode III loading along the crack front is related to Poisson´s ratio and the increasing values adjacent to the free side surfaces of the specimen are due to the decreasing lateral constraints there.

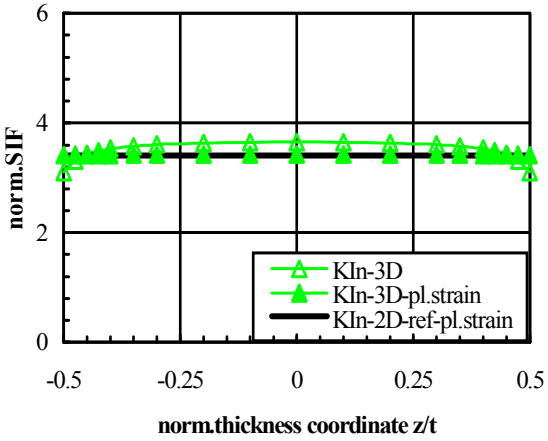

Figure 2. Norm. SIFs along the crack front of a CTS-specimen with a straight crack front (β=90°) under pure tension loading (α=0°)

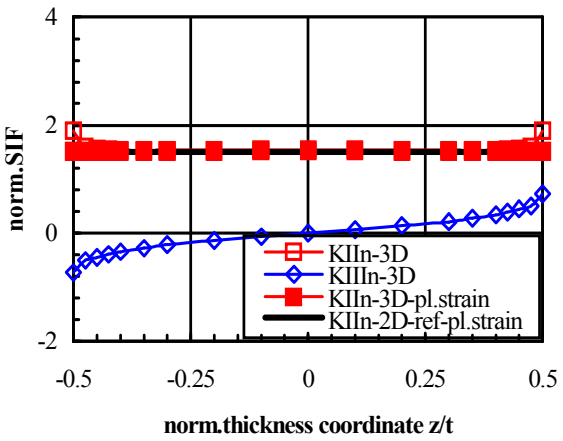

Figure 3. Norm. SIFs along the crack front of a CTS-specimen with a straight crack front (β=90°) under pure in-plane shear loading (α=90°)

But although for these real 3D analyses there are no reference solutions available in Handbooks or in the literature, we can check the accuracy of the Kin-3D curves, i=I,II and III in Figs. 2 and 3. The way how to relate these results of the 3D-model of the CTS-specimen to 2D reference solutions given by RICHARD is to suppress all displacements in the thickness or global z-direction of the specimen by setting $u_{z0}(x,y,z/t=\pm 0.5)=0$ as boundary conditions (BCs) at both side surfaces of the specimen. By this trick plane strain conditions with $u_z(x,y,\ 0 \le z/t \le \pm 0.5) \equiv 0$ can be enforced also for the real 3D FE-model of the CTS-specimen and the SIFs evaluated along the crack front through the thickness of the specimen should be constant and related to the corresponding 2D reference values. The normalised SIF-values KIn-3D-pl.strain or KIIn-3D-pl.strain, as plotted in Figs. 2 and 3, respectively, are found to be perfectly constant along the crack front for both loading cases and through the small relative errors of $\Delta_{rel}=+0.5\%$ or $\Delta_{rel}=+0.9\%$ between the corresponding 2D plane strain reference values and the mean values of KIn-3D-pl.strain or KIIn-3D-pl.strain, respectively, the quality of the chosen FE-model and the high accuracy of the Kin-3D curves, i=I,II and III in Figs. 2 and 3 can be taken as approved.

The corresponding findings for the modified CTS-specimen with an angle γ=45° of the inclined crack plane are given in Figs.4 and 5. For pure tension loading again dominating mode I loading conditions are generated along the crack front of the inclined crack plane (Fig. 4), with a maximum value of the related KIn-incl.cr.plane(45°) curve in the mid plane of the specimen and distinctly decreasing values adjacent to the free side surfaces of the specimen ($z/t \rightarrow \pm 0.5$). But due to the inclined crack plane also considerable mode III loading conditions are generated along the crack front. Quantitatively they are given in form of the KIIIn-incl.cr.plane(45°) curve in Fig. 4, showing about constant values for $0 \le z/t \le \pm 0.4$ and values of about the same magnitude as of the KIn-incl.cr.plane(45°) curve. But in contrast to KIn-incl.cr.plane(45°), distinctly increasing values are found for KIIIn-incl.cr.plane(45°) for $z/t \rightarrow \pm 0.5$. But furthermore the 3D-analysis by the MVCCI-method shows that also remarkable mode II loading conditions are induced locally along the crack front with strongly increasing values adjacent to the free side surfaces of the specimen ($z/t \rightarrow \pm 0.5$). For $z/t = \pm 0.5$ they even exceed the corresponding KIn and KIIIn-values. In contrast to the related KIn and KIIIn-curves, which are symmetric with respect to the mid plane of the specimen, the KIIn-incl.cr.plane(45°) curve is skew-symmetric and changes sign at z/t=0. The locally induced mode II

loading conditions along the crack front are correct and have also been found in case of a Three-Point Bend(3PB)-specimen with an inclined crack plane [4].

For pure in-plane shear loading of the modified CTS-specimen with an inclined crack plane (γ=45°) we find in Fig. 5 results for KIIn and KIIIn-incl.cr.plane(45°) which are very similar to those discussed in Fig. 3 for the CTS-specimen with a straight crack front (β=90°) and thus the corresponding curves are nearly coinciding. This means that in contrast to the case of tension loading, for in-plane shear loading the inclination of the crack plane has hardly any influence on the mode-mixture which may be achieved locally along the crack front of the modified CTS-specimen. But furthermore also skew-symmetric mode I loading conditions are found along the crack front. For values KIn-incl.cr.plane(45°) > 0 this means crack opening, but for values < 0 this means crack face contact in a real laboratory specimen, which will affect experimental investigations performed with this type of modified CTS-specimen in case of pure in-plane shear loading.

Due to limited space in this paper a Figure showing results for an in-plane tension/shear loading of this specimen, e.g. with a loading angle of α=45°, had to be cancelled. But it appears obvious and has been proved in this investigation that in this case also another superposition of all fracture modes I, II and III can be generated along the crack front of this modified CTS-specimen. For sure the mixed-mode ratios which can be achieved are limited, although angles of crack plane inclinations up to γ=60° may be considered (γ=0°, crack plane normal to free side surfaces of spec.).

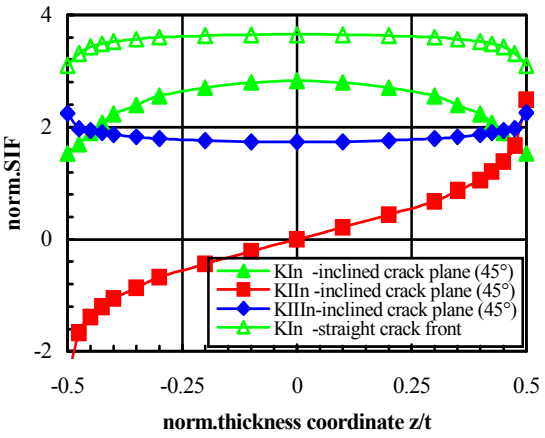

Figure 4. Norm. SIFs along the crack front of a CTS-specimen with an inclined crack plane (γ=45°) under pure tension loading (α=0°)

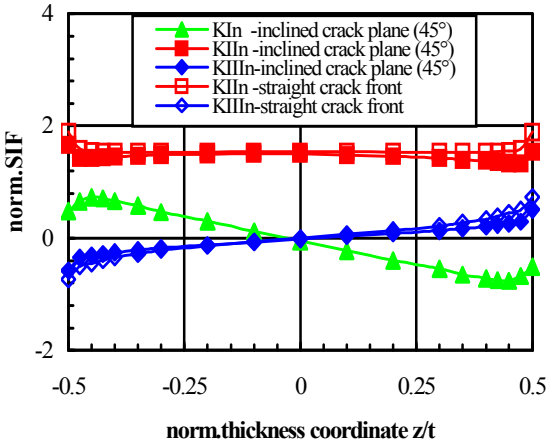

Figure 5. Norm. SIFs along the crack front of a CTS-spec. with an inclined crack plane (γ=45°) under pure in-plane shear loading (α=90°)

References

[1] Richard, H.A., An new compact shear specimen. *Int. J. Fracture* **17**, R105-R107, (1981).

[2] Richard, H.A. and Benitz, K., A loading device for the creation of mixed mode in fracture mechanics. *Int. J. Fracture* **22,** R55-R58, (1983).

[3] Buchholz, F.-G., Finite Element Analysis of a 3D Mixed-Mode Fracture Problem by Virtual Crack Closure Integral Methods. In: *Fracture Mechanics* (Eds. A.V. Krishna Murthy, F.-G. Buchholz), Proc. of the Indo-German Workshop on Advances in Fracture Mechanics, Indian Institute of Science, Bangalore, India, March 1994, Interline Publ., Bangalore, 7-12, (1994).

[4] Buchholz, F.-G., Richard, H. A., Comparison of Computational Crack Path Predictions with Experimental Findings for SEN-Specimens Under Different Loadings. In *Computational Mechanics*, (Eds. Z. H. Yao et al.), CD-ROM Proc. of the 6th World Congress of Computational Mechanics (WCCM VI) in conjunction with APCOM'04, Beijing, China, September 2004. Tsinghua University Press & Springer-Verlag, 2004.

Key Engineering Materials Vols. 385-387 (2008) pp 745-748
© (2008) Trans Tech Publications, Switzerland
doi:10.4028/www.scientific.net/KEM.385-387.745

Impact Properties of Sn-0.75Cu Lead-free Solder Ball Joint

Ikuo Shohji[1, a], Tsutomu Osawa[1], Takeshi Okashita[2] and Hirohiko Watanabe[3, b]

[1]Graduate school of engineering, Gunma University, Tenjin-cho, Kiryu, 376-8515, Japan

[2]Faculty of engineering, Gunma University, Tenjin-cho, Kiryu, 376-8515, Japan

[3]Fuji Electric Advanced Technology Co., Ltd., 1 Fuji-machi, Hino, 191-8502, Japan

[a]shohji@me.gunma-u.ac.jp, [b]watanabe-hirohiko@fujielectric.co.jp

Keywords: Sn-0.75mass%Cu, Impact properties, Fracture, Ball shear impact test, Lead-free solder

Abstract. Impact properties of a solder ball joint with a Sn-0.75mass%Cu lead-free solder were investigated under aging conditions at 393 K. Moreover, obtained impact properties were compared with those of the joints with Sn-3.5mass%Ag and Sn-3.5mass%Ag-0.5mass%Cu solders. Ball impact force of a Sn-0.75Cu joint was stable at 4.5~5 N, which is similar to that of a Sn-3.5Ag-0.5Cu joint without aging, upon aging at 393 K for 1000 h. In the Sn-0.75Cu joint without aging, main fracture mode was complex fracture of the solder and an intermetallic compound (IMC) formed in a joint interface. Main fracture mode changed from the complex mode to solder fracture upon aging, and thus the impact toughness improved.

Introduction

A Sn-Cu solder is an attractive lead-free solder because the material cost is cheaper than any other lead-free solders such as Sn-Ag-Cu solders. Since the melting point of the Sn-Cu solder is higher than those of Sn-Ag-Cu solders, the Sn-Cu solder has been expected to be used for wave soldering process [1]. In recent years, it was reported a Sn-0.7Cu solder has better low cycle fatigue performance [2] and better thermal fatigue performance for flip chip application [3] compared with a Sn-37Pb solder. Thus, the Sn-Cu solder is expected to be used not only for wave soldering but also for area array type packages such as ball grid array (BGA) [4] and flip chip with a low-k insulation layer [5].

In solder ball joints of area array type packages, the impact reliability is one of the crucial issues besides thermal fatigue, heat resistance and so on. For the Sn-Cu solder, many researches have been conducted on tensile properties [6, 7], creep properties [8], fatigue properties [2, 9], intermetallic compound layer growth upon heating and aging [4, 10] and so on. On the contrary, the study on the impact properties of the Sn-Cu solder joint is a little. The aim of this study is to investigate the impact properties of the Sn-Cu solder ball joints under aging conditions. Moreover, obtained data were compared with those of the solder ball joints with Sn-Ag and Sn-Ag-Cu.

Experimental

Sn-0.75mass%Cu solder balls with 0.3 mm diameter were prepared and Sn-3.5mass%Ag and Sn-3.5masss%Ag-0.5masss%Cu solder balls were also prepared for comparison. Following the experimental procedure of the previous reports [11], the solder ball was joined on a Cu pad on an FR-4 substrate by reflow soldering with non-clean flux. The diameter of the Cu pad was 0.2 mm and the surface of the Cu pad was finished with organic solderability preservative. The peak temperature and duration time over 500 K in reflow soldering were set to be 516 K and 33 s, respectively. After reflow soldering, the subsequent aging treatment were conducted at 393 K for 300 h, 600 h and 1000 h. For the Sn-0.75Cu joints before and after aging, microstructural observation was conducted using an electron probe X-ray microanalyzer (EPMA).

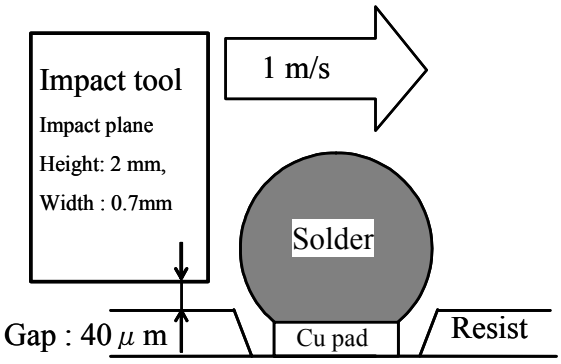

Fig. 1 Schematic of the impact test [13].

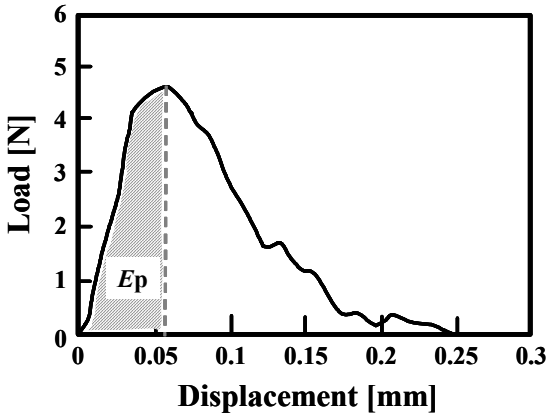

Fig. 2 Example of a result of impact test with a Sn-0.75Cu solder ball joint (without aging).

The impact test of the solder ball joint was conducted at room temperature using Instron Micro Impactor [12]. Fig. 1 shows a schematic of the impact test. The thickness of the Cu pad and the resist were 36 μm and 46 μm, respectively. The velocity before impact was set at 1 m/s. Fig. 2 indicates an example of the result of the impact test with a Sn-0.75Cu solder ball joint. In this study, energy to peak load was defined as *E*p, and thus the ball impact force (peak load) and the impact toughness (*E*p) were investigated. Eight joints were tested under each condition, and the averages of the peak load and *E*p were evaluated by the data except maximum and minimum values. Fracture surfaces and cross sections after the impact test were observed with the EPMA to investigate the fracture mode.

Results and discussion

Microstructures. Fig. 3 shows microstructures of the joint interfaces between Sn-0.75Cu solders and Cu pads. In the as-reflowed joint, a scallop-shape reaction layer approximately 2 μm thick forms in the joint interface. From the EPMA mapping analysis, Cu and Sn were detected in the reaction layer. The reaction layer seems to be a Cu-Sn compound. Two reaction layers form in the joint interface upon aging as shown in Fig. 3(b). A bright gray layer and a dark gray layer form in the Sn-0.75Cu side and in the Cu side in the joint interface, respectively. From the result of EPMA quantitative analysis, the bright gray layer and the dark gray layer were identified as Cu_6Sn_5 and Cu_3Sn, respectively.

Impact properties. Fig. 4 shows the impact test results of the solder ball joints. The ball impact force of the Sn-0.75Cu joint is relatively stable at 4.5 – 5 N, which is similar to that of the Sn-3.5Ag-0.5Cu joint without aging, regardless of the aging time. On the contrary, the impact force of the Sn-3.5Ag-0.5Cu joint gradually decreases with increasing aging time. Although the impact force of the Sn-3.5Ag joint is higher than those of Sn-0.75Cu and Sn-3.5Ag-0.5Cu before aging, it decreases upon aging and becomes almost the same as that of the Sn-3.5Ag-0.5Cu after aging for 600 h.

The impact toughness, *E*p, of the Sn-0.75Cu joint is 0.15 mJ before aging. This value is smaller than that of the Sn-3.5Ag joint but higher than that of the Sn-3.5Ag-0.5Cu joint. *E*p of the Sn-3.5Ag-0.5Cu joint is stable approximately at 0.1 mJ upon aging. *E*p of the Sn-3.5Ag joint reduces upon aging and it becomes the same as that of the Sn-3.5Ag-0.5Cu joint after aging for 600 h in the same manner as the ball impact force. On the other hand, *E*p of the Sn-0.75Cu joint improves by aging and becomes approximately double after aging for 600 h.

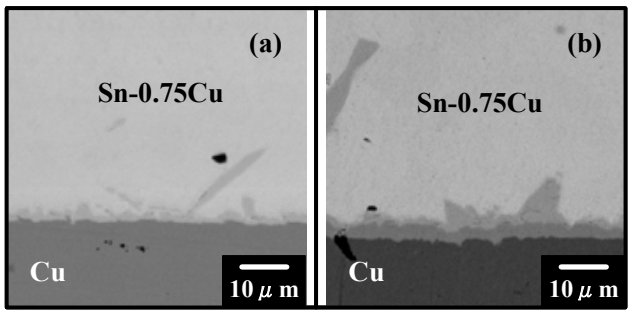

Fig. 3 Back-scattered electron images of Sn-0.75/Cu joints. (a) as-reflow, (b) after aging at 393 K for 1000 h.

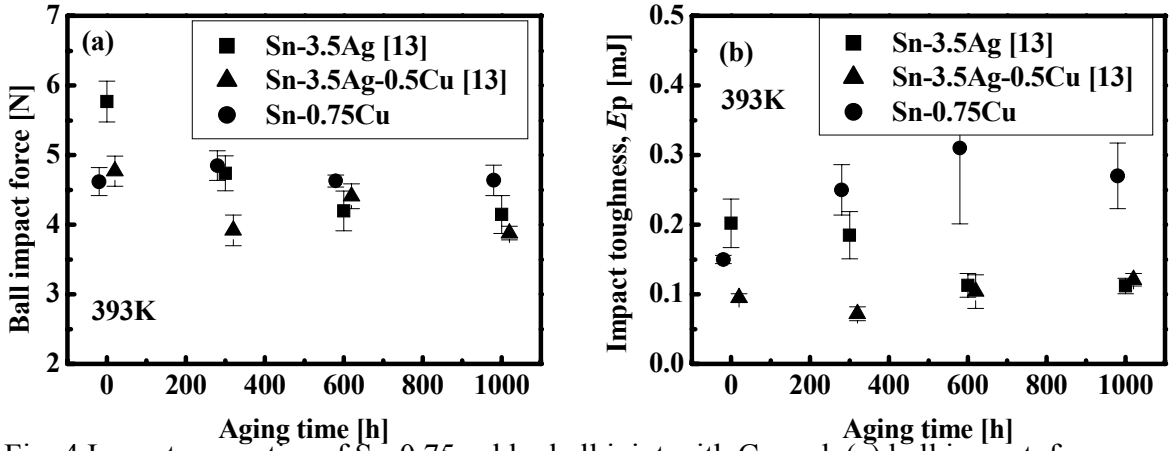

Fig. 4 Impact properties of Sn-0.75 solder ball joint with Cu pad. (a) ball impact force, (b) impact toughness (*E*p).

Fracture mode. Three fracture modes were observed in fracture surfaces after the impact test in this study. Examples of fracture modes are shown in Fig. 5. Figs. 5(a), (b) and (c) show solder fracture, IMC fracture and their complex fracture, respectively. Fig. 6 indicates the change of the fraction of fracture mode upon aging for each solder joint. For the Sn-3.5Ag-0.5Cu joint, fracture occurred in a brittle IMC layer regardless of aging treatment. Thus, the Sn-3.5Ag-0.5Cu joint seems to have poor impact properties as shown in Fig. 4.

For the Sn-3.5Ag joint, although the main fracture mode was IMC fracture, the solder fracture mode was also observed in as-reflow joints. Since an as-cast Sn-3.5Ag solder has higher tensile strength than as-cast Sn-Ag-Cu and Sn-Cu solders [14], higher ball impact force and *E*p are shown in the as-reflow Sn-3.5Ag joint. However, all fracture mode became IMC fracture after aging for 600 h and thus impact properties degraded to the same level of the Sn-3.5Ag-0.5Cu joint.

On the contrary, the complex fracture of solder and IMC was dominant in as-reflow Sn-0.7Cu joints. When the IMC layer grows upon aging, the main fracture mode changes from the complex fracture to solder fracture. This change makes *E*p of the joint improve as shown in Fig. 4(b). After aging at 393 K for 1000 h, the impact toughness of the Sn-0.75Cu joint became approximately double those of the joints with Sn-3.5Ag and Sn-3.5Ag-0.5Cu. In the Sn-0.75Cu joint, the Cu_3Sn layer, which is stiffer than the Cu_6Sn_5 layer, grows upon aging. Thus, fraction of the complex fracture increases with increasing aging time, although the impact force of the joint scarcely changes over the aging conditions investigated.

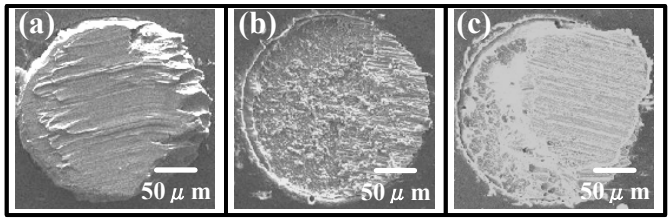

Fig. 5 Examples of observed fracture surfaces in Sn-0.75Cu solder ball joints (secondary electron images). (a) solder fracture after aging at 393 K for 300 h, (b) IMC fracture after reflow soldering, (c) complex fracture after aging at 393 K for 1000

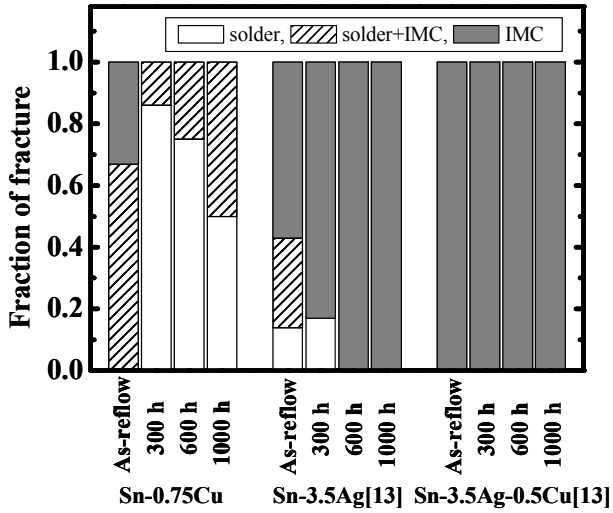

Fig. 6 Relationship between fraction of fracture and aging time.

Summary

The impact properties of the Sn-0.75Cu solder ball joint were investigated under aging conditions and were compared with those of Sn-3.5Ag and Sn-3.5Ag-0.5Cu joints. The ball impact force of the Sn-0.75Cu joint was stable at 4.5~5 N, which is similar to that of the as-reflow Sn-3.5Ag-0.5Cu joint, upon aging at 393 K for 1000 h. Ball impact forces of Sn-3.5Ag and Sn-3.5Ag-0.5Cu joints decreased with increasing aging time, and they were lower than that of the Sn-0.75Cu joint after aging at 393 K for 600 h. Main fracture mode changed from the complex mode of the solder and the IMC to the solder fracture by aging in the Sn-0.75Cu joint, and thus the impact toughness of the Sn-0.75Cu joint improved. After aging at 393 K for 1000 h, the impact toughness of the Sn-0.75Cu joint became approximately double those of the joints with Sn-3.5Ag and Sn-3.5Ag-0.5Cu.

Acknowledgement

The authors would like to thank Instron Ltd. for conducting the impact test for solder ball joints.

References

[1] M. Abtew and G. Selvaduray: Mater. Sci. Eng. R, Vol. 27 (2000), p. 95

[2] J. H. L. Pang, B. S. Xiong and T. H. Low: Int. J. Fatigue, Vol. 26 (2004), p. 865

[3] D. R. Frear, J. N. Arnold and R. C. Pfahl: 2001 ICEP(International Conference on Electronics Packaging) Proceedings (IEEE CPMT Society Japan, IMAPS Japan and JIEP, 2001) p. 54

[4] J. W. Yoon, S. W. Kim and S. B. Jung: J. Alloys Compd., Vol. 385 (2004), p. 192

[5] M. Uchida, H. Ito, K. Yabui, H. Nishiuchi, T. Togasaki, K. Higuchi and H. Ezawa: Proc. of 14th Symposium on Microjoining and Assembly Technology in Electronics (The Japan Welding Society, 2008) p. 217

[6] S. H. Huh, K. S. Kim and K. Suganuma: Mater. Trans., Vol. 42 (2001), p. 739

[7] I. Shohji, T. Yoshida, T. Takahashi and S. Hioki: Transactions of the Materials Research Society of Japan, Vol. 29 (2004), p. 2001

[8] W. J. Plumbridge, C. R. Gagg and S. Peters: J. Electron. Mater., Vol.30 (2001), p. 1178

[9] T. Takahashi, S. Hioki, I. Shohji and O. Kamiya: Key Engineering Materials, Vol. 326-328 (2006), p. 1035

[10] M. J. Rizvi, C. Bailey, Y. C. Chan, M. N. Islam and H. Lu: J. Alloys Compd., Vol. 438 (2007), p. 122

[11] I. Shohji, S. Tsunoda, H. Watanabe, T. Asai and M. Nagano: Mater. Trans., Vol. 46 (2005), p. 2737

[12] E. H. Wong, Y-W. Mai, R. Rajoo, K. T. Tsai, F. Liu, S. K. W. Seah and C-L. Yeh: Proc. of 2006 Electronic Components and Technology Conference (IEEE, 2006) p. 64

[13] I. Shohji, H. Watanabe, T. Okashita and T. Osawa: Mater. Trans., Vol. 49 (2008), in press.

[14] T. Osawa, I. Shohji, T. Matsuki, Y. Kariya, K. Yasuda and T. Takemoto: Proc. of 14th Symposium on Microjoining and Assembly Technology in Electronics (The Japan Welding Society, 2008) p. 115

Key Engineering Materials Vols. 385-387 (2008) pp 749-752
© (2008) Trans Tech Publications, Switzerland
doi:10.4028/www.scientific.net/KEM.385-387.749

Evaluation of the Failure Elongation of Steel Sheets for an Auto-body at the Intermediate Strain Rate

Seokbong Kim[1,a] and Hoon Huh[1,b]

[1]School of Mechanical, Aerospace and System Engineering, KAIST, Daeduck Science Town, Daejeon, 305-701, Korea

[a]ksb79@kaist.ac.kr, [b]hhuh@kaist.ac.kr

Keywords: Failure elongation, Intermediate strain rate, Steel sheets

Abstract. This paper deals with the dynamic failure elongation of mild steel, SGACD and advanced high strength steel sheets such as TRIP600, DP600 and TWIP steels. The failure elongation has been obtained from the high speed tensile testing machine with various strain rates ranged from 0.003/s to 200/s. The experimental result demonstrates that the tensile elongation does not simply decrease as the strain rate increases, but it decreases from the quasi-static state to the strain rate of 0.1 or 1/s and increases again up to the strain rate of 100/s. Furthermore, some high strength steels have the tendency that the tensile elongation increases as the strain rate increases. Moreover, the localized strain rate hardening in the necking region induces the increase of elongation.

Introduction

The sheet metal forming process is one of the most important fabrication processes for an auto-body with development of forming techniques. Although the formability is important and indispensable for success in very complicated sheet metal forming, few studies have been done about the formability of sheet metal since it was difficult to make the tensile test of sheet metal at the intermediate strain rate ranged from several tens to hundreds per second. The dynamic tensile properties of auto-body steel sheets are important since the range of the strain rate is under 500/s in a real auto-body crash and at which the dynamic response of steel sheets is different from static one [1,2]. Mechanical, pneumatic and servo-hydraulic loading methods have been used to measure mechanical properties of materials at this range of intermediate strain rate. Nowadays, servo-hydraulic material testing machines are employed in most research works [3]. However, a few in-depth studies have been published about the dynamic material properties such as the yield and tensile strength as well as the tensile elongation at the intermediate strain rates.

In this paper, the tensile elongation has been obtained from various steel sheets for an auto-body at the intermediate strain rates. Dynamic tensile tests of four different steel sheets for an auto-body such as SGACD, TRIP600, DP600 and TWIP steels were performed to investigate the relation between the strain rate and the tensile elongation.

Experimental Conditions

In this research, a high speed material testing machine of the servo-hydraulic type was utilized in order to obtain the dynamic mechanical properties at the intermediate strain rates. The machine has the maximum stroke velocity of 7800 mm/s, the maximum load of 30 kN and the maximum displacement of 300 mm. Two electric motors are used to compress the operating hydraulic oil up to the pressure of 300 bars and two accumulators with the capacity of 5 liters are used to make the response time faster. The machine equipment is set up with the Kistler 9051A piezo-electric type load cell in a specially designed loading fixture to reduce the noise level and to increase the noise frequency from the load-ringing phenomenon. Several tests were conducted at the same condition to verify repeatability and the results were very satisfactory for repeatability with robust calibration and indicated that the machine response, testing procedure and material response were consistent.

Tensile specimens for the standard test are specified in the regulations of ASTM, BSI and KS as well as the testing method. These regulations, however, do not include the high speed tensile testing method and the corresponding specimens. Therefore, an appropriate high speed tensile testing method and specimen need to be determined for accurate tensile tests at the high strain rate ranged from 1 to 500/s. The dimension of specimen was determined from the finite element analysis result and the tensile test result considering the shape factors [4]. The dynamic tensile specimen has length of the parallel region of 30 mm and 6 mm in both gauge width and fillet radius.

The materials tested were auto-body steels such as SGACD, TRIP600, DP600 and TWIP steels prepared along the rolling direction. Experiments were carried out at room temperature of 294K at the strain rates ranged from quasi-static to 200/s. Quasi-static tensile tests were carried out at the strain rate of 0.003/s using the static tensile machine, Instron 5583. Dynamic tensile tests were carried out at strain rates from 0.1/s to 200/s using a high speed material testing machine developed.

Dynamic Tensile Characteristics of Steel Sheets

Flow Stress with Strain Rate. The mechanical properties of auto-body steel sheets obtained from the static test are given in Table 1. TWIP steel has highest elongation and lower yield ratio than any other steel sheets due to the massive twinning in the austenitic matrix during deformation. Twinning induced plasticity (TWIP) effect is the most useful effect on the work hardening because deformation twins increase the work hardening rate by acting as obstacles for gliding dislocations. TRIP600 has higher elongation and good ductility than DP600 steels due to the TRIP effect. This effect improves the elongation and strength of materials as the phase of remained austenite transforms into the phase of martensite during deformation.

Dynamic tensile tests were carried out at the strain rate ranged from 0.003/s to 200/s. Engineering stress-strain curves of auto-body steel sheets are shown in Fig. 1 at various strain rates. As the strain rate increases, the flow stress of steel sheets gradually increases but in case of TWIP steel, although the yield stress is positively sensitive to the strain rate, the tensile strength shows negative strain rate sensitivity. The slope of the stress-strain curve for mild steels such as SGACD decreases as the strain rate increases. As a result, the ultimate tensile strength occurs at the lower strain and the hardening exponent becomes smaller with the increase of the strain rate. This phenomenon seems to occur with the mechanism of grain sliding and the heat dissipated from the plastic work at the high strain rate. The yield stress of SGACD increases by more than two times while the increases of the yield stress of the advanced high strength steel, TRIP600, DP600 and TWIP steels is below 1.2 times. In general, the yield stress of the mild steel is more sensitive to the strain rate than that of the high strength steel. DP600 is more sensitive to the strain rate than TRIP600 in terms of the ultimate tensile strength. This result represents that the strain rate hardening of DP sheets is more advantageous than that of TRIP sheets because the strain rate in most auto-body crashes is under 500/s. Although the TWIP steel has prominent hardening and elongation properties at static state, TWIP steel will be disadvantageous in the auto-body crash event because flow stress is negatively sensitive to the strain rate.

Material	Thickness [mm]	Yield Stress [MPa]	UTS [MPa]	YS/UTS	Failure Elongation [%]
SGACD	0.79	166	308	0.539	56.7
TRIP600	1.45	414	612	0.676	34.0
DP600	1.43	422	632	0.668	26.9
TWIP	1.50	427	937	0.456	58.3

Table 1. Mechanical properties from the static test

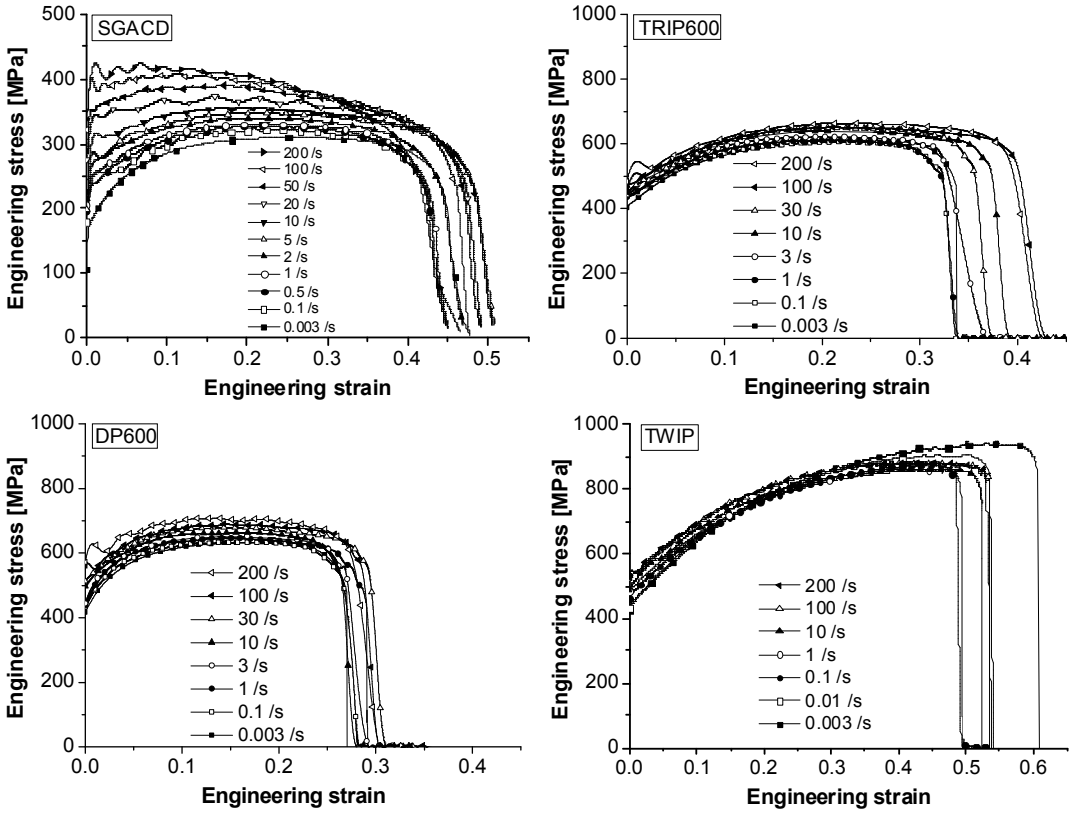

Fig. 1 Stress-strain curves of SGACD, TRIP600, DP600 and TWIP steels at various strain rates

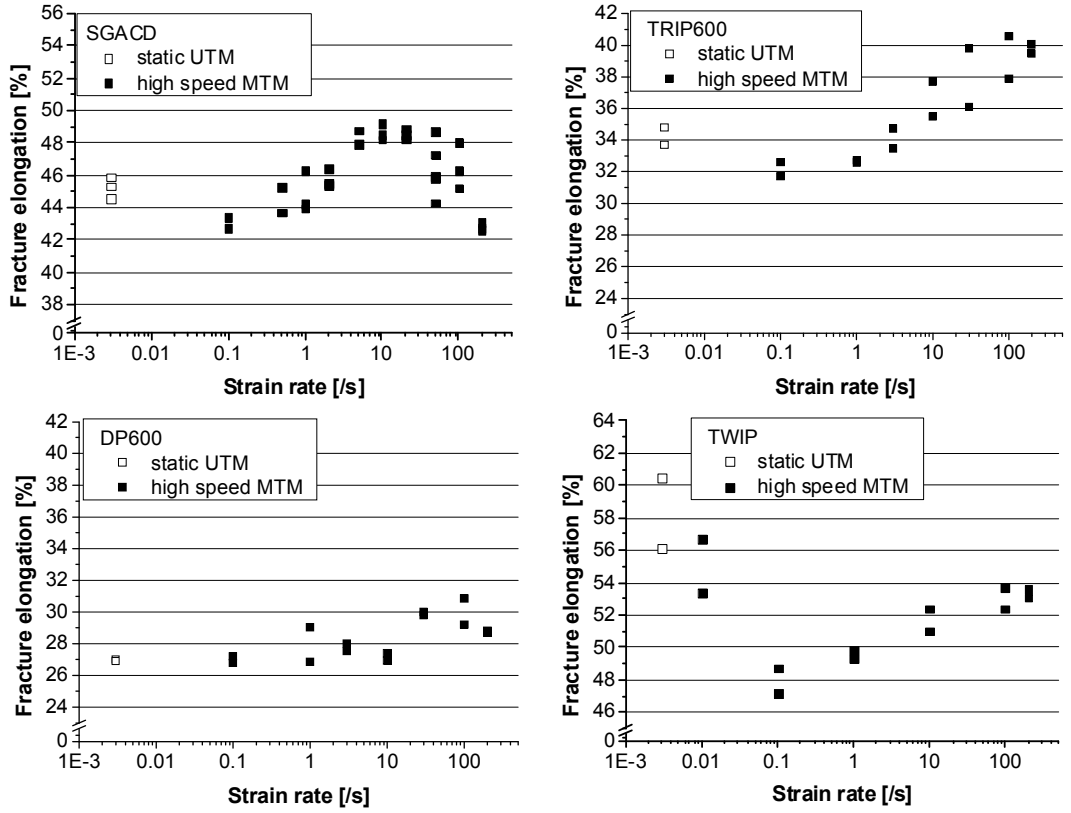

Fig. 2 Failure elongation of SGACD, TRIP600, DP600 and TWIP steels at various strain rates

Failure Elongation. The failure elongation was obtained from the engineering stress-strain curves at various strain rates. Fig. 2 shows the failure elongation distribution with the same elongation range of 18% against the logarithmic scale of the strain rate. It is known from classical conjecture that the strength of steel increases due to the strain rate hardening and the fracture elongation is expected to

decrease as the strain rate increases. However, the tensile test results show that the failure elongation of SGACD and TRIP600 decreases with increasing strain rate from 0.003/s to 0.1/s, and then increases up to the strain rate of 50/s or 100/s. The failure elongation of TWIP steel also shows this tendency although the elongation at quasi-static is higher than that at the dynamic state. On the other hand, the failure elongation of DP600 increases monotonically as the strain rate increases. Peixinho et al. [5] obtained the similar experimental result that ductility of TRIP600 and DP600 does not simply decrease with increasing the tensile speed. When the necking phenomenon occurs in simple static tensile tests, deformation is concentrated at the gauge region in a narrow band of the gauge region. On the other hand, in tensile tests at the high stain rates, local strain rate hardening restrains the progress of necking and diffuse necking region expands in the adjacent region forming a wide band of necking. It is because the strain rate at the necking region becomes particularly higher than the other region and the flow stress in the necking region exceeds the flow stress in the other region due to the rapid increase of the strain rate. Consequently, the necking region becomes stronger than the neighboring region despite thinning in the necking region, and finally the failure elongation increases as the strain rate increases. This experimental result is worthy of attention for the crashworthiness of an auto-body especially in terms of the fracture and tearing of auto-body members. This result is also applicable to sheet metal forming processes of auto-body members in order to enhance the formability of sheet metals. This increment of fracture elongation is due to the strain rate hardening in the proper strain rate range. This result reveals that forming processes at an adequate strain rate can enhance the formability compared to the static forming process.

Conclusions

This paper represents the tensile failure elongation that has been obtained for various steel sheets for an auto-body at the intermediate strain rate. The high speed material testing machine and the dynamic tensile specimen has been used for dynamic tensile tests at intermediate strain rates ranging from 0.1/s to 200/s. Dynamic tensile tests of SGACD, TRIP600, DP600 and TWIP steels for an auto-body were performed to investigate the relation between the strain rate and the elongation from the stress-strain curves at various strain rates. Several remarks are deduced from the experimental results as follows:

The failure elongation and the formability of TRIP600 are better than those of DP600 at the intermediate strain rates. TWIP steel shows prominent failure elongation compared to other steel sheets although flow stress is negatively sensitive to the strain rate.

The failure elongation of auto-body steels decreases with increasing strain rates from 0.003/s to 0.1/s, and then increases up to the strain rate of 50/s or 100/s due to the local strain rate hardening. The elongation of DP600 increases monotonically as the strain rate increases in contrast to the classical conjecture. This phenomenon is very interesting and important in sheet metal forming and the high speed deformation such as the auto-body crash from a viewpoint that the increment of the strain rate does not deteriorate the elongation.

References

[1] A.S. Khan and S. Huang: Int. J. Plasticity Vol. 8 (1992), p. 397

[2] H. Huh, J.H. Lim, S.B. Kim, S.S. Han and S.H. Park: Key Eng. Mat. Vol. 274 (2004), p. 403

[3] J.S. Kim, H. Huh, K.W. Lee, D.Y. Ha, T.J. Yeo and S.J. Park: Int. J. Auto. Tech. Vol. 7 (2006), p. 571

[4] H. Huh, S.B. Kim, J.H. Song and J.H. Lim: Int. J. Mech. Sci. in printing (2008)

[5] N. Peixinho and A. Pinho: Proc. of EURODYN (2005), p. 1767

Key Engineering Materials Vols. 385-387 (2008) pp 753-756
© (2008) Trans Tech Publications, Switzerland
doi:10.4028/www.scientific.net/KEM.385-387.753

Investigation of Rheological Properties of Asphalt Binders Containing Conductive Fillers

Shaopeng Wu[1,a], Bo Li[2,b], Junfeng Huang[3,c], Zhifei Liu [4,d]

[1] Key Laboratory of Silicate Materials Science and Engineering
(Wuhan University of Technology), Ministry of Education, Wuhan 430070, China

[2] Key Laboratory of Silicate Materials Science and Engineering
(Wuhan University of Technology), Ministry of Education, Wuhan 430070, China

[3] Key Laboratory of Silicate Materials Science and Engineering
(Wuhan University of Technology), Ministry of Education, Wuhan 430070, China

[4] Key Laboratory of Silicate Materials Science and Engineering
(Wuhan University of Technology), Ministry of Education, Wuhan 430070, China

[a]wusp@whut.edu.cn, [b]lip@whut.edu.cn, [c] hjf0808@163.com, [d]liuzhifei@whut.edu.cn

Keywords: Asphalt Binders, Conductive, Rheological Properties

Abstract: It is currently interesting to use thermal or electrical conductive asphalt mixtures for snow-melting and maintenance of asphalt pavements in winter or strain-sensing application. Graphite is the principal conductive filler for asphalt mixtures. The addition of Graphite not only makes asphalts conductive but also has effects on other properties. Considering the visco-elastic property of asphalt, the effects of graphite on rheological properties of asphalt binders were investigated by *Viscosity Test(VT)* and *Dynamic Shear Rheometer(DSR)*. The results of *Viscosity Test* indicate that viscosity of asphalt binder increases with an increasing amount of graphite. And the effect is more prominent at higher amount and lower temperature. It means that graphite makes asphalt binders stiffer. The results from DSR tests present that the values of complex modulus increase while phase angles decrease under a proper amount of graphite. It infers that proper amount of graphite can make asphalt a more elastic like material. And the results of rutting parameter point out that graphite can improve the rutting resistance of asphalts.

Introduction

Asphalt mixtures are widely used for highways, airport runways, bridge decks and city roads. However, the simultaneous use of these materials for non-structural functions is desired for the purpose of providing smart structures. It is currently interesting to use an asphalt solar collector or electrical conductive asphalt mixtures for pavement deicing in winter [1-2] or strain-sensing application [3]. The strain-sensing is valuable for weighing (as strain relates to stress, which in turn relates to the force), traffic monitoring, and structural vibration control (as strain relates to vibration). Since asphalt mixture is a kind of insulated material with electrical resistivity of 10^{12}-$10^{14}\Omega\cdot$m, fillers that are conductive are selected to provide low resistivity to asphalt mixtures. One of the ideal fillers that have been used in prior work for this purpose is graphite. The addition of graphite can greatly improve the electrical conductive property but also has effects on mechanical properties [4].

Asphalt is a visco-elastic material and may exhibit either elastic or viscous behavior, or combination of these, depending on temperature and time over which the asphalt is observed. The rheological properties of asphalt binders may significantly influence the performance of asphalt mixtures during mixing, compaction and in service. For this reason, it is very important to investigate rheological properties of asphalt binders containing conductive fillers. This paper presents a rheological investigation of asphalt binders with different contents of conductive fillers by Viscosity Test (VT) and Dynamic Shear Rheometer (DSR).

Materials and Experimental Design

Raw Materials Microcrystal graphite powders were selected as conductive fillers. Graphite powders are with particle size of 150μm, carbon content of 98.9%, electrical resistivity of $10^{-4}\Omega\cdot m$. A heavy-duty Asphalt binder AH-90 was obtained from Panjin Northern Asphalt Ltd., Co. in Liaoning Province, P.R. China, with penetration of 85.9 (0.1 mm at 25°C, 100 g and 5 s), ductility of more than 120cm at 15°C, and softening point of 41.1°C.

Specimens preparation The graphite contents of 8, 12, 18, and 22% by volume of asphalt binders were chosen according to the percolation model results of reference [5]. The asphalt binders containing different contents of graphite particles were prepared using a low shear mixer at 140 °C and a speed of 125 rpm. The mixing time was one hour. For the accurate evaluation of graphite effects, the base asphalts were also subjected to the same treatment as the graphite-asphalt blends.

Viscosity Test The viscosity tests of asphalt binders with different contents of graphite were conducted by a Brookfield viscometer (model DV-II + Pro) according to ASTM D 2170. The test temperatures covered a range of 60-170°C.

Dynamic Shear Rheometer Test A strain-controlled rheometer (Anton Paar, Austrilia) with parallel plate geometry (25 mm in diameter) was used to determine the rheological properties of asphalt binders. A frequency sweep was applied over the range of 0.1-100 rad/s at a fixed temperature of 50°C. The frequency sweep was conducted in an order decreasing frequency. Various visco-elastic parameters, such as complex shear modulus, phase angle, were collected automatically by the software. The visco-elastic parameters were also used to evaluate the rutting resistance of asphalt mixtures. Research has shown that the use of rutting parameter was a good indicator of rutting resistance.

Results and Discussions

Results of Viscosity

The effects of graphite contents and temperature on viscosity are shown in Fig.1. It can be observed from Fig.1 that at the same temperature, the viscosity of asphalt binders increases with an increasing amount of graphite. And under the same graphite amount, the viscosity of asphalt binders decreases while the temperature increases. For example, the viscosity increases from 355 up to 2330 mP· s at 135°C when the contents of graphite range from 0 to 22%. It means that the addition of graphite can make asphalts stiffer, which is good for the high temperature property.

Normally, the evaluation of rutting resistance of asphalt mixtures is conducted at 60°C. For this reason, the viscosity at 60°C is very important. Higher value of viscosity results in excellent rutting resistance. As shown in Fig.1, the viscosity of asphalt binders increases in magnitude when graphite contents range from 0 up to 22%. It implies that the addition of graphite can reduce the fluidity deformation of asphalts, which leads excellent rutting resistance.

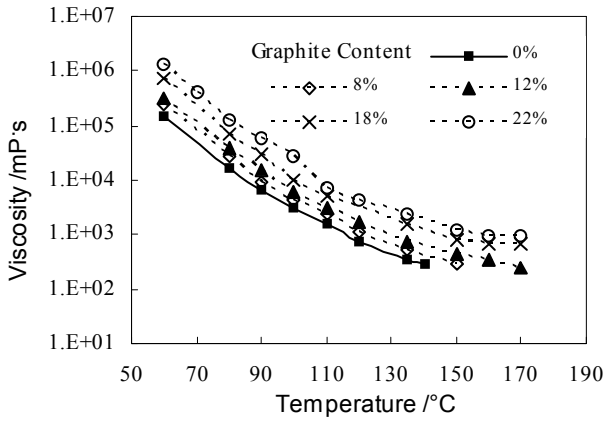

Figure 1 Viscosity versus temperatures

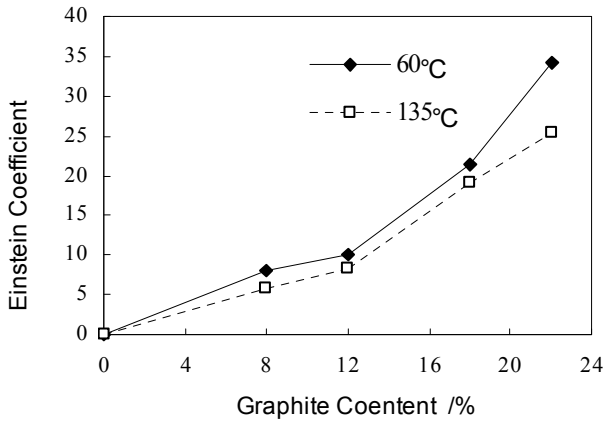

Figure 2 Results of Einstein Coefficients

Einstein coefficient is introduced to further evaluate the effects of graphite on the viscosity of asphalt binders according to equation 1:

$$K_E = (\eta / \eta_0 - 1) / \phi_f \tag{1}$$

Where: η—viscosity of asphalt with graphite, P·s; η_0—viscosity of base asphalt, P·s ;
K_E—Einstein coefficient ; ϕ_f—graphite content by volume of asphalt binders.

The effects of graphite contents on Einstein coefficient at 60°C and 135°C are shown in Fig. 2. It can be seen from Fig.2 that Einstein coefficient significantly increases with an increasing amount of graphite. For example, Einstein coefficient increases from 5.9 up to 25.3 when graphite contents range from 8% to 22% at 135°C. It means that the increasing effects are more prominent when graphite content is higher. It also can be observed form Fig. 2 that Einstein coefficients are higher at 60°C than those at 135°C. It refers that graphite can absorb asphalts more stably when the temperature is relatively low.

Results of DSR

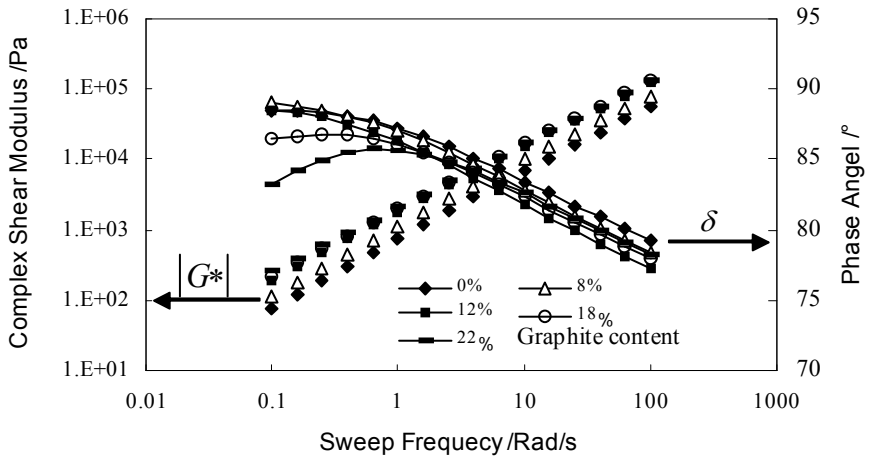

Figure 3 Complex shear modulus and phase angle of asphalt binders at 50°C

The complex shear modulus (G*) and phase angle (δ) at 50°C for asphalts with different contents of graphite are shown in Fig. 3. For clarity, curves of phase angles are plotted as solid line. It can be seen that G* of asphalt binders increase with the increasing of graphite contents and

frequencies. But the increasing effect is limited when the content of graphite exceeds 12%, especially under high frequency. It also can be observed from Fig.3 that phase angles present a decreasing trend with the increasing of graphite contents and frequencies. But when the content of graphite exceeds 12%, phase angles increase again. It means that a proper content of graphite can reduce the phase angle and make the asphalt a more elastic like material.

Rutting parameter, $E^*/\sin\varphi$, is considered to be an effective parameter to characterize the rutting resistance of asphalt binders. Fig. 4 depicts the rutting parameters of asphalt binders with different contents of graphite at 50°C, 63.1 rad/s (equal to 10Hz). It can be found that the rutting parameters of asphalt binders increase dramatically with an increasing content of graphite. But there is no further increasing effect when the content exceeds 18%. It means that the addition of graphite can greatly improve the rutting resistance of asphalts.

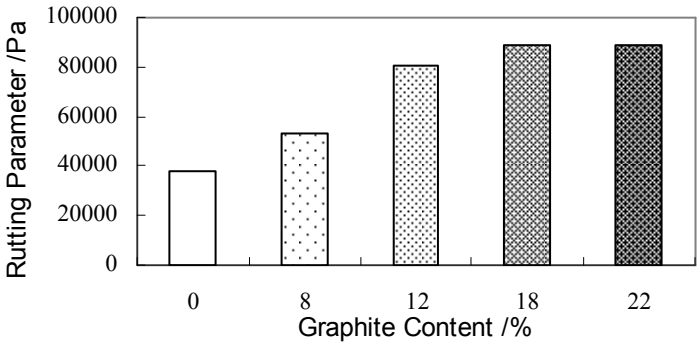

Figure 4 Rutting parameters of asphalt binders at 50°C, 63.1 rad/s

Conclusions

Rheological properties of asphalt binders containing graphite were investigated by Viscosity Test and Dynamic Shear Rheometer. The addition of graphite can lead a dramatic increase in viscosity due to its excellent absorption property to asphalts. And the effect is more prominent at higher amount and lower temperature. A proper content of graphite can lead an increase of complex shear modulus and decrease of phase angles. And the rutting resistance of asphalts can also be greatly improved by the addition of graphite.

Acknowledgements

The support of Education Ministry for New Century Excellent Talent Project (NCET-05-0656) is gratefully acknowledged.

Reference

[1] Van Bijsterveld, W.T. Houben, L.J.M.: Transportation Research Record Vol. 1778(2001), p.140

[2] Huang Baoshan, Cao Jingyao, Chen Xingwei : Journal of the Association of Asphalt Paving Technologists Vol. 75 (2006), p.1235

[3] Wu Shaopeng, Liu Xiaoming: Key. Eng. Mater Vol. 326-328 (2006), p.1499

[4] Wu Shaopeng, MoLiantong and Shui Zhonghe: Carbon Vol. 43-7(2005), p.1358

[5] Mo Liantong, Wu Shaopeng, Liu Xiaoming: Mater.Sci.Ed. Journal of Wuhan University of Technology Vol. 20-1(2005), p.111

Key Engineering Materials Vols. 385-387 (2008) pp 757-760
© (2008) Trans Tech Publications, Switzerland
doi:10.4028/www.scientific.net/KEM.385-387.757

Dimple Fracture Simulation under Mixed Mode Loading Condition.

Masanori Kikuchi[1,a] and Shougo Sannoumaru[2,b]

[1]Department of Mechanical Engineering, Tokyo University of Science, 2641 Yamazaki, Noda, Chiba, 278-8510, Japan
[2]Graduation School of Tokyo University of Science, 2641 Yamazaki, Noda, Chiba, 278-8510, Japan
[a]kik@me.noda.tus.ac.jp, [b]sun@me.noda.tus.ac.jp

Keywords: Ductile fracture, Mixed mode loading, Void, FEM simulation, Shear-lip fracture, Gurson's constitutive equation

Abstract. Dimple fracture under mixed mode loading condition is studied experimentally and numerically. By the mixed mode loading, it is found that fracture surface becomes much rougher than that of mode I fracture. It is also found that ductile fracture growth direction deviates from the original plane. It becomes clear that there are two factors affecting ductile fracture processes, one is mixed mode ratio and another is thickness effect. Three-dimensional finite element analyses are conducted to study effects of these factors. For the simulation of ductile fracture, Gurson's constitutive equation is used with large deformation theory. These numerical results agree with experimental observation very well qualitatively.

Introduction

In the elastic-plastic fracture mechanics, J integral [1] is considered to be one of the most important parameters, which controls the fracture process. It is known that J integral is not available under different constraint condition. It is called constraint effect, and thickness effect[2] is one of the constraint effect problems. Recently, as the machine becomes smaller, thin plate structures are used and plane stress fracture problem should be considered. Under plane stress state, shear-lip fracture occurs. The mechanism of shear-lip fracture has not been studied yet well. The effect of mixed mode loading to dimple fracture is another important problem. Authors have simulated mode I dimple fracture process precisely [3]. But dimple fracture under mixed mode loading has not been studied well.

In this paper three point bending specimen is used for the dimple fracture tests. Loading condition is changed from Mode I to mixed mode conditions. Ductile fracture process was simulated numerically by Gurson's constitutive equation. Results are compared with experimental ones and thickness effect and mixed mode loading effect are discussed.

Dimple fracture test.

Fig.1 shows three-point bending specimen used in this study. The material is A533B steel, which is used for nuclear power plant. As shown in Fig.1, crack is located near to left-side supporting point, and mixed mode loading condition is changed by changing this crack location. The mixed mode is expressed by the ratio of K_{II} to K_I as K_{II}/K_I. K_{II}/K_I is changed in 5 cases. Dimple fracture tests are conducted by changing specimen thickness in two cases, 2mm and 8mm.

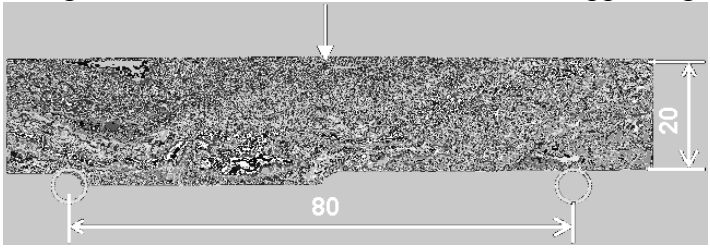

Figure 1 Three-point bending specimen under mixed mode loading.

Fig.2 shows SEM photos on dimple fracture surface. This is a result of test K_{II}/K_I=0.25, where mixed mode ratio is the largest. Fig.2 (a) shows dimples at mid-plane of the specimen, and (b) shows fracture surface in shear-lip zone. In mid-plane of the specimen, large dimples are observed. But shear-lip zone is covered by very small dimples. In shear-lip zone under mixed mode loading, it is also shown that dimple fracture, void nucleation and growth, is dominant phenomenon as well as under mode I loading condition.

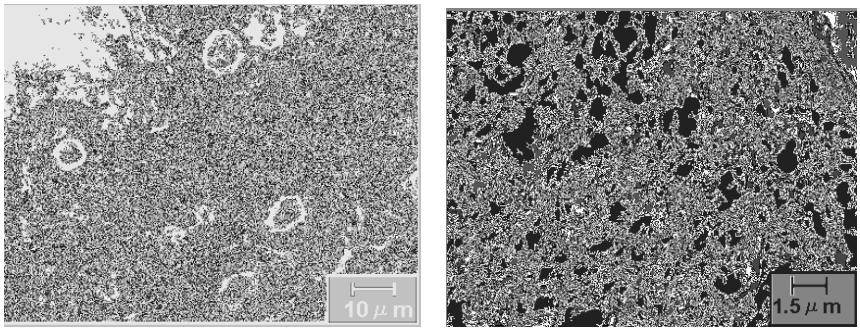

(a) Mid-plane (b) Shear-lip zone

Figure 2 Dimples on fracture surfaces.

By mixed mode loading, crack front does not grow along the initial crack direction. Then the crack growth direction is measured by using displacement measurement machine. By the change of mixed mode ratio and specimen thickness, these angles also change. Results are shown in Fig. 3. At shear-lip zone, crack growth angle is large. For mixed mode condition, crack growth angle in mid-plane increases a little, and at shear-lip zone, it does not change largely with the change of mixed mode ratio. It is interesting to note that crack growth direction at specimen surface is opposite to each other in 2mm and 8mm thick specimens. In 8mm-thick specimen, crack growth directions at mid-plane and at specimen surface are opposite to each other, though they are same directions in 2mm-thick specimen.

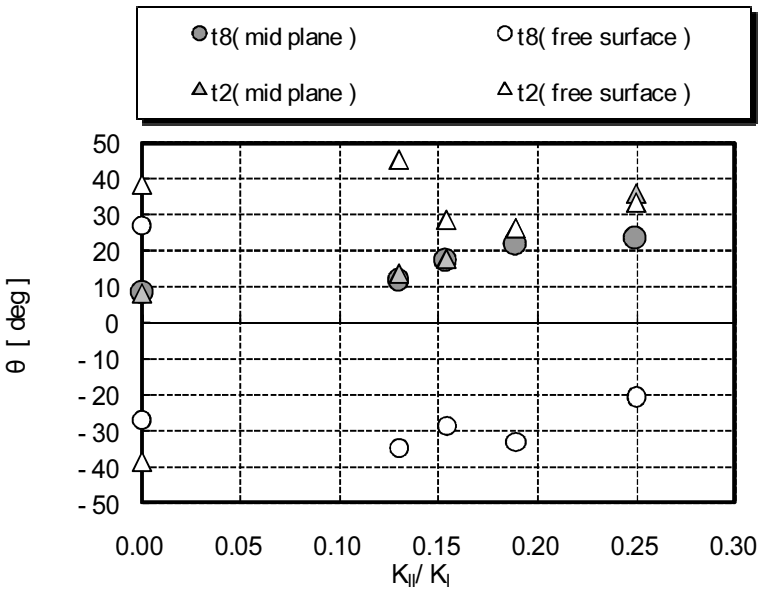

Figure 3 Crack growth angle.

Numerical simulation

Constitutive equation Based on experimental results, numerical simulation was conducted using Finite Element Method (FEM). To consider dimple fracture process, such as void nucleation, growth and coalescence, yield function proposed by Gurson for ductile material [4] is used as a constitutive equation, which is expressed as follows:

$$\Phi = \frac{3}{2}\frac{\sigma'_{ij}\sigma'_{ij}}{\bar{\sigma}_m^2} + 2f^* q_1 \cosh\left(\frac{q_2\sigma_{kk}}{2\bar{\sigma}_m}\right) - \left(1 + q_1^2 f^{*2}\right) = 0 \qquad (1)$$

where f^* is void volume fraction, σ_{ij} is deviatric stress and σ_m is equivalent stress. Constants q_1 and q_2 are parameters introduced by Tvergaard [5].

Void volume fraction, f^*, increases due to the increase of plastic deformation. It is expressed by the next equation.

$$f = f_{nucleation} + f_{growth} \qquad (2)$$

where $f_{nucleation}$ is increment of f due to nucleation of new voids, and f_{growth} is increment of void by the growth of existing void. Growth term is controlled by the dilatational strain, and it has been proposed that nucleation term is controlled by stress state and plastic strain, which is expressed as follows [10].

$$\dot{f}_{nucleation} = A\left(\dot{\bar{\sigma}}_m + \frac{1}{3}\dot{\sigma}_{kk}\right) + B\dot{\bar{\varepsilon}}_m^p \qquad (3)$$

In the following numerical simulation, both term are used and values of A and B are determined as $A=5.0\times10^{-6}$ and $B=5.0\times10^{-2}$, respectively.

Three-dimensional simulation. Fig.4 shows three-dimensional model of three point bend specimen. This is a model of $K_{II}/K_I=0.25$. By the symmetry of the specimen shape, half model is used for mixed mode fracture simulation. Mode I problem is also solved, and only quarter part is enough for this modeling. By introducing pre-crack by fatigue load, crack front has some curvature. It is called tunneling effect. For accurate simulation, this curvature is measured experimentally, and is used for modeling. In three-dimensional field, super-box element is used for FEM analyses.

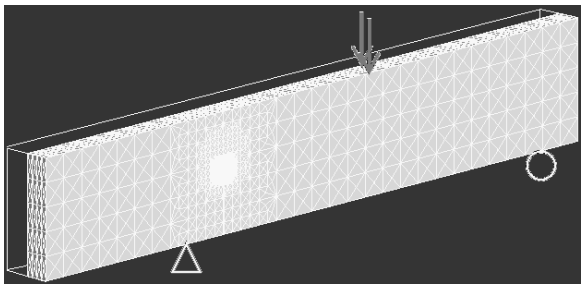

Figure 4 Half model of specimen under mixed mode loading.

Crack growth directions of mode I and mixed mode cases are compared with each other. Fig.5(a), (b) and (c) show crack growth behavior at mid-plane of the specimen. Fig.5(a) is a result of mode I crack problem. Crack grows straight along initial crack direction. Stress triaxiality distribution around crack tip is also shown in this figure. It is understood that crack grows to maximum stress triaxiliality area. In Fig.5 (b) and (c), results of mixed mode loading condition, $K_{II}/K_I=0.25$, are shown. As same as Fig.5(a), crack grows to maximum stress triaxiality direction, and grows toward to loading point, which agrees with experimental one qualitatively. Comparing with these figures, it is noticed that stress triaxiality of mode I specimen is larger than that of mixed mode specimen. It means that void easily grows larger in mode I specimen, and is rather difficult to grow in mixed mode specimen. These results agree again qualitatively that average void diameter of mode I specimen is larger than that of mixed mode specimen

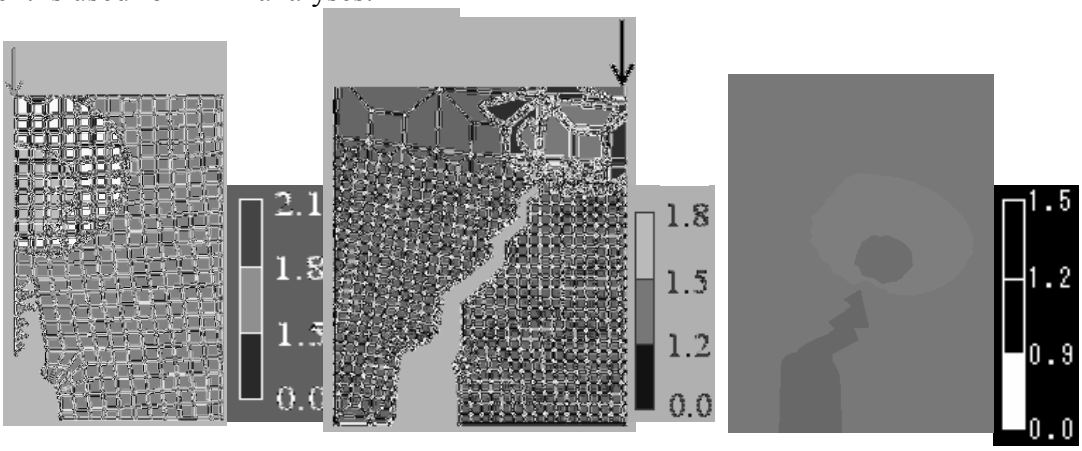

(a) Mode I crack (b) $K_{II}/K_I=0.25$ (8mm) (c) $K_{II}/K_I=0.25$ (2mm)

Figure 5 Crack growth at mid-plane and distribution of stress triaxiality.

Fig.6 shows crack growth behaviors of three specimens at surface of specimen. At specimen surface, stress state is plane stress condition, and fracture occurs in shear-lip zone. In these figures, distributions of equivalent plastic strain are also shown. In all figures, it seems that crack growth occurs to along large equivalent plastic strain area. In Fig.6(b), for 8mm thick specimen, crack growth occurs to opposite direction to that at mid-plane, as shown in Fig.5(b). But in Fig.6(c), 2mm thick specimen, crack growth direction is same as that at mid-plane shown in

Fig.5(c). It is interesting to note that crack growth direction changes with the change of the specimen thickness. The reason of this change is due to the effect of mid-plane. Ductile crack growth occurs earlier at mid-plane, and fracture at surface occurs later. As a result, fracture direction at surface of 2mm thick specimen follows the direction at mid-plane. But for 8mm thick specimen, there is a distance between mid-plane and surface. By this reason, fracture directions at mid-plane and surface are determined independently. These results agree with experimental observations in Fig.2 qualitatively.

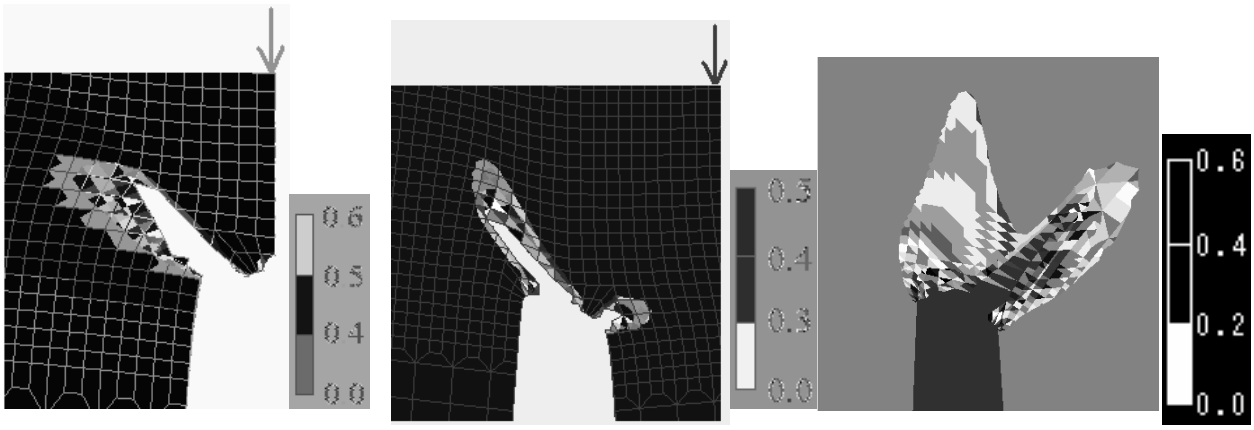

(a) Mode I crack. (b) K_{II}/K_I=0.25

Figure 6 Plastiac strain distribution around crack tip.

Through these numerical simulation, it becomes obvious that mixed mode dimple fracture process can be simulated using Gurson's constitutive equation. Comparing with mode I dimple fracture, it is interesting to note that assumptions for void nucleation should be considered in two ways. One is plastic strain controlled nucleation (PSCN), and another is stress controlled nucleation (SCN). In mode I fracture, only PSCN assumption is enough. But under mixed mode conditions, both assumptions are needed to simulate fracture process.

Summary

Dimple fracture process under mixed mode loading condition is studied experimentally and numerically. It has been shown that void nucleation and growth play important role in both at mid-plane and at free surface. Including shear-lip zone, these phenomena could be simulated using Gurson's constitutive equation by considering PSCN and SCN conditions. By further detailed simulation, transformation process from plane strain condition to plane stress condition will be understood, which gives basic understanding for plane stress fracture mechanics..

References

[1] Rice, J.R .Trans. ASME, J. Appl. Mech., vol.35(1968), p379.

[2] William. A. Et al., International Journal of Fracture, Vol.47(1991), pp.105-126

[3] M.Kikuchi and S.Sannoumaru, proceedings of JSEM, No.7(2007),pp.122-124

[4] A.L.Gurson, Continuum , J. Engineering materials and technology, vol.99, No.1(1977), pp.2-15

[5] V.Tvergaard. International Journal of Fracture, vol.17(1988), p.389

Key Engineering Materials Vols. 385-387 (2008) pp 761-764
© (2008) Trans Tech Publications, Switzerland
doi:10.4028/www.scientific.net/KEM.385-387.761

Fatigue Crack Growth Simulation by using S-version FEM

M. Kikuchi, Y. Wada, Maigefeireti and Y. Li

Department of Mechanical Engineering, Tokyo University of Science

2641 Yamazaki, Noda, Chiba, 278-8510, Japan

kik@me.noda.tus.ac.jp

Keywords: fatigue crack growth; s-version FEM; mix-mode condition; 3-dimensional plural cracks;

Abstract. Fatigue crack growth under mixed mode loading conditions is simulated using S-version FEM (Superposition FEM, S-FEM). By using S-FEM technique, only local mesh should be re-meshed and it becomes easy to simulate crack growth. By combining with re-meshing technique, local mesh is re-meshed automatically, and curved crack path is modeled easily.

Introduction

Fatigue fracture can always be detected in the broken machine. This leads to not only the economic loss but also human hurt. The analysis of fatigue crack can provide necessary information for component design and offer effective ways for machine maintenance. Until now, the study came across two major problems. One is the prediction of fatigue crack growth direction for mixed-mode condition; another is involved to the re-meshing technique in finite element analysis. Although there are many literature presented good simulation results of 2-dimensinal problem. For 3-dimensional problem which is real problem, the DOF increased and regular element type needed at the crack tip for accurate SIF calculation. So the re-meshing becomes difficult. A flexible method of FEM which is S-FEM is introduced to resolve this problem. Using this method two mix-mode condition single crack cases were simulated using an analytical crack growth direction criterion. And then interaction problem of two through cracks was discussed.

Methodology

S-FEM was proposed to resolve the high gradient laminate plate problem at earliest [1]. Its flexibility is embodied that using the computer resource to analysis the key part of complex problem, like the vicinity of hole, inclusion and crack. It extracts the key area from the whole structure and combines them by mathematical relationship.

This method defines the whole problem using two models. Those are global model and local model which are expressed in Ω_G and Ω_L respectively. These two models are continuous at the boundary Γ^{GL} and the displacement in Ω_L, u^L_i, at the boundary is defined to be zero. Displacements are written to be

$$u_i = \begin{cases} u_i^G & i \in \Omega_G - \Omega_L \\ u_i^G + u_i^L & i \in \Omega_L \end{cases} \qquad (1)$$

The variation of displacements can be written in the same way. Then insert the displacement and variation of displacement into virtual work principle then the equation of S-FEM are derived as Eq.(2).And the matrix form is illustrated as Eq.(3)

In Eq. (3), the stiffness matrix is symmetric and is

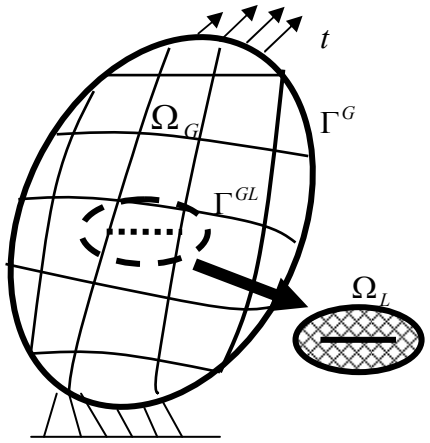

Fig. 1 A schematic illustration of S-FEM

consisted of four parts in which $[K^{GL}]=[K^{LG}]^T$. These two parts expressed the relationship between two models

$$\int_{\Omega^G}\delta u^G_{i,j}D_{ijkl}u^G_{k,l}d\Omega+\int_{\Omega^L}\delta u^G_{i,j}D_{ijkl}u^L_{k,l}d\Omega+\int_{\Omega^L}\delta u^L_{i,j}D_{ijkl}u^G_{k,l}d\Omega+\int_{\Omega^L}\delta u^L_{i,j}D_{ijkl}u^L_{k,l}d\Omega=\int_{\Gamma^{tG}}\delta u^G_i t_i d\Gamma \tag{3}$$

$$\begin{bmatrix}[K^{GG}] & [K^{GL}]\\ [K^{LG}] & [K^{LL}]\end{bmatrix}\begin{Bmatrix}\{u^G\}\\ \{u^L\}\end{Bmatrix}=\begin{Bmatrix}\{t^G\}\\ 0\end{Bmatrix} \tag{4}$$

The detail of the theory was presented in the literature of one of the author [2].

Criteria of crack growth simulation

Under mixed-mode condition, a kinking angle φ_0 caused by K_{II} and a twisting angle ψ_0 by K_{III} appear. There are many criteria related to crack growth simulation for both 2-dimensional and 3-dimensional problems. Some of these equations are not explicit. In literature an analytical criterion named Criterion of Richard[3], was introduced. It is an approximation function to simply predict the crack growth direction under mix-mode condition.

$$\varphi_0=\mp\left[140^\circ\frac{|K_{\text{II}}|}{K_{\text{I}}+|K_{\text{II}}|+|K_{\text{III}}|}-70^\circ\left(\frac{|K_{\text{II}}|}{K_{\text{I}}+|K_{\text{II}}|+|K_{\text{III}}|}\right)^2\right] \tag{5}$$

where $\varphi_0<0^\circ$ *for* $K_{\text{II}}>0$ and $\varphi_0>0^\circ$ *for* $K_{\text{II}}<0$.

$$\psi_0=\mp\left[78^\circ\frac{|K_{\text{III}}|}{K_{\text{I}}+|K_{\text{II}}|+|K_{\text{III}}|}-33^\circ\left(\frac{|K_{\text{III}}|}{K_{\text{I}}+|K_{\text{II}}|+|K_{\text{III}}|}\right)^2\right] \tag{6}$$

where $\psi_0<0^\circ$ *for* $K_{\text{III}}>0$ and $\psi_0>0^\circ$ *for* $K_{\text{III}}<0$

Also there are many formulas for the equivalent stress intensity factor. Richard also gives out a equation

$$\Delta K_{eq}=\frac{\Delta K_{\text{I}}}{2}+\frac{1}{2}\sqrt{\Delta K_{\text{I}}{}^2+4(\alpha_1\Delta K_{\text{II}})^2+4(\alpha_2\Delta K_{\text{III}})^2} \tag{7}$$

when $\alpha_1=1.155$ and $\alpha_2=1$, the result had good agreement with theoretical value。The simulation of fatigue crack growth is conducted by using these criteria.[3]

3-dimensional fatigue crack growth simulation.

Single Crack. **(a)** Single edge crack

Three-point bending loading was given to an edge cracked specimen. The edge crack was positioned a distance offset from the center of model and the load was also bias. At the initial crack condition the crack tip loading is mixed-mode. The stress intensity factor was calculated by VCCM for each element at the crack tip. Fig.1 shows the stress intensity factor distributions along crack tip. It indicates that the crack tip loading condition is

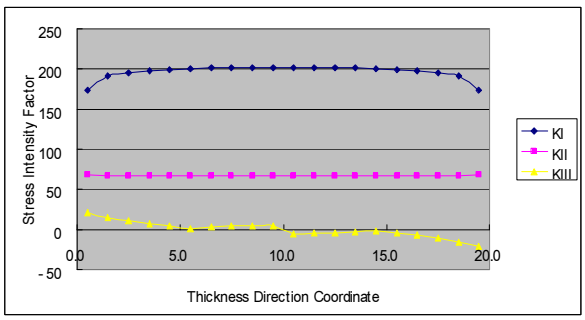

Fig.1 Stress Intensity Factor for initial crack

combined by mode I and II while mode III has little influence. Using above mentioned crack growth criteria, the crack growth direction was predicted. And the model was re-meshed, S-FEM calculation was conducted and crack growth parameters were predicted again and these procedures repeated. Finally the crack growth path was simulated as shown in Fig.2. Initially crack under mixed-mode grew in a direction with itself and then grew along this direction because the crack tip condition changed to pure mode I as shown in Fig.3.

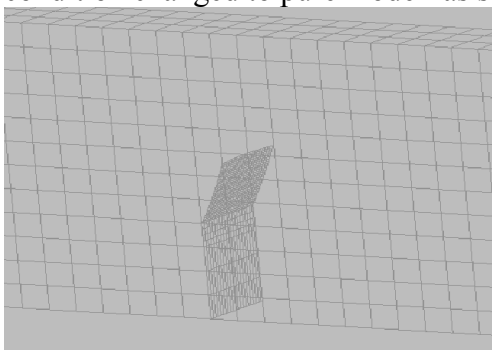

Fig.2 Final crack configuration of edge crack

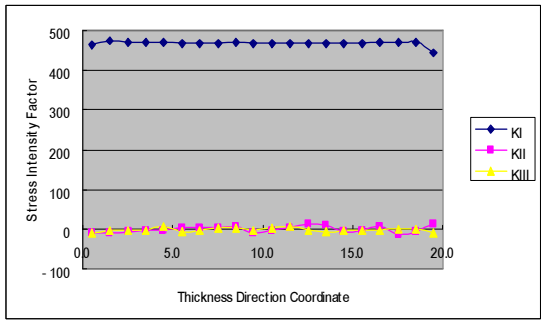

Fig.3 Stress Intensity Factor for final crack

(b) Twist Edge crack

A model containing an inclined edge crack with a twisted angle with the side surface of model was subject to three-point bending. The initial crack was in the mixed-mode which is a combination of mode I, II and III, as shown in Fig.4. Owing to the anti-symmetric distribution of K_{Π}, the crack grew with a variable kinking angle along crack tip. After several steps of growth simulation procedure, the crack grew from initial inclined angle to a nearly 90º angle with the side surface of model as shown in Fig.5. Finally the mode condition became pure mode las shown in Fig.6. This simulation result agreed with the reference [4].

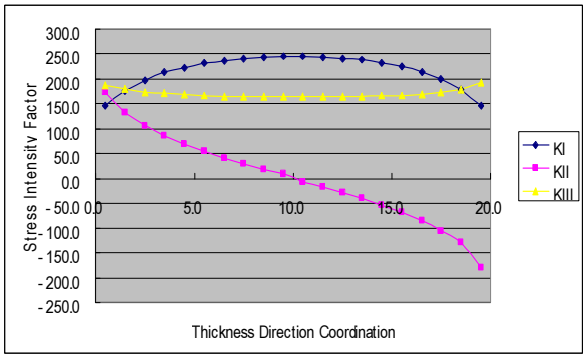

Fig.4 Stress Intensity Factor of twist edge crack

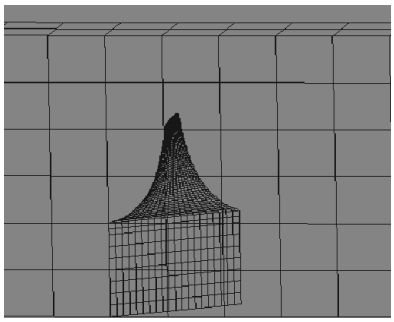

Fig.5 Final crack configuration of twist crack

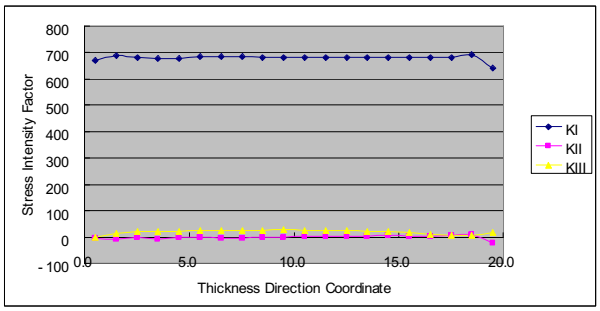

Fig.6 Stress Intensity Factor for final crack

Plural Cracks. In real situation, structure always contains not only one but also plural cracks. The interaction will appear between cracks. The S- FEM formula will have a little change because two local models are involved. The sub-matrix of coefficient matrix on the diagonal line indicated the relationships between global model, local-1 model and local-2 model.

Eq.7 is re-written as,

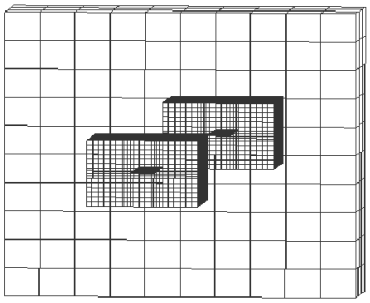

Fig.7 Two cracks S- FEM model

$$\begin{bmatrix} [K^{GG}] & [K^{GL_1}] & [K^{GL_2}] \\ [K^{L_1G}] & [K^{L_1L_1}] & [K^{L_1L_2}] \\ [K^{L_2G}] & [K^{L_2L_1}] & [K^{L_2L_2}] \end{bmatrix} \begin{Bmatrix} \{u^G\} \\ \{u^{L_1}\} \\ \{u^{L_2}\} \end{Bmatrix} = \begin{Bmatrix} \{t^G\} \\ 0 \\ 0 \end{Bmatrix} \tag{8}$$

Fig.7 shows two through cracks located in the structure with vertical distance 8mm and horizontal distance 3mm between two cracks. At the beginning, two cracks grow under mode Ⅰas shown in Fig.8. With distances decrease, the interaction became noticeable. The crack tip loading condition was affected by mode Ⅱ and kinking angle appeared, shown as Fig.9. Until now only the reference [5] is recorded the plural cracks problem but it is refined in two-dimensional problem. The result in this paper showed the spatial crack growth of plural cracks. The growth trend was almost same with two-dimensional result.

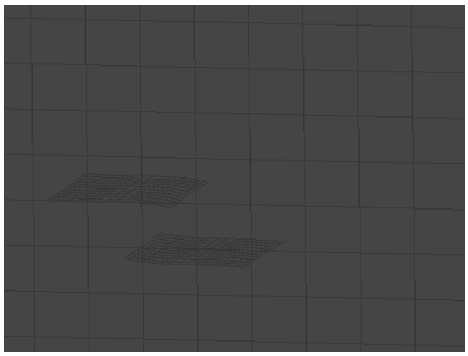

Fig. 8 two cracks configuration at step 10

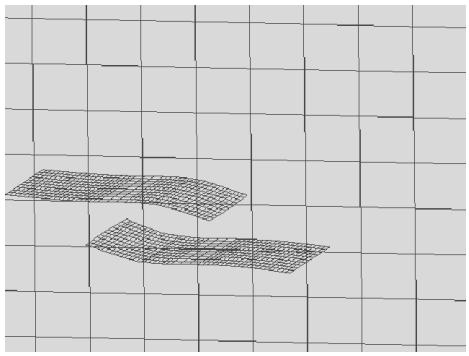

Fig. 9 two cracks configuration at step 15

Using S-FEM to conduct plural cracks is more flexible because the local models containing crack were re-meshed seperately. Using the general FEM, re-meshing will become complex and difficult when two crack tips get closer. S-FEM avoid this difficulty and can also get good simulation result.

Summary

S-FEM was adopted to calculate several fatigue crack problems. From the result, we can find that S-FEM is a feasible. And combined with Richard's criteria it is easy to applied to fatigue fracture. Especially, it is very useful in three-dimensional problem. It can avoid some difficulties occurred in general FEM.

References

[1] J. Fish AND S. Markolefas, in: The S-version of the Finite Element Method for Multilayer Laminates International Journal for Numerical Methods in Engineering, vol. 33, 1081-1 105 (1992)

[2]H. Okada, S. Endoh and M. Kikuchi, in: On Fracture Analysis using an Element Overlay Technique Engineering Fracture Mechanics 72(2005) 773-789

[3]H.A. Richard, M. Sander, M. Fulland, and G. Kullmer, in: *Development of Fatigue crack Growth in Real Structures* Engineering Fracture Mechanics 75(2008) 331-340

[4] R. Citarella and F.-G. Buchholz, in: *Comparison of crack growth simulation by DBEM and FEM for SEN-specimens undergoing torsion or bending loading* Engineering Fracture Mechanics, Volume 75, Issues 3-4, 2008, Pages 489-509

[5]J.R. Yates, M. Zanganeh, R.A. Tomlinson and M.W. Brown, in: *Crack paths under mixed mode loading* Engineering Fracture Mechanics 75(2008) 319-330

Key Engineering Materials Vols. 385-387 (2008) pp 765-768
© (2008) Trans Tech Publications, Switzerland
doi:10.4028/www.scientific.net/KEM.385-387.765

Modeling of Chloride Penetration in Surface Treated Concrete

In-Seok Yoon[1,a]

[1] Dept. of Civil Engineering, Induk Institute of Technology, Seoul, Korea

[a] isyoon@induk.ac.kr

Keywords: Surface treatment system, Surface chloride content, Chloride Penetration

Abstract. The surface treatment system is one of the best options to extend the service life of marine concrete in terms of cost effectiveness versus durability performance. In order to establish rational maintenance strategies for surface treated concrete structures, however, it is necessary to define how to quantify and how to optimize the performance of the surface treatment system. The solution could be obtained from the prediction of chloride in surface treated concrete. In this study, theoretical solution to predict the behavior of chloride diffusion in surface treated concrete is constructed.

Introduction

Surface treatment system is one of the best solutions to extend service life of concrete structures under marine environment in terms of cost effective versus performance [1-2]. In particular, its effectiveness can be optimized if surface treatment system is applied to prevent chloride ingression from the initial stage of construction. The purpose of this paper is to assess the performance of surface treatment systems to reduce the rate of chloride penetration and to predict the chloride penetration of surface treated concrete. So far, the only known solution deals with a semi-infinite medium with a surface layer, which has a different (constant) diffusivity from the diffusivity of the concrete itself. In this study, how to define surface chloride content of surface treated concrete is developed and this is useful for predicting its chloride profiles. This can make a realization about diffusion analysis for surface treated concrete without specific mathematical expressions or assumptions for a surface layer.

Chloride Diffusion in Surface Treatment Systems and Experiment

For surface treatment system, performance to resist chloride penetration depends on its densification, thickness and number of layer, as shown in Fig. 1. The materials properties of used surface treatment material are presented in Table 1. Surface treated concrete specimens are cured for 28 days. The diffusion cell is shown in Fig. 1. The specimens separate half cells containing 0.47 M NaCl and 0.054 $MgCl_2$ solution at cell I and saturated $Ca(OH)_2$ at cell II. Chloride concentration is measured using the method of ion chromatography.

Meanwhile, the diffusion resistance R of specimen can be defined as T/D. Since surface treated concrete is a composite material (com) which consists of surface treatment material (st) and substrate (su), its diffusion resistance R can be described as $R_{com} = R_{st} + R_{su}$ [3]. Thus, chloride diffusivity of only surface treatment systems can be derived as;

$$D_{st} = \frac{T_{st}}{\frac{T_{com}}{D_{com}} - \frac{T_{su}}{D_{su}}} \tag{1}$$

Table 1 Material properties of surface treatment systems

	Main materials	Color	pH	Specific gravity
CT	Redispersible polymer modified cementious materials	Light grey powder	-	2.30

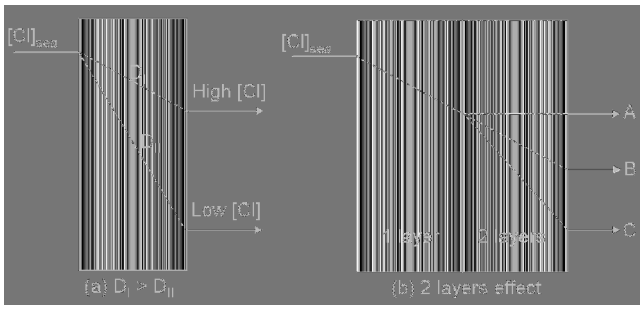

Fig. 1 The effect of diffusivity of working condition on penetrated chloride concentration

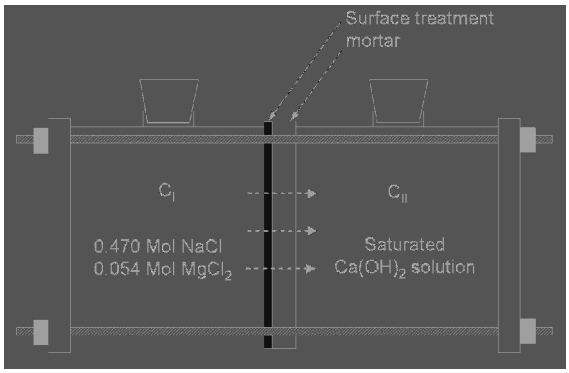

Fig. 2 Chloride diffusion cell stet-up

in which, D_{com}: diffusivity of composite materials, D_{st}: diffusivity of surface treatment system, D_{su}: diffusivity of substrate, T_{com}: thickness of composite material, T_{st}: thickness of surface treatment, T_{su}: thickness of substrate. It is avaiable to calculate passed chloride content with D_{st}, as shown in Fig. 1.

Material Parameters Modeling [4]

Surface Chloride Content, $[Cl]_s$. If it is assumed that the pores of concrete are saturated with sea water and total content of salt ingredients is 35.0 ‰, $[Cl]_s$ is calculated by the procedure of presented Fig. 3. For surface treated concrete, it is possible to formulate surface chloride content in non-treated concrete if concrete is saturated with passed chloride content through surface treatment system

Quantity (Q_C) of chemical composite salt (c)	→	Cl quantity (Q_C^{Cl}) of chemical compositions of salt	→	Maximum surface chloride content ($[Cl]_s$)
$Q_C = (Q_e \cdot AW_e / 35) \cdot \rho_c$ (2)		$Q_C^{Cl} = Q_C \dfrac{W_{Cl}}{(W_C + W_{Cl})}$ (3)		$[Cl]_S = \dfrac{(Q_{NaCl}^{Cl} + Q_{MgCl_2}^{Cl}) \cdot \phi}{W_{con'c}}$ (4)

Fig. 3 Calculation of surface chloride content (Q_e: Quantity of chemical element e, AW_e: atomic weight of chemical element e, W_c: weight of composite salt c (c : NaCl or $MgCl_2$), Q_{NaCl}^{Cl} : quantity of chloride in NaCl, ρ_c : density of composite salt c, ϕ : porosity of concrete)

Chloride Diffusivity. Analytical solution for chloride diffusivity of cement paste is designed as multi factors function including (a) water diffusivity, (b) pore structures, (c) tortuosity, (d) hindrance effect.

Chloride Binding. Based on the Freundlich isotherm, chloride binding model is modified as;

$$\frac{d[Cl(aq)]_f}{d[Cl]_t} = \frac{1}{1+\dfrac{d[Cl]_b}{d[Cl(aq)]_f}} = \frac{1}{1+\left(\dfrac{0.379\cdot 10^{1.14}}{\rho_W \cdot \mathrm{MW}_{Cl}}\right)\left(\dfrac{[\text{C-S-H}]\cdot \mathrm{MW}_{CSH}}{V_W \cdot V_{cp}}\right)\left(\dfrac{[\mathrm{Cl(aq)}]_f}{\mathrm{MW}_{Cl}\cdot \phi_W \cdot V_{cp}/W_{conc}}\right)^{-0.623}} \quad (5)$$

in which, MW_i: molar weight of i, ρ_W : density of water, ϕ_W : water content in the unit volume of cement paste(= porosity for full saturation), V_{cp}: volumetric fraction of cement paste in the unit volume of concrete, W_{conc} : unit weight of concrete, [C-S-H] : C-S-H content in concrete[13].

Critical Chloride Content, $[Cl(aq)]_{cr}$. Critical chloride content $[Cl(aq)]_{cr}$ is formulated, as shown in Eq.(13). $[OH^-]$ concentration is calculated by the HYMOSTRUC. In this equation, 0.287 is induced from the ratio of $[Cl^-]$ to $[OH^-]$ of Gouda experiment.

Modeling of Surface Treated Concrete and Results

Modeling of Surface Treated Concrete. Basic strategy to predict chloride profile in surface treated concrete is explained in Fig. 4. The passed chloride content, $[Cl]_{out}$, can be useful to calculate surface chloride content for non-surfaced treated concrete.

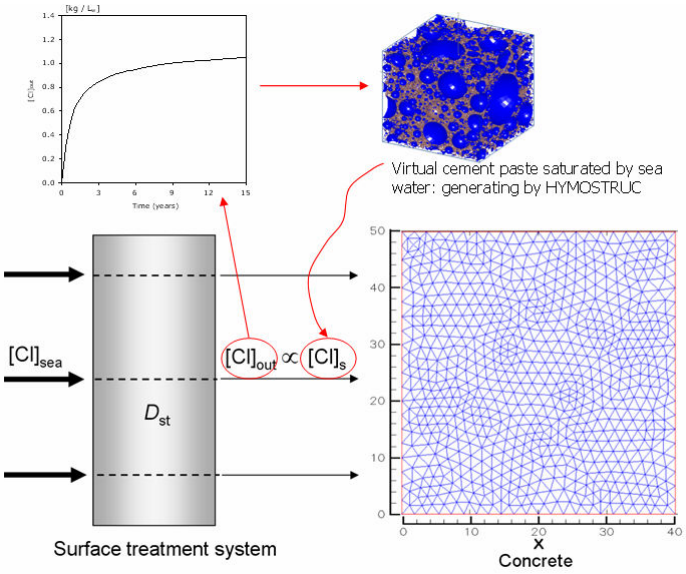

Fig. 4 Basic concept for chloride diffusion in surfaced treated concrete

Eq. (6) is a governing equation for analysis of chloride diffusion in the non-surface treated concrete. Here, [Cl(aq)]w and [Cl(s)] mean water soluble Cl^- content and bound Cl^- content, respectively. Table 2 is an example of mixing proportion of concrete for a calculation.

$$\frac{d[Cl(aq)]_W}{dt} = \frac{d[Cl(aq)]_W}{d[Cl(s)]_T} div\{D_{Cl}\ grad[Cl(aq)]_W\} \quad (6)$$

Table 2 Mix proportion of concrete

Unit weight (kg/m^3)			
Water	Cement	Sand	Gravel
185	370	720	1021

Calculation of Chloride Profile & Service Life. Experimental result of chloride diffusivity for only surface treatment system is represented in Fig. 5. Surface chloride content of surface treated concrete is computed on the basis of assumption that surface concrete is saturated with passed chloride content, as shown in Fig. 6.

It has been generally recognized that surface treatment materials have finite lives and therefore need to be renewed due mostly to degradation caused by the effect of ultra-violate radiation, temperature & water distribution, and so on [5]. Life of surface treatment material is assumed to be 5 years in this study.

Fig. 7 shows the prediction on the chloride profile in aqueous phase of pores of concrete with various condition of surface concrete. The value of surface chloride content of concrete, whose surface treatment is degraded after 5 years, is equivalent to that of plain concrete because its surface condition can not be prevented by surface treatment system any more. Fig. 8 represents computational results of required cover depth. It can be concluded from this figure that surface treatment system should be effective to prevent reinforcement from corroding even though it would be difficult to expect its effectiveness after 5 years. It is necessary to take into account active strategies to reduce chloride ingress into concrete from the initial stage.

Summary

The purpose of this study is to set up a framework for optimizing durability design using surface treatment system to extend service life of marine concrete. It is believed that this work will lead to more reasonable methodologies for the prediction of chloride diffusion in surface treated concrete.

References

[1] E. Nolan, P. A. M. Basheer, and A. E. Long: Effects of Three Durability Enhancing Products on Some Physical Properties of Near Surface Concrete, *Construction and Building Materials*, Vol.9, No.5 (1995) p.267-272.

[2] D. W. Pfeifer, M. J. Scali: Concrete Sealers for Protection of Bridge Structures, NCHRP Report 224 (1981) TRB Washington.

[3] N. R. Buenfeld, and J. -Z. Zhang: Chloride Diffusion Through Surface-Treated Mortar Specimens, *Cement and Concrete Research*, Vol.28, No.5 (1998) p.665-674.

[4] I. S. Yoon: Modeling of Material Parameters of Marin Concrete for Service Life Prediction, Vol.348-349 (2007) p.753-756.

[5] O. N. Sunny, and D. James: A Practical Approach to In-situ Evaluation of Surface-treated Structures, *Construction and Building Materials*, Vol.15 (2000) p.199-212.

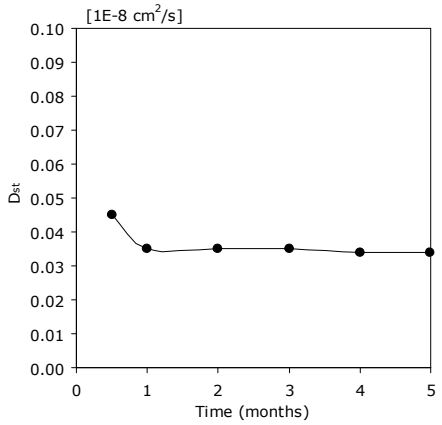

Fig. 5 Chloride diffusivity of surface treatment materials

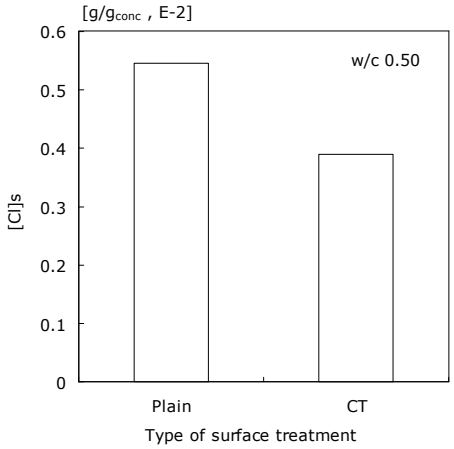

Fig. 6 Surface chloride content

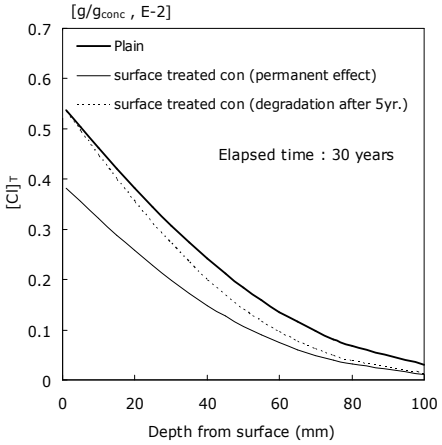

Fig. 7 Chloride profile with various condition of surface concrete

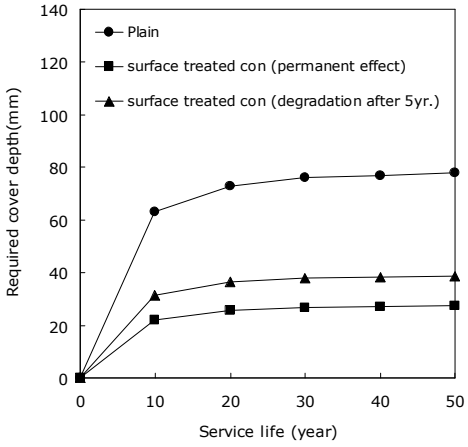

Fig. 8 Required cover depth

Key Engineering Materials Vols. 385-387 (2008) pp 769-772
© (2008) Trans Tech Publications, Switzerland
doi:10.4028/www.scientific.net/KEM.385-387.769

Influence of Cracks on the Durability of RC Structures

Lucio Nobile

Department Distart, University of Bologna, Viale Risorgimento 2, 40136 Bologna, Italy

email: lucio.nobile@unibo .it

Keywords: RC structures, Cracks, Corrosion, Durability, Fracture Mechanics, Failure.

Abstract. To carry out maintenance and assessment of reinforced concrete (RC) structures, a good understanding of the effect of the change in bond behaviour of reinforcement during service life is essential. Steel reinforcement is subjected to corrosion due to carbonation and chloride attack. The former ordinarily induces uniform corrosion, the latter induces generally localised corrosion at cracks level. The existence of cracks and the crack width affect the starting points of corrosion, as indicated by the results of the exposure test carried out by Shiessl et al.[1].

Corresponding techniques, such as non-destructive in-situ testing for concrete cover thickness, permeability and the positions of the reinforcing bars, are helpful to model the real behaviour.

Cracked portion around the tensile reinforcement in a flexural member can be considered to be equivalent to a concrete member having a single reinforcement subjected to pull-out force at both ends. In this paper a damage process model is proposed based on slip crack propagation in order to evaluate the effective load capacity.

Introduction

In a general design of RC structures, the tensile stress of concrete is neglected and the reinforcement is provided to resist all tensile stresses induced in a section. Normally cracking of concrete due to tensile stresses does not directly lead to the failure of RC structures. However, in the case of design which has to consider the tensile resistance of concrete such as plain concrete structures, the failure of such structures is highly related to the cracking of concrete. Even in the case of RC structures subjected to relatively low shear stresses, the tensile resistance of concrete is considered implicitly and hence diagonal cracking is expected. Besides, in the anchorage zone of a deformed bar, since the tensile resistance of concrete is taken into account, it is necessary to pay attention on cracking along the bar.

In the case of RC structures subjected to flexure under the service loads, cracks occur in the flexural tension zone of the section. The excessive crack width leads to unfavorable consequences as follows [1,2].

Due to the penetration of water and air through the crack, the corrosion of reinforcement inside the concrete occurs. This will increase the volume of reinforcing steel and spall the concrete cover out. The rate of corrosion of uncovered reinforcement increases very rapidly. The corrosion of concrete deteriorates not only the aesthetic view but also the durability of concrete structures.

In the design of structures with special attention on air as well as water tightness, the function of the structure will be lost if a crack having excessive width occurs.

In the aesthetic view point, excessive crack is undesirable.

The reinforcement inside the concrete with relatively good quality will not be corroded. In general, RC structures are considered to be very durable compared with other types of structures. In spite of cracking of concrete, the corrosion of reinforcement will not occur if the concrete cover is sufficiently thick, and the surface crack width is less than a limit value. One of the serviceability limit states is the limit state on crack width , since it is related to the durability of concrete structures and not to the failure.

A simple model to describe the behaviour until failure of reinforced concrete in tension is proposed. The theoretical analysis is based on the concept by Fracture Mechanics where the debonded zone closed to a transversal crack can be considered as an interfacial crack.

Cracked portion around the tensile reinforcement in a flexural member can be considered to be equivalent to a concrete member having a single reinforcement subjected to pull-out force at both ends. In this paper a damage process model is proposed based on slip crack propagation in order to evaluate the effective load capacity.

Damage model

Consider a concrete member having a single reinforcement subjected to pull-out force at both ends (Fig.1).

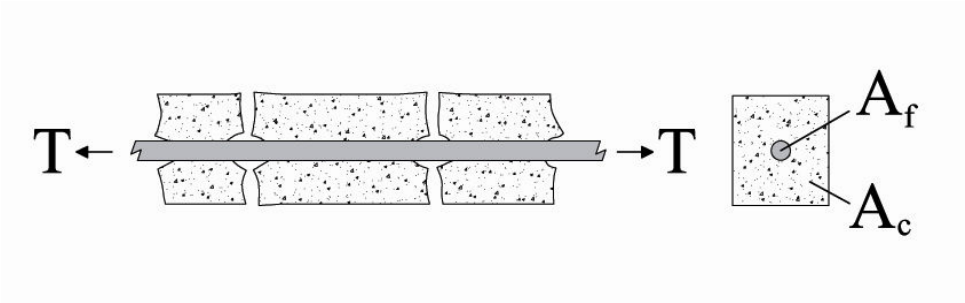

Fig.1. Schematic of cracked RC bar

Concrete fails to resist tensile stresses only where the actual crack is located, when:

$$T = A_s f_t \,, \tag{1}$$

where f_t *is* the tensile strength of concrete and A_s is the area of reinforcement bar. Steel tensile stress is maximum and local bond stress adjacent to the crack are very high.

Gradually moving away from the first crack, steel tensile stress reduces of moderate amount of tension introduced by bond:

$$t = \tau_d(z) p dz \,, \tag{2}$$

in which $\tau_d(z)$ is the shear stress acting on the contact surface between bars and concrete and p is the rebar perimeter.

The length necessary to reach the full tensile strength of concrete, where a new crack develops, can be calculated from:

$$\pi\phi \int_0^{\Delta l} \tau_d(z) dz = A_s f_t \,, \tag{3}$$

where ϕ is the rebar diameter.

By neglecting concrete deformation and assuming $\tau_d(z)$ constant, it can be found:

$$\Delta l = \frac{A_s f_t}{\pi \phi \tau_d} \,. \tag{4}$$

Note that the debonded zone between concrete and rebar close to the transverse crack can be considered as an interfacial slip crack, as shown in Fig.2.

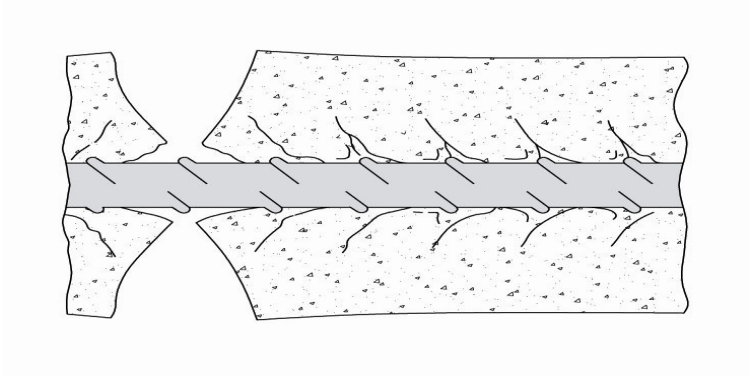

Fig.2. Debonded zone

By solving the modified problem of Kelly [3], the critical force T at which the crack begins to move is:

$$T_{cr} = \frac{\pi}{\sqrt{2}} \phi^{3/2} \sqrt{\gamma_i E_s} \,, \tag{5}$$

where γ_i is the irreversible work spent to increase a unit area of the surface of the slip crack, a physical constant, and E_s is the Young modulus for steel. This force is independent of crack length, i.e. its propagation, once it begins, will continue. Some increase in force is required only to overcome lateral friction. This force can be easily estimated by measuring "force-movement" diagram in the same experiment, as shown in Fig.3.

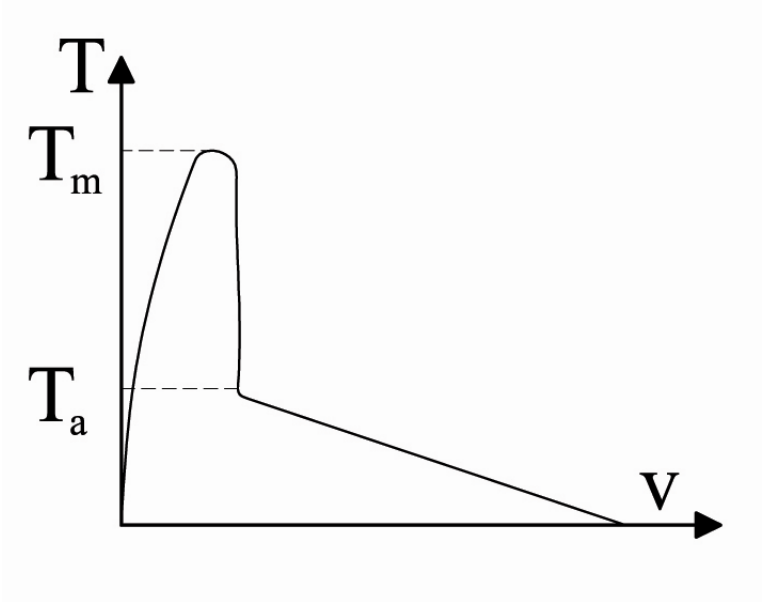

Fig.3. Typical force-movement experimental diagram

The plateau section corresponds to the stage of the process in which the crack has encompassed the entire lateral surface of the rebar and resistance results only from lateral friction. Therefore the maximum value of force required to extract the rebar is:

$$T_m = T_{cr} + T_a \,, \tag{6}$$

where $T_a = \pi\phi \Delta l / 2 \tau_f$, being τ_f the tangential stress due to friction between concrete and steel, i.e. a physical parameter.

Extraction of steel rebar without yielding will take place if:

$$T_m \le A_s f_{yk} \tag{7}$$

or if:

$$2\sqrt{\frac{2\gamma_i E_s}{\phi} + \frac{2}{\phi}\Delta l \tau_f} \le f_{yk} \,, \tag{8}$$

with f_{yk} the yield strength of steel.

If the tensile rebar force is lesser than T_m, the corrosion process in cracked beam starts with increase of the volume of reinforcing steel and spall of the concrete cover out.

Recently, a Finite Element model has been developed to simulate the flexural behaviour of corroded RC elements with a set of limitations[4].

Summary

Cracks are unavoidable in RC structures. A simple model to describe the behaviour until failure of reinforced concrete in tension has been proposed. The theoretical analysis is based on the concept by Fracture Mechanics where the debonded zone closed to a transversal crack can be considered as an interfacial crack.

Cracked portion around the tensile reinforcement in a flexural member can be considered to be equivalent to a concrete member having a single reinforcement subjected to pull-out force at both ends. In this paper a damage process model has been proposed based on slip crack propagation in order to evaluate the effective load capacity.

Acknowledgments

This research has been supported by Italian Ministry for University and Scientific and Technological Research (MIUR).

References

[1] P. Schiessl, in: Colloque Inter-Association de Liege: Comportment en service des ouvrages en bèton. Contribution II.3 (1975).

[2] M. Kavyrchine: Annales de l'Institu Technique du Batiment et des Travaux Publics, 38(1981).

[3] A. Kelly: Proc.Roy.Soc.,vol.A282 (1970), p.95.

[4] F. Buyle-Bodin, A.L. Thang, M. Dekoster, O. Blanpain,O. Maurel,in: 10DBMC International Conférence on Durability of Building Materials and Components, LYON [France] 17-20 April 2005.

Key Engineering Materials Vols. 385-387 (2008) pp 773-776
© (2008) Trans Tech Publications, Switzerland
doi:10.4028/www.scientific.net/KEM.385-387.773

Weibull Stress Analysis for An Embedded Crack in Reactor Pressure Vessels Under Pressurized Thermal Shock

Xudong Qian[1, a] and Robert H. Dodds Jr.[2,b]

[1]Department of Civil Engineering, National University of Singapore, Singapore 117576

[2]Department of Civil and Environmental Engineering, University of Illinois at Urbana Champaign, IL 61801, USA

[a]cveqx@nus.edu.sg, [b]rdodds@uiuc.edu

Keywords: Cleavage fracture, Weibull stress, embedded crack, pressurized thermal shock (PTS), reactor pressure vessel (RPV), ductile-to-brittle transition.

Abstract. This paper describes the Weibull stress approach in predicting the cumulative probability of cleavage fracture for an axially embedded crack in the wall of a reactor pressure vessel (RPV) subjected to a thermal-mechanical transient typical for an accidental, pressurized thermal shock (PTS) event. This study demonstrates the need for detailed elastic-plastic analyses in the integrity assessment of RPVs under PTS loadings, and proposes both a simplified approach and a refined approach to assess the probability of fracture for RPVs subjected to such events.

Introduction

Nuclear reactor pressure vessels (RPV) often embed crack-like, fabrication defects over the wall thickness, which experiences significant material damage caused by accumulated radiation over years of service life. Pressurized thermal shock (PTS) defines an accidental event characterized by sudden overcooling concurrent with or followed by significant changes in the internal pressure, causing potentially brittle, catastrophic failure of the vessel. The integrity assessment for RPVs under a PTS event becomes extraordinary complex due to: 1) a large combination of crack locations, sizes and orientations together with a wide spectrum of thermal-mechanical transients; and 2) the variation of material properties and hence the fracture toughness along the curved crack front caused by the temperature gradient over the wall thickness generated by the thermal transient.

The very large scatter in the experimentally measured fracture toughness K_{Jc}-values for ferritic steels in the ductile-to-brittle transition (DBT) region drives the development of probabilistic approaches in describing the cleavage fracture failure. Previous research efforts utilize extensively the weakest-link based, Weibull stress framework to characterize the cumulative probability of fracture. The Weibull stress approach, originally proposed by the Beremin Group [1], couples the Griffith fracture criterion with an assumed power-law distribution of micro-cracks in small but finite volumes of materials ahead of the crack tip. The probability of fracture thus depends on a local driving force, measured by the scalar Weibull stress. This study extends the application of the Weibull stress framework to an RPV with an axially embedded flaw under a PTS transient.

Finite Element Details

Fig. 1 shows the geometric configuration of an RPV with an axially embedded flaw, together with the finite element (FE) mesh. The RPV consists of a cylinder made of ferritic steels and an internal cladding layer fabricated from stainless steels. The FE model employs 20-node brick elements. The semi-elliptical crack front consists of 30 crack-front elements with 31 and 10 rings of elements around each crack-front node for the elastic-plastic analyses and for linear-elastic analyses, respectively. Fig. 2 illustrates the mechanical and thermal properties of the ferritic and stainless steels. Fig. 3 describes the PTS transient corresponding to a critical probability of crack initiation

based on a previous investigation. The computational procedure utilizes the finite-element research code, WARP3D, which includes the finite strain formulation and the nonlinear material responses.

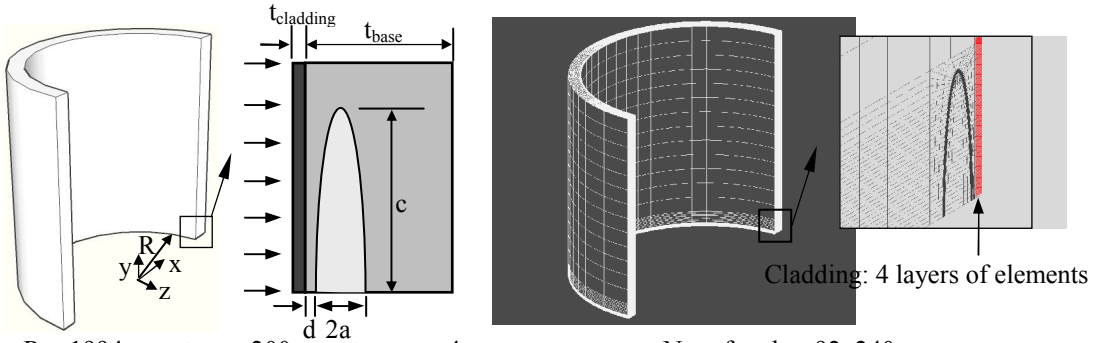

R = 1994 mm; t_{base} = 200 mm; $t_{cladding}$ = 4 mm;
2a = 17 mm; c = 51 mm; d = 1.9 mm

No. of nodes: 92, 240
No. of elements: 20, 800

Fig. 1: Geometric configuration and a sample FE mesh for an RPV with an axially embedded crack.

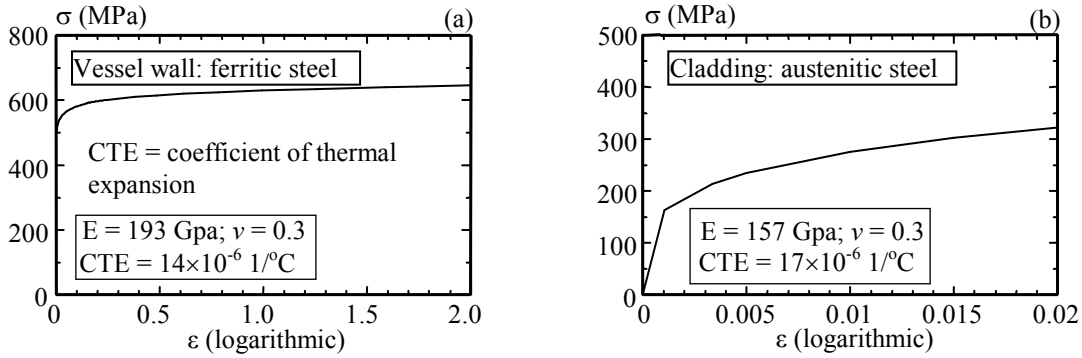

Fig. 2: Mechanical and thermal properties for: (a) ferritic; and (b) cladding; steels.

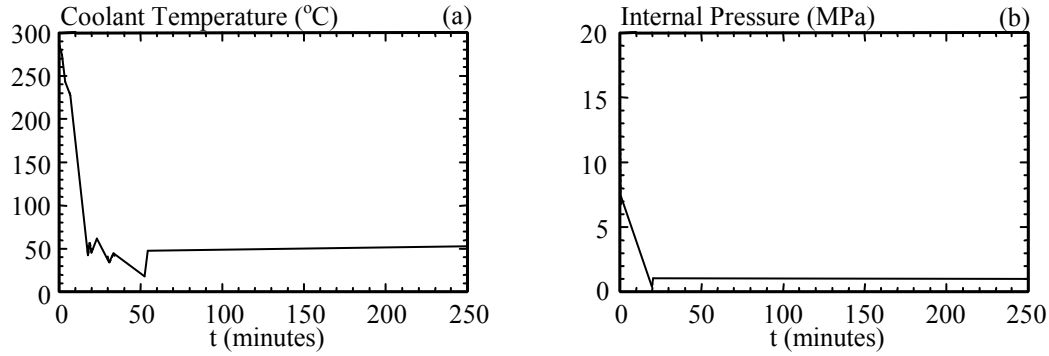

Fig. 3: (a) Thermal; and (b) mechanical; transients for a pressurized thermal shock event.

Results and Discussions

Weibull Stress Framework. The current study adopts the 3-parameter Weibull stress model proposed by Petti and Dodds [2] to predict the cumulative probability of cleavage fracture, P_f,

$$P_f\left(\sigma_w\right) = 1 - \exp\left[-\left(\frac{\sigma_w^{m/4} - \sigma_{w-min}^{m/4}}{\sigma_u^{m/4} - \sigma_{w-min}^{m/4}}\right)^4\right]. \quad (1)$$

On a macroscopic level, Eq. 1 should reflect the cumulative probability function, Eq. 2, in ASTM E-1921 [3] obtained by curve-fitting the experimental fracture toughness data for high-constraint, small-scale yielding specimens,

$$P_f\left(K_J\right)=1-\exp\left[-\left(\frac{K_J-K_{min}}{K_0-K_{min}}\right)^4\right]. \quad (2)$$

where K_0 follows the temperature dependent master curve [3]. The comparison of Eqs. 1-2 yields,

$$\sigma_w^m = CBK_J^4 g\left(M,m\right), \quad (3)$$

where B denotes the thickness of the fracture specimen, C is a constant determined from the high-constraint, small-scale yielding model, and g(M, m) (≤ 1.0) defines the constraint loss in the fracture specimen (M is a non-dimensional loading parameter and g(M, m) = 1.0 for high constraint, small-scale yielding conditions). The Weibull stress integrates an effective stress (the maximum principal stress, σ_1, in this study) over the fracture process zone, V_f, defined by $\sigma_1 > 2\sigma_{ys}$ in this paper, where σ_{ys} defines the material yield strength,

$$\sigma_w = \left[\frac{1}{V_0}\int_{V_f}\sigma_{eff}^m\, dV_f\right]^{1/m}, \quad (4)$$

where V_0 denotes the normalizing reference volume, and equals to unity in the current study.

The Weibull scale parameter, σ_u in Eq. 1, characterizes the temperature dependent microcrack toughness. The temperature insensitive Weibull modulus, m, equals to 18-20, for ASTM A533B ferritic steels typically used in RPVs, as calibrated by Wasiluk et al. [4]. The threshold Weibull stress, σ_{w-min}, computes from Eq. 3 with $K_J = K_{min} = 20\ MPa\sqrt{m}$ [4].

Macroscopic Crack Driving Force. Fig. 4(a) compares the macroscopic crack driving force, K_J, at location P (the point with the lowest temperature along the crack front as shown in Fig. 4(b)), computed from the linear-elastic and elastic-plastic analyses. The crack driving force reaches the maximum value at t = 18 min. The linear-elastic analysis underestimates significantly the macroscopic crack driving force, with K_J-values at t = 18 min 30% lower than the elastic-plastic values. Fig. 4(b) shows the biaxiality ratio, β, along the semi-elliptical crack front. The variable T defines the linear-elastic T-stress computed from an interaction integral scheme. The thermal loads at t = 10 and 18 min increase significantly the constraint condition at point O ($\phi = 0$), but vary only marginally the low-constraint condition at crack-front points P and Q. Fig. 4(b) shows that the majority of the crack-front experiences very low constraints, sufficient to impinge on the high-constraint, small-scale yielding assumption in the ASTM E-1921 approach (Eq. 2).

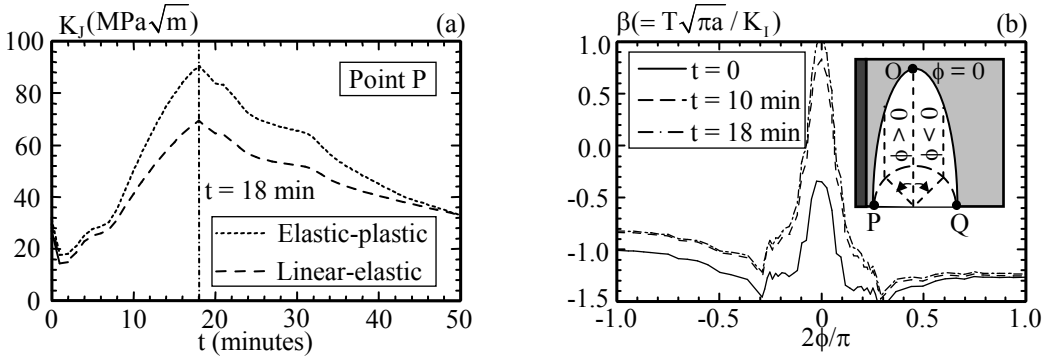

Fig. 4: (a) Macroscopic crack driving force; and (b) crack-front constraints; under the PTS transient.

A Simplified Weibull Stress Approach. The simplified approach utilizes Eq. 1 with the lowest microcrack toughness (σ_u) along the crack front (location P in Fig. 4(b)), and the σ_w values computed for the entire crack front using Eq. 4. Fig. 5 shows the evolution of σ_w for different m values and the corresponding probability of fracture. P_f continues to increase beyond the peak K_J at t = 18 min due to the decrease in temperature and hence σ_u for t > 18 min.

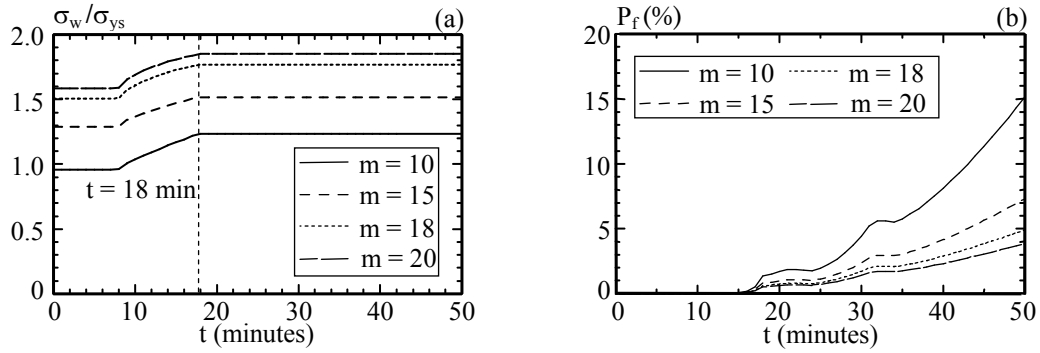

Fig. 5: (a) Weibull stress along the entire crack front; and (b) P_f computed from the simplified method.

A Refined Weibull Stress Approach. The refined approach treats the curved crack front as multiple segments of idealized fracture specimens, each with a spatially constant temperature and therefore spatially constant Weibull material properties (σ_u and $\sigma_{w\text{-}min}$ values). The probability of fracture at time t computes from,

$$P_f^{Total}(t) = 1 - \exp\left[-\sum_{i=1}^{n} \left(\frac{\sigma_{w_{(i)}}^{m/4} - \sigma_{w-min_{(i)}}^{m/4}}{\sigma_{u_{(i)}}^{m/4} - \sigma_{w-min_{(i)}}^{m/4}} \right)^4 \right]. \quad (5)$$

The subscript (i) denotes the ith segment of the total n crack-front segments. Eq. 5 follows the weakest link model, which assumes that failure occurs when fracture initiates in the most critical segment. Fig. 6 shows σ_w along the crack front and P_f for the RPV computed from Eq. 5.

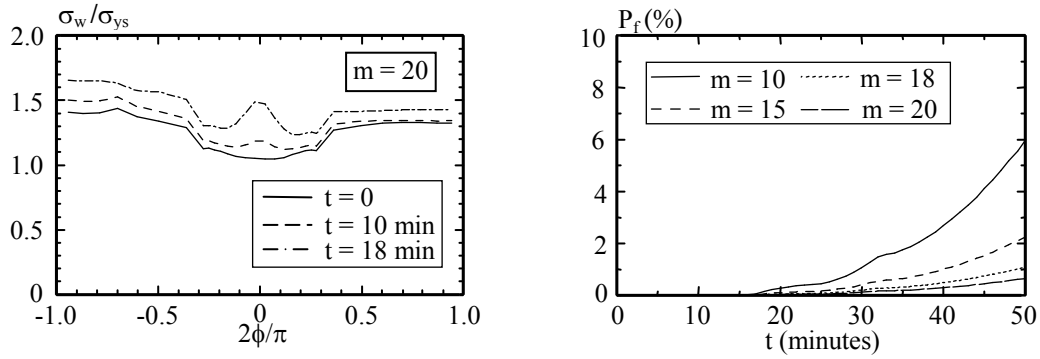

Fig. 6: (a) Weibull stress along the crack front for m = 20; and (b) P_f based on the refined Weibull stress approach.

Summary and Conclusions

This study demonstrates that linear-elastic analysis significantly underestimates the macroscopic crack driving force compared to the elastic-plastic K_J values. The simplified Weibull stress approach provides a conservative estimation of the failure probability by using the weakest material scaling parameter (σ_u) for the entire crack front. The refined approach offers a more detailed assessment of the failure probability.

References

[1] F.M. Beremin: Metallur. Trans. Vol 14(a) (1983), p. 2277

[2] J.P. Petti, R.H.Jr. Dodds: Engng. Fract. Mech., Vol 71 (2004), p. 2079

[3] ASTM E-1921. 2002.

[4] B. Wasiluk, J.P. Petti, and R.H.Jr. Dodds: Engng. Fract. Mech., Vol 71 (2006), p. 1046

Key Engineering Materials Vols. 385-387 (2008) pp 777-780
© (2008) Trans Tech Publications, Switzerland
doi:10.4028/www.scientific.net/KEM.385-387.777

The enhancement of corrosion resistance of titanium in high temperature acidic solutions by microarc oxidation

Jianshu Lu[1, a] Chuang Lu[2, b]

1 College of Chemical Engineering and Materials Sciences, Zhejiang University of Technology, Hangzhou 310014, P R China;
2 The Surface Engineering Center, Ningbo Branch of Ordnance Science Institute of China, Ninbo 315103, P R China
[a] jianshul@zjut.edu.cn, [b] hbluchuang@163.com

Key Words：titanium, microarc oxidation, corrosion, high temperature

Abstract. Microarc oxidation technique (MAO) is an electrochemical process which can be used to make ceramic coatings on the surfaces of titanium and its alloys. In this investigation samples of a commercially pure titanium (TA3) were anodized in 30g/L $NaAlO_2$ solution under 280V voltage for 75 minutes to form a 3-10μm coating. XRD analysis showed that the main phase of the coating is $TiAl_2O_5$. Samples of the titanium and the MAO treated titanium were immersed in HCl and H_2SO_4 acid solutions at 250ºC in an autoclave. Results show that in 0.1 mol/L concentration both the titanium and the MAO treated titanium have good corrosion resistance in the acid solutions. However, in 1 mol/L concentration the titanium samples completely dissolved in 24 hour immersion. The MAO-treated titanium samples did not dissolved away although some degree of weight losses took place. SEM shows that there are corrosion products on the surfaces of MAO treated titanium samples. XRD analysis showed that the corrosion products are titanium oxides (rutile and anatase). A corrosion resistance mechanism, which is based on the synergic protection of aluminum titanium oxides and titanium oxides for the titanium substrate, is proposed for explaining the enhancement of the corrosion resistance.

1 Introduction

Titanium and its alloys are well known for their excellent corrosion resistance in many environments. But in some environments (e.g. supercritical water oxidation) titanium may suffer failure by general corrosion, stress corrosion cracking and creep fracture. In some extremely corrosive media, such as hot strong mineral acids[1] and supercritical water oxidation environments[2-4], titanium is not strong enough in corrosion resistance for long term service. Therefore, it is highly desirable to enhance the corrosion resistance of titanium.

The well known methods to increase the corrosion resistance of titanium are noble metal alloying, anodizing, and coatings. The corrosion resistance of titanium is largely due to the formation of titanium oxides on its surface. The coating thickness can be increased by anodic oxidation or heat treated at high temperature in air or oxygen atmosphere. Conventional anodic oxidation of titanium is normally practiced with direct current under 30 volts in electrolytes such as sulfuric acid or ammonium sulfate. A special anodic oxidation technique is called microarc oxidation (MAO)[5,6] or plasma electrolytic oxidation[7,8] in which metals are anodically oxidized at high voltage (a few hundred volts) in some special electrolytes. MAO is an electrochemical process that can make relatively thick ceramic coatings (tens of micrometer) on the surface of some light

metals such as magnesium, aluminum, and titanium.

In this paper, a study on the corrosion resistances of a commercially pure titanium and the MAO-treated titanium in high temperature acidic solutions was carried out. The results show that enhancement of corrosion resistance of the titanium in high temperature acid solutions can be achieved by MAO treatment.

2 Experiments

2.1 Commercially Pure Titanium

A 1 mm thick commercially pure titanium sheet (TA3) was purchased from Baotai New Metals Ltd. (Baoji, China). The chemical composition of the titanium is (wt%): Ti >99.2, Fe 0.16, O 0.29 and other minor impurities (<0.3). The titanium is similar in composition to the ASTM grade 3 titanium. Plate samples of 20×13×1 mm in size were cut from the sheet.

2.2 Microarc Oxidation of Titanium Samples

The titanium samples were first polished using 1200# grit SiC paper and then ultrasonically cleaned in ethanol for 5 minutes. Microarc oxidations of the titanium samples were carried out in a 30g/L $NaAlO_2$ aqueous solution bath at room temperature for 75 minutes with maximum applied voltage of 280V. After the oxidation, the titanium samples appear grayish white in color.

2.3 High Temperature Corrosion Tests

The titanium samples with and without MAO treatment were immersed respectively in chloride acid and sulfuric acid at 250ºC in an autoclave. The autoclave was lined with PTFE and has 250 mL volumetric capacity. Two concentrations of the acids (0.1 mol/L and 1 mol/L) were used in the tests. The duration of the tests was 24h. Corrosion products were collected from the immersion solutions by centrifugation and dried at 110ºC for 12 hours.

2.4 Characterization

An X-ray diffraction instrument (ThermoARL SCINTAG xtra) with Cu Kα radiation (λ=0.15406nm) was used for phase analysis of the corrosion products. The morphology of corroded sample surfaces and the corrosion products were showed by electron scanning microscopes (Hitachi S-4700 or JEOL6300F).

3 Results and Discussion

3.1 Oxide Coating by the MAO Treatment

Fig.1 shows the micrograph of oxide coating on titanium by the MAO treatment. The coating is rather rough in surface and has many pores. The thickness of the coating is about 6μm which are measured by SEM. Fig.2 shows the XRD diagram of the MAO treated titanium. The reflection came mainly from Al_2TiO_5 (marked by #, PDF number 01-070-1434) and the substrate α-Ti (marked by $, PDF number 44-1294). For the Al_2TiO_5 phase, the diffraction peaks from left to right were reflected by (200), (101), (230), and (002) planes, respectively. For the α-Ti, the diffraction peaks from left to right were reflected by (001), (002), (101), (102), (110), (103), and (201) planes, respectively. There are other four peaks (at 2θ= 45.96º, 48.20º, 66.96º and 72.60º) for which we are not able to identify their corresponding substance. Unexpectedly, no anatase or rutile peaks existed in the XRD diagram. However, the titanium oxides may exist in amorphous form[9]. From this XRD result, it is clear that Al_2TiO_5 is the main product of the MAO process of the titanium. In this respect our work is in agreement with those of Yerokhin[10].

3.2 Corrosion of titanium and MAO titanium in 0.1 mol/L and 1 mol/L acid solutions at 250ºC

In 0.1 mol/L HCl and H_2SO_4 solutions the titanium and MAO treated samples showed only slight color change (darkening) after 24 h immersion test. Table 1 shows the weight changes of the

samples. All the samples gained weight. The weight changes are very small. They are close to the sensitivity of the balance (0.1 mg). The MAO treated titanium samples had a little more weight gain than the untreated titanium samples in the two acid solutions. The results showed that both the titanium and the MAO treated titanium have good corrosion resistance in these conditions.

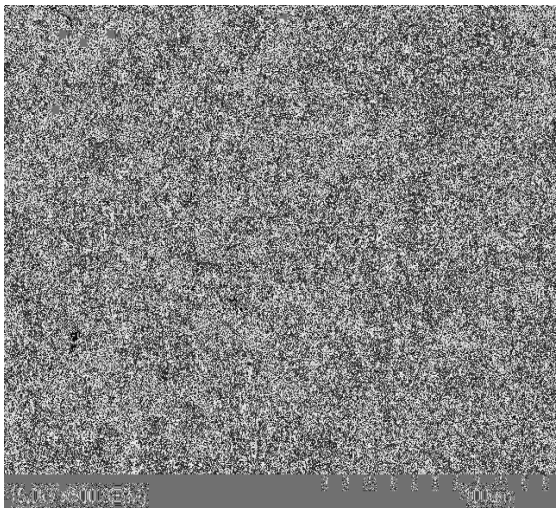

Fig.1 Micrographs of the MAO coating

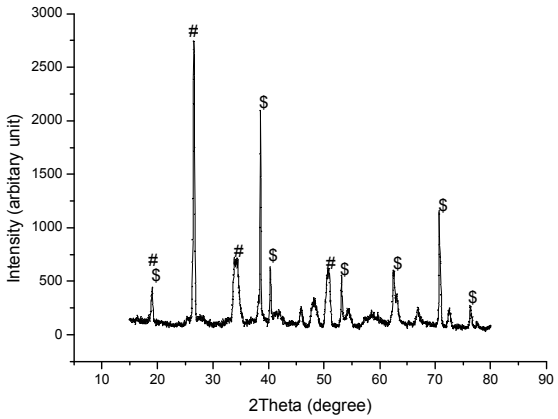

Fig.2 XRD diagram of the MAO coating

Table 1 the corrosion data of titanium and MAO titanium samples in acid solutions at 250ºC for 24h

Acid concentration	weight change after test (mg)		corrosion rate (mg/cm^2, h)	
(mol/L)	Ti	MAO treated Ti	Ti	MAO treated Ti
0.1 HCl	+0.2	+0.4	/	/
1.0 HCl	dissolved (-1189)	-162.7	>8.5	1.17
0.1 H_2SO_4	+0.3	+0.6	/	/
1.0 H_2SO_4	dissolved (-1175)	-9.2	>8.4	0.07

However, in 1 mol/L HCl and H_2SO_4 solutions the corrosions are very heavy. The titanium samples were totally dissolved after 24 h immersion in 1 mol/L HCl. The MAO treated titanium samples were also heavily corroded but not dissolved. Table 1 shows the corrosion rates of the samples. The average weight loss of MAO Ti samples was 162.7mg. The calculated corrosion rate is 1.17 mg/(cm^2,h). This result shows that the MAO treatment improve the corrosion resistance of the titanium. Fig.3 shows the corrosion product of the MAO titanium after the immersion test. XRD analysis revealed that the main phase of the corrosion product is rutile. The rutile crystal grew into flower like morphology. The rutile corrosion product may contribute in the corrosion resistance.

In 1.0 mol/L sulfuric acid solution, the titanium samples were also totally dissolved after 24 hours immersion test at the high temperature, while the MAO titanium samples lost 9.2 mg in weight. The small weight loss shows that corrosion resistance of MAO treated titanium is much better that untreated titanium. Fig.4 is the micrograph of the corrosion product in MAO titanium after the immersion test. XRD analysis revealed that the corrosion product is anatase. The corrosion product consists of very fine crystal grains which may have protection effect.

From the above experimental results it is clear that the MAO coating can enhance the corrosion resistance of titanium in hot chloride acid and sulfuric acid solutions. The main component of the MAO coating is Al_2TiO_5, which is a functional ceramic with properties of low thermal expansion and low thermal conductivity. It is reasonable to assume that the MAO coating acted as a barrier

coating that protects the titanium substrate in the hot acid solutions. Although the MAO coating was porous, the pores can be filled by the corrosion products produced *in situ*. If the acids attack the titanium substrate through the pores of the MAO coating, the pores will be automatically filled by titanium oxides that are the corrosion products of the titanium. In this way, further corrosion is inhibited. This is actually a synergic protection mechanism. Moreover, the MAO coatings were reported consisting of two layers: a porous outer layer and a dense inner layer. The dense inner layer can act as a barrier coating to protect the substrate.

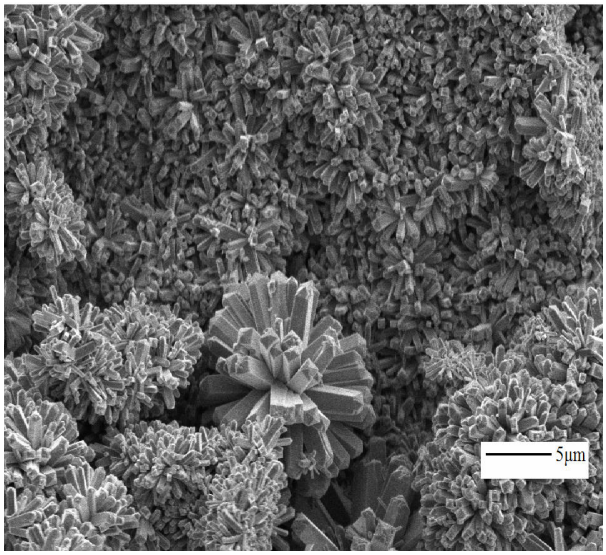

Fig.3 Corrosion product of MAO treated Ti in HCl

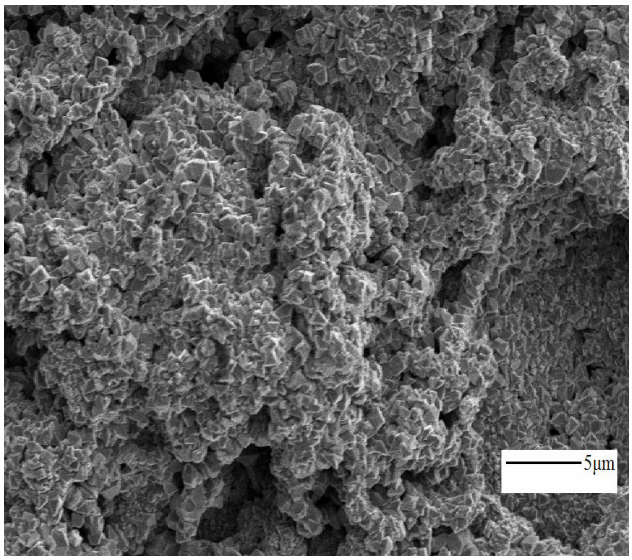

Fig.4 Corrosion product of the MAO treated Ti in H_2SO_4

4 **Summary**

The MAO treatment forms $TiAl_2O_5$ coating on the commercially pure titanium surface. Both the commercially pure titanium and the MAO treated titanium have good corrosion resistance in the acid solutions with 0.1 mol/L concentration at 250ºC. The MAO treated titanium has better corrosion resistance than the untreated titanium in 1 mol/L HCl and H_2SO_4 acid solutions at the high temperature.

Acknowledgement

The authors are grateful for the financial support by the Natural Science Foundation of China under the grant 50371078.

References

[1] J. Vaughan, A. Alfantazi, J. Electrochem. Soc., 153 (2006) B6
[2] D. F. Taylor, Indus. and Engi. Chem.. 42 (1950) 639
[3] N. Boukis, C. Friedirich, E. Dinjus, Corrosion98. Paper no.417.
[4] J. Lu, J. Zhang, Z. Mao, Transaction of Non-ferrous Metals Soc. of China. 12 (2002) 1391
[5] D. Wei, Y. Zhou, D. Jia, Y. Wang. Surf. Coat. Tech. 201 (2007) 8715
[6] Y. Shin, W. Chae, Y. Song, Y. Sung. Electrochem. Communi. 8 (2006) 465
[7] A. L. Yerokhin, A. Leyland, A. Matthews, Appl. Surf. Sci., 200 (2002) 172
[8] T. H. Teh, A. Berkani, S. Mato, P. Skeldon, G.. E. Thompson, H. Habazaki, K. Shimizu, Corrosion Science 45 (2003) 2757
[9] A. Afshar, M. R. Vaezi, Surf. Coat. Tech. 186 (2004) 398
[10] A. L. Yerohkin, X. Nie, A. Leyland, A. Matthews, Surf. Coat. Tech. 130 (2000) 195

Key Engineering Materials Vols. 385-387 (2008) pp 781-784
© (2008) Trans Tech Publications, Switzerland
doi:10.4028/www.scientific.net/KEM.385-387.781

The Effect of Volume Fraction of Steel Fiber on the Tensile Softening Behavior in Ultra High Performance Concrete

Su-Tae Kang[1, a], Jung-Jun Park[1,b], Sung-Wook Kim[1,c] and Kee Nam Hong[2,d]

[1] Structure Material Research Division, Korea Institute of Construction Technology, Goyang, 411-712, Korea

[2] Department of Civil Engineering, Chungbuk National University, Cheongju, 361-763, Korea

[a]alphard@kict.re.kr, [b]jjpark@kict.re.kr, [c]swkim@kict.re.kr, [d]hong@chungbuk.ac.kr

Keywords: Steel fiber, Volume fraction, High performance, tensile softening, Inverse analysis

Abstract. This paper estimated the influence of volume of steel fiber on the tensile softening behavior in Ultra High Performance Concrete. Tensile softening curves were obtained from Three-Point Bending Test(TPBT) with notched beam. Inverse analysis method by Uchida et al. was introduced to obtain the tensile softening behaviors from the results of TPBT. We could find out that the increase of volume fraction of steel fiber makes the tensile strength higher but all of the curves converged on an asymptote with crack width. We proposed the equation of softening curve expressed by combination of plastic area and exponential descending area considering the volume fraction of steel fiber and ω_0, which is corresponding to the maximum crack width of plastic area. We also carried out the crack propagation analysis using finite element method with smeared crack model and confirmed that the proposed equation had a good agreement with the experimental results.

Introduction

As a material exhibiting remarkable compressive strength and durability, concrete represents one of the mostly adopted materials for the construction of bridges together with steel. However, its inherent poor tensile and flexural strengths make it prone to cracking, and the gradual increase of brittleness according to the increase of the compressive strength is also bringing numerous problems in its application. Recent researches on ultra high performance concrete revealed that its mechanical characteristics are showing high tensile strength and continue to develop large ductility even after cracking. Regard to the tensile characteristics, such ultra high performance concrete is playing a critical role in the ductile behavior of the structure until flexural failure and shear failure. Since the application of ultra high performance concrete in structures can contribute in reducing and lightening the structural members owing to its remarkable material performances, noticeable reduction of construction costs can be realized. Need is thus to develop design and structural analysis technologies using the mechanical characteristics of ultra high performance concrete in order to explore and diversify its efficient exploitation so as to promote the applicability of ultra high strength fiber reinforced concrete structures. However, the lack of experimental data for quantitative assessment including the load sharing capacity of the fibers together with the absence of relevant methods analyzing the final state of ultra high performance concrete structural members are currently impeding the exploitation of the promising large deformation performance brought by such material. Reliable tension softening model appears thus to be necessary to estimate accurately the deformation performance through FEM analysis.

Accordingly, this study intends to examine experimentally the tensile softening characteristics of ultra high performance concrete and to establish a tension softening model for the accurate estimation of the deformability through FEM analysis based on the corresponding experimental data and results.

Test planning and method

The test methods allowing the determination of the tension softening curve of ultra high performance concrete are bending test [1], uni-axial tensile test [2] and compact tension (CT) test [3] similarly to those applied for ordinary concrete. Among them, the bending test is the most widely adopted method owing to its simplicity. Even if the uni-axial tensile test offers the advantage to determine directly the tension softening curve, difficulties are encountered in securing accuracy. CT test presents the noticeable advantage to be practically free from the effects of the self-weight of the specimen because of the large failure area produced in specimens with small volumes. However, CT method is determining the tension softening curve indirectly such as the bending test, and has been rarely applied due to the need of special equipment.

This study performed 3-point bending test for the determination of the tension softening curves in compliance with JCI-S-002-2003 test method for the load-deflection curve of fiber reinforced concrete proposed by the Japan Concrete Institute [4]. Fiber content was selected as test variable and was classified into 5 groups corresponding volume ratio increased by 1% from 1% to 5%. The adopted steel fibers were straight with length of 13 mm and diameter of 0.2 mm. Bending test specimens were manufactured with dimensions of 100×100×400 mm and notched at the center of the 300 mm supported span with notch depth of 30 mm. Five specimens were manufactured per test variable. Table 1 summarizes the concrete mix design proportions used in this study.

Table 1. Mix design of concrete (relative ratios*)

Cement	Water	Silica fume	Fine aggregates	Filler	Superplasticizer	Steel fiber
1.00	0.25	0.25	1.10	0.30	0.018	2% vol.

(*) Relative ratios: weight ratio to cement, except steel fiber expressed as volumetric ratio to the whole volume.

Three-point bending tests were conducted to determine the tension softening curves of ultra high performance concrete. The specimens were cut with a notch at mid-length using a diamond cutter prior to the execution of the test and after completion of concrete curing. The notch was set with a constant width of 4 mm. A universal testing machine with capacity of 2,000 was used for the bending test. Load was applied through displacement control at speed of 1/1500 of the specimen span length (300 mm) per minute. In addition, one LVDT with capacity of 10 mm was installed at both sides to measure the deflection of the center of the specimen during the test. Clip gage was attached at the bottom of the specimen to measure the crack width at the notch. Figure 1 illustrates the characteristics of the bending test specimens and equipment.

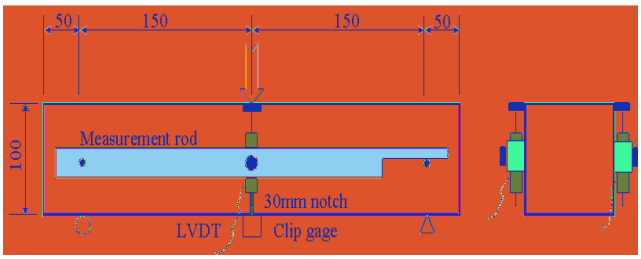

Figure 1. Three-point bending test

Experimental results and discussion

Figures 2 and 3 plot the experimentally obtained mean load-CMOD curves and load-deflection curves for each fiber content of the 100×100×400 mm specimens. In Figure 2, CMOD has been measured within values below 4 mm because of the capacity (5 mm) of the clip gage used in this study. Accordingly, larger crack widths could not be measured. Figure 3 reveals that the initial stiffness does not experience significant change according to the increase of the fiber content, while the maximum load is increasing gradually together with gradual change into brittle behavior in the softening section. The inverse analysis method suggested by Uchida et al. [5] has also been applied in this study for the determination of the tension softening curves of ultra high performance concrete. This method exploits the load-deflection curves obtained from flexural tensile test to perform inverse analysis using FEM model and the poly-linear approximation method proposed by Kitsutaka et al. [6, 7] was applied to derive the tensile stress-crack mouth opening displacement (CMOD) relationship. The poly-linear approximation method is an established technique of which accuracy has been sufficiently

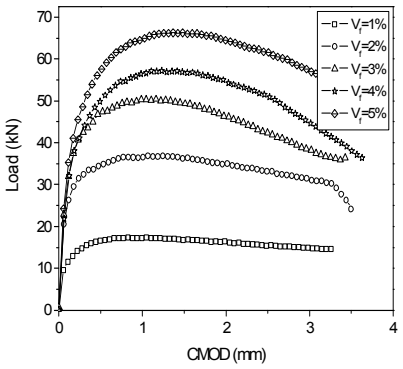

Figure 2. Comparison of mean load-CMOD curves

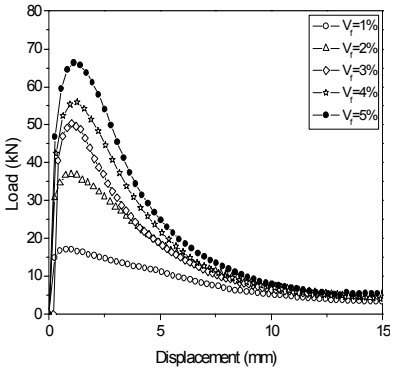

Figure 3. Comparison of mean load-displacement curves

verified for ordinary concrete, its accuracy regard to ultra high performance concrete similar to the material of concern in this study has also been verified by several researchers. Figure 3 illustrates the concept of such poly-linear approximation method. Figure 4 depicts the process deriving the tensile stress-crack width relationship through inverse FEM analysis using the results of flexural tensile test. The finite element model is composed of 1203 triangular plane stress elements and 684 nodes. The notch at the center has been modeled in details with denser meshing in order to evaluate exactly the crack propagation.

Figure 5 arranges the tension softening curves for each of the considered steel fiber contents obtained from inverse FEM analysis. It can be observed that the tensile strength increases gradually with larger steel fiber content. It is also verified that the material continues to maintain its tensile strength during a definite period after having reached the tensile strength prior to reduce and converge toward a definite stress in all the tension softening curves. In addition, the gradual decreasing slope of the tensile stress is seen to become gradually steeper with increasing steel fiber content.

As shown in Figure 5, the tension softening curves obtained in this study are featured by a domain where the tensile stress remains constant and a domain where the stress is decreasing. Accordingly, this study expresses the constant tensile strength domain be means of a straight line and the decreasing stress domain be means of an exponential function. In view of Figure 5, the maximum displacement, w_0, in the domain exhibiting constant tensile stress appears to remain practically constant regardless of the fiber content. Its value was determined to be 0.26 mm corresponding to the mean value of the 5 classes of fiber content, and defined as the critical crack width. The tension softening model expressed in Equations 1 to 3 was then proposed based on the regression analysis of the experimental data.

$$f_t = 131 \cdot \left(V_f\right)^{1/3} - 2 \text{ (MPa)}$$

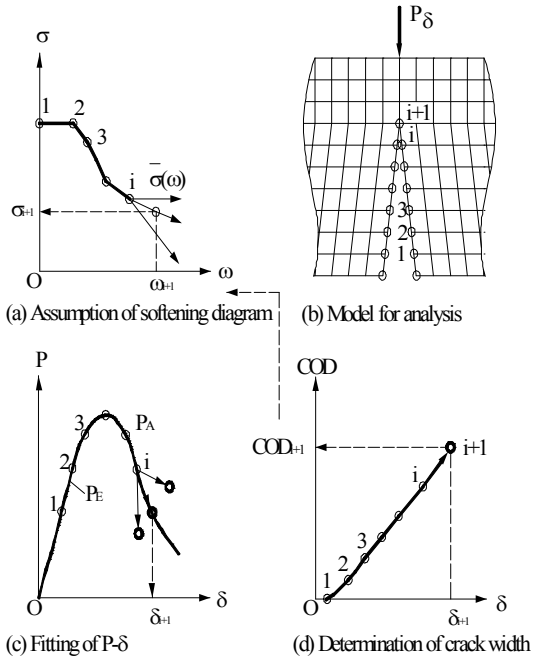

Figure 4. Poly-linear approximation method

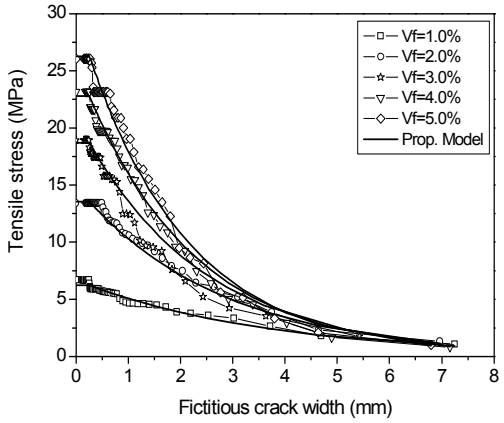

Figure 5. Comparison of inverse analysis results and tension softening model

(1)

$$\sigma_w = \begin{cases} f_t & (for \quad w \le w_0) \\ f_t \cdot b^{(w-w_0)} & (for \quad w \ge w_0) \end{cases} \tag{2}$$

where w_0 = 0.26 mm and $b = 0.3 - 0.1 \cdot \ln(V_f)$.

Conclusions

This study investigated the effects of the fiber content on the tension softening behavior of ultra high performance concrete.

(1) Ultra high performance concrete has been seen to develop definite initial stiffness regardless of the fiber content.
(2) Larger steel fiber content appeared to increase the flexural tensile strength of ultra high performance concrete and to favor the brittleness of the softening behavior.
(3) The inverse analysis method proposed by Uchida et al. for the determination of the tension softening curve of ultra high performance concrete has been adopted. A tension softening model has been proposed and expressed as a function of the fiber content and critical crack width.

Acknowledgements

This study was carried out as a partial research of the "Development of UHPC for hybrid cable-stayed bridges" in the Korea Institute of Construction Technology. The authors express their gratitude for the support.

References

[1] Kitsutaka, Y., Oh-oka, T., in: Influence of short cut fiber on fracture parameters of high strength mortar matrix : Fracture behavior of high-strength fiber Reinforced concrete(HFRC), Journal of structural and construction engineering Transactions of AIJ, Vol. 501, 1997, pp. 7-12. (in Japanese)
[2] Wang, Y, Li, V. C. and Backer, S., in: Experimental Determination of Tensile Behavior of Fiber Reinforced Concrete, ACI Materials Journal, Vol. 87, No. 5, 1990, pp. 461-468.
[3] Hirozo, M., Noriaki, N., and Kazuki, K., in: Mechanical properties of FRCC on the basis of fracture mechanics, Journal of structural and construction engineering Transactions of AIJ, Vol. 449, 1993, pp. 1-7. (in Japanese)
[4] Japan Concrete Institute, in: JCI Standards for test methods of fiber reinforced concrete (JCI-SF4), 1984, pp. 11- 17. (in Japanese)
[5] Uchida, Y., Kurihara, N., in: Determination of tension softening diagrams of various kinds of concrete by means of numerical analysis, FRAMCOS-2, Germany, AEDIFICATION, 1995.
[6] Kitsutaka, Y., in: Fracture parameters by poly-linear tension softening analysis, Journal of Engineering Mechanics 123(5), 1997, pp 444-450.
[7] Kitsutaka, Y., in: Fracture parameters for concrete based on poly-linear approximation analysis of tension softening diagram, FRAMCOS-2, Germany, AEDIFICATION, 1995.
[8] Tanaka, Y., Fukuura, N., Uzawa, T., Sakamoto, J., Maehori, S., and Katagiri, M., in: Tensile characteristics and modeling of tension softening behavior for ultra high performance fiber-reinforced concrete, Journal of Materials, Concrete Structures and Pavements, JSCE, Vol. 67, No. 788, 2005, pp. 159-173. (in Japanese)

Key Engineering Materials Vols. 385-387 (2008) pp 785-788
© (2008) Trans Tech Publications, Switzerland
doi:10.4028/www.scientific.net/KEM.385-387.785

Reinforcement of Aluminum by TiB dissolution

P. Agrianidis[1,a], K.G. Anthymidis[2,b] and C. David[3,c]

[1,2,3]Technical University of Serres, Mechanical Engineering Department,

Magnesias Campus, 62124 – Serres, Greece

[a]pagri@teiser.gr, [b]kanth@teiser.gr, [c]david@teiser.gr

Keywords: composite materials, mechanical properties, aluminum reinforcement

Abstract. Interactions between solid materials and liquid aluminum lead to a dissolution of solid elements into aluminum, which in turn results in a subsequent growth of intermetallic and intermediate phases. It was established that the growth of the intermetallic phases could be governed by chemical reactions at the interfaces and by interdiffusion of the reacting elements through the different phases. Dissolution on the other hand mainly depends on thermodynamic conditions, experimental parameters such as temperature, stirring time, and reacting holding time and on the degree of the saturation of aluminum as well as on the chemical composition of the solid materials in the reaction zone.

The above-mentioned factors play also an important role in the formation of the different phases during dissolution. Nevertheless, a non-uniform distribution of the solute elements may causes a local concentration of these elements into the liquid aluminum, which practically delays the process or alters the equilibrium of the growth of the phases. Thus it is crucial to control the dissolution conditions so that the instabilities induced at the solid materials/aluminum interface are limited.

The main objective of this study was to investigate both the formation of intermetallic and intermediate phases in the reaction zone and to examine the development of the diffusion structures of pure aluminum reinforced with TiB particles and to investigate the mechanical properties of the as-produced composite materials.

Introduction

It is well known that the addition of ceramic phases in an alloy e.g. aluminum, in form of fibers or particles infects its mechanical properties [1]. This leads to a new generation of materials, which are called metal matrix composites. They have found a lot of application during the last twenty-five years due to their low density, high strength and toughness, good fatigue and wear resistance [2-12]. Automobiles industry use aluminum alloy matrix composites reinforced with SiC or Al_2O_3 particles for the production of pistons, brake rotors, calipers and liners [13]. However, no reference could be cited in the international literature concerning aluminum reinforced with TiB although these composites are very promising for improving the mechanical properties of this metal without significantly alter it's corrosion behavior. Several processing techniques have been developed for the production of reinforced aluminum alloys. This paper is concerned with the study of TiB reinforced aluminum produced by the stir-casting method.

Experimental procedure

The aluminum metal was heated and thawed at about 800°C vigorous stirring of the matrix with a tungsten impeller at 800 rpm. After fifteen minutes of isothermal holding stirring a satisfactory vortex was created and then TiB particles were gradually added in it. When this was completed of the mix was maintained under stirring for further fifteen minutes and then the alloy was left to rest for about eight minutes and afterwards was poured in a preheated mold and left to be cooled in the atmosphere. The morphology of the produced composite materials was examined using optical and SEM microscopy. The composition of microstructural features was determined by EDX

spectroscopy. The tribological properties of the as-produced composite material were evaluated using a pin on disc type equipment under dry wear conditions. Test conditions: pressure 154 KPa, SiC paper 220 grit, testing time 5 min, velocity 47.1 m/min. The experimental set up for tribological testing has been described in a previous publication[14].

Results and discussion

Figure 1 shows the typical morphology of the produced aluminum reinforced with TiB particles. In the present experiment synthesis of composite materials was carried out with the method described above, by mixing of 90% w.t. Al metal, 5% w.t. K_2TiF_6 and 5% w.t. KBF_4 at temperature of 800°C. The Vickers microhardness of the produced composite material was measured 44 Hv (Fig.2).

Figure 1: Typical morphology of the aluminum reinforced with TiB particles produced by the stir-casting method.

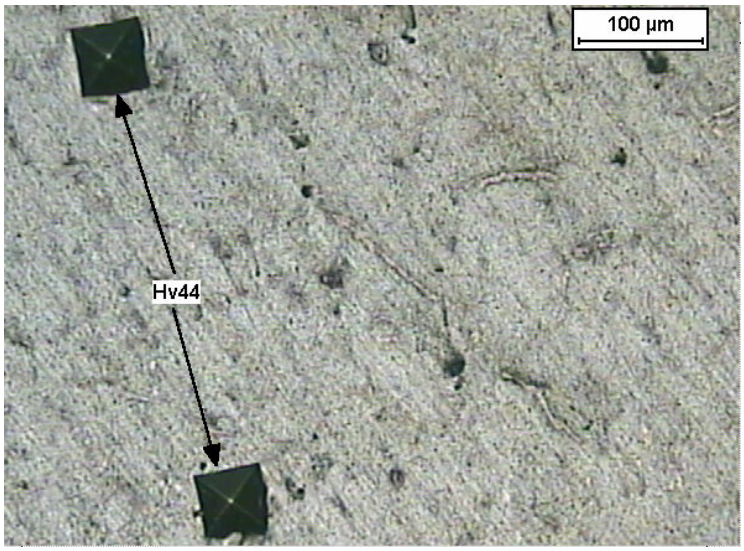

Figure 2: Microhardness measurements of the aluminum reinforced with TiB particles (black spots) produced by the stir-casting method.

From the EDX spectroscopy it was concluded that the as prepared material consists of two different phases: white phase comprises 95%w.t. Al and 5% w.t. Ti and dark color phase which is almost pure Aluminum metal, TiB particles are scattered mainly within the white phase (Fig.3).

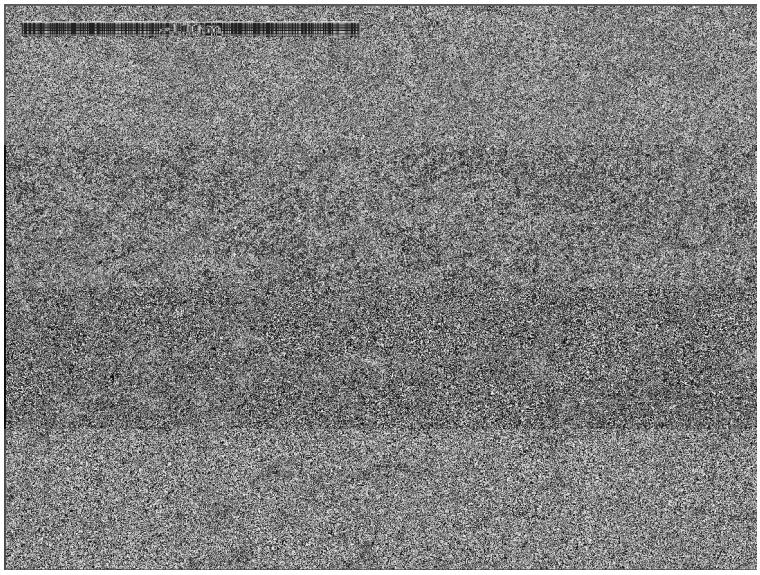

Figure 3: SEM photos of the aluminum reinforced with TiB particles produced by the stir-casting method.

The SEM mapping of the produced metal matrix composite material is presented in Figure 4 and it is in good agreement with the above analysis of the experimental results.

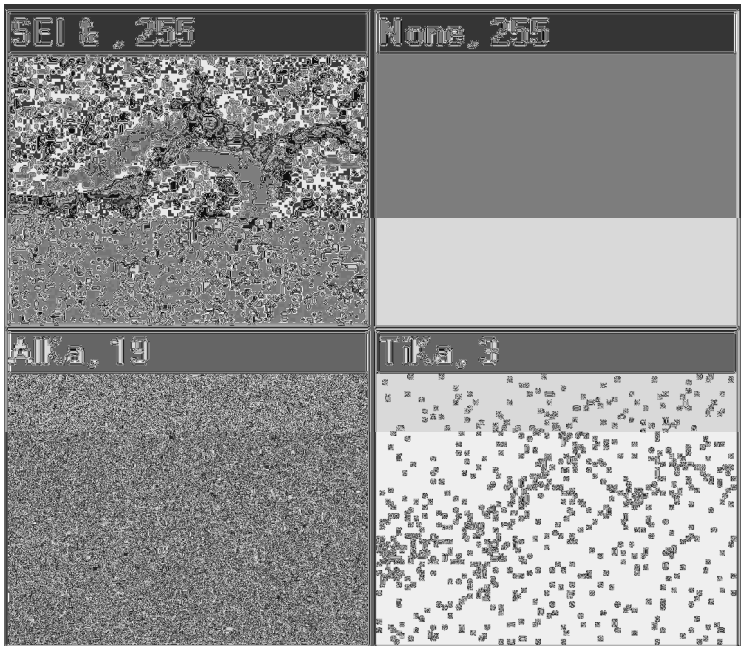

Figure 4: SEM mapping of the aluminum reinforced with TiB particles produced by the stir-casting method.

In the tribological tests under dry wear conditions the produced reinforced composite material showed an approximately 50% increased resistance to wear compared to pure Al metal (Fig. 5).

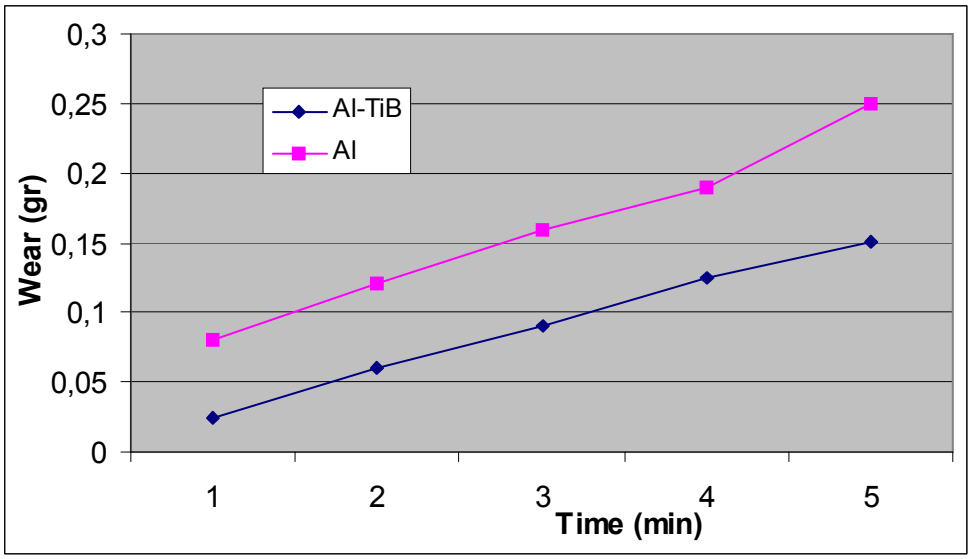

Figure 5: Effect of the TiB particles on dry wear resistance of Al. Test conditions: pressure 154 KPa, SiC paper 220 grit, velocity 47.1 m/min.

Acknowledgments

The authors are greatly indebted to the Research Committee of the Technical University of Serres (T.E.I) for funding of this research project.

References

[1] D. Aylor, in: *Metals Handbook Vol.13 9th ed.*, edited by ASM, Metals Park, OH, 1987, p. 859
[2] G.E. Kiourtsidis and S.M. Skolianos: Wear Vol. 253 (2002), p. 946
[3] K.J. Blansali and R. Mehrabian: J. Met. Vol. 34 (1982), p. 30
[4] M.K. Surappa, S.V. Prasad and P.K. Rohatgi: Wear Vol. 77 (1982), p. 295
[5] P.K. Rohatgi, R. Asthana and S. Das: Int. Met. Rev. Vol. 31 (1986), p. 115
[6] R.L. Deuis, C. Subramanian and J.M. Yellup: Wear Vol. 201 (1996), p. 132
[7] S. Skolianos and T.Z. Kattamis: Mater. Sci. Eng. A Vol. 163 (1993), p. 107
[8] W.Q. Song, P. Krauklis, A. Mouritz and S. Bandyopadhyay: Wear Vol. 185 (1995), p. 125
[9] B. Venkataraman and G. Sundararajan: Acta Mater. Vol. 44 (1996), p. 451
[10] Z.F. Zhang, L.C. Zhang and Y.W. Mai: J. Mater. Sci. Vol. 30 (1995), p. 5999
[11] S. Das, D.P. Mondal and G. Dixit: Metall. Mater. Trans. A Vol. 32 (2001), p. 633
[12] P.N. Bindumadhavan, H.K. Wah and O. Prabhakar: Wear Vol. 248 (2001), p. 112
[13] K.M. Prewo: Am. Ceram. Soc. Bull. Vol. 68 (1989), p. 395
[14] S. Skolianos, A. Hatziaugoustis and A. Papaefthimiou, "Tribological properties of the squeeze cast Al-6001", Proceed. Of the First Balkan Conference of Tribology Balkantrib 93, 1-3 October 1993, Sofia Bulgaria, p.239-246, vol.1, Ed. E. Assenova, K. Danev, Technical University of Sofia, Bulgaria

Key Engineering Materials Vols. 385-387 (2008) pp 789-792
© (2008) Trans Tech Publications, Switzerland
doi:10.4028/www.scientific.net/KEM.385-387.789

Fiber Alignment of Steel Fiber Reinforced High Strength Concrete (SFR-HSC) in Flexural Members and its Effect on the Flexural Strength

Su-Tae Kang[1, a], Jung-Jun Park[1,b], Gum-Sung Ryu[1,c] and Sung Wook Kim[1,d]

[1] Structure Material Research Division, Korea Institute of Construction Technology, Goyang, 411-712, Korea

[a]alphard@kict.re.kr, [b]jjpark@kict.re.kr, [c]ryu0505@kict.re.kr, [d]swkim@kict.re.kr

Keywords: Steel fiber, high strength, concrete, alignment

Abstract. The fibers alignment in steel fiber reinforced high strength concrete (SFR-HSC) has naturally significant influence on the mechanical properties of concrete. Fiber-reinforced concrete being manufactured by means various kinds of specimen shape and diversified filling methods and directions, these variables are likely to produce effect on the fibers alignment leading to large differences in its mechanical properties. This study intended to evaluate the effect of placing and flow direction not only on the fibers alignment but also on the tensile behavior of SFR-HSC. Section analysis using photographic shooting was adopted to investigate the fiber alignment and revealed considerable difference in the fiber alignment according to the placing and flow direction. The best alignment appears to be achieved when placing is done in the direction of the flexural tensile stress and the alignment was change with the flow distance although the same flow direction. Such placing and flow direction produce little difference in the first cracking strength but significant discrepancy up to 50% in the ultimate tensile strength.

Introduction

The evolution of concrete technology has attained a level dealing with ultra high strength features going beyond the classic concept of high strength and has even permit the development of steel fiber reinforce high strength concrete (SFR-HSC) solving also the problem of brittleness that was the most critical one for the high strengthening of concrete [1]. The matrix based on RPC (Reactive Powder Concrete) commonly called as cement is composed of an adequate proportion of particles with diameter below 1mm and is characterized by a brittle behaviour. In order to supplement such brittleness, SFR-HSC uses steel fibres which allow it to develop extremely high strength together with remarkable performance regard to toughness and durability aspects [2]. The mechanical characteristics of SFR-HSC are its compressive strength ranging from about 180 to 200MPa, its splitting tensile strength averaging 10 to 12MPa and its flexural tensile strength running on the mean from 30 to 35MPa. The most important advantages of fibre reinforced concrete are the increase of tensile strength and improvement of toughness. The improvement of such mechanical properties can be optimized through an arrangement of the fibers suited to the orientation of the stress. This can be achieved through the control of the orientation and dispersion of continuous long fibers in the matrix. Short fibers with length of 15 to 30mm are generally adopted in fiber reinforced concrete. These fibers are dispersed randomly in all directions so as to exhibit isotropy. However, since SFR-HSC are not using coarse aggregates and show high fluidity, the fibers alignment may rely on the flow direction owing to the casting sequence or shape of the structure. So many studies were carried out with the fiber distribution in fiber-reinforced concrete since the early seventies [3-5]. However the studies were focused on the material mechanics but did not deal with the flow characteristics. Recently, Ozyurt et al. [6], Stähli et al. [7] did this kind of studies, which were still restricted in specimen scale. Accordingly, this study examines the fibers distribution according to placing and flow directions in order to evaluate the corresponding effects on the cracking strength and flexural strength.

Test setup and method

The composition of matrix used is given in Table 1 and 2% vol. steel fibers were used. The flow test showed the flowabiliy of about 230mm. This study performed at first specimen level tests using rectangular specimens with dimensions of 100mm× 100mm×400mm to evaluate the orientation and dispersion of the fibres according to the placing and flow directions of SFR-HSC in fresh state. The specimens were tested by four point bending test. Two cases were considered for the placing and flow directions: casting in the longitudinal direction and guided flow, and casting in the vertical direction. Figure 1 illustrates each of the placing and flow directions adopted during the manufacture of the specimens.

Table 1. Mix design of concrete (relative ratios*)

Cement	Water	Silica fume	Fine aggregates	Filler	Superplasticizer	Steel fiber
1.00	0.25	0.25	1.10	0.30	0.018	2% vol.

* weight ratio to cement, except steel fiber expressed as volumetric ratio to the whole volume.

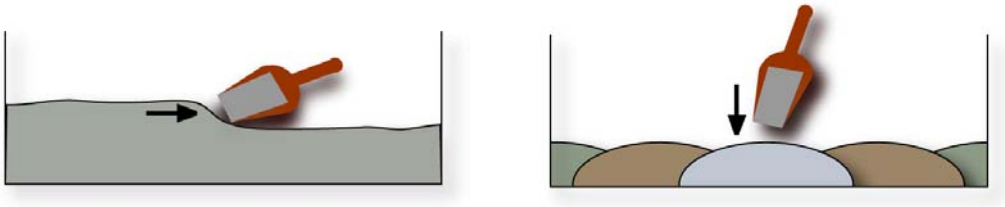

(a) Placed parallel to flexural tension (CASE1) (b) Placed perpendicularly to flexural tension (CASE2)
Figure 1. Placing and flow directions of concrete

Survey was done by cutting the specimens to evaluate the characteristics of the fibres' arrangement within the specimens according to the placing and flow direction. High resolution photographs were taken at each of the cutting planes to investigate the alignment of the fibres. Thereafter, 4-point bending tests were conducted to examine the relationship between the alignment of the fibers and the tensile characteristics of SFR-HSC.

In the previous, tests were carried out at the specimen level regard to the alignment of the fibres according to the placing and flow directions. However, the flow in rectangular specimens of 100mm×100mm×400mm is disturbed by the small dimensions of the members, which is likely to produce differences in the flow characteristics and the corresponding alignment of the fibres in real structures. Chao et al.[8] reported that the tensile strength and behaviour was different according to the scale in the direct tensile test. More realistic alignment of the fibres can be evaluated for specimens presenting dimensions closer to those of real structures. Accordingly, we investigated these effects at a level comparable to actual structures. Plate with dimensions of 1320mm×1320mm× 100mm was thus manufactured and cut into rectangular pieces of about 100mm×100mm×440mm to evaluate the cracking strength and flexural tensile strength with respect to the position by four point bending test. Placing was done by free fall from a height of about 200mm at the centre of the plate. The fresh SFR-HSC was let to flow radially by itself. Since SFR-HSC exhibits fluidity reaching its self-filling possibility, complete filling was realized without additional finishing work except surface finishing. Figure 2 depicts the placing and flow directions during the manufacture of the plate structure. Figure 3 illustrates the cutting directions of the manufactured plate and the designation of

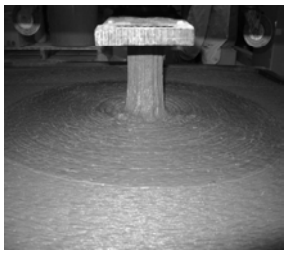

Figure 2. Placing and flow directions

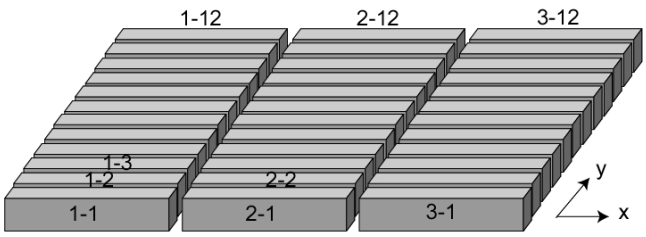

Figure 3. Label and shape of plate pieces

(a) Placed parallel to flexural tension (b) Placed perpendicularly to flexural tension

Figure 4. Distribution of fibers according to the placing and flow directions

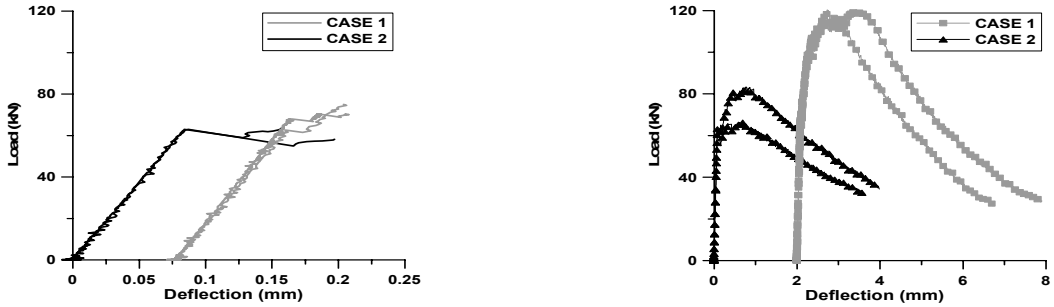

(a) Load-deflection curve regard to crack initiation (b) Load-deflection curve regard to flexural tensile behavior

Figure 5. Bending test results at specimen level according to the placing and flow directions

each of the resulting pieces.

Experimental results and discussion

Figure 4 presents the results at the specimen level related to the alignment of the fibres according to the placing and flow directions of SFR-HSC. Figure 4 shows the alignment of the fibres at the cutting planes perpendicular to the direction in which the principle tensile stress acts at the bottom. In the case of placing parallel to the flexural tension, the fibres are seen to be evenly dispersed with most of them being oriented vertically, whereas when placing is done perpendicularly to the flexural tension, the alignment of the fibres becomes improper and the number of fibers is comparatively small. Figure 5(a) illustrates the behaviour until the initiation of crack and Figure 5(b) represents the whole flexural tensile behaviour. Even if CASE 1 presents a first cracking load slightly larger than CASE 2, the corresponding maximum tensile load is seen to be larger by about 50%. This means that, even if the initial cracking strength is relatively less influenced by the effect of the orientation and dispersion of the fibres, this effect becomes considerable on the maximum tensile strength. These results can be explained by the dependency of the initial cracking strength to the strength of the matrix and the large influence of the pullout strength of the fibres acting per unit area on the maximum tensile strength.

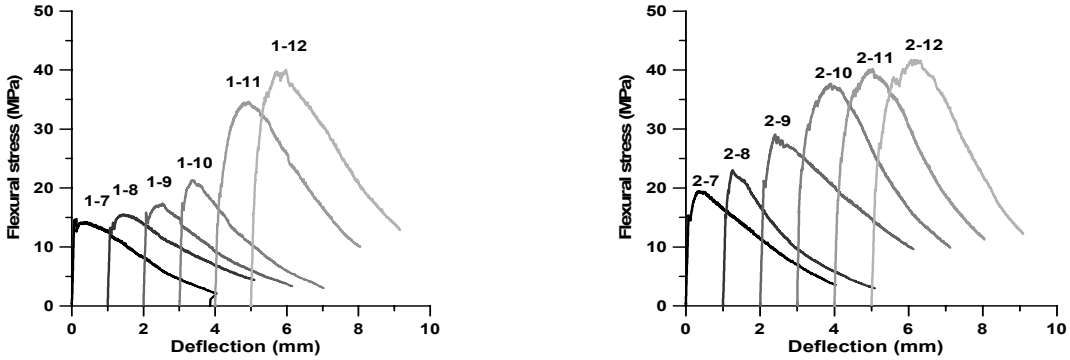

(a) Flexural behavior of series“1” by position (b) Flexural behavior of series“2” by position

Figure 6. Bending test results at structure level according to the placing and flow directions

When it comes to plate test results, the initial cracking stress appears to have no particular difference.

However, it was verified that the maximum flexural stress exhibits significant difference with respect to the position. Figures 6(a) and 6(b) plot respectively the flexural behaviours of series “1” and series “2” according to the position. It can be seen that both series develop flexural strength increasing from the centre toward the edges. In the case of series “1”, pieces 7, 8, 9, and 10 are seen to have nearly no or very short hardening region whereas pieces 11 and 12 are presenting large increase of the flexural strength and also hardening after cracking. On the other hand, a comparison of series “2” with series “1” reveals the occurrence of relatively larger flexural strength for identical y coordinates as well as hardening.

Conclusions

The changes in the alignment of fibres according to the placing and flow directions of steel fiber reinforced high strength concrete (SFR-HSC) have been evaluated at the specimen and structure levels. Investigation of the effect of these results on the flexural behaviour of SFR-HSC also has been conducted. Large differences in the distribution of the fibers were verified according to the placing and flow directions. The best alignment of fibers was obtained when placing and flow occurred in the flexural tension direction. The evaluation of the effects of the placing and flow characteristics at the structure level revealed that the flexural strength increased when the flow of SFR-HSC is oriented perpendicularly to the direction of the principal tensile stress. It was verified that the alignment of the fibres approaches the normal to the flow for larger flow distance from the pouring site. Accordingly, the evaluation of the tensile strength of SFR-HSC shall imperatively consider the effects of the placing and flow directions. During the design of the structure, the design tensile strength shall be determined with sufficient consideration of the placing conditions on field and the flow characteristics according to the shape of the relevant member.

Acknowledgements

The work presented in this paper was funded by Center for Concrete Corea(05-CCT-D11), supported by Korea Institute of Construction and Transportation Technology Evaluation and Planning (KICTTEP) under the Ministry of Construction and Transportation (MOCT).

References

[1] P. Richard and M. Cheyrezy, in: Composition of Reactive Powder Concrete, Cement and Concrete Research, Vol. 25, No. 7, 1995, pp. 1501-1511.
[2] O. Bonneau et al., in: Mechanical Properties and Durability of Two Industrial Reactive Powder Concretes, ACI Materials Journal, Vol. 94, No. 4, 1997, pp. 286-290.
[3] A. E. Naaman, and H. W. Reinhardt, in: Characterization of High Performance Fiber Reinforced Cement Composites-HPFRCC, Proceedings of the Second International Workshop 'HPFRCD2', 1995, pp. 3-6.
[4] S. P. Shah and C. Ouyang, in: Mechanical Behavior of Fiber-reinforced Cement-based Composites, Journal of American Ceramic Society, Vol. 74, No. 11, 1991, pp. 2727-2738.
[5] Y. Akkaya, J. Picka, and S. P. Shah, in: Spatial Distribution of Aligned Short Fibers in Cement Composites, ASCE Materials in Civil Engineering, Vol. 12, No. 3, 2000, pp. 272-279.
[6] N. Ozyurt, T. O. Mason, S. P. Shah, in: Correlation of Fiber Dispersion, Rheology and Mechanical Performance of FRCs, Cement and Concrete Composites, Vol. 29, 2007, pp. 70-79.
[7] P. Stähli, M. Sutter and J. G. M. van Mier, in: Improving the Mechanical Properties of HFC by Adjusting the Filling Method, Proceedings of the Fifth International RILEM Workshop 'HPFRCC5', 2007, pp. 23-30.
[8] S. Chao, W. Liao, T. Wongtanakitcharoen, and A. E. Naaman, in: Large Scale Tensile Tests of High Performance Fiber Reinforced Cement Composites, Proceedings of the Fifth International RILEM Workshop 'HPFRCC5', 2007, pp. 77-86.

Key Engineering Materials Vols. 385-387 (2008) pp 793-796
© (2008) Trans Tech Publications, Switzerland
doi:10.4028/www.scientific.net/KEM.385-387.793

An Iterative Algorithm of Hypersingular Integral Equations for Crack Problems

Kazuhiro Oda[1, a] and Nao-Aki Noda[2, b]

[1] Tokuyama College of Technology, 3538 Gakuendai, Shunan, Yamaguchi 745-8585, Japan

[2] Kyushu Institute of Technology, 1-1 Sensui-cho, Tobata, Kitakyushu 804-8550, Japan

[a]oda@tokuyama.ac.jp, [b]noda@mech.kyutech.ac.jp

Keywords: Iterative Algorithm, Hypersingular Integral Equation, Body Force Method, Crack Problem, Gauss-Chebyshev Quadrature Formula

Abstract. Crack problems are reducible to singular integral equations with strongly singular kernels by means of the body force method. In the ordinary method, the integral equations are reduced to a system of linear algebraic equations. In this paper, an iterative method for the numerical solution of the hypersingular integral equations of the body force method is proposed. This method is based on the Gauss- Chebyshev numerical integration rule and is very simple to program. The solution is achieved without solving the system of linear algebraic equations. The proposed method is applied to some plane elasticity crack problems and is seen to give convergent results.

Introduction

The body force method (BFM) [1] has been widely applied to the analysis of the stress concentration factors and the stress intensity factors for various notch and crack problems. In the analysis of the method, two-dimensional crack problem is formulated as an integral equation with higher singularity of the form r^{-2}. The singular integral equation is called the hypersingular integral equation and can be accurately analyzed by using the fundamental density function and the Chebyshev polynomials [4]. In order to analyze this equation, it is necessary to perform a numerical integration of kernel function and a numerical solution of linear algebraic equation. Recently, the versatile program based on the body force method is developed to satisfy the both conditions of accuracy and efficiency [2]. This program contains no numerical integration and uses the boundary condition expressed by resultant force.

As the different way of the efficient computation, Ioakimidis [3] has considered the iterative method for numerical solution of singular integral equation with the Cauchy type kernel. The iterative algorithm is useful for the solution of the equation and the determination of stress intensity factor.

In this paper, a simple iterative algorithm for solving the hypersingular integral equation of the body force method is proposed and is applied to some crack problems. The solutions are achieved without solving system of linear algebra equations.

Method of Analysis

In the body force method, the problem of mode I crack is expressed by the following integral equation having a strongly singular kernel [4].

$$\frac{1}{\pi}\int_{-1}^{1}\frac{w(t)}{(t-x)^2}g(t)dt+\frac{1}{\pi}\int_{-1}^{1}w(t)h(t,x)g(t)dt=-p(x),\quad(-1<x<1), \tag{1}$$

where $w(t)=\sqrt{1-t^2}$ is the weight function [1, 4], *g(t)* is the unknown function (proportional to the density of force doublets along the crack [1, 4]), *h(t,x)* is a regular kernel and *p(x)* is a normal

traction on the crack surface. The first integral in (1) should be interpreted as a Hadamard finite-part integral.

The ordinary body force method has been used to reduce eq.(1) to a system of linear algebraic equations [1, 2, 4]. In this study, the iterative method for the numerical solution of eq.(1) is proposed.

Gauss-Chebyshev Quadrature Formula. Korsunsky [5] has proposed the following quadrature formula for the finite-part integral

$$\frac{1}{\pi}\int_{-1}^{1}\frac{w(t)}{(t-x)^2}g(t)dt \cong \sum_{i=1}^{\mathrm{m}}\frac{(1-t_i^2)}{(m+1)}\frac{g(t_i)}{(t_i-x_j)^2} - (m+1)g(x_j), \tag{2}$$

The nodes t_i and x_j are given by

$$t_i = \cos\left(\frac{i\pi}{m+1}\right), \quad x_j = \cos\left(\frac{(2j-1)\pi}{2(m+1)}\right), \quad (i=1,...,m,\ j=1,...,m+1), \tag{3}$$

where t_i, $(i=1,...,m)$ and x_j, $(j=1,...,m+1)$ are zeros of $U_m(t_i)$ and $T_{m+1}(x_j)$, the Chebyshev polynomials of the first and second kinds, respectively [5].

Since the Korsunsky's integration formula (2) is valid only at the discrete set of points $x = x_j$, we derive the modified integration rule from the relation between the Cauchy principal-value integral and the hypersingular integral as follows [6],

$$\frac{1}{\pi}\int_{-1}^{1}\frac{w(t)g(t)}{(t-x)^2}dt \cong \sum_{i=1}^{m}\left\{\frac{1-t_i^2}{(m+1)(t_i-x)^2}\left(1-\frac{T_{m+1}(x)}{T_{m+1}(t_i)}\right)-\frac{1-t_i^2}{t_i-x}\frac{U_m(x)}{T_{m+1}(t_i)}\right\}g(t_i). \tag{4}$$

Moreover, by using the Lagrangian interpolation (5), we obtain the integration formula (6).

$$g(x)=\sum_{i=1}^{m}\frac{U_m(x)}{U_m'(t_i)(x-t_i)}g(t_i), \quad U_m'(x)=\frac{xU_m(x)-(m+1)T_{m+1}(x)}{1-x^2}, \tag{5}$$

$$\frac{1}{\pi}\int_{-1}^{1}\frac{w(t)g(t)}{(t-x)^2}dt \cong \sum_{i=1}^{m}\frac{1-t_i^2}{(m+1)(t_i-x)^2}\left(1-\frac{T_{m+1}(x)}{T_{m+1}(t_i)}\right)g(t_i)-(m+1)g(x). \tag{6}$$

It is seen that (4) and (6) are considered as the more general integration formula for hypersingular integrals which is valid at any points *x*. Clearly, (6) coincides with the Korsunsky's integration formula (2) when $x = x_j$. In the following section, we propose two methods of iterative algorithm using the formulae (2) and (6).

Iterative Method (A). Substituting from (2) into (1), eq.(1) becomes

$$(m+1)g_k(x_j)=p(x_j)+\sum_{i=1}^{m}\frac{1-t_i^2}{(m+1)}\left\{\frac{1}{(t_i-x_j)^2}+h(t_i,x_j)\right\}g_k(t_i), \quad (k=0,1,2,...), \tag{7}$$

where the nodes t_i and x_j are defined by (3). Eq.(7) is not sufficient for the construction of the algorithm because both values of $g_k(t_i)$ and $g_k(x_j)$ are involved. Hence, we use the Lagrangian interpolation to calculate the values $g_{k+1}(t_i)$,

$$g_{k+1}(t_i)=\sum_{j=1}^{m+1}\frac{T_{m+1}(x_j)}{T_{m+1}'(x_j)(t_i-x_j)}g_k(x_j), \quad T_{m+1}'(x)=(m+1)U_m(x). \tag{8}$$

Eqs. (7) and (8) describe the iterative algorithm (A) proposed in this study. The values $g_k(x_j)$ are calculated from (7) when the values $g_k(t_i)$ are given, and the values $g_{k+1}(t_i)$ are determined from (8). These values can then be used for the next iteration.

After the determination of the convergent values $g_k(t_i)$ and $g_k(x_j)$, the stress-intensity factors $K_I(\pm 1)$ are determined by the interpolation method in [7].

$$K_I(\pm 1) = g_k(\pm 1)\sqrt{\pi a}, \quad g_k(\pm 1) = \frac{1}{m}\sum_{j=1}^{m+1} U_{2m-2}\left(\left(\frac{1 \pm x_j}{2}\right)^{\frac{1}{2}} \right) g_k(x_j) \ . \tag{9}$$

In (9), the notation 'a' means a half crack length.

Iterative Method (B). Next, we consider different algorithm using the integration formula (6) because the values $g_k(\pm 1)$ at the crack tip cannot be directly calculated in the method (A). By applying (6) at the points $x = t_j$ to (1), we obtain

$$(m+1) g_k(t_j) = p(t_j) + \sum_{i=1}^{m} \frac{1-t_i^2}{(m+1)} \left(1 - \frac{T_{m+1}(t_j)}{T_{m+1}(t_i)} \right) \left\{ \frac{1}{(t_i - t_j)^2} + h(t_i, t_j) \right\} g_k(t_i), \tag{10}$$

where the points t_j are defined by

$$t_j = \cos\{ i\pi/(m+2) \}, \quad (j = 0,1,...,m+2). \tag{11}$$

To calculate the next values $g_{k+1}(t_i)$ from the values $g_k(t_j)$ in (10), we use (6) once more with degree m+1 at the points $x = t_j$. Then,

$$(m+2) g_{k+1}(t_i) = p(t_i) + \sum_{j=1}^{m+1} \frac{1-t_j^2}{(m+2)} \left(1 - \frac{T_{m+2}(t_i)}{T_{m+2}(t_j)} \right) \left\{ \frac{1}{(t_j - t_i)^2} + h(t_i, t_j) \right\} g_k(t_j). \tag{12}$$

Eqs. (10) and (12) describe completely the iterative method (B). The calculation of (10) and (12) are repeated until the values $g_k(t_i)$ and $g_k(t_j)$ converge. The stress-intensity factors $K_I(\pm 1)$ are directly obtained from the crack-tip values $g_k(\pm 1)$ when j=0 and m+2 in (10).

Results and Discussion

In this section, we apply the iterative methods (A) and (B) of the previous section to mode I crack problems. In all problems the initial value for $g_0(t_i)$ in (7) and (10) is selected as the same value of the traction $p(t_i)$, that is $g_0(t_i) = p(t_i)$.

Two Collinear Cracks. As a first application, consider the problem of two collinear cracks with length $2a$ in an infinite plane. In this case

$$h(t,x) = 1/(d-t-x)^2, \quad p(x) = 1, \tag{13}$$

where d is the distance between centre of cracks. Numerical results are presented in Tables 1 and 2 when a/d=0.25. The exact solution of the problem is analyzed by Erdogan [8]. As shown in tables, numerical results obtained by both proposed methods are in remarkable agreement with the theoretical values. The present iterative methods give rapidly converging numerical results even when m=3.

Table 1 Convergence of SIFs for two collinear cracks with increasing iteration k [method (A)]

Method (A)	m=3		m=4		m=5		m=6	
k	g(1)	g(-1)	g(1)	g(-1)	g(1)	g(-1)	g(1)	g(-1)
10	1.0456	1.0257	1.0436	1.0239	1.0414	1.0220	1.0393	1.0202
20	1.0478	1.0278	1.0475	1.0275	1.0469	1.0269	1.0461	1.0261
30	1.0479	1.0279	1.0479	1.0279	1.0478	1.0278	1.0475	1.0275
40	1.0479	1.0280	1.0480	1.0279	1.0479	1.0279	1.0479	1.0279
Erdogan [8]	1.0480	1.0280	1.0480	1.0280	1.0480	1.0280	1.0480	1.0280

Table 2 Convergence of SIFs for two collinear cracks with increasing iteration k [method (B)]

Method (B)	m=3		m=4		m=5		m=6	
K	g(1)	g(-1)	g(1)	g(-1)	g(1)	g(-1)	g(1)	g(-1)
10	1.0470	1.0275	1.0471	1.0273	1.0465	1.0266	1.0456	1.0258
20	1.0473	1.0278	1.0478	1.0280	1.0478	1.0279	1.0478	1.0278
30	1.0473	1.0278	1.0478	1.0280	1.0479	1.0279	1.0479	1.0279
40	1.0473	1.0278	1.0478	1.0280	1.0479	1.0280	1.0480	1.0280
Erdogan [8]	1.0480	1.0280	1.0480	1.0280	1.0480	1.0280	1.0480	1.0280

Table 3 Convergence of SIFs for an internal crack in a semi-infinite plate with increasing *k* [method (A)]

Method (A)	m=3		m=4		m=5		m=6	
k	g(1)	g(-1)	g(1)	g(-1)	g(1)	g(-1)	g(1)	g(-1)
10	1.1247	1.3561	1.1109	1.3373	1.0986	1.3171	1.0880	1.2983
20	1.1443	1.3836	1.1402	1.3795	1.1347	1.3715	1.1284	1.3622
30	1.1464	1.3865	1.1454	1.3868	1.1436	1.3840	1.1411	1.3801
40	1.1466	1.3868	1.1463	1.3880	1.1458	1.3869	1.1448	1.3854
50	1.1466	1.3869	1.1464	1.3882	1.1463	1.3876	1.1460	1.3870
Noda et al [9]	1.1464	1.3875	1.1464	1.3875	1.1464	1.3875	1.1464	1.3875

Table 4 Convergence of SIFs for an internal crack in a semi-infinite plate with increasing *k* [method (B)]

Method (B)	m=5		m=6		m=7		m=8	
k	g(1)	g(-1)	g(1)	g(-1)	g(1)	g(-1)	g(1)	g(-1)
10	1.1317	1.3617	1.1250	1.3553	1.1185	1.3467	1.1118	1.3370
20	1.1450	1.3803	1.1439	1.3820	1.1425	1.3812	1.1404	1.3789
30	1.1459	1.3816	1.1458	1.3847	1.1458	1.3859	1.1454	1.3858
40	1.1460	1.3817	1.1460	1.3850	1.1463	1.3865	1.1462	1.3870
50	1.1460	1.3817	1.1461	1.3850	1.1463	1.3866	1.1464	1.3872
Noda et al [9]	1.1464	1.3875	1.1464	1.3875	1.1464	1.3875	1.1464	1.3875

Internal Crack in a Semi-Infinite Plate. We also considered the problem of internal crack with length *2a* in a semi-infinite plane. In this case

$$h(t,x) = -\frac{1}{(t+x+2d)^2} + \frac{12(x+d)}{(t+x+2d)^3} - \frac{12(x+d)^2}{(t+x+2d)^4}, \quad p(x) = 1, \tag{14}$$

where *d* is the distance between the center of crack and the free edge of the semi-infinite plate. Numerical results are shown in Tables 3 and 4 when a/d=0.8. The accurate stress-intensity factor of the problem is analyzed by the singular integral equation method [9]. As shown in tables, in spite of this inconvenient geometry condition, numerical results are in close agreement with the previous results in [9]. From Table 4, in method (B) larger number of *m* (compared with those used in method (A)) must be used to obtain the same accuracy in the final numerical results.

From Tables 1-4, the present iterative methods were found to give the good convergence of the numerical results and to be useful for determining the stress intensity factor.

References

[1] H. Nisitani: *Journal of the Japan Soc. Mech. Engng.*, Vol.70, No.580 (1967), p.627.

[2] H. Nisitani, D.-H. Chen and A. Saimoto: *Versatile Program of Two-dimensional Stress Analysis Based on Body Force Method* (Baifukan Publications, Japan 1994).

[3] N.I. Ioakimidis: *Journal of Computational Physics*, Vol. 43 (1981), p. 164.

[4] N.-A. Noda and K. Oda: *International Journal of Fracture*, Vol.58, No. 4 (1992), p. 285.

[5] A.M. Korsunsky: *Quarterly of Applied Mathematics*, Vol. LVI, No. 3 (1998), p. 461.

[6] G. Monegato: *Numer. Math.*, Vol. 50 (1987), p. 273.

[7] S. Krenk: *Quarterly of Applied Mathematics*, Vol. 32 (1975), p. 479.

[8] F. Erdogan: *Proc. 4th U.S. Nat. Congr. Appl. Mech.*, (1962), p. 547.

[9] N.-A. Noda and T. Matsuo: *International Journal of Fracture*, Vol. 63, No. 3 (1993), p. 229.

Key Engineering Materials Vols. 385-387 (2008) pp 797-800
© (2008) Trans Tech Publications, Switzerland
doi:10.4028/www.scientific.net/KEM.385-387.797

Observation of the Behavior of Fatigue Cracks in Friction Stir Welded Aluminum Alloy Joints

Keiji Katsuki[1, a], Markus Gutensohn[2, b], Masahiro Endo[1, c] and Dietmar Eifler[2, d]

[1]Department of Mechanical Engineering, Fukuoka University, Jonan-ku, Fukuoka 814-0180, Japan

[2] Institute of Materials Science and Engineering, University of Kaiserslautern, Kaiserslautern, Germany

[a]td070004@cis.fukuoka-u.ac.jp, [b]gutensohn@mv.uni-kl.de, [c]endo@fukuoka-u.ac.jp, [d]eifler@mv.uni-kl.de

Keywords: Friction stir welding, Aluminum alloy, Small fatigue cracks, Microstructure, Hardness, Residual stress

Abstract. Friction stir welding (FSW) is a new solid-state welding process that can produce low-cost and high-quality joints of especially aluminum and mgnesium alloys. The welding zone consists of different regions with characteristic microstructuralal details such as a weld nugget, a thermo-mechanically-affected zone (TMAZ) and a heat-affected zone (HAZ). Tension-compression fatigue tests were performed using FSW aluminum alloy AA5454 sheet specimens at a stress ratio of –1. To investigate the propagation behavior of small fatigue cracks in those regions, an artificial defect was introduced into different defined locations in the FSW specimens as well as into the parent material specimens. The crack propagation rates depended on the defined locations and were a function of the hardness; that is, the lower the hardness was, the higher the propagation rate was. The crack paths were mostly perpendicular to the applied stress axis, but some crack paths exhibited deviations by the influence of the local anisotropy of the microstructure.

Introduction

The use of lightweight structural materials is increasing with an increase in the demands for global environmental protection and energy saving in recent years. Aluminum and magnesium alloys are in particular used widely in automotive, rail and aircraft industries as well as for shipbuilding. The fatigue strength of welded joints in the components of those machines and structures has been of major concern. Friction stir welding (FSW), an innovative solid-state joining technique developed in 1991, has been integrated into the manufacturing process as an effective joining method of aluminum and magnesium alloys. The FSW offers advantages over conventional arc weldments such as lower welding temperature, less distortion, lower residual stress, fewer weld defects and no shielding gas requirement. For expanding the application of FSW, it is necessary to clarify the fatigue characteristics of FSW joints. In the present study, tension-compression fatigue tests were performed using friction stir welded AA5454 aluminum alloy plates and the growth behavior of small fatigue cracks was investigated with respect to the microstructure in the welding zone.

Materials and Experimental Method

The investigations were carried out with the AA5454 aluminum alloy. The chemical composition (wt. %) is listed in Table 1.The aluminum alloy was rolled and then annealed to a hardness of 90 HV10. The microstructure of the longitudinal section of an AA5454 sheet is shown in Fig.1. The microstructure consists of an intermetallic Al-Mg-phase (β-phase) embedded in an aluminum solution α-phase. Both phases are elongated due to the rolling process.

The AA5454 sheets, with the dimensions of 125 × 300 × 3.5 mm^3, were butt welded by use of a standard milling machine and a standard tool geometry with a shoulder diameter of approximately 15 mm and an M3.5 pin. In systematic investigations the parameters of the welding process were

optimized to attain high tensile strength FSW joints. It was found that a rotation of 1500 rpm and a welding speed of 200 mm/min were suitable for producing pore free and high strength welds[1].

Fig. 2 shows the microstructural changes of the cross section of a friction stir welded AA5454-joint. The welding zone is characterized by different regions like a central nugget with a typical onion ring structure, a thermo-mechanically-affected zone (TMAZ), and a heat-affected zone (HAZ)[2]. Table 2 shows the mechanical properties of parent metal and FSW joint. After welding, the sheets were cut and milled into the shape of specimen shown in Fig. 3. Specimens were electropolished after finishing with an emery paper of #2000. An artificial defect shown in Fig. 4 was introduced into the surface of the FSW specimens as well as the parent material specimens. The Martens hardness distribution on the cross section of the welding zone was determined by use of a Fischerscope. The X-ray residual stress measurements were also made along the axial centerline on the top and bottom surfaces of a polished specimen.

Tension-compression tests were carried out using a servo-hydraulic fatigue testing machine with a test frequency of 40 Hz and a stress ratio R of −1. The surface length of cracks was measured by the plastic replica method.

Results and Discussion

As shown in Fig. 2, the welding zone consists of different regions with the nugget, the TMAZ and the HAZ. In order to observe individually the growth behavior of fatigue cracks in these regions with different microstructures, the artificial defect shown in Fig. 4 was used to cause a fatigue crack to start at the appointed locations. The applied stress amplitude, σ_a, was a constant of 160 MPa for all the fatigue tests. Fig. 5 shows the experimental results of the fatigue crack length as a function of the number of cycles. The locations of defects are illustrated in the figure. Fig. 6 shows the relationship between the crack growth rate, da/dN, and the stress intensity factor (SIF) range, ΔK. The value of SIF was calculated using the equation of $K_I = F\sigma\sqrt{\pi a}$, where F, the geometrical correction factor of SIF,

Table 1 Chemical composition of AA5454 in wt. %.

Mg	Mn	Fe	Si	Zn	Ti	Cr	Cu
2.85	0.84	0.31	0.13	0.01	0.01	0.08	0.03

Table 2 Mechanical properties of AA5454.

	Base metal	FSW joint
0.2% offset yield point [MPa]	220	125
Tensile strength [MPa]	300	265
Elongation [%]	8	18

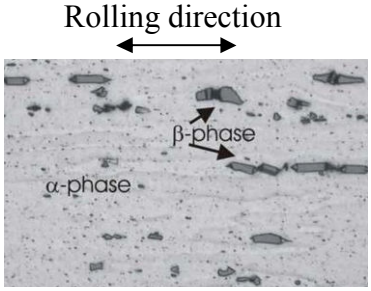

Fig. 1 Microstructure of AA5454.

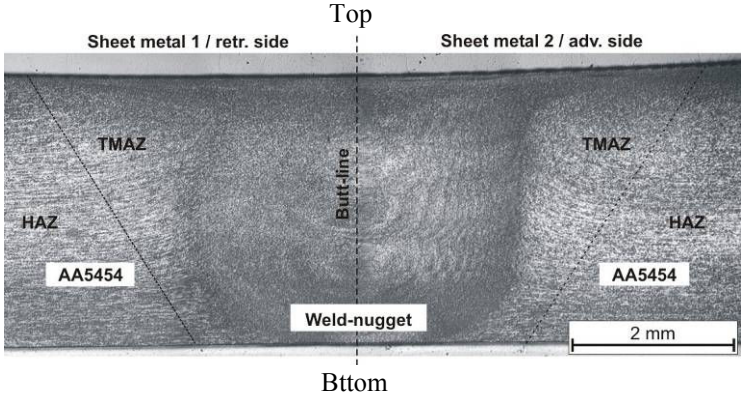

Fig. 2 Micrograph of the cross section of FSW-joint.

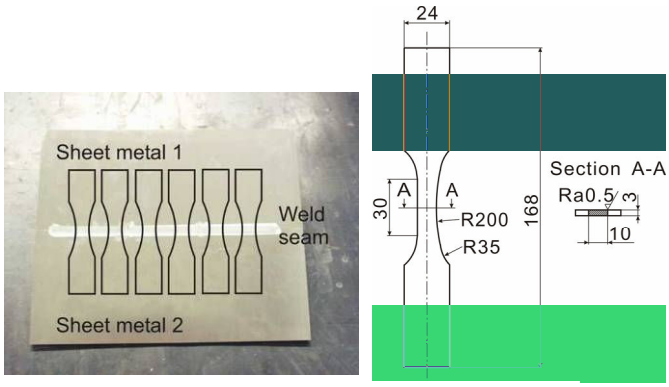

Fig. 3 Extraction position and specimen geometry.

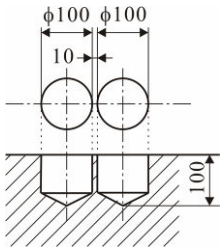

Fig. 4 Two adjacent holes used as a crack starter, in μm; the two holes were aligned in the direction perpendicular to the loading axis.

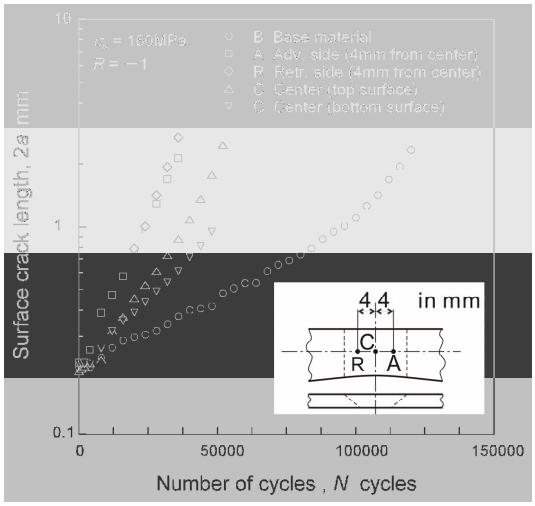

Fig. 5 Relationship between 2*a* and *N*.

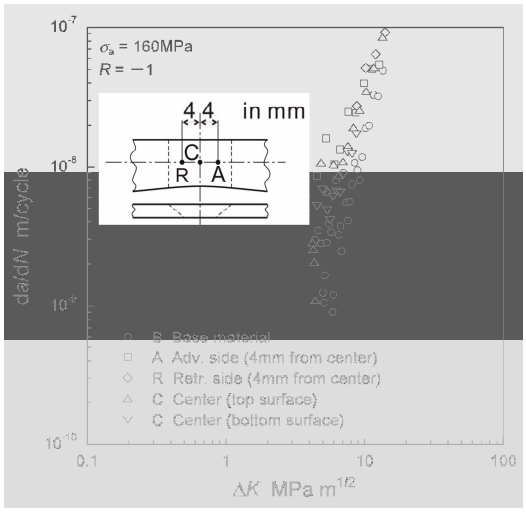

Fig. 6 Relationship between d*a*/d*N* and *ΔK*.

is 0.73 for a semi-circular crack assumed herein, σ is the remote applied stress, and *a* is the crack depth; i.e., half the surface length. The crack growth rates, d*a*/d*N*, differed largely depending on the locations. The highest rate was observed near the interface of TMAZ and HAZ.

Fig. 7 shows the Martens hardness distribution in the welded region. A trapezoidal shape of the softened area was observed. The hardness of base metal was about 1000 whereas that of softened area was reduced to about 700, resulting in a significant difference of the local crack growth rate. From the comparison of Figs. 6 and 7, it is found that the crack growth rate increases with decreasing hardness.

Fig. 8 shows the distributions of axial and radial residual stresses measured on the top and bottom surfaces. The axial residual stress acting in the direction of cyclic stress can affect the fatigue crack growth as a mean stress. However, the change in axial residual stress in the present FSW specimens is small and in addition, the compressive residual stress is larger in the welded region than in the remote parent metal. Therefore, the residual stress is not responsible for the large difference in the crack growth rates.

Fig. 9 shows the path of a crack propagating from a defect that was introduced just on the oxide fragments line on the bottom surface. It is seen that the right hand side of the crack has deviated from the direction normal to the loading axis, relating to the direction of β-phase particles flow that may have been caused by a mechanical action of the welding tool.

Conclusions

The fatigue crack growth behavior was observed in the friction star welded AA5454 aluminum alloy. The crack growth rates differed depending on the locations in the welded region. The hardness had a

good correlation with the crack growth rate. The crack path was influenced by the local anisotropy of the microstructure.

References

[1] G. Wagner, M.Gutensohn, and D. Eifler: *Proceedings of the 7th International Conference on Magnesium Alloys and Their Applications*, Ed: K. U. Kainer (2006),1092-1098.
[2] Y. Sato and H. Kokawa: *Key Engineering Materials*, Vols 345-346 (2007), 1493-96.

Acknowledgements

This work was in part supported by funds from the Center Research Institute of Fukuoka University (No. 081501).

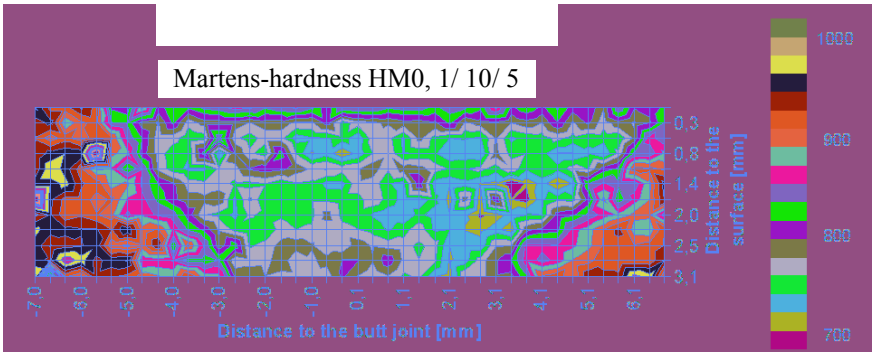

Fig. 7 Martens hardness distribution on the cross section of friction stir welded AA5454–joint.

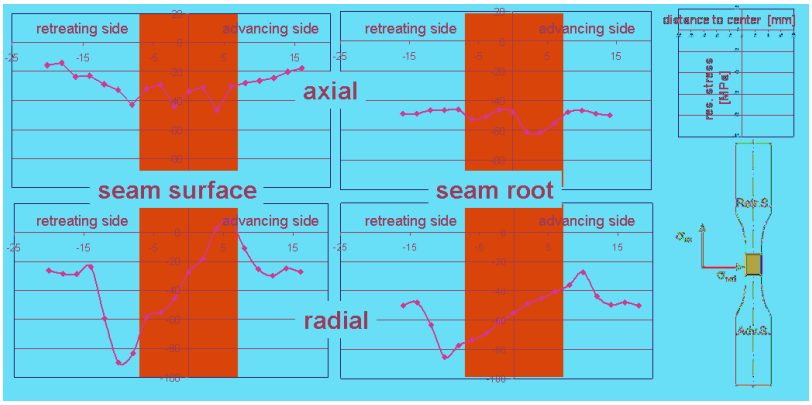

Fig. 8 Residual Stresses in FSW-AA5454-joints after polishing.

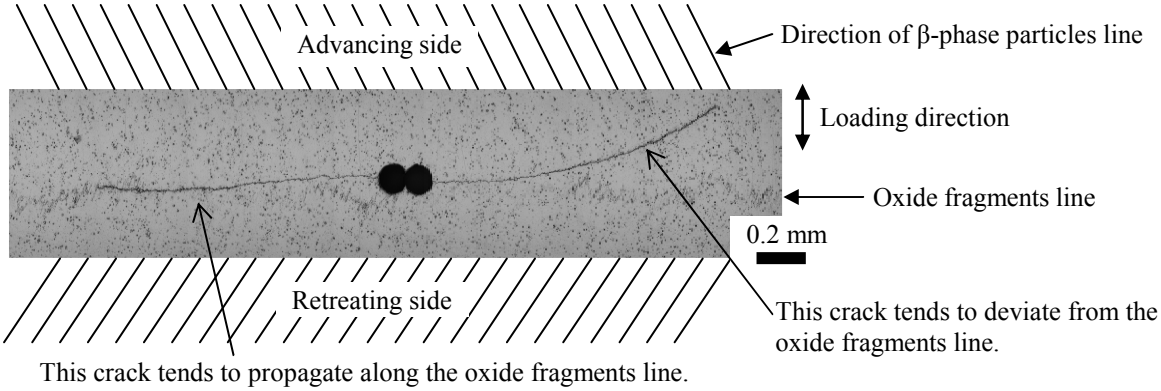

Fig. 9 Path of a crack emanating from a crack starter at central position on bottom surface.

Key Engineering Materials Vols. 385-387 (2008) pp 801-804
© (2008) Trans Tech Publications, Switzerland
doi:10.4028/www.scientific.net/KEM.385-387.801

AN ORIENTATION-DEPENDENT FAILURE CRITERION FOR FCC CRYSTALS

Nam N. Huynh[1a], Cheng Lu[1b], Liangying Si[2,1c], and Kiet Tieu[1d]

[1]School of Mechanical, Materials and Mechatronic Engineering, University of Wollongong, Wollongong, NSW 2500, Australia
[2]State Key Laboratory of Rolling and Automation, Northeastern University, Shenyang, Liaoning 110004, P. R. China
[a] nnh275@uow.edu.au, [b] chenglu@uow.edu.au, [c] lsi@uow.edu.au, [d] ktieu@uow.edu.au

Keywords: orientation-dependent failure criterion, crystal plasticity, FCC crystal, fracture

Abstract. The crystalline orientation significantly affects the fracture behavior of crystals. However, the orientation-dependent failure criterion is still lacking up to now. In this paper the failure criteria for different crystalline planes of aluminum have been developed. The critical normal stresses to separate two parallel crystallographic planes have been calculated based on Morse potential. The critical stresses on four different planes ({100}, {111}, {110} and {120}) were obtained. It has been found that plane {120} had the minimum critical normal stress. The developed failure criteria have been applied in the crystal plasticity finite element method (CPFEM) model to simulate the uniaxial tensile deformation of single crystal aluminum with a notch. The lattice orientation evolution during deformation has been predicted by the CPFEM model. Elements at notch tip reaching predefined orientation-dependent failure criterion were removed from the mesh so that the crack growing could be determined explicitly without any path assumption.

1. Introduction

Simulation of dynamic crack growth in crystalline materials has been widely investigated. Most of these simulation works employed cohesive zone technique to simulate the propagation of crack tip [1-2]. Tang et al. [1] numerically studied the crack growing in a ductile FCC single crystal specifically on (010) plane in [101] direction. Zavattieri et al. [2] investigated the dynamic fragmentation of ceramic microstructures, in which the open-up and growing of micro-cracks were assumed along grain boundaries. The main drawback of above works is that a crack path should be presumed in advance, which is not always realistic. Others employed molecular dynamics method to simulate the crack propagation at the nano scale [3,4], which is more physically based. However, this method is difficult to be applied for polycrystals and large deformation due to limitation of computing time. Another common approach to simulating crack growth is using cell models, which has been widely used to model porous solids and rupture of multi-phase solid or having micro-defects.

Various experimental observations have been reported regarding rupture of bicrystals as well as single crystals [5-8]. Specifically for tensile tests on (100) wafer of single crystal silicon, stretched along the <110> direction, and notched on one edge, Li et al. [5] observed that {110} were dominant cleavage planes. It was also concluded that micro-scale fracture path of single crystal silicon was influenced by both direction of tensile load and orientation of cleavage planes relative to sample surface. These experimental observations indicate that the fracture behaviors of crystals are strongly orientation-dependent. Unfortunately, the failure criteria considering the effect of the crystalline orientation are currently not available [9].

This paper presents an orientation-dependent failure criterion, which has been applied into the crystal plasticity finite element method (CPFEM) model. The uniaxial tensile deformation of single crystal aluminum with a notch has been investigated. The lattice orientation evolution during deformation has been predicted by the CPFEM model. Elements at notch tip reaching predefined

orientation-dependent failure criterion were removed from the mesh so that the crack growing could be determined explicitly without any path assumption.

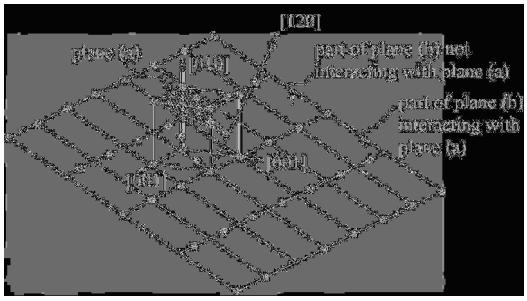

Figure 1. Sketch of two parallel adjacent {120}planes.

2. Simulation model

The failure criterion is defined by critical normal stress required to break atomic bond between two parallel adjacent crystallographic planes. Let us consider force interaction between atoms on, for example, two parallel adjacent {120} planes, as shown in Fig. 1. A unit area of the plane (a), as shown as the hatched region, is considered. It contains three atoms. It is assumed that the atoms on plane (a) are attracted from the atoms on half of plane (b) since a crack exists in another half space. Normal force (F) acting on an atom (i) on plane (a) from atoms on plane (b) is

$$F_i^{(120)} = \sum_{j=1}^{n} f(r_{ij}) \frac{d}{r_{ij}} \tag{1}$$

where r_{ij} is the distance between atom i on plane (a) and atom j on plane (b); d is normal distance between two planes; n is the number of atoms on plane (b), which is chosen to be 22. $f(r_{ij})$ is force between atom i and atom j, defined from Morse potential [10]. The effective force on the hatched region for each atom is one sixth of the force calculated by Eq. (1). Normal stress (σ) acting on plane (a) is approximated by taking the effective total normal force acting on the hatched region divided by its area. We have

$$\sigma^{(120)} = \frac{\sum_{i=1}^{3} \frac{1}{6} F_i^{(120)}}{S} = \frac{\sum_{i=1}^{3} \frac{1}{6} F_i^{(120)}}{\sqrt{5}/4\, a_0^2} \tag{2}$$

where S is the area of the hatched region and a_0 is the lattice constant.

Figure 2 shows the normal stress (σ) on plane (120) versus the distance (d). The normal stress increases with the distance to the maximum of about 330.5 MPa, then decreases. The maximum stress is the critical normal stress. For FCC crystal, there exist four sets of independent crystallographic planes, namely {100}, {120}, {111}, {110}. The critical normal stresses, i.e. failure criteria, for planes {100}, {111}, and {110} are 1755 MPa, 2205 MPa, 750 MPa, respectively. It can be found that critical stress on {120} is minimal and is about two to four times smaller than those on other planes.

A comprehensive review of the crystal plasticity constitutive model was provided in ref. [11]. In this study, the crystal plasticity theory is implemented into the finite element code Abaqus/Standard by means of user-defined subroutine UMAT. The subroutine was originally developed by Huang and has been modified to implement Bassani and Wu's hardening law [12]. Parameters used for hardening law as well as constitutive theory were described in one of our previous studies [13]. Cube (001)[100] initial orientation is assigned to the single crystal. The single crystal is meshed by 40,000 C3D8R elements (8-node linear brick, reduced integration with hourglass control).

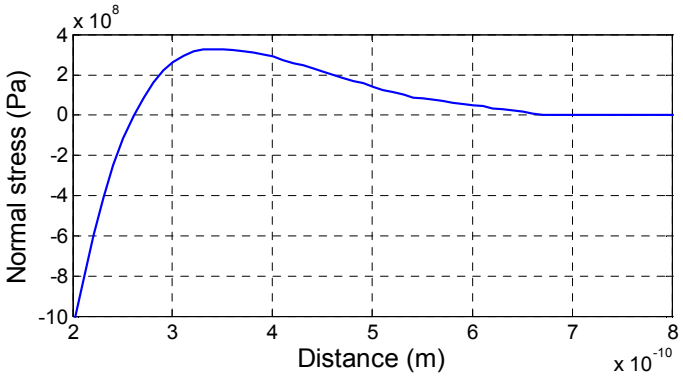

Figure 2. Stress normal to two parallel adjacent {120} planes against normal distance between them

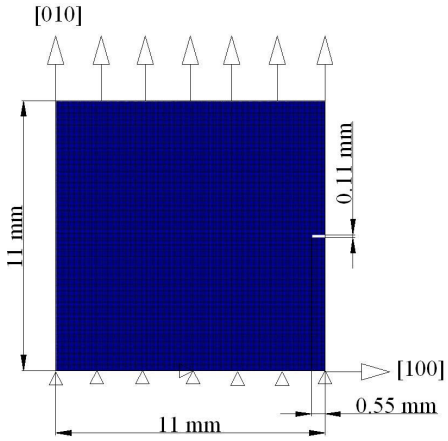

Figure 3. Geometry of notched single crystal, load direction and boundary conditions.

Fig. 3 shows geometry of the single crystal, as well as direction of tensile load applied and initial boundary conditions. The strain rate is 0.01 s^{-1}. Strain load is applied in small loading steps so that elements reaching predefined failure criteria (dead elements) can be detected at the end of each step. The analysis is then saved and restarted. Dead elements, if any, are removed at the beginning of the restarting analysis. Forces exerted by these removed elements on the remaining part of the model are ramped down to zero gradually, so that the effect of the removed region on the whole model is completely absent at the end of the removing step. In the following loading step, calculations are performed on the newly formed mesh.

3. Results and discussions

One main advantage of the theory of crystal plasticity compared to the classic continuum theory is its ability to capture the revolution of crystal orientation during deformation. Stress normal to twelve possible {120} planes are calculated and compared with critical value calculated above to determine crack moving as they revolve under the tensile load.

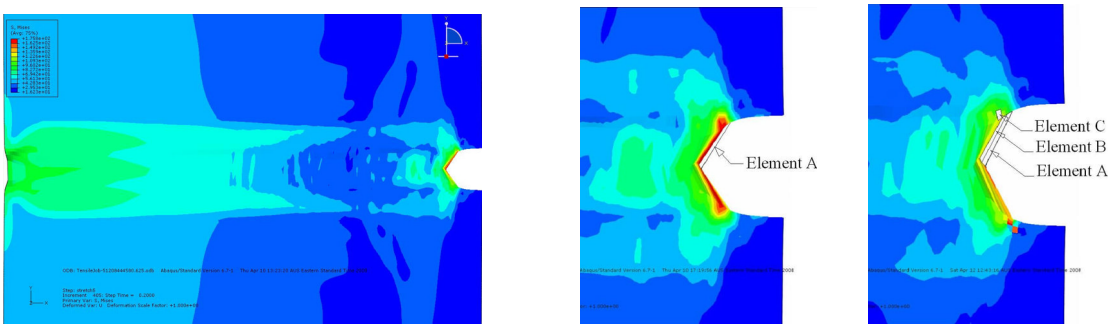

(a) (b) (c)

Figure 4. Mises stresses and results of crack growth using element removal technique.

Mises stress around notch before crack starts moving (dead elements detected) at 8% strain load are shown in Figure 4(a). Figure 4(b) and 4(c) demonstrate the first elements removed at 8% at notch tip and subsequent crack growth at 10% strain, respectively.

Table 1. Angles between normal to {120} planes with [010] and corresponding normal stresses

Planes	(120)	$(\bar{1}20)$	(210)	$(\bar{2}10)$	(102)	$(\bar{1}02)$	(201)	$(\bar{2}01)$	(012)	$(0\bar{1}2)$	(021)	$(0\bar{2}1)$
Stress (Mpa)	177.1	379.9	178.1	380.9	281.1	274.3	282.7	275.9	275.4	279.3	276.0	280.0
Angles (deg)	75.1	26.1	110.4	21.6	123.7	85.2	139.1	58.6	86.9	121.6	62.7	133.9

Angles between loading direction [010] and vectors normal to {120} planes are listed in Table 1 together with their corresponding normal stresses for element A in Fig. 4a prior to its removal. The maximum normal stress occurs on plane $(\bar{2}10)$, which also has the minimum angle with loading direction. The same tendency is obtained for element B and C.

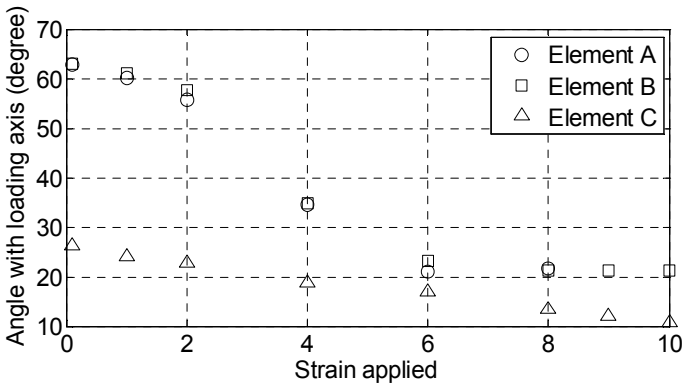

Figure 5. Angles between normal to ruptured planes with loading axis versus strain applied.

Further analysis of lattice orientation in these elements along loading history also reveals that vectors normal to planes reaching the damage criteria evolve toward the loading axis, as shown in Fig. 5. This agrees well with conclusion made from experimental observations by Li et al. [4] that dominant cleavage planes are normal to the principal tensile stress.

4. Conclusions

In this paper the critical normal stresses to separate two parallel crystallographic planes have been calculated based on Morse potential. The critical stresses on four different planes ({100}, {111}, {110} and {120}) have been obtained. It has been found that plane {120} has the minimum critical normal stress. The developed failure criteria have been applied in the crystal plasticity finite element method (CPFEM) model to simulate the uniaxial tensile deformation of single crystal aluminum with a notch. The orientation evolution during deformation has been predicted by the CPFEM model. Elements at the notch tip reaching predefined orientation-dependent failure criterion were removed from the mesh so that the crack growth could be determined explicitly without any path assumption.

References

[1] H. Tang, Y.S. Choi, A. Acharya, S. Saigal: *J. Mech. Phys. Solids*, vol. 52, (2004), p. 2841.
[2] P.D. Zavattieri, H.D. Espinosa: *Acta Mater.*, vol. 49, (2001), p. 4291.
[3] H. Rafii-Tabar, L. Hua, M. Cross: *J. Phys.: Condensed Matter*, vol. 10, (1998), p. 2375.
[4] B. Wang, V. Karuppiah, H. Lu, S. Roy, R. Komanduri: *Mech. Adv. Mater. Struct.*, vol. 12, (2005), p. 471.
[5] J.W. Kysar: *Acta Mater.*, vol. 48, (2000), p. 3509
[6] J.S. Wang, P.M. Anderson: *Acta Metall. Mater.*, vol. 39, (1991), p. 779.
[7] G. Elssner, D. Korn, M. Rühle: *Scripta Metall. Mater.*, vol. 31, (1994), p. 1037.
[8] X. Li, T. Kasai, S. Nakao, H. Tanaka, T. Ando, M. Shikida, K. Sato: Transducers, (2003), p.444.
[9] S. Hao, W.K. Liu, C.T. Chang: *Comp. Methods App. Mech. and Eng.*, vol. 187, (2000), p. 401.
[10] R.C. Lincoln, K.M. Koliwad, P.B. Ghate: *Phys. Rev. Vol.157, (1967), p. 463.*
[11] R.J. Asaro: *Adv. Appl. Mech.*, vol. 23, (1983), p. 1.
[12] Y.G. Huang, *Mech Report 178*, Division of Engineering and Applied Sciences, Harvard University, Cambridge, Massachusetts.
[13] N.N. Huynh, C. Lu, L. Si, K. Tieu, *J. Eng. Tribology*, (2008) accepted for publication.

Key Engineering Materials Vols. 385-387 (2008) pp 805-808
© (2008) Trans Tech Publications, Switzerland
doi:10.4028/www.scientific.net/KEM.385-387.805

Influence of Rolling Reduction on Fatigue Behaviour of AA6016/FeP06 Material Compound

Abdelrhani Lamik, Heinz Leitner , Wilfried Eichlseder

Chair of Mechanical Engineering, University of Leoben, Austria

Abdelrhani.lamik@unileoben.ac.at, Heinz.leitner@unileoben.ac.at, Eichlseder.wilfried@unileoben.ac.at

Keywords: material compound, rolling reduction, AA6016/FeP06, simulation model, hardening.

Abstract. The goal of this research project is the development of a simulation model for lifetime estimation of components manufactured from the AA6016-T4/FeP06 material compound.
Components composed of this material are manufactured predominantly by rolling and deep-drawing. For this reason, the influence of the plastic deformations during the manufacturing process on the fatigue behaviour must be investigated. Particularly the cyclic hardening behaviour of FeP06 steel has a relevant effect on the fatigue life of this aluminium-steel compound. Simulation models for fatigue life estimation therefore have to consider the influence of this hardening effect, which occurs during the manufacturing process. In this work, test results and a simulation model to take into account the influence of the rolling reduction on the fatigue behaviour of components manufactured from the AA6016/FeP06 material compound are presented.

Introduction

Many areas of mechanical engineering are characterized by a permanent development of components and modules with the aim of reducing weight, increasing reliability, under the consideration of physical properties such as corrosion resistance or thermal conductivity. In many cases conflicting requests do not allow for the finding of a solution with a single specific material. New material compounds are suitable for new application areas. Each single material of the compound has specific advantages. A carefully selected material combination is a prerequisite for the construction of components that exhibit the advantages of each material used. Often a combination of different materials is the only possibility to achieve the desired goal. In addition to the described requirements above, the component must exhibit appropriate fatigue strength, i.e. sufficient durability under cyclic load as described by the S/N-curve. The strength of a material in a component under operating conditions is not identical with the strength, which is determined on idealised specimens under laboratory conditions. The local fatigue strength in the component is influenced by rolling reduction, stress concentrations, forming process, residual stress and by other factors. The local effects have to be allocated to their fatigue behaviour; (they have to be matched).
Afterwards, the influences of these effects can be considered in a step by step simulation.
In this investigation, each component of the material compound (AA6016-T4 and FeP06) was first analysed separately, and then the material compound itself was studied. The characterization of the AA6016-T4/FeP06 material compound was introduced in [1].

Overview of the manufacturing process of the material compound

The material compound was manufactured using the roll-bonding process. Before rolling, the aluminium and steel sheets were degreased. Then the surfaces of the sheets were scratch brushed. The pressure in the roll gap elongates the strips and causes the interface layers to break up simultaneously. The underlying metal is then exposed and extruded under the action of the roll pressure through widening cracks in the surface layers. The freshly created metal surfaces come into intimate contact and are welded together. The welding quality is affected by the rolling reduction,

the metal under consideration, the welding temperature, pressure, welding duration, lattice structure, solubility of oxygen in the metal, metal purity and surface preparation. The mechanism of cold pressure welding is explained in detail in [2] [3]. An investigation of the deformation behaviour and bonding strength of the bimetal strip is presented in detail in [4] [5] and [6]. Furthermore, bonding does not occur until a threshold deformation of 20% reduction of the thickness has been reached.

Influence of the rolling reduction on the fatigue behaviour

According to literature [4] [7] and experimental investigations, a heat treatment (solution annealing at 540 °C) of the material compound is optimal to obtain a good bond strength. Material hardening occurs during the manufacturing of the material compound by cold rolling. Due to the heat treatment at 540°C, a recrystallization of the AA6016 occurs. Therefore mechanical behaviour of the material can be considered independent from the manufacturing process and there is no influence of the rolling reduction on the mechanical properties of AA6016 (see Fig.2). In fact, 540°C is too low to cause a recrystallization of the material FeP06. Hence, the influence of the cold rolling reduction which causes a hardening of the material FeP06 represents the main influence factor that has to be considered in this simulation model. A series of rolling experiments were carried out using several rolling reductions to investigate the influence of the plastic deformation due to rolling process on the static and cyclic behaviour of the steel.

Influence of rolling reduction on static and cyclic behaviour of AA6016-T4

Fig.1 and Fig.2 show the influence of the rolling reduction (RR) on the static and cyclic material behaviour of the AA6016-T4, respectively. As a result of the heat treatment at 540°C (recrystallization effect), this influence is still marginal for both static and fatigue behaviour. Hence, the influence of the rolling reduction on fatigue life of the AA6016-T4 will not be considered in the presented simulation model.

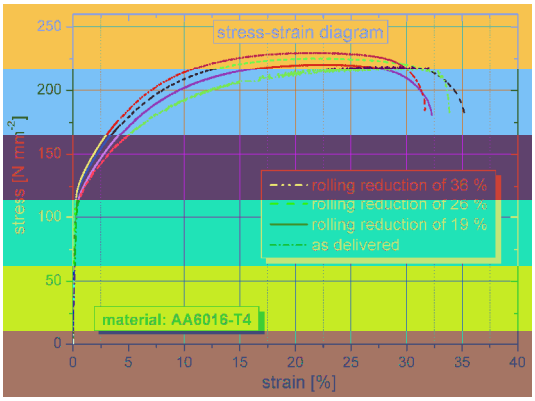

Fig.1: Influence of the RR on the static material behaviour

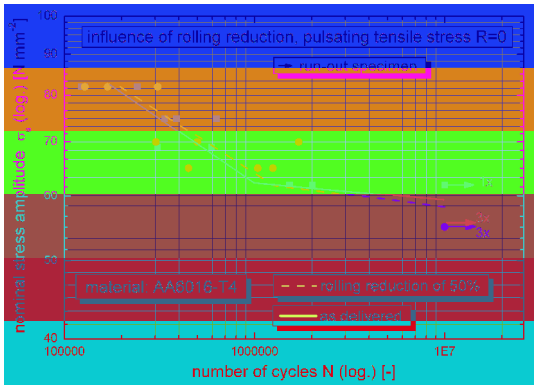

Fig.2: Influence of the RR on the cyclic material behaviour

Influence of rolling reduction on static mechanical properties of FeP06

Tensile tests were performed on specimens which were machined from plates with different rolling reductions (as delivered, 16%, 19%, 25% and 37%). The influence of the rolling process on the mechanical properties is significant. The yield strength $R_{p0.2}$, the ultimate tensile stress R_m and the fracture stress σ_B were established as an empirical function of the RR, see Equ. (1).

$$R_{p0.2} = 78.9 \cdot \ln(RR) + 82.9$$
$$R_m = 89.9 \cdot \ln(RR) + 78.5 \qquad \text{Equ. (1)}$$
$$\sigma_B = 75.7 \cdot \ln(RR) + 314.9$$

Influence on cyclic material behaviour, pulsating tensile stress

Several fatigue tests (see Fig.3) were performed in order to find a model that describes the fatigue behaviour as a function of the rolling reduction. On the basis of these results the properties of the S/N curve (fatigue limit σ_D, slope k and the number of cycles at fatigue limit N_D) were established as a function of the rolling reduction (RR) using logarithmic approximation, Equ. (2).

$$\sigma_D = 34.1 \cdot \ln(RR) - 59.3$$
$$k = 9.1 \cdot \ln(RR) - 6.9 \qquad \text{Equ. (2)}$$
$$N_D = 1902000 \cdot \ln(RR) + 395300$$

Influence on cyclic material behaviour, tension/compression

Fig.4 shows S/N curves for the material FeP06 under tension/compression (*R=-1*) at different rolling reductions. The relation between the properties of the S/N curve and the rolling reduction is shown in Equ. (3).

$$\sigma_D = 46 \cdot \ln(VG) + 45$$
$$k = 12.2 \cdot \ln(VG) - 25.4 \qquad \text{Equ. (3)}$$
$$N_D = 5147000 \cdot \ln(VG) - 12980000$$

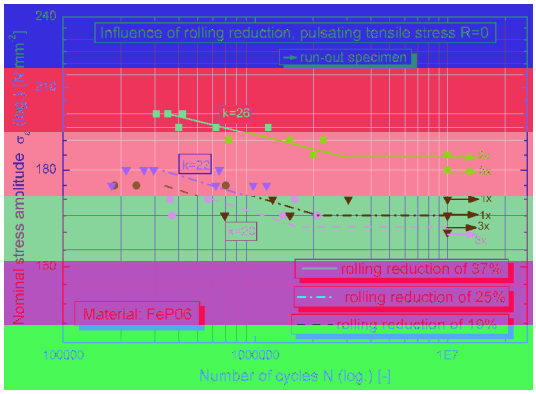

Fig.3: Influence of the RR on the cyclic behaviour, R=0

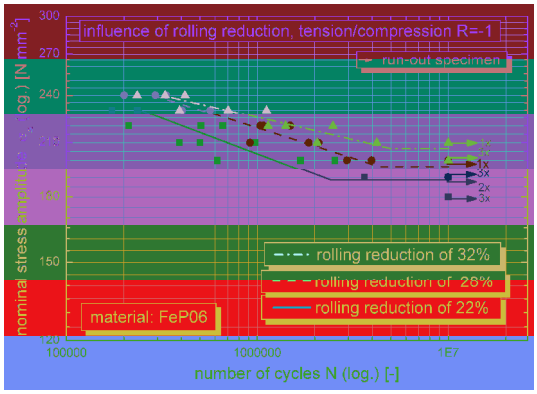

Fig.4: Influence of the RR on the cyclic, R=-1

Verification of the generated models for lifetime estimation

The material compound is manufactured by means of the deep drawing technique. We therefore used a simple drawn part, in this case a component with a cup shape, to verify the simulation model. Several fatigue tests were performed at stress ratio of R=0,1. The results of the fatigue tests were compared to the simulation results. The lifetime estimation shows a considerable improvement of accuracy by the consideration of the influence of the rolling reduction, see Fig. 5.

Conclusion

Due to the conflict between the requirements (low weight and high strength), the design of components from a thin sheet of metal manufactured of different compounds, still poses optimisation problems. To reduce the development effort, it is important to minimize the number of prototypes. Therefore the use of a simulation model to predict behaviour is necessary for component optimisation. A computation concept is presented for the lifetime estimation of cyclic loaded components from an Al6016-T4/FeP06 material compound. This considers the influence of the rolling reduction as the main influence factor on the lifetime of such components. A yield curve as a

function of the rolling reduction of the material FeP06 was also generated during this research project [8]. This curve is the basis for every elastic plastic deep drawing simulation. To verify this simulation model, fatigue tests on the component itself were performed. The lifetime estimation shows a considerable improvement of accuracy by the consideration of the influence of the rolling reduction. The consideration of the forming ratio during the deep drawing process [9] changes marginally the accuracy of lifetime estimation.
In order to approve the general applicability of this model, other materials have also to be tested.

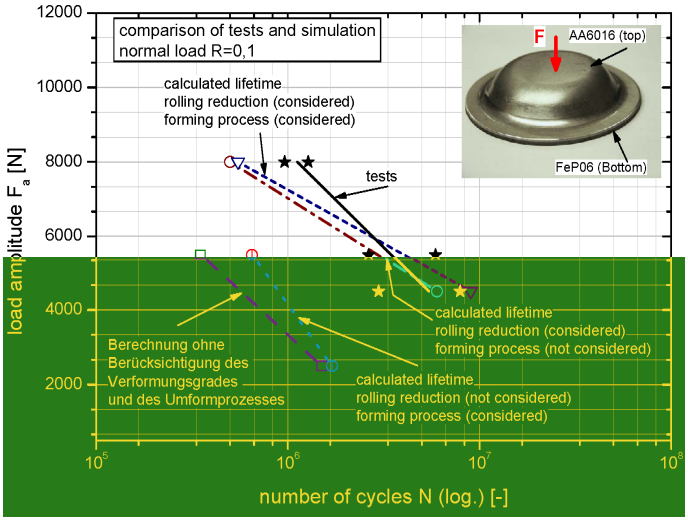

Fig. 5: comparison of tests and simulation

References

[1] A. Lamik, H. Leitner, W. Eichlseder, F. Riemelmoser: *A Study of the fatigue behaviour of an aluminium-clad steel material compound*, submitted to Strain Journal 2007.

[2] J. A. Cave, J.D. Williams: *the mechanism of cold pressure welding by rolling*, Department of Mechanical engineering, Ashby Institute, Journal of the institute of metals, Vol. 101, 1973.

[3] K. J. B. McEwan, D. R. Milner: *pressure welding of dissimilar metals*, Department of Industrial Metallurgy at Birmingham University, British welding journal, July 1962.

[4] H. Danesh Manesh, A. Karimi Taheri: *bond strength and formability of an aluminium-clad steel sheet*, Journal of Alloys and Compounds 361, 2003, 138-143.

[5] H. Danesh Manesh, A. Karimi Taheri: *an investigation of deformation behavior and bonding strength of bimetal strip during rolling*, Mechanics of Materials 37, 531-542, 2005

[6] T. Mori and S. Kurimoto: *press-formability of stainless steel and aluminum clad sheet*, Journal of Materials Processing Technology 56, 242-253, 1996.

[7] H. Danesh Manesh, A. Karimi Taheri: *the effect of annealing treatment on mechanical properties of aluminium clad steel sheet*, Materials & Design 24, 617-622, 2003.

[8] A. Lamik, H. Leitner, W. Eichlseder, F. Riemelmoser: *A concept for the fatigue life prediction of components from an aluminium-steel compound*, seventh international ASTM/ESIS, Tampa 2007, submitted to journal of ASTM International.

[9] R. Masendorf: *Einfluss der Umformung auf die zyklischen Werkstoffkennwerte von Feinblech*, TU-Clausthal, Dissertation 2000.

Key Engineering Materials Vols. 385-387 (2008) pp 809-812
© (2008) Trans Tech Publications, Switzerland
doi:10.4028/www.scientific.net/KEM.385-387.809

Dynamic Stability of Lateral Vibration of Bottom Hole Assemblies

Guanghui Zhao[a], Zheng Liang[b]

Mechatronic Engineering College, Southwest Petroleum University, Chengdu 610500, China

[a]wy_zgh@yahoo.com.cn, [b]liangz_2242@126.com

Keywords: Bottom hole assemblies, parametric resonance, air drilling, mud drilling.

Abstract. Bottom hole assemblies (BHA) of oil drilling engineering were simplified as simply supported beam, and parametric resonances of BHA in mud drilling and air drilling were studied. Lateral vibration of BHA, which was induced by bit/formation interaction, was described and reduced into Mathieu equation by means of separation of variables and Galerkin method. Modified strained parameter method was adopted in stability analysis. The parametric resonance zones expressed by weight on bit (WOB) are presented here. It is found that drilling method, speed of rotation (SOR), material properties, and length of compression drillstring all can influence parametric resonance zones. So unstable responses can be avoided by adjusting these parameters.

Introduction

BHA of drilling engineering is subjected to axial compression under drilling working condition. Rapidly growing lateral vibrations triggered by axial vibration (induced by WOB fluctuation) is known in mechanics as the parametric resonance phenomenon, and may happen when the energy associated with axial vibrations is diverted to lateral vibrations [1]. As a result, drillstring would collide with borehole wall severely. It is found that bending stress wave induced by this collision is the main cause of early failure of drillstring. Parametric resonance differs fundamentally from the conventional resonance. In conventional resonance, the critical frequency spectrum is made up solely of the discrete set of natural drillstring frequencies. In parametric resonance, however, this spectrum is a set of bands. Avoiding parametric resonance is an important way to protect drillstring from severe collision, and therefore decrease fracture failure of drillstring.

Stability Model

BHA is simplified as simply supported elastic beam with uniformity and homogeneous section. Severe lateral vibration may happen when the beam is loaded by longitudinal compressive force that fluctuates periodically in time. Considering the drilling fluid that flows inside and outside the drillstring, and simplifying the gravity of BHA as two compressive single forces that exerts on both end of the beam, the governing equation of lateral vibration of BHA could be derived as follow [2]:

$$L[y(x,t)] = \frac{EI}{M}\frac{\partial^4 y}{\partial x^4} + \frac{\left(F_0 + P_t \cos \Omega t\right)}{M}\frac{\partial^2 y}{\partial x^2} + \frac{2m_d v}{M}\frac{\partial^2 y}{\partial x \partial t} + \frac{\partial^2 y}{\partial t^2} = 0. \tag{1}$$

In which, $F_0 = P_0 - W_e l/2 + m_d v^2$, $M = m_d + m_c + \pi D^2 \rho_d C_d / 4$. y is lateral deflection of drillstring and x is the axial direction. P_0 is the constant part of WOB. P_t and Ω are the amplitude and frequency of fluctuating WOB respectively; in which Ω is usually three times of SOR for three cone bits and is called parameter-induced frequency. W_e is the buoyant weight of drillstring for unit

length, m_c and m_d are mass of drillstring and drilling fluid for unit length respectively. ρ_d is density of drilling fluid. l is length of the compression section of drillstring. v is velocity of drilling fluid inside the drillstring. C_d is associated mass coefficient, which is due to the effect of drilling fluid in annular space on the lateral vibration of drillstring. Regardless of compressibility and viscosity of drilling fluid, it can be derived as: $C_d = (D_w^2 + D^2) / (D_w^2 - D^2)$, where D_w is diameter of borehole. The solution of Eq. (1) is assumed to have the form of separated variables, and could be approximated as the sum of symmetric and anti-symmetric spatial modals. That is suitable to the term $\partial^2 y / (\partial x \partial t)$ and simply supported boundary conditions.

$$y(x,t) = \sum_{n=1,3,5,\cdots} u_n(t)\sin(n\pi x / l) + \sum_{n=2,4,6,\cdots} u_n(t)\sin(n\pi x / l). \tag{2}$$

By means of Galerkin method, Eq. (1) can be reduced as:

$$\int_0^l L[y(x,t)]\sin(n\pi x / l)dx = 0, \quad n = 1,2,3,\cdots \tag{3}$$

When n is odd, Eq. (3) is rewritten as follow (If n is even, we have the similar equation form):

$$\frac{\partial^2 u_n(t')}{\partial t'^2} + \omega_n^2 u_n(t') + 2\varepsilon_n \cos 2t' \cdot u_n(t') + \sum_{m=2,4,6,\cdots} \varepsilon^* \mu_{nm}^* \frac{\partial u_m(t')}{\partial t'} = 0. \tag{4}$$

In which,

$$\omega_n^2 = \frac{4}{\Omega^2}\left[\frac{EI}{M}\left(\frac{n\pi}{l}\right)^4 - \frac{F_0}{M}\left(\frac{n\pi}{l}\right)^2\right];\ 2\varepsilon_n = \frac{4P_t}{M\Omega^2}\left(\frac{n\pi}{l}\right)^2;\ \varepsilon^*\mu_{nm}^* = \frac{8m_d v}{lM\Omega}\cdot\frac{2mn}{n^2-m^2};\ t' = \frac{2}{\Omega}t. \tag{5}$$

Generally, there is no multiple's relation between ω_n with different n. So when a certain ω_n of Eq. (4) is near to the multiple of parameter-induced frequency Ω, the natural frequency of lateral vibration for other n is not close to the multiple of Ω. As a result, the terms in Σ of Eq. (4) have no effect on stability analysis. Considering that the term with cosine function is uncoupled, the stability analysis of Eq. (4) equals to that of the following system:

$$\frac{\partial^2 u_n(t')}{\partial t'^2} + \omega_n^2 u_n(t') + 2\varepsilon_n \cos 2t' \cdot u_n(t') = 0. \tag{6}$$

Dynamic Stability Analysis

Eq. (6) is Mathieu equation. The following analysis is suitable for all the values of n, and the subscript n and prime on time variable are omitted. Here ω_n is rewritten as:

$$\omega_n^2 = \omega_{n0}^2 + (\omega_1 - 2)\varepsilon + \omega_2'\varepsilon^2 + \cdots \tag{7}$$

Because that ε, which is related to fluctuating WOB, is not always small, modified strained parameter method [3] is adopted and a new small parameter is introduced as: $\alpha = \omega_1\varepsilon/(1+\omega_1\varepsilon)$. In which $|\omega_1\varepsilon| < |1+\omega_1\varepsilon|$ is satisfied. So ε, ω_n and u can be described by α as: $\varepsilon = \omega_1^{-1}(\alpha + \alpha^2 + \cdots)$, $\omega_n^2 = \omega_{n0}^2 + (\omega_1 - 2)\omega_1^{-1}\alpha + \omega_2\alpha^2 + \cdots$ and $u = u_0 + \alpha u_1 + \alpha^2 u_2 + \cdots$, where $\omega_{n0}^2, \omega_1, \omega_2', \omega_2, \cdots$ are all arbitrary constants. Inserting the above expressions into Eq. (6), comparing the terms with the same power of α and eliminating secular terms, returning the variables into ε and ω_n, the transition curve of natural frequency between stable and unstable dynamic responses of drillstring could be derived.

Under the condition of ω_{n0}=1. This condition corresponds to the case that natural frequency of the linearly derived system of Eq. (6) equals to the parameter-induced frequency Ω. The parametric resonance zone, which is called secondary parametric resonance zone, is the area that is limited by the two curves as follow:

$$\omega_n^2 = 1 - \frac{\varepsilon}{1+\varepsilon} - \frac{9}{8}\cdot\left(\frac{\varepsilon}{1+\varepsilon}\right)^2; \qquad \omega_n^2 = 1 + \frac{1}{3}\cdot\frac{3\varepsilon}{1+3\varepsilon} + \frac{23}{72}\cdot\left(\frac{3\varepsilon}{1+3\varepsilon}\right)^2. \tag{8}$$

For certain SOR, this unstable zone described by P_0 and P_t is got by inserting Eq. (5) into Eq. (8):

$$\begin{cases} P_0 = \dfrac{1}{EM}\left[AM - \dfrac{\Omega^2}{4} + \dfrac{\Omega^2}{\dfrac{2\Omega^2}{EM\cdot P_t}+4} + \dfrac{9\Omega^2}{8}\left(\dfrac{1}{\dfrac{\Omega^2}{EM\cdot P_t}+2}\right)^2\right] \\ P_0 = \dfrac{1}{EM}\left[AM - \dfrac{\Omega^2}{4} - \dfrac{\Omega^2}{\dfrac{2\Omega^2}{EM\cdot P_t}+12} - \dfrac{23\Omega^2}{8}\left(\dfrac{1}{\dfrac{\Omega^2}{EM\cdot P_t}+6}\right)^2\right] \end{cases}. \tag{9}$$

Where:

$$AM = [EI(n\pi/l)^4 + (W_e l/2 - m_d v^2)(n\pi/l)^2]/M, \quad EM = (n\pi/l)^2/M \ , n=1,\ 2,\ 3,\ \ldots \tag{10}$$

From the unstable zone expressed by Eq. (9) and Eq. (10), we could see that SOR (which is related to Ω), length of compression section (l), the mechanical behavior of drillstring and drilling fluid (EI, W_e, m_d, v) and so on all can influence the location of parametric resonance zone. So it is possible to avoid parametric resonance by adjusting these parameters.

Under the condition of ω_{n0}=2. This condition corresponds to the case that natural frequency of the linearly derived system of Eq. (6) equals to Ω/2. The parametric resonance zone, which is called principal resonant zone, could be derived similarly and described by P_0 and P_t as follow:

$$P_0 = \frac{1}{EM}\left[AM - \Omega^2 - \frac{5\Omega^2}{12}\left(\frac{1}{\dfrac{\Omega^2}{EM\cdot P_t}+4}\right)^2\right]; \quad P_0 = \frac{1}{EM}\left[AM - \Omega^2 + \frac{\Omega^2}{12}\left(\frac{1}{\dfrac{\Omega^2}{EM\cdot P_t}+4}\right)^2\right]. \tag{11}$$

In the case of air drilling, the effect of air flowing on the dynamic stability of drillstring could be ignored. So AM and EM in expressions (10) could be simplified.

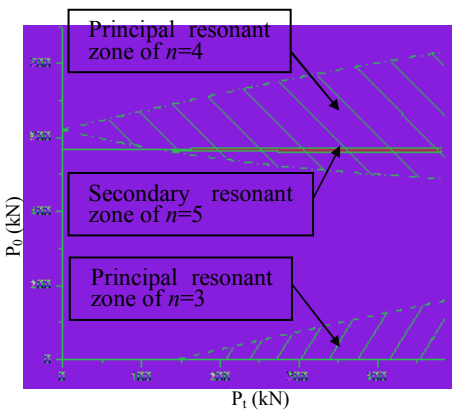

Fig. 1 Parametric resonance zones in air drilling with SOR=60rpm.

Case Study and Numerical Results

Here BHA is simplified as drill collar with outer and inner diameters as D=203mm and d=71.44mm respectively. The other mechanical and size parameters are chosen as follows: m_c=228.28kg/m, E=206×10^{9}Pa, D_w=314mm, T=120kN. The length of this model is chosen as that of compression section in air drilling as: l=T/($m_c g$)=53.585m. For mud

drilling, ρ_d=1200kg/m^3, and rate of flow is Q=0.025m^3/s.

Fig. 1 shows the parametric resonance zones in air drilling with SOR being 60rpm. From which we find that principal resonance zone is much larger than secondary resonance zone, and several resonance zones with different modals coexist (The 3rd, 4th, and 5th resonant modals coexist in the parametric ranges of Fig. 1). When the values of WOB fall in the resonance zones, rapidly growing lateral vibrations triggered by axially fluctuated WOB would happen. Fig. 2 is comparison of the 4th principal parametric resonance zones between air drilling and mud drilling for SOR being 80rpm. It presents that parametric resonance zone occupies different area for different drilling methods. Fig. 3 illustrates the influence of SOR on principal parametric resonance zone in air drilling. From Fig. 3(a) we can see that the location of unstable zone would shift remarkably for different SOR. Fig. 3(b) is derived from Fig. 3(a), and shows ΔP_0, the span of P_0 that corresponding to certain P_t, varying with P_t. It illustrates that the area of unstable zone is larger along with higher SOR. As a result, it's possible to avoid parametric resonance by adjusting SOR or drilling method.

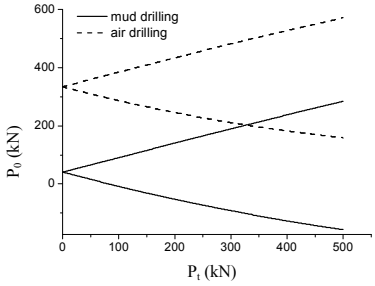

Fig.2 Comparison of the 4th principal parametric resonance zones for SOR=80rpm.

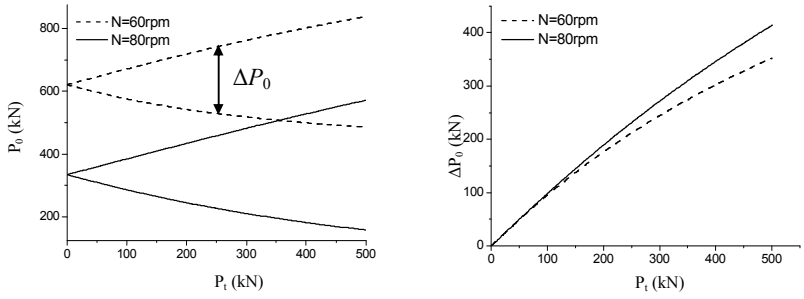

(a) (b)

Fig.3 Comparison of the 4th principal parametric resonance zones in air drilling.

Conclusion

BHA is in a compressive state longitudinally under drilling working condition. Severe lateral vibrations, which are induced as a result of axial excitations caused by bit/formation interaction, may happen under some conditions. Here the parametric resonance zones, which are described by the fluctuating amplitude and constant part of WOB, are derived for air drilling and traditional mud drilling. Influence of drilling method and SOR on the unstable dynamic response is discussed.

It's found that parametric resonance of BHA may happen under many modals. The area covered by parametric resonance will increase along with larger SOR. The locations of parametric resonance zones in parametric plane (P_0, P_t) shift obviously when SOR or drilling method changes. Apart from SOR and drilling method, other factors such as material properties, length of compression drillstring and so on can also influence parametric resonance zones. As a result, it is possible to avoid parametric resonance by varying these parameters.

Acknowledgements

This work is supported by Key Laboratory of Oil and Gas Equipment from Ministry of Education (2006STS02) and Science Foundation of Southwest Petroleum University.

References

[1] V.A. Dunayevsky, F. Abbassian and A. Judzls: SPE 14329 (1993), p.84
[2] Zheng Liang, X. Deng and X. L. Yu: Well Testing Vol. 8 (1999), p. 5
[3] Y.W. Yuan, W. Zhang: Chinese Journal of Applied Mechanics Vol. 17 (2000), p.128

Key Engineering Materials Vols. 385-387 (2008) pp 813-816
© (2008) Trans Tech Publications, Switzerland
doi:10.4028/www.scientific.net/KEM.385-387.813

Shape Optimization of Metal Welded Bellows Seal based on the Turing Reaction-diffusion Model coupled with FEM

Mamtimin Geni[1a] and Masanori Kikuchi[2b]

[1]School of Mechanical Engineering, Xinjiang University, Urumqi, China, 830008
[2] Mechanical Department, Tokyo University of Science, Noda,Chiba,278,Japan

[a] mgheni@263.net, [b]kik@me.noda.tus.ac.jp

Key Words: Reaction-diffusion Model, FEM, iBone, Metal Welded Bellows, Flexibility

Abstract. In this paper, the Turing reaction-diffusion model coupled with Finite Element Method (FEM) is implemented first by considering the biomechanical model iBone (Imitation Bone). Then the shape optimization of Metal Welded Bellows Seal (MWBS) is conducted based on the biomechanical bone forming process by considering the osteoclasts and osteoblasts process. The MWBS mass and shape is changed by changing the initial boundary condition, then some reasonable results are obtained by keeping the required forming value, and the new S type wave of metal welded bellow of mechanical seal are obtained. Finally, the strength evaluations are conducted for new optimized S type model and original V and S type models by using the FEM software.

Introduction

The mechanical properties of the metal welded seal are strongly affected by the structures of the wave. In order to improve the life-span and durability of the metal welded bellow, the structure of the bellow wave should be improved. If the design requirements were satisfied, bellow shapes and parameters were chosen properly, the manufactures not only be able to save materials, but also decrease the cost of the bellow.

Bellows is the sealed elastic component of welded metal bellows machinery. Its main function, in order to compensate and buffer the ring of moving to wear and tear, the axial displacement is reasons, such as a bunch of quantity of axial and vibration etc. In addition, bellows also plays a role in enabling working up the ring to rotate with the rotation axis. Bellows also to utilize elastic strength of bellows make sealed terminal surface produce a certain one than pigeonhole together with sealed medium pressure, make the terminal surface produce certain bearing capacity and play a sealed role[1]-[2].

The V, U and S type shape of welded metal bellows are widely used in practical application. The shape of the bellows largely affects the welded metal bellows mechanical characteristics and technical targets. However, how to get the optimized shape of the welded metal bellows still the open question.

Numerical Model for Shape Optimization

In this study the iBone model based on the reaction-diffusion model is used for the shape optimization of welded metal bellows. The reaction-diffusion model was firstly proposed by Turing and has been studied in various fields, such as chemistry and biology[3]. Testuka observed the cell condensation patterns in his previous work and the results shown similar to these Turing patterns, and then introduce iBone model[4]. This model was made by assumption of bone remodeling and

assumed that bone formation and resorption are proportional to local concentrations of activator and inhibitor in reaction-diffusion system, respectively. The local stress was introduced into the differential equation of the activator to make the entire reaction respond to it. In this model bone formation occurred near the stress concentration area and bone resorption activity occurs where the surrounding stress concentration smaller area. This model required only one global parameter that determined the balance between total bone formation and resorption. All the other information was obtained locally and the cells communicated each other via diffusion of local factors.

The hypothetical bone remodeling behaves as a shape adaptation system to the given stress in iBone model, and by using a simple two dimensional model considering the reaction-diffusion system by using main variables activator A and inhibitor I[4] .

Numerical Results of Shape Optimization

The structure of the metal welded bellow seal is given as the Fig1. A welded metal bellow is a kind of pipe, which is delicately welded with many slices so that the bellow can be flexible and bendable. Punching a hole into a slice of bellow forms the slice. The two punched-hole pieces of bellow are welded together at the inner edge so that the centers are the same. Many of these two-welded slices can be welded together at the outer edge. In this way a welded metal bellow is completed as shown below in Fig1 (d). Composing a bellow in this way will allow the bellow to work smoothly in the same axial direction with the other components in the seal. Many types of bellows shapes are used as a seal component. Based on the shape of the bellow wave, there are three types of bellows as shown in Fig. 1(a),(b),(c).

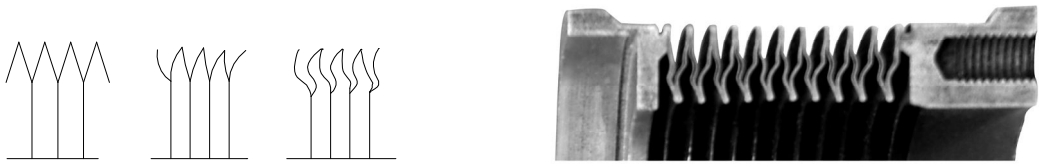

(a) V-type (b) U-type (c) S-type (d) Cross Section of S-type Bellow

Fig.4 Shapes of the bellow wave

For the shape optimization, due to the symmetry of the slices and loading condition, only one slice can be considered and the initial iBone model boundary conditions can be made as shown in Fig.2 (a). The shape optimization process is shown in Fig.2 (b) to (d) by using the iBone model[5]. It is shown that the element largely reduced and final shape nearly close to S type as shown Fig.2 (d) at 100 stage. The maximum effective stress nearly 1526.6MPa at 10 stages and it is decreased 624MPa at 100 stages. This is indicated that the stress concentration largely reduced and the optimized structure close to uniform stress distribution model is obtained.

(a) Initial iBone Model and Boundary Condition (b) Optimization Results after 10 Stage

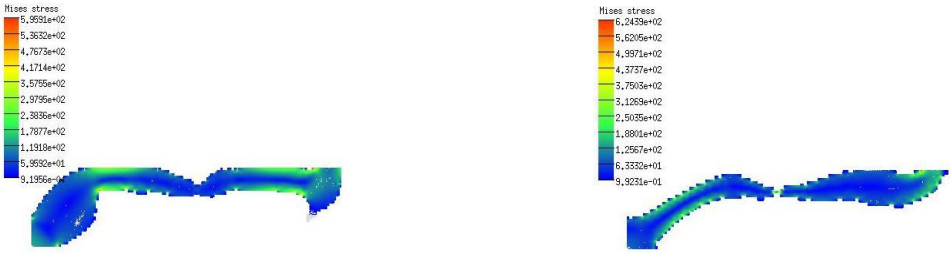

(c) Optimization Results after 50 Stage (d) Optimization Results after 100 Stage

Fig.2 The Initial iBone Model Boundary Conditions and the Shape Optimization Process

FEM Analysis of Bellow

The geometry modelings are conducted by using the MSC. Patran by considering the shape optimized model using iBone model. Then the 3D model of welded metal bellows diaphragms are made. Due to the symmetry of the structure and continuity of the loading transfer condition as shown in Fig.3, only one piece of diaphragm is considered and 1/4 slice is used to 3 dimensional numerical calculations [6].

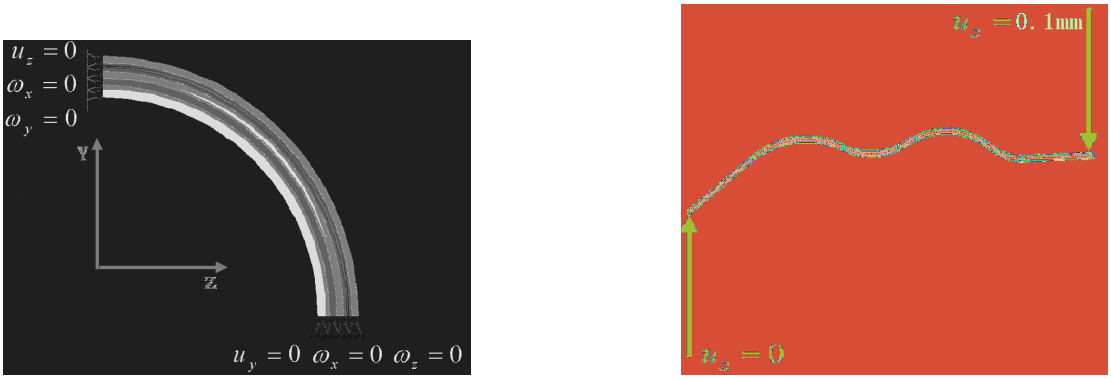

(a) Geometrical Symmetry (b) Loading Continuity

Fig. 3 Numerical Model for Welded Metal Bellows Diaphragm and Boundary Conditions

The 20 nodal hexahedron meshes are used and the FEM analysis based on the large deformation theory are conducted. The boundary conditions are supplied by considering the symmetry of the model as shown Fig.3(a). However, the bellows type machinery seal mainly supporting load is axial load, so the axial load transfer each other continuously from diaphragms to diaphragms, then the loading condition mainly consider the axial loading and controlled by displacement as shown in Fig.3(b).

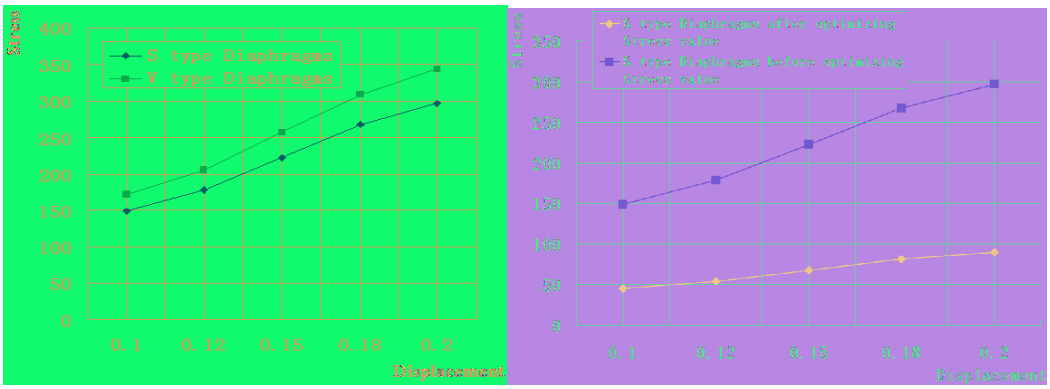

Fig. 4 Stress and Displacement Relations of the S type and the V type and New S type Models

Fig.4 (a) shows the stress and displacement relations of the S and V type model. It is shown that the stresses are increased with increases of the both model, but at the same displacement the stress in S type model smaller than the V type model. Fig.4 (b) shows the stress and displacement relations of the original S type models before and after improving the shape optimization. The results shown, that the biggest stress value of S type model after optimizing is smaller than the minimum stress value of S type model before optimization. Under the same displacement load, it is shown that the new model nearly reduced stress value over 70%. This is indicated that the S type model gives the good flexibility under the same loading condition than the V type one, and the new optimized model of S type diaphragm also give a good flexibility than the old S type model.

Conclusion

The reasonable new type of the welded metal bellow diaphragm shape was designed by using the biomechanical shape optimization method based on the iBone (imitation bone) model, and the 2D FEM strength evaluation based on the new optimized shape and the original type shape are conducted to improve the iBone model.

The 3D FEM analyses are conducted by using S type and V type diaphragms for the detailed strength and flexibility evaluations. The S type model gives the good flexibility under the same loading condition than the V type one, and the new optimized model of S type diaphragm also give a good flexibility than the old S type model with the same strength.

Acknowledgement

This work was supported by Ministry of Science and Technology 973 Project of China (No:2007CB707706) and National Natural Science Foundation of China (No:50775193) .

Reference

[1]. Lifubao.The discussions of metal welded bellow. Institute of Liaoyang petrol chamistry (Liaoyang111003).TG457.1,(in Chinese)

[2]. Liu Ren-Huai, Wang Zhi-Wei. Nonlinear deformation analysis of a U-shaped bellows With varying thickness.

[3]. Turing A.M., *The Chemical Basis of Morphogenesis*, Phil. Trans. R. Soc. London B237, 1952, pp.37-72.

[4]. Tezuka, K., Wada Y. & Kikuchi M., iBone:A Reaction Diffusion Based Shape Optimization Method. Key engineering Materials. 2003, 243-24.

[5]. Halida Musha, Mamtimin Geni, Buhalqam, Shape Optimization and Strength Evaluation of Metal Welded Bellows Wave of Mechanical Seal, Advanced Materials Research, Vols. 33-37,2008, 1377-1382.

[6]. Rabiya Nuer, Mamtimin Geni, Ahmat Mutellip, Li Hua Jia, FEM Analysis and Optimization for Welded Metal Bellows Seal, Advanced Materials Research, Vols. 33-37,2008, 1371-1376.

Key Engineering Materials Vols. 385-387 (2008) pp 817-820
© (2008) Trans Tech Publications, Switzerland
doi:10.4028/www.scientific.net/KEM.385-387.817

Shrinkage Performance and Cracking Resistance Mechanism of Rubberized Lightweight Aggregate Concrete with Polymer

Wang Ji[1,a], Li Yue[1,b] , Zhang Ming-zhong[1,c]

[1]Design Institute of Wuhan University of Technology, Wuhan 430070, P.R.China

[a]hmywj@263.net, [b]leeyue321@whut.edu.cn , [c]zmzcn@whut.edu.cn

Keywords: rubber particle; polymer; lightweight aggregate concrete; shrinkage performance; interface transition zone (ITZ)

Abstract. To improve the cracking resistance of lightweight aggregate concrete, rubber particles and polymer were added. Experimental results showed that the shrinkage rate increased when rubber particles were added into lightweight aggregate concrete, but when polymer was mixed, the shrinkage rate decreased dramatically. Microstructure analysis indicated that the interface transition zone (ITZ) influenced the shrinkage performance of rubberized lightweight aggregate concrete with polymer directly; the ITZ bondage between rubber particles and cement matrix was very poor and the restriction to shrinkage was weak, which were the main reasons for the increase of shrinkage rate of rubberized lightweight aggregate concrete; when polymer was mixed into the concrete, the hole and ITZ structure of concrete were improved, which made the strain energy absorbing function of rubber particles can be exerted entirely and the flexibility of ITZ was boosted, thereby the shrinkage performance and cracking resistance of lightweight aggregate concrete were improved.

Introduction

The volume contraction caused by water ratio change, chemical reaction and temperature change etc, in concrete is called concrete shrinkage [1~3]. Lightweight aggregate concrete is consisted of aggregates with low elastic modulus and great abundance of cement, which will cause great shrinkage in concrete and after hardening the brittleness will increase also, so the cracking resistance of lightweight aggregate concrete is very poor, which confine the wide use of lightweight aggregate concrete[4,5]. Rubber particles which are easy to deform can help to decrease the stress in concrete caused by temperature and moisture change, and can absorb some strain energy, which can help to improve the shrinkage performance of concrete[6~8].

In this paper, lightweight aggregate concrete was modified by mixed with rubber particles and polymer latex, which decreased the brittleness of lightweight aggregate concrete and improved the cracking resistance. Furthermore, the working mechanisms of rubber particles and polymer latex in lightweight aggregate concrete were analyzed.

1 Materials and Experimental

1.1 Materials

(1) Cement: ordinary Portland cement P.O42.5;

(2) Coarse aggregate: 5~20 mm crushed shale lightweight aggregate;

(3) Fine aggregate: river sand of 2.6 fineness modulus, specific gravity is 1450 kg/m^3;

(4) Rubber aggregate: 2360μm rubber particles mixed with 830μm rubber particles with quality ratio of 4:6, specific gravity is 560 kg/m^3;

(5) Polymer latex: styrene-butadiene latex (ab. SD) with solid content of 47%;

(6) Additive: water reducing agents (FDN), the water reducing rate is 18% when its content is 1.0% by the cement quality.

1.2 Experimental

Specimens (100 mm×100 mm×515 mm) were prepared according to T0551-2005, the mix ratio can be seen in Table 1. Rubber particles were considered as fine aggregate by the volume of sand that was replaced. Polymer latex was used as additive.

All specimens were curing in standard curing room, and should be stripped after curing 1~2d. The specimens were taken out of the curing room after curing 3 days, and at the same time, were put into shrinkage room (the temperature was controlled at 20°C±2°C and the relative humidity was 60%±5%) and began to measure the initial length. The initial length should be measured three times repeated, and the arithmetic mean value was taken. Measure the length of specimens at 1d, 3d, 7d, 14d, 28d, 60d and 90d since the specimens were put into the shrinkage room, shrinkage rate can be calculated according to the Eq.1 below:

$$S_d = \frac{X_0 - X_d}{L_0} \times 100\% . \qquad (1)$$

Where: S_d is the shrinkage rate of the specimen at age of d day; L_0 is the norm length of the specimen (mm); X_0 is the initial length of the specimen (mm); X_d is the testing length of the specimen at age of d day (mm).

Table 1 Mix ratio for shrinkage test (kg/m^3)

NO.	Water	Cement	shale lightweight aggregate	Sand	Rubber particles	Water reducing agents	Styrene-butadiene latex
LC35	152	380	645	660	0	1.9	0
R60	152	380	645	504.6	60	1.9	0
R150	152	380	645	156.8	150	1.9	0
J2+R150	143.4	380	645	156.8	150	1.9	16.17

2 Results and discussions

Evolution curves of shrinkage rate changing with age can be seen in Fig.1. It is seen from Fig.1 that the shrinkage rate increased with age gradually.

The shrinkage rates of specimen R60 and R150 (rubber particles content of 60 kg/m^3 and 150 kg/m^3) were comparative to that of specimen LC35 (lightweight aggregate concrete) at early ages, but in later time, the shrinkage rates of R60 and R150 were bigger than that of LC35.

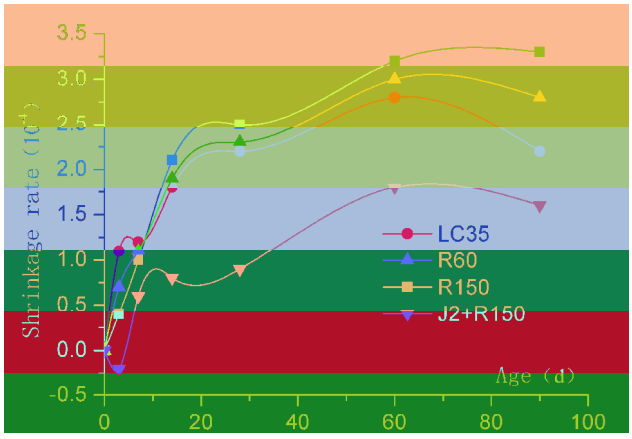

Fig.1 Evolution curves of shrinkage rate changing with age

Compare specimen R60 with R150, it can be seen that the shrinkage rate of rubberized lightweight aggregate concrete increased with the content of rubber particles. Specimen J2+R150 (with rubber

particles of 150 kg/m^3 and polymer latex) had a much smaller shrinkage rate than specimen R150, and the shrinkage performance was even better than that of LC35 which had no rubber particles.

3 Microstructure and Mechanism Analysis

To study the working mechanism of rubber particles and polymer latex, and discover the relations between microstructure and shrinkage performance, polarizing microscope image analysis and scan electron microscope (SEM) study were carried on and ITZ structures between cement matrix and rubber particles or lightweight aggregate were observed, which can be seen in Figs.2~4.

3.1 Polarizing Microscope Image Analysis

ITZ structure between rubber particles and cement matrix was observed by polarizing microscope, seen in Fig.2.

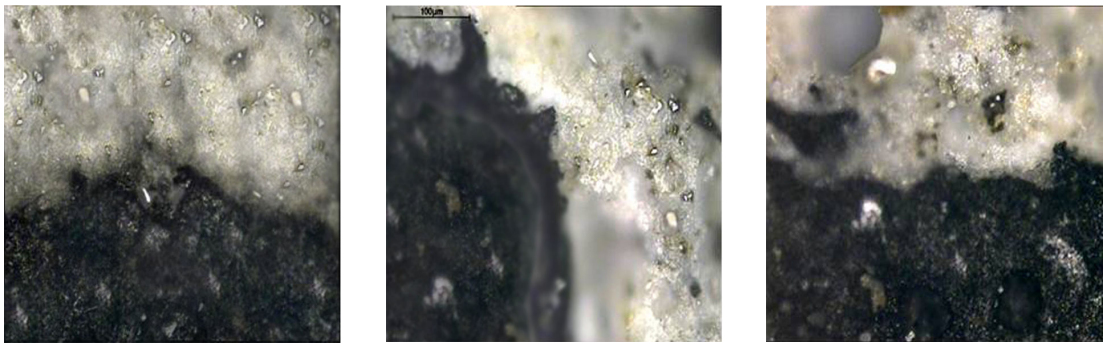

(a) Specimen R60 (b) Specimen R150 (c) Specimen J2+R150

Fig.2 Polarizing microscope photos for rubber particles-cement matrix interface (×200)

It can be seen from Fig.2 that with the increase of rubber particles content, the ITZ width between rubber particles and cement matrix was enlarged obviously, the density was lessened and the bondage between rubber particles and cement paste was weakened evidently. But when polymer latex was mixed in (such as specimen J2+R150), the bondage was strengthened greatly.

3.2 SEM Study

ITZ structure between lightweight aggregate and cement matrix was observed by SEM, seen in Fig.3a, b, c, and d.

It can be seen from Fig.3 that with the increase of rubber particles content, the bondage of ITZ between lightweight aggregate and cement paste was weakened, the ITZ structure was porous and the ITZ width was enlarged evidently. But the ITZ structure of specimen J2+R150 was compact, the density of hydration products was enhanced and the interface of ITZ was clear and regular, even better than that of specimen LC35.

Fig.4 shows the cement paste structure

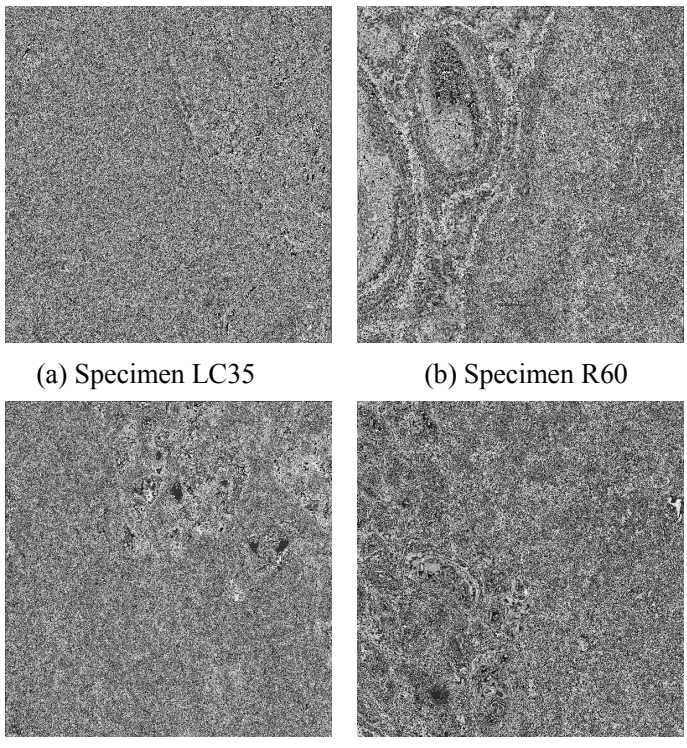

(a) Specimen LC35 (b) Specimen R60

(c) Specimen R150 (d) Specimen J2+R150

Fig.3 SEM photos for lightweight aggregate-cement paste interface

of specimen LC35 (with no polymer latex) and J2+R150. It can be seen from Fig.4 that the cement paste structure of J2+R150 was more compact than that of LC35 and the hole structure was improved evidently. The polymer particles filled the holes in cement paste and the meshy polymer film was formed like cement gel, which made the structure of cement paste strengthened.

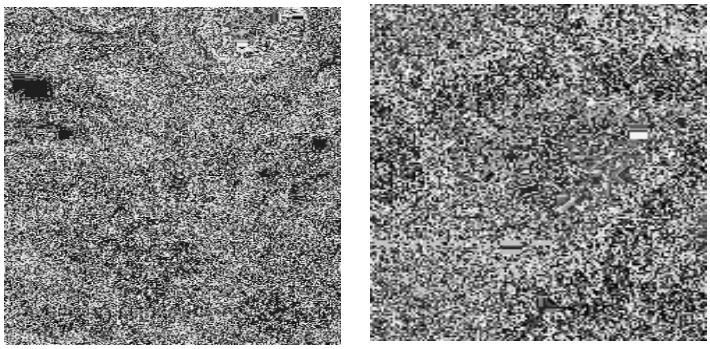

(a) Specimen LC35 (b) Specimen J2+R150

Fig.4 Cement paste structure

3.3 Mechanism Analysis

Rubber particles as organism were mixed into cement matrix, the interface bondage was very poor and rubber particles as elastic material had little restriction to the shrinkage of cement paste, so when the rubber particles content increased, the shrinkage of concrete increased also.

Figs.2~4 indicate that the functions of polymer latex in rubberized lightweight aggregate concrete are: (1) polymer particles can fill fine cracks in lightweight aggregate, which can strengthen the lightweight aggregate and prevent crack spreading; (2) meshy polymer film can be formed and combine with cement hydration products to form network structure, the network cover the acicular AFt and AFm crystal in ITZ, which improves the ITZ structure and strengthens the bondage between aggregate and cement matrix; (3) strain energy absorbing function of rubber particles can be exerted entirely when ITZ structure is improved and the flexibility of the interface is boosted.

4 Conclusions

(1) Shrinkage rates of rubberized lightweight aggregate concrete were bigger than that of lightweight aggregate concrete and increased with the content of rubber particles;

(2) When polymer latex was mixed, the shrinkage rate of concrete decreased greatly;

(3) The main reasons for the increase of shrinkage rate of rubberized lightweight aggregate concrete were that interface bondage between rubber particles and cement paste was very poor, and rubber particles as elastic material had little restriction to the shrinkage of cement paste;

(4) When polymer latex was mixed, the hole and ITZ structure of concrete were improved and the bondage between aggregate and cement matrix was strengthen, thereby the shrinkage performance and cracking resistance of concrete were improved.

References

[1] Sidney Mindess, J. Francis Young, David Darwin:Concrete (Pearson Education, Inc., USA 2003).

[2] Mei Ming-rong, Ge Shi-pin, Chen Jun: submitted to Journal of Hehai University (2002).

[3] Shao Ping, Hu Xin-gang: submitted to Journal of Hei Longjiang transportation technology (2002).

[4] Liu Xun-bo, Ji Yi-qi, Chi Jian-ye: submitted to Journal of Concrete (2006).

[5] Hu Shu-guang, Wang Fa-zhou: submitted to Journal of Wuhan University of Technology (2000).

[6] Li Yue, Wang Ling: submitted to Journal of Concrete (2006).

[7] Eldin N N, Senouci A B: submitted to Journal of Materials in Civil Engineering (1993).

[8] Toutanji H A.: submitted to Journal of Cement and Concrete Composites (1996).

Key Engineering Materials Vols. 385-387 (2008) pp 821-824
© (2008) Trans Tech Publications, Switzerland
doi:10.4028/www.scientific.net/KEM.385-387.821

Delamination of Laminates Governed by Free Edge Interlaminar Stresses using Interface Element

H. Hosseini-Toudeshky[1,a], M. Jalalvand[1,b] , B. Mohammadi[1,c]
[1]Aerospace Engineering Department & Centre of Excellence in Computational Aerospace Engineering
Amirkabir University of Technology, 424 Hafez Ave, Tehran, Iran
Fax: +98-21 6695 9020, Tel: +98-21 6454 3224
[a]Hosseini@aut.ac.ir, [b]M_jalalvand@aut.ac.ir, [c]Bijan_Moh@aut.ac.ir

Keywords: Interface Element – Free Edge Delamination - Damage Mechanics- FEM

Abstract. In this paper, interface element with de-cohesive constitutive law is used to predict the delamination progress of laminates in which delamination is the prominent failure mode. For this purpose, a finite element program is developed to perform nonlinear damage analysis. The analyses are carried out based on the interlaminar constitutive law of elastic-plastic-damage proposed before in the literature. Delamination initiation and propagation of several laminates with dominant interlaminar shear stresses at free edges are investigated to find the failure load. It is shown that the difference between the predicted failure loads using the present study and the experimental results are 3.1% to 19.4% for various laminates.

Introduction

Delamination analysis is normally performed to predict the delamination initiation using some stress-based criteria or to model crack propagation using fracture mechanics. An alternative method which is capable to predict both initiation and propagation of delamination is defining an interface damage zone. In this type of modeling, the composite laminate is conceived as an assemblage of two main constituents of the fiber-reinforced layer and the separation interface. In this approach, the interface is considered as the third independent material entity which links two components and is defined by its own constitutive law [[1]]. The constitutive law is attributed to the damage zone. Implementing a softening constitutive law into the FEM using interface elements is usually a straight forward task which is one of the main advantages of this method comparing with the FEM fracture mechanics [[2]-[3]].
In most of the investigations dealing with interface elements, a new constitutive model have been purposed or they used this approach to analyze standard fracture tests such as DCB, ENF and simple mixed mode laminates. In addition, most of the effort devoted in this area has been restricted to the investigation of interlaminar crack propagation while delamination initiation is much more open for research [[1]]. The objective of this paper is to apply the meso-modeling approach in the prediction of final failure of laminates in which delamination is the dominant phenomenon. The dominant failure mode of the composite laminates is strongly related to the stacking sequence of the layers [[4]]. The interlaminar stresses at free edges may lead to the edge delamination and failure of laminated composites. Experimental results indicate that if free edge delamination is caused by interlaminar normal stress, the laminate can withstand loads beyond the onset of delamination, however, the free edge failure caused by the interlaminar shear stresses often results in immediate laminate failure [[5]]. Therefore, it is possible to find the final failure load due to the catastrophic crack propagation of laminates by simulating the crack initiation and propagation of the interlaminar crack using interface elements. For this purpose a generalized nonlinear finite element program named AUTDMA-IF85 was developed. In this program a sixteen-node interface element compatible with the twenty-node brick elements for layers are used.

Interfacial Constitutive Law

Plastic deformation and damage parameter vectors are two variables determining the nonlinear state. The constitutive law must be formulated using a differential equation in which the response of

the structure can be calculated for each load increment. Eq. 1 describes the variation of interlaminar stress components with respect to nonlinear state variables.

$$d\tau_i = K_i(1-\varphi_i)du_i^e - u_i^e K_i\, d\varphi_i . \quad (1)$$

Where τ_i, K_i, ϕ_I, and u^e_i are stress, interface penalty stiffness, damage parameter and elastic displacement discontinuity components respectively.

The yield criterion, which determines the initiation of non-linear state variables, is presented by Eq. 2. This equation is similar to the classic quadratic interlaminar crack initiation criterion while the effective stress values of undamaged state are substituted in that.

$$F(\tau_i,\varphi_i) = \sqrt{a_1\left(\frac{\tau_1}{1-\varphi_1}\right)^2 + a_2\left(\frac{\tau_2}{1-\varphi_2}\right)^2 + a_3\left(\frac{<\tau_3>^+}{1-\varphi_3}\right)^2} \quad \text{where} < \tau_3 >^+ = \begin{cases}\tau_3 & \text{if } \tau_3 > 0\\ 0 & \text{if } \tau_3 \le 0\end{cases} . \quad (2)$$

$h(\lambda)$ describes the softening rule and $h(\lambda)=-\lambda$ where λ is the plastic-damage multiplier which governs the magnitude of plastic deformation and damage variables. Parameters of a_i are material constants that should be identified for each model independently. To avoid penetration of damage and considering the closure effect in the direction 3 or opening mode, an exceptional condition was exerted in this direction and positive quantities of normal interlaminar stresses are only considered to be effective on damage and plasticity development. The variation of plastic displacement discontinuity and damage parameters are governed by the flow rule and evolution law which have already been proposed in [[6]] and they are not explained here due to the pages limitation.

Analyses and Results

Six laminates with different lay-up configurations are analyzed using the developed method to find the final failure load of them. The lay-ups of $[15_2/\text{-}15_2]_s$, $[15/\text{-}15]_{2s}$, $[5/30/\text{-}5/\text{-}30]_s$, $[15/0/0/\text{-}15]_s$, $[10/25/\text{-}10/\text{-}25]_s$, and $[30/10/\text{-}10/\text{-}30]_s$ are selected. The stacking sequences of the laminates are selected in which the interlaminar shear stress (τ_{xz}) at the free edges is much larger than the other stress components. The composite material of graphite/epoxy AS4/3501-6 is used for the laminates with the ply thickness of 0.14 *mm*. The geometry of the laminates is shown in Fig.1. The length and width of them are L=200 *mm* and W=20 *mm* respectively. The material properties are: E_{11}=138.9 GPa, E_{22}=E_{22}=9 GPa, G_{12}=G_{13}=6.0 GPa, G_{23}=5.0GPa, ν_{12}=ν_{12}=0.3, ν_{23}=0.45, X=2200 MPa, X′=-2010 MPa, Y=57 MPa, Y′=-207MPa, S=110MPa and G_c=0.4 N/mm. The experimental results of these lay-ups are presented in [[5]] and the obtained results in this paper are compared with them. Due to the symmetric condition of the lay-ups, half of the laminates in the thickness direction was modeled and symmetry boundary conditions on the plane of z=0 were applied. To predict the high stress gradient near the free edges, very fine meshes are used in these areas. Six uniform element along the x-direction, and 20 non-uniform elements in the y-direction are used. The top view of typical mesh is shown in the Fig. 1 (a).

Effect of various penalty stiffness values on the obtained shear stress, τ_{xz}, along the y-direction for a typical laminate with $[15_2/\text{-}15_2]_s$ lay-up is shown in Fig. 2. This figure shows that the larger values of penalty stiffness result in larger quantity of shear stress at free edges. It is also clear that the stress gradient at the vicinity of the free edge and especially at the edge node is quite large indicating an acceptable mesh refinement in the modeling.

It is assumed that, delamination may potentially initiate and grows at one of the existed three interfaces in each model where the interface elements should be located, Fig. 1(b). The location of the interface elements along the thickness in which the maximum τ_{xz} value occurs is found from the elastic analysis results. The obtained interlaminar normal and shear stress components of interfaces at (x=100mm and y=0) are listed in Table 1 for each laminate. The results in this table are obtained with the penalty stiffness value of 10^5 and the applied strain of 0.5% while the interface behavior is assumed to be linear elastic. To reduce the number of elements and consequently the run time of each laminate, one interface element row is only applied for each model and the interface row location is found according to the maximum stresses depicted in Table 1. The selected interface for

delamination occurrence of each laminate is also depicted in Table 1. The relevant mesh scheme of each laminate is also shown in Fig.1(c) and (d).

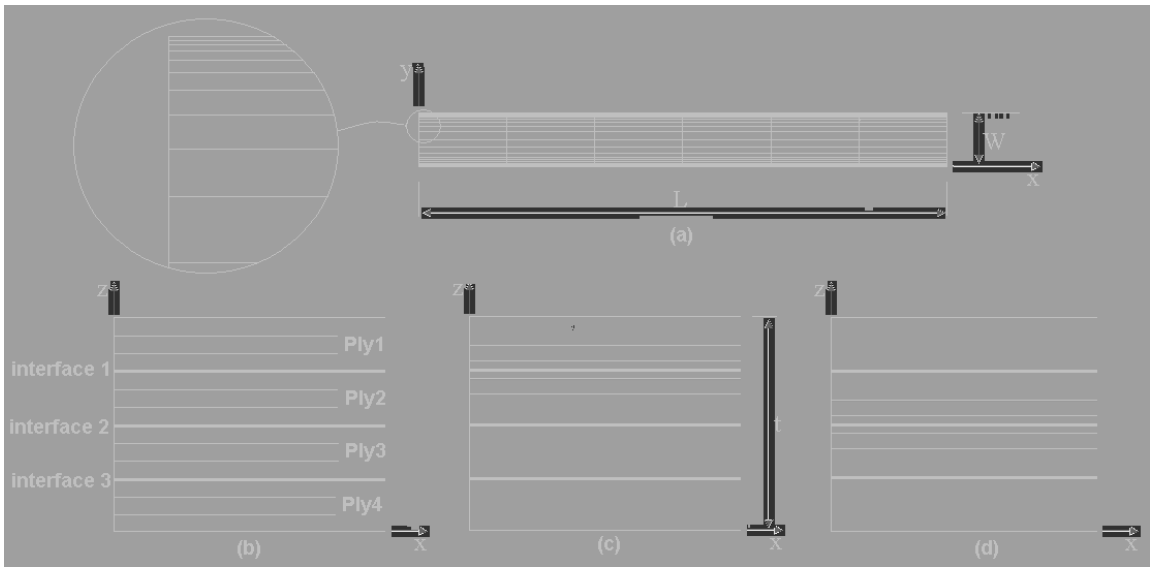

Fig. 1 Typical mesh and selected interfaces through the thickness, a) 2D mesh, b) three interfaces for elastic analysis c) Interface-1 selected for laminates of 1, 3, 5 and 6, d) Interfaces-2 selected for laminates 2 and 4 (See Table 1 for laminates numbers.)

Table 1. Elastic interlaminar stress components at laminates interfaces

No.	Laminate	Interface 1			Interface 2			Interface 3			Selected interface
		τ_{xz}	τ_{yz}	σ_z	τ_{xz}	τ_{yz}	σ_z	τ_{xz}	τ_{yz}	σ_z	
1	$[15/15/-15/-15]_S$	41.2	-0.4	0.4	169.3	0.2	-2.9	41.1	1.1	3.2	2
2	$[15/-15/15/-15]_S$	127.8	-0.5	-1.3	-86.8	0.3	-0.1	127.5	1.5	2.5	1
3	$[5/30/-5/-30]_S$	20.7	-3.3	-4.0	110.9	9.1	-7.1	37.1	-3.6	-2.3	2
4	$[15/0/0/-15]_S$	80.6	4.5	3.2	48.5	-0.1	9.0	80.7	-5.0	-1.5	1
5	$[10/25/-10/-25]_S$	42.4	-1.6	-2.2	149.9	7.0	-6.8	31.5	-0.9	-0.1	2
6	$[30/10/-10/-30]_S$	18.2	-0.1	2.9	142.9	0.1	4.9	18.0	0.2	3.4	2

The axial load in each laminate is incrementally applied during the solution procedure. It has been observed that, in a certain little load increment, the global behaviour of the laminate becomes unstable and also all of the applied interface elements become completely damaged. Damage grows, ϕ_1, in a final load increment and various iterations for a typical laminate are shown in Fig. 3. When all of the interface elements are destroyed, the solution of the problem diverges and this load step can be interpreted as the catastrophic interlaminar crack growth or unstable delamination propagation.

The predicted final failure axial stress and strain of different laminates using this study are compared with those obtained from the experiments [5] in Table 2. This table shows that the predicted failure loads using the present study are non-conservative by 3.1% to 19.4% for different laminates. The non-conservative results may be due to the neglect of other type of damages such as matrix cracking and possibility of multi interface delaminations in some cases. It was already shown in Table 1 that the shear stress τ_{xz} at one of the interfaces is considerably larger than the τ_{xz} at the other interfaces for laminates 1, 3, 5 and 6 in which there are good agreements between the predicted failure loads and experiments. But for laminates 2 and 4 the obtained elastic shear stress in different interfaces are close to each other and the shear stress at interfaces 1 and 3 are almost equal. Such a situation may be interpreted as the tendency of multi interface delamination growth. More investigations considering multi interface elements rows can be performed to obtain more accurate results. The applied method indicates the capability of damage analysis to predict the failure load of laminates in which the prominent damage mode is delamination.

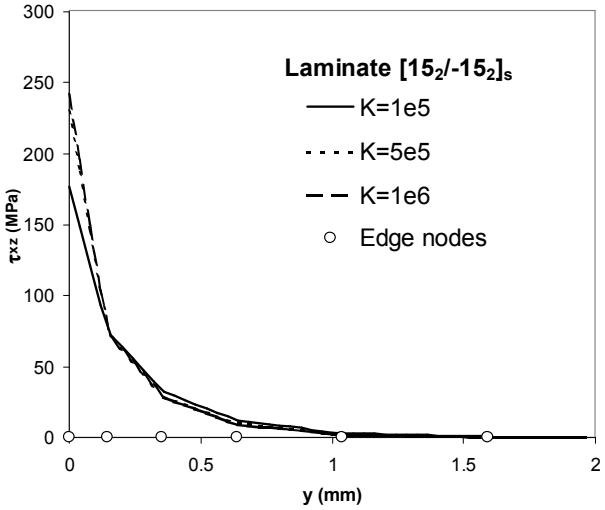

Fig. 2. Comparison of shear stress, τ_{xz}, along the laminate width for various penalty stiffness values

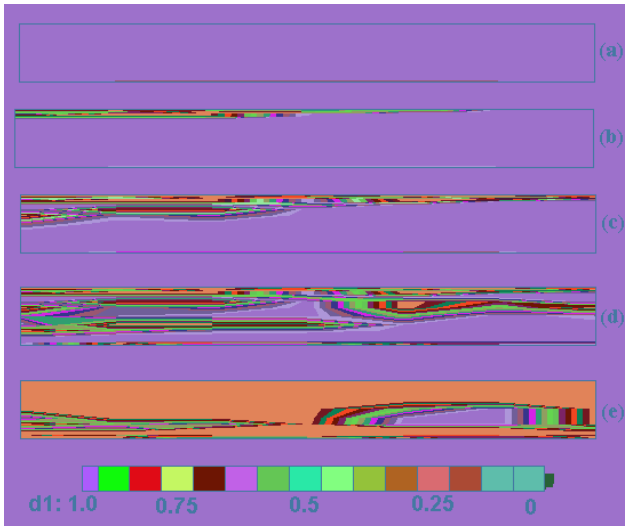

Fig. 3 Damage grows (black areas) in final load increment and various iterations a-e, (unstable delamination propagation)

Table 2. Comparison between predicted final failure load and experimental results

No.	Laminate	Present Study		Experimens [[5]]	
		ε_x	σ_x (MPa)	ε_x	σ_x (MPa)
1	$[15/15/-15/-15]_S$	0.0051	572	0.0050	555
2	$[15/-15/15/-15]_S$	0.0082	927	0.0076	855
3	$[5/30/-5/-30]_S$	0.0076	722	0.0075	709
4	$[15/0/0/-15]_S$	0.0097	1232	0.0080	1032
5	$[10/25/-10/-25]_S$	0.0057	573	0.0059	545
6	$[30/10/-10/-30]_S$	0.0062	564	0.0060	508

Conclusion

Interface elements with de-cohesive constitutive law were used to predict the delamination progress of laminates under quasi-static axial loading. Delamination initiation and propagation of several laminates were investigated to find the final failure load of them. It was shown that in a certain load increment, the interface elements between the two layers with different angles were suddenly destroyed. This phenomenon, always leads to produce a singular global stiffness matrix and numerical instability which can be interpreted as the unstable delamination propagation. It was shown that the predicted failure loads using the present study are non-conservative by 3.1% to 19.4% for different laminates.

References

[1] A.Corigliano, O.Allix, (2000), Comput. Methods Appl. Mech. Engrg., Vol. 185, pp. 203-224.

[2] C. Balzani , W. Wagner, (2007), Engineering Fracture Mechanics, Vol. 75 (9), pp. 2597-2615.

[3] Zou Z., Reid S.R., Li S.,(2003), *J. of the Mechcs and Physics of Solids*, Vol. 51, pp. 333-356.

[4] N.J.Ppagano and R.B.Pipes (1971), J. Composite Materials, Vol.5, pp.50-57.

[5] J.W.Joo, C.T.Sun, (1992) J. Composite Materials Vol.26, No.10, pp. 1510-1522.

[6] Corigliano A , (1993), *J. of Solid Structures*, Vol. 30, No 20, pp. 2779-2811.

Key Engineering Materials Vols. 385-387 (2008) pp 825-828
© (2008) Trans Tech Publications, Switzerland
doi:10.4028/www.scientific.net/KEM.385-387.825

On sensitivity of thermal parameters for concrete box girder in the sunshine

Jianzhuang Xiao[1,a], Zhiwen Song[1,b], Ch. Zhang[2,c]

[1] Department of Building Engineering, Tongji University, Shanghai 200092, China

[2] Department of Civil Engineering, University of Siegen, D-57068 Siegen, Germany

[a]jzx@mail.tongji.edu.cn,[b]songjiman66@163.com,[c]zhang@uni-siegen.de

Keywords: concrete box girder, sensitivity analysis, thermal parameters, temperature field, thermal effects.

Abstract: In this paper, the temperature field and the thermal effects on a concrete box girder in the sunshine are investigated. For this purpose, the finite element method (FEM) package ANSYS is applied. By varying the values of different thermal parameters, the sensitivity of the thermal parameters is explored. Numerical results are presented and discussed to show the influences of the thermal parameters and the temperature field on the deflection and the tensile stress of a single-span concrete bridge with a box cross section.

Introduction

With the increasing requirements on the performance, the reliability and the durability of civil engineering structures, design of exterior concrete structures especially concrete bridge structures should take the thermal effects into account. Reinforced concrete box girder as main load-bearing structure in concrete bridges is ineluctably exposed to temperature loading induced by solar radiation. In summer time, the temperature difference between the inner and the outer side of a concrete girder could be very high, which may lead to micro-cracking or damage and considerable deformation of the girder structure. The gradual evolution of micro-cracks is favorable to moisture ingress and permeability, which may lead to corrosion damage of the steel reinforcement. Thus, the reliability and the durability as well as the deformation of a reinforced concrete girder structure can be affected significantly by the thermal loading. To describe the temperature field, the main thermal parameters are the thermal conductivity, the specific heat, the thermal expansion coefficient, the convection heat transfer coefficient, and the absorption coefficient of solar radiation. These parameters obviously influence the temperature field and consequently the reliability, the durability and the deformation behavior of a concrete box girder under in-service condition. Generally, the effects of heat flow by convection and radiation can be combined in an overall heat transfer coefficient for practical purposes [1]. Many investigators have presented different values of these thermal parameters based on their experiments and analysis. However, the sensitivity of thermal parameters to the temperature field and the temperature effects of concrete box girder in the sunshine still need to be studied further. Based on a series of transient finite element analyses, the present paper investigates the influence of the thermal parameters on the temperature field and the temperature effects for a simple-supported concrete box girder. By varying the values of different thermal parameters, the sensitivity of thermal parameters including thermal conductivity, coefficient of thermal expansion, overall heat transfer coefficient and absorption coefficient of solar radiation is analyzed.

Sensitivity analysis of thermal parameters

A bridge with the cross section as shown in Fig.1 is assumed to be located in Shanghai of PR China (31.2° N and 121.5° E). A two-dimensional analysis along the bridge cross-section is conducted using the finite element method with CuteTEA. Triangular elements are used to model the concrete box girder. The transient analyses are performed for a starting time at 0:00AM in the summer, and the initial temperature in the bridge is considered to be uniform and equal to the ambient temperature at the time. The analyses are conducted for six days in order to eliminate the effect of the assumed initial conditions. In the following sections, the results corresponding to the last day of the analyses are presented.

The following parameters are assumed for the numerical simulation: Young's modulus of the concrete $E = 3.5\times10^4$MPa, bridge span L = 24m, orientation of the bridge axis = west-east, meteorological parameters for a return period of 30 years in summer with a maximum total solar radiation 30.89MJ/m^2, a maximum daily range of ambient temperature 15.48°C and a daily mean ambient temperature 28°C.

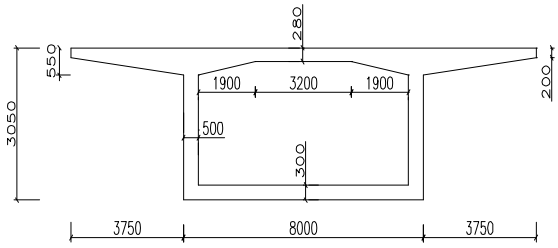

Fig. 1. Cross section of a box girder (mm)

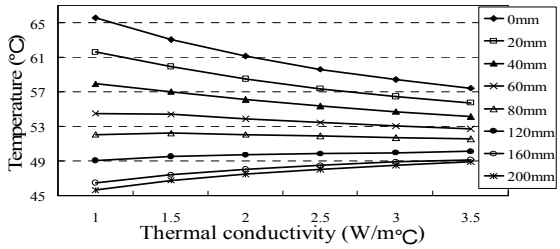

Fig. 2. Temperature in the upper slab

Sensitivity analysis of thermal conductivity

Thermal conductivity λ determines the capacity of the heat transmission, and earlier investigations reveal that the type of aggregate, porosity and moisture content have maximum influence on the thermal conductivity of concrete [2]. Thermal conductivity values have been chosen within the range of 1.0~3.5 W/m·°C.

Figure 2 shows the influence of the thermal conductivity on the temperature at different depth points in the upper slab. As can be seen, the thermal conductivity increase has significant effect on the temperature in the range of 60mm depth. Table 1 shows the influence of the thermal conductivity on the deflection and the tensile stress. It can be seen that a higher thermal conductivity results in a higher vertical deflection at the mid-span of the bridge, but the increase speed is gradually slow down and tends stable. Further, a higher thermal conductivity tends to bring the temperature distribution of cross section more uniform, reducing temperature stress.

Table 1: Influence of thermal conductivity on the deflection and the tensile stress

Thermal conductivity λ (W/m·°C)	1.0	1.5	2.0	2.5	3.0	3.5
Vertical deflection at the mid-span Δ_v (mm)	1.69	1.91	2.06	2.16	2.24	2.30
Maximum tensile stress σ_{tmax} (MPa)	4.34	4.26	4.16	4.06	3.98	3.90

Sensitivity analysis of coefficient of thermal expansion

The coefficient of thermal expansion α_c has no effect on the temperature field, but it has significant influence on the thermal effects. According to [3], the coefficient of thermal expansion depends on the type of aggregate and moisture content of concrete, and the values range from 6×10^{-6} °C^{-1} to 15×10^{-6} °C^{-1}.

Figure 3 (a) shows the maximum tensile stress due to solar radiation for different coefficients

of thermal expansion. According to Fig. 3(a), the maximum tensile stress increases linearly with the increase of the coefficient of thermal expansion. The influence of the coefficient of thermal expansion on the vertical deflection is shown in Fig. 3(b). It can be observed that the vertical deflection at the mid-span obviously increases with increasing coefficient of the thermal expansion and their relationship is also linear.

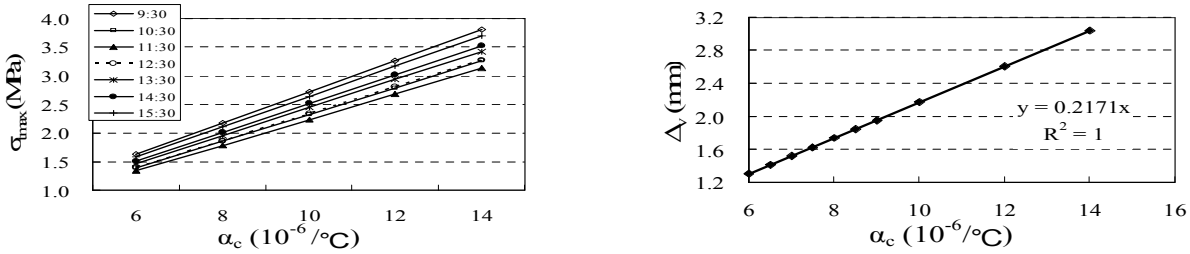

(a) The maximum tensile stress (b) The vertical deflection at the mid-span

Fig. 3. Influence of the coefficient of thermal expansion on thermal effects

Sensitivity analysis of overall heat transfer coefficient

For the overall heat transfer coefficient h (W/m^2·°C), there are no assured research results known in literature at the present time. Most previous investigations assume that the overall heat transfer coefficient is a linear function of the wind speed v (m/s) [4,5,6]. The heat transfer magnitude and speed depend on the value of wind speed. Sensitivity analysis of the overall heat transfer coefficient actually investigates the influence of wind speed. In this analysis, the overall heat transfer coefficient is obtained by means of the following equation [7].

$$h = 4.0v + 11.34 \qquad (v \le 5\text{m/s}) \tag{1}$$

Fig. 4(a) shows the diurnal temperature variation of the upper slab-surface for different wind speed. It can be observed that the temperature of upper slab-surface obviously decreases with the increase of wind speed but the decrease speed is gradually slow down. The maximum tensile stress due to solar radiation decreases pronouncedly with the higher wind speed (Fig. 4(b)). Therefore, when the wind speed is smaller the necessary measures must be taken to prevent cracking induced by solar radiation. Further, increasing wind speed decreases the vertical deflection at the mid-span (see Fig. 4(c)), and their relationship can be approximated by a quadratic function.

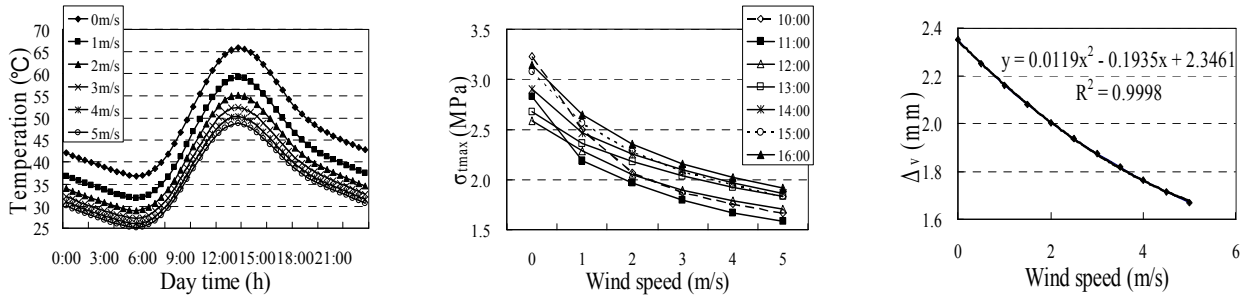

(a) Daily temperature variation (b) The maximum tensile stress (c) The vertical deflection

Fig. 4. Influence of wind speed on temperature field and thermal effects

Sensitivity analysis of absorption coefficient of solar radiation

The absorption coefficient of solar radiation α $(0 < \alpha < 1)$ is defined as the fraction of the solar radiation absorbed by concrete surfaces. The variation of the coefficient of solar radiation depends mainly on the material type, the roughness and the coloration of surface etc. The coefficient of solar radiation of concrete surfaces lies between 0.5-0.7 [7].

Fig. 5(a) shows the diurnal temperature variation of upper slab-surface for different absorption

coefficients of solar radiation. It can be seen that the absorption coefficient of solar radiation has significant effect on the temperature field. With the increase of the absorption coefficient of solar radiation, the temperature variation of upper slab-surface increases. The temperature rise varies linearly with the absorption coefficient of solar radiation. And the maximum temperature of upper slab-surface can rise about 2.5°C when the absorption coefficient of solar radiation increases by 0.05.

The maximum tensile stress due to solar radiation increases with the increase of the absorption coefficient of solar radiation and their relationship is nearly linear (Fig. 5(b)). Similarly, a higher absorption coefficient of solar radiation results in a larger vertical deflection at the mid-span, and their relationship is also linear (Fig. 5(c)).

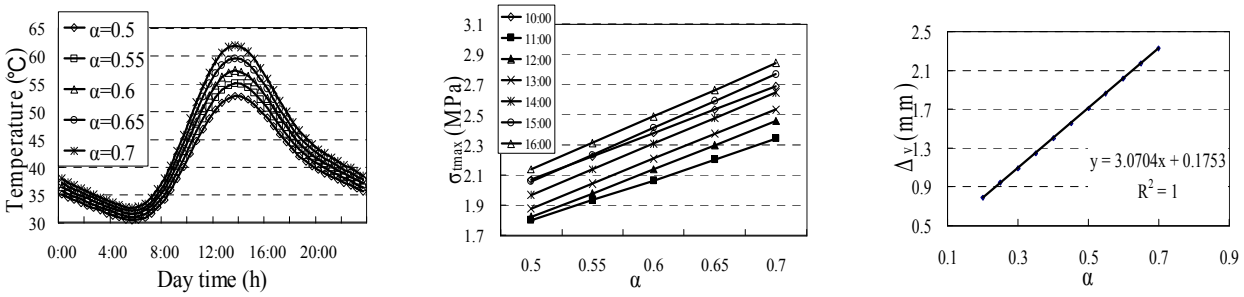

(a) Daily temperature variation (b) The maximum tensile stress (c) The vertical deflection

Fig. 5. Influence of absorption coefficient of solar radiation on temperature field and thermal effects

Conclusions

Thermal parameters have different influences on the temperature field and the thermal effects of concrete structures. The thermal conductivity has effect on the surface temperature of concrete structures, but the influence depth is less than 60mm. The coefficient of thermal expansion has no effect on the temperature field, but has marked influences on the stress and the strain induced by temperature difference. The influence of the overall heat transfer coefficient and the absorption coefficient of solar radiation on the temperature field and the thermal effects is very pronounced. They are the key factors for analyzing the temperature field and the thermal effects of concrete structures subjected to solar radiation. Thus, they should be chosen properly. However, so far there exist no unitized test methods and assured research results for the overall heat transfer coefficient and the absorption coefficient of solar radiation. Thus, future research works are needed and should be directed to: (1) further studies of thermal parameters, especially the overall heat transfer coefficient and the absorption coefficient of solar radiation, (2) sampling of standard and normal test methods.

Acknowledgement

This work was supported by the Shanghai Rising-Star Program under the project-no. 06QH14012.

References

[1] M.M. Elbadry, Amin Ghail: Journal of Structural Engineering, ASCE, Vol. 109 (1983), p. 2355.
[2] M.I. Khan: Building and Environment, Vol. 37 (2002), p. 607.
[3] Thomas Telford: CEB-FIP Model Code 1990. London, 1993.
[4] S. Moorty, C.W. Roeder: Journal of Structural Engineering, ASCE, Vol. 118 (1992), p. 1090.
[5] Guangping Wei: Journal of Southwest Jiaotong University, Vol. 4 (1989), p. 90, (in Chinese).
[6] D.S. Prakash Rao: ACI Journal, Vol. 83 (1986), p. 588.
[7] Jun Wang: Ph.D Dissertation, Tongji University, Shanghai, 2004, (in Chinese).

Key Engineering Materials Vols. 385-387 (2008) pp 829-832
© (2008) Trans Tech Publications, Switzerland
doi:10.4028/www.scientific.net/KEM.385-387.829

Effects of DLC on Fatigue Properties of Eutectoid Steel

Mian Zhang[1,a] , Nobusuke Hattori[2,b], and Shin-ichi Nishida[2,c]

[1] Department of Mechanical Engineering, Graduate School of Science and Engineering, Saga University,Honjo-machi 1, Saga 840-8502, Japan

[2] Department of Mechanical Engineering, Faculty of Science and Engineering, Saga University, Honjo-machi 1, Saga 840-8502, Japan

[a] zhangwango@hotmail.com, [b] hattori@me.saga-u.ac.jp, [c] nishida@me.saga-u.ac.jp

Key Words: Fatigue properties; DLC; Eutectoid Steel; Compressive residual stress.

Abstract: Diamond-like carbon (DLC) is an amorphous hard carbon, which has very high hardness, high resistivity, and dielectric optical properties. Economically and technologically attractive properties have drawn almost unparalleled interest towards the coatings. Eutectoid steel is a kind of material that has been widely used in shafts and various kinds of industrial components. Three kinds of fatigue specimens with different DLC conditions were used in this study. Fatigue test had been performed to investigate the effects of DLC on fatigue properties of eutectoid steel. The fractography was analyzed by a scanning electron microscope (SEM), and surface hardness was also evaluated. The fatigue limits of the DLC coated specimens did notincrease after DLC process, though the compressive residual stress which produced by DLC process can prevent fatigue fracture. According to the results of fatigue test, the optimal DLC method for improving the fatigue properties of eutectoid steel is determined and the relationship between fatigue limits and coating bias are obtained.

1. Introduction

As one of the most important industrial materials, eutectoid steel is used in many industrial fields. For example, rails, wheels, wires, and other machine parts. To protect such components from wear and corrosion, the parts are put through selective surface treatments via surface finish and coatings [1]. However, such treatments should not be detrimental to the fatigue life of the parts. In general, coatings that protect the surface from physio-chemical damage such as corrosion and wear tend to reduce the fatigue life. It is reported that more than 80–90% of failures in steel structural components are directly or indirectly caused by fatigue [2]. How to improve the fatigue strength is a major research subject in mechanical engineering.

The free surface of a steel component in general is a site for the nucleation of a fatigue crack, though sometimes defects and or inclusions inside the material may be the origin of a fatigue crack. Therefore surface preparation of a component plays a major role in fatigue crack initiation. A number of methods such as shot peening, nitriding or deposition of other coatings that impart high strength, wear and corrosion resistance are implemented have been developed.

Diamond-like carbon (DLC) coatings are one of the most popular surface treatments, which is widely used in the various molds and dies, cutting tools, drills, wear resistant tools, machine parts, hard discs of the computer, mirrors, etc. which have good chemical stability, low adhesion, low

static and dynamic coefficient of friction, and high wear resistance[3]. DLC coatings are amorphous in structure and contain sp^3 hybridized (diamond configuration) carbon clusters surrounded by a matrix of sp^2-bonded carbon and polymer-like network. DLC coatings contain about 20% hydrogen that is bonded to carbon [4]. The typical deposition methods of the DLC films included cathodic arc, plasma-enhanced CVD, ion beam deposition, dc or rf sputtering, and ion plating, etc.

2. Experimental Procedure

Table 1 lists chemical composition of the tested material. The shape and dimensions of the fatigue test specimen is showed in Fig.1. All of the specimens were annealed in vacuum at 520°C for 30 minute and then electro-polished to the depth of 50μm in diameter to relief the residual stress and remove the work hardened layer. Three kinds of DLC surface treatment method were used in this study. The DLC film of specimen A, B and C were normative film, double coat film and soft film, respectively. For specimen B, a silicon-based thin interlayer was used as a bonding layer between the steel substrate and DLC film. The DLC surface treatment conditions are listed in Table 2. The bias of specimens A and B are -2.5kv. For specimen C, the bias is -4.0kv.

In the fatigue test, Ono-type rotating bending fatigue-testing machine was used at the frequency of 60Hz in laboratory air atmosphere and was carried out until complete failure of specimens. There is a digital counter on the machine which had recorded the number of load cycles of the test specimens. The fatigue test machine stopped automatically as soon as the specimen failure occurred. The tests were terminated if no failure had occurred after 10^7 cycles. The fractography was analyzed using a scanning electron microscope (SEM).

Table 1 Chemical composition mass%

C	Si	Mn	P	S	Cr	T-Al
0.78	0.21	0.89	0.023	0.08	0.03	0.002

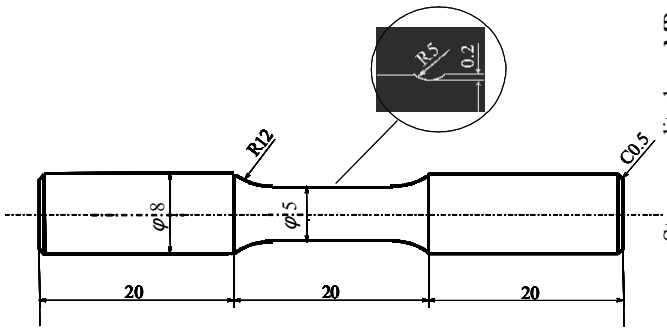

Fig.1. Shape and dimensions of the fatigue specimen

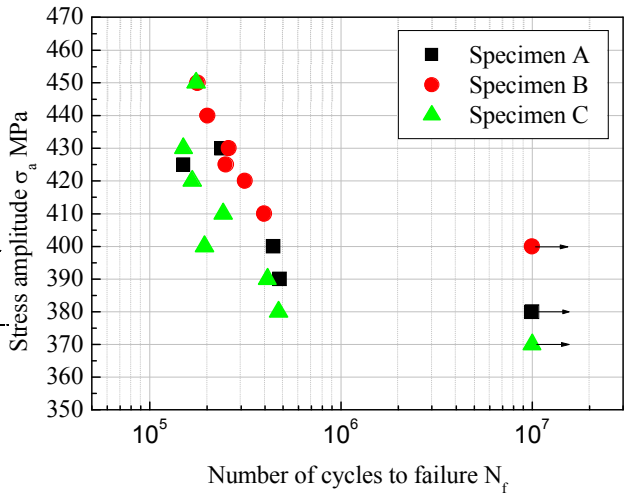

Fig.2. S-N curves

Table 2 DLC surface treatment conditions

Specimen	DLC film	Bias [kv]	Temperature [℃]	Time [hrs]	Pressure [Pa]
A	Normative	-2.5	150	3	2.0×10^{-1}
B	Double coat	-2.5	150	3	2.0×10^{-1}

Table 3 Fatigue limit and surface hardness

Specimen	Film thickness [μm]	σ_w [MPa]	Surface hardness [HV]
A	1	380	2100
B	1.5	400	2100
C	1	370	1750

3. Results and discussion

The fatigue limit and surface hardness are listed in Table 3. The fatigue limits of specimens A, B and C are 380MPa, 400MPa and 370MPa, respectively. The S–N curves obtained from rotating bending fatigue tests are given in Fig. 2. The surface hardness numbers are 2100Hv, 2100Hv and 1700Hv for specimens A, B and C, respectively.

The residual stresses that are induced by the surface treatments have an important effect on the fatigue life. Residual stresses arising from surface treatments when superimposed with the applied fatigue loads alter the mean level of fatigue cycle and the fatigue crack nucleation. Residual stresses affect the fatigue behavior of the materials in the same way as the static mechanical stresses that are superimposed on cyclic stress amplitude. In general, residual stresses are favorable if compressive, and detrimental, if tensile. In many brittle coatings, fatigue crack initiation is primarily due to tensile overload. The high residual compressive stress (nearly 1 Gpa) and strain limit of the hard coating such as DLC may contribute to the improved fatigue strength. The coating with compressive stress should behave similarly to a compressive layer induced by shot peening [4].

In general, DLC films do not adhere well to steel due to the presence of native oxides on the surface. Prior to DLC film deposition, the substrates were in-situ sputter etched using argon plasma. However, along with this sputter cleaning an intermediate bonding layer is needed to yield consistently well adherent DLC films. Elements belonging to groups IVb, Vb and VIb are all capable of forming hard carbides with high melting points, indicating the formation of strong covalent bonds and therefore can be used as bonding intermediate layers between steel and DLC [5]. In this study, for specimen B, a silicon-based thin interlayer was used as a bonding layer between the steel substrate and DLC film. Deposition of the silicon-based layer was carried out in-situ prior to DLC deposition by using a silicon-containing source gas. The reason why specimen B has the greatest fatigue limit can be considered that good adhesion can contribute to generating of compressive residual stress efficiently. Both fatigue limits of specimen A and B are greater than that of specimen C. This can be considered that the bias of -4.0kv is too low to form nice DLC film for improving fatigue strength. For all of the fatigue fracture surfaces, fatigue cracks initiated in the surface of the specimens. Fig. 3 shows the microstructure of fracture surface of the DLC coated

specimen. It is clear that the fatigue crack initiated at the surface of the specimens and then propagated to opposite side.

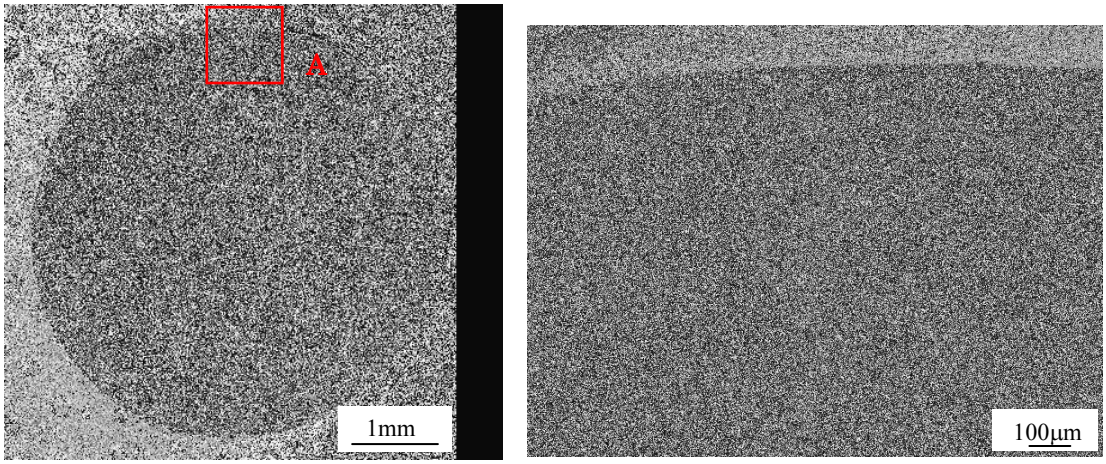

(a) Specimen A σ_a =400MPa, N_f =4.421×10^5cycles (b) Magnified point A

Fig.3. SEM microstructure of fatigue fracture surface

4. Conclusions

The main results obtained in this study are as follows:

(1) The fatigue limits of specimens A, B and C are 380MPa, 400MPa and 370MPa, respectively. The double coat method of specimen B is the optimum one on contributing to fatigue strength.

(2) Fatigue cracks initiate in the surface for all of the DLC coated specimens.

(3) The decreasing of the bias can decrease the fatigue limit of DLC coated eutectoid steel.

References

[1] K.N. Strafford, Surf. Coat. Technol. 81 (1996) 106.

[2] Nishida S. Failure analysis in engineering applications. Butterworth Heinemann Co. Ltd; 1992, p. 4.

[3] S. Zhang, B. Wang, T.Y. Tang, Processing and characterization of diamondlike carbon films, Surf. Eng. 13 (1997) 303–309.

[4] Vasan S. Sundaram, Diamond like carbon film as a protective coating for high strength steel and titanium alloy, Surface & Coatings Technology (2006)

[5] K. Bentzon, et al., Surf. Coat. Technol. 68 (1994) 651.

Key Engineering Materials Vols. 385-387 (2008) pp 833-836
© (2008) Trans Tech Publications, Switzerland
doi:10.4028/www.scientific.net/KEM.385-387.833

Plastic Limit Analysis of an Elbow with Various Wall-Thinning Geometries

Sang-Min Lee[1,a,*], Young-Hwan Choi[1,b], Hae-Dong Chung[1,c], Yoon-Suk Chang[2,d] and Young-Jin Kim[2,e]

[1]Korea Institute of Nuclear Safety, 19 Guseong-dong, Yuseong-gu, Daejeon 305-338, Korea

[2]School of Mechanical Engineering, Sungkyunkwan University,

300 Chunchun-dong, Jangan-gu, Suwon-si, Kyonggi-do 440-746, Korea

[a]sangmin.lee@kins.re.kr, [b]young@kins.re.kr, [c]hdchung@kins.re.kr, [d]yschang7@skku.edu, [e]yjkim50@skku.edu

Keywords: Bend Angle, Elbow, Limit Load Analysis, Limit Pressure, In-plane/out-of-plane Limit Moment, Wall-Thinning.

Abstract. A piping system including straight pipes, elbows and tee branches in a nuclear power plant is mostly subjected to severe loading conditions with high temperature and pressure. In particular, the wall-thinning of an elbow due to flow accelerated corrosion is one of safety issues in the nuclear industry. In this respect, it is necessary to investigate the limit loads of an elbow with a wall-thinned part for evaluating integrity. In this paper, three dimensional plastic limit analyses are performed to obtain limit loads of an elbow with different bend angles as well as defect geometries under internal pressure and in-plane/out-of-plane bending moment. The limit loads are also compared with the results from limit load solutions of an uninjured elbow based on the von Mises yield criteria. Finally, the effects of significant factors, bend angle and defect shape, are quantified to estimate the exact load carrying capacity of an elbow during operation.

Introduction

A piping system consists of straight pipes, elbows and tee branches in a nuclear power plant, which are mostly subjected to severe loading conditions with high temperature and pressure, and may undergo the wall-thinning due to erosion/corrosion and flow accelerated corrosion (FAC). Hence, it is necessary to assess the limit load under different loading conditions. To preserve integrity, provisions in guidelines such as, ANSI/ASME B31G [1] and ASME Code Case N-597 [2], have been established. In despite of their efficiency and inherent conservatisms, however, they can lead to unnecessary repair and change of a wall-thinned pipe.

Most of previous researches for pipe bend have focused on the simplest loading configuration such as merely the internal pressure or in-plane bending moment. For instance, limit moments for short radius pipe bends were obtained by conducting several experiments [3]. Marcal [4] presented the results for elastic-plastic behavior of pipe bends with in-plane bending moment. Chattopadhyay [5] determined the limit loads of an elbow with circumferential cracks under a bending moment. Recently, several limit load solutions for a flawless elbow have been reported to assess the limit pressure and bending moment under internal pressure, in-plane bending, out-of-plane bending and/or combined load. For example, the effect of internal pressure on the load-carrying capacity of pipe bends with different pipe bend factors, subjected to out-of-plane moment load, was investigated by Mourad and Younan [6]. Chattopadhyay [7] proposed a closed-form collapse moment equation of elbows under combined internal pressure and in-plane bending moment using elastic-plastic finite element (FE) analysis results. Also, Balan and Redekop [8] determined the effect of bi-directional load on the fatigue assessment of pressurized 90° piping elbows with local thinned areas. However, most of solutions were introduced by investigating global behaviors of pipe bends without a flaw and there

have been few researches focused on limit loads of pipe bends with a wall-thinned part subjected to mechanical loads.

The objective of this paper is to assess the limit load of a wall-thinned elbow under internal pressure or in-plane/out-of-plane bending moment. For this purpose, three dimensional limit load analyses were carried out to obtain the limit pressure (p_{limit}) and limit moment (M_{limit}) of elbows with different bend angles (φ) as well as defect geometries (d/t, $2\theta/\pi$, $2l/D_o$). The calculated limit pressure and moment were compared with results from plastic limit load solutions based on the von Mises yield criteria [9, 10].

Finite Element Analysis

Model Description. In order to calculate the limit pressure for pipe bends, three dimensional FE analyses were performed using the general purpose FE program, ABAQUS Ver 6.5 [11]. Figures 1 and 2 show the geometry and typical FE meshes for wall-thinned elbows with three different bend angles (φ). The radius of curvature (R), outer diameter (D_o), pipe thickness (t) and pipe bend factor ($h=Rt/r^2$) were fixed at 5, 2.5, 0.276 inch and 1.12, respectively. In FE models, symmetry conditions were fully utilized to reduce the computing cost. The elbow is modelled with a connecting straight pipe. The length of the straight pipe is chosen as ten times the radius of the pipe to eliminate the effect of ovalisation at the point where the load is applied.

To avoid problems associated with incompressibility, the reduced integration element (C3D20R) within ABAQUS was invoked. The number of nodes and elements in a typical FE mesh are 7,812 and 1,440. In the FE analysis, the internal pressure was applied as a distributed load to the inner surface of the FE model, together with an end-cap force applied at the end of the straight pipe as a distributed load. To avoid problems associated with convergence in elastic-perfectly plastic calculations, the RIKS option within ABAQUS was used. In case of bending moment, the nodes at the end of the elbow were constrained using MPC (multi-point constraint) option with ABAQUS. In addition, an elastic-perfectly plastic material model is used to eliminate the effect of strain hardening. The material of the pipe bend is SA106 Gr.B and the relevant material properties are shown in Table 1 [12].

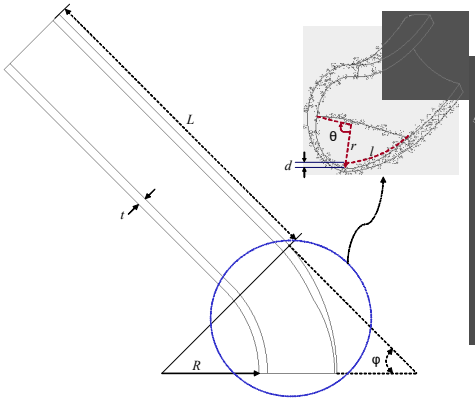

Fig. 1 Schematic geometry of an elbow

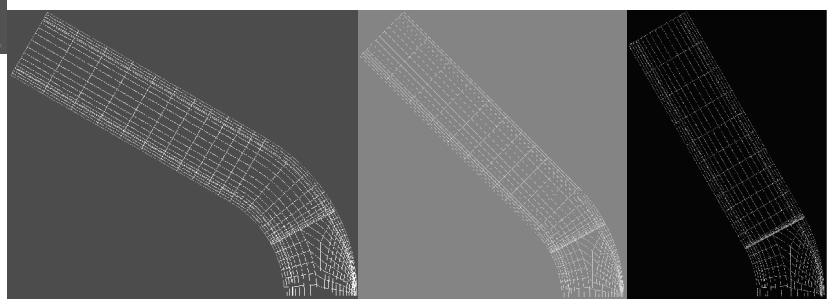

(a) $\varphi=\pi/6$ (b) $\varphi=\pi/4$ (c) $\varphi=\pi/3$

Fig. 2 Typical finite element mesh

Table 1 Material properties of SA106 Gr.B at 70℉

Young's modulus (psi)	σ_y (psi)	σ_u (psi)	Poisson's ratio
29.5×10^6	35×10^3	60×10^3	0.3

Parametric Study. For the pipe connections such as elbows and tee branches, the internal pressure and bending moment are the primary external loads. Therefore, the present limit analysis focused on only these loading types. To investigate the effect of non-dimensional key parameters (d/t, $2\theta/\pi$, $2l/D_o$, φ) on the limit pressure and limit moment, a detailed FE parametric study was performed. For

the internal pressure, total of 81 separate cases were investigated in the parametric study as listed in Table 2. In case of bending moment, limit analyses of 14 cases were selectively carried out.

Table 2 Parametric study matrix

R (in)	D_o (in)	t (in)	d/t	$2\theta/\pi$	$2l/D_o$	φ	$h(=Rt/r^2)$
5	2.5	0.276	1/4, 1/2, 3/4	1/4, 1/2, 1	1/2, 1, 2	$\pi/6$, $\pi/4$, $\pi/3$	1.12

Results and Discussion

As listed in Table 2, three different wall-thinned depths, angles, lengths, bend angles were systematically varied to quantify their effects on the limit pressure and limit moment. Based on the FE results, the limit loads were calculated for each analysis case. In the following figures, the resultant limit pressure (p_{limit}) and limit moment (M_{limit}) were normalized with the corresponding limit pressure (p_o) and limit moment (M_o) based on the von Mises yield criteria such as p_{limit}/p_o and M_{limit}/M_o.

Figure 3 shows the limit pressure for three different bend angles with the constant wall-thinned length ($2l/D_o$=1). By increasing the wall-thinned depth from 0.25 to 0.75, the limit pressures at $\varphi=\pi/6$ decreased about 10~70% with a variation of the wall-thinned angles ($2\theta/\pi$=1/4, 1/2, 1). For the case of the shallow wall-thinned depth (d/t=0.25), the limit pressures had a constant value as the wall-thinned angle increased. Also, the variation of bend angles had negligible effects on the limit pressure with the variations of the wall-thinned depth and angle.

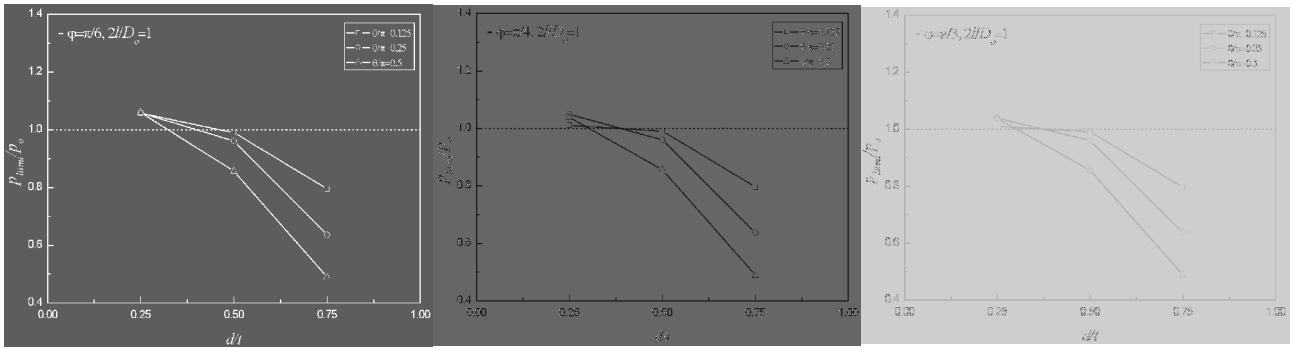

Fig. 3 Limit pressure obtained from FE results for three different bend angles with the constant wall-thinned length ($2l/D_o$=1)

Figure 4 depicts the limit pressure and limit moment for three different wall-thinned depth, length and angle. As the wall-thinned depth increased from 0.25 to 0.75, the limit pressure at $\varphi=\pi/4$, $2\theta/\pi$=1/2, $2l/D_o$=1.0 decreased about 40% and the in-plane/out-of-plane limit moments were maintained at the similar level of 0.5 or 0.4, respectively. By increasing the wall-thinned length from 0.5 to 2.0, the limit pressure at $\varphi=\pi/4$, $2\theta/\pi$=1/2, d/t=0.5 decreased about 20% and the limit moments nearly had constant values. As the wall-thinned angle increased from 0.125 to 0.5, the limit pressure at d/t=0.5, $2l/D_o$=1.0 decreased a maximum of 14% with the variation of bend angles ($\varphi=\pi/6$, $\pi/4$, $\pi/3$). In case of out-of-plane bending moment, the limit moment decreased about 7% regardless of the variation of bend angles. In case of in-plane bending moment, on the other hand, the value of limit moment at $\varphi=\pi/4$ was about 8% greater than those of limit moment at $\varphi=\pi/6$ and $\pi/3$.

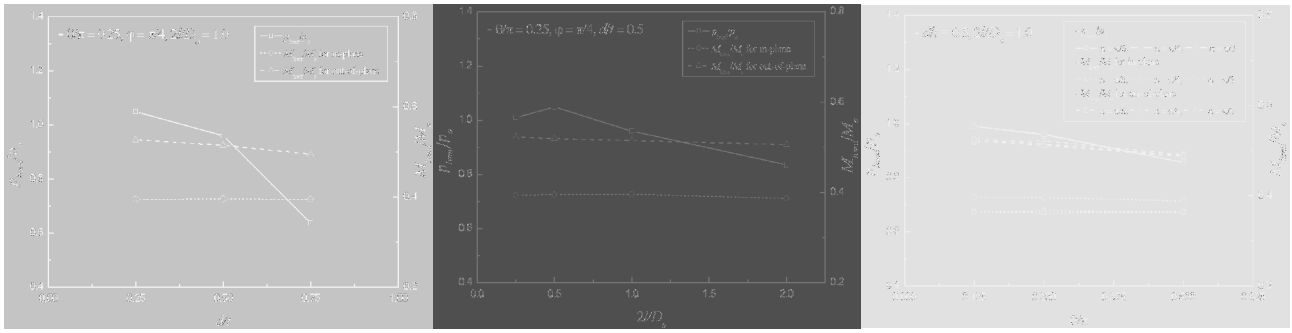

Fig. 5 Limit loads obtained from FE results for three different wall-thinned depth, length and angle

In order to verify the effect of an elbow shape, additional static FE analyses were performed with the variation of three different bend angles ($\varphi=\pi/6$, $\pi/4$, $\pi/3$) at d/t=0.5, $2l/D_o$=1 and $2\theta/\pi$=1/4. The stress concentration factor was obtained from an averaged von Mises stress in net section of a wall-thinned part and the calculated limit pressure. The stress concentration factors showed the similar values compared with three different bend angles. Therefore, the bend angles of elbows had no effect on the limit pressure under internal pressure.

Concluding Remarks

In this paper, three dimensional FE limit analyses were performed for wall-thinned elbows under internal pressure or in-plane/out-of-plane bending moment. In FE analyses, the failure of elbows with a local wall-thinning was assumed to occur when the stress in the thinnest ligament reaches the yield strength. Based on such a criterion, additional FE analyses were carried out to investigate the effect of key parameters on the limit loads, which lead to the following conclusions.

(1) In cases of the constant wall-thinned angle, length and bend angle, the limit pressure decreased a maximum of 40% and the in-plane/out-of-plane limit moments had similar values of 0.4 or 0.5 according to the variation of the wall-thinned depth.

(2) In cases of the constant wall-thinned angle, depth and bend angle, the limit pressure decreased a maximum of 20% and the in-plane/out-of-plane limit moments were maintained at the similar level of 0.4 or 0.5 according to the variation of the wall-thinned length.

(3) For the cases of the identical wall-thinned depth and length, and increasing wall-thinned angle, the limit pressure decreased about 14% regardless of the variation of bend angle while the value of in-plane limit moment at $\varphi=\pi/4$ was about 8% greater than those of limit moment at $\varphi=\pi/6$ and $\pi/3$.

(4) For the cases of different bend angles with the constant wall-thinned length, and increasing wall-thinned depth, the wall-thinned angles showed considerable effects on the limit pressure.

References

[1] ASME: *ANSI/ASME B31G* (1991).

[2] ASME: *ASME B&PV Code, Code Case N-597* (1998).

[3] N. Gross: Proc. Inst. Mech. Eng. Vol. 1-B (1952-1953), pp. 465-479.

[4] P.V. Marchal: J. Strain Anal. Vol. 2 (1967), pp. 84-90.

[5] J. Chattopadhyay, B.K. Dutta, H.S. Kushwaha, S.C. Mahajan and A. Kahodkar: Int. J. Press. Ves. & Piping Vol. 62 (1995), pp. 109-116.

[6] H.M. Mourad and M.Y.A. Younan: J. Press. Vess-T. Vol. 124 (2002), pp. 32-37.

[7] J. Chattopadhyay, D.K. Nathani, B.K. Dutta and H.S. Kushwaha: J. Press. Vess-T. Vol. 122 (2000), pp. 431-436.

[8] C. Balan and D. Redekop: Int. J. Press. Ves. & Piping Vol. 82 (2005), pp. 235-242.

[9] I.W. Goodall: CEGB Report RD/B/N4360, Central Electricity Generating Board (1978).

[10] C.R. Calladine: J. Mech. Eng. Sci. Vol. 16 (1974), pp. 85-87.

[11] ABAQUS: *ABAQUS User's manual Ver. 6.5* (Hibbitt, Karlsson and Sorensen, Inc., USA 2005).

[12] ASME: *ASME B&PV Code Section II* (1998).

Key Engineering Materials Vols. 385-387 (2008) pp 837-840
© (2008) Trans Tech Publications, Switzerland
doi:10.4028/www.scientific.net/KEM.385-387.837

Fracture Analysis for Stiffened Aircraft Fuselage Using Substructure Method

Jinsan Ju[1, a], *Xiugen Jiang[1,b] and Xiangrong Fu[1,c]

[1]Dept. of Civil Engineering, China Agricultural University, Beijing 100083, China;

[a]jujinsan@tsinghua.org.cn, [b]jiangxiugen@tsinghua.org.cn, [c]fuxiangrong@tsingua.org.cn

Keywords: substructure, hiearchical analysis, stress intensity factor, crack, stiffened fuselage.

Abstract. This paper primarily describes the development and application of substructure computational analysis techniques in two-step hirarchical strategy to determine stress intensity factors for the stiffened damaged panels subjected to fatigue internal pressure. A program based on substructure analysis technique and global-local hierarchical strategy has been developed for the fracture analysis of curved aircraft panels containing cracks. This program may create superelements in global and local models, and obtain fracture parameter of the crack in local model by expanding results in superelements automatically. The technique is applied to the analysis of a cracked panel with 7 frames and 10 stringers. SIFs of four cracks in it with different crack lengths are obtained efficiently.

Introduction

To obtain fracture parameter such as stress intensity factor has been made difficult by the complex nature of the airframe structures where the detail of the frames, stringers, shear clips, rivets etc. play a very important role in the nature of the damage process and on the possible propagation of any cracks that might occur. For an aircraft fuselage, there is a need to consider the fully pressurised airframe with various arrangements of frames and stringers at the model level. At the same time, fracture is essentially a local event and it is necessary to capture the full stress field in the vicinity of the crack [1]. Therefore the analysis must be sufficiently robust to ensure that all relevant phenomena can be evaluated. The traditional approach to calculate stress intensity factors of aircraft panels containing damages is to use a large number of elements and embed local details using mesh refinement in the vicinity of the crack/damage. The approach needs a very powerful computer and takes a considerable time and effort to produce a reasonable result.

The hierarchical methods are one of the best ways then. There were three-stage method [2-4] and two-stage method [5,6]. There are three or two calculations in the methods. The boundary condition data transfer between different stage models are little complicated. The large mount of work must be done to create the local models with much more details when the crack propagates.

Substructuring is a procedure that condenses a group of finite elements into one element represented as a matrix. The single-matrix element is called a superelement. Once a superelement is created by performing a substructure generation analysis, it can be used in an analysis as any other element type. Substructuring reduces computer time and allows solution of very large problems with limited computer resources. In global and local models the structure with repeated patterns except the local area in which the cracks with different lengths embed. One superelement can generated to represent the pattern of the rest area and simply make copies of it in some calculations, and the other superelement is created for the local area both in global and local models. So this method can save a significant amount of model creation time.

Technique Approach

In general, the purpose of the global model is to capture global load flow in the panel, the mesh around crack tips is rather simple, the local model is performed to extract more accurate load flow

around the crack tips and to calculate fracture parameters, taking structural detail of stiffeners and joint configurations onto account[6].

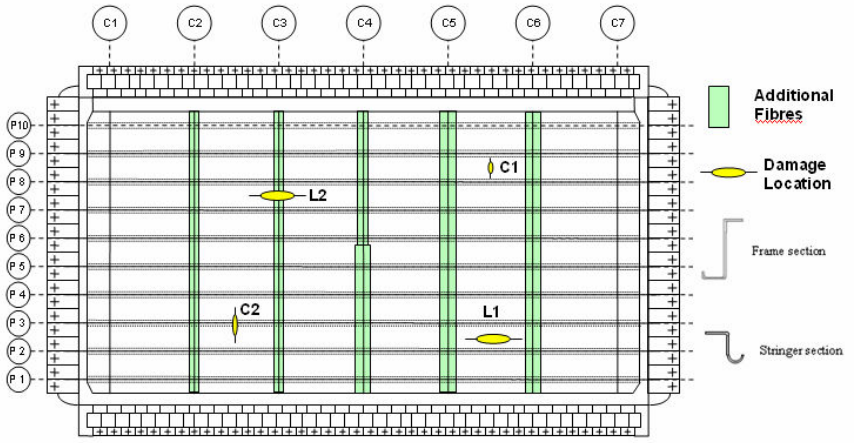

Fig. 1 Fuselage Panel with four cracks

This paper primarily describes the development and application of substructure computational analysis techniques to determine stress intensity factors for the damaged panels subjected to fatigue pressure.A typical curved panel with 4 cracks consists of 7 frames and 10 stringers and is shown in Fig. 1. The frame and stringer sections are also shown. A longitudinal crack L1 is in the centre of a bay surrounded by frame C5-C6 and stringer P2-P3. Under fatigue load, these pre-existing cracks can grow under the internal pressure and sometimes can cross from one bay into the next. During this growth process, the frame/stringer can be broken or unbroken.

One of the important requirements in the development of the analysis methodology was the automation of the model creation, superelement creation, data transfer and stress intensity factor calculation for a crack of a given length. This is necessary as the time associated with mesh generation for problems of this nature can be extremely time consuming.The detailed using the substructure to model the panel with a specified crack are now described, including the automation hierarchical process. In global model, some significant simplifications are used with respect to the frames and stringers and these are modeled using beam elements while the fuselage is modeled using shell elements. In the local model, the frames and stringers are now modeled explicitly using shell elements as is the fuselage skin, while spring elements are used for the rivets [3]. The crack tip region is carefully modeled to allow accurate calculation of the stress intensity factors. In these two models, only the superelement region the crack embeds is needed to be modeled each time, there is no change of the other superelement of the rest region.

A program system based on finite element software ANSYS is used to create models and to calculate the stress intensity factor (SIF) of crack in superelement of local model. The typical curved panel global mode consisting of 7 frames and 10 stringers model is divided into two superelements shown in Fig. 2. The crack is in the small one and its length can be changed. Aftrer calculation of the two super elements of global model, the calculation displacement results of local region corresponding to local model will be trandferred to local model as its boundary condition.

The typical local region model consisting of 2 frames and 3 stringers model is divided into two superelements shown in Fig. 3. The crack is in the small one and the crack tip region is now carefully modeled to allow accurate calculation of the stress intensity factors. In the coming calculation, the superelements in global and local models without crack need not be generated again and the small superelements will be generated with different crack lengths. The program can make the same node number at the boundary between two superelements in global and local models. The whole process including creation of superelements and the result expanding are automated by the program. The input was parameterised to allow for variations in stringer/frame size, shape and spacing. Once a number of key parameters of global and local model are input, then the two superelements are automatically generated and the calculation result of the superelement with crack can be expanded automatically as well. It is also possible to vary the size of the superelement with crack.

Calculation Results and Analysis

The skin thickness of the panel shown in Fig.1 is 1.8mm, radius of panel is 2820mm, stringer thickness is 1.8mm, frame thickness is 2.5mm, and clip thickness is 1.8mm. The material is aluminium and the elastic modulus is 73,100MPa. The distance between the frames is 533.4 mm, and the distance between stringers is 185.9 mm. The 0.3mm thickness additional carbon fibre is used stiffened the panel as shown in Fig. 1.

Both longitudinal and circumferential cracks were present in the panels and it was necessary to cater for the full range of crack growth in the analysis. The length of a longitudinal crack can vary from 26.6 mm to 1066 mm and can span up to two frames with the possibility of the frame being broken.

The small superelement model's deformation of the local model is shown in Fig. 4. This paper refined the mesh of global and local model using ½ element size of that shown in above figures, the SIF results were the same. It means that the SIF is not sensitive to the element size.

The hoop stress distribution of the local area around the crack tip in small superelement of local model is shown in Fig. 5. The hoop stress in global model is very coarse due its poor mesh around the crack tips while that of local model is very fine. The SIF is obtained from the stress distribution in Fig.5.

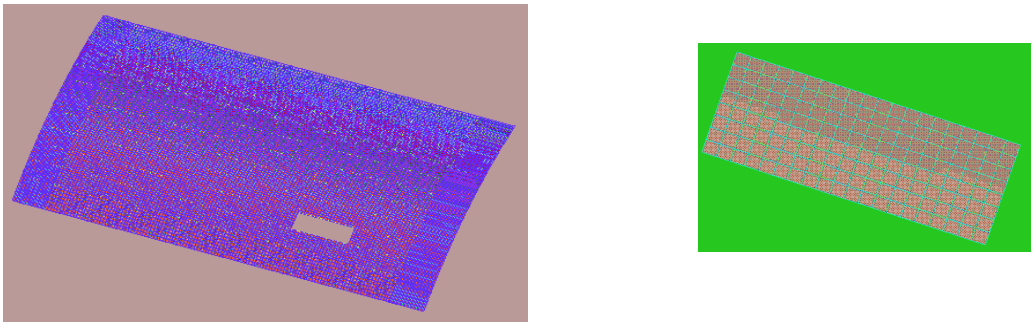

Fig.2 Two superelements of the global model

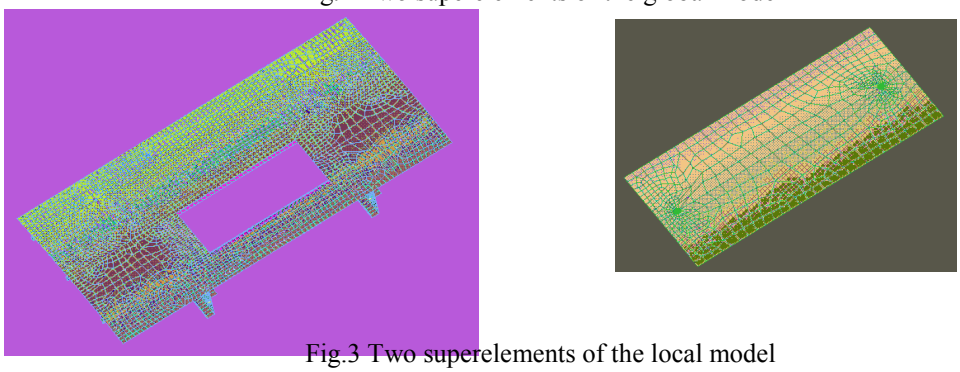

Fig.3 Two superelements of the local model

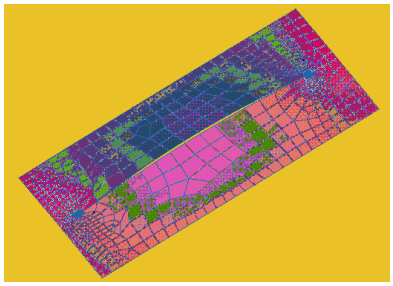

Fig.4 Deformation of the substructure

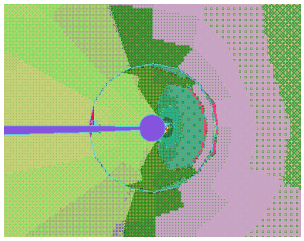

Fig.5 Stress distributions of area around the crack tips

Fig. 6 shows stress intensity factors of four cracks in Fig.1 by using above method. It can be seen that L2 encounter a fibre strap when the half length is about 400 mm and the SIF decreases due to the added stiffness of the strap. For larger crack lengths, the SIF for L1 decreases as it approached frames. The same conclusions can be gotten for circumferential cracks. The SIF here can be used to predict the duration of the stiffened aircraft panel.

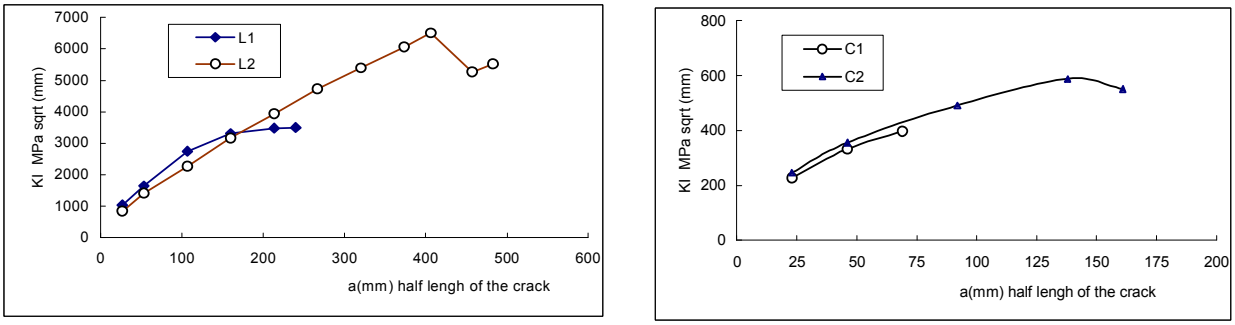

Fig.6 SIF results of 4 cracks

Conclusions

A highly efficient substructure technique combining two-step hierarchical strategy is developed here for the analysis of curved stiffened aircraft panels containing cracks. A global model consisting of two superelements is used to get the general stress distribution in the structure while a smaller, more detailed local model with two superelements is used to capture the stress distribution in the vicinity of the crack tip and the stress intensity factor by expanding calculation results of superelement containing crack region. To facilitate the requirements for repeated analysis such as different crack lengths, the approach has been automated by parameterisation of all the process from models creation, superelement creation, analysis, data transfer and result expanding. Thus, the substructure method based on two-steps hierarchical strategy is highly efficient for the analysis of a complicated cracked aircraft fuselage.

References

[1] S.N. Atluri: *Structural Integrity and Durability* (Tech Science Press, Georgia, USA 1997).

[2] J. Ju, X.Jiang, and X. Fu: Fracture analysis for damaged aircraft fuselage subjected to blast. Key Engineering Materials, Vol. 348-349(2007), p. 705.

[3] H. Kawai, L. Wang, D. S. Pipkins, K. O'Sullivan, P. E. O'Donoghue, S. N. Atluri: Automation of Global-Intermediate-Local Analysis Based on Feature Based Modelling and the Finite Element Alternating Method. Computer Modeling and Simulation in Engineering, Vol. 4 (1999), p. 457.

[4] P.E. O'Donoghue, S.N. Atluri: Computational Strategies for Fatigue Crackgrowth in Three Dimensions with Application to Aircraft Components. Engineering Fracture Mechanics, Vol. 52(1995), p.51.

[5] J. Ju, X. Jiang: Effect of Bugling Deformation on Fracture Analysis of Aircraft Panel Containing Damage and Automation Calculation. In: *Proceedings of World Conference of Computational Mechanics VI*, edited by M.YUAN, Tsinghua University Press, China, 2004, p.356.

[6] J. Ju, X.Jiang, and X. Fu: Global-local Hierarchical Analysis Techniques for Damaged Aircraft Fuselage Considering Bulging Deformation of Crack. Key Engineering Materials, Vol. 324-325 (2006), p. 871.

Key Engineering Materials Vols. 385-387 (2008) pp 841-844
© (2008) Trans Tech Publications, Switzerland
doi:10.4028/www.scientific.net/KEM.385-387.841

Research on the Metal Forming Process of the Muffler Tube using Finite Element Method

Kyu-Taek Han[1,a] , Yijiong Jin[2,b*]
[1] School of Mechanical Engineering, Pukyong National University, Busan, 608-739, Korea
[2] Dept. of Mechanical Engineering, Graduate School, Pukyong National University, Busan, 608-739, Korea
[a]e-mail: kthan@pknu.ac.kr ,[b]e-mail:bennyjin32@hotmail.com

Keywords: muffler tube; shear clearance; plate holder; punch radius; Finite Element Analysis.

Abstract: A muffler is an important part used to reduce noise and to purify exhaust gas in cars and heavy equipments. Recently there has been a growing interest in the designing and manufacturing the muffler tube due to the strict environmental regulations. The technique of perforating on the muffler tube has been largely affected by the shear clearance. And considering the concentration of the force around the punch edge, it is essential to reduced it through the punch radius. In this research, finite element analysis has been carried out to predict optimal forming conditions of the muffler tube using DEFORM^{TM}-3D. In analysis, using one-fourth component of the punch and die, metal forming process is simulated and Cockcroft-Latham ductile fracture theory is used. According to the simulation results, when the shear clearance is 0.04mm, the punch radius is 0.05mm and the value of plate holder force is 250KN, the relation of load-stroke for punch is optimized. Also the burr is minimized and optimal shear section is obtained. The simulation results are reflected to the forming process design for the muffler tube.

1. Introduction

A muffler is an important part used to reduce noise and to purify exhaust gas in cars and heavy equipments. Recently there has been a growing interest in the design and manufacturing of the muffler tube due to the strict environment regulation.

In this study, we analyzed the burr and deformation of product as shear clearance, punch radius and plate holder force. The part of tube, punch, and die shape are modeled using the commercial S/W, CATIA. Also we studied the tube deformation, stress on punch using finite element code, DEFORM^{TM}-3D, and analyzed the results through the simulation.

2. Perforating Process Analysis of Muffler Tube

2.1 Muffler tube

Fig.1 shows the muffle tube after perforating process. The specification and material property of the muffler tube are shown in Table 1 and Table 2.

Table 1 Specification of muffler tube

Diameter (mm)	Length (mm)	Thickness (mm)	Hole Diameter (mm)	Material
101.6	430	2	40	AISI-304 [70-2020F(20-1100C)]

Table 2 Material property of the muffler tube

Tensile strength (MPa)	Yield point (MPa)	Elongation (%)	Hardness (HRc)
Min 500	Min 210	Min 35	50

Fig.1 Muffler tube

2.2 Perforating process design

In the perforating process, the die is inserted at the inside of the tube and the punch to be put to fixed arrangement operates to the vertical. Shearing process is processed in the part that the tube contacts with the punch. At this time we simulated by a proper shear clearance. Additional, in order to optimize the simulation, a plate holder and a punch radius will be applied in the process, the best one will be shown at last.

2.3 Theoretical background

The fracture of metal happens when maximum shear stress(τ_{max}) or maximum tension stress(σ_{max}) reached the critical slip shear stress(τ_{cr}). The conditional expression is as follows.

$\tau_{max} = \tau_{cr}$ or $\sigma_{max} = \sigma_{cr}$
where, $\tau_{max}=(\sigma_1 - \sigma_3) / 2 = H(\varepsilon)$
$\sigma_{max} = \sigma_1 = H\sigma(\varepsilon)$
$\tau_{cr}=a+b\sigma_H+c\varepsilon$, $\sigma cr=a'+b'\sigma_H+c'\varepsilon$
where, ε:effective strain, σ_H:hydrostatic stress
Also a, b, c, a', b', c' is the function of temperature, deformation, and each velocity.

Ductile fracture condition is adopted to investigate the shear plane formation process of the piercing part using finite element method.

Cockroft proposed a growth model of pore and ductile fracture condition by the plastic deformation energy concept.

$$\int_0^{\varepsilon_f} \sigma^* d\bar{\varepsilon} = C$$

where, ε_f is fracture strain, σ^* is maximum tension principal stress, ε is effective strain, and C is material constant.

2.4 Finite element analysis

2.4.1 Modeling

The assembly of model is shown in Fig.2.

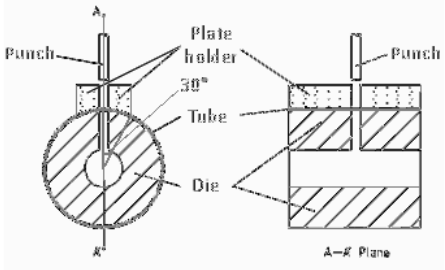

Fig.2(a) Schematic diagram of shearing apparatus

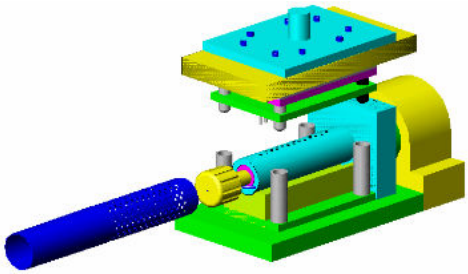

Fig.2(b) The part of perforating process

The material is assumed plastic as shown the Fig.3(a) and the anisotropy of material according to the rolling direction is ignored. Also we assumed the punch, die and plate holder to the rigid body as shown in Fig.3(b), Fig.3(c) and Fig.3(d). Fig.4 is one-fourth component of the piercing punch and die of fifteen column arrangement which is modeled for the observation of the total behavior.

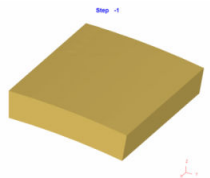

Fig.3(a) Tube

Fig.3(b) Punch

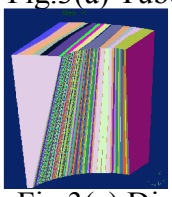

Fig.3(c) Die

Fig.3(d) Plate holder

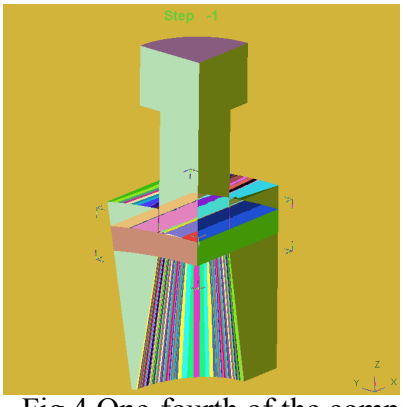

Fig.4 One-fourth of the component

2.4.2 Meshing

Solving the perforating process problem by three dimensional modeling instead of two dimensional analysis is used due to tube characteristics. In the analysis of three dimensional piercing process, the stress concentration occurred at edge level needing the mesh size to make smaller. Notably, it is modeled so that the observation of the part to be sheared is simple. The mesh condition is shown in table 3 and the picture after mesh is shown in Fig. 5.

Table 3 Mesh condition

Number of Nods	14839
Number of Elements	66434
Surface Polygons	13986
Min Element Size	0.09 mm
Max Element Size	0.3 mm

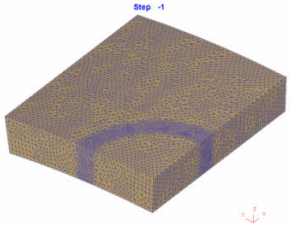

Fig.5 Mesh condition

2.4.3 Process parameter

The constant physical properties in the analysis are shown in Table 4.

Table 4 Simulation parameter

Parameter	Unit	Value
Temperature	°C	20
Stroke per step	mm	0.03
Friction coefficient	-	0.12
Punch speed	mm/sec	300
Shear angle	°	10

In the simulation, the stroke per step is defined as one-third of the minimum element size, the friction coefficient is chosen based on the recommendable value in DEFORM^{TM}-3D, and the punch speed is according to the real speed in the factory.

2.4.4 Simulation

In order to testify the effect of plate holder and punch radius in the process of muffler tube, three cases of the one-fourth component muffler tubes are simulated in this paper.

Case 1 is the normal case with the fixed plate holder. In case 2 the plate holder force is exerted and in case 3 a punch radius is used to optimized the design. The exact date is shown in Table 5 and the result of the simulation is shown in Fig.6.

Table 5 Condition of simulation data

	Clearance (mm)	Stroke (mm)	Plate holder force (N)	Punch radius (mm)
Case 1	0.08	3.6	Fixed	0
Case 2	0.08	3.6	1500	0
Case 3	0.04	3.6	1500	0.05

Case 1 Case 2 Case 3

Fig.6 Comparison of shear section according to the given cases

3. Results and Discussions

Fig.7 shows the relation of load-stroke according to the punch and die for Case 1, Case 2 and Case 3. Fig.8 shows the die load between Case 1 and Case 2. Fig.9 shows the punch load between Case 2 and Case 3.

As we can see from Fig.7, the die load of Case 2 is very big compared to the other cases and it is almost 43000N. Fig.8 also demonstrates this point. So if there is a proper plate holder force in the process, the load of die can be reduced.

From Fig.9, the punch load of Case 3 is smoother than Case 2, it means when the tube is being processed the vibration is slight.

From Fig.6 we can see that Case 3 is the best among these three cases because the burr is minimized and optimal shear section is obtained.

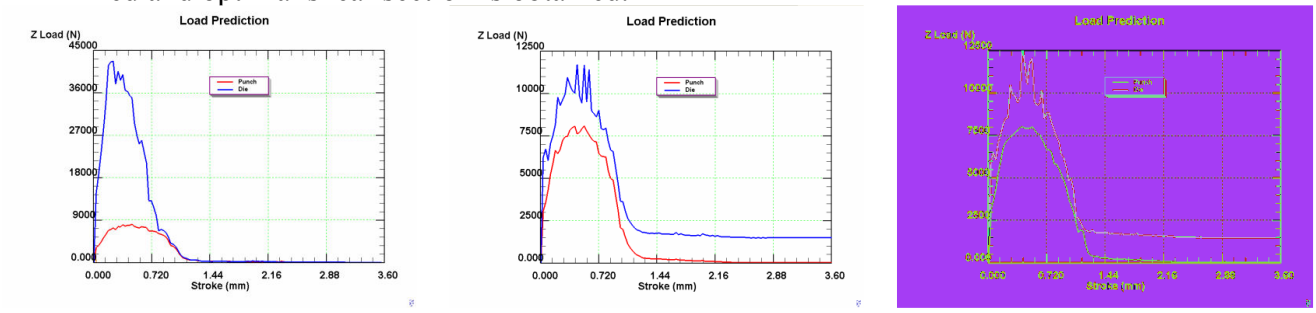

Case 1 Case 2 Case 3

Fig.7 Relation of load-stroke for punch and die

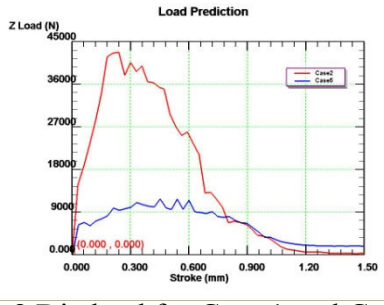

Fig.8 Die load for Case 1 and Case 2 (Stroke 1.5mm)

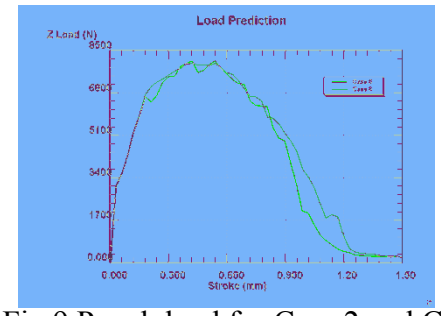

Fig.9 Punch load for Case 2 and Case 3 (Stroke 1.5mm)

Fig.10 shows damage of these three cases according to step which is the last step before fracture.

From Fig.10, the maximum damage in Case 3 is the smallest among these three cases which means that when the tube is being processed, it is a low probability to occur an unexpected problem comparing with another two cases. So the punch radius can reduce the value of damage and make the process stable.

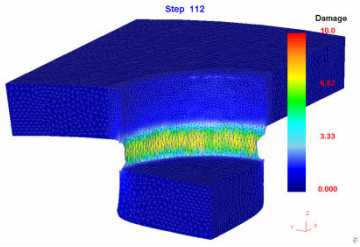

Damage of Case 1 at step 112

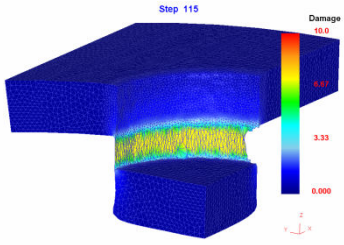

Damage of Case 2 at step 115

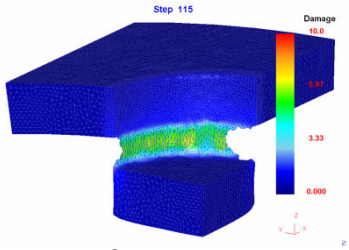

Damage of Case 3 at step 115

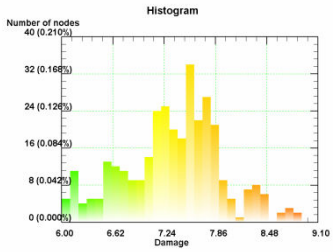

Histogram of nodes for Case 1 (Max 8.85)

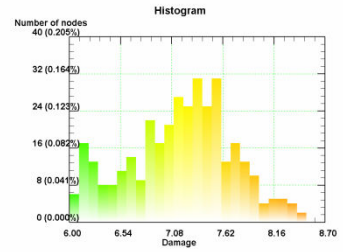

Histogram of nodes for Case 2 (Max 8.48)

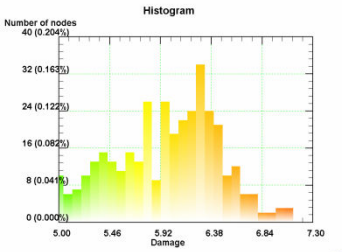

Histogram of nodes for Case 3 (Max 7.05)

Fig.10 The value of damage before fracture

4. Conclusions

In this study, the conditions to decide the perforating process of the muffler tube for automobiles are studied using finite element analysis.

The conclusions of this study obtained can be summarized as follows:

1. When the shear clearance is 0.04mm, the value of plate holder force is 250KN, the punch radius is 0.05mm, the burr is minimized and optimal shear section is obtained.
2. The plate holder can reduce the value of die load and extend the life of it.
3. The punch radius can make the punch load smoother and reduce the value of damage, it results the process stable.
4. The analysis results by FEM simulation are reflected in the perforating process design for the muffler tube and better products in dimension and quality are obtained.

References

[1] Faura, A.Garcia M.Estrems, "Finite element analysis of optimum clearance I the blanking process", Journal of Materials Processing Technology 80-81, pp.121~125, 1998.
[2] Scientific Forming Technologies Corporation, DEFORM^{TM}-3D User 's Manual, 1995.
[3] Kobaysahi, S. Oh, S. I and Altan, T., "Metal forming and the finite element method", Oxford University Press. 1989.
[4] T. C. Lee, I. C. Chan and P. F. Zheng, "Application of the Finite Element Deformation Method in the Fine Blanking Process", Journal of Materials Process Technology 63, pp.744~749, 1997.
[5] M. G. Cockcroft and D. J. Latham, "Ductility and the workability of metals", J. Inst. Metals. Vol. pp33~39. 1968.

Key Engineering Materials Vols. 385-387 (2008) pp 845-848
© (2008) Trans Tech Publications, Switzerland
doi:10.4028/www.scientific.net/KEM.385-387.845

Life Cycle Cost Management Strategy on Corrosion Deterioration and Fatigue Damage of Steel Girder Bridge

Moe M S CHEUNG[1, a], Kevin K L SO [2, b] and Xueqing ZHANG [3, c]

[1]Chair Professor and Head, [2]PhD Candidate, and [3]Assistant Professor,

Department of Civil Engineering

The Hong Kong University of Science and Technology

Clear Water Bay, Kowloon, Hong Kong, China

[a]mscheung@ust.hk, [b]kevin@ust.hk, and [c]zhangxq@ust.hk

Keywords: Corrosion, Fatigue, Deflection, Moment, Shear, Condition Index, LCC

Abstract: This paper proposes a life-cycle cost (LCC) management methodology that integrates corrosion deterioration and fatigue damage mechanisms. This LCC management methodology has four characterized features: (1) corrosion deterioration and fatigue damage models are used to predict the time when the pre-defined limits are reached; (2) the performance of the steel girder is measured by condition state sets in which deflection, moment and shear capacities and fatigue strength limits are considered altogether; (3) the cost-effectiveness of management strategies are measured by the performance improvement per unit of money spent; and (4) the LCC model includes initial design/construction cost, inspection cost, maintenance cost, repair/rehabilitation cost and failure cost. A steel girder bridge is used as an example to demonstrate the application of the proposed LCC management methodology.

Introduction

In U.S., more than 43% of the bridges are made of steel. Currently, there are 190,000 steel bridges (simply supported and continuous) of which over 40,000 (25%) are structurally deficient and over 35,000 (18.5%) are functionally obsolete [1]. The majority of the problems affecting the service life of bridges are related to fatigue sensitive details, the need to increase the service load, corrosion and the lack of proper maintenance [2]. Among typical types of steel girder bridge damages, corrosion deterioration and fatigue damage are the most common ones which are influenced by the environment and the vehicle loadings and its stress ranges. To relieve the long term financial burden on maintenance, a whole life cycle cost (LCC) management concept was introduced in recent decade and is now getting more important in engineering design, construction and management. In the whole LCC management model, the mechanism and prediction of structural member deterioration is essential. In most research works, very few of them have addressed a management strategy considering major structural assessment factors all together: the serviceability limit – deflection, the ultimate capacity limits – bending and shear, and the fatigue limit. This paper focuses on the integration of corrosion deterioration and fatigue damage models to the proposed LCC management strategy by using a steel girder bridge as an example to demonstrate its application.

`

Corrosion Model. Corrosion is influenced by the environment such as the amount of moisture in the air and the presence of salt. There is a common agreement that the corrosion time versus penetration rate can be modeled, with a good approximation, by an exponential function [1]. Lee et al. [3], based on the previous study, introduced a modified corrosion propagation model with consideration of periodic repainting. Lee's model is adopted for service life prediction in the paper.

Fatigue Model. Several models were developed to describe the process of fatigue deterioration, including the S-N model, the Miner's linear cumulative fatigue damage model and the crack growth model under linear-elastic fracture mechanics (LEFM) approach [4]. S-N and Miner's models both have limitation in addressing the probabilistic nature whereas LEFM approach based on crack propagation theory yields more accurate results for fatigue and fracture reliability assessment if the current crack size is measured [5].The most commonly used crack growth model is the well known Paris-Erdogan Model which can be further simplified to determine the required cycles for fatigue failure and this model is adopted for service life prediction in the paper. Having estimated the fatigue life in cycles for the component, the data on average daily traffic specific to the bridge roadway, distribution of traffic volume per traffic lane and expected traffic growth in future years are used to convert fatigue cycles in terms of time (years).

Corrosion and fatigue damages will weaken structural members and result in increment of deflection, reduction of ultimate bending moment and shear capacities and reduction of fatigue strength. The aforesaid models with integration of pre-defined limits as below form service life prediction models to predict the service condition of members at any time throughout its life.

Proposed LCC Management Strategy. Conventional LCC management strategy is based on fixed pre-defined limit states either serviceability control (i.e. deflection), or structural capacity control (i.e. moment and shear capacities) or fatigue control. However, it may not be always true that the one limit state dominates over one another or vice versa in all circumstances. This paper proposes the consideration of serviceability, structural ultimate capacity and fatigue life simultaneously which are essential in LCC analysis.

Definition of Limits. The paper defines the structural condition limits as follows:

- **Serviceability Limit**. It is defined in terms of deflection of the girder at any time, $\delta(t)$, throughout its life. If the deflection exceeds to code-allowable deflection requirement, δ_{all}, serviceability failure is assumed to occur. It is assumed that repair/rehabilitation works must be conducted before the deflection of girder reached its limit.
- **Structural Ultimate Limits.** Ultimate limits are governed by condition of structural capacities of bending moment, M, and shear, V. It is assumed that repair/rehabilitation works must be conducted before the total applied bending moments or shears reached the ultimate bending moment or shear capacity, $M_u(t)$ and $V_u(t)$ of girder at any time throughout its life. .

`

- **Fatigue Strength Limit.** The fatigue strength limit suggested in this paper is defined in terms of accumulated number of stress cycle at any time, *N(t)*, throughout its life. If the number of stress cycles exceeds to its allowable, N_{all}, fatigue failure is assumed to occur. It is assumed that repair/rehabilitation works must be conducted before reached its limit.

To mathematically present the condition of structural member towards its limits at particular time, buffer function, *F(t)*, measured in percentage for each limit are then formulated accordingly as Eqs 1 to 4 where subscripts *δ, M, V* and *N* for *F(t)* refer to buffer function for deflection, bending moment, shear and fatigue strength respectively; and subscripts *DL, SDL, LL* and *I* for M or V refer to moment or shear induced by dead load, superimposed dead load, live load and impact respectively.

$$F_{\delta}(t) = \frac{\delta_{all} - \delta(t)}{\delta_{all}} \tag{1}$$

$$F_{M}(t) = \frac{M_u(t) - M_{DL} - M_{SDL} - M_{LL} - M_I}{M_u(t)} \tag{2}$$

$$F_{V}(t) = \frac{V_u(t) - V_{DL} - V_{SDL} - V_{LL} - V_I}{V_u(t)} \tag{3}$$

$$F_{N}(t) = \frac{N_{all} - N(t)}{N_{all}} \tag{4}$$

Condition States for Girder. To assist systematic management, four proposed discrete condition states, Good (G), Satisfactory (S), Fair (F), and Poor (P) are assigned with respect to the percentage range of deflection, moment, shear and fatigue buffer functions. Let Ω_j denote the set of possible limit states, then,

$$\Omega_j = \begin{cases} G & F_{\delta}(t) \geq 15\%;\quad F_M(t) \geq 40; F_V(t) \geq 40; F_N(t) \geq 40 \\ S & 10\% \leq F_{\delta}(t) < 15\%;\quad 30\% \leq F_M(t)\ or\ F_V(t) or\ F_N(t) < 40\% \\ F & 5\% \leq F_{\delta}(t) < 10\%;\quad 20\% \leq F_M(t)\ or\ F_V(t) or\ F_N(t) < 30\% \\ P & F_{\delta}(t) < 5\%;\quad F_M(t)\ or\ F_V(t)\ or\ F_N(t) < 20\% \end{cases} \tag{5}$$

where j=1, 2, 3 and 4 with respect to different limits: deflection, bending moment, shear and fatigue. Once acceptable service condition states for each limit are defined, the repair/rehabilitation actions to be carried out at particular time before reaching its acceptable condition limits can be predicted. The predicted action time will then be used in the LCC model.

Methodology of Integrated Life Cycle Cost (LCC) Model.

To evaluate the cost-effectiveness of different management strategies, LCC model is used as the basis. In which, proper maintenance or repair/rehabilitation actions taken at proper time is the key elements to the accuracy of the LCC model. The LCC model is a combination of initial design/construction cost, C_i and present value of costs of inspection $C_{ins}(t)$, maintenance $C_m(t)$, repair/rehabilitation $C_{rep}(t)$ and failure $C_f(t)$ respectively at particular occurring time, *t*, throughout its life period, *T, in* years with a discount rate, *r*. The minimum expected LCC denoted as LCC_{ET} has been the most widely used criterion in design optimization of new structural systems considering lifetime performance. LCC_{ET} of a structure over its life is generalized as Eq. 6.

$$LCC_{ET} = C_i + \sum_{t=1}^{T}\left[\frac{C_{ins}(t)}{(1+r)^t} + \frac{C_m(t)}{(1+r)^t} + \frac{C_{rep}(t)}{(1+r)^t} + \frac{C_f(t)}{(1+r)^t}\right] \tag{6}$$

`

Example of LCC Management Strategy of Steel Girders

A two-lane steel girder bridge with 75-years designed life is adopted to illustrate the proposed LCC management strategy. The example steel girder bridge as shown in Figure 1 has a simple span of 28.0 m with two lane traffic in same direction. It is assumed that repair/rehabilitation actions only be taken places when the condition reaches 'Poor-P' state range.

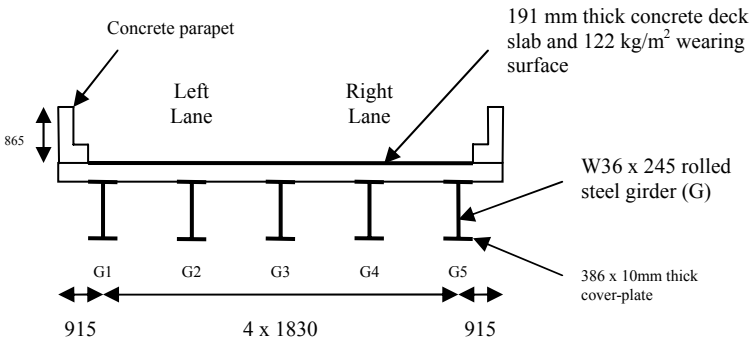

Figure 1 Typical Cross Section of Steel Girder Bridge (unit: mm)

	G1	G2	G3	G4	G5
Moment	26	Remain 'F' State		Remain 'S' State	
Fatigue	48	43	47	50	62

Table 1 Time (yr) to 'P' State of Moment and Fatigue Buffers

From Eqs. 1 to 5, results show condition of bridge deck in terms of deflection buffer and condition of all girders with respect to shear buffer will remain 'Satisfactory-S' state throughout its life. While simulated time to reach 'P' state in terms of moment and fatigue buffer limits at 80 percentile value are shown in Table 1. From service life prediction models, future conditions at predicted time can be obtained. Management strategy covering inspection, maintenance, repair/rehabilitation works with associated costs for each girder can then be prioritized accordingly and cost of each works at particular time will then be incorporated into Eq. 6 to obtain the minimum $LCC_{ET.}$

Conclusion

This paper proposes a LCC management methodology with a service life prediction model that integrates serviceability limit, structural ultimate limit and fatigue strength limit. An example is provided to demonstrate the application of the proposed LCC model.

Acknowledgement

This paper is financially supported by RGC of HKSAR, China under Grant No. 610505.

References

[1] Czarnecki, A. A. and Nowak, A. S. (2008). "Time-variant reliability profiles for steel girder bridges", *Structural Safety* 30 (2008), pp. 49-64

[2] Tavakkolizadeh, M., and Saadatmanesh, H. (2003). "Fatigue strength of steel girders strengthened with carbon fiber reinforced polymer patch", Journal of Structural Engineering, Vol. 129, No. 2, 1 February 2003, pp. 186-196.

[3] Lee, K. M., Cho, H. N. and Cha, C. J. (2006). "Life-cycle cost-effective optimum design of steel bridges considering environmental stressors", Engineering Structures 28 (2006), pp. 1252-1265

[4] Yanaka, Y. and Kitagawa, M. (2002). "Maintenance of steel bridges on Honshu-Shikoku crossing", Journal of Construction Steel Research 58 (2002) 131 -150

[5] Dexter, R. J., Wright, W. J. and Fisher, J. W. (2004). "Fatigue and fracture of steel girders", Journal of Bridge Engineering, Vol. 9, No. 3, 1 May 2004, pp. 278-286.

`

Key Engineering Materials Vols. 385-387 (2008) pp 849-852
© (2008) Trans Tech Publications, Switzerland
doi:10.4028/www.scientific.net/KEM.385-387.849

Fatigue properties of Al-Li plates joined by Friction Stir Welding

P. Cavaliere[1, a], F. Panella[1,b] and A. Squillace[2,c]

[1]Department of Innovation Engineering, University of Salento, Via per Arnesano 73100 Lecce, Italy
[2]Department of Materials and Production Engineering, University of Naples "Federico II", 80125 Naples, Italy

[a]pasquale.cavaliere@unile.it, [b]francesco.panella@unile.it, [c]squillac@unina.it

Keywords: Friction Stir Welding; Al-Li; Fatigue; Fatigue crack behavior; Thermoelastic stress analysis.

Abstract. Al-Li alloys are characterized by a strong anisotropy in mechanical properties and microstructure with respect to the rolling direction. Plates of 2198 Al-Li alloy were friction stir welded by employing maximum rotation speed: 1000 rev/min and welding speed of 80 mm/min, both in parallel and orthogonal directions with respect to the rolling one. The joints mechanical properties were evaluated by means of tensile tests at room temperature. In addition, fatigue tests performed with a resonant electro-mechanical testing machine under constant amplitude control up to 250 Hz loading, were conducted in axial control mode with $R(\sigma_{min}/\sigma_{max})=0.33$, for all the welding and rotating speed conditions. The fatigue crack propagation experiments were performed by employing single edge notched specimens.With the aim to characterize the weld performances, both the microstructure evolution at jointed cross sections, related to the welding variables, and the fractured surfaces were respectively analyzed by means of optical and scanning electron microscopy.

Introduction

The Friction Stir Welding (FSW) technology is being targeted by modern aerospace industry for high performance structural applications [1]. If compared to traditional welding techniques, FSW strongly reduces the presence of distortions and residual stresses [2-4]. Recently some papers were published regarding the microstructural and mechanical properties of friction stir welded Al-Li alloys. In particular Hao et al. presented some interesting results of tensile and bending mechanical properties as a function of processing parameters in 1420 alloy [5]. In different other papers, the authors showed the fatigue properties of FSW plates as a function of processing parameters and microstructural evolution [6, 7].

Experimental procedure

The material under investigation was a 2198-T851 aluminium-lithium alloy produced by ALCAN (Toronto, Canada) under the form of rolled sheets of 5 mm thickness with the following composition (wt%): Si 0.03, Fe 0.04, Cu 3.3, Mn 0.01, Mg 0.32, Cr 0.01, Ni 0.01, Zn 0.02, Ti 0.03, Zr 0.11, Pb 0.01, Li 1.0, Al bal. 200mm length x 80mm rectangular plates were welded in perpendicular and parallel direction with respect to the rolling one. The employed rotating velocities (in clockwise direction) of the cylindrical threaded tool was 1000 RPM while the advancing selected speed was 80 mm/min the tilt angle was set equal to 2°. Some sheets were instrumented with thermocouples embedded in the parent material, in different position, in order to monitor the temperature profiles as a function of the distance from the weld line. K-type thermocouples with a sheath diameter of 2 mm were employed. Endurance fatigue tests were performed by a resonant electro-mechanical testing machine under constant loading control up to 250 Hz sine wave loading (TESTRONIC^{TM} 50±25 kN, produced by RUMUL, SUI). The cyclic fatigue tests were conducted under axial total stress amplitude control mode under fully reversed, push-pull, tension loading ($R=\sigma_{min}/\sigma_{max}=0.33$). The fatigue specimens gauge dimensions measured 12.5-mm width, 50-mm

length. The fatigue crack propagation experiments were performed with the same machine and by employing single edge (1 mm) notched specimens obtained on the advancing side. Due to such inhomogeneities, when a clock wise direction rotation is employed the less resistant zone results the one on the advancing side of the tool. From previous studies performed by the authors, in fact, it was demonstrated for 6082 aluminium alloy that the fractured zone for tensile and fatigue specimens resulted the one on the advancing side of the tool.

Results and discussion

The temperature variation as a function of the distance from the welds centerline for both the joining configurations was calculated. For both the cases, the maximum measured temperature (at a distance of 10 mm from the centerline) was close to 250 °C and then decreasing by increasing the distance, for both the welding configurations, the temperature behavior is very similar. In all the measurements, the temperatures in the retreating sides resulted lower, respect to the advancing one, by increasing the distance from the welds centerline. For the L welding configuration, the absolute temperatures resulted higher (in the same zone) respect to the T configuration. Such different thermal history for the two welding configurations led to different profiles in the microhardness measurements. In Fig. 1 they are plotted the microhardness profiles for the L and T welds, for comparison the mechanical properties are plotted in the same graphs with the provisional thermal profiles obtained by the polynomial fit calculated from the measured temperatures. In the case of L configuration it seems that the material is less effective in dissipating the thermal energy developed by the tool movement, in fact, for both the configurations the highest temperature is very similar (close to 320 °C in the center of the nugget zone) but the profile describes that the temperature decreases much more faster in the T configuration with respect to the L one.

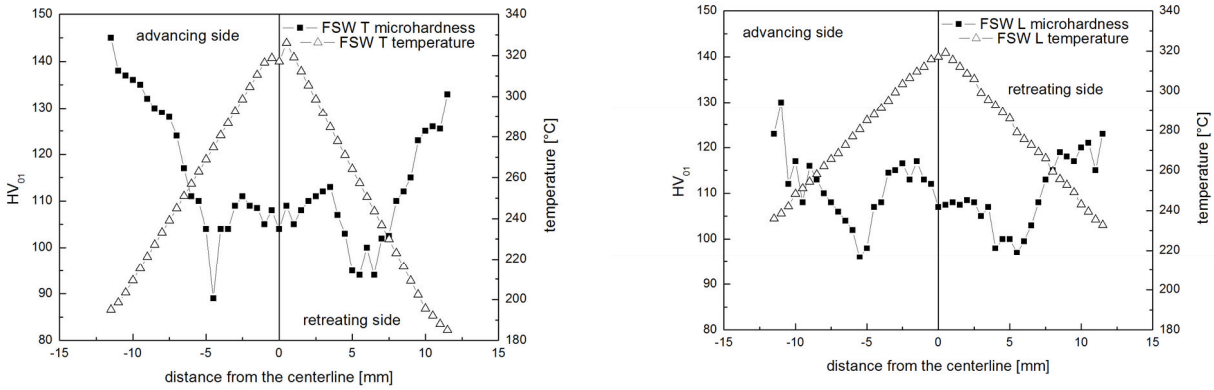

Figure 1: Temperature profiles coupled with the microhardness values, in the T and L configurations, on both the advancing and the retreating sides of the tool.

The fatigue properties of the FS Welded joints can be observed in S-N curves for the toughest studied joints, as shown in Fig. 2. The fatigue specimens have been cut from the welded plates in a number of 25 for each condition and polished, according to standard procedures and avoiding superficial defects. The bead material in all the welding configurations shows similar fatigue behavior in the low cycle regime, since extremely narrow data differences are produced in terms of stresses especially in the intermediate region; in the high cycle regime, the Wöhler curves did not show clear differences. It can be observed decreasing stress amplitude limits as function of life endurance up to the fatigue limit (~$4x10^6$ cycles to failure) and such value is very similar for both the configurations at a value of the cyclic maximum stress of 200 MPa.

In different configuration and with the same used welding parameters it was reached a good combination between the material plasticization during tool rotation and the mixing affect produced by the advancing movement leading to the disappearance of the effects due to the rolling process.

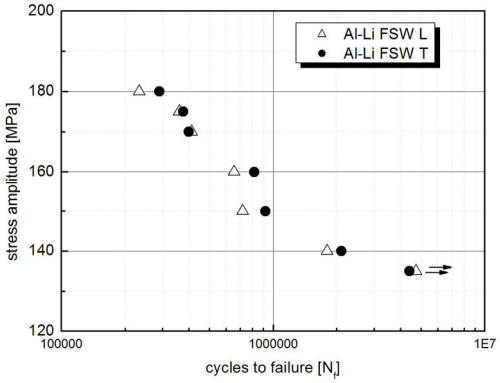

Figure 2: Fatigue endurance curves of the friction stir welded 2198 Al-Li plates in both T and L directions.

With a revolutionary pitch in the range of 0.07 – 0.1, the process is in the optimal temperature and strain rates conditions to produce good microstructure quality without defects for butt joints and therefore sound welds are achieved. The longitudinal residual stresses were measured in the cross sections of the welds by X-ray diffraction using the $\sin^2\Psi$ method. Residual stress profiles of the two studied joints configuration is shown in Fig. 3a. It must be observed that the residual stresses can be relaxed for the cut of the mechanical testing specimens, for this reason the residual stresses showed in the present work are related to the measurements performed on the cut material. As a general behavior, the residual stresses have compressive character by approaching the weld line, changing to a tensile character in the weld zone from the heat affected one. It can be observed that the higher values of residual stresses are achieved in the advancing side of the tool, the profiles show a very similar behavior in both the configurations with higher values experienced in the case of T joints.

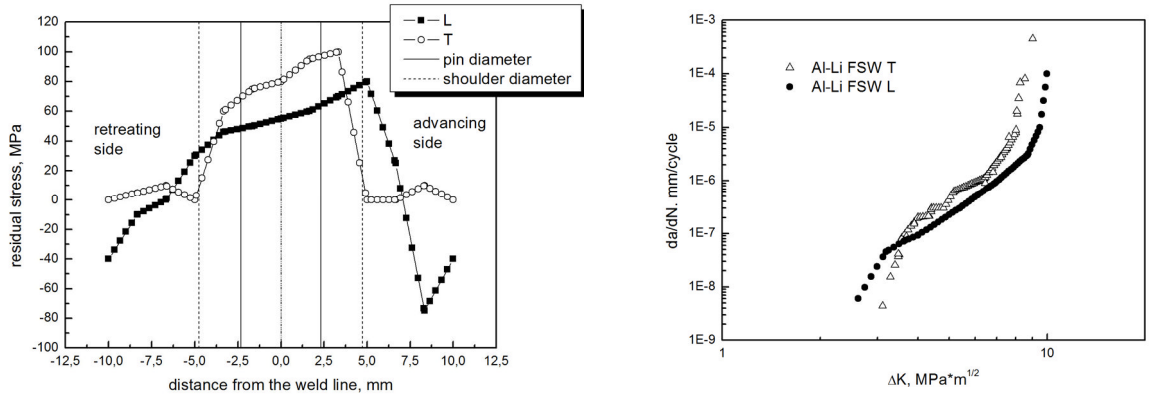

Figure 3: Residual stresses in the studied joints a); rack growth behaviour for the 2198 Al-Li plates friction stir welded in T and L configurations b).

The crack initiation and growth behaviour, for both the studied configurations is shown in Fig. 3b. The fatigue crack growth rate results are shown in the curves processed at a load ratio of R = 0.33. Both the L and T welds show a similar behaviour in the crack initiation and growth leading to the conclusion that the FSW process eliminates the effect of rolling direction on the fatigue properties of the welds.

Summary
The effect of rolling direction respect to the welding one on the mechanical behavior of FSW Al-Li plates was studied and the results reported in the present paper. The thermal profiles of the material during welds was very similar for both the configurations with a temperature of 250 °C at 10 mm from the centerline to 320 °C in the center of the welds. The mechanical strength of the base material results much more higher in the L direction respect to the T one accompanied with a reduction in ductility and an increase in the necking value, demonstrating the strong anisotropy of such kind of Al-Li alloys with respect to the rolling direction. In the high cycle fatigue regime, the Wöhler curves did not show clear differences. It was observed decreasing stress amplitude limits as function of life endurance up to the fatigue limit (~$4x10^6$ cycles to failure) and such value was very similar for both the configurations at a value of the cyclic maximum stress of 200 MPa.
Both the L and T welds show a similar behaviour in the crack initiation and growth leading to the conclusion that the FSW process eliminates the effect of rolling direction on the fatigue properties of the welds.

References

[1] R.S. Mishra, Z.Y. Ma ZY. Friction stir welding and processing. Mater. Sci. Engineering Vol. R50 (2005), p. 1.

[2] G. Bussu, P.E. Irving. Int. J. Fatigue Vol. 25 (2003), p. 77.2003;25:77–88.

[3] R. John, K.V. Jata, K. Sadananda Int. J. Fatigue Vol 25 (2003), p. 939.

[4] K.V. Jata, K.K. Sankaran, J. Ruschau Met. Mat. Transactions Vol 31A (2000), p. 2181.

[5] S. Wei, C. Hao, J. Chen. Mater. Sci. Engineering Vol A 452–453 (2007), p. 170.

[6] P. Cavaliere, A. Squillace, F. Panella. J. Mater. Proc. Technology Vol 200 (2008), p. 364.

[7] P. Cavaliere, A. Squillace, F. Panella. J. Mater. Proc. Technology Vol 180 (2006), p. 263.

Key Engineering Materials Vols. 385-387 (2008) pp 853-856
© (2008) Trans Tech Publications, Switzerland
doi:10.4028/www.scientific.net/KEM.385-387.853

A Viscoplastic Constitutive Model for Single Crystals and Its Application in a Numerical Simulation of Creep-Plasticity Behaviors

Xiangguo Zeng[1,a] Huayan Chen[1,b], Zhanhua Gao[2, c]

[1.] College of Architecture and Environment , Sichuan University, Chengdu, P.R. China, 610065

[2.] School of Engineering, University of Southern California, Los Angeles, CA, USA 90089

[a]xiangguo_zeng@yahoo.com.cn, [b]kay_chy@126.com, [c]zanhua_gao@hotmail.com

Keywords: Slip System, Viscoplasticity, KBW Model, Creep-Plasticity Interaction.

Abstract. Founded on the energy storing characteristics of microstructure during irreversible deformation, a viscoplastic constitutive model with no yielding surface introduced was developed for single crystals by adopting a spring-dashpot mechanical system. Both plastic dashpots reflecting the material time-independent responses and Newtonian dashpots mirroring the material time-dependent viscous responses were introduced to describe the viscoplasticity of slip systems. The single crystal constitutive model was established based on the thermodynamics of internal variables and the theory of absolute reaction rate. By implementing the KBW self-consistent theory, a polycrystal viscoplastic constitutive model was formed. The numerical analysis in corresponding algorithm was significantly simplified as no searching process for the activation of the slip systems and slip directions was required. The numerical simulation of creep-plasticity behaviors demonstrated excellent agreement with the corresponding experimental data.

Introduction

In recent years, great attentions have been paid to the development of polycrystal plastic constitutive models based on microstructure deformation mechanism [1]. These microstructure-based models are essential for describing material behavior under the effects of rate, microstructure and loading history, etc. [2]. Nowadays, more efforts are being made for the study of polycrystal viscoplastic constitutive models [3-4].The existence of presumed yielding shear stresses and the adoption of the corresponding slip principles in the classic plasticity theory involve the numerical analysis into additional iterations to search for the activation of slip systems and slip directions, which not only complicates the numerical analysis but also adversely affects the accuracy, convergence, and efficiency of the polycrystalline analysis.

Rate-dependent Non-classic Single Crystal Constitutive Model

In single crystals, the overall deformation of a slip system under the resolved shear stress is contributed by three individual displacements: 1) Elastic deformation of the microstructure of the slip system; 2) Time-independent slip of the slip system; 3) Time-dependent intrinsic displacement of the slip system. The principle described above can be illustrated by the simple mechanical model shown in Fig. 1. The model consists of a spring representing the elastic deformation of the slip system m, a plastic dashpot $a^{(m)}$ representing the time-independent slip $p^{(m)}$, and a Newtonian dashpot $b^{(m)}$ representing the intrinsic displacement $q^{(m)}$. $\gamma^{(m)}$ is the overall deformation of the slip system m and C represents the spring stiffness. The following relations between the three individual displacements and the resolved shear stress $\tau^{(m)}$ can be obtained.

$$\tau^{(m)} = C(\gamma^{(m)} - p^{(m)} - q^{(m)}) \tag{1}$$

The time-independent slip can be given as:

$$\tau^{(m)} = a^{m} dp^{(m)} / d\varsigma_{(m)} \tag{2}$$

where a^m is the material parameter of the slip system m.
ζ_k denotes the intrinsic time of the slip system m, which
can be defined by the following differential form:

$$dz_m = \frac{d\varsigma_m}{f_m H_m} = \frac{\Gamma_m d\gamma_m}{f_m H_m}, \Gamma_m = \frac{d\gamma_m}{d\varsigma_m} \qquad (3\text{-a, b})$$

where $z^{(m)}$ & f_m are the intrinsic time and hardening coefficient. H_m stands for the effect on the hardening of the slip system m from other slip systems. The evolution of f_m meets:

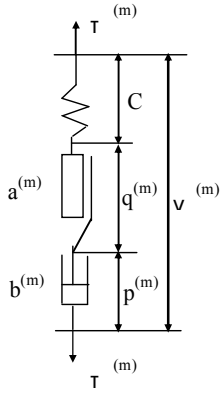

Fig. 1 Rate-dependent mechanical model

$$\frac{df_m}{dz^{(m)}} = \beta_1 (d_1^* - f_m) \;\; ; \;\; d_1^* = \begin{cases} (1+\eta\zeta_m^c) d_1 \\ d_1 \end{cases} \qquad (4\text{-a, b})$$

where d_1 is the saturation value and β_1, η are material constants. $\eta\zeta_m^c$ refers to additional hardening caused by creep deformation. Latent hardening from Bassani[5] is referred as a function of hardening, i.e.

$$H_m = 1 + \sum_{k \neq m} f_{mk} \tanh(2\beta_s \zeta_k) \qquad (\text{m} = 1, 2, 3 \ldots \text{N}) \qquad (5)$$

where ζ_k is the slip amount of slip system k. β_s and f_{mk} are material parameters[6]. β_s denotes the rate of H_m in approaching to the saturation value. The $q^{(m)}$ can be assumed as the average displacement of atomic crowd overcoming the energy barrier of the slip system m formed by the random distributions of point defects, dislocations, etc. The average velocity of atomic crowd overcoming the energy barrier with the height of $\varepsilon_0^{(r)}$ depends on energy tilt $\omega^{(r)}$ under external stresses [7-8].An approximation can be made as following:

$$dq^{(m)} / dt = Ke^{-\beta\bar{\varepsilon}_0^{(r)}} \sinh(\beta\overline{\omega}^{(r)}) \qquad (6)$$

where K and $\bar{\varepsilon}_0^{(r)}$ are material constants. $\beta = 1/KT$ in which T is absolute temperature and K is Boltzmann constant. Assuming that the energy barrier height has an exponential relationship with the effective stress in external stress field, the Eq.(7) can be obtained:

$$dq^{(m)} / dt = ASinh(\left|\tau^{(m)} - \chi^{(m)}\right| / D)^n \quad ; \quad (\overline{\omega} = \left((\tau^{(m)} - \chi^{(m)}) / D\right)^n \quad ; \quad \chi^{(m)} \text{ could be zero }) \qquad (7)$$

As the first approximation, assuming that the resistance of the dashpot is proportional to $dq^{(m)} / dt$, i.e. $\tau^{(m)} = bdq^{(m)} / dt$, where b is a constant. In Eq.(1) taking derivative about intrinsic time $z^{(m)}$ can get:

$$d\tau^{(m)} / dz^{(m)} = C(d\gamma^{(m)} / dz^{(m)} - dp^{(m)} / dz^{(m)} - dq^{(m)} / dz^{(m)}) \qquad (8)$$

Combining Eq.(2) , Eq.(7) and Eq.(8), non-classic single crystal constitutive model can be obtained:

$$d\tau^{(m)} + ACdtSinh(\frac{\left|\tau^{(m)} - \chi^{(m)}\right|}{D})^n = (C - \frac{\alpha\tau^{(m)}\Gamma_m}{f_m H_m}) d\gamma^{(m)} \qquad (9)$$

Algorithm Derivation of Rate-dependent Polycrystal Constitutive Model

The incremental form of KBW self-consistent model can be described as Eq. (10)[9]:

$$\Delta\sigma_c - \Delta\sigma = -\frac{2(7-5\nu)}{15(1-\nu)} G(\Delta\varepsilon_C^P - \Delta\varepsilon^P) \tag{10}$$

Where G and ν stand for the shear modulus and Poisson ratio of polycrystals, respectively. $\Delta\sigma_c$ and $\Delta\varepsilon_c^p$ denote local stress and strain of a single crystal while $\Delta\sigma$ and $\Delta\varepsilon^p$ are the overall stress and strain that are considered as the average of the local stresses and strains over all randomly distributed single crystal grains. This work applied a mixed average approach based on icosahedrons [6], which ensures to derive 20 homogeneously-distributed directions in space and can be expressed as

$$\Delta\bar{\varepsilon}^p = \frac{1}{20}\sum_{i=1}^{20}\frac{1}{2\pi}\int_{-\pi}^{\pi}\Delta\varepsilon_c^p(\theta_i,\phi_i,\omega)d\omega \tag{11}$$

Noticing the plastically incompressible characteristic of crystals, Eq.(10) can be rewritten as:

$$\Delta\sigma_{KK_c} = \Delta\bar{\sigma}_{KK} \tag{12}$$

which implies that the stress increments of volumetric stress inside the crystal spheres are identical to the macroscopic one. Combining the (10) and (12), Eq.(13) can be obtained:

$$\Delta\underline{q} = \Delta\underline{S} + \frac{2(7-5\nu)}{15(1-\nu)} G\Delta\underline{\varepsilon}^p \quad \text{and} \quad \Delta q = \Delta S_c + \frac{2(7-5\nu)}{15(1-\nu)} G\Delta\varepsilon_c^p \tag{13}$$

where $\Delta\underline{S}_c, \Delta\underline{S}$ are the deviator stress incremental of single crystal and polycrystal. Multiplying both sides of Eq.(13) by $\alpha^{(m)}$ and noticing that $\Delta\underline{\varepsilon}^p = \sum_n \Delta\gamma^n \underline{\alpha}^n$, Eq.(14) can be obtained as following from Eq.(9):

$$\Delta\underline{q}\alpha^{(m)} + ACdt\sinh\left(\frac{\left|\tau^{(m)} - \chi^{(m)}\right|}{D}\right)^n = \left(C - \frac{\alpha\tau^{(m)}\Gamma_m}{f_m H_m}\right)d\gamma^{(m)} + 2G\frac{(7-5\nu)}{15(1-\nu)}\sum_n \Delta\gamma^{(n)}\alpha^{(n)}\alpha^{(m)} \tag{14}$$

Let $B^{(m)} = \Delta\underline{q}\alpha^{(m)} + ACdt\sinh\left(\left|\tau^{(m)} - \chi^{(m)}\right| / D\right)^n$; $A_{nm} = \left(C - \frac{\alpha\tau^{(m)}\Gamma_m}{f_m H_m}\right)d\gamma^{(m)} + 2G\frac{(7-5\nu)}{15(1-\nu)}\sum_n \Delta\gamma^{(n)}\alpha^{(n)}\alpha^{(m)}$ (15)

Then Eq.(14) can be expressed as

$$\sum_{n=1}^{N} A_{nm}\Delta\gamma^{(n)} = B^{(m)} \tag{16}$$

Where A, C, α and D are material constants. Eq.(7) suggests that $\Delta\underline{q}$ is solely dependent on the deviator stress increment and plastic strain increment of polycrystals.

Comparison of Experimental and Computational Results

The creep-plasticity behavior of type 316 stainless steel at elevated temperature of 600℃ was studied. The specimens were loaded to σ_A =190 MPa along pure shear direction. Then the stress was held and creep occurred. After creep strain reached γ_c =0.5%, 0.75%, 1.0%, respectively, the specimens were plastically loaded to equivalent strain of 5.0%[10]. Meanwhile, the experiments were conducted to compare the effects of different loading histories in which the specimens were only plastically loaded to the same strain level of 5.0%. The experimental results in Fig. 6 (a) illustrates that when the material is deformed to the same strain level of 5%, the applied stresses for the specimens with prior creep $\gamma_c / \sqrt{3}$ =0.5%, 0.75% and 1.0% are significantly higher than that in the pure plasticity case. The computational results shown in Fig. 6(b) well reproduce the basic

characteristics of the above creep-plasticity material responses. The different hardening effect on materials caused by the same amount of creep and plastic deformation can attribute to the difference between the substructures resulted from the different loading history. The computational results in Fig. 6(b) show excellent agreement with the experimental results.

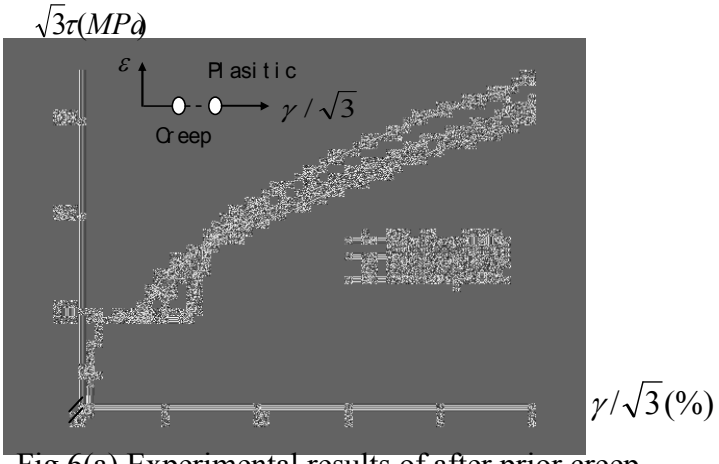

Fig.6(a) Experimental results of after prior creep

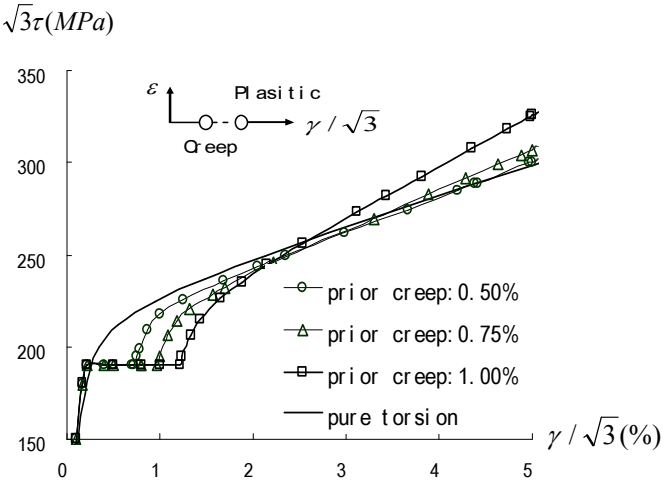

Fig. 6(b) Calculated results of after prior creep

Acknowledgments

Financial support from the Chinese National Science Foundation through the contract of 10776023 is appreciated.

Reference

[1] Voyiadjis, G. Z., Al-Rub, R. K. A., Palazotto, A. N., Thermodynamic framework for coupling of non-local viscoplasticity and non-local anisotropic viscodamage for dynamic localization problems using gradient theory, Int. J. of Plasticity, 20, 981-1038. (2004).

[2] Glazoff, M. V., Barlat, F., Weiland, H., Continuum physics of phase and defect microstructures: bridging the gap between physical metallurgy and plasticity of aluminum alloys, Int. J. of Plasticity, 20, 363-402. (2004).

[3] K. C. Hwang, Y. Guo, H. Jiang, Y. Huang , and Z. Zhuang, The finite deformation theory of Taylor-based nonlocal plasticity Int. J. of Plasticity, 20, 831-839, (2004).

[4] Valanis, K. C. 1979, An Internal Variable Model of Viscoplasticity, Int. J. Enging Sci.,Vol. 22,No. 8-10, pp. 1041-1053, (1984).

[5] Bassani J.L., Single crystal hardening. Appl Mech Rev, 43(5):320-327, (1990).

[6] Pengxianghe Zengxiangguo Fanjinghong , Peng Xianghe Zeng Xiangguo A Nonclassical Model for Slip and Its Application Acta Mechanica Solida Sinica, Vol.21,No.2, pp. 131-137. (2000).

[7] E.H.Jordan, K.P.Walker, A Viscoplastic Model for Single Crystals, Journal of Engineering Materials and Technology, 114, 19-26. (1992).

[8] K.C.Valanis and S. Lalwani, Thermodynamics of internal variables in the constitutive of the absolute reaction rate theory, The Journal of Chemical Physics, Vol.67,No.9,pp. 3980-3990. (1977).

[9] Budiansky B, Wu TT. Theoriticals Prediction of Plastic Strains of Polycrystals. Proc. 4th Congr. Appl. Mech., pp. 1175-1185. (1962).

[10] Ohashi Y, Kawai M and Ahimizu H. Effects of Prior Creep on Subsequent Plasticity of Type 316 Stainless Steel at Elevated Temperature, Journal of Engineering Materials and Technology, Vol.105,pp. 257-263. (1983).

Key Engineering Materials Vols. 385-387 (2008) pp 857-860
© (2008) Trans Tech Publications, Switzerland
doi:10.4028/www.scientific.net/KEM.385-387.857

An Experimental Study on Shear Reinforcement Methods of Interior Flat Plate-Column Connections

H. K. Choi[1, a], J. S. Kim[2, b], E. S. Jin[3, c], C. S. Choi[4, d]

[1]Ph.D Candidate, Division of Architectural Engineering, Hanyang Univ., Seoul, Korea(R)

[2]Graduate Student, Division of Architectural Engineering, Hanyang Univ., Seoul, Korea(R)

[3]Director, BYUCKSAN Engineering & Construction CO., LTD., Seoul, Korea(R)

[4]Professor, Division of Architectural Engineering, Hanyang Univ., Seoul, Korea(R)

[a]chk7796@naver.co.kr, [b]ggojilee2@naver.com, [c]jinstar@becco.co.kr, [d]ccs5530@hanyang.ac.kr

Keywords: Flat Plate, Punching Shear, Shear reinforcement

Abstract. This research is an experimental study on full-scale interior slab-column connections of flat-plate. Three types of shear reinforcements were proposed to prevent brittle punching shear failure that could result in collapse of whole flat plate structures. A series of four flat plate specimens including a specimen without shear reinforcement and three specimens with the reinforcements was tested. The dimension of the slabs was 2620*2725*180mm and the specimens had a 600*800mm square column at the center of the slabs. The slabs were tested up to failure using monotonic vertical shear forces. The presences of the shear reinforcements substantially increased punching shear capacity and ductility of the interior slab-column connections.

Introduction

Flat plates can be substitutive structural systems for shear walls used in most apartment buildings and moment resisting frames used in office buildings. It has already been widely used in buildings which carry small amount of live loads such as office and residential buildings in North America. Reinforced concrete flat plates are much more economical system than other structural systems. Flat plate system has some structural weaknesses such as punching shear failure compared to beam-column connections. Direct transferring of loads from slabs to columns causes stress concentration around columns, and this is leading to punching shear failure of connections.

Purpose of this study was to evaluate the capacity of the proposed three shear reinforcements of interior slab-column connections that can resist punching shear. An experimental and analytical study on punching shear was executed using the results of four tests of interior slab-column connections. The test variables of the study included three types of shear reinforcements. The major difference of three reinforcements was material and shape.

EXPERIMENTAL PROGRAM

Design of Specimens. The test specimens of this experiment is full-scale representations of interior slab-column connections from a twenty-story apartment buildings designed to use as reinforced concrete shear walls as lateral force resistance system and flat plates as vertical force resistance system. To evaluate shear capacity of proposed shear reinforcements, an unreinforced specimen and three reinforced specimens which had different types of shear reinforcements were manufactured and the experiments were carried out. The size of the slab was 2620*2725*180mm and the specimens had a 600*800mm square column at the center of the slabs. In order to ease the production of specimens and execution of tests, the test specimens were cut 1/4 points of the slabs under the assumption that inflection points were generated at the points of 1/4 from slabs when subjected to relatively low levels of gravity load. Both sides of the slab were enlarged as much as 150mm to meet the condition of simple supports of the slab.

Reinforce Method and Reinforcement Details. By using the shear reinforcements shown in Fig. 1 and Fig. 2, the expected advantages are as follows. It's economical because manufacture process is simple and applications on the site are excellent. Besides, the shear reinforcements play a role of spacers when arranging bars, and it enables to secure effective depth between top and bottom longitudinal bars, which secures structural stability. By using the reinforcements, Spacers are not needed separately. The shear reinforcements were installed at every 75mm (0.5d) intervals, from column face to 5d distance.

(a) SS/bar (b) CS/bar (c) Wiremesh

Fig. 1. Reinforcement details

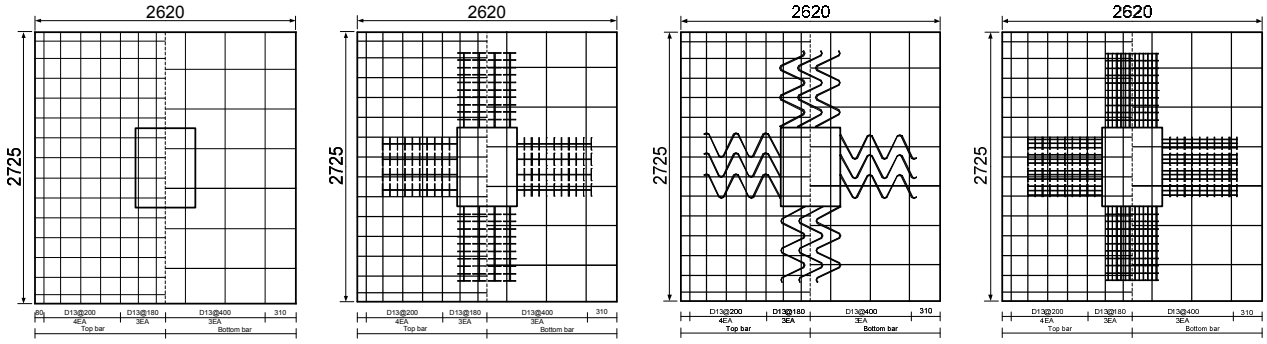

(a) Control (b) FP-SS/bar (c) FP-CS/bar (d) FP-Wiremesh

Fig. 2. Specimens size and reinforcements arrangement

Test Setup. As shown in Fig. 3 the specimens were tied to steel support beams and were loaded using pull-out method by an actuator linked to a reaction frame. The method was used to simulate the loads causing deflection and punching shear failure in the real slab structures. The experiment was proceeded using the load control system. The deformation of each steel bar and shear reinforcement was measured by installing four strain gauges located at 0.5d, d, 3d, and 5d distance of short slab direction from the column face. The strain gauges were installed to provide information on internal force distribution and yielding of the reinforcements.

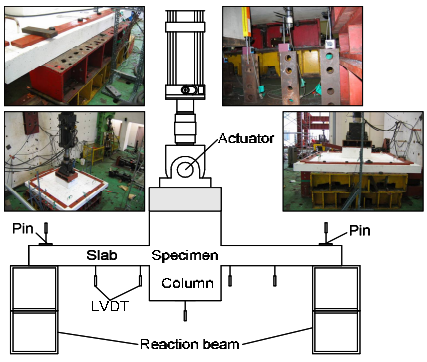

Fig. 3 Test setup

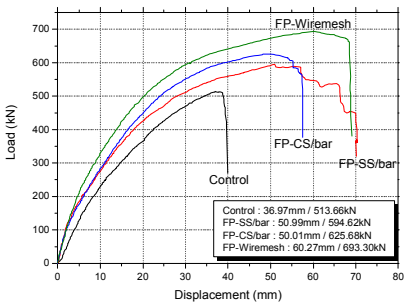

Fig. 4 Load-displacement relationship

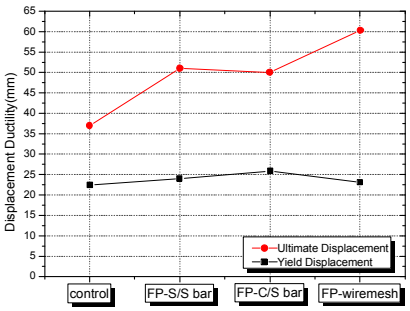

Fig. 5 Comparison of Ductility

TEST RESULT

Load-Displacement. Fig. 4 shows the load-displacement curves for the specimens and Table 1 shows the test results. A control specimen which was a specimen without shear reinforcements had ultimate strength of 513.66kN at 37mm displacement and sudden punching shear failure at 40mm displacement. On the other hand, a FP-S/S bar specimen had ultimate strength of 594.62kN at 51mm displacement. The specimen maintained the strength for a while and then failed after repeated strength degradations. A FP-CS/bar specimen showed ultimate strength of 625.68kN at 50mm displacement and gradual reduction of strength until 57mm displacement. The test was stopped at 57mm displacement due to sudden reduction of strength. A FP-Wiremesh specimen showed ultimate strength of 693.30kN at 58mm displacement.

Based on observation of load-displacement curves of the specimens, the specimens with shear reinforcements showed 23% increase strength on the average compared to the control specimen. Punching shear resistance of FP-Wiremech was the highest among the reinforced specimens. This was the result of truss action because of jointing between longitudinal bars and web reinforcements and dowel action on top and bottom bars.

Table 1. Test result

Specimen	Yield load V_y(kN)	Ultimate load V_{max}(kN)	Yield deflection δ_y(mm)	Ultimate deflection δ_{max}(mm)	Strength ratio	Deflection ratio	Displacement Ductility δ_{max}/δ_y
Control	441.10	513.66	26.45	36.97	-	-	1.40
FP-SS/bar	473.10	594.62	25.16	50.99	1.16	1.38	2.03
FP-CS/bar	521.18	625.68	26.38	50.01	1.22	1.35	1.90
FP-wiremesh	541.44	693.30	23.94	60.27	1.35	1.63	2.52

Crack and Failure Mode. Fig. 6 shows crack patterns of the specimens. The control specimen showed the diagonal initial cracks were developed from the edge of the column at the load of 162kN. As the load increased gradually, these cracks were concentrated at the critical sections of the slab-column connection and eventually sudden punching shear failure occurred after increasing of crack width. On the other hand, three specimens with shear reinforcements generated both flexural cracks and shear cracks at the same time, and failed outside of shear reinforced area after cracks were uniformly developed throughout the slabs.

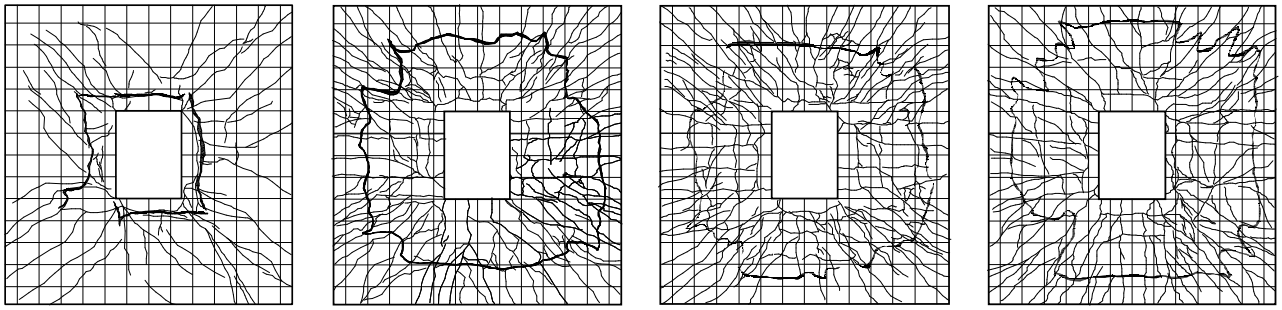

(a) Control (b) FP-SS/bar (c) FP-CS/bar (d) FP-Wiremesh

Fig. 6 Crack patterns

Displacement Ductility. Fig. 5 shows displacement ductility of the specimens. Yield displacements of all specimens were closed to each other since yield displacement of the reinforced specimens showed maximum yield displacement increase of 17% compared to that of control specimen. However, displacements at ultimate strength were increased 38% in FP-S/S bar, 35% in FP-CS/bar, and 63% in FP-Wiremesh. FP-Wiremesh showed higher increase in strength and displacement than those of the other specimens. This is because of increase of bonding strength between deformed shear reinforcements and concrete, and increase of dowel

action caused by welding of web reinforcements and top and the bottom longitudinal reinforcements.

Secant Stiffness. Fig. 6 shows secant stiffness of the specimens. Stiffness of the connections significantly affected on the deflections of the flat slab.

The stiffness of the control specimen was 24.11kN/mm. Stiffness of the reinforced specimens increased stiffness of 15.3~42.8% compared to that of the control specimen. Thus, these specimens were having advantages of resisting deflection of flat plate compared to unreinforced flat plate. The stiffness of the connections was increased 15.3% in FP-SS/bar, 16.9% in FP-CS/bar, and 42.8% in FP-Wiremesh.

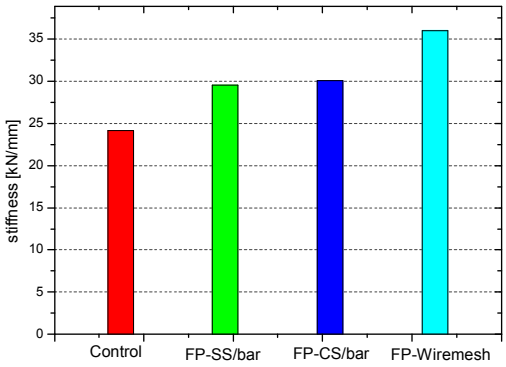

Fig. 6 Comparison of Secant Stiffness

Summary

Following conclusions were made from the experimental results of interior slab-column connections of flat-plate.

1) For the shear reinforced specimens, ultimate strength was increased within the range of 16~35% and deflection was increased within the range of 35~63% compared to the control specimen. These show that proposed three types of reinforcements can be considered as shear reinforcements which improve shear strength and deformation capacity on slab-column connections.
2) After cracks were generated at the critical sections of the slab, the width of the cracks did not increase while these cracks were spread throughout the slab. This happened by avoiding stress concentration and distributing stress equally throughout the whole slab, while stress concentration at the critical sections occurred at the control specimen.
3) The stiffness of reinforced connections was increased 15.3~42.8% range compared to the control connection. In the case of using the three shear reinforcements, reduction of deflection may be predicted.

Acknowledgment

This work was supported by SRC/ERC program of MOST(grant R11-2005-056-030020-0), the CCTRD of MOCT (grant C105A1050001-05A0505-00210), Regional Research Centers Program(Bio-housing Research Institute) and 07urbanRenaissanceA03.

References

[1] Neil Hammill., Amin Ghali, "Punching Shear Resistance of Corner Slab-Column Connection." ACI Structure Journal Vol.91, No.6 Nov-Dec 1994 pp.697-707

[2] Broms C. E., "Shear Reinforcement for Deflection Ductility of Flat Plates." ACI Structure Journal, V.87, No.6, Nov-Dec 1990 pp.696-705

[3] Yamada, T., Nanni., A., And Endo, D., "Punching Shear Resistance of Flat Slab : Influence of Reinforcement Typeand ratio." ACI Structure journal, V.89, No.4 Sept-Oct 1992 pp.555-563

[4] Austin, D. Pan and Jack P. Moehle, "An experimental study of slab-column connections", ACI 89-S59, 1992. pp.626-638.

[5] Rudiger Beutel and Josef Hegger., “The effect of anchorage on the effectiveness of the shear reinforcement in the punching zone" Cement & Concrete Composite 24 (2002) 539-549

Key Engineering Materials Vols. 385-387 (2008) pp 861-864
© (2008) Trans Tech Publications, Switzerland
doi:10.4028/www.scientific.net/KEM.385-387.861

A Study on Retrofit Methods of Shear Walls with New Openings

H. K. Choi[1,a],J. A. Lee[2,b], M. S. Lee[3,c], Y. C. Choi[4,d] and C. S. Choi[5,e]

[1] Ph.D, Candidate Division of Architectural Engineering, Hanyang Univ., Seoul, Korea(R)

[2] Graduate Student, Division of Architectural Engineering, Hanyang Univ., Seoul, Korea(R)

[3]Postdoctoral Researcher, BK21 Architectural Engineering Program (SAPEC), Hanyang Univ., Seoul, Korea(R)

[4]Professor, Department of Architectural Environmental Engineering and Building Service, Chung-Woon Univ., Hong-Sung, Korea(R)

[5]Professor, Division of Architectural Engineering, Hanyang Univ., Seoul, Korea(R)

[a]chk7796@naver.com , [b]sjinahya@naver.com, [c]moonlee33@yahoo.com, [d]21ycchoi@naver.com,[e]ccs5530@hanyang.ac.kr

Keywords: Shear wall, Remodeling, Opening, Retrofit method, Steel plate, CFS, Wire

Abstract. A series of five shear wall specimens were tested under constant axial stress and reversed lateral cyclic loading in order to evaluate the seismic retrofit methods that had been proposed for shear walls with new openings. The test results showed that the failed specimens had shear fractures and two different retrofit methods had different effects on the strengths of each specimen.

Introduction

Remodeling is an environmentally-friendly approach that reduces the amount of wastes in construction sites. Remodeling can sometimes include partial destruction of the structural members of a building. The objective of this paper is to present the test results and structural behavior of perforated RC walls and to introduce effective retrofitting methods by evaluating efficacy of passive and active retrofit methods. These methods using carbon fiber sheets, steel plates, and wires are widely used for strengthening the members of existing buildings.

EXPERIMENT PROGRAM

Table 3. List of specimens

Specimen	Opening ratio	Retrofit material	Reinforcement		$l_w \times h_w \times t$ [mm]
WB-Solid	23% (900mm×1050mm)		Vert. D6 @255	Horiz. D6 @255	3000×130×100
WB-0.23		Without retrofit			
WB-CFS		Carbon fiber sheet			
WB-St. Plate		Steel plate			
WB-Wire		P.S Wire			

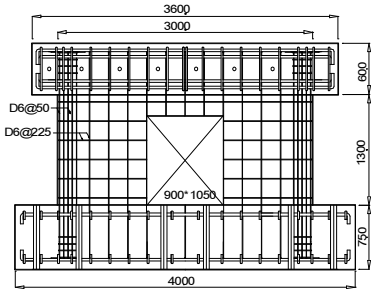

Fig. 1. Specimen details

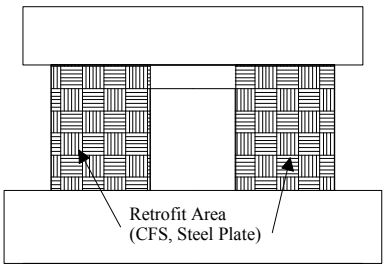

Fig. 2. Retrofit area

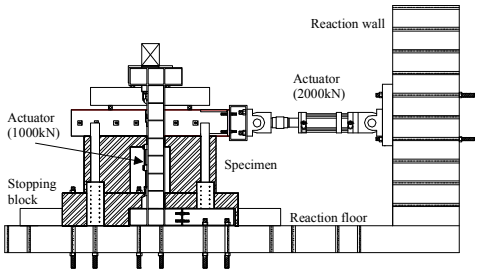

Fig. 3. Test setup

Specimen Description. Specimens were representations of one-story walls of a 1980's apartment in Korea. Prototype walls represented undamaged walls which had 21MPa compressive strength of concrete and 400MPa tensile strength of reinforcement. Four other walls had 900mm*1050mm artificial openings located in the bottom center of the specimens. Three of them were retrofitted using PS-Wires, Steel Plates and CFS (carbon fiber sheets). A series of five shear wall specimens is listed in Table 1 and details of one of the retrofitted specimen are shown in Fig 1. Fig. 2 represents retrofitted area.

Test Set-up. A picture of the test setup is shown in Fig. 3. Two actuators were mounted vertically both ends of the wall to apply the load approximately 10% of the computed concentric capacity of the wall. Displacement controlled lateral load was applied at the top of the wall by a 2000kN hydraulic actuator mounted between the specimen and a reaction wall. Guide beams and ball zigs were used to minimize out-of-plane movement and simulate the diaphragm effect.

Experimental Results

Observed Crack and Load-Displacement Relationship. Fig. 4 illustrates the specimens' crack pattern. Fig. 5 illustrates the specimen's load-displacement relationship. Each specimen showed shear failure rather than flexural failure. WB-Solid showed typical shear failure because it has a low aspect ratio. WB-0.23 showed shear failure and peeling off of the concrete surface at the opening's

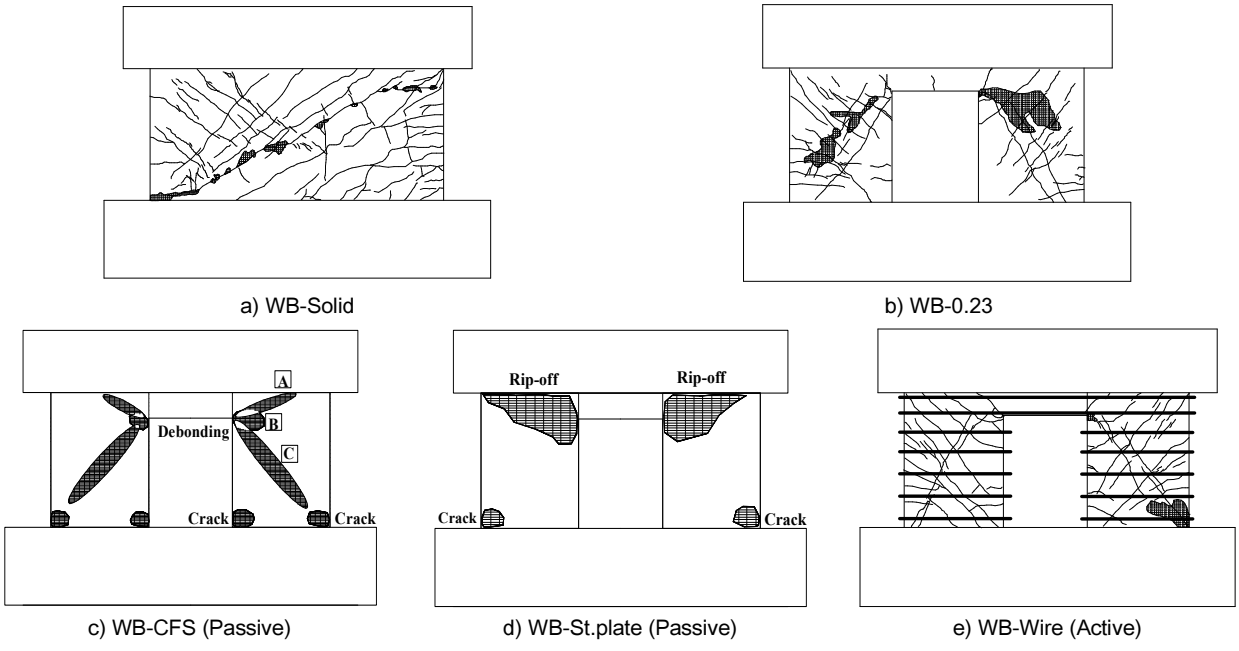

Fig. 4. Crack Patterns

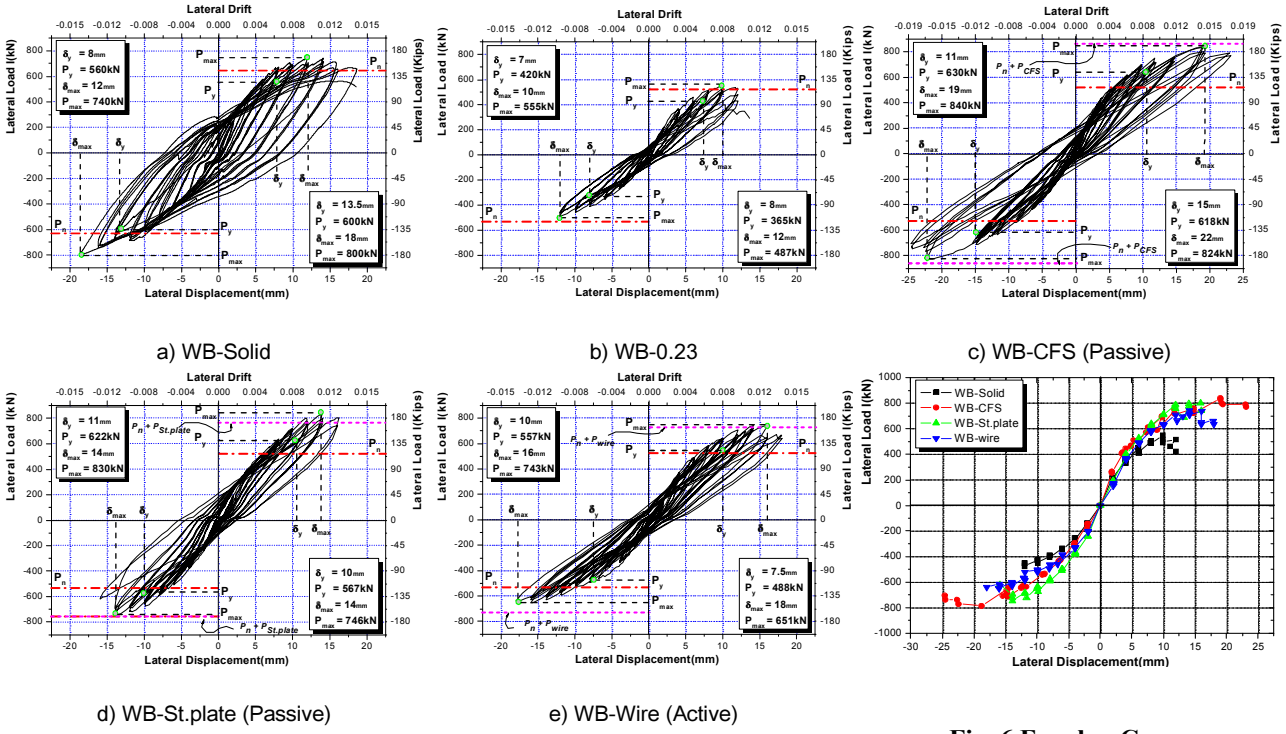

Fig. 5 Load-Displacement Relationship

Fig. 6 Envelop Curve

corners. WB-ST. Plate failed by debonding of the reinforcing materials, steel plates. Behavior of WB-CFS was similar to that of WB-St.Plate. In the case of WB-Wire specimen, initial cracks occurred at the anchorages and then the cracks were generated in diagonal directions. Fig. 6 represents envelop curves of retrofitted specimens and a solid specimen. All retrofitted specimens' ultimate strength was larger than WB-Solid specimen's. WB-Wire specimen showed little retrofitting effects compared to the other retrofitted specimens. It is believed that anchorage method of WB-Wire induced stress concentration at the edge of the wall.

Stiffness and Ductility. Stiffness degradation ratio of WB-Solid and WB-0.23 at rotational angle of 1.2% was 30% and 10% as shown in Fig. 7. In accordance with the result from the observation of crack patterns, unclosed diagonal tension cracks contributed to stiffness degradation at the end of the test. Stiffness degradation curves of WB-St.Plate, WB-CFS, and WB-Wire generally showed gentle slopes. However, WB-Wire showed the lowest degradation ratio because WB-ST.Plate and WB-CFS exhibited their retrofitting capacities after ultimate strength of the walls was reached while WB-Wire showed uniformly distributed retrofitting capacity from the start to the end of the test.

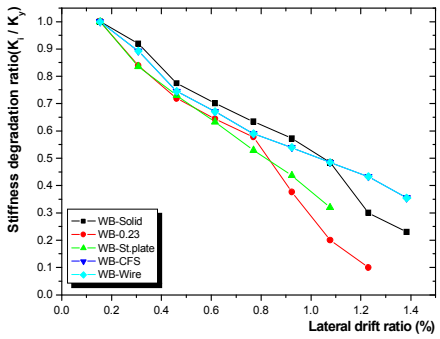

Fig. 7. Stiffness Degradation

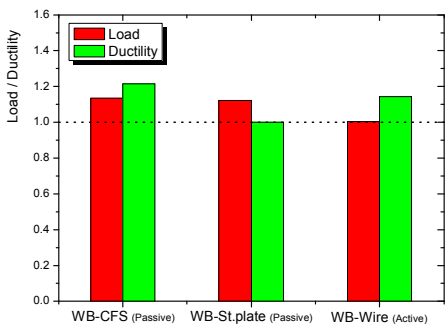

Fig. 8. Comparison of ultimate load and ductility

Summary.

1) In the case of WB-0.23 which was damaged by installing an opening, ultimate strength decreased by 25% compared to WB-Solid, a wall without opening. It is believed that this is the result of loss of bonding strength due to cutting of reinforcing bars and reduction of effective concrete area caused by an opening installation.

2) All specimens with opening had initial flexural cracks because of stress concentration at the edge of the walls, and the cracks developed as shear cracks as the load increased. It was not effective to close the diagonal tension cracks because of horizontal installation of wires.

3) WB-St.Plate and WB-CFS showed 12% higher strength than WB-Solid and 50% higher strength than WB-0.23. However, WB-Wire had small increase in strength compared to those specimens.

4) WB-Wire showed its retrofitting capacity throughout the whole load history by uniform distribution of the stress from the start to the end of the test.

Acknowledgment

This work was supported by SRC/ERC program of MOST(grant R11-2005-056-030020-0), the CCTRD of MOCT (grant C105A1050001-05A0505-00210), Regional Research Centers Program(Bio-housing Research Institute) and 07urbanRenaissanceA03.

References

[1] H. D. Yun, C. S. Choi, “Shear Strength and deformability of R/C Framed Shear Walls with Opening”, Journal of the Architectural Institute of Korea, Structure & Construction, vol. 21 n.3, 2005, 03, pp 11-18.

[2] Darwin, D, and Nmai, C.K, "Energy Dissipation in RC Beams under Cyclic Load", Journal of Structural Div, ASCE, Vol. 112, No. 8, Aug, 1986, pp. 1829-1846.

[3] Konstantios K. Antoniades, Thomas N. Salonikios, Andreas J. Kappos, "Test on seismecally damaged reinforced concrete walls repaired and strengthened using fiber-reinforced ploymers", Journal of Structure Eng., ASCE, Vol. 9, No. 3, June 1, 2005, pp.236-246.

[4] J. I. Daniel, K. N. Shiu, W. G. Corley F., "Openings in Earthquake-Resistant Structural Walls", Journal of Structure Eng., ASCE, June 1, 1997, pp.1660-1675.

[5] ACI Committee 318 (2002), "Building Code Requirements for Structural Concrete (ACI 318-02) and Commentary (ACI 318 R-02)", American Concrete Institute, Michigan.

[6] H. D. Yun, C. S. Choi, “Shear Strength of High-Strength Concrete Shear Walls”, Journal of the Architectural Institute of Korea, Structure & Construction, vol. 19 n.5, 2003, 05, pp 53-60.

Key Engineering Materials Vols. 385-387 (2008) pp 865-868
© (2008) Trans Tech Publications, Switzerland
doi:10.4028/www.scientific.net/KEM.385-387.865

A Study on Shear Reinforcement of Exterior Joints for Flat Plate

H. K. Choi[1, a], S. W. Beck[2, b], Y. S. Baik[3, c], C. S. Choi[1, d]

[1]PhD. Candidate, Division of Architectural Engineering, Hanyang Univ., Seoul, Korea(R)

[2]PhD. Division of Architectural Engineering, Hanyang Univ., Seoul, Korea(R)

[3]Deputy Manager. Hyundai Development Company., Seoul, Korea(R)

[4]Professor. Division of Architectural Engineering, Hanyang Univ., Seoul, Korea(R)

[a]chk7796@naver.com, [b]skea16@hotmail.com, [c]bbys@hananet.com, [d]ccs5530@hanyang.ac.kr

Keywords: Flat Plate, Punching Shear, Shear reinforcement, Exterior connection, Curve steel

Abstract. The purpose of this research was to study the response of slab-column connections containing various types of shear reinforcement when subjected to the combination of gravitational and lateral cyclic loads. The three test specimens were full-scale representations of exterior slab-column connections of a prototype apartment building in Korea. The control specimen had no shear reinforcements, while the other specimens had CS-Bar and SS-Bar as shear reinforcements. The control specimen failed due to the punching shear around the slab-column connection at 4.0% drift. None of the specimens with shear reinforcement experienced punching shear failure up to 4.4% drift. The two types of slab shear reinforcements proved to be equally effective in resisting punching shear failure of these connections subjected to relatively low levels of gravity load. The presence of shear reinforcements significantly increased the lateral load ductility of the connections. The test results showed that the strength and ductility of the specimens with SS-Bar and CS-Bar were improved by 23% and 15% compared to the specimen without shear reinforcements.

Introduction

Flat plate structure which is 2-way slab system without beams is more economical structure than other structures. Specifically this structural system has benefits of reducing the story height, using the space in various ways, and saving the time and money for construction. However, it is weaker structural system than beam-column frame. The main problem is punching shear failure. Little study was conducted for exterior slab-column connections compared to their interior counterparts. This exterior connection usually has short critical section area, and tends to have unbalanced moment caused by their asymmetric geometry and eccentric shear occurred by both gravitational and lateral loads. Main objective for this study is to evaluate the earthquake resistance capability of exterior slab-column connections with aspect ratio of 2.5. Main objectives are represented below

- Evaluation of structural performance of the exterior slab-column connection without shear reinforcement.
- Reinforcing effects on different shear reinforcing methods.

Experimental Program

Test Specimens. A series of three specimens was tested in this study. Two specimens were specially reinforced for shear, while the other one contained no shear reinforcements. As shown in Fig. 1 test specimens were produced based on exterior connections of a flat plate residential structure built in Korea. The slab specimens were constructed in full scale and had the size of 4640mm×2820mm. Although column height was originally designed to have 2.7m, it was reduced to 1920mm because of the limitation of the testing facilities. The specimens were designed to satisfy KBC 05[2] code and they were designed as a dual system which has a combination of flat plate and moment resisting frame. 25% of the loads were resisted by flat plate system while rest of the loads was resisted by moment resisting frame system. All re-bars were D13. Upper re-bars were

placed in column strip of the slab and lower re-bars were distributed uniformly in all slab width. In order to satisfy structural integrity in the standards, two lower re-bars were placed through the column.

Special Shear Reinforcement. Fig. 2 (a) and (b) shows specially designed shear reinforcements. Curvilinear shear reinforcement is made up of curved upper anchorage bent bars which will be placed on the bottom of the top longitudinal reinforcements, middle shear reinforcements which are welded to upper and lower anchorage bent bars, and lower anchorage bent bars which have the same shape of upper bent bars. Upper and lower bent bars work as anchorages for slabs and middle shear reinforcements resist shear. These bent bars maintain a uniform distance. This distance between them is determined based on the thickness of the slabs and the space for flexural reinforcements.

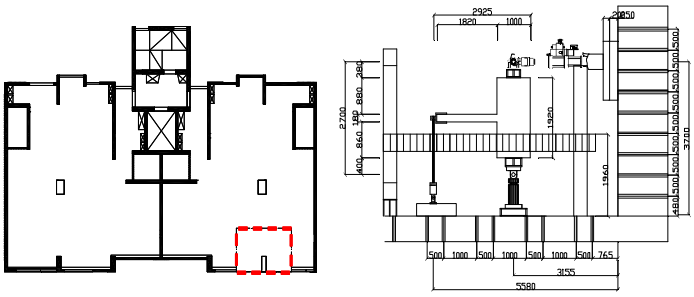

Fig. 1. Test Specimen

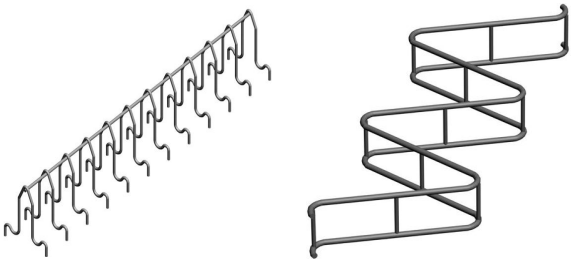

(a) SS/bar (b) CS/bar

Fig. 2. Shear Reinforcements details

Material Test and Test Setup. Test results of the compressive strength for concrete and the tensile strength for re-bar is shown in Tables 1 and 2. Test setup is illustrated in Fig. 1. Test specimens were installed with a hydraulic jack in lower part of the column, and a 2000kN actuator for lateral loads in upper part of the column. Uniform gravitational loads on the slabs were represented using load blocks. These loads were controlled using a hydraulic jack which was installed edge of the slab. According to the past researches (Hawkins et al.)[3], shear-moment ratio at the column surface affects the behaviors of slab-column connections significantly. In this test, load blocks were adjusted to simulate the shear-moment ratio of the original building. Lateral loads were applied through 2000kN actuator using displacement control. Displacements were represented in rotational angle which is lateral displacement of top of the column over length of the column. 13 steps (0.2%, 0.25%, 0.35%, 0.5%, 0.75%, 1%, 1.4%, 1.75%, 2.2%, 2.75%, 3.5%, 4.5%, 6%) of displacement were applied and each phase had 3 cycles. Data were gathered by load cells installed to the actuator, slab supports, and hydraulic jack, wire strain gauges attached to the reinforcements, and LVDTs installed under the slab.

Table 1. Compressive strength for concrete

Materials	Compressive Strength (MPa)	Young's Modulus (GPa)	Maximum Strain (ε_u)	Poisson's ratio
Concrete	22.8	21.92	0.00171	0.15

Table 2. Tensile strength for re-bar

Materials	Yield strength (MPa)	Yield strain (ε_y)	Tensile strength (MPa)	Poisson's ratio
D6(SS-Bar)	358.19	0.0019	375.01	0.28
D10(CS-Bar)	420.08	0.0024	675.1	0.31
D13(Slab rebar)	420.08	0.0025	665.8	0.31

Experimental Results

Crack and Failure. Crack patterns of each specimen are illustrated in Fig. 3. All specimens were failed in flexural-shear and showed similar patterns except crack distribution. Based on the observation of all specimens, initial cracks on the slabs were flexural cracks developed due to the gravitational loads. As lateral displacements applied, additional flexural cracks were generated orthogonal to the loading direction throughout the slab. By applying more lateral displacements,

tensile cracks were developed in lower part of the slabs, and diagonal torsion cracks were developed. Finally, the specimens were failed due to punching shear. As a result of the analysis using the standard strength equation, the failure of the specimens was governed by shear and flexure.

The control specimen which had no shear reinforcements failed due to development of a small amount of concentrated deep and wide cracks, while two specimens which had special shear reinforcements failed with widely distributed shallow and narrow cracks. It was believed that the special reinforcements provided additional shear resistance by distributing shear stresses which develop diagonal cracks.

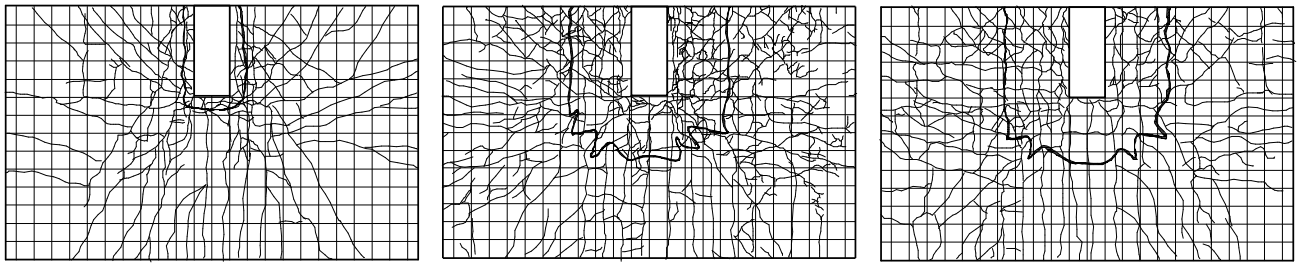

(a) Control (b) FP-SS/bar (c) FP-CS/bar

Fig. 3 Crack patterns

Stress-Strain Relationship. Fig. 4 shows stress-strain relationship of the specimens from the test. All specimens showed story drift larger than 4.4%. It is an adequate capacity for seismic design limitation, since it is larger than limit drift ratio of 1.5%.

Based on the strength measured from each specimen, strength of CS-Bar and SS-Bar specimens increased 24% and 27% compared to the control specimen. The specially reinforced specimens showed 5% story drift while the control specimen showed 4.4% story drift. The specially reinforced specimens had 13% increase of drift capacity. Table 3 shows details of the specimens and test results. In order to ensure lateral load resisting capacity of the shear reinforcements in slab-column connections, continuous placement of the shear reinforcements with top and bottom longitudinal reinforcements is important. The special reinforcements improved strength and ductility of the system efficiently by satisfying this placement condition.

Table 3. Details of specimens & Test results

Specimen	C_1/C_2 [-]	ρ_{c+3h} [%]	d [mm]	f'_c [MPa]	f_y [MPa]	V_g/V_c [%]	P_{peak} [kN]	D_u [mm(%)]	$M_{u\ Test}$ [kN•m]	$M_{u\ ACI}$ [kN•m]	$M_{u\ Test}/M_{u\ ACI}$	μ [D_u/D_y]
Control	2.5	0.0053	150	22.8	410	0.38	63	120 (4.4)	200	193	1.03	2
FP-CS/Bar				22.7		0.52	78	135 (5.0)	210	193	1.08	2.77
FP-SS/Bar				22.9		0.54	80	135 (5.0)	216	193	1.11	2.71

V_g/V_c : gravity shear ratio P_{peak} : peak horizontal load measured D_u : ultimate drift $M_{u\ test}$: unbalanced moment measured
$M_{u\ ACI}$: unbalanced moment computed by ACI μ : ultimate displacement ductility ratio

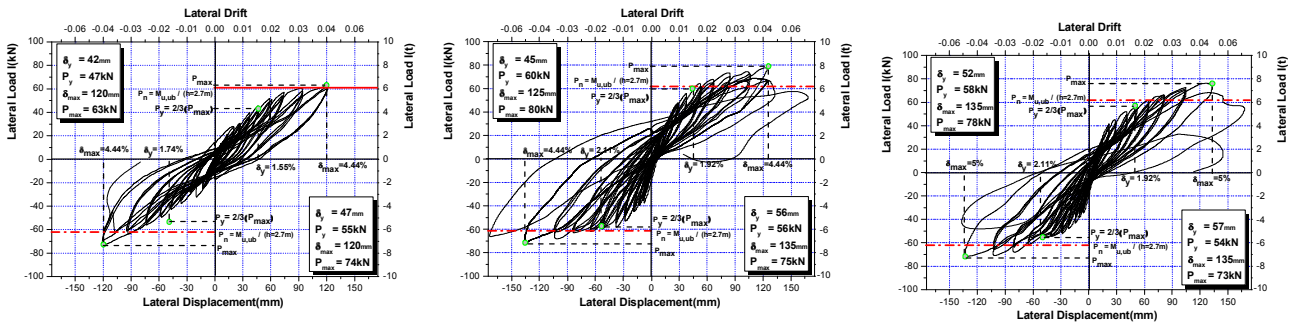

(a) Control (b) FP-SS/bar (c) FP-CS/bar

Fig. 4 Stress-strain relationship

Shear strength. Shear strength evaluation of specimens are executed based on eccentric shear stress model described in ACI318-05[1]. According to this model shear stress is decided from two stresses. One is direct shear stress which is applied to centroid of critical section of slab and the other is developed by unbalanced moment. Table 4 represents the shear strength of the result for this study and conventional studies. ACI strength evaluation is well predicted the control specimen shear strength. However, prediction for special reinforcing specimens' shear strength is relatively small than test results. It is believed that different geometric characteristics of special reinforcement show different resistance capacity for diagonal crack and shear failure caused by unbalanced moment.

Relationship between Gravity-Shear Ratio & Story Drift. ACI318-05 ensures drift capacity of 2-way slab connections by limiting drift for $0.035\text{-}0.05(V_g/V_c) \geq 0.005$. Fig. 5 shows influence of gravity to shear ratio (GSR). Most existing specimens satisfied gravity to shear ratio limit of 0.4 and story drift limit of 1.5%, while the specially reinforced specimens showed better performance than most specimens. Current design specification only considers gravity to shear ratio but it needs to consider other variables such as column aspect ratio and reinforcement ratio to distinguish capacity of these connections.

Table 4. Evaluation of eccentric shear stress

Specimen	$\upsilon_{u.Test}$ [MPa]	$\upsilon_{u.ACI}$ [MPa]	$\upsilon_{u.Test}/\upsilon_{u.ACI}$ [-]
Control	1.18	1.22	0.967
FP-CS/Bar	1.32	1.80	1.733
FP-SS/Bar	1.37	1.85	1.714

$\upsilon_{u.Test}$: shear stress tested $\upsilon_{u.ACI}$: shear stress computed by ACI

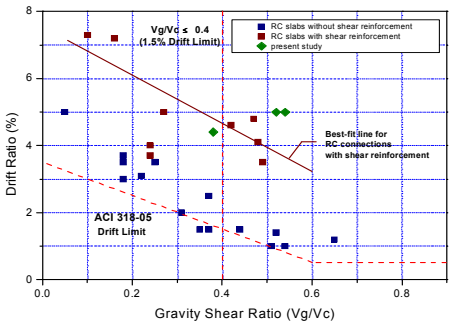

Fig. 5. Influence GSR

Conclusion

The objective of this study is to evaluate the special reinforcing methods for punching shear failure of flat plate structure.

- According to the test results, the lateral resistant capacity for each specimen was different. Strength and drift of the specially reinforced specimens showed 23% and 12% improvement over those of the control specimen.
- The specially reinforced specimens showed uniformly distributed steel strain while the control specimen showed concentrated steel strain around the column.
- All specimens satisfied limit of gravity to shear ratio of ACI, and the specially reinforced specimens outperformed existing slab-column connections with shear reinforcements.
- Based on results, performance of flat plate structure using special reinforcements was sufficiently ensured.

Acknowledgment

This work was supported by SRC/ERC program of MOST(grant R11-2005-056-030020-0), the CCTRD of MOCT (grant C105A1050001-05A0505-00210), Regional Research Centers Program(Bio-housing Research Institute) and 07urbanRenaissanceA03.

References

[1] ACI Committee 318: "Building code requirements for structural concrete (ACI 318-05)", American Concrete Institute, 2005.

[2] AIK : "Korean Building Code-Structural (KBC 05)", Architectural Institute of Korea, 2005.

[3] Akitama, H. and Hawkins, N.M: *Response of Flat Plate Connection Structures to Seismic and Wind Force*, Structure and Mechanics Report SM 84-1, University of Washington, Seattle, July, 1984

[4] Luo, Y. H and Durrani, A.J: *Equivalent Beam Model for Flat-Slab Buildings-Part II: Exterior Connections*, ACI Structural Journal, Vol.86, No. 3, May-June 1989, pp. 250-258.

Key Engineering Materials Vols. 385-387 (2008) pp 869-872
© (2008) Trans Tech Publications, Switzerland
doi:10.4028/www.scientific.net/KEM.385-387.869

Elastic-Plastic Torque Analysis of Notched Cross-Section Bars Using the Finite Difference Method

HUI-PENG LIU[1,4], XIANG-RONG FU[1*], SONG CEN[2,3], XIU-GEN JIANG[1], JIN-SAN JU[1], WEN-JIE WANG[1]

1. Department of Civil Engineering, China Agricultural University, Beijing 100083, China
2. Department of Engineering Mechanics, School of Aerospace, Tsinghua University, Beijing 100084, China
3. Failure Mechanics Laboratory, Tsinghua University, Beijing 100084, China
4. China Academy of Building Research, Beijing 100013, China

Key words: Finite Differences Method; Sand Heap Analogy Method; Elastic-plastic Torque; Stress Singularity; Notched Cross-section Bar; Fracture Mechanics

Abstract: A new strategy of finite differences method is proposed for analysis of notched cross-section bars under elastic-plastic torsion. Relation curves of the elastic-plastic torque responding with different positions, angles and lengths of the notches in one section are obtained by numerical tests. It can be seen that these relation curves exhibit obvious nonlinearity. Meanwhile, the stress intensity factors can also be easily calculated by utilizing the results of above finite differences method. It provides an effective way for solving such elastic-plastic fracture mechanics problem.

Introduction

In this paper, the finite differences method is employed to analyze the elastic-plastic torsion problem of notched cross-section bars. With the increase of torque, three different stages of the bar are considered. The first one is the elastic stage, i.e., the whole section of the bar is in the elastic state, so the stress solutions can be evaluated by the conventional finite differences method, and the magnitude of torque has linear relation with the torsion angle. The second one is the plastic stage, i.e., the whole section of the bar is in the plastic state, and the yield condition for shear stresses is satisfied. This stage can be analyzed by the sand heap analogy method. The third one is the elastic-plastic stage, in which results obtained from the previous two stages are simultaneously utilized. Obviously, here the relation curves between torque and torsion angle is nonlinear as the torque increases.

Above study strategy can be used for analysis of torsion bars with various notched cross-sections. As long as the meshes are fine enough, the elastic-plastic torque can be calculated exactly. And the stress intensity factors can also be calculated by utilizing the results of above finite differences method. By using the proposed method, such solution strategy can be generalized to elastic-plastic calculations for torsion bars with other defects.

The finite differences method for dealing with the elastic torsion problem of bars

Torsion problem of bar can be treated as a simple 2-D problem with only two non-zero stress components τ_{xz} and τ_{yz}. In elastic stage, these two stresses must satisfy following equations

$$\frac{\partial \tau_{yz}}{\partial x} - \frac{\partial \tau_{xz}}{\partial y} = 2G\alpha \quad , \quad \frac{\partial \tau_{xz}}{\partial x} + \frac{\partial \tau_{yz}}{\partial y} = 0 \tag{1}$$

where G is the shear module of the isotropic material; α is the torsion angle along the unit length of the bar. τ_{xz} and τ_{yz} can be expressed in terms of stress function Φ_e as

$$\tau_{xz} = \frac{\partial \Phi_e}{\partial y}, \qquad \tau_{yz} = -\frac{\partial \Phi_e}{\partial x} \tag{2}$$

Substitution equation (2) into the first expression of equation (1) yields

$$\nabla^2 \Phi_e = \left(\frac{\partial^2 \Phi_e}{\partial x^2} + \frac{\partial^2 \Phi_e}{\partial y^2} \right) = -2G\alpha \tag{3}$$

And the elastic torque T_e can be evaluated by

$$T_e = 2\iint_A \Phi_e dxdy \tag{4}$$

So, at this stage, once the stress function is obtained, the stresses and the torque can be determined.

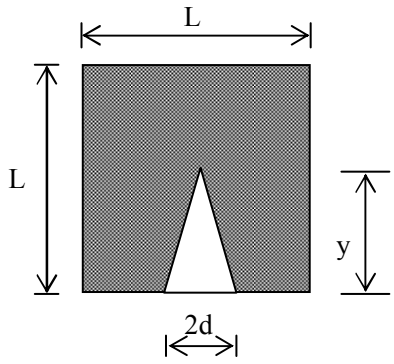

Figure 1. Notched cross-section

Here, equation (3) can be solved by finite differences method with following iteration equation

$$\Phi_e(i,j) = \frac{1}{4}\left(\Phi_e(i-1,j) + \Phi_e(i+1,j) + \Phi_e(i,j-1) + \Phi_e(i,j+1) + 2G\alpha \cdot h^2\right) \tag{5}$$

where h is the mesh dimension; and the boundary condition is $\overline{\Phi}_e = 0$. As long as the cross-section is simply connected, above equation can also be used for those bars with notched cross-section, as showed in Figure 1. The configurations of the stress function Φ_e and its corresponding resultant stress τ of the notched cross-section bar (Figure 1) are plotted in Figures 2 and 3.

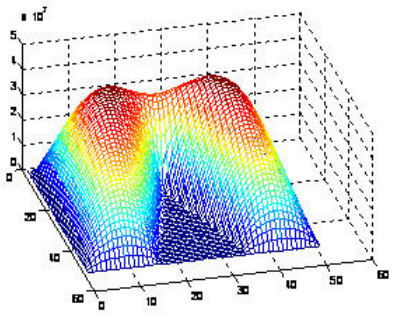

Figure 2. Configuration of Φ_e

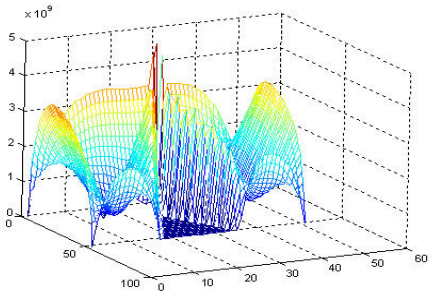

Figure 3. Configuration of τ

The finite differences method for dealing with the elastic-plastic torsion problem of bars

When the whole section of the bar is under plastic state, we have (yield condition)

$$\tau_{xz}^2 + \tau_{yz}^2 = \left(\frac{\partial \Phi_p}{\partial x} \right)^2 + \left(\frac{\partial \Phi_p}{\partial y} \right)^2 = \tau_s^2 \tag{6}$$

where Φ_p is the plastic stress functions, which should satisfy the boundary condition $\overline{\Phi}_p = 0$ and can be obtained by usual sand heap analogy method; τ_s is the yield stress of the material. The configuration of Φ_p is plotted in Figure 4.

Elastic-plastic analysis of the notched cross-section bar can be carried out by combination of above results in elastic and plastic cases. Firstly, the interfaces ($\Phi_e = \Phi_p$) between elastic and plastic regions can be obtained by comparing the values of Φ_e in Figure 2 with Φ_p in Figure 4. Then, these

interfaces are treated as the new boundaries of the elastic region. Thirdly, the stress function Φ_e in the elastic region will be recalculated using the iteration equation (5), and the configuration of resultant stress τ is plotted in Figure 5.

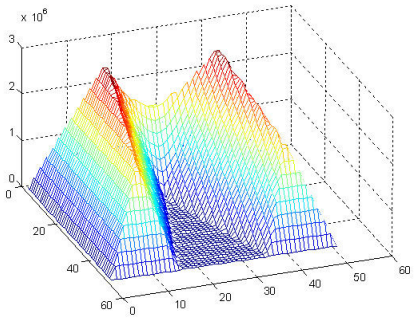

Figure 4. Configuration of Φ_p

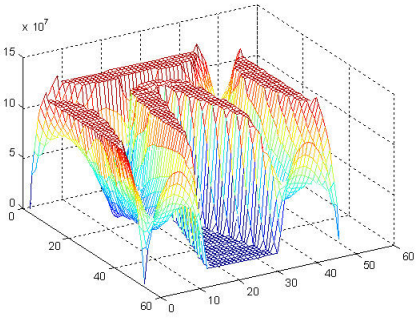

Figure 5 Configuration of τ

As shown In Figure 5, it is obvious that both elastic and plastic regions exist in the cross-section simultaneously. The plastic regions occur near the tip of V-notch and the long sides of free boundaries, while the rest of the section is still in elastic state. The elastic-plastic interfaces have been clearly illustrated in Figure 5. Finally, the torque of the bar can be calculated by sum of the volumes of the elastic stress function Φ_e and the plastic stress function Φ_p.

Numerical examples

Example 1. A bar with notched square cross-section showed in Figure 1 is considered. The side length of the section L = 0.1m; the shear module G = 8.0×10^{10} N/m^2; and the yield shear stress τ_s = 1.2×10^8 N/m^2. A V-notch is located at one side (see Figure 1). The bottom length and the height of the V-notch are denoted by 2d and y, respectively. The variation of the elastic-plastic torque T with the torsion angle α is analyzed by proposed method.

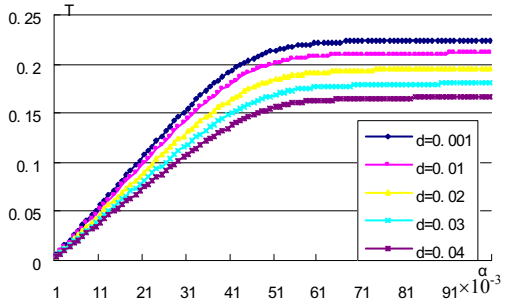

Figure 6 T~α curves in elastic-plastic analysis

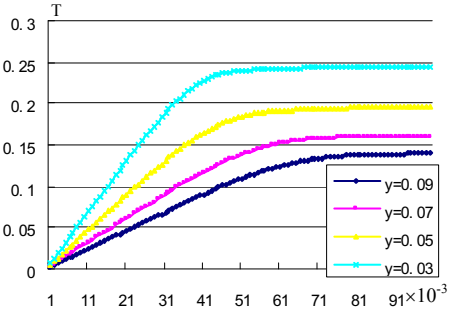

Figure 7 T~α curves in elastic-plastic analysis

The resulting elastic-plastic T-α curves with y=0.05m and different d (varies from 0.002m to 0.08m) are plotted in Figure 6. From the figure, it can be seen that, with the increase of d, the plastic limit torque decreases and the bar behaves more softly.

The resulting elastic-plastic T-α curves with d=0.02m and different y (varies from 0.03m to 0.09m) are plotted in Figure 7. From the figure, it can be seen that, with the increase of y, the plastic limit torque decreases and the bar behaves more softly.

Example 2. The bar in previous example is considered again. Here, the elastic stress intensity factor K_{III} of the notch is evaluated by $K_{III} = \sqrt{2\pi r}\cdot\tau_{xz}$, in which r is the distance to the tip. For the case

of α=0.001, results of K_{III} with different h, d and y are given in Table 1.

Table 1 Results of K_{III} (MPa$\cdot\sqrt{m}$) with different h, d and y

d=…	0.001	0.01	0.02	0.03	0.04	0.02	0.02	0.02	0.02
y=…	0.05	0.05	0.05	0.05	0.05	0.03	0.05	0.07	0.09
h=0.002	0.7978	0.7677	0.7247	0.6816	0.6443	0.8529	0.7247	0.4721	0.08448
h=0.001	0.8329	0.7845	0.7277	0.6915	0.6677	0.8594	0.7277	0.4977	0.13346
h=0.0005	0.8490	0.7823	0.7260	0.6974	0.6763	0.8694	0.7260	0.4994	0.15331

From Table 1, it can be seen that the values of K_{III} can converge with the decrease of h. In first five columns, the values of K_{III} are decreasing continually with the increasing of d. This may be caused by the change of the open angle. In last four columns, the values of K_{III} also decrease continually with the increasing of y. This phenomenon is quite interesting because it is not consistent with common sense.

Conclusions

In this paper, the differences method and the sand heap analogy method are combined together to calculate the elastic-plastic torque of the notched cross-section bars. It is found that this solution strategy is an efficient way to solve the stress analysis of the torsion bar with notched cross-section. In the elastic stage, the stress factor K_{III} can be calculated directly using the results of the differences method. As long as the mesh is fine enough, the solution can be very exactly. So this solution strategy of the finite differences method can be generalized to elastic-plastic calculations for torsion bars with other defects.

Acknowledgement

This study was supported by the National Natural Science Foundation of China (10502028), the Foundation for the Author of National Excellent Doctoral Dissertation of PR China (200242), the Program for New Century Excellent Talents in University (NCET-07-0477), the Science Foundation of China Agricultural University (2004016), and the National Science Support Plans (2006BAJ01B07).

References

[1] M.L. Williams. On the stress distribution at the base of a stationary crack. Journal of Applied Mechanics, 1957,24:109-114.

[2] H. Neuber, Theory of notch stresses, Springer-Verlag, Berlin, 1958.

[3] N. Noda, Y. Takase, Stress concentration formula useful for all notch shape in a round bar (comparison between torsion, tension and bending), Int. J. Fatigue 28 (2006) 151–163.

[4] J. Qian, N. Hasebe, Property of eigenvalues and eigenfunctions for an interface V-notch in antiplane elasticity, Eng. Fract. Mech. 56(1997) 729–734.

[5] M.L. Dunn, W. Suwito, S. Cunningham, Stress intensities at notch singularities, Eng. Fract. Mech. 57 (1997) 417–430.

[6] E. Smith, The elastic stress distribution near the root of an elliptically cylindrical notch subjected to mode III loadings, Int. J. Eng. Sci.42 (2004) 1831–1839.

[7] E. Smith, A comparison of Mode I and Mode III results for the elastic stress distribution in the immediate vicinity of a blunt notch,Int. J. Eng. Sci. 42 (2004) 473–481.

[8] E. Smith, A comparison of the Modes I and III elastic stress distribution near a circular cylindrical notch, Int. J. Eng. Sci. 42 (2004)483–490.

Key Engineering Materials Vols. 385-387 (2008) pp 873-876
© (2008) Trans Tech Publications, Switzerland
doi:10.4028/www.scientific.net/KEM.385-387.873

Dynamic Tensile Properties of TiCp/Ti Composite

Fang Jiang[1,a], Dong Zhao[2,b], Jian-guo Ning[3,c]

[1]School of Technology, Beijing Forestry University, China, 100083

[2] School of Technology, Beijing Forestry University, China, 100083

[3]State Key Laboratory of Explosion Science and Technology, Beijing Institute of Technology, China, 100081

[a]jf0620@gmail.com, [b]zhaodong68@bjfu.edu.cn, [c]jgning@bit.edu.cn

Keywords: TiCp/Ti composite; dynamic tensile properties; strain rate hardening; constitutive relation

Abstract: The tensile properties of a titanium alloy reinforced with 3% by volume fraction of TiC particles and of an unreinforced titanium alloy are studied over a range of strain rates from $0.0001s^{-1}$ to $1300s^{-1}$ using quasi-static material testing system (MTS810) and split Hopkinson tensile bar apparatus. The experimental results show that both the TiCp/Ti composite and its matrix alloy exhibit an obvious strain-rate hardening property. But the high strain-rate sensitivity of the TiCp/Ti composite is significantly higher than that of the matrix. The high strain-rate sensitivity of the TiCp/Ti composite is considered to be originated from the high dislocation accumulation rate during dynamic deformation and the constraint of TiC particles on the surrounding matrix, which dramatically enhances rate of the matrix. Finally, a phenomenological dynamic constitutive relation is established considering the composite is elastic-perfectly plastic material.

Introduction

Metal matrix composites such as Al, Ti and Ni alloy reinforced particulates of whiskers have the potential to provide desirable mechanical properties including high specific stiffness, high plastic flow strength and creep resistance and good oxidation and corrosion resistance. This suit of properties makes particle reinforced MMCs attractive to a wide range of applications in automobile, aerospace and defense industries. Largely driven by these applications, extensive theoretical and experimental studies have been made in recent years to uncover the mechanics and mechanism underlying the behavior of particle reinforced metal matrix composites [1-7].

Most metals harden with increasing strain rate, so do metal matrix composite. Under dynamic loading conditions, such as the impact of foreign objects on aerospace structures, the components made of particle reinforced MMCs often sustain high strain rate deformation. And rate sensitivity of MMCs is controlled by rate sensitivity of the matrix and the interaction of the particles and the matrix. In this paper, the rate-dependent stress-strain behavior of the TiCp/Ti composite is obtained and a comparison is made between titanium alloy matrix and composite.

1. Experimental Approach

The rate-dependent mechanical behavior of the composite and the matrix were studied over a strain rate range of $0.0001s^{-1}$ to $1300s^{-1}$ using quasi-static material testing system and split Hopkinson tensile bar apparatus. And the dynamic impact tests were conducted in a rotating-disk

bar-bar tensile impact apparatus shown in Fig.1. As the hammer (1) on the high-speed rotating disk impacts the block (2), the short metal bar (3) made of aluminum alloy breaks and an approximately rectangular input stress impulse is produced and transmitted through the input bar (4) to the specimen (5). The partial impulse is reflected to the input bar and the survival impulse is transferred to the output bar (6). Adjusting the impact speed and diameter or length of the short metal bar, the amplitude, width and rising gradient for different tensile impulses can be obtained. By applying stress impulses of different amplitude, tensile impact tests at different strain rates of different materials can be carried out. If a short stress impulse is used, tensile impact loading-unloading tests at different strain rates can be achieved.

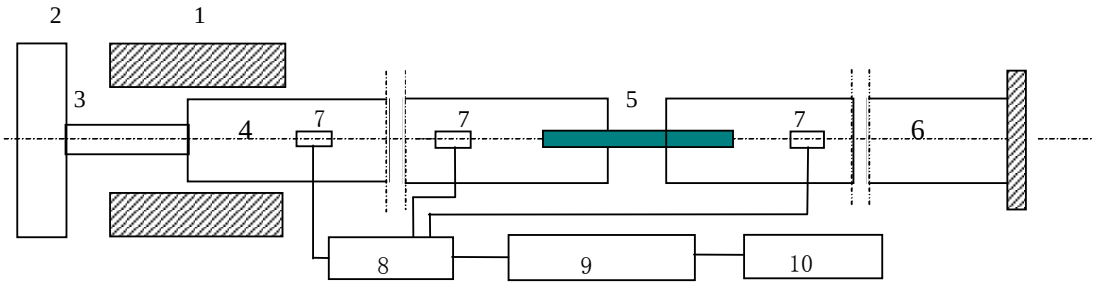

1-hammer; 2- block; 3-short metal bar; 4-input bar; 5-specimen; 6-output bar;
7-strain gauges; 8-superdynamic strain meter; 9-transient converter; 10-computer

Fig.1 Schematic diagram of tensile impact set-up and principle of measurement

According to the one-dimensional simple-wave theory, the stress, strain and strain rate, in the specimen can be obtained as follows

$$\sigma(t)=\frac{EA_0}{A}\varepsilon_t(t) \tag{1}$$

$$\varepsilon(t)=\frac{2C_0}{l}\int_0^t\left[\varepsilon_i(\tau)-\varepsilon_t(\tau)\right]d\tau \tag{2}$$

$$\dot{\varepsilon}(t)=\frac{2C_0}{l}\left[\varepsilon_i(t)-\varepsilon_t(t)\right] \tag{3}$$

where, A and l are the cross-section area and the length of the testing region of the specimen, respectively. C_O, A_O and E are the one-dimensional elastic stress wave velocity, the cross-section area and Young's modulus of the input/output bar respectively.

The composite used in theses experiments was a titanium matrix reinforced with 3% by volume of TiC particles (nominal size is 5μm). The titanium alloy is T650 (Chinese material code) with composition of 6.0% Al, 2.5% Sn, 4.0% Zr, 0.5% Mo, 1.0%Nb, 0.45% Si and the rest of Ti alloy. The composite was fabricated by pre-treatment melt process.

2. Experimental Results and Discussion

2.1 Experimental Results

Fig.2 and Fig.3 show the stress/strain curves of TiC_P/Ti and the matrix in the strain rate range from 200 to 1300 1/s. In addition, quasi-static tensile experiments have been performed on MTS810 shown in Fig.4 and Fig.5 respectively for comparison with the above tensile impact results.

On these curves, no obvious strain hardening effect can be observed. Both the composite and the matrix are strain-rate hardening materials. And the ultimate stress and yield stress of the composite are higher than those of the matrix.

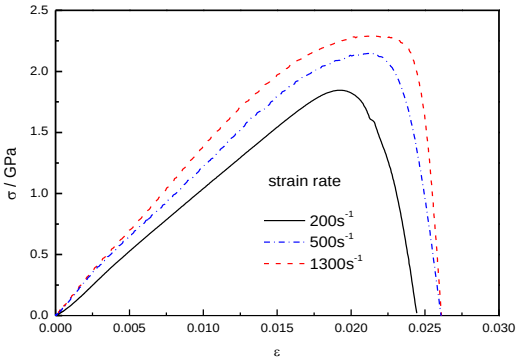

Fig 2. Stress/strain curves of TiC_P/Ti matrix composite at different strain rates

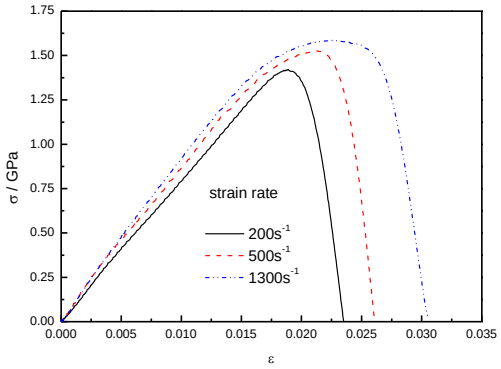

Fig 3. Stress/strain curves of Titanium alloy matrix composite at different strain rates

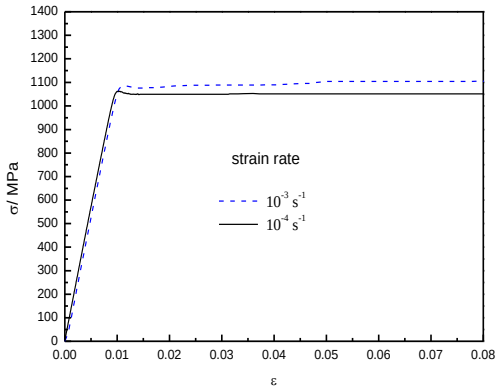

Fig 4. Quasi-static stress/strain curves of the matrix

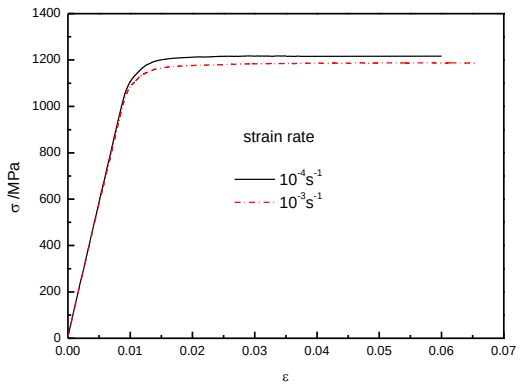

Fig 5. Quasi-static stress/strain curves of the composite

2.2 Constitutive relations of TiCP/Ti

Fig.6 shows the relationship between $\sigma-\sigma_{ref}$ and $\dot{\varepsilon}-\dot{\varepsilon}_{ref}$, and the strain-rate hardening of the composite is assumed to follow a power law:

$$\sigma=\sigma_{ref}+a\left(\frac{\dot{\varepsilon}}{\dot{\varepsilon}_{ref}}\right)^{m} \qquad (4)$$

where, σ, $\dot{\varepsilon}$, $\dot{\varepsilon}_{ref}$ and σ_{ref} are ultimate stress, strain rate, reference strain rate and reference stress, respectively.

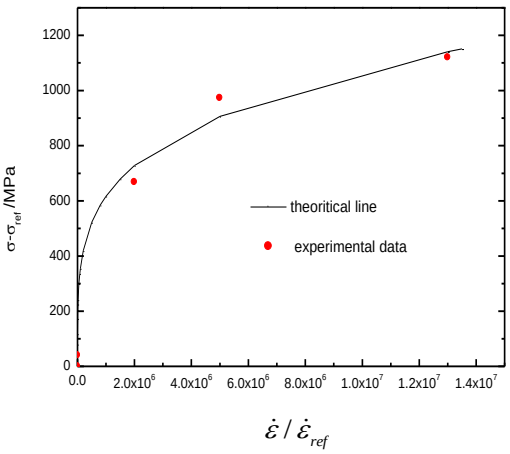

Fig6. Effect of strain rate on the stress

Assuming $\dot{\varepsilon}_{ref}=10^{-4}\mathrm{s}^{-1}$, and $\sigma_{ref}=1170\mathrm{MPa}$, the strain rate sensitivity coefficients, a and m can be obtained by using the least squares method, $a=22.38\,\mathrm{MPa}$, $m=0.24$.

The quasi-static constitutive relation of the composite can be simplified as

$$\varepsilon=\begin{cases}\sigma/E, & \sigma\le\sigma_s\\ \sigma_s/E, & \sigma>\sigma_s\end{cases} \qquad (5)$$

where, E is elastic modulus of the composite. It is related to the elastic modulus of the matrix and the reinforced particles, Poisson ratio of the matrix and the volume fractions of the reinforced particles etc. The formula can be referenced [8].

2.3 Strain-rate response

Fig.7 show that the rate-sensitivity comparison between TiCP/Ti composite and its matrix at different strain rate. Assuming $\dot{\varepsilon}_0$ =1×10^{-4}s^{-1}, the ultimate stress of the composite and the matrix, σ_{b0} are 1050MPa and 1170MPa.

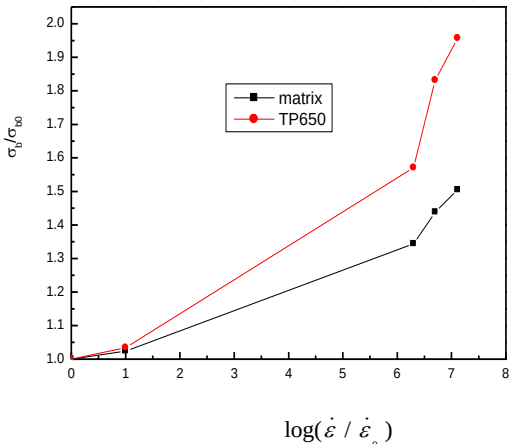

Fig 7. The rate-sensitivity comparison between TiC$_P$/Ti composite and its matrix at different strain rates

The strain rate hardening of the composite is higher than that of the matrix. The high strain-rate sensitivity of the composite is considered to be originated from the high dislocation accumulation rate during dynamic deformation and the constraint of TiC particles on the surrounding matrix, which dramatically enhances rate of the matrix.

3. Conclusion

The experimental results show that both the TiCp/Ti composite and its matrix alloy exhibit an obvious strain-rate hardening property. But the high strain-rate sensitivity of the TiCp/Ti composite is significantly higher than that of the matrix. The high strain-rate sensitivity of the composite is considered to be originated from the high dislocation accumulation rate during dynamic deformation and the constraint of TiC particles on the surrounding matrix, which dramatically enhances rate of the matrix. A phenomenological dynamic constitutive relation is established considering the composite is elastic-perfectly plastic material.

Acknowledgement:

The financial support provided by the Chinese National Natural Science Foundation (No.90305018).

References

[1] G. Bao, J.W.Hutchinson and R.M. McMeeking: Acta. Metal. Mater, Vol. 39 (1991), p.1871

[2] J.W. Ju, L.Z. Sun: Int. J. of Solids Struct., Vol. 38 (2001), p.183

[3] J.W. Ju, L.Z. Sun: Int. J. of Solids Struct., Vol. 38 (2001), p.203

[4] V.A. Buryachenko: Acta. Mech., Vol. 119 (1996), p.93

[5] G.J. Dvorak: Buryachenko: Int. J. of Solids Struct., Vol. 37 (2000), p.155

[6] G.P. Tandon: Buryachenko: Transactions of the ASME, Vol. 55 (1998), p.126

[7] G.K. Hu: Buryachenko: Int. J. plasticity, Vol. 12 (1997), p.1007

[8] F. Jiang: Ph.D. Thesis, Beijing Institute of Technology, Beijing (2006)

Key Engineering Materials Vols. 385-387 (2008) pp 877-880
© (2008) Trans Tech Publications, Switzerland
doi:10.4028/www.scientific.net/KEM.385-387.877

Damage identification of mechanical system with artificial neural networks

Lijuan Cao[1, a], Shouju Li[2,b] and Zichang Shangguan[3,c]

[1]Institute of Mechanical Engineering, Dalian Fisheries University, Dalian, Liaoning Province, China

[2]State Key Laboratory of Structural Analysis of Industrial Equipment,

Dalian University of Technology, Dalian, Liaoning Province, China

[3]Institute of Civil Engineering, Dalian Fisheries University, Dalian, Liaoning Province, China

[a]clj@dlfu.edu.cn, [b]lishouju@dlut.edu.cn, [c]shangguan@dlfu.edu.cn

Key words: natural frequency, damage identification, neural network, hybrid optimization, inverse problem

Abstract. The inverse problem of structure damage detection is formulated as an optimization problem, which is then solved by using artificial neural networks. Based on the hybrid optimization strategy, the parameter identification algorithm was presented according to the measured data of vibrating frequency and mode shapes in the damaged structure. The proposed algorithm combines the local optimum method having fast convergence ability with the neural networks having global optimum ability. By doing this, the local minimization problem of the local optimum method can be solved, and the convergence speed of the global optimum method can be improved. The investigation shows that to identify the location and magnitude of the damaged structure by using an artificial neural network is feasible and a well trained artificial neural network by Levenberg-Marquardt algorithm reveals an extremely fast convergence and a high degree of accuracy.

1 introduction

Non-destructive inspection techniques are generally used to investigate the critical changes in the structural parameters so that an unexpected failure can be prevented. These methods concentrate on a part of the structure and in order to perform the inspection, the structure needs to be taken out of service. Since these damage identification techniques require a large amount of human intervention, they are passive and costly methods. On the other hand, damage can be detected, quantified and localized by on-line damage assessment techniques using vibration-based analysis data in the service life of a structure. Mechanics engineering structures are prone to damage and deterioration during their service life. Damage assessment attempts to determine whether structural damage has occurred, as well as the location and extent of any such damage. However, detecting structural damage and identifying damaged elements in a large complex structure are challenging tasks since the in situ measured data of large Mechanics engineering structures such as water turbine and electric generator are inaccurate (owing to noise corruption) and often incomplete (for economy consideration). Vibration-based damage identification has attracted the attention of a number of researchers. Budipriyanto reported numerical investigations on uncracked and cracked steel cantilever beams. Strain frequency response functions of the beams were examined to determine the crack severity and location. They stated that strain frequency response functions were sensitive to cracks and can be employed to identify the crack location and extent [1]. The effects of common damage on a structure are changes in natural frequencies, mode shapes and structural damping. Since the measurement of natural frequencies is easier than that of changes in structural damping, damage can be detected from dynamic analysis using natural frequencies and mode shapes. Damage detection techniques based on changes in the structural dynamic characteristics have been studied [2]. Conventional damage assessment methods are inevitably direct process methods, proceeding linearly from causes to effects. These methods involve first constructing a mathematical model for the structure, and then applying that model to elucidate structural behavior and establish correlations between specific member damage conditions and changes in structural response.

Despite their many attractive features, conventional damage assessment methods may encounter difficulties, such as measurement noise and modeling errors, when detecting difficult to model systems. Additionally, commonly adopted damage assessment algorithms are generally complex and inappropriate where measured data are inappropriate [3]. Many efforts have been made on health monitoring and damage assessment of mechanics structure for avoiding catastrophic structural failure and making proper decision on repair, partial replacement or demolition. Among others, the vibration-based damage identification technique has attracted significant interest for researchers and engineers in the past two decades. This approach usually uses measured change in natural frequencies and modal shapes to evaluate change in physical properties that may indicate structural damage or degradation. Also, vibration-based damage detection using measured frequency response functions (FRFs) has been studied by a number of researchers. As modal parameters (natural frequency, mode shape and modal damping) are indirectly-measured test data, they could be contaminated by measurement error as well as modal extraction error, and provide less information than FRF data [4]. Neural networks are computational models inspired in the architecture and operation of the human brain. They are an assembling of connected processing units called neurons. The strength of the connection is represented by the ‘‘weights’’ or parameters, which are determined in the training process. The technique used here aims to test the efficacy of global or local vibration parameters and their different combinations as input to feed-forward back-propagation ANNs for accurate prediction of damage location and severity. The purpose of the present study is to investigate the capability of identifying the damage extent and location of damage on the simple mechanics part model. Finite element models for the stiffened shaft e were developed to simulate the dynamic response of the undamaged and damaged structures. The modal frequencies and modal shapes obtained from the finite element calculations were used as input to the network.

2 Neural networks for damage identification

Among the many different types of ANN, the feed forward, multilayered, supervised neural network with the error back-propagation algorithm, generally known as the back-propagation (BP) network, is by far the most commonly applied owing to its simplicity. Before an ANN can be applied, it needs to learn or be trained from an existing training set comprising pairs of input–output elements. The training of a supervised neural network using BP learning algorithm usually involves two stages, the first of which is the data feed forward.

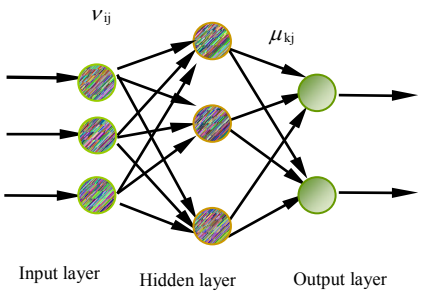

Fig. 1. Topography structure of artificial neural network

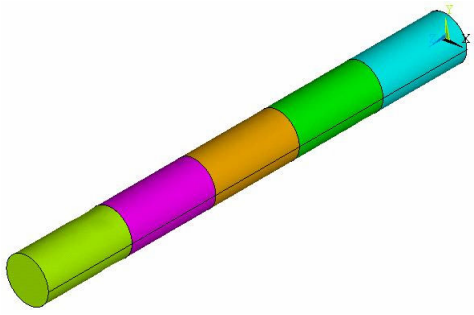

Fig. 2 FEM model of a beam structure

The architecture of BP networks, depicted in Figure 1, includes an input layer, one or more hidden layers, and an output layer. The nodes in each layer are connected to each node in the adjacent layer. Notably, Hecht-Nielsen proved that one hidden layer of neurons suffices to model any solution surface of practical interest. Hence, a network with only one hidden layer is considered in this study. Before an ANN can be used, it must be trained from an existing training set of pairs of input-output elements. The training of a supervised neural network using a BP learning algorithm

normally involves three stages. The first stage is the data feed forward. The computed output of the i-th node in output layer is defined as follows [5]

$$y_i = f(\sum_{j=1}^{N_h}(\mu_{ij} f(\sum_{k=1}^{N_i} v_{jk} x_k + \theta_j) + \lambda_i)) \quad (1)$$

Where μjk is the connective weight between nodes in the hidden layer and those in the output layer; vjk is the connective weight between nodes in the input layer and those in the hidden layer; θj or λi is bias term that represents the threshold of the transfer function f, and xk is the input of the kth node in the input layer. Term Ni, Nh, and No are the number of nodes in input, hidden and output layers, respectively. The transfer function f is selected as Sigmoid function

$$f(\cdot) = 1/[1 + \exp(-\cdot)] \quad (2)$$

The second stage is error back-propagation through the network. During training, a system error function is used to monitor the performance of the network. This function is often defined as follows

$$E(w) = \sum_{p=1}^{P}(\sum_{i=1}^{N_o}(y_i^p - o_i^p)^2 \quad (3)$$

Where y_i^p and o_i^p denote the practical and desired value of output node i for training pattern p, P is the number of sample. Training methods based on back-propagation offer a means of solving this nonlinear optimization problem based on adjusting the network parameters by a constant amount in the direction of steepest descent, with some variations depending on the flavor of BP being used. The optimization algorithm used to train network makes use of the Levenberg-Marquardt approximation. This algorithm is more powerful than the common used gradient descent methods, because the Levenberg-Marquardt approximation makes training more accurate and faster near minima on the error surface [6].

The number of neurons in the input layer depends on the number of input features in each input pattern set. The measured modal data include the first 10 frequencies and vertical mode shape at the middle point of model. Therefore, the number of neurons in the input layer is equal to 20. The output layer has 2 neurons, which must be equal to the number of identified parameters. The number of neurons in the hidden layer is equal to two times of the number of neurons in the input layer. So the topology structure of neural network is 20-41-2. After selecting the architecture of the neural networks, the database for training and testing was generated by using finite element method.

3 Numerical simulation validations

A Finite Element (FE) model is used to generate the data for training and testing the NNs. As the information contained in the features is limited, the definition of both the damage and the FE model should be consistent with it. Thus, the damage should be defined by a number of independent parameters less than or equal to the number of available modal parameters. Otherwise, the NNs would be unable to generalize. This is because different states of damage lead to very close sets of modal parameters. Local damage in a mechanics structure always causes reduction of local structural stiffness, so that these variations can be denoted using change of material elastic coefficients of the local structure. Dynamics model of a damaged structure can be established using the modified material elastic coefficients in local damage position of the structures, and it may not be necessary to depict the geometry of small damage. Thus, it is possible to avoid troubles caused by direct meshing structures using current commercial software in modeling damaged structures.

As shown in Fig. 2, a beam structure is fixed at the right side and simply supported at the left side. The length and diameter of the beam structure are 2m and 200mm, respectively. Material density and elastic modulus are 7800kg/m3 and 206E9, respectively. The beam structure is simply divided into five blocks. Modal shapes of the fourth and seventh order are shown in Fig. 3 and 4.

The samples for training and testing the NNs are generated by FEM. After training NNs, the testing samples are used to validate the effectiveness of proposed damage identification procedure. Table 1 lists the modal frequency characteristics of damaged beam structure. Table 2 depicts the comparison between the identified and hypothetical values.

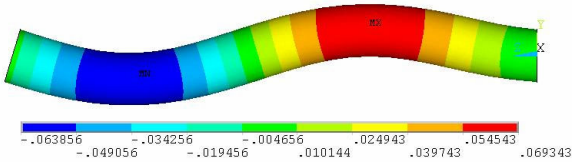

Fig. 3 Modal shapes of the fourth order

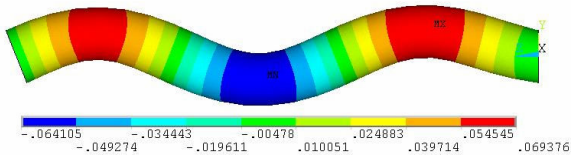

Fig. 4 Modal shapes of the eighth order

Table 1 Modal frequency characteristics of damaged beam[Hz]

No.	Damage cases				
	A	B	C	D	E
1	33.437	35.262	35.083	35.712	35.821
2	148.62	153.82	146.88	147.42	153.24
3	211.54	216.92	203.54	210.62	217.84
4	470.10	475.50	472.05	464.10	474.42
5	573.30	579.80	575.80	556.99	582.83
6	616.10	633.92	618.62	635.95	644.30
7	748.32	773.04	777.17	764.41	755.47
8	934.02	950.28	917.48	938.02	941.24
9	1066.1	1086.3	1048.8	1061.9	1079.6
10	1512.9	1541.1	1461.5	1510.1	1528.8

Table 2 Comparison between the identified and hypothetical values

No.	Damage location		Damage index[%]	
	Hypothetical values	Identified values	Hypothetical values	Identified values
1	Block 1	Block 1	15.0	15.149
2	Block 2	Block 2	25.0	24.897
3	Block 3	Block 3	35.0	35.351
4	Block 4	Block 4	45.0	45.459

Note(Table 1): A denotes block 1 damage index 20%; B denotes block 2 damage index 10%; C denotes block 3 damage index 30%; D denotes block 4 damage index 25%; E denotes block 5 damage index 15%.

4 Conclusion

A method based on neural networks (NNs) is proposed to identify damage location and index for the mechanical system in this paper. The objectives of the method are to detect and quantify the damage location and index using low natural frequencies and mode shapes of the beam structure. The inputs of the neural networks are the frequencies and mode shapes at each principal direction of the structure and the outputs are the damage location and index. A simplified finite element model was used to generate the data needed to train the networks. The investigation shows that to identify the location and magnitude of the damaged structure by using an artificial neural network is feasible and a well trained artificial neural network by Levenberg-Marquardt algorithm reveals an extremely fast convergence and a high degree of accuracy.

References

[1] A. Budipriyanto, M.R. Haddara and A.S.J. Swamidas: Ocean Engineering 34 (2007), p.709–716

[2] M. Sahin, R.A. Shenoi : Engineering Structures 25 (2003), p. 1785–1802

[3] C.Y. Kao, Shih-Lin Hung: Computers and Structures 81 (2003), p. 2631–2644

[4] Y.Q. Ni, X.T. Zhou and J.M. Ko: Journal of Sound and Vibration 290 (2006), p. 242–263

[5] Shouju Li, Yingxi Liu: Lecture Notes in Computer Science, 2005, 3644: p.276-285

[6] Li, Shouju, Liu Yingxi: International Journal Of Nonlinear Sciences And Numerical Simulation (7)2006, p.177-182

Key Engineering Materials Vols. 385-387 (2008) pp 881-884
© (2008) Trans Tech Publications, Switzerland
doi:10.4028/www.scientific.net/KEM.385-387.881

Crack Analysis of 3D Functionally Graded Materials by a BEM

J. Wang[1, a], X. W. Gao[1, b] and Ch. Zhang[2, c]

[1]Department of Engineering Mechanics, Southeast University, Nanjing 210096, PR China

[2]Department of Civil Engineering, University of Siegen, D-57068 Siegen, Germany

[a]wangjing060730@qq.com, [b]xwgao@seu.edu.cn, [c]c.zhang@uni-siegen.de

Keywords: Fracture mechanics, Crack analysis, Functionally graded materials, Stress intensity factors, Boundary element method.

Abstract. This paper presents an elastostatic crack analysis in three-dimensional (3D), isotropic, functionally graded and linear elastic solids. A boundary element method (BEM) based on boundary-domain integral equations is applied. A multi-domain technique and discontinuous elements at the crack-front are adopted. To show the effects of the materials gradients on the crack-opening-displacements (CODs) and the stress intensity factors (SIFs), numerical results for a penny-shaped crack are presented and discussed.

Introduction

Functionally graded materials (FGMs) are advanced composite materials with continuously nonhomogeneous material properties. FGMs are introduced in recent years to benefit from the ideal performance of its constituents, e.g., high heat and corrosion resistances of ceramics on one side, and large mechanical strength and toughness of metals on the other side. Cracks or crack-like defects may be induced in ceramic/metal FGMs by materials processing and in-service conditions. Thus, fracture and damage analysis of FGMs is an important issue to their reliability and durability in engineering applications. In general cases, fracture and damage analyses of FGMs require advanced and efficient numerical methods such as finite element method (FEM) or boundary element method (BEM). Due to the mathematical complexity of the arising boundary value problems, most research works reported in literature have been devoted to crack analysis in two-dimensional (2D), isotropic and linear elastic FGMs. In contrast to this, only very few investigations are directed to the corresponding 3D problems. This paper presents an elastostatic crack analysis in 3D, isotropic, continuously nonhomogeneous and linear elastic FGMs. A BEM based on a boundary-domain integral equation formulation is applied for this purpose. Normalized displacements are introduced in the BEM to avoid the displacement gradients in the domain-integrals. Numerical results for a penny-shaped crack are presented and discussed to show the effects of the material gradation on the crack-opening-displacements (COD) and the stress intensity factors (SIFs).

Boundary Element Method for Isotropic and Linear Elastic FGMs

Let us consider 3D, isotropic, continuously nonhomogeneous and linear elastic solids. The Young's modulus E is a function of spatial coordinates, while the Poisson's ratio ν is regarded as constant. Under this assumption, boundary-domain integral equations for boundary and internal nodes can be obtained as [1,2]

$$c\tilde{u}_i(\mathbf{x}^p) = \int_\Gamma U_{ij}(\mathbf{x},\mathbf{x}^p)t_j(\mathbf{x})d\Gamma - \int_\Gamma T_{ij}(\mathbf{x},\mathbf{x}^p)\tilde{u}_j(\mathbf{x})d\Gamma + \int_\Omega V_{ij}(\mathbf{x},\mathbf{x}^p)\tilde{u}_j(\mathbf{x})d\Omega\,, \tag{1}$$

where $c=1$ for internal points and $c=1/2$ for smooth boundary points, U_{ij} and T_{ij} are the Kelvin displacement and traction fundamental solutions [3] for an isotropic, homogeneous and linear elastic solid with $\mu = 1$, and

$$V_{ij} = \frac{-1}{4\pi\alpha(1-\nu)r^{\alpha}}\left\{\tilde{\mu}_{,k}r_{,k}[(1-2\nu)\delta_{ij}+\beta r_{,i}r_{,j}]+(1-2\nu)(\tilde{\mu}_{,i}r_{,j}-\tilde{\mu}_{,j}r_{,i})\right\}, \tag{2}$$

where β=3 for 3D problems and $\alpha=\beta-1$. In Eqs. (1) and (2), $\tilde{u}_j(\mathbf{x})$ and $\tilde{\mu}$ are the normalized displacements and shear modulus defined by

$$\tilde{u}_i(\mathbf{x}) = \mu(\mathbf{x})u_i(\mathbf{x}), \qquad \tilde{\mu}(\mathbf{x}) = \log\mu(\mathbf{x}). \tag{3}$$

Equation (1) shows that no displacement gradients are involved in the boundary-domain integral equations. This is a result of the use of the normalized quantities defined in Eq. (3). In comparison to the conventional boundary integral equations for isotropic, homogeneous and linear elastic solids [3], there is now a domain-integral in the integral equations (1). This domain-integral is converted into an equivalent boundary integral using the radial integral method (RIM) [4]. Since the unknown variables $\tilde{u}_j$ are included in the domain-integral, some internal points inside the analyzed domain are required to improve the computational accuracy in the approximation of $\tilde{u}_j$ in terms of the radial basis functions (RBFs) in the application of RIM [2,4]. More details to the numerical implementation of the present BEM can be found in references [1,2,4].

Numerical Results

As numerical example we consider a functionally graded solid with a penny-shaped crack located at the center of the solid as shown in Fig. 1. The geometry of the cracked solid is determined by B=100mm, H=300mm and a=20mm. Poisson's ratio is taken as $\nu = 0.25$.

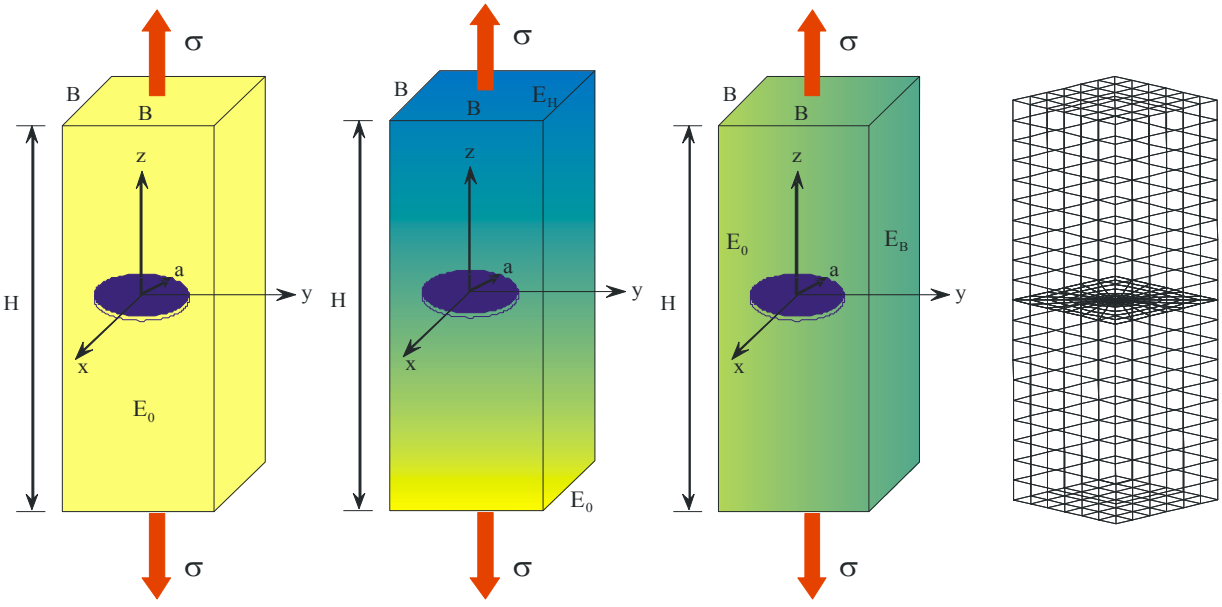

Fig. 1. Homogenous and functionally graded solids with a central penny-shaped crack

For the Young's modulus, three different cases are considered:

Case I: Homogenous solid: $E = E_0 = 1000\text{GPa}$ (4)

Case II: Material gradation in z-direction: $E = E(z) = E_0 e^{\alpha(z+H/2)}$ (5)

Case III: Material gradation in y-direction: $E = E(y) = E_0 e^{\beta(y+B/2)}$ (6)

The gradient parameters α and β in Eqs. (5) and (6) are determined by

$$\alpha = \frac{1}{H}\log\left(\frac{E_H}{E_0}\right), \qquad \beta = \frac{1}{B}\log\left(\frac{E_B}{E_0}\right), \tag{7}$$

where $E_H / E_0 = 10$ and $E_B / E_0 = 10$ are used in the numerical calculations. Case I is considered here for the comparison purpose. The BEM mesh is also shown in Fig. 1, which consists of 936 8-noded quadrilateral boundary elements with 2524 boundary nodes. 450 internal nodes are applied to compute the domain-integrals. In the two element rows behind and ahead of the crack-front, discontinuous 8-noded quadrilateral boundary elements are implemented.

For two selected sections Fig. 2 shows the numerical results for the normalized crack-opening displacement normal to the crack-surface, which is defined by

$$\Delta\bar{u}_3(r) = \frac{\Delta u_3(r)}{\Delta u_3^0}, \qquad \Delta u_3^0 = \frac{8(1-\nu^2)}{\pi E_0}\sigma a \tag{8}$$

where Δu_3^0 is the normal COD of a penny-shaped crack in an infinite, isotropic, homogeneous and linear elastic solid with the Young's modulus E_0 subjected to a remote tensile loading $\sigma_{33}^{\infty} = \sigma$. It can be seen from Fig. 2 that a material gradation in *y*-direction (Case III) affects the variation of the normal COD with the radial coordinate *r/a*. In this case, the soft side at *r/a*=-1 shows a larger COD, while the hard side at *r/a*=1 shows a smaller COD.

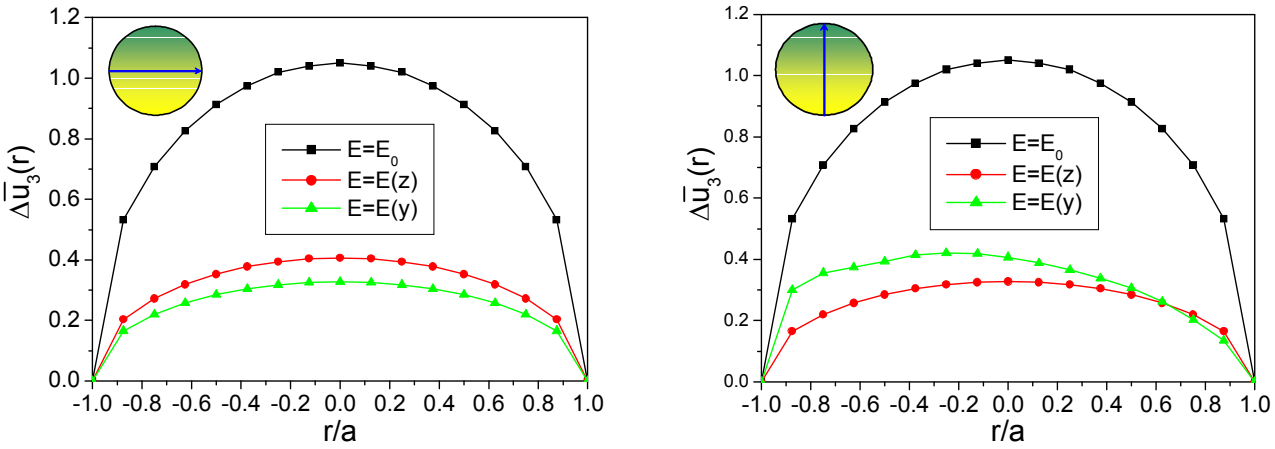

Fig. 2. Normalized CODs for two selected sections

Figure 3 presents the normalized stress intensity factors defined by

$$\bar{K}_I(\theta) = \frac{K_I(\theta)}{K_I^0}, \quad \bar{K}_{II}(\theta) = \frac{K_{II}(\theta)}{K_I^0}, \quad \bar{K}_{III}(\theta) = \frac{K_{III}(\theta)}{K_I^0}, \quad K_I^0 = \frac{2}{\pi}\sigma\sqrt{\pi a}, \tag{9}$$

where K_I^0 is the mode-I stress intensity factor of a penny-shaped crack in an infinite, isotropic, homogeneous and linear elastic solid subjected to a remote tensile loading $\sigma_{33}^{\infty} = \sigma$. Figure 3 implies that a material gradation in *y*-direction not only changes the distribution of the SIFs in the circumferential direction, but also results in mode-II and mode-III SIFs. For a material gradation in the *z*-direction, the mode-II and the mode-III SIFs are negligibly small. These negligibly small values are presumably caused by the numerical inaccuracies of the present BEM.

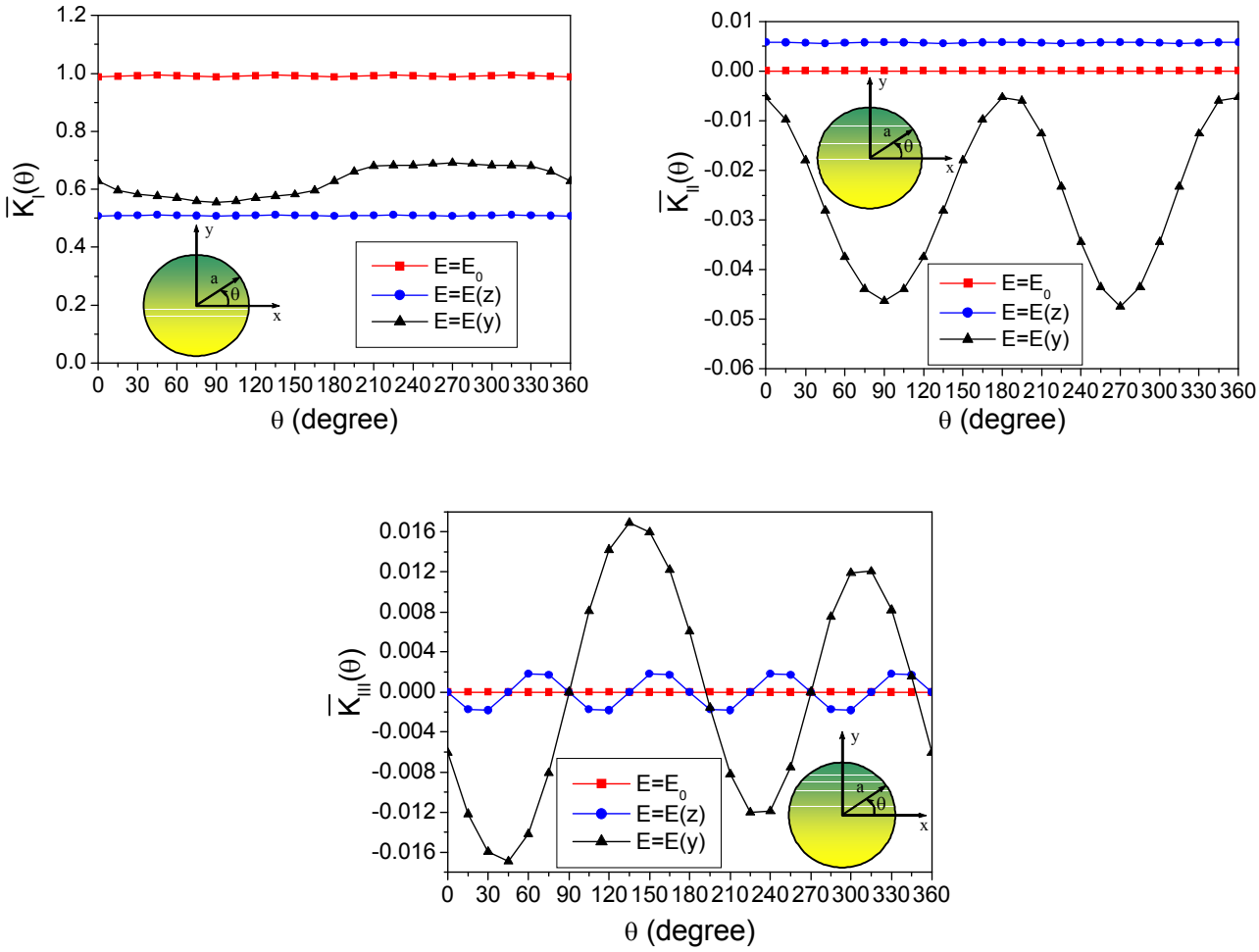

Fig. 3. Normalized stress intensity factors versus the polar angle

Summary

Elastostatic crack analysis in 3D, isotropic, functionally graded and linear elastic solids is presented in this paper. A BEM based on boundary-domain integral equations is applied for this purpose. A multi-domain technique and discontinuous elements at the crack-front are adopted. Numerical results for a penny-shaped crack are presented and discussed to explore the effects of the material gradation on the crack-opening-displacements and the stress intensity factors.

Acknowledgement

Support by the German Research Foundation (DFG) under the project number ZH 15/10-1 is gratefully acknowledged.

References

[1] X.W. Gao, L. Guo, and Ch. Zhang: Eng. Anal. Bound. Elem. Vol. 31 (2007), p. 965.
[2] X.W. Gao, Ch. Zhang and L. Guo: Eng. Anal. Bound. Elem. Vol. 31 (2007), p. 974.
[3] X.W. Gao and T.G. Davies: *Boundary Element Programming in Mechanics* (Cambridge University Press, 2002).
[4] X.W. Gao: Eng. Anal. Bound. Elem. Vol. 26 (2002), p. 905.

Key Engineering Materials Vols. 385-387 (2008) pp 885-888
© (2008) Trans Tech Publications, Switzerland
doi:10.4028/www.scientific.net/KEM.385-387.885

Finite Element Modelling of Piezoelectric Sensors for Damage Identification in Composite Panels

M H Aliabadi[1, a], Apicella [2,b] and A. Sanqirgo-Rodriguez[1,c]

[1] Department of Aeronautics, Imperial College London, South Kensington, London, SW7 2BZ

[2] Alenia Finmeccanica, Viale dell'Aeronautica, 80038 Pomigliano d'Arco, Naples, Italy

[a]m.h.aliabadi@imperial.ac.uk, [b]aapicella@aeronautica.alenia.it, [c]albert.sanquirgo-rodriguez07@imperial.ac.uk

Keywords: Structural health monitoring, Composite materials, Damage detection

Abstract. In this paper the application of the finite element method is presented to modeling piezoelectric sensors and actuators for use in structural health monitoring of composite panels. It this demonstrated that FEM can be used to simulate sensorised composite panels and investigate the damage detection capability of sensors.

Introduction

Future aircraft structures contain new structural designs, processes and materials to achieve higher environmental and economical efficiency due to reduced weight and therefore lower fuel consumption. The advanced composite materials such as monolithic CFRP, sandwich structures and laminates are widely used in modern civil aircrafts to achieve these goals. In aircraft industry these innovative ideas can only become reality if a sensitive, reliable and efficient quality assurance concept is available and integral part of aircraft manufacturing process.

The identification of damage in composite panels, including characterization of damage location and severity, if of great importance. To date, many damage detection methods have been proposed that utilize global structural response measurements to hypothesize the existence of structural damage. The accuracy and robustness of current damage detection methodologies could be improved through the use of active sensors. Active sensors, such as piezoelectric pads, impart low-energy acoustic excitation into structural elements and can be record corresponding system behaviour [1-4].

Recent developments in sensor technologies, signal processing and electronics have shown the potential for new monitoring techniques that could be used for aircraft damage detection. In general damage monitoring systems which utilize smart structures and materials technologies are concerned with a design philosophy directed to the integration of actuators, sensors and signal processors. The attractive potential of such technologies arises from the added value in terms of more reliable damage monitoring system, reduced inspection and improved safety location and severity, if of great importance. To date, many damage detection methods have been proposed that utilize global structural response measurements to hypothesize the existence of structural damage. The accuracy and robustness of current damage detection methodologies could be improved through the use of active sensors. Active sensors, such as piezoelectric pads, impart low-energy acoustic excitation into structural elements and can be record corresponding system behaviour.

Recent developments in sensor technologies, signal processing and electronics have shown the potential for new monitoring techniques that could be used for aircraft damage detection. In general damage monitoring systems which utilize smart structures and materials technologies are concerned with a design philosophy directed to the integration of actuators, sensors and signal processors. The attractive potential of such technologies arises from the added value in terms of more reliable damage monitoring system, reduced inspection and improved safety

In this paper the effectiveness of the finite element method to model piezoelectric sensors mounted on the surface of a composite panel is investigated. The special piezo-elements are used as actuators

to generate lamb waves as well as sensors to detect the change due to possible damage in the panel. Sensor outputs due to damage at different locations and level of damage are investigated.

Finite Element Model

Consider a fibre reinforced laminated composite with distributed piezoelectric sensors that are bonded on it surface as shown in Figure 1.

The mechanical and electric response of piezoelectric can be described by equation of motion

$$\sigma_{ji,j} + f_i = \rho \ddot{u}_i \tag{1}$$

and the Maxwell's equation for

$$D_{i,i} = 0 \tag{2}$$

where σ_{ij}, f_i, ρ, $\ddot{u}$ and D_i are stress, body force, acceleration and displacement acceleration. The constitutive equations for the piezoelectric can be presented as

$$\varepsilon_{ij} = S_{ijkl}\sigma_{kl} + d_{klj}E_k \tag{3}$$

and

$$D_i = d_{ikl}\sigma_{kl} + x_{ij}E_j \tag{4}$$

where S_{ijkl} are elastic compliances for a constant electric filed, x_{ij} are the premittivities for a constant stress, d_{ikl} are the piezoelectric strain constants, and E_j are the electric field components.

Generating a lamb wave is done by applying a voltage in a piezoelectric actuator. The amplitude is be defined as a triangular function to simulate an impulse. For simulations in this paper the lamb wave is generated by applying a voltage of 10 V on the top surface of the piezoelectric actuator. The location of this actuator and four sensors are shown in Figure 1.

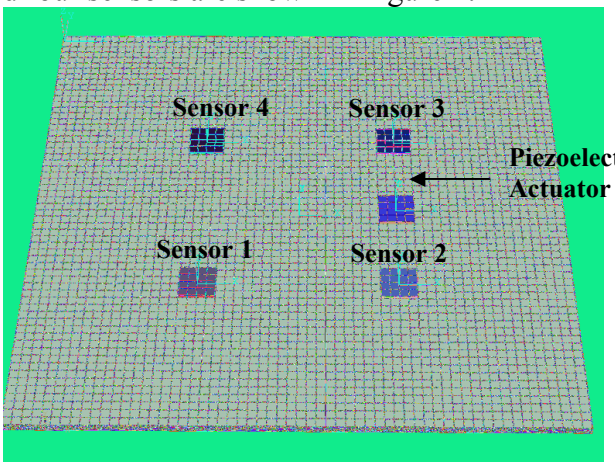

Figure 1. Location of the piezoelectric actuator

The composite plate has the following properties

Stacking sequence: $[45_2/-45_4/45_2]_s$

E_L: 142 Gpa

E_T: 10.8 Gpa

G_{LT}: 5.49Gpa

Poisson's ratio: 0.30

Density: 1600 Kg/m

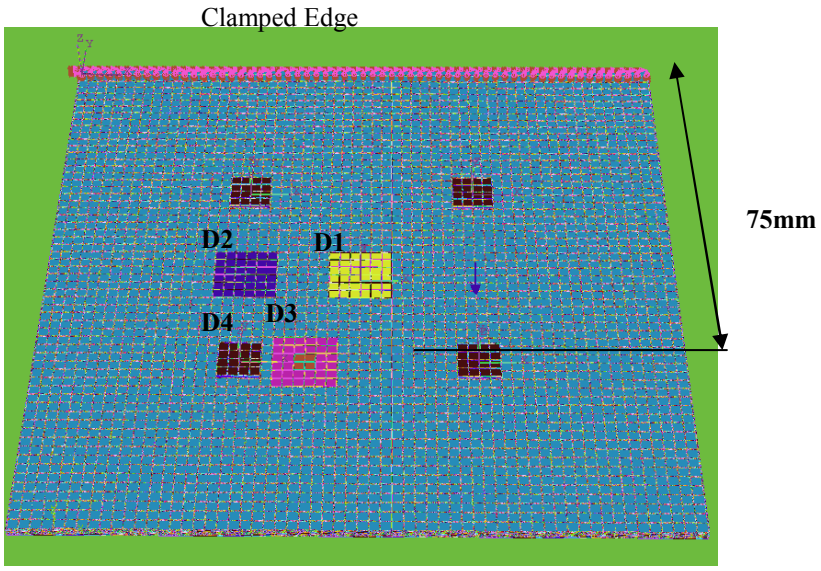

Figure2. Location of damaged areas (D1, D2, D3 and D4)

Damaged areas D1, D2 and D3 are 15x15 mm^2 and D4 is 5x5 mm^2. The notation for these damage areas are the same used to present the results in the figures. The results obtained for sensors 1 is presented in figure 3. As it can be seen the sensor picks up the change between different damage location.

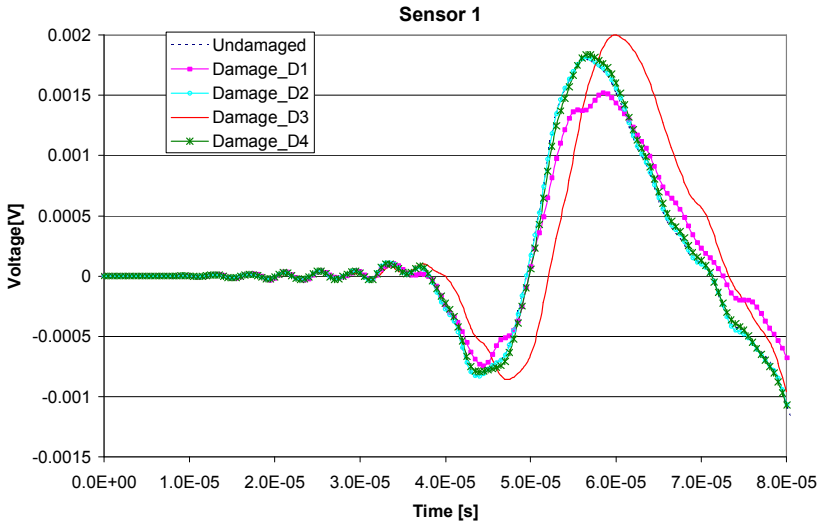

Figure 3. Comparison of sensor responses for different damaged areas in Sensor 1

The effectiveness of the sensors in sensing different level of damage is next investigated. Three levels of damage 25%, 50% and 75% modeled by reducing materials stiffness at damage location D1 was studied. In figure 3 and 4 outputs from sensors 1 and 2 are presented. As it can be seen sensor 1 is able to sense the damage, where as the output for sensor 2 remained unchanged. This goes to highlight the importance of sensor positioning for effective structural health monitoring.

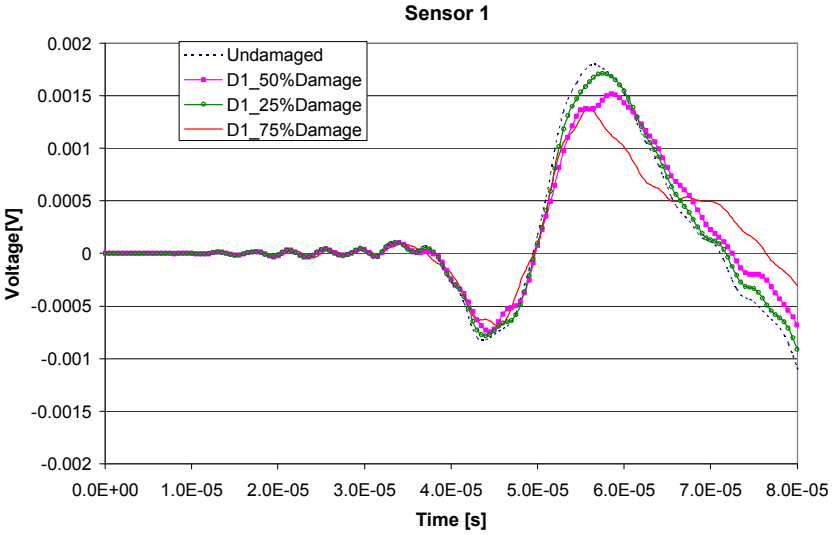

Figure 4. Sensor 1 outputs for different level of damage.

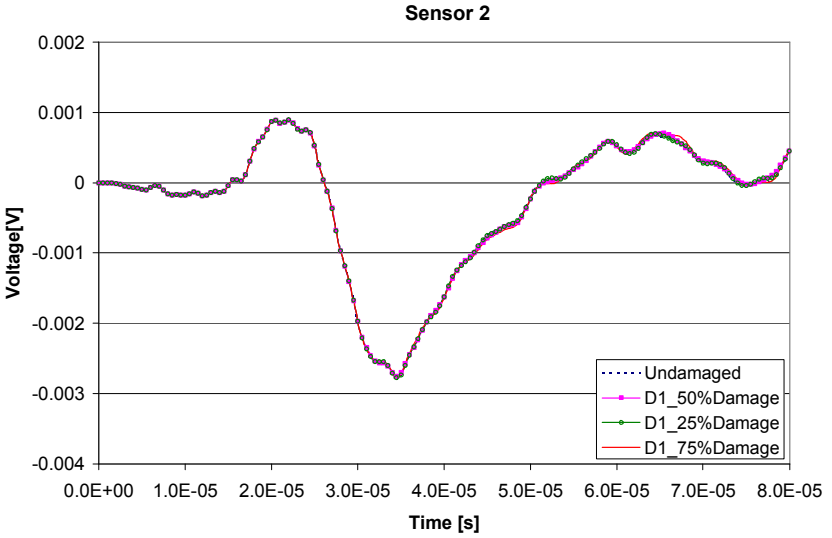

Figure 5. Sensor 2 output for different level of damage.

Conclusions

In this paper the application of the 3D finite element method for modeling piezoelectric sensors was investigated. The piezo finite elements were used for both sensing and actuating. Test cases studied included difference location and level of damage.

References

[1] Schulz,M.J., Pai, P.F and Inman, D.J. *Composites*, **30,** 713-725, 1999.

[2] Sung Kyu Ha, Keilers,C., Fu-Kuo *AIAA Journal*, **30**, 772-780, 1992.

[3] Lin,X and Yuan,F.G *Smart Material Structures*, **10,** 907-913, 2001

[4] Leme, S.P.L. Aliabadi, M.H. Bezerra, L.M. Partridge, P.W., *Structural Health Monitoring and Durability,* **3**, 121-132, 2007

Key Engineering Materials Vols. 385-387 (2008) pp 889-892
© (2008) Trans Tech Publications, Switzerland
doi:10.4028/www.scientific.net/KEM.385-387.889

Application of Instrumented Indentation Technique to Evaluate Residual Stress and Stress Directionality

Min-Jae Choi[1,a], Ingeun Kang[1,b], Kwang-Ho Kim[2,c] and Dongil Kwon[1,d,*]

[1]Department of Materials Science and Engineering, Seoul National University, Seoul, Korea

[2]Frontics, Inc., Research Institute of Advanced Materials, Seoul National University, Seoul, Korea

[a]mjtake1@snu.ac.krmail, [b]neviny1@snu.ac.kr, [c]khkim@frontics.com, [d]dongilk@snu.ac.kr

Keywords: Instrumented Indentation Technique, IIT, Residual Stress, Directionality, Knoop

Abstract. The instrumented indentation technique (IIT) is a powerful method for evaluating mechanical properties of materials such as elastic modulus, tensile strength, fracture toughness and residual stress. Especially, IIT is a promising alternative to conventional methods of residual stress measurement such as hole drilling, saw cutting, X-ray/neutron diffraction, and ultrasonic methods because of its various advantages of nondestructive specimen preparation, easy process, characterization of material properties on local scales and measurement of in-service structures. Evaluation of residual stress using IIT is based on the key concepts that the deviatoric-stress part of the residual stress affects the indentation load-depth curve and that the quantitative residual stress in a target region can be evaluated by analyzing the difference between the residual stress-induced indentation curve and residual stress-free curve. To verify the applicability of the suggested technique, indentation tests were performed on the welded zone.

Introduction

Indentation technique is one of the most popular methods to measure the mechanical properties of materials, especially the hardness of materials which is a measure of resistance to plastic deformation. The extensive use of indentation technique in-field and in-research is owing to its simple and non-destructive experimental procedure. The development of instrumented indentation technique (IIT), which gives accurate measurements of the continuous variation in indentation load as a function of indentation depth, paved the way for significant progresses in the researches on indentation tests [1]. In IIT, observing the residual impression area is unnecessary, and elastic modulus which is a measure of resistance to elastic deformation is also measurable. In addition, various material properties such as tensile properties and fracture toughness are measured by analyzing the indentation load-depth curve [2-4]. Residual stress also can be evaluated by IIT, which has great advantages of non-destructive and simple/easy process in comparison with conventional method such as hole-drilling, saw-cutting and X-ray/neutron diffraction [5-6].

Residual stress caused by inhomogeneous thermal and mechanical loads during welding affect subsequent fracture and fatigue behavior, stress-corrosion cracking, and the like [7]. Thus the quantitative measurement of welding residual stress is important for the safe use and economical maintenance of industrial structures and facilities. Welding thermal cycles generate inhomogeneous heating and cooling in the regions near the heat source and thus cause residual stress in the weldment, sometimes so large as to surpass the yield strength of the welded material. It is widely recognized that welding residual stresses is detrimental to the performance of the weldment, the tensile-stressed region is particularly harmful because of its susceptibility to fatigue and stress corrosion cracking [8]. In this study, instrumented indentation tests were performed on the welding specimen. We confirmed the heat-affected zone and welding zone by optical observation and surface etching and we quantified the residual stress through the indentation testing on weld zone and heat-affected zone. The profile of residual stress was obtained by numerous tests along the perpendicular line to welding direction.

Evaluation of Residual Stress Using Instrumented Indentation Technique

The change in indentation deformation caused by the residual stress was identified in the indentation loading curve in Fig. 1. The applied load in the tensile stressed state is lower than that in the stress-free state for the same maximum indentation depth. On the contrary, the applied load in the compressive stressed state is higher than that in the stress-free state. The residual stress can be evaluated by analyzing the load difference at the same indentation depth in the indentation load-depth curve that obtained from the stressed zone and stress-free zone [5,6].

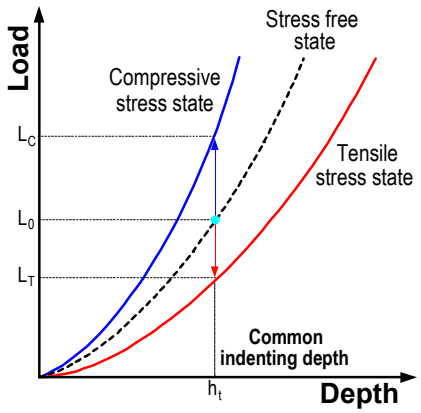

Fig. 1. Variation of indentation loading curves with changes in the stress state.

The degree of curve shift caused by residual stress is defined ΔL at the same indentation depth, h_t, and ΔL is assumed to be product of selected deviatoric stress component and its corresponding contact area A_S at h_t. If the stress directionality p is defined as the ratio of residual stress of each direction, an equation for non-equibiaxial residual stress is determined as follow:

$$\sigma_{res}^{x} = \frac{3}{(1+p)} \frac{1}{\Psi} \frac{\Delta L}{A_S} . (1)$$

Lee and Kwon demonstrated the validity of Eq. 1 by empirical indentation tests on biaxially strained specimens [6]. Several preliminary observations on the welded joints showed that the value of residual stress directionality is about 0.33, and this value was used in subsequent biaxial stress analyses [9].

Experimental Procedure

The material used in this study was a carbon steel. The chemical compositions of the materials and weld metal are shown in Table 1. The dimensions of the plates were 200 mm x 100 mm x 12 mm. Instrumented indentation tests were performed along perpendicular line to welding direction and 30 tests were performed along the line for drawing the residual stress profile. The distance between test point and next point was 3mm and maximum indentation load was 80kgf. The equipment for instrumented indentation tests was Frontics Inc.'s AIS3000.

Table 1. Chemical composition of the parent and weld metal (in wt.%)

Composition	C	Mn	Si	S	P	Ni	Cr	Mo	Cu	V	Ti	Co	Al
Parent metal	.12	.63	.13	.01	.02	.02	.01	.01	.01	<.01	<.01	<.01	.03
Weld metal	.10	1.7	.68	.02	.02	.05	.03	.04	-	.04	-	-	-

Results

The instrumented indentation curves of the HAZ, weld zone and the reference curve for the welding specimen are presented together in Fig. 2.

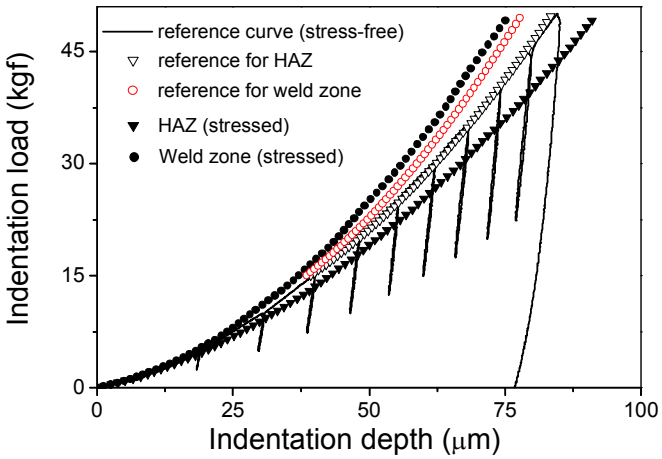

Fig. 2. Experimental indentation curves (solid triangles and circles) from the welded joint in residual stress state and analytical reference curves (open triangles and circles) in stress-free state.

The load decrease due to surface stress at a given indentation depth means that the residual stress is tensile stress. On the contrary, the load increases at a given indentation depth means that the residual stress is compressive stress. Fig. 2 is one example of the experimental indentation load-depth curve on the specimen. Through the analysis of the experimental data of 30 indentation tests along the testing line, residual stress values classified by distance from welding center line were obtained as Fig. 3. To analyze the residual stress, contact area A_S were calculated from the contact depth considered pile-up height based on the geometry of the Vickers indenter, $A_S = 24.5h^2$, and by inserting $p = 0.33$ into Eq. 1, the quantitative residual stress distribution inside the specimen was calculated.

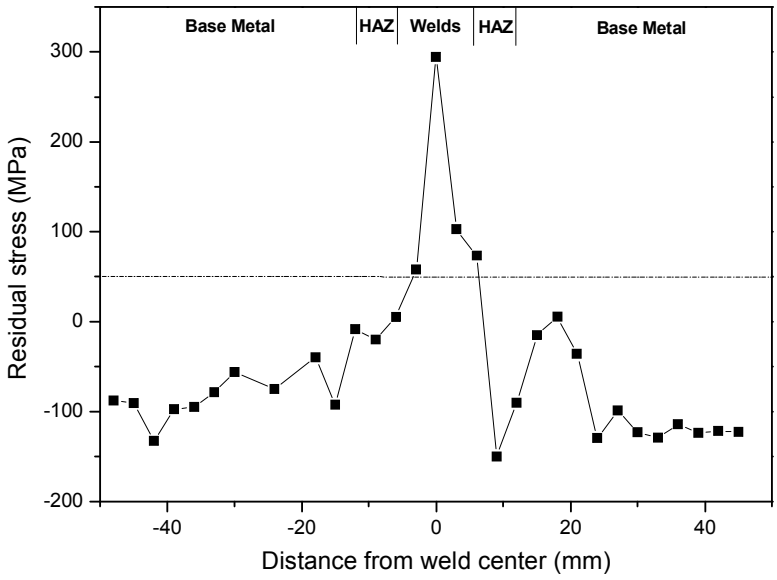

Fig. 3. Residual stress distributions measured from the instrumented indentation technique

The maximum tensile residual stress, about 300MPa, was estimated on the center of weldment, and the minimum compressive residual stress, about -150MPa, was measured on the right heat-affected zone.

The experimental results show good agreement with general tendency of distribution of welding residual stress that maximum tensile stress exists in weld zone and minimum compressive stress exists in heat-affected zone. These results suggest that the instrumented indentation technique is a promising non-destructive residual stress measurement technique, especially weld joints. If additional tests using conventional residual stress measurement methods are performed, it will be good comparison data between each method to measure residual stress.

Summary

Welding residual stresses were evaluated by the instrumented indentation technique based on the key concept that the load differences at the same indentation depth were occurred by residual stress. The modeling of contact morphology and stress decomposition under a rigid indenter can explain the quantitative relation of residual stress and indentation load. To verify the indentation technique, welding residual stresses in the specific welding specimen were evaluated. Good agreement was found between the results of instrumented indentation technique and general tendency of welding residual stress.

References

[1] W.C. Oliver and G.M. Pharr: J. Mater. Res. Vol. 7 (1992), p. 1564

[2] J.-H. Ahn and D, Kwon: J. Mater. Res. Vol. 16 (2001), p. 3170

[3] J.-Y. Kim, K.-W. Lee, J.-S. Lee and D. Kwon: Surf. Coat. Technol. Vol. 201 (2006), p. 4278

[4] J. S. Lee, J. I. Jang, B. W. Lee, Y. Choi, S. G. Lee and D. Kwon: Acta Mater. Vol. 54 (2006), p.1101

[5] Y.-H. Lee and D. Kwon: Scripta Mater. Vol. 49 (2003), p. 459

[6] Y.-H. Lee and D. Kwon: Acta Mater. Vol. 52 (2004), p. 1555

[7] J. Lu, M. R. James and G. Roy, in: *Handbook of Measurement of Residual Stresses*, Fairmont Press, Lilburn (1996)

[8] I. C. Noyan and J. B. Cohen, in: *Residual Stresses*, Springer-Verlag, New York (1987)

[9] Y. Choi, Y.-H. Lee, J.-i. Jang, S.-K. Park, K.-H. Kim, Y.-W. Seo and D. Kwon: Key Eng. Mater. Vol. 297-300 (2005), p. 2122

Key Engineering Materials Vols. 385-387 (2008) pp 893-896
© (2008) Trans Tech Publications, Switzerland
doi:10.4028/www.scientific.net/KEM.385-387.893

Nondestructive Estimation of Fracture Toughness Using Instrumented Indentation Technique

Kyung-Woo Lee[1, a], Hyun-uk Kim[1, b], Sang-Wook Park[2, c], Jung-suk Lee[3, d], Kwang-Ho Kim[4, e] and Dongil Kwon[1,f]

[1]Dept. of Materials Science and Engineering, Seoul National University, Seoul, South Korea

[2]POSCO, Gyeongbuk Pohang, South Korea

[3] Corporate R&D Division, Hyundai·Kia Motors, Gyeonggi-Do, South Korea,

[4]Frontics, Inc., Seoul, South Korea,

[a]case77@snu.ac.kr, [b]easygo03@snu.ac.kr, [d]jslee119@hyundai-motor.com,

[e]khkim@frontics.com, [f]dongilk@snu.ac.kr

Keywords: Fracture toughness, Instrumented Indentation, Mechanical properties, nondestructive

Abstract. This study focused on the determination of fracture toughness by instrumented indentation technique. A theoretical model to estimate the fracture toughness of ductile materials is proposed and used to verify those results. Modeling of IIT to evaluate fracture toughness is based on two main ideas; the energy input up to characteristic fracture initiation point during indentation was correlated with material's resistance to crack initiation and growth, and this characteristic fracture initiation point was determined by concepts of continuum damage mechanics. The estimated fracture toughness values obtained from the indentation technique showed good agreement with those from conventional fracture toughness tests based on CTOD. In addition, we confirmed that the proposed model can be also applied in the brittle material through modification of void volume fraction.

Introduction

Most structural failures generally caused by negligence during design, construction, or operation of the structure. It could bring about safety problems and economical loss. These are related with mechanical properties of materials. So, the evaluation of mechanical properties of structural steels in service and other equipments plays an important role in diagnosing the material degradation under high temperature and pressure. Especially, fracture toughness which represents the resistance to crack propagation is important for life prediction and safety of structures in service and so on. However, conventional standard methods generally require specific specimen geometry and size, usually complex shape to make, which are single-edge notched beam sample for 3-point bending or compact-tension for tensile loading. In addition, the complex test process including fatigue pre-cracking and crack length measurement were not easy to control for accurate estimation. Excepting above difficulties about fracture toughness evaluation methods, the conventional fracture toughness evaluation methods cannot be directly applied to industrial structures and equipments in service due to the fact that they are destructive methods.

To overcome those problems, we present the non-destructive method to evaluate the fracture toughness by using instrumented indentation technique [1]. The concept of a critical void volume fraction was adopted to identify a characteristic fracture initiation point during the indentation process. Fracture toughness from this model using only indentation data compared well with those from standard fracture toughness tests.

Theoretical model for estimating fracture toughness

The relation of the fracture energy, w_f and plane-strain fracture toughness, K_{JC} is expressed as following:

$$K_{JC} = \sqrt{2Ew_f} \tag{1}$$

where E is the elastic modulus. To estimate K_{JC} on the basis of Eq.(1) by using the indentation technique, w_f must be determined using only indentation parameters. Triaxiality ahead of the indenter tip is in the range 2~3, and the degree of constraint in the deformed indentation region is similar to that ahead of the crack tip [2~4]. Hence the indentation energy per unit contact area to the characteristic point can be related to w_f if there exists a characteristic fracture initiation point during or over the indentation process. This energy, henceforth called the critical indentation energy, is calculated from the indentation load-depth curve:

$$2w_f = \lim_{h \to h^*} \int_0^h \frac{4P}{\pi d^2} dh \tag{2}$$

where P is the applied load, h is the indentation depth, d is the chordal diameter of the impression and h^* is the critical indentation depth corresponding to the characteristic fracture initiation point. $2w_f$ indicates the formation of two crack surfaces.

Since there are no distinguishing marks that can be used to identify fractures occurring during indentation, h^* in Eq. (2) cannot be measured by direct methods (optical microscope or SEM observation). Thus to determine h^*, continuum damage mechanics (CDM) was applied to the indentation process. CDM is used mainly to predict failure in structures loaded statically and dynamically. According to Lemaitre's strain equivalence principle [5], damage variable D can be represented as following:

$$E_{eff} = E(1-D) \tag{3}$$

where E_{eff} is the effective elastic modulus of the damaged material and E is the elastic modulus of the initial non-damaged material. E_{eff} decreases as h increases due to the increase in damage beneath the indenter [1]. In addition, E_{eff} is represented by a function comprised only of indentation parameters [6]:

$$E_r = \frac{\sqrt{\pi}}{2} \cdot \frac{S}{\sqrt{A_c}} \quad \text{and} \quad E_{eff} = \frac{1-\nu^2}{E_r} + \frac{1-\nu_i^2}{E_i} \tag{4) and (5}$$

where E_r is the reduced modulus, A_C is the contact area and S is the unloading slope. The υ and υ_i are the passion ratio of material and indenter, respectively. From multiple loading-unloading, the values of E_{eff} for various indentation depths can be calculated from each unloading and E_{eff} vs. h may be plotted as in Fig. 1. If critical value of the elastic modulus is determined, h^* can be determined from the corresponding value of h. Since the indentation load is compressive in terms of the loading axis, the deformed region beneath the indenter experiences compressive stress. Hence, voids will be nucleated by localized shear due to compressive stress, and the void volume fraction, f will increase as h increases [7]. The D can be represented in terms of f as [5]:

$$D = \frac{\pi}{(1.3\pi)^{2/3}} f^{2/3} \tag{6}$$

From previous experimental and computational researches [8, 9], the void volume fraction, f of two types is proved; the values $f_C = 0.15$ (void volume fraction at onset of coalescence) and $f_F = 0.25$ (void

volume fraction at initiation of stable crack growth). The concept of critical void volume fraction was adopted to determine the critical value of the elastic modulus. Critical CTOD (crack tip opening displacement) are classified as δ_C, δ_U and δ_m, but ductile structural materials generally have δ_U and δ_m [10]. Since δ_U-type materials are brittle and have poor resistance to strain localization between voids compared to δ_m materials, they experience abrupt loss of load-carrying capacity soon after void coalescence begins. On the other hand, δ_m-type materials retain load-carrying capacity even after the onset of void coalescence, showing gradual loss of this capacity at the initiation of stable crack growth. With these phenomena in mind, f_C is used as the fracture criterion for δ_U-type materials and f_F is used for δ_m-type materials. The f_C and f_F can be converted into corresponding damage variables D_C and D_F through Eq. (6); then corresponding values of E_C and E_F are calculated by Eq. (4) and (5). Therefore, h^* is determined as the corresponding h by using critical value of elastic modulus, $E^* = E_C$ for δ_m-type materials and $E^* = E_F$ for δ_U-type materials.

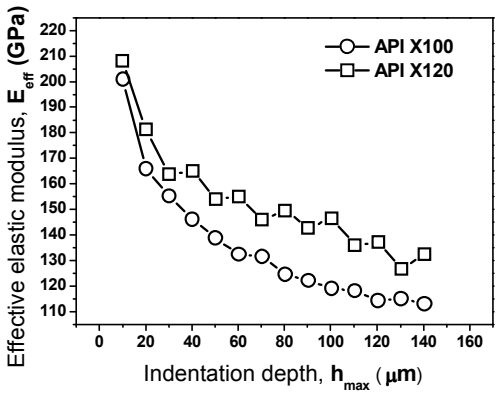

Figure. 1. Decreasing elastic modulus with indentation depth of API steels.

Experiments

To verify this critical indentation energy model, fracture toughness tests and indentation tests were performed for API X100 and 120 (ductile materials), which have been newly developed as pipeline steels, and four Ti-alloys as brittle materials. CTOD tests were performed according to ASTM E1290 [10]. Indentation tests were performed under displacement-controlled conditions: the maximum indentation depth was 150 μm and multiple loading-unloading cycles were applied at 10 μm intervals using a 500 μm diameter ball indenter with $\nu_i = 0.07$ and $E_i = 600$ GPa. The loading and unloading rates were both 0.1 mm/min.

Results and discussions

Table 1 lists the fracture toughness values, K_{JC} from the indentation technique and that from CTOD tests for API X100 and 120. They are showed good agreement the results between the indentation technique and the CTOD test.

Table 1 Fracture toughness of API X100 and X120

Material	K_{JC}_Indentation (MPam$^{0.5}$)	K_{JC}_CTOD (MPam$^{0.5}$)
API X100	286.5 ± 12.7	257.9 ± 33.7
API X120	292.9 ± 13.8	277.6 ± 40.3

As above mentioned, the fracture type of materials by CTOD test is distinguished as three types: δ_m, δ_u and δ_c type. Except for δc-type materials, physical meaning of void volume fraction to calculate damage variables was already explained. The void volume fraction for δc-type materials can be

calculated through the reverse operated method based on current modeling, if K_{JC} measured from CTOD tests were assumed the true values for materials. For four Ti-alloys for representing δc-type materials, void volume fraction values calculated by reverse method were illustrated in Fig.2. Range of void volume fraction 0.04~0.06 were acceptable for δc-type materials. As the results, void volume fraction value 0.05 could be reasonable for δc-type materials even though physical meaning was not found theoretically. The results of indentation fracture toughness using this assumption is illustrated in Fig. (3), and showed also good agreement compared with K_{JC} obtained from CTOD tests.

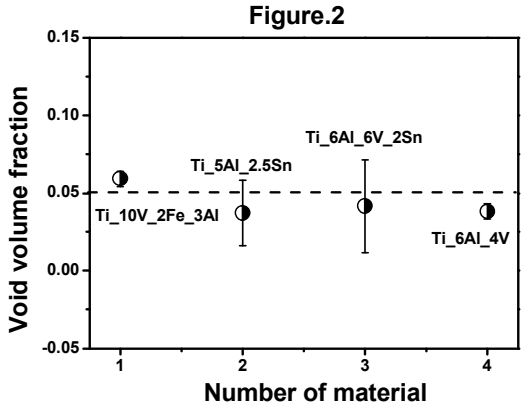

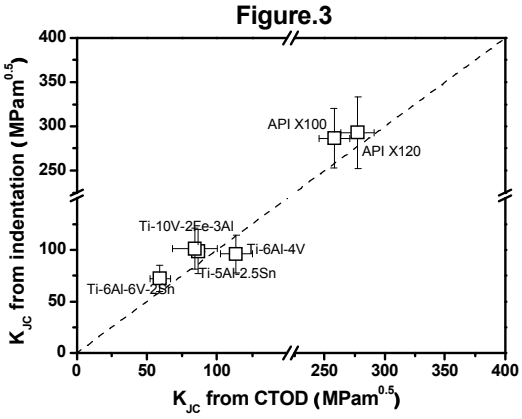

Figure.2. Void volume fraction for dc-type materials.
Figure.3. Comparison of KJC between indentation and CTOD.

Summary

A nondestructive method for evaluating fracture toughness using indentation technique is presented. The concept of critical void volume fraction was introduced to identify a characteristic fracture initiation point. By taking into account the decrease in elastic modulus due to internal damage during the indentation process based on damage mechanics, the criteria were established. To verify the model, indentation and CTOD tests were performed for six materials. The test results show good agreement between KJC from the indentation model and KJC from CTOD test, boding well for practical use of the model in the future.

References

[1] J.-S. Lee, J.-i. Jang, B.-W. Lee, Y. Choi, S.-G. Lee, and D. Kwon: Acta Mater., Vol. 54 (2006), p.1101

[2] Francis, HA: J. Engng. Mater. Tech., Vol 98 (1976), pp 272

[3] Murty, KL, Mathew, MD, Wang, Y, Shah, VN, and Haggag, FM: Int. J. Press. Ves. Piping, Vol 75 (1998), pp 831

[4] Byun, TS, Kim, SH, Lee, BS, Kim, IS, and Hong, JH: J. Nucl. Mater., Vol 277 (2000), pp 263

[5] Lemaitre, J: J. Engng. Mater. Tech., Vol 107 (1985), pp 83

[6] Oliver, WC, and Pharr, GM: J. Mater. Res., Vol 7 (1992), pp 1564.

[7] Fougere, GE, Riester, L, Ferber, M, Weertman, JR, and Siegel RW: Mater. Sci. Engng. A, Vol 204 (1995), pp 1

[8] Brown, LM, and Embury, JD: Proc. 3rd Int. Conf. Strength of Metals and Alloy, Vol 1 (1973), pp 164

[9] Goods, SH, and Brown, LM: Acta Metall., Vol 27 (1979), pp 1

[10] ASTM Standard E1290: Standard Test Method for Plane-Strain Fracture Toughness of Metallic Materials, (1993)

3-Dimensional Plural Cracks 761
3D Mixed-Mode Fracture 741
3D VCCT 713
6005 Al Alloy 721
ΔK_{IIIth} 449
ΔK_{IIth} 449

A

AA6016/FeP06 805
Accumulating 37
Accumulative Damage Model 97
Adhesion Strength 613
Adhesive Postinstalled Method 77
Admixture 605
Aerospace 5
Aging 481, 493
Air Drilling 809
Al 5052 Alloy 725
Al-Li 849
Alignment 789
Alloy 617 693
Alloy 783 501
Aluminium Panel 141
Aluminum Alloy 397, 417, 565, 797
Aluminum Reinforcement 785
Amido 497
Analysis of Variance (ANOVA) 285
Analytical Trial Function Method (ATFM) 617
Anisotropy 193
Annealing 725
Anti-Corrosion 613
Anti-Fatigue Design 109
Anti-Loosening 249
Artificial Neural Network (ANN) 533
Asphalt 481
Asphalt Binders 753
Asphalt Concrete 297, 301
Asphalt Pavement 597
Asphalt-Stone Adhesion 473
Assessment Method 109
Austenitic Heat Resistant Steel 425
Austenitic Stainless Steel 505
Austenitic Steel 49
Autogenous Shrinkage 629
Average Penetration Depth 681
Axial Loading 185

B

Ball Shear Impact Test 429, 745
Ballistic Range 129
Barkhausen Noise 357
BCC Iron 453
Bearing Resistance 25
Bearing Steel 449
BEM 573
Bend Angle 833
Bending 37
Bending Tensile Stress 513
Bi-Material 217
Bi-Material Notch 409
Biaxiality 545
Biaxiality Ratios 193
Bifurcation 53
Bilinear SDF System 437
Bimaterial Interface 125, 541
Biomaterial 637
Blade 393
Blast Furnace Slag 625
Body Force Method 793
Bogie Frame 645
Bottom Hole Assemblies 809
Boundary Element Method (BEM) 881
Brake Hose 169
Brittle Fracture 1, 9
Buckle 173
Buckling 377, 609
Buckling Failure 257
Bushing Bearing 237

C

$Ca(OH)_2$ 625
CAMT 293
Carbon Fiber Reinforced Polymer/Plastic (CFRP) 241
Carbon Material 533
Carbon/Carbon Composite 537
Carbonation 281, 625, 633
Cathodic Protection Method 665
Cavity 53

Cement 605
Cement Loop Damage 61
Cement Matrix 445
Cement Mortar 337
Ceramic Matrix Composite (CMC) 689
CFRP Strip 165
CFS 861
Chaos Synchronization 309
Chip Size Package 433
Chloride 661
Chloride Diffusivity 281
Chloride Ion 677
Chloride Penetration 765
Circular Hole 105
Cleavage 225
Cleavage Fracture 773
Coaxing Effect 505
COD 293
Coefficient of Seepage 681
Coffin-Manson's Relation 433
Cohesive Crack 81
Cold Region 597
Collision Analysis 153
Compliance 293
Composite 85, 141, 365
Composite Crack 105
Composite Fatigue 545
Composite Frame Column 145, 149
Composite Material 785, 885
Compression Test 205
Compressive Deformation 177
Compressive Residual Stress 829
Compressor Blade 401
Computational Fracture Analysis 741
Concrete 21, 69, 73, 233, 661, 789
Concrete Box Girder 825
Concrete Bridge 597
Concrete Repair Material 677
Concrete Strength 77
Condition Index 845
Conductive 753
Conductive Asphalt-Based Composite 469
Connection 709
Constitutive Relation 873
Contact Explosion 45
Contact Fatigue 57
Continuum Damage Mechanics 277
Controlled Cooling 509
Controlled Rolling 509
Corner Singularity 125
Corrosion 385, 393, 621, 657, 769, 777, 845
Crack 201, 273, 349, 353, 661, 769, 837
Crack Analysis 881
Crack Arrest 245
Crack Closure 369
Crack Growth 5
Crack Growth Rate 293
Crack Initiation 113, 161, 197, 397
Crack Kinking 9
Crack Localization 245
Crack Permeability 569
Crack Problem 793
Crack Propagation 89, 113, 161, 197, 337, 397, 453
Crack Propagation Behavior 297, 301
Crack Propagation Criterion 233
Crack Restart 245
Crack Tip 101, 585
Crack Width 93
Crack/Notch Problem 617
Cracked Beam 465
Crash Test 685
Creep 393
Creep Curve 693, 705
Creep-Plasticity Interaction 853
Creep Property 425
Critical Blasting Charge 45
Critical Damage 45
Critical Deformation 45
Critical Plane 209
Crumb Rubber 489
Crystal Plasticity 801
CT 297, 301
CT Scan 69
Cu-Nl Alloy 385
Cumulative Damage Model 165
Cumulative Dissipated Hysteretic Energy 145
Curing Temperature 141
Curve Steel 865
Cyclic Stress-Strain Curve 581

D

Damage 81, 201, 673
Damage Analysis 97
Damage Coupling 137
Damage Detection 561, 885
Damage Evaluation 589
Damage Identification 313, 877
Damage Index 145
Damage Mechanics 361, 821
Damage Variable 373
Darcy's Law 681
Debonded Length 61
Deflection 845
DEFORM 41
Deformation-Induced Transformation 509
Delamination 253, 609
Deterioration 37
Differential Governing Equation 521
Diffusion 661
Diffusion Coefficient 677
Digital Correlation Method 361
Digital Image Correlation (DIC) 369
Directionality 889
Displacement Mode of Scattering Wave for Far Field 157
Distribution of Displacement Field 61
Distribution of Stress 61
DLC 829
DMA 33
Double-Notch 417
Ductile Fracture 757
Ductile-to-Brittle Transition 773
Ductility 445, 697
Dugdale Model 641
Durability 621, 769
Durability Design 657, 677
Dynamic Balance Equation 373
Dynamic Brittle Fracture 245
Dynamic Failure 685
Dynamic Formation 53
Dynamic Fracture 45
Dynamic Growing 101
Dynamic Mechanical Analysis 473
Dynamic Shear Rheology 481
Dynamic Stability Map 465
Dynamic Stress Concentration Factor (DSCF) 389
Dynamic Stress Intensity Factor (DSIF) 105, 217, 273, 389
Dynamic Tensile Properties 873
Dynamic Tension Stress Test 473

E

Eco-Material for Erosion Control of Slope 461
Edge Dislocation 457
Effective Fatigue Threshold 49
Eigen-Equation 217
Eigenanalysis 573
Eigenstrain 517
Elastic Modulus 333
Elastic Modulus Decrease 325
Elastic-Plastic Deformation 5
Elastic-Plastic Model 413
Elastic-Plastic Torque 869
Elastic-Viscoplastic Material 321
Elasticity 513
Elastodynamic 577
Elbow 833
Electrochemical Testing 121
Electromechanical Admittance 561
Elevated Temperature 161
Embedded Crack 773
Energetic Balance 81
Energy Release Rate 253
Environmental Factor 33
Epoxy 225, 417
Epoxy Matrix 421
Equal Channel Angular Processing 721, 725
Eshelby Equivalent Inclusion Theory 329
Eutectoid Steel 829
Expansion 289, 305
Expansive Deformation 305
Experiment 201, 245, 345, 545
Experimental Stress Analysis 193
Expert System 189
Explanation Mechanism 189
Exterior Connection 865
Extreme Value 561
Extrinsic Toughening 49

F

Failure 353, 769
Failure Analysis 29
Failure Elongation 749

Failure Evolution 361
Failure Mechanism 265
Failure Mode 261, 269
Failure Pattern 149
Fatigue 5, 113, 161, 197, 241, 393, 397, 505, 593, 845, 849
Fatigue Analysis 413
Fatigue Behaviour 485, 537
Fatigue Crack 317, 557, 601
Fatigue Crack Behaviour 849
Fatigue Crack Growth 761
Fatigue Crack Propagation 529
Fatigue Damage Parameter 649
Fatigue Life 109, 221, 285
Fatigue Life Curve 581
Fatigue Life Prediction 649
Fatigue Limit 645
Fatigue Load 325
Fatigue Mechanism 537
Fatigue Property 469, 553, 829
Fatigue Resistance 133
Fatigue Test 549, 649
Fatigue Threshold 49
Faulty Assembly 29
FCC Crystal 801
Fe_2Si Steel 1
Fiber Composite 421
Fiber Reinforced Composite 337
Fiber Reinforcement 289
Fibrous Composite Model 61
Finite Difference Method (FDM) 869
Finite Element (FE) 525, 617
Finite Element (FE) Simulation 501, 757
Finite Element Analysis (FEA) 17, 253, 265, 417, 649, 653, 685, 841
Finite Element Model (FEM) 37, 117, 169, 217, 277, 369, 401, 413, 465, 513, 541, 561, 645, 713, 813, 821
Fire-Resistance 717
Fish-Eye 185
Fitness for Service 173
Flat Plate 857, 865
Flexibility 813
Flexural Fatigue 673
Flexural Rigidity 165
Flexural Strength 337
Flow Instability 501
Flow Stress 89
Flywheel Governor 309
Focused Ion Beam (FIB) 1
Forecast 533
FOSM 621
Fractal Dimension 461
Fractography 1
Fracture 69, 73, 401, 429, 489, 745, 801
Fracture Behaviour 177, 457
Fracture Energy 93
Fracture Failure 65
Fracture Flow 137
Fracture Mechanic 13, 189, 193, 525, 569, 617, 769, 869, 881
Fracture Parameter 713
Fracture Toughness 89, 293, 893
Frame Column 97
Free Edge Delamination 821
Freight Car 653
Fretting Fatigue 401, 565
Friction Stir Welding (FSW) 797, 849
Full Scale Panel 549
Functionally Graded Material (FGM) 881
Fuzzy Optimization 285

G

Garofalo Model 705
Gauss-Chebyshev Quadrature Formula 793
Gear 345, 601
General Singular Stress Concentrator 125
Generalized Stress Intensity Factor 409
Glass Fiber 545
Glass/ED6 Composite 329
Grain Size 113, 197
Green's Function 105, 157, 273, 389
Ground Motion 437
Guided Wave 729
Gurson's Constitutive Equation 757

H

Half-Cell Potential 665
Hardening 805
Hardening-Softening Curves 581

Hardness 797
Heat Treatment 357, 721
Hiearchical Analysis 837
High Arch Dam 269
High Cycle Fatigue 185
High Performance 781
High-Performance Cement Paste 629
High-Strength 789
High Strength Concrete 717
High Temperature 777
High Temperature Deformation 501
High Temperature Gas Cooled Reactor (HTGR) 693
Hopf Bifurcation 309
Hopkinson Press Bar 21
Hose Life 169
Hot Spot 669
Humidity 113, 197, 397
Hybrid Layered Composites 485
Hybrid Optimization 877
Hydration 605, 633, 661
Hydro-Mechanical Coupling 137
Hypersingular Integral Equation 793
Hypervelocity Impact 129, 201

I

iBone 813
IIT 889
Image Correlation 341
Impact Loading 485
Impact Property 429, 745
Impact Ratio 29
Impact Testing 133
Impedance Analysis 729
Impregnation 205
In-Plane/Out-of-Plane Limit Moment 833
Inclined Crack 541
Incompressibility 53
Inconel 738LC 581
Indirect Tensile Strength 469
Inelastic Displacement 437
Inference Engine 189
Infrared Thermography 669, 689
Instrumented Indentation 893
Instrumented Indentation Technique 889
Integral Structure 529
Interacting Crack and Circular Cavity near the Surface 389
Interaction of Circular Cavity and Crack 157
Interface 9
Interface Crack 585
Interface Element 277, 821
Intermediate Strain Rate 749
Inverse Analysis 781
Inverse Problem 877
Irregular Loading 209
Isochronous Stress-Strain Curve 705
Iterative Algorithm 793

J

J-Integral 569

K

KBW Model 853
Knoop 889
Knotted Fiber 421
Kolsky Bars (SHPB) 245

L

Laminate Theory 253
Laminated Composite 377
Lapped Splice 349
Lattice Model 73
Lattice Orientation 453
Layer-Wise 277
Layered Hybrid Fiber Reinforced Concrete (LHFRC) 673
Layered Steel Fiber Reinforced Concrete (LSFRC) 673
LCC 845
Lead-Free Solder 429, 433, 745
Life Prediction 405
Lifetime Safety Factor Method 657
Light Weight Collision Safety Device 685
Lightweight Aggregate Concrete (LWAC) 817
Limit Load Analysis 833
Limit Pressure 833
Linear Damage Rule 209
Linear Friction Welding 517
Lining Structure 273
Load Test 645
Loading Rate 301
Lock-In Thermography 485
Low Cycle Fatigue 581, 721, 725

Low Cycle Fatigue Damage 17
Low Cyclic Reversed Loading Test 97
Low Electrical Resistance Measurement 589
Low-Temperature Performance 493

M

Machine Element 249
Magnesium Alloy 129
Maraging Steel 113, 161, 197
Marine Environment 385
Martensitic Transformation (MT) 505
Matched Asymptotic Expansion 541
Matched Asymptotics 9
Material 297
Material Compound 805
Mathematical Model 345
Maximum Green-Lagrange Strain 649
Maximum Likelihood Estimation 241
Maximum Tensile Stress 513
McEvily Method 641
Mechanical Model 213
Mechanical Property 441, 637, 785, 893
Mechanical Stress 357
Meshfree Method 333
Meta Kaolin 717
Metal 589
Metal Matrix Composite (MMC) 517
Metal Spray 613, 665
Metal Welded Bellows 813
Metallic Material 657
Micro-Arc Oxidation (MAO) 777
Micro-Surfacing 489
Microbiological Influenced Corrosion (MIC) 385
Microcracking 445
Microemulsion 497
Micromechanics 137, 221, 445
Microstructural Characterization 689
Microstructure 701, 797
Minimum Creep Rate 693
Mix-Mode Condition 761
Mixed Damage Model 137
Mixed-Mode Crack-Tip under Compression and Shear 321
Mixed Mode I-II Fracture 233
Mixed Mode Loading 245, 757
Mode Switching Algorithm 729
Modeling 253
Modified 497
Modified Virtual Crack Closure Integral Method 741
Moduli Prediction 329
Molecular Dynamic Simulation 453
Molecular Dynamics (MD) 457
Moment 845
Monkman-Grant (M-G) Strain 693
Morphological Evolution 221
Mortar 633
Mud Drilling 809
Muffler Tube 841
Multi-Components Hydration Model 629
Multi-Wall 201
Multiaxial Fatigue 209

N

Natural Frequency 877
Neural Network (NN) 877
Neutron Diffraction 517
Ni-Cr-Mo Steel 185
Ni-Ti Thin Films 89
Nickel-Based Super Alloy 221
Nitrogen Effect 425
Non-Circular Cutout 365
Non-Conservative System 577
Non-Contact 349
Non-Equilibrium Grain-Boundary Segregation Kinetics 65
Non-Linear Behavior 709
Non-Local Model 81
Non-Propagating Crack 641
Nonconservative Force 465
Nondestructive 893
Nonlinear 577
Nonlinear Least Square Fitting (NLSF) 693, 705
Normal Load 565
Notch Effect 241, 641
Notched Cross-Section Bar 869
Notched Part 553
Numerical Analysis 345, 373, 733
Numerical Calculation 409
Numerical Model 57
Numerical Simulation 233, 629

O

Oblique Crack 733

Opening 861
Optical Measurement 361
Optimum Vector Method 261
Orientation-Dependent Failure Criterion 801
Orthogonal Array 717
Orthotropic 585

P

Parametric Resonance 809
Paris Law 557
Particle Size Effect 289
Pasternak Soil 465
Patch 377
Perforated Plate 365, 377
Permalloy 357
pH Value 605, 625
Phase Characterization 121
Phenomenological Approach 137
Piezoelectric Patch 561
Pipeline 173
Plane-Strain Fracture Toughness 21
Plastic Working 249, 553
Plastic Zone Size 641
Plastic Zone's Correction 341
Plate Assemblies 13
Plate Holder 841
Poincaré Map 309
Polymer 817
Polymethylmethacrylate (PMMA) 245
Polysiloxane 497
Polystyrene 353
Polyurethane Foam 205
Pore Volume-Size Distribution 461
Porosity 281
Post-Buckling 253
Pozzolanic Behavior 289
Pre-Stressed Glass-Epoxy Composite 733
Precast Concrete 349, 353
Precipitation 425
Press Working 249
Pressurized Thermal Shock (PTS) 773
Prestrain 421
Prestressed CFRP 41
Prevailing Torque 249
Processing Map 501
Product Lifecycle Management (PLM) 109
PT Flat Plate 709
Pulsating Fatigue 553
Punch Radius 841
Punching Shear 857, 865
Pushover 709
PVA Fiber Reinforced Cementitious Composites 697
PVD Coating 57
PZT Sensor 729

Q

Quantitative Analysis 625
Quasi-Static Propagating 321
Quasi-Variational Principle 577

R

Railway Application 653
Railway Brake Disc 669
Rain-Flow Cycle Counting 209
Range of Pore-Size 461
Rationale 77
RC Crane Girder 165
RC Frame Structure 313
RC Structure 769
Reaction-Diffusion Model 813
Reactor Pressure Vessel (RPV) 773
Recessing 225
Reciprocal Theorem 541
Recycled Aggregate Concrete (RAC) 381, 521
Reduced Web Connection 265
Regression Analysis 437
Rehabilitation 697
Reinforced Concrete Beam 41
Relative Displacement 565
Reliability 621
Reliability-Based Structural Optimization 261
Reliability Calculating of System Overall Instability 257
Remodeling 861
Repair 141, 377, 697
Residual Force Vector Method 313
Residual Resistance 257
Residual Strain 413
Residual Strength 325, 485
Residual Stress 25, 57, 413, 517, 529, 593, 797, 889
Residual Thermal Stress 573
Resonance 733

Retrofit Method 861
Reversion Austenite 113, 197
Rheological Properties 753
Rim Stress 117
Rim Thickness 117
Ring-Opening 497
Risk Analysis 269
Riveted Joints 25
Road Accident 153
Rolling Reduction 805
Rotating Bending 185
Rubber Engine Mount 649
Rubber Particle 817

S

S-N Curve 593
S-Version FEM 761
Salt Ingredient 181
Sample Size 285
Sand Heap Analogy Method 869
Scaling Law 609
Scarf Joint 17
Scattering of SH-Wave 157, 273
Sealing Performance 169
Seawater 181
Section Modulus 257
Seismic Damage Model 145
Self-Stress 305
Semi-Infinite Piezoelectric Medium 389
Sensitivity Analysis 825
Service Life 237, 281
Service Life Design 181
SH-Wave Scattering 105
Shallow Shell Assemblies 13
Shape Memory Alloy Actuator 213, 421
Shear 845
Shear Clearance 841
Shear Deformable 13
Shear-Lip Fracture 757
Shear Mechanism 149
Shear-Mode Fatigue Crack 449
Shear Reinforcement 857, 865
Shear Strength 149
Shear Wall 861
Shrinkage Performance 817
SHS/PHIP Method 177
SHTB 361
Silica Fume 701
Similitude 609
Simulation Model 805
Sines Criterion 549
Single Crystal 1
Single Lap Joint 417
Single-Side 141
Single-Variable 713
Slip Markings 581
Slip System 853
Slurry Coating 133
SM 490 A 593
SMA 493
Small Crack 449
Small Fatigue Cracks 797
Sn-0.75mass%Cu 745
Sn-3mass%Ag-0.5mass%Cu 429
Sn-9mass%Zn 429
Sn-Ag-Cu 433
Softening 69, 73
Soil 461
Solid Oxide Fuel Cell (SOFC) 441
Solidification Age 381
Spalling 717
Spark Plasma Sintering (SPS) 637
Specific Sustained Crushing Stress 85
Sphere 53
Spiral 37
Spur Gear 57, 117
Squeeze Cast 397
SRC Frame Structure 373
Stability 261
Stacking Fault 457
State Function 269
Static Behavior 485
Statistical Tests 285
Steel 225
Steel 2.25Cr1Mo 509
Steel Fiber 305, 781, 789
Steel Frame 525
Steel Frame Connection 265
Steel Plate 861
Steel Reinforced Concrete (SRC) 93
Steel Reinforced High Strength and High Performance Concrete (SRHSHPC) 97, 145, 149
Steel Sheet 749
Stiffened Box 85
Stiffened Fuselage 837
Stiffness Connectivity Vector 313
Stiffness Reliability Index 325

Stochastic Finite Element Method 325
Stochastic Structure System 261
Strain 381
Strain Localization 581
Strain-Rate 21
Strain Rate Hardening 873
Strength 381, 521
Stress 365, 381, 521
Stress Analysis 169, 645
Stress Concentration 641
Stress Distribution 225, 417
Stress Field 585
Stress Intensity Factor (SIF) 193, 341, 401, 525, 837, 881
Stress Singularity 573, 617, 869
Stress Singularity Exponent 125
Stress Transfer 421
Structural Health Monitoring (SHM) 341, 885
Structural Steel 553
Structural Strength 653
Sub-Region Accelerated Müller Method 617
Substructure 837
Sulfide Stress Corrosion Cracking (SSCC) 121
Supporting Condition 109
Surface Chloride Content 181, 765
Surface Finish 633
Surface Roughness (SR) 613
Surface Treatment System 765
Sustainable Steel Structure 657

T

Tangential Load 565
Temperature Field 413, 825
Temperature-Sensitivity 473
Temperature Stress 597
Tensile 489
Tensile Fatigue Life 533
Tensile Softening 781
Tensile Test 73, 205
Tension 69
Tension Bolt 685
Tension Stiffening 93
Testing Techniques 293
Thermal Barrier Coating (TBC) 405
Thermal Effect 825
Thermal Fatigue 405
Thermal Fatigue Life 433
Thermal Parameters 825
Thermo-Mechanical Couple 33
Thermoelastic Stress Analysis 849
Thermopiezoelectric Ceramics 569
Thin Structure 317
Thin-Walled Tube 249
Three-Dimensional Joint 573
Three Point Bend Test 205
Three-Point Bending 493
Threshold Values 557
Ti_3AlC_2 Ceramics 177
TiAl 5
TiCp/Ti Composite 873
Tilting Train 33
Timoshenko Beam 465
Titanium (Ti) 777
Titanium Powder 637
Tooth Root Stress 117
Torsion Actuator 213
Torsional Fatigue Test 449
Tortuosity 281
Triaxiality Function 17
Tribology 237
Truss Model of Concrete 149
Tubular Specimen 713
Twin 1
Type 316LN Stainless Steel 705

U

Ultra Fine Grained Material 721
Ultra High Performance 701
Ultrafine Grained 725
Ultraviolet 481
Unified Closure Model 49
Unsaturated Porous Medium 137
Unterface Transition Zone (ITZ) 817
UTM 33

V

V-Notch 217
Valve 29
Vertex Singularity 125, 317
Vibration 601
Visco-Elastic Compressible Material 101
Visco-Elastic Model 329
Viscoplasticity 853
Viscosity Effect 321
Void 757

Volume Fraction 781

W

Wall-Thinning 833
Waste Glass 289
Water Penetration of Mortar 681
Wavelet Signal Analysis 601
Wear of Materials 237
Web Opening 265
Web Stress 117
Web Thickness 117
Weibull Stress 773
Weld Joint 593
Wire 861
Woodfibres 445
Woven Fabric Composite 333
Wrinkle 173

X

X-FEM 245

Y

Young's Modulus 405

Z

Zirconia 441

A

Abdel Wahab, M.M. 17
Aberšek, B. 345
Adachi, M. 397
Adachi, T. 441
Adden, S. 545
Agrianidis, P. 785
Akita, M. 505
Aliabadi, M.H. 13, 333, 885
Alidoust, O. 289, 337
An, H. 257, 325
An, W.G. 257, 325
Anghel, V. 485
Anthymidis, K.G. 133, 785
Apicella, A. 549, 885
Araki, W. 441
Armentani, E. 549
Arson, C. 137
Ashcroft, I.A. 17
Avila, J.A. 229

B

Bae, M.S. 437
Baik, Y.S. 865
Baiz, P.M. 13
Bao, C. 293
Baragetti, S. 57
Beck, S.W. 865
Belsak, A. 601
Buchholz, F.G. 741
Buciumeanu, M. 565

C

Cai, L.X. 293
Calabrese, A. 237
Camas-Peña, D. 369
Cao, L.J. 877
Cao, T.W. 473
Caputo, F. 25, 153
Carabineanu, A. 733
Cascini, L. 657
Cavaliere, P. 849
Cazes, F. 81
Cen, S. 617, 869
Ceschini, L. 517
Cha, J.H. 721, 725
Chang, S.H. 645
Chang, Y.S. 833
Chang, Y.X. 309
Chen, H.B. 509
Chen, H.Y. 713, 853
Chen, S.Y. 361
Chen, X.M. 361
Chen, Z. 489
Chen, Z.T. 269
Cheung, M.M.S. 845
Chi, R.Q. 201
Chlupová, A. 581
Cho, H.H. 721, 725
Choi, C.S. 857, 861, 865
Choi, H.K. 857, 861, 865
Choi, M.J. 889
Choi, S.S. 501
Choi, W.M. 685
Choi, Y.C. 861
Choi, Y.H. 833
Chu, Y.D. 309
Chung, H.D. 833
Chung, Y.H. 425
Combescure, A. 81, 245
Constantin, N. 485
Constantinescu, D.M. 205
Coret, M. 81
Craciun, E.M. 733
Crocker, A.G. 1
Crocombe, A.D. 17
Cui, N.G. 201
Cui, S.Q. 41, 77

D

David, C. 133, 785
Ding, L. 525
Ding, X.Z. 329
Dini, D. 5
Dodds Jr., R.H. 773
Dong, S.L. 389
Dong, W. 233
Dong, X.M. 121

E

Eichlseder, W. 805
Eifler, D. 797
Endo, M. 449, 637, 641, 797
Eryürek, B. 29

F

Fan, T. 577
Fan, X.C. 673
Feng, C. 101
Flasker, J. 601
Flašker, J. 345
Flewitt, P.E.J. 1
Fu, X.R. 617, 837, 869

G

Gao, X.W. 881
Gao, Y. 453, 457
Gao, Z.H. 853
Gao, Z.Q. 533, 537
Gatmiri, B. 137
Găvan, M. 485
Ghasemnejad, H. 85
Gheni, M. 813
Göksenli, A. 29
González-Herrera, A. 369
Goo, B.C. 593, 669
Gravouil, A. 81
Grégoire, D. 245
Grimaldi, A. 153
Guan, G.S. 201
Guo, Y.F. 221
Guo, Y.M. 589
Gutensohn, M. 797

H

Ha, S.S. 349
Hadavinia, H. 85
Haghi, A.K. 289, 337, 393
Han, K.T. 841
Han, M.H. 665
Han, S.H. 621
Han, S.W. 437, 709
Harada, M. 357
Hasan, W. 465
Hattori, N. 553, 829
Häusler, S.M. 529
He, H.N. 305
Hendra, 513
Higo, S. 37
Hilmy, I. 17
Hong, D.P. 729
Hong, J.K. 501
Hong, K.N. 781
Hong, Y. 729
Horníková, J. 49
Horst, P. 529, 545
Hosseini-Toudeshky, H. 141, 277, 821
Hou, P.J. 165
Hu, Z.L. 461
Huang, C.K. 305
Huang, J.F. 753
Huang, S.Q. 497
Huh, H. 685, 749
Hur, S. 649
Hutař, P. 125, 317, 557
Huynh, N.N. 801
Hwang, S.H. 729
Hwang, Y.E. 33

I

Ikeda, S. 641
Ishikawa, H. 429
Iwamoto, T. 161

J

Jafari, M. 365
Jalalvand, M. 821
Jeon, C.S. 645
Jiang, F. 873
Jiang, X.G. 617, 837, 869
Jiang, Y.B. 381
Jiang, Z.Z. 297, 301
Jin, D. 209
Jin, E.S. 857
Jin, H.B. 709
Jin, J.H. 613
Jin, L. 265, 293
Jin, M. 421
Jin, Y.J. 841
Ju, J.S. 617, 837, 869
Jun, T.S. 517
Jung, E.J. 501
Jung, I.H. 693, 705
Jung, J.W. 505

Jung, W.S. 425

K

Kanemaru, T. 197
Kang, I.G. 889
Kang, I.S. 353
Kang, S.T. 697, 701, 781, 789
Katsuki, K. 797
Kawagoishi, N. 113, 161, 197, 397
Kawahara, H. 169
Kawakami, Y. 637
Kawano, T. 433
Kermanpur, A. 401
Kikuchi, M. 757, 761, 813
Kim, H.U. 893
Kim, J.B. 437
Kim, J.G. 645, 653, 669, 689
Kim, J.H. 501
Kim, J.S. 685, 857
Kim, K.H. 889, 893
Kim, S.B. 749
Kim, S.H. 349, 353
Kim, S.J. 705
Kim, S.W. 701, 781, 789
Kim, W.D. 649
Kim, W.G. 693, 705
Kim, W.H. 721, 725
Kim, W.K. 645
Kim, Y.H. 717
Kim, Y.J. 605, 681, 833
Kim, Y.U. 425
Kim, Y.W. 693, 705
Klusák, J. 409
Knésl, Z. 317, 557
Koguchi, H. 573
Koh, K.T. 697
Kojima, K. 357
Kojima, M. 429
Kondo, E. 113, 161, 197
Kondo, Y. 49
Kong, W.G. 361
Kong, W.W. 285
Kong, X.W. 77
Korsunsky, A.M. 5, 517
Kossivas, F. 477
Kotoul, M. 409, 541
Koyanagi, D. 641
Kubota, R. 129
Kuhara, M. 249
Kumar, S.B. 173
Kuna, M. 569
Kwon, D.I. 889, 893
Kwon, S.T. 653, 669
Kwon, T.S. 685
Kwun, S.I. 425, 721, 725
Kyprianou, A. 477

L

Lamanna, G. 25
Lamik, A. 805
Lan, B. 297, 301
Lan, T. 361
Landolfo, R. 657
Lee, C.S. 501
Lee, H.S. 353, 605, 613, 625, 629, 633, 661, 665, 677, 681
Lee, J.A. 861
Lee, J.C. 717
Lee, J.S. 893
Lee, K.J. 353
Lee, K.K. 353
Lee, K.W. 893
Lee, M.H. 717
Lee, M.S. 861
Lee, S.H. 625
Lee, S.M. 833
Leguillon, D. 9
Leitner, H. 805
Lewis, E. 85
Li, B. 597, 753
Li, C. 177
Li, C.H. 385
Li, D. 389
Li, H. 33, 105, 413
Li, H.L. 105
Li, H.W. 77
Li, J. 421
Li, J.L. 585
Li, L. 93, 97, 145, 149, 165, 373
Li, N. 469
Li, Q.F. 33, 65, 177, 189, 385, 509, 741
Li, Q.N. 149
Li, S.J. 877

Li, X. 405
Li, X.F. 309
Li, Y. 761, 817
Li, Y.H. 89
Li, Y.T. 109, 217
Li, Z. 225, 417
Liang, W.Y. 321
Liang, Z. 809
Liao, X.L. 533, 537
Lim, S.M. 629
Ling, H. 381
Liu, C.H. 469, 493, 597
Liu, C.S. 89
Liu, E.B. 65
Liu, H.B. 265, 525
Liu, H.P. 869
Liu, J.S. 497
Liu, Q.T. 473
Liu, Y.J. 713
Liu, Z. 41
Liu, Z.F. 753
Long, Y.Q. 617
López-Crespo, P. 341, 369
Lu, C. 453, 457, 777, 801
Lu, J.S. 777
Lv, H.Q. 321

M

Ma, H.Q. 405
Ma, P. 109
Maeda, H. 357
Maeda, Y. 397
Maigefeireti, 761
Maigre, H. 245
Marsavina, L. 205
Martínez, E. 229
Marunić, G. 117
Marzani, A. 465
Matsumoto, S. 357
Matsunaga, H. 449
Meng, F.L. 89
Michal, G. 453
Minak, G. 241
Miranda, A.S. 565
Miyazono, M. 113
Mochizuki, Y. 185
Mohammadi, B. 141, 277, 821
Mohammadi, K. 393
Moon, B.C. 605
Moon, K.H. 709
Morelli, P. 237, 241
Morino, K. 161
Moriyama, S. 449, 637
Morri, A. 237
Muramoto, S. 449
Murer, S. 9

N

Nagano, T. 113
Nagawa, M. 249
Náhlík, L. 125, 317
Nakajima, M. 185, 505
Nakayama, K. 553
Nam, J.H. 193
Nam, J.P. 33
Negru, R. 205
Ni, G.Q. 361
Ning, J.G. 873
Nishida, S. 553, 829
Nishihara, H. 357
Nishimoto, M. 433
Niu, P. 253
Nobile, L. 769
Noda, N. 37, 169, 249, 513, 793
Norigoe, H. 441
Nourbakshnia, N. 401
Numata, D. 129

O

Obrtlík, K. 581
Oda, K. 793
Ogasawara, A. 249
Ogawa, Y. 433
Ogino, T. 357
Ohkawara, H. 193
Ohtsuka, N. 357
Ohzono, Y. 197
Okashita, T. 745
Okutani, K. 397
Osawa, T. 745

P

Panella, F.W. 849
Pang, B.J. 201
Pang, L. 481, 489, 493

Park, J.J. 697, 701, 781, 789
Park, N.K. 501
Park, S.W. 893
Park, W.S. 621
Patterson, E.A. 341, 369
Pei, Z.Z. 41
Peride, N. 733
Petrenec, M. 581
Pokluda, J. 49
Polák, J. 581
Portioli, F. 657
Priore, S. 549
Profant, T. 409, 541
Providakis, C.P. 561

Q

Qi, G.Y. 741
Qi, H.Y. 405
Qian, X.D. 773
Qiao, Y.J. 385
Qiu, Y.J. 297, 301
Qu, J. 21
Qu, W.L. 313

R

Ren, H.L. 413
Ren, Z.Y. 177
Rezaeepazhand, J. 365, 377, 609
Ricoeur, A. 569
Rotundo, F. 517
Rui, Z.Y. 217
Ryu, G.S. 697, 701, 789

S

Sabori, H. 377
Sadowski, T. 205
Sadr-Lahidjani, M.H. 277
Sadrmomtazi, A. 289, 337
Sagae, T. 357
Saito, K. 249
Sakamoto, Y. 637, 641
Sambogna, G. 237
Šandera, P. 49
Sannoumaru, S. 757
Sanqirgo-Rodriguez, A. 885
Schlangen, E. 69, 73, 445
Seitl, S. 557
Seo, J.W. 653
Sepehri Amin, H. 401
Šestáková, L. 125
Shamboli, M. 141
Shangguan, Z.C. 877
Shao, Y.S. 265, 525
Shi, D.Q. 405
Shi, X.H. 45
Shimamoto, A. 129, 193
Shimizu, T. 185
Shimoyama, S. 429
Shin, D.H. 721, 725
Shin, S.H. 677
Shindo, Y. 357
Shohji, I. 429, 433, 745
Shterenlikht, A. 341
Si, L.Y. 801
Sierra Beltran, M.G. 445
Silva, F.S. 565
Simatos, A. 81
Slámečka, K. 49
Smith, G.E. 1
So, K.K.L. 845
Sofuku, Y. 397
Song, H.Y. 577
Song, M. 109
Song, T.S. 389
Song, X.R. 285
Song, Z.W. 825
Soprano, A. 25, 153
Sorbello, F. 1
Sorohan, Ş. 485
Squillace, A. 849
Sun, B.T. 157, 273
Sun, B.X. 589
Sun, S.Z. 61

T

Takamatu, Y. 37
Takase, Y. 513
Takayama, K. 129
Tang, L.Q. 53, 61, 101, 329
Taniguchi, A. 573
Taniguchi, S. 357
Tarterini, F. 237
Terranova, A. 57
Tian, Q.C. 121
Tieu, A.K. 453, 457

Tieu, K.A. 801
Tohei, T. 433
Tokaji, K. 505
Tordini, F. 57
Tronskar, J.P. 173
Tsipas, D.N. 133
Tsuyunaru, M. 513

U

Uematsu, Y. 505

V

Viola, E. 465

W

Wada, Y. 761
Walsh, M.J. 5
Wang, B. 93, 97, 145, 149, 165, 373
Wang, D.Z. 381
Wang, G.P. 729
Wang, H. 597
Wang, H.B. 253
Wang, J. 65, 461, 673, 817, 881
Wang, J.S. 41, 77
Wang, Q.Y. 113, 197, 713
Wang, S. 45
Wang, W. 373, 381, 521
Wang, W.J. 869
Wang, X.N. 381, 521
Wang, X.W. 389
Wang, X.Y. 629, 633, 661
Wang, Y. 53, 101
Wang, Y.M. 89
Wang, Y.S. 221
Wang, Z.Q. 213, 321
Watanabe, H. 745
Wen, P.H. 333
Withers, P.J. 341
Woo, C.S. 649
Wu, C.C. 61
Wu, G.H. 53
Wu, J.H. 209
Wu, M.Z. 93
Wu, S.P. 469, 473, 481, 489, 493, 497, 597, 753
Wu, W.P. 221
Wu, Z.M. 233

X

Xia, T. 381
Xiao, J.Z. 825
Xiao, Y. 249, 473
Xie, L.L. 265
Xie, M. 145
Xie, T. 297, 301
Xu, M.J. 273
Xu, Q. 233
Xu, W.F. 533, 537

Y

Yan, C.F. 217
Yan, N. 161
Yan, P.L. 157
Yan, S.Y. 741
Yan, X.C. 261
Yan, Z.M. 225
Yang, G. 253
Yang, L.J. 521, 589
Yang, X.G. 405
Yang, Y. 53, 101, 105
Yang, Z.L. 157, 273
Yang, Z.M. 173
Yao, H.S. 585
Yates, J.R. 341, 369
Yeom, J.T. 501
Yin, S.N. 693, 705
Yonemaru, K. 37
Yoo, J.Y. 681
Yoon, I.S. 181, 281, 765
Yoon, S.C. 645, 653, 669
Yoon, S.H. 33, 213
Yoshimura, S. 169
Yoshizawa, K. 433
You, M. 225, 417
Yu, S. 417
Yu, X.M. 61
Yu, Z.H. 189
Yumoto, A. 249
Yun, S.Y. 677

Z

Zapatero, J. 369
Zeng, L. 93, 97
Zeng, X.G. 713, 853

Zerafatangiz, F.	337
Zhai, C.H.	525
Zhang, A.F.	253
Zhang, B.	37
Zhang, C.Z.	825, 881
Zhang, J.	45
Zhang, J.G.	309
Zhang, J.R.	461
Zhang, L.	97, 145, 149, 165, 373
Zhang, M.	553, 829
Zhang, M.Z.	461, 673, 817
Zhang, Q.A.	121
Zhang, S.Q.	585
Zhang, T.	489
Zhang, X.Q.	845
Zhang, Y.	209
Zhang, Y.Y.	257, 325
Zhao, D.	873
Zhao, D.F.	285
Zhao, G.H.	809
Zhao, M.R.	417
Zhao, Y.L.	421
Zheng, S.S.	93, 97, 145, 149, 165, 373
Zheng, X.L.	225, 417
Zhou, B.	213, 321
Zhu, G.J.	481, 493
Zhu, H.T.	457
Zhu, S.F.	189
Ziaei-Rad, S.	401
Zou, G.P.	21, 213
Zou, W.J.	313